Copyrighted Material

Methods in Cell Biology • Volume 114

Digital Microscopy

4th Edition

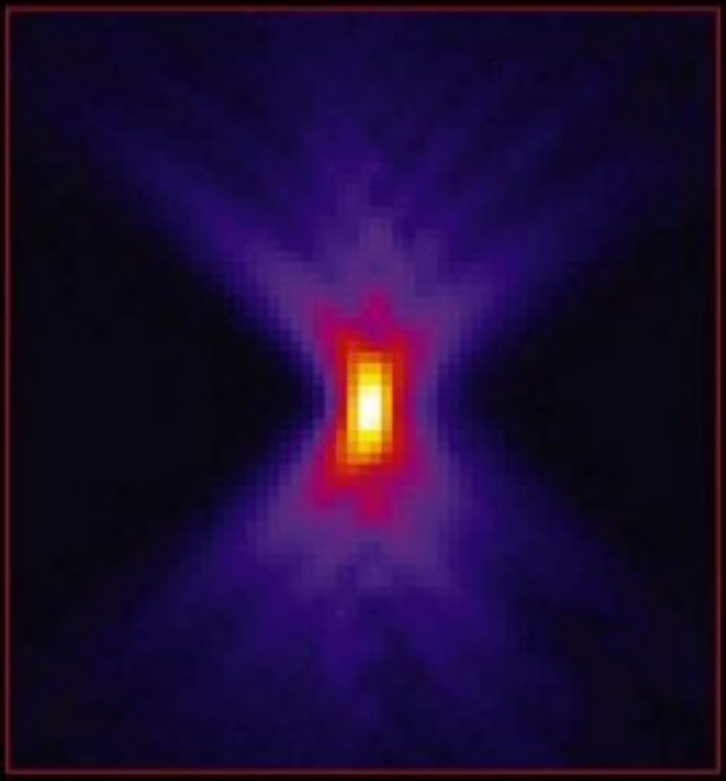

Edited by

Greenfield Sluder and David E. Wolf

Copyrighted Material

Series Editors

Leslie Wilson
Department of Molecular, Cellular and Developmental Biology
University of California
Santa Barbara, California

Paul Matsudaira
Department of Biological Sciences
National University of Singapore
Singapore

Phong Tran
Department of Cell and Developmental Biology
University of Pennsylvania
Philadelphia, Pennsylvania

Academic Press is an imprint of Elsevier
525 B Street, Suite 1800, San Diego, CA 92101-4495, USA
225 Wyman Street, Waltham, MA 02451, USA
The Boulevard, Langford Lane, Kidlington, Oxford, OX5 1GB, UK
32 Jamestown Road, London NW1 7BY, UK
Radarweg 29, PO Box 211, 1000 AE Amsterdam, The Netherlands

Copyright © 2013, 2007, 2003, 1998 Elsevier Inc. All rights reserved

No part of this publication may be reproduced, stored in a retrieval system or transmitted in any form or by any means electronic, mechanical, photocopying, recording or otherwise without the prior written permission of the publisher

Permissions may be sought directly from Elsevier's Science & Technology Rights Department in Oxford, UK: phone (+44) (0) 1865 843830; fax (+44) (0) 1865 853333; email: permissions@elsevier.com. Alternatively you can submit your request online by visiting the Elsevier web site at http://elsevier.com/locate/permissions, and selecting *Obtaining permission to use Elsevier material*

Notice
No responsibility is assumed by the publisher for any injury and/or damage to persons or property as a matter of products liability, negligence or otherwise, or from any use or operation of any methods, products, instructions or ideas contained in the material herein. Because of rapid advances in the medical sciences, in particular, independent verification of diagnoses and drug dosages should be made

ISBN: 978-0-12-407761-4
ISSN: 0091-679X

For information on all Academic Press publications visit our website at store.elsevier.com

Printed and bound in USA
13 14 15 16 11 10 9 8 7 6 5 4 3 2 1

Contributors

Keith Berland
Physics Department, Emory University, Atlanta, Georgia, USA

Kerry Bloom
Department of Biology, University of North Carolina, Chapel Hill, North Carolina, USA

Jose Javier Bravo-Cordero
Department of Anatomy and Structural Biology, and Gruss Lipper Biophotonics Center, Albert Einstein College of Medicine of Yeshiva University, Bronx, New York, USA

Dylan A. Bulseco
Sensor Technologies, LLC, Shrewsbury, Massachusetts, USA

Richard A. Cardullo
Department of Biology, The University of California Riverside, California, USA

Ching-Wei Chang
Department of Biomedical Engineering, University of Michigan, Ann Arbor, Michigan, USA

Leng-Chun Chen
Department of Biomedical Engineering, University of Michigan, Ann Arbor, Michigan, USA

Graham T. Dempsey
Department of Chemistry and Chemical Biology, Harvard University, Cambridge, Massachusetts, USA

Gabriella Ficz
Laboratory of Developmental Genetics and Imprinting, The Babraham Institute, Cambridge, United Kingdom

Todd French
Molecular Devices Corporation, Sunnyvale, California, USA

Paul C. Goodwin
GE Healthcare, Issaquah, and Department of Comparative Medicine, University of Washington, Seattle, Washington, USA

Rainer Heintzmann
Randall Division of Cell and Molecular Biophysics, King's College London, London, United Kingdom

Edward H. Hinchcliffe
Cellular Dynamics Section, Hormel Institute, University of Minnesota, Austin, Minnesota, USA

Louis Hodgson
Department of Anatomy and Structural Biology, and Gruss Lipper Biophotonics Center, Albert Einstein College of Medicine of Yeshiva University, Bronx, New York, USA

Ken Jacobson
Department of Cell and Developmental Biology, and Lineberger Comprehensive Cancer Center, University of North Carolina, Chapel Hill, North Carolina, USA

Whitney L. Johnson
Department of Biochemistry, Stanford Medical School, Stanford University, Stanford, California, USA

Alexey Khodjakov
Wadsworth Center, NYS Department of Health, Albany, and Rensselaer Polytechnic Institute, Troy, New York, USA

Noah Kolodziejski
Radiation Monitoring Devices, Watertown, Massachusetts, USA

William R. Lloyd III
Department of Biomedical Engineering, University of Michigan, Ann Arbor, Michigan, USA

Paul S. Maddox
Department of Biology, University of North Carolina, Chapel Hill, North Carolina, USA

Valentin Magidson
Wadsworth Center, NYS Department of Health, Albany, New York, USA

Veronika Miskolci
Department of Anatomy and Structural Biology, and Gruss Lipper Biophotonics Center, Albert Einstein College of Medicine of Yeshiva University, Bronx, New York, USA

Butch Moomaw
Hamamatsu Photonic Systems, Division of Hamamatsu Corporation, Bridgewater, New Jersey, USA

Yasmin Moshfegh
Department of Anatomy and Structural Biology, and Gruss Lipper Biophotonics Center, Albert Einstein College of Medicine of Yeshiva University, Bronx, New York, USA

John M. Murray
Department of Biology, Indiana University, Bloomington, Indiana, USA

Mary-Ann Mycek
Department of Biomedical Engineering, University of Michigan, Ann Arbor, Michigan, USA

Joshua J. Nordberg
Department of Cell Biology, University of Massachusetts Medical School, Worcester, Massachusetts, USA

Nathan O'Connor
Department of Physiology and Biophysics, Weill Medical College of Cornell University, New York, New York, USA

Ivan Rasnik
Physics Department, Emory University, Atlanta, Georgia, USA

Rudi Rottenfusser
Carl Zeiss Microscopy, LLC, Woods Hole, Falmouth, Massachusetts, USA

Edward D. Salmon
Department of Biology, University of North Carolina, Chapel Hill, North Carolina, USA

Champika Samarasekera
Sensor Technologies, LLC, Shrewsbury, Massachusetts, USA

Sidney L. Shaw
Biology Department, Indiana University, Bloomington, Indiana, and Department of Biology, University of North Carolina, Chapel Hill, North Carolina, USA

Randi B. Silver
Department of Physiology and Biophysics, Weill Medical College of Cornell University, New York, New York, USA

Greenfield Sluder
Department of Cell Biology, University of Massachusetts Medical School, Worcester, Massachusetts, USA

Désirée Spiering
Department of Anatomy and Structural Biology, and Gruss Lipper Biophotonics Center, Albert Einstein College of Medicine of Yeshiva University, Bronx, New York, USA

Kenneth R. Spring
Laboratory of Kidney and Electrolyte Metabolism, National Heart, Lung, and Blood Institute, National Institutes of Health, Bethesda, Maryland, USA

Aaron F. Straight
Department of Biochemistry, Stanford Medical School, Stanford University, Stanford, California, USA

Dhruv Sud
Department of Biomedical Engineering, University of Michigan, Ann Arbor, Michigan, USA

Jason R. Swedlow
Division of Gene Regulation and Expression, College of Life Sciences, University of Dundee, Dundee, Scotland, United Kingdom

Clare M. Waterman-Storer
Department of Biology, University of North Carolina, Chapel Hill, North Carolina, USA

Jennifer C. Waters
Department of Biology, University of North Carolina, Chapel Hill, North Carolina, and Department of Cell Biology, Harvard Medical School, Boston, Massachusetts, USA

David E. Wolf
Sensor Technologies, LLC, Shrewsbury, Massachusetts, USA

Elaine Yeh
Department of Biology, University of North Carolina, Chapel Hill, North Carolina, USA

Preface

Each year in May, a new class of students joins the Analytical and Quantitative Light Microscopy course at the Marine Biological Laboratory in Woods Hole, Massachusetts. For three decades, this course, started by Shinya Inoue, has played a major role in the development and implementation of modern light microscopy. Much of the material in this book derives from lectures and laboratories in this course.

The first edition of this book appeared in 1998 as "Video Microscopy," and we find it remarkable that 15 years later we are putting the final touches on the fourth edition. By the time of the second edition, in 2003, it became clear that technology trends mandated that the name be changed to "Digital Microscopy." Like all technology, light microscopy is caught up in the whirlwind of Raymond Kurzweill's singularity. That is how we got from the early microscopes of Hooke and von Leuwenhoek to the modern microscope. It used to be that microscopes were limited by the fundament resolution limit of physical optics (a subject covered in Chapter 2). One of the great scientific advances of this past year was the discovery at European Organization for Nuclear Research (CERN) of the elusive Higgs boson. In a very real sense, the Large Hadron Collider at CERN is the world's largest microscope, and its resolution is limited by the same fundamental physics as the light microscope.

However, and increasingly, in biological science, this resolution limit has been overcome by super resolution techniques (such as structured illumination, PALM, STORM, and STED) (see Chapters 22 and 24) on the one hand and confocal microscope (Chapter 18) on another. Now we routinely speak about resolution 10 times finer than the classical limit. As shown in the chapter on Tip-Enhanced Raman Spectroscopy (Chapter 26) microscopy, two more orders of magnitude finer resolution can be achieved in some instances. It is not that the laws of physical optics no longer apply, but rather that they may be used in new ways by asking different questions. Understanding these subtle points is an important element of this book. It is the old question that scientists forever deal with—namely how to think "outside the box" in imaginative ways.

Whereas early microscopy largely focused on structural issues, biologists demanded, and technologists delivered, molecular identification as well. Now it is routine to look at a single-molecule level at the distribution and dynamics of individual molecular species on the timescales of the living cell. This revolution began with immunofluorescence, was expanded by the development of a host of molecular probes (see for instance Chapter 16), and finally by the development of the family of green fluorescent proteins, covered in Chapter 5, for which Osamu Shimomura, Martin Chalfie, and Roger Y. Tsien were awarded the Nobel Prize in Chemistry in 2008.

It is easy to sigh and ask where and when will it all end? The exciting point is that it will never end and we look forward to seeing the next advances and techniques in the years to come. This takes us to the principal goal that defines both this book and the Analytical and Quantitative Light Microscopy course. We hope to impart a real

understanding of the physics and chemistry involved in modern light microscopy. So when the next great question in biology arises, our readers and students will have the tools to respond with creative new solutions.

The preparation of a book of this sort cannot be done in isolation, and many people have contributed both directly and indirectly to this volume. First, we want to recognize Zoe Kruze, Acquisitions Editor at Serials and Elsevier Insights, for her infinite patience and professionalism in dealing with us and bringing this edition along to completion. Above all, we thank our contributors for taking the time to write articles covering the basics and practical aspects of digital microscopy. Although this may be less glamorous than describing the latest and greatest aspects of their work, their efforts will provide a valuable service to the microscopy community. We also thank the members of the commercial faculty of the Analytical and Quantitative Light Microscopy course for their years of patience, inspired teaching of both students and us. Through their interaction with students, these people, principals in the video and microscopy industries, have defined how the material covered in this book is best presented for use by researchers in biology. We are grateful that some of them have taken the time from their busy schedules to write chapters for this book. The job of editing a book like this is a dubious honor, and after a season of arm twisting, we can only hope that we have as many friends at the end of the process as we had at the beginning. Our gratitude also goes out to the many individuals who have and continue to administer the educational programs at the Marine Biological Laboratory. We pray that the Marine Biological Laboratory in its new association with the University of Chicago will never lose sight of its singular role in science education. Five generations of scientists are indebted to this remarkable institution.

In recognition of the contributions of the many past students of the Analytical and Quantitative Microscopy course, the commercial faculty, the instrument manufacturers, and the academic faculty, we respectfully dedicated this volume to them all.

Greenfield Sluder
David E. Wolf

CHAPTER

Microscope Basics 1

Greenfield Sluder and Joshua J. Nordberg
Department of Cell Biology, University of Massachusetts Medical School, Worcester, Massachusetts, USA

CHAPTER OUTLINE

Introduction **2**
1.1 How Microscopes Work **2**
1.1.1 The Finite Tube-Length Microscope 2
1.1.2 Infinity Optics Microscopes 6
1.2 Objective Basics **6**
1.2.1 Types of Objectives 6
1.2.2 "Mixing and Matching" Objectives 7
1.2.3 Coverslip Selection 8
1.3 Mounting Video Cameras on the Microscope **8**
1.3.1 Basic Considerations 8
1.3.2 Empty Magnification 9
1.3.3 Camera Pixel Number and Resolution 10
Reference **10**

Abstract

This chapter provides information on how microscopes work and discusses some of the microscope issues to be considered in using a video camera on the microscope. There are two types of microscopes in use today for research in cell biology–the older finite tube-length (typically 160 mm mechanical tube length) microscopes and the infinity optics microscopes that are now produced. The objective lens forms a magnified, real image of the specimen at a specific distance from the objective known as the intermediate image plane. All objectives are designed to be used with the specimen at a defined distance from the front lens element of the objective (the working distance) so that the image formed is located at a specific location in the microscope. Infinity optics microscopes differ from the finite tube-length microscopes in that the objectives are designed to project the image of the specimen to infinity and do not, on

Methods in Cell Biology, Volume 114 **ISSN 0091-679X**
Copyright © 2003 Elsevier Inc. All rights reserved.
http://dx.doi.org/10.1016/B978-0-12-407761-4.00001-4

their own, form a real image of the specimen. Three types of objectives are in common use today–plan achromats, plan apochromats, and plan fluorite lenses. The concept of mounting video cameras on the microscope is also presented in the chapter.

INTRODUCTION

The first part of this chapter provides basic background information on how microscopes work and some of the microscope issues to be considered in using a video camera on the microscope. In this we do not intend to reiterate the material covered in the chapters by Ernst Keller on microscope alignment and by Jan Hinsch on mating cameras to the microscope; the material outlined here is intended to provide an introduction to these more detailed presentations.

1.1 HOW MICROSCOPES WORK

There are two types of microscopes in use today for research in cell biology: the older finite tube length (typically 160 mm mechanical tube length) microscopes and the infinity optics microscopes that are now produced.

1.1.1 The finite tube-length microscope

The objective lens forms a magnified, real image of the specimen at a specific distance from the objective known as the intermediate image plane (Fig. 1.1A). All objectives are designed to be used with the specimen at a defined distance from the front lens element of the objective (the working distance) so that the image formed (the intermediate image) is located at a specific location in the microscope. The working distance varies with the objective and is typically greater for lower-power objectives, but the location of the intermediate image in the microscope is fixed by design. The intermediate image is located at the front focal plane of the ocular, another sophisticated magnifying lens. Because the intermediate image is located at the focal length of the ocular, the image, now further magnified, is projected to infinity (Fig. 1.1B). The human eye takes the image projected to infinity and forms a real image on the retina. In practice, this means that one can observe the specimen as if it is at infinity and the eye is relaxed. If one makes the mistake of trying to use one's eye to accommodate for focus, eye strain and a headache are likely to occur. The combination of the objective lens and the ocular lens is shown in Fig. 1.1C; this is the basic layout of the microscope.

The photo-detecting surface of the digital or video camera must be located at the intermediate image plane or a projection of the intermediate image. Modern microscopes are designed to accept a variety of accessories and consequently have multiple light paths and relay lenses that project the intermediate image to a number of locations as outlined below and shown for an upright microscope in Fig. 1.2. In the path to the eye, the intermediate image plane is by convention located 10 mm toward the objective from the shoulder of the eyepiece tube into which the ocular is inserted. In other words, if one removes an ocular, the intermediate

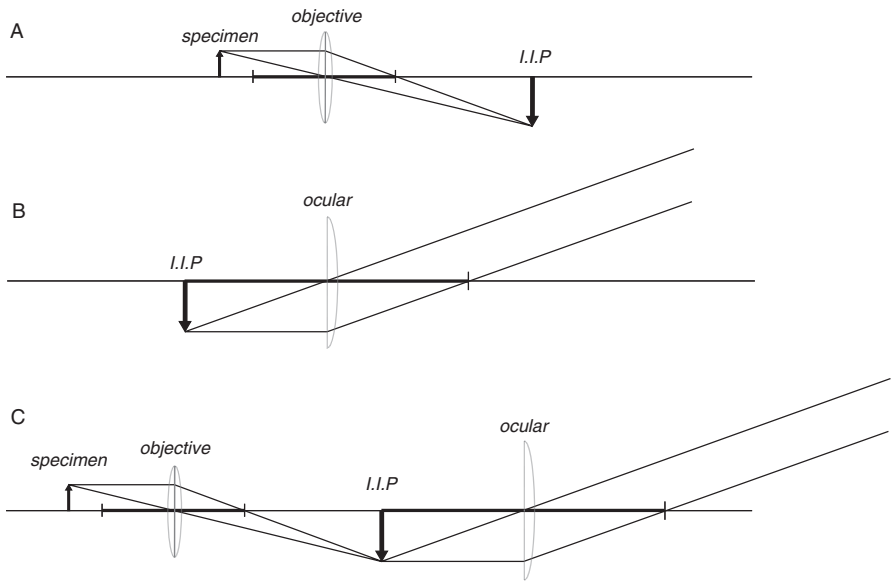

FIGURE 1.1

Geometric optics of the compound microscope of finite tube length design. (A) Objective lens. The specimen (small arrow on left) is located outside the focal length of the objective lens, and a real magnified image (large inverted arrow) is formed at the intermediate image plane (IIP). (B) Ocular lens. The image of the specimen at the IIP is located at the focal length of the ocular lens, and light from every point on the intermediate image is projected to infinity. Shown here is the ray path for the light coming from a point at the tip of the arrow image. (C) The layout of the compound microscope. The specimen is imaged at the IIP, and this image is projected to infinity by the ocular. The eye takes the light coming from the ocular and forms a real image on the retina. The dark bars along the optic axis denote the focal lengths of the lenses.

image will be 10 mm down in the tube. This holds true whether the microscope is relatively small and simple or is large with a long optical train leading to the oculars. In the latter case, the manufacturer uses relay optics to project the intermediate image to the front focal plane of the ocular. For older microscopes with a long thin camera tube on the trinocular head, the intermediate image plane is located 10 mm from the tip of the tube or shoulder into which one mounts a projection ocular that is used in conjunction with a 35-mm camera. If one has a video camera tube with a C mount thread on the trinocular head, the intermediate image plane is above the C mount at the intended position of the photo-detecting surface. For camera ports on the sides or front of inverted microscopes, the location of the intermediate image plane (or its projected image) is located at the intended location of the photo-detecting surface, be it a 35-mm film camera or a digital or video camera.

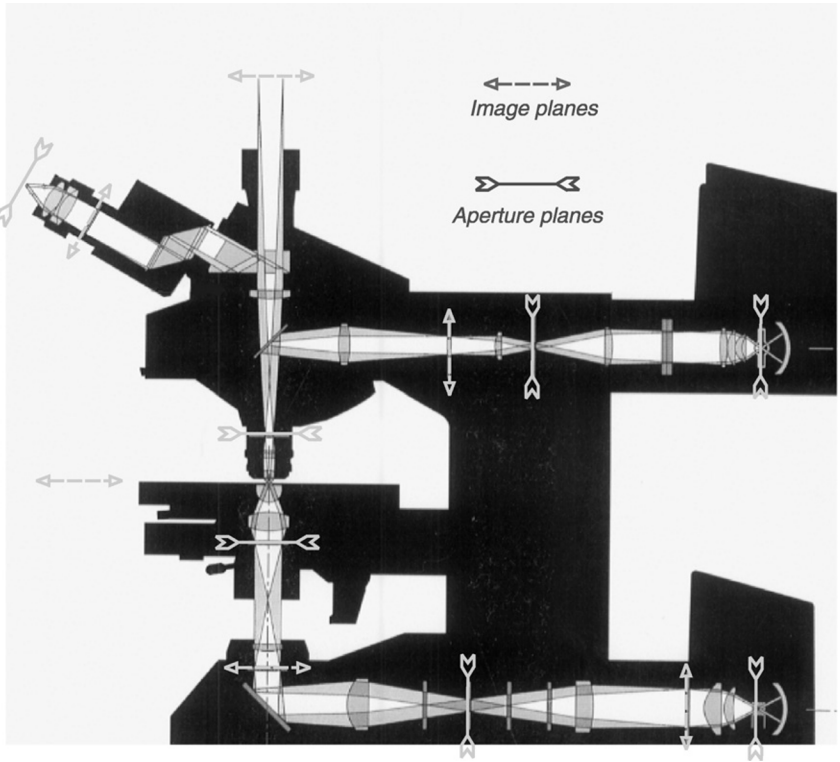

FIGURE 1.2

Diagrammatic cross section of a modern upright microscope equipped for transmitted and epi-illumination. For both the illumination and imaging pathways, the conjugate image planes are shown by the dashed arrows with outward-facing arrowheads. The conjugate aperture planes are shown by the solid arrows with inward-facing arrowheads. For this particular microscope, the photosensitive surface of the digital or video camera would be placed at the image plane located above the trinocular head. Diagram of microscope kindly provided by R. Rottenfusser of Carl Zeiss Corporation.

For research-grade microscopes that are designed to accommodate optical accessories for specialized contrast modes, such as differential interference contrast, polarization microscopy, or epifluorescence, the manufacturer puts a color-corrected negative lens (often called a "telan" lens) in the nosepiece to project the image of the specimen to infinity and adds an additional lens in the body of the microscope (the tube lens) to form a real image of the specimen at the intermediate image plane (Fig. 1.3A, upper, for a specimen point off the optical axis; and Fig. 1.3A, lower, for a point on the optical axis). This is done because these optical accessories work properly only with light projected to infinity, and additional space is needed to accommodate these optical components.

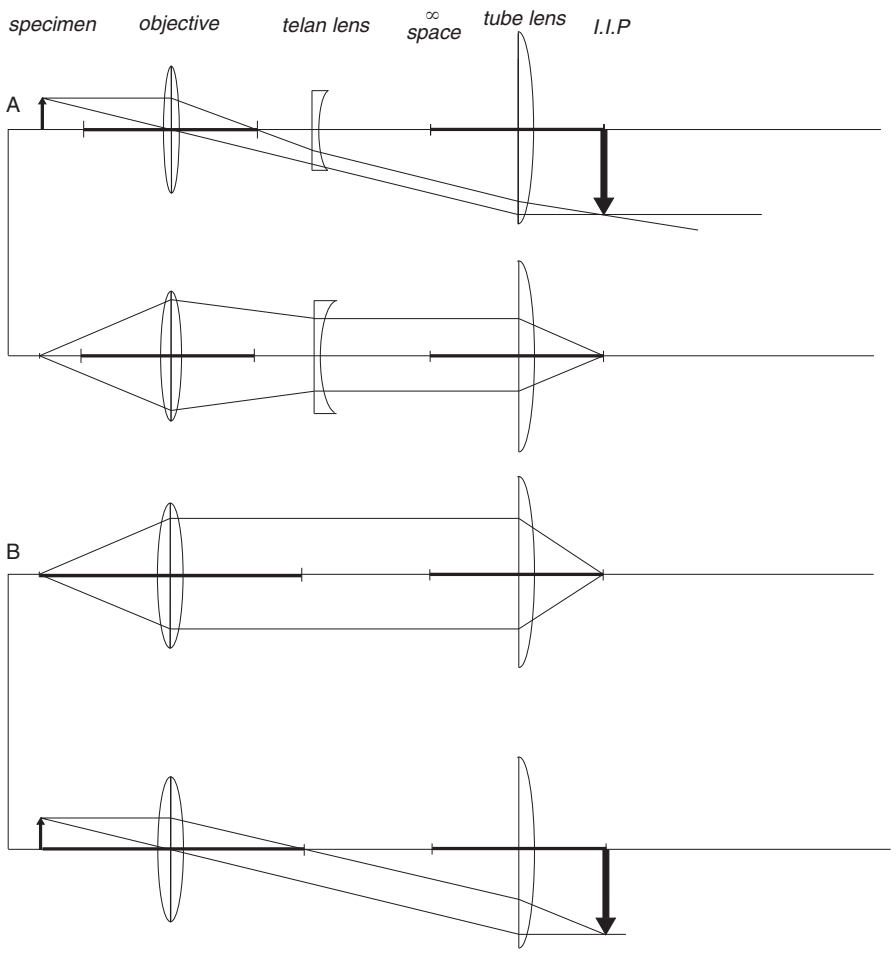

FIGURE 1.3

Comparison of the practical use of finite tube-length and infinity-corrected microscope optics. (A) Finite tube length optics. A "telan" lens (negative lens) is put in the nosepiece of the microscope to project to infinity the light coming from every point on the specimen. Further up the microscope body, the tube lens forms a real image of the specimen at the IIP. The upper diagram shows the ray paths for light coming from an off-axis point on the specimen. The lower diagram shows the same for light coming from an on-axis point on the specimen. (B) Infinity-corrected optics. The objective takes light from every point on the specimen and projects it to infinity. Farther up the microscope body, the tube lens forms a real image of the specimen at the intermediate image plane (IIP). The upper diagram shows the ray paths for light coming from an on-axis point on the specimen. The lower diagram shows the same for light coming from an off-axis point on the specimen. The dark bars along the optic axis denote the focal lengths of the lenses.

The total magnification of the specimen image is, in the simplest case, the product of the magnification of the objective and that of the ocular. If the microscope has an auxiliary magnification changer with fixed values (say 1×, 1.5×, and 2×), this magnification value must also be multiplied times the magnification of the objective and ocular. In the case of camera couplers, the magnification of the coupler (if any) should be substituted for the ocular magnification, and the size of the charge-coupled device (CCD) chip in the camera should be taken into account when calculating the magnification of the image on the monitor: The smaller the chip, the greater the magnification of the image on the monitor and the smaller the field of view (Hinsch, 1999).

1.1.2 Infinity optics microscopes

These microscopes differ from the finite tube-length microscopes in that the objectives are designed to project the image of the specimen to infinity and do not, on their own, form a real image of the specimen (Fig. 1.3B, upper, for a specimen point on axis; Fig. 1.3B, lower, for a specimen point off axis). A real image of the specimen is formed at the intermediate image plane by a tube lens mounted in the body of the microscope. By convention, the intermediate image plane is located 10 mm toward the objective from the shoulder of the tubes that hold the oculars (see Fig. 1.2). As for the finite tube-length microscopes, the intermediate image is located at the focal length of the ocular, and the specimen image is projected to infinity. In practice, the use of infinity-corrected optics means that the manufacturers do not need to put a "telan" lens in the nosepiece of the microscope to provide the "infinity space" for optical accessories for specialized contrast modes.

Because different manufacturers use tube lenses of different focal lengths and use different strategies to correct for lateral chromatic aberration of the objectives, it is no longer practical to use objectives of one manufacturer on the microscope of another even though all modern objectives are infinity corrected. In addition, Leica and Nikon no longer use the Royal Microscopical Society thread on their objectives, and consequently, other objectives will not physically fit on their microscopes.

1.2 OBJECTIVE BASICS

1.2.1 Types of objectives

Three types of objectives are in common use today: plan achromats, plan apochromats, and plan fluorite lenses. The first, plan achromats, are color corrected for two wavelengths—red (656 nm) and blue (486 nm)—and are corrected for spherical aberration in the green (546 nm). The term "plan" refers to correction for flatness of field so that a thin specimen will be in focus across the entire field not just in the center (or at the margins of the field at a different focus setting). Plan achromats have a number of good features, particularly for monochromatic applications. They cost less than other types of objectives, and they have fewer lens elements. This latter characteristic can be important for polarization and differential interference contrast microscopy, in which one

wants strain-free optics to optimize contrast. With fewer lens elements, there is often less birefringent retardation associated with the lens.

Plan apochromats are the most highly corrected objectives available. They are corrected for four wavelengths (red, green, blue, and violet 405 nm), and the chromatic aberration is relatively well corrected for other wavelengths between those that are fully corrected. These objectives are also corrected for spherical aberration at four wavelengths and have a high degree of flatfield correction. These corrections are optimized for most of the field of view, with some loss of correction at the margins of the field. These lenses are put together by hand to exacting specifications and are expensive. Great care should be used in handling them because a mechanical shock or temperature shock can irreversibly degrade their optical performance. In addition, they contain many more lens elements than achromats, and consequently, they often are not as well suited for polarization or differential interference applications as achromats in monochromatic applications. For white light or polychromatic applications, however, these lenses excel.

In regard to optical performance and cost, fluorite lenses (or semiapochromats) occupy a niche between the achromats and the apochromats. They are corrected for chromatic and spherical aberrations at three wavelengths (blue, green, and red).

It should also be mentioned that any objective, no matter how well it is designed or built, is engineered to work within a defined region of the visible spectrum. In specialized applications, such as the use of the near ultraviolet or near infrared, the optical performance of the lens may degrade substantially. Not only will the chromatic and spherical aberration corrections fail but also the transmission characteristics may suffer because the antireflection coatings are not designed to work outside a given range of wavelengths. This is also part of the reason why it is important to have an efficient infrared blocking filter in the illumination pathway when one is using transmitted light in normal applications or in fluorescence when working with red emission. If the video camera is sensitive to infrared, one may superimpose a poorly corrected infrared image on the image one is recording. For near ultraviolet and near infrared applications, one should seek objectives that are specifically designed for these specialized uses.

1.2.2 "Mixing and matching" objectives

For finite (160 mm) mechanical tube-length microscopes one can use objectives of one manufacturer on the microscopes made by others, particularly in applications where only one wavelength of light is to be used. For critical applications in which more than one illumination wavelength is used, one should bear in mind that 160-mm tube-length Olympus and Nikon objectives are "chrome free"; that is, the objective provides complete color correction for the intermediate image. Zeiss and Leica objectives are designed to be used with compensating eyepieces to correct for defined residual chromatic aberration. Mismatching objectives and oculars can produce color fringing, particularly at the margins of the field, when a specimen is observed with white light. In fluorescence microscopy, when two different wavelengths are used, one will obtain slightly different sized images at the two wavelengths. Leica objectives designed for 170-mm mechanical tube length should not be used on stands of other manufacturers if optimal image quality is desired.

It is important to note that one should not use infinity-corrected optics on finite tube-length microscopes. Infinity-corrected objectives are not designed to produce a real image; even if one can obtain an image, it will be of extremely poor quality. The only time one can use infinity-corrected objective lenses on a microscope designed for finite tube-length optics is in conjunction with specialized objective lens adapters, which are available from all the microscope manufacturers. Similarly, one should not try to use 160-mm tube-length lenses on a stand designed for infinity-corrected objectives without an adapter designed for this purpose. One can tell whether the objective in hand is designed for a finite tube-length or infinity-corrected microscope by simple inspection of the engraved numbers on the barrel of the objective. Finite tube-length objectives typically have the number 160 followed by a slash and 0.17, the thickness in millimeters of the coverslip for which the lens is designed. Infinity-corrected objectives have an infinity symbol followed by a slash and the coverslip thickness.

1.2.3 Coverslip selection

All objectives, be they finite tube length or infinity corrected, are designed to be used with number 1.5 coverglasses that are 0.17 mm thick. This holds true even for oil, glycerol, and water immersion objectives. A coverslip that is too thin or too thick will introduce spherical aberration that will noticeably degrade image contrast. For example, if one images tiny fluorescent beads with a coverslip of inappropriate thickness, there is a pronounced halo of diffuse light around each bead, and one cannot find a point at which the bead is in perfect focus. This is particularly evident with objectives with a numerical aperture greater than 0.4. The exceptions to this rule are special dipping objectives that are designed to be used without a coverslip and objectives that have a correction collar that allows the use of a range of coverslip thicknesses.

1.3 MOUNTING VIDEO CAMERAS ON THE MICROSCOPE

1.3.1 Basic considerations

Typically the video camera is mounted directly on a C mount thread without screwing an imaging lens into the camera. In such a case, the photo-detecting surface, be it a tube or a CCD chip, must be located at either the intermediate image plane or the projected image of the intermediate image plane. If the detecting surface is located at some other plane, one will notice that the focus for the specimen in the oculars will be different from the focus needed to obtain an image on the monitor. This represents more than just an inconvenience; the image quality as seen by the camera will be less than optimal, because the objective corrections are designed for an image that is projected to the design distance of the intermediate image plane. This means that one should purchase video adapter tubes that are designed to be used on the particular microscope one is using.

In addition, one should be aware that the degree of lateral chromatic correction at the intermediate image plane will depend on the objective design. For finite

tube-length microscopes, Olympus and Nikon objectives manufactured within the last 20 years provide complete color correction for the image at the intermediate image plane. Older Zeiss and Leica objectives were designed to have some residual chromatic aberration that was corrected by compensating eyepieces. This is not a practical problem when using just one wavelength of light to image a specimen, but it is a factor to consider when imaging with white light or when seeking to superimpose images taken sequentially at two wavelengths, as is often done when producing multicolor images of fluorescent specimens, using a monochrome video camera. One may find that images formed by shorter wavelengths will be slightly larger than images formed by longer wavelengths of light. To deal with this problem, one should use camera tubes (even if they are $1\times$) that have optics that compensate for lateral chromatic aberration. When using CCD cameras with $\frac{1}{3}$- or $\frac{1}{2}$-inch chips, residual lateral chromatic aberration may not be a practical problem for noncritical applications because one is imaging only the center of the field. For infinity corrected systems, the intermediate image is fully color corrected in all microscopes.

Although not commonly used, a second way to mount a camera is to use a projecting ocular to form a real image of the specimen on the detecting surface of the camera. In such cases, it is important to use a projecting ocular because a conventional ocular will not produce a real image of the specimen on the photo-detecting surface unless the camera is put at a grossly inappropriate location. If one is to use a conventional ocular, an imaging lens, such as one used to image outdoor scenes, must be mounted on the camera. The camera is put on a rail or stand close to the ocular with a light-absorbing sleeve between the ocular and the camera lens to block stray light. In such a case, the camera lens should be set at infinity so that slight changes in the distance between the ocular and the camera lens will not change the focus of the image on the photo-detecting surface. This is a practical concern when one is using a microscope in which the whole head moves when one changes focus.

1.3.2 Empty magnification

For higher numerical aperture lenses, the resolution provided by the objective at the intermediate image plane is often higher than the resolution provided by the photo-detecting surface. That is, the detector undersamples the image, and consequently, the image on the monitor or the image recorded digitally on the hard drive of a computer is limited by the pixel spacing of the camera, not the optical resolution of the objective. Thus, it is often of great importance to introduce additional magnification or "empty magnification" to the image formed on the photo-detecting surface. This is normally done with the auxiliary magnification wheel found on most modern microscopes or magnification in the phototube that holds the camera. The extent of empty magnification needed depends on the resolution or magnification of the objective lens and the physical pixel dimensions of the camera. To fully capture the resolution provided by the objective, the camera should oversample the image so that the most closely spaced line pair imaged by the objective will be separated by at least one and preferably two rows of unstimulated detector pixels. However, in introducing empty

magnification, one should bear in mind that increases in magnification will reduce image intensity per unit area by a factor of the magnification squared and reduce the field of view.

1.3.3 Camera pixel number and resolution

It is tempting to think that cameras with large pixel arrays (say 1000 × 1000) will produce higher-resolution images than cameras with smaller pixel arrays (say 500 × 500). This is not strictly true, because empty magnification can always be used with a small-pixel array camera to capture the full resolution offered by the objective lens. The advantage of larger-array cameras is that one can image a larger field at a magnification that matches camera pixel spacing with the objective resolution. Put another way, at a given specimen field size, the larger-array cameras will capture an image with greater resolution.

Reference

Hinsch, J. (1999). Mating cameras to microscopes. *Methods in Cell Biology*, *56*, 147–152.

CHAPTER

The Optics of Microscope Image Formation

2

David E. Wolf
Sensor Technologies, LLC, Shrewsbury, Massachusetts, USA

CHAPTER OUTLINE

Introduction **12**
2.1 Physical Optics: The Superposition of Waves **13**
2.2 Huygens' Principle **14**
2.3 Young's Experiment: Two-Slit Interference **15**
2.4 Diffraction from a Single Slit **18**
2.5 The Airy Disk and the Issue of Microscope Resolution **19**
2.6 Fourier or Reciprocal Space: The Concept of Spatial Frequencies **23**
2.7 Resolution of the Microscope **28**
2.8 Resolution and Contrast **30**
Conclusions **31**
2.9 Appendix A **31**
2.9.1 Fourier Series 31
2.10 Appendix B **35**
2.10.1 Kirchoff's Scalar Theory of Diffraction: Recasting Huygens' principle in an Electrodynamic Context 35
2.10.2 Generalizing the Problem 36
2.10.3 Scalar Spherical Waves 36
2.10.4 Green's Theorem 37
2.10.5 Solution for a Plane 37
2.10.6 Huygens' Principle 39
2.11 Appendix C **39**
2.11.1 Diffraction by a Circular Aperture from Which the Airy Disk Comes 39
Acknowledgments **42**
References **42**

Methods in Cell Biology, Volume 114 **ISSN 0091-679X**
Copyright © 2007 Elsevier Inc. All rights reserved.
http://dx.doi.org/10.1016/B978-0-12-407761-4.00002-6

Abstract

Although geometric optics gives a good understanding of how the microscope works, it fails in one critical area, which is explaining the origin of microscope resolution. To accomplish this, one must consider the microscope from the viewpoint of physical optics. This chapter describes the theory of the microscope-relating resolution to the highest spatial frequency that a microscope can collect. The chapter illustrates how Huygens' principle or construction can be used to explain the propagation of a plane wave. It is shown that this limit increases with increasing numerical aperture (NA). As a corollary to this, resolution increases with decreasing wavelength because of how NA depends on wavelength. The resolution is higher for blue light than red light. Resolution is dependent on contrast, and the higher the contrast, the higher the resolution. This last point relates to issues of signal-to-noise and dynamic range. The use of video and new digital cameras has necessitated redefining classical limits such as those of Rayleigh's criterion.

The nature of light is a subject of no material importance to the concerns of life or to the practice of the arts, but it is in many other respects extremely interesting.

(Thomas Young[1], 1773–1829)

(M. Shamos, 1987)

INTRODUCTION

Although geometric optics gives us a good understanding of how the microscope works, it fails in one critical area: explaining the origin of microscope resolution. Why is it that one objective will resolve a structure whereas another will not? This is the question we will examine in this chapter. To accomplish this, we must consider the microscope from the viewpoint of physical optics. Useful further references are

[1]There is a coincidental connection between the lives of Jean Baptiste Fourier and Thomas Young that transcends optics. In 1798, Fourier joined Napoleon's army during the invasion of Egypt. Word of the French Expeditionary Force had reached Admiral Nelson, who unsuccessfully chased the French fleet across the Mediterranean. On August 1, his luck changed. The French fleet was anchored in a wide crescent at the bay at Aboukir, 37-km east of Alexandria. Secure on their shoreward side, the French had moved all of their cannons to the seaward side. At 5:40 PM, Nelson began the assault. British men-of-war Goliath and Zealous managed to wedge their way between the French and the shore. It was a bold move that led to the destruction of the French fleet and stranded the French Expeditionary Force in Egypt, among them Fourier (www.discovery.ca/napoleon/battle.cfm). The French Expeditionary Force is perhaps most famous for its discovery in 1799 by Dhautpol and Pierre-Francois Bouchard of the Rosetta stone near the town of Rosetta in the Nile delta. Translation of the Rosetta stone represented one of the great intellectual challenges of time and, similar to the work of Young and Fourier in physics and mathematics, respectively, it expanded humanity's worldview. Thomas Young was a brilliant linguist and was the first to recognize that some of the hieroglyphics on the Rosetta stone were alphabetic characters. Young's work was the critical starting point that ultimately enabled Jean Francois Champollion to complete the translation of the Rosetta stone (www.rosetta.com/RosettaStone.html).

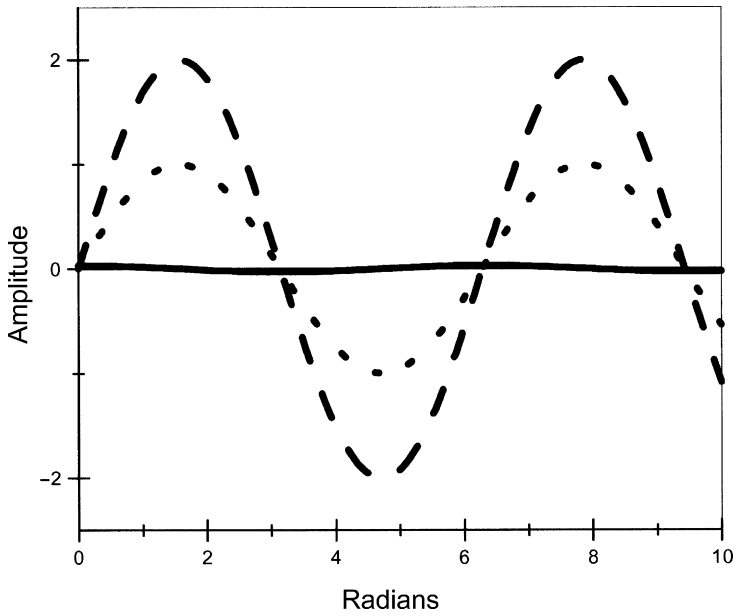

FIGURE 2.1

Superposition of sine waves: *dotted line*, $\sin(x)$; *dashed line*, the condition of constructive interference $\sin(x) + \sin(2\pi + \phi)$; *solid line*, the condition of destructive interference $\sin(x) + \sin(x + \pi - \phi)$ where $\phi \ll 1$.

Inoué & Spring, 1997; Jenkins & White, 1957; Sommerfeld, 1949a; Born & Wolf, 1980 for the optics of microscope image formation.

2.1 PHYSICAL OPTICS: THE SUPERPOSITION OF WAVES

Let us consider a simple type of wave, namely, a sine or cosine wave, such as that illustrated in Fig. 2.1. Mathematically, the equation of the wave shown in Fig. 2.1 (dotted line) is

$$y(t) = y_0 \sin(\omega t). \tag{2.1}$$

Here, we are considering the abstract concept of a wave in general. However, a clear example of a wave is the light wave. Light is a wave in both space and time. The equation for its electric field vector, E, takes the form

$$E(x, t) = E_0 \sin(kx - \omega t), \tag{2.2}$$

where ω (the frequency in radians per second) is related to the frequency of the light, v, by the relation $\omega = 2\pi v$; k is the wave number, which is related to the wavelength, λ, by the relation $k = 2\pi/\lambda = 2\pi v/c$, where c is the speed of light; and E_0 is the amplitude. In

Appendix A, we show that Eq. (2.2) represents the unique solution of the wave equation, which governs optics. Two additional points are worth mentioning here: First, that the intensity of light is the square of the electric field vector; second, that the spatial and temporal components of the light wave can be separated. As a result, you can view light as being a spatial sine or cosine wave moving through space with time.

Now let us suppose that we have two simultaneous waves with the same frequency,

$$y(t) = y_0 \sin(\omega t) + y_1 \sin(\omega t + \phi), \tag{2.3}$$

but that are phase-shifted with respect to one another with a phase shift ϕ. The composite wave is determined by pointwise addition of the individual waves, a principle known as the superposition theorem. When the two waves are completely in phase (i.e., $\phi = 0$), we have the condition of constructive interference shown in Fig. 2.1 (dashed line). When the two waves are 180° out of phase, we have the condition of destructive interference shown in Fig. 2.1 (solid line).

This can be most readily shown by adopting the exponential form of the wave. In general, a complex number can be expressed in one of two ways, the right- and left-hand sides of Eq. (2.4):

$$e^{i\theta} = \cos\theta + i \sin\theta. \tag{2.4}$$

Thus, our sine wave may be expressed as

$$\begin{aligned} E(x,t) &= E_0 \,\mathbf{Re}\{e^{-i(kx-\omega t)}\}, \\ E(x,t) &= E_0 \,\mathbf{Re}\{e^{-ikx} e^{+i\omega t}\}, \end{aligned} \tag{2.5}$$

where **Re** stands for "the real part of."

2.2 HUYGENS' PRINCIPLE

In 1678, the Dutch physicist Christiaan Huygens (1629–1695) evolved a theory of wave propagation that remains useful in understanding such phenomena as reflection, refraction, interference, and diffraction. Huygens' principle is that:

> *All points on a wave front act as point sources for the production of spherical wavelets. At a later time the composite wave front is the surface which is tangential to all of these wavelets.*
>
> **(Halliday & Resnick, 1970)**

In Fig. 2.2, we illustrate how Huygens' principle or construction can be used to explain the propagation of a plane wave. We have chosen this example because it seems otherwise counterintuitive that one can construct a plane out of a set of finite radius spheres.

Expressed in this way, Huygens' principle is an empirical construct that will not explain all aspects and phenomena of light. Clearly, a complete description requires the application of James Clerk Maxwell's (1831–1879) wave equation and the

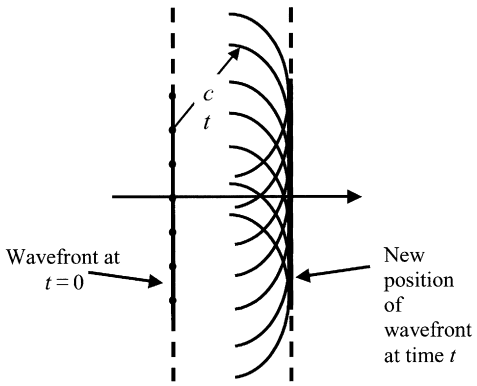

FIGURE 2.2

Huygens' construct illustrating how a plane wave front at time $t = 0$ propagates as a plane wave front at time t.

boundary conditions of his electromagnetic theory. In Appendix A, we demonstrate that Eq. (2.2) is, indeed, a solution to Maxwell's wave equation. Gustav Kirchoff (1824–1887) has developed a more robust form of Huygens' principle that incorporates electromagnetic theory. In Appendix B, we develop the rudiments of Kirchoff's approach. Subsequently, in Appendix C, we use Kirchoff's solution to develop a mathematical treatment of the Airy disk. The reader is referred to Sommerfeld (1868–1951) (Sommerfeld et al., 1949) for an excellent description of diffraction theory.

2.3 YOUNG'S EXPERIMENT: TWO-SLIT INTERFERENCE

One usually sees Huygens' principle described using the quotation above. In practice, however, it is more often applied by considering a wave surface and then asking what the field will be on at some point, P, away from the surface. The composite field will be given by the sum of spherical wavelets reaching this point at a given time. Because the distances between points on the surface and point P vary, it must be the case that for them to arrive simultaneously, they must have been generated at different points in the past. In this context, Huygens' principle is really an expression of the superposition theorem.

This was the approach taken by Thomas Young (1773–1829) in 1801 in explaining interference phenomena (Young, 1801). Young's now classic experiments demonstrated the fundamental wave nature of light and brought Young into conflict with Sir Isaac Newton (1643–1727) and his Corpuscular Theory of Light. Young's experiment is illustrated in Fig. 2.3. Young used a slit at A to convert sunlight to a coherent spherical wave (Huygens' wavelet). Two slits are symmetrically positioned on B relative to the slit at A. Huygens' wavelets propagate from the two slits and will,

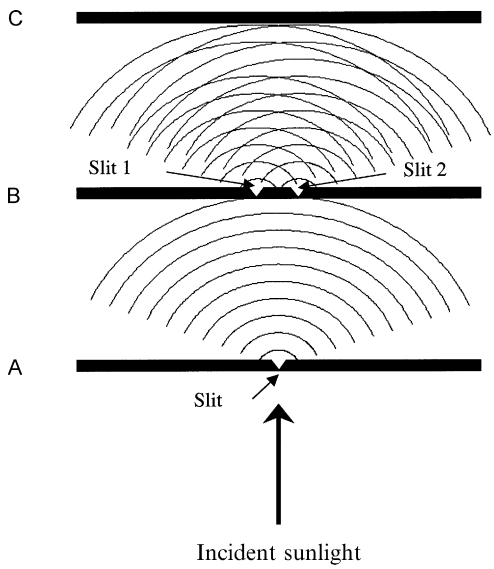

FIGURE 2.3

Young's double-slit experiment in terms of Huygens' construct.

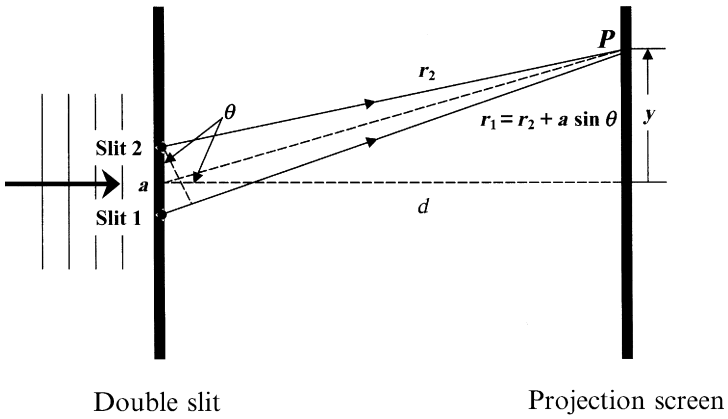

FIGURE 2.4

Young's double-slit experiment showing the source of the phase shift geometrically.

at various points, constructively and destructively interfere with one another. Figure 2.4 considers some arbitrary point P, a distance y from the center of the surface C, which is a distance D from B. If the distance between the slits is d, the path length difference between the two wavelets at P will be $d \sin(\theta)$ and intensity maxima caused by constructive interference will occur when

$$d \sin(\theta) = m\lambda, \tag{2.6}$$

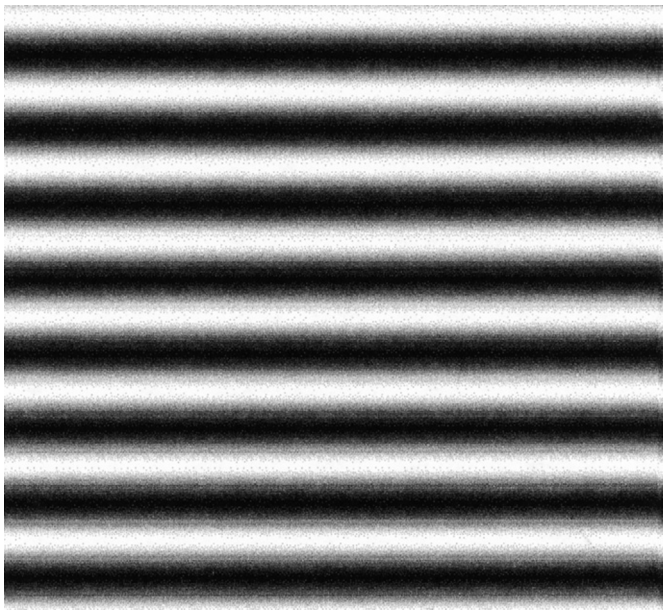

FIGURE 2.5

Young's double-slit interference pattern.

where $m = 0, 1, 2, 3$, and so forth. The pattern that Young saw is shown in Fig. 2.5 and is referred to as the double-slit interference pattern. One clearly observes the alternating intensity maxima and minima. The maxima correspond to the angles θ given by Eq. (2.4).

It is worthwhile to examine this problem more closely and to determine the actual intensity profile of the pattern in Fig. 2.5. Huygens' principle promises us that it derives from the superposition theorem. If the time-dependent wave from slit 2 is $E_2 = E_0 \sin \omega t$ and the wave from the slit 1 is $E_1 = E_0 \sin(\omega t + \phi)$, then the time-dependent wave at point P is:

$$E = E_1 + E_2 = E_0(\sin \omega t + \sin [\omega t + \phi]), \tag{2.7}$$

where again $\phi = a \sin \theta$. Eq. (2.5) may be algebraically manipulated as follows:

$$\begin{aligned} E &= E_0(\sin \omega t + \sin \omega t \cos \phi + \cos \omega t \sin \phi) \\ &= E_0(\sin \omega t\,(1 + \cos \phi) + \cos \omega t \sin \phi). \end{aligned} \tag{2.8}$$

The intensity is given by E^2, therefore,

$$I = E_0^2(\sin^2 \omega t(1 + \cos \phi)^2 + \cos^2 \omega t \sin^2 \phi + 2 \sin \omega t \cos \omega t \sin \phi[1 + \cos \phi]). \tag{2.9}$$

What we observe physically is the time-averaged intensity, I_{AV}. Recalling that the time average of $\sin^2\omega t$ and $\cos^2\omega t$ is 1/2 whereas that of $2\sin\omega t\cos\omega t = \sin 2\omega t = 0$, we obtain

$$I_{AV} = \frac{E_0^2}{2}\left([1+\cos\phi]^2 + \sin^2\phi\right) \tag{2.10}$$

$$\begin{aligned} I_{AV} &= \frac{E_0^2}{2}\left(1 + 2\cos\phi + \cos^2\phi + \sin^2\phi\right) \\ &= E_0^2(1+\cos\phi) \\ &= 2E_0^2\cos^2\frac{\phi}{2}. \end{aligned} \tag{2.11}$$

Considering Fig. 2.4, because the angle θ is small,

$$\phi = a\sin\theta \simeq a\tan\theta = \frac{ay}{d}, \tag{2.12}$$

and therefore,

$$I_{AV} = 2E_0^2\cos^2\left(\frac{ay}{2d}\right). \tag{2.13}$$

In deriving Eq. (2.11), we have ignored the $1/r^2$ falloff of intensity. To allow for this, one would have to replace E in Eq. (2.5) by E/r. That is, we assume a spherical rather than a plane wave. This, of course, causes the intensity of the bands to fall off with increasing y.

In this derivation, one sees the fundamental application of the superposition theorem to derive the composite wave. In this case, the application is relatively straightforward as the wave at P is the superposition of only two waves. In other cases, such as the single-slit diffraction example that follows, the composite is a superposition of an infinite number of waves, and the summation becomes an integration. In Appendix B, we consider Kirchoff's generalization of this problem to a scalar theory of diffraction.

2.4 DIFFRACTION FROM A SINGLE SLIT

The double-slit interference experiment is an example of Huygens' principle of superposition where we have only two generating sites. A related interference phenomenon is that of single-slit diffraction, which is illustrated in Fig. 2.6. Here, we envision a plane wave impinging on a narrow slit of width a. We imagine the slit divided into infinitesimally narrow slits separated by distance dx, each of which acts as a site that generates a Huygens' wavelet. Two neighboring wavelets generate parallel wavelets. A lens collects these wavelets and brings them to a focus at the focal plane. We consider two wavelets from neighboring regions of the slit, which ultimately converge on point P of the focal plane. The path difference will be $dx\sin(\theta)$. Calculation of the resulting interference pattern referred to as single-slit

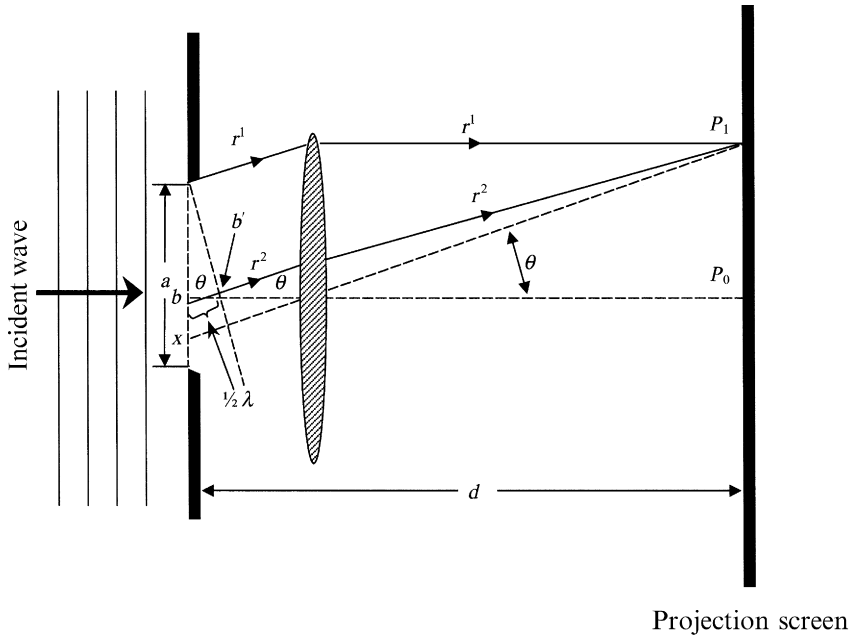

FIGURE 2.6

The single-slit experiment showing the source of the phase shifts geometrically.

Fraunhoffer (we define in the appendixes what we mean by Fraunhoffer diffraction) diffraction requires summing or integrating over the entire surface of the slit and is illustrated in Fig. 2.7. Effectively, the single slit acts as an infinite set of slits. Indeed, you are probably more familiar with diffraction produced by a grating, which is an infinite set of equally spaced slits separated by some fixed distance.

2.5 THE AIRY DISK AND THE ISSUE OF MICROSCOPE RESOLUTION

We are now in a position to turn our attention to how interference affects microscope images: How does a microscope treat a point source of light? You might ask, why do we care? We care because ultimately all objects can be represented as the sum of an infinite set of point sources. If we know how the microscope treats (distorts, if you will) a point object, we know how it treats any object. This is the concept of the point spread function because a point of light is confused or spread out by both the optical and the electronic systems of the digital or video microscope system. We will encounter this concept progressively throughout this volume. This spreading is an example of what mathematicians refer to as convolution. In Chapter 9 by Salmon et al., this volume, we will be introduced to the concept of convolution.

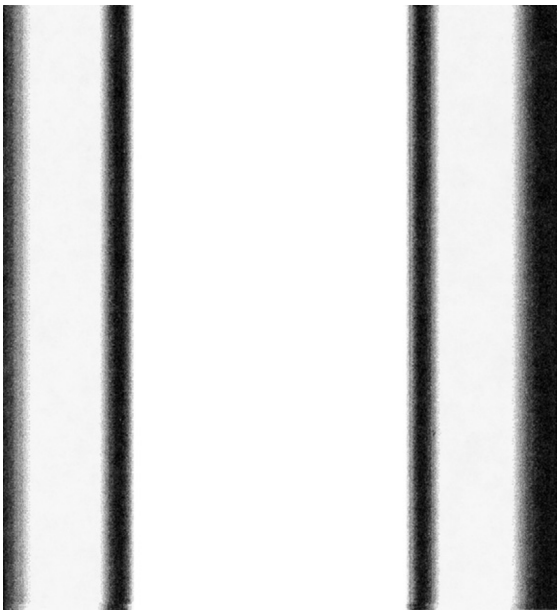

FIGURE 2.7

The single-slit diffraction pattern.

Unfortunately, the reverse process, which we might refer to as deconvolution, is not mathematically trivial. Later in this chapter, we will introduce the concept of Fourier series and transforms, both as an introduction to the idea of spatial frequencies and to provide the mathematical tools necessary to understand deconvolution. The concept of deconvolution using Fourier transforms will finally be considered in Chapter 16 by Salmon and Tran, this volume; and Chapter 14 by Wolf et al., this volume.

In Fig. 2.8, we illustrate how a microscope views a point source of light. One expects from consideration of geometric optics that a point of light at A will be focused by the objective to a point on the image plane. However, Huygens teaches us that the two points on the wave front act as generation sites for Huygens' wavelets. Although most of the light goes to the center point on the image plane, where it constructively interferes to produce a bright spot, some of it also goes to other points. At the second point shown in the figure, the two waves will be phase-shifted. The result is an interference pattern on the image plane. Rather than focusing the point source to a spot, the actual image shown in Fig. 2.9 is known as the Airy disk, after George Biddell Airy (1801–1892). The ability of the microscope to resolve two spots as two ultimately relates to how sharply the Airy disks are defined (Fig. 2.10). For self-luminous point sources, such as the ones obtained in fluorescence microscopy, the Airy disks are independent and do not interfere with one another.

An empirical criterion for resolution for such self-luminous objects that is related to the separation where the primary maximum of the second Airy disk coincides with the primary minimum of the first is

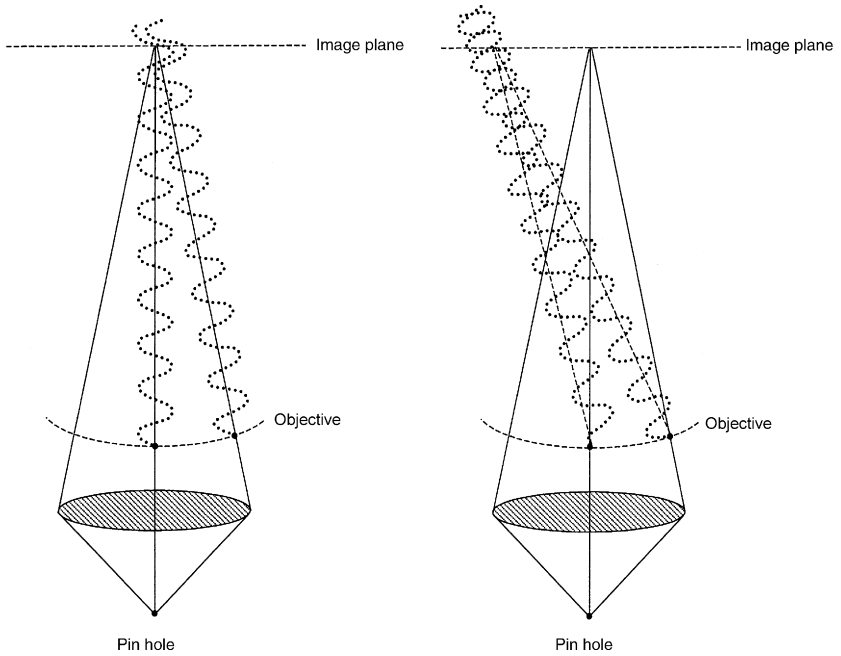

FIGURE 2.8

A point of light viewed in the microscope showing how interference leads to the Airy disk pattern.

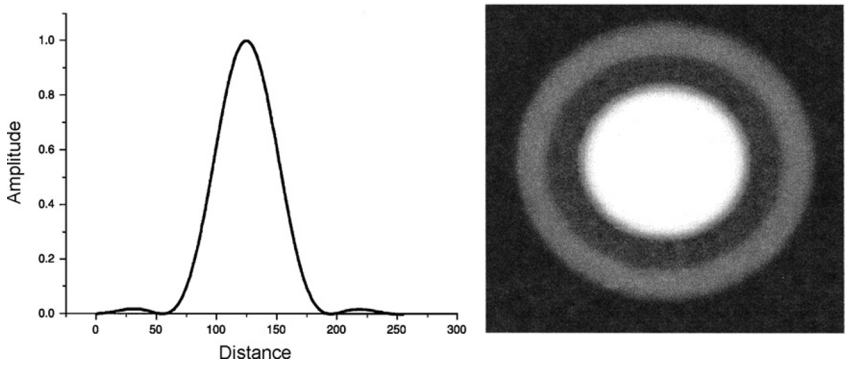

FIGURE 2.9

The Airy disk: Notice how the intensity of the secondary ring is only about 2% of the intensity of the primary maximum. The ability to see this ring in the microscope offers an empirical test of noise rejection in the microscope.

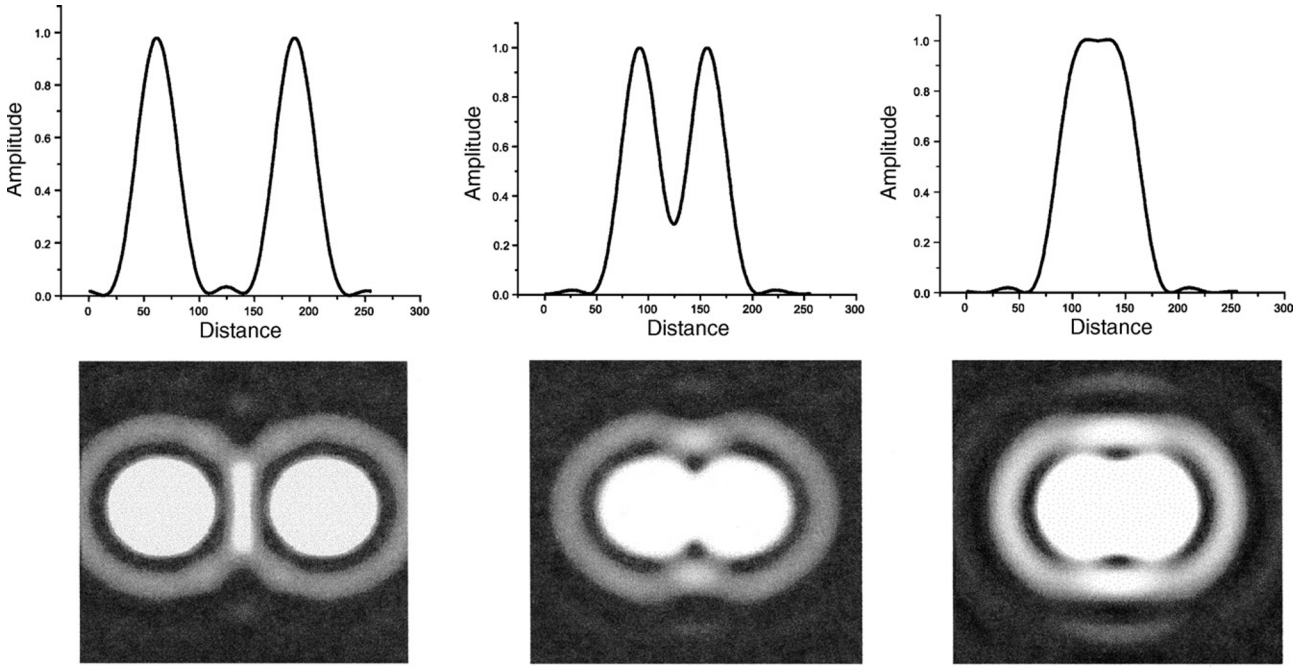

FIGURE 2.10

Defining resolutions as the ability to distinguish two Airy disks: as the disks come closer, the intensity dip between them becomes smaller. Resolution definitions such as Rayleigh's criteria set are based on the ability of the human eye to detect this dip. Other criteria may be more appropriate for digital systems.

$$r = \frac{1.22\lambda_0}{2\mathrm{NA}_{\mathrm{obj}}} \tag{2.14}$$

and is known as Rayleigh's criterion. The NA (numerical aperture) of an objective is related to the collection angle θ and is given by

$$\mathrm{NA} = n\sin(\theta), \tag{2.15}$$

where n is the index of refraction. For bright field images, the point sources will be partially coherent, and the resolution will also be dependent on the NA of the condenser. Thus, for bright field point sources, resolution is given by

$$r = \frac{1.22\lambda_0}{\mathrm{NA}_{\mathrm{obj}} + \mathrm{NA}_{\mathrm{cond}}}. \tag{2.16}$$

In a modern context, it is important to recognize that Rayleigh's criterion is empirical and ultimately based on the human eye's ability to resolve intensity differences. It asks the question, or more accurately, states the answer to the question, what is the minimum intensity dip between the two maxima required for the human eye to resolve them as two Airy disks? With modern image detectors and image processing, it is possible to push these limits. We will explore this issue further in subsequent chapters.

On deeper consideration of Fig. 2.8, the reader may be tempted to cry foul. There is a point at which the spherical wavelets emitted from the two points destructively interfere, but what about wavelets from all of the other generating centers between these points? In reality, we must consider and superimpose all of the wavelets to generate the composite field at any point P. In Appendix B, we will discuss Kirchoff's approach to this problem, and in Appendix C, we will apply the approach to the problem of the Airy disk.

2.6 FOURIER OR RECIPROCAL SPACE: THE CONCEPT OF SPATIAL FREQUENCIES

The issue of resolution also relates to the amount of contrast (the difference between light and dark) and the sharpness of edges. To understand these questions, we must take a detour into what may at first appear to be a strictly mathematical domain. This is the concept of Fourier, or reciprocal, space. This concept is fundamental to understanding the optics of microscope image formation.

We must begin with the concept of a spatial frequency. Consider, for instance, the picture in Fig. 2.11A. When we look at this (or any) scene, our first inclination is to say that the sizes of the objects are random. On closer examination, we realize that this is not really the case. Every scene has certain characteristic spacings in it. We have drawn some of these characteristic frequencies as sine^2 waves over the figure. Mathematically, these spacings are referred to as spatial frequencies (more accurately, we might refer to spatial wavelengths, L, and define the spatial frequencies as $2\pi/L$). In every scene, certain spatial frequencies dominate over others. This

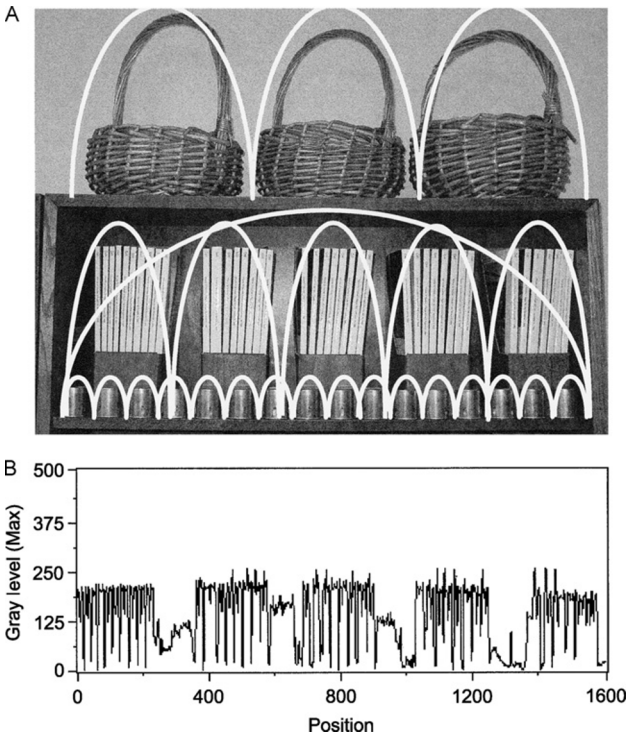

FIGURE 2.11

(A) Every object or image has characteristic spatial frequencies. (B) A line scan across the books in Fig. 2.11.

concept may seem very abstract at first. When you think about it, one point that you will probably recognize is that fine detail is described by high spatial frequencies. So in some sense, the highest spatial frequency, which we can detect, must be related to the resolution limit of our optical system. If you take a magnifying glass and examine Fig. 2.11A closely, you will see dots. What this tells us is that there is a cutoff, a highest spatial frequency, beyond which the printer did not need to go to accurately portray the photograph. This is very clear in digital photography. When you look at a high-resolution digital photograph, it is nice and sharp; as you zoom in, however, you will eventually see the pixels. The maximum spatial frequency used in the photograph is 2π divided by the interpixel distance.

One might think that although light waves can be represented by sine waves, or more accurately a sum of sine waves, this might not be the case for all waves. Let us phrase this differently: Can we put this abstract concept of spatial frequencies into a coherent mathematical context? To approach this problem, let us simplify it a bit. Suppose that rather than dealing with the two-dimensional image of Fig. 2.11A, we scan one horizontal line across this image and look at the intensity as a function of position. Such a line is shown in Fig. 2.11B. Again, the information is not random. We can clearly see characteristic spatial frequencies.

Jean-Baptiste Fourier (1768–1830), in the early nineteenth century, demonstrated the remarkable fact that any wave or function could be described as a sum of sine waves (actually, sine + cosine waves). Rather than work with the scan of Fig. 2.11B, let us consider a simpler but more challenging pattern, namely, that of a step function, as illustrated below in Fig. 2.12A—a step function that is an

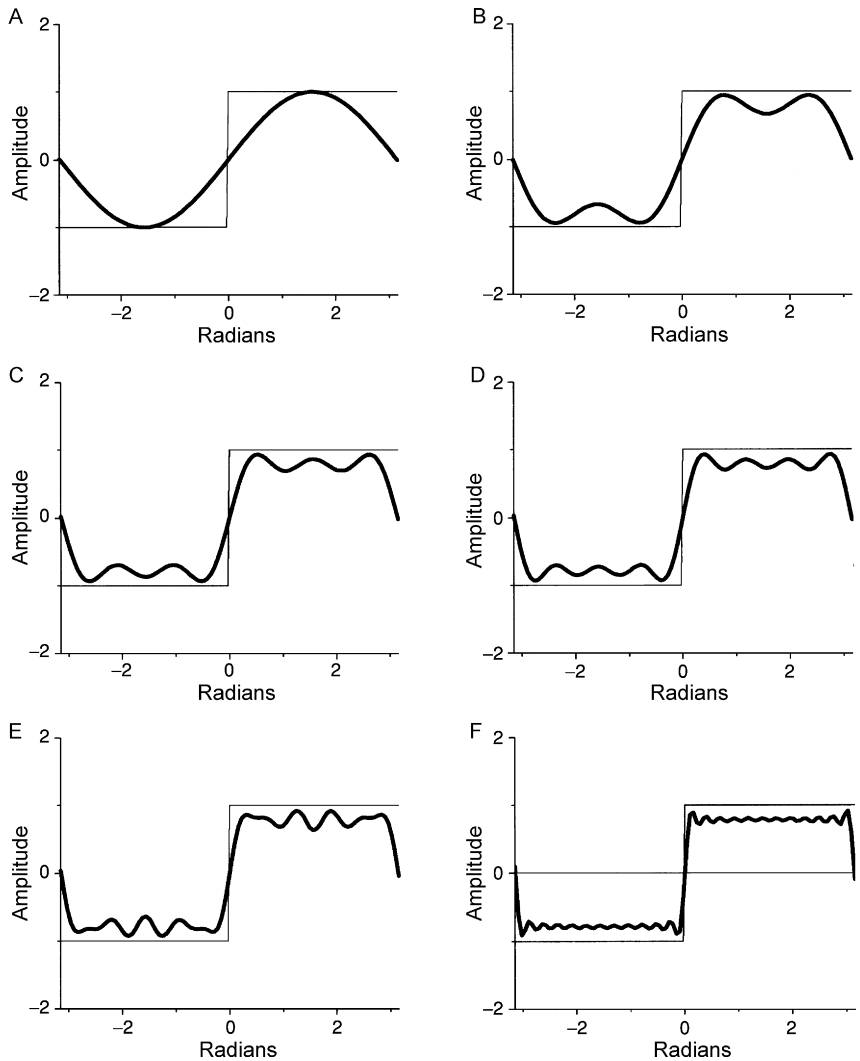

FIGURE 2.12

Fourier's construction of a step from a composite of sine waves: (A) sin x, (B) sin $x + 1/3$ sin $3x$, (C) sin $x + 1/3$ sin $3x + 1/5$ sin $5x$, (D) sin $x + 1/3$ sin $3x + 1/5$ sin $5x + 1/7$ sin $7x$, (E) sin $x + 1/3$ sin $3x + 1/5$ sin $5x + 1/7$ sin $7x + 1/9$ sin $9x$, and (F) up to the term $1/23$ sin $23x$. Notice that even in (F) there is ringing of the intensity pattern.

alternating pattern of white and black bands. One might think that nothing is farther from a sine wave.

However, think about it a little more closely. If we draw a sine wave with the same spacing, it approximates the step function (Fig. 2.12A). This is the lowest spatial frequency, $2\pi/L$. We next try to fill in the gaps by adding some amount of a sine wave with spatial frequency $3(2\pi/L)$ (Fig. 2.12B). As one successively adds sine waves of shorter and shorter wavelength [spatial frequencies $m(2\pi/L)$, where m is odd] (Fig. 2.12C–F) in the appropriate proportions, the resulting sum looks more and more like a step function. To achieve perfect match, one has to use an infinite number of sine waves. However, as the amplitudes of the waves decrease rapidly and monotonically, any given degree of approximation can be achieved with a finite number of sine functions. It is significant to note that when one cuts off the summation at a finite number of sine waves, the resultant wave shows oscillations or "ringing," which is most apparent at the edge of the step (Fig. 2.12F). As we will see, the optical ringing at the edges of objects in the light microscope is caused by incomplete reconstruction of Fourier series. Indeed, microscopes always act as low-pass filters with some maximum spatial frequency making it through, and as we shall see, is the basis of resolution in the microscope.

In Fig. 2.13, we show the amplitudes of the spatial frequencies of the step function. Such a plot is referred to as the Fourier transform of the original function. Note that in the case of the step function, the function is not continuous but rather discrete.

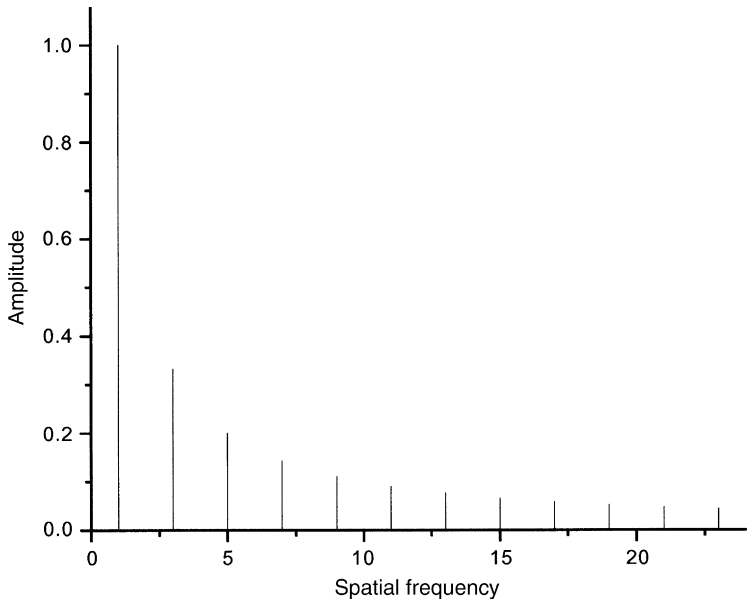

FIGURE 2.13

The amplitudes of the frequency terms: this is the so-called Fourier transform of the step function.

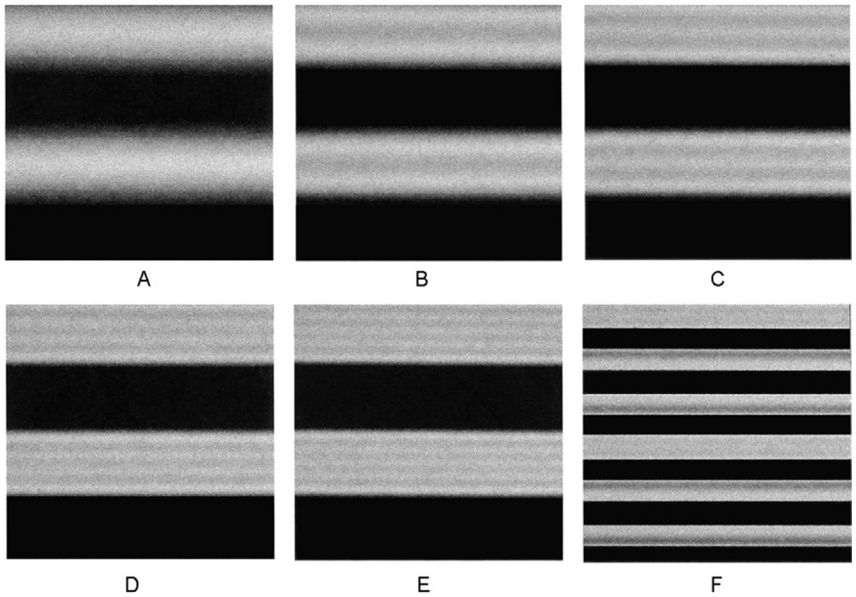

FIGURE 2.14

The Fourier series of Fig. 2.13 shown as an image; (A–E) correspond to Fig. 2.13. In (F), we have removed the sin *x* term, which causes a doubling of the frequency pattern.

That is, only those spatial frequencies that are odd numbers have nonzero amplitude. In fact, for a spatial frequency m, the amplitude is $1/m$.

In Fig. 2.14, we use the Fourier series to recreate the step function as an image. In Fig. 2.14A, we have generated an image with a sinusoidally varying intensity. We can get a sense of the bars of the step function, but the edges are very fuzzy. In Fig. 2.14B–E, we progressively add the sin $3\times$, sin $5\times$, sin $7\times$, and sin $9\times$ terms. With the addition of each higher-order spatial frequency, the edges become more and more distinct. However, in each case we can see ringing at the edges because we lack higher order terms.

Next we ask the question, what will happen if we eliminate the first term in the series? This is shown in Fig. 2.14F. What happens is that we now have a perfectly reasonable looking step function, only its bars are now twice as close as before.

In this discussion, we have considered a one-dimensional Fourier series. One can also perform Fourier transforms on two-dimensional patterns (i.e., images) or even three-dimensional patterns such as a z-stack of images. In Appendix A, we develop the mathematics of Fourier series and transforms. Reducing a wave to a Fourier series is derived, following Carl Friedrich Gauss (1777–1855), as being essentially equivalent to a problem in nonlinear least squares curve fitting: the solution of the step function is derived explicitly, the integral form is developed, and finally, the application of Fourier transforms to solving the wave equation of electrodynamics and optics is discussed.

2.7 RESOLUTION OF THE MICROSCOPE

Physical systems such as microscopes tend to pass only a certain set of spatial frequencies. In a sense, the highest frequency passed becomes a measure of resolution. An object such as diffraction grating, which is essentially the step wave shown in Fig. 2.14, requires all spatial frequencies to see it correctly. How a microscope treats such an object is illustrated in Fig. 2.15. When the grating is illuminated with a bundle of planar light, say at the center, the zeroth-order undiffracted light propagates straight through as one bundle, whereas higher orders are diffracted and propagate as parallel bundles at appropriate angles. Because all of these bundles are parallel, they will be focused by the objective at the back focal plane, with higher orders appropriately displaced from the center. A Fourier transform of the image forms at the

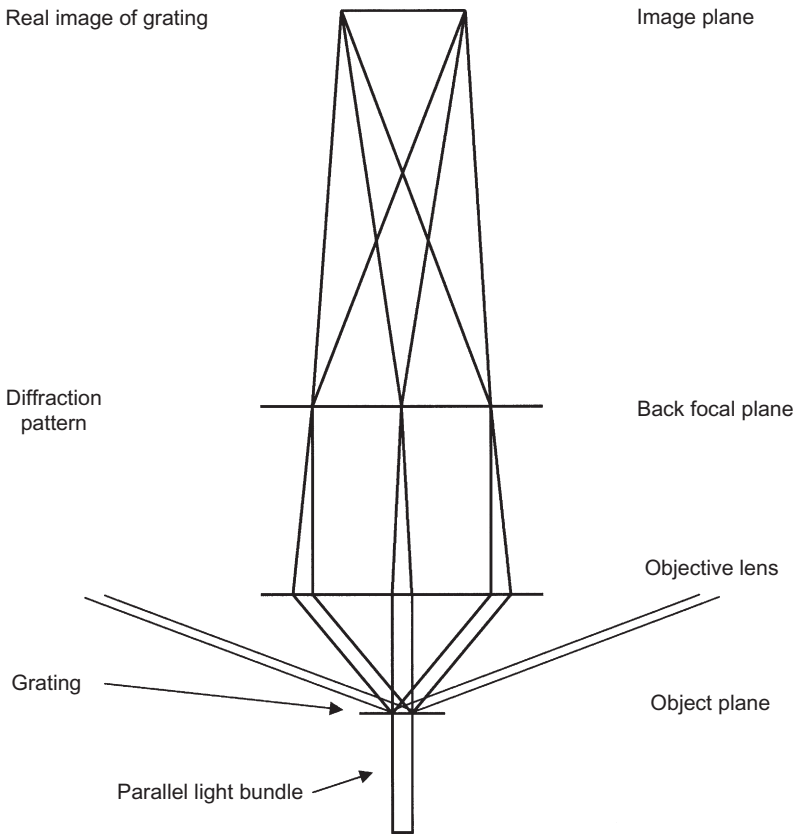

FIGURE 2.15

In the microscope, the resolution limit results from the microscope's inability to collect all spatial frequencies. Objects act as diffraction gratings and Fourier transform of the object forms at the back focal plane.

back focal plane. These bundles recombine at the image plane to form a real image of the diffraction grating. You can see the problem immediately: Not all of the orders will make it through the objective. There is a cutoff and higher orders fail to enter the objective. The larger the collection angle (the NA) of the objective, the higher the cutoff and the higher the resolution. So far, we have discussed what is going on at the center of the object. The situation becomes more complex as one moves away from the center. The cutoff frequency on the two sides becomes asymmetric. The resolution limit is effectively defined by the highest spatial frequency that enters the objective.

In Fig. 2.16, we image the back focal plane for Fourier transform of biological specimens. We have chosen specimens with some well-defined structure.

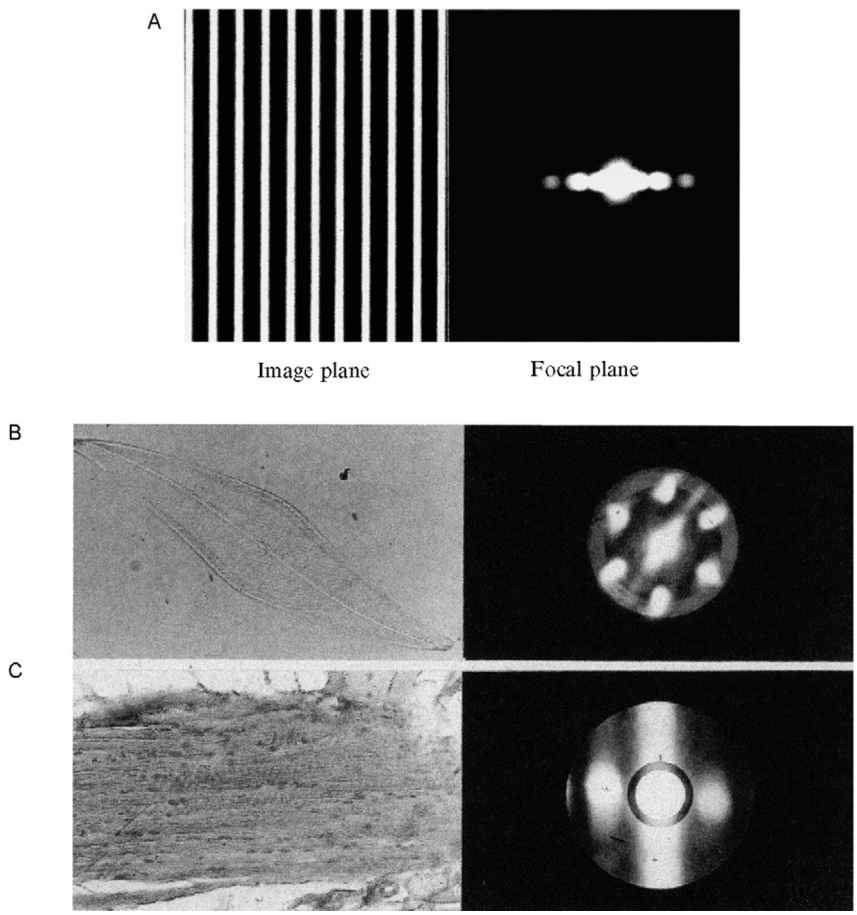

FIGURE 2.16

Fourier patterns at the back focal plane of the objective for: (A) a Ronchi ruling, (B) a diatom, and (C) a muscle fiber. Courtesy of Greenfield Sluder.

Figure 2.16A shows a diatom and Fig. 2.16B a muscle section. For comparison, we also show the specimens viewed in the image plane.

2.8 RESOLUTION AND CONTRAST

We have previously seen how resolution can be defined in terms of our ability to distinguish between two Airy disks. As the disks come closer and closer, which corresponds to trying a higher and higher spatial frequency, the contrast between the two disks decreases. The resolution limit is reached when the contrast between the two points becomes sufficiently small such that they can no longer be distinguished as two separate points. We see that image contrast and resolution become highly intertwined factors. This is illustrated in Fig. 2.17, where sine waves of increasing spatial frequency (left to right) and increasing contrast (bottom to top) are displayed as an image; the higher the contrast, the higher the detectable spatial frequency. In Fig. 2.18, we show this same fact for hypothetical microscope

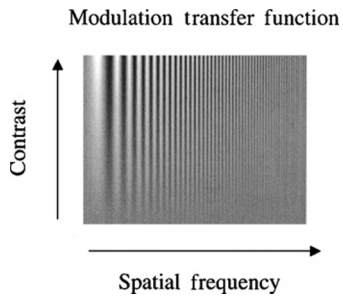

FIGURE 2.17

Increasing contrast increases resolution (the highest detectable spatial resolution).

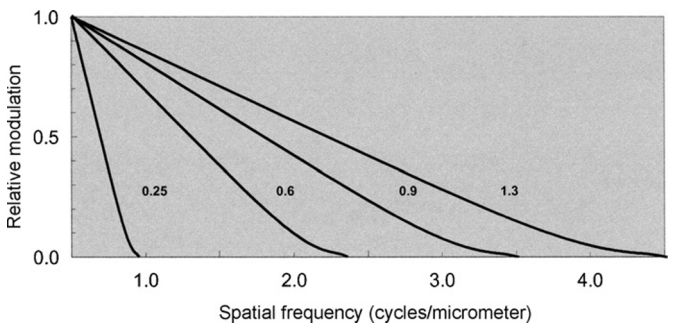

FIGURE 2.18

The relationship between contrast (relative modulation) and resolution (highest discernable spatial frequency) for objectives with NA = 0.25, 0.6, 0.9, and 1.3.

objectives. Resolution (highest collected spatial frequency) clearly increases with increasing NA. However, for a given objective, the greater the contrast, the greater the resolution becomes.

CONCLUSIONS

In this chapter, we have described Abbe's theory of the microscope-relating resolution to the highest spatial frequency that a microscope can collect. We have shown that this limit increases with increasing NA. As a corollary to this, resolution increases with decreasing wavelength because of how NA depends on wavelength. The resolution is higher for blue light than for red light. Finally, we see that resolution is dependent on contrast and that the higher the contrast, the higher the resolution.

Ultimately, this last point relates to issues of signal-to-noise and dynamic range. The use of video and new digital cameras has necessitated redefining classical limits such as those of Rayleigh's criterion. In subsequent chapters, we will further explore these critical issues.

2.9 APPENDIX A

2.9.1 Fourier series

In this chapter, we indicated that a light wave could be represented by the equation

$$E(x_1 t) = E_0 \mathrm{e}^{-i(kx-\omega t)}. \tag{2.A1}$$

One might ask, where this comes from? We know that the mathematical form of the wave must satisfy Maxwell's wave equation, and we can, indeed, show that it is a solution of this equation. Yet we may still ask to what extent is it the only solution? It was considerations such as these that led to the development of Fourier series and transforms. At the end of this appendix we will see why. We begin by exploring briefly the concept of the Fourier series and their importance in optics. For a more extensive discussion, the reader is referred to the elegant treatment by Arnold Sommerfeld in his book *Partial Differential Equations in Physics* (Sommerfeld, Sommerfeld, 1949b).

Suppose that one has an arbitrary function, a wave form, $f(x)$, which is defined over the interval of $-\pi$ to π (by suitable rescaling, any interval $-L/2$ to $L/2$ can be redefined to meet this criterion). We next suppose that this function can be approximated by a function $S_n(x)$, which is the sum of a series of n sine waves and n cosine waves with coefficients A_m and B_m plus a constant A_0. That is,

$$S_n(x) = A_0 + \sum_{m=1}^{n} \{A_m \sin(mx) + B_m \cos(mx)\}. \tag{2.A2}$$

The problem, then, is to determine the $2n+1$ coefficients, A_m and B_m, that define the $S_n(x)$. This problem is equivalent to the problem of fitting experimental data to a curve or mathematical function. As in the curve-fitting problem, we recognize that for every value of x, there is a deviation or difference $\delta(x)$ between the approximation $S_n(x)$ and the function $f(x)$. That is,

$$f(x) = S_n(x) + \delta(x). \tag{2.A3}$$

The goal is to minimize the sum of the squares of the deviations over the entire interval $-\pi$ to π. That is, we seek to minimize χ^2, where

$$\chi^2 = \frac{1}{2\pi}\int_{-\pi}^{+\pi} \delta_n^2(x)\mathrm{d}x. \tag{2.A4}$$

Minimization requires that all of the partial derivatives of χ^2 with respect to the A_m's and the B_m's be simultaneously equal to 0. For an arbitrary value of m, we have that,

$$\begin{aligned} -\frac{\partial\chi^2}{\partial A_m^2} &= \frac{1}{\pi}\int_{-\pi}^{+\pi}\{f(x) - S_n(x)\}\cos(mx)\mathrm{d}x = 0 \quad \text{and} \\ -\frac{\partial\chi^2}{\partial B_m^2} &= \frac{1}{\pi}\int_{-\pi}^{+\pi}\{f(x) - S_n(x)\}\sin(mx)\mathrm{d}x = 0. \end{aligned} \tag{2.A5}$$

One can then solve Eq. (2.A5) for the $2n+1$ coefficients by putting Eq. (2.A2) into Eq. (2.A5) and making use of the orthogonal properties of the sine and cosine functions, namely, that:

$$\frac{1}{\pi}\int_{-\pi}^{+\pi}\cos(px)\sin(qx)\mathrm{d}x = 0 \quad \text{for (all values of } p \text{ and } q), \tag{2.A6a}$$

$$\begin{aligned} \frac{1}{\pi}\int_{-\pi}^{+\pi}\cos(px)\cos(qx)\mathrm{d}x &= 0 \quad \text{for} \quad p \neq q, \\ &= 1 \quad \text{for} \quad p = q, \end{aligned} \tag{2.A6b}$$

$$\begin{aligned} \frac{1}{\pi}\int_{-\pi}^{+\pi}\sin(px)\sin(qx)\mathrm{d}x &= 0 \quad \text{for} \quad p \neq q, \\ &= 1 \quad \text{for} \quad p = q. \end{aligned} \tag{2.A6c}$$

Substituting the conditions of Eq. (2.A6) as well as the trivial condition that

$$\frac{1}{2\pi}\int_{-\pi}^{+\pi}\mathrm{d}x = 1, \tag{2.A7}$$

we find that

$$A_m = \frac{1}{\pi}\int_{-\pi}^{+\pi} f(x)\cos(mx)\mathrm{d}x, \tag{2.A8a}$$

$$B_m = \frac{1}{\pi}\int_{-\pi}^{+\pi} f(x)\sin(mx)\mathrm{d}x, \tag{2.A8b}$$

$$A_0 = \frac{1}{2\pi}\int_{-\pi}^{+\pi} f(x)\mathrm{d}x. \tag{2.A8c}$$

The $2n+1$ coefficients can be determined by means of Eq. (2.A8).

A rigorous mathematical treatment must demonstrate three critical points: that as $n \to \infty$, then χ^2, indeed $\delta(x)$ for all values of x, goes to 0; that a solution exists; and that the solution is unique. Here, we will refer the reader to Sommerfeld et al., 1949 on these three points and go on to examine the problem of the step function.

The step function is given by

$$\begin{aligned} f(x) &= -1 \qquad \text{for} \quad -\pi < x < 0 \\ f(x) &= +1 \qquad \text{for} \quad 0 < x < +\pi. \end{aligned} \tag{2.A9}$$

Before applying Eqs. (2.A7) and (2.A8), we recognize that as we are centering the step function around a DC level of 0 then $A_0 = 0$. Furthermore, we recognize that as the function must have a node at $-\pi$, 0, and $+\pi$, the function is a series in sines with odd coefficients, m. This last condition means that all of the B_m's equal 0 and the A_m's equal 0 where m is even. Inserting Eq. (2.A9) into Eq. (2.A8a) gives us the Fourier series for the step function, namely,

$$f(x) = \sum_{m=0}^{\infty}\left(\frac{1}{2m+1}\right)\sin[(2m+1)x]. \tag{2.A10}$$

Related to the Fourier series is the concept of the Fourier transform. The function in real space is described by $f(x)$. We alternatively speak of the function being described in frequency or reciprocal space. This frequency space description is referred to as the Fourier transform, $\mathfrak{J}(\nu) = \mathfrak{J}\{f(x)\}$, of the function. For the step functions, $\mathfrak{J}(\nu) = 0$ except for $\nu = 2m+1$, where $\mathfrak{J}(\nu) = 1/(2m+1)$ and m is an integer. For completeness we also speak of the inverse Fourier transform $\mathfrak{J}^{-1}$. This leads to the trivial identity that

$$\mathfrak{J}^{-1}[\mathfrak{J}\{f(x)\}] = f(x). \tag{2.A11}$$

The requirement that the function have nodes at $-\pi$, 0, and $+\pi$, or more generally, the requirement that the function is defined over a finite interval with specific boundary values, leads to series like that of Eq. (2.A9) wherein the series contains only a subset of all possible sine waves defined by the eigenvalues m. In the more general case, all possible sine and cosine waves represent possibilities, and the summation in the equation is replaced by an integral. In such cases, it is more convenient to use the exponential form of the wave, e^{ikx}. The connection between this representation and the sine/cosine representation has already been discussed in the text of the chapter and is contained in the trigonometric identities

$$\sin(kx) = \frac{\mathrm{e}^{ikx} - \mathrm{e}^{-ikx}}{2i}, \tag{2.A12a}$$

$$\cos(kx) = \frac{e^{ikx} + e^{-ikx}}{2i}. \tag{2.A12b}$$

We may then define the Fourier transform of the function $f(x)$ as

$$\Im(v) = \frac{1}{\sqrt{2\pi}} \int_{-\infty}^{+\infty} f(x) e^{-ivx} dx, \tag{2.A13a}$$

and the inverse Fourier transform by

$$\Im^{-1}(x) = \frac{1}{\sqrt{2\pi}} \int_{-\infty}^{+\infty} \Im(v) e^{ivx} dv. \tag{2.A13b}$$

We have here derived the concept of Fourier series and Fourier transforms as a means of introducing the fact that the diffraction pattern is the Fourier transform of the object and that the diffraction pattern may be observed at the back focal plane of the microscope objective. As the reader will see in subsequent chapters (i.e., Chapter 9 by Salmon et al., this volume; Chapter 16 by Salmon and Tran, this volume; and Chapter 14 by Wolf et al., this volume), the Fourier transform becomes a powerful tool in digital deconvolution techniques to remove out-of-focus fluorescence. Ultimately, this results from the fact that the Fourier transform of the object is the diffraction pattern observed at the back focal plane of the objective. Indeed, some laboratories have created Fourier filters of the image not by digital transformation but by physically masking specific frequencies at the back focal plane (Hui & Parsons, 1975).

Fourier transforms also are very powerful tools for solving partial differential equations such as the wave equations. Let us suppose, as an example, that we have an electromagnetic wave, which is propagating in the x-direction and polarized so that it is confined to the z-direction. Then we can write the wave equation for the electric field as:

$$\frac{\partial^2 E}{\partial t^2} = c^2 \frac{\partial^2 E}{\partial z^2}. \tag{2.A14}$$

We next Fourier transform both sides of Eq. (2.A14). If we reverse the order of integration and differentiation, we obtain

$$\frac{d^2 \Im(E)}{dt^2} = -v^2 c^2 \Im(E). \tag{2.A15}$$

Note that this is a simple rather than a partial differential equation. We can then write,

$$\Im(E) = \Im_0(E) e^{-ivct}. \tag{2.A16}$$

All that remains to be done to determine E is to inverse Fourier transform Eq. (2.A14). Let us assume that $E(x) = E_0 e^{ikx}$. Fourier has already taught us that this is not a big assumption, as even if it is not true, it will be the case that the wave can be represented as a sum or distribution of terms $E_0 e^{ikx}$. Then the Fourier transform is determined by putting Eq. (2.A11) into Eq. (2.A14):

$$\mathfrak{J}(E) = E_0 e^{-ivct} \frac{1}{\sqrt{2\pi}} \int_{-\infty}^{+\infty} e^{i(k-v)x} dx. \tag{2.A17}$$

The integral Eq. (2.A17) is the Dirac Delta Function given by

$$\delta(k-v) = \frac{1}{\sqrt{2\pi}} \int_{-\infty}^{+\infty} e^{i(k-v)x} dx, \tag{2.A18}$$

then

$$\mathfrak{J}(E) = E_0 e^{-ivct} \delta(k-v). \tag{2.A19}$$

The critical property of the Dirac Delta Function is that it is 0 for all values of s except for $s = k$, where the function has the value of 1.

We next inverse Fourier transform Eq. (2.A19)

$$E = E_0 \int e^{-i(vct-vx)} \delta(k-v) dv. \tag{2.A20}$$

The properties of the Dirac Delta Function lead us to

$$E = E_0 e^{i(kx-kct)}, \tag{2.A21}$$

remembering that

$$k = \frac{2\pi}{\lambda} = \frac{2\pi\upsilon}{c} = \frac{\omega}{c}. \tag{2.A22}$$

We obtain

$$E = E_0 e^{i(kx-\omega t)}. \tag{2.A23}$$

We have now come full circle. We have shown that e^{ikx} is a solution to the spatial part of the wave equation. We have further shown that any solution can be represented as a Fourier sum or distribution of such solutions. Finally, we have used the Fourier transform to demonstrate that given the form e^{ikx} of the spatial dependence, e^{-iwt} must be the solution of the temporal dependence.

2.10 APPENDIX B

2.10.1 Kirchoff's scalar theory of diffraction: Recasting Huygens' principle in an electrodynamic context

Our goal in this appendix is to describe Kirchoff's formulation of Huygens' principle in terms of electrodynamic field theory. Here we will follow the derivation of Sommerfeld in his book *Optics, Lectures on Theoretical Physics* (Sommerfeld et al., 1949). We present an outline of the theory, and the reader is referred to the original for more details. Other texts with excellent discussions of this problem and the problem of the diffraction pattern from a circular aperture are *An Introduction to Fourier Optics* (Goodman, 1968) and *Electrodynamics* (Jackson, 1975). The latter is particularly

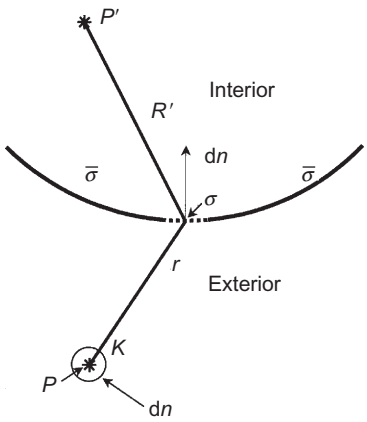

FIGURE 2.A.1

The generalized condition of an opaque surface $\bar{\sigma}$ with an aperture σ.

valuable as it treats the full vectorial solution rather than the scalar approximation. The reader is further referred to *Principles of Optics* (Born & Wolf, 1980).

2.10.2 Generalizing the problem

Figure 2.A.1 represents a generalized view of diffraction problems. We have a point P and a surface. The surface consists of an opaque region, $\bar{\sigma}$, and an aperture region, σ. The basic question is how the field at P relates to the field in the aperture, σ.

For mathematical purposes, we define an exterior and an interior to the surface and we create a second infinitesimally small spherical surface K around the point P. This serves to isolate the singularity at P and to create a closed surface for purposes of investigation. In the figure, dn represents the normal to the surface at any point r.

2.10.3 Scalar spherical waves

In this chapter, we have dealt with plane waves of the form e^{ikx}, which depend only on the coordinate x. Here we must deal with a scalar spherical wave, which depends only on the radial value r. Such waves must, in general, be solutions of the equation

$$\frac{1}{r}\cdot\frac{\partial^2(ru)}{\partial r^2}+k^2u=0. \tag{2.B1}$$

Equation (2.B1) is the wave equation in spherical coordinates assuming spherical symmetry, that is, no angular dependence.

The so-called principal solution of Eq. (2.B1) has the form

$$u=\frac{1}{r}e^{ikr}. \tag{2.B2}$$

2.10.4 Green's theorem

Here we need to integrate over the surface σ to find our solution. This is accomplished using Green's function, G, to find the solution, which we call v_p for the field at P. In general, Green's theorem tells us that

$$\int \left\{ G\frac{1}{r}\left(\frac{\mathrm{d}^2 rv}{\mathrm{d}r^2}\right) - v\frac{1}{r}\times\frac{\mathrm{d}^2 rG}{\mathrm{d}r^2}\right\}\mathrm{d}\tau = \int \left(G\frac{\partial v}{\partial n} - v\frac{\partial G}{\partial n}\right)\mathrm{d}\sigma, \tag{2.B3}$$

where $\mathrm{d}\tau$ represents the volume element within the surface and $\mathrm{d}\sigma$ represents the surface element.

The use of $G = u$ leads to contradictions because of the requirement that $v = 0$ and $\partial v/\partial n = 0$ everywhere on the surface $\overline{\sigma}$. Instead, we define G by the conditions that

$$\frac{1}{r}\times\frac{\partial^2 rG}{\partial r} + k^2 G = 0 \quad \text{within the volume,} \tag{2.B4a}$$

$$G = 0 \ \text{ on } \ \sigma, \tag{2.B4b}$$

$$G \to u \ \text{ as } \ r \to 0, \tag{2.B4c}$$

$$r\left(\frac{\partial G}{\partial n} - ikG\right) \to 0 \ \text{ as } \ r \to \infty. \tag{2.B4d}$$

It is Eq. (2.B4d) that enables the boundary conditions on v without contradiction. If we define the volume as the exterior exclusive of the volume surrounding P by K, then the left-hand side of Eq. (2.B3) vanishes. Integration of the right-hand side over K leads to $-4\pi v_p$. Thus, Eq. (2.B3) reduces to

$$4\pi v_p = \int_\sigma \left\{\frac{\partial v}{\partial n}G - v\frac{\partial G}{\partial n}\right\}\mathrm{d}\sigma. \tag{2.B5}$$

Applying the condition $\partial v/\partial n = 0$ on σ, Eq. (2.B5) becomes

$$4\pi v_p = \int_\sigma -v\frac{\partial G}{\partial n}\delta\sigma. \tag{2.B6}$$

The boundary conditions on v are

$$v = 0 \ \text{ on } \ \overline{\sigma}, \tag{2.B7a}$$

$$v = \frac{A \ \exp \ ikr'}{r'} \ \text{ on } \ \sigma. \tag{2.B7b}$$

2.10.5 Solution for a plane

This problem simplifies where the screen or surface is a plane. In that case, Green's function can be conveniently expressed by the method of images [to satisfy the condition in Eq. (2.B4b) that $G = 0$ on σ]. Referring to Fig. 2.A.2, if the point P

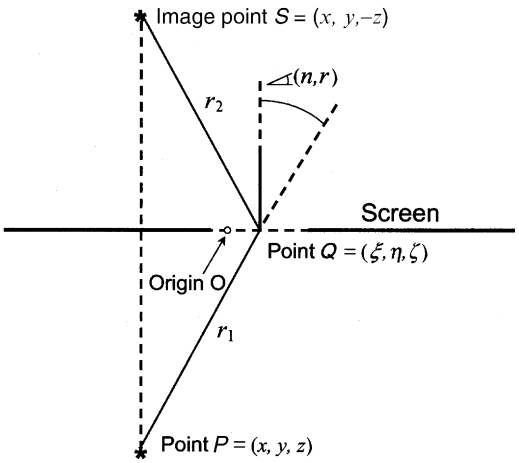

FIGURE 2.A.2

Method of images applied to the generalizable diffraction problem.

is at arbitrary coordinate (x,y,z), then the image point is at coordinates $(x,y,-z)$. For an arbitrary point Q with coordinates (ξ,η,ζ), we have

$$G = \frac{e^{ikr_1}}{r_1} - \frac{e^{ikr_2}}{r_2}, \tag{2.B8a}$$

where

$$r_1^2 = (\xi - x)^2 + (\eta - y)^2 + (\zeta - z)^2 \tag{2.B8b}$$

and

$$r_2^2 = (\xi - x)^2 + (\eta - y)^2 + (\xi + z)^2. \tag{2.B8c}$$

We next calculate

$$\frac{\partial G}{\partial \zeta} = \frac{d}{dr_1}\left(\frac{e^{ikr_1}}{r_1}\right)\frac{\partial r_1}{\partial \zeta} - \frac{d}{dr_1}\left(\frac{e^{ikr_1}}{r_1}\right)\frac{\partial r_2}{\partial \zeta}, \tag{2.B9}$$

$$\frac{\partial G}{\partial n} = \frac{-\partial G}{\partial \zeta} - 2\frac{\partial}{\partial r}\left(\frac{e^{ikr}}{r}\right)\cos(n,r). \tag{2.B10}$$

We then have that

$$\begin{aligned}\frac{\partial}{\partial r}\left(\frac{e^{ikr}}{r}\right) &= \frac{ike^{ikr}}{r} - \frac{1}{r^2}e^{ikr} \\ &= \frac{ike^{ikr}}{r}\left(1 - \frac{1}{ikr}\right).\end{aligned} \tag{2.B11}$$

In the limit of large r we have that $kr = 2\pi r/\lambda \gg 1$ and

$$\frac{\partial}{\partial}\left(\frac{e^{ikr}}{r}\right) \sim \frac{2\pi i}{\lambda}\frac{e^{ikr}}{r}. \tag{2.B12}$$

Putting Eq. (2.B12) into Eq. (2.B10), and that into Eq. (2.B6), we can solve for v_p.

$$i\lambda v_p = \int_\sigma \frac{e^{ikr}}{r}\cos(n,r)v\mathrm{d}\sigma. \tag{2.B13}$$

2.10.6 Huygens' principle

Equation (2.B13) is mathematically equivalent to Huygens' principle. A light wave falling on the aperture σ propagates as if every element $\delta\sigma$ emitted a spherical wave, the amplitude and phase of which are given by that of the incident wave v.

If we assume point source illumination, then

$$v = \frac{Ae^{ikr'}}{r'}, \tag{2.B14}$$

in which case,

$$i\lambda v_p = A\int e^{ik(r+r')}\frac{\cos(n,r)\delta\sigma}{rr'}. \tag{2.B15}$$

2.11 APPENDIX C

2.11.1 Diffraction by a circular aperture from which the airy disk comes

Our next goal is to understand the origin of the Airy disk in the context of Kirchoff's formulation of Huygens' principle. We again follow Sommerfeld in this discussion. If we take as our starting point Eq. (2.C15) of Appendix B and further assume that dimensions of the aperture are small compared to the distance r_1 and r_2, then the term $\cos(n,r)/r_1r_2$ varies little within the opening. Hence, that term may be taken outside of the integral. Replacing r and r' with R and R', their respective values at the center of the aperture, Eq. (2.C15) of Appendix B becomes

$$i\lambda v_p = \frac{A}{RR'}\cos(n,r)\int e^{ik(r+r')}\delta\eta\delta\xi, \tag{2.C1}$$

where η and ξ have the same meaning as in Appendix B. Now,

$$r = \sqrt{(x-\xi)^2 + (y-n)^2 + z^2}. \tag{2.C2}$$

Because $R^2 = x^2 + y^2 + z^2$,

$$\begin{aligned} r &= \sqrt{R^2 - 2(x\xi + y\eta) + \xi^2 + \eta^2} \\ &\cong R - \frac{x}{R}\xi - \frac{y}{R}\eta + \frac{\xi^2 + \eta^2}{2R} - \frac{(x\xi + y\eta)^2}{2R^2} \\ &= R - \alpha\xi - \beta\eta + \frac{\xi^2 + \eta^2 - (\alpha\xi + \beta\eta)^2}{2R}, \end{aligned} \tag{2.C3}$$

to second order in ξ and η.

Where α and β are respectively the directional cosines of the diffracted ray $O \rightarrow P'$,

$$r' = R' + \alpha_0\xi + \beta_0\eta + \frac{\xi^2 + \eta^2 - (\alpha_0\xi + \beta_0\eta^2)}{2R'}. \tag{2.C4}$$

It then follows that

$$e^{ik(r+r')} = e^{ik(R+R')}e^{-ik\Phi}, \tag{2.C5}$$

where

$$\Phi = (\alpha - \alpha_0)\xi + (\beta - \beta_0)\eta - \left(\frac{1}{R} + \frac{1}{R'}\right)\frac{\xi^2 + \eta^2}{2} + \frac{(\alpha\xi + \beta\eta)^2}{2R} + \frac{(\alpha_0\xi + \beta_0\eta)^2}{2R'}. \tag{2.C6}$$

With these modifications, Eq. (2.C1) becomes

$$i\lambda v_p = \frac{A}{RR'}\cos(n, R)e^{ik(R+R')}\int e^{-ik\Phi}\delta\xi\delta\eta. \tag{2.C7}$$

We have, as they say, reached the proverbial end of the tunnel. For the microscope, both R and R' are large in comparison to the dimensions of the aperture. This is the important condition of Fraunhoffer diffraction. In this limit, Φ becomes linear in ξ and η:

$$\Phi \cong (\alpha - \alpha_0)\xi + (\beta - \beta_0)\eta. \tag{2.C8}$$

We define

$$a = \alpha - \alpha_0, \tag{2.C9a}$$

and

$$b = \beta - \beta_0, \tag{2.C9b}$$

in which case,

$$\Phi \cong a\xi + b\eta. \tag{2.C10}$$

Considering the problem of a small circular aperture in the microscope, we recognize that in the Fraunhoffer limit RR' and $\cos(n, r)$ vary very little. Because $|\exp ik(R + R')\xi| = 1$ and A is a constant, we may rewrite Eq. (2.C7) as

$$v_p = C \int e^{ik\Phi} \delta\xi \delta\eta, \tag{2.C11}$$

where C is a constant.

If we replace the coordinates (ξ, η) and the directional cosines (a, b) with polar coordinates, that is

$$\xi = r \cos \varphi, \tag{2.C12a}$$

$$\eta = r \sin \varphi, \tag{2.C12b}$$

$$a = s \cos \psi, \tag{2.C12c}$$

$$b = s \sin \psi, \tag{2.C12d}$$

where r is the distance from the center of the opening, and s is the sine of the deflection angle between the diffracted ray and the perpendicular incident ray (the undiffracted ray), thus we may rewrite Eq. (2.C11) as

$$v_p = Ck \int_0^{d/2} r\mathrm{d}r \int_{-\pi}^{\pi} e^{-ikrs\cos(\varphi-\psi)} \mathrm{d}\varphi. \tag{2.C13}$$

We recognize the φ integral to be the cylindrical Bessel function:

$$J_0(\rho) = \frac{1}{2\pi} \int_{-\pi}^{+\pi} e^{+i\rho\cos\alpha} \mathrm{d}\alpha. \tag{2.C14}$$

Thus,

$$v_p = 2\pi Ck \int_0^{d/2} J_0(krs) r\mathrm{d}r, \tag{2.C15}$$

$$v_p = \frac{2\pi Ck}{k^2 s^2} \int_0^{ksd/2} J_0(\rho') \rho' d\rho', \tag{2.C16}$$

where $\rho = ikrs$. Then,

$$v_p = \frac{\pi Cd}{s} J_1\left(ks\frac{d}{2}\right). \tag{2.C17}$$

What we actually observe is not v_p but $|v_p|^2$. If we also normalize this by dividing by the intensity squared at $s = 0$, we obtain

$$\frac{v_p^2}{v_{p_0}^2} = \frac{J_1^2(ks(d/2))}{J_1^2(0)}. \tag{2.C18}$$

This is the equation of the Airy disk observed in the microscope for a point source of light.

Acknowledgments

I thank Ryan and Kathryn Sears, Leya Bergquist, Dylan Bulseco, and Angela Perno for help in the preparation of this chapter, and Robin G. Jordan, professor of physics at Florida Atlantic University, for the quotation by Thomas Young at the beginning of this chapter.

References

Born, M., & Wolf, E. (1980). *Principles of optics: Electromagnetic theory of propagation interference and diffraction of light* (6th ed.). New York: Pergamon Press.

Goodman, J. W. (1968). *Introduction to Fourier optics*. New York: McGraw-Hill Book Company.

Halliday, D., & Resnick, R. (1970). *Fundamentals of physics*. New York: John Wiley & Sons.

Hui, S. W., & Parsons, D. (1975). Direct observation of domains in wet lipid bilayers. *Science*, *190*, 383.

Inoué, S., & Spring, K. R. (1997). *Video microscopy* (2nd ed.). New York: Plenum Publishing.

Jackson, J. D. (1975). *Classical electrodynamics* (2nd ed.). New York: John Wiley & Sons.

Jenkins, F. A., & White, H. E. (1957). *Fundamentals of optics* (3rd ed.). New York: McGraw-Hill Book Company.

Shamos, M. (1987). *Great experiments in physics*. New York: Dover Publications.

Sommerfeld, A. (Ed.), (1949a). *Optics: Lectures on theoretical physics* (Vol. 4). New York: Academic Press.

Sommerfeld, A. (Ed.), (1949b). *Physics: Partial differential equations* (Vol. 6). New York: Academic Press.

Young, T. (1801). *Course of lectures on natural philosophy and the mechanical arts*. Lecture 39. London: Press of the Royal Institution.

CHAPTER

Proper Alignment of the Microscope

3

Rudi Rottenfusser

Carl Zeiss Microscopy, LLC, Woods Hole, Falmouth, Massachusetts, USA

CHAPTER OUTLINE

3.1 Key Components and Image Locations of the Light Microscope 44
3.1.1 Illumination Section 44
3.1.1.1 Light Source 44
3.1.1.2 The Lamp Collector 49
3.1.1.3 Internal Components of Illumination Paths 50
3.1.1.4 Field Diaphragm 50
3.1.1.5 Condenser 52
3.1.1.6 Aperture Diaphragm 53
3.1.1.7 Condenser Carrier (Substage Carrier) 55
3.1.1.8 Stage and Specimen Holder 55
3.1.2 Imaging Section 56
3.1.2.1 Objective 56
3.1.2.2 Objective Back Focal Plane BFP 57
3.1.2.3 Revolving Nosepiece Turret 58
3.1.2.4 Infinity Space 58
3.1.2.5 Tube Lens 58
3.1.2.6 Tube, Intermediate Image Plane, Camera Mount 58
3.1.2.7 Eyepieces 59
3.2 Working the Microscope: Basic Setup 60
3.2.1 Koehler Illumination 60
3.2.2 Koehler Illumination: Detailed Step by Step 62
3.2.3 Conjugated Light Paths in Koehler Illumination 62
3.2.3.1 Conjugated Planes in the Illumination Pathway 62
3.2.3.2 Conjugated Planes in the Imaging Pathway 64
3.3 Addendum 66
Acknowledgments 67

Methods in Cell Biology, Volume 114
ISSN 0091-679X
http://dx.doi.org/10.1016/B978-0-12-407761-4.00003-8
Copyright © 2013 Elsevier Inc. All rights reserved.

Abstract

The light microscope is merely the first element of an imaging system in a research facility. Such a system may include high-speed and/or high-resolution image acquisition capabilities, confocal technologies, and super-resolution methods of various types.

Yet more than ever, the proverb "garbage in–garbage out" remains a fact. Image manipulations may be used to conceal a suboptimal microscope setup, but an artifact-free image can only be obtained when the microscope is optimally aligned, both mechanically and optically.

Something else is often overlooked in the quest to get the best image out of the microscope: Proper sample preparation! The microscope optics can only do its job when its design criteria are matched to the specimen or vice versa. The specimen itself, the mounting medium, the cover slip, and the type of immersion medium (if applicable) are all part of the total optical makeup.

To get the best results out of a microscope, *understanding* the functions of all of its variable components is important. Only then one knows *how* to optimize these components for the intended application.

Different approaches might be chosen to discuss all of the microscope's components. We decided to follow the light path which starts with the light source and ends at the camera or the eyepieces. To add more transparency to this sequence, the section up to the microscope stage was called the "Illuminating Section", to be followed by the "Imaging Section" which starts with the microscope objective.

After understanding the various components, we can start "working with the microscope." To get the best resolution and contrast from the microscope, the practice of "Koehler Illumination" should be understood and followed by every serious microscopist. Step-by-step instructions as well as illustrations of the beam path in an upright and inverted microscope are included in this chapter.

A few practical considerations are listed in Section 3.

3.1 KEY COMPONENTS AND IMAGE LOCATIONS OF THE LIGHT MICROSCOPE

3.1.1 Illumination section

3.1.1.1 Light source

Long before electricity was invented, people already used microscopes, and the only source then was the sun. A cloudy sky would be best because it provided for perfectly even illumination. A mirror directed the light toward the specimen to be illuminated. "Daylight" had another advantage besides its uniformity—it provided for the most natural representation of colors (Fig. 3.1). While there is nothing wrong to use this source now, modern microscopes are mostly located in areas where there are no windows, or in special rooms, or at times of the day when it is dark outside. For these and other diverse reasons, "artificial" sources for illumination are used today for most applications.

With Edison's invention of the light bulb, external, attached, and later built-in illuminators came into use. The first one consisted of the incandescent light bulb

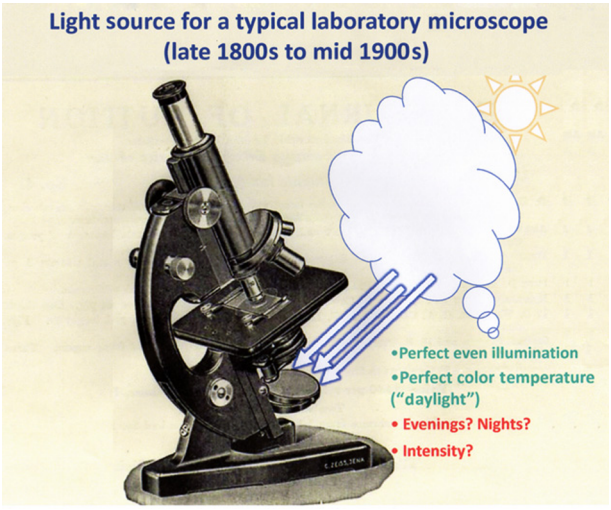

FIGURE 3.1

Light source for a typical laboratory microscope in the late 1800's.

which contains a *tungsten filament* wire heated to a high temperature by an electric current passing through it, until it glows. The hot filament is protected from oxidation with a glass bulb that is evacuated. Incandescent bulbs work equally well on either alternating current or direct current. They were widely used in microscopy applications, particularly after tightly wound flat filament coils, rather than round ones, allowed for proper imaging without "hot spots" during Koehler illumination (see Section 3.2.1). The shape of the filament can be rectangular or square.

In most modern microscopes, the power supply for the illumination is integrated into the stand (Fig. 3.2).

One of the down sides of regular tungsten filament lamps is that with age the inside of the glass envelopes gradually becomes more opaque, changing its spectrum more toward yellowish hues as well as reducing the intensity, due to the deposit of tungsten particles (Fig. 3.4).

In the 1980s, *tungsten-halogen* bulbs (Fig. 3.3 and 3.4) began to replace the tungsten (vacuum) lamps. Tungsten-halogen sources have a continuous spectral emission over the visible and near-infrared (IR) ranges with a color temperature up to 3200°K at nominal voltage. Like their ancestor tungsten (vacuum) bulbs, they are also not very energy efficient in that they convert less than 5% of the energy they use into visible light, with the remaining energy being converted into heat. This disadvantage may be an advantage, however, for microscope applications in the IR range.

The envelope in tungsten-halogen lamps is filled with an inert gas (either nitrogen, argon, krypton, or xenon) that is mixed during assembly with a minute amount of a halogen compound (usually hydrogen bromide, HBr) and trace levels of molecular oxygen. The halogen compound serves to initiate a reversible chemical reaction

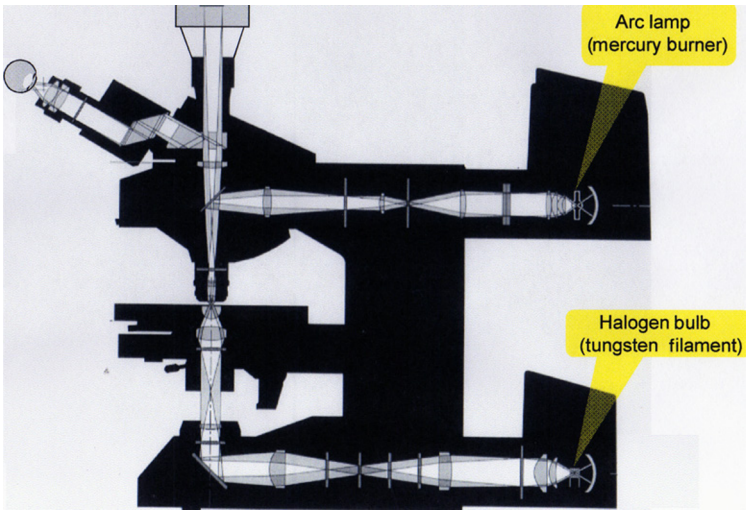

FIGURE 3.2

External lamp housings.

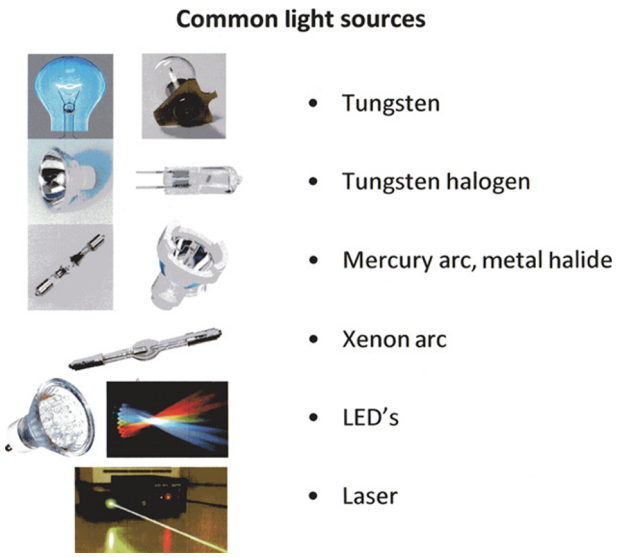

FIGURE 3.3

Common Light Sources in Microscopy.

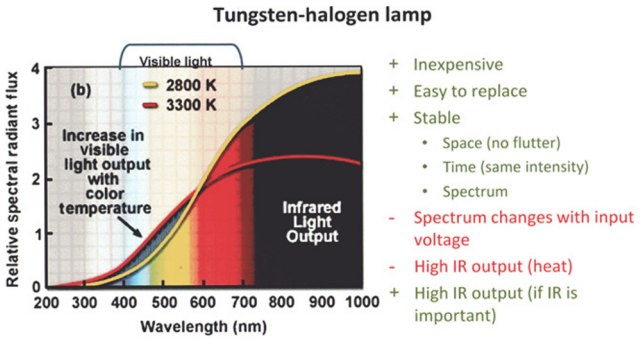

FIGURE 3.4

Tungsten-Halogen bulb spectra, advantages and disadvantages.

with tungsten evaporated from the filament to yield gaseous tungsten oxyhalide molecules in the vapor phase. Thermal gradients formed as a result of the temperature differential between the hot filament and the cooler envelope contribute to interception and recycling of tungsten to the lamp filament through a process known as the *halogen regenerative cycle*. The benefits of the halogen regenerative cycle include the ability to use smaller and stronger quartz envelopes that are maintained in a clean, deposit-free condition during the life span of the lamp. Higher internal gas pressure assists in suppression of filament vaporization, thus allowing increased filament temperatures, producing more luminous output, and shifting emission profiles to feature a greater proportion of the more desirable visible wavelengths. As a result, tungsten-halogen lamps retain their original brightness throughout their life span. They also convert electric current to light somewhat more efficiently than their precursors, although their output in the visible light range is still much lower than in the IR. Eventually, the lamps fail due to decreased filament thickness in the hottest regions. To see how the halogen regenerative cycle works, go to the following interactive tutorial: http://zeiss-campus.magnet.fsu.edu/tutorials/halogencycle/index.html.

Proper alignment of the bulbs within their lamp housings is important and most of the modern microscopes either use pre-aligned bulbs which are part of the microscope stand or bulbs in external lamp housings with pre-aligned concave reflectors. In this case, the image of the source may be directed to the ceiling of the lab, while the lamp housing is detached. One only needs to focus and superimpose the image of the filament and its mirror image and reattach the lamp housing for proper alignment.

Gas discharge or *arc lamps* (Fig. 3.4) originated as carbon arc sources, with mercury arc and xenon arc lamps to follow. The most common current arc lamp is either a mercury arc or a combination of mercury/halide lamp. Illumination sources based on plasma discharge (arc lamps) are much brighter than tungsten-halogen lamps and therefore often used as a source in fluorescence microscopy. Since they require considerable time after ignition to reach thermal equilibrium, temporal, spatial, and spectral instability need to be addressed. In many cases, a period of up to 1 h is required until the illumination source is sufficiently stable to enable reproducible measurements

or to record time-lapse video sequences without significant temporal variations in intensity. Generally, gas discharge lamps are the most unstable illumination sources currently used in optical microscopy. Besides the fact that the arc exhibits a significant degree of chaotic, flickering discharge that worsens with age (see tutorial http://zeiss-campus.magnet.fsu.edu/tutorials/arclampinstability/index.html), the light output can also be affected by ambient electromagnetic fields or an unstable power supply. Eventually, the electrodes deteriorate to the point that the lamp will no longer ignite, which occurs, depending on the type, after 300 up to 2000 h with reflector-type lamps. Proper installation and alignment of arc lamps are easier now than it used to be because of pre-aligned concave reflectors. Due to their emission of large amounts of ultraviolet (UV) radiation, *never* align the light source by shining its arc on a wall or the ceiling. Read the manufacturer's instructions and warnings closely before installing and aligning high-pressure discharge lamps. This is especially important for Xenon bulbs. They are especially fragile because they are under pressure even while cold. Make sure to wear safety goggles when changing those.

A safe and easy procedure to perform a rough alignment of gas discharge lamps is to view the electrodes directly through the collector lens of a detached lamp housing (while the lamp is switched off!), with your unaided eye. You can center and focus the electrodes and mirror image thereof without any risk, while you turn the alignment screws for x, y, and focus.

Another route to simplify the alignment of an arc lamp is to use a pre-aligned external reflector-type bulb, connecting it to the microscope via a flexible fiber optics cable and appropriate coupler. This bulb is usually of a *metal-halide* type which contains not only mercury but also other inert gases, increasing its useful lifetime. A special mount assures its proper fit within a specific external power supply. No alignment is needed when the bulb is changed. This and its longer lifetime of up to 3000 h are reasons why this type of arc lamp has become very popular (Fig. 3.5).

LEDs (light-emitting diodes) have become one of the most promising of emerging technologies for illumination in optical microscopy (Fig. 3.3, 3.4). These versatile semiconductor devices possess many of the desirable features that incandescent (tungsten-halogen) and arc lamps lack and are now efficient enough to be powered by low-voltage batteries or relatively inexpensive switchable power supplies. The diverse spectral output afforded by LEDs makes it possible to select an individual diode light source to supply the optimum excitation wavelength band for fluorophores spanning the UV, visible, and near-IR regions.

During the past four decades, LEDs have advanced at a pace that rivals microprocessors. They have historically doubled in brightness every 2 years and are expected to continue this dramatic growth in performance. As their brightness and the range of available colors has increased, LEDs have been put to use in a variety of new applications, including the role of an energy efficient and durable replacement for incandescent lamps for home and industrial lighting, as well as microscopy. Their advantages in microscopy are numerous such as: No warm-up period (instant on and off), long life (10,000 + h), stable temporal output, consistent spectral output which does not vary with voltage, cool, no lamp alignment needed, usable for shuttering (no vibration), and quick switching (see Figure 3.5).

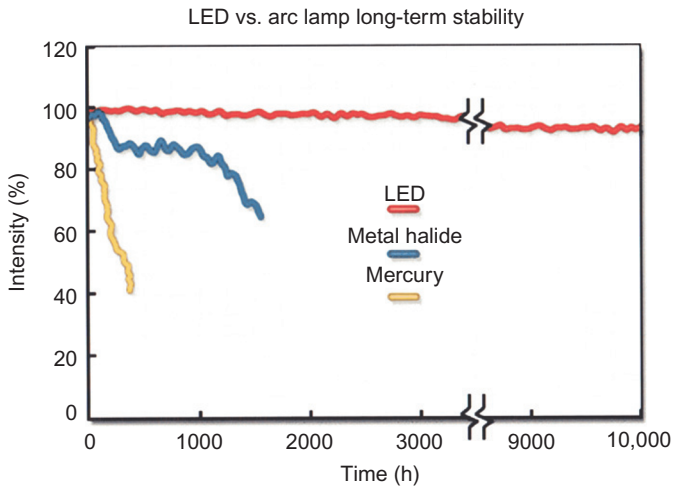

Source: zeiss-campus.magnet.fsu.edu/articles/lightsources/led.html

FIGURE 3.5

LED vs. Arc Lamp long-term stability.

Demands in a variety of industrial, medical, and military application areas of the economy that require substantially higher quantities of LEDs than the field of optical microscopy, will provide a driving force for the development of more LEDs, emitting in all spectral regions, thus benefiting all illumination modalities in optical microscopy.

Laser Light Sources: In spite of the high cost, because of their high light output and other features, lasers are increasingly used for applications which have very special requirements. Lasers are used for total internal reflection fluorescence, confocal microscopy, and super-resolution microscopy. Different types of lasers provide unique emission spectra. Pulsed lasers are used in multiphoton microscopy, also known as nonlinear or multiphoton microscopy. Samples are illuminated at about twice of their normal excitation wavelength. The longer wavelength is advantageous because the radiation is less damaging to live cells. Longer wavelength light also travels further into tissues. This is important in 3D and also for live-cell imaging. Thus live samples survive studies over longer time periods. Examples of multiphoton microscopy techniques include second harmonic generation, third harmonic generation, coherent anti-Stokes Raman spectroscopy, and stimulated-emission-depletion microscopy.

3.1.1.2 The lamp collector

The collector captures as much light as possible from the source and converts it into a collimated beam. Collectors are part of external lamp housings and they are either focusable or fixed. In the latter case, the lamp can be axially moved to provide proper focus of the source. The image of the source should be several meters away.

This makes it possible that initial alignment of tungsten or tungsten-halogen sources can be carried out by sending their images to the ceiling or a wall.

After the attachment of the lamp housing and collector to the microscope stand, the internal optics of the microscope focuses the source image into the front focal plane (aperture) of the condenser for even, uniform illumination. See Section 3.2.1.

Focal length, aperture, and optical correction of the collector lens directly influences the light flux and uniformity of illumination at the specimen. A collector with a single aspheric lens will provide for highest light throughput, but collectors which contain 2–4 lens elements still provide for best image quality.

Please note that different sources require different collectors. High energy sources such as mercury or xenon or lasers should NEVER be aligned outside of the microscope because of the danger to damage someone's eyesight.

An IR blocking filter is usually mounted at the end of the collector, facing the microscope. It greatly reduces the amount of radiated heat from the source which can potentially damage internal elements such as polarizers, as well as keeping heat away from sensitive specimens. In addition, since detectors for digital cameras amplify IR very efficiently, images in the visible range may be overwhelmed by IR. Thus the IR filter also improves the image on a detector (if it is not already equipped with an IR blocking filter).

Make sure you know if such an IR blocking filter is in place because if you need to perform special techniques in the near-IR such as for applications in electrophysiology, you may have to remove the IR filter to permit the longer wavelengths to pass through to the detector. Keep in mind that after removing this filter, you have to be careful to keep the intensity of the illumination down, to prevent potential overheating of internal elements. If in doubt, hold your hand over the light output. If it is too warm for your hand, it is too warm for optics and polarizers (Fig. 3.6)!

3.1.1.3 Internal components of illumination paths

Following the light after the collector, it may be passing through several components such as a shutter, filters, or light attenuators, before it arrives at the location of the "field diaphragm" (see Section 3.1.1.4). Ideally, these internal components assure controlled and even illumination from edge to edge at the field diaphragm level.

In transmitted- or incident-light illumination, diffusers are sometimes used to more evenly distribute the nonuniform character of a filament or arc. This is especially important for low magnifications (objectives 10× or lower). Filters serve a variety of functions, including correcting for color balance, enhancing contrast of stained specimens, or attenuating light intensity without changing its spectral nature.

Receptacles for inserting special components such as filter turrets or a slider for Dodt Contrast (useful for imaging into deep tissues) are present on some of the research microscope stands.

3.1.1.4 Field diaphragm

All research grade microscopes should include a field diaphragm, sometimes called "luminous field diaphragm" or "field iris diaphragm" or "field stop." As the name implies, its function is connected to the field size which illuminates the specimen.

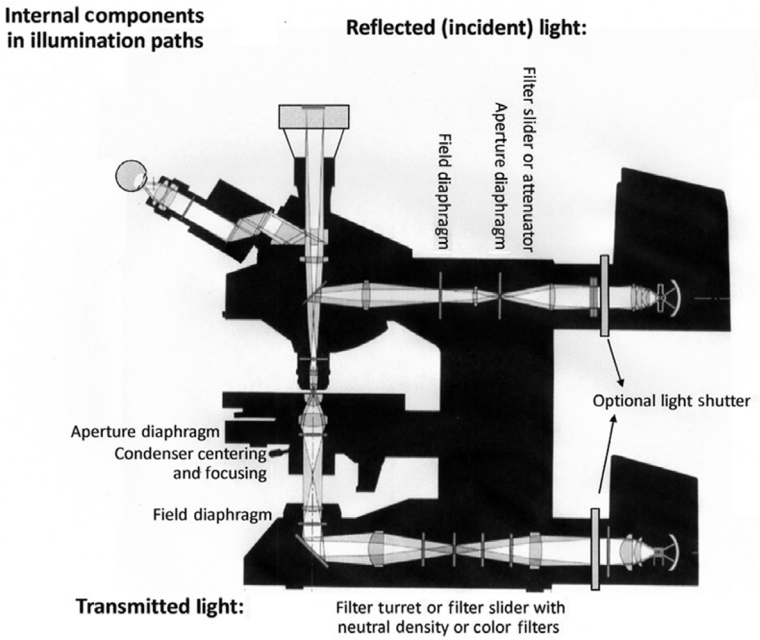

FIGURE 3.6

Location of Internal Components in Illumination Pathways.

Uniform illumination of the field diaphragm will assure uniform illumination of the specimen since one is imaged into the other (see Section 3.2.1).

Depending on the type and brand of microscope, the field diaphragm may be located at various locations inside its stand.

While field diaphragms with a fixed size of illumination are often part of routine microscopes, a research grade system should incorporate a variable field iris diaphragm. It serves to illuminate only the area which the objective projects to the eye or the camera, not more and not less. The adjustment of the iris may be manual or motorized, depending on the degree of sophistication of the microscope. The iris generally provides for a circular illuminated field. Optional adjustable rectangular diaphragms may be used in place of circular ones to match the rectangular size of the detector even better, which may be particularly useful to prevent unintended excitation of the specimen in fluorescence applications.

In a transmitted light setup, the field diaphragm is imaged into the plane of the specimen via the microscope's condenser which needs to be adjusted accordingly (see Section 2.1). In an incident-light setup, the objective acts also as condenser, consequently, the field diaphragm is automatically in correct focus when the specimen is in focus.

The advantages and proper settings of the field diaphragm are outlined in Section 2.1.

3.1.1.5 Condenser

The condenser is the key element to provide for the type of lighting which brings out the desired details of the specimen. It allows for the highest possible resolution and, via its variable aperture, adjustment of optimal contrast, and depth of field of the image.

When the cone angle of light which exits the condenser matches the cone angle of the objective, the condenser effectively doubles the resolving power of the microscope if compared to a setup without condenser. For an illustration of different condenser light cones, you can go to interactive tutorials: http://zeiss-campus.magnet.fsu.edu/tutorials/basics/condenserlightcones/index.html and http://zeiss-campus.magnet.fsu.edu/tutorials/basics/substagecondensernumericaperture/index.html.

If the illumination comes from the top such as in fluorescence applications, the objective which images the specimen simultaneously acts also as a "perfect" condenser (Fig. 3.7).

3.1.1.5.1 Numerical aperture

The "Numerical Aperture" (NA) is the most important number associated with the light gathering ability of an objective or condenser. It is directly related to the angle of the cone which is formed between a point on the specimen and the front lens of the objective or condenser, determined by the equation $NA = n \sin \propto$. It can never get any larger than 1 if air is the medium between the specimen and the lens. To obtain NA values larger than 1, a medium with a larger refractive index than air has to be applied.

Please note that Fig. 3.8 reflects a simplified depiction of an objective (shown to be plane convex). Objectives actually consist of 2–14 internal lens elements, depending on correction, magnification, etc.

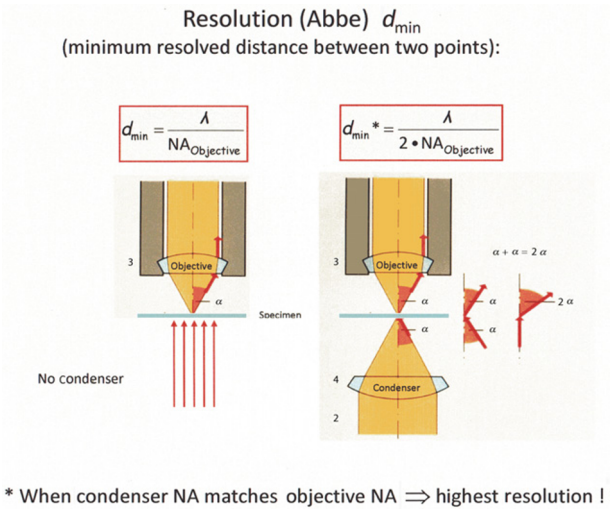

FIGURE 3.7

Resolution without and with condenser.

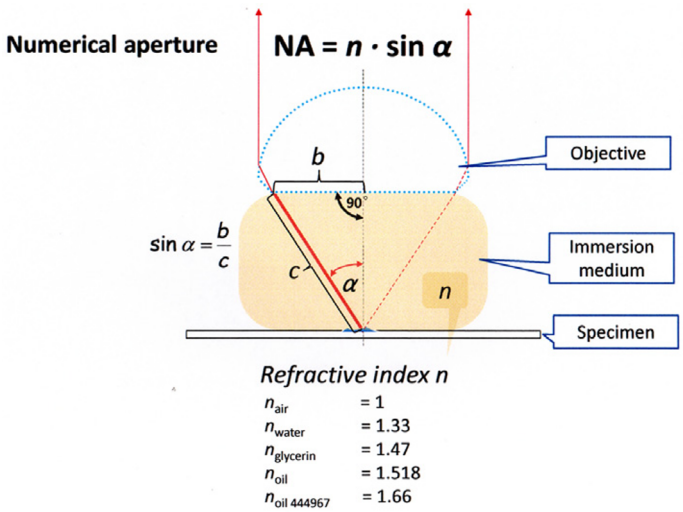

FIGURE 3.8

Numerical Aperture (NA).

Most condensers are used "dry," that is, the medium between their front lenses and the specimen is air, and they are often labeled with their maximum NA (e.g., 0.9) (Fig. 3.9).

For highest resolution, obtained by objectives with NA's larger than 1.0, special immersion type condensers are available which are able to match the NA of such an objective. These condensers require the application of immersion media such as water or oil between their front lens and the specimen. Whenever the label on the condenser indicates a value higher than 0.95, it should be used with the specified immersion medium, for best image quality.

Research-type condensers are optically corrected to produce a minimum of aberrations and a sharply defined image of the field diaphragm. They also have a variable iris diaphragm (see next section). Some include a revolving turret for optical elements which are used for special imaging techniques such as Phase Contrast, Darkfield, or Differential Interference Contrast (DIC).

3.1.1.6 Aperture diaphragm

The aperture or condenser diaphragm which is part of a research microscope's condenser plays a major role in the quality and rendition of an image. Located at the condenser's front focal plane, the aperture diaphragm controls the *angle* of the illuminating cone of light. An experienced microscopist knows how to use the aperture diaphragm as *the* tool to balance resolution against contrast and depth of field of the microscope image (Fig. 3.10).

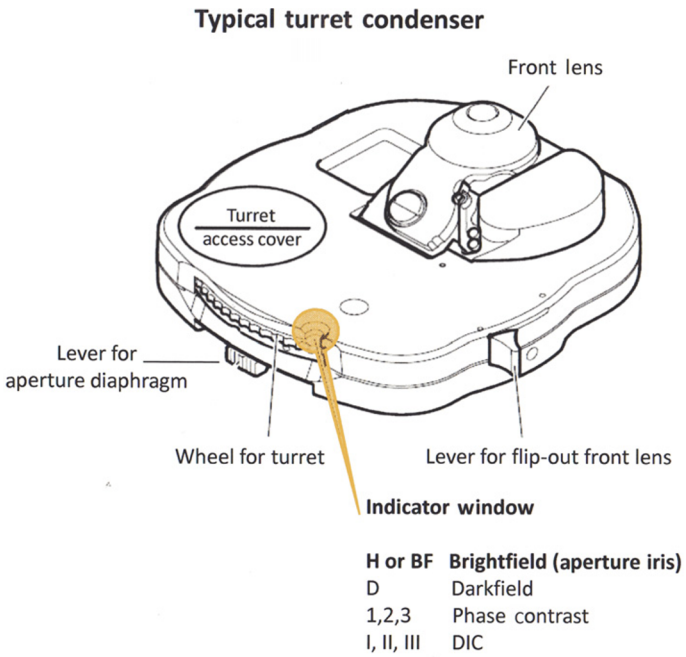

FIGURE 3.9

Typical Turret Condenser.

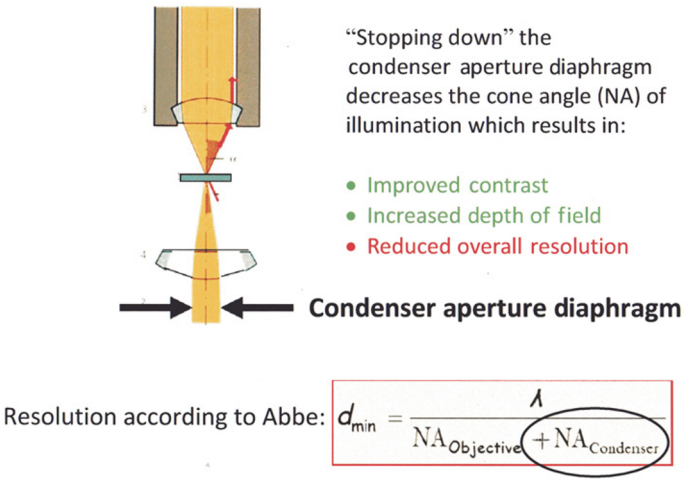

FIGURE 3.10

Condenser Aperture Diaphragm.

Closing down the aperture diaphragm results in improved contrast and greater depth of field. This applies for the coarser structures of the specimen, but the finest details will start to merge together and become invisible. For thick specimens, this is exacerbated by the increased depth of field which results in superposition of structures at different depths of the specimen.

Highest resolution is obtained if the size of the condenser aperture is matched to the size of the objective's back aperture. An optimum image is reached by balancing the resolution versus contrast and depth of field by closing the aperture diaphragm only as little as needed for sufficient contrast. This setting which is different for each objective depends on what information one needs to obtain from the observed specimen. See example at: http://www.olympusmicro.com/primer/java/kohler/contrast/index.html.

Please note that the best possible image can only be obtained if the optics at hand are properly matched with the type and nature of the specimen, mounting material, cover glass, etc.

For incident-light techniques, the aperture diaphragm is important both in materials science applications as well as interference reflection contrast techniques. It is located within the "epi" light path and optically conjugated to the objective's back focal plane (BFP). For fluorescence applications it is normally kept fully open, but it *can* be used for light attenuation, because the resolution in fluorescence is independent of the angle of illumination.

Note: Closing down the aperture diaphragm will also decrease the brightness of the image, but it is never be used for this purpose! The brightness of the image should only be adjusted via regulating the power supply and/or by applying filters!

3.1.1.7 Condenser carrier (substage carrier)

The condenser carrier is usually attached to the stage carrier on an upright microscope. It moves with the stage focus, but also has its own control knobs which are specific only for condenser focus and centration, independent of specimen focus. The condenser carrier routinely features mounting holes or receptacles for swing-in filters or polarizers.

3.1.1.8 Stage and specimen holder

The specimen stage typically attaches to a focusable stage carrier of the upright microscope, or the frame of the inverted microscope. For special applications, for example, electrophysiology, stages are usually fixed in the *Z*-direction or they consist of separate platforms which enable the attachment of manipulators and/or probes. In this case, the nosepiece or the whole upper part of an upright microscope must be focusable.

Stages are often interchangeable and, depending on the application, may consist of a plain platform, movable platform in *x* and *y*, or a rotating platform. Nonrotating stages offer convenient and ergonomic *x*–*y* controls via coaxial knobs. These vertically oriented knobs are close to the hand, resting on the table surface, and therefore comfortable for long-term use. Working with polarized light requires rotating stages.

These are also used for DIC or other techniques which produce orientation-dependent images. Hanging (vertical) *x*–*y* controls are possible if the stage rotates 240° or less; for 360° rotations (required in quantitative Pol studies), *x*–*y* controls of the specimen are possible only by attaching an additional carrier to the top of the stage.

Images with high resolution at high magnification require a very stable and reliable focus drive and a solid suspension of the stage. This is especially important with heavy stages and motorized *x*–*y* drives. It is prudent to select a microscope stand which is built to accommodate these needs.

Holders for specimens are available to accommodate typical microscope slides, with spring fingers for quick change. Special holders are available for petridishes and plates of various sizes. Some of them are adjustable and usable for different types of samples.

3.1.2 Imaging section

3.1.2.1 Objective

The objective is the most important optical component of the microscope. Its parameters and its degree of optical correction determine not only the magnification ratio but also resolution, contrast, image brightness, depth of field, sharpness from center to edge, and color fidelity. Additional factors to consider may be: working distance, spectral transmission, absence of internal strain (Pol work), absence of autofluorescence, temperature tolerance and isolation (heated samples), electrical shielding (electrophysiology), and shape of front part (access for probes, etc.).

Between Achromats and Plan-Apochromats and a variety of specialized lenses, the microscope objective needs to be carefully selected for its intended application (Fig. 3.11).

Objectives may or may not be fully corrected by themselves. Since the concept of infinity optics always necessitates a tube lens, objectives from Leica and Zeiss utilize the tube lens to correct for inherent lateral chromatic aberration (LCA) of their objectives. Nikon and Olympus incorporate the LCA correction into the objective itself. At any rate, whatever the method, the intermediate images are fully corrected.

Note: The designs between microscope manufacturers in terms of focal lengths of tube lenses, thread diameters, and dimensions of the infinity space are not the same. Because of these different approaches, it is generally not a good idea to mix objectives of different manufacturers on a given platform.

Time to determine the appropriate objective out of a wealth of options is well spent. More detailed information is available within the Websites of the major microscope companies such as:

Leica: www.leica-microsystems.com,
Nikon: www.nikon.com,
Olympus: http://microscope.olympus-global.com,
Zeiss: www.zeiss.com/campus and www.micro-shop.zeiss.com/index.php?p=us&f=o.

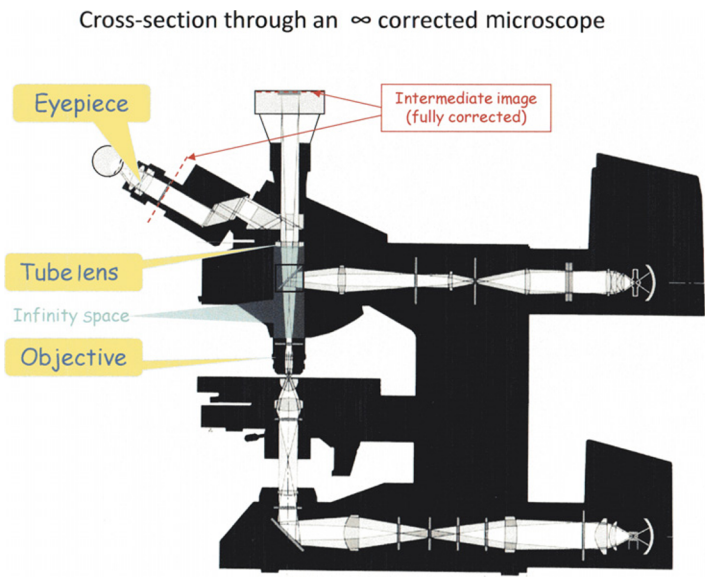

FIGURE 3.11

Imaging Components in the infinity-corrected microscope.

Whenever the "best" objective for a specific application has been selected, the optical pathway between the objective and the specimen has to be considered for the total calculation of the objective. Mounting media and/or cover slips with different thicknesses change these properties. Best images can only be expected if the design parameters of the objective are met. Many objectives are made for one specific purpose and some have a correction collar to adjust for different environments (see tutorial example http://www.microscopyu.com/tutorials/java/aberrations/correctioncollar/index.html).

3.1.2.2 Objective Back Focal Plane BFP

The BFP of the objective (i.e., the optical plane where beams coming from infinity will come into focus) resides inside the barrel of the objective, with few exceptions. It is a significant optical plane because the diameter of the BFP directly relates to its NA. As stated before, NA determines the obtainable resolution and brightness. The BFP is also the place where phase rings are located, allowing an objective to be used for "Phase Contrast" applications. A few select high magnification objectives are available with a built-in iris diaphragm at the BFP. These objectives are usable for transmitted light Darkfield techniques.

The image which appears at the BFP can be viewed in the microscope by (a) removing the eyepiece or (b) replacing the eyepiece with a phase telescope or (c) engaging a Bertrand lens.

3.1.2.3 Revolving nosepiece turret

Precisely machined turrets with receptacles for four to seven objectives allow for fast changing between magnifications and help maintain focus (parfocality) and registration (parcentration) of the specimen. Special nosepieces with individually centerable threads are used primarily for quantitative polarized light work where it is crucial to maintain the exact center of stage rotation between different objectives. DIC requires the addition of a "DIC" slider behind the objective. Many research microscopes now have nosepieces with built-in receptacles for DIC sliders, which make it simple to add this technique to an existing system.

The thread size of objective mounts was almost universally the same for all microscopes for more than a century. Called the "RMS" thread where "RMS" stands for "Royal Microscopy Society," its dimension is 0.8″ (diameter) with a pitch of 1/36″. Larger thread sizes allow for more flexibility to accommodate special requirements. Therefore, M25 (25 mm) and M27 (27 mm) threads are becoming more common among research microscopes. Intermediate rings allow objectives with the smaller RMS thread to be used on the same nosepiece.

3.1.2.4 Infinity space

Most current research microscopes incorporate "infinity-corrected" objectives, initially introduced in the 1970s. They have become standard for all major microscope manufacturers. "Infinity-correction" means that the objective is calculated with the specimen being located at its front focal plane, consequently sending the image to infinity. The space between the objective mount and the tube lens is appropriately called the "infinity space."

This concept is of great benefit for components such as compensators, beam splitters, reflectors, and filters because, as long as these components are plane-parallel, they have no negative effect on focus, alignment, or quality of the image.

3.1.2.5 Tube lens

The "tube lens" at the far end of the infinity space is usually part of the tube. It focuses the infinite conjugate rays of the specimen to *its* BFP, the intermediate image plane. Objective and tube lens together perform the same optical function as the objective alone in a "finitely corrected" system (no tube lens) which was the norm before the advent of infinity optics.

The focal length of the tube lens is linked to the magnification of the objective, for example, a 10× objective designed for a 200-mm tube lens will be only an 8× objective when used on a system with a 160-mm tube lens. In addition, different manufacturers use diverse design concepts for the full correction of the image. This means that in general one should *not* mix and match objectives of different manufacturers because of the likelihood of degraded images.

3.1.2.6 Tube, intermediate image plane, camera mount

The name "tube" dates back to the early microscopes where a straight (monocular) tube on top of the objective accommodated an eyepiece for observation, requiring the observer to look straight down.

It was much more convenient and comfortable for microscopists, when the simple straight tube was superseded by the "inclined" binocular tube. For a long time, inclination angles varied between 30° and 60°. Ergonomy studies pioneered in Scandinavia determined that for long observations, an inclination of 15° from the horizontal or less seems to be best to prevent strain on the neck muscles.

Most research microscope tubes are equipped to accommodate not only the eyepieces for the observer but also a camera system of one type or another. These tubes are called trinocular tubes or binocular phototubes. Prisms or mirrors inside may have a fixed beam splitting ratio or are switchable to send the image to the observer, or to a camera, or to both.

The intermediate image, that is, the image projected by objective and tube lens together is located within the binocular part of the tube, usually 10 mm from the flange where the eyepieces are inserted.

A different flange on top of the photo port allows for adaptation of camera systems with their detectors placed directly at the intermediate image. The distance between the mounting flange and the intermediate image plane determines how many detectors of different sizes and parameters can be used without the addition of "relay optics" for a 1 × image ratio. This leads to the "cleanest" possible image, that is, the minimum amount of glass which the image passes through on its way to the detector. An adapter with a different magnification (and built-in optics) may be required to match the pixel resolution of the detector to the resolution of the microscope image.

3.1.2.7 Eyepieces

The eyepiece or ocular represents part two of the compound microscope. Its magnification permits the observer to clearly see all details which are projected into the intermediate image plane by the objective and the tube lens. 10 × eyepieces are by far the most common ones. Most manufacturers now supply "high-eyepoint" eyepieces which make it possible to use eyeglasses while maintaining the full field of view.

Both eyepieces should be individually focusable. If one is fixed, arrange to replace the fixed-focus eyepiece with its focusable counterpart. The reasons are explained in the Addendum, Section 3.3 - "Setting your microscope to be parfocal".

If you want to capture all of the image information which is available in a given setup, it is good to know about two boundaries which are outlined by the term "useful magnification range." This range is delineated by two limits:

1. *The eye*: You will miss fine nuances in the image if the objective projects details through the eyepiece which are smaller than the resolving power of the eye, given by the distance of rods and cones in the retina. This is often the case when using low magnification/high-NA objectives. As a rule of thumb, the *minimum* magnification necessary for details in an image to be visible by the eye is ∼500 × NA of the objective. Details which are smaller cannot be recognized by a person with normal vision.
2. *The microscope*: You will reach "empty magnification" if you enlarge an image beyond the physical resolving power of the objective. Again, a rule of thumb states that the *maximum* magnification of an image to the eye

should not exceed $\sim 1000\times$ NA of the objective. Magnifications higher than this value will only lead to the finest details being spread further apart with no added information to the eye. The image would simply be larger but become increasingly more blurry. This is why it is called "empty" magnification.

Note: The same principle holds for detectors which capture the image information directly at the intermediate image plane. In this case, the *minimum* magnification to the sensor has to be large enough for the finest details to occupy at least two to three times the distance of individual pixels on the sensor (Nyquist criterion). The upper limit for magnification is still governed by the microscope optics' resolution limit.

Through the widespread use of computers, various types of display media are being increasingly used for viewing the specimen, in place of eyepieces. One might be tempted to say that eyepieces will not be needed any more in the future. However, there still may be good reasons for eyepieces:

1. Even with the best imaging systems and monitors, the image as it is seen in the eyepiece reveals a "presence" and color fidelity which cannot be duplicated by other means. As an example, for pathologists where small color nuances are essential for proper diagnosis, co-observation tubes are used for teaching with multiple sets of eyepieces. Every collaborator sees the same fine detail and color through "his" or "her" eyepieces.
2. Another reason for eyepieces is that they generally project a larger field of view than "seen" by cameras. Being commonly more than twice the field diameter, they help to speed up the initial search for specimen details, before switching over to the camera or a confocal system.
3. Important but often overlooked—eyepieces present the observed image at "infinity" which is akin to observing open space in nature. Computer monitors are comparably much closer, resulting in eye strain especially when used for extensive periods of time.
4. An eyepiece can also be used as a magnifier. To use it as such, remove it from the tube and hold it close to the eye, with the outside part facing the object. At about $1''$ distance, objects will come into focus. This is very useful for checking out the cleanliness of objectives' front lenses and other optical components.

3.2 WORKING THE MICROSCOPE: BASIC SETUP

3.2.1 Koehler illumination

August Koehler, in German spelled Köhler (1866–1948), developed his famous illumination technique while he was an assistant professor at the Institute of Zoology in Giessen, Germany. His technique was originally published in 1893 in the *Zeitschrift für wissenschaftliche Mikroskopie*, to be followed in English in the

August Koehler 1866–1948

FIGURE 3.12

Journal of the Royal Microscopical Society. In 1900, August Koehler joined the Zeiss Optical works where he remained until his retirement in 1945 (Fig. 3.12).

To this day, no other technique beats the "Koehler" method for optimizing illumination in a microscope. Koehler illumination provides for most homogenous and even lighting, highest resolution and minimum effect of stray light or dust. It also allows for optimizing contrast and depth of field. As an additional benefit, "koehlering" helps to quickly locate difficult-to-find structures by establishing the field diaphragm as a reference for proper focus.

When one follows the Koehler method, the condenser is positioned properly not only for Brightfield but also for other techniques such as Darkfield, Phase Contrast, DIC, etc. Optical components required for these techniques will be at the proper location after setting up the microscope for Koehler illumination.

Necessary components to perform Koehler illumination:

- Adjustable Field Diaphragm,
- Focusable and Centerable Condenser,
- Adjustable Condenser Aperture Diaphragm.

3.2.2 Koehler illumination: Detailed step by step

To begin with, turn on the microscope, set the eyepieces at "0" and adjust the binocular tube to your own interpupillary distance.

- Move condenser via substage controls to top of its range (condenser top lens in place)
- Open the field diaphragm all the way.
- Open the aperture (condenser) diaphragm all the way.
- Swing a low power (5× to 10×) objective in place, focus specimen and set intensity to a comfortable level (varying lamp intensity setting and/or neutral density filters).
- Close down field diaphragm until its outline becomes visible in the field of view.
- Lower the condenser until the edges of the field diaphragm are in focus (e.g., as a hexagonal shape), along with the specimen.
- Center the image of the field diaphragm with the centering screws located on both sides of the condenser carrier (usually at 4° clock and 8° clock, viewed from the top).
- Open field diaphragm until its edges are just outside of the field of view, while fine-tuning the condenser's focus and centering settings. If using a camera, the field diaphragm should be adjusted to disappear just beyond the field of view of the camera image.
- Remove one of the eyepieces or replace it with a centering telescope. You can now observe the objective's BFP in the tube.
- Close the aperture diaphragm which is visible within the objective's BFP, until its diameter is about ¾[1] of the size of the BFP.
- Insert the eyepiece again. Your microscope is now set up in Koehler illumination.

Whenever a different objective is moved into place, field and aperture diaphragms need to be readjusted for a perfect image (Fig. 3.13).

3.2.3 Conjugated light paths in Koehler illumination

The illumination and imaging pathways in Koehler illumination are intertwined and often shown superimposed together in illustrations. For the sake of clarity, they are shown here separately on the facing page (Fig. 3.14).

3.2.3.1 Conjugated planes in the illumination pathway

The light path starts at the source, shown here to be a tungsten filament. The center of the filament (shown as an orange star symbol) is imaged by the collector system of the lamp housing first to infinity. As this collimated light beam enters the microscope's internal illumination path and passes through the luminous field diaphragm, it is

[1]The ¾ rule for the aperture diaphragm size is only a starting point. The best compromise between contrast and resolution should be determined by critically observing the specimen.

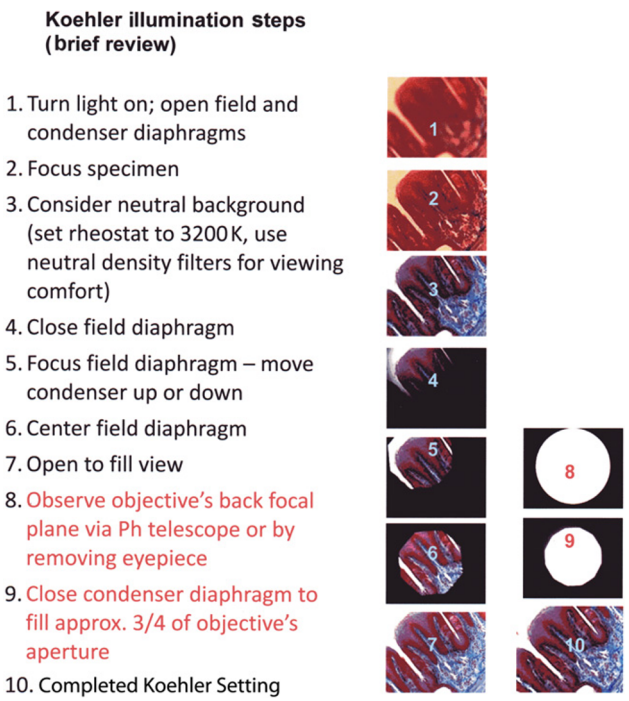

FIGURE 3.13

10 steps to proper Koehler Illumination (abbreviated).

refocused into the aperture diaphragm, located at the front focal plane of the condenser. The image of the source which is now in the same optical plane as the aperture diaphragm is in other words *conjugated* to the aperture plane. The condenser then images the aperture diaphragm along with the superimposed source image to infinity, that is, the image of the source is "maximally out of focus" as it passes through the specimen. This causes the specimen to be evenly illuminated. The objective now refocuses the source image into its BFP which is located approximately at the front focal plane of the tube lens. From here, the tube lens relays the image from the objective's BFP again to infinity. The eyepiece refocuses this image to *its* BFP which is conventionally called the "eyepoint." The eyepoint of the eyepiece matches up with the front focal plane of the eye. The internal optics of the eye (cornea and lens together) subsequently fill the whole retina evenly with light. If one observes a point at the filament which is off-center, for example, to the right as shown, the same sequence as explained before takes place except that the images of this peripheral source point are now also appearing off-center at the aperture diaphragm plane, the BFP of the objective, and the eyepoint. A total of four planes conjugated to each other are thus present in this pathway.

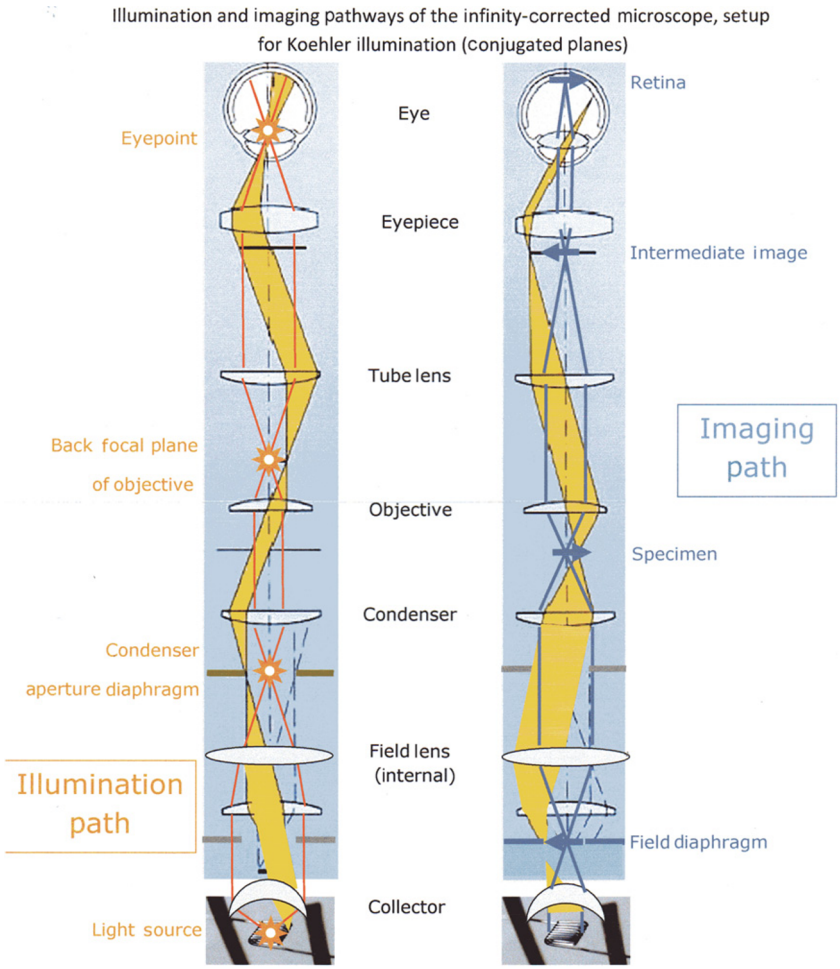

FIGURE 3.14

Illumination and Imaging pathways of the infinity-corrected microscope; conjugated planes.

3.2.3.2 Conjugated planes in the imaging pathway

The imaging pathway starts at the field diaphragm of the microscope. It is evenly illuminated because all points of the source are at infinity (maximally out of focus) as stated before. Being at the front focal plane of internal lenses in the base of the microscope or an auxiliary lens associated with the condenser, the image of the field diaphragm is projected as a conglomerate of infinite number of parallel pencils of light into the condenser. The condenser thus receives the image of the field diaphragm from infinity and now focuses it at its BFP which is where the specimen (shown as a blue arrow) is located. The objective picks up the image of the specimen

along with the superimposed image of the field diaphragm and sends these images to infinity (infinity optics!) until they arrive at the tube lens. The tube lens again focuses the image of the specimen into its BFP (the "intermediate image plane") which is situated at the front focal plane of the eyepiece. The eyepiece now relates the image back to infinity and the eye completes this cycle by focusing the specimen to the retina. At this point, the field diaphragm, specimen, and anything located at the intermediate image plane (e.g., a reticle) are visible simultaneously by the observer. Again, four planes conjugated to each other are visible in this pathway.

See Fig. 3.15

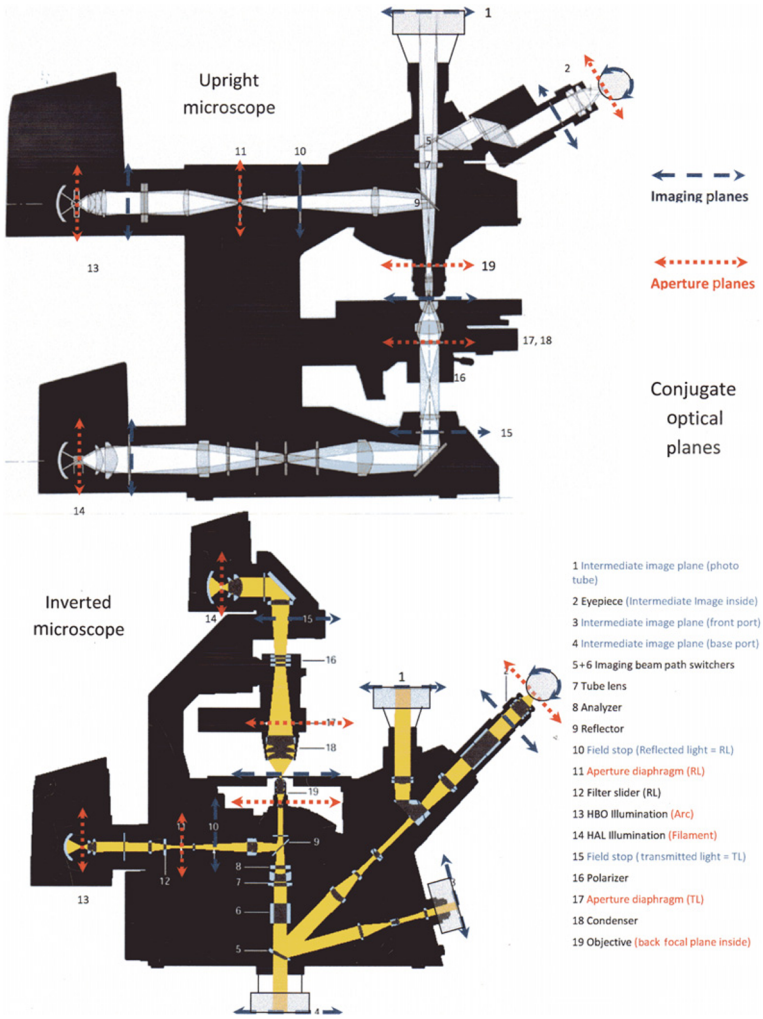

FIGURE 3.15

Conjugated imaging and aperture planes in the upright and inverted microscope.

3.3 ADDENDUM

See Fig. 3.16.

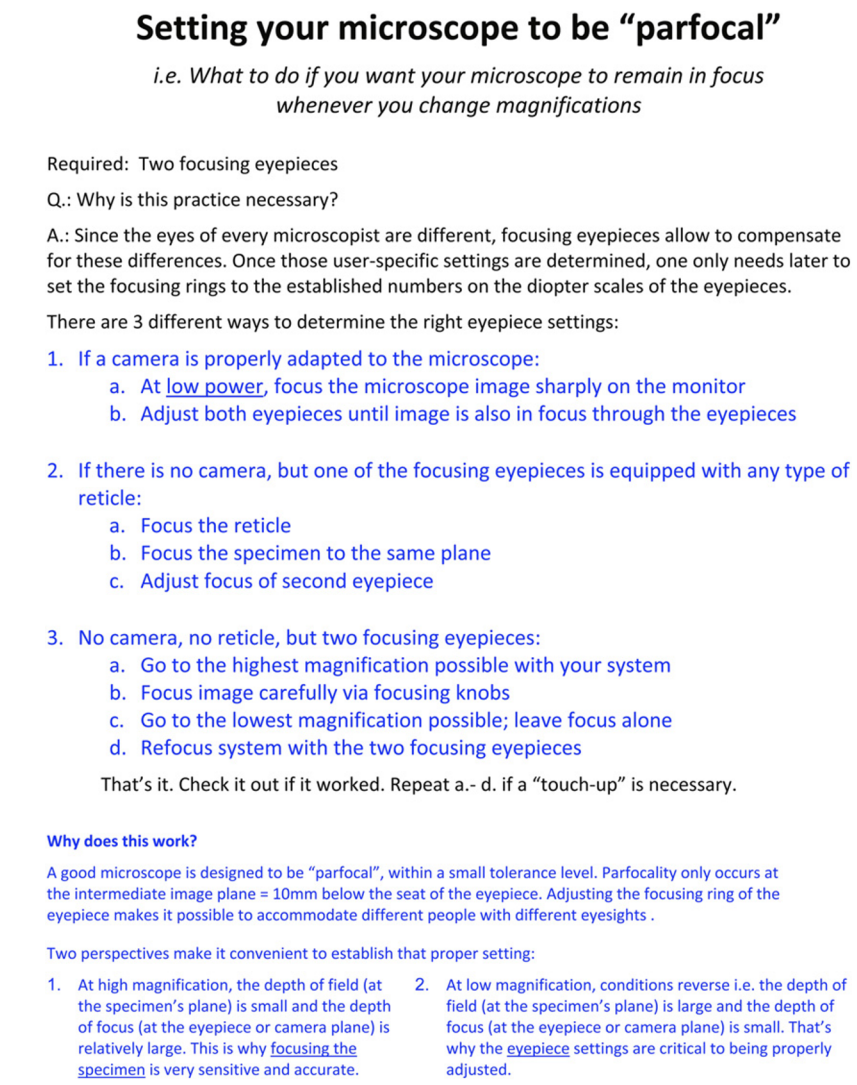

Setting your microscope to be "parfocal"

i.e. What to do if you want your microscope to remain in focus whenever you change magnifications

Required: Two focusing eyepieces

Q.: Why is this practice necessary?

A.: Since the eyes of every microscopist are different, focusing eyepieces allow to compensate for these differences. Once those user-specific settings are determined, one only needs later to set the focusing rings to the established numbers on the diopter scales of the eyepieces.

There are 3 different ways to determine the right eyepiece settings:

1. If a camera is properly adapted to the microscope:
   a. At low power, focus the microscope image sharply on the monitor
   b. Adjust both eyepieces until image is also in focus through the eyepieces

2. If there is no camera, but one of the focusing eyepieces is equipped with any type of reticle:
   a. Focus the reticle
   b. Focus the specimen to the same plane
   c. Adjust focus of second eyepiece

3. No camera, no reticle, but two focusing eyepieces:
   a. Go to the highest magnification possible with your system
   b. Focus image carefully via focusing knobs
   c. Go to the lowest magnification possible; leave focus alone
   d. Refocus system with the two focusing eyepieces

That's it. Check it out if it worked. Repeat a.- d. if a "touch-up" is necessary.

Why does this work?

A good microscope is designed to be "parfocal", within a small tolerance level. Parfocality only occurs at the intermediate image plane = 10mm below the seat of the eyepiece. Adjusting the focusing ring of the eyepiece makes it possible to accommodate different people with different eyesights .

Two perspectives make it convenient to establish that proper setting:

1. At high magnification, the depth of field (at the specimen's plane) is small and the depth of focus (at the eyepiece or camera plane) is relatively large. This is why focusing the specimen is very sensitive and accurate.
2. At low magnification, conditions reverse i.e. the depth of field (at the specimen's plane) is large and the depth of focus (at the eyepiece or camera plane) is small. That's why the eyepiece settings are critical to being properly adjusted.

FIGURE 3.16

Acknowledgments

H. Ernst Keller is responsible for much of my initial understanding of the microscope which I acquired over the years while attending his lectures and in my position as product manager at Zeiss' New York office. One of Mr. Keller's many accomplishments during his over 50 years with Zeiss was to write the chapter "*Proper Alignment of the Microscope*" for the previous editions of this handbook.

I am also grateful for having had the chance during my 15 years at the Marine Biological Laboratory in Woods Hole to encounter many experts in various fields and applications, while I was supporting courses and research there. My interactions with course directors, faculty, and students presented a unique opportunity to pick the best approaches for teaching basic concepts. Obviously, there are many different ways to explain various criteria. Since everyone has a different background, I encourage the reader to study different approaches until he/she *really* understands.

Michael Davidson and his team at Florida State University (Website http://micro.magnet.fsu.edu/) have been creating excellent articles, on-line tutorials, and animated simulations of many aspects in microscopy and in general. The Davidson team also developed sections which are more specific for the equipment of various microscope manufacturers, that is

Zeiss: http://www.zeiss.com/campus,
Olympus: http://www.olympusmicro.com,
Nikon: http://nikon2.magnet.fsu.edu/.

CHAPTER

Fundamentals of Fluorescence and Fluorescence Microscopy

4

David E. Wolf

Sensor Technologies, LLC, Shrewsbury, Massachusetts, USA

CHAPTER OUTLINE

Introduction **70**
4.1 Light Absorption and Beer's Law **71**
4.2 Atomic Fluorescence **73**
4.3 Organic Molecular Fluorescence **74**
4.4 Excited State Lifetime and Fluorescence Quantum Efficiency **76**
4.5 Excited State Saturation **77**
4.6 Nonradiative Decay Mechanisms **77**
4.7 Fluorescence Resonance Energy **78**
4.8 Fluorescence Depolarization **80**
4.9 Measuring Fluorescence in the Steady State **82**
4.10 Construction of a Monochromator **83**
4.11 Construction of a Photomultiplier Tube **84**
4.12 Measuring Fluorescence in the Time-Domain **84**
4.12.1 Boxcar-Gated Detection Method 85
4.12.2 Streak Camera Method 87
4.12.3 Photon Correlation Method 89
4.12.4 Note on the Process of "Deconvolution" 90
4.12.5 Phase Modulation Method 90
4.13 Filters for the Selection of Wavelength **92**
4.14 The Fluorescence Microscope **94**
4.15 The Power of Fluorescence Microscopy **95**
Some Useful Web Sources 96
Acknowledgments **96**
References **96**

Methods in Cell Biology, Volume 114
ISSN 0091-679X
Copyright © 2007 Elsevier Inc. All rights reserved.
http://dx.doi.org/10.1016/B978-0-12-407761-4.00004-X

Abstract

This chapter discusses the fundamental physics of fluorescence. The application of fluorescence to microscopy represents an important transition in the development of microscopy, particularly as it applies to biology. It enables quantitating the amounts of specific molecules within a cell, determining whether molecules are complexing on a molecular level, measuring changes in ionic concentrations within cells and organelles, and measuring molecular dynamics. This chapter also discusses the issues important to quantitative measurement of fluorescence and focuses on four of quantitative measurements of fluorescence—boxcar-gated detection, streak cameras, photon correlation, and phase modulation. Although quantitative measurement presents many pitfalls to the beginner, it also presents significant opportunities to one skilled in the art. This chapter also examines how fluorescence is measured in the steady state and time domain and how fluorescence is applied in the modern epifluorescence microscope.

INTRODUCTION

The application of fluorescence to microscopy represents an important transition in the development of microscopy, particularly as it applies to biology. It was the transition from asking the question, what are the structures of a cell, to asking the question, where are specific molecules located within the cell? Combined with immunofluorescence techniques and later with polynucleic acid technology, biologists could now answer this question for essentially any molecule within the cell, including the location of specific genes within a chromosome. Fluorescence does more than answer this qualitative question of molecular localization. It enables us to quantitate the amounts of specific molecules within a cell, to determine whether molecules are complexing on a molecular level, to measure changes in ionic concentrations within cells and organelles, and to measure molecular dynamics. A recurring theme throughout this volume is how to accurately extract quantitative information from microscope images, particularly from fluorescence images. The reason is that, in an age of dramatic pseudocolor images, it is easy to mislead first oneself and then, in turn, others. The accurate application of correct quantitative technique in fluorescence microscopy requires careful attention to detail. Sadly, the custom is as Hamlet expressed it:

> *"But to my mind, though I am native here And to the manner born, it is a custom More honour'd in the breach than the observance."*
>
> **William Shakespeare, Hamlet the Prince of Denmark; Act I, Scene IV, lines 16–19**

Our goals in this chapter are fourfold. First, we will consider the fundamental physics of fluorescence. Second, we will begin to look at some of the issues important to quantitative measurement of fluorescence. Although quantitative measurement presents many pitfalls to the beginner, it also presents significant opportunities to one skilled in the art. Third, we will examine how fluorescence is measured in the steady state and time-domain. Finally, we will examine how fluorescence is applied in the modern epifluorescence microscope. Because the scope of this chapter is broad, we

must apologize at the outset, as we can only begin to examine these issues. For a more complete discussion of fluorescence and fluorescence microscopy, the reader is referred to several excellent texts on these subjects (Becker, 1969; Cundall & Dale, 1980; Demas, 1983; Guibault, 1973; Haugland, 1996; Lakowicz, 1986; Mavrodineanu, Shultz, & Menis, 1973; Parker, 1968).

4.1 LIGHT ABSORPTION AND BEER'S LAW

In considering the phenomenon of fluorescence emission, it is useful to take a step back and consider the absorption of light by a solute in solution. Many substances, such as multiring organic molecules, are colored, which is to say they absorb light at specific visible wavelengths. Let us consider (Fig. 4.1) a solution of some absorbing solute of concentration C, molecules per cubic centimeter, in a cuvette. We shine a light of intensity I_0, photons per centimeter squared per second, on the front surface of this cuvette. What we would like to know is the output intensity at the other side of the cuvette. Let us call the thickness of the cuvette l, and the cross-sectional area A. Let us generalize the question a bit. If we define the front surface to be at a position $x = 0$ and the back surface at $x = 1$, then we can consider an infinitesimal slab at some x inside the cuvette of thickness $\mathrm{d}x$. If we know $I(x)$, what is $I(x+\mathrm{d}x)$? $\mathrm{d}I = I(x+\mathrm{d}x) - I(x)$ is the number of photons absorbed per unit area per second, and the total number of photons absorbed within the slab per second is $A\mathrm{d}I$. Now, if you think of the photons as being a shower of bullets blasting into clay spheres (the absorbing solute molecules), then you predict that the number of photons absorbed by the slab will be proportional to the number of bullets, $I(x)$, times the number of clay spheres, $C\mathrm{d}x$. If we let ε' be the constant of proportionality, we have

$$\mathrm{d}I = -\varepsilon' CI\mathrm{d}x. \tag{4.1}$$

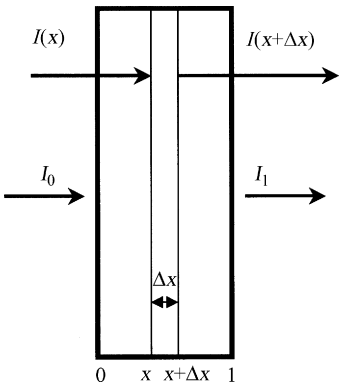

FIGURE 4.1

Schematic of an absorbance measurement. A cuvette of thickness l is shown in cross section. The intensity at $x = 0$ is I_0 and at $x = l$ is I_1. At some arbitrary point x within the volume, the intensity is $I(x)$ and at some Δx later is $I(x + \Delta x)$.

A little rearranging gives us

$$\frac{dI}{I} = -\varepsilon' C dx, \tag{4.2}$$

which is a differential equation that, on integration, gives us

$$\ln\left(\frac{I}{I_0}\right) = -\varepsilon' Cx, \tag{4.3}$$

or, equivalently,

$$I = I_0 \exp(-\varepsilon' Cx). \tag{4.4}$$

This is known as Beer's law.

We can bring this into a more familiar form if we consider the logarithmic form of the equation at $x = 1$. The fraction of light transmitted through the cuvette is $I(1)/I_0$; call it T. Then,

$$\ln(T) = -\varepsilon' C1.$$

Let us then change over to base 10 logarithms:

$$\begin{aligned} \log(T) &= 2.303 \ln(T) = -2.303\varepsilon' C1; \\ \ln\left(\frac{1}{T}\right) &= 2.303\varepsilon' C1. \end{aligned} \tag{4.5}$$

$\log(1/T)$ is known as the optical density of the sample, OD, and if we define $\varepsilon = 2.303\varepsilon'$, we come to the familiar form of Beer's law

$$\text{OD} = \varepsilon C1, \tag{4.6}$$

where ε is the molar extinction coefficient and has units $\text{M}^{-1}\ \text{cm}^{-1}$.

Filters used to reduce light intensity in fluorescence microscopy are typically designated by their optical density. An optical density of one will attenuate light tenfold, of two, 100-fold, and so forth.

ε, of course, is wavelength dependent. Typical values for ε are $5 \times 10^4\ \text{M}^{-1}\ \text{cm}^{-1}$ for organic molecules. This puts us in a position to estimate the sensitivity of adsorbance measurements. Let us assume that we can measure ODs as low as 0.01. If you look at a 0.01 OD solution in a test tube, you will realize that this is about right. Then, if we are using a standard 1-cm path-length cuvette, the lowest concentration we can reliably detect or measure will be

$$C = \frac{\text{OD}}{\varepsilon 1} = \frac{0.01}{5 \times 10^4}(1) = 0.2\ \mu\text{M}.$$

Thus, the detection limit of a standard adsorbance measurement is a few tenths of a micromolar. In contrast, the detection limit for fluorescence samples can be as low as a picomolar. As a solution assay method, if one uses 100-μl cuvettes, this translates to being able to detect an atto, 10^{-18}, moles of a fluorescent substance. In the fluorescence microscope, one can readily see surface concentrations on the order of

100 mol/μ^2. Recognize, also, that this concentration refers to fluorophore density. Thus, if necessary, one can multilabel a probe to push this limit. Webb's group, for instance, has succeeded in visualizing the surface dynamics of individual LDL receptors by preparing LDL labeled with 100 C_{16}dil molecules/LDL molecules (Barak & Webb, 1982).

All of this I offer as a rationale for turning our attention to the phenomenon of fluorescence.

4.2 ATOMIC FLUORESCENCE

Figure 4.2 is meant to illustrate the energy levels of some atom. This kind of energy level diagram is referred to as a Jablonski diagram. Jablonski diagrams fly in the face of what we were all taught in school. The abscissa has no label. The energy levels are labeled S_n, where n is the principal quantum number. S_0 is, of course, the ground state of the atom. We can get the atom into some excited state S_n by shining light of energy $S_n - S_0$ on it. The frequency, ν, and wavelength, λ, of this light can be determined by the Planck's radiation law, namely,

$$S_n - S_0 = h\nu = \frac{hc}{\lambda}, \tag{4.7}$$

where h is Planck's constant. Once in the excited state, the molecule will stay there for a while and then decay back to the ground state by emitting light of identical wavelength. Thus, atomic adsorbance and emission spectra are identical, very sharp, and very boring from our point of view.

It should also be noted that one can excite atomic fluorescence by other forms of energy. If you sprinkle salt crystals onto a candle's flame, you excite the sodium ions with heat and they then emit yellow light. Similarly, we can excite with electrical

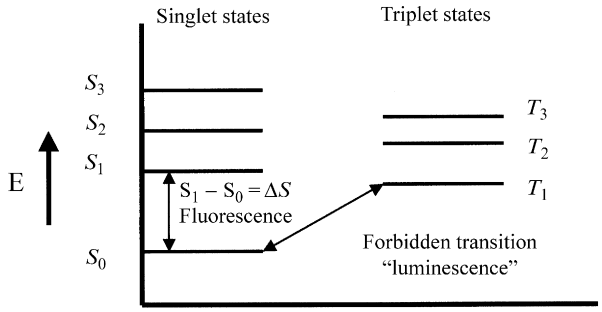

FIGURE 4.2

Jablonski diagram showing the energy levels of a hypothetical atom. The energy levels and therefore the spectral lines that occur are very discrete. A set of triplet states parallels the set of singlet states at slightly reduced energy. Transition between triplet and singlet states violate conservation of angular momentum and is said to be forbidden.

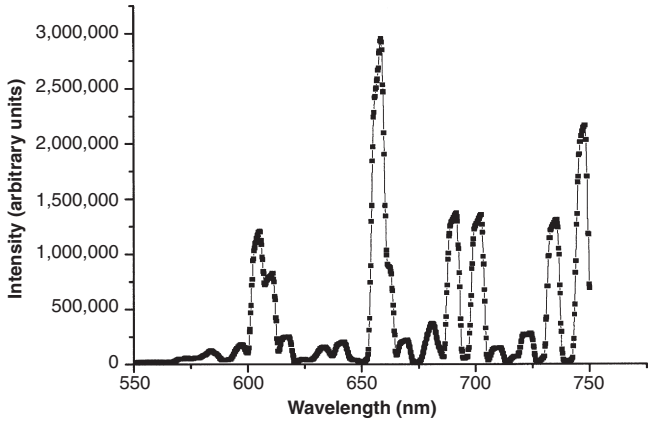

FIGURE 4.3

Atomic fluorescence spectrum of a He–Ne gas showing the discrete nature of the spectral lines. Excitation and emission occur at the same wavelengths.

energy. Figure 4.3 shows the so-called plasma glow of a helium–neon laser. Here electrons bombard the atoms of gas, stripping off their electrons. The atoms then emit at very precise wavelengths corresponding according to Eq. (4.7) to transitions between the various energy levels.

You may also remember that the principal quantum number does not tell the whole story. Electronic orbitals are also defined by whether they have an angular momentum. The ground state cannot have angular momentum and is known as a singlet state. In Fig. 4.2, we have shown the other singlet, that is no angular momentum levels for the nonzero quantum numbers. For $n > 0$, we have a set of parallel states that have angular momentum. Because angular momentum can be in any of three possible directions, these states are threefold degenerate and are known as triplet states. They have energy levels slightly less than the corresponding singlet states. Angular momentum must be conserved. As a result, a transition from a triplet state to a singlet state, such as T_1 to S_0, or vice versa, is forbidden. In quantum mechanics, we can never say never. Forbidden transitions are not absolutely forbidden, just very unlikely. Thus, if one can trick an atom into T_1, it will stay there for a very long time. For organic molecules, we have fast fluorescence with excited state lifetimes on the order of nanoseconds and slow fluorescence, or luminescence, with lifetimes that can be as long as several seconds.

4.3 ORGANIC MOLECULAR FLUORESCENCE

When we consider organic molecules, we are considering the molecular orbitals as shown in Fig. 4.4. The critical difference is that by virtue of the many vibrational states of organic molecules, the energy levels become bands. This causes the absorbance and emission spectra to broaden, as shown in Fig. 4.5. In a typical scenario, a molecule is sitting in the lowest energy level of the ground state. It can absorb light of

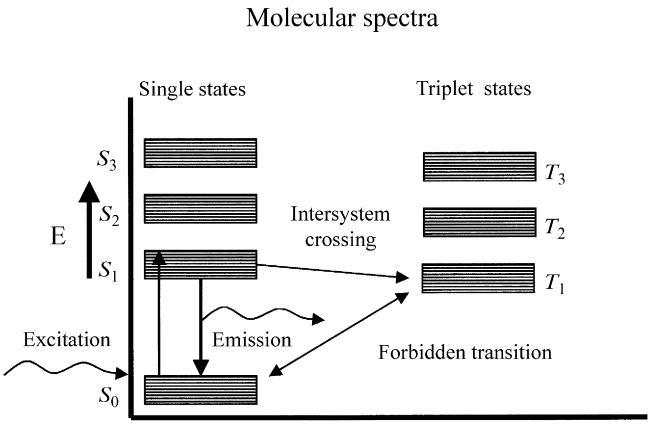

FIGURE 4.4

Jablonski diagram showing the energy levels of a hypothetical organic molecule. In contrast to atomic energy levels, the energy levels are broadened because the molecule can exist in a large number of vibrational states.

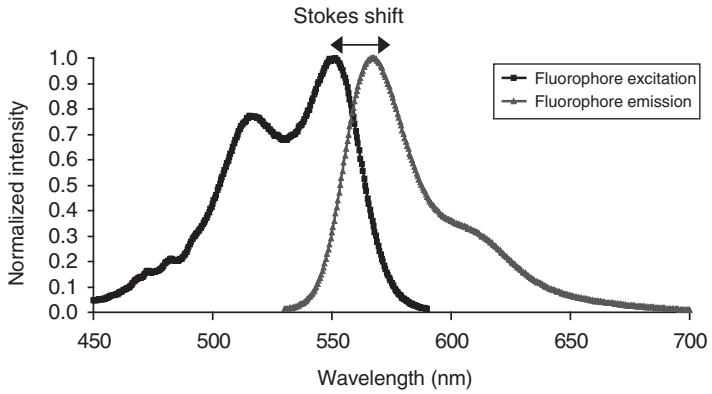

FIGURE 4.5

Molecular fluorescence spectrum illustrating the broadening of the spectral lines because of vibrational energy levels and the Stoke's shift between the excitation and emission maxima.

a variety of wavelengths, bringing it to some vibrational level of, say, the first singlet excited state. It then decays nonradiatively to the lowest level of the excited state, where it sits for a while and then decays to any of the vibrational levels of the ground state. Finally, it gives up energy nonradiatively to return to the lowest vibrational level of the ground state. In addition to broadening the spectra, these vibrational levels result in several other interesting phenomena. First of all, we see that the energy of emission is less than that of excitation. Thus, the emitted light is redder; it has a longer wavelength than the exciting light. This is known as the Stoke's shift after the father of fluorescence, George Gabriel Stokes (1819–1903) (see for instance http://www.cmde.dcu.ie/Stokes/GGStokes.html). Second, and almost

counterintuitively, the excitation spectrum's shape reflects the distribution of excited state vibrational levels, whereas the emission spectrum's shape reflects the distribution of ground state energy levels. Third, it can happen, as illustrated in Fig. 4.4, that the vibrational levels of the triplet states can overlap the vibrational levels of the singlet states. This affords the molecule a way of nonradiatively going from a singlet state into the corresponding triplet state, a phenomenon known as intersystem crossing.

Now, one would assume, from our discussion so far, that the excitation spectrum corresponds to the absorbance spectrum. This is not always the case and typically means that nonfluorescent spectroscopic species, such as dimers, are forming.

4.4 EXCITED STATE LIFETIME AND FLUORESCENCE QUANTUM EFFICIENCY

Up to this point, we have spoken in very vague terms about the excited state lifetime, τ_0. It is, of course, the case that not every molecule spends exactly time τ_0 in the excited state. In reality, τ_0 defines the probability, $p(t)$, that a fluorophore that is in the excited state at time 0 will still be there at time t. $p(t)$ is given by

$$p(t) = p_0 \exp\left(-\frac{t}{\tau_0}\right), \tag{4.8}$$

where p_0 is a normalization constant. We have expressed this equation in terms of the language of physics. Recognize, however, that it is equivalent to the experimental condition where we flash a cuvette with light and then watch the decay of fluorescence following the flash.

It is often convenient to think in terms of a rate of decay of the excited state, $k = 1/\tau_0$. Then

$$p(t) = p_0 \exp(-kt). \tag{4.9}$$

Of course, decay can occur by processes that compete with fluorescence. It is useful then to separate out a radiative k_r and nonradiative k_{nr}, part. Then,

$$k = k_r + k_{nr}. \tag{4.10}$$

We can then define the fluorescence quantum efficiency (QE) as the fraction of radiative decay. That is,

$$\mathrm{QE} = \frac{k_r}{k_r + k_{nr}}. \tag{4.11}$$

If we define a hypothetical excited state lifetime in which there would be no nonradiative decay and call this τ_0, we can express QE in terms of the excited state lifetimes:

$$\mathrm{QE} = \frac{\tau}{\tau_0}. \tag{4.12}$$

This last equation supports one's intuitive feeling that if one adds a nonradiative decay mechanism to a system, one shortens its excited state lifetime and makes it less fluorescent.

An analogy may be drawn to a bucket full of water. A pump fills the bucket at a constant rate. A hole in the bucket represents radiative decay. Poking a new hole (nonradiative decay) decreases both the amount of water in the bucket (fluorescence intensity) and the average time that any given water molecule spends in the bucket (excited state lifetime).

4.5 EXCITED STATE SATURATION

We can state this last point differently. Fluorescence intensity is proportional to the number of fluorophores in the excited state. Suppose that we have a very simple system of fluorophores at a total concentration C_T, which we excite with light of intensity I_0. Suppose that the system is driven up into its first excited singlet state, S_1, with a forward rate constant k_f and then comes back down with a reverse rate constant of k_r. Then, at equilibrium, we will have

$$k_f I_0 (C_T - [S_1]) = k_r [S_1]. \tag{4.13}$$

Equation (4.13) can be rearranged to obtain

$$[S_1] = \frac{k_f I_0 C_T}{k_f + k_f I_0}. \tag{4.14}$$

Equation (4.14) illustrates two important points. First, that for a constant illumination intensity, $[S_1]$ and therefore fluorescence intensity is proportional to the total concentration of the fluorophore. Second, fluorescence intensity is not proportional to illumination intensity. Doubling input intensity does not necessarily double output intensity. Rather, the excited state and the fluorescence intensity saturate with increasing illumination intensity. If you try to define quantum efficiency, not as we have above, but as (power out)/(power in), you paradoxically get an intensity-dependent quantum efficiency. This phenomenon of saturation is particularly important when dealing with laser illumination, for instance, in the confocal microscope.

4.6 NONRADIATIVE DECAY MECHANISMS

There is, of course, a whole battery of nonradiative decay mechanisms. Many of these mechanisms can be developed into tools, providing valuable information in biological experiments. Fundamentally, fluorescence is sensitive to molecular environment. Environmental changes such as ion concentrations, hydrophobicity, and pH can alter not only quantum efficiency but also the actual spectra of fluorophores. Now classic examples are the Ca^{2+}- and pH-sensitive fluorophores (Haugland, 1996). Using a membrane impermeable fluorescence-quenching agent, our laboratory has been able to determine the distribution of a fluorophore across a biological membrane (Wolf, 1985).

Excited states are chemically unstable. This is particularly true of triplet states, and results from the asymmetric charge distributions of excited states. The familiar phenomenon of fluorescence photobleaching on prolonged illumination is typically caused by chemical reactions of the triplet state, often with oxygen (Lakowicz, 1986). For fixed samples, one can slow photobleaching by using agents that inhibit such reactions. Photobleaching also has enabled us to develop the technique of fluorescence recovery after photobleaching (FRAP) to measure lateral diffusion (Axelrod, Koppel, Schlessinger, Elson, & Webb, 1976).

4.7 FLUORESCENCE RESONANCE ENERGY

An important example of a nonradiative decay mechanism is nonradiative fluorescence resonance energy transfer (FRET). FRET provides a "spectroscopic ruler" enabling one to measure distances of the order of 1–5 nm (Förster, 1948; Stryer & Haugland, 1967). The principle of FRET is illustrated in Figs. 4.6 and 4.7. FRET-based systems use two fluorophores, referred to as the donor–acceptor pair. Figure 4.6 shows the fluorescence excitation and emission spectra of a well-matched donor–acceptor pair. For the case shown, if the system is illuminated with light at ~480 nm, the donor will be excited and fluoresce, but the acceptor will not. Because the emission spectrum of the donor overlaps the absorbance spectrum of the acceptor, it is theoretically possible that light emitted by the donor would be reabsorbed by the acceptor and subsequently emitted by the acceptor in the red region of the spectrum at wavelengths >650 nm. In fact, such radiative energy transfer does not occur at typical biological concentrations <1 μM. Significantly, however, a different form of energy transfer, FRET, can occur when the two fluorophores are in close proximity. As shown in Fig. 4.7, if one has the donor alone and excites it with blue 480-nm light, the donor molecule absorbs the light and is driven into an excited state. Because these excited states typically have asymmetric molecular orbitals, we have illustrated them as dipoles. Organic

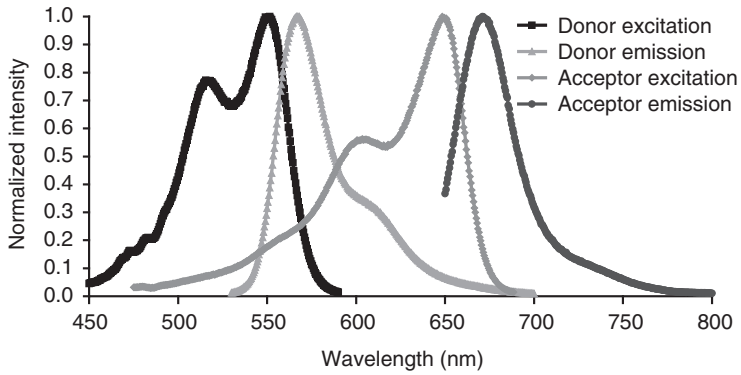

FIGURE 4.6

Spectral overlap between donor emission and acceptor excitation spectra in fluorescence resonance energy transfer.

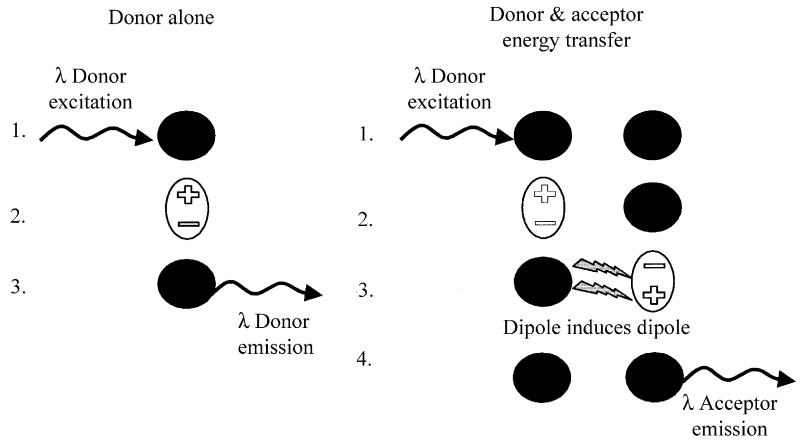

FIGURE 4.7

Schematic of the mechanism of fluorescence resonance energy transfer.

fluorophores remain in this state for a time, referred to as the excited state lifetime, that is typically ~10 ns, before they decay back to the ground state by emitting light, in this case, green light at a longer wavelength. However, if an acceptor molecule is in close proximity to the donor molecule, the donor's dipole can induce the acceptor molecule into its own dipolar-excited state. The acceptor can then decay to its own ground state, emitting red light with a wavelength >650 nm. FRET manifests itself in four major ways: (1) a decrease of donor fluorescence, (2) an increase in sensitized acceptor fluorescence, (3) a decrease in donor excite state lifetime, and (4) a depolarization of donor fluorescence relative to its excitation.

As described, FRET represents a dipole-induced dipole interaction. Therefore, the efficiency of this transfer falls off as the reciprocal of the sixth power of the intermolecular distance. Because the laws of quantum mechanics govern these processes, an individual donor molecule cannot give away part of its energy. It must give all of it or none of it to an acceptor. That is, there is a transfer process that represents a stochastic distribution of molecules transferring energy and molecules not transferring energy. Furthermore, transfer can only occur if the energy levels overlap. That is, there must be spectral overlap of the donor emission and acceptor absorbance spectra, as shown in Fig. 4.6. For transfer between a single donor and acceptor molecule, the efficiency of transfer, E_T, is given by

$$E_r = \frac{R_0^6}{R^6 + R_0^6}, \tag{4.15}$$

where R is the intermolecular distance, and R_0 is the distance where E_T is 50%. In the case where the donor is proximal to more than one acceptor, the relationship is more complex. Typically, R_0 is ~50 Å. However, with careful choice of the donor and acceptor pair, it can easily be manipulated between ~30 and 75 Å. The R^{-6} dependence of FRET makes it exquisitely sensitive to intermolecular distance. FRET only occurs when the donor and acceptor are in extremely close proximity to one another.

There is an important caveat to mention here, mainly the assumption of an R^{-6} dependence of the transfer efficiency. Early experimenters in this field were very rigorous in proving the validity of this assumption (see for instance Stryer & Haugland, 1967). We will not quote Hamlet again, but if one is going to use FRET quantitatively, it is important that the R^{-6} assumption holds. This assumption is equivalent to assuming singlet–singlet transfer. There are a number of cases in which the assumption is not valid. Also, it is quite often the case that FRET is not between a single donor–acceptor pair, but between a donor and a distribution of acceptors, in which case Eq. (4.15) does not apply (Dewey & Hammes, 1980; Fung & Stryer, 1978; Wolf, Winiski, Ting, Bocian, & Pagano, 1992).

An example of FRET is shown in Fig. 4.8 (Cardullo, Agrawal, Flores, Zamecnik, & Wolf, 1988). Here the 5′ ends of complementary oligonucleotides were labeled with fluorescein and rhodamine. Hybridization results in FRET between the two fluorophores. As the hybridization is melted by increased temperature, FRET is lost, as observed in a loss of sensitized rhodamine fluorescence and an increase or "dequenching" of the fluorocein fluorescence. The later is seen to parallel the absorbance at 260 nm, the hyperchromicity.

4.8 FLUORESCENCE DEPOLARIZATION

Polarization, as applied to fluorescence, can also yield useful information about biological systems (Weber, 1952). Figure 4.9 shows a cuvette in an L-format fluorimeter illuminated with polarized light. If one uses vertically polarized light, then

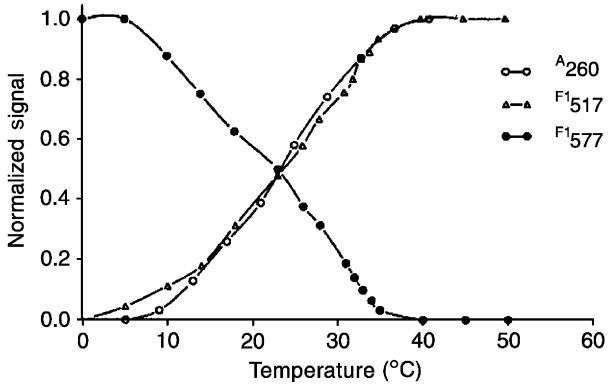

FIGURE 4.8

Oligonucleotide hybridization detected by FRET. The 5′ termini of a complementary oligonucleotide are labeled respectively with fluorescein and rhodamine. When hybridization occurs, there is FRET between the fluorescein and rhodamine. As the hybridization is melted, FRET is lost, as shown by the loss of sensitized rhodamine fluorescence, FI577, and the increase (dequenching) of fluorescein fluorescence, FI517. The later may be compared to the hyperchromicity as measured by absorbance at 260 nm, A260 (Cardullo et al., 1988).

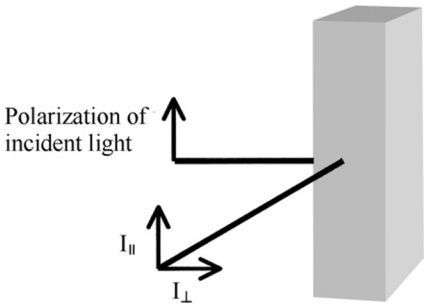

FIGURE 4.9

Schematic of a fluorescence polarization measurement.

one can measure an intensity parallel to the illumination polarization, $I_{\|}$, and an intensity perpendicular to the illumination polarization, $I_{\perp}$. You can think of a fluorophore as being an antenna. Those antennae parallel to the light's electric field vector become excited. If the molecules are not free to rotate, they stay in their initial orientation, so that when they emit light, the fluorescence is polarized parallel to the illumination. However, if the molecules are completely free to randomize their orientation before emitting light, they are just as likely to emit perpendicular as parallel to the exciting light, and the fluorescence is completely depolarized. In a real situation, the critical question is how much rotation occurs within the excited state lifetime. We can define the polarization

$$p = \frac{I_{\|} - I_{\perp}}{I_{\|} + I_{\perp}}, \tag{4.16}$$

or the anisotropy

$$r = \frac{I_{\|} - I_{\perp}}{I_{\|} + 2I_{\perp}}. \tag{4.17}$$

Then, for totally fluid medium, p and $r = 0$, whereas for totally rigid medium, p and $r = 1$.

A practical complication is that p and r are dependent not just on the rate of rotation but also on the excited state lifetime. Factors changing the rotation rate tend to also change the lifetime. Thus, from steady state measurements alone, one can never be sure what is changing. What one really needs to measure is the decay of fluorescence polarization using a fluorescence lifetime instrument. It often proves to be the case, particularly with membrane systems, that changes in fluorescence depolarization reflect not changes in the rates of molecular rotation, but changes in the limits of the rotation envelope.

Fluorescence polarization can also be used to answer such questions as how a given fluorophore orients itself in a membrane. Classic examples of this are papers from Webb's and Axelrod's groups studying the orientation of cyanine dyes in artificial and red blood cell membranes, respectively (Axelrod, 1979; Dragsten & Webb, 1978).

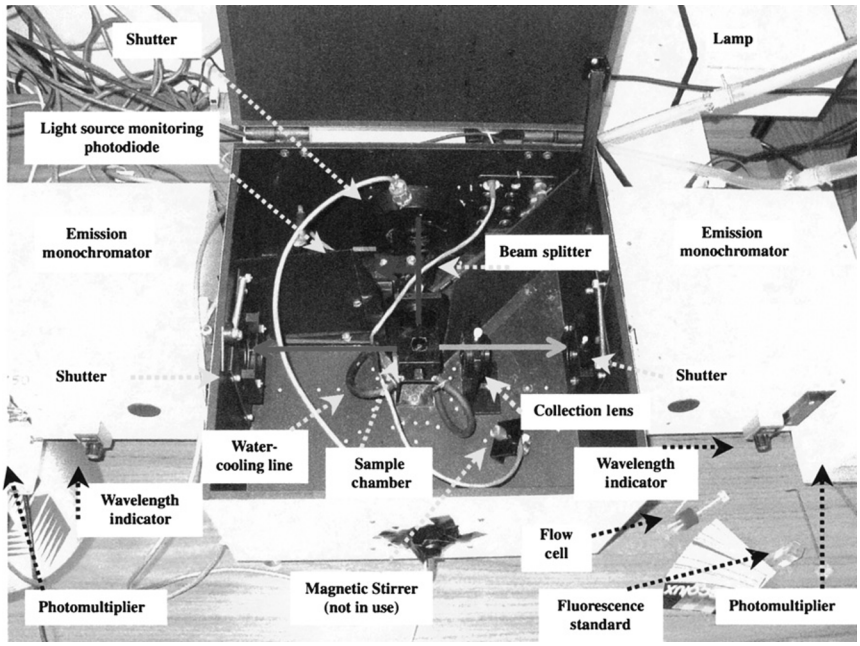

FIGURE 4.10

Typical fluorescence spectrofluorimeter. The instrument (from Photon Technologies, Inc.) shown is set up in the so-called "T configuration," where there is a single excitation monochromator and two emission monochromators.

4.9 MEASURING FLUORESCENCE IN THE STEADY STATE

Fluorescence is typically measured by an instrument called a spectrofluorimeter. Figure 4.10 illustrates the design of a spectrofluorimeter. Light from a xenon or mercury lamp is sent through a monochromator, which selects light from a narrow band of wavelengths. This light is sent through the sample. Fluorescence is typically measured perpendicular to the direction of illumination, the so-called L configuration. Emitted light is collected into a second monochromator, which selects the particular band of wavelengths to be measured. This light is then sent to a photomultiplier tube, which measures the fluorescence intensity. Typical photomultiplier tubes have quantum efficiencies of 10–15%. The monochromators of a fluorimeter can be driven individually so as to produce either excitation or emission spectra.

Spectrofluorimeters are more complicated devices than spectrophotometers in that they must correct for a number of factors: First, illumination intensities change with time. To correct for such fluctuations, a second light detector, typically a photodiode, is often employed to measure the illumination intensity, and the photomultiplier output is divided by this intensity. Second, lamps do not produce the same intensity at all wavelengths. Third, photomultipliers are not equally sensitive to all wavelengths.

The second and third factors must be corrected for if one needs to obtain absolute rather than relative spectra. Similar issues, as well as spatial corrections, must be applied to video detectors on microscopes if one wants to obtain quantitative spectral information.

4.10 CONSTRUCTION OF A MONOCHROMATOR

Figure 4.11 illustrates the construction of a monochromator, which is a device that selects for a light of a narrow band of wavelengths. A typical spectrofluorimeter has two monochromators, one at the excitation and one at the emission end. Let us consider the excitation monochromator in the figure. Light from a xenon arc lamp strikes a concave mirror directing the light to a diffraction grating. The grating, in turn, separates the light into its spectral components. This spectrum is then focused by a second concave mirror onto a surface. A slit selects the wavelengths that one wishes to use or measure. A lens in the fluorimeter focuses the light to the center of the sample cuvette. You will notice the drive mechanism coupled by universal joints that rotates the diffraction grating. This moves the spectrum at the slit and thereby changes the wavelength.

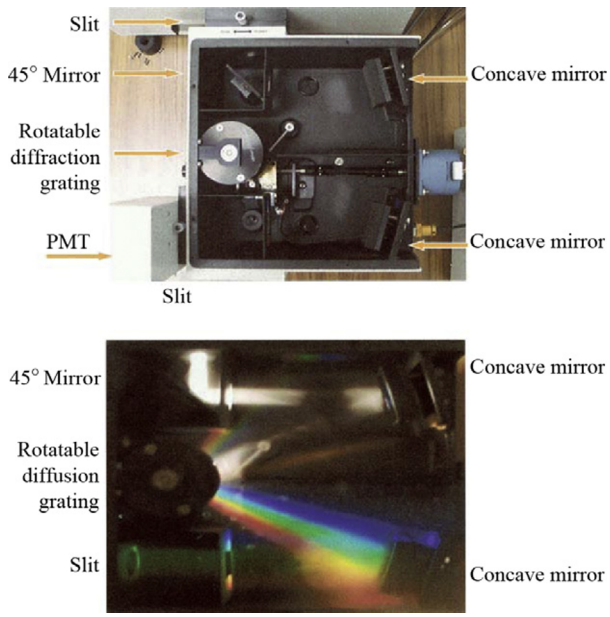

FIGURE 4.11

Design of a monochromator for fluorescence spectroscopy.

(from Photon Technology, Inc.)

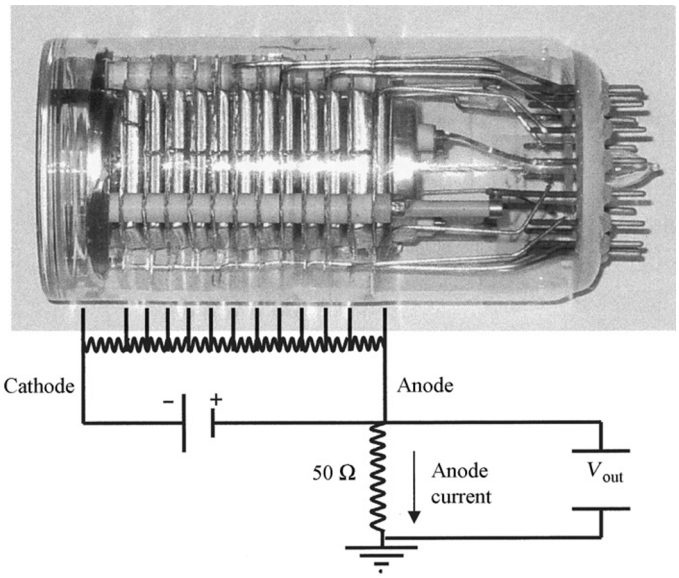

FIGURE 4.12

End-window photomultiplier tube.

4.11 CONSTRUCTION OF A PHOTOMULTIPLIER TUBE

The detector in most spectrofluorimeters, as well as microscope photometry systems, including confocal microscopes, is a photomultiplier tube (PMT) (Fig. 4.12). PMTs are highly sensitive linear devices for light detection. Light strikes a photosensitive photocathode held at voltage V_c. In response to light, the photocathode emits electrons on its back surface. These electrons are accelerated by voltage difference, $V_1 - V_c$, toward the first dynode. Because of the acceleration, an electron striking the dynode's front surface causes multiple electrons to be emitted from the dynode's back surface. These emitted electrons are then accelerated toward the second dynode by the voltage difference $V_2 - V_1$. The process continues down the dynode chain (typical photomultipliers today have as many as 11 dynodes) until a considerable current is generated by this multiplication process at the PMTs anode.

4.12 MEASURING FLUORESCENCE IN THE TIME-DOMAIN

Considerable information about the environment of a fluorophore can be obtained by measuring the excited state lifetime or, inversely, the rate of fluorescence decay [Eq. (4.9)]. Solvated molecules are in equilibrium with their environments, and driving them into excited states alters this equilibrium. The solvent environment must adjust to the new charge distribution presented by the excited state. As a result, lifetime can be very sensitive to the local environment. Although similar information is contained in the quantum efficiency and spectrum, these parameters represent an

average over the ensemble of fluorophores. Lifetime measurement offers the possibility of heterogeneity analysis in which the populations emitting at different lifetimes can be mathematical or physically distinguished.

The measurement of fluorescence excited state lifetimes is a very complex field, and we can only touch on some of the critical issues. The reader is referred to several standard texts on this subject (Cundall & Dale, 1980; Demas, 1983; Lakowicz, 1986), as well as to Chapter 17 by Swedlow, this volume on lifetime imaging in the microscope.

We have already described, in Section 4.5, the concept of flashing with a pulse of light and measuring the decay of fluorescence. In Eq. (4.9), we spoke about a single exponential decay. Here we will generalize this slightly, allowing for two exponential decay times τ_1 and τ_2 with fractions f_1 and f_2, respectively. Then Eq. (4.9) becomes

$$p(t) = p_0\left\{f_1\left[\exp\left(-\frac{t}{\tau_1}\right)\right](1-f_1) + \left[\exp\left(-\frac{t}{\tau_2}\right)\right]\right\}, \tag{4.18}$$

where we have recognized that $f_2 = 1 - f_1$. Of course, we can generalize this even further to, say, N decay times:

$$p(t) = p_0\left\{\sum_i^N F_i \exp\left(-\frac{t}{\tau_2}\right)\right\}, \tag{4.19}$$

where

$$\sum_i^N f_i = 1. \tag{4.20}$$

In reality, although some systems can be treated as one or two exponential decay times, many fluorescent systems are best treated as a continuum distribution of lifetimes.

Although the conceptual experiment of flashing with a pulse and measuring the decay of fluorescence can be done in some cases, in most instances it proves difficult for two reasons. First, as most organic lifetimes are in the nanosecond time scale, to be effectively an impulse, the light pulse must have a picosecond or faster width. This can only be achieved with relatively high-cost pulsed laser systems. Second, the response of the detector limits our ability to measure fluorescence decay as illustrated ideally in Fig. 4.13. Here we have illuminated with an impulse. The first photon locks up the detector for some dead time, and this dead time is followed by a ringing in the detector. As a result, the simple experiment of pulse and measure continuously is difficult.

A number of strategies have been developed to overcome these problems. We will here focus on four of them: boxcar-gated detection, streak cameras, photon correlation, and phase modulation.

4.12.1 Boxcar-gated detection method

The concept of boxcar-gated detection is illustrated in Fig. 4.14 for Photon Technology Incorporated's (PTI's) fluorescence lifetime system. Here a nitrogen laser pulses a dye laser that is coupled to the sample chamber with a fiber optic. A beam splitter carries

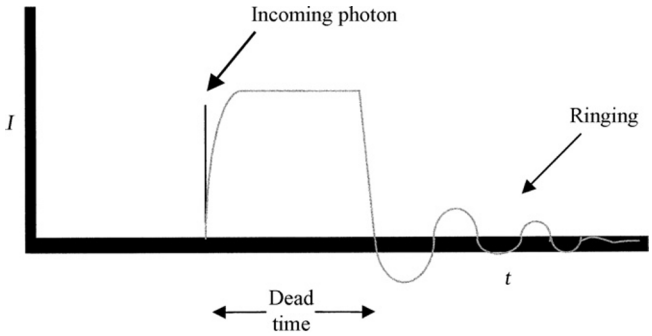

FIGURE 4.13

Schematic of the response of a photomultiplier to an incoming photon illustrating rise time, dead time, and after-pulsing or ringing.

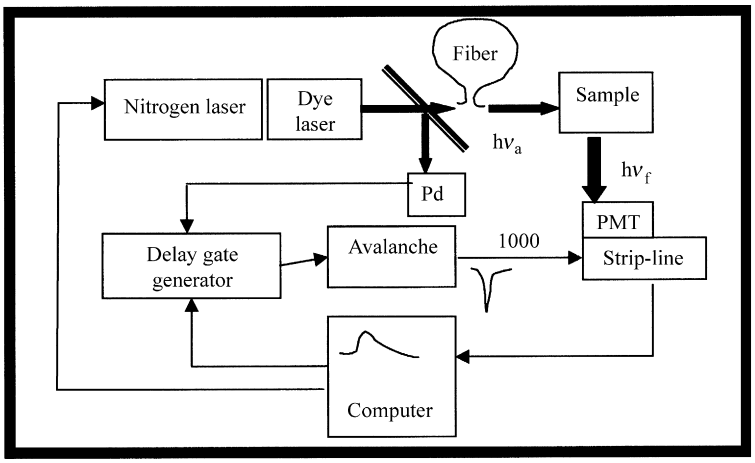

FIGURE 4.14

Boxcar-gated detection measurement of fluorescence excited state lifetimes (from Photon Technologies, Inc.). PMT, photo multiplier tube.

some of the pulse to a photodiode, which triggers a delay gate generator. This causes a pulse delay relative to the input pulse. This pulse is used to trigger a PMT. The PMT only measures during this delayed pulse. As a result, current is only measured by the PMT during the delayed pulse. By systematically sweeping the delay time, one can, over the course of many pulses, build up a measurement of the decay process. Recent advances in light emitting diode (LED) technology have enabled pulsed nitrogen lasers to be replaced by rapidly pulsed LEDs. One such instrument is PTI's "Easy Life System." In addition to the cost advantage of the LEDs compared to pulsed laser sources, LEDs are now available in a relatively wide spectrum of wavelengths, making application of this technology to most common fluorescent dyes possible.

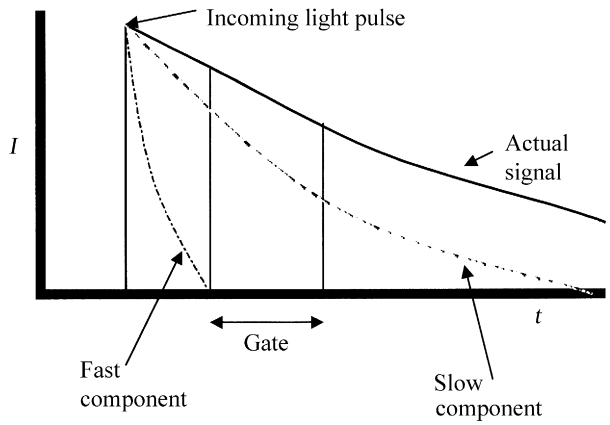

FIGURE 4.15

Schematic of how gating can be used to suppress a fast lifetime component.

An interesting feature of this approach is illustrated in Fig. 4.15. Suppose that one has a double exponential decay with a relatively fast and a relatively slow lifetime component. By judicious choice of the delay, one can effectively "tune out" the fast lifetime component. As discussed in Chapter 17 by Swedlow, this volume, this can be effectively exploited in lifetime imaging analysis.

As we have already discussed, one must often correct for the finite pulse width of the light source. Effectively, the light pulse, $I_{ex}(t')$ can be divided into an infinite number of infinitely narrow slices each occurring at its own time t'. Each slice will elicit an exponential decay:

$$I(t) = \int_0^\infty I_{ex}(t')e^{-(t-t')/\tau}dt'. \tag{4.21}$$

This can, of course, be generalized to multiple exponential decay. An example of such an analysis made on the PTI instrument is shown in Fig. 4.16. One sees the incident light pulse, the fluorescence response, the fit of the fluorescence response assuming the pulse width, and the exponential decay correcting for this finite width of the incident pulse.

4.12.2 Streak camera method

Streak cameras measure fluorescence lifetimes by translating a temporal difference into a spatial difference. Figure 4.17 illustrates how this is accomplished in the Hamamatsu streak camera. In the figure, the incident light has been split along the horizontal axis into different wavelengths using, for instance, a diffraction grating. A horizontal slit is placed immediately behind the photocathode. The electrons are accelerated toward a microchannel plate. Vertical electrodes are used to rapidly sweep the electron beam along the vertical axis as electrons accelerate toward the

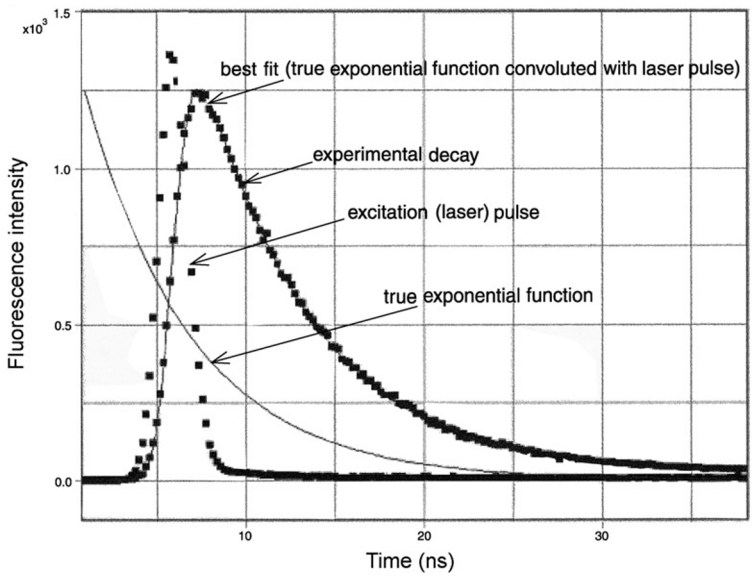

FIGURE 4.16

Fluorescence lifetime data from the Photon Technology, Inc., gated-boxcar detection system. Note that because the illumination is not a perfect pulse, the pulse must be deconvolved from the emission signal to obtain the "true" exponential decay.

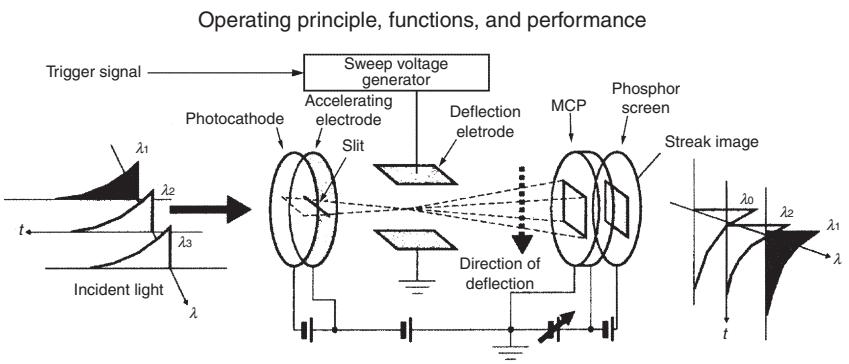

FIGURE 4.17

Operating principle of measurement of fluorescence lifetimes using a streak camera.

(from Hamamatsu Photonics)

microchannel plate. As a result, the vertical axis becomes time and the horizontal axis is wavelength. A phosphor screen at the anode end of the microchannel plate converts this image back to light, which can then be examined using a video camera. The signal from the camera is integrated over multiple pulses. Data obtained from the streak camera give not only the fluorescence decay with time but also the wavelength

dependence of this decay. As the solvent surrounding the fluorophores adjusts to the altered electronic distribution of the excited state, the energy levels and, therefore, the lifetimes change. Time-resolved spectra provide a further level of information about the molecular *milieu*.

4.12.3 Photon correlation method

The decays $p(t)$ in Eqs. (4.18) and (4.19) represent the probability that a molecule in the excited state at time 0 is still in the excited state at some later time t. This probability is equivalent to the distribution of times between absorption of a photon by the fluorophores and emission of a photon of fluorescence. The photon correlation method seeks to directly measure that distribution function. The instrumentation is shown schematically in Fig. 4.18. Here a photodetector detects the illuminating light pulse and initiates a timing circuit. The timing circuit is turned off by the detection of the fluorescence by the photomultiplier. As a result, the circuit measures the time between excitation and emission. By repeating this measurement many times, one obtains the probability distribution of times between excitation and emission. The advantage here is that it is a low-light level technique, as the goal is to measure only one photon per pulse. The photon correlation technique has now been extended to imaging lifetime analysis (see Chapter 24 by Chang et al., volume 81, 2007) and commercial systems are available from Becker and Hickl (Berlin, Germany).

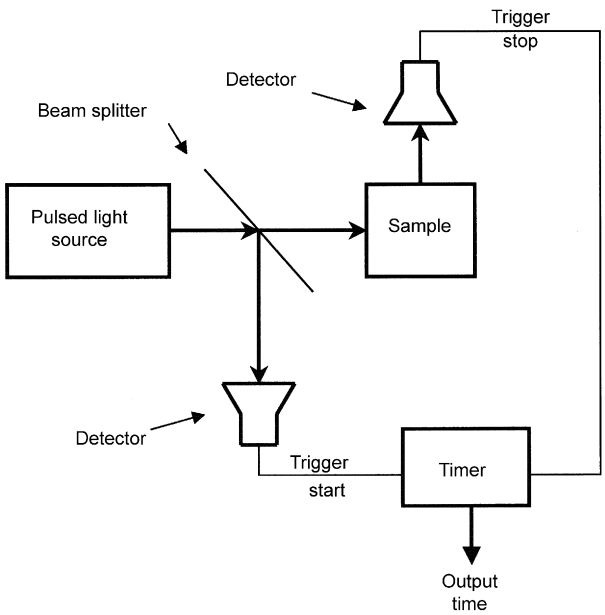

FIGURE 4.18

Schematic diagram of the photon correlation method of measuring fluorescence lifetimes.

4.12.4 Note on the process of "deconvolution"

As is the case in the boxcar method, one must "deconvolve" the shape of the excitation pulse to obtain the true shape of the decay for a pulse of infinitesimal width. The process of "deconvolution" represents starting with $I(t)$ and solving Eq. (4.21) for the exponential term or, in the more general case, terms. After spending a few moments considering how this might be done, one soon realizes that it is not a trivial problem. The issue of temporal deconvolution of the light pulse directly parallels the issue of spatial deconvolution of out of focus fluorescence, which will be discussed in the Chapter 20 by Wang, volume 81, 2007 and Chapter 17 by Swedlow, this volume. Indeed, the temporal problem can be solved by very similar Fourier and iterative reconvolution techniques. For a discussion of Fourier transforms see Chapter 2 by Wolf, this volume. The reader is referred to Cundall & Dale, 1980; Demas, 1983 for a discussion of iterative reconvolution applied to fluorescence lifetime analysis, for a discussion of a different approach known as the method of moments.

4.12.5 Phase modulation method

In Chapter 2 by Wolf, this volume, we discussed the fact that determining the response to an impulse, the so-called point spread function, defines the systems response to any real distribution of intensities because any real object in the microscope is composed of an infinite number of points. We went on to describe the concept of Fourier transforms, where we consider not the response to a point but to a sine wave in space. We introduced the concept of spatial frequencies and the fact that any object is composed of an infinite number of sine waves or spatial frequencies. We also described the Fourier treatment of a step function and of its first derivative, the impulse. This connected the two treatments by demonstrating that an impulse is composed of an infinite number, which is all of the spatial frequencies.

Let us now consider Fig. 4.19, which shows a conventional spectrofluorimeter that is modified by introducing modulators of the incident light intensity and the detector sensitivity. For the input side, this modulation is readily accomplished with an acousto-optical modulator. Suppose that we modulate the incident light sinusoidally, as shown in Fig. 4.20A. Now suppose that the sample is fluorescent and has a single exponential decay rate. We can then determine the systems response by application of Eq. (4.21) in which $I_{ex}(t') = \sin(\omega t)$, where ω is the frequency in rad/s. In Fig. 4.20B, we have applied Eq. (4.21) numerically to the sine wave of Fig. 4.20A. Conceptually, this involves dividing the sine wave into an infinite number of slices. Each slice causes an exponential decay, and the composite effect is the sum of this infinite number of exponentials. We observe that this convolution has two effects. First, the resultant wave is shifted in time or phase relative to the excitation wave, and second, it is filled in or modulated in intensity. For a single exponential decay, the fluorescence lifetime can be calculated from the phase shift, ϕ, from the equation (Lakowicz, 1986):

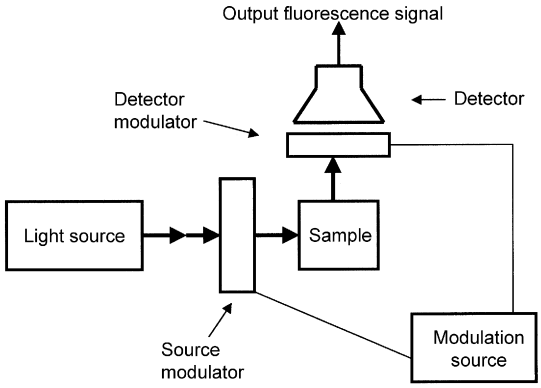

FIGURE 4.19

Schematic diagram of a phase modulation spectrofluorimeter. The light source and the detector can be independently modulated. This is typically done either at the same frequency as a phase shift (homodyne detection) or at different frequencies (heterodyne detection).

$$\tau = \frac{\arctan(\phi)}{\omega}, \tag{4.22}$$

or from the demodulation of the sine wave, m:

$$\tau = \frac{m^2 - 1}{\omega^2}. \tag{4.23}$$

For the single exponential decay, the phase and demodulation lifetimes are the same. The two become different for multiple exponential decay. For a more complete discussion of this important aspect of fluorescence spectroscopy, the reader is referred to several excellent texts (Cundall & Dale, 1980; Demas, 1983; Lakowicz, 1986).

Now suppose that we modulate the detector as well as the excitation light. In the case of photomultiplier tubes, this is accomplished by modulating the cathode to anode voltage. Suppose that we modulate the detector at the same frequency as the excitation, a condition referred to as homodyne detection. If we introduce an adjustable phase shift between the excitation and detector modulations, then what will happen is that the range or modulation of the detector signal will be maximized when the phase shift $= \phi$ as shown in Fig. 4.20C, and will be a minimum when the phase shift $= \phi + 180°$, as shown in Fig. 4.20D. Effectively, one can tune in or out a signal based on its fluorescence lifetime.

As typical lifetimes are on the order of nanoseconds, modulation frequencies need to be on the order of 100 MHz, which also requires measurement of the sine wave at this time scale as well. This problem can be overcome by modulating the detector at a slightly different frequency. The resultant signal is then a "beat" signal of frequency equal to the difference between the two modulation frequencies. This is a condition known as heterodyne detection.

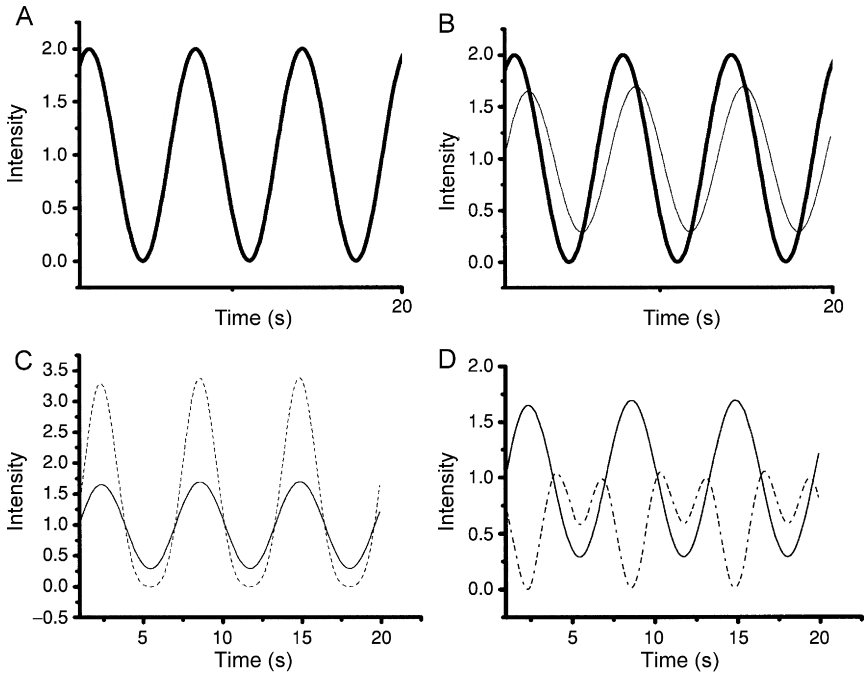

FIGURE 4.20

Phase modulation spectrofluorimetry (homodyne detection). (A) The illuminating light source is modulated sinusoidally (—). (B) In response to this modulation, and as a result of the probabilistic nature of emission, the fluorescence shows a phase shift and demodulation of the signal amplitude (—). (C) Modulating the detector in phase with the illumination modulation enhances the fluorescence (----). (D) Modulating the detector 180° out of phase with the illumination modulation suppresses the fluorescence (- - -).

Commercial instruments for phase modulation imaging microscopy are now available from companies such as Intelligent Imaging Innovations (Denver, CO). The Chapter 24 by Chang et al., volume 81, 2007 shows how pulse, photon correlation, and phase modulation techniques can be applied to microscopy. Examples of data obtained through a microscope with both techniques are illustrated.

4.13 FILTERS FOR THE SELECTION OF WAVELENGTH

Wavelength selection for fluorescence microscopy is usually accomplished with filters rather than monochromators. Given that fluorescence signals are typically 10^6-fold less than the incident exciting light, the design specifications of such filters are demanding. We will confine our discussion here to the types of filters typically available on fluorescence microscopes. The top panel in Fig. 4.21 shows the percentage transmission of

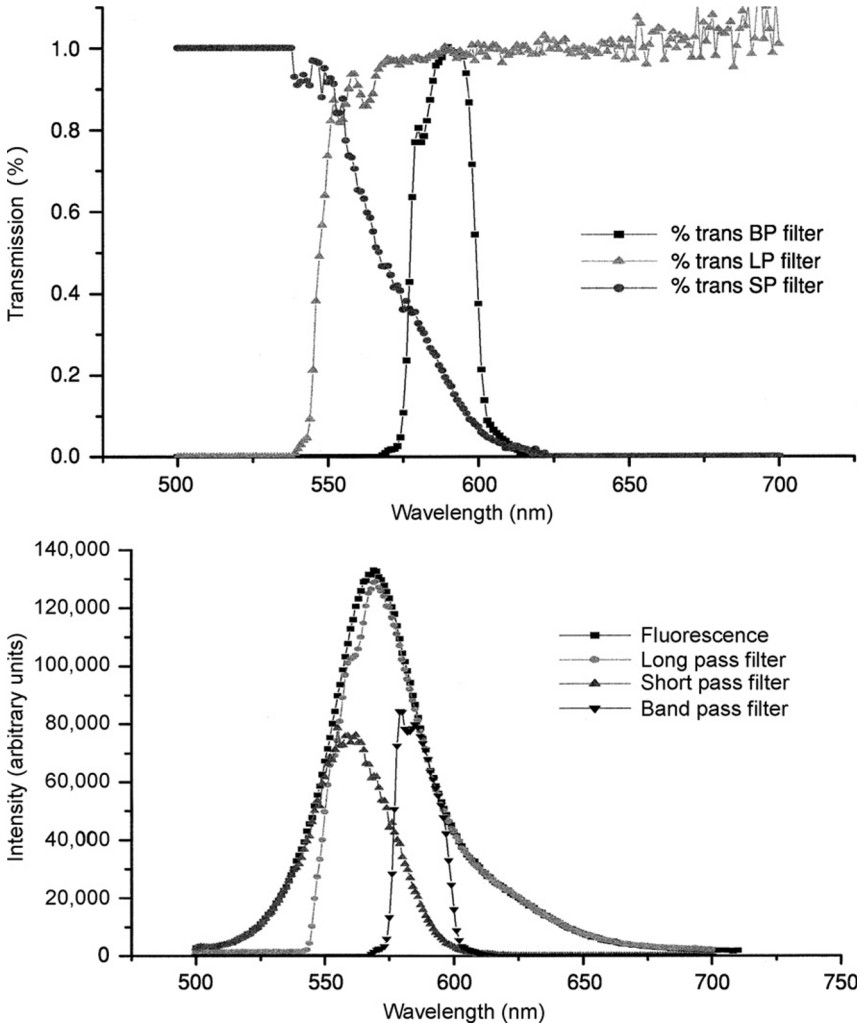

FIGURE 4.21

Filters for wavelength detection. (Top) The percentage transmission of a short-pass, long-pass, and band-pass filter. (Bottom) Fluorescence emission spectrum unaltered and subjected to these filters.

a short-pass, band-pass, and long-pass filter. The lower panel shows a fluorescence emission spectrum of a fluorescent dye; first, in the absence of any filter and second, through the short-pass, band-pass, and long-pass filters of the top panel. There are, in addition, multipass filters that allow more than one band or region to pass.

Most of the filters encountered in fluorescence microscopy are either absorbing glass filters or interference filters made by depositing a set of thin films on the glass.

The distinction is important. Unlike absorbing glass filters, thin film filters respond differently to the different components of plane polarization and, additionally, are designed for a particular incident angle, usually either 0° or 45°. One can, in fact, shift the wavelength selection properties of such filters by rotating them around either of the axes, which are perpendicular to the direction of light propagation.

4.14 THE FLUORESCENCE MICROSCOPE

The fundamental design of the epiillumination fluorescence microscope is illustrated in Fig. 4.22. One will immediately recognize that this design is essentially a folded form of Kohler illumination (see Chapter 1 by Sluder and Nordberg, this volume; and Chapter 3 by Ernst Keller, volume 81, 2007). The folded epiillumination design enables one to use the objective simultaneously as the condenser. Note that the light source is typically a mercury or xenon lamp. In most systems, the lamp is parallel to a parabolic mirror, which is adjusted so that the reflection of the lamp is focused back on the source. In a different design, an elliptical mirror, pioneered by Photon Technologies, Inc., NJ, is used and the lamp penetrates and is perpendicular to the mirror. The lamp is situated at a focus of the ellipse. As described in Chapter 1 by Sluder and Nordberg, this volume, the lamp is focused to and, therefore, conjugates with the back focal plane of the objective. The specimen plane forms a real image at and is therefore conjugate with the intermediate image plane. Combining these two terminologies, we say that the intermediate image plane is a conjugate image plane to the specimen or object plane. Significantly, in fluorescence microscope, there is a second intermediate

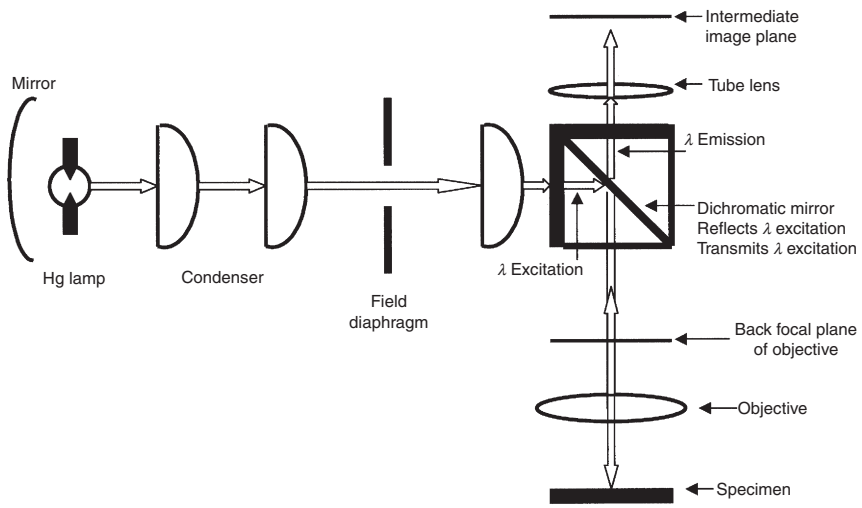

FIGURE 4.22

Schematic diagram of the epiillumination optics of a fluorescence microscope.

image plane, which falls at the field diaphragm of the illuminator. This can usually be located because there is a diaphragm or aperture, the field stop, at this position. This intermediate image plane is significant to people who wish to focus a laser onto the sample. A beam focused at the image plane is focused on the sample. To minimize the beam at the object plane, one often needs to expand it so that it fills the back focal plane of the objective. For more on coupling lasers to microscopes either directly or with fiber optics see Chapter 22 by Murray, volume 81, 2007.

Incident light from the lamp passes through the fluorescence filter cube. The excitation filter, usually a low-pass or band-pass filter, selects the excitation wavelengths. Further selection is accomplished by a second filter, referred to as the dichromatic mirror, which typically is a long-pass filter that reflects the excitation light into the objective. The fluorescence light returns through the objective. However, its longer wavelengths are transmitted by the dichromatic mirror. Further selection of fluorescence wavelengths is affected by the emission filter, typically a long-pass or band-pass filter, which selects wavelengths for observation. Most modern fluorescence microscopes have multiple filter cubes and a slider or turret for choosing between these cubes.

4.15 THE POWER OF FLUORESCENCE MICROSCOPY

We began this chapter with a discussion of physical advantages of fluorescence as a molecular detection technique. It is perhaps fitting to end with the biological advantages. The real power of the fluorescence spectroscopy and microscopy as tools of modern biology and biochemistry results not only from the exquisite sensitivity of fluorescence to detect down to even single molecules but also from our ability to selectively label specific biomolecules of interest. This began with the use of antibodies to localize specific molecules within a cell, but today has broadened to include a wide and ever-growing variety of molecular probes (Haugland, 1996). The various properties of the phenomenon of fluorescence have opened windows to explore the environments within cells and to study the dynamics of molecules. It is easy to fall into the trap of becoming seduced and enamored of "pretty pictures," and it is the responsibility of investigators to learn to properly treat quantitative data obtained with the fluorescence microscope.

In this chapter, we have tried to introduce and provide a basis for understanding some of these issues. Several further chapters, particularly those concerned with detectors, image processing, ratio-imaging, FRET, deconvolution, fluorescence correlation spectroscopy, and lifetime imaging, follow up on this quintessential theme. I am tempted to paraphrase Shakespeare, again, and say that, "The fault, dear reader, is not in our fluorescence microscopes, but in ourselves that we are underlings." However, I prefer to end more positively and point out that if one takes the time and effort to understand the proper use of the tools one is using, then one has heeded the advice of Lady Macbeth when asked what happens if we fail:

"We fail! But screw your courage to the sticking place, and we'll not fail."

William Shakespeare, Macbeth; Act I, Scene VII, lines 60–70

Some Useful Web Sources

There are a large number of useful Web-based resources about fluorescence and fluorescence microscopy, for instance, http://probes.invitrogen.com/resources/education/?&CID=KNC-GOOGLE&s_kwcid=fluorescence|510808419. *The Handbook of Fluorescence* by Haugland is now available on the Web at http://probes.invitrogen.com/handbook/. The major manufacturers of fluorescence microscopes each have tutorial Websites with the added advantage that the guide the user to product specific information: Carl Zeiss, http://www.micro-shop.zeiss.com/us/us_en/spektral.php; Leica, http://www.fluorescence-microscopy.com; Nikon, http://www.microscopyu.com/articles/fluorescence/index.html; and Olympus, http://www.olympusmicro.com/primer/techniques/fluorescence/fluorofiltershome.html. Manufacturers of filters for fluorescence microscopy similarly offer very useful information and tools for custom filter cube design: Omega Filters, http://www.omegafilters.com and Chroma, http://www.chroma.com.

Acknowledgments

I thank Kathryn Sears, Leya Bergquist, Dylan Bulseco, and Kip Sluder for help in the preparation of this chapter.

References

Axelrod, D. (1979). Carbocyanine dye orientation in red cell membrane studied by fluorescence polarization. *Biophysical Journal*, *26*, 557–574.

Axelrod, D., Koppel, D. E., Schlessinger, J., Elson, E. L., & Webb, W. W. (1976). Mobility measurement by analysis of fluorescence photobleaching kinetics. *Biophysical Journal*, *16*, 1055–1069.

Barak, L. S., & Webb, W. W. (1982). Diffusion of low density lipoprotein-receptor complex on human fibroblasts. *The Journal of Cell Biology*, *95*, 846–852.

Becker, R. (1969). *Theory and interpretation of fluorescence and phosphorescence*. New York: John Wiley-Interscience.

Cardullo, R. A., Agrawal, S., Flores, C., Zamecnik, P., & Wolf, D. E. (1988). Detection of oligonucleotide hybridization by nonradiative fluorescence resonance energy transfer. *Proceedings of the National Academy of Sciences of the United States of America*, *85*, 8790–8794.

Cundall, R. B., & Dale, R. E. (1980). *Time-resolved fluorescence spectroscopy in biochemistry and biology*. New York: Plenum Press.

Demas, J. N. (1983). *Excites state lifetime measurements*. New York: Academic Press.

Dewey, T. G., & Hammes, G. G. (1980). Calculation of fluorescence resonance energy transfer on surfaces. *Biophysical Journal*, *32*, 1023–1035.

Dragsten, P., & Webb, W. W. (1978). Mechanism of the membrane potential sensitivity of the fluorescent membrane probe merocyanine 540. *Biochemistry*, *17*, 5228–5240.

Förster, T. (1948). Intermolecular energy migration and fluorescence. *Annalen der Physik (Leipzig)*, *2*, 55–75.

Fung, B. K. K., & Stryer, L. (1978). Surface density determination in membranes by fluorescence energy transfer. *Biochemistry*, *17*, 5241–5248.

Guibault, G. G. (1973). *Practical fluorescence theory, methods, and techniques.* New York: Marcel Dekker.

Haugland, R. (1996). *Handbook of fluorescent probes and research chemicals.* Eugene, OR: Molecular Probes.

Lakowicz, J. R. (1986). *Principles of fluorescence spectroscopy.* New York: Plenum Press.

Mavrodineanu, R., Shultz, J. I., & Menis, O. (1973). *Accuracy in spectrophotometry and luminescence measurements.* Washington, DC: U.S. Department of Commerce, NBS.

Parker, C. A. (1968). *Photoluminescence of solutions.* Amsterdam: Elsevier.

Stryer, L., & Haugland, R. P. (1967). Energy transfer: A spectroscopic ruler. *Proceedings of the National Academy of Sciences of the United States of America*, *58*, 719–726.

Weber, G. (1952). Polarization of the fluorescence of macromolecules. 1. Theory and experimental method. *The Biochemical Journal*, *51*, 145–155.

Wolf, D. E. (1985). Determination of the sidedness of carbocyanine dye labelling of membranes. *Biochemistry*, *24*, 582–586.

Wolf, D. E., Winiski, A. P., Ting, A. E., Bocian, K. M., & Pagano, R. E. (1992). Determination of the transbilayer distribution of fluorescent lipid analogues by nonradiative fluorescence resonance energy transfer. *Biochemistry*, *31*, 2865–2873.

CHAPTER

Fluorescent Protein Applications in Microscopy

5

Whitney L. Johnson and Aaron F. Straight

Department of Biochemistry, Stanford Medical School, Stanford University, Stanford, California, USA

CHAPTER OUTLINE

5.1 The Identification of Green Fluorescent Protein 100
5.2 Formation of the GFP Chromophore 101
5.3 The Structure of GFP 103
5.4 Mutagenesis to Alter the Properties of GFP 104
5.5 Imaging FPs 108
5.5.1 Components of the Optical System 108
5.5.2 Reducing Unwanted Fluorescence 108
5.5.3 Selecting Appropriate Filters and Chromatic Mirrors 109
5.5.4 Selecting the Appropriate FP 109
5.5.5 Constructing FP Fusions 111
5.5.6 Note on Fixation of FPs 112
5.5.7 Time-Lapse Imaging of FPs 112
5.6 Applications of FP Imaging 114
5.6.1 Multiwavelength Imaging of FPs 114
5.6.2 Monitoring Intracellular Environments Using FPs 114
5.6.3 Monitoring Protein–Protein Interactions in vivo 115
5.6.4 Protein Dynamic Measurements using FP Photobleaching and Activation 116
5.6.5 Super-resolution Imaging with Photoactivatable FPs 117
Conclusion 117
References 118

Abstract

The use of fluorescent proteins (FPs) in modern cell biology and microscopy has had an extraordinary impact on our ability to investigate dynamic processes in living cells. FPs are unique in that fluorescence is encoded solely by the primary amino

Methods in Cell Biology, Volume 114 **ISSN 0091-679X**
Copyright © 2013 Elsevier Inc. All rights reserved.
http://dx.doi.org/10.1016/B978-0-12-407761-4.00005-1

acid sequence of the FP and does not require enzymatic modification or cofactors. This genetically encoded fluorescence enables the expression of FPs in diverse cells and organisms and the detection of that fluorescence in living systems. This chapter focuses on microscopy-based applications of FP detection to monitor protein localization, dynamics, interaction, and the cellular environment.

5.1 THE IDENTIFICATION OF GREEN FLUORESCENT PROTEIN

The isolation of green fluorescent protein (GFP) was first described by Shimomura, Johnson, & Saiga, 1962 as a footnote to their studies about the aequorin protein from the jellyfish *Aequorea aequorea*. *A. aequorea* normally emits a greenish luminescence from the light organs around the rim of the jellyfish. During the isolation of the luminescence system of *Aequorea*, Shimomura and colleagues noted that the luminescence from aequorin was blue rather than the green luminescence of the intact organism. However, they also noted that

> *A protein giving solutions that look slightly greenish in sunlight though only yellowish under tungsten lights, and exhibiting a very bright, greenish fluorescence in the ultraviolet of a Mineralite, has also been isolated from squeezates. No indications of a luminescent reaction of this sustance [sic] could be detected. Studies of the emission spectra of both this protein and aequorin are in progress.*

Shortly after their observation of the green fluorescence, the protein was purified and characterized and eventually given the name green fluorescent protein (Hastings & Morin, 1969; Johnson et al., 1962).

Prior to the cloning of GFP, its fluorescent properties were characterized in detail through careful biochemical analysis. Purified aequorin emits blue light when stimulated with calcium as the result of oxidation of coelenterazine to coelenteramide, but the light organs of *Aequorea* emit a greenish light upon stimulation of the organism. Morin and Hastings provided an explanation for this wavelength shift by demonstrating that the excited state energy of calcium-stimulated aequorin could be transferred to GFP via the Förster mechanism, resulting in the longer wavelength green emission from GFP (Fig. 5.1; Morin & Hastings, 1971). Through a combination of intuition and brute force biochemistry, Shimomura, 1979 first deciphered the structure of the GFP chromophore as a *p*-hydroxybenzyl imidazolone. GFP was even crystallized in 1974 using protein isolated from tens of thousands of jellyfish, and the energy transfer reaction between aequorin and GFP was studied in detail (Morise, Shimomura, Johnson, & Winant, 1974).

Although these elegant biochemical studies had demonstrated many of the properties of GFP, the experiments that catapulted GFP into widespread use were the cloning of the gene for GFP from *Aequorea* and the subsequent expression of the protein in other organisms. Prasher, Eckenrode, Ward, Prendergast, & Cormier, 1992 isolated a full-length cDNA clone encoding GFP, and the primary sequence demonstrated that the chromophore of the protein was derived from the amino acid triplet Ser-Tyr-Gly at positions 65-66-67. Chromophore formation is resulted from cyclization of the peptide backbone and oxidation of the tyrosine side chain (Cody, Prasher, Westler, Prendergast, & Ward, 1993), but as Cody et al. pointed out

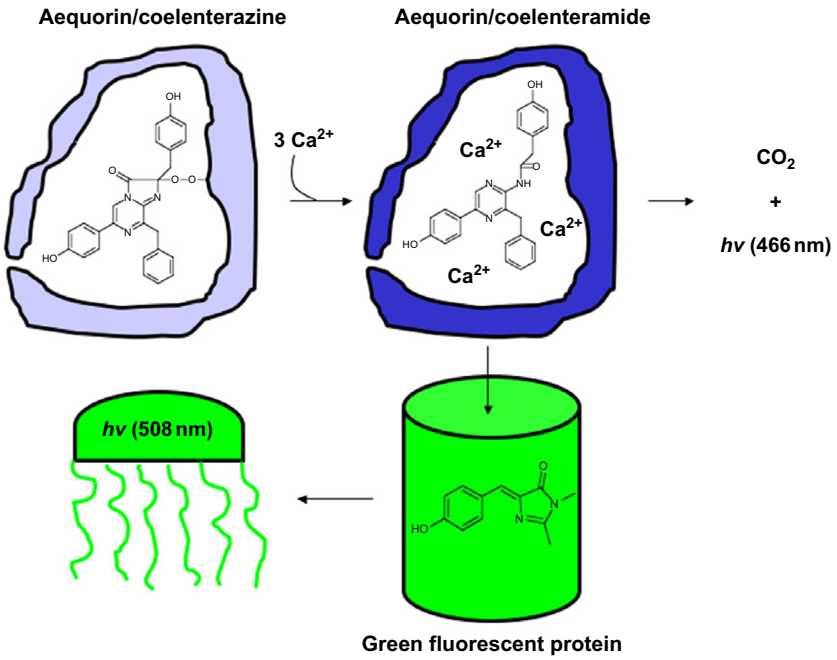

FIGURE 5.1

Energy transfer between aequorin and GFP. Aequorin with its attached cofactor coelenterazine is stimulated to luminesce when calcium ions bind. In the absence of GFP, aequorin emits light of 466 nm. In the presence of GFP, the excited state energy of aequorin can be transferred to GFP resulting in the longer wavelength emission at 508 nm.

> *It is very unlikely that the chromophore forms spontaneously, but its formation probably requires some enzymatic machinery.*

Truly surprising were the experiments that followed from Chalfie, Tu, Euskirchen, Ward, & Prasher, 1994 and Inouye & Tsuji, 1994 showing that GFP could be expressed in other organisms and still become fluorescent. This demonstrated that no *Aequorea* specific cofactors were required for chromophore formation, and also led to the realization that GFP could be used in virtually any organism to track gene expression, protein dynamics, and more. The discovery, characterization, and optimization of GFP have since revolutionized imaging in live biological systems, and earned Osamu Shimomura, Martin Chalfie, and Roger Y. Tsien the Nobel Prize in Chemistry in 2008.

5.2 FORMATION OF THE GFP CHROMOPHORE

The primary amino acid sequence of GFP is sufficient to direct the formation of the functional chromophore. Heim, Prasher & Tsien, 1994 first proposed a reaction scheme to explain how GFP might spontaneously mature into a fluorescent protein

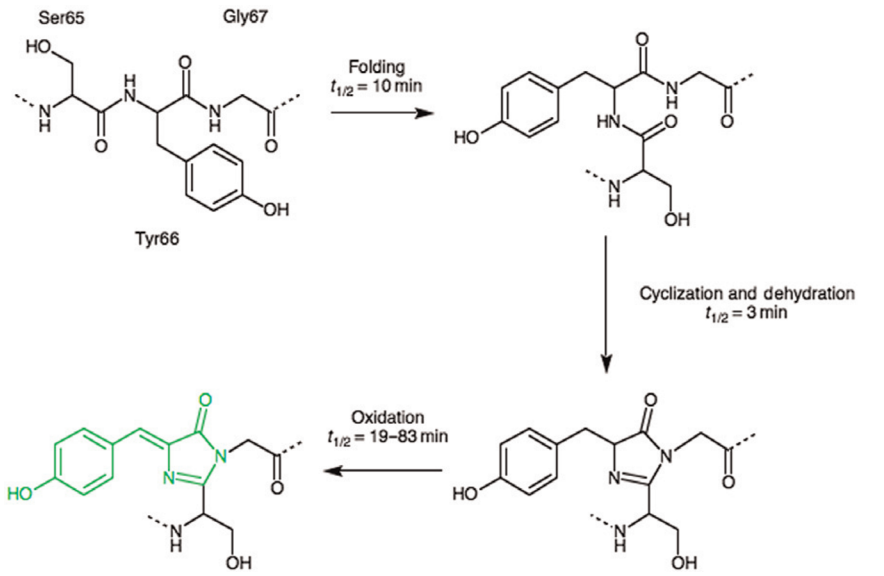

FIGURE 5.2

Formation of the GFP chromophore. Three steps in GFP chromophore formation are shown. The first step is the folding of the GFP protein that has a half-time of approximately 10 min. Once folded, cyclization of the peptide backbone and dehydration occur rapidly. The rate-limiting step in chromophore formation is the oxidation of the tyrosine side chain. The final deprotonation of the tyrosine hydroxyl group is not shown.

(FP; Fig. 5.2). Four key steps were proposed to control chromophore formation: (1) the folding of the GFP protein, (2) the cyclization and dehydration of the peptide backbone between the amide nitrogen of Gly67 and the carbonyl of Ser65, (3) the oxidation of the Tyr66 side chain to introduce a vinyl group, and (4) the deprotonation of the Tyr66 hydroxyl. The rate constants for each step in GFP chromophore formation have been measured, and the rate-limiting step in the reaction is the oxidation of the Tyr66 side chain (Reid & Flynn, 1997).

The initial folding of the GFP molecule precedes all other steps in chromophore formation. As researchers began to express GFP in a variety of organisms, it was quickly realized that the conversion of GFP to its fluorescent state was highly temperature dependent. Expression of GFP at 37 °C in *Escherichia coli* resulted in most of the protein being incorporated into inclusion bodies, while expression at 25 °C produced soluble FP (Siemering, Golbik, Sever, & Haseloff, 1996). Following proper folding, the rate-limiting step for functional chromophore formation is the oxidation of the Tyr66 side chain that brings the aromatic ring of Tyr66 into conjugation with the imidazolone ring. Because this oxidation can take as long as 2 h, there may be a significant lag between GFP translation in cells and GFP fluorescence. The excitation spectrum of *Aequorea* GFP exhibits two absorbance peaks, one at 395 nm and another

at 475 nm, that are thought to result from the protonation state of the chromophore. Protonation of the tyrosine hydroxyl group results in absorbance at 395 nm, and deprotonation to the anionic form of the chromophore yields the 475-nm peak.

5.3 THE STRUCTURE OF GFP

The crystal structure of GFP revealed the importance of the entire GFP protein to the fluorescence of the chromophore. GFP is formed by an 11-stranded β-barrel that folds into a structure that has been termed as β-can (Fig. 5.3; Ormo et al., 1996; Yang, Moss, & Phillips, 1996). The chromophore is completely buried in the center of the β-can structure, protected from solvent quenching effects. Folding of the GFP protein into the β-can structure prevents access of other proteins to the chromophore region; thus, a nonenzymatic mechanism is required for spontaneous chromophore formation. The β-can structure also explains why attempts to truncate GFP to a lower molecular weight were unsuccessful. Almost the entire GFP sequence participates in forming the β-can structure; therefore, the deletion of any part of the sequence would disrupt the overall conformation.

Since the discovery of *Aequorea* GFP, several other FPs from various organisms have been discovered and characterized. Despite their very different sources, all FPs appear to be about 25 kDa and contain similar β-can structures that are necessary for creating the unique environment in which the functional chromophore is formed. So far, only four residues are totally conserved in naturally occurring FPs: Tyr66, Gly67,

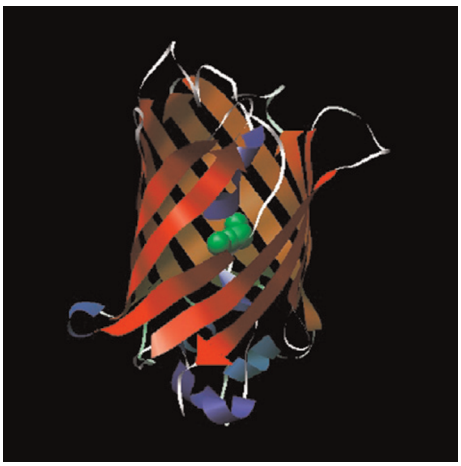

FIGURE 5.3

The structure of GFP. GFP folds into a barrel-like structure composed of 11 strands of β-sheet (shown in red). Buried in the center of the barrel is the GFP chromophore (shown in green).

Arg96, and Tyr222 (Remington, 2006). These residues are necessary for proper chromophore formation and maturation, although studies have shown that other aromatic residues can replace Tyr66 (Heim et al., 1994). Most residues of FPs are not highly conserved, which has allowed for extensive mutagenesis of FPs to optimize and alter their characteristics.

5.4 MUTAGENESIS TO ALTER THE PROPERTIES OF GFP

The thermosensitivity, slow maturation rate, and complex absorbance spectrum of *Aequorea* GFP were some of the factors that prompted multiple research groups to begin mutagenizing GFP to alter its functional properties. Initial mutagenesis studies on GFP were directed at improving its folding and expression at 37 °C and at altering its excitation and emission spectrum (Cormack, Valdivia, & Falkow, 1996; Crameri, Whitehorn, Tate, & Stemmer, 1996; Delagrave, Hawtin, Silva, Yang, & Youvan, 1995; Heim, Cubitt, & Tsien, 1995; Heim et al., 1994; Siemering et al., 1996). These and subsequent studies were quite successful in generating GFP variants that matured rapidly to fluorescence and that absorbed and emitted light at different wavelengths. Excellent reviews of GFP mutagenesis have recently been published that describe a wide variety of mutations and their consequences for GFP fluorescence (Chudakov, Matz, Lukyanov, & Lukyanov, 2010; Day & Davidson, 2009; Kremers, Gilbert, Cranfill, Davidson, & Piston, 2011; Lippincott-Schwartz, & Patterson, 2003; Rizzo, Davidson & Piston, 2009; Shaner, Steinbach, & Tsien, 2005; Zacharias & Tsien, 2006). Furthermore, many other mutations in GFP were generated that favorably altered its properties by reducing its tendency to aggregate, dimerize, or tetramerize, reducing its pH and halide ion sensitivity, and improving its photobleach characteristics.

A major barrier to expanding the applications of GFP was that, despite extensive mutagenesis, no research group had been able to extend its emission spectrum beyond approximately 530 nm so that GFP variants were not available that emitted longer wavelength red light. The solution to this problem came from the isolation of an FP from a coral species *Discosoma* that naturally exhibited a red fluorescence (Matz et al., 1999). This protein, termed drFP583 or dsRed, exhibited an emission peak at 583 nm. The chromophore of dsRed is formed by cyclization of the peptide backbone at amino acids Gln66-Tyr67-Gly68 in a manner analogous to GFP chromophore formation. The extended wavelength fluorescence is due in large part to an additional oxidation of the peptide backbone at Gln66 that extends the conjugated system of the chromophore (Fig. 5.4; Gross, Baird, Hoffman, Baldridge, & Tsien, 2000; Wall, Socolich, & Ranganathan, 2000). However, dsRed exhibits an extremely slow maturation time (>10 h) proceeding through a green intermediate and is an obligate tetramer (Baird, Zacharias & Tsien, 2000).

The discovery of a red fluorescent protein (RFP) provided the platform for further mutagenesis to optimize dsRed for use in cell biology. Bevis & Glick, 2002 first addressed the slow maturation time of dsRed and generated mutants that matured 15 times faster than the original dsRed protein, as well as mutants that reduced

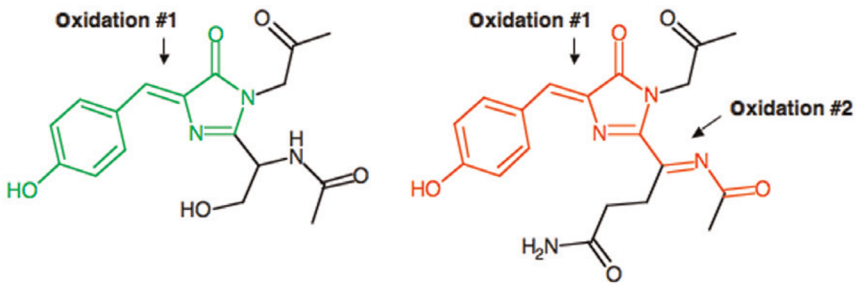

FIGURE 5.4

Comparison of the GFP and dsRed chromophores. The GFP chromophore is shown in green on the left. dsRed (right) contains an additional double bond that extends the conjugated system of the chromophore.

the green intermediate. Through an extensive series of mutagenesis and optimization experiments, Campbell et al., 2002 systematically disrupted the dimer–dimer interface and then the dimer–monomer interface of dsRed to generate a truly monomeric RFP called mRFP1. This monomeric RFP then served as the starting point to diversify the wavelength distribution of RFPs. Continued mutagenesis and optimization allowed Roger Tsien's laboratory to produce an extraordinary array of monomeric RFP derivatives that span the emission spectrum from 537 to 649 nm (Shaner et al., 2004; Wang, Jackson, Steinbach, & Tsien, 2004). Recent advances in expanding the FP color palette include the development of FP variants with improved brightness and photostability, and variants that extend the FP spectrum into the violet and far-red regions (Davidson & Campbell, 2009; Day & Davidson, 2009; Kremers et al., 2011; Rizzo et al., 2009b; Shaner et al., 2008; Shaner, Patterson, & Davidson, 2007; Shcherbo et al., 2009). Development and optimization of more FPs that excite in the far-red end of the spectrum will not only extend the possible number of colors but also most likely improve many aspects of imaging, as longer excitation wavelengths can penetrate deeper into biological tissues, causing less background autofluorescence and less phototoxicity. Table 5.1 lists current GFP variants, grouped by wavelength, that are recommended for conventional imaging applications. This represents a small subset of the diversity of FPs that are available and others that are not listed may be more suitable for specialized applications.

A major advance in FPs was the development of photoactivatable FPs. Patterson & Lippincott-Schwartz, 2002 developed a variant of *Aequorea* GFP by directed mutagenesis called photoactivatable GFP, or PA-GFP, that exhibited very low fluorescence when irradiated with 488-nm light but when activated by irradiation with 413-nm light became 100-fold more fluorescent upon 488 nm excitation. This ability to switch an FP from an "off" state to an "on" state made it possible to spatially activate a subpopulation of the FP within a cell to follow its dynamics through time and space. In the same year, Ando, Hama, Yamamoto-Hino, Mizuno, & Miyawaki, 2002 described an FP from a stony coral that normally exhibits green fluorescence

Table 5.1 Characteristics of selected fluorescent proteins

Fluorescent protein	Ex	Em	ε	QY	Brightness
Violet					
Sirius	355	424	15,000	0.24	3600
Blue					
EBFP2	383	448	32,000	0.56	17,920
Azurite	384	450	26,200	0.55	14,410
mTagBFP	399	456	52,000	0.63	32,760
Cyan					
mTurquoise	434	474	30,000	0.84	25,200
ECFP	434	476	32,500	0.40	13,000
Cerulean	433	475	43,000	0.62	26,660
CyPet	435	477	35,000	0.51	17,850
mTFP1	462	492	64,000	0.85	54,400
Green					
EGFP	488	507	56,000	0.60	33,600
Emerald	487	509	57,500	0.68	39,100
mWasabi	493	509	70,000	0.80	56,000
T-Sapphire	399	511	44,000	0.60	26,400
Yellow					
EYFP	514	527	83,400	0.61	50,874
Venus	515	528	92,200	0.57	52,554
Citrine	516	529	77,000	0.76	58,520
YPet	517	530	104,000	0.77	80,080
Orange					
Kusabira Orange2	551	565	63,800	0.62	39,556
mOrange2	549	565	58,000	0.60	34,800
tdTomato	554	581	138,000	0.69	95,220
TagRFP	555	584	100,000	0.48	48,000
Red					
mApple	568	592	75,000	0.49	36,750
mStrawberry	574	596	90,000	0.29	26,100
mCherry	587	610	72,000	0.22	15,840
Far-red					
mKate2	588	633	62,500	0.40	25,000
mPlum	590	649	41,000	0.10	4100

Ex, excitation maximum (nm); Em, emission maximum (nm); ε, extinction coefficient (M^{-1} cm^{-1}); QY, quantum yield; Brightness, ε × QY (M^{-1} cm^{-1}). For a comprehensive analysis of fluorescent protein properties, we recommend these reviews: Chudakov et al. (2010); Davidson and Campbell (2009); Day and Davidson (2009); Kremers et al. (2011); Rizzo et al. (2009a, 2009b); Shaner et al. (2007); Wiedenmann, Oswald, and Nienhaus (2009).
Adapted from Chudakov et al. (2010), Kremers et al. (2011), and Rizzo et al. (2009b) and values in the literature.

but can be switched to red fluorescence by activation with UV light. These initial observations then led to the discovery of several new FPs that can be photoactivated or photoconverted to a new wavelength (Chudakov et al., 2003, 2004; Gurskaya et al., 2006; Tsutsui, Karasawa, Shimizu, Nukina & Miyawaki, 2005; Wiedenmann et al., 2004). Ando, Mizuno, & Miyawaki, 2004 described a novel FP from the coral *Pectiniidae* that could be photoactivated with 400-nm light to become fluorescent-like PA-GFP, but could then be reversibly switched off by irradiation with 490-nm light. This process of "reversible protein highlighting" with reversibly switchable FPs, or RSFPs, allows exquisite spatial control of FP activation in cells. Recent years have seen continued development and optimization of photoactivatable, photoconvertible, and photoswitchable FPs, as they are extremely useful in selectively marking subcellular regions to understand protein dynamics within living systems, as well as in achieving subdiffraction-resolution images of labeled cellular structures when combined with super-resolution imaging techniques (Fig. 5.5; Gould, Verkhusha, & Hess, 2009; Hofmann, Eggeling, Jakobs, & Hell, 2005; Hoi et al., 2010; Lippincott-Schwartz & Patterson, 2009; Lukyanov, Chudakov, Lukyanov, & Verkhusha, 2005; Patterson, Davidson, Manley, & Lippincott-Schwartz, 2010; Wiedenmann et al., 2011; Wiedenmann & Nienhaus, 2006).

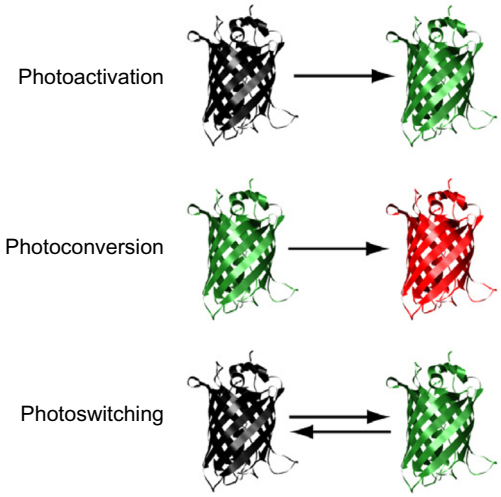

FIGURE 5.5

Switching states in fluorescent proteins. Photoactivation (top) is the process of changing a fluorescent protein from a dark state to a fluorescent state. Photoconversion (middle) involves switching a fluorescent protein from one wavelength emission to a new wavelength emission. Photoswitching (bottom) is the reversible activation and inactivation of a fluorescent protein either from a dark to a fluorescent state or between different wavelengths.

5.5 IMAGING FPs

There are several simple factors to consider and control when planning an imaging experiment that will dramatically improve the ability to detect FPs in fixed or live specimens. Most of these factors are just as applicable to imaging conventional fluorophores as they are to FPs and thus can be considered as general guidelines for fluorescence imaging. The challenge with any live cell experiment is to image the specimen over a long enough time frame to extract meaningful data. This is almost always practically limited by bleaching of the fluorophore and the death of the specimen. These two limitations are often linked through radical generation during photobleaching that causes cellular damage leading to cell death.

5.5.1 Components of the optical system

Designing an optical system to most effectively detect fluorescent signal while minimizing phototoxicity is the first important step in FP imaging. The efficiency of the optical system to detect the fluorescence signal depends on the numerical aperture of the lens, the quality of transmission of the light through the system, and the sensitivity of the detector. High numerical aperture objective lenses allow the collection of more of the fluorescence emission into the optical system and provide more photons for detection. Thus, the highest numerical aperture objective that is available in an appropriate magnification should be selected. Unnecessary optical elements in an imaging system can absorb significant amounts of light. Controlling the light path so that emitted light takes the most direct path to the detector through the least number of optical elements will ensure maximum transmission of signal through the optical system. Finally, once the light reaches the detector, it is important to maximize the detector sensitivity so that as many incident photons as possible are acquired. CCD cameras vary significantly in their spectral response and sensitivity, thus choosing a camera that has high quantum efficiency and sensitivity in the visible wavelengths is recommended.

5.5.2 Reducing unwanted fluorescence

Fluorescence from sources other than the FP of interest can obscure the relevant fluorescence signal. Some of the most common sources of unwanted fluorescence are additives of the imaging medium. Cultured cell media often contain pH indicators such as phenol red or serum components that are fluorescent, and yeast and bacterial rich media also contain significant sources of unwanted fluorescence. Because the sample is bathed in the imaging medium, even dimly fluorescent components in the medium can obscure the detection of the desired fluorescence signal. It is often not possible to exclude all components that contribute to media fluorescence; however, using media that lack additives such as phenol red or defined media that do not contain fluorescent components can eliminate a significant source of unwanted fluorescence.

A second major source of unwanted fluorescence is autofluorescence of the sample itself. There are many examples of cellular compartments and tissues that have an intrinsic fluorescence, such as yolk platelets in embryos, chloroplasts in plants, and vacuolar compartments in fungi to name a few. These sources of intrinsic fluorescence are usually not possible to remove; however, they can often be excluded by the appropriate choice of optical filters.

5.5.3 Selecting appropriate filters and chromatic mirrors

One of the most important factors in maximizing fluorescent signal detection while minimizing unwanted fluorescence signal is the proper matching of the excitation and emission wavelengths of the optical system to the excitation and emission spectrum of the FP. Many imaging systems come equipped with standard filters for DNA dyes such as DAPI or Hoechst, and common fluorophores such as fluorescein or rhodamine. Laser-based systems depend on the emission spectrum of the laser for the excitation wavelength and select emission wavelengths using a variety of methods, ranging from standard emission filters to diffraction-based wavelength selection. However, commonly used wavelengths may not be well suited to the spectrum of a particular FP, and improper matching of the excitation and emission wavelengths will result in significant loss of fluorescence emission signal as well as excessive irradiation of the specimen. The spectrum of EGFP is reasonably well matched to conventional fluorescein excitation and emission filters, and EGFP is efficiently excited by the strong 488-nm emission of the Argon laser. Other FPs, however, require excitation and emission filters that are appropriately matched to their spectra. The yellow fluorescent protein (YFP) variants listed in Table 5.1 are an excellent example. These variants are bright and photostable, but if conventional filter sets are used, the vast majority of the excitation and emission light will be wasted while unnecessarily irradiating the sample. Figure 5.6 shows the difference in image intensity when GFP is imaged through a well-matched filter set versus a poorly matched set.

5.5.4 Selecting the appropriate FP

Although a large number of FPs are currently available, selecting an FP for a specific experiment can be simplified with a few straightforward considerations. The most important consideration in choosing an FP is to maximize its brightness and stability. The data in Table 5.1 can be used to determine the relative brightness of a particular FP in comparison with others. Brightness is calculated by multiplying the extinction coefficient, a measure of how efficiently an FP absorbs light, and the quantum yield, the fraction of absorbed photons that are emitted as fluorescence. For instance, the cyan fluorescent protein (CFP) variant Cerulean is more than twice as bright as ECFP and thus would likely perform better in a standard imaging experiment. Several other factors will also contribute to the apparent brightness of an FP in cells. The expression of the protein can have a major effect on the FP signal. Most available FP variants have been codon optimized for efficient expression in mammalian cells;

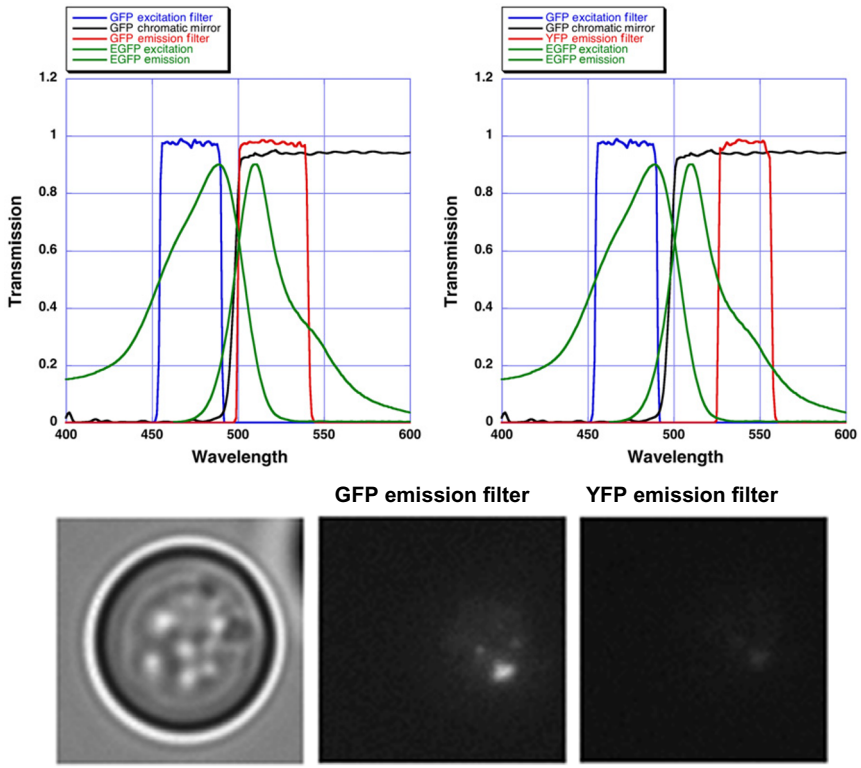

FIGURE 5.6

Choosing the appropriate filter sets for fluorescent protein imaging. Top left panel: excitation and emission spectrum of EGFP (green) and transmission profile of excitation filter (blue), chromatic mirror (black), and emission filter (red) designed for GFP. The top right panel shows the same curves except the emission filter is designed for YFP (red). Bottom panel: brightfield image of yeast cell (left), fluorescence image of yeast cell acquired using GFP filter (center), and fluorescence image of yeast cell acquired using the YFP emission filter.

however, these constructs may be suboptimal when introduced into another organism. We recommend altering the codon bias of the FP so that it matches the most frequently used codons in a particular organism. As previously mentioned, FP folding and maturation rate can have a dramatic effect on apparent fluorescence in cells. Furthermore, wild type GFP is both halide and pH sensitive, a significant consideration if an FP must function in acidic cellular compartments such as the lysosome. Many of the most commonly used FPs have been engineered to fold efficiently at 37 °C, to mature rapidly, and to fluoresce at a wide range of pH and salt concentrations, but being aware of their limitations will help one to circumvent easily avoidable pitfalls.

Several additional factors can affect the ability to image FPs in living cells. FPs exhibit distinctly different quantum photobleach rates, and these rates will determine the duration of imaging experiments (Shaner et al., 2004). Although it is difficult to compare data from many sources on photobleach rates for different FP variants, selecting FPs that have slow bleaching rates can significantly improve the duration and reliability of an imaging experiment. Finally, protein multimerization provides a major obstacle to the use of some FP variants. As mentioned earlier, dsRed is an obligate tetramer when expressed (Baird et al., 2000). Thus, the fusion of a protein of interest to dsRed will naturally tetramerize the protein of interest, leading to unpredictable and likely unwanted effects. Two solutions to this multimerization problem have been devised. The first was to encode a multimer as a fusion in a single repeated reading frame so that a tandem dimer was produced (Campbell et al., 2002). Although this solves the multimerization problem, it also more than doubles the size of the FP and may have deleterious results. An alternative strategy is to use the available monomeric versions of FPs that have very low intermolecular affinities. This will ensure that artifacts of dimerization or multimerization do not adversely affect the imaging experiment. For a more comprehensive analysis and recommendations on FP choice, we recommend the following reviews (Chudakov et al., 2010; Day & Davidson, 2009; Kremers et al., 2011; Lippincott-Schwartz & Patterson, 2003; Rizzo, Davidson, & Piston, 2009a; Rizzo et al., 2009b; Shaner et al., 2005; Wiedenmann et al., 2009; Zacharias & Tsien, 2006).

5.5.5 Constructing FP fusions

One of the most widely used applications of FPs is the fluorescent tagging of another protein of interest in order to follow its localization and dynamics in living systems. However, proteins tagged with FPs may not always recapitulate the behavior of the endogenous protein (Landgraf, Okumus, Chien, Baker, & Paulsson, 2012). In order to have the highest confidence that the behavior of the FP fusion accurately reflects the behavior of the endogenous protein, three criteria should be met. First, one should determine whether fusing an FP to a protein of interest alters the localization of the fusion with respect to the endogenous protein. If an antibody is available to the protein of interest, the localization of the endogenous protein can be determined and compared with that of the FP fusion. In the absence of an antibody, it is often useful to compare N- and C-terminal fusion of proteins to FPs to determine if they report the same localization. Because GFP is 27 kDa, it is also often useful to compare the localization of the FP fusion with the localization of a fusion protein with an alternative antigen tag of smaller size. Second, the construction of an FP should not alter the activity of the protein of interest. If the protein of interest can be produced *in vitro* and has an enzymatic activity, then the FP fusion can easily be tested in the same assay to determine whether the fusion protein changes the activity or kinetics of the enzyme. In practice, it can be difficult to monitor the activity of the protein if its function is unknown or if it is difficult to express or purify. Third, the FP fusion should not alter the stability or expression of the protein of interest. This can often be determined if an antibody to the protein of interest is available. By comparing the

levels of the fusion protein with the levels of the endogenous protein, one can determine whether the FP fusion is produced at a level comparable to the endogenous protein or whether the half-life of the protein changes when fused to the FP. Although satisfying all of these criteria is often not feasible, addressing as many as possible will help one to ensure that the data acquired with the FP fusion accurately reports the behavior of the cellular protein.

5.5.6 Note on fixation of FPs

The advantage of FP imaging comes as a result of detecting the protein in living cells, but there are many instances where fixation of the cells and imaging of the FP are desirable. Fixation of FP fusions can give highly variable results. Excessive fixation or the use of harsh fixatives can destroy the fluorescence of GFP. As a general rule, short fixation with paraformaldehyde or formaldehyde often preserves the fluorescence of GFP as well as maintains the localization of the protein of interest, whereas soluble GFP has been shown to be extracted by methanol fixation (Wang, Miller, Shaw, & Shaw, 1996). As a cautionary note, the spectral properties of CFP have been reported to change significantly after aldehyde fixation, although this does not seem to be a general property of FPs (Domin Lan, & Kaminski, 2004). A careful analysis of FP redistribution was performed under different fixation conditions to monitor the localization of the epidermal growth factor receptor (EGFR; Brock, Hamelers, & Jovin, 1999). These authors observed that methanol fixation completely removed EGFR from cells while paraformaldehyde preserved the localization and fluorescence of the fusion protein. These authors also noted that the use of the Mowiol mounting media caused redistribution of the GFP signal in cells. Properties of the mounting media such as pH and halide concentration should be checked for compatibility with the FP used in the experiment. Thus, careful attention should be paid to the fixation and mounting conditions used when analyzing FP distribution in fixed specimens.

5.5.7 Time-lapse imaging of FPs

FP imaging in live cells allows one to study the dynamics of proteins over time and under different stimuli (Fig. 5.7). In order to image labeled cells over long time periods without undue damage to the specimen, it is necessary to optimize the cell growth conditions on the microscope as well as limit the amount of excitation light to which cells are exposed. Many different methods for stage incubation have been developed from simple chambers that hold the specimen on the microscope stage to enclosures for the entire imaging platform that regulate temperature, gas, and humidity. Depending on the sample, finding an appropriate specimen incubator that preserves viability will allow long-term imaging of cells. Finally, limiting the exposure time and intensity of the excitation light will have a substantial effect on sample viability. Most current platforms for time-lapse microscopy include electronic shutters that gate the excitation light and use neutral density filters or electronic modulation to alter the intensity of the excitation beam. Either reducing the time of

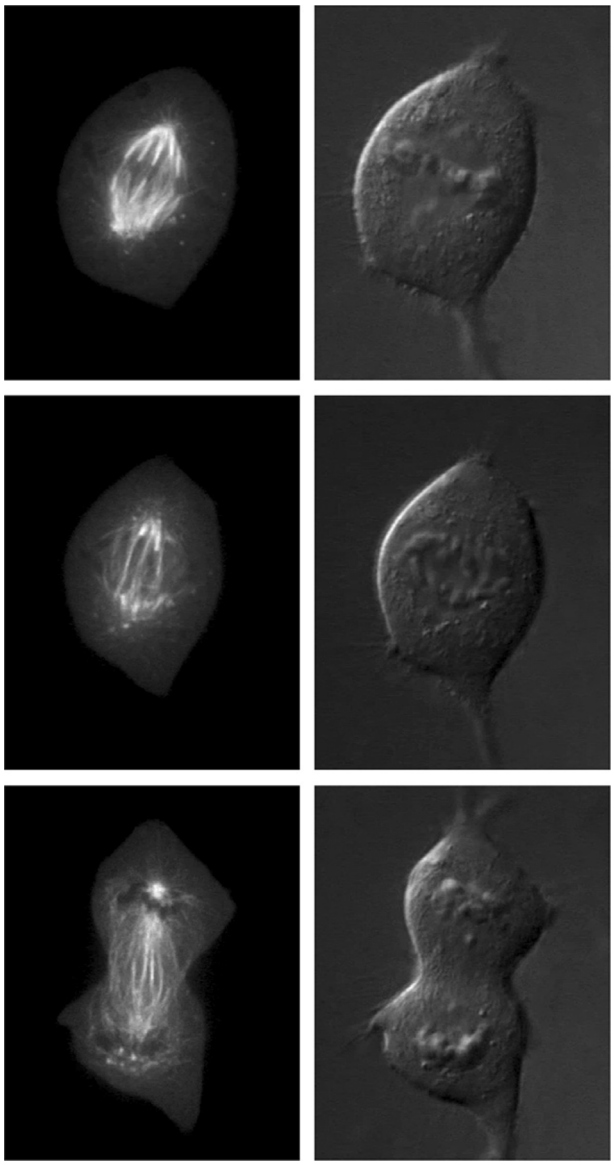

FIGURE 5.7

Example of time-lapse image sequence. Mammalian tissue culture cells growing at 37 °C and expressing a fusion of EGFP to α-tubulin were imaged through the process of mitosis using fluorescence (left panels) and differential interference contrast microscopy (right panels). Top panel, metaphase; center panel, early anaphase; and bottom panel, late anaphase.

excitation with high-intensity light or decreasing the intensity of excitation in a given timeframe is an effective means of reducing photodamage, and the choice between these alternatives should be empirically determined as appropriate for the specimen. Reducing photobleaching and photodamage to the specimen and optimizing growth conditions will facilitate effective live cell imaging over longer time periods.

5.6 APPLICATIONS OF FP IMAGING

The development of FP variants that possess diverse properties such as spectral differences, sensitivity to environmental factors, and photoswitchable responses to light has opened many new avenues in live cell imaging. Here, we discuss a few examples of microscopy-based FP applications to investigate cell biological questions.

5.6.1 Multiwavelength imaging of FPs

The development of many different spectral variants of FPs has enabled the simultaneous imaging of multiple tagged proteins in living cells. There are several combinations of FPs that are well separated in their fluorescence excitation and emission spectra so that they can be easily distinguished with appropriate filter sets. One of the most commonly used pair of FPs for multiple labeling are the cyan and YFPs. Their widespread use primarily reflects the timing of their development, because the longer wavelength dsRed variants were not available until more recently. The bright CFP variants such as Cerulean and CyPet can be easily combined with the YFP variants such as Citrine, YPet, and Venus for simultaneous imaging. The development of longer wavelength FPs has enabled dual wavelength imaging of GFP variants and Red variants such as mStrawberry, mCherry, and mPlum. It is now common practice to distinguish three and four FP variants simultaneously within a single cell, given the appropriate selection of excitation and emission filters (Shaner et al., 2005). With the continued development of spectral unmixing technologies, one may be able to distinguish several FPs within a single cell.

5.6.2 Monitoring intracellular environments using FPs

The sensitivity of some FP variants to factors such as pH and halide ion concentration served as a starting point to generate reporters of cellular environment. One of the first examples of this was to exploit the changes in excitation and emission spectra of FPs in response to pH changes to obtain a readout of the pH of different cellular compartments (Llopis, McCaffery, Miyawaki, Farquhar, & Tsien, 1998; Miesenbock, De Angelis, & Rothman, 1998). In an elegant study describing pH-dependent indicators called pHluorins, Miesenbock and Rothman demonstrated that the ratio of emission intensity of pHluorins when excited at 410 and 470 nm depended upon the pH of the environment. Using the ratio of emission intensities at different excitation wavelengths, they were able to accurately calculate the pH of different compartments of the secretory pathway.

The discovery of spectral variants of GFP made possible the use of Förster resonance energy transfer (FRET) to generate sensors of intracellular environment and enzyme activity. Two fluorescent molecules such as CFP and YFP have excitation and emission spectra such that there is significant overlap of the CFP emission spectrum with the excitation spectrum of YFP. When brought in close proximity ($<$100 Å), excitation of CFP can result in the radiationless transfer of the excited state energy to YFP, resulting in fluorescence emission at longer wavelengths as YFP returns to the ground state. This FRET process is extremely sensitive to distance, as the efficiency of the energy transfer process drops proportional to the sixth power of the distance between the FP molecules. Miyawaki et al., 1997 used this distance dependence to create intracellular sensors for calcium ion concentration. By inserting the calmodulin protein and a calmodulin-binding peptide between either BFP and GFP or CFP and YFP, the authors were able to generate a sensor that would bring the two FPs into close proximity, and thus increase the energy transfer efficiency, as a function of calcium binding. A number of different biosensors based upon this energy transfer system have now been used to detect cyclic-AMP, sugars, protease activity, kinase activity, and more (Fig. 5.8; Blakeley, Chapman, & McNaughton, 2012; Fehr et al., 2005; Frommer, Davidson, & Campbell, 2009; Honda et al., 2001; Luo, Yu, Pu, & Chang, 2001; Sato, Hida, Ozawa, & Umezawa, 2000; Zaccolo et al., 2000).

5.6.3 Monitoring protein–protein interactions in vivo

The application of FP-based reporters of proximity can also be applied to study the interaction between proteins within living cells. By fusing two different FPs that can act as an energy transfer pair to two different proteins of interest, it is possible to monitor the spatial and temporal interactions between those proteins in cells by monitoring the energy transfer efficiency. This approach was first used to demonstrate that the transcription factor Pit1 could dimerize in the cell nucleus by monitoring the energy transfer efficiency between Pit1 fused to GFP and BFP in the same cell (Periasamy & Day, 1998). Although in principle using energy transfer seems a simple approach to detecting protein–protein interactions in living cells, accurate calculation of energy transfer efficiency can be hampered by many factors. A discussion of the microscopic methods for calculating transfer efficiency between FPs is beyond the scope of this chapter, but these techniques have been extensively reviewed elsewhere (Day & Davidson, 2009; Miyawaki & Tsien, 2000; Piston & Kremers, 2007; Sekar & Periasamy, 2003; Vogel, Thaler, & Koushik, 2006).

Split-FP systems have also proven to be useful as alternatives to FRET-based methods for detecting protein–protein interactions in living cells (Chun, Waldo, & Johnson, 2010; Kerppola, 2008; Shekhawat & Ghosh, 2011). Putative interacting proteins are fused to two nonfluorescing fragments of a split-FP, and when interacting proteins come into close proximity and bind, they reconstitute the intact FP as well as FP fluorescence. This system avoids some of the issues that arise in FRET-based assays, such as low signal and the need to overexpress protein above endogenous levels, but may introduce unique disadvantages, such as slow FP reassembly and susceptibility to aggregation.

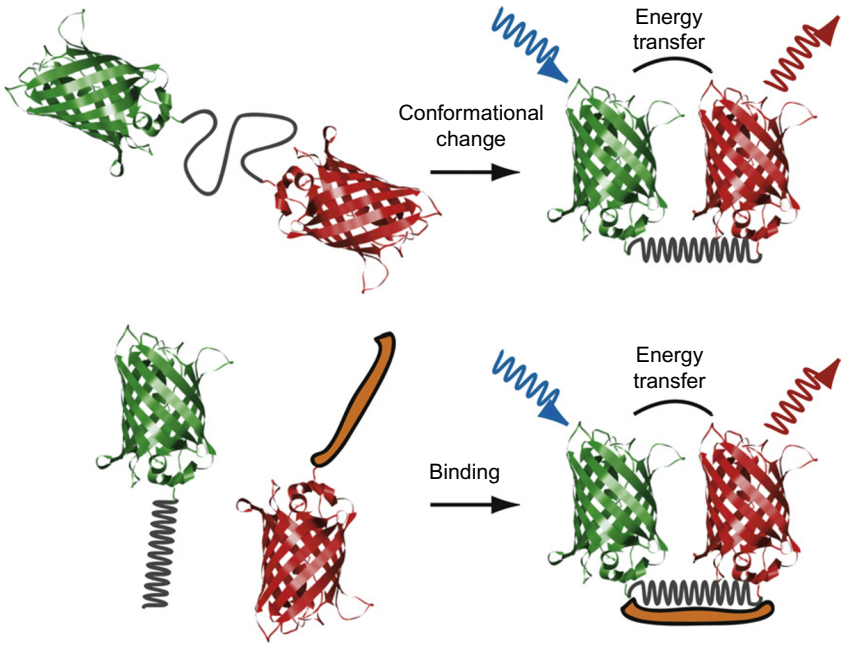

FIGURE 5.8

Using energy transfer between fluorescent proteins to monitor cellular environment and protein interactions. Top panel: a linker between two fluorescent proteins whose conformation changes upon protein or small molecule binding brings two fluorescent proteins into close proximity so that FRET occurs and can be measured to determine the concentration or activity of the linker binding moiety. Bottom panel: two proteins or protein domains that bind to one another when fused to fluorescent proteins can bring the fluorescent proteins into close proximity and thus generate a readout for the interaction of the two proteins within the cell.

5.6.4 Protein dynamic measurements using FP photobleaching and activation

The dynamic properties of proteins in cells can be effectively studied using spatially localized photobleaching and photoactivation of FPs. The best known of these techniques is fluorescence recovery after photobleaching (FRAP), where a defined region of fluorescence signal is ablated using high-intensity light and then the recovery of fluorescence is monitored over time (Axelrod, Koppel, Schlessinger, Elson, & Webb, 1976). This allows an estimate of the mobility of protein within the photobleached region as well as an estimate of how completely fluorescence can be recovered. A companion technique to FRAP is fluorescence loss in photobleaching (FLIP). FLIP employs continuous ablation of the fluorescence in a region of the cell until all cellular fluorescence signal is gone or no more decay due to the bleaching light is observed (Lippincott-Schwartz & Patterson, 2003). This provides an estimate of the total mobility of fluorescent signal within a cell. Finally, the

discovery of FP photoactivation and photoconversion allows a region of the cell to be activated to the fluorescent state and then the relocalization of the fluorescent molecules can be monitored over time as they redistribute (Patterson & Lippincott-Schwartz, 2002). These three techniques allow calculation of protein mobility throughout cells, in specific regions or organelles, and even allow estimates of bulk association, dissociation, and diffusion kinetics in living specimens.

5.6.5 Super-resolution imaging with photoactivatable FPs

The development of photoactivable FPs has led to a revolution in super-resolution imaging. Conventional imaging is limited by the diffraction of light, so that the highest possible resolution is about half the wavelength of the light used, or at least 200 nm. However, many cellular structures and processes are on the level of tens of nanometers, and cannot be resolved by conventional imaging. After the development of the first photoactivable FP, Betzig et al. described a technique called photoactivated localization microscopy, or PALM, which uses low-level illumination to photoactivate a small percentage of PA-FP molecules in a sample (Betzig et al., 2006). The spots corresponding to individual fluorescent PA-FP molecules are still diffraction limited; however, they are sparse enough that they do not overlap, and therefore the center of each spot can be precisely calculated using the point spread function of the microscope. These molecules are then photobleached, and low-level illumination of the sample is repeated to photoactivate new subsets of molecules, eventually resulting in a complete, super-resolution image. PALM, as well as fluorescent photactivation localization microscopy and stochastic optical reconstruction microscopy developed around the same time, are imaging techniques that take advantage of the unique properties of photoactivatable and photoswitchable molecules to achieve subdiffraction resolution (Hess, Girirajan, & Mason, 2006; Rust, Bates, & Zhuang, 2006). These techniques continue to develop and expand to different imaging realms such as multicolor imaging, 3D imaging, and live cell imaging (Chang et al., 2012; Gould et al., 2009; Gunewardene et al., 2011; Huang, Babcock, & Zhuang, 2010; Lippincott-Schwartz & Patterson, 2009; Patterson et al., 2010; Schermelleh, Heintzmann, & Leonhardt, 2010).

CONCLUSION

The examples described earlier represent just a few of the many applications of FP imaging used to understand the dynamics of proteins in cells and to monitor the intercellular environment. Additional applications whose descriptions are outside the scope of this chapter include FP-based sensors of cell cycle state (Sakaue-Sawano et al., 2008), optical control of protein activity (Zhou, Chung, Lam & Lin, 2012), all-optical writing with a photoswitchable GFP (Grotjohann et al., 2011), and many more. As more FP variants are discovered in nature and as more derivatives of FPs are developed in the laboratory, the scope of FP applications will continue to expand. A great deal of work has been done to generate FP wavelength variants with improved brightness and photostability, and new variants continue to be developed

at a rapid rate. Our ability to examine the behavior of proteins within living cells and cells within living organisms has been transformed by the discovery of GFP and will continue to improve with the further development of novel FP applications.

References

Ando, R., Hama, H., Yamamoto-Hino, M., Mizuno, H., & Miyawaki, A. (2002). An optical marker based on the UV-induced green-to-red photoconversion of a fluorescent protein. *Proceedings of the National Academy of Sciences of the United States of America*, *99*(20), 12651–12656.

Ando, R., Mizuno, H., & Miyawaki, A. (2004). Regulated fast nucleocytoplasmic shuttling observed by reversible protein highlighting. *Science*, *306*(5700), 1370–1373.

Axelrod, D., Koppel, D. E., Schlessinger, J., Elson, E., & Webb, W. W. (1976). Mobility measurement by analysis of fluorescence photobleaching recovery kinetics. *Biophysical Journal*, *16*(9), 1055–1069.

Baird, G. S., Zacharias, D. A., & Tsien, R. Y. (2000). Biochemistry, mutagenesis, and oligomerization of DsRed, a red fluorescent protein from coral. *Proceedings of the National Academy of Sciences of the United States of America*, *97*(22), 11984–11989.

Betzig, E., Patterson, G. H., Sougrat, R., Lindwasser, O. W., Olenych, S., Bonifacino, J. S., et al. (2006). Imaging intracellular fluorescent proteins at nanometer resolution. *Science*, *313*(5793), 1642–1645.

Bevis, B. J., & Glick, B. S. (2002). Rapidly maturing variants of the Discosoma red fluorescent protein (DsRed). *Nature Biotechnology*, *20*(1), 83–87.

Blakeley, B. D., Chapman, A. M., & McNaughton, B. R. (2012). Split-superpositive GFP reassembly is a fast, efficient, and robust method for detecting protein–protein interactions in vivo. *Molecular BioSystems*, *8*(8), 2036.

Brock, R., Hamelers, I. H., & Jovin, T. M. (1999). Comparison of fixation protocols for adherent cultured cells applied to a GFP fusion protein of the epidermal growth factor receptor. *Cytometry*, *35*(4), 353–362.

Campbell, R. E., Tour, O., Palmer, A. E., Steinbach, P. A., Baird, G. S., Zacharias, D. A., et al. (2002). A monomeric red fluorescent protein. *Proceedings of the National Academy of Sciences of the United States of America*, *99*(12), 7877–7882.

Chalfie, M., Tu, Y., Euskirchen, G., Ward, W. W., & Prasher, D. C. (1994). Green fluorescent protein as a marker for gene expression. *Science*, *263*(5148), 802–805.

Chang, H., Zhang, M., Ji, W., Chen, J., Zhang, Y., Liu, B., et al. (2012). A unique series of reversibly switchable fluorescent proteins with beneficial properties for various applications. *Proceedings of the National Academy of Sciences of the United States of America*, *109*(12), 4455–4460.

Chudakov, D. M., Belousov, V. V., Zaraisky, A. G., Novoselov, V. V., Staroverov, D. B., Zorov, D. B., et al. (2003). Kindling fluorescent proteins for precise in vivo photolabeling. *Nature Biotechnology*, *21*(2), 191–194.

Chudakov, D. M., Matz, M. V., Lukyanov, S., & Lukyanov, K. A. (2010). Fluorescent proteins and their applications in imaging living cells and tissues. *Physiological Reviews*, *90*(3), 1103–1163.

Chudakov, D. M., Verkhusha, V. V., Staroverov, D. B., Souslova, E. A., Lukyanov, S., & Lukyanov, K. A. (2004). Photoswitchable cyan fluorescent protein for protein tracking. *Nature Biotechnology*, *22*(11), 1435–1439.

Chun, W., Waldo, G. S., & Johnson, G. V. W. (2010). Split GFP complementation assay for quantitative measurement of tau aggregation in situ. *Methods in Molecular Biology*, *670*, 109–123 (Chapter 9).

Cody, C. W., Prasher, D. C., Westler, W. M., Prendergast, F. G., & Ward, W. W. (1993). Chemical structure of the hexapeptide chromophore of the Aequorea green-fluorescent protein. *Biochemistry*, *32*(5), 1212–1218.

Cormack, B. P., Valdivia, R. H., & Falkow, S. (1996). FACS-optimized mutants of the green fluorescent protein (GFP). *Gene*, *173*(1 Spec. No.), 33–38.

Crameri, A., Whitehorn, E. A., Tate, E., & Stemmer, W. P. (1996). Improved green fluorescent protein by molecular evolution using DNA shuffling. *Nature Biotechnology*, *14*(3), 315–319.

Davidson, M. W., & Campbell, R. E. (2009). Engineered fluorescent proteins: Innovations and applications. *Nature Methods*, *6*(10), 713–717.

Day, R. N., & Davidson, M. W. (2009). The fluorescent protein palette: Tools for cellular imaging. *Chemical Society Reviews*, *38*(10), 2887.

Delagrave, S., Hawtin, R. E., Silva, C. M., Yang, M. M., & Youvan, D. C. (1995). Red-shifted excitation mutants of the green fluorescent protein. *Biotechnology (NY)*, *13*(2), 151–154.

Domin, A., Lan, M. J., & Kaminski, C. (2004). Effects of fixation on cyan fluorescent protein and its fluorescence resonance energy transfer efficiency. Paper presented at the Laser Applications to Chemical and Environmental Analysis.

Fehr, M., Okumoto, S., Deuschle, K., Lager, I., Looger, L. L., Persson, J., et al. (2005). Development and use of fluorescent nanosensors for metabolite imaging in living cells. *Biochemical Society Transactions*, *33*(Pt 1), 287–290.

Frommer, W. B., Davidson, M. W., & Campbell, R. E. (2009). Genetically encoded biosensors based on engineered fluorescent proteins. *Chemical Society Reviews*, *38*(10), 2833.

Gould, T. J., Verkhusha, V. V., & Hess, S. T. (2009). Imaging biological structures with fluorescence photoactivation localization microscopy. *Nature Protocols*, *4*(3), 291–308.

Gross, L. A., Baird, G. S., Hoffman, R. C., Baldridge, K. K., & Tsien, R. Y. (2000). The structure of the chromophore within DsRed, a red fluorescent protein from coral. *Proceedings of the National Academy of Sciences of the United States of America*, *97*(22), 11990–11995.

Grotjohann, T., Testa, I., Leutenegger, M., Bock, H., Urban, N. T., Lavoie-Cardinal, F., et al. (2011). Diffraction-unlimited all-optical imaging and writing with a photochromic GFP. *Nature*, 1–5.

Gunewardene, M. S., Subach, F. V., Gould, T. J., Penoncello, G. P., Gudheti, M. V., Verkhusha, V. V., et al. (2011). Superresolution imaging of multiple fluorescent proteins with highly overlapping emission spectra in living cells. *Biophysical Journal*, *101*(6), 1522–1528.

Gurskaya, N. G., Verkhusha, V. V., Shcheglov, A. S., Staroverov, D. B., Chepurnykh, T. V., Fradkov, A. F., et al. (2006). Engineering of a monomeric green-to-red photoactivatable fluorescent protein induced by blue light. *Nature Biotechnology*, *24*(4), 461–465.

Hastings, J. W., & Morin, J. G. (1969). Comparative biochemistry of calcium-activated photoproteins from the Ctenophore, Mnemiopsis and the coelenterates Aequorea, Obelia, Pelagia and Renilla. *The Biological Bulletin*, *137*, 402.

Heim, R., Cubitt, A. B., & Tsien, R. Y. (1995). Improved green fluorescence. *Nature*, *373*(6516), 663–664.

Heim, R., Prasher, D. C., & Tsien, R. Y. (1994). Wavelength mutations and posttranslational autoxidation of green fluorescent protein. *Proceedings of the National Academy of Sciences of the United States of America*, *91*(26), 12501–12504.

Hess, S. T., Girirajan, T. P. K., & Mason, M. D. (2006). Ultra-high resolution imaging by fluorescence photoactivation localization microscopy. *Biophysical Journal*, *91*(11), 4258–4272.

Hofmann, M., Eggeling, C., Jakobs, S., & Hell, S. W. (2005). Breaking the diffraction barrier in fluorescence microscopy at low light intensities by using reversibly photoswitchable proteins. *Proceedings of the National Academy of Sciences of the United States of America*, *102*(49), 17565–17569.

Hoi, H., Shaner, N. C., Davidson, M. W., Cairo, C. W., Wang, J., & Campbell, R. E. (2010). A monomeric photoconvertible fluorescent protein for imaging of dynamic protein localization. *Journal of Molecular Biology*, *401*(5), 776–791.

Honda, A., Adams, S. R., Sawyer, C. L., Lev-Ram, V., Tsien, R. Y., & Dostmann, W. R. (2001). Spatiotemporal dynamics of guanosine 3′,5′-cyclic monophosphate revealed by a genetically encoded, fluorescent indicator. *Proceedings of the National Academy of Sciences of the United States of America*, *98*(5), 2437–2442.

Huang, B., Babcock, H., & Zhuang, X. (2010). Breaking the diffraction barrier: Super-resolution imaging of cells. *Cell*, *143*(7), 1047–1058.

Inouye, S., & Tsuji, F. I. (1994). Aequorea green fluorescent protein. Expression of the gene and fluorescence characteristics of the recombinant protein. *FEBS Letters*, *341*(2–3), 277–280.

Johnson, F. H., Shimomura, O., Saiga, Y., Gershman, L. C., Reynolds, G. T., & Waters, J. R. (1962). Quantum efficiency of Cypridina luminescence, with a note on that of Aequorea. *Journal of Cellular and Comparative Physiology*, *60*, 85–104.

Kerppola, T. K. (2008). Bimolecular fluorescence complementation (BiFC) analysis as a probe of protein interactions in living cells. *Annual Review of Biophysics*, *37*(1), 465–487.

Kremers, G. J., Gilbert, S. G., Cranfill, P. J., Davidson, M. W., & Piston, D. W. (2011). Fluorescent proteins at a glance. *Journal of Cell Science*, *124*(15), 2676.

Landgraf, D., Okumus, B., Chien, P., Baker, T. A., & Paulsson, J. (2012). Segregation of molecules at cell division reveals native protein localization. *Nature Methods*, *9*(5), 480–482.

Lippincott-Schwartz, J., & Patterson, G. H. (2003). Development and use of fluorescent protein markers in living cells. *Science*, *300*(5616), 87–91.

Lippincott-Schwartz, J., & Patterson, G. H. (2009). Photoactivatable fluorescent proteins for diffraction-limited and super-resolution imaging. *Trends in Cell Biology*, *19*(11), 555–565.

Llopis, J., McCaffery, J. M., Miyawaki, A., Farquhar, M. G., & Tsien, R. Y. (1998). Measurement of cytosolic, mitochondrial, and Golgi pH in single living cells with green fluorescent proteins. *Proceedings of the National Academy of Sciences of the United States of America*, *95*(12), 6803–6808.

Lukyanov, K. A., Chudakov, D. M., Lukyanov, S., & Verkhusha, V. V. (2005). Innovation: Photoactivatable fluorescent proteins. *Nature Reviews. Molecular Cell Biology*, *6*(11), 885–891.

Luo, K. Q., Yu, V. C., Pu, Y., & Chang, D. C. (2001). Application of the fluorescence resonance energy transfer method for studying the dynamics of caspase-3 activation during UV-induced apoptosis in living HeLa cells. *Biochemical and Biophysical Research Communications*, *283*(5), 1054–1060.

Matz, M. V., Fradkov, A. F., Labas, Y. A., Savitsky, A. P., Zaraisky, A. G., Markelov, M. L., et al. (1999). Fluorescent proteins from nonbioluminescent Anthozoa species. *Nature Biotechnology*, *17*(10), 969–973.

Miesenbock, G., De Angelis, D. A., & Rothman, J. E. (1998). Visualizing secretion and synaptic transmission with pH-sensitive green fluorescent proteins. *Nature*, *394*(6689), 192–195.

Miyawaki, A., Llopis, J., Heim, R., McCaffery, J. M., Adams, J. A., Ikura, M., et al. (1997). Fluorescent indicators for Ca^{2+} based on green fluorescent proteins and calmodulin. *Nature*, *388*(6645), 882–887.

Miyawaki, A., & Tsien, R. Y. (2000). Monitoring protein conformations and interactions by fluorescence resonance energy transfer between mutants of green fluorescent protein. *Methods in Enzymology*, *327*, 472–500.

Morin, J. G., & Hastings, J. W. (1971). Energy transfer in a bioluminescent system. *Journal of Cellular Physiology*, *77*(3), 313–318.

Morise, H., Shimomura, O., Johnson, F. H., & Winant, J. (1974). Intermolecular energy transfer in the bioluminescent system of Aequorea. *Biochemistry*, *13*(12), 2656–2662.

Ormo, M., Cubitt, A. B., Kallio, K., Gross, L. A., Tsien, R. Y., & Remington, S. J. (1996). Crystal structure of the *Aequorea victoria* green fluorescent protein. *Science*, *273*(5280), 1392–1395.

Patterson, G., Davidson, M., Manley, S., & Lippincott-Schwartz, J. (2010). Superresolution imaging using single-molecule localization. *Annual Review of Physical Chemistry*, *61*(1), 345–367.

Patterson, G. H., & Lippincott-Schwartz, J. (2002). A photoactivatable GFP for selective photolabeling of proteins and cells. *Science*, *297*(5588), 1873–1877.

Periasamy, A., & Day, R. N. (1998). FRET imaging of Pit-1 protein interactions in living cells. *Journal of Biomedical Optics*, *3*(2), 154–160.

Piston, D. W., & Kremers, G.-J. (2007). Fluorescent protein FRET: The good, the bad and the ugly. *Trends in Biochemical Sciences*, *32*(9), 407–414.

Prasher, D. C., Eckenrode, V. K., Ward, W. W., Prendergast, F. G., & Cormier, M. J. (1992). Primary structure of the *Aequorea victoria* green-fluorescent protein. *Gene*, *111*(2), 229–233.

Reid, B. G., & Flynn, G. C. (1997). Chromophore formation in green fluorescent protein. *Biochemistry*, *36*(22), 6786–6791.

Remington, S. J. (2006). Fluorescent proteins: Maturation, photochemistry and photophysics. *Current Opinion in Structural Biology*, *16*(6), 714–721.

Rizzo, M. A., Davidson, M. W., & Piston, D. W. (2009a). Fluorescent protein tracking and detection: Applications using fluorescent proteins in living cells. *Cold Spring Harbor Protocols*, *2009*(12), pdb.top64.

Rizzo, M. A., Davidson, M. W., & Piston, D. W. (2009b). Fluorescent protein tracking and detection: Fluorescent protein structure and color variants. *Cold Spring Harbor Protocols*, *2009*(12), pdb.top63.

Rust, M. J., Bates, M., & Zhuang, X. (2006). Sub-diffraction-limit imaging by stochastic optical reconstruction microscopy (STORM). *Nature Methods*, *3*(10), 793–796.

Sakaue-Sawano, A., Kurokawa, H., Morimura, T., Hanyu, A., Hama, H., Osawa, H., et al. (2008). Visualizing spatiotemporal dynamics of multicellular cell-cycle progression. *Cell*, *132*(3), 487–498.

Sato, M., Hida, N., Ozawa, T., & Umezawa, Y. (2000). Fluorescent indicators for cyclic GMP based on cyclic GMP-dependent protein kinase Ialpha and green fluorescent proteins. *Analytical Chemistry*, *72*(24), 5918–5924.

Schermelleh, L., Heintzmann, R., & Leonhardt, H. (2010). A guide to super-resolution fluorescence microscopy. *The Journal of Cell Biology*, *190*(2), 165–175.

Sekar, R. B., & Periasamy, A. (2003). Fluorescence resonance energy transfer (FRET) microscopy imaging of live cell protein localizations. *The Journal of Cell Biology*, *160*(5), 629–633.

Shaner, N. C., Campbell, R. E., Steinbach, P. A., Giepmans, B. N., Palmer, A. E., & Tsien, R. Y. (2004). Improved monomeric red, orange and yellow fluorescent proteins

derived from *Discosoma* sp. red fluorescent protein. *Nature Biotechnology*, *22*(12), 1567–1572.

Shaner, N. C., Lin, M. Z., McKeown, M. R., Steinbach, P. A., Hazelwood, K. L., Davidson, M. W., et al. (2008). Improving the photostability of bright monomeric orange and red fluorescent proteins. *Nature Methods*, *5*(6), 545–551.

Shaner, N. C., Patterson, G. H., & Davidson, M. W. (2007). Advances in fluorescent protein technology. *Journal of Cell Science*, *120*(24), 4247–4260.

Shaner, N. C., Steinbach, P. A., & Tsien, R. Y. (2005). A guide to choosing fluorescent proteins. *Nature Methods*, *2*(12), 905–909.

Shcherbo, D., Murphy, C. S., Ermakova, G. V., Solovieva, E. A., Chepurnykh, T. V., Shcheglov, A. S., et al. (2009). Far-red fluorescent tags for protein imaging in living tissues. *The Biochemical Journal*, *418*(3), 567.

Shekhawat, S. S., & Ghosh, I. (2011). Split-protein systems: Beyond binary protein–protein interactions. *Current Opinion in Chemical Biology*, *15*(6), 789–797.

Shimomura, O. (1979). Structure of the chromophore of Aequorea green fluorescent protein. *FEBS Letters*, *104*, 220–222.

Shimomura, O., Johnson, F. H., & Saiga, Y. (1962). Extraction, purification and properties of aequorin, a bioluminescent protein from the luminous hydromedusan, *Aequorea*. *Journal of Cellular and Comparative Physiology*, *59*, 223–239.

Siemering, K. R., Golbik, R., Sever, R., & Haseloff, J. (1996). Mutations that suppress the thermosensitivity of green fluorescent protein. *Current Biology*, *6*(12), 1653–1663.

Tsutsui, H., Karasawa, S., Shimizu, H., Nukina, N., & Miyawaki, A. (2005). Semi-rational engineering of a coral fluorescent protein into an efficient highlighter. *EMBO Reports*, *6*(3), 233–238.

Vogel, S. S., Thaler, C., & Koushik, S. V. (2006). Fanciful FRET. *Science's STKE*, *2006*(331), re2.

Wall, M. A., Socolich, M., & Ranganathan, R. (2000). The structural basis for red fluorescence in the tetrameric GFP homolog DsRed. *Natural Structural Biology*, *7*(12), 1133–1138.

Wang, L., Jackson, W. C., Steinbach, P. A., & Tsien, R. Y. (2004). Evolution of new nonantibody proteins via iterative somatic hypermutation. *Proceedings of the National Academy of Sciences of the United States of America*, *101*(48), 16745–16749.

Wang, D. S., Miller, R., Shaw, R., & Shaw, G. (1996). The pleckstrin homology domain of human beta I sigma II spectrin is targeted to the plasma membrane in vivo. *Biochemical and Biophysical Research Communications*, *225*(2), 420–426.

Wiedenmann, J., Gayda, S., Adam, V., Oswald, F., Nienhaus, K., Bourgeois, D., et al. (2011). From EosFP to mIrisFP: Structure-based development of advanced photoactivatable marker proteins of the GFP-family. *Journal of Biophotonics*, *4*(6), 377–390.

Wiedenmann, J., Ivanchenko, S., Oswald, F., Schmitt, F., Rocker, C., Salih, A., et al. (2004). EosFP, a fluorescent marker protein with UV-inducible green-to-red fluorescence conversion. *Proceedings of the National Academy of Sciences of the United States of America*, *101*(45), 15905–15910.

Wiedenmann, J., & Nienhaus, G. U. (2006). Live-cell imaging with EosFP and other photoactivatable marker proteins of the GFP family. *Expert Review of Proteomics*, *3*(3), 361–374.

Wiedenmann, J., Oswald, F., & Nienhaus, G. U. (2009). Fluorescent proteins for live cell imaging: Opportunities, limitations, and challenges. *IUBMB Life*, *61*(11), 1029–1042.

Yang, F., Moss, L. G., & Phillips, G. N., Jr. (1996). The molecular structure of green fluorescent protein. *Nature Biotechnology*, *14*(10), 1246–1251.

Zaccolo, M., De Giorgi, F., Cho, C. Y., Feng, L., Knapp, T., Negulescu, P. A., et al. (2000). A genetically encoded, fluorescent indicator for cyclic AMP in living cells. *Nature Cell Biology*, *2*(1), 25–29.

Zacharias, D. A., & Tsien, R. Y. (2006). Molecular biology and mutation of green fluorescent protein. *Methods of Biochemical Analysis*, *47*, 83–120.

Zhou, X. X., Chung, H. K., Lam, A. J., & Lin, M. Z. (2012). Optical control of protein activity by fluorescent protein domains. *Science*, *338*(6108), 810–814.

CHAPTER

Live-Cell Fluorescence Imaging

6

Jennifer C. Waters

Department of Cell Biology, Harvard Medical School, Boston, Massachusetts, USA

CHAPTER OUTLINE

Introduction **126**
6.1 Preparing a Specimen for Fluorescence Live-Cell Imaging **127**
6.1.1 Choice of Fluorophore 127
6.1.2 Mounting the Specimen for Viewing 128
6.1.2.1 Avoiding Spherical Aberration and Light Scattering 128
6.1.2.2 Chambers for Live-Cell Imaging 129
6.1.3 Maintaining Temperature 131
6.1.4 Cell Culture Media for Imaging 131
6.1.5 Preventing Photobleaching 132
6.2 Choice of Microscope **132**
6.2.1 The Microscope Stand 132
6.2.2 Mode of Fluorescence Microscopy 133
6.3 Wide-Field Illumination of the Specimen **134**
6.3.1 Light Source 134
6.3.2 Diaphragms 135
6.3.3 Filter Sets 136
6.3.4 Automation of Filter Selection 137
6.4 Choosing the Best Objective Lens for Your Application **138**
6.4.1 NA: Resolution and Brightness 138
6.4.2 Magnification 139
6.4.3 Correction for Aberrations 139
6.4.4 Phase and DIC Objective Lenses 140
6.5 Acquiring Digital Images Over Time **141**
6.5.1 Cameras 141
6.5.1.1 Quantum Efficiency and Gain 141
6.5.1.2 Camera Noise 142
6.5.1.3 Determining Exposure Time 142
6.5.1.4 Signal (aka Shot Or Poisson) Noise 143
6.5.1.5 Camera Binning 143

Methods in Cell Biology, Volume 114 **ISSN 0091-679X**
Copyright © 2007 Elsevier Inc. All rights reserved.
http://dx.doi.org/10.1016/B978-0-12-407761-4.00006-3

6.5.2 Shutters 144
6.5.3 Maintaining Focus 144
6.6 nD Imaging 145
6.7 Verifying Cell Health and Troubleshooting Sick Cells 146
Conclusion 148
Acknowledgments 148
References 148

Abstract

This chapter examines the ways to optimize the signal-to-noise ratio while keeping the specimen healthy. Live cells expressing fluorescent protein fusions are usually dim compared to fixed specimens, both because the fluorescent proteins are not very bright and because there is, in most cases, only one fluorophores per protein. It is also favorable to choose cells that are expressing low levels of fluorescent protein fusions to minimize the difference from the levels of the endogenous protein *in vivo*. Long camera exposure times, which allow accumulation of weak signals, must be often avoided to reduce photobleaching and phototoxicity and to acquire images quickly enough to capture cell dynamics. Choices, such as objective lens and camera, determine the signal-to-noise ratio of an imaging system. Optimizing the imaging system to maximize signal and minimize noise is critical for live-cell fluorescence imaging. Imaging with high signal-to-noise ratio will allow detection of low concentrations of fluorescent fusion proteins with illumination conditions that are less likely to damage cells. Automation of an imaging system allows collection of multidimensional data while helping to maintain focus and minimize specimen exposure to light. Under all imaging conditions, maintaining and verifying cell health is essential to the validity of the experimental results.

INTRODUCTION

With the discovery of genetically encoded fluorescent proteins, such as green fluorescent protein (GFP; Chapter 6 by Straight, volume 81, 2007; Shaner, Steinbach, & Tsien, 2005), many molecular and cell biologists who previously used microscopy only for simple localization experiments in fixed specimens now wish to use microscopy for both localization and quantitation of fluorescence in live cells over time. Accurate localization and quantification of fluorescence requires images of the highest possible quality (Chapter 14 by Wolf et al., this volume; and Chapter 22 by Murray, volume 81, 2007), which is particularly difficult to achieve in live cells. The ideal fluorescence image has a high signal-to-noise ratio and adequate spatial resolution. While spatial resolution is necessary to discern specimen detail, the most challenging and critical parameter for live-cell imaging is detection of weak fluorescent signals above background noise generated by the specimen and the imaging system. Imaging systems with high signal detection to noise ratio are essential both for detecting weak fluorescence signals and for accurate quantitation of small changes in concentration of fluorophore.

Imaging live cells poses many more problems than imaging fixed specimens. For live-cell fluorescence imaging, attaining an adequate image must be balanced with minimizing illumination to protect the specimen against photodamage and photobleaching. Live cells expressing fluorescent protein fusions are usually dim compared to fixed specimens, both because the fluorescent proteins are not very bright and because there is, in most cases, only one fluorophore per protein. It is also favorable to choose cells that are expressing low levels of fluorescent protein fusions to minimize the difference from levels of the endogenous protein *in vivo*. Long camera exposure times that allow accumulation of weak signals must often be avoided to reduce photobleaching and phototoxicity, and to acquire images quickly enough to capture cell dynamics. With these challenges, it is especially important that the specimen, microscope, and detector be optimized to maximize the signal while minimizing the addition of noise to the image (Table 6.1). Live-cell imaging is further complicated by the need to keep the specimen at the appropriate temperature and pH and to maintain focus over time. In this chapter, we will begin with the specimen and work our way through the optical path to the detector, examining ways to optimize the signal-to-noise ratio while keeping the specimen healthy.

6.1 PREPARING A SPECIMEN FOR FLUORESCENCE LIVE-CELL IMAGING

6.1.1 Choice of fluorophore

Fluorophores are molecules that absorb light of particular wavelengths, leading to the emission of longer wavelengths of light (Chapter 4 by Wolf, this volume; Herman, 1987; Tsien, Ernst, & Waggoner, 2006). Fluorophores vary greatly in their

Table 6.1 Fluorescence Live-Cell Imaging Checklist

To increase signal
- ☐ Choose a bright fluorophore
- ☐ Image through a clean No. 1.5 coverslip
- ☐ Mount specimen as close to coverslip as possible
- ☐ Use high NA, minimally corrected oil immersion clean objective lens with lowest acceptable magnification
- ☐ Choose fluorescence filter sets that match fluorophores
- ☐ Align arc lamp for Koehler illumination
- ☐ Use antiphotobleaching inhibitors
- ☐ Remove DIC Wollaston prism and analyzer from light path
- ☐ Use cooled CCD camera with at least 60% quantum efficiency
- ☐ Use camera binning

To decrease background/noise
- ☐ Turn off the room lights
- ☐ Close down the field diaphragm
- ☐ Use phenol red-free media
- ☐ Use cooled CCD camera with low readout noise

brightness and rate of photobleaching. Among the many fluorescent proteins that are now available, there can be brightness differences as much as 30-fold (Thorn, 2000). To attain the highest possible signal-to-noise and signal-to-background ratio in our final image, we want to start with the brightest possible fluorophore. Brightness is determined by the fluorophore's extinction coefficient and quantum yield. Extinction coefficient is a measure of how efficiently a fluorophore absorbs light while quantum yield is the ratio of the number of photons emitted to the number of photons absorbed. These numbers are usually available from the manufacturer or in the published articles in which the proteins were introduced. Fluorescent proteins are discussed in more detail in Chapter 6 by Straight, volume 81, 2007.

6.1.2 Mounting the specimen for viewing

6.1.2.1 Avoiding spherical aberration and light scattering

Spherical aberration is an axial elongation and asymmetry of the image, which decreases axial resolution (resolution in "z"; Keller, 2006; Wallace, Schaefer, & Swedlow, 2001). Spherical aberration also greatly reduces the intensity and clarity of the image (North, 2006; Fig. 6.1) and should therefore be avoided as much as possible in live-cell fluorescence imaging. To avoid spherical aberration, one should consider the specifications of the objective lens (Chapter 1 by Sluder and Nordberg, this volume; and Chapter 3 by Ernst Keller, volume 81, 2007; Abramowitz, Spring, Keller, & Davidson, 2002; Keller, 2006) when deciding how to mount a specimen for imaging. The highest resolution objective lenses are designed to image a specimen that is just beneath a 170-μm thick coverslip and mounted in a media with the same refractive index as the lens immersion medium. Spherical aberration is introduced when there is a mismatch in refractive index between the media surrounding the

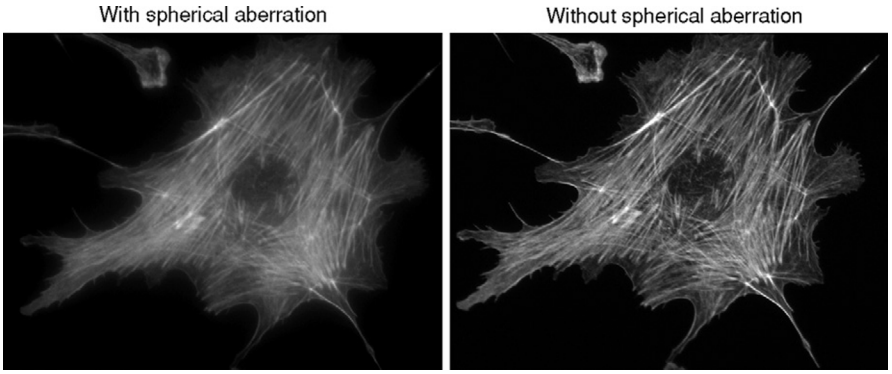

FIGURE 6.1

Spherical aberration can be introduced by the specimen. Fluorescence images of tissue culture cells labeled with Alexa 488 phalloidin. A difference in refractive index between the lens immersion medium and the specimen itself (i.e., immersion oil and an aqueous medium) causes spherical aberration. Spherical aberration was generated using an immersion oil with a higher refractive index (1.534) than that of the specimen mounting media (~1.45). Spherical aberration results in decreased intensity and resolution.

specimen and the objective lens immersion medium, as is the case when a specimen mounted in aqueous cell culture media is imaged with an oil immersion objective lens (Egner & Hell, 2006). The effect gets worse and image intensity decreases as distance from the coverslip increases, so every effort should be made to mount the specimen as close to the coverslip as possible. Water immersion lenses can be used to reduce spherical aberration when imaging a specimen mounted in an aqueous medium and are particularly useful when imaging deep into an aqueous solution. Water immersion lenses are used with a No. 1.5 coverslip, and should not be confused with water-dipping lenses (such as those used for electrophysiology work) which are designed to be used without a coverslip. Care must be taken when using water immersion lenses, as tilt in the coverslip relative to the lens can result in additional aberrations (Arimoto & Murray, 2004).

With high numerical aperture (NA) air objectives in particular, using the wrong thickness of coverslip increases spherical aberration and decreases image intensity (Spring & Davidson, 2006). The thickness of coverslip (in millimeters) that the lens is designed to be used with is marked just after the infinity symbol (which refers to the now almost universally used infinity corrected optics) on the barrel of most modern objective lenses, and is 0.17 mm (grade No. 1.5) in most cases (Abramowitz et al., 2002). The effect of coverslip thickness on images formed with high NA dry objectives is so detrimental to image quality that many high resolution air objective lenses come with a correction collar that is used to compensate for error in coverslip thickness. These collars wrap around the barrel of the objective and are adjusted by rotating the collar relative to the objective lens. If such a collar is present, it should be adjusted for each specimen every time the lens is used to minimize spherical aberration (Fig. 6.2A and B).

It is also very important for image quality that the coverslip surface proximal to the objective lens and the top lens of the objective are clean (see Inoué & Spring, 1986 for thorough instructions on how to clean an objective lens). Prior to imaging, use a gentle glass cleaner such as Sparkle (www.glasscleaner.com) or a weak solution of a mild detergent to wipe any dirt and excess media from the coverslip. This is especially important when using an oil immersion objective, as residue on the coverslip will mix with the immersion oil, leaving the objective lens in need of cleaning as well. Also note that immersion oil from different manufacturers does not necessarily mix, and old immersion oil accumulates dirt. Clean old immersion oil off of the coverslip surface with Sparkle or pure ethanol before adding fresh immersion oil.

6.1.2.2 Chambers for live-cell imaging

Chambers for live-cell imaging serve multiple purposes (Dailey, Focht, et al., 2006; Swedlow & Andrews, 2005). They hold the specimen on a coverslip and allow for a volume of cell culture media necessary to keep the cells alive. Chambers designed for live-cell imaging may be open or sealed closed. Open chambers are used when the cells need to be accessed directly before or during imaging, for experiments which require drug delivery or microinjection, for example. Chambers that can be sterilized are preferable for long-term imaging experiments. And finally, specialized chambers provide temperature and CO_2 control (described in Section 6.1.3).

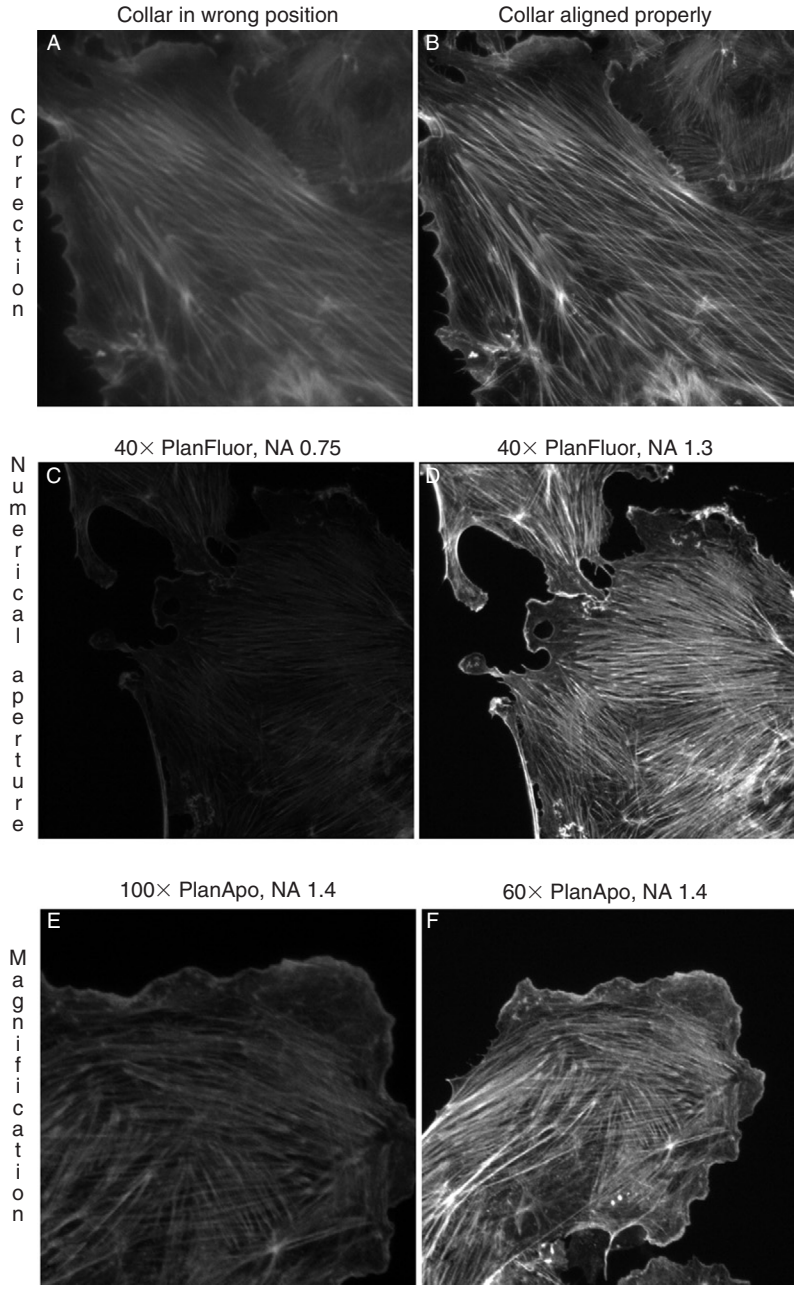

FIGURE 6.2

Image quality and brightness depend on the objective lens. Fluorescence images of tissue culture cells labeled with Alexa 488 phalloidin (Invitrogen, Eugene, OR). Each image pair was collected and is displayed identically to demonstrate differences in intensity. (A and B) High NA dry objectives (in this case, a 40× PlanApo NA 0.95) often have a correction collar for coverslip thickness. Neglecting to adjust these collars introduces spherical aberration which degrades image quality. (C and D) An image formed with a high NA oil immersion lens (NA 1.3) is much brighter than an image formed with a lower NA dry lens (NA 0.75). (E and F) Increasing magnification without increasing NA results in a dimmer image.

There are several commercially available dishes for use in optical microscopy. One commonly used simple design is a round plastic tissue culture dish with a coverslip bottom (MatTek, Ashland, MA). Rectangular coverlips with plastic multiple well chambers are also available (LabTek II Chambered Coverglass, Nalgene Nunc, Rochester, NY), as are coverslip bottomed 6 through 96-well plates (MatTek; Nalgene Nunc). With all of these commercially available dishes, be sure to order No. 1.5 thickness of coverslip glass. These dishes are available sterilized and/or with coatings such as poly-l-lysine to enhance cell adherence to the glass. For a more economical solution, reusable metal chambers that hold standard coverslips can be made with easily obtainable materials and the help of a machine shop (Dailey, Focht, et al., 2006; Rieder & Cole, 1998; Sluder, Nordberg, Miller, & Hinchcliffe, 2005).

6.1.3 Maintaining temperature

Cells must be kept at physiological temperature during imaging to ensure health and to be confident that cell behavior on the microscope is an accurate representation of behavior *in vivo* (Swedlow & Andrews, 2005). For the most commonly used mammalian cell types, this requires heating the sample to 37 °C. There are many commercially available solutions to heating specimens on a microscope stage. Simple and economical designs use heating elements to warm metal chambers that hold a coverslip (20/20 Technology, Inc., Wilmington, NC; Warner Instruments, Hamden, CT). These work well for shorter term experiments. However, in this design, oil objective lenses and the stage act as heat sinks, drawing heat way from the specimen. Maintaining focus during live-cell imaging can be a major source of frustration, and heating only the chamber which holds the sample introduces thermal drift as the heater cycles on and off. One way to help alleviate this problem is to add a heated collar that is placed around the barrel of the objective lens (Bioptech, Butler, PA). However, heating the objective lens does not completely eliminate thermal drift, and cycles of heating and cooling are not particularly good for the objective lens. The most reliable way to maintain temperature over time is to build an incubator around the body of the microscope (Solent Scientific Limited, Segensworth, UK). Microscope incubators are usually made of plexiglass and are custom designed to fit around the microscope and peripheral devices. These incubators enclose the majority of the microscope and keep it at a stable temperature, which helps to eliminate thermal drift. With microscope incubation chambers, a specimen prepared on a coverslip bottomed dish (as described above) can move directly from the cell culture incubator to the microscope stage, without the need to remount the specimen in a chamber. This is not only convenient but also maintains sterility.

6.1.4 Cell culture media for imaging

Typical media used for tissue cell culture, such as D-MEM, contains phenol red to monitor pH and is buffered by sodium bicarbonate and an atmosphere of 5% CO_2. Phenol red-free versions of these media should be used for fluorescence live-cell imaging, as phenol red is fluorescent and increases background in the image. A method of

buffering the media while the cells are on the microscope stage is also needed. Some commercially available temperature control chambers deliver humidified 5% CO_2 to the specimen, so traditional sodium bicarbonate buffered media can be used. With simple sealed chambers, media can be purged with CO_2 prior to sealing the chamber. Another common approach is to change to a prewarmed media that maintains pH in atmospheric CO_2 just prior to imaging such as Gibco CO_2-Independent Media (Invitrogen, Eugene, OR) or Leibowitz. Supplementing sodium bicarbonate buffered media with 10–25-mM HEPES can also help to maintain pH under atmospheric CO_2. It is critical that the cells be tested for viability in the media used for imaging (discussed in Section 6.6).

Evaporation of the cell culture media can be a problem with a specimen in an open chamber, especially when heated to 37 °C. We have had good results using a layer of mineral oil poured over the cell culture media to prevent evaporation. The oil allows sufficient gas exchange (to maintain pH in an atmosphere of 5% CO_2 when necessary) while minimizing evaporation for, in our tests, as long as 4 days. A capillary needle can also be moved through the layer of mineral oil to reach the cells, providing a convenient way to "seal" a chamber during microinjection or micromanipulation experiments.

6.1.5 Preventing photobleaching

Photobleaching is the irreversible destruction of the fluorophore that can occur when the fluorophore is in an excited state, which leads to the familiar fading of fluorescence during observation (Diaspro, Chirico, Usai, Ramoino, & Dobrucki, 2006). Photobleaching is best prevented by optimizing the imaging system to maximize signal and minimize noise (Table 6.1) so that the lowest possible level of illumination can be used. A lot of photobleaching occurs when searching for the perfect cell through the eyepiece or while focusing the image of the specimen on the camera. The amount of time spent illuminating the specimen when not acquiring images should be kept at a minimum. If photobleaching is still a problem, it can be prevented by depleting oxygen from the media. One commercially available solution is Oxyrase or OxyFluor (www.oxyrase.com), which was originally made for growing anaerobes and has been successfully used to prevent photobleaching during live-cell imaging (0.5–1.0 units oxyrase per milliliter imaging media; Wittmann, Bokoch, & Waterman-Storer, 2003).

6.2 CHOICE OF MICROSCOPE

6.2.1 The microscope stand

Inverted microscope stands are preferable for most live-cell imaging applications. With the inverted microscope design, the specimen is imaged with an objective lens from beneath the microscope stage. This allows for sufficient room on the microscope stage for cell culture dishes filled with media and heated incubation chambers, and allows easy access to the specimen for perfusion or microinjection. High-quality

inverted microscope stands are heavy and stable, making them resistant to focus drift. To prevent vibration that can degrade resolution, the microscope stand should be mounted on a vibration isolation table.

6.2.2 Mode of fluorescence microscopy

There are various modes of fluorescence imaging, including wide-field fluorescence microscopy (Herman, 1987), multipoint scanning confocal [(Toomre & Pawley, 2006); such as spinning disk (Adams et al., 2003; Maddox, Moree, Canman, & Salmon, 2003), swept field, or slit scanning confocal (Liebling et al., 2006)], laser scanning confocal (Chapter 21 by Bulseco and Wolf, this volume; Conchello & Lichtman, 2005), multiphoton excitation microscopy (Piston, 1999), and total internal fluorescence microscopy (TIRF; Axelrod, 2001). Confocal and TIRF are dealt with in more detail in other chapters of this volume; this section provides general guidelines for choosing the appropriate technique for a live-cell imaging experiment.

Standard fluorescence microscopy (Herman, 1987) is referred to as wide-field to differentiate it from other fluorescence microscopy techniques. Unlike confocal techniques, wide-field uses full-field illumination, and all of the emission light that passes through the objective is sent to the detector. For live-cell imaging, wide-field can be used with a high quantum efficiency, low noise cooled charge-coupled device (CCD) camera (Section 6.4.1; Chapter 8 by Spring, this volume; Spring, 2000), helping to make it a high signal-to-noise ratio technique (Swedlow, Hu, Andrews, Roos, & Murray, 2001) and an excellent choice for live-cell imaging experiments. If a focus motor (Section 6.4.3) is used to collect multiple focal planes at regular intervals ("z-series"), constrained iterative digital deconvolution can be used to increase the signal-to-noise ratio of wide-field images (Wallace et al., 2001).

It is a common misconception that confocal microscopy is a higher resolution technique that is always preferable to wide-field when available. The benefit of confocal microscopy over wide-field is not increased resolution as much as the removal of out-of-focus fluorescence. Therefore, in specimens where there is no significant out-of-focus fluorescence, there is no benefit of using a confocal microscope. The resolution of both wide-field and confocal are limited by the NA of the objective lens (Section 6.3) and the wavelength of emission light (Inoué, 2006). While there is a modest increase in axial resolution when using a confocal microscope, it is difficult to achieve and rarely enough to uncover new information in specimens with minimal out-of-focus fluorescence. The use of the pinhole in confocal microscopy leads to a 20% loss of in focus light from the image plane (Pawley, 2006), significantly reducing the useful signal that makes it to the detector. Since wide-field fluorescence with a high-quality cooled CCD camera has been shown to be a lower noise technique than laser scanning confocal (Swedlow et al., 2001), in cases where a decrease in out-of-focus fluorescence is not needed, wide-field microscopy will produce a higher signal-to-noise image than laser scanning confocal. The test that works well in most cases is as follows: if the wide-field fluorescence image looks good through the eyepiece, you do not need a confocal microscope.

In live specimens that do have significant out-of-focus information that degrades the wide-field image, confocal microscopy can produce a very satisfying increase in the signal-to-noise ratio (Dailey, Mander, Soll, & Terasaki, 2006). Laser scanning confocal (also called point scanning confocal) has the benefit of variable pinhole, so its size can be matched to the objective lens and wavelength of light to provide maximum removal of out-of-focus information. For low light level live-cell applications, however, it can be difficult to get a reasonable signal-to-noise image at laser levels that do not bleach the specimen and at speeds fast enough to capture fast cell dynamics.

There are now several designs of faster multipoint or slit scanning confocals available (Toomre & Pawley, 2006). A commonly used model is the Yokogawa spinning disk confocal, which has been shown to be excellent for low light level live-cell imaging (Adams et al., 2003; Maddox et al., 2003). This model is designed for high resolution work, as the fixed pinhole size provides maximum reduction of out-of-focus fluorescence only when used with a 100× 1.4 NA objective lens. These confocals acquire high signal-to-noise images with reduced out-of-focus fluorescence at a much faster rate than laser scanning confocals and are therefore favorable for live-cell confocal imaging.

When deep penetration into biological tissue (100 μm or more) is needed, multiphoton excitation is necessary. The long wavelengths of illumination used for multiphoton penetrate deeply into biological specimens, and emission light scattered by the specimen is collected and used for image formation (Piston, 1999). Since longer wavelengths of light are less damaging to cells, multiphoton excitation can also be useful for imaging fluorophores that are normally excited by high energy shorter wavelength photons. However, multiphoton is expensive, difficult to execute well, and a lower resolution technique, and should therefore only be used when the specimen demands it.

In TIRF microscopy (Axelrod, 2001), the evanescent wave of energy that forms at the boundary between two media of different refractive index (usually the coverslip and the aqueous specimen) when light totally internally reflects is used to excite fluorophores in the specimen. The evanescent wave penetrates only 50–100 nm into the specimen, so only fluorophores very close to the coverslip surface are excited, resulting in a very high signal-to-noise image with a much thinner optical section than confocal or wide-field (50–100 nm vs ~700 nm). However, it is only useful for studying parts of the specimen that are close to the coverslip surface, such as membrane proteins and focal adhesions.

6.3 WIDE-FIELD ILLUMINATION OF THE SPECIMEN

6.3.1 Light source

The most commonly used light source for fluorescence microscopy is a mercury or xenon arc lamp (Nolte, Pawley, & Horing, 2006; Ploem, 1999). These are intense light sources that produce a large amount of heat, which can damage live specimens.

A heat absorption filter (available from the microscope manufacturer) should therefore be placed in the light path, just after the lamp housing.

In order to get even illumination across the entire field of view, it is essential to align the arc lamp so that it is in focus and centered at the back focal plane of the objective lens, referred to as Koehler illumination (Inoué & Spring, 1986; Waters, 2005). When the arc lamp is in focus at the back focal plane of the objective lens, the objective lens will project a maximally out-of-focus image of the light source onto the specimen. This provides even illumination of the specimen. To view the image of the arc at the back focal plane of the objective, unscrew an objective lens from the nosepiece and place a piece of paper on the stage. Use the collector lens, found at the front of the lamp housing, to focus the image of the arc onto the paper. Two translation screws on the lamp housing allow movement of the bulb in X and Y to center it in the field of view. Many lamp housings have a mirror behind the arc to reflect down the optical path light that would otherwise be lost. If a mirror is present, there will be three additional screws at the back of the lamp housing that move the mirror in Z, X, and Y so that the reflected image of the bulb can also be focused and centered at the back focal plane of the objective.

When you are in the fortunate position of having a specimen that is too bright for the camera, there are often neutral density filters in the light path between the lamp housing and filter sets that can be used to attenuate illumination. These filters are most often labeled "ND" and then a number which is the denominator in the fraction of light that the filter allows through. For example, an ND 4 filter allows one-fourth of the illuminating light through to the specimen.

6.3.2 Diaphragms

There are two diaphragms present in the fluorescence light path (Inoué & Spring, 1986; Ploem, 1999). Both diaphragms are located in the light path between the lamp housing and the fluorescence filter sets. The aperture diaphragm (found in some but not all fluorescence microscopes) is in focus at the back focal plane of the objective. Its location means that closing down the diaphragm decreases the NA of the illumination and decreases intensity of illumination. The second diaphragm is the field diaphragm. The field diaphragm is placed in a position in the optical path such that it is in focus at the image plane. When closed down while looking at the image of the specimen, the in-focus edges of the octagonal-shaped field diaphragm can be seen. It is very important in live-cell imaging to properly adjust the field diaphragm to frame the field of view. The field diaphragm should be open just enough to illuminate only the area of the sample you are interested in. Note that the area imaged by the camera is often smaller than that seen through the eyepiece, and the field diaphragm should therefore be closed down further when imaging with a camera. If the field diaphragm is open more than is needed, parts of the specimen are illuminated that you are not imaging, and light scattered from these parts of the specimen can contribute background to the image (Fig. 6.3A and B).

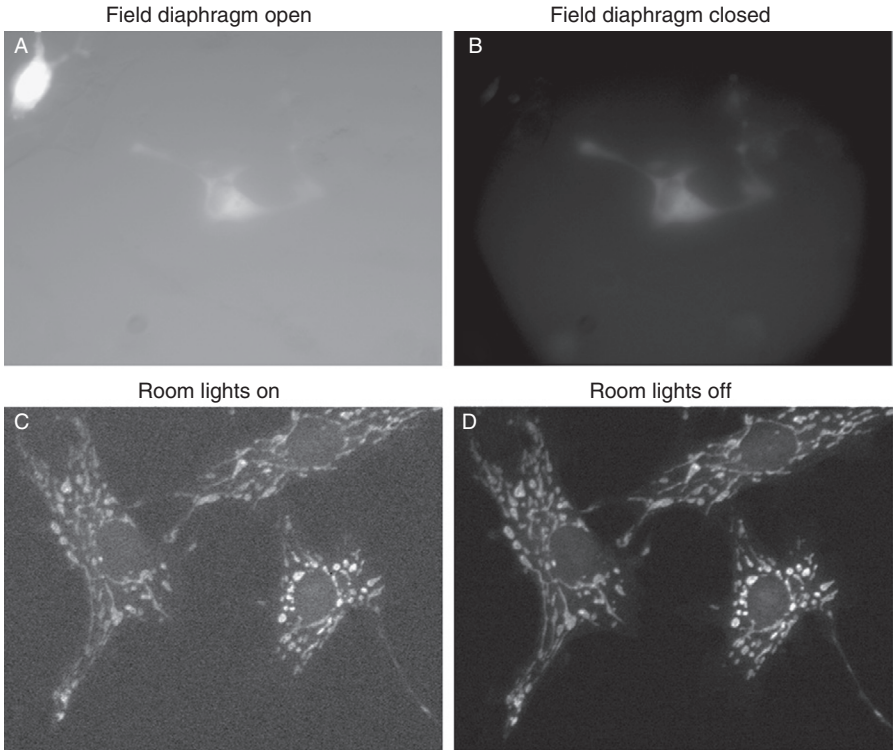

FIGURE 6.3

Stray light adds noise to fluorescence images. (A and B) Fluorescence images of live tissue culture cells expressing a GFP fusion protein. (A) With the field diaphragm all the way open, cells which are not of interest (top left corner) contribute scattered light to the image. (B) Closing down the field diaphragm so that only the cell of interest is illuminated greatly decreases the background fluorescence. (C and D) Fluorescence images of cells labeled with MitoTracker Red (Invitrogen, Eugene, OR). Light from the room is collected by the objective lens, increasing the background in the image. Images were collected and are displayed identically to demonstrate differences in intensity.

6.3.3 Filter sets

A set of three filters is used to visualize fluorophores in the wide-field fluorescence microscope (Kinoshita, 2002; Ploem, 1999; Reichman, 2000). The illuminating light first encounters the excitation filter, which is chosen to allow through the wavelengths of light that excite the fluorophore. The light then hits the dichromatic mirror (or beam splitter), which is positioned at a 45° angle relative to the incident light. The excitation light is reflected 90° by the dichromatic mirror, down the optical axis of the microscope. The light is collected by the objective lens and projected onto the specimen. The fluorophores in the specimen absorb the excitation wavelengths of

light and emit longer wavelengths of light. The emission light is collected by the objective, and then must pass back through the dichromatic mirror. The dichromatic mirror is therefore designed to reflect the excitation wavelengths, but transmit the emission wavelengths. The reflection of the excitation wavelengths is not 100%—a small amount of this light passes through the dichromatic mirror. However, the emission light is only 10^{-4} to 10^{-10} as intense as the excitation light, so the excitation light that passes through the dichromatic mirror must be blocked from reaching the detector or it will contribute background to the image. This light is blocked by the third and final filter, the emission filter (also called the barrier filter). The emission filter can also be used to select more carefully for the emission wavelengths of light expected from the fluorophore. A "band-pass" filter is more selective, allowing through a narrow band of wavelengths. A "long-pass" filter is less selective, allowing through light above a specified wavelength. Choice of band-pass versus long-pass emission filter is an important one. The band-pass has the advantage of selectivity, making it the best choice for specimens labeled with more than one fluorophore. The lack of selectivity of the long-pass filter is beneficial if your specimen is labeled with only one fluorophore and does not have autofluorescence that needs to be filtered out. The long-pass filter will allow through all of the fluorescence from the fluorophore, resulting in the brightest possible image.

It is important to accurately match the fluorophore(s) you are imaging with an appropriate filter set (Kinoshita, 2002; Ploem, 1999; Reichman, 2000). Absorption and emission spectra for fluorophores are available online from the company where they were purchased, or can be easily produced with a spectrofluorometer. Transmission spectra for filter sets are also available online from the microscope or filter manufacturer. These spectra should be compared so that the fluorophore is illuminated with wavelengths of light that it maximally absorbs, and so that all or the majority of the emission light coming from the fluorophore passes through the dichromatic mirror and emission filter. There are several websites that offer useful tools to create overlays of fluorophore and filter spectra (e.g., the "Curv-o-matic" at www.omegafilters.com).

6.3.4 Automation of filter selection

For live-cell imaging of more than one fluorophore, switching between filter sets must be automated. Motorized microscope stands are now available from all of the major microscope manufacturers. These stands include motorized fluorescence filter turrets and shutters that can be controlled by commercially available image acquisition software packages. The speed of movement varies among microscope models and manufacturers, but can take as long as 1 s or more to move between adjacent filter set positions. If rapid switching between wavelengths is required for your experiments, a faster solution is necessary.

Motorized filter wheels (Dailey, Focht, et al., 2006; Salmon & Waters, 1996; Prior Scientific, Rockland, MA; Sutter Instrument, Novado, CA) can be used to switch between wavelengths at faster speeds; filter wheels switch between adjacent positions on the order of 20 ms. In this setup, excitation filters are removed from the

filter cubes and placed in a motorized wheel that is positioned in front of the lamp housing. A multiple band-pass dichromatic mirror is used that reflects multiple excitation wavelengths and transmits multiple emission wavelengths. To select for emission wavelengths, a multiple band-pass emission filter can be used, but these allow more bleed through than single-pass emission filters. Single-pass emission filters can be used by adding a second filter wheel in front of the camera. This design is more thoroughly described in Chapter 9 by Salmon et al., this volume.

For even faster switching between excitation wavelengths, a monochromator can be used (Dailey, Focht, et al., 2006). Monochromators use prisms or diffraction gratings to spatially separate colors of light. The dispersed or diffracted light is then moved mechanically to direct a narrow band of select wavelengths through an exit pinhole or slit. Switching between excitation wavelengths using these devices takes only ~1 ms. Multiple band-pass emission filters are then used to select for emission wavelengths. Monochromators are commonly used for live-cell ratio imaging of calcium probes, where rapid switching between excitation wavelengths is critical (Chapter 16 by O'Connor and Silver, this volume).

Some experiments call for simultaneous imaging of two or more fluorophores. This can be accomplished by simultaneously exciting the multiple fluorophores, and using a device which splits the emission light into two or four images that are focused side by side onto the same CCD camera chip (Dailey, Focht, et al., 2006; Optical Insights, Tuscan, AZ; Hamamatsu Photonics, Bridgewater, NJ). These devices are very useful for fast moving specimens or for live-cell ratio imaging experiments such as Förster resonance energy transfer (FRET; Chapter 16 by O'Connor and Silver, this volume).

6.4 CHOOSING THE BEST OBJECTIVE LENS FOR YOUR APPLICATION

In fluorescence microscopy, the objective lens is used for both illumination of the specimen and image formation. It is critical to live-cell imaging applications that an objective lens is carefully selected, with properties that will help to optimize the signal-to-noise ratio of the image.

6.4.1 NA: resolution and brightness

The NA of a lens is defined as $n(\sin \theta)$, where n is the refractive index of the medium between the specimen and the coverslip (such as air or immersion oil) and θ is the half angle of light acceptance (Keller, 2006). NA is arguably the most important property of an objective lens. In fluorescence microscopy, both the resolution of the microscope and the brightness of the image are dependent on the NA of the objective lens.

The NA of the objective is marked on the barrel of the lens, just after the magnification (Abramowitz et al., 2002; Keller, 2006). A lens with an NA above the refractive index of air (~1) is designed to be used with an immersion medium of higher refractive index such as immersion oil, water, or glycerol. Use of an immersion

medium decreases refraction and total internal reflection at the glass–air interface, resulting in a significantly brighter image (Fig. 6.2C and D). While immersion media are messy to work with, the increase in signal is well worth the effort.

The resolution of an objective lens can be defined as size of the smallest possible point source in the image, the radius of which is given by $0.61\lambda/\mathrm{NA}$, where λ is the wavelength of emission light (Inoué, 2006). The axial resolution (resolution in "z") of the light microscope is different and significantly worse. The axial resolution of the microscope is defined as $(2\lambda n)/(\mathrm{NA})^2$, where n is the refractive index of the medium the specimen is immersed in.

The brightness of an objective lens is equal to $10^4\mathrm{NA}^4/M^2$, where M is the magnification (Abramowitz et al., 2002; Keller, 2006; Fig. 6.2E and F). High NA lenses are exquisitely sensitive to light. It is therefore important that the room lights be turned off, especially on an inverted microscope where the objective lens points directly toward ceiling lights (Fig. 6.3C and D). For very low light level imaging, it can also be beneficial to turn off bright computer monitors after acquisition has begun, or to position the monitor away from the microscope.

6.4.2 Magnification

If all other properties of the lens remain the same, image intensity decreases with magnification ($10^4\mathrm{NA}^4/M^2$; Fig. 6.2E and F). The lowest possible magnification should therefore be used for fluorescence live-cell imaging. For maximum resolution, sufficient magnification is necessary to ensure that the resolution of the microscope is matched to the size of the detector elements in the camera (Chapter 8 by Spring, this volume; Spring, 2000; Waters, 2006). Sacrificing some resolution by using a high NA, lower magnification lens is one way to increase signal in low light level applications.

6.4.3 Correction for aberrations

There are several aberrations that can be found in objective lenses (Keller, 2006; Chapter 3 by Ernst Keller and Chapter 18 by Goodwin and Visiting Scientist, volume 81, 2007), two of which are of particular concern for fluorescence live-cell imaging—chromatic aberration and spherical aberration. Chromatic aberration causes a shift between different wavelengths along the axial axis of the microscope and is, therefore, problematic when imaging more than one fluorophore (North, 2006). Chromatic aberration occurs because different wavelengths of light refract at different angles as they pass through the lens. Spherical aberration can be introduced by the wrong thickness of coverslip or by a change in refractive index between the coverslip and specimen, as was described earlier. Spherical aberration can also be inherent in an objective lens, since light that travels through the periphery of a spherical refractive lens comes into focus at a different plane than light that travels through the center of the lens. Objective lenses with spherical aberration will produce images that are less intense and have worse axial resolution than lens that are free of spherical aberration (Figs. 6.1A and B and 6.2A and B).

Objective lenses that are corrected for spherical and chromatic aberrations are called achromatic (least corrected), fluorite, or apochromatic (most highly corrected). Most research grade microscopes use fluorite or apochromatic lenses, which are marked Fluor (or Fluar) or Apo, respectively, on the objective lens barrel (Abramowitz et al., 2002). Correction for chromatic and spherical aberration is not perfect and the extent of correction varies with individual lenses. The best way to characterize both the resolution capabilities and the extent of aberrations in a particular lens is to collect three-dimensional images of small beads (less than 200 μm in diameter) that fluoresce in multiple wavelengths (available from Invitrogen/Molecular Probes, Eugene, OR; Chapter 14 by Wolf et al., this volume; Hiraoka, Sedat, & Agard, 1990). These images will reveal the extent of spherical aberration in the lens and any shifts between wavelengths. See exercise 8a in Chapter 14 by Wolf et al., this volume.

Objectives are corrected for aberrations by adding additional elements to the lens. Unfortunately, these also decrease the transmission of light through the objective, particularly in the UV range (Keller, 2006). When imaging only one fluorophore, chromatic aberration is not a concern and a less highly corrected Fluor lens may produce a brighter image than an Apo lens. Most of the lenses we use are also marked Plan to indicate correction for an additional aberration, curvature of field (Keller, 2006). Lenses that are not Plan corrected have higher transmission in the UV range and are essential for applications such as ratio imaging of the calcium indicator dye FURA (Chapter 16 by O'Connor and Silver, this volume).

6.4.4 Phase and DIC objective lenses

When working on a fluorescence microscope that is also set up for the transmitted light methods phase or differential interference contrast (DIC), it is important to understand the effect of the phase or DIC components on the fluorescence image (Inoué & Spring, 1986).

Phase objective lenses (usually marked Ph1, Ph2, or Ph3) have a ring in the back focal plane that is necessary for generating the phase effect (Inoué & Spring, 1986). The ring is designed to absorb light and decreases the transmission of light through the objective by as much 30%. Phase objective lenses are therefore not ideal for fluorescence live-cell imaging and should not be used unless the acquisition of phase images during fluorescence time-lapse recording is necessary.

DIC objectives (usually marked DIC or Pol) are not modified in a way that affects light transmission and are therefore a good choice for fluorescence live-cell imaging. However, when a microscope is configured for DIC imaging, there are two additional components in the light path that do affect the fluorescence image (Chapter 13 by Moomaw, volume 81, 2007; Inoué & Spring, 1986). The analyzer is a piece of polarization film that is located between the objective and the eyepieces, and when placed in the light path decreases transmission by 50%. The Wollaston prism is most often found just after the objective lens in the optical path. It shears each point source of light into two point sources separated by up to a few hundred nanometers (Inoué & Spring, 1986). When the

Wollaston prism is in the light path, it decreases lateral resolution of the fluorescence image and decreases the intensity of each point source of light (and is especially harmful for confocal microscopy). Both the analyzer and Wollaston prism should therefore be removed from the light path when collecting a fluorescence image. If both fluorescence and DIC images are collected during a time-lapse experiment, the Wollaston prism is usually left in place. However, the analyzer can be placed in a motorized emission filter wheel in front of the camera so that its removal from the light path during fluorescence image acquisition can be automated (Chapter 9 by Salmon et al., this volume). Motorization of removal and insertion of the analyzer into the light path is also an option on many motorized microscope stands.

6.5 ACQUIRING DIGITAL IMAGES OVER TIME

6.5.1 Cameras

Acquiring fluorescence images of live cells is especially challenging because a relatively low number of photons are emitted from the specimen. It is therefore essential that a sensitive detector is used that contributes minimal noise to the image. The CCD cameras commonly used for wide-field fluorescence imaging are covered in detail in Chapter 8 by Spring, this volume; Chapter 10 by Rasnik et al., this volume; and Chapter 13 by Moomaw, volume 81, 2007 (Spring, 2000; Waters, 2006). This section will review the most important considerations for acquiring high signal-to-noise ratio digital images of live fluorescent cells.

6.5.1.1 Quantum efficiency and gain

Quantum efficiency is the percentage of incident photons that are recorded by the CCD camera (Inoué & Spring, 1986; Spring, 2000; Spring & Davidson, 2004). Higher quantum efficiency means that the detector is more sensitive and will therefore require lower exposure times. Lower exposure times mean the specimen is exposed to less light, which helps to prevent photobleaching and phototoxicity. It also means that images can be collected with the higher temporal resolution necessary for capturing fast dynamic processes. The CCD cameras that are most commonly used for fluorescence microscopy have quantum efficiencies in the range of 50–70% (meaning that 30–50% of the photons coming from the specimen are disregarded; Spring & Davidson, 2004), which is tolerable for most live cell work. Back-thinned CCD chips have quantum efficiencies as high at 90% (Spring & Davidson, 2004), but they are also expensive and have fragile detectors. Color cameras should never be used for fluorescence live-cell imaging, since the filters needed to create the color image decrease the quantum efficiency substantially. Graphs of the quantum efficiency of a camera, which varies with the wavelength of light, are usually available on the manufacturer's website.

For very low-intensity fluorescence, amplification of the signal may be necessary. Such amplification is referred to as "gain." This can be accomplished with an intensifier placed in front of a standard CCD chip (Inoué & Spring, 1986). While

intensifiers offer very high gain, they have low quantum efficiency. Newer electron multiplication (EM) CCDs (Basden, Haniff, & Mackay, 2003) amplify the signal on the CCD chip, prior to readout (so readout noise is not amplified). EM-CCDs add more noise to an image than a standard CCD chip, so they should only be used when all other options for increasing signal have been exhausted (Chapter 10 by Rasnik et al., this volume; and Chapter 13 by Moomaw, volume 81, 2007).

6.5.1.2 Camera noise

All CCD cameras contribute noise to each pixel in the resulting digital image (Inoué & Spring, 1986; Spring, 2000; Waters, 2006). High noise levels can mask weak signals coming from the specimen, effectively decreasing the sensitivity and dynamic range of the camera. In fluorescence live-cell imaging, the signal is often weak, making it very important to choose a low noise camera. The two main types of camera noise are dark (also called thermal) noise and readout noise. Cooled CCD cameras have negligible dark noise and are therefore preferable for imaging fluorescence. Readout noise is generated as the signal is read from the CCD chip, and is significantly higher than dark noise in cooled CCD cameras. Readout noise increases with readout rate, so faster cameras generally have more readout noise.

Noise levels for a camera can be found on specification sheets available from the manufacturer's website. Noise is given in electrons to make it easy to compare one camera to another, that is for instance, the camera has a DC readout level of 100 electrons with a standard deviation of eight electrons, then eight electrons is the noise. For live-cell fluorescence imaging, readout noise of eight electrons or less is acceptable. [To make the expected noise contribution easier to appreciate, electrons can be converted into gray scale values with the following equation: gray scale value = electrons/(full well capacity/maximum gray scale value).]

6.5.1.3 Determining exposure time

The optimal fluorescence digital image uses the full dynamic range of the camera without saturating. A maximum gray scale value in the image which is ~90% of the maximum gray scale value the camera can produce is ideal. Realistically, this is difficult if not impossible to achieve with dim live fluorescent specimens. Even with brighter specimens, it may be preferable to underexpose the image in order to maintain cell viability and reduce photobleaching. When an image is underexposed, the maximum gray scale value decreases and gets closer to the noise level of the camera. The noise therefore becomes more noticeable, resulting in a grainy appearance to the image. More importantly, when an image is underexposed, signal noise (explained in Section 6.5.1.4) degrades the accuracy of fluorescence intensity measurements.

A common error when determining the best exposure time for a specimen is to look at the image on the monitor to judge image quality. Images from the cooled CCD cameras most commonly used for live-cell fluorescence imaging are 12 or 14 bit (2^{12} or 2^{14} gray scale values, respectively). The monitor can display only 256 gray scale values and our eyes can see only about 60. Therefore, to determine image quality, we must use the image acquisition software to measure gray scale values in the image. This can be

accomplished with a histogram that displays the range of gray scale values in the image, a utility offered in most image acquisition software packages.

"Auto-expose" functions in image-processing software usually expose the specimen to light for an undesirable amount of time while calculating the optimal exposure time. The optimal exposure time is better determined by guessing an exposure time (which will become easier as you get to know your camera and specimen) and then looking at the gray scale values in the image to determine if the exposure time needs to be adjusted.

6.5.1.4 Signal (aka shot or poisson) noise

The intrinsic statistical variation in the detected fluorescence signal, called signal noise, is equal to the square root of the signal. Signal noise is always present and there is nothing that can be done to eliminate it from an image, so its effect on the accuracy of fluorescence intensity measurements must be considered. The danger of underexposing a digital image is as the maximum gray scale value in the image decreases, signal noise becomes a larger percentage of the measurement, rendering the result less accurate.

6.5.1.5 Camera binning

Camera binning is very useful for fluorescence live-cell imaging. Binning is a function of some CCD cameras and is set in the image acquisition software. When an image is binned, the signal from subarrays of adjacent pixels (i.e., 2×2 pixels) is pooled together prior to readout. The outcome is a larger pixel that is four times brighter, but that has same readout noise as one single pixel. This results in a significant increase in the signal-to-noise ratio of the image (Fig. 6.4). The trade-off is resolution, as the pixels in

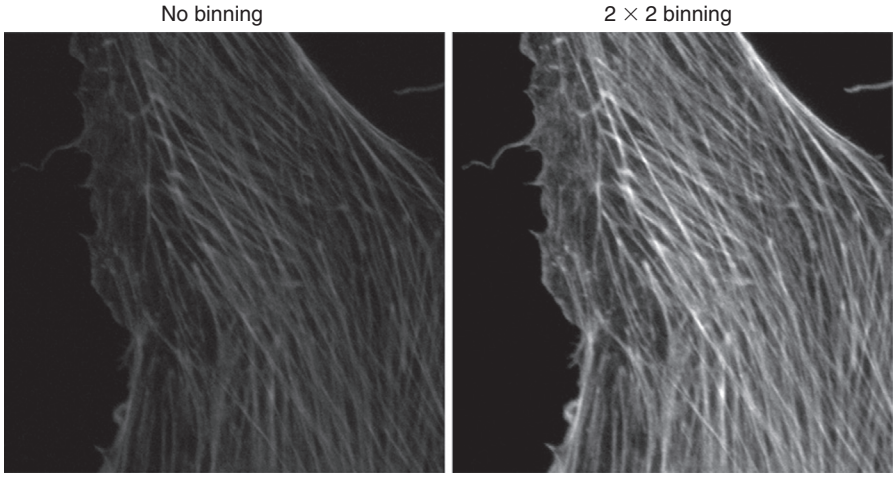

FIGURE 6.4

Camera binning increases the signal of a digital image, without increasing read noise. Some resolution is lost, but this is often a worthwhile sacrifice in exchange for increase in signal-to-noise ratio. The loss of resolution is barely noticeable in these images of fluorescently labeled actin in tissue culture cells, while the increase in signal is dramatic.

the image are now effectively twice the size. However, since detection of weak fluorescence signals is often more important than acquiring the highest possible resolution images, the increase in signal-to-noise is often well worth the decrease in resolution. Binning has the added benefit of decreasing the image file size and transfer time, which is especially useful when faster acquisition rates are required.

6.5.2 Shutters

It is essential that the light source is shuttered between camera exposures to minimize illumination of the specimen. This is most often accomplished with a mechanical shutter (Dailey, Focht, et al., 2006; Prior Scientific; Sutter Instrument) controlled with image acquisition software. When choosing image acquisition software, it is important to be sure that the software opens the shutter just before and closes the shutter directly after the camera acquires the image. A delay (on the order of 20 ms) is sometimes needed after the shutter is opened and before the camera acquires the image to ensure vibration caused by the shutter opening has dissipated. However, software that allows the shutter to remain open significantly longer than is necessary to properly expose the image will result in unnecessary photodamage and photobleaching of the specimen. This problem can usually be detected by acquiring an image with a very short exposure time (10 ms).

6.5.3 Maintaining focus

Maintaining focus during live-cell imaging can be a major source of frustration. Focus changes over time due to gravity acting on the gears within the focus mechanism, changes in temperature, and movement of the specimen.

On most inverted microscopes used for live-cell imaging, the nosepiece is moved up and down by the focus mechanism. Making the nosepiece as light as possible by removing objectives that are not being used can help to reduce focus drift. For many microscope models, torque of the focus mechanism can be adjusted so that more force is needed to move the gears. The presence of a focus motor directly coupled to the fine focus mechanism of the microscope also helps to stabilize focus.

As described earlier, microscope incubators are the best way to minimize focus drift resulting from fluctuations in temperature. After placing a dish into a microscope incubator, or after assembling a localized heated chamber, it should be expected that there will be some focus drift for 10–20 min while the temperature equilibrates. It is also important to maintain as constant an ambient room temperature as is possible. Air conditioning and heating vents should be positioned in the room so that the air does not directly blow onto the microscope. With high NA objective lenses, the smallest shifts in temperature and air currents in the room can result in loss of focus.

Focus drift can also occur as a result of a specimen that is mounted in a chamber that "settles" over time. When placing the specimen onto the microscope stage, it is important to make sure that the specimen is held as tightly to the stage as is possible. Use stage clips or tape to hold dishes to the stage and be sure that the stage plate is locked or screwed into place. This is especially important when collecting

z-series—if the specimen is at all loose it will move as the focus position is changed, rendering the z-series inaccurate.

Specimens that do not naturally adhere to the glass coverslip should be immobilized during imaging to prevent movement out of the focal plane or blurring in the digital image. For example, a common way to immobilize yeast during imaging is to place them in a solidified media containing gelatin. In this design, the cells should be sandwiched between the gelatin and a coverslip so that the light between the specimen and the objective does not need to pass through the gelatin (Maddox, 2000), which would cause spherical aberration.

There are a couple of ways to deal with persistent focus drift, both of which require automation of focus (Section 6.5). One way is to use autofocusing algorithms available with many image acquisition software packages. These can work very well, with a few caveats. The focal plane that the software chooses based on image intensity and sharpness may not be the focal plane you are interested in, and autofocusing can be slow depending on the speed of the algorithm and focus motor. Autofocusing on the fluorescence image is not a good idea, since several images need to be collected in the process resulting in additional photodamage and photobleaching. Instead, autofocusing should be performed on a transmitted light image. This requires mechanical shutters on both the fluorescence and the transmitted light path so that the software can switch between the two modes of microscopy.

There are clever new commercially available technological solutions to maintaining focus that give excellent results (Hogan, 2006; Applied Scientific Instrumentation, Eugene, OR; Nikon Instruments, Melville, NY; Olympus America Inc., Melville, NY). In these systems, an infrared laser beam is sent through the back of the objective lens. The beam exits the objective at a high angle such that it totally internally reflects at the interface between the coverslip and the specimen. The light that reflects back into the objective is monitored. As the distance between the objective lens and the coverslip changes, so does the intensity and position of the light reflected back into the objective. A focus motor is used to continuously adjust the focus to maintain a single focal plane. These instruments are currently most commonly used in conjunction with TIRF microscopes in which focus is critical, but they work so reliably it is likely that they will soon be found on all microscopes used for live-cell imaging.

6.6 nD IMAGING

With the development of fast and accurate motorized components of the microscope, we can now collect z-series images of multiple fluorophores at multiple stage positions over time—so-called multidimensional or nD imaging. Collecting multiple focal planes is necessary for analyzing specimens that move in three dimensions and for quantitative digital deconvolution (Wallace et al., 2001). Motorized stages can be used to collect images of multiple fields of view over time, greatly increasing the amount of data that can be collected in one experiment.

Collecting multiple focal planes at precise intervals ("z-series" optical sections or image stacks) requires automation of focus controlled by image acquisition software (Dailey, Focht, et al., 2006). This is most often accomplished with a stepper motor that drives the focus mechanism of the microscope. Stepper motors are available built within motorized microscopes, or as peripheral devices that attach to the fine focus mechanism. To increase accuracy, linear encoders can be added which monitor the distance the stepper motor moves and make adjustments as needed. Piezoelectric focus devices are alternatives to stepper motors that offer higher accuracy and speed. Piezoelectric devices can be attached to the nosepiece to move a single objective up and down along the optical axis of the microscope. Newer piezoelectric designs move a stage plate relative to the objective lens to focus and have the advantage of being easier to use with multiple objective lenses. Piezoelectric devices are much faster and more accurate than traditional stepper motors, but only operate over a limited working range (usually between 50 and 400 μm, depending on the model).

Movement between fields of view or between wells in multiwell dishes can be automated with motorized stages controlled with image-processing software (Dailey, Focht, et al., 2006). X and Y positions of the stage are memorized in the software, and the stage can be moved back to memorized positions with the click of a mouse or at each time point in a time-lapse experiment. Images from each field of view can then be collated and made into a movie. The motorized stage must return to memorized positions with high accuracy for this to work well, as inaccuracy will cause shifts between images in the movie (this can be corrected for later with software, if there is a stationary object within the field of view that can be used as a reference point). As with focus stepper motors, accuracy in motorized stage movement can be increased with the addition of linear encoders.

6.7 VERIFYING CELL HEALTH AND TROUBLESHOOTING SICK CELLS

When imaging fluorescence in live cells, two important questions should be addressed. Is the fluorescently labeled protein behaving like the endogenous protein, and is the illuminating light damaging the cells?

It must be demonstrated that the localization of the fluorescently labeled protein is the same, over time, as the endogenous protein. If the localization of the protein has not been established, a method of fluorescently labeling the endogenous protein is required. This is most commonly achieved with indirect immunofluorescence labeling of the protein. Whenever possible, fixed time point assays should be used to verify the behavior of the protein over time with live-cell imaging results. For fluorescent protein fusions, it should also be shown that the fusion protein's expression level and stability is similar to the endogenous protein (Chapter 6 by Straight, volume 81, 2007; Spector & Goldman, 2005). Optimizing the signal-to-noise ratio of your imaging setup will allow you to choose cells that are expressing lower levels of fluorescent fusion proteins to image.

Light damages cells. This is especially true of shorter wavelengths such as the blue light used to image GFP (Chu, Zheng, Chen, & Hu, 2006; Gorgidze, Oshemkova, & Vorobjev, 1998; Seko, Pang, Tokoro, Ichinose, & Mochizuki, 2001; Sparrow & Cai, 2001). Excitation of fluorophores also generates free radicals that damage cells. We must therefore always be concerned about the health of our live specimens during fluorescence imaging. It is essential that control tests are performed to ensure that the imaging conditions are not changing cell behavior. After an imaging experiment is complete, the cells that were imaged should be compared to cells outside of the imaged field of view. Using transmitted light (phase or DIC), look for the accumulation of vacuoles within cells, fragmented mitochondria, or unusually large numbers of apoptotic cells (for sample images of light-damaged cells see Dailey, Focht, et al., 2006). Many of the live-cell imaging experiments we perform are short in duration, but damage to cells may not be obvious until hours later. It is good practice to continue to image cells for a long period of time (on the order of 24 h) after the experiment, collecting transmitted light images every 20–30 min, to look for long-term effects. Mitotic index and duration of mitosis are also good indicators of cell health.

What if the cells do look sick or behave abnormally? If all of the cells in the dish appear affected, you should check the imaging media and temperature. Ensure that the pH of the media is maintained over the course of the experiment and use a thermometer to measure the temperature of the media on the microscope stage. Try removing any antiphotobleaching reagents (e.g., Oxyrase), as they may be toxic to some cell types. On occasion, coverslips used right out of the packaging can contain contaminants that are harmful to cells. Vigorous cleaning of coverslips prior to plating cells can alleviate this problem (Canman & Salmon, 2000).

A next test would be to replace the growth medium in a fresh batch of cells with the imaging media (if it is different than the growth medium), and place the cells on the microscope stage in the heated chamber (if one is being used) or in a tissue culture incubator. Do not image the cells, but wait to see if the cells still look healthy after 24 h. If they do not, another imaging media should be tried.

If the cells tolerate the imaging media, be sure that the imaging system is optimized as much as is possible for maximum signal and minimum noise, as described throughout this chapter and summarized in Table 6.1. Use a very low level of illumination (by using a low exposure time and/or neutral density filters) to image the cells such that the fluorescent labeling is barely visible. Use camera binning whenever possible, and make sure that there is a heat absorption filter in front of the light source that cuts out infrared light. Slowly increase the exposure time and remove the neutral density filters until you determine the maximum level of light the cells will tolerate. You should then image as far away from that maximum as is possible while still attaining an adequate signal-to-noise ratio for your experiment. Experiment with illumination light level versus exposure time—some cells tolerate short exposure times at high-intensity levels while others do better with long exposure times at lower light levels. If the lowest possible light exposure still cause appreciable damage, and the imaging system has been optimized for signal-to-noise, free radical scavengers such as vitamin C or Trolox may help (Swedlow & Andrews, 2005).

CONCLUSION

Choices such as objective lens and camera determine the signal-to-noise ratio of an imaging system. Optimizing your imaging system to maximize signal and minimize noise is critical for live-cell fluorescence imaging. Imaging with high signal-to-noise ratio will allow detection of low concentrations of fluorescent fusion proteins with illumination conditions that are less likely to damage cells. Automation of an imaging system allows collection of multidimensional data while helping to maintain focus and minimize specimen exposure to light. Under all imaging conditions, maintaining and verifying cell health is essential to the validity of the experimental results.

Acknowledgments

Many thanks to Dr. Meg Bentley for critical reading of this chapter. Thanks also to Lara Petrak, without whom I would never find the time to write. I am also very grateful to Ted Salmon, Jason Swedlow, David Wolf, Kip Sluder, Ken Spring, John Murray, Tim Mitchison, Clare Waterman-Storer, Conly Rieder, Rich Cole, Butch Moomaw, Paul Goodwin, and Charles Felts for many helpful discussions on specimen preparation, microscopy, and digital imaging.

References

Abramowitz, M., Spring, K. R., Keller, H. E., & Davidson, M. W. (2002). Basic principles of microscope objectives. *Biotechniques*, *33*(4), 772–781.

Adams, M. C., Salmon, W. C., Gupton, S. L., Cohan, C. S., Wittman, T., Prigozhina, N., et al. (2003). A high-speed multispectral spinning-disk confocal microscope system for fluorescent speckle microscopy of living cells. *Methods*, *29*, 29–41.

Arimoto, R., & Murray, J. M. (2004). A common aberration with water-immersion objective lenses. *Journal of Microscopy*, *216*(1), 49–51.

Axelrod, D. (2001). Total internal reflection fluorescence microscopy in cell biology. *Traffic*, *2*, 764–774.

Basden, A. G., Haniff, C. A., & Mackay, C. D. (2003). Photon counting strategies with low light level CCDs. *Monthly Notices of the Royal Astronomical Society*, *345*(3), 985–991.

Canman, J., & Salmon, E. D. (2000). *Protocols: Coverslip preparations*. http://www.bio.unc.edu/faculty/salmon/lab/protocolscoverslippreps.html.

Chu, R., Zheng, X., Chen, D., & Hu, D. N. (2006). Blue light irradiation inhibits production of HGF by human retinal pigment epithelium cells *in vitro*. *Photochemistry and Photobiology*, *82*(5), 1247–1250.

Conchello, J.-A., & Lichtman, J. (2005). Optical sectioning microscopy. *Nature Methods*, *2*, 920–931.

Dailey, M. E., Focht, D. C., Khodjakov, A., Rieder, C. L., Patterson, G. H., Lippincott-Schwartz, J., et al. (2006). Introduction to live-cell imaging techniques. http://www.microscopyu.com/articles/livecellimaging/index.html.

Dailey, M. E., Mander, E., Soll, D. R., & Terasaki, M. (2006). Confocal microscopy of living cells. In J. B. Pawley (Ed.), *Handbook of biological confocal microscopy* (3rd ed., pp. 126–144). New York: Springer.

Diaspro, A., Chirico, G., Usai, C., Ramoino, P., & Dobrucki, J. (2006). Photobleaching. In J. B. Pawley (Ed.), *Handbook of biological confocal microscopy* (3rd ed., pp. 690–699). New York: Springer.

Egner, A., & Hell, S. W. (2006). Aberrations in confocal and multi-photon fluorescence microscopy induced by refractive index mismatch. In J. B. Pawley (Ed.), *Handbook of biological confocal microscopy* (3rd ed., pp. 404–412). New York: Springer.

Gorgidze, L. A., Oshemkova, S. A., & Vorobjev, I. A. (1998). Blue light inhibits mitosis in tissue culture cells. *Bioscience Reports*, *18*, 215–224.

Herman, B. (1987). *Fluorescence microscopy* (2nd ed.). New York: Springer Verlag.

Hiraoka, Y., Sedat, J. W., & Agard, D. A. (1990). Determination of three-dimensional imaging properties of a light microscope system. *Biophysical Journal*, *57*, 325–333.

Hogan, H. (2006). Focusing on the experiment. *Biophotonics International*, *13*, 48–49.

Inoué, S. (2006). Foundations of confocal scanned imaging in light microscopy. In J. B. Pawley (Ed.), *Handbook of biological confocal microscopy* (3rd ed., pp. 1–16). New York: Springer.

Inoué, S., & Spring, K. (1986). *Video microscopy* (3rd ed.). New York: Plenum Press.

Keller, H. E. (2006). Objective lenses for confocal microscopy. In J. B. Pawley (Ed.), *Handbook of biological confocal microscopy* (3rd ed., pp. 145–160). New York: Springer.

Kinoshita, R. (2002). Optimize your system with the right filter set. *Biophotonics International*, *9*(9), 46–50.

Liebling, M., Forouhar, A. S., Wolleschensky, R., Zimmerman, B., Ankerhold, R., Fraser, S. E., et al. (2006). Rapid three-dimensional imaging and analysis of the beating embryonic heart reveals functional changes during development. *Developmental Dynamics*, *235*(11), 2940–2948.

Maddox, P. (2000). *Protocols: Yeast growth chambers*. http://www.bio.unc.edu/faculty/salmon/lab/protocolsyeastchambers.html.

Maddox, P. S., Moree, B., Canman, J. C., & Salmon, E. D. (2003). Spinning disk confocal microscope system for rapid high-resolution, multi-mode, fluorescence speckle microscopy and green fluorescent protein imaging in living cells. *Methods in Enzymology*, *360*, 597–617.

Nolte, A., Pawley, J. B., & Horing, L. (2006). Non-laser light sources for three-dimensional microscopy. In J. B. Pawley (Ed.), *Handbook of biological confocal microscopy* (3rd ed., pp. 126–144). New York: Springer.

North, A. (2006). Seeing is believing? A beginners' guide to practical pitfalls in image acquisition. *The Journal of Cell Biology*, *172*, 9–18.

Pawley, J. (2006). Fundamental limits in confocal microscopy. In J. B. Pawley (Ed.), *Handbook of biological confocal microscopy* (3rd ed., pp. 20–41). New York: Springer.

Piston, D. W. (1999). Imaging living cells and tissues by two-photon excitation. *Trends in Cell Biology*, *9*, 66–69.

Ploem, J. S. (1999). Fluorescence microscopy. *Fluorescent and luminescent prones for biological activity* (2nd ed.). London: Academic Press, pp. 3–13.

Reichman, J. (2000). *Handbook of optical filters for fluorescence microscopy*. Oxford: Oxford University Press. www.chroma.com.

Rieder, C. L., & Cole, R. (1998). Perfusion chambers for high-resolution light microscopic studies of vertebrate cell monolayers: Some considerations and a design. *Methods in Cell Biology*, *56*, 253–275.

Salmon, E. D., & Waters, J. C. (1996). A high resolution multimode digital imaging system for fluorescence studies of mitosis. *Analytical use of fluorescent probes in oncology*. New York: Plenum Press.

Seko, Y., Pang, J., Tokoro, T., Ichinose, S., & Mochizuki, M. (2001). Blue light-induced apoptosis in cultured retinal pigment epithelium cells of the rat. *Graefes Archives for Clinical and Experimental Ophtalmology*, *239*(1), 47–52.

Shaner, N. C., Steinbach, P. A., & Tsien, R. Y. (2005). A guide to choosing fluorescent proteins. *Nature Methods*, *2*(12), 905–909.

Sluder, G., Nordberg, J. J., Miller, F. J., & Hinchcliffe, E. H. (2005). *A sealed preparation for long-term observations of cultured cells. Live cell imaging: A laboratory manual*. CSHL Press, Cold Spring Harbor, pp. 345–349.

Sparrow, J. R., & Cai, B. (2001). Blue light-induced apoptosis of A2E-containing RPE: Involvement of caspase-3 and protection by Bcl-2. *Investigative Ophthalmology & Visual Science*, *42*(6), 1356–1362.

Spector, D. L., & Goldman, R. D. (2005). *Constructing and expressing GFP fusion proteins. Live cell imaging: A laboratory manual*. CSHL Press, Cold Spring Harbor, pp. 25–31.

Spring, K. (2000). Scientific imaging with digital cameras. *Biotechniques*, *29*(1), 70–76.

Spring, K. R., & Davidson, M. W. (2004). Concepts in digital imaging technology: Quantum efficiency. http://micro.magnet.fsu.edu/primer/digitalimaging/concepts/quantumefficiency.html.

Spring, K. R., & Davidson, M. W. (2006). Basic concepts in formulas in microscopy: Coverslip correction. http://www.microscopyu.com/articles/formulas/formulascoverslipcorrection.html.

Swedlow, J. R., & Andrews, P. D. (2005). In vivo *imaging of mammalian cells. Live cell imaging: A laboratory manual*. CSHL Press, Cold Spring Harbor, pp. 329–343.

Swedlow, J. R., Hu, K., Andrews, P. D., Roos, D. S., & Murray, J. M. (2001). Measuring tubulin content in Toxoplasma gondii: A comparison of laser-scanning confocal and wide-field fluorescence microscopy. *Proceedings of the National Academy of Sciences of the United States of America*, *99*(4), 2014–2019.

Thorn, K. (2000). THORNLab resources: Fluorescent proteins. http://www.sysbio.harvard.edu/csb/thornlab/gfps.htm.

Toomre, D., & Pawley, J. B. (2006). Disk-scanning confocal microscopy. In J. B. Pawley (Ed.), *Handbook of biological confocal microscopy* (3rd ed., pp. 221–237). New York: Springer.

Tsien, R. Y., Ernst, L., & Waggoner, A. (2006). Fluorophores for confocal microscopy: Photophysics and photochemistry. In J. B. Pawley (Ed.), *Handbook of biological confocal microscopy* (3rd ed., pp. 338–348). New York: Springer.

Wallace, W., Schaefer, L. H., & Swedlow, J. R. (2001). A workingperson's guide to deconvolution in light microscopy. *Biotechniques*, *31*, 1076–1097.

Waters, J. C. (2005). Arc alignment. http://nic.med.harvard.edu/arcalignment.pdf.

Waters, J. C. (2006). *An introduction to electronic image acquisition during light microscopic observation of biological specimens. Cell biology: A laboratory handbook* (Vol. 3). London: Elsevier, pp. 49–56.

Wittmann, T., Bokoch, G. M., & Waterman-Storer, C. M. (2003). Regulation of leading edge microtubule and actin dynamics downstream of Rac1. *The Journal of Cell Biology*, *161*(5), 845–851.

CHAPTER

Practical Aspects of Adjusting Digital Cameras

7

Joshua J. Nordberg and Greenfield Sluder

Department of Cell Biology, University of Massachusetts Medical School, Worcester, Massachusetts, USA

CHAPTER OUTLINE

Introduction **152**
7.1 Measuring Gray-Level Information **152**
7.1.1 The Histogram 152
7.1.2 The Line Scan 152
7.1.3 Other Strategies 154
7.2 Camera Settings **154**
7.2.1 Exposure Time 154
7.2.2 Offset 154
7.2.3 Gain 155
7.3 Contrast Stretching **157**
7.3.1 Setting the Exposure Time 157
7.3.2 Adjusting Offset and Gain 157
7.4 Camera Versus Image Display Controls **159**
Acknowledgments **161**
References **162**

Abstract

This chapter introduces the adjustment of digital camera settings using the tools found within image acquisition software and discusses measuring gray-level information such as (1) the histogram, (2) line scan, and (3) other strategies. The pixel values in an image can be measured within many image capture software programs in two ways. The first is a histogram of pixel gray values and the second is a line-scan plot across a selectable axis of the image. Understanding how to evaluate the information presented by these tools is critical to properly adjusting the camera to maximize the image contrast without losing grayscale information. This chapter discusses the 0–255 grayscale

Methods in Cell Biology, Volume 114 **ISSN 0091-679X**
Copyright © 2007 Elsevier Inc. All rights reserved.
http://dx.doi.org/10.1016/B978-0-12-407761-4.00007-5

resolution of an 8-bit camera; however, the concepts are the same for cameras of any bit depth. This chapter also describes camera settings, such as exposure time, offset, and gain, and the steps for contrast stretching such as setting the exposure time, adjusting offset and gain, and camera versus image display controls.

INTRODUCTION

The purpose of this chapter is to introduce the adjustment of digital camera settings using the tools found within image acquisition software. The principles are the same as those outlined in Chapter 8 by Hinchcliffe and Sluder, volume 81, 2007. Here we have reiterated some material in order to provide a treatment of the subject for those using digital cameras. The theme of this chapter is how to use camera image acquisition and display settings to optimize image contrast without irreversibly losing grayscale information.

7.1 MEASURING GRAY-LEVEL INFORMATION

The pixel values in an image can be measured within many image capture software programs in two ways. The first is a histogram of pixel gray values and the second is a line-scan plot across a selectable axis of the image. Understanding how to evaluate the information presented by these tools is critical for properly adjusting the camera to maximize the image contrast without losing grayscale information. For simplicity, we will work with the 0–255 grayscale resolution of an 8-bit camera; the concepts are the same for cameras of any bit depth.

7.1.1 The histogram

The histogram presents the number of image pixels (ordinate) as a function of gray level (abscissa) for the whole image or a region of interest. For an 8-bit camera, the pixel gray levels range from 0 on the left to 255 on the right. Fig. 7.1B shows the histogram of the entire image shown in panel A [a differential interference contrast (DIC) image of several cultured mammalian cells]. The sharp peak about one-third of the way from the origin indicates that the majority of the pixels in this image range from gray levels 40 to 110 with relatively few pixels of higher and lower values. It is important to note that the histogram is heavily weighted toward the background of the field (area around the cells) and that the brighter and darker portions of the specimen detail are represented in the histogram "tails" to the right and left of the main peak. For setting the camera acquisition and display parameters, these are the histogram values of interest, not just the primary peak.

7.1.2 The line scan

Most software packages allow the user to draw a line across a selectable part of the image and measure pixel gray levels along that line. Many such packages enable the user to draw an arbitrary line rather than lines confined to the camera's horizontal and vertical axes. The readout is a graph that shows pixel location along the *x*-axis with

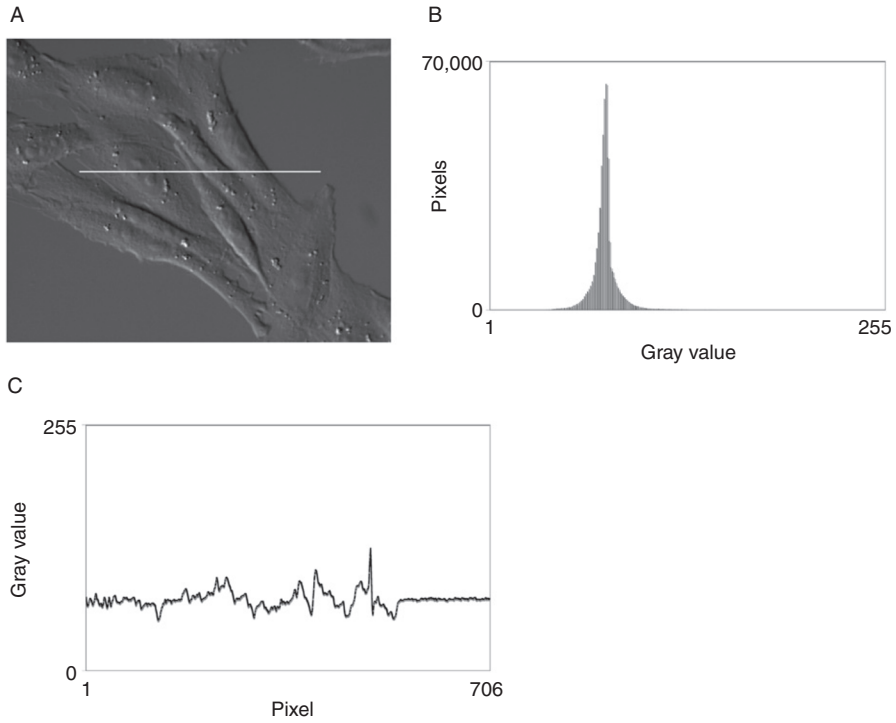

FIGURE 7.1

Two ways to measure pixel gray values. Panel A is a differential interference contrast (DIC) image of cultured mammalian cells. Panel B shows a pixel gray-level histogram with the gray values ranging from 0 to 255 along the *x*-axis and the pixel number for each gray value shown on the *y*-axis. The histogram represents all pixels in the image. Panel C is a plot of pixel gray levels along the line scan shown in panel A. The *x*-axis is the pixel position along the line, and the *y*-axis represents gray values from 0 to 255. Usually, the position and orientation of the line can be user defined.

the corresponding gray value on the *y*-axis, ranging from 0 to 255. Figure 7.1C shows a line-scan plot of the gray levels found along the line seen in Fig. 7.1A. The line scan is particularly useful because the user can access the intensity information for any pixel of interest. This, as we will describe in the next section, allows the operator to know exactly how the adjustments made to the camera are applied to each pixel along the scan line.

While the information from a histogram is sometimes more difficult to interpret than the line scan, a histogram is often present in the corner of the display screen, and is updated in real time while the user is making imaging adjustments. The line-scan function usually requires an extra step to capture the image and measure the intensities afterward, making live adjustments difficult.

7.1.3 Other strategies

In addition to the histogram and line-scan functions for determining proper camera settings, some software packages offer a tool that detects over- and underexposed pixels for the user. These pixels are displayed in a color overlay on the monochrome image being captured. Some software packages even allow the user to choose how many gray levels below white or above black will be detected and displayed. Pixel colorization is an easily visible but not quantitative measure of camera performance.

7.2 CAMERA SETTINGS

7.2.1 Exposure time

Just as with a film camera, the exposure time setting determines how long the photoreactive element (here the CCD chip) is exposed to the light from the microscope. The result of underexposing is an image with a low signal-to-noise ratio. Overexposure will lead to saturated pixels within which there will not be any detectable image detail. Also, saturation of pixels can lead to an effect known as "blooming" (Davidson, 2005).

When blooming occurs, adjacent pixels can also acquire signal leading to degradation of specimen detail in that region. Therefore, care must be taken to determine a proper exposure time that provides an image that is neither under- nor overexposed before adjusting any of the camera parameters as described below.

7.2.2 Offset

The offset control (sometimes referred to as "brightness" or "black level") allows one to add or subtract an adjustable value from all pixels in the image. Normally, this is used to set the darkest portion of the specimen detail from some gray value down to a level close to zero when stretching the contrast in a low contrast image (described below). The effects of changing the offset are shown in Fig. 7.2. Figure 7.2A, bottom panel, shows a gray scale ranging from 0 to 255 with the corresponding line-scan plot of this gray scale in the top panel. Figure 7.2B shows what happens when the offset is made more negative; the lowest four gray values are driven to zero and the others are correspondingly reduced. Any specimen information contained in the lowest four gray levels is lost from the image. Figure 7.2C shows the consequence of increasing the offset; the highest four gray levels are driven to white and the other values are correspondingly increased. Any specimen information contained in the highest four gray levels is lost from the image. The effect of driving pixel intensity values off-scale is often referred to as "clipping." The reader is referred to Chapter 14 by Wolf et al., this volume for a further discussion of camera optimization specifically as it relates to dynamic range and the maximization of quantitative information.

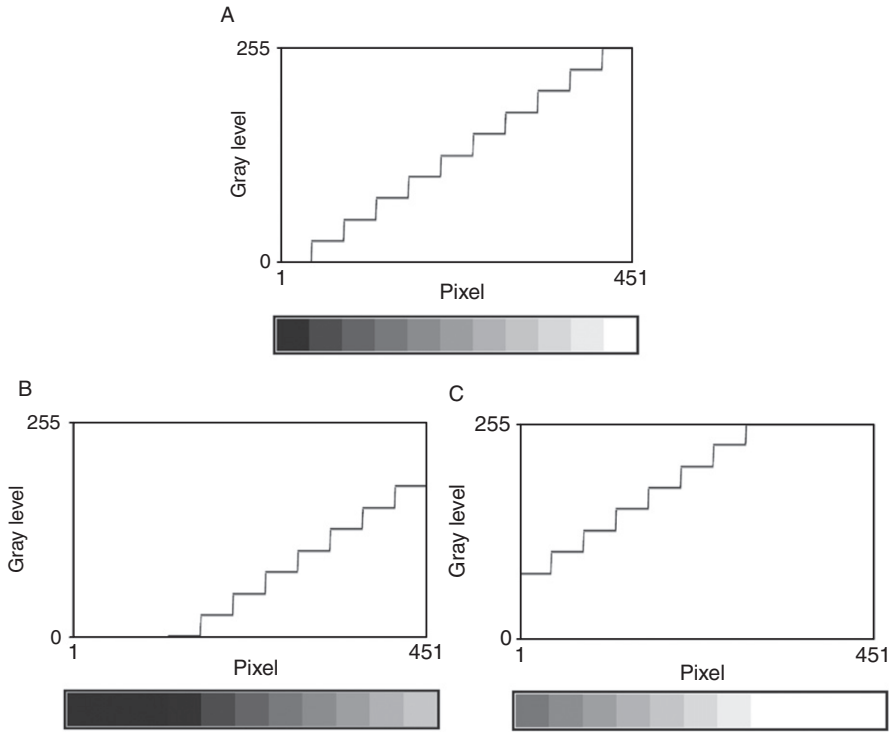

FIGURE 7.2

Adjusting camera offset. Top panels are line scan plots of the grayscale test patterns shown in the bottom panels. The *y*-axis shows gray level ranging from 0 to 255 and the *x*-axis shows position across the image. Panel A shows the original image of the grayscale test pattern that includes the entire 256 gray-level range. Panel B shows what happens to the image and its line scan when the offset is decreased so that the fourth lowest gray value has been set to 0. Panel C shows what happens when the offset is increased such that the fourth highest gray level is set to 255—that is, white. Notice that varying the offset does not alter the difference between each gray value.

7.2.3 Gain

Camera gain acts as an amplifier that varies the output value from the camera for a given change in input. It is expressed as a ratio of the number of electrons from the CCD chip that are converted into analog-to-digital units (ADU). Increasing the camera gain effectively means reducing the number of electrons required to produce one ADU (Roper Scientific, 2006). The effect this has on the captured image is to multiply all pixel values by the same value. For example, if two pixels initially have a difference of 5 gray values (say 45 and 50), increasing the gain multiplies all gray values by the same factor (say, 3); the new values of the pixels are 135 and 150—a gray value difference of 15.

Figure 7.3 shows the effects of changing camera gain on the grayscale test pattern. Panel A shows the full range of pixel gray levels ranging from black (0) to white (255). Figure 7.3B shows what happens to the grayscale test pattern when one increases the gain. Notice that the differences between the output gray values increases and there is clipping of the higher gray values. When the gain is decreased, as shown in Fig. 7.3C, the differences between pixel gray values are decreased in the output. Although gray-level information is retained in principle, the resulting image is of low contrast. We also note that changing the gain does not alter the signal-to-noise ratio; both the signal and the noise in the camera signal are amplified.

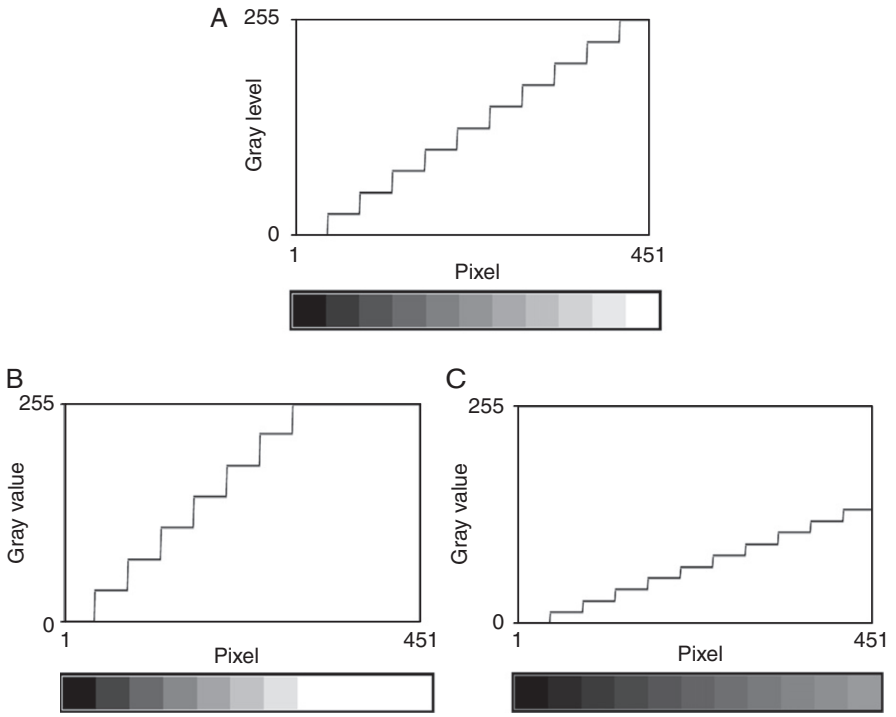

FIGURE 7.3

Adjusting camera gain. Panel A shows the original image of the grayscale test pattern that includes the entire 256 gray-level range. Panel B shows what happens to the image and its line scan when the gain is increased. Notice that the differences between gray values (size of the steps) has been increased for all intensities (except 0). However, the highest gray values are now indistinguishable from each other because they have been "pushed" to saturation (255). In panel C, the gain has been decreased. While no gray values have been lost, it is more difficult to distinguish between gray values because the difference between steps has been decreased.

7.3 CONTRAST STRETCHING

Most real-life specimens are not represented by the entire 256 gray value range; often the specimen detail is found within a relatively narrow range of grays. By controlling exposure, offset, and gain, one can enhance the contrast and visibility of specimen detail without loss of essential gray-level information. In doing this, there are two primary considerations. First, one seeks to use the full dynamic range of the camera output and second, one does this for the specimen detail of interest. Specimen or background information not of interest can be allowed to saturate or go to black.

7.3.1 Setting the exposure time

Exposure is the light intensity per unit area at the detector multiplied by the amount of time the detector is exposed to the light. For a given exposure, one can use higher intensity illumination for a short time or a lower intensity for a longer time. The natures of the sample and the experiment will determine what combination of illumination intensity and exposure duration one will use. Regardless, one must use the histogram or the line-scan measurement tools to ensure that one does not saturate (drive to 255) pixels representing the brightest specimen details of interest and to ensure that there is adequate exposure to produce a gray level (>0) for the dimmest specimen detail of interest. Over- or underexposure can lead to irretrievable loss of specimen information. Obviously, the key consideration is the range of specimen gray levels, not necessarily the gray level of the background. For example, when imaging a fluorescent specimen, one might not want to increase the exposure to the point that the background has a gray value, particularly if this means that the pixels representing the brightest specimen fluorescent intensity become saturated. Likewise, in a brightfield image of an absorbing specimen, one might allow the background values to saturate in order to capture the dimmest specimen detail.

7.3.2 Adjusting offset and gain

After an exposure time has been determined, the gray levels in the specimen detail of interest can be "stretched" to maximize the visibility of information captured. This is useful for images in which the specimen detail is represented by a relatively narrow range of gray values (i.e., a low contrast image of the specimen). The first step is to identify the specimen detail of interest that has the lowest gray value—even if it has a light gray value in the raw image. The offset is then adjusted to bring this gray level down to a lower gray-level value. Our example, shown in Fig. 7.4, is a DIC image of cultured cells. Figure 7.4A, left panel, shows the raw image with a line scan through one of the cells (white line). The pixel values along this line are shown in the right-hand panel. By reducing the offset, we set the lowest gray values to a value close to 0 (Fig. 7.4B). We also decrease the gray value of every pixel in the image, resulting in a similar line scan graph that is shifted closer to 0 on the y-axis.

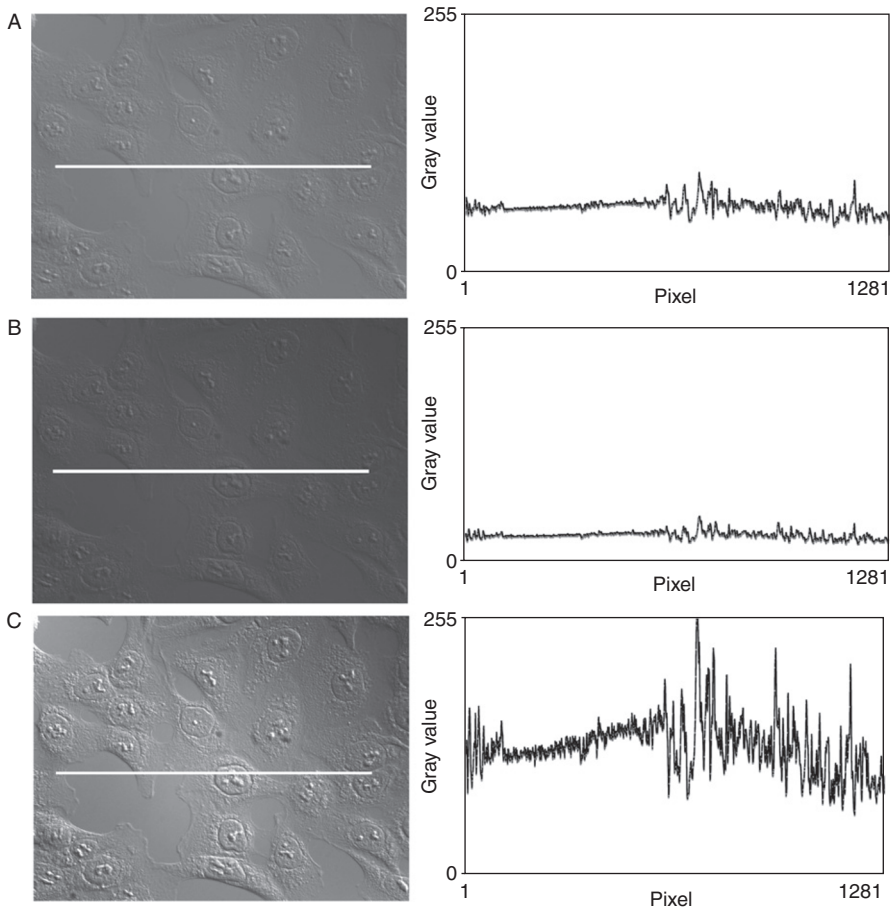

FIGURE 7.4

Optimizing image contrast using the line scan plot. The left-hand panels are DIC images of fixed cells. The right-hand panels are line scan plots of pixel gray values along the line seen in each of the DIC images. Panel A shows an image with low contrast specimen detail. The corresponding line scan plot shows that the gray values of our image fall within a narrow range. Panel B shows the result of decreasing the offset. The gray values in the line scan plot are now closer to 0. In panel C, the gain has been increased so that the differences between the pixel values are increased. Notice that the highest specimen gray value in panel C is now close to 255. By making these adjustments, the range of pixel intensities for the specimen detail is now closer to the entire 256 gray value spectrum.

The next step is to increase the gain to drive the lightest gray specimen detail of interest to a value close to 255 as shown in Fig. 7.4C. This multiplies all pixel values by the same factor thereby increasing the contrast between the highest and lowest values in the image. When done properly, this operation results in the conversion

of an image of the specimen detail that starts with a limited range of gray values and represents it as an image that has the full range of gray values. Most importantly, there is no loss of essential gray-level information.

Figure 7.5 shows the contrast stretch operation conducted on the same specimen using the histogram of the pixel values of the entire image. In using the histogram display, it is important to bear in mind that the prominent peak of pixel values can be dominated by the background values and that the pixel values for the specimen detail may lie to the right and left of the peak. An extreme case is shown in Fig. 7.6; panel A (left) shows a fluorescence image of a cell in which the objects of interest are centrosomes immunolabeled for γ-tubulin. The automatically scaled histogram of this image (panel A, right) shows that almost all the pixel values are close to zero with no values at lighter-gray levels. However, rescaling of the histogram (panel B) reveals that $\sim$375 pixels are at 255 and their presence is difficult to detect with a single bar at the right margin of the histogram. Thus, the image of the centrosomes is saturated and substructure, if any, would not be detectable. The more important implication of finding these saturated pixels is that contrast stretching the prominent peak would not be of use. The histogram-scaling problem illustrated here can be addressed by using a histogram of a user-defined region of interest or by using a histogram with a logarithmic *y*-scale, an option found in some software packages.

7.4 CAMERA VERSUS IMAGE DISPLAY CONTROLS

An important distinction to draw is the difference between altering the camera's output parameters and the displayed image. In some software, one can only modify the characteristics of the camera output and consequently, the monitor display reflects the results. The image recorded to the hard drive also reflects the modifications made to the camera output.

In other image acquisition packages, one can independently vary camera output characteristics and the display characteristics. If modifications are made to the camera output, they are reflected in the monitor display and in the image that is recorded. However, if a contrast stretch is made through just the display controls, only the image on the monitor is modified. The raw image remains unaltered and the recorded image will not reflect any changes made.

Although it is possible to record the raw image and later conduct a contrast stretch, there is a penalty to be paid. For example, Figure 7.5A–C shows the image gray-level histogram throughout the process of contrast stretching the image at the camera output level. Figure 7.5D shows the same raw image that has been contrast stretched after capture using image-processing software. The histogram shows that the gray levels have been spread across approximately the same range of grays as in Fig. 7.5C. There are fewer bars, however, indicating that fewer gray levels represent the image. In principle, this means that there is loss of gray-level resolution, particularly for 8-bit cameras (compare the histograms in Fig. 7.5C and D).

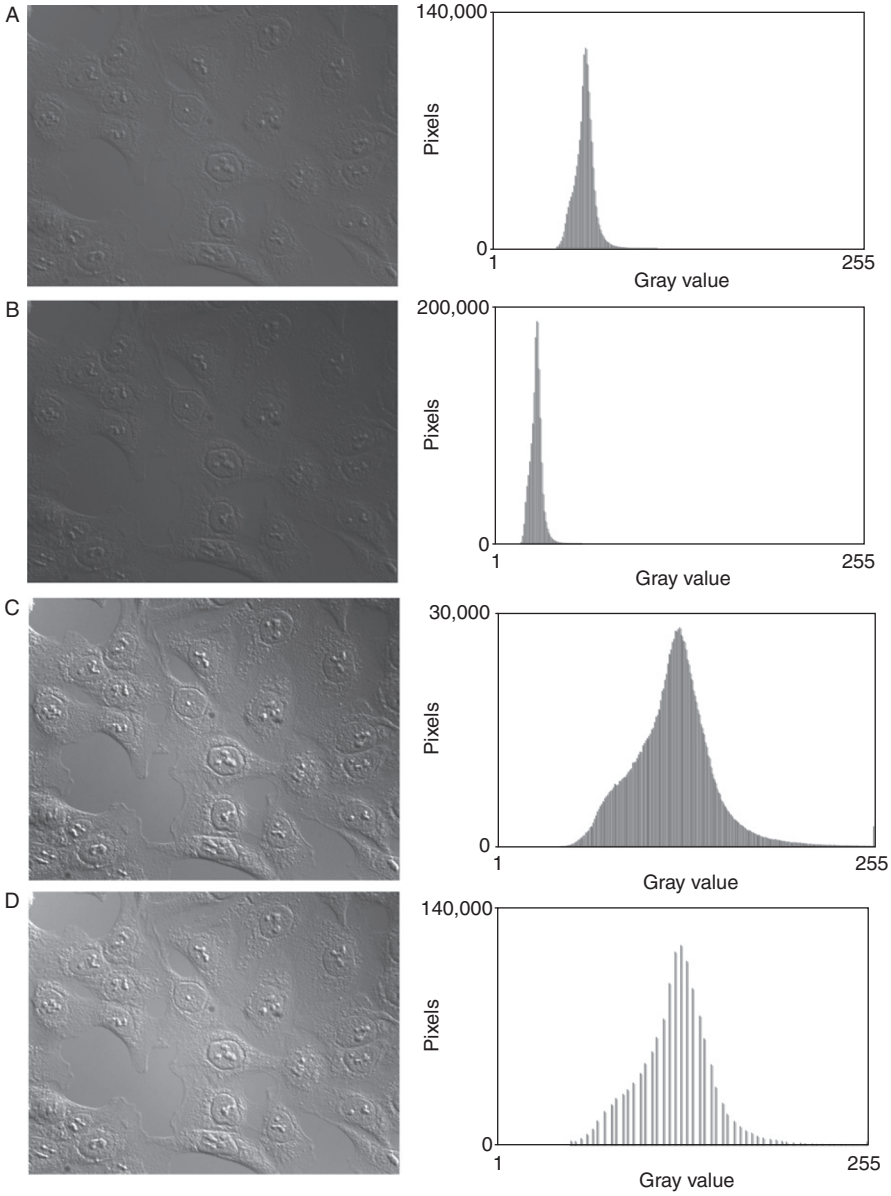

FIGURE 7.5

Optimizing the image using the histogram. The left-hand panels are the DIC images of living cells used in Fig. 7.4. The right-hand panels are histograms of pixel gray values for the whole image. The adjustments made are identical to those in Fig. 7.4. Panel A shows an image with low specimen contrast. The corresponding histogram shows that the image contains a narrow range of gray values. In panel B, the offset has been decreased. Note that all histogram values have been pushed closer to 0. In panel C, the gain has been increased so that the differences between gray values are increased producing a higher contrast image with, in principle, no loss of gray-level information. Note, however, that in this particular example, a few pixels have been driven to saturation as indicated by the small peak at the far right margin of the histogram. In a real world situation, one would decide whether or not this is a problem. In panel D, the image in panel A has been contrast stretched using image-processing software after capture of the raw image. Note that the histogram in D has a gray-level range similar to that in C, but with fewer bars. This indicates a loss of grayscale resolution.

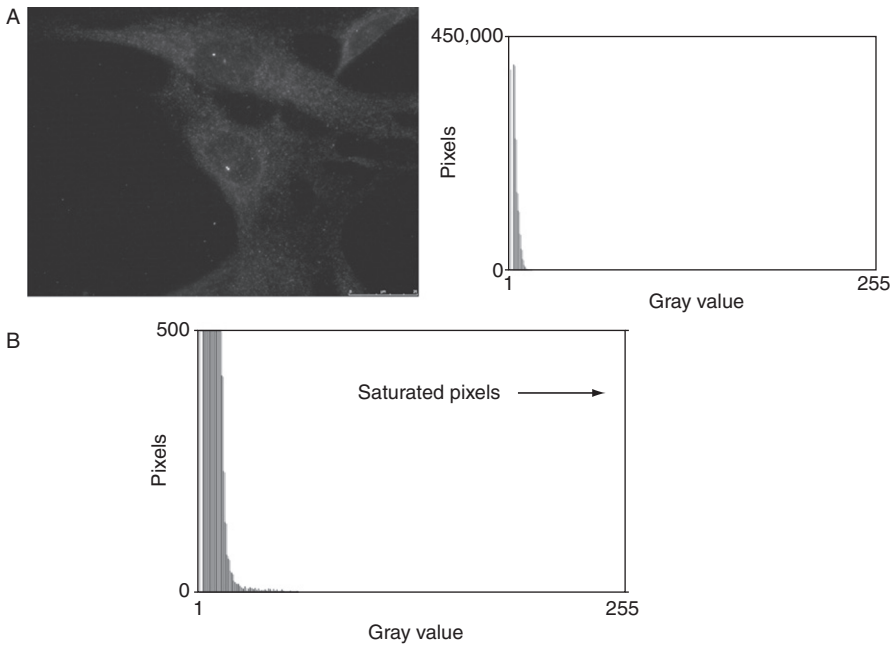

FIGURE 7.6

The importance of scaling the *y*-axis of the histogram under some circumstances. Panel A (left) shows a fluorescence image of several cultured cells immunostained for γ-tubulin at the centrosomes (the two round, bright dots next to the nucleus). Panel A (right) shows the corresponding image gray-level histogram. All pixel gray values of the image appear to be concentrated near 0. Panel B shows the same histogram, but the scale has been changed from 0–450,000 to 0–500. Note that a number of pixels representing the γ-tubulin fluorescence are saturated (peak at far right margin of the histogram). If the centrosomes are the specimen detail of interest, one will have to decide if saturation of these pixels is acceptable or not.

Since camera and display controls are not standardized, it is incumbent on the user to explore the options available in his/her software, understand what the controls modify, and proceed accordingly.

Acknowledgments

This work was supported by National Institutes of Health (NIH) grant GM 030758 to G. Sluder.

References

Davidson, M. W. (2005). *Molecular expressions microscopy primer: Digital imaging in optical microscopy—Concepts in digital imaging—CCD saturation and blooming*. Mortimer Abramowitz, Olympus America, Inc. and The Florida State University. http://micro.magnet.fsu.edu/primer/digitalimaging/concepts/ccdsatandblooming.html.

Roper Scientific (2006). Photometrics encyclopedia. http://www.photomet.com/library_enc_gain.shtml.

CHAPTER

Cameras for Digital Microscopy

8

Kenneth R. Spring

Laboratory of Kidney and Electrolyte Metabolism, National Heart, Lung, and Blood Institute, National Institutes of Health, Bethesda, Maryland, USA

CHAPTER OUTLINE

8.1 Overview **164**
8.2 Basic Principles **164**
8.2.1 Sources of Noise 165
8.2.2 Quantum Efficiency 166
8.2.3 Dynamic Range 167
8.2.4 Image Integration 168
8.2.5 CCD Architecture 168
8.2.6 Scan Formats 170
8.2.7 Binning 170
8.2.8 Color 171
8.2.9 Image-Intensified CCD Camera 173
8.2.10 Gating of the ICCD 175
8.2.11 Electron-Bombarded CCD 175
8.2.12 On-Chip Multiplication 175
8.3 Application of CCD Cameras in Fluorescence Microscopy **176**
8.4 Future Developments in Imaging Detectors **178**
Further Reading **178**

Abstract

This chapter reviews the fundamental characteristics of charge-coupled devices (CCDs) and related detectors, outlines the relevant parameters for their use in microscopy, and considers promising recent developments in the technology of detectors. Electronic imaging with a CCD involves three stages—interaction of a photon with the photosensitive surface, storage of the liberated charge, and readout or measurement of the stored charge. The most demanding applications in fluorescence

Methods in Cell Biology, Volume 114 **ISSN 0091-679X**
Copyright © 1998 Elsevier Inc. All rights reserved.
http://dx.doi.org/10.1016/B978-0-12-407761-4.00008-7

microscopy may require as much as four orders of greater magnitude sensitivity. The image in the present-day light microscope is usually acquired with a CCD camera. The CCD is composed of a large matrix of photosensitive elements (often referred to as "pixels" shorthand for picture elements, which simultaneously capture an image over the entire detector surface. The light-intensity information for each pixel is stored as electronic charge and is converted to an analog voltage by a readout amplifier. This analog voltage is subsequently converted to a numerical value by a digitizer situated on the CCD chip, or very close to it. Several (three to six) amplifiers are required for each pixel, and to date, uniform images with a homogeneous background have been a problem because of the inherent difficulties of balancing the gain in all of the amplifiers. Complementary metal oxide semiconductor sensors also exhibit relatively high noise associated with the requisite high-speed switching. Both of these deficiencies are being addressed, and sensor performance is nearing that required for scientific imaging.

8.1 OVERVIEW

The image in the present-day light microscope is usually acquired with a charge-coupled device (CCD) camera. The CCD is composed of a large matrix of photosensitive elements (often referred to as "pixels" shorthand for "picture elements") that simultaneously capture an image over the entire detector surface. The light-intensity information for each pixel is stored as electronic charge and is converted to an analog voltage by a readout amplifier. This analog voltage is subsequently converted to a numerical value by a digitizer situated on the CCD chip, or very close to it. In this chapter, I will review the fundamental characteristics of CCDs and related detectors, point out the relevant parameters for their use in microscopy, and consider promising recent developments in the technology of detectors.

8.2 BASIC PRINCIPLES

Electronic imaging with a CCD involves three stages: interaction of a photon with the photosensitive surface, storage of the liberated charge, readout or measurement of the stored charge. The CCDs in modern cooled and intensified cameras contain large arrays of silicon photoconductors, typically 1200 (H) $\times$ 1000 (V), incorporating surface channels for transfer of the signal to the output amplifier. An individual pixel absorbs a photon in a specialized region known as the depletion layer, resulting in the liberation of an electron and the formation of a corresponding positively charged hole in the silicon crystal lattice. External voltages are applied to the individual pixels to control the storage and movement of the generated charges. Initially, the pixels act as "wells," storing the charge for a given time interval; the amount of stored charge is linearly proportional to the light flux incident on the pixel up to the capacity of the well. After the charges are collected, a series of voltage steps are applied to shift the charge along the transfer channels to the readout amplifier, where

the signal is converted to a voltage. Virtually all CCDs used at present accumulate holes rather than electrons—so-called "HAD" or hole-accumulator-diode CCDs. HAD technology has dominated because there is more electronic noise associated with the storage and transfer of electrons than of holes. However, for convenience I will refer to all charges as electrons.

The charge storage capacity of a potential well in a CCD is largely a function of the physical size of the individual pixel. Most pixels are square in present-day CCDs, and the charge storage capacity of the potential well may be approximated by the area of the pixel in microns multiplied by 1000. Thus, a 4μ-square pixel will have a charge storage capacity of about 16,000 electrons. This full-well capacity (FWC) determines the maximum signal that can be sensed in the pixel.

8.2.1 Sources of noise

The minimum detectable signal is determined by both the photon statistical noise and the electronic noise of the CCD. Conservatively, a signal can only be discriminated from noise when it exceeds the noise by a factor of ~2.7; that is, a signal/noise (S/N) ratio = 2.7. How low a signal will yield a S/N ratio of 2.7? Even with an ideal noiseless detector there is inherent noise associated with the signal because of random variations of the photon flux. This photon statistical noise is equal to the square root of the number of photons. Therefore, the maximum achievable S/N for a perfect detector is given by $S/\sqrt{S}$, equal to $\sqrt{S}$; a light flux of 8 photons will be required to achieve a S/N of 2.7.

Real cameras add electrical noise from two sources—dark noise and readout amplifier noise—to the photon statistical noise. Dark noise is the random fluctuation in the amount of electronic charge that is accumulated in a potential well when the detector is in total darkness. Dark charge accumulation is a consequence of thermal excitations of the CCD that liberate electrons or holes. Dark noise cannot simply be subtracted, as it represents the uncertainty in the magnitude of the dark charge accumulation in a given time interval. Dark noise has been drastically reduced by the storage of holes rather than electrons, as there is a far greater likelihood of thermal generation of electrons than holes. CCDs for scientific applications are usually cooled because the accumulation of dark charge is reduced by an order of magnitude for every 20 °C temperature decrease. Cooling to −30 °C, or even to 0 °C, reduces dark noise to a negligible quantity in most microscopy applications.

Readout amplifier noise is the other major electronic noise source in a cooled CCD. Readout noise may be thought of as the price that must be paid for converting the accumulated charge into a voltage. Because it is noise, its magnitude cannot be precisely determined but only approximated by an average value. Readout noise increases with the speed of measurement of the accumulated charge in each pixel. Higher readout speeds require greater amplifier bandwidths, and inevitably, increased amplifier bandwidth is associated with greater noise. Cooling the CCD helps to reduce readout amplifier noise, but there is a temperature below which readout amplifier performance is reduced.

An alternative strategy for achieving high-speed readout with lower noise is equipping the CCD with multiple output taps, so that four or more readout amplifiers

are used to extract the image information. The image information is then obtained in the form of adjoining blocks that are later stitched together by processing software.

An additional benefit of cooling the CCD is an improvement in the charge transfer efficiency (CTE). Each time a packet of charge is shifted along the transfer channels there is a possibility of leaving some behind. When this occurs, the image is less crisp because the charge from adjacent pixels is inadvertently admixed leading to blurring. The large format of modern CCDs necessitates a very high CTE to prevent the loss of a significant magnitude of the charge from pixels that are far from the readout amplifier. The pixel farthest from the readout amplifier undergoes thousands more transfer steps than the pixel closest to the amplifier. When CTE values in a cooled CCD are 0.9999 or greater, charge loss is negligible. However, when the CTE is lower than 0.999, such loss occurs and the region farthest from the output amplifier appears dimmer than that near it; then the camera is said to exhibit "shading."

Shading may be compensated for in two different ways: with software or with hardware. When the software correction method is used, an image of uniform intensity is captured and a pixel-by-pixel gain correction map is generated. This map can then be used to correct the intensity values in all subsequent images. This approach is satisfactory as long as the magnitude of the correction factors is not greater than 10%–20%. The hardware method involves sampling the intensities of dark or blank pixels in five to six reference columns at the end of each row of the CCD. These reference columns are outside of the image area and serve as controls for charge loss during the transfer. Large corrections, up to three- to fivefold, can then be made by adjusting the gain factors for an individual row. The voltage readout from each row of pixels in the image are multiplied by the correction factor for that row. When the multiplication factors are large, as in the most distant regions of a video-rate CCD, the noise is also substantially increased. Although the signal does not appear to be reduced by this correction process and the shading is gone, the *S*/*N* is not uniform over the entire image.

8.2.2 Quantum efficiency

Quantum efficiency (QE) is a major determinant of the minimum detectable signal in a CCD camera, particularly in low-light-level applications. QE is a measure of the likelihood that a photon of a particular wavelength (and therefore energy) will be captured in the detector. If the photon is not detected because it never reaches the depletion layer or passes completely through it, no signal is generated. CCDs typically used in fluorescence microscopy can detect photons with wavelengths between 400 and 1100 nm. Most CCDs used in scientific imaging are interline transfer devices, described in detail below. Only about 25% of the surface area of these devices is photosensitive because the remainder is covered by the opaque charge transfer channels. A decade ago, manufacturing techniques were developed to bond microscopic lenses onto the surface of each pixel in register with the photosensitive regions. The lenses extend over the charge transfer channels and act to direct the incident photons to the sensitive area, increasing their effective surface area threefold.

The latest-generation CCD sensors have a QE of 70% in the green, so seven out of every 10 incident photons are detected in this range of the visible spectrum. If the

readout noise is relatively high, the charge generated by a detected photon cannot be discriminated from the amplifier noise, and the signal is obscured. Assuming a detectable signal must be about 2.7 times larger than the noise, a CCD camera that has a readout noise of 10 electrons/pixel plus signal-dependent noise given by $\sqrt{S}$ requires a minimum detectable signal of 35 electrons. Because present-day CCD cameras use unity gain readout amplifiers, each photon that is detected results in liberation of a single electron or hole. If the QE is 70%, 50 photons must impinge on a single pixel before a signal can be identified with certainty. If a video-rate CCD camera is used, the readout noise is much higher, $\sim$150 electrons/pixel, and the minimum detectable signal is then $-$450 electrons/pixel.

Additional strategies are occasionally used to further improve QE in both the visible and ultraviolet wavelength ranges. The charge transfer gates that lie on the surface of the CCD sensor are not perfectly transparent and absorb or reflect blue or ultraviolet light. The transparency of these gates has been increased in recent years by the use of indium-tin oxide in place of aluminum. When even higher QE is deemed necessary, a back-illuminated CCD may be employed. In the back-illuminated CCD sensor, the detector is flipped over so that light is incident on the back surface after the CCD has been substantially thinned by etching. A QE as high as 90% can be achieved in such back-thinned detectors, but these devices are delicate and relatively costly. Performance of back-thinned CCDs in the ultraviolet wavelengths may be further improved by the addition of special antireflection coatings.

Coatings of wavelength conversion phosphors to the front face of conventionally oriented CCD sensors have also been used to enhance sensitivity to wavelengths outside of the normal spectral range of an unmodified CCD. Such conversion phosphors absorb light energy in the spectral region of interest and emit at a wavelength compatible with the spectral sensitivity of the CCD. For example, CCD sensitivity at $\sim$200 nm is very low, even in a back-thinned CCD, but conversion phosphors are available that efficiently absorb light at 200 nm and emit at 560 nm.

8.2.3 Dynamic range

Dynamic range is the extent of signal variation that can be quantified by a detector. It is typically expressed in units of 2^n, where n is the dynamic range in bits; a detector that can support $2^8 = 256$ discrimination levels (i.e., gray levels) has a dynamic range of 8 bits. Most CCD camera manufacturers specify the dynamic range of the camera as the ratio of the FWC to the readout noise. Thus, a camera with a 16,000 electron FWC and a readout noise of 10 electrons would have a dynamic range of 1600, or between 10- and 11-bit resolution. This specification is not a realistic measure of the useful dynamic range; rather, it represents the maximum dynamic range within a scene in which some regions are just at saturation and others are lost in the noise. The useful dynamic range is smaller both because the CCD becomes nonlinear when the wells are about 90% full and because a signal equal to the readout noise is unacceptable visually and of virtually no use quantitatively. For our hypothetical camera, the useful dynamic range can be calculated as the ratio of 90% of 16,000 (the FWC) or 14,400 electrons divided by 27 electrons (the signal needed to achieve a S/N of 2.7

with a readout noise of 10 electrons). The ratio is 533, or a little better than 9 bits. Thus, a more realistic dynamic range designation of such a camera would be 10-bit resolution or 1024 gray levels. Each gray level would then correspond to about 14–16 stored charges; this relationship is often denoted as $\sim 14e^{-}$/A.D.U. (analog to digital unit).

The maximum dynamic range is not equivalent to the maximum achievable *S*/*N*, a parameter that is also a function of FWC. Because the FWC represents the maximum signal that can be accumulated, the associated photon statistical noise is the square root of the FWC, or 126.5 electrons for a FWC of 16,000 electrons. The maximum *S*/*N* is given by the signal, 16,000 electrons, divided by the noise, 126.5 electrons, and is equal to 126.5, the square root of the signal itself. Electronic noise, as well as stray light, will decrease the maximum achievable *S*/*N* to values below the 126.5 in our example, as they both diminish the effective FWC by filling the wells with charge that is not signal.

8.2.4 Image integration

When the light flux incident on the CCD is low, as is the case in fluorescence microscopy, the period of image integration before read out may be lengthened to accumulate more charges in each well. Image integration on the sensor (on-chip integration) is essential for most applications of CCD cameras, cooled or room temperature, under low-light-level conditions. The maximum integration period is a function both of the sensor FWC and of the rate of dark charge accumulation. Ideally, the integration period should be sufficiently long to nearly fill the wells of the pixels in the brightest regions. Most microscopy applications do not require integration periods longer than 30 seconds, and dark charge is still a very small fraction of FWC for such a time interval.

Careful examination of the image from a room-temperature CCD obtained after a long integration period in total darkness often reveals a small number of white spots that represent "hot" pixels. These are individual sensors with abnormally high rates of dark charge accumulation that saturate long before the neighboring pixels exhibit significant signal. The usual practice is to discard the information from the hot pixels by subtraction of a "spot mask" or background image.

Accumulation of charge beyond the FWC may result in "blooming," a situation in which the excess charge spills out into adjacent pixels and contaminates their wells. Most CCDs are equipped with antiblooming capabilities, where the excess charge is siphoned off and discarded instead of being allowed to spread to nearby pixels. In either case, the remaining charge fails to faithfully represent the incident light flux, and the upper limit of the dynamic range of the detector is exceeded. The pixel is saturated and the stored intensity information is compromised.

8.2.5 CCD architecture

There are three basic designs for a CCD—full frame, frame transfer, and interline transfer—as shown in Fig. 8.1. The full-frame device has virtually no dead space between the photosensitive regions and requires the incorporation of a mechanical

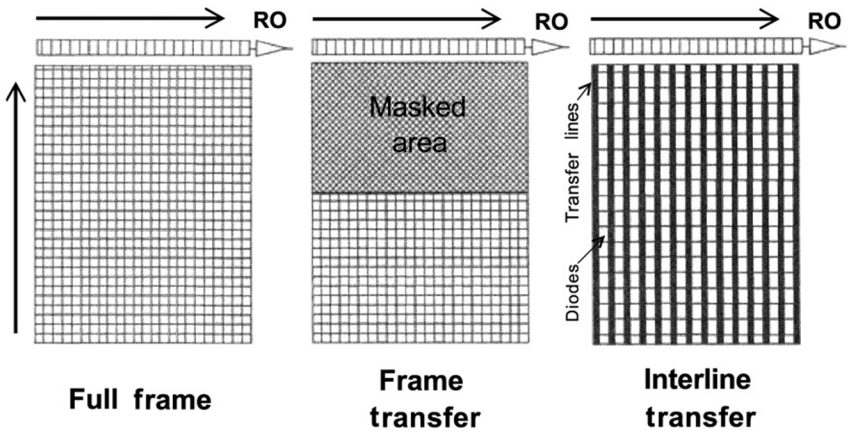

FIGURE 8.1

Designs for CCD detectors. See text for details.

shutter. The charge accumulated while the shutter is open is transferred and read out while the shutter is closed. Full-frame devices have the largest photosensitive area of all the CCDs, but their operation is limited by the speed of the mechanical shutter and the charge-transfer and readout steps. They have proven most useful in applications involving long exposure times—several seconds to hours—in which speed is not a concern.

Frame-transfer CCDs resemble a full-frame CCD in which the sensor has been subdivided vertically into two equal regions. The lower region is photosensitive, and the upper is covered by an opaque metal mask. Charge, accumulated in the photosensitive pixels during the integration period, is rapidly shifted vertically to the masked region at the end of the integration period. The stored charge in the masked region is then systematically shifted and read out at a slower rate to ensure efficiency while the next image is simultaneously being integrated on the photosensitive portion of the sensor.

The interline-transfer CCD has a charge-transfer channel adjacent to each photosensitive region. Stored charge need only be shifted horizontally once by a small distance to move into the masked transfer channels. The interline-transfer CCD allows very short integration periods and enables electronic control of exposure or "electronic shuttering." Once the charge has been shifted to the transfer channels, it moves vertically to the serial register for readout. As discussed above, the area of the sensor occupied by the transfer channels is substantial, amounting to 75% of the surface, so the use of adherent microlenses is essential. Interline transfer CCDs may also be electronically shuttered, or made effectively light insensitive, by discarding the accumulated charge instead of shifting it to the transfer channel.

When CCDs were first developed, they were in competition with vidicon tube cameras and were required to produce an electronic output that conformed to the prevailing standards for video (see Chapter 4). This history is relevant today because it

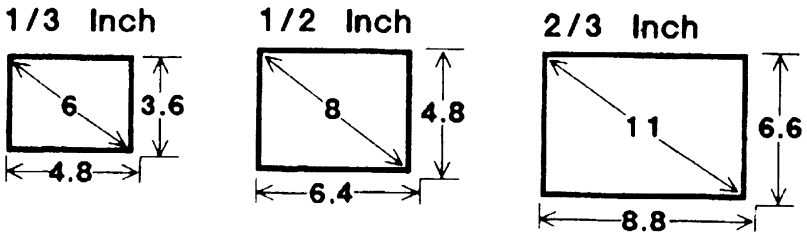

FIGURE 8.2

Geometry of commonly used CCD sensors. All dimensions are in millimeters.

has dictated the geometry of the CCD and its numerical description. As illustrated in Fig. 8.2, CCDs are available in a number of rectangular sizes that are designated in inches. Careful examination of Fig. 8.2 reveals that none of the dimensions listed correspond to their designations in inches. The notation arose because the rectangles represented the size of the rectangular scanned area in the corresponding round vidicon tube. Thus, a "one-inch" CCD has a sensor size of 9.6 $\times$ 12.8 mm, with a diagonal of 16 mm, as this was the scanned area of a 1-inch tube with a 25.4-mm outside diameter and an $\sim$18-mm-diameter input window.

8.2.6 Scan formats

Because early CCDs were designed for video standards such as RS-170 and NTSC, they were required to produce an interlaced scan output. Interlaced scanning was an engineering solution to the speed limitations of early video equipment. It entailed the assembly of each image from two lower-resolution images known as "fields" taken 16 msec apart so that the final picture was a composite of the two fields in which the odd and even horizontal scan lines were obtained at different times. These speed limitations are no longer a concern, and modern CCDs use a "progressive scan" output in which the sensor is read progressively from top to bottom so that each image contains the simultaneously acquired stored information of all the rows of the sensor. In video-rate devices, the charge transfer and readout steps are accelerated so that the entire image is produced in the requisite 33 msec. The speed increase results in greater noise and reduced charge transfer efficiency, as described above.

8.2.7 Binning

When the incident light flux is very low, the process of binning may substantially improve the *S/N* of a CCD camera. Binning is an operation by which the signals from several adjacent pixels are pooled and treated as if they came from a single larger sensor (superpixel). Binning involves shifting the charge from a number of adjacent pixels into the output node and delaying the readout until the signal from all of the selected pixels has accumulated in the node. Binning trades off spatial resolution for sensitivity. The improvement in *S/N* comes from the fact that the pooled signal from

several pixels is read out only once. The relative contribution of the readout amplifier noise is reduced in proportion to the number of pixels that are binned. When 3×3 binning is employed, the signal is increased ninefold, whereas the noise is 1/9th of the noise obtained on sampling each of the nine pixels individually. The only physical limitation to the number of pixels that can be combined is the charge storage capacity of the serial register and output node of the CCD, both of which are typically two to three times larger than the FWC of a single pixel. This is not usually a significant concern because binning is employed when the signal is weak and the amount of stored charge does not approach the FWC. The associated reduction in spatial resolution is often a more important limitation to the extent of binning.

8.2.8 Color

There are three strategies for producing color images with CCD sensors: (1) cover each pixel of the CCD with a mask containing either red, green, or blue filters (RGB) usually arranged in the Bayer mosaic pattern; (2) divide the incident light with a beam-splitting prism and attached filters into three components (R, G, B) and three CCDs to capture the relevant images; (3) use a liquid crystal filter or rotating filter wheel to capture the R, G, and B images in succession (frame-sequential color). Although each approach has its strengths and weaknesses, all color cameras are less sensitive than their monochrome counterparts because of unavoidable losses associated with the color filters or other optical components.

When a Bayer mosaic filter is used, the color information is distributed over four pixels, one red, one blue, and two green (Fig. 8.3). The emphasis on green in the filter distribution pattern accomplishes good color fidelity with human vision and has only modest decreases in spatial resolution. Spatial resolution is largely determined by the

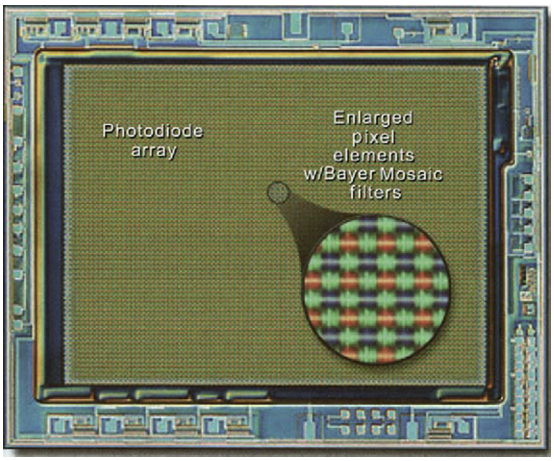

FIGURE 8.3

A Bayer mosaic filter CCD for color imaging.

luminance portion of a color image—that part associated with the monochrome signal. Each pixel, regardless of the color of the filter, contains considerable luminance information, so the resolution is not diminished in proportion to the number of pixels that constitute a sensor unit. Our visual system requires that only rather coarse color information be admixed with the monochrome structural information to produce a visually satisfying image. Some single-CCD color cameras improve the spatial resolution by shifting the CCD small amounts between a series of images and then interpolating between the images. This approach slows acquisition considerably because of the mechanical repositioning between frames. The single-chip CCD with an adherent color filter is the most widely used color camera in light microscopy.

The three-CCD color camera combines rapid image acquisition with high spatial resolution (Fig. 8.4). Spatial resolution may be greater than that of the individual CCD sensors, as each CCD may be slightly offset by a subpixel amount. Thus, the RGB images all represent slightly different samples and can be combined in software to produce a higher-resolution image. Commercial broadcast television cameras are all of the three-CCD variety, and many scientific applications that require high-resolution color and good temporal resolution employ these devices. They are often used in microscopy, particularly in applications involving histology or pathology.

Frame-sequential color cameras equipped with a liquid crystal filter are widely used in light microscopy (Fig. 8.5). Because the same sensor is used for all three colors, image registration is not an issue. The acquisition of three frames in succession slows the process considerably. Proper color balance often requires longer integration times for one color than for another. In addition, the transmission of the liquid crystal or color filter is not the same for the three wavelengths, so the

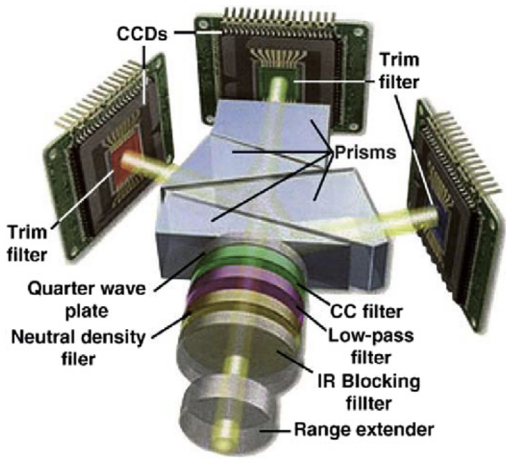

FIGURE 8.4

A three-CCD color camera.

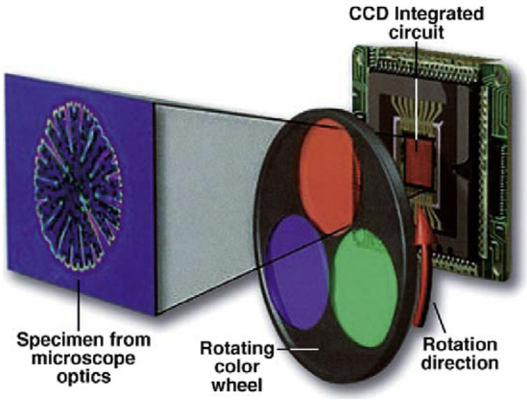

FIGURE 8.5

A frame-sequential color camera using a filter wheel.

integration time must be adjusted accordingly. When a rotating filter wheel is used, more than three colors may be acquired. In remote sensing applications, up to 10 different wavelengths are captured in succession. A readily visible problem with such multiwavelength systems is image registration. Small positional shifts occur because the filter surfaces are not absolutely flat or the filters are not mounted perfectly. These artifacts can be corrected by postprocessing, but the acquisition time is further lengthened.

Liquid crystal filters have a lower transmission than the colored glass or interference filters used in the filter wheel systems. Liquid crystal filters only transmit one polarization, so half of randomly polarized incident light is lost. Additional losses in the filters themselves reduce transmission to about 40%. The polarization sensitivity of the liquid crystal filters also can distort the colors of objects imaged under polarized light. In fact, the analyzer can be removed in some cases as the filter fulfills that role.

Finally, some new technologies are on the horizon that may become relevant to the light microscopist. As discussed earlier, the depth of penetration of a photon into the silicon of a CCD depends on its energy and, hence, its wavelength. A new sensor exploits this property by layering the sensing regions and determining the "color" of an incident photon from its depth of penetration.

8.2.9 Image-intensified CCD camera

Image intensification is a widely used alternative to prolonged on-chip integration and binning when the image must be obtained in a short time period. Image intensifiers are an integral part of many low-light-level cameras, particularly video-rate devices. When the intensifier is coupled to a CCD camera, the device is designated an ICCD (intensified CCD). Image intensifiers are three-stage devices: The first stage is

photon detection by a photocathode and the liberation of photoelectrons, the second stage is an electron accelerator or multiplier, and the third stage is conversion of the electron beam to visible light or a detectable electronic signal.

Photons impinge on the front surface of a photocathode that absorbs their energy and releases an electron from its back surface. The released electron is accelerated by a substantial voltage and strikes the wall of a microscopic capillary in a microchannel plate (MCP) electron multiplier. The impact of the electron on the capillary surface results in the release of a cloud of electrons that cascade through the capillary driven by a voltage gradient along its length. The capillary is slightly tilted so that subsequent additional impacts with the capillary wall occur and result in a large increase in the number of electrons that emerge from the end of the channel in the MCP. A high voltage accelerates the electron cloud across a small gap to impact on a screen coated with a phosphor that converts the electron energy to light. The process results in an overall light gain of as high as 10^6, although 10^5 is more commonly achieved. Thus, a single detected photon at the input of the intensifier may result in an emission at the output of tens or hundreds of thousands of photons. This output light flux is usually relayed to the CCD sensor by a tapered fiber optic coupler that is designed to collect as much of the emitted light as possible.

The gain of image intensifiers is controlled by variation in the voltage across the MCP and can usually be adjusted over about a 1000-fold range. MCP gain can be adjusted very rapidly (within a few milliseconds) and reproducibly so that frequent gain alteration is an integral part of many quantitative imaging systems using an ICCD. When the gain of the MCP is fixed, image intensifiers have a limited dynamic range within a scene compared to a CCD camera. The dynamic range is largely determined by the maximum current that can flow through a region of the MCP. Well-designed ICCD cameras exhibit a 1000-fold dynamic range within a scene and, therefore, just achieve 10-bit resolution. When the gain of the intensifier is adjusted, a much larger intensity range can be accommodated, but the limitations still apply for the dynamic range within a scene. Because each detected photon results in the generation of thousands of photons at the output window of the image intensifier, the potential wells in the CCD sensor to which the intensifier is coupled may quickly fill to overflowing with charge. Therefore, unless the CCD employed has very large pixels, dynamic range limitations will also arise in the CCD itself. Thus, just a few frames of integration on the CCD sensor may saturate regions of interest and preclude the accurate measurement of their intensity. Often when integration is performed with an ICCD, the gain of the intensifier is substantially reduced to prevent such regional saturation.

Spatial resolution of an ICCD is always less than that of the CCD alone. The intensification process tends to blur the signal from individual photons and obscure fine image details. The extent of the resolution loss is a function of the size of the MCP capillaries, the geometry of the fiber optic coupling, and the pixel size and number of the CCD sensor. The latest designs use 6-μm diameter MCP capillaries, tapered fiber optic couplers, and CCDs with array sizes of 1000×1000 or greater. The spatial resolution achieved is about 75% of that of the CCD alone.

8.2.10 Gating of the ICCD

The photocathode of the image intensifier can be rapidly turned off or on (gated) by altering its voltage from negative to positive. Gating effectively shutters the intensifier, eliminating the need for a mechanical shutter and allowing the intensified camera to tolerate much higher-input light intensities. When the input light intensity is overly bright, gating can be used to reduce the "on" time to as little as a few nanoseconds. Gated intensified CCD cameras are used in spectroscopy and high-speed imaging for sampling the photon fluxes that are obtained during such brief exposures.

8.2.11 Electron-bombarded CCD

The first intensified video camera, the silicon intensifier target or SIT, used a photocathode and large accelerating voltage to generate energetic photoelectrons that impacted directly on the target of a silicon diode vidicon tube. Because of the high energy of the electrons, each electron impact generated many charge pairs in the silicon diode target. The SIT differed from the image-intensified cameras that followed because the electrons were not used to generate photons by impacting on an output phosphor but instead acted directly on the detector surface. The electron bombarded (EEB) CCD is the modern-day, solid-state embodiment of the SIT. The photosensitive surface is a photocathode as in the SIT and image intensifiers, and the photoelectrons are accelerated by a large voltage, but they impact onto a back-thinned CCD, where they liberate a large number of charge carriers.

The EBCCD has several advantages over the old SIT, including faster response, lower geometric distortion, and better uniformity of sensitivity across the detector surface. The spatial resolution of the EBCCD is generally higher than that of a comparable ICCD, but the EBCCD has substantially smaller dynamic range than a cooled CCD with the same size pixels. Each detected photon generates hundreds of charges, so the potential wells of the CCD fill very quickly. As with the ICCD, this limitation can be partially overcome by using a CCD with larger pixels.

8.2.12 On-chip multiplication

Two recent developments in CCD sensor technology are useful to light microscopists. As discussed above, the readout amplifier in a conventional CCD has unity gain, and each detected photon liberates a single electronic charge. Conventional CCD cameras incorporate subsequent amplification stages that allow multiplication of the output of the readout amplifier. This mode of amplification has the disadvantage of increasing both the signal and the readout noise to the same extent. Ideally, the readout amplifier itself should have variable gain, so that the signal can be increased without any amplification of the readout amplifier noise. Recently, two new designs were announced for a low-noise, on-chip charge multiplication stage interposed between the sensors and the readout amplifier of a CCD.

In one version, the serial register pixels are modified to enable voltage-controlled avalanche multiplication of the charge stored in that pixel. Thus, as each row of a 512 $\times$ 512 array CCD is transferred to the serial register, the corresponding 512 pixels in the serial register allow variable multiplication of the stored charge before read-out. Because the serial register pixels are twice as large as the sensor pixels and the output node pixel is three times as large, there are limits to the maximum multiplication that can occur. Usually, however, multiplication is used when the signals are small and the stored charge in the pixels is nowhere near FWC. Avalanche multiplication occurs when the bias voltages of the serial register pixels are substantially increased, a process that also results in an increase in noise.

In the second version, the stored charges are transferred as usual to a modified serial register that contains a long, specialized region in which a variable number of impact ionization steps may occur. Each of these steps leads to charge carrier multiplication with little increase in noise, much as in the dynode chain of a photomultiplier tube. Thus, the signal that reaches the readout amplifier may be increased up to 50-fold depending on the gain that is selected, whereas the readout amplifier noise is unaffected. A single electronic charge resulting from the detection of one photon could result in as many as 50 charges at the output node. For a CCD with a readout noise of 10 electrons, the *S/N* would be 5 for a single photon event.

Low noise amplification of the stored charge before read out is preferable to the amplification of the incident light flux that occurs in ICCD cameras or to the electron multiplication that occurs in the EBCCD. In both of these devices, amplification of the signal substantially reduces the dynamic range because the charge storage wells are filled at a rate that is directly related to the amplification factor.

8.3 APPLICATION OF CCD CAMERAS IN FLUORESCENCE MICROSCOPY

Although fluorescence microscopy is considered a "low-light-level" technique, the emitted light flux may vary over several orders of magnitude. In the past, low-light level referred to conditions in which a video-rate camera is incapable of capturing an image. The weakest light flux that can be detected by a tube or solid-state video-rate camera is about 10^{-2} lux (or 10^{-3} foot candles), equivalent to the nighttime incident light of a full moon or to the levels observed in polarized light microscopy near extinction. The most demanding applications in fluorescence microscopy may require as much as four orders of magnitude greater sensitivity.

In addition to the physical limits of fluorescence, the need for sensitive detectors is driven by the low collection efficiency of conventional wide-field microscopes. The geometric constraints imposed by the numerical aperture of the objective lens as well as the inevitable losses in the optical train of the microscope lead to a loss of 80% or more of the original fluorescence signal. Depending on the properties of the detector, the resultant electronic signal may represent as little as 3% or as much as 16% of the fluorescence emission.

When a veteran video camera company representative was once asked about the basis for deciding between a cooled or intensified CCD camera for fluorescence microscopy, he replied, "It's all a matter of time." Indeed, given sufficient time for integration, a cooled CCD camera will always outperform an ICCD with a comparable sensor (see also chapter by Moomaw Deu). However, some biological events occur on such fast time scales and yield so few photons that a useful image cannot be obtained with a cooled CCD camera. The recent emphasis on the application of fluorescence microscopy to study the dynamics of living cells results in many such situations. The high illumination intensities or prolonged integration periods needed to capture an image using a cooled CCD camera may produce such serious photodynamic damage. How does one decide which detector to use?

The ICCD has the strengths of high speed and sensitivity but the weaknesses of limited dynamic range and resolution, both bit depth and spatial. The cooled CCD has the virtues of high quantum efficiency, large dynamic range, virtually perfect linearity, and excellent spatial resolution. These strengths come at the price of limited speed, both in the period of integration required to capture an image with acceptable *S/N* and in the time taken to read that image out. In many cases, the EBCCD and the On-Chip Multiplication CCD cameras offer an attractive compromise between the extremes of the cooled and ICCD cameras. The break-even point is determined by the experimental requirements, particularly the speed/sensitivity concern.

A rule of thumb for minimization of photodynamic damage during live cell imaging by reducing the excitation light intensity can be summarized as follows: 'If you can see the fluorescence through the eyepieces, the excitation light is too bright.' The limiting sensitivity of the dark-adapted human eye is about 10^{-4} lux or 10^{-5} foot candles, a light level that requires an integration time of about 200 ms on a cooled CCD camera to produce an acceptable *S/N*. If the biological event of interest occurs in less than this time, an ICCD, EBCCD or On-Chip Multiplication CCD is the appropriate detector. In many fluorescence microscopy applications to the study of living cells, the concentration of fluorophore in the cell or organelle may be limited either by loading limitations or by interaction of the probe with the process of interest, such as the undesired calcium buffering by the calcium indicator dye. Under these conditions the signal may be so weak that a longer integration time is required for a cooled CCD or EBCCD to capture a useful image, even when binning is employed. Again, the ICCD or On-Chip Multiplication CCD may prove more appropriate under these circumstances because the gain may be increased to compensate for the weak signal while maintaining the requisite sampling speed.

It is important to note that the dynamic range limitations of the ICCD and EBCCD can make it difficult to capture events that exhibit large variations in brightness, as in specimens containing both thick and thin regions. When imaging Ca^{++} in neurons, for example, the cell body may be 40 times thicker than the dendrites, which requires a minimum of 12-bit resolution to simultaneously monitor the fluorescence from both sites. Because ICCDs generally have at most 10-bit dynamic range, one would have to capture several images at different gain settings with an ICCD. High

gain could be used to visualize the small structures, and low gain to capture the image of the thick cell body. With a cooled CCD or On-Chip Multiplication CCD, however, it would be possible to effectively image both sites at once.

8.4 FUTURE DEVELOPMENTS IN IMAGING DETECTORS

A promising development is the recently improved performance of the CMOS (complementary metal oxide semiconductor) sensors. These devices have large charge storage capacity, very fast readout of regions of interest, and extremely large dynamic range. Several (three to six) amplifiers are required for each pixel, and to date, uniform images with a homogeneous background have been a problem because of the inherent difficulties of balancing the gain in all of the amplifiers. CMOS sensors also exhibit relatively high noise associated with the requisite high-speed switching. Both of these deficiencies are being addressed, and sensor performance is nearing that required for scientific imaging.

Further Reading

Inoué, S., & Spring, K. R. (1997). *Video microscopy: The fundamentals.* New York: Plenum.

Murphy, D. B. (2001). *Fundamentals of light microscopy and electronic imaging.* New York: Wiley-Liss.

Sluder, G., & Wolf, D. E. (1998). *Methods in cell biology, video microscopy* (Vol. 56). San Diego: Academic Press.

CHAPTER

A High-Resolution Multimode Digital Microscope System

9

Edward D. Salmon, Sidney L. Shaw, Jennifer C. Waters, Clare M. Waterman-Storer, Paul S. Maddox, Elaine Yeh, and Kerry Bloom

Department of Biology, University of North Carolina, Chapel Hill, North Carolina, USA

CHAPTER OUTLINE

Introduction **181**
9.1 Design Criteria **182**
9.1.1 Fluorescence Considerations 182
9.1.2 Live Cell Considerations 184
9.1.3 Phase Contrast and DIC Imaging 185
9.1.4 The Need for Optical Sections 186
9.2 Microscope Design **186**
9.2.1 Imaging Optics 186
9.2.1.1 Objectives and Matching Condenser 186
9.2.1.2 Magnification 187
9.2.1.3 Determining Focus 188
9.2.1.4 Phase Contrast 188
9.2.1.5 DIC and the Analyzer Filter Wheel 188
9.2.2 Epiillumination Optics 189
9.2.2.1 Mercury Lamp and Housing 189
9.2.2.2 Heat Reflection Filter 189
9.2.2.3 Köhler Illumination 189
9.2.2.4 Dual Filter Wheel and Epishutter 189
9.2.2.5 Condenser Diaphragm 189
9.2.2.6 Field Stops 190
9.2.2.7 Correction for Longitudinal Chromatic Aberration 191
9.2.2.8 Filter Cube Turret 191
9.2.2.9 Multiple Band-Pass Dichromatic Mirror and Emission Filter 191
9.2.3 Transillumination Optics 191
9.2.3.1 Quartz-Halogen Lamp and Housing 191
9.2.3.2 Heat-Reflecting Filter 192
9.2.3.3 Thermal Isolation 192
9.2.3.4 Köhler Illumination and the Ground–glass Diffuser 192
9.2.3.5 Band-Pass Filters 192
9.2.3.6 Transshutter 192

Methods in Cell Biology, Volume 114 **ISSN 0091-679X**
Copyright © 1998 Elsevier Inc. All rights reserved.
http://dx.doi.org/10.1016/B978-0-12-407761-4.00009-9

9.2.4 Focus Control 193
9.2.5 Vibration Isolation 193
9.3 Cooled CCD Camera 193
9.3.1 Camera Features 193
9.3.2 Quantum Efficiency 194
9.3.3 Readout 196
9.3.3.1 AD Conversion 196
9.3.3.2 Transfer Time 196
9.3.3.3 Size 196
9.3.3.4 Binning 197
9.3.4 Linearity, Noise Sources, and the Advantages of Cooling 198
9.3.5 Dark and Background Reference Image Subtraction 199
9.3.6 Shading 199
9.3.7 Signal-to-Noise 200
9.4 Digital Imaging System 201
9.4.1 Microscope Automation and Camera Control 201
9.4.1.1 Computer Control of the Microscope 201
9.4.1.2 Image Processing and Analysis 202
9.4.2 Other Useful Software and Devices 202
9.5 Example Applications 203
9.5.1 DE-DIC 203
9.5.2 Multimode Imaging of Anaphase *in Vitro* 203
9.5.3 Fluorescence Photoactivation 205
9.5.4 Microtubule and ER Dynamics in Migrating Tissue Cells 206
9.5.5 GFP-Dynein-Labeled Microtubules in Yeast 207
9.5.6 Immunofluorescent Specimens 208
References 209
Further Reading 210

Abstract

This chapter describes the development of a high-resolution, multimode digital imaging system based on a wide-field epifluorescent and transmitted light microscope, and a cooled charge-coupled device (CCD) camera. The three main parts of this imaging system are Nikon FXA microscope, Hamamatsu C4880 cooled CCD camera, and MetaMorph digital imaging system. This chapter presents various design criteria for the instrument and describes the major features of the microscope components—the cooled CCD camera and the MetaMorph digital imaging system. The Nikon FXA upright microscope can produce high resolution images for both epifluorescent and transmitted light illumination without switching the objective or moving the specimen. The functional aspects of the microscope set-up can be considered in terms of the imaging optics, the epi-illumination optics, the transillumination optics, the focus

control, and the vibration isolation table. This instrument is somewhat specialized for microtubule and mitosis studies, and it is also applicable to a variety of problems in cellular imaging, including tracking proteins fused to the green fluorescent protein in live cells. The instrument is also valuable for correlating the assembly dynamics of individual cytoplasmic microtubules (labeled by conjugating X-rhodamine to tubulin) with the dynamics of membranes of the endoplasmic reticulum (labeled with $DiOC_6$) and the dynamics of the cell cortex (by differential interference contrast) in migrating vertebrate epithelial cells. This imaging system also plays an important role in the analysis of mitotic mutants in the powerful yeast genetic system *Saccharomyces cerevisiae*.

INTRODUCTION

In this chapter we describe the development of a high-resolution, multimode digital imaging system based on a wide-field epifluorescent and transmitted light microscope and a cooled charge-coupled device (CCD) camera. Taylor and colleagues (Farkas et al., 1993; Waterman-Storer, Sanger, & Sanger, 1993) have reviewed the advantages of using multiple optical modes to obtain quantitative information about cellular processes and described instrumentation they have developed for multimode digital imaging. The instrument described here is somewhat specialized for our microtubule and mitosis studies, but it is also applicable to a variety of problems in cellular imaging including tracking proteins fused to the green fluorescent protein (GFP) in live cells (Cubitt et al., 1995; Heim & Tsien, 1996; Pawley, 2006). For example, the instrument has been valuable for correlating the assembly dynamics of individual cytoplasmic microtubules (labeled by conjugating X-rhodamine to tubulin) with the dynamics of membranes of the endoplasmic reticulum (ER, labeled with $DiOC_6$) and the dynamics of the cell cortex [by differential interference contrast (DIC)] in migrating vertebrate epithelial cells (Waters, Mitchison, Rieder, & Salmon, 1996). The instrument has also been important in the analysis of mitotic mutants in the powerful yeast genetic system *Saccharomyces cerevisiae*. Yeast cells are a major challenge for high-resolution imaging of nuclear or microtubule dynamics because the preanaphase nucleus is only about 2 μm wide in a cell about 6 μm wide. We have developed methods for visualizing nuclear and spindle dynamics during the cell cycle using high-resolution digitally enhanced DIC (DE-DIC) imaging (Zhai, Kronebusch, & Borisy, 1995; Inoué & Salmon, 1995). Using genetic and molecular techniques. Bloom and coworkers (Shotten, 1995; Spencer, 1982) have been able to label the cytoplasmic astral microtubules in dividing yeast cells by expression of cytoplasmic dynein fused to GFP. Overlays of GFP and DIC images of dividing cells have provided the opportunity to see for the first time the dynamics of cytoplasmic microtubules in live yeast cells and how these dynamics and microtubule interactions with the cell cortex change with mitotic cell cycle events in wild-type and in mutant strains (Shotten, 1995; Spencer, 1982).

Our high-resolution multimode digital imaging system is shown in Fig. 9.1 and diagrammed in Fig. 9.2. The legend to Fig. 9.2 provides model numbers and sources of the key components of the instrument. There are three main parts to the system:

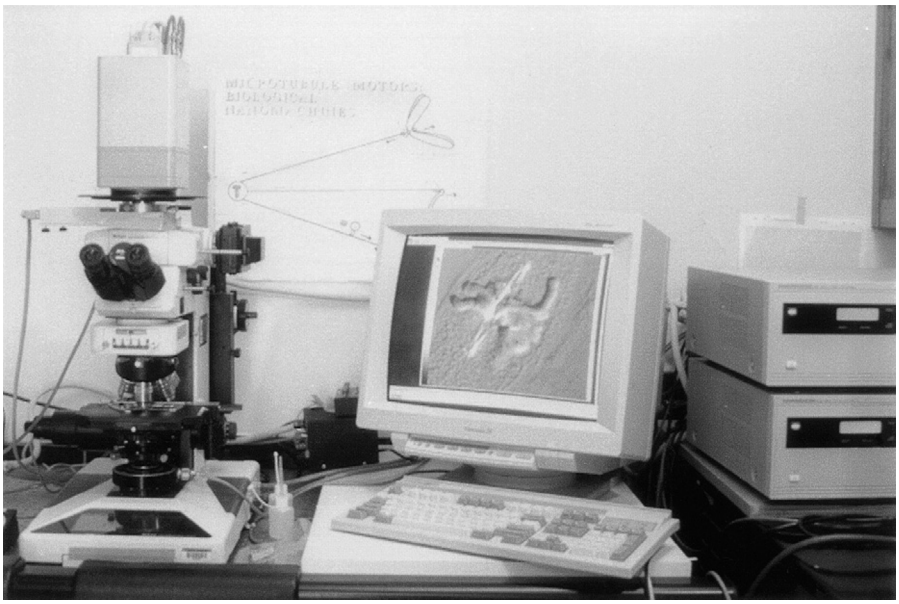

FIGURE 9.1

Photograph of the multimode digital imaging system including the Nikon FXA upright microscope sitting on an air table (Newport Corp., Irvine, CA, VW-3660 with 4-inch-high tabletop). Images are captured with a Hamamatsu C4880 cooled CCD camera. Image acquisition, storage, processing, analysis, and display are controlled by MetaMorph Digital Imaging software in a Pentium-based computer.

a Nikon FXA microscope, a Hamamatsu C4880 cooled CCD camera, and a MetaMorph digital imaging system. First we will consider our design criteria for the instrument, then consider separately the major features of the microscope components, the cooled CCD camera, and the MetaMorph digital imaging system. The reader is referred to other sources for general aspects of microscope optics (Inoué & Oldenbourg, 1993; Mitchison, 1989; Taylor & Salmon, 1989); DIC microscopy (Salmon, 1998); fluorescence microscopy (Waterman-Storer & Salmon, 1997); video cameras, slow-scan cameras, and video microscopy (Aikens, Agard, & Sedat, 1989; CLMIB staff, 1995; Inoué, 1986; Keller, 1995; Taylor, Nederhof, Lanni, & Waggoner, 1992) and 3D imaging methods (Carrington et al., 1995; Hiroka, Sedlow, Paddy, Agard, & Sedat, 1991; Salmon, Inoué, Desai, & Murray, 1994).

9.1 DESIGN CRITERIA

9.1.1 Fluorescence considerations

When we began building our instrument 4 years ago, our primary objective was to obtain quantitative time-lapse records of spindle microtubule dynamics and chromosome movements for mitosis in live tissue culture cells and in *in vitro* assembled spindles

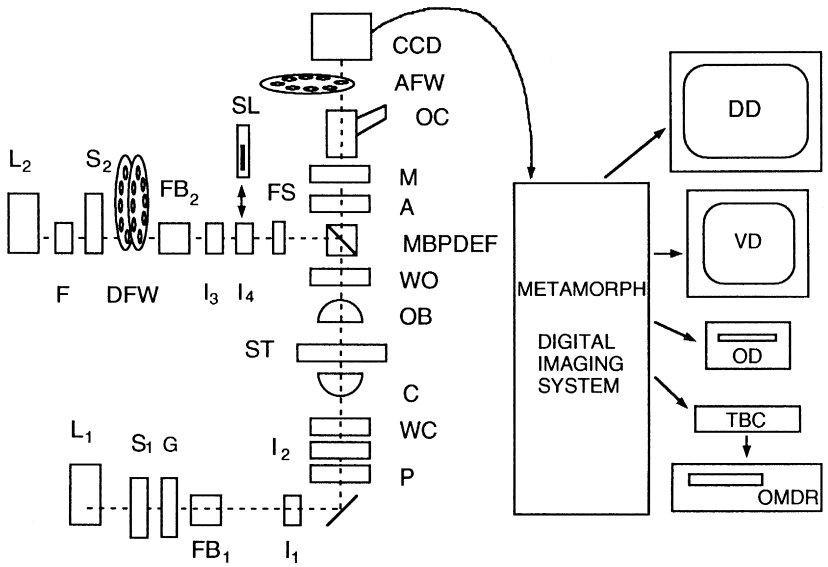

FIGURE 9.2

Component parts are L1, 100-watt quartz halogen lamp; S1, Uniblitz shutter (No. 225L2A1Z523398, Vincent Associates, Rochester, NY); G, ground glass diffuser: FB1, manual filter changers including KG4 heat cut and green interference filters; I_1, field iris diaphragm; I_2, condenser iris diaphragm; P and A, high transmission Nikon polaroid polarizer and removable analyzer; WC, and WO, Wollaston prisms for condenser and objective: C. Nikon NA = 1.4 CON A. Achr-Apl condenser; ST, rotatable stage with focus position controlled by *z*-axis stepper motor (Mac2000, Ludl Electronic Products, LTD., Hawthorne, NY); OB, 20X/NA = .75 or 60X/NA = 1.4 Nikon objectives; MBPDEF, epifilter block with multiple bandpass dichromatic mirror and emission filter (Nos. 83101 and 83100. Chroma Technology Corp., Brattleboro, VT); L2, 100-watt HBO mercury lamp; F, KG4 heat cut filter; S2 shutter; DFW, dual 8-position filter wheel (Metaltek, Raleigh, NC), one wheel containing neutral density filters (No. FNQ011, Melles Griot, Irvine, CA) and the other a series of narrow bandpass excitation filters (Nos. 83360, 83490, and 83570, Chroma Technology Corp.); FB_2, manual filter changer; I_3, epicondenser iris diaphragm; I_4, epifield diaphragm slider; SL, slit (25 μm width. No. 04PAS004, Melles Griot, Irvine, CA) cemented to Nikon pinhole slider (No. 84060) for photoactivation; FS, filter slider; M, optivar magnification changer, $1-2\times$ OC, oculars; AFW, 4-position filter wheel (Biopoint filter wheel No. 99B100, Ludl Electronic Products, LTD., Hawthorne, NY) with one position containing a Nikon high transmission polarizer for the analyzer and another position an optical glass flat of the same thickness as the analyzer; CCD, cooled CCD camera (No. C4880, Hamamatsu Photonics, Bridgewater, NJ); DD, 1024 × 768-pixel, 20-inch digital graphics display monitor (No. 2082, Viewsonic); VD, RGB video display monitor (No. PVM1271Q, Sony); MetaMorph digital imaging system (Universal Imaging Corp., West Chester, PA) with a 166-MHz Pentium computer having both EISA and PCI bus. 128-MByte RAM memory, Imaging Technology AFG digital and video

Continued

in *Xenopus* egg extracts. Fluorescence optical components were chosen, in part, based on the fluorophores that were available for labeling microtubules, chromosomes, and other microtubule- or spindle-associated components. Microtubules could be fluorescently labeled along their lengths by incorporating X-rhodamine-labeled tubulin into the cytoplasmic tubulin pool (Fig. 9.3; Olson, McIntosh, & Olmsted, 1995; Sawin & Mitchison, 1991). In addition, we needed to use fluorescence photoactivation methods to produce local marks on spindle microtubules to study the dynamics of their assembly (Murray, Desai, & Salmon, 1996; Yeh, Skibbens, Cheng, Salmon, & Bloom, 1995). This is accomplished by the addition of a cagedfluorescein-labeled tubulin to the cytoplasmic pool and fluorescence photoactivation with a 360-nm microbeam as described by Mitchison and coworkers (Mitchison & Salmon, 1993; Shamu & Murray, 1992; Sawin, Theriot, & Mitchison, 1992). In extracts and some living cells, chromosomes can be vitally stained with the DNA intercalating dyes DAPI or Hoescht 33342 (Olson et al., 1995; Shamu & Murray, 1992). Thus, in fluorescence modes, we needed to be able to obtain images in a "red channel" for X-rhodamine microtubules, a "green channel" for photoactivated fluorescein marks, and a "blue channel" for chromosomes.

9.1.2 Live cell considerations

Photobleaching and photodamage are a major concern during time-lapse imaging of fluorescently tagged molecules in live cells or in *in vitro* extracts. Minimizing these problems requires that the specimen be illuminated by light shuttered between camera exposures, that the imaging optics have high transmission efficiencies, that the camera detectors have high quantum efficiency at the imaging wavelengths, and that light can be integrated on the detector to reduce illumination intensity and allow longer imaging sessions without photo-damage. This later point is true not only for epifluorescence but also for transmitted light (phase-contrast or DIC) imaging. In our studies, the detector also needed a high dynamic range (12 bits = 4096 gray levels), as we wanted to be able to quantitate the fluorescence of a single microtubule or the whole mitotic spindle, which could have 1000 or more microtubules. In addition, the red, green, and blue images needed to be in focus at the same position on the detector so that the fluorophores within the specimen could be accurately correlated.

---

image processing card, Hamamatsu C4880 CCD controller card, Matrox MGA Melenimum 4-M RAM graphics display card, SVGA graphics display to S-VHS converter card (Hyperconverter, PC Video Conversion Corp., San Jose, CA). 1.4-MByte floppy drive, 2-GByte hard drive, 1-Gbyte Iomega Jaz drive, Hewlett Packard SureStore CD Writer 40201, ethernet card, and parallel port cards for controlling shutter S1 and driving laser printer; 8–serial port card for controlling MetalTek filter wheel, Ludl *z*-axis stepper, CCD camera, and OMDR; OD, Pinnacle Micro 1.3-GByte optical drive; TBC, time-base corrector; OMDR, Panasonic 2028 Optical Memory Disk Recorder. Video is also recorded on a Panasonic AG-1980P S-VHS recorder and a Panasonic AG-6750A time-lapse S-VHS recorder. Modified from Salmon et al. (1994).

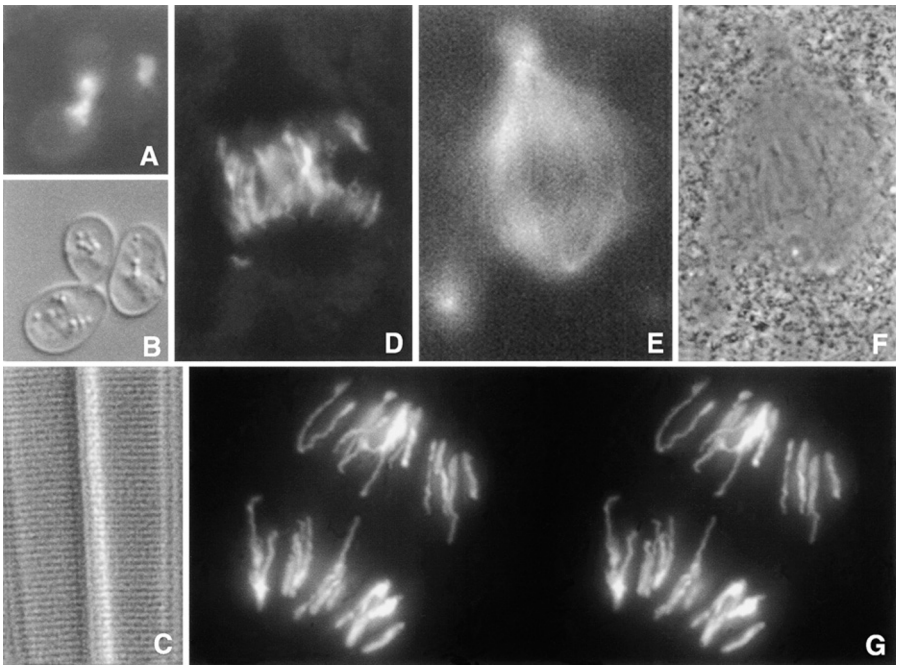

FIGURE 9.3

Views of a living, dividing yeast, *Saccharomyces cerevisiae*, by (A) fluorescence of GFP protein bound to nuclear histones and (B) DIC.* (C) Images in DIC of the 0.24-μm spacing between rows of surface pores of the diatom *Amphipleura* illuminated with green light.* Images of a spindle undergoing *in vitro* anaphase in *Xenopus* cytoplasmic egg extracts: (D) DAPI-stained chromosomes, (E) X-rhodamine-tubulin-labeled spindle and aster microtubules, and (F) phase contrast (Nikon 20X/NA = 0.75 Fluar Phase 3 objective). See Murray et al. (1996) for details. Stereo-pair images (G) of DAPI-stained chromosomes generated from a stack of 0.5-μm optical sections through a *Xenopus* spindle fixed in the extracts in midanaphase.* (*, Nikon 60X/NA = 1.4 Plan Apo DIC objective and NA = 1.4 condenser illumination for DIC.) With permission from Salmon et al. (1994).

9.1.3 Phase contrast and DIC imaging

Phase contrast or DIC-transmitted light images allow the localization of fluorescently tagged molecules in the cells to be correlated with overall cell structure or the positions of the chromosomes, nucleus, cell cortex, and so on (Fig. 9.3). DIC has much better resolution than phase contrast (Inoué & Oldenbourg, 1993) and excellent optical sectioning abilities (Inoué, 1989), but unlike phase contrast, an analyzer must be placed in the light path after the objective. Conventional analyzers typically transmit 35% or less of incident unpolarized light, and thus for sensitive fluorescence methods, the analyzer must be removed from the light path for fluorescence imaging and inserted for DIC imaging.

9.1.4 The need for optical sections

In some of our studies, three dimensional images from "z-axis" series of images or four dimensional microscopy where a z-axis image series is recorded at each time point in a time-lapse series have been required. For example, proteins localized to the kinetochore of one chromosome may be 5 μm out of focus with the kinetochore of another chromosome in the same cell. To see all of the kinetochores in the cell, several focal planes are acquired along the z-axis and projected into a single two dimensional representation of the three dimensional data.

9.2 MICROSCOPE DESIGN

The Nikon FXA upright microscope (Figs. 9.1 and 9.2) can produce high-resolution images for both epifluorescent and transmitted light illumination without switching the objective or moving the specimen. The functional aspects of the microscope set-up can be considered in terms of the imaging optics, the epiillumination optics, the transillumination optics, the focus control, and the vibration isolation table.

9.2.1 Imaging optics

Light collected by the objective passes through the body tube, the filter cube holder of the epifluorescence illuminator, a magnification changer, then either straight to the camera or by a prism into the binocular tube for viewing by eye. The cooled CCD camera is mounted at the primary image plane of the microscope.

9.2.1.1 Objectives and matching condenser

In epifluorescence microscopy, the intensity of the image varies as the fourth power of objective numerical aperture (NA) and inversely with the square of the magnification (M) between the objective and the detector (Waterman-Storer & Salmon, 1997):

$$I_{sp} = I_{il}\mathrm{NA}_{obj}^{4}/M^{2}, \tag{9.1}$$

where I_{il} is the intensity of the epiillumination light entering the objective aperture. For high-resolution work, we typically use the highest NA possible (NA = 1.4) to maximize fluorescence intensity. Most of our specimens are less than 10 μm thick, so that lower-NA objectives or water-immersion objectives that have better performance for thicker specimens (Mitchison, 1989) have not been necessary. For high-resolution work, we use a Nikon 60X/NA = 1.4 Plan-Apochromatic objective, either the one designed for phase-contrast or the one designed for DIC. The specimen is illuminated in the transmitted light mode through a Nikon NA = 1.4 condenser containing a turret for selecting matching phase annulus or DIC Nomarski prism and a polarizer for DIC. For the highest-resolution work, immersion oil must be used with the condenser as well as the objective. For lower-resolution work and magnification, we have also found the Nikon Fluar 20X/NA = 0.6 and 40X/NA = 1.3 to be very useful lenses. The Fluar lenses have better transmission efficiency, at 360 nm, in comparison to the PlanApochromat lenses, so they are better for photoactivation experiments.

9.2.1.2 Magnification

The magnification changer is an important feature of the imaging path because the camera is fixed in position at the primary image plane above the objective, and different specimens often require different magnifications. It provides 1.0, 1.25, 1.5, and 2.0 × selectable intermediate magnifications to the camera detector. The body tube above the objective provides additional magnification of 1.25×. Therefore, for the 60X objective, the final possible magnifications to the detector are 75, 93.75, 112.5, and 150×.

How much magnification is necessary so that resolution is not limited by the pixel size of the cooled CCD detector? As discussed below, the Hamamatsu cooled CCD detector uses a chip with a pixel size of 12 × 12 μm. To resolve two adjacent specimen points as distinct points, their images at the detector must be at least two pixel elements apart, or 24 μm (Fig. 9.4). With the specimen points separated by three pixel elements, or 36 μm, the problem of aliasing (Keller, 1995) is avoided. The diffraction limited lateral resolution, r, of two adjacent points in the specimen for the Nikon 60X/NA = 1.4 objective is about:

$$r = 0.61\lambda/\mathrm{NA}_{\mathrm{obj}} = 0.24\mu\mathrm{m} \tag{9.2}$$

for $\lambda = 550$ nm green light. The magnifications needed so that 0.24 μm in the specimen is magnified to 24 or 36 μm on the detector is 24/.24 = 100 × or 36/.24 = 150×. Thus, for resolution limited by the objective and not the detector we must use at least the 1.5× setting of the magnification changer and the 2× setting for the best resolution. Magnifications less than 100× produces brighter images as predicted by Eq. (9.1), but resolution in these images is limited by the resolution of the detector.

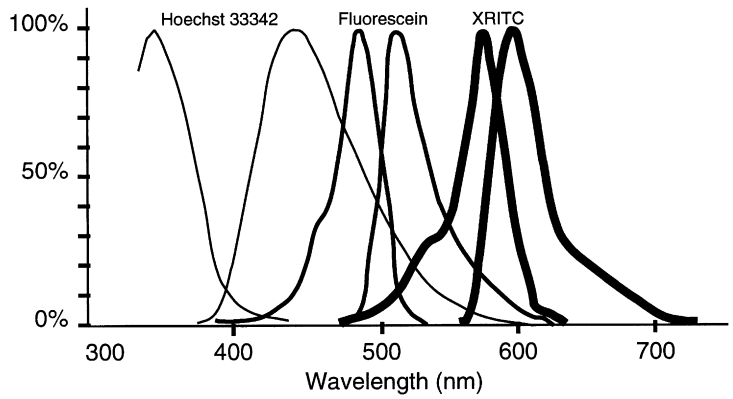

FIGURE 9.4

Excitation and emission spectra for the blue, green, and red fluorophores we commonly use. The excitation and emission spectra for S65TGFP is similar to the fluorescein spectrum and we have had great success using the multiband pass filter (Fig. 9.5) and the fluorescein excitation filter.

9.2.1.3 Determining focus

We have found that an effective way to focus the specimen image on the camera is with dark-adapted eyes. Adjustments are available on the FXA microscope so that the oculars can be made parfocal with the camera. During an experiment, the specimen is viewed by eye and quickly brought into focus. Then the light is switched to the camera for recording. The Hamamatsu C4880 camera has a fast-scan mode that can produce displayed video images as fast as 10 Hz. We have also used this camera feature for achieving focus, but for most situations, we have found that achieving focus with the dark-adapted eye is quicker than switching the camera's mode of operation back and forth between the fast-scan mode of focusing and the slow-scan mode for image recording.

9.2.1.4 Phase contrast

When phase images are recorded along with fluorescent images, we use the phase objective and the matching phase annulus on the condenser turret. The DIC objective Nomarski prism and the DIC analyzers are removed from the imaging path. The phase ring in the back aperture of the objective produces some loss of fluorescent image brightness, but it has not proven significant.

9.2.1.5 DIC and the analyzer filter wheel

For DIC, a Normarski prism is inserted just above the objective, and the condenser turret is switched to the Nomarski prism that matches the objective. The Nikon polarizer beneath the condenser uses high-transmission (35%) Polaroid materials mounted between optical glass flats.

For focusing by eye, a high-transmission DIC analyzer is slid temporarily into the light just above the objective Normarski prism. For the best DIC image contrast, the bias retardation of the objective Nomarski prism is typically adjusted to about 1/15th to 1/10th the wavelength of light (see Salmon et al., 1998) by the following procedure. First, the prism is adjusted to extinguish the background light. Then it is translated further, brightening the background and making one side of the structure of interest maximally dark. At this position, this side of the structure will be darker than the background whereas the other side of the structure will be brighter than the background, producing the "shadowed" appearance of the DIC image (Fig. 9.3).

For DIC image recording, the focusing analyzer is removed from the light path. A filter wheel just beneath the camera (Fig. 9.2) is used to insert a high-transmission DIC analyzer into the light path. For fluorescence imaging, the filter wheel is rotated to an adjacent position that contains an optical glass flat of equivalent optical thickness to the analyzer. The Ludl filter wheel was chosen in part because it was sufficiently thin to fit between the top of the microscope and the camera without changing the position of focus of the primary image on the detector. It was also selected because it can change filter positions without inducing noticeable vibration of the objective. This filter wheel is relatively slow, requiring about 1 second to change filter positions; a time that has not proven a problem for our applications. Finally, the filter wheel is rotated by a stepping motor. There are 4000 steps between adjacent

filter positions, and the ability of the filter wheel to repeatedly bring the analyzer back to the exact same position (crossed with the polarizer) is excellent.

9.2.2 Epiillumination optics

There are a number of important features of the epiillumination pathway for our multimode microscope, including the mercury lamp housing, dual filter wheel, condenser, condenser diaphragm, field stop (diaphragm or slit), optical flat slider, and filter cubes.

9.2.2.1 Mercury lamp and housing

The lamp housing contains a mirror in the back so that both the direct light from the arc and the reflected light from the mirror pass through the lamp collector lens and become projected into the objective aperture by the epiillumination optics. The mirror image helps obtain a more intense and even illumination of the objective aperture.

9.2.2.2 Heat reflection filter

This filter prevents harmful infrared light from heating the shutters, filters, or the specimen. Many conventional fluorescence filter sets do not block infrared light, which shows up as a hot spot on cameras though it is invisible to the eye.

9.2.2.3 Köhler illumination

Nikon has a mirror within an objective mount that can be used for focusing and aligning the images of the arc lamp centered and in focus at the position of the objective back aperture. This is the procedure for Köhler illumination, the alignment that gives the most even illumination of the specimen. See the microscope manual for detailed alignment procedures.

9.2.2.4 Dual filter wheel and epishutter

There are two eight-position filter wheels mounted near the lamp collector lens where the illumination light is out of focus. The wheels hold 1-inch-diameter filters. The filter wheel assembly includes a 1-inch electronic shutter. The sides of the blades facing the lamp are silvered to reflect the light when the shutter is closed and to prevent overheating of the shutter mechanism. The filter wheel position and the shutter are under computer control.

The first wheel has a series of neutral density filters including 0, 0.3, 0.5, 1.0, 1.3, 2.0, 2.3, and 3.0 O.D. The second filter wheel has one open position, and the rest contain a series of band-pass filters. The open position is used with conventional filter cubes. Three of the band-pass filters are excitation filters used to excite the blue, green, and red fluorophores (Fig. 9.4) through a multiple band-pass dichromatic filter cube (Fig. 9.5). These have central wavelengths of 360, 480, and 570 nm. Other filter positions contain filters for 340, 408, and 546 nm.

9.2.2.5 Condenser diaphragm

The epiillumination condenser diaphragm is often useful for making manual "on-the-fly" adjustments of illumination intensity. Closing this diaphragm can reduce illumination intensity by about 1 O.D.

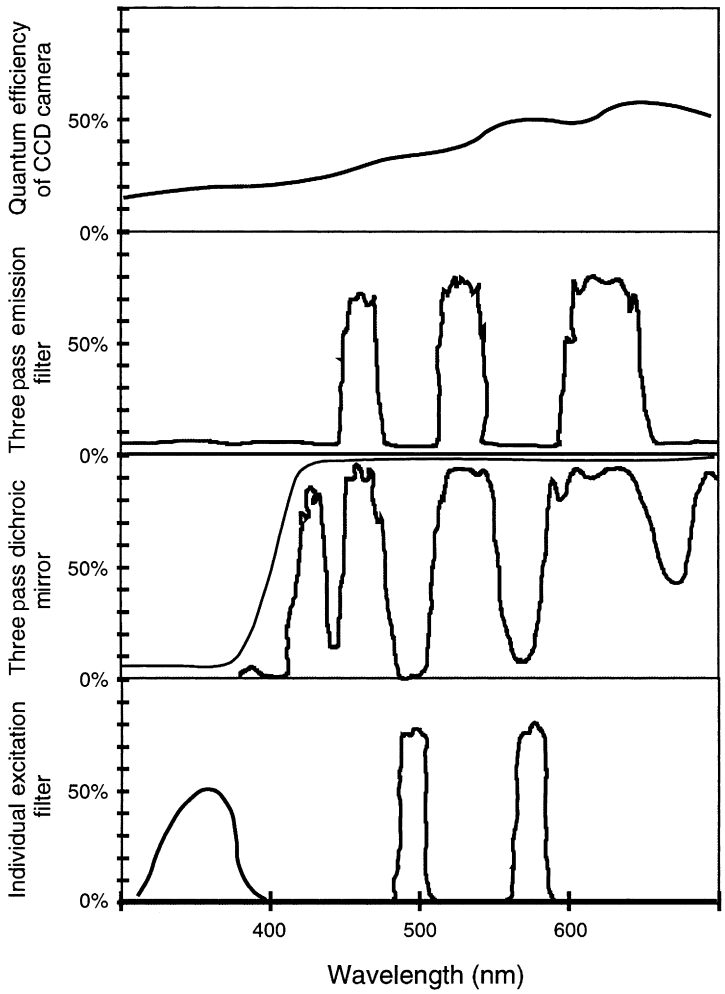

FIGURE 9.5

The quantum efficiency of the TC-215 CCD chip in the Hamamatsu C4880 camera compared to the spectra of the Chroma excitation filters, multiple band pass dichromatic mirror, and multiple band pass emission filter. For the filters, the *y*-axis is percentage transmission. The thin line in the curves for the three-pass dichromatic mirror is produced by a coating on the backside for reflecting 360-nm excitation light.

9.2.2.6 Field stops

We use two field stops. One is a diaphragm that is used during fluorescence imaging to restrict the field of illumination to only the region of interest. As this diaphragm is closed down, the amount of fluorescent scattered light from the specimen decreases, which can significantly enhance the contrast in fluorescence images. Thus, we take care to adjust this diaphragm for each specimen.

The other field stop that can be exchanged easily for the diaphragm is a strip of slits and spots that we use for fluorescence photoactivation. There are translation screws for centering the position of the field stops.

9.2.2.7 Correction for longitudinal chromatic aberration

Between the field stop and the filter cube holder is a slider for 1.5-cm filters. For fluorescence imaging we use an open position. For photoactivation at 360 nm, we insert a 3-mm-thick optical glass flat to make the 360-nm excitation light image of the field spot or slit parfocal with the green or red light images we use for focusing the slit on the specimen, as described in the following photoactivation section.

9.2.2.8 Filter cube turret

The Nikon FXA epiilluminator has four positions for filter cubes. These filters must be rotated into position by hand. We usually leave one of these positions open for the highest- resolution DIC imaging when fluorescence images are not required. We use conventional filter cubes, or specialized cubes, in the other positions.

We initially tried to use a motor-controlled filter turret to select different filters. However, when different filter cubes were used, they had slightly different optical properties (tilted optical elements, nonparallel surfaces, etc.) so that the different-colored images were deflected to different positions on the CCD detector. Their alignment was often not repeatable each time a particular filter was rotated into place. Taylor and colleagues have had better repeatable position accuracy using a linear filter slider (Farkas et al., 1993; Waterman-Storer et al., 1993); however, this does not eliminate the problem of image registration on the detector.

9.2.2.9 Multiple band-pass dichromatic mirror and emission filter

This problem was solved by using a multiple band-pass dichromatic mirror and emission filter set manufactured by Chroma similar to one described by Sawin et al., 1992. In combination with the appropriate excitation filters, these have excitation and emission spectra similar to DAPI or Hoescht DNA intercalating dyes (360 ex/450 em), fluorescein and GFP (480 ex/510–530 em), and X-rhodamine (570 ex/620–650 em) (Fig. 9.5). This has been an important filter cube for our work because the image for the three different fluorophores project to the same focus on the detector. This is because they all use the same dichromatic mirror and emission filter.

Another important aspect of the Chroma filter set is the high transmission efficiency within each bandpass (Fig. 9.5). This is important for maximizing sensitivity and minimizing the effects of photobleaching and photodamage. The same principle applies to the selection of any filter cube for live-cell experiments.

9.2.3 Transillumination optics

9.2.3.1 Quartz-halogen lamp and housing

The 100-watt quartz-halogen lamp is mounted in a housing that contains a rear mirror. The combination of the primary filament image with the mirror filament image produces more even illumination of the condenser aperture than occurs for the primary image of the filament alone.

9.2.3.2 Heat-reflecting filter

As described for the epiillumination pathway, it is important to remove infrared light from the illumination beam. A 1.5-inch-diameter heat-reflecting filter is inserted in front of the lamp collector lens.

9.2.3.3 Thermal isolation

We initially had considerable trouble with the stage drifting downward over time. Stage drift is a significant problem in time-lapse recording because the specimen continually goes out of focus. Stage drift was reduced substantially for the FXA stand by isolating the heat of the lamp from the base of the stand using a ceramic connector between the lamp housing and the base of the microscope stand.

9.2.3.4 Köhler illumination and the ground–glass diffuser

To achieve the highest resolution in DIC, it is essential that the objective aperture be uniformly illuminated (Inoué, 1989; Inoué & Oldenbourg, 1993), and the procedures outlined below are designed to achieve that goal:

1. Initially, the slide is oiled to the condenser (without air bubbles) and viewed with a low-power (10× or 20×) objective.
2. The condenser focus and horizontal position screws are adjusted so that the image of the field diaphragm in the transillumination light path is in focus and centered on the specimen when the specimen is in focus to the eye.
3. The objective is moved away and a small drop of oil (without air bubbles) is placed on the coverslip.
4. The 60X objective is rotated into place. The specimen is focused and the centration of focus of the field diaphragm readjusted. For best contrast, the field diaphragm should be closed till it just surrounds the specimen of interest.
5. The telescope (Bertrand lens) in the magnification changer is then used to focus on the objective back aperture. In that position the condenser diaphragm plane is also in focus. The condenser diaphragm is opened all the way, the ground-glass diffuser is removed from the light path, and the position controls for the bulb and the mirror are adjusted so that the primary and mirror filament images sit side by side in focus at the condenser diaphragm plane. The condenser diaphragm is adjusted to just be visible at the periphery of the objective aperture.
6. The ground-glass diffuser is then placed in the light path to produce more uniform illumination of the 1.4-NA condenser aperture.

9.2.3.5 Band-pass filters

The base of the FXA stand contains a filter changer. For live-cell illumination we use a wide-band (40-nm) green 546-nm band-pass filter.

9.2.3.6 Transshutter

Transillumination of the specimen is controlled by a 1-inch Vincent electronic shutter that is under computer control. The shutter sits on top of the base of the microscope underneath the condenser carrier.

9.2.4 Focus control

Z-axis focus is controlled by a Ludl stepping motor attachment to the fine-focus knob. Coarse focus can be done by hand using the inner focus ring on the microscope. The stepping motor has a manual focus knob with three sensitivity positions: coarse, medium, and fine. The sensitivity is selected with a toggle switch on the knob box. We use the coarse setting for focusing at low magnification and the fine setting for focusing at the highest resolution.

During image recording, focus can be controlled by the computer system to yield a stack of images at equal z-axis steps through the specimen (0.1-μm steps are possible, but we typically use either 0.5- or 1-μm intervals).

We also use the stepping motor to correct for the shift in focus as the stage drifts. Often stage drift occurs at a uniform rate in one direction. During time-lapse recordings, focus is stepped at each recording interval to compensate for the stage drift.

9.2.5 Vibration isolation

To prevent vibration from destroying image fine structural detail, the FXA microscope is mounted on a Newport vibration isolation table (Fig. 9.1). An attractive feature of this table is that it provides arm rests and shelves for computer monitors and other equipment, which are supported independent of the air table.

9.3 COOLED CCD CAMERA

9.3.1 Camera features

Our current camera is a Hamamatsu C4880 dual mode cooled CCD. The CCD detector is a rectilinear array of photodetectors (photodiodes) deposited on a silicon substrate. When the shutter is opened, incoming photons at each photodiode are converted to electrons that are accumulated in potential wells created by an electrode array on the surface of the chip. Thermal motion also knocks electrons into the potential well, and the C4880 is cooled by a Peltier device to about $-30\ ^{\circ}$C to reduce "thermal noise." At the end of a light exposure, the shutter is closed. The C4880 camera uses a Texas Instrument TC-215 CCD chip, which has a 1024×1024-pixel array in which each pixel element is $12 \times 12\ \mu$m in size. The well capacity is 60,000 electrons; beyond this number, the electrons will flow into adjacent wells. CCD detectors are graded for quality and defects. A grade 1 chip like the one in the C4880 camera has few defective pixel elements and few "hot pixels."

Both photons and thermally accumulated electrons in the rows and columns of the CCD array are "read out" by a combination of parallel and serial transfers of charge to a readout amplifier and analog-to-digital (AD) converter. The C4880 uses two readout amplifiers to increase readout speed. "Readout noise" depends on rate; the slower the better, and the C4880 uses a 500-KHz rate to readout pixel values in its precision slow-scan mode. The C4880 also has a fast-scan mode (7 frames/second), which is much (about $5\times$) noisier but is useful for imaging brighter light sources and for focusing.

The C4880 is not a conventional video-rate camera equipped with a Peltier cooler. Video-rate CCD chips readout at 30 frames/second, and the CCD chips are constructed differently from full-frame, slow-scan CCD chips like the TC-215 in the C4880 camera (CLMIB staff et al., 1995; Keller, 1995; Shaw, Yeh, Maddox, Salman, & Bloom, 1997).

We use the slow-scan mode of the C4880 for most of our applications, and several significant features of its operation are described in more depth next. Details on the construction and properties of CCD chip cameras, including the various ways of obtaining images from slow-scan CCDs, are available elsewhere (Aikens et al., 1989; Keller, 1995).

9.3.2 Quantum efficiency

Quantum efficiency measures the percentage of incident photons that yield measurable photoelectrons in a pixel well. Quantum efficiency depends on wavelengths, as shown in Figs. 9.5 and 9.6D. The TC-215 chip has a peak quantum efficiency of 55% at 650 nm, the emission wavelength for the X-rhodamine fluorescence for our labeled microtubules in living cells. At 510 nm, the emission wavelengths for fluorescein and GFP, the quantum efficiency is about 35%. In general, CCD chips are more quantum efficient toward red and infrared wavelengths and significantly less toward the blue and violet wavelengths (Fig. 9.6D). Our chip has been coated with a fluorophore, which enhances the sensitivity in the blue-to-ultraviolet region of the spectrum (Fig. 9.6D).

The quantum efficiency of the TC-215 CCD is 1.5 to 2 times better than most slow-scan, full-frame readout CCDs in the visible wavelengths and much better than conventional interline video-rate CCD cameras (Fig. 9.6D). In full-frame readout CCD arrays such as the T1215, the potential wells are illuminated through the metal electrode array, which reduces the quantum efficiency. Back-thinned, rear-illuminated CCD chips are much harder to manufacture, but they have become available for almost reasonable prices. These chips can have quantum efficiencies as high as 80% (Fig. 9.6D).

Video-rate CCD cameras that allow "on-chip integration" are very economical ($800–$2000) and useful for bright fluorescence applications like immunofluorescence, as reviewed by Shaw et al., 1997. Compared to the full-frame readout chips, the quantum efficiency of conventional interline transfer chips is poor (15% peak) in part because half of the chip is masked (Fig. 9.6D). Sony has developed more sensitive chips by fabricating microlenses over each pixel element that collect light hitting the masked regions and direct it into a pixel element. This technique was developed for the "hyperhad" or HAD (hole accumulation diode) video-rate CCD chips by Sony. The quantum efficiency is still only 30% for most of these chips, and the readout noise is much higher than slow-scan, cooled CCD chips. A new Sony HAD chip exhibits 55% quantum efficiency near 510 nm (HAD ICX-061 in Fig. 9.6D), the peak emission wavelength for GFP fluorescence imaging. For longer-wavelength probes, these chips are much less sensitive than the conventional full-frame transfer chips. Because it is an interline chip, the Sony supports video

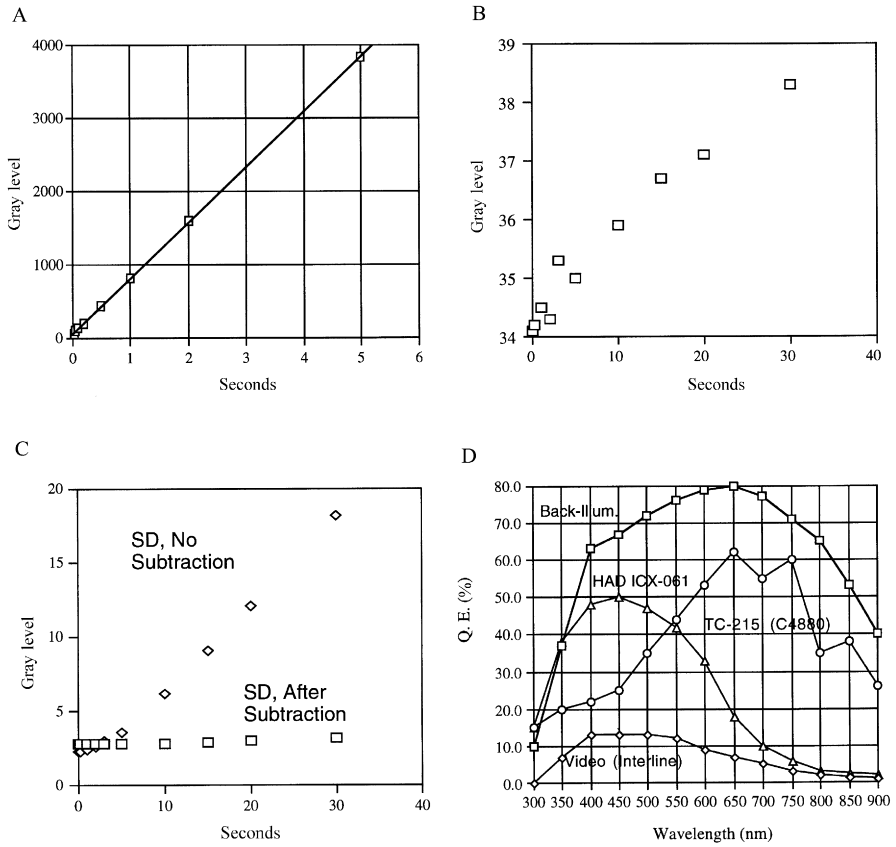

FIGURE 9.6

Performance of the C4880 cooled camera with TC-215 CCD. (A) Measured linearity where 1 gray-level count equals 5 electrons read from the CCD. Light intensity was held constant, and integration time (sec) varied. (B) Measured average values of "dark" gray-level verses integration time (seconds) when the camera shutter is closed. The offset in converting electrons to gray-level is the intercept at zero time. (C) Measured values for camera noise obtained from the standard deviations (SDs) of the dark signal versus integration time (open diamonds) and the SD after pairs of images taken for the same time were subtracted from each other to remove the "hot pixel" contributions (open squares). (D) Comparison of the quantum efficiency of the TC-215 CCD to other types of detectors. Data taken from manufacturer's specifications.

or near-video readout rates and does not need a shutter. The pixel detectors are about 9 μm in size with a well capacity of 15,000 electrons. The readout and thermal noise are remarkably low and comparable to the high-quality slow-scan full-frame transfer devices. Hence, the gap between slow-scan "scientific-grade" cameras and more commercial-grade videorate cameras continues to narrow.

9.3.3 Readout

The C4880 has two readout modes: slow scan and fast scan. In either mode, a shutter is used to control light exposure to the CCD chip. We mainly use the slow-scan mode because it has much better signal-to-noise and higher dynamic range (4096 versus 1024 gray levels). Potentially, the fast-scan mode is useful for focusing, as it can run as fast as 10 frames/second. In practice, however, we have found it easier to focus using the dark-adapted eye as described earlier. The following describes the operation of the camera in the slow-scan mode.

9.3.3.1 AD conversion

The number of accumulated electrons generates a voltage that is scaled and converted into a digital signal. The analog-to-digital converter is 12 bits or 4096 gray levels, and the pixel value is transferred and stored in the computer as a 16-bit or 2-byte (1 byte = 8 bits) value. There are three gain factors (GFs) selectable with this camera. One gray level equals 25, 5, and 1 accumulated electrons at low, high, and super-high values of GF, respectively. We use the high gain setting normally because $5 \times 4096 = 20{,}480$, about a third of the full-well capacity for the TI-215 detector.

9.3.3.2 Transfer time

It takes about 4.5 seconds after the chip is exposed to transfer a 1024×1024-pixel image into the computer display. About 4 seconds is the time of the slow-scan readout from the chip at a rate of 500,000 bytes/sec. The other 0.5 seconds is the time required to move the image from the frame buffer in the Imaging Technology AFG card in the computer to the computer's own RAM memory. This later delay can now be greatly eliminated using PCI bus adapter cards. Transfer time can be substantially shortened by reducing image size, now the time needed depends on the number of pixels in the image.

9.3.3.3 Size

In most of our applications, we do not need the full-chip image. The time taken for image acquisition depends on the size of the image transferred, and this time can be substantially reduced by transferring a smaller region of the chip. For example, we often use a 300×300-pixel image size in our mitosis studies. The total number of pixels for these images is about 1/10th the number for the full chip, and the rate of transfer is proportionately faster.

The other big advantage of smaller-sized images is that they take less memory in RAM or disk recording. For example, a 300×300-pixel image requires 1/10th the storage capacity as the full-chip image. We often record 500 images or more in time lapse. A 300×300-pixel image requires 90,000 pixels $\times$ 2 bytes = 0.18 Mbytes of memory or disk space. A full-chip image requires 1,048,576 pixels $\times$ 2 bytes = 2.1 Mbytes of storage, 23 times more than the 300×300-pixel image.

9.3.3.4 Binning

During readout, the C4880 camera controller can combine adjacent pixel values into one value. This "binning" increases the sensitivity of the camera and reduces the image size in proportion to the number of binned pixels. Binning of 2×2, 4×4, or 8×8 produces increases in sensitivity and reduces image size by factors of 4-, 16-, or 64-fold, respectively. The enhanced sensitivity is shown in Fig. 9.7 for a field of immunofluorescently stained microtubules, where the excitation light intensity is

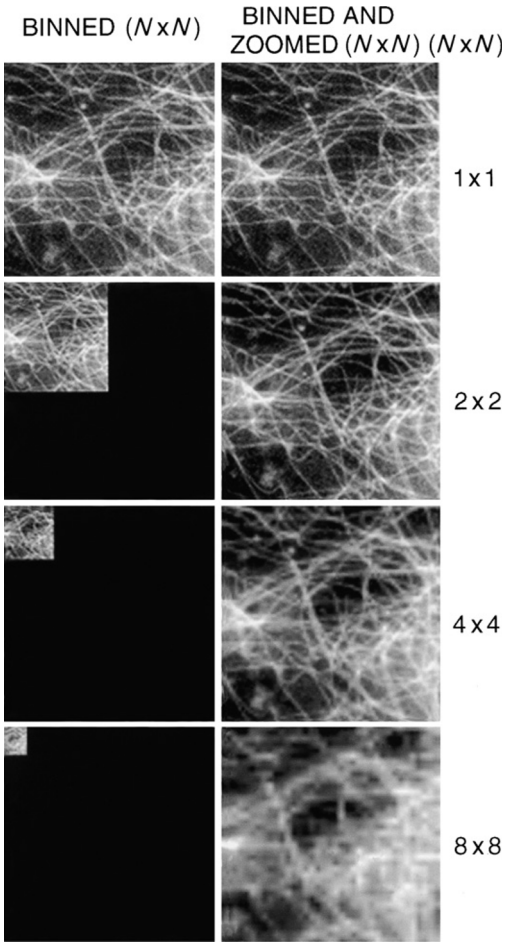

FIGURE 9.7

Binning increases sensitivity, reduces image size, and reduces resolution. Images of a field of microtubules in a cell fixed and stained with fluorescent antibodies to tubulin. Images were taken with $N \times N$ binning at constant integration time and excitation light intensity. Image brightness increased as N^2. The final images were scaled to the same maximum brightness in the print.

reduced by insertion of neutral density filters as binning is increased. Note that binning also reduces resolution in proportion to the binned pixels in each direction. We often use 2 × 2 or 4 × 4 binning in our fluorescence applications where resolution is limited not by optical limitations, but by too few photons. The 4- or 16-fold gain in sensitivity by binning can make substantial improvements in image quality.

9.3.4 Linearity, noise sources, and the advantages of cooling

CCD detectors are ideal for quantitative two-dimensional intensity measurements and position measurements because the signal (S) for each pixel is proportional to light intensity over a wide range and there is no geometrical distortion. Fig. 9.6A shows the output linearity of the C4880 camera measured for a region of a fluorescent specimen in which the light intensity was held constant, but the exposure time was varied from 20 ms to 5 seconds.

Essentially, the CCD detector is a geometrical array of pixel detectors, where the pixel gray-level value (0–4096 gray levels for 12-bit digitization) acquired by the computer, $P_{i,j}$, for a single readout of the chip is:

$$P_{i,j} = (I_{i,j}Q_{i,j}t + N_{T_{i,j}}t + N_{R_{i,j}})\ \mathrm{GF}, \tag{9.3}$$

where $I_{i,j}$ is the light intensity, $Q_{i,j}$ is the quantum efficiency, $N_{T_{i,j}}$ is the thermally generated electrons/second, t is the exposure time, $N_{R_{i,j}}$ is the electron equivalent error in the readout process, and GF is the gain factor in the conversion of accumulated electrons to gray level.

Thermal noise N_T is usually specified as the number of electrons per second at a given temperature. This number decreases by about 50% for each 8° of cooling (Fig. 9.8). So, for example, if a detector element accumulates 400 thermal electrons/second at 20 °C (about room temperature), there will be only 6 at −28 °C. Our C4880 camera has a specified average value of $N_T = .1$ electrons/pixel/per second at −40 °C (Fig. 9.6B). Some pixel elements on the chip are much worse than most, and these are termed "hot" pixels. For a chip cooled to −30 °C these hot pixels only become apparent for exposures longer than several seconds, as seen in Fig. 9.8. For uncooled chips, these hot pixels are not

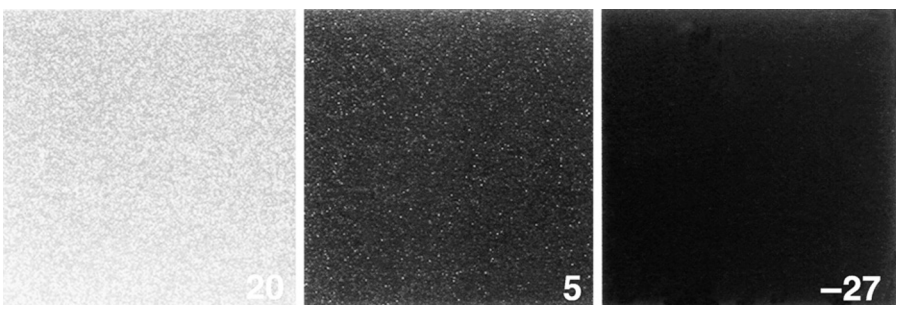

FIGURE 9.8

Dark images from the C4880 camera as a function of temperature of the CCD chip. Exposures were for 5 seconds, and temperature in degrees centigrade is indicated on each frame.

apparent at video rates (1/30-second exposures), but they can become very apparent even for exposures of .1 to 1 second (Shaw et al., 1997). The new HAD Sony chips, however, have remarkably low thermal noise and few hot pixels.

The other major source of noise is readout noise, N_R. Unlike the photon and thermal noise, it does not depend on integration time, but occurs once when the chip is readout to the computer. N_R depends on how fast and on the way readout is achieved (Aikens et al., 1989; Keller, 1995).

We measured the thermal and readout noises by measuring the standard deviations (SDs) of "dark" images obtained by capping the camera and recording for durations between 20 ms to 40 second when the camera was cooled to −30 °C (Fig. 9.6B). Both thermal and readout noise are governed by random number statistics, where SD is a measure of their noise contributions. For exposures less than 5 seconds, readout noise dominates (Fig. 9.6C). Readout noise is constant, independent of exposure time, at $N_R =$ 2.6 gray levels or 5 (electrons per gray level) × 2.6 = 11.3 electrons. Thermal noise increases with exposure time and begins to be more significant than readout noise for exposures longer than 5 seconds, mainly because of the "hot pixels."

9.3.5 Dark and background reference image subtraction

The average values of the contributions of thermal and readout noise can be subtracted from a specimen image by subtracting a "dark" reference image. The dark reference image is obtained by blocking light to the camera for the same exposure time t used for the specimen image, and their difference is given from Eq. (9.3) by:

$$\begin{aligned} P_{i,j} &= \text{specimen image} - \text{dark reference image} \\ &= \left[I_{i,j}\, Q_{i,j}\, t + (N_T \pm \Delta N_T)_{i,j} + (N_R \pm \Delta N_R)_{i,j}\right] \text{GF} \\ &\quad - \left[N_T \pm \Delta N_T)_{i,j} + (N_R \pm \Delta N_R)_{i,j}\right] \text{GF} \\ P_{i,j} &= (I_{i,j}\, Q_{i,j}\, t + N_{T_{i,j}} \pm \Delta N_{R_{i,j}})\, \text{GF}, \end{aligned} \tag{9.4}$$

where $\Delta N_{T_{i,j}}$ and $\Delta N_{R_{i,j}}$ represent the random noise in the thermal and readout contributions. For bright specimens, these noise values are small and insignificant. For low-intensity specimens near the "noise floor" of the camera, these values are significant and generate poor image quality and large uncertainty in image measurements. Dark image subtraction reduces substantially the dark image noise from hot pixels (Fig. 9.6C), and this subtraction is essential for good image quality for weakly fluorescent specimens.

There are other sources of noise from the microscope, including out-of-focus fluorescence, reflections from the coverslip and optical components, and fluorescence from the optical components. The average values of these contributions to the specimen image can be subtracted out by obtaining a "reference" image from a region of the slide lacking the specimen or by focusing up or down so the specimen is out of focus.

9.3.6 Shading

Quantum efficiency is remarkably constant between different pixel elements for the highest-quality CCD chips and does not have to be corrected except in the most critical applications. Variation in sensitivity between different pixels is termed

"shading." This shading can be corrected for any signal by multiplying each pixel value with a scaling factor ($SF_{i,j}$). $SF_{i,j}$ is obtained by acquiring a bright image (B) with constant light intensity (I) across the detector and acquiring a dark image (D) with the shutter closed on the camera. In the computer, the average values for all the pixels in the bright image (B_{avg}) and the dark image (D_{avg}) are calculated, and the scale factor for each pixel ($SF_{i,j}$) is obtained from the ratio

$$SF_{i,j} = (B_{avg} - D_{avg})/(B_{i,j} - D_{i,j}). \tag{9.5}$$

9.3.7 Signal-to-noise

The ratio of signal (S) to noise (N) is a measure of image quality, and the reciprocal (N/S) represents the uncertainly in making an image measurement. After background subtraction and shading correction, the ability to see image detail and the uncertainty of intensity measurement depends on random sources of noise in the integrated signal ($I_{i,j}\, Q_{i,j}\, t$) as well as from thermal noise (ΔN_T) and readout noise (ΔN_R). Noise in the specimen signal (called photon noise or shot noise) depends on random-number statistics just as do the other sources of noise in the camera. For S photon-produced electrons, the SD (ΔS) is a measure of the noise of S, just as the SDs are a measure of thermal and readout noise. For example, if the other sources of noise are neglected and the average number of signal electrons recorded for one pixel is 100, then the ΔS is the square root of 100, or 10. $S/N = 10$, and the uncertainty in measurement = 10%. There is a 63% chance of measuring $S \pm$ square root of S electrons in a subsequent measurement made the same way.

In general, the more photoelectrons accumulated by photon absorption by silicon in the CCD chip the better the image quality. This is shown in Fig. 9.9. An image of a fluorescent specimen was acquired for 20-, 200-, and 2000-ms exposure time at constant illumination intensity then scaled to the same peak brightness for printing. At 20-ms exposure, the image is very "grainy," and the fluorescent actin filament

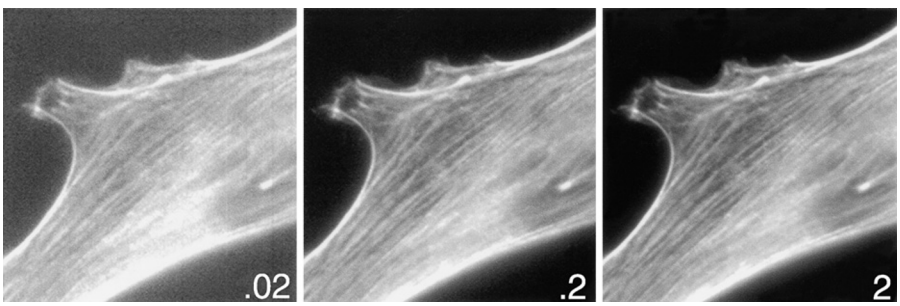

FIGURE 9.9

Images of actin filaments in a cell that was fixed and stained with rhodamine-labeled phaloidin, taken at the same illumination light intensity but different integration times, as indicated in seconds on each frame. Too few photons makes a noisy image.

bundles in the cell are indistinct and poorly resolved because of too few photons. The image is much better at 200 ms and beautiful at 2 seconds. Quantitatively, signal-to-noise in the camera is given by:

$$S/N = S/(\Delta S^2 + \Delta N_T^2 + \Delta N_R^2)^5. \quad (9.6)$$

Note from Fig. 9.6B that at short exposure times (less than 2 seconds), thermal noise is insignificant in the C4880 camera and image quality is determined by photon statistics and readout noise.

9.4 DIGITAL IMAGING SYSTEM

9.4.1 Microscope automation and camera control

9.4.1.1 Computer control of the microscope

Essential to using the multimode microscope system is a flexible software package that allows control of the microscope components. Commercial software packages operating on Windows, Macintosh, and UNIX platforms are now available. We have selected the MetaMorph software package from Universal Imaging Corporation running under Windows95 for the majority of our image acquisition and processing. Figure 9.2 details the hardware components that run the software to control the illumination, focus, and camera.

The software contains instructions (drivers) for controlling auxiliary devices attached to the microscope. As an example, a driver within MetaMorph controls the dual eight-position filter wheels containing O.D. and fluorescence excitation filters. An excitation wavelength and light intensity can be selected from a pull-down menu for a dim rhodamine-labeled specimen and a second set of filters chosen for brighter DAPI staining. The two sets of selections are saved as preset filter combinations and are automatically selected during time-lapse experiments when rhodamine and DAPI images are taken sequentially. In addition to filter wheels, the MetaMorph software contains drivers for controlling the focusing motor, epi- and transillumination shutters, and output to devices such as an optical memory disk recorder.

The MetaMorph camera driver allows us to take advantage of several properties specific to the Hamamatsu C4880 CCD camera. The time of exposure, area of CCD chip readout, binning of pixels, and camera gain and offset can all be saved as a preset file. Having these variables saved affords us the ability to obtain images of a specimen brightly illuminated for DIC or dimly illuminated for fluorescence without manually reconfiguring the camera.

Critical to our use of the software is a scripting language (or journaling) for customized control of the parameters, sequence, and timing of image acquisition. Journals are a sequence of instructions to the MetaMorph imaging software generated by recording a sequence of selections from the program menus. For example, to take phase contrast, DAPI, and rhodamine images of the same spindle in time lapse, journals are recorded that control image acquisition for each optical mode. For phase contrast, the transmitted shutter is opened and the CCD camera instructed to open its shutter for 600 ms, close the camera shutter, and then transfer the 12-bit image

to computer memory. Similarly, journals are written to control image acquisition for DAPI and rhodamine epifluorescence that specify the exposure time of the camera, the neutral density filter, the excitation filter, and the opening and closing of the epifluorescence light shutter. A time-lapse journal then calls the phase contrast, DAPI, and rhodamine journals in sequence at a specified time interval.

9.4.1.2 Image processing and analysis

In addition to automated control of the microscope, the software contains routines for manipulating the size, scale, and contrast of images and allows handling of multiimage stacks. Image stacks are created in circumstances such as multimode time-lapse experiments where all DAPI images in a series remain in the DAPI stack and all rhodamine or DIC images remain in their respective stack. The ability to perform contrast enhancements or arithmetic (such as background image subtraction) on all images in a stack rather than performing the function on each image individually saves tremendous amounts of labor. Our camera and digital-to-analog converter generate images with greater than 4000 gray levels (12 bits). The MetaMorph software has tools for linear and nonlinear modification of image contrast as well as scaling from 12 bits to 10- or 8-bit images. The contrast enhancement allows presentation of very bright specimen information in the same image as very dim information, as is often the case when microtubules in a spindle are shown next to astral microtubules (Fig. 9.3E).

The software has excellent routines for creating 24-bit RGB image stacks and for overlaying fluorescent colors onto grayscale DIC or phase-contrast images. For example, an RGB stack can be easily obtained from three stacks taken in a time-lapse series where one stack is the rhodamine image, another a fluorescein or GFP image, and the third a DAPI or DIC or phase-contrast image. Separate gain and contrast adjustment controls are available for each channel of the RGB image. The RGB image stack can be treated like any other image stack and displayed by a movie player.

Many of our experiments require quantitative analysis of images for relative fluorescence intensity or for motion. Analysis is helped tremendously by the use of calibration files. The MetaMorph software package contains routines for saving distance measurements, made from images of a stage micrometer, and intensity measurements from florescence standards. These measurements can be called on to provide calibrated values instantly. The time and date of image acquisition are contained in the header of all MetaMorph image files, allowing accurate rates to be calculated from distance measurements of time-lapsed images. The ability to couple image processing with analysis greatly increases the quantity and variety of measurements available. The journaling language described above for automating image acquisition can also be applied to image-processing routines to automatically link repetitive processes.

9.4.2 Other useful software and devices

We have found several other software packages useful for image presentation and production of movies. These include Adobe Photoshop for making complicated montages of images generated in MetaMorph and saved as TIFF-formatted files

and Adobe Premiere for making digital movies in .mov or .avi file formats. For making slides and labeling prints, images are copied into Microsoft PowerPoint, where lettering and annotation of images is convenient. Black-and-white draft prints of images are obtained with a Hewlett Packard Laser Jet 4M printer, and photographic-quality prints are generated with a Tektronics Phaser SDXII Dye Sublimation printer. Other ways of image processing and presentation are described by Shaw et al., 1997 in a paper concerning a low-cost method of digital photography using NIH-Image software and a Macintosh computer.

9.5 EXAMPLE APPLICATIONS

9.5.1 DE-DIC

Our DE-DIC images are recorded typically with 600-ms on-chip integration. The standard test specimen for high resolution in the light microscope is the frustrule pore lattice of the diatom *Amphipleura*. These pores in the silica shell are aligned with about 0.19-μm separation along rows and 0.25-μm separation between rows. As seen in Fig. 9.3C, the rows of pores are clearly resolved by our DE-DIC system, and the individual pores are almost resolvable with green light illumination. A major advantage of this system for living cells is the low illumination intensity and the computer control of shutter, which illuminates the specimen only during camera exposure. As a result, cells are viable for long periods of time-lapse recording.

Using this system we have obtained high-resolution real-time images of yeast nuclear motion in the cell division cycle. In one series of experiments (Sawin & Mitchison, 1991), GFP histones were expressed to visualize the nucleus (Fig. 9.3A) and cellular structural detail recorded by DIC (Fig. 9.3B). The native GFP fluorescence excited at 490 nm was photoactivated using a several-second pulse of 360-nm light, then images were recorded using the fluorescein channel and excitation filter. In other studies (Zhai et al., 1995; Inoué & Salmon, 1995), we discovered that the cooled CCD camera produces high-contrast and high-resolution DE-DIC images, such that the positions of the spindle pole bodies and the anaphase elongation of the mitotic spindle within the 2-μm diameter preanaphase nucleus can be clearly seen (Fig. 9.10). To achieve the images shown in Fig. 9.10, it is necessary to reduce the refractive index mismatch between the cell wall and the media. This is achieved by embedding the cells in 25% gelatin-containing LPD yeast growth medium (Inoué & Salmon, 1995). Slides are prepared with a 10-μm-thin film of the 25% gelatin, a 5-μL drop of cell suspension is added, a number 1.5 22 $\times$ 22-mm coverslip is pressed down on the preparation, and the preparations are then sealed with VALAP (1:1:1 vasoline, lanolin, and paraffin).

9.5.2 Multimode imaging of anaphase *in vitro*

The multimode microscope system has also been particularly useful for recording anaphase spindle dynamics and chromosome segregation for the first time *in vitro* (Olson et al., 1995; Sawin & Mitchison, 1991) by reconstituting mitosis in a test tube

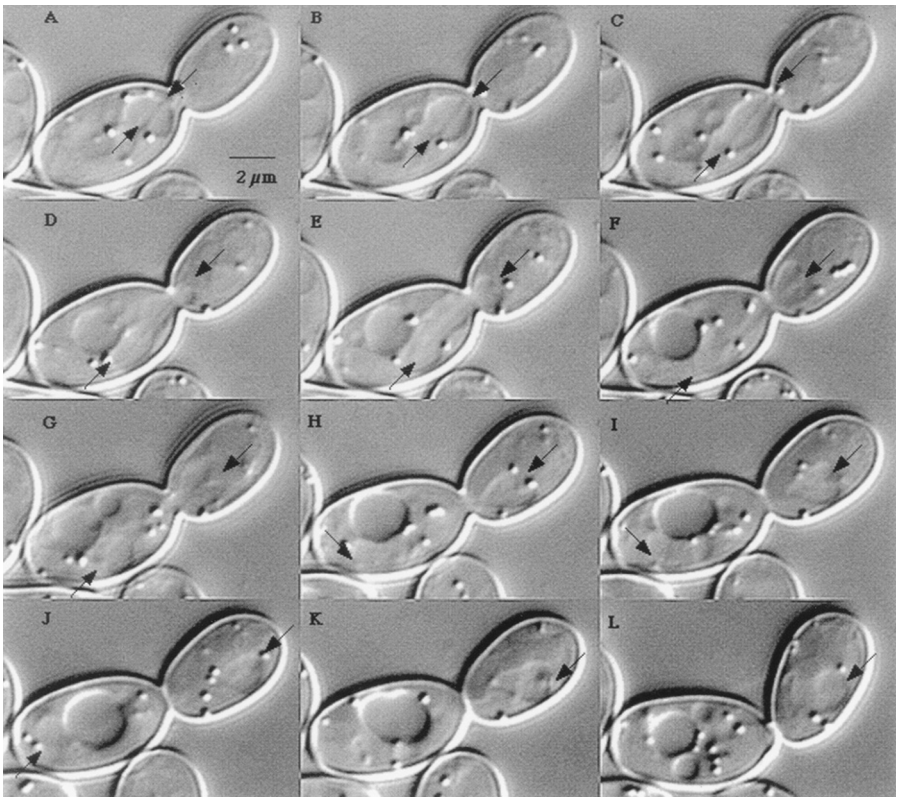

FIGURE 9.10

DE-DIC images of a dividing yeast *Saccharomyces cerevisiae*. The spindle extends through the center of the nucleus and is formed from an overlapping bundle of microtubules extending from opposite spindle pole bodies (arrows). (A) Preanaphase. (B–K) Anaphase. (L) Cytokines. The preanaphase nucleuse in A is about 2.5 μm in diameter. Modified from Yeh et al. (1995).

from sperm nuclei and cytoplasmic extracts prepared from *Xenopus* eggs (Holloway, Glotzer, King, & Murray, 1993; Shaw, Yeh, Bloom, & Salman, 1997) (Fig. 9.3D–F). Here phase DAPI fluorescence image stacks record chromosome movements while X-rhodamine-labeled tubulin fluorescence shows spindle microtubule assembly dynamics. The spindles in cytoplasmic extracts are held in a chamber between a slide and a coverslip separated by 12-μm latex beads and sealed with halocarbon oil and VALAP. For time lapse, sequential 600-ms exposures of rhodamine and DAPI or phase images are recorded to their respective image stacks at either 30- or 60-second intervals. The *Xenopus* egg cytoplasm is very optically dense, making the rhodamine and DAPI fluorescent images the most useful for recording spindle and chromosome dynamics. Three-dimensional images derived from a single time-point stack of optical

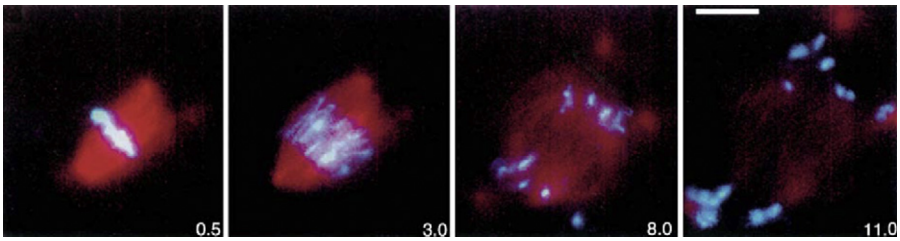

FIGURE 9.11

Anaphase recorded for mitotic spindles assembled in the test tube from *Xenopus* egg extracts as described (Murray et al., 1996). At 30-second intervals, an X-rhodamine-tubulin image and a DA PI-stained chromosome image were recorded. Red and blue image stacks were overlaid with MetaMorph and printed in Adobe Photoshop. Time in minutes is indicated on each frame taken from the time-lapse sequence.

sections have also proved very useful for determining the behavior of all of the chromosomes and their kinetochore regions within the spindle (Olson et al., 1995; Sawin & Mitchison, 1991) (Fig. 9.3G). Figure 9.11 shows frames from an RGB digital movie of *in vitro* anaphase in which the DAPI blue chromosome images are overlaid on the rhodamine tubulin red image of the spindle microtubules (Olson et al., 1995).

9.5.3 Fluorescence photoactivation

Another application of our multimode system has been in the analysis of the dynamics of kinetochore microtubules within mitotic tissue cells using fluorescence photoactivation methods (Murray et al., 1996; Yeh et al., 1995). Figure 9.12 shows a metaphase newt lung epithelial cell that has been microinjected with X-rhodamine-labeled tubulin to label all the spindle microtubules and C2CF caged-fluorescein-labeled tubulin for photoactivation of tubulins within the spindle fiber microtubules as developed by Mitchison & Salmon, 1993. For photoactivation, the field diaphragm in the epiilluminator is replaced with a 25-μm slit cemented to a Nikon pinhole slider (Fig. 9.2). The spindle is marked with 350-nm illumination for 2 seconds using the Chroma DAPI exciter filter within the excitation filter wheel and no neutral density filters. Image stacks for rhodamine, fluorescein, and phase are acquired at 30-second intervals. The exposures are 600 ms, using two OD-neutral filters in front of the 100-watt Hg lamp and using a 2 $\times$ 2-pixel binning of pixels in the Hamamatsu Cooled CCD detector. The 2 $\times$ 2-pixel binning reduces the 300 $\times$ 300 central image capture area to 150 $\times$ 150 pixels and increases image sensitivity fourfold. This has proven to be important in allowing lower excitation light intensity, which reduces photobleaching and has not significantly reduced useful resolution in these low-light-level images. The images in Fig. 9.12 show that photoactivated marks on the kinetochore fibers flux poleward, demonstrating that at metaphase, the kinetochore microtubules that connect the chromosomes to the poles have a net addition of tubulin subunits at their kinetochore ends and a net disassembly of

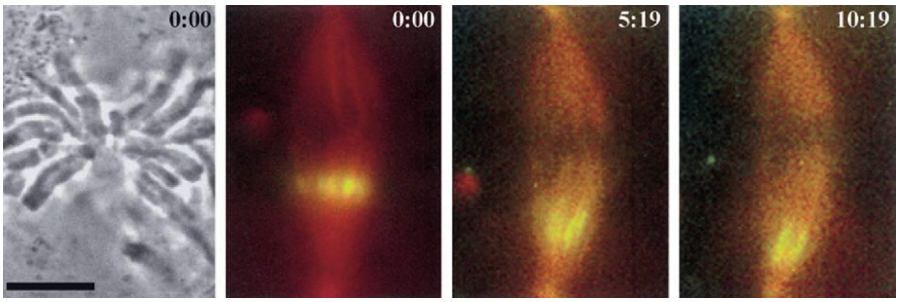

FIGURE 9.12

Multimode imaging and local fluorescence photoactivation to see the dynamics of kinetochore fiber microtubules in metaphase newt lung epithelial cells. Cells were injected in early mitosis with X-rhodamine-labeled tubulin and C2CF caged-fluorescein-labeled tubulin. At each time point, a phase image showed chromosome position, an X-rhodamine image showed spindle microtubule assembly, and the C2CF fluorescein image recorded the poleward flux and turnover of photoactivated fluorescent tubulin within the kinetochore fiber microtubules. In the color frames, the green photoactivated C2CF fluorescein fluorescence is overlaid on the red image of the X-rhodamine tubulin in the spindle fiber microtubules. Time is given in minutes after photoactivation. See Waters et al. (1996) for details. Scale = 10 μm.

subunits at their polar ends. In anaphase, this poleward flux of kinetochore microtubules persists as chromosomes move poleward (Murray et al., 1996; Yeh et al., 1995; Schotten, 1993). Photoactivation has also been used to show that poleward flux of spindle microtubules occurs in other cell types (Shamu & Murray, 1992). This has important implications for how kinetochore microtubule dynamics are coupled to force generation-for-chromosome movement and proper alignment of the chromosomes for accurate segregation during mitosis (Murray et al., 1996; Yeh et al., 1995).

9.5.4 Microtubule and ER dynamics in migrating tissue cells

The sensitivity of the imaging system has made it possible to track with great clarity the assembly dynamics of individual microtubules and ER in migrating epithelial cells (Waters et al., 1996). Microtubules are fluorescently labeled red by microinjecting X-rhodamine-labeled tubulin into cells. Endoplasmic reticulum is fluorescently labeled green using the membrane-intercalating dye $DiOC_6$ (Yang, Yeh, Salmon, & Bloom, 1997), and the leading edge lamellopodia and the lamella of the cell are recorded by DIC. Sets of image stacks are recorded every 7 seconds. Figure 9.13A–C show a pair of images, one from the rhodamine channel showing the microtubules and the other by DIC showing the leading edge of the lamella. Figure 9.13D–F show a pair of images, one from the rhodamine channel and the other from the $DiOC_6$ channel. One significant advance in the prevention of photobleaching in a sealed

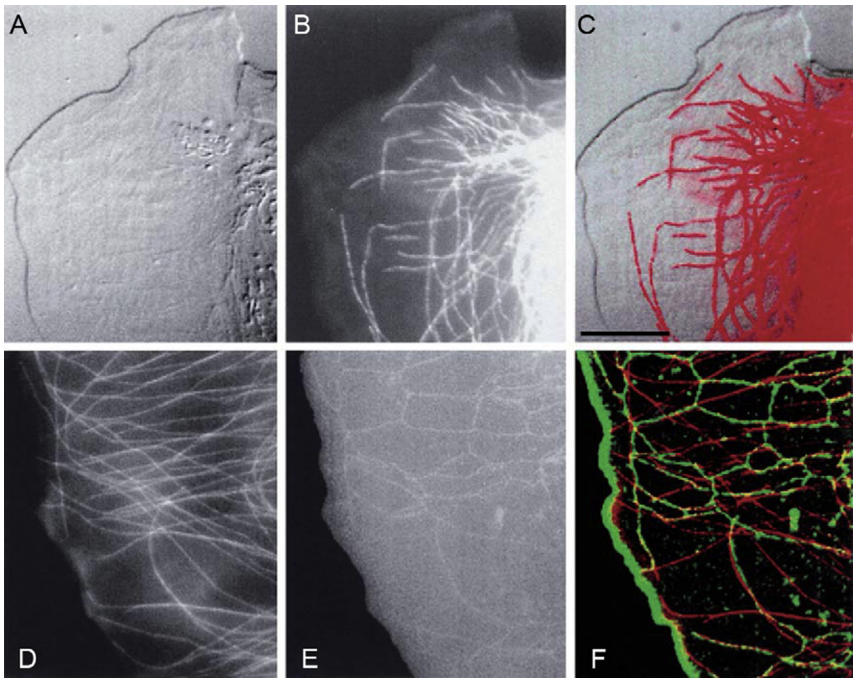

FIGURE 9.13

Microtubules in the lamella of a live migrating newt lung epithelial cell. Microtubules are fluorescently labeled by microinjection of X-rhodamine-labeled tubulin into the cytoplasm and ER-labeled with $DiOC_6$ (A) DIC image of leading edge of lamella. (B) X-rhodamine microtubule image. (C) RGB color overlay of A and B. (D) X-rhodamine tubulin image of another cell. (E) $DiOC_6$ image of the ER. (F) RGB color overlay of E and F. See text for details.

slide–coverslip preparation is the oxygen-scavenging enzyme system Oxyrase (Yang et al., 1997), used in these experiments.

9.5.5 GFP-dynein-labeled microtubules in yeast

Shotten, 1995, imaged the dynamics and organization of the cytoplasmic microtubules in live budding yeast (Fig. 9.14). GFP dynein expressed in yeast binds all along the lengths of the cytoplasmic but not the nuclear microtubules. The fluorescence is barely detectable with the dark-adapted eye with no attenuation of the Hg illumination to the specimen. Images with distinct astral microtubules are recorded using exposures of 3 seconds. 1 OD illumination attenuation, and the field diaphragm closed down around the specimen to reduce the out-of-focus fluorescence from the gelatin layer that holds the yeast against the coverslip surface. We found that a single optical

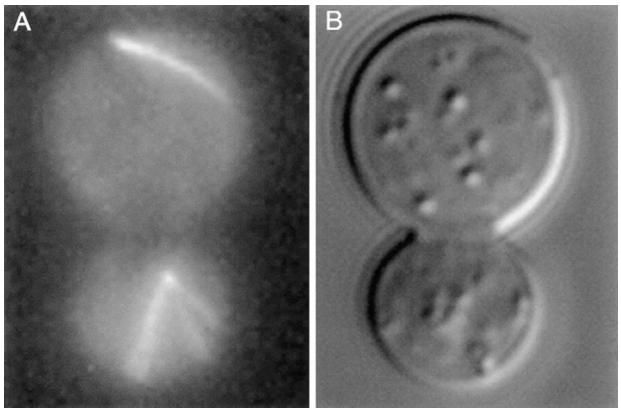

FIGURE 9.14

(A) Fluorescent image of GFP-dynein bound to astral microtubules and (B) the corresponding DIC image of an anaphase yeast *Saccharomyces cerevisiae*. The elongated nucleus is mostly out of focus in the DIC image. See text for details.

section was not sufficient to see the organization of astral microtubules in these small cells, which are about 5 μm in diameter. As a result, we developed an image acquisition procedure where for each time-lapse point (1-minute intervals), a series of five fluorescent optical sections is taken through the yeast at 1-μm intervals along the *z*-axis (Spencer, 1982). In the position of the middle section, a DIC image is taken by inserting the analyzer before the camera with the emission filter controller described earlier. After the completion of the time lapse over the yeast cell cycle of about 90 minutes, the fluorescent image stack is processed so that at each time interval, the fluorescent microtubule images in each five-plane stack are projected onto one plane. This projected image can then be displayed side by side or overlaid with the corresponding DIC image (Fig. 9.14). Movies of these images show the organization and dynamics of astral microtubules relative to the cell nucleus and other structural features of the cell visible by DIC.

9.5.6 Immunofluorescent specimens

We have found that the cooled CCD image acquisition system produces images of immunofluorescent-stained specimens with great clarity. Often our specimens do not have high levels of out-of-focus fluorescence, and the advantages of confocal imaging are not required. Figure 9.15 shows an example where mammalian PtK1 tissue cells are stained with antibodies for a protein implicated in the control of the anaphase onset during mitosis. MAD2 (Chen, Waters, Salmon, & Murray, 1996). The hypothesis is that when bound to kinetochores. MAD2 signals the cell to "stop" the cell cycle. When kinetochores become properly attached to microtubules emanating from opposite poles, MAD2 antibody staining of kinetochores disappears (all the "red stop lights" are off) and the cell enters anaphase.

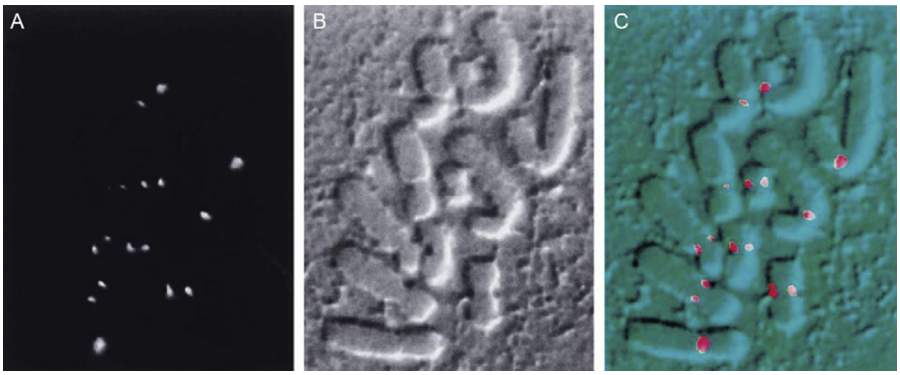

FIGURE 9.15

The mitotic arrest protein MAD2 localizes to kinetochores on chromosomes in mitotic PtK1 cells when they are unattached from spindle microtubules. The cell was treated with nocodazole to induce spindle microtubule disassembly and then lysed and fixed for immunofluorescence staining with antibodies to the MAD2 protein (Chen et al., 1996). (A) A single optical fluorescence section. (B) The corresponding DIC image. (C) The fluorescent MAD2 image and the DIC image combined in an RGB image to show the localization of MAD2 on either side of the centomeric constriction of the chromosomes where the sister kinetochore are located. Some kinetochores are above or below the plane of focus and not visible.

References

Aikens, R. S., Agard, D. A., & Sedat, J. W. (1989). *Methods in cell biology*. (Vol. 29). San Diego: Academic Press, pp. 292–313.

Carrington, W. A., Lynch, R. M., Moore, E. D. W., Isenberg, G., Forarty, K. E., & Fay, E. S. (1995). *Science*, *268*, 1483–1487.

Chen, R. H., Waters, J. C., Salmon, E. D., & Murray, A. W. (1996). *Science*, *274*, 242–246.

CLMIB staff (1995). *American Laboratory*, 25–40.

Cubitt, A. B., Heim, R., Adams, S. R., Boyd, A. E., Gross, L. A., & Tsien, R. Y. (1995). *Trends in Biochemical Sciences*, *20*, 448–455.

Farkas, D., Baxter, G., DeBiasio, R., Gough, A., Nederlof, M., Pane, D., et al. (1993). *Annual Reviews of Physics*, *55*, 785.

Heim, R., & Tsien, R. (1996). *Current Biology*, *6*, 178–182.

Hiroka, Y., Sedlow, J. R., Paddy, M. R., Agard, D., & Sedat, J. W. (1991). *Seminars in Cell Biology*, *2*, 153–165.

Holloway, S. L., Glotzer, M., King, R. W., & Murray, A. W. (1993). *Cell*, *73*, 1393.

Inoué, S. (1986). *Video microscopy*. New York: Plenum.

Inoué, S. (1989). *Methods in cell biology*. (Vol. 30). San Diego: Academic Press, pp. 112.

Inoué, S., & Oldenbourg, R. (1993). Optical society of America. In *Handbook of optics*. (2nd ed.). New York: McGraw-Hill.

Keller, H. E. (1995). J. B. Pawley (Ed.), *Handbook of biological confocal microscopy* (pp. 111–126). New York: Plenum.

Mitchison, T. J. (1989). *The Journal of Cell Biology*, *109*, 637.

Mitchison, T. J., & Salmon, E. D. (1993). *The Journal of Cell Biology*, *119*, 569.
Murray, A. W., Desai, A., & Salmon, E. D. (1996). *Proceedings of the National Academy of Sciences of the United States of America*, *93*, 12327–12332.
Olson, K., McIntosh, J. R., & Olmsted, J. B. (1995). *The Journal of Cell Biology*, *130*, 639.
Pawley, J. (Ed.), (2006). *Handbook of biological confocal microscopy*. (2nd ed.). New York: Plenum.
Salmon, E. D., Inoué, T., Desai, A., & Murray, A. W. (1994). *The Biological Bulletin*, *187*, 231–232.
Sawin, K. E., & Mitchison, T. J. (1991). *The Journal of Cell Biology*, *112*, 941.
Sawin, K. E., Theriot, J. A., & Mitchison, T. J. (1992). *Fluorescent probes for biological activity in living cells*. San Diego: Academic Press.
Shamu, C. E., & Murray, A. W. (1992). *The Journal of Cell Biology*, *117*, 921.
Shaw, S. L., Yeh, E., Bloom, K., & Salman, E. D. (1997). *Current Biology*, *7*, 701–704.
Shaw, S. L., Yeh, E., Maddox, P., Salman, E. D., & Bloom, K. (1997). *The Journal of Cell Biology*, *139*, 327–338.
Shotten, D. M. (1995). *Histochemistry and Cell Biology*, *104*, 97–137.
Spencer, M. (1982). *Fundamentals of light microscopy*. London: Cambridge University Press.
Taylor, D. L., Nederhof, M., Lanni, F., & Waggoner, A. S. (1992). *American Scientist*, *80*, 322–335.
Taylor, D. L., & Salmon, E. D. (1989). *Methods in cell biology*. (Vol. 29). San Diego: Academic Press, pp. 207–237.
Waterman-Storer, C. M., & Salmon, E. D. (1997). *The Journal of Cell Biology*, *139*, 417–434.
Waterman-Storer, C. M., Sanger, J. W., & Sanger, J. M. (1993). *Cell Motility and the Cytoskeleton*, *26*, 19.
Waters, J. C., Mitchison, T. J., Rieder, C. L., & Salmon, E. D. (1996). *Molecular Biology of the Cell*, *7*, 1547–1558.
Yang, S. S., Yeh, E., Salmon, E. D., & Bloom, K. (1997). *The Journal of Cell Biology*, *136*, 1–10.
Yeh, E., Skibbens, R. V., Cheng, J. W., Salmon, E. D., & Bloom, K. (1995). *The Journal of Cell Biology*, *130*, 687–700.
Zhai, Y., Kronebusch, P., & Borisy, G. (1995). *The Journal of Cell Biology*, *131*, 721.

Further Reading

Inoué, S., & Salmon, E. D. (1995). *Molecular Biology of the Cell*, *6*, 1619–1640.
Inoué, S., & Spring, K. (1997). *Video microscopy* (2nd ed.). New York: Plenum.
Schotten, D. (1993). *Electronic light microscopy*. New York: Wiley-Liss.
Shaw, S. L., Salmon, E. D., & Quatrano, R. S. (1995). *BioTechniques*, *19*, 946–955.

CHAPTER

Electronic Cameras for Low-Light Microscopy

10

Ivan Rasnik*, Todd French†, Ken Jacobson‡,§, and Keith Berland*

*Physics Department, Emory University, Atlanta, Georgia, USA

†Molecular Devices Corporation, Sunnyvale, California, USA

‡Department of Cell and Developmental Biology, University of North Carolina, Chapel Hill, North Carolina, USA

§Lineberger Comprehensive Cancer Center, University of North Carolina, Chapel Hill, North Carolina, USA

CHAPTER OUTLINE

Introduction **212**
Low-Light Imaging in Biology 212
The Importance of Proper Optical Imaging 213
Detection of Low Light 215
10.1 Parameters Characterizing Imaging Devices **216**
10.1.1 Sensitivity and Quantum Efficiency 216
10.1.1.1 Spectral Response 217
10.1.1.2 Units 217
10.1.1.3 Fill Factor (CCD Format) 218
10.1.2 Camera Noise and the Signal-to-Noise Ratio 218
10.1.2.1 Shot Noise 220
10.1.2.2 Readout Noise 220
10.1.2.3 Background and Noise 221
10.1.2.4 Example Calculation 221
10.1.3 Spatial Resolution 222
10.1.3.1 Example 224
10.1.4 Linearity and Uniformity 224
10.1.5 Time Response 225
10.1.6 Dynamic Range 225
10.1.7 Gain 226
10.1.8 Frame Rate and Speed 227
10.1.9 Resolution, Sensitivity, and Imaging Rate 227
10.2 Specific Imaging Detectors and Features **228**
10.2.1 Video CCD Cameras 228
10.2.2 Slow-Scan CCD Cameras 229

Methods in Cell Biology, Volume 114 **ISSN 0091-679X**
Copyright © 2007 Elsevier Inc. All rights reserved.
http://dx.doi.org/10.1016/B978-0-12-407761-4.00010-5

10.2.3 Fast-Scan CCDs 231
10.2.4 Intensified Cameras 231
10.2.4.1 Intensifier Formats 233
10.2.4.2 Cameras for Image Intensifiers 234
10.2.5 Internal Image Amplification Cameras 234
10.2.5.1 On-Chip Multiplication Gain (EMCCD) 234
10.2.5.2 Electron Bombardment Cameras 235
10.2.6 Color Video Cameras 236
10.2.7 Digital Still Cameras 236
10.2.8 SIT Cameras 237
10.2.9 CMOS Imagers 237
10.2.10 Image Acquisition 238
Conclusions 239
References 239

Abstract

This chapter introduces to electronic cameras, discusses the various parameters considered for evaluating their performance, and describes some of the key features of different camera formats. The chapter also presents the basic understanding of functioning of the electronic cameras and how these properties can be exploited to optimize image quality under low-light conditions. Although there are many types of cameras available for microscopy, the most reliable type is the charge-coupled device (CCD) camera, which remains preferred for high-performance systems. If time resolution and frame rate are of no concern, slow-scan CCDs certainly offer the best available performance, both in terms of the signal-to-noise ratio and their spatial resolution. Slow-scan cameras are thus the first choice for experiments using fixed specimens such as measurements using immune fluorescence and fluorescence *in situ* hybridization. However, if video rate imaging is required, one need not evaluate slow-scan CCD cameras. A very basic video CCD may suffice if samples are heavily labeled or are not perturbed by high intensity illumination. When video rate imaging is required for very dim specimens, the electron multiplying CCD camera is probably the most appropriate at this technological stage. Intensified CCDs provide a unique tool for applications in which high-speed gating is required. The variable integration time video cameras are very attractive options if one needs to acquire images at video rate acquisition, as well as with longer integration times for less bright samples. This flexibility can facilitate many diverse applications with highly varied light levels.

INTRODUCTION

Low-light imaging in biology

The demand for low-light-level cameras in biological microscopy is mainly for fluorescence imaging. Modern low-light-level cameras provide much better

technological solutions than even just a few years ago, and continuing improvements in sensitivity and ease of use are facilitating their integration into a wide variety of biological applications, ranging from imaging the distribution of labeled molecules in fixed specimens to measuring rapid changes in ion concentration in live cells or the motion of molecular motors and virus (Arndt-Jovin, Robert-Nicoud, Kaufman, & Jovin, 1985; Babcock, Chen, & Zhuang, 2004; Bastiaens & Squire, 1999; Brownlee, 2000; Shotton, 1995; Wang & Taylor, 1989; Yildiz et al., 2003). Sensitive cameras allow observation of cells labeled with a variety of fluorescent probes at illumination levels that cause insignificant perturbation of cellular function over extended periods, providing a means to study real-time changes in structure, function, and concentration (Taylor, Woo, & Giuliano, 2001). As the technology of digital camera evolves, new applications appear that take advantage of their better characteristics, for example, parallelized confocal microscopy in the last few years (Blom & Gosch, 2004). Detection with low-illumination levels can also help reduce photobleaching or "fading" of fluorescent probes to manageable levels. Moreover, low-light electronic cameras have replaced the traditional role of film cameras for microscopic imaging.

There are many different types of electronic cameras and a wide variety of requirements in biological imaging. Thus, it can be difficult to determine which cameras best fit a particular application. The aim of this chapter is to provide an introduction to electronic cameras, including a discussion of the parameters most important in evaluating their performance, and some of the key features of different camera formats. This chapter does not present a comprehensive list of all available devices, a difficult task given the rapid and continuous changes in camera technology. Rather, it is hoped that this chapter will provide the reader with a basic understanding of how electronic cameras function and how these properties can be exploited to optimize image quality under low-light conditions. The best sources for up-to-date product information and explanatory materials are the camera manufactures.[1]

The importance of proper optical imaging

Broadly speaking, most fluorescence imaging can be characterized as "low light," and highly sensitive cameras are invaluable for recording quality images. However, one should not overlook the microscope itself, as the actual image intensity that must be measured by the camera depends critically on the microscope and imaging optics. The goal in light-limited imaging will be to optimize the collection efficiency of the microscope; that is, to get as much light as possible from a luminescent specimen to the camera. Choosing appropriate optical components for each application, such as objectives, filters, and dichroic mirrors, is thus very important. This may require some extra work, but is easy to do and well worth the effort, as poor optical design

[1]Although there are more camera manufacturers than we can list here; there are at least a few with very good materials that explain the underlying technology such as Andor Technology (http://www.andor-tech.com), Apogee Instruments (www.ccd.com), Hamamatsu Photonics (www.hamamatsu.com), and Roper Scientific (www.roperscientific.com).

can result in significant light loss. Using a high-quality microscope together with the proper optical components should result in substantially higher light levels reaching the camera. More light translates into better images, even for the most sensitive cameras.

There are several important factors that determine the collection efficiency of a microscope. First, the fraction of fluorescence emission that can be collected by the objective lens is determined by its numerical aperture (NA). Higher-NA lenses collect more light. A second factor is the throughput (transmission) of the objective, which varies for different lens designs and is also dependent on lens materials and coatings (Keller, 1995). Manufacturers can be consulted regarding which lenses have higher throughput. Filters and dichroic mirrors also reduce the collection efficiency, although they are necessary to attenuate the illumination relative to the fluorescence emission. These elements should be carefully chosen to optimize the signal relative to the background, based on the excitation and emission spectra of the particular fluorescent molecule to be imaged. Finally, microscopes often have multiple mirrors, lenses, and windows between the back aperture of the objective and the camera, resulting in light loss. Microscopes with multiple camera ports do not usually send the same amount of light to each port, and one should determine which port receives the most light. When low-light imaging is a priority, it may prove fruitful to upgrade the microscope itself, as many designs now have a direct optical path from the back of the objective to the camera, which can improve throughput substantially (Herman & Tanke, 1998).

Table 10.1 shows the total fluorescence detection efficiency for two different cameras and highly optimized optics. The total collection efficiency of about 10% represents an optimistic upper limit on the collection efficiency. Although it may be difficult to actually reach 10% with any given microscope or fluorescent probe

Table 10.1 Factors which Determine the Efficiency of a Fluorescence Microscope

Microscope Elements	Optimized Collection Efficiency
Objective lens: numerical aperture[a]	0.3
Objective lens: transmission	0.9
Dichroic mirror	0.8
Microscope throughput[b]	0.8
Filters[c]	0.6
Total collection efficiency	10%
Total detection efficiency (camera = 50% quantum efficiency)	5%
Total detection efficiency (camera = 10% quantum efficiency)	1%

[a]Represents the fraction of emitted light that is collected by the objective.
[b]The light transfer efficiency from the objective to the camera, excluding other listed elements.
[c]Filter transmission can be higher if excitation and emission wavelengths are well separated.
The total collection efficiency is given by the product of the different factors shown. Some of the values shown will be difficult to achieve, as described in the text. The total detection efficiency represents the percentage of emitted photons detected by the camera.

molecule, it should be possible to get reasonably close, say within a factor of 2–10. However, it is also not uncommon to collect much less light than the numbers shown in the table. For example, use of low-NA objectives or a camera port that receives, for example, 50% (or less) of the light, will both reduce the efficiency. Other potential sources of light loss include the use of too many or inappropriate filters; use of differential interference contrast (DIC) microscopes without the slider or analyzer removed; dirty optics, perhaps covered with dust or immersion oil; and optical misalignment. Without proper attention to optical imaging, the total collection efficiency could easily be much less than 1%, or even less than 0.1%, throwing away much-needed light.

Detection of low light

The total detection efficiency can be used to estimate the camera signal amplitude for various applications, beginning with a single fluorescent molecule. If we estimate that with moderate illumination a single probe will emit about 10^5 photons/s, the microscope and two cameras from Table 10.1 would detect 10,000 and 1000 photons, respectively, for a 1-s exposure (neglecting photobleaching; Harms, Cognet, Lommerse, Blab, & Schmidt, 2001; So et al., 1995; Tsien & Waggoner, 1995).[2] In contrast, a shorter exposure, say one video frame (1/30th second exposure), would detect 330 and 33 photons, respectively. A very important point one should notice from these numbers is that it is possible to measure reasonably large numbers of photons, especially with a high-efficiency camera, even from a single fluorophore, provided it does not photobleach too rapidly (Funatsu, Harada, Tokunaga, Saito, & Yanagida, 1995; Schmidt, Schutz, Baumgartner, Gruber, & Schindler, 1995). The development of fluorescent probes with better photophysical and specific binding properties is an active field of research in itself (Giepmans, Adams, Ellisman, & Tsien, 2006; Zhang, Campbell, Ting, & Tsien, 2002). The microscope magnification and camera pixel size will determine across how many pixels the image from a single fluorophore will be spread, as discussed later. In any case, the technology is available to reliably measure fluorescence even from only a small number of probe molecules, particularly when the optical collection efficiency is also optimized. The remainder of this chapter is devoted to the discussion of electronic camera technology.

[2]This photoemission rate can vary greatly depending on the photophysics of the specific probe and the illumination level, but 10^5 is a reasonable estimate for this illustration. In fact, this number can realistically, in some cases, be 10–1000 times larger or as low as desired if illumination is reduced. Photobleaching will normally limit the total number of photons emitted, as fluorescent molecules often will photobleach after 10^3–10^5 excitations. Thus, the rates of 10^5 or higher may not be sustainable, depending on the exposure time. If long or multiple exposures were needed, one would often use lower intensity illumination to limit photobleaching. One might also use lower illumination to limit perturbation of live-cell preparations.

10.1 PARAMETERS CHARACTERIZING IMAGING DEVICES

The fundamental purpose of any electronic camera is to generate an electrical signal that encodes the optical image projected on its surface. When the light intensity is reasonably high, there are a number of cameras that perform very well. As the image intensity declines, it becomes increasingly more difficult to obtain high-quality images. Applications with the lowest light levels generally require some compromises between spatial resolution, temporal resolution, and signal-to-noise levels. However as cameras become more sophisticated, the required compromises are less severe. Ideally, a camera would record the arrival of every photon with high spatial and temporal precision, without introducing any extraneous signal or noise. Of course, ideal detectors are hard to come by, and it is thus important to understand how real detectors perform. In Section 10.1.1, we discuss the key parameters that determine a camera's characteristic response.

Although there are many types of cameras available for microscopy, it seems the most relied on type is the charge-coupled device (CCD) camera (Aikens, Agard, & Sedat, 1989; Hiraoka, Sedat, & Agard, 1987). The other common type of camera, the complementary metal-oxide semiconductor (CMOS) camera, is mainly used for consumer devices, as it can be made very inexpensively. There are CMOS cameras appropriate for microscopy, yet it would appear that CMOS cameras are destined for the low-cost market, whereas CCD technology will remain preferred for high-performance systems.

Hence we will concentrate on CCD camera performance, although the basic ideas are generally valid for any camera type. There are many excellent references available for readers interested in more details about vacuum tube-based cameras, as well as solid state cameras and microscopy in general (Inoué & Spring, 1997; Miura, 2001; Periasamy and American Physiological Society, 2001; Sluder & Wolf, 1998; Tsay, Inman, Wray, Herman, & Jacobson, 1990).[3]

10.1.1 Sensitivity and quantum efficiency

Camera sensitivity refers to the response of the camera to a given light level. A convenient measure of this quantity is the quantum efficiency (QE), which refers to the fraction of photons incident on the detector surface that generate a response (photoelectrons). Different CCD materials and designs can have vastly different quantum efficiencies, from a few percent to above 90% in some devices. The higher quantum efficiency cameras are generally more sensitive, although a camera's minimum noise level must also be considered to determine how "sensitive" it is. Camera sensitivity is thus sometimes expressed in terms of the minimum amount of light that can be reliably measured, often called the noise equivalent floor. In this case, a lower sensitivity rating means the camera can detect dimmer light (i.e., it is more sensitive). To be completely clear, it is best to specify the signal-to-noise ratio (see below) that can be achieved for a given light level. The use of different definitions in reporting the sensitivity can lead to confusion, and the manufacturer should be consulted when data sheets are unclear.

[3]For an example of an on-line resource, see http://bsir.bio.fsu.edu

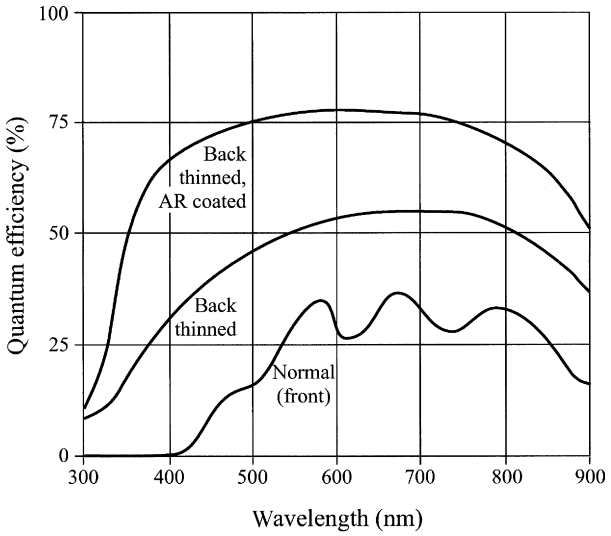

FIGURE 10.1

Quantum efficiency of a CCD as a function of wavelength, showing typical curves for three devices—normal (front face), back thinned, and back thinned with antireflective (AR) coating.

10.1.1.1 Spectral response

The quantum efficiency of an image detector is wavelength dependent. This property is called the spectral response and is the result of the nonuniform response of the device materials to different colors of light. Some typical curves of quantum efficiency versus wavelength are shown in Fig. 10.1 for three different CCDs. The spectral response is dominated by the material response (silicon) but is modified by how the CCD is manufactured. Most CCDs have their peak response in the visible wavelengths and are normally more sensitive to red light than to blue. The sensitivity can be enhanced for particular applications by tuning the thickness of the photoactive region (blue or red enhancement), for example, adding antireflective coatings (enhancing the peak light acceptance) or down-conversion coatings (improving the UV response). Other enhancements such as changing the design of overlying control structures (e.g., open electrode or ITO electrode designs) offer a double enhancement of improving the light gathering of the sensor (less blocked light, see Section 10.1.1.1 below) and shifting the peak spectral response more toward the blue. No matter what enhancements are offered, it is most important to verify that a camera has reasonably high sensitivity to the wavelengths of light that are to be imaged in your particular experiment.

10.1.1.2 Units

Camera sensitivity is also often reported in units of radiant sensitivity, which is equivalent to the QE, but expressed in units of amperes per watt rather than electrons per photon. One can easily switch between quantum efficiency and radiant sensitivity using

$$\mathrm{QE} = 1240\frac{R_s}{\lambda}$$

where R_s is the radiant sensitivity in amperes per watt and λ is the wavelength in nanometers. Both quantum efficiency and radiant sensitivity are radiometric units.

When the sensitivity is reported as the smallest resolvable signal, as mentioned above, it is usually expressed in photometric units such as lux, lumen, or candela. Quoting sensitivity in lux is ambiguous unless the light spectrum is specified. Photometric units are adjusted for the response of the average human eye to different colors of light, and thus differ from radiometric units such as energy or number of photons. The integrated product of the radiant quantity and the efficiency of the eye yields the corresponding photometric (sometimes called luminous) quantity. The luminous efficiency function of the eye is called the CIE $V(\lambda)$ curve (CIE publication, 1990). Note that 1 lumen is equivalent to 1/683 W (about 1.5 mW) of monochromatic light whose frequency is 540×10^{12} Hz (a wavelength of about 555 nm in air). Figure 10.2 shows the conversion between radiometric and photometric units as a function of wavelength for monochromatic light.

10.1.1.3 Fill factor (CCD format)

The sensitivity of a CCD detector is also affected by its geometry. Not all the light reaching the CCD falls on photoactive areas (the pixels), as some of the surface may be obstructed as part of the device design for transferring stored photoelectrons. The surface electrodes obscure some incoming light. Interline transfer CCDs (see -Section 10.2.2 for different CCD formats), for example, have inactive space between each row of pixels for charge transfer, resulting in reduced collection efficiency. The fill factor refers to the fraction of the detector that is active, determined mainly by the surface area of the pixels. For interline transfer CCDs, the fill factor can be as low as 25%. This loss can be diminished by positioning microlenses over each pixel to refract light that would be blocked by the control structure into the active pixel area, thus increasing the effective collection area on an active pixel. Current microlens techniques (sometimes two layers of lenses) along with improvements in pixel design (e.g., Sony's hole accumulation diode, HAD, design) can achieve fill factors of more than 70% for interline transfer devices. Other CCD formats, such as frame-transfer CCDs, do not have masked areas between pixels and have higher fill factors, 70–90%. Devices that are prepared for backside illumination have no obscuring control structures and thus are normally quoted as 100% fill factor devices, although some light may still be lost to buried pixel control structures such as antiblooming schemes. Note also that some CCD manufacturers combine the effect of the quantum efficiency and the fill factor and just report the product as the quantum efficiency. The quantum efficiency in this sense is that of the whole device, whereas the quantum efficiency we defined above is for the active area. The net result is the same, but the terminology can be confusing.

10.1.2 Camera noise and the signal-to-noise ratio

Electronic imaging is complicated by the presence of noise, which degrades image quality. If the response of a camera to a given light level is below the noise level,

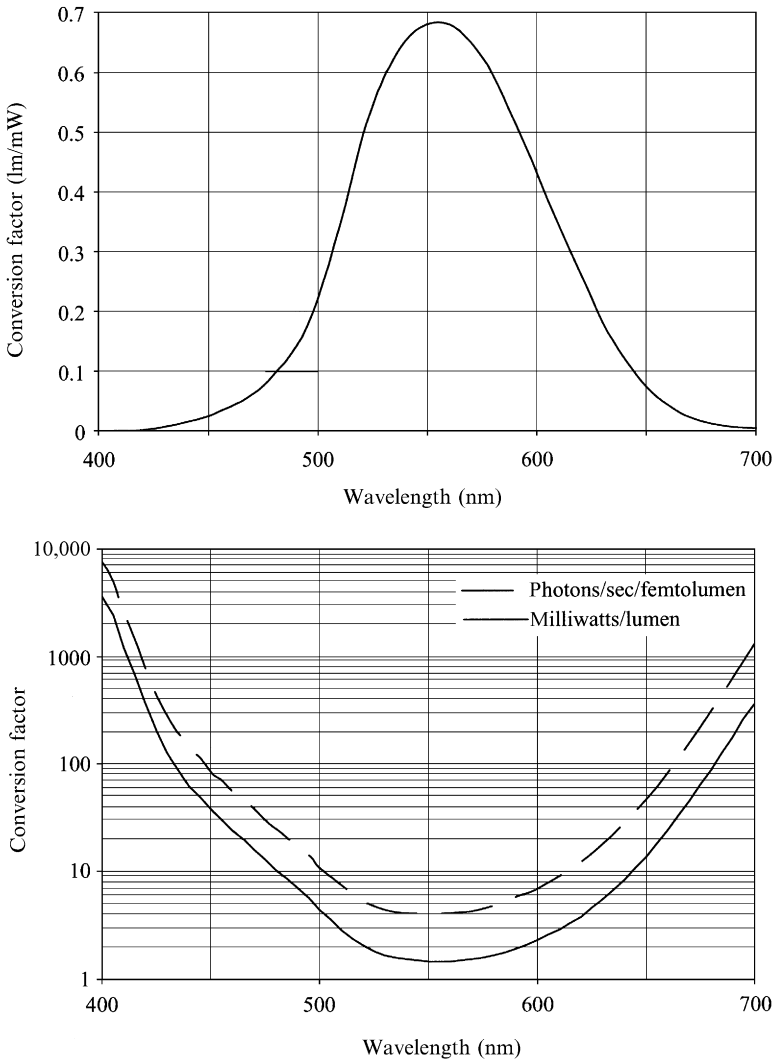

FIGURE 10.2

Factors for converting between radiant flux (milliwatts or photons per second) and luminous flux (lumens) for monochromatic light. The two panels are shown for reader convenience although they contain the same information.

the image will not be resolved. The most important measure of a camera's response is therefore not the sensitivity itself but, rather, the signal-to-noise ratio, which can be achieved for a given light level reaching the detector. The signal-to-noise ratio (S/N) is defined as the signal level generated by the camera's response to light divided by the average noise level. The higher the signal-to-noise ratio is, the better the image

quality. The signal-to-noise ratio is often expressed in equivalent forms, decibels (dB), or bits. To convert the signal-to-noise ratio to decibels, the following formula is used:

$$\left(\frac{S}{N}\right)_{\mathrm{dB}} = 20\log\left(\frac{S}{N}\right)$$

The equivalent number of bits can be found by calculating the base 2 logarithm of the signal-to-noise ratio (S/N) or dividing $(S/N)_{\mathrm{dB}}$ by 6, as 1 bit is equivalent to 6 dB ($20\log(2) \approx 6$).

Noise plays an important role in determining the performance of imaging devices, particularly in low-light-level imaging, where the signal is small by definition (see Section 10.2.4 for techniques to amplify the signal). To achieve a good signal-to-noise ratio, therefore, requires a camera that has very low noise. Knowledge of noise sources and how their effects can be minimized is thus valuable in understanding how various cameras are designed and in determining which camera types are most appropriate for a given application.

10.1.2.1 Shot noise

Using an electronic camera to detect an image is essentially an experiment in counting the number of photoelectrons stored in the pixel wells. The electron counting is a random process and will follow Poisson statistics. The uncertainty in the measured result, called shot noise or photon noise, will be the familiar "square root of N," where N, in this case, is the number of electrons collected in each pixel. Shot noise is intrinsic to the photon statistics of the image and cannot be reduced. As the light level increases, the shot noise increases, eventually exceeding the level of other noise sources (this is a good thing). When shot noise is the dominant noise source for an image, the signal to noise grows as the square root of the number of photons measured at any pixel. This condition is the best obtainable, that is, the signal-to-noise ratio cannot exceed the shot noise limit. The signal-to-noise ratio will vary between applications depending on whether the camera noise sources are most important or are insignificant when compared with shot noise.

10.1.2.2 Readout noise

Intimately coupled to the design of image detectors is the method they use to transfer the recorded image from the detector to a usable electronic format. This process, called readout, will introduce noise to the signal. The main source of readout noise in CCDs is an on-chip preamplifier required before digitization. The noise level is independent of the amount of light reaching the camera, and high readout noise will reduce the signal-to-noise ratio, particularly for low-light images. The readout noise level is highly dependent on the readout rate, increasing approximately as the square root of the readout rate. Thus, cameras with lower readout rates will have better signal-to-noise ratios than cameras with higher readout rates, other things equal. The cost of a lower readout rate is a reduced frame rate. For high-end video CCDs, readout noise can be as low as a few electrons per pixel, increasing to several hundred electrons per pixel for lower end devices. The readout noise level is determined by the electronics of each device, but some typical numbers for high-performance

electronics are 3 electrons/pixel at 50-kHz, 10 electrons/pixel at 1-MHz, and 20/pixel electrons at 20-MHz readout rates. Although there are no other systematic ways to reduce the readout noise, it can be effectively reduced by a new type of CCD that multiplies the number of photoelectrons before the read out occurs, thus applying gain to the signal without affecting the readout noise (Section 10.2.5.1).

10.1.2.3 Background and noise

There are a number of sources of background signals in electronic imaging. Thermally generated electrons get collected in the same pixels as the photoelectrons. These electrons, called dark charge, are generated even when the CCD is not illuminated.[4] The associated noise, called dark noise, will grow as the square root of the dark charge, as does shot noise. Other factors such as Rayleigh and Raman scattered illumination or stray light leaking through to the camera can also contribute to the background signal, again contributing to the noise as the square root of the number of electrons generated. The background level ultimately lowers the dynamic range (discussed below) of the camera and raises the noise. With image processing, the average background level can be subtracted from an image, although this subtraction will not reduce the noise. Although it is valuable to understand the various noise sources, there is no need in actual experiments to distinguish between shot noise and various other background noise sources. Rather, the total noise (excluding readout noise) can be calculated directly as the square root of the total number of electrons collected in any pixel.

In general, for video rate applications, the dark noise is not as important as readout and shot noise. In contrast, for longer image acquisition times, dark noise can be significant at room temperature. By cooling the camera with thermoelectric coolers or liquid nitrogen, dark charge, and thus dark noise, can be drastically reduced. High-quality-cooled scientific cameras can achieve extremely low dark charge levels of less than a single electron per pixel per hour. This is in contrast to the dark charge of a few hundred electrons per pixel per second for standard, uncooled cameras.

Cooling is not the only strategy used to reduce dark charge. Some camera chips have multipinned phasing (MPP), which helps reduce collection of surface electrons on the CCD chip during image integration. MPP devices can reduce dark charge several hundred times. The major drawback of MPP is that it usually results in a reduction of pixel well capacity, and thus limits the dynamic range.

10.1.2.4 Example calculation

Assume a cooled slow-scan CCD camera has quantum efficiency of 50%, read noise of $N_r = 10$ electrons/pixel, and is cooled such that much less than one thermal electron is generated per pixel during a 1-s exposure. What will be the signal-to-noise ratio when the number of photons per pixel per second reaching the camera is 100, 1000, and 10,000? First, the number of electrons generated is given by the

[4]Camera data sheets often specify a dark current, in amperes per centimeter squared, rather than dark charge, in electrons per second per pixel. The conversion between the two is determined by the size of each pixel and the charge of the electron which is 1.6×10^{-19} C.

number of photons multiplied by the quantum efficiency, or 50, 500, and 5000. The shot noise, N_s, is then 7, 22, and 71, respectively. The total noise is given by $N = \sqrt{N_r^2 + N_s^2 + N_d^2}$, where the dark noise, N_d, is negligible for this example. Total noise is thus 12, 24, and 71 electrons, with corresponding signal-to-noise ratio of 4, 19, and 70, respectively, or 12, 26, and 37 dB.

How would the signal-to-noise ratio be changed using a 1-s or 1-min exposure if the same camera is illuminated by 1000 photons/pixel/s, and also has dark charge of 50 electrons/pixel/s? The total number of photons reaching the detector would be 1000 or 60,000 for the long exposure, generating 500 or 30,000 electrons, respectively. The total dark charge for the two integration times is 50 or 3000 electrons, respectively. The combination of dark noise and shot noise would then be 23 or 182, respectively. Adding in read noise results in noise of 25 or 182 electrons. The signal-to-noise ratio is then 20 (26 dB) or 165 (44 dB). Note that the shot noise limit for these two cases is a signal-to-noise ratio of 22 (27 dB) for the 1-s exposure and 173 (45 dB) for the 1-min exposure. The signal-to-noise ratio can, of course, be calculated in one step rather than the two shown, but this method nicely illustrates how read noise becomes less significant for long exposures. Figure 10.3 further illustrates this point with plots of the signal-to-noise ratio as a function of signal intensity for three different values of the read noise.

10.1.3 Spatial resolution

Electronic cameras form images by sampling the optical image in discrete pixels, as shown in Fig. 10.4. The spatial resolution of a camera system is determined by the pixel spacing and is independent of the optical resolution of the microscope, although

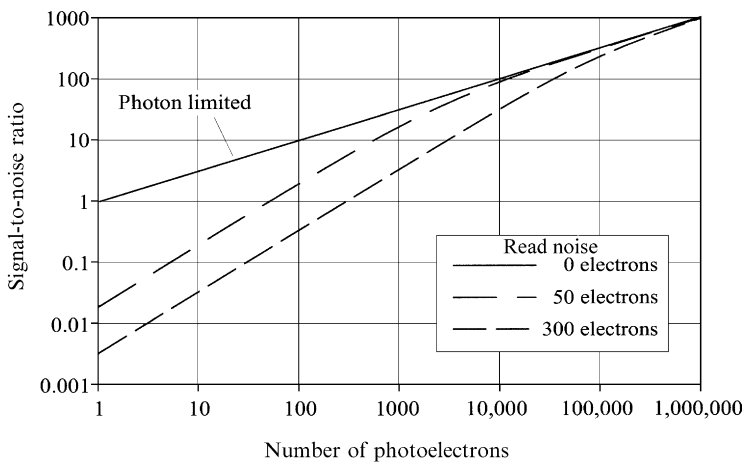

FIGURE 10.3

The signal-to-noise ratio as a function of image intensity, assuming negligible dark noise. The three curves correspond to three different values for the read noise.

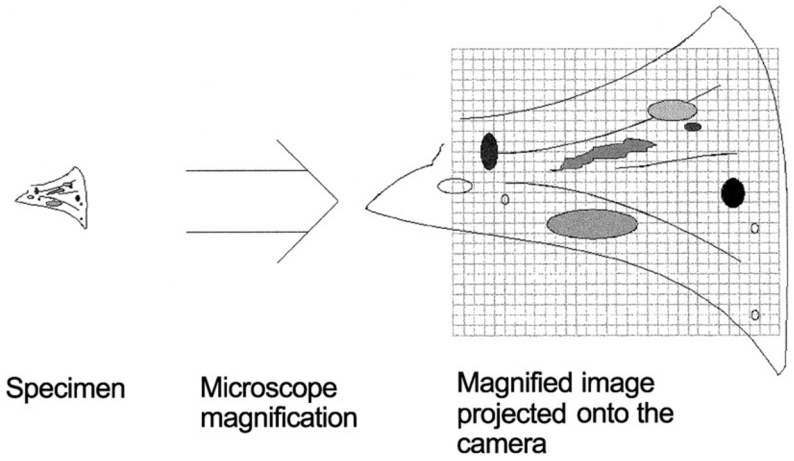

FIGURE 10.4

Spatial resolution in electronic cameras is determined by the pixel size as described in the text. The magnified image is projected onto the camera, where it is sampled in discrete pixels. Image features that change over distance scales smaller than two pixels are not resolved in the electronic image. A real camera would have many more pixels than this cartoon.

limited by it (Castleman, 1993). To resolve image features of a given spatial frequency, the camera must sample the image with at least twice that frequency. This requirement can be roughly understood as simply stating that image details will be resolved only when the pixel spacing is smaller than the scale over which image features change. As an extreme but intuitive example, one can imagine a "camera" with only a single large pixel, for example, a photomultiplier tube, that can measure light intensity, but has no spatial resolution. By dividing the detector into pixels, the image will begin to be resolved, and as the number of pixels is increased, higher levels of detail will become apparent, up to the diffraction-limited resolution of the microscope optics. CCDs generally have a pixel spacing from about 2 to 40 μm. The smallest resolvable details in the magnified image on the detector's active area are therefore about 4–80 μm in size, because of the sampling requirements stated above.

Most image detectors are physically small devices, typically 1 in.^{2} for image tubes and even less for many CCD chips. Choosing how much an image is expanded or compressed in projecting the image on the device will involve a trade-off between the resolution and the field of view. Image magnification also involves a trade-off between spatial resolution and image brightness—the more an image is magnified, the more the light from each fluorophore is spread out, reducing the signal in any given pixel and, thus, the signal-to-noise ratio (Shotton, 1993).

A closely related topic to resolution is the localization of individual fluorophores. The subject has received increasing attention as experiments have shown the ability to determine individual translocation steps of molecular motors with subwavelength

resolution and ultraresolution image reconstruction based on localization of multiple individual fluorophores. The concept behind subwavelength localization is that the position of the maximum of the point spread function of a diffraction-limited spot can be determined with accuracy that increases with the number of photons detected from the fluorophore and limited by the background noise (including all noise sources). For these type of applications, not only the image amplification is important but also the level of noise and background of each individual pixel (Betzig et al., 2006; Yildiz et al., 2003).

10.1.3.1 Example

The size of a microscope image is governed by the object size and the microscope magnification, the smallest size being limited by the point spread function of the microscope (diffraction-limited resolution). The spatial resolution of an imaging system can easily be calculated if the camera pixel size and magnification are known. Consider a CCD camera with 10×10-μm^2 pixels on a microscope with a $63\times$ objective (NA $= 1.4$) and no further magnification. For each dimension of the camera chip, the 10-μm pixel at the camera corresponds to 159 nm (10 μm/$63\times$) in the specimen plane. This camera/lens combination would thus correctly sample image details down to 318 nm (2×159). This would not, however, fully exploit all the available image detail. The Rayleigh criteria for the optical resolution limit is given by 0.61λ/NA, which specifies the minimum separation at which two point objects can be resolved (Castleman, 1993). Assuming we have 500-nm light, this limit is 218 nm for a 1.4-NA objective. To correctly recover all the available image detail would require sampling at 109-nm (218/2) pixel spacing. This could, in fact, be achieved with additional magnification of $\sim 1.5\times$, which would sample the image every 106 nm. This extra magnification can be added to the microscope, or sometimes to the camera itself.

10.1.4 Linearity and uniformity

In general, cameras are designed to be linear, that is, the detector has a linear relation between input signal and output signal intensities. This feature is essential for quantitative imaging and must be verified for each camera. A CCD is a linear detector, although linearity is lost if the detector is overexposed. In this case, photoelectrons from adjacent pixels overflow into neighboring wells, causing blooming. Antiblooming circuitry and the improved design of modern CCDs reduce this problem. Also, the camera response across the detector surface is not always uniform and leads to image distortion, or shading. The camera response is not the only source of this problem, as the illumination itself is often not uniform over the entire field of view. Shading (flat field) correction can be added to some cameras to electronically correct their response, or the image may be corrected at a later time using image processing provided that the necessary correction is known from imaging a uniform sample.

Sometimes, video cameras are intentionally coupled to an output stage that is not linear. Two common sources of nonlinearity built into a video CCD camera are

automatic brightness control and gamma correction. Automatic brightness control changes the output preamplifier's gain when the number of stored charges in a pixel becomes too large. This change in gain is not normally under the camera operator's control and is therefore difficult to compensate for quantitative imaging. The best solution is to turn off automatic brightness control. Many cameras (especially video CCD cameras) also have gamma-compensated output. Gamma correction is useful to properly transfer an image from the detector to a video monitor but is generally harmful to quantitative analysis. Monitors have a nonlinear response to the voltage applied to them. If monitor brightness is M_B and monitor voltage is M_v, then this nonlinearity is closely modeled by a power function:

$$M_B = M_v^{\gamma} \tag{10.1}$$

where the exponent gamma (γ) is about 2.5. Then the words "the signal, S" and the second equation become

$$M_v = S^{1/\gamma} \tag{10.2}$$

Cameras that perform gamma correction convert the linear CCD signal into a gamma-corrected one [using Eq. (10.2)]. This means a digitizer will quantize the data at nonlinear intensity levels. The advantage is that the first digitization controls the precision in the signal, and there is no further loss of precision when using a digital-to-analog converter for the video signal sent to the monitor. The disadvantage is that to make quantitative comparisons in the linear space of the original CCD signal, some of the original signal precision may be lost.

10.1.5 Time response

Cameras do not always respond immediately to a change in input intensity, introducing lag and a decrease in temporal resolution. Lag can be introduced in several ways, including the time response of the phosphor screen in image intensifiers and the incomplete readout of all accumulated charges in any one frame of tube cameras. Lag is not significant in CCD cameras. If fast time resolution is of interest, it is very important to make sure the camera lag does not affect the measurement. For example, ratio imaging will likely contain artifacts if performed using a camera with lag, such as a SIT camera.

10.1.6 Dynamic range

There are a finite number of intensity levels, or gray levels, that can be detected by a given device, which can limit the detection of fine details. The range of levels is called the dynamic range. High dynamic range is important whenever there is a wide range of signal levels that must be recorded for a given imaging application. Dynamic range may be specified both within one frame (intrascene) and between frames (interscene). The dynamic range is determined by two factors: the overall operating range or pixel well depth in the case of CCDs, and the average noise level and

is calculated by dividing the maximum signal level (for each pixel) by the minimum average noise level (excluding shot noise).

For example, a CCD with pixel capacity of 200,000 electrons and an average noise floor of 50 electrons has a dynamic range of 4000:1. Normally, similar to the signal-to-noise ratio, the dynamic range is expressed in either dB or the equivalent number of bits. For this example, 4000 gray levels are equivalent to 72 dB or 12 bits.

Another way to think about dynamic range is that it specifies the smallest difference in signal level that can be resolved when the camera is operating at full range; that is, the smallest difference in image brightness that can be observed on top of a bright background. Although this second definition is technically not quite correct, it is useful in as much as it gives some intuitive feeling for what the dynamic range is. The signal-to-noise ratio and dynamic range should not be confused. Whereas the dynamic range describes the camera's ability to respond over a range of signal levels, the signal-to-noise ratio is dependent on the conditions for each image acquired, comparing actual signal levels and camera noise. The signal-to-noise ratio is always less than the dynamic range.

The dynamic range of a camera can be limited by the choice of digitizer. For most video-grade CCDs this is not a problem, as they often have a dynamic range of only 40 dB or less, which is less than a dynamic range of an 8-bit digitizer (256:1). In contrast, scientific-grade CCDs may have a dynamic range of greater than 100 dB (16 bit, or 66,000:1). In this case, a digitizer with equivalent precision is required, or digitization of the camera signal will reduce the dynamic range.

10.1.7 Gain

Gain refers to signal amplification by the camera to create an electrical signal that can be accurately measured. Although sensitivity describes the input response of the device, gain determines the total output response. Gain stages can only increase the noise, but some gain is normally necessary to transmit a signal that can be reliably read by the digitizing electronics. If the digitization is performed in proximity to the detector, the gain requirements are less. Not all gain is provided by an electronic amplifier. Sometimes, it is an inherent part of the photodetector, as in SIT cameras image intensifiers and electron multiplying CCDs, although these devices still have electronic gain as well.

When gain can be changed between frames, the camera can accommodate an interscene dynamic range that may be several orders of magnitude larger than the intrascene dynamic range. However, the response characteristics of a camera are normally not precisely known for different gain settings. For example, altering the gain may affect the slope of the camera's linear response or may even result in a nonlinear response. These differences must be measured and calibrated to use the detector with multiple gain settings. Without precise knowledge of the response of the detector at different gain settings, it is impossible to make quantitative measurements that can be compared. Therefore, when the gain response is not well known, it is important that all the images of a time sequence, for example, use the same gain setting for proper

quantitative analysis. Unfortunately, some images may have points that exceed the normal intrascene dynamic range. However, without changing the gain there is nothing that can be done, and the detector gain should be set to the best compromise. One exception is the gain of the output preamplifier of CCD cameras, which does not normally affect the response of the detector. However, the effect of the system gain must be measured to verify linearity.

10.1.8 Frame rate and speed

Different applications require image acquisition at varying speeds, or frame rates. The frame rate is determined by the pixel read rate and the number of pixels in the image. For a fixed number of pixels, the main drawback to higher frame rates is increased noise caused by higher readout rates (faster readout also has less light per pixel per frame). Digitization is normally the rate-limiting step in image readout. For a certain level of noise and digitization depth (number of bits), the maximum digitization rate is consistent across all manufacturers. The frame rate is then determined by the number of pixels. Most video cameras have a fixed frame rate of 30 frames/s. Scientific cameras and other specialized systems can offer variable frame rates. If a camera contains many pixels (one million or more), the frame rate will in almost all cases be lower than video rate, particularly for low-light applications. This is because the high read noise associated with fast readout would overwhelm the small signal levels inherent to low-light imaging, resulting in poor signal-to-noise ratios.

10.1.9 Resolution, sensitivity, and imaging rate

A properly operated electronic camera is essentially an array of independent photodetectors. When the signal-to-noise ratio is reasonably high for most pixels, the result will be high-quality images. Various camera design choices employ different strategies to maximize signal-to-noise ratios, usually involving some compromise between spatial resolution, frame rate, and the signal-to-noise ratio. For example, when the signal per pixel is small compared with readout noise, one can simply acquire an image for a long time, provided the camera has low dark noise, to build up the required signal level. This describes the basic design of slow-scan CCD detectors, which increase the signal-to-noise ratio at the expense of time resolution. Another strategy is to use a camera with fewer (larger) pixels, effectively increasing the amount of signals per pixel. This will also increase the signal-to-noise ratio at the expense of spatial resolution. Conversely, for a given light level reaching the camera, increasing spatial resolution (more, but smaller, pixels) will lead to a decrease in the signal-to-noise ratio, as will increasing the frame rate. The required resolution and the image characteristics (intensity, spatial and temporal frequency) will determine which strategy and suitable camera design to employ for a given application.

Sometimes, when spatial resolution can be sacrificed, a technique called binning can be used to optimize the signal-to-noise ratio or the frame rate for a given

application. Binning is an electronic technique, available only on certain camera models, that combines the stored charges of adjacent pixels on the CCD chip. Binning is effectively equivalent to using a camera with a smaller number of larger pixels than the actual camera in use—there is essentially no time loss associated with binning, as combining electrons from multiple pixels can be completed much faster than pixel readout. There are several reasons one might choose to use binning. One is that there will be fewer pixels to digitize per frame, which will allow for higher frame rates. Another reason is to increase the signal level by increasing the active area of each effective pixel. This is especially useful for low-light situations in which the number of photoelectrons collected by each single pixel is low compared to the readout noise. Getting more light to each pixel can also be accomplished using lower optical magnification, but electronic binning, when it is available, is certainly more convenient than changing optical hardware. The obvious drawback in either case is reduced spatial resolution. Another drawback of binning is that the full well capacity cannot always be used without saturation, as binning transfers all of the charge from multiple wells into one well before readout. This should not be a problem in most low-light imaging applications, as the pixels are generally nearly empty rather than full, and binning is used to increase the number of electrons to measurable levels.

10.2 SPECIFIC IMAGING DETECTORS AND FEATURES

There are currently many options available in choosing electronic cameras, and devices with improved performance characteristics are constantly being released. More cameras are being manufactured with application-specific designs, resulting in exciting possibilities for biological imaging. In this section, we present some of the basic camera types that are commonly available and highlight the major features. For up-to-date information on the latest product specifications, one should consult camera manufacturers. In choosing a camera for special applications, it is wise to evaluate several models, on a trial basis, to compare their performance and image quality using an investigator's actual samples.

10.2.1 Video CCD cameras

Monochrome video CCDs are the most commonly available and least expensive CCD-based cameras for microscopy. These are not considered low-light cameras, as they do not have particularly high quantum efficiency (10–20%). The typical minimum sensitivity of low-end devices is 0.5 lux (noise equivalent), which is barely low enough for microscopy. High-end video CCD cameras can have sensitivity as low as 0.01 lux, which can be used for fluorescence imaging of brightly labeled specimens. Readout noise is the main noise source since dark noise is usually minimal for video rate acquisition. The high readout noise and relatively low pixel capacity (36,000–100,000 electrons) limit the dynamic range. In the highest quality video CCDs, the dynamic range can be as high as 8 bits, although noise often limits the true dynamic

range of many video CCDs to around 6 bits. Typical spatial resolution is $\sim 700 \times 500$ pixels (interlaced) on a 1/4- to 2/3-in. chip. Video CCDs have a fixed frame rate of 30 Hz. These basic cameras have little flexibility, but they are easy to use and are compatible with standard video equipment.

Some video CCD cameras have been modified to enhance performance and increase flexibility. Circuits have been added that allow variable "on chip" integration time, from a short 100 s (300 times less than video rate exposures) up to several hundred seconds. Long integration times are very useful for low-light applications, increasing the total amount of light reaching the detector before it is read. On-chip integration has a major advantage over frame-averaging standard video camera output, as on-chip integration incurs read noise only once, rather than each time the image is read for averaging. Variable frame rate video CCDs incorporate cooling to reduce dark charge, which is important for the longer exposure times. These modified video CCDs are much more powerful and flexible than standard video cameras and provide an economical option for low-to-moderate light-level imaging.

10.2.2 Slow-scan CCD cameras

Slow-scan, or scientific, CCDs are designed specifically for low-light applications, with the ideal attributes of both very high sensitivity and low noise. Slow-scan CCDs are currently the best available low-light cameras, provided fast time resolution is not required. These cameras are substantially more flexible than video cameras, and this flexibility can be exploited to achieve superior image quality for many applications. They come in many different formats, and the particular CCD chip will determine the camera performance. The quantum efficiency of scientific CCDs ranges from 20% to above 90% significantly better than video devices. The highest quantum efficiency is found in back-illuminated CCDs, which collect the image from the back surface of the chip rather than the front, to reduce light losses incurred in passing through the electrodes and protective layers on the front surface of the chip. Applying antireflective coatings can also help achieve maximum quantum efficiency. Back-thinned CCDs are more expensive than other scientific CCDs, and the application will determine whether this added sensitivity is required and worth the investment.

In addition to high sensitivity, scientific CCD cameras also have very high spatial resolution, which is achieved by using CCDs with more pixels. Arrays may contain upward of 5000×5000 pixels. Some devices are built such that they can be placed side by side to create even larger pixel arrays. The growth in the number of pixels results in longer read times and, thus, slower frame rates. This should not pose a major problem unless fast time resolution is required, in which case the highest spatial resolution may be too much to hope for at present, at least for low-light applications. If only a small number of images are required, frame-transfer CCDs can be used to acquire several images rapidly, with the images stored on inactive areas of the CCD and read out later at slow readout rates. This approach works because charge transfer to the inactive regions of the CCD chip can be completed much faster than the actual readout. As mentioned above, binning can also be employed to increase the frame rate.

Slow-scan cameras have very low background, and hence low noise, allowing for long image acquisition times. The readout and thermal noise are minimized through slow readout rates and cooling or multipinned phasing. Readout noise as low as 5 electrons/pixel is common, and dark charge can be reduced to just a few electrons per pixel per hour. This results in the potential for very high signal-to-noise ratios in high-light conditions, or with long integration times for low-light levels. Basically, using slow-scan CCDs, low-light images can be integrated (on-chip integration) for whatever time is necessary to achieve a reasonable signal-to-noise ratio, provided the sample is stable. The low noise also makes it possible to exploit the full dynamic range of each pixel. The electron well capacity of scientific CCDs is generally at least several hundred thousand electrons per pixel, with some devices holding over one million electrons per pixel. The dynamic range of scientific cameras is 10–16 bits (1000:1–66,000:1), much greater than the 8-bit (maximum) video CCD.

An important factor in determining camera quality is the image transfer method. Because scanning pixels in the vertical direction limits the speed of the camera, the CCD manufacturers developed different scan procedures to speed up this process. Some CCDs transfer pairs of pixels in adjacent horizontal rows. The rows are scanned in one single sweep, and their charge is added together. This procedure diminishes the vertical resolution, resulting in an image with a poorer resolution than the actual number of pixels in one direction. An alternative method is interlaced transfer, in which odd-numbered rows are read in one step and even-numbered rows in the next one. The result is the loss of scan synchronicity. Both methods are not suitable for precise measurements, though there are software algorithms that can deinterlace the image, basically splitting it into two separate images (with half the perpendicular resolution). Recent advances in CCD chip design, especially improvements in the vertical electron transfer rate, allowed development of progressive interline scanning. In this method, every single pixel is read in one scan, preserving full vertical resolution and synchronicity.

Aside from electronic methods to transfer the image, CCDs employ physical structures that enable specific types of image transfer. Frame-transfer devices are the most basic sort, where the image is formed on the active area and then read out directly from the active area. The image is shifted across the active area, one column at a time, for a total time that is slightly greater than the number of pixels divided by the readout rate. For example, a 1000×1000-pixel camera read at 20 MHz will require 50 ms to shift the image and read it out. In frame-transfer cameras, it is important that the transfer time is a small fraction of the total integration time, or the image may smear as more photons fall on the active area while the image is shifted out to the readout register. Alternatively, shutters are used to block light during readout. Another more complicated camera is based on full-frame-transfer devices. In these systems, the CCD size is essentially doubled. The excess area (frame storage area) is storage for a single image during readout. It is typically the same size and material as the active area except that it has a masking layer that blocks incoming light. When an image is ready to be read, the collected charge is rapidly moved to the frame storage area and then read out at the normal rate. The transfer time to the storage area is normally the number of columns

divided by the readout rate. For the same example, the transfer time would be 50 μs. Readout still occurs in the original 50 ms except that while one frame is being read, the next can be accumulated. A simple alternative to this design is the split-frame-transfer device, where the frame storage area is split into multiple regions for multiple readout registers. A final type of camera is based on interline transfer devices. In these devices, the CCD is also about double the required photoactive area, except that the masked regions are interspersed every other row. The transfer of the image from the active to the storage area moves all rows in parallel. This takes one charge transfer cycle, significantly faster than the other alternatives. Again, with the same example, that would mean it would take 50 ns to transfer the entire image. As with the full-frame-transfer devices, the next image can be accumulated while the first is being read. Although possessing a clear advantage in image transfer time, the interline transfer devices do suffer from poor fill factor as discussed earlier.

10.2.3 Fast-scan CCDs

When experiments require greater time resolution than slow-scan CCDs provide, fast-scan CCDs are another option. These are integrating cameras like the slow-scan CCD, but they have faster readout to achieve higher frame rates. Unfortunately, high readout rates result in increased noise, and the specimen must by fairly bright to acquire good images with these cameras. Fast-scan cameras generally sacrifice noise, dynamic range, or resolution for the higher frame rates. The advantages of the fast-scan camera over an intensified video camera (see following) are greater resolution, higher dynamic range, and ease of use (Ramm, 1994). These features can be important if signal levels are highly variable. The fast-scan camera also features variable integration times, providing flexibility for different applications. The high readout noise limits the dynamic range to 8–12 bits, compared to the 10- to 16-bit resolution of comparable slow-scan cameras.

10.2.4 Intensified cameras

In some imaging applications, the amount of light reaching the detector may be too low to acquire high-quality images in the requisite amount of time. Image intensifiers are designed to overcome this limitation by amplifying the amount of light reaching the camera. Figure 10.5 presents a schematic of an intensified CCD camera setup. In the nonintensified camera, the poor image quality is the result of the low signal-to-noise ratio, that is, the low-light levels do not result in a signal level sufficiently above the noise. Image intensifiers can increase the signal level substantially without a corresponding increase in dark noise or readout noise, resulting in better signal-to-noise ratios. Image intensifiers do not reduce the shot noise inherent in the image and actually add some noise of their own to the system. If there were no dark noise or readout noise, the image intensifier would be of no help. The increase in signal-to-noise ratio without the need for long integration times, as with slow-scan cameras,

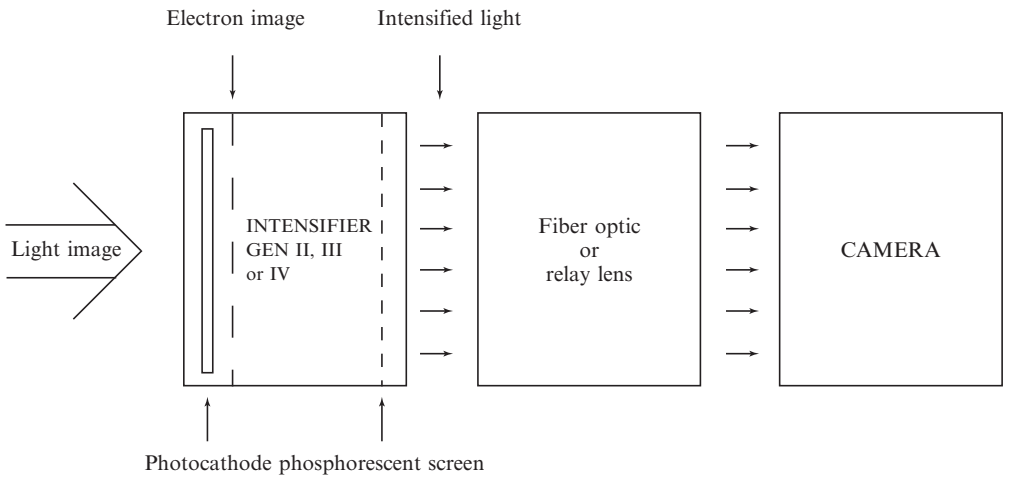

FIGURE 10.5

Schematic of an intensified CCD camera. Light reaching the photocathode generates an electron image, which generates an intensified light image on striking the phosphor screen. The image on the screen is then projected to the camera.

makes intensified cameras very useful for low-light applications where fast time resolution is required, such as measuring the kinetics of rapid calcium changes.

A second major application of image intensifiers is to achieve very high time resolution through gating. Intensifiers can normally be turned on and off very rapidly, for some devices in less than 1 ns. Thus, light can be collected from very short time windows to record transient events. Another application of high-frequency gating is fluorescence lifetime imaging (Lakowicz & Berndt, 1991; Marriott, Clegg, Arndt-Jovin, & Jovin, 1991; Verveer, Wouters, Reynolds, & Bastiaens, 2000).

10.2.4.1 Intensifier formats

There are several different types of image intensifiers. Gen I intensifiers employ vacuum tubes similar to standard tube-type cameras. Electrons generated at the photocathode (each by a single photon) are accelerated onto a phosphor screen. The electrons striking the screen produce multiple photons in proportion to the electron energy, thus amplifying the signal. The image produced on the phosphor screen is then viewed by a suitable camera. Typical gain for a Gen I intensifier may be as high as several hundred times. The quantum efficiency of the cathode is generally about 10%.

Gen II, III, and IV intensifiers employ a microchannel plate, which is a collection of small glass tubes, with metal surface coatings on the inside walls. Electrons collide with the surfaces as they are accelerated through the tubes, resulting in a cascade of electrons reaching the phosphor screen. The gain can be very high, up to 1,000,000 times. This method of amplification has very low thermally induced dark noise. The main differences between Gen II, III, IV intensifiers are the efficiency of the cathode material and the method of construction. These intensifiers can have respectable quantum efficiencies, reaching 30–50% in high-quality devices.

Although intensifiers can greatly increase sensitivity, there are some drawbacks. First, their spatial resolution may be limited, depending on the size and spacing of the glass capillaries and the phosphor material. Although in some cases, the intensifier may have comparable resolution to the camera itself, it is probably best not to use an intensifier if very high spatial resolution is required. The second drawback is that intensifiers often exhibit some nonuniformity and, therefore, require flat field correction. Intensifiers also often produce images with a lot of "snow," caused by thermally generated background noise. Finally, the phosphor screen may introduce lag, caused by long-lived phosphorescence. Proper choice of phosphor material can reduce lag at the cost of image intensity. If very fast time resolution is important in a particular application, the intensifier and phosphor material must be chosen appropriately.

Image intensifiers must be coupled to the camera in some manner. The two main methods are lens coupling and fiber optic coupling. The principal difference is in the coupling efficiency. Lens coupling is easy, but the transfer efficiency from the phosphor screen to the camera is typically less than 10%. Fiber coupling, however, results in 50–60% transfer efficiency. Lens coupling of image intensifiers is more convenient if the intensifier and camera need to be separated, for example, if either component fails or use the camera alone, without an intensifier.

10.2.4.2 Cameras for image intensifiers

All the camera types described above can be coupled to image intensifiers, although it is rare to couple them to slow-scan scientific cameras. Intensified video CCDs are very popular and are reasonably affordable low-light cameras. The main drawbacks are high noise and low dynamic range (less than 8 bits). The low dynamic range may cause difficulty in trying to find the proper gain settings or may not be sufficient to resolve the details of images with wide variations in signal level. Fixed frame rate and lack of flexibility are limitations, just as with the nonintensified video CCDs. An expensive but attractive option is to couple an image intensifier to a fast-scan scientific CCD. The major advantage of this pairing is the much larger dynamic range of 8–12 bits, which is useful when using high-end intensifiers. This configuration is most commonly seen in high-speed (faster than video rate) applications.

10.2.5 Internal image amplification cameras

The progress in the field of low-light microscopy is inherently connected with the development of more sensitive, fast, and accurate image sensors. Until recently, the use of image intensifiers was the primary choice for low-light-level/high-speed event applications, but recent technological advances in CCD technology are challenging this dogma. The main problem with the use of CCDs in these applications is the increase of read noise with the pixel readout rate (which effectively sets the detection limits) or the need for long exposure times (which limits the time resolution). Intensifiers overcome these limitations by amplifying the signal above the noise level with minimal introduction of additional noise.

10.2.5.1 On-chip multiplication gain (EMCCD)

CCD chips with internal image amplification have been introduced by several manufacturers. These new devices use an "on-chip multiplication gain" technology that allows boosting the photon-generated electron signal directly on the CCD chip. The signal amplification is performed in an additional part of the readout register (inserted before the output amplifier). Electrons collected from each pixel in the CCD are transferred to the extended readout register (also called a gain or multiplication register), where a much higher transfer voltage is applied than is necessary to transfer electrons alone. The electrons are accelerated from pixel to pixel, causing generation of secondary electrons by impact ionization, thereby amplifying the original signal. The generation of secondary electrons is a stochastic process, causing statistical variation in the level of signal amplification. That is, there is gain noise, typically expressed as the noise factor. The noise factor is reported to be from 1.0 to 1.4 (Jarram et al., 2001). It is the multiplier (NF) of the signal (S) in the modified shot noise calculation (shot noise, $N_s = \sqrt{NF \times S}$). The gain of one transfer within the gain register is small (1–1.5%), but with enough pixels in the gain register, the gain can become significant. Gains of several hundreds can be achieved, and they are dependent on the applied voltage, the temperature, and the number of pixels in the gain

register. Gain increases with the applied voltage and number of pixels in the gain register and decreases with the operating temperature. Thus, it is very important to cool the CCD chip, which also fortuitously reduces dark current and dark noise. Although the signal is amplified, the net effect of the gain is to reduce the effect of the read noise. The read noise relative to the amplified signal is decreased. The other most common noise source, the dark current, is amplified with the signal. The net reduction of the read noise, however, cannot be arbitrarily low, as there is another unusual noise source lurking called spurious charge or clock-induced charge. Spurious charge is generated during the charge transfer process. Usually, it is much smaller than the read noise. However, spurious charge effects will add an extra electron to every 10–100 transfers depending on conditions (Jarram et al., 2001).

This new on-chip multiplication gain technology has evolved considerably in the last few years and found utility in applications that demand high readout rate with low incident light, for example in single-molecule fluorescence measurements (Haustein & Schwille, 2004). These nonintensified-light-amplifying cameras do not carry the risk of chip damage from exposure to high-light levels that is a constant threat with traditional external image-intensified cameras.

10.2.5.2 Electron bombardment cameras

A different approach to the problem of internal image amplification is provided in electron bombardment cameras. In a conventional image-intensified camera, electrons produced by photons striking a photocathode are subsequently multiplied by the intensifier and converted back to photons by the phosphor screen at the back of the intensifier. The intensified image is optically transferred to the camera by a lens or a fiber–optic coupling (Fig. 10.5). The electron bombardment technique eliminates the image intensifier (and two-stage conversion of incident light to electrons and electrons back to light) and the optical coupling to the CCD camera. In the electron bombardment camera, the incident light is converted to electrons on the photocathode. These photoelectrons are accelerated directly into a back-thinned CCD by applying a high voltage between photocathode and CCD chip. These accelerated electrons "bombard" the CCD chip and generate multiple electron–hole pairs on the impact that amplifies the initial signal. This process yields gains of over 1000. As a result, the initial image is amplified with similar gain as in the traditional intensifier, but with very much reduced noise (the CCD chip and photocathode are both in a cooled, high-vacuum compartment). The amplified image is also distortion free (because of the relative proximity of the photocathode and CCD chip). In short, this technique has advantages of the traditional intensified cameras but eliminates drawbacks introduced by external image intensifiers. In the past, the use of this technique was severely limited by the short life span of the CCD chip when bombarded by the strong electron beam. However, the new Hamamatsu cameras now have a life span comparable to that of normal CCDs. Even though at this stage of development, electron bombardment cameras are expensive, prices should fall as the market develops.

10.2.6 Color video cameras

Color cameras, designed primarily for the commercial and surveillance markets, are mass manufactured (found in the family camcorder or Webcam) and are often optimized to reproduce the response of the human eye to different colors of light. They are less sensitive than their monochrome counterparts because they must split the incoming light into its different colors, and the extra optics cause some light loss. Normally the light is sent through red, green, and blue filters or, on high-end systems, multiple beam splitters or prisms to separate the color components. Each component is then imaged on a different region of a CCD, or sometimes on three different CCDs. An alternate, less attractive strategy is to image the three colors sequentially, using a filter wheel, and then combine the three images to form a single color image.

Although color video cameras are also not sensitive enough for ultra-low-light-level microscopy, they can sometimes be used with good results for conventional immunofluorescence and FISH. The best models have a minimum sensitivity reaching below 0.1 lux (some advertised even as 0 lux). Although most color cameras have fixed video format (30-Hz frame rate), some offer flexible exposure times, similar to the modified video cameras discussed above. These cameras are cooled to accommodate longer exposure times and may, therefore, prove quite useful in low- to moderate-light applications. The noise and dynamic range are comparable to monochrome video, as color video cameras use the same types of CCDs. The resolution is therefore also comparable (up to about 700×500 pixels), although a few higher resolution models are available. Color cameras are easy to use and normally couple directly to monitors and video recording equipment.[5] Some also offer digital output that can be directly sent to a computer. The color separation schemes used in color cameras are not always optimal for fluorescence microscopy with various fluorescent probes. If multiple indicators must be imaged simultaneously, color cameras may be convenient, but for quantitative fluorescence imaging, it is often better to use monochrome cameras with customized filters.

10.2.7 Digital still cameras

A new alternative for capturing still images is the digital still camera. These cameras are almost always color cameras and are intended to replace traditional photographic cameras. They incorporate a CCD camera into a convenient camera body, often the same body as for film-based SLR cameras. Still cameras are easy to operate, commonly have high resolution (usually $>1000 \times 1000$ pixels), reasonable dynamic range (12 bits typical), and may collect up to several images per minute. The high-sensitivity color versions may just be acceptable for fluorescence microscopy. These cameras were very expensive not long ago, but their commercial popularity has now made their price quite attractive.

[5]Standard video recording equipment has much lower resolution and dynamic range than the camera itself; except for professional video equipment.

10.2.8 SIT cameras

Silicon intensified target (SIT) cameras are built around an image tube rather than a solid state detector. Photons striking a photocathode create photoelectrons, which are accelerated onto a silicon target. The accelerated electrons generate many electron–hole pairs in the target, resulting in the signal amplification of the SIT camera. Charges stored in the target are read out with a scanning electron beam, as in other television tube cameras.

These cameras have significant lag caused by incomplete charge readout of each frame, which effectively results in some degree of on-chip integration or image averaging between frames. This results in visually pleasing images, although it can also be a drawback if high time resolution is needed, such as in ratiometric calcium imaging, where lag produces significant artifacts. When a SIT camera is coupled to a Gen I intensifier, it is called an ISIT camera. This type of camera has very high gain and is suitable for low-light-level video, but as with the SIT camera, the ISIT has little flexibility, and significant lag SIT cameras were fairly popular for video microscopy not long ago and are still available, although for most fluorescence applications they are not competitive with CCD-based devices.

10.2.9 CMOS imagers

The promise of CMOS imaging devices is a single integrated imaging sensor with on-chip processing and control, that is, no external electronics. These devices are similar to CCDs but are far less commonly used in microscopy. The first CMOS imagers were charge-injection devices (CIDs). The CID has an array of pixels, each independently addressed, and differs from CCDs in that electrons in each pixel are not removed by the readout process. The ability to randomly address pixels could be useful for imaging a small area of interest at higher rates. In addition, pixels of the CID can have different image integration times. This allows CID detectors the possibility of obtaining the maximum signal-to-noise ratio for each pixel, even though there may be large differences in light intensity for various pixels. For example, pixels with low-light levels can be averaged on-chip for a longer time, whereas reading out bright pixels before overflow leads to blooming. CIDs have promising characteristics, although they often have high readout and dark noise. The high noise makes them difficult to use for low-light-level imaging.

Another CMOS imager is the active pixel device, developed primarily to overcome the high readout noise of CIDs. An active pixel sensor is a CID with an amplifier at each pixel. These active pixel sensors bring the readout noise to levels comparable to high-quality CCDs. However, an active pixel sensor may still have a large dark current making it difficult to use for microscopy except for high-speed imaging. These devices have low power consumption and are cheap to produce. In many respects (dynamic range, resolution, addressability), CMOS imagers are comparable to or better than CCDs (Golden & Ligler, 2002). However, most current sensors are not well suited to low-light-level imaging. On the other hand, while not yet

available, there is some indication that CMOS cameras may soon become useful for specialized applications in bioimaging such as for high-speed imaging with high dynamic range.[6]

10.2.10 Image acquisition

Electronic cameras do not all have the same output format, and evaluating the image acquisition system is an important part of choosing a camera. The basic objective is to get an image into digital format and read into a computer. Another important consideration is to make sure that the computer will be able to process the data at the required speed; in general, manufacturers will provide information regarding system requirements. For many cameras, such as slow-scan CCDs, cameras with variable integration modes, and cameras with other unique designs (multiple outputs, very high speeds), the manufacturer incorporates a dedicated digitizer as part of the camera system. This is the most desirable performance choice, and it should normally be easy to get the digital image into a computer for whatever processing is necessary. Video cameras, however, usually have an output that can be directly sent to standard equipment such as videocassette recorders. When it is necessary to digitize the signal and import it into a computer for further processing, a frame grabber can be used. Frame grabbers can often be customized to capture analog signals from many different cameras (almost always fast-scan cameras).

There are numerous ways of processing an image once it is stored in digital format. Some basic capabilities can prove useful, such as flat field correction and background subtraction. Flat field correction accommodates nonuniform response in an image. It is normally required even for cameras with uniform response because the illumination or collection may not be uniform. Sometimes additional processing is required just to visualize the data. For example, high-bit depth images do not typically display directly on monitors. They must be rescaled for the normal 8-bit (grayscale) display. Note that this is true even for a 24-bit display because there are 8 bits each devoted to the red, green, and blue channels, thus leaving only 256 possible gray levels displayable. Finally, the most useful data is not always the initial intensity images but rather a combination of images as in ratio imaging, or fluorescence lifetime imaging. Although basic image processing and storage are usually straightforward, it can become quite complicated if interfacing electronics and camera components are not correctly matched. It is therefore sensible to discuss output formats and image handling with manufacturers to avoid headaches after the camera is delivered.

[6]Personal communication, Raymond DuVarney of SciMeasure Analytical Systems. Contact info at www.scimeasure.com.

CONCLUSIONS

The requirements for electronic camera performance are as varied as its diverse applications, particularly those of fluorescence microscopy. Digital camera technology evolves fast. In the last few years, a strong emphasis has been placed on the development of EMCCDs, but other technologies may provide alternatives and better solutions for specific problems.

The information presented in this chapter will hopefully aid the reader in understanding how to appropriately apply the available technology to suit their imaging requirements. A good place to start when evaluating cameras for a particular biological application is to address the following questions: What time resolution and frame rate are required? Is high spatial resolution a priority? How bright is a typical sample?

The answers to these questions can narrow down the appropriate choices considerably. For example, if time resolution and frame rate are of no concern, slow-scan CCDs certainly offer the best available performance, both in terms of the signal-to-noise ratio and their spatial resolution. Slow-scan cameras are thus the first choice for experiments using fixed specimens, such as measurements using immunofluorescence and fluorescence *in situ* hybridization. However, if video rate imaging is required, one need not evaluate slow-scan CCD cameras. A very basic video CCD may suffice if samples are heavily labeled or are not perturbed by high-intensity illumination. When video rate imaging is required for very dim specimens, the EMCCD camera is probably most appropriate at this technological stage. Intensified CCDs provide a unique tool for applications in which high-speed gating is required. The variable integration time video cameras are a very attractive option if one needs to acquire images at video rate acquisition as well as with longer integration times for less bright samples. This flexibility can facilitate many diverse applications with highly varied light levels. Whichever camera type is chosen, it is always best to evaluate the camera performance in the laboratory before making a purchase.

Finally, we reiterate that obtaining quality fluorescence images requires not only a good camera but also optimal optical imaging. By maximizing the microscope light collection efficiency, one can substantially increase the amount of light reaching the camera. This is an important consideration that can greatly benefit any application using fluorescence microscopy.

References

Aikens, R. S., Agard, D. A., & Sedat, J. W. (1989). Solid-state imagers for microscopy. In Y. L. Wang & D. L. Taylor (Eds.), *Fluorescence microscopy of living cells in culture. Part A. Fluorescent analogs, labeling cells, and basic microscopy* (pp. 291–313). New York: Academic Press.

Arndt-Jovin, D. J., Robert-Nicoud, M., Kaufman, S. J., & Jovin, T. M. (1985). Fluorescence digital imaging microscopy in cell biology. *Science*, *230*, 247–256.

Babcock, H. P., Chen, C., & Zhuang, X. W. (2004). Using single-particle tracking to study nuclear trafficking of viral genes. *Biophysical Journal*, *87*(4), 2749–2758.

Bastiaens, P. I. H., & Squire, A. (1999). Fluorescence imaging microscopy: Spatial resolution of biochemical processes in the cell. *Trends in Cell Biology*, *9*, 48–52.

Betzig, E., Patterson, G. H., Sougrat, R., Lindwasser, O. W., Olenych, S., Bonifacino, J. S., et al. (2006). Imaging intracellular fluorescent proteins at nanometer resolution. *Science*, *313*(5793), 1642–1645.

Blom, H., & Gosch, M. (2004). Parallel confocal detection of single biomolecules using diffractive optics and integrated detector units. *Current Pharmaceutical Biotechnology*, *5*(2), 231–241.

Brownlee, C. (2000). Cellular calcium imaging: So, what's new? *Trends in Cell Biology*, *10*, 451–457.

Castleman, K. R. (1993). Resolution and sampling requirements for digital image processing, analysis, and display. In D. Shotton (Ed.), *Electronic light microscopy* (pp. 71–94). New York: Wiley-Liss.

CIE publication 86 (1990). Spectral luminous efficiency function for photopic vision.

Funatsu, T., Harada, Y., Tokunaga, M., Saito, K., & Yanagida, T. (1995). Imaging of single fluorescent molecules and individual ATP turnovers by single myosin molecules in aqueous solution. *Nature*, *374*, 555–559.

Giepmans, B. N. G., Adams, S. R., Ellisman, M. H., & Tsien, R. Y. (2006). Review—The fluorescent toolbox for assessing protein location and function. *Science*, *312*(5771), 217–224.

Golden, J. P., & Ligler, F. S. (2002). A comparison of imaging methods for use in an array biosensor. *Biosensors and Bioelectronics*, *17*, 719–725.

Harms, G. S., Cognet, L., Lommerse, P. H. M., Blab, G., & Schmidt, T. (2001). Autofluorescence proteins in single-molecule research: Applications to live-cell imaging microscopy. *Biophysical Journal*, *80*, 2396–2408.

Haustein, E., & Schwille, P. (2004). Single-molecule spectroscopic methods. *Current Opinion in Structural Biology*, *14*(5), 531–540.

Herman, B., & Tanke, H. J. (1998). *Fluorescence microscopy*. Oxfordshire, UK: Bios Scientific Publishers.

Hiraoka, Y., Sedat, J. W., & Agard, D. A. (1987). The use of a charge-coupled device for quantitative optical microscopy of biological structures. *Science*, *238*, 36–41.

Inoué, S., & Spring, K. R. (1997). *Video microscopy: The fundamentals*. New York, NY: Kluwer Academic.

Jarram, P., Pool, P. J., Bell, R., Burt, D. J., Bowring, S., Spencer, S., et al. (2001). The LLCCD: Low light imaging without the need for an intensifier. *Proceedings of SPIE*, *4306*, 178–186.

Keller, E. H. (1995). Objective lenses for confocal microscopy. In J. B. Pawley (Ed.), *Handbook of biological confocal microscopy* (2nd ed., pp. 111–126). New York: Plenum.

Lakowicz, J. R., & Berndt, K. W. (1991). Lifetime-selective fluorescence imaging using an RF phase-sensitive camera. *The Review of Scientific Instruments*, *62*, 1727–1734.

Marriott, G., Clegg, R. M., Arndt-Jovin, D. J., & Jovin, T. M. (1991). Time resolved imaging microscopy. *Biophysical Journal*, *60*, 1374–1387.

Miura, K. (2001). Imaging and detection technologies for image analysis in electrophoresis. *Electrophoresis*, *22*, 801–813.

In A. Periasamy (Ed.) and American Physiological Society (2001). *Methods in cellular imaging*. Oxford: Oxford University Press.

Ramm, P. (1994). Advanced image analysis systems in cell, molecular, and neurobiology applications. *Journal of Neuroscience Methods*, *54*, 131–149.

Schmidt, T., Schutz, G. J., Baumgartner, W., Gruber, H. J., & Schindler, H. (1995). Characterization of photophysics and mobility of single molecules in a fluid lipid membrane. *The Journal of Physical Chemistry*, *99*, 17662–17668.

Shotton, D. (1993). An introduction to the electronic acquisition of light microscope images. In D. Shotton (Ed.), *Electronic light microscopy* (pp. 1–38). New York: Wiley-Liss.

Shotton, D. M. (1995). Electronic light microscopy: Present capabilities and future prospects. *Histochemistry and Cell Biology*, *104*, 97–137.

Sluder, G., & Wolf, D. E. (Eds.), (1998). *Video microscopy*. San Francisco: Morgan Kaufmann.

So, P. T. C., French, T., Yu, W. M., Berland, K. M., Dong, C. Y., & Gratton, E. (1995). Time-resolved fluorescence microscopy using two-photon excitation. *Bioimaging*, *3*, 49–63.

Taylor, L. D., Woo, E. S., & Giuliano, K. A. (2001). Real-time molecular and cellular analysis: The new frontier of drug discovery. *Current Opinion in Biotechnology*, *12*, 75–81.

Tsay, T. T., Inman, R., Wray, B., Herman, B., & Jacobson, K. (1990). Characterization of low-light-level cameras for digitized video microscopy. *Journal of Microscopy*, *160*, 141–159.

Tsien, R. Y., & Waggoner, A. (1995). Fluorophores for confocal microscopy. In J. B. Pawley (Ed.), *Handbook of biological confocal microscopy* (pp. 267–279). New York: Plenum.

Verveer, P. J., Wouters, F. S., Reynolds, A. R., & Bastiaens, P. I. H. (2000). Quantitative imaging of lateral ErbB1 receptor signal propagation in the plasma membrane. *Science*, *290*, 1567–1570.

Wang, Y. L., & Taylor, D. L. (Eds.), (1989). *Fluorescence microscopy of living cells in culture. Part A. Fluorescent analogs, labeling cells, and basic microscopy*. New York: Academic Press.

Yildiz, A., Forkey, J. N., McKinney, S. A., Ha, T., Goldman, Y. E., & Selvin, P. R. (2003). Myosin V walks hand-over-hand: Single fluorophore imaging with 1.5-nm localization. *Science*, *300*(5628), 2061–2065.

Zhang, J., Campbell, R. E., Ting, A. Y., & Tsien, R. Y. (2002). Creating new fluorescent probes for cell biology. *Nature Reviews. Molecular Cell Biology*, *3*(12), 906–918.

CHAPTER

11 Camera Technologies for Low Light Imaging: Overview and Relative Advantages

Butch Moomaw

Hamamatsu Photonic Systems, Division of Hamamatsu Corporation, Bridgewater, New Jersey, USA

CHAPTER OUTLINE

11.1 Overview 244
11.2 CCD and sCMOS Technologies 245
11.3 Low Light Camera Review 247
11.3.1 Cooled CCD 248
11.3.2 Cooled sCMOS 248
11.3.3 ICCD or IsCMOS 249
11.3.4 Electron Multiplier CCD 250
11.3.5 Summary of Low Light Camera Technologies 252
11.4 Sensitivity 252
11.4.1 What Does "Sensitivity" Mean? 252
11.5 Signal to Noise 255
11.5.1 Signal Shot Noise (N_{shot}) 255
11.5.2 Camera Noise (N_{camera}) 255
11.5.3 Total Noise (N) 256
11.5.4 Noise and Light Level 257
11.6 Comparing Camera Noise in Different Technologies 258
11.6.1 Noise Effects in CCCD Cameras 258
11.6.2 Noise Effects in sCMOS Cameras 259
11.6.3 Noise Effects in Signal Amplification Cameras 260
11.7 DR and Detectable Signal Change 261
11.7.1 Definition of DR for a Camera 262
11.7.2 Definition of DS 262
11.7.3 Increasing DR and DS 263
11.7.3.1 Methods for Increasing Signal 263
11.7.3.2 Methods for Reducing Noise 266
11.8 Required Levels of Signal to Noise 271

Methods in Cell Biology, Volume 114 **ISSN 0091-679X**
Copyright © 2013 Elsevier Inc. All rights reserved.
http://dx.doi.org/10.1016/B978-0-12-407761-4.00011-7

11.9 Sensitivity Comparison 275
11.10 Spatial Resolution Considerations 276
11.10.1 Cooled CCD and sCMOS 277
11.10.2 Intensified Camera 277
11.10.3 Electron Mulitplier CCD 278
11.11 Temporal Resolution Considerations 278
11.11.1 For CCCD, sCMOS, and EMCCD Cameras 278
11.11.2 For ICCD Cameras 278
11.12 Geometric Distortion 279
11.13 Shading 279
11.13.1 Cooled CCD 279
11.13.2 sCMOS 279
11.13.3 Intensified CCD 279
11.13.4 Electron Multiplier CCD 279
11.14 Usability 280
11.14.1 Cooled CCD and sCMOS 280
11.14.2 Intensified Cameras With Video Readout 280
11.14.3 Intensified Cameras With CCCD Or sCMOS Camera Readout 280
11.14.4 Electron Multiplier Cameras 281
11.15 Advanced Technology Nutshell 282
11.15.1 High Sensitivity 282
11.15.2 High Spatial Resolution 282
11.15.3 High Temporal Resolution 282
11.15.4 Convenience 283
Acknowledgments 283
Reference 283

Abstract

"Camera Technologies for Low Light Imaging" is designed to offer the reader a summary of the current camera choices for low light imaging with special emphasis on the practical aspects related to each. Four major camera technologies, cooled charge-coupled device, cooled sCMOS, intensified cameras, and electron multiplier cameras, are discussed and compared. Supporting information about noise characteristics of photoelectrons and camera noise are provided and used for illuminating the practical aspects of using these cameras.

11.1 OVERVIEW

Electronic imaging has become an important tool in the area of biological sciences due to many advantages of modern detectors compared with the human eye. These advantages offer great benefits to scientists and researchers.

- The flexibility of imaging detectors enables one to observe objects that are too dark or too bright to be seen by the unaided human eye.

- The spectral sensitivity of the human eye is limited from 400 to 700 nm. The spectral sensitivity range of imaging detectors is wider, offering observation and acquisition of images over the range from X-ray to infrared wavelengths.
- The intensity discrimination of the human eye is narrow (about 20 gray levels) compared with that of a camera. Electronic detectors offer up to a 64,000 gray levels of intensity discrimination if the signal level is sufficient.
- The human eye cannot follow an object if it moves too fast or too slow. Modern detectors can capture images in time ranges from femtoseconds to hours and compress or expand real-time events into a time scale that is meaningful for human observation.
- Images can be analyzed to characterize the objects.
- Images can be stored in electronic formats for future reference and quantitative analysis.
- Images can be modified to reveal information that cannot be observed with the human eye.

To meet to the requirements of modern science, a variety of imaging detectors are available. Currently, charge-coupled device (CCD) and complementary metal oxide semiconductor (CMOS) detectors are the two most common choices for scientific imaging. Advanced CMOS detectors with the trade name sCMOS are becoming the first choice for scientific imaging and will be described in this chapter.

Special methods of imaging are needed for low light imaging, that is, when the available light intensity (signal) at the detector decreases to a level that approaches the average noise of the detection system. The ratio of the amount of signal collected to the amount of noise in the system is called the signal-to-noise ratio (SNR). Achieving a suitable SNR is the goal of all low light cameras, and there are many methods and technologies available for this purpose but the four most common technologies are cooled CCD (CCCD), cooled sCMOS (CsCMOS), intensified CCD (ICCD) or intensified sCMOS (IsCMOS), and electron multiplier CCD (EMCCD).

11.2 CCD AND sCMOS TECHNOLOGIES

A brief review of CCD technology and sCMOS technology is helpful in understanding how low light imaging schemes work and what noise sources must be overcome as well as in understanding signal amplification devices that rely on these basic technologies.

A CCD device converts photons to electrons in an array of photodiodes and stores the resulting charge in each pixel of the array. When readout of the pixel charges occurs, a high-voltage gate is opened between each row of pixels and the charges from each row are transferred to the row below in a few microseconds. The very bottom row of pixels is transferred to a serial register. In the serial register, charges are then transferred horizontally to the readout amplifier where they are converted to a voltage and then sent to the digitizer. This process is repeated until all rows of the device have been read out (see Fig. 11.1).

This process requires that a CCD camera provides several different voltages to the chip; a timing generator is needed and the readout amplifier must operate in

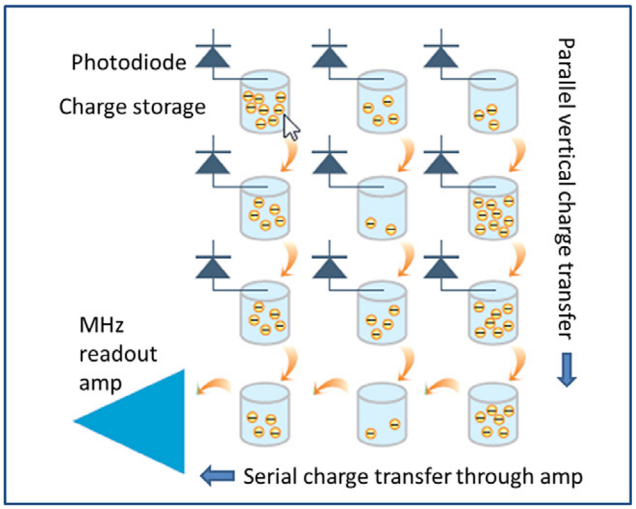

FIGURE 11.1

CCD readout.

the 10- to 40-MHz range if reasonable frame rates are required. The additional components needed to operate a CCD detector increase cost, complexity, and heat in a CCD camera. As the speed of the readout amp increases, the readout noise increases and this sets the limit for low light detection when a CCD is used alone.

An sCMOS device shares little with a CCD device beyond the photodiode converting photons to electrons in a pixel. While the charge from this conversion is stored in the pixel, it is immediately converted to a voltage by an amplifier in the same pixel. Rather than store and move a pixel charge through the device, a CMOS camera can just turn on or off transistors to move the voltage in the pixels through the device, similar to turning on and off light switches in a home. In an sCMOS device, readout of the signal is done in either a "Global Shutter" mode or a "Rolling Shutter" mode, and some models include both modes. There are numerous articles about each of these modes and the advantages and limitations associated with them, but a detailed analysis is beyond the scope and space limitations of this chapter. In short, the Global Shutter mode offers simultaneous exposure of all the pixels but reduces readout rates by 50% compared with the Rolling Shutter mode and increases both dark current and readout noise. The Rolling Shutter mode offers the fastest readout rates and lowest dark current and lowest readout noise but each horizontal row of pixels in the image has a sequential exposure leading to a time shift of a few microseconds between each row. Practical experience with these devices indicates that the time difference is not detectable in most biological microscope applications but the user should try the device with a typical sample for evaluation.

Readout of the sCMOS device involves simply switching on the transistors in each horizontal row of pixels, each of which is directly connected to a line that leads to a correlated doubling sampling amplifier below each column of pixels. Having a

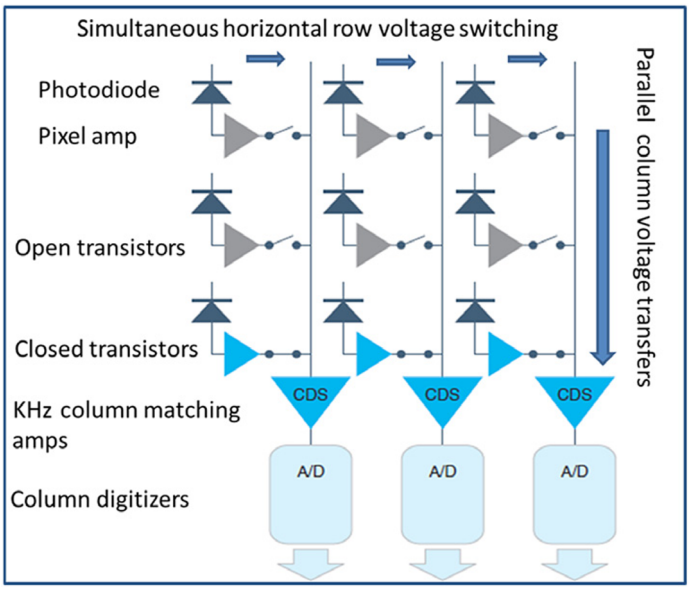

FIGURE 11.2

sCMOS readout.

separate amplifier for each column means that there are as many amplifiers as there are horizontal pixels in the array, and the pixel clock rate for each column needs to operate only in the KHz range rather than in the MHz range of a CCD. This slower clock rate greatly reduces the readout noise compared with a CCD while offering frame rates at least 50 times faster than a CCD.

Additional benefits of the sCMOS camera include having a digitizer for each column built onto the chip, larger pixel formats for larger fields of view, smaller and less expensive camera heads, and low power and cooling requirements (see Fig. 11.2 for details).

It should be mentioned that comparing "readout noise" between CCD and CMOS cameras is not a simple endeavor. CCD cameras are simple to measure using pair of images and a typical root mean square calculation as all pixels share a common amplifier. CMOS cameras have thousands of amplifiers running in parallel so it is necessary to measure the readout noise of each pixel from a hundred or more images and plot the distribution of all the pixels.

11.3 LOW LIGHT CAMERA REVIEW

For low light applications, there are four types of cameras commonly available.

- Integrating CCCD
- Integrating CsCMOS
- ICCD or IsCMOS
- EMCCD

11.3.1 Cooled CCD

The CCCD camera uses just a CCD chip, similar to a high-light-level camera. In this device, chip design and materials selection are optimized to increase signal collection efficiency and reduce camera noise factors, so exposure integration can be used to accumulate the signal over time. Reducing camera noise is a key requirement in making this device useful for low light images. Lowering the temperature of the CCD in a hermetic vacuum chamber greatly reduces the dark current component of the camera noise and slowly reading out the accumulated signal minimizes the readout noise component of the camera noise to levels of 3–8 electrons depending on the pixel clock speed (see Fig. 11.3). CCD cameras with 1 or 2 million pixels typically readout 10–20 frames per second (fps) at 6–8 electrons of readout noise. This requires the readout amplifier to run at 15–40 MHz.

When frame rate is not the key requirement, integration with a CCCD provides the best *S/N* ratio in an image since the primary noise source is the signal shot noise itself once the readout noise is overcome. CCCDs will produce an image with a good SNR, good intrascene dynamic range (DR), and clean backgrounds. The intrascene DR is limited only by the full-well capacity (FWC) of the CCD at the bright end of the scale and the camera noise at the low light end of the scale.

11.3.2 Cooled sCMOS

The CsCMOS camera is similar in design to a CCCD camera but with an sCMOS chip in place of the CCD chip. The camera can be smaller due to the simpler requirements of an sCMOS chip but the cooled hermetic vacuum chamber offers the same benefit of reducing the dark current. Figure 11.3 is representative of both cameras at this point.

Beyond the dark current values, sCMOS cameras excel at low readout noise at high frame rates due to the multiple, low-speed column amplifiers. It is common to see camera formats with 4–5 million pixels reading out at 100 fps with less than 2 electrons of readout noise since the individual column amplifiers need to run only at 60–80 KHz in this device.

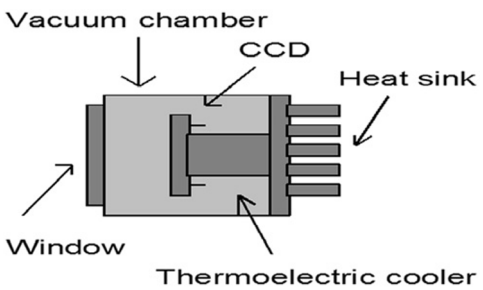

FIGURE 11.3

Cooled CCD.

Depending on the number of transistors in the pixel of an sCMOS camera, a pixel with the same spatial dimensions as a similar CCD chip may have twice the FWC. This increased signal capacity and much lower readout noise translates into huge DR capabilities in sCMOS compared with a CCD.

There is almost always a trade-off when getting new and better features in a detector, and in the case of sCMOS, the trade-off is in the form of fixed pattern noise due to pixel gain fluctuation (the small differences between all of the individual pixel amplifiers). Although the median readout noise of the pixels in an sCMOS device is very low, there are always a few pixels with higher readout noise and this results in a noise that is related to the signal level in the pixels. When the signal levels are low or even in the midrange of the FWC, this noise is so small that it is undetectable. When signal levels approach the maximum FWC, the noise can be detected statistically. Compared with a CCD camera, an sCMOS camera performs better at very low light levels but may have higher noise at higher light levels but at those levels a similar CCD would be saturated due to the inherently smaller FWC of the CCD.

11.3.3 ICCD or IsCMOS

An intensified camera uses an image intensifier (II) coupled to a CCD or an sCMOS camera. The II is a vacuum tube device that converts incoming photons into electrons at the photocathode, multiplies the electrons with high voltage acceleration through a microchannel plate, then reconverts the multiplied electrons back to photons at a phosphor-coated window.

The photons emitted at the phosphor-coated window are then projected onto a CCD or an sCMOS camera through a relay lens set or a fiber optic plate (FOP; see Fig. 11.4A and B).

The advantage of the relay lens coupling is flexibility. It is possible to remove the camera or change it for a different model but the efficiency of the lenses is only a fraction of the efficiency of a FOP. The advantage of the FOP is much greater efficiency but the camera must be cemented to the fiber optic and there is no way to remove it for other purposes.

Either configuration enables one to observe a low light image by amplifying the original signal to a great extent (tens of thousands of times are possible) compared with the noise of the camera. Although the multiplication process adds some small noise to the total camera noise, the overall gain in the signal level helps separate the signal from the camera noise by reducing the "relative readout noise" of the camera compared with the "multiplied signal." This technology provides full frame, rapid imaging at low light levels with the frame rate limited only by the readout camera and the number of photoelectrons per frame time. Very short exposures for stop action are another feature of ICCD cameras since the photocathode or the MCP can be turned on and off very quickly to provide "gating" of the electron conversion or multiplication. Even with slow readout cameras, the effective exposure time can be only a few nanoseconds.

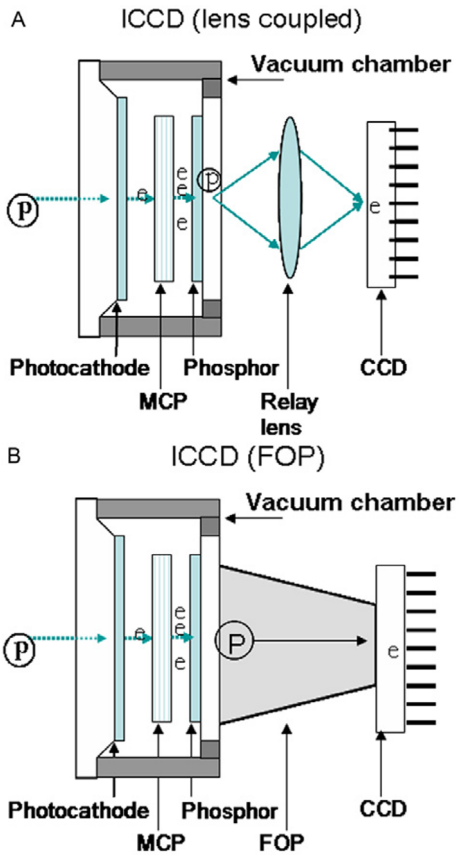

FIGURE 11.4

Coupling methods in Intensified cameras.

Intrascene DR is limited due to the high gain. As the gain is increased, the signal levels in the brightest and dimmest portions of the image, the intrascene DR, will each be multiplied, and the difference will also become greater. At the point where the difference is greater than the DR of the coupled detector, the intrascene DR starts to decrease due to saturation of the CCD or sCMOS detector or saturation of the phosphor screen within the intensifier.

High light levels may damage the intensifier photocathode and microchannel plate so the ICCD is not suited to bright-image applications.

11.3.4 Electron multiplier CCD

EMCCD cameras have become the most popular choice for low light imaging when fast frame rates are required or where both high and low light imaging is required. For very fast frame rates, the binning (summation of adjacent pixel charges) and subarray

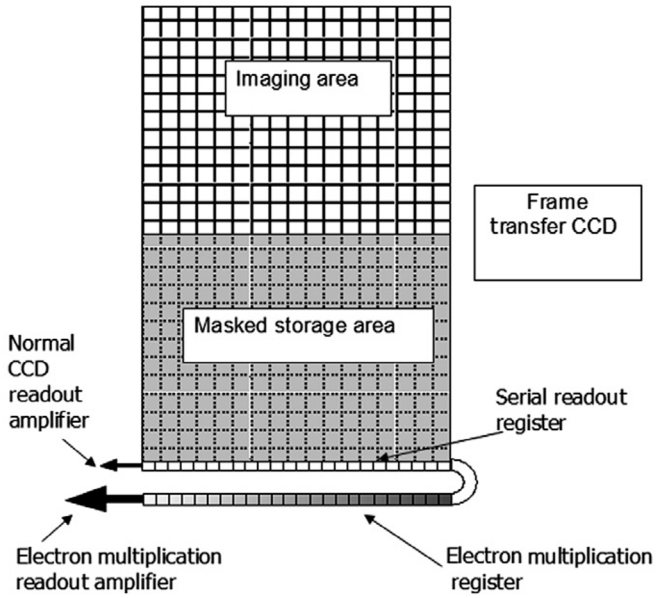

FIGURE 11.5

Electron multiplier CCD.

(selected region of pixels) functions can be used to reach frame rates in the range of several 100 fps.

This type of camera employs "impact ionization" for signal amplification but no vacuum tube or photocathode is required. A frame-transfer CCCD is used, and a special multiplication register is added between the image storage area and the readout amplifier. In this special register, a large voltage (30–50 V) is applied to each of the 400–500 stages in the register as the signal is transferred through the register resulting in an extra electron being occasionally generated through a process called "impact ionization" within each stage of the register (see Fig. 11.5). From this sequential multiplication, more than a thousand times signal gain can be realized before the amplified signal reaches the readout amplifier. Compared with the original camera readout noise, this multiplication of the signal reduces the "relative readout noise" to undetectable levels. Additional noise factors are introduced however and the signal noise itself is increased slightly. This additional noise limits the statistical accuracy of measurements and reduces the "effective quantum efficiency (QE)" of the device by 50%, but the trade-off for speed is often acceptable. The intrascene DR is reduced in proportion to the gain applied when the gain register is used due to saturation within the multiplication register itself.

It is also possible to use this camera and bypass the multiplication register to create low light images by integration like a normal CCCD and in very bright situations as well. This is a major advantage over intensified cameras when a multipurpose

camera is required although the readout noise in this operating method is much higher than most other low light cameras.

Some attention to input light levels is still required however. When the EM gain is employed, a phenomenon called Gain Aging occurs and results in declining gain factors over time. The high voltages used in the multiplication register and the number of electrons in the original signal combine to create the loss of gain. Although the true cause of this is currently not known for certain, the general opinion of engineers studying this is that the impact ionization process traps electrons in the device and reduces the available gain. To reduce the rate at which this happens, it is good practice to reduce the gain to the EM register and reduce or eliminate light to the device when not actually imaging a sample.

11.3.5 Summary of low light camera technologies

Even though the main goal of all these different kinds of cameras is higher sensitivity (better SNRs) at low light levels, each has different characteristics that may be seen as advantages or disadvantages when they are used in low light applications. There is no simple answer to the question which is better. It is often necessary to look at the application, construct a prioritized list of requirements, and make a comparison between the benefits of each type of camera. In this manner, it is possible to make an educated choice from the large selection of cameras available.

11.4 SENSITIVITY

Sensitivity is one of the most often requested characteristics for low light cameras. The word "sensitivity" can be used to describe a number of different properties of a camera. This often creates some misunderstandings about "high-sensitivity cameras." Depending on the application, "high sensitivity" may mean the ability to detect a small signal or the ability to detect a small change in a signal. While this difference may not seem like much at first, there is a tremendous difference in the camera specifications to meet each of these requirements.

11.4.1 What does "sensitivity" mean?

- A brighter image on the display monitor?

We naturally think that a highly sensitive camera generates a brighter image compared with a less sensitive camera. Brightness of the image on a monitor screen is an important factor for the human eye to recognize the image; however, it is not an accurate way to judge sensitivity. Monitor controls need to be properly adjusted to see the full range of intensities or some bright or dark portions of the image may be lost to view. If camera noise and the signal are similar in intensity, no amount of brightness will make the signal appear separately from the noise.

- A larger gray level value in the captured image?

The seemingly logical conclusion that a larger value in the gray level scale means more sensitivity in the detector is a very common misconception. The gray level

value is really just an undefined value from the digitizer and so requires knowledge of how the digitizer and the signal are related. The digitizer simply divides the signal (in electrons) into some number of gray levels. It is possible for each gray level to represent any number of actual electrons, so it is important to multiply the gray level values in an image by the electrons/gray level conversion factor. In CCCDs, one photon in the signal is converted to 1 electron in the CCD, but the digitizer is set up to use some specific number of electrons to equal one gray level in the output. This conversion number is variously referred to as the "conversion efficiency (CE)," "analog to digital unit," or "digitizer count (DC)." You may find a lower gray level number that represents more real signal collected when comparing "sensitivity" in this manner! A helpful interactive tutorial on CE can be found at the Hamamatsu learning site (http://learn.hamamatsu.com/tutorials/flash/conversionefficiency/index.html, accessed January 2013).

For example, compare two cameras using the same sample and same illumination level. If the two cameras have the same field of view or the optics are adjusted to provide the same field of view to both cameras, then the light level per pixel at the detector will be equal for both cameras. Camera "A" has 20,000 electrons FWC and Camera "B" has 15,000 electrons FWC. Both cameras are using 12-bit digitizers with 4096 gray levels and the digitizer offset (Zero signal input level in the digitizer) is 200 gray levels. The number of electrons per gray level is calculated by dividing the FWC by the number of gray levels available in the digitizer. See Formula (11.1)

$$\mathrm{CE(e/gl)} = \frac{\mathrm{FWC(e)}}{\mathrm{Bit\,depth(gl)} - \mathrm{dig\,offset(gl)}} \tag{11.1}$$

Camera "A" 20,000 e/4096 gl = 5.1 e/gl

Camera "B" 15,000 e/4096 gl = 3.8 e/gl

As illustrated in Table 11.1, the "sensitivity" of both cameras is the same. Each collected the same number of electrons, but the displayed gray level is different. Camera "B," with fewer electrons per count will indicate more gray levels in the same time than Camera "A." Although the gray level seems to indicate that it acquired more signal, there was no real difference. The advantage of Camera "A" is that is can acquire more total signal and the accuracy in every gray level is greater. The advantage of Camera "B" is that it will offer finer discrimination between adjacent gray levels but the precision will not be as good as Camera "A." It is important to find and subtract the digitizer offset of each camera to get the actual CE. The digitizer offset can be found by taking the shortest possible exposure with the camera when absolutely no light is falling on the chip. The mean value from this image represents zero intensity and this is the digitizer offset for the camera.

- A better SNR?

If we consider that an image consists of signal and noise, we cannot recognize a signal smaller than the noise. Suppose we try to compare sensitivity between two cameras, one generates higher signal than noise and the other generates lower signal than noise. In this case, we can say that the former camera is more sensitive than the latter. In other words, the ratio of signal to noise indicates "sensitivity." So, it would seem that a better SNR would be a good indication of low light sensitivity but is this really so?

Table 11.1 Real Sensitivity Comparison, Cameras with Equal Pixel Size

Camera	FWC (Electrons)	Bit Depth (2^{Bits})	Gray Levels at Bit Depth	Digital Offset	Available Gray Levels	Conversion Efficiency	Measured Gray Level	Actual Signal Acquired
A	20,000	12	4096	200	3896	5.1	500	2567
B	15,000	12	4096	100	3896	3.8	684	2568

11.5 SIGNAL TO NOISE

Signal-to-noise ratio: SNR is expressed by a very simple formula. Simply divide the detected signal (S electrons) by the total noise (N electrons). See Formula (11.2).

$$\mathrm{SNR} = \frac{S}{N} \tag{11.2}$$

Signal: S (electrons) is calculated by multiplying the input light level I (photons/s), the QE (electron/photon) of the detector, and the integration time T (s) as in Formula (11.3).

$$S = I \cdot \mathrm{QE} \cdot T \tag{11.3}$$

11.5.1 Signal shot noise (N_{shot})

The minimum unit of light is a photon. As photons create electrons in each pixel of the detector, the distribution in the number of electrons is equal to the distribution of the number of incoming photons and is considered to be a Poisson distribution. In a given amount of time, repeated measurements of the number of electrons result in an average "intensity" with a Poisson distribution of intensities around that average. This distribution can be thought of as a normal fluctuation of the average and represents the statistical noise of the average signal. This statistical noise is called signal shot noise N_{shot}

From the signal S (electron) the signal shot noise N_{shot} is calculated using Eq. (11.4) for most CCDs.

When calculating the signal shot noise of an EMCCD or ICCD, there is an additional noise factor that must be included. Since the original signal must pass through the multiplication process (ICCD) or register (EMCCD), the multiplication noise, called excess noise factor (F) created by the additional uncertainty of the multiplication process, must be squared and multiplied by the signal using Eq. (11.4a).

$$N_{\mathrm{shot}} = \sqrt{S} \tag{11.4}$$

$$N_{\mathrm{shot}} = \sqrt{S \times F^2} \tag{11.4a}$$

11.5.2 Camera noise (N_{camera})

There are two major sources of camera noise. One is camera read noise N_{read} (electrons) created when the signal is read from a detector and converted to a voltage signal. Camera read noise N_{read} is independent of temperature and is normally constant at a given readout speed. The other is camera dark noise N_{dark} (electrons) which is the fluctuation of the dark current D (e/pix/s) generated in the CCD or sCMOS substrate. The total dark current is the function of the integration time T (s) and the rate at which

dark current D is generated. From Eq. (11.5), the dark noise can be seen to be the square root of the dark current in standard CCDs, ICCDs, and sCMOS.

$$N_{\text{dark}} = \sqrt{D \cdot T} \tag{11.5}$$

For EMCCDs, the dark current is multiplied in the multiplication register by a factor (M) and the multiplication noise, called F created by the additional uncertainty of the multiplication process as in Eq. (11.5a).

$$N_{\text{dark}} = \sqrt{F^2 \cdot M^2 (D \cdot T)} \tag{11.5a}$$

Camera noise N_{camera} (electron) is calculated using Eq. (11.6) for most CCDs.

For EMCCDs, again there are additional noise factors that must be included. During the transfer process of the signal from the imaging area to the storage area, there is some additional noise created called clock-induced charge (C), noise, and the excess noise from the multiplication register (F) that must be included. Since the electrons from all sources on the CCD pass through the multiplication register, a factor (M) must be included as shown in Fig. 11.6A.

$$N_{\text{camera}} = \sqrt{N_{\text{read}}^2 + N_{\text{dark}}^2} \tag{11.6}$$

$$N_{\text{camera}} = \sqrt{F^2 \cdot M^2 [(N_{\text{dark}}) + C]^2 + [N_{\text{read}}/M]^2} \tag{11.6a}$$

11.5.3 Total noise (*N*)

Total noise N (electrons) is the square root of the sum of the noise generated by the camera and the noise that is a component of the signal itself. The combination of both noise terms becomes the total noise (N).

Total noise is the combination of signal shot noise N_{shot} (electron) and camera noise N_{camera} (electron) and is calculated using Eq. (11.7). From this calculation, it becomes evident that total noise (N) is only found in an image.

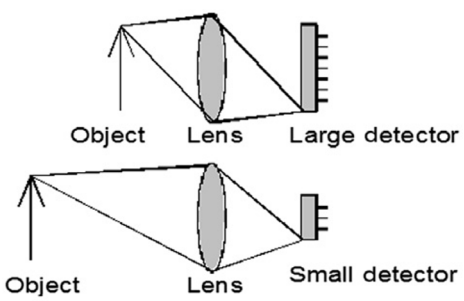

FIGURE 11.6

Larger detector shortens the distance and results in higher light collection efficiency.

$$N = \sqrt{N_{\text{shot}}^2 + N_{\text{camera}}^2} \tag{11.7}$$

Interestingly, in the very latest low-noise EMCCD and sCMOS cameras, camera noise has dropped to less than 1 or 2 electrons so optical noise in the microscope has become the limiting factor in low signal detection. Internal light leaks, internal reflections, and ambient stray light have to be considered as serious issues and cannot be neglected. A deep discussion of the effects of small noise terms on both sCMOS and EMCCD cameras used for super resolution (Long, Zeng, & Huang, 2012) was recently published and is recommended to those interested in more details.

11.5.4 Noise and light level

Chart 11.1 shows the camera noise, signal shot noise, and total noise based on the light level using a constant exposure time. Under these conditions, camera noise stays the same at all light levels but signal shot noise increases with the light level increase. In lower light levels, camera noise is higher than signal shot noise and total noise is determined primarily by camera noise. In higher light levels, signal shot noise is higher than camera noise and total noise is determined primarily by signal shot noise. The large arrow indicates the point at which the major noise component switches over from camera noise to signal shot noise, about 200 photons for this camera under these conditions. In other words, the camera noise is an important factor in

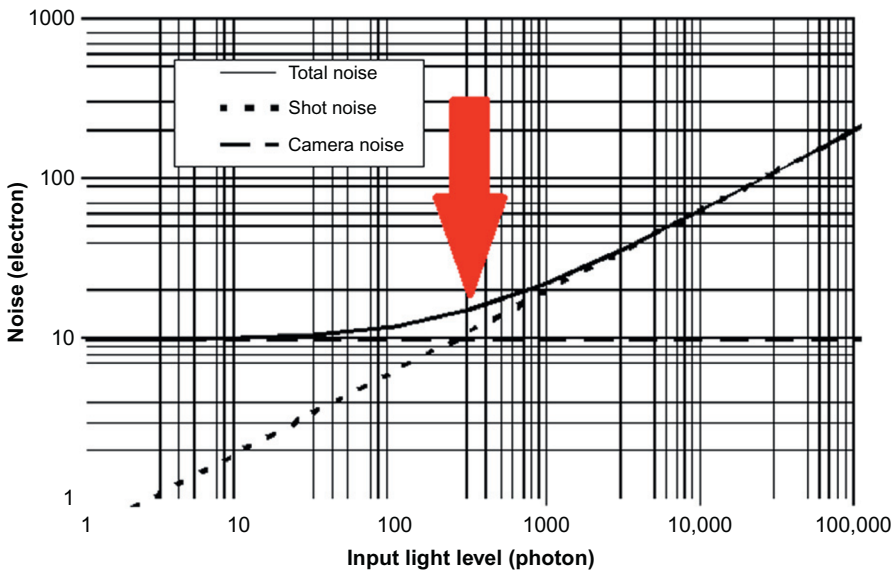

CHART 11.1

Noise versus light level (camera noise = 10 electrons, QE = 0.4).

Table 11.2 Camera Noise is a Better Indicator than S/N for Low Light Cameras

Camera	Full Well Cap. (Electrons)	Camera Noise (Electrons)	*S/N* Ratio	Low Light Use?
A (60% QE)	100,000	100	1000:1	No
B (60% QE)	20,000	20	1000:1	Yes

achieving higher SNR only in low light situations. If you know the properties of any camera, it is easy to construct a similar graph for that camera at a particular wavelength to determine how much signal is required with that camera to overcome the camera noise limitations. When the signal shot noise becomes dominant, the imaging system is said to be "signal shot noise limited" and the camera noise terms become negligible in the equations and images.

From this chart, we can also learn the secret to detecting small signals. We need minimum camera noise and maximum QE, so we can become limited only by the signal noise at lower light levels. An interactive version of this chart is available on the Hamamatsu learning Web site (http://learn.hamamatsu.com/tutorials/java/noisegraph/, accessed January 2013).

The SNR of a camera by itself is not indicative of the ability to detect small signals. This is illustrated in Table 11.2 by comparing two cameras with different characteristics but with the same SNR. The low noise is more important than the FWC.

11.6 COMPARING CAMERA NOISE IN DIFFERENT TECHNOLOGIES

If a "perfect camera" were available, it would have no noise and the noise of the signal would be the only noise source. Such a camera would make a good standard with which to compare other technologies to see what the noise of the camera has to do with the total noise in an image and detection limits. For the purposes of such a comparison, Charts 11.2–11.4 show how each camera technology and the noise associated with that technology change the total noise characteristics in images taken at light levels between 1 detected photon and 30,000 detected photons, assuming the QE of all the systems is the same. In reality, the QE of each cameras is different and there is no perfect camera.

11.6.1 Noise effects in CCCD cameras

For the calculations in Chart 11.2, it is assumed that the saturation level of the CCD is about 20,000 electrons and readout noise is the only significant camera noise source which is typical for a modern CCCD camera. Compared with a perfect camera where the noise of the signal is equal to the square root of the signal at all light levels we see that having 6 electrons of readout noise means that we need about 40 photons of signal to reach the region where shot noise and read noise have equal contributions and about 250 photons to be completely signal shot noise limited.

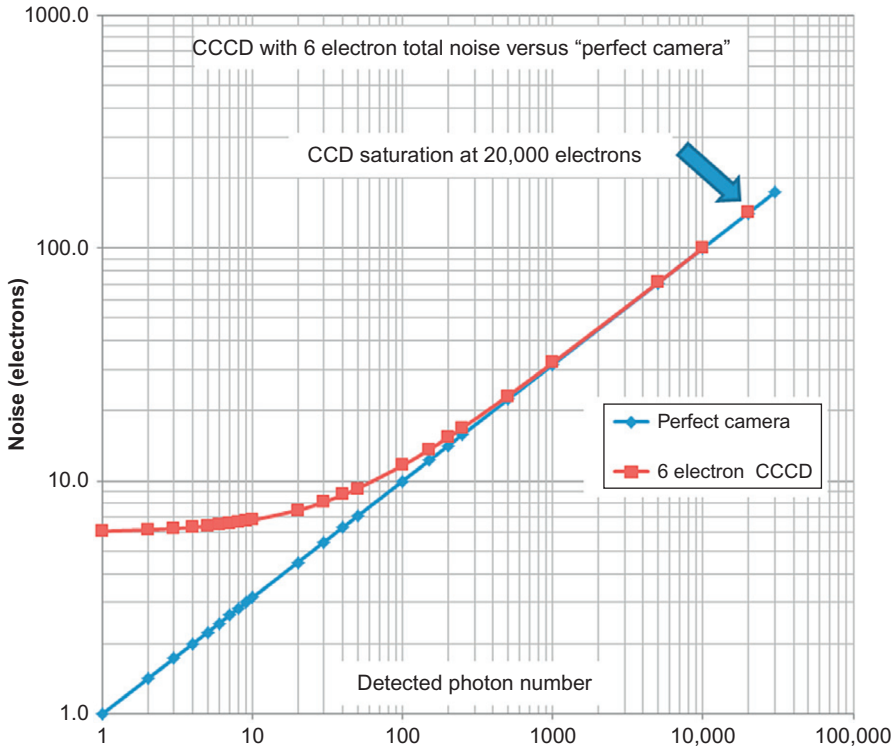

CHART 11.2

Noise effects in a CCCD with 6 electrons readout noise.

Since Chart 11.2 is calibrated in electrons, the effect of noise is more apparent than it would be in a typical digital camera since the signal would be digitized. In the digitization process, the CE of the digitizer limits the resolution of the chart. For example, a typical CCD camera with a FWC of 20,000 electrons would have a 12-bit digitizer and a CE of about 4.5 electrons per DC. To increment the DC by 1 requires a signal change of 4.5 electrons so that the digitizer would not see any change in the total noise over the readout noise until the total noise reached 10.5 electrons, (6 electrons readout noise plus 9 electrons of detected signal) $10.8 = \sqrt{6^2 + 9^2}$. For a detailed description of digitization of images, there are numerous sources including Chapter 18.

11.6.2 Noise effects in sCMOS cameras

In Chart 11.3, the noise of the signal in a perfect camera is again equal to the square root of the signal at all light levels. In the sCMOS camera, we see the readout noise is small so we need only about 20 photons of signal to reach the region where shot noise dominates

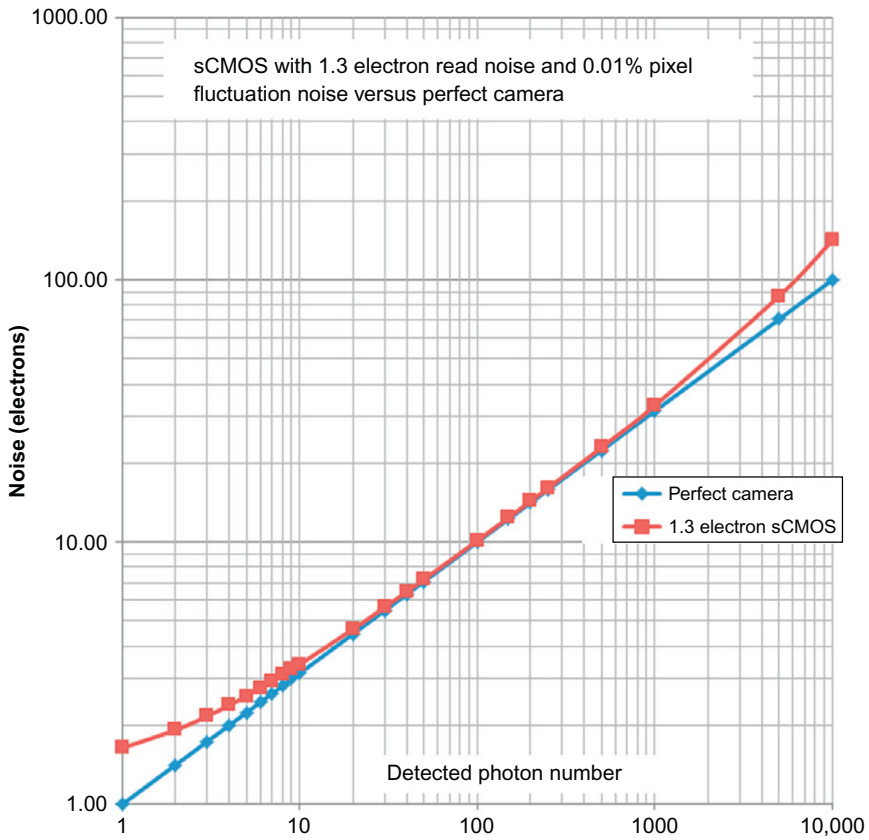

CHART 11.3

Noise effects in sCMOS cameras.

and about 30 photons to be almost completely shot noise limited until the signal becomes very bright. At intensity values above 1500 photons in this example, the pixel fluctuation noise of about 0.01% begins to become evident. In this chart, we make the assumption that only read noise, signal noise, and pixel fluctuation noise are present.

11.6.3 Noise effects in signal amplification cameras

Chart 11.4 assumes that the QE of both cameras is the same and compares the perfect camera to an EMCCD camera. Since the EM camera has gain, the readout noise value depends on the gain. In this calculated chart, it is assumed that at a gain of 100, the readout noise is 1 electron, and at a gain of 1000, the readout noise is undetectable. Another assumption in this calculation is that the maximum linear FWC of the multiplication register is 100,000 electrons, so the original signal, when multiplied by the

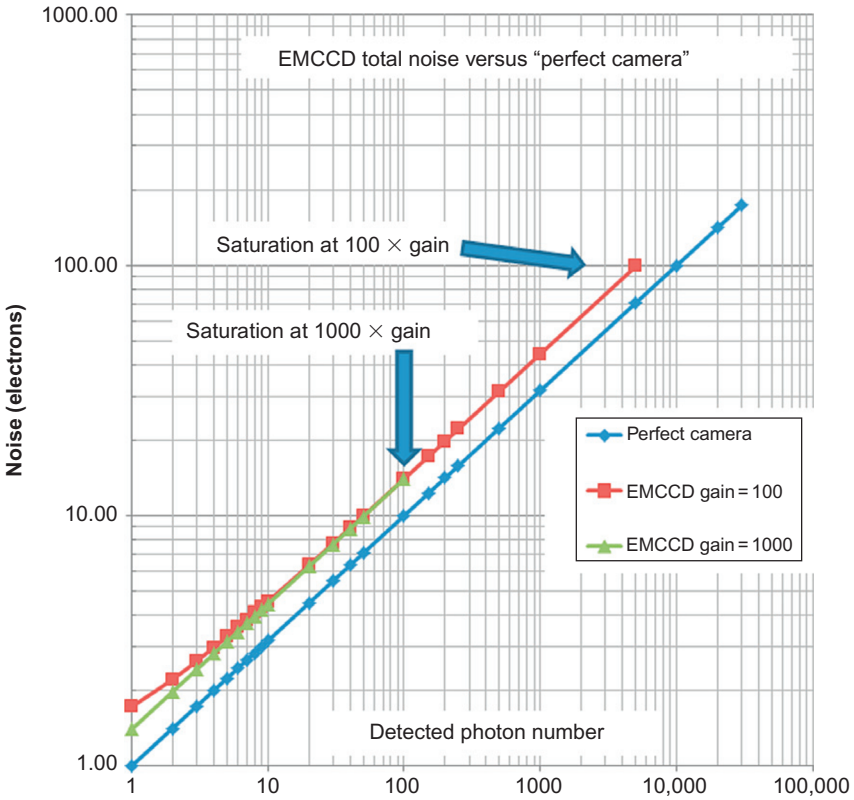

CHART 11.4

Noise effects in EMCCD cameras.

gain factor, must be less than 100,000 electrons, thus the DR of the original signal is limited as shown when gain is applied.

We observe that at gain 100, the readout noise of 1 electron makes little difference after the signal level is greater than10 photons but the multiplication noise (F) increases the signal noise at all levels. This increase in signal noise is equivalent to reducing the QE of the detector by 50%. To understand this, compare the two cameras at 100 photons input. The noise of the signal is 10 electrons in the perfect camera but 14 electrons in the EMCCD at both gain settings, equivalent to the noise of $\sqrt{200}$ photons of signal.

11.7 DR AND DETECTABLE SIGNAL CHANGE

DR and detectable signal change (DS) are important but completely different characteristics for low light cameras. DR indicates the ratio of the brightest to the darkest signal that can be detected in the same scene, and DS defines the precision of a

change in the signal level. Neither is a measure of the sensitivity to low light levels however.

11.7.1 Definition of DR for a camera

The DR of a CCD camera is defined by the ratio of camera noise N_{camera}, which limits the lowest signal detectable, and saturation SAT, which is equivalent to the FWC, and represents the highest signal detectable.

$$\text{DR} = \frac{\text{SAT}}{N_{\text{camera}}} \tag{11.8}$$

The DR is a ratio of the electrons of signal to the electrons of camera noise. The signal is assumed to equal the FWC (saturation level) of the CCD. It will be obvious that the result of Eq. (11.8) is the same as the SNR from Eq. (11.2) for the camera. Significantly, unless the values for SAT and N_{camera} are in electrons, the true meaning of the term cannot be defined.

The term DR is often confused with the number of gray levels in the digitizer but these are not equivalent. A digitizer will divide the DR up into as many gray levels as desired, but the DR is not altered. As more gray levels are created from the same number of electrons, the accuracy of each gray level is diminished, but the DR is not affected unless the digitizer saturates before the FWC is reached.

For example, 8-bit conversion gives 256 gray levels and 12-bit conversion gives 4096 gray levels. However, the original DR is unchanged, just divided into a different number of gray levels. If this done with the same FWC, then each gray level represents fewer and fewer electrons as bit depth is increased.

The DR defined by Eq. (11.7) is useful information when the application requires one to image bright and dark objects in the same scene. However, if the application requires one to see a small signal in a bright background or measure a small fluctuation in a bright signal, Eq. (11.7) will not provide an accurate value for the minimum DS.

11.7.2 Definition of DS

Since a camera has a maximum FWC, it is possible to calculate the maximum DS potential of the camera using Eq. (11.9) since FWC and SAT are the same.

$$\text{DS} = \frac{\text{SAT}}{N_{\text{SAT}}} = \frac{\text{SAT}}{\sqrt{\text{SAT}}} = \sqrt{\text{SAT}} \tag{11.9}$$

In the cases where the signal level is below the saturation level of the camera but above the camera noise, then the DS is calculated using just the number of electrons in the signal divided by the noise of that signal as in Eq. (11.9a). To find the number of electrons in the signal, it is always necessary to multiply the indicated gray level by the number of electrons in each gray level (CE) and subtract the digitizer offset of the camera.

$$\mathrm{DS} = \frac{\mathrm{SIG}}{N_{\mathrm{SIG}}} = \frac{\mathrm{SIG}}{\sqrt{\mathrm{SIG}}} = \sqrt{\mathrm{SIG}} \tag{11.9a}$$

Example: Camera with 100,000 electrons FWC, 10 electrons camera noise. Compare DR and DS using Eqs. (11.10) and (11.11)

$$\mathrm{DR} = \frac{\mathrm{SAT}}{N_{\mathrm{camera}}} = 10,000 \tag{11.10}$$

$$\mathrm{DS} = \sqrt{\mathrm{SAT}} = 316 \tag{11.11}$$

In this case, it is only possible to detect a signal change of one part in 316 (0.3%) compared with the DR of 10,000:1.

From Eqs. (11.10) and (11.11), we learn the secret to high sensitivity to small changes in signal levels. The major requirement is large FWC and enough signal to fill the statistical requirements for percentage change desired.

Comparing again the same two cameras from Table 11.2, we see the importance of FWC to DS in Table 11.3. Camera A can detect a change of 0.03% in a signal and Camera B can detect a change of only 0.7%.

11.7.3 Increasing DR and DS

Both the DR and DS can be improved by increasing the signal level at the detector or reducing noise in the signal or camera. There are many ways to do either but experimental conditions will often limit the choices. It is helpful to at least be aware of those choices.

11.7.3.1 Methods for increasing signal

11.7.3.1.1 Higher QE (more electrons)

Imaging detectors convert incoming photons into electrons. The conversion rate or percentage is known as QE. Higher QE generates more electrons and results in a higher signal. Chart 11.5 shows the SNR for different QE factors. In brighter light levels, the QE is not a significant influence in the SNR since the signal noise is the dominant factor. QE becomes increasingly important as light level decreases.

There are several basic designs for CCD chips and each has different characteristics, including the QE. A standard front illuminated full-frame CCD has about 40–50% QE at peak wavelength, while a back-thinned CCD has over 90% QE at peak wavelength. New interline transfer CCDs and sCMOS detectors with micro

Table 11.3 DS is Independent of S/N or DR

Camera	Full Well Cap. (Electrons)	Camera Noise (Electrons)	*S/N* Ratio (DR)	DS
A (60% QE)	100,000	100	1000:1	316:1 (0.03%)
B (60% QE)	20,000	20	1000:1	141:1 (0.7%)

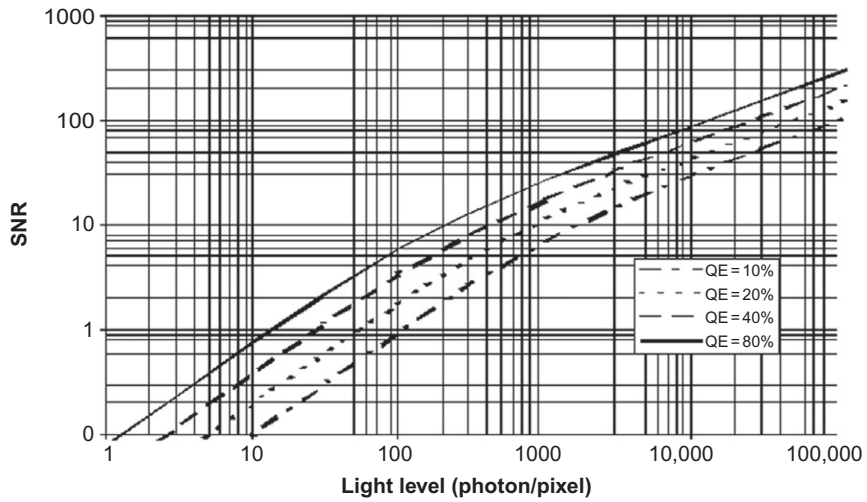

CHART 11.5

SNR versus QE (camera noise = 10 electrons).

lenses approach 75% QE. The higher QE helps to increase the signal and results in higher sensitivity.

Notice the location of the change in slope in the above lines as the dominant noise changes from camera noise on the left to signal shot noise on the right at different QE values.

11.7.3.1.2 On-chip signal integration (spatial/temporal)

The signal can be integrated spatially and/or temporally and/or spatially. Temporal integration is the accumulation of signal over longer exposures. This will yield increased signal at the expense of frame rate but not affect the spatial resolution of the image. Spatial integration will increase the signal and improve the frame rate at the expense of spatial resolution in the image.

Spatial integration is referred to as binning. This process sums the signals of adjacent pixels in a specified array (example: 2×2) to create a larger signal that is read out as if it were one pixel.

In a CCD camera, this means the signal increases by the factor of the number of binned pixels (example: $2 \times 2 = 4$ times increase in signal) while the readout noise it that of a single pixel. The result from a 2×2 binning in a CCD is a SNR increase of four times as in Eq. (11.12) This works best with CCD cameras that have low dark noise since dark noise is summed as well.

$$(S \times 4)/\mathrm{Rn} \tag{11.12}$$

In an sCMOS camera, there is no possibility of binning on the chip but many cameras have the on-board capability of binning the pixels after the readout. This is not as

effective as CCD binning since the signal of in the pixels is summed and the readout noise of the pixels is summed as well. At first, it would seem that there is no benefit to this scheme but since the signal summation is a simple sum and the readout noise summation is done in quadrature as in Eq. (11.13), the net result of a 2×2 binning of an sCMOS camera is a SNR increase of only two times compared with four times of the CCD binning.

$$(S \times 4)/\sqrt{(\mathrm{Rn}_1)^2 + (\mathrm{Rn}_2)^2 + (\mathrm{Rn}_3)^2 + (\mathrm{Rn}_4)^2} \tag{11.13}$$

This method creates higher sensitivity at the expense of spatial resolution. In some CCDs, spatial integration can also improve the DR of a camera by increasing the maximum signal level (the FWC), if the readout register pixels have larger FWC than the image acquisition pixels.

Summing multiple images in a computer will result in brighter images, but since the noise of the readout is included, the camera noise is summed as well. This is not the same as integration on the CCD.

Temporal integration on a detector is the single best way to increase SNR in an image as long as the rate of signal accumulation is greater than the camera noise accumulation. Since camera noise has many factors, it is important to properly sum these values to determine how much signal is required or how long of an integration period is possible with a given signal level.

For example, using a CCD camera with an FWC of 18,000 electrons, a 12-bit digitizer, a readout noise of 6 electrons and cooled to maintain a dark current level of 0.5 e/pix/s, we can use Eq. (11.14) to create a table that describes how long an integration period is possible before the camera noise equals a single count in the digitizer, that is, at what point does the camera noise become detectable.

$$\mathrm{Cn} = \sqrt{(\mathrm{Rn})^2 + (\mathrm{Dc} \times T)} \tag{11.14}$$

By calculating the sum of the readout noise (Rn) and dark noise (Dc) per second (T), we can find the camera noise for this camera at any exposure time. With that information and the digitizer CE (4.4 e/count), we can determine how long we can integrate with this camera before camera noise will increment one count in the digitizer. In Table 11.4, we will find that it takes 90 s of integration before the increase in dark current is sufficient to increase the DC by a single gray level. If the signal accumulation is greater than the accumulation of camera noise in the same amount of time, then signal integration on the chip will provide an increased S/N ratio.

11.7.3.1.3 Increase detector area (macro applications)

When the imaging object is considered as a point light source, the light collection efficiency of the detector is determined by the diameter of the lens and the distance between the imaging target and the lens. The distance is proportional to the imaging object size and the inverse factor of detector size. With a larger detector it is possible to shorten the distance and it results in a higher signal level due to the increased collection angle on the object side of the lens as seen in Fig. 11.6.

Table 11.4 Integration and Detectable Camera Noise

Exp. Time	Readout Noise	Dark Current (Dark Noise^2)	Camera Noise	Electrons Per Gray Level	Gray Level in Image
T (s)	*Rn (Electrons)*	*Dc*T (e/pix/s)*	*Cn (Electrons)*	*E/GL (e/gl)*	*GL (Gray Value)*
1	6	0.5	6.042	4.4	1.37
5	6	2.5	6.205	4.4	1.41
10	6	5	6.403	4.4	1.46
15	6	7.5	6.595	4.4	1.50
20	6	10	6.782	4.4	1.54
30	6	15	7.141	4.4	1.62
45	6	22.5	7.649	4.4	1.74
60	6	30	8.124	4.4	1.85
90	6	45	9.000	4.4	2.05
120	6	60	9.798	4.4	2.23

11.7.3.1.4 Selection of microscope objectives and magnification factors

The relationship between the magnification and numerical aperture (NA) of a microscope objective is a key to the brightness of an image at the camera.

Increasing NA is one of the most effective methods of increasing signal.

In transmitted light, intensity increases by the square of the change in NA. In reflected light fluorescence, intensity increases by the fourth power of the change in NA. A seemingly small increase in the NA of an objective can make a considerable difference in the signal level.

Similarly, the intensity in an image is inversely proportional to the magnification, again by a factor of 2. As magnification is reduced, the intensity at the camera increases by the square of such change.

This leads to Eq. (11.15), a useful tool for evaluating the relative brightness of two objectives or finding the resulting brightness difference in a contemplated objective change between objective "a" and objective "b" in an epi-fluorescence microscope.

$$\underset{\text{(fluorescence)}}{\text{Relative brightness}} = \frac{1}{\left(\frac{NA_a}{NA_b}\right)^4 \times \left(\frac{MAG_b}{MAG_a}\right)^2} \tag{11.15}$$

11.7.3.2 Methods for reducing noise

11.7.3.2.1 Averaging images after readout

Averaging of images in a computer is another form of temporal integration and can benefit the SNR since the noise values of both the signal shot noise and the camera noise will be reduced. DR and DS will improve by the square root of the number of images averaged but the intensity of the signal will not increase.

For example, Eqs. (11.16) and (11.17) show the result of image averaging in both the DR and DS by the function of the number of images I that are averaged

$$\mathrm{DR}_I = \frac{\mathrm{SIG}}{\sqrt{I}\cdot N_{\mathrm{camera}}} = \sqrt{I}\cdot\mathrm{DR} \tag{11.16}$$

$$\mathrm{DS}_I = \sqrt{I\cdot\mathrm{SIG}} = \sqrt{I}\cdot\mathrm{DS} \tag{11.17}$$

For example, Eqs. (11.18) and (11.19) show the result of averaging 16 images.

$$\mathrm{DR}_1 \cong 256:1 \tag{11.18}$$

$$\mathrm{DR}_{1,16} \cong \sqrt{16}\times 256 = 1024:1 \tag{11.19}$$

For example, in Table 11.5, we see the benefits of image averaging. Since both the camera noise and signal shot noise are divided by $\sqrt{I}$ even averaging two frames or four frames produces significant improvements in both DR and DS.

11.7.3.2.2 Signal intensification

Historically, standard CCD and tube cameras did not have enough sensitivity for low light applications because of high camera noise. Signal intensification is one way to reduce the "relative" noise of a camera by multiplying the original signal before the camera detects the signal. In this manner, the noise of the camera becomes relatively lower compared with the multiplied signal. In this process, the signal shot noise is multiplied by a factor F that represents the uncertainty associated with the outcome of the multiplication process. F can be slightly different for different types of electron multiplication schemes but the value is generally considered to be about $\sqrt{2}$ and is referred to as multiplication noise. The combination of an II and a CCD or an sCMOS camera makes it possible to achieve sufficient sensitivity for imaging at low light level and rapid rates.

An II converts incoming photons into electrons at the photocathode. Each electron can be intensified (multiplied) by acceleration and/or by a microchannel plate, by tens of thousands of times. Intensification of the signal is not equivalent to increasing the original signal but allows separation of the signal from the noise by amplifying the signal but not the camera noise. Chart 11.6 is an example that

Table 11.5 S/N versus QE

Camera Noise = 10			Signal Level = 2560		
Images Averaged	**Camera Noise (Electrons)**	**Signal Level (Electrons)**	**Signal Noise (Electrons)**	**DR**	**DS**
1	10.0	2560	50.6	256	51
2	7.1	2560	35.8	362	72
4	5.0	2560	25.3	512	101
8	3.5	2560	17.9	724	143
16	2.5	2560	12.6	1024	202

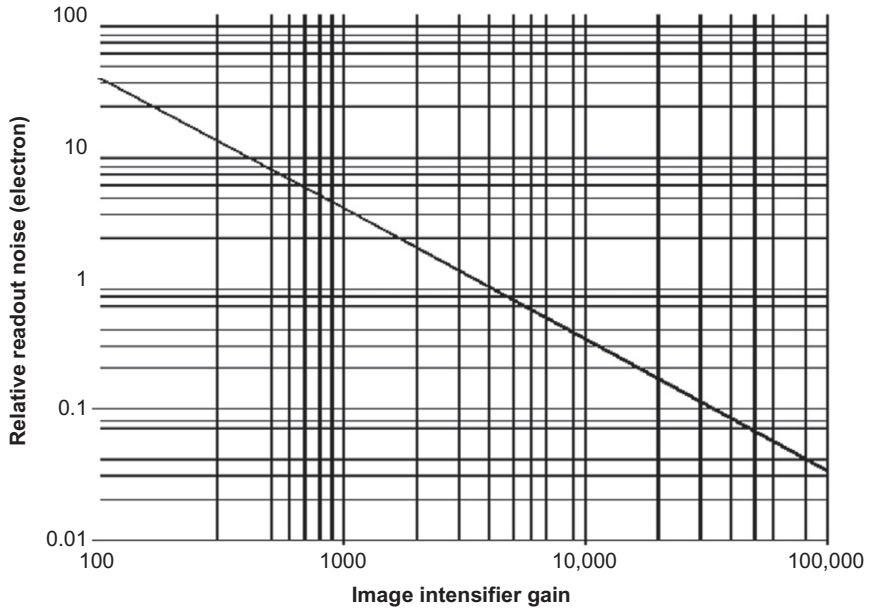

CHART 11.6

Relative readout noise of intensified CCD.

shows the relative noise for various gains of the II based on the condition that the CCD camera noise is 150 electrons and the relay lens coupling efficiency is 0.045.

Modern ICCD cameras incorporate improved intensifiers with higher QE photocathode materials, better microchannel plate technology for higher spatial resolution, and very efficient fiber coupling to a wide variety of low-noise CCD or sCMOS cameras. These improvements have extended the usefulness of the ICCD camera and improved the image quality and intrascene DR of this technology. The presence of the microchannel plate still limits the resolution compared with a plain CCD and requires careful attention to light levels to prevent damage to this very sensitive device.

In high light levels, multiple photons arrive together, and the light level can be measured as a function of signal intensity. In other words, higher signals yield higher gray levels and lower signals yield lower gray levels (refer to Fig. 11.7).

In very low light levels, individual photons arrive at the detector at discrete intervals. At this light level, signal intensity cannot be measured in gray levels. The signal only means the arrival of a single photon. Therefore, light intensity must be measured as a function of the number of photon events per unit of time. In other words, higher number of pulses within a certain time means a higher light level, and lower number of pulses means a lower light level (refer to Fig. 11.7). For such low light applications, a very special type of ICCD, called a photon counting camera, is designed to have enough signal intensification for a single input photon to greatly exceed the noise of the camera. This enables real-time discrimination of photon

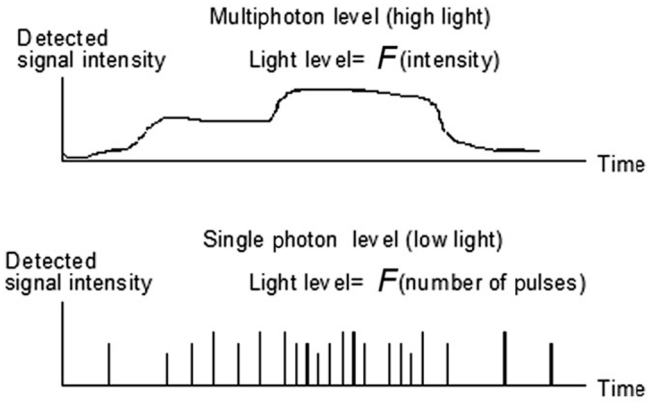

FIGURE 11.7

Multiphoton and single photon.

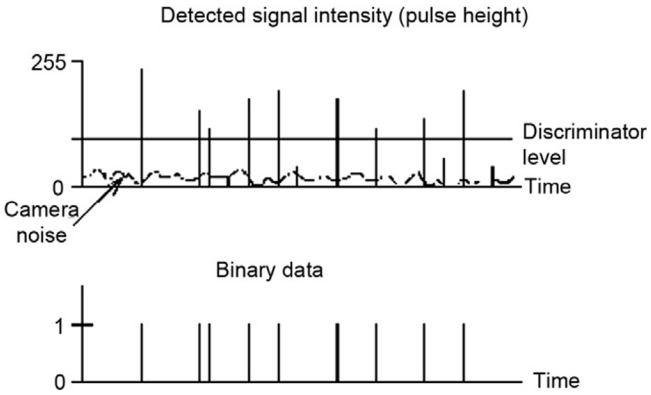

FIGURE 11.8

Photon counting discrimination.

events and rejection of camera noise to reveal single photon interaction at the detector. Photon counting is used to detect very weak light, such as luminescence where there is no background illumination.

A photon counting intensified camera amplifies each detected photon to an intensity level that is so far above the camera noise that the pulse from the photon is easily discriminated from camera noise and is converted to a binary data count of 1. Each time the camera is read out this binary data is summed in a computer memory and displayed as a gray level equal to the number of pulses accumulated at that point in the image. Gray levels in this case are simply the numbers of pulses detected at each pixel in the image over the total accumulation time (see Fig. 11.8).

This method eliminates camera noise completely and the only noise sources are the signal shot noise and some small noise from the dark current of the photocathode in the intensifier. Normally, the photon counting detector is designed to have minimum noise and very high signal gain. The limiting factor to this technology is the readout rate of the camera. Each pixel can count only one photon in each readout period. If the photons arrive in a single pixel at a faster rate than they can be read, then the camera will not detect the additional photons in that pixel for that readout period.

Intensified photon counting cameras are most useful at very low light levels and in situations where some kinetic information is required over the course of a long integration time. The ability to read out the camera information at rapid rates and still maintain an accurate photon count over long periods can offset the disadvantage of relatively low overall QE and resolution when compared with cooled slow scan cameras.

11.7.3.2.3 Signal amplification

Signal amplification is different from signal intensification although the goal is the same. A signal amplification EMCCD camera eliminates the need for an II by using an on-chip multiplication register as described earlier in Section 3.4. The primary advantage of this low light scheme is the tremendous increase in overall efficiency but the additional multiplication noise F reduces the effective QE by 50% and blurs the mathematical differences between background and objects if the intensities are similar.

Cooled slow scan EMCCD cameras take advantage of the very high QE of CCD chips and recent improvements in reducing total camera noise.

With deep, properly stabilized cooling, and good electronic design to minimize the CIC noise, EMCCDs offer a very low-noise, high-speed imaging device at low light levels when there is no background in the image.

The advantages of EMCCD cameras over intensified cameras are the increase in spatial resolution, broad spectral response, and hardiness, but there is no ability to see kinetic events within the total exposure time.

11.7.3.2.4 Reducing camera noise

Camera noise in CCCD cameras is comprised of the dark noise (fluctuation of the dark current) and the read noise (noise generated in the readout process). In most modern cameras, the dark noise has become so low it is not a factor in most biological imaging. For ultra-low light applications where long integration times are used, dark noise still needs to be considered.

sCMOS camera noise is comprised of dark noise, readout noise, and pixel gain fluctuation noise. Since pixel gain fluctuation is a multiplicative noise, it has no detectable influence in low light but may be a factor in higher light images. Recent advances in sCMOS technology have reduced read noise to less than 2 electrons while dramatically increasing pixel count and readout speed. For fast imaging at low light levels with samples that include some background illumination, sCMOS cameras offer the lowest overall noise.

For EMCCD cameras when using the gain feature, the noise list includes dark noise, readout noise, clock-induced charge noise, and multiplication noise. In these

cameras, the dark noise and clock-induced charge noise are multiplied in the gain system while the readout noise is divided by the gain factor.

The dark current in all detectors is primarily generated in the silicon substrate of the device and temperature-dependent. It is significant that the dark current is most critical in low light situations when using an EMCCD or any time when longer integration is required.

Normal CCD and sCMOS cameras are limited in their low light abilities primarily by the readout noise of the camera at short exposure times and by the dark noise as exposure time increases. For low light applications, cameras are designed with some additional features to improve the ratio of the signal electrons to the camera noise. These features include very low temperature cooling to reduce the dark current, double-correlated sampling circuits in the readout node, and flexible or multiple pixel clock speeds to provide a selection of readout noise levels/frame rate compromises.

11.8 REQUIRED LEVELS OF SIGNAL TO NOISE

Applications determine the level of SNR required. Images in Pictures 11.1–11.5 are taken with a photon counting camera but illustrate the concept common to all images. Longer integration gives better SNR and results in higher resolution and higher DR.

PICTURE 11.1

1/30 s Photon counting.

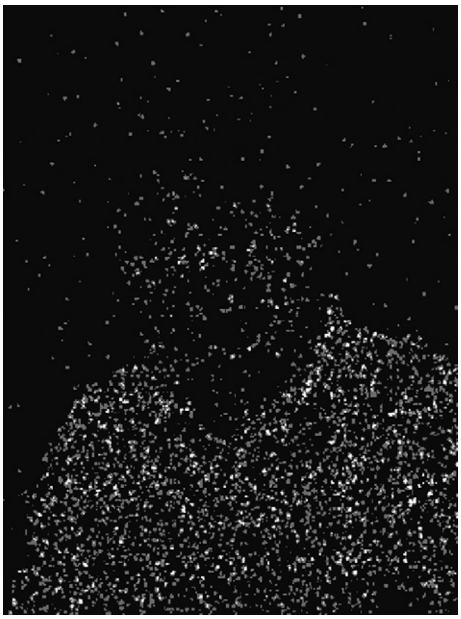

PICTURE 11.2

1 s Photon counting.

PICTURE 11.3

10 s Photon counting.

PICTURE 11.4

100 s Photon counting.

PICTURE 11.5

1000 s Photon counting.

If the application requires the recognition of detail in the image or the measurement of gray levels in the image, higher image quality (SNR) such as Picture 11.5 is required. If the application requires one to simply recognize the rough shape of the image, it does not require high image quality, and Picture 11.3 will be sufficient. If the application requires one to just detect the existence of an object, Picture 11.1 will be sufficient. It is important to determine the required image quality (SNR) from the application and choose the best detector to accomplish this requirement.

Comparing Picture 11.5 with Picture 11.6, it is easy to see that the integration time would have to be very long to achieve similar results in the SNR and the spatial resolution.

Signal multiplication cameras are most frequently used in Fluorescence microscopy where the signal levels are low but the background is not zero, as it was in the photon counting example above. In the situation where background is not zero, additional consideration must be given to multiplication noise and the effect it has on the ability to discriminate the sample intensity from the background intensity.

Multiplication noise has the effect of broadening the distribution of the histogram for a particular mean value and if two values have little difference in their mean intensities, broadening the histogram will blur the discrimination between the two. For example, if an object with a mean intensity of 40 electrons is imaged in a background with a mean intensity of 10 electrons, how would the image be different if it were imaged with a low-noise CCCD or sCMOS camera versus an EMCCD or ICCD camera signal amplification or signal amplifier camera? In Fig. 11.9A and B, it can be

PICTURE 11.6

High light image.

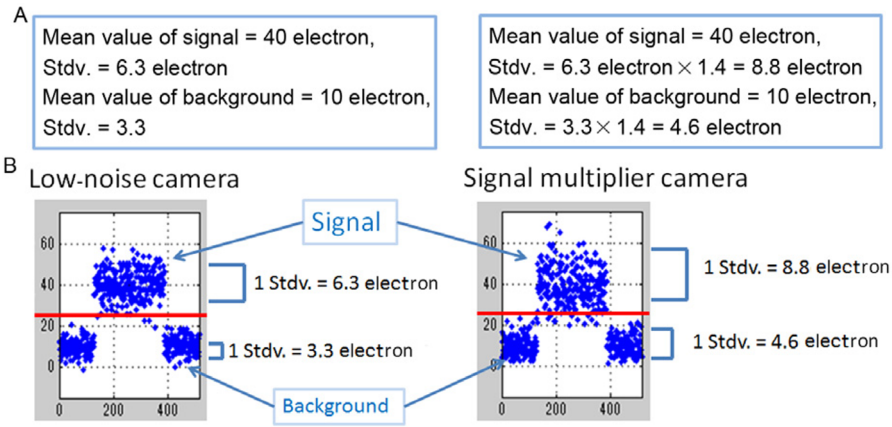

FIGURE 11.9

(A) Signal Multiplication noise Increases Stdv. of a signal by a factor of 1.4. (B) Increased Signal Stdv. in an image blurs intensity differences between objects.

seen how the multiplication noise spreads the standard deviation and the ability to clearly distinguish one from the other.

In a low-noise camera, it is possible to draw a line between the signal values and the background values with almost no points of uncertainty on that line; while with a signal multiplier camera, there are numerous points that fall on the line. In practical terms, this means that the CCCD or CsCMOS user has a high chance to see and threshold the difference between the sample signal and the background in the low-noise cameras, while there is low chance that the user can make and accurate decision where the sample ends and where the background begins with a signal multiplier camera.

In images containing background levels above zero, the required signal level for signal amplification cameras is nearly two times greater than a standard CCD or sCMOS to achieve equivalent SNR.

11.9 SENSITIVITY COMPARISON

Signal multiplication cameras, such as ICCD and EMCCD, CCCD and sCMOS cameras are all used for low light applications. There is no easy answer to determine which is more sensitive without adding the conditions and requirements of the experiment. If we look at a comparison of the different camera types over the same range of light intensities, we can determine the technology that provides the best SNR at a given light level and then design our experiment to achieve that level or at least understand what trade-off we must make. From Charts 11.2–11.4 we can create Chart 11.7 to compare the cameras at various light levels.

This chart does not take into account the effects of backgrounds, different pixel sizes, or QE so experimental conditions would have to be adjusted to reach the appropriate light levels but some general observations can be made.

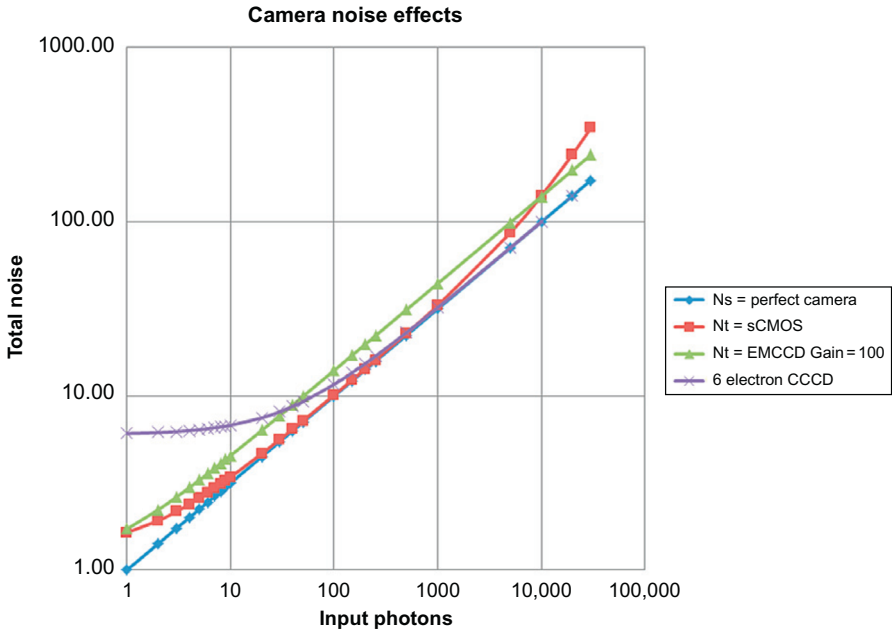

CHART 11.7

Effects of camera noise at different light levels in CCD, EMCCD and sCMOS cameras.

1. The EMCCD at 1000× gain will produce better SNR at light levels under 4 photons but the signal noise will be twice what a perfect camera would offer and it will saturate at a maximum signal level of 100 photons.
2. The sCMOS camera will produce better SNR beginning at 6 photons and offer signal noise limited data from about 30 photons up to about 1500 photons. It will make images up to the full 30,000 electron level without saturation but there will be an additional noise factor as the signal increases beyond 1500 photons.
3. The CCCD will be read noise limited until the signal level reached about 40 photons but will be shot noise limited from 250 photons up to the saturation level of 20,000 photons.

11.10 SPATIAL RESOLUTION CONSIDERATIONS

New computational imaging methods such as super-resolution are changing the ultimate limits of resolution. For standard microscopy applications in widefield, fluorescence microscopy, TIRF microscopy, and spinning disk confocal microscopy, the NA of the optics is the limiting factor when there is sufficient light to become shot noise limited in the image.

With a bright signal, detector spatial resolution is determined by the number of pixels, the size of the pixels, and the magnification between the object and the detector.

In all cameras, resolution is limited by the amount of light (photons). In other words, the possible resolution of any detector may not be fully utilized in low light situations. This is illustrated in Pictures 11.1–11.6 in the photon counting section.

11.10.1 Cooled CCD and sCMOS

A CCCD or an sCMOS camera normally has square pixels and gives the same resolution in both vertical and horizontal directions. The resolution of the CCCD or sCMOS is expressed as the size and number of pixels in both horizontal and vertical directions.

To match the resolution of the CCD chip to the resolution of a microscope, it is necessary to divide the pixel dimension by the required resolution in the image. This will indicate the minimum magnification required between the object and the CCD. This value will provide the minimum magnification for detection. For maximum resolution in the image, it is necessary for the smallest image dimension to cover two to three pixels on the CCD so two to three times the minimum magnification is required. A helpful interactive tutorial can be found at the Hamamatsu learning site (http://learn.hamamatsu.com/tutorials/java/airymag/, accessed January 2013).

Matching the magnification to the resolution may lead to very small fields of view due to the small size of CCD chips compared with the eyepiece field of view! It will also lead to very low light levels. Remember both field of view and intensity will be reduced by the change in magnification squared. If you double the magnification at a fixed NA, both the field of view and the intensity are reduced by four times.

Example: Camera with 10-μ square pixels and a desired image resolution of 0.5 μ.

10 μ/0.5 μ = 20× magnification for detection, and 40–60× magnification for good resolution. The next qualification is that the NA of the 20× lens must be sufficient to produce the resolution of 0.5 μ at the wavelength in use.

11.10.2 Intensified camera

An intensified camera such as the ICCD is made up of an II and a CCD camera with relay optics. The resolution of an II is expressed as lp/mm (number of black and white line pairs in 1 mm of the photocathode that can be resolved). The image from the phosphor screen of the intensifier must be transferred to the CCD with an appropriate magnification to maintain the resolution when projected on the CCD and this depends on the pixel size of the CCD.

For example, if the intensifier is rated at 25 line pairs/mm, then there are 50 lines in each millimeter. Each line must therefore be 20 μ in width. If this intensifier is used with a camera with 10 μ pixels, then it would be necessary to have a 2:1

reduction lens factor between the phosphor screen and the CCD. This also means that the intensifier output window must be twice the diameter of the CCD chip diagonal dimension or vignetting will occur.

11.10.3 Electron mulitplier CCD

The resolution of an EMCCD is just the same as a regular CCCD when there is sufficient light intensity. As the intensity decreases, the resolution of an EMCCD becomes more and more limited by the number of signal photons, the gain, and the multiplication noise effects on differences between the sample and the background.

Temporal resolution is limited by the type of CCD used and the pixel clock of the camera when the exposure time is very short. Temporal resolution can be described as the shortest possible exposure or the maximum frame rate. It is important to define which meaning is desired in any dialog about temporal resolution.

11.11 TEMPORAL RESOLUTION CONSIDERATIONS

11.11.1 For CCCD, sCMOS, and EMCCD cameras

The shortest possible exposure is limited by the pixel transfer speed and the design of the readout system. Full-frame cameras are normally the slowest since there is a shutter of some sort that has to be opened and closed to expose the CCD. This can take 10 ms to open and 10 ms to close, so the minimum frame time is 20 ms plus the exposure time. Frame-transfer cameras are much faster, often in the 10-μs exposure range depending on how close to the image storage area the imaging pixels are located. Interline transfer cameras normally have the shortest possible exposure for the entire chip since each pixel has only to move the signal one pixel to the storage area. This means the fastest exposure time is a few microseconds.

The frame rate for any CCD also depends on the design of the CCD. For frame-transfer and interline CCDs, it is calculated from the total number of pixels and the pixel clock rate. For example, a CCCD that has 1000×1000 pixels with 1-MHz pixel clock has 1 fps as the fastest frame rate. This assumes that the exposure time is equal to or shorter than the readout time. If the exposure time is longer than the readout time, the exposure time determines the frame rate since the exposure and readout occur simultaneously in these CCDs.

11.11.2 For ICCD cameras

The shortest possible exposure time can be in the nanosecond and picosecond range thanks to the ability to rapidly gate the MCP. The readout speed of the camera will limit the frame rate but the exposure time can be extremely short.

In the case of an ICCD, there is another limitation of temporal resolution: decay time of the phosphor screen of the II. Normally, the decay time of the typical P43 phosphor screen is several hundred microseconds. This is fast enough when the

intensifier is used with most CCD cameras but if the frame rate nears 1000 fps, this decay time may limit the frame rate.

11.12 GEOMETRIC DISTORTION

Intensified cameras have 2–3% geometric distortion. This is caused by the II itself and relay optics. Normally, the inverter type II has higher distortion compared with the proximity type II. A CCCD or an EMCCD will have no geometric distortion since there is no transfer optics or coupling systems. sCMOS cameras have the possibility of distortion when used in the rolling shutter mode with fast moving objects. The shape and degree of distortion depends on the direction of motion in relation the axis of the chip.

11.13 SHADING

11.13.1 Cooled CCD

A CCCD camera has very little shading due to the on-chip pixel correction features in every CCD. There is also the possibility of shading on the CCD due to heat from amplifiers that are part of the CCD itself. Cooling helps diminish this but it may still be obvious in long integrations.

11.13.2 sCMOS

sCMOS cameras can exhibit great pixel-to-pixel variability plus large column to column differences unless very detailed corrections are applied by the camera manufacturer in the camera head. A well-designed sCMOS camera will have very little shading.

11.13.3 Intensified CCD

Intensified cameras have up to 20% shading. This is caused by the II itself and the type of coupling to the CCD. In the intensifier, normally the center of view is brighter than the corners. A fiber optic coupling generally has less shading than a lens coupling.

11.13.4 Electron multiplier CCD

EMCCD cameras, like CCCD cameras, normally have very little shading but the dark current from any cooling nonuniformity will be multiplied by the same factor in the multiplication register. When shading is seen in these cameras, it is usually a small light leak in the microscope.

11.14 USABILITY

It is important to understand basic advantages and limitations in practical use when considering the different technologies.

11.14.1 Cooled CCD and sCMOS

1. Low light to high light applications are possible with these cameras. Very high resolution and DR images are possible with these cameras and there is no risk of detector burn in high light conditions.
2. Pixel manipulation (binning, subarray).
3. As discussed earlier, pixel binning and subarray capabilities can be used to make these cameras very flexible and useful in many applications.
4. CCD and sCMOS cameras have digital interfaces like RS-422, RS-644, IEEE1394, Camera Link, USB 2, and USB 3. This makes it possible to interface with most computer/software packages but care needs to be taken to assure the computer data bus and storage capabilities match the camera data rates.
5. Cooling required for low light applications to minimize dark current.
6. CCDs and sCMOS cameras are normally cooled with a Peltier thermoelectric cooler. This cooler requires some additional method to remove the heat. Convection, fans, and water circulation are common ways of handling this.
7. Slow frame rate at low intensities can make focusing difficult.

11.14.2 Intensified cameras with video readout

1. Interfaces include RS-170 and CCIR with video frame grabbers
   a. The standard video format is disappearing but historically it made it easy to use video peripherals such as video recorders, image processors, and image processing software.
   b. The standard frame rate of video cameras is 30 fps and this is fast enough formost real-time applications and focusing, but the resolution is higher in the horizontal axis than the vertical axis and lower than modern digital cameras.

11.14.3 Intensified cameras with CCCD or sCMOS camera readout

1. CCD and sCMOS cameras with bigger DRs and on-chip integration offer greater flexibility than video rate cameras and can be used in combination with gating of the intensifier for special applications like fluorescence lifetime imaging.
2. Usable only at low light levels.
3. Background levels are always an issue but the multiplication noise of ICCD cameras decrease the contrast differences and broaden the histograms of both sample and background intensities, so extra care should be taken to minimize background levels when using these cameras.

4. The intensified camera can be used for high light applications such as DIC and Phase Contrast if the light source level is adjusted low enough for the detector but the image quality is not as good as that of high light detectors due to the limited number of photons in the image. The II also has a risk for burn-in when excessive light is applied. The damage will be minimized with the tube protection circuit; however, special caution is required.
5. Because of long integration times, slow read out, the existence of a mechanical shutter, or the sheer number of pixels, the frame rate of a CCCD can be slow. This limits the temporal resolution and makes focusing difficult under low light conditions. Frame-transfer and interline-transfer CCD cameras usually generate faster frame rates.
6. sCMOS cameras offer much faster readout and can be matched with gating of the intensifier for very short exposures and very fast frame rates.

11.14.4 Electron multiplier cameras

1. Low light to high light imaging is possible with these versatile cameras.
2. At high light levels, EMCCD cameras can operate as a standard CCCD camera and produce high DR images. The models currently available have larger pixels than most CCCD camera so spatial resolution will be different unless additional magnification is added to the optical system.
3. At low light levels, the gain amplifier is employed, and in this operating mode, high light levels must be avoided to reduce the chance of damaging the multiplication register, a process called gain aging.
4. Background levels are always an issue but the multiplication noise of EMCCD cameras decrease the contrast differences and broaden the histograms of both sample and background intensities, so extra care should be taken to minimize background levels when using these cameras.
5. Pixel manipulation (binning, subarray) is identical to the binning described for a CCCD.
6. EMCCD cameras use the same interfaces as CCCD and sCMOS cameras.
7. Cooling requirements for EMCCDs are very stringent since not only is dark current reduced but also the gain factor depends on the temperature and the stability of the temperature. Small changes in the temperature result in changes in dark current which is multiplied by the gain register and the gain itself. Accurate and repeatable scientific images can only be obtained if the cooling stability is very well regulated. Temperature fluctuations of a single degree can make detectable differences in the camera output.
8. Slow frame rate can make focusing difficult.
9. Slow frame rates can be overcome with the gain feature of the camera. (Changing the gain or changing between the normal mode and gain mode can take tens of milliseconds so this needs to be considered when planning an experiment.)

11.15 ADVANCED TECHNOLOGY NUTSHELL

Imaging technology is improving every day and it is important to have up-to-date information about this in a modern research setting. Dramatic improvements are leading to higher sensitivity, higher spatial resolution, and higher temporal resolution and the rate at which these changes are occurring is increasing.

11.15.1 High sensitivity

The QE of an II is lower than that of a CCCD or an sCMOS or an EMCCD, but new photocathode materials with more than 50% QE and broader spectral ranges have been developed to reduce the gap between CCCDs and IIs. Back-thinning of CCDs can increase the QE to over 90% and sCMOS cameras may soon have this feature as well. When evaluating the QE of an EMCCD, it is critical to think of the "effective QE" of the device which changes when used with or without the multiplication register, where multiplication noise in the multiplication register reduces the QE of the chip by 50%.

Improvements in Micro Lens technology have given interline cameras and sCMOS cameras nearly the same QE as a back-thinned type CCDs especially when compared with back-thinned EMCCDs. Spectral sensitivity limits are being expanded at the same time. It is not unusual to find good QE numbers over the range of ultra-violet to near IR.

11.15.2 High spatial resolution

The spatial resolution of ICCDs is improving due to new photocathode materials and microchannel plates with finer spacing and less shading. Better coupling methods to newer style CCDs and sCMOS have eliminated many of the older video rate CCD camera limitations.

New, larger scale CCDs with as many as 4000×4000 pixels are available though they require a slow frame rate and large image storage capacity while new sCMOS cameras offer 2000×2000 or more pixels at frame rates of 100 fps.

11.15.3 High temporal resolution

New technologies like the sCMOS cameras have tremendously increased the temporal resolution of cameras. While still limited by the photon levels in the signal, the current limit to frame rate has become the speed at which data can be transferred and stored in computers. At this time, sCMOS cameras are capable of creating and transferring 800 MB or more of data per second when each image contains 4–5 million pixels at sustained frame rates of 100 fps. Computer configurations for cameras like this take on the same importance as the camera selection itself.

11.15.4 Convenience

Using an advanced imaging detector is becoming easier due to increasing standardization of interface protocols. These new detectors also place additional burdens on the user to understand the technology, design experiments with tighter controls, and know the limitations of each piece of equipment used in the experiment. As camera noise decreases to the level of a single electron, optical noise in the background, internal reflections in the optics, and stray light in the laboratory are becoming the limiting factors to low light detection. Optical cleanliness, microscope alignment and sample preparation, and bench skills need to be fully considered in a modern laboratory and in experimental design.

It is very popular to use image processing software to analyze and/or modify images. In this case, the imaging detector has to be physically connected to the computer and the control of the imaging detector has to be linked to the image processing software. Hardware standards such as IEEE1394, Camera Link, USB 2, USB 3, and AIA (RS-422 and RS-644) are common. It is now possible to run more than one camera on the same computer, and image processing software can combine this data for advanced applications. With a bit of study, we can now choose the best system for the application from a variety of combinations.

Acknowledgments

The author gratefully acknowledges the work of Mr. Masafumi Oshiro of Hamamatsu Photonics K.K. Japan who taught me about cameras for microscopy and wrote the original chapter on which this edition is based and Dr. Ken Spring for his ideas and experience in teaching these subjects in a clear manner. Additional thanks are due to Dr. Stephanie Fullerton and Dr. Keith Bennett of Hamamatsu Corp, Mr. T. Maruno, Mr. H. Iida and Mr. T. Hayakawa, and the engineers of 14th Group of Hamamatsu Photonics K.K. Japan for their helpful discussions and advice over many years.

Reference

Long, F., Zeng, S., & Huang, Z. (2012). Localization-based super-resolution microscopy with an sCMOS camera. Part II: Experimental methodology for comparing sCMOS with EMCCD cameras. *Optics Express*, *20*(16), 17741–17759.

CHAPTER

Post-Processing for Statistical Image Analysis in Light Microscopy

12

Richard A. Cardullo* **and Edward H. Hinchcliffe†**

*Department of Biology, The University of California Riverside, California, USA

†Cellular Dynamics Section, Hormel Institute, University of Minnesota, Austin, Minnesota, USA

CHAPTER OUTLINE

Introduction **286**
12.1 Digitization of Images **286**
12.2 Using Gray Values to Quantify Intensity in the Microscope **288**
12.3 Noise Reduction **289**
12.3.1 Temporal Averaging 290
12.3.2 Spatial Methods 292
12.3.2.1 Arithmetic Operations Between an Object and a Background Image 292
12.3.2.2 Concept of a Digital Mask 292
12.3.2.3 Averaging Versus Median Filters 293
12.4 Contrast Enhancement **294**
12.5 Transforms, Convolutions, and Further Uses for Digital Masks **299**
12.5.1 Transforms 301
12.5.2 Convolution 304
12.5.3 Digital Masks as Convolution Filters 306
12.5.3.1 Point Detection in a Uniform Field 309
12.5.3.2 Line Detection in a Uniform Field 309
12.5.3.3 Edge Detection-Computing Gradients 310
12.5.3.4 Laplacian Filters 311
12.6 Thresholding **312**
Conclusions **314**
References **314**

Abstract

Image processing of images serves a number of important functions including noise reduction, contrast enhancement, and feature extraction. Whatever the final goal, an understanding of the nature of image acquisition and digitization and subsequent

Methods in Cell Biology, Volume 114 **ISSN 0091-679X**
Copyright © 2013 Elsevier Inc. All rights reserved.
http://dx.doi.org/10.1016/B978-0-12-407761-4.00012-9

mathematical manipulations of that digitized image is essential. Here we discuss the basic mathematical and statistical processes that are routinely used by microscopists to routinely produce high quality digital images and to extract key features of interest using a variety of extraction and thresholding tools.

INTRODUCTION

The theoretical basis of image processing along with its applications is an extensive topic that cannot be adequately covered here but has been presented in a number of texts dedicated exclusively to this topic (Andrews & Hunt, 1977; Bates & McDonnell, 1986; Chellappa & Sawchuck, 1985; Gonzalez & Wintz, 1987; Inoue & Spring, 1997; Russ, 1994; Shotton, 1993). In this chapter, the basic principles of image processing used routinely by microscopists will be presented. Since image processing allows the investigator to convert the microscope/detector system into a quantitative device, this chapter will focus on three basic problems: (1) reducing "noise," (2) enhancing contrast, and (3) quantifying intensity of an image. These techniques can then be applied to a number of different methodologies such as video-enhanced differential interference microscopy (VEDIC; Chapter 16 by Salmon and Tran, volume 81, 2007), nanovid microscopy, fluorescence recovery after photobleaching, fluorescence correlation spectroscopy, fluorescence resonance energy transfer, and fluorescence ratio imaging (Cardullo, 1999). In all cases, knowledge of the basic principles of microscopy, image formation, and image-processing routines is absolutely required to convert the microscope into a device capable of pushing the limits of resolution and contrast.

12.1 DIGITIZATION OF IMAGES

An image must first be digitized before an arithmetic, or logical, operation can be performed on it (Pratt, 1978). For this discussion, a digital image is a discrete representation of light intensity in space (Fig. 12.1). A particular scene can be viewed as being continuous in both space and light intensity and the process of digitization converts these to discrete values. The discrete representation of intensity is commonly referred to as gray values whereas the discrete representation of position is given as picture elements, or pixels. Therefore, each pixel has a corresponding gray value which is related to light intensity [e.g., at each coordinate (x,y) there is a corresponding gray value designated as $GV(x,y)$]. The key to digitizing an image is to provide enough pixels and grayscale values to adequately describe the original image.

Clearly, the fidelity of reproduction between the true image and the digitized image depends on both the spacing between the pixels (e.g., the number of bits that map the image) and the number of gray values used to describe the intensity of that image. Figure 12.1B shows a theoretical one-dimensional scan across a portion of an image. Note that the more pixels used to describe, or sample, an image, the better the

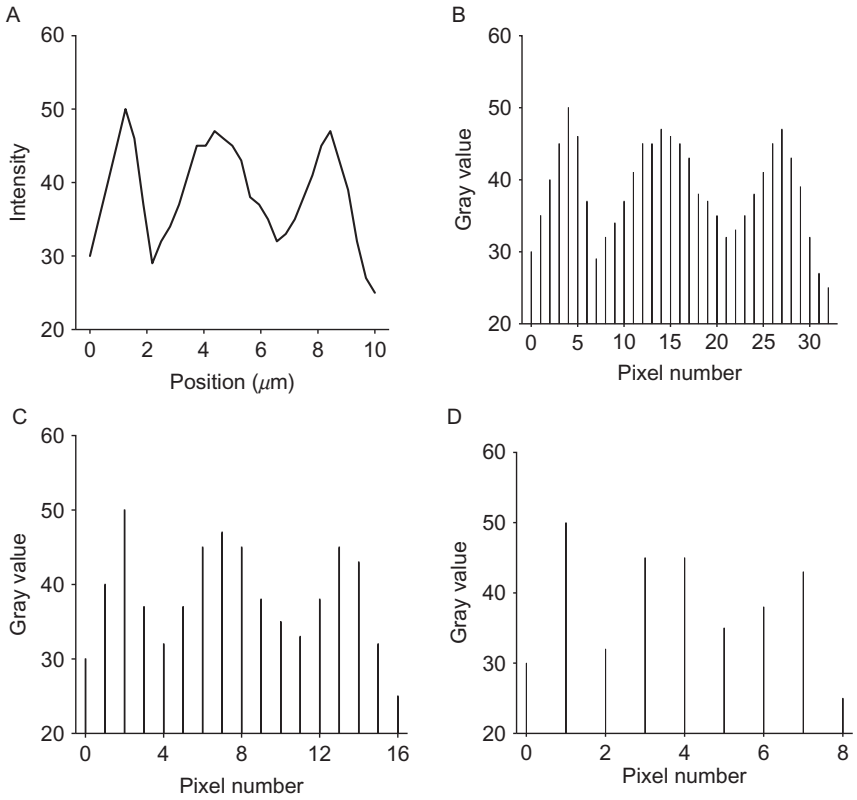

FIGURE 12.1

(A) A densitometric line scan through a microscopic image is described by intensity values on the *y*-axis and its position along the *x*-axis. (B) A 6-bit-digitized representation (64 gray values) of the object in (A), with 32 bits used to describe the position across 10 μm. The digital representation captures the major details of the original object but some finer detail is lost. Note that the image is degraded further when the position is described by only (C) 16 bits or (D) 8 bits.

digitized image reflects the true nature of the original. Conversely, as the number of pixels is progressively reduced, the true nature of the original image is lost. When choosing the digitizing device for a microscope, particular attention must be paid to matching the resolution limit of the microscope ($\sim$0.2 μm for visible light, see Chapter 1 by Sluder and Nordberg, this volume) to the resolution limit of the digitizer (Inoue, 1986). A digitizing array that has an effective separation of 0.05 μm per pixel is, at best, using four pixels to describe resolvable objects in a microscope resulting in a highly digitized representation of the original image (note that this is most clearly seen when using the digitized zoom feature of many imaging devices which results in a "boxy" image representation). In contrast, a digitizer which has pixel elements separated by 1 μm effectively averages gray values five times above the resolution limit of the microscope resulting in a degraded representation of the original image.

In addition to assigning the number of pixels for an image, it is also important to know the number of gray values needed to faithfully represent the intensity of that image. In Fig. 12.1B, the original image has been digitized at 6-bit resolution (6 bits $= 2^6 = 64$ gray values from 0 to 63). The image could be better described by more gray values (e.g., 8 bits = 256 gray levels) but would be poorly described by less gray values (e.g., 2 bits = 4 gray values).

The decision on how many pixels and gray values are needed to describe an image is dictated by the properties of the original image. Figure 12.1 represents a low-contrast, high-resolution image which needs many gray scales and pixels to adequately describe it. However, some images are by their very nature high contrast and low resolution and require less pixels and gray values to describe it (e.g., a line drawing may require only 1 bit of gray-level depth, black or white). Ultimately, the trade-off is one in contrast, resolution, and speed of processing. The more descriptors used to represent an image, the slower the processing routines will be performed. In general, an image should be described by as few pixels and gray values as needed so that speed of processing can be optimized. For many applications, the user can select a narrower window, or region of interest (ROI), within the image to speed up processing.

12.2 USING GRAY VALUES TO QUANTIFY INTENSITY IN THE MICROSCOPE

A useful feature shared by all image processors is that they allow the microscopist a way to quantify image intensity values into some meaningful parameter (Green, 1989; Russ, 1990). In standard light microscopy, the light intensity—and therefore the digitized gray values—is related to the optical density (OD) which is proportional to the log of the relative light intensity. In dilute solutions (i.e., in the absence of significant light scattering), the OD is proportional to the concentration of absorbers, C, the molar absorptivity, ε, and the path length, l, through the vessel containing the absorbers. In such a situation, the OD is related to these parameters using Beer's law:

$$\mathrm{OD} = \log\left(\frac{I_0}{I}\right) = \varepsilon C l$$

where I and I_0 are the intensities of light in the presence and absence of absorber, respectively. Within dilute solutions, it therefore might be possible to equate a change in OD with changes either in molar absorptivity, path length, or concentration. However, with objects as complex as cells, all three parameters can vary tremendously and the utility of using OD to measure a change in any one parameter is difficult.

Although difficult to interpret in cells, measuring changes in digitized gray values in an OD wedge offers the investigator a good way to calibrate an entire microscope system coupled to an image processor. Figure 12.2 shows such a calibration using a brightfield microscope coupled to a CCD camera and an image processor. The wedge had 0.15-OD increments. The camera/image processor unit was digitized to 8 bits

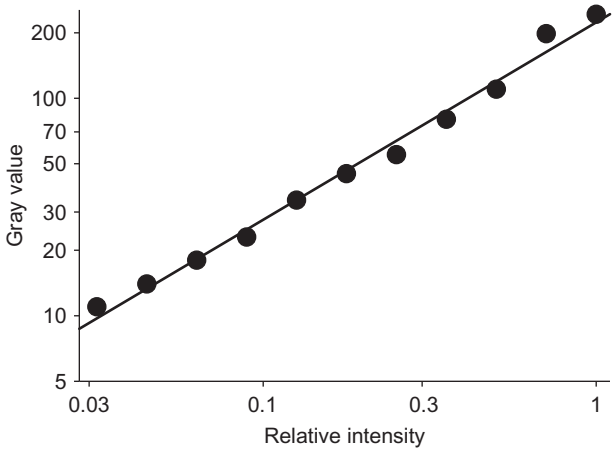

FIGURE 12.2

Calibration of a detector using an image processor. The light intensity varied incrementally using an OD step wedge (0.15-OD increments), and the gray value was plotted as a function of the normalized intensity. In this instance the camera/image processor system was able to quantify differences in light intensity over a 40-fold range.

(0–255) and the median gray value was recorded for a 100 × 100 pixel array (the ROI) in each step of the wedge. In this calibration, the black level of the camera was adjusted so that the highest OD corresponded to a gray value of 5. At the other end of the scale (the lowest OD used), the relative intensity was normalized so that I/I_0 was equal to 1 and the corresponding gray value was ~95% of the maximum gray value (~243). As seen in Fig. 12.2, as the step wedge is moved through the microscope, the median value of the gray value increased as the log of I/I_0. In addition to acting as a useful calibration, this figure shows that an 8-bit processor can reliable quantify changes in light intensity over two orders of magnitude.

12.3 NOISE REDUCTION

The previous sections have assumed that the object being imaged is relatively free of noise and is of sufficient contrast to generate a usable image. Although this may be true in some instances, the ultimate challenge in many applications is to obtain reliable quantitative information from objects which produce a low-contrast, noisy signal (Erasmus, 1982). This is particularly true in cell physiological measurements using specialized modes of microscopy such as VEDIC, fluorescence ratio imaging, nanovid microscopy, and so on. There are different ways to reduce noise and the methods of noise reduction chosen depend on many different factors, including the source of the noise, the type of camera employed for a particular application, and the contrast of the specimen. For the purposes of this chapter, we shall distinguish between temporal and spatial techniques to increase the signal-to-noise ratio (SNR) of an image.

12.3.1 Temporal averaging

In most low-light level applications, there is considerable amount of shot noise associated with the signal. If quantitation is needed, it is often necessary to reduce the amount of shot noise in order to improve the SNR. Because this type of noise reduction requires averaging over a number of frames ($\geq$2 frames), this method is best used for static objects. Clearly, temporal averaging can be difficult to use for optimizing contrast for dynamic processes such as cell movement, detecting rapid changes in intracellular ion concentrations over time, quantifying molecular motions using fluorescence recovery after photobleaching, or single particle tracking. The trade-off is between improving SNR versus blurring or missing the capture of a dynamic event. Current digital microscopy equipment allows for very short exposure times, even with the low-light levels associated with live cell imaging. Thus, frame averaging can be an acceptable solution to improve SNR, provided that the light exposures are sufficiently short (Fig. 12.3).

Assume that at any given time, t, within a given pixel, a signal, $S_i(t)$, represents both the true image, I, which may be inclusive of background, and some source of noise, $N_i(t)$. Since the noise is stochastic in nature, $N_i(t)$ will vary in time, taking on both positive and negative values, and the signal, $S_i(t)$, will vary about some mean value. For each frame, the signal is therefore just:

$$S_i(t) = I + N_i(t)$$

As the signal is averaged over M frames, an average value for $S_i(t)$ and $N_i(t)$ is obtained:

$$\langle S_i \rangle_M = I + \langle N_i \rangle_M$$

where $\langle S_i \rangle_M$ and $\langle N_i \rangle_M$ represent the average value of $S_i(t)$ and $N_i(t)$ over M frames. As the number of frames, M, goes to infinity, the average value of N_i goes to zero and therefore:

$$\langle S_i \rangle_{M \to \infty} = I$$

The question facing the microscopist is how large M should be so the SNR is acceptable. This is determined by a number of factors including the magnitude of the

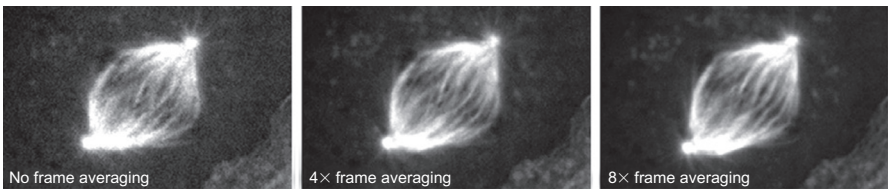

FIGURE 12.3

Frame averaging improves the SNR. A dividing mammalian cell expressing GFP-α tubulin was imaged using a spinning disk confocal microscope. Images were collected with no frame averaging, 4 frames averaged or 8 frames averaged. Random noise is reduced due to frame averaging.

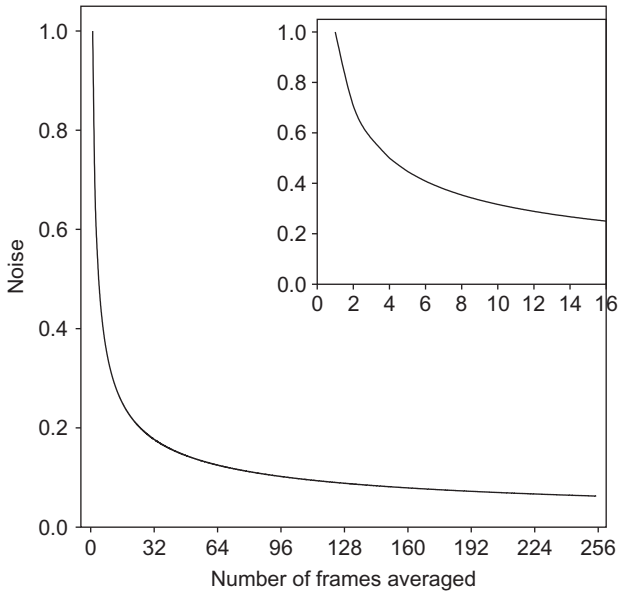

FIGURE 12.4

Reduction in noise as a function of the numbers of frames averaged. The noise is reduced inversely as the square root of the number of frames averaged. In this instance, the noise was normalized to the average value obtained for a single frame. The major gain in noise reduction is obtained after averaging very few frames (inset) and averaging for more than 64 frames leads to only minor gains in the SNR.

original signal, the amount of noise, and the degree of precision required by the particular quantitative measurement. A quantitative measure of noise reduction can be obtained by looking at the standard deviation of the noise, which decreases inversely as the square root of the number of frames ($\sigma_M = \sigma_0/\sqrt{M}$). Therefore, averaging a field for 4 frames will give a 2-fold improvement in the SNR, averaging for 16 frames yields a 4-fold improvement, while averaging for 256 frames yields a 16-fold improvement. At some point the user obviously reaches a point of diminishing returns where the noise level is below the resolution limit of the digitizer and any improvement in SNR is minimal (Fig. 12.4).

Although frame-averaging techniques are not always appropriate for moving objects, it is possible to apply a running average where the resulting image is a weighted sum of all previous frames. Because the image is constantly updated on a frame-by-frame basis, these types of recursive techniques are useful for following moving objects but improvement in SNR is always less than that obtained with the simple averaging technique outlined in the previous paragraph (Erasmus, 1982). Additional recursive filters are possible which optimize the SNR but these are typically not available on commercial image processors.

12.3.2 Spatial methods

A number of spatial techniques are available which allow the user to reduce noise on a pixel-by-pixel basis. The simplest of these techniques generally uses simple arithmetic operations within a single frame or, alternatively, between two different frames. In general, these types of routines involve either image subtraction or division from a background image or calculate a mean or median value around the neighborhood of a particular pixel. More sophisticated methods use groups of pixels (known as masks, kernels, or filters), which perform higher-order functions to extract particular features from an image. These types of techniques will be discussed separately in Section 12.5.

12.3.2.1 Arithmetic operations between an object and a background image

If one has an image, which has a constant noise component in a given pixel in each frame, the noise component can be removed by performing a simple subtraction that removes the noise and optimizes the SNR. Although SNR is improved, subtraction methods can also significantly decrease the dynamic range but these problems can generally be avoided when the microscope and camera systems are adjusted to give the optimal signal.

Any constant noise component can be removed by subtraction and, in general, it is always best to subtract the noise component from a uniform background image (Fig. 12.5). Thus, if a pixel within an image has a gray value of say 242, with the background having a gray value of 22 in that same pixel, then a simple subtraction would yield a resultant value of 220. Image subtraction therefore preserves the majority of the signal, and the subtracted image can then be processed further using other routines. In order to reduce temporal noise, both images can be first averaged as described in Section 12.3.1.

12.3.2.2 Concept of a digital mask

A number of mathematical manipulations of images involve using an array (or a digital mask) around a neighborhood of a particular pixel. These digital masks can be used either to select particular pixels from the neighborhood (as in averaging or median filtering discussed in Section 12.3.2.3) or alternatively can be used to apply some mathematical weighting function to an image on a pixel-by-pixel basis to extract particular features from that image (discussed in detail in Section 12.5). When the mask is overlaid on an image, the particular mathematical operation is performed and the resultant value is placed into the same array position and the operation is performed repeatedly until the entire image has been transformed. Although a digital mask can take on any shape, the most common masks are square with the center pixel being the particular pixel being operated on at any given time (Fig. 12.6). The most common masks are 3×3 or 5×5 arrays so that only the nearest neighbors will have an effect on the pixel being operated on. Additionally, larger arrays will greatly

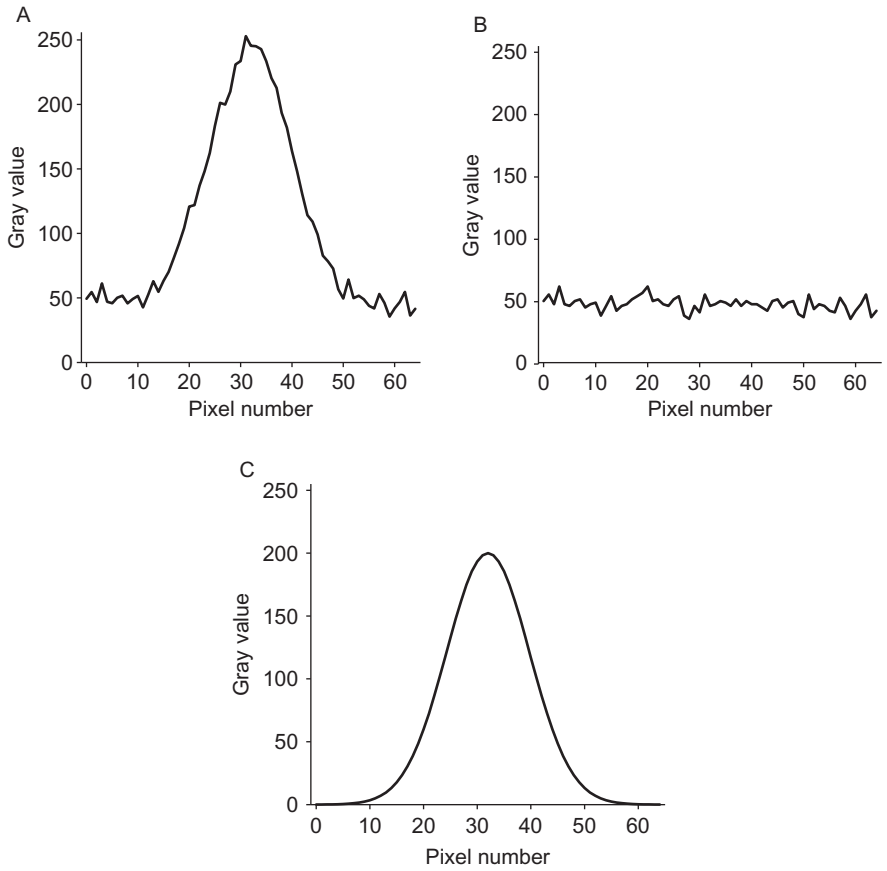

FIGURE 12.5

Subtracting noise from an image. (A) Line scan across an object and the surrounding background. (B) Line scan across the background alone reveals variations in intensity that may be due to uneven light intensity across the field, camera defects, dirt on the optics, and so on. (C) Image in (A) subtracted from image in (B). The result is a "cleaner" image with a higher SNR in the processed image compared to the original in (A).

increase the number of computations that need to be performed which can significantly slow down the rate of processing a particular image.

12.3.2.3 Averaging versus median filters

When an image contains random and infrequent intensity spikes with particular pixels, a digital mask can be used around each pixel to remove them. Two common ways to remove these intensity spikes are to calculate either the average value or the median value within the neighborhood and assign that value to the center pixel in the processed image (Fig. 12.7). The choice of filter used will depend on the type of

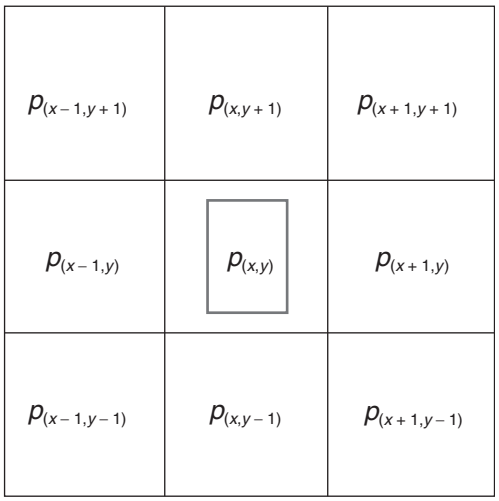

FIGURE 12.6

Digital mask used for computing means, averages, and higher-order mathematical operations, especially convolutions. In the case of the median and average filters, the mask is overlaid over each pixel in the image and the resultant value is calculated and placed into the identical pixel location in a new image buffer.

processed image that is desired. Although both types of filters will degrade an image, the median filter preserves edges better than the averaging filter since all values with the digital mask are used to compute the mean. Further, averaging filters are seldom used to remove intensity spikes because the spikes themselves contribute to the new intensity value in the processed image and therefore the resultant image is blurred.

The median filter is more desirable for removing infrequent intensity spikes from an image since those intensity values are always removed from the processed image once the median is computed. In this case, any spike is replaced with the median value within the digital mask, which gives a more uniform appearance to the processed image. Hence, a uniform background that contains infrequent intensity spikes will look absolutely uniform in the processed image. Since the median filter preserves edges (a sharpening filter), it is often used for high-contrast images (Fig. 12.8).

12.4 CONTRAST ENHANCEMENT

One of the most common uses of image processing is to digitally enhance the contrast of the image using a number of different methods (Castleman, 1979). In brightfield modes such as phase contrast or differential interference contrast, the addition of a camera and an image processor can significantly enhance the contrast so that specimens with inherent low contrast can be observed. Additionally, contrast routines can be used to enhance an image in a particular region, which may allow the investigator to quantify structures or events not possible with the microscope alone. This is the

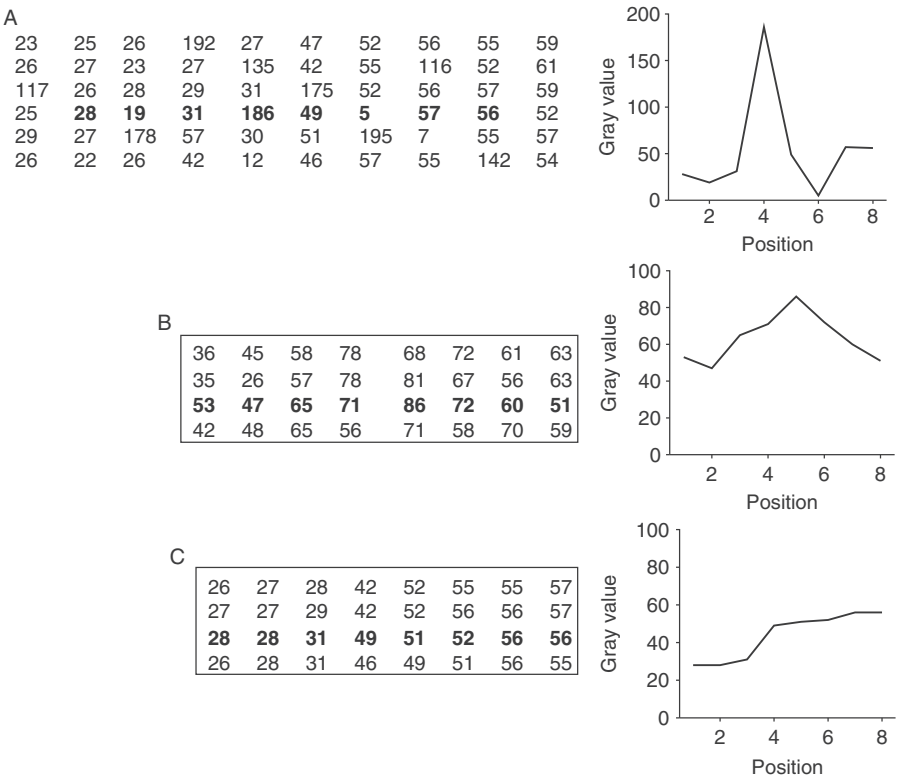

FIGURE 12.7

Comparison of 3 × 3 averaging and median filters to reduce noise. (A) Digital representation of an image displaying gray values at different pixel locations. In general, the object possesses a boundary which is detected as a line scan from left to right. However, the image has a number of intensity spikes which significantly mask the true boundary. A line scan across a particular row (row denoted by arrow and scan is on the right-hand side) reveals both high- and low-intensity values which greatly distort the image. (B) When a 3 × 3 averaging filter is applied to the image, the extreme intensity values are significantly reduced but the image is smoothed in the vicinity of the boundary. (C) In contrast, a 3 × 3 median filter removes the extreme intensity values while preserving the true nature of the boundary.

basis for VEDIC, which allows, for example, the motion of low-contrast specimens such as microtubules or chromosomes to be quantified (Chapter 16 by Salmon and Tran, volume 81, 2007).

In order to optimize contrast enhancement digitally, it is imperative that the microscope optics and the camera be adjusted so that the full dynamic range of the system is utilized. This is discussed further in Chapter 14 by Wolf et al., this volume. The gray values of the image and background can then be displayed as a histogram (Fig. 12.9) and the user is then able to adjust the brightness and contrast within a particular region of the image. Within a particular gray value range, the user can then

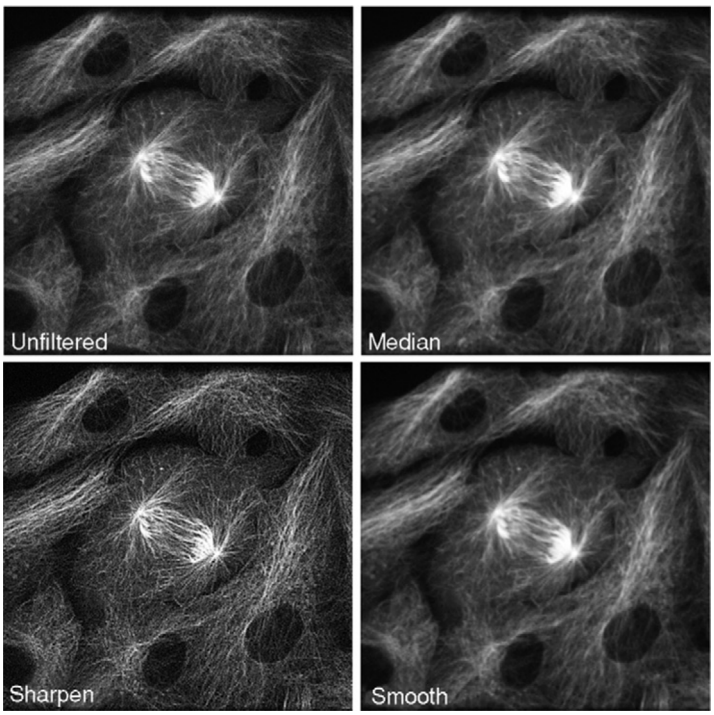

FIGURE 12.8

Effects of median sharpen and smooth filters on image contrast. A dividing mammalian cell expressing GFP-α tubulin was imaged using a spinning disk confocal microscope. After collection, separate digital filters were applied to the image.

stretch the histogram so that values within that range are spread out over a different range in the processed image. Although this type of contrast enhancement is artificial, this allows the user to discriminate features which otherwise may not have been detectable by eye in the original image.

Stretching gray values over a particular range in an image is one type of mathematical manipulation, which can be performed on a pixel-by-pixel basis. In general, any digital image can be mathematically manipulated to produce an image with different gray values. The user-defined function that transforms the original function is known as the image transfer function (ITF), which specifies the value and the mathematical operation that will be performed on the original image. This type of operation is a point operation, which means that the output gray value of the ITF is dependent only on the input gray value on a pixel-by-pixel basis. The gray values of the processed image, I_2, are therefore transformed at every pixel location relative to the original image using the same ITF. Hence, every gray value in the processed image is transformed according the generalized relationship:

$$\mathrm{GV}_2 = f(\mathrm{GV}_1)$$

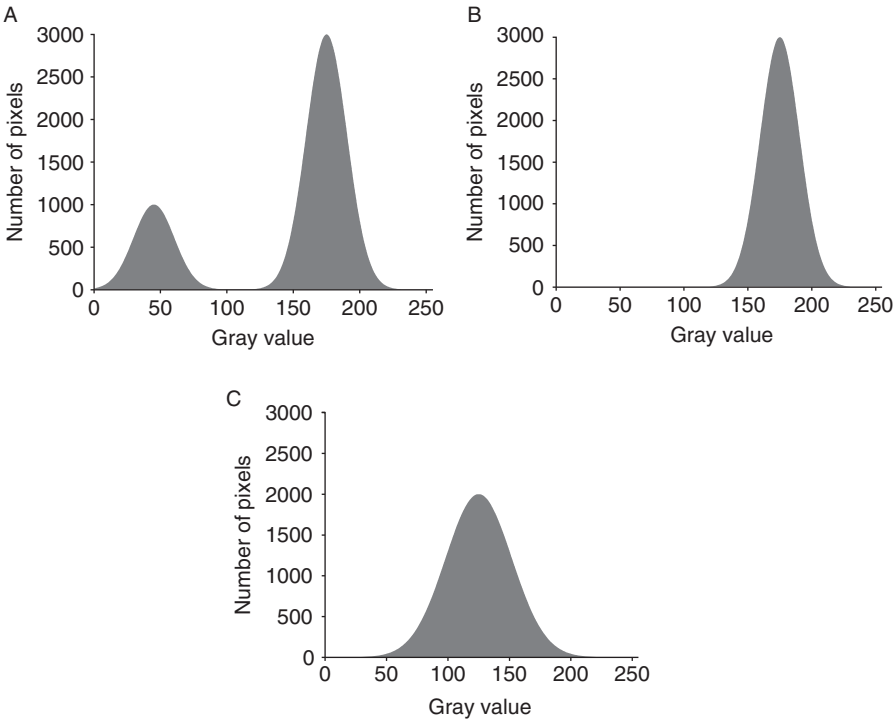

FIGURE 12.9

Histogram representation of gray values for an entire image. (A) The image contains two distributions of intensity over the entire gray value range (0–255). (B) The lower distribution can be removed either through subtraction (if lower values are due to a uniform background) or by applying the appropriate ITF which assigns a value of 0 to all input pixels having a gray value less than 100. The resulting distribution contains only information from input pixels with a value greater than 100. (C) The histogram of the higher distribution can be stretched to fill the lower gray values resulting in a lower mean value than the original.

where GV_2 is the gray value at every pixel location in the processed image, GV_1 is the input gray value of the original image, and $f(GV_1)$ is the ITF acting on the original image.

The simplest type of ITF is a linear equation of slope m and intercept b:

$$GV_2 = mGV_1 + b$$

In this case, the digital contrast of the processed image is linearly transformed with the brightness and contrast determined by both the value of the slope and intercept chosen. In the most trivial case, choosing values of $m = 1$ and $b = 0$ would leave all gray values of the processed image identical to the original image (Fig. 12.10A). Raising the value of the intercept while leaving the slope unchanged would have the effect of increasing all gray values by some fixed value (identical to increasing the DC or black level control on a camera).

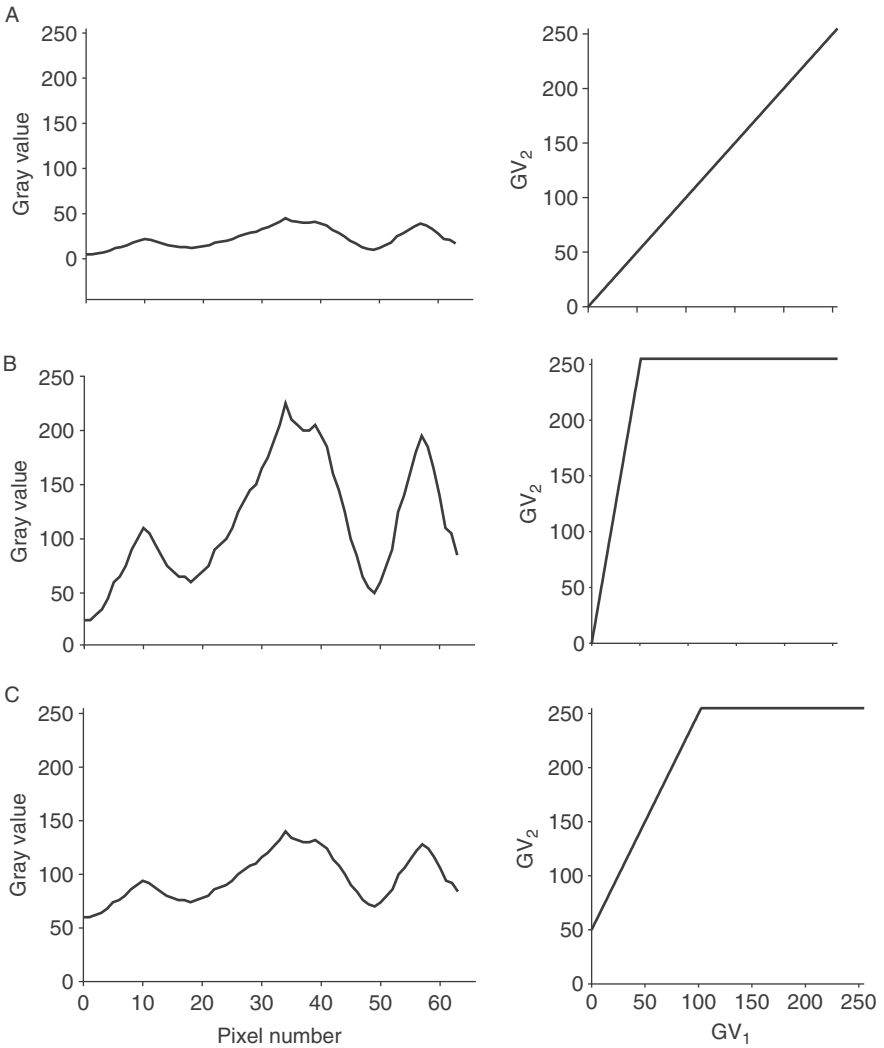

FIGURE 12.10

Application of different linear ITFs to a low-intensity, low-contrast image. (A) Intensity line scan through an object which is described by few gray values. Applying a linear ITF with $m = 1$ and $b = 0$ (right) will result in no change from the initial image. (B) Applying a linear ITF with $m = 5$ and $b = 0$ (right) leads to significant improvement in contrast. (C) Applying a linear ITF with $m = 2$ and $b = 50$ (right) slightly improves contrast and increases the brightness of the entire image.

Similarly, decreasing the value of the intercept will produce a darker image than the original. The value of the slope is known as the *contrast enhancement factor* and changes in the value of m will have significant effects on how the gray values are distributed in an image. A value of $m > 1$ will have the effect of spreading out

the gray values over a wider range in the processed image relative to the original image. Conversely, values of $m < 1$ will reduce the number of gray values used to describe a processed image relative to the original (Fig. 12.10). As noted by Inoue, 1986, although linear ITFs can be useful, the same effects can be best achieved by properly adjusting the camera's black levels and gain controls. However, this may not always be practical if conditions under the microscope are constantly changing or if this type of contrast enhancement is needed after the original images are stored.

The ITF is obviously not restricted to linear functions, and nonlinear ITFs can be extremely useful for enhancing particular features of an image while eliminating or reducing others (Fig. 12.11). Nonlinear ITFs are also useful for correcting sources of nonlinear response in an optical system or to calibrate the light response of an optical system (Inoue, 1986). The actual form of the ITF, being linear or nonlinear, is generally application dependent and user defined. For example, nonlinear ITFs that are sigmoidal in shape are useful for enhancing images, which compress the contrast in the center of the histogram and increase contrast in the tail regions of the histogram. This type of enhancement would be useful for images where most of the information about the image is in the tails of the histogram while the central portion of the histogram contains mostly background information. One type of nonlinear ITF, which is sigmoidal in shape, will enhance an 8-bit image of this type is given by the equation:

$$GV_2 = \frac{128}{(b-c)^a}\left[(b-c)^a - (b-GV_1)^a + (GV_1+c)^a\right]$$

where b and c are the maximum and minimum gray values for the input image, respectively and are arbitrary contrast enhancement factors (Inoue, 1986). For values of $a = 1$, this normally sigmoidal ITF becomes linear with a lope of $256(b-c)$. As a increases beyond 1, the ITF becomes more sigmoidal in nature with greater compression occurring at the middle gray values.

In practice, ITFs are generally calculated in memory using a lookup table (LUT). An LUT represents the transformation that is performed on each pixel on the basis of that intensity value (Figs. 12.12 and 12.13). In addition to LUTs, which perform particular ITFs, LUTs are also useful for pseudo-coloring images where particular user-defined colors represent gray values in particular ranges. This is particularly useful in techniques such as ration imaging where color LUTs are used to represent concentrations of Ca^{2+}, pH, or other ions, when various indicator dyes are employed within cells.

12.5 TRANSFORMS, CONVOLUTIONS, AND FURTHER USES FOR DIGITAL MASKS

In the previous sections, the most frequently used methods for enhancing contrast and reducing noise using temporal methods, simple arithmetic operations, and LUTs were described. However, more advanced methods are often needed to extract

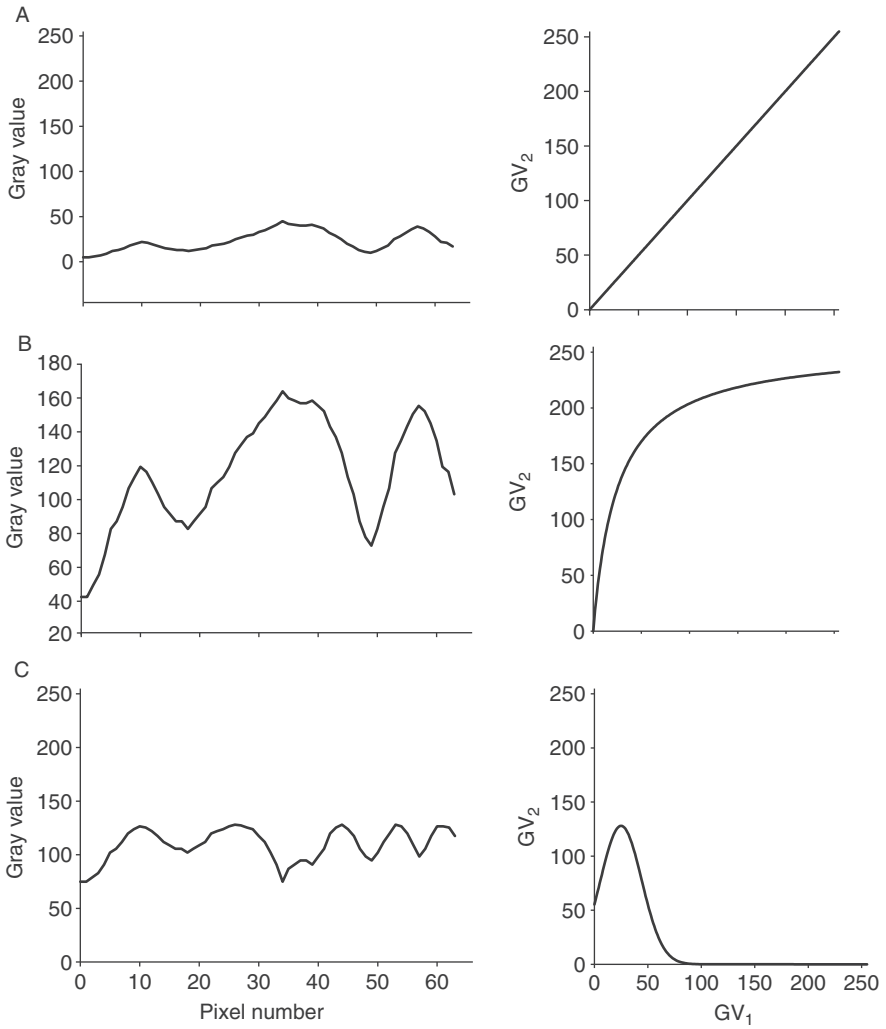

FIGURE 12.11

Application of different nonlinear ITFs to the same low-intensity, low-contrast image in Fig. 12.8. (A) Initial image and ITF (right) resulting in no change. (B) Application of a hyperbolic ITF (right) to the image results in amplification of lower input values and only slightly increases the gray values for higher input values. (C) Application of a Gaussian ITF (right) to the image results in amplification of low values, with an offset, and minimizes input values beyond 100.

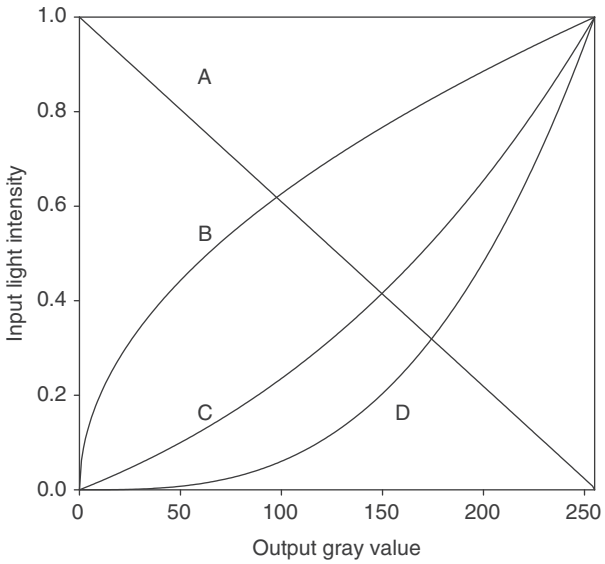

FIGURE 12.12

Some different gray value LUTs used to alter contrast in images. (A) Inverse LUT, (B) logarithmic LUT, (C) square root LUT, (D) square LUT, and (E) exponential LUT. Pseudo-color LUTs would assign different colors instead of gray values.

particular features from an image which may not be possible using these simple methods (Jahne, 1991). In this section, some of the concepts and applications associated with transforms and convolutions will be introduced.

12.5.1 Transforms

Transforms take an image from one space to another. Probably, the most used transform is the Fourier transform which takes one from coordinate space to spatial frequency space (see Chapter 2 by Wolf, this volume for a discussion of Fourier transforms). In general, a transform of a function in one dimension has the form:

$$T(u) = \sum_x f(x)g(x,u)$$

where $T(u)$ is the transform of $f(x)$ and $g(x,u)$ is known as the forward transformation kernel. Similarly, the inverse transform is given by the relation:

$$f(x) = \sum_u T(u)h(x,u)$$

where $h(x,u)$ is the inverse transformation kernel. In two dimensions, these transformation pairs simply become:

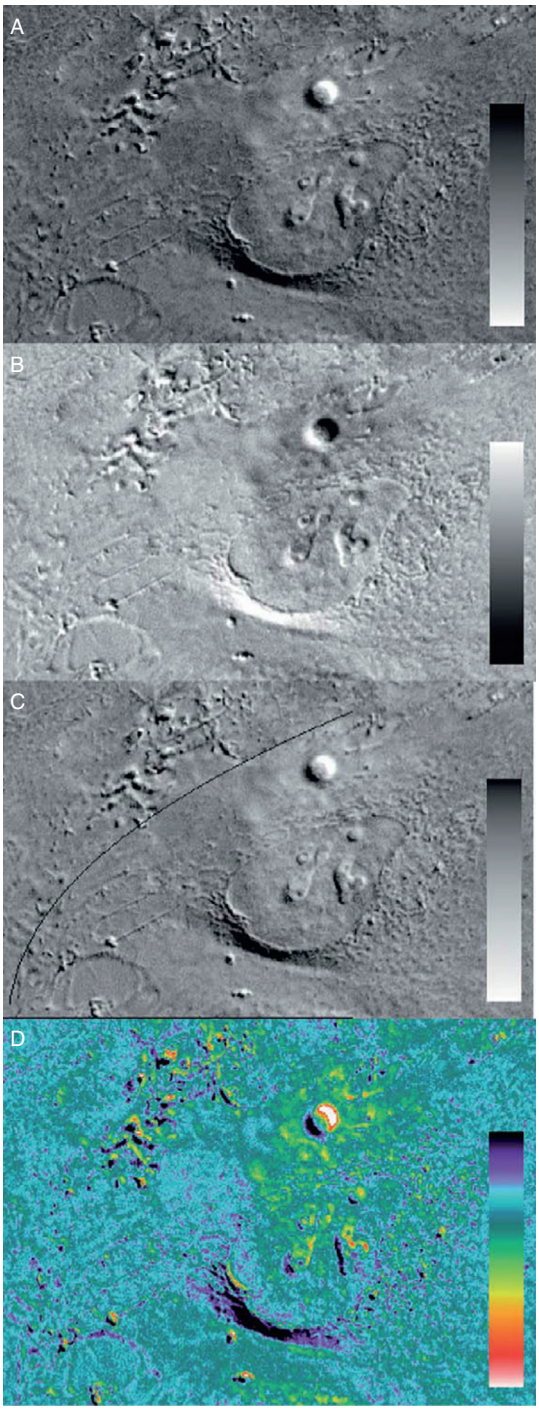

FIGURE 12.13

Different LUTs applied to the image of a check cell. (A) No filter, (B) reverse contrast LUT, (C) square root LUT, (D) pseudo-color LUT.

$$T(u,v) = \sum_x \sum_y f(x,y)g(x,y,u,v)$$

$$f(x,y) = \sum_u \sum_v T(u,v)h(x,y,u,v)$$

It is the kernel functions that provide the link, which brings a function from one space to another. The discrete forms shown above suggest that these operations can be performed on a pixel-by-pixel basis and many transforms in image processing are computed in this manner (known as a discrete Fourier transform or DFT). However, DFTs are generally approximated using different algorithms to yield a fast Fourier transform, or FFT.

In the Fourier transform, the forward transformation kernel is:

$$g(x,u) = \frac{1}{N} e^{-2\pi iux}$$

and the reverse transformation kernel is:

$$f(x,u) = \frac{1}{N} e^{+2\pi iux}$$

Hence, a Fourier transform is achieved by multiplying a digitized image pixel-by-pixel whose gray value is given by $f(x,y)$ by the forward transformation kernel given above. Transforms, and in particular Fourier transforms, can make certain mathematical manipulations of images considerably easier than if they were performed in coordinate space directly.

One example where conversion to frequency space using an FFT is useful is in identifying both high- and low-frequency components on an image that allows one to make quantitative choices about information that can be either used or discarded. Sharp edges and many types of noise will contribute to the high-frequency content of an image's Fourier transform. Image smoothing and noise removal can therefore be achieved by attenuating a range of high-frequency components in the transform range. In this case, a filter function, $F(u,v)$, is selected that eliminates the high-frequency components of that transformed image, $I(u,v)$. The ideal filter would simply cut off all frequencies about some threshold value, I_0 (known as the cutoff frequency):

$$F(u,v) = 1 \quad \text{if} \quad |I(u,v)| \leq I_0$$
$$F(u,v) = 0 \quad \text{if} \quad |I(u,v)| > I_0$$

The absolute value brackets refer to the fact that these are zero-phase shift filters because they do not change the phase of the transform. A graphical representation of an ideal low-pass filter is shown in Fig. 12.14. Just as an image can be blurred by attenuating high-frequency components using a low-pass filter, so they can be sharpened by attenuating low-frequency components (Fig. 12.14). In analogy to the low-pass filter, an ideal high-pass filter has the following characteristics:

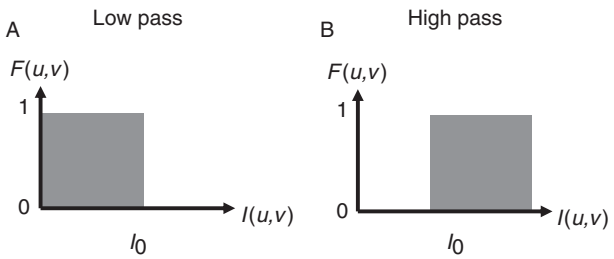

FIGURE 12.14

Frequency domain cutoff filters. The filter function in frequency space, $F(u,v)$, is used to cut off all frequencies above or below some cutoff frequency, I_0. (A) A high-pass filter attenuates all frequencies below I_0 leading to a sharpening of the image. (B) A low-pass filter attenuates all frequencies above I_0 which eliminates high-frequency noise but leads to smoothing or blurring of the image.

$$F(u,v) = 0 \quad \text{if} \quad |I(u,v)| \leq I_0$$
$$F(u,v) = 1 \quad \text{if} \quad |I(u,v)| > I_0$$

Although useful, Fourier transforms can be computationally intense and are still not routinely used in most microscopic applications of image processing. A mathematically related technique known as convolution, which utilizes digital masks to select particular features of an image, is the preferred method of microscopists since many of these operations can be performed at faster rates and perform the mathematical operation in coordinate space instead of frequency space. These operations are outlined in Section 12.5.2.

12.5.2 Convolution

The convolution of two functions, $f(x)$ and $g(x)$, is given mathematically by:

$$\int_{-\infty}^{+\infty} f(\alpha)g(x-\alpha)\mathrm{d}\alpha$$

where α is a dummy variable of integration. It is easiest to visualize the mechanics of convolution graphically as demonstrated in Fig. 12.15, which, for simplicity, shows the convolution for two square pulses. The convolution can be broken down into three simple steps:

1. Before carrying out the integration, reflect $g(\alpha)$ about the origin, yielding $g(-\alpha)$ and then displace it by some distance x to give $g(x-\alpha)$.
2. For all values of x, multiply $f(\alpha)$ by $g(x-\alpha)$. The product will be nonzero at all points where the functions overlap.
3. Integrating this product yields the convolution between $f(x)$ and $g(x)$.

Hence, the properties of the convolution are determined by the independent function $f(x)$ and a function $g(x)$ that selects for certain desired details in the function $f(x)$. The selecting function $g(x)$ is therefore analogous to the forward transformation

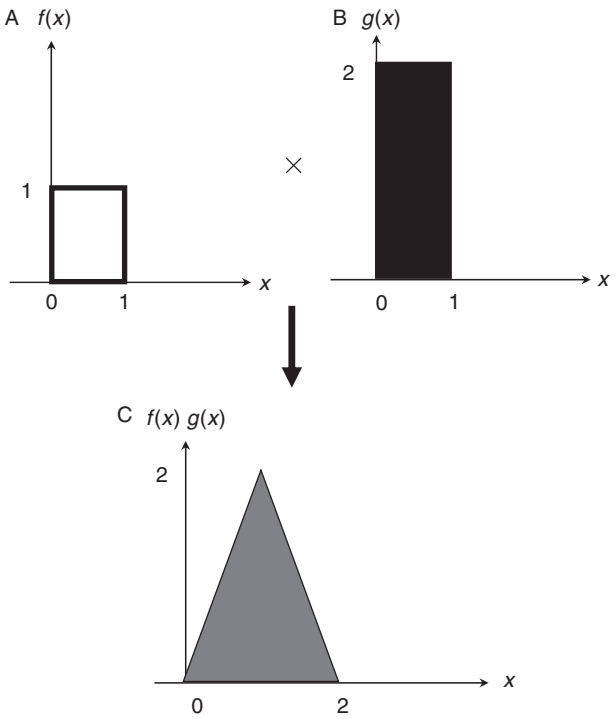

FIGURE 12.15

Graphical representation of one-dimensional convolution. (A) In this simple example, the function, $f(x)$, to be convolved is a square pulse of equal height and width. (B) The convolving function, $g(x)$, is a rectangular pulse which is twice as high as it is wide. The convolving function is then reflected and is then moved from $-\infty$ to $+\infty$. (C) In all areas where there is no overlap, the products of $f(x)$ and $g(x)$ is zero. However, $g(x)$ overlaps $f(x)$ in different amounts from $x = 0$ to $x = 2$ with maximum overlap occurring at $x = 1$. The operation therefore detects the trailing edge of $f(x)$ at $x = 0$ and the convolution results in a triangle which increases in height from 0 to 2 for $0 < x \leq 1$ and decreases in height from 2 to 0 for $1 \leq x < 2$.

kernel in frequency space except that it selects for features in coordinate space instead of frequency space. This clearly makes the convolution an important image-processing technique for microscopists who are interested in feature extraction.

One simple application of convolutions is the convolution of a function with an impulse function (commonly known as a delta function), $\delta(x - x_0)$:

$$\int_{-\infty}^{+\infty} f(x)\delta(x - x_0)\mathrm{d}x = f(x_0)$$

For our purposes, $\delta(x - x_0)$ is located at $x = x_0$ and the intensity of the impulse is determined by the value $f(x)$ at $x = x_0$ and is zero everywhere else. In this example, we will let the kernel $g(x)$ represent three impulse functions separated by a period, τ:

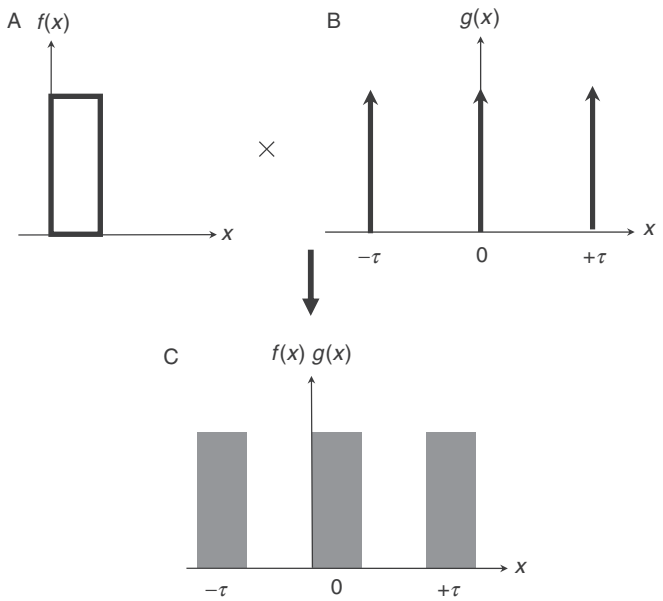

FIGURE 12.16

Using a convolution to copy an object. (A) The function $f(x)$ is a rectangular pulse of amplitude, A, with its leading edge at $x = 0$. (B) The convolving functions $g(x)$ are three delta functions at $x = -\tau$, $x = 0$, and $x = +\tau$. (C) The convolution operation $f(x)g(x)$ results in copying of the three rectangular pulses at $x = -\tau$, $x = 0$, and $x = +\tau$.

$$g(x) = \delta(x + \tau) + \delta(x) + \delta(x - \tau)$$

As shown in Fig. 12.16, the convolution of the square pulse $f(x)$ with these three impulses results in a copying of $f(x)$ at the impulse points.

As with Fourier transforms, the actual mechanics of convolution can rapidly become computationally intensive for a large number of points. Fortunately, many complex procedures can be adequately performed using a variety of digital masks as illustrated in Section 12.5.3.

12.5.3 Digital masks as convolution filters

For many purposes, the appropriate digital mask can be used to extract features from images. The convolution filter, acting as a selection function $g(x)$, can be used to modify images in a particular fashion. Convolution filters reassign intensities by multiplying the gray value of each pixel in the image by the corresponding values in the digital mask and then summing all the values; the resultant is then assigned to the center pixel of the new image and the operation is then repeated for every pixel in the image (Fig. 12.17). Convolution filters can vary in size (i.e., $3 \times 3, 5 \times 5, 7 \times 7$, and so on) depending on the type of filter chosen and the relative weight that is required from neighboring values from the center pixel.

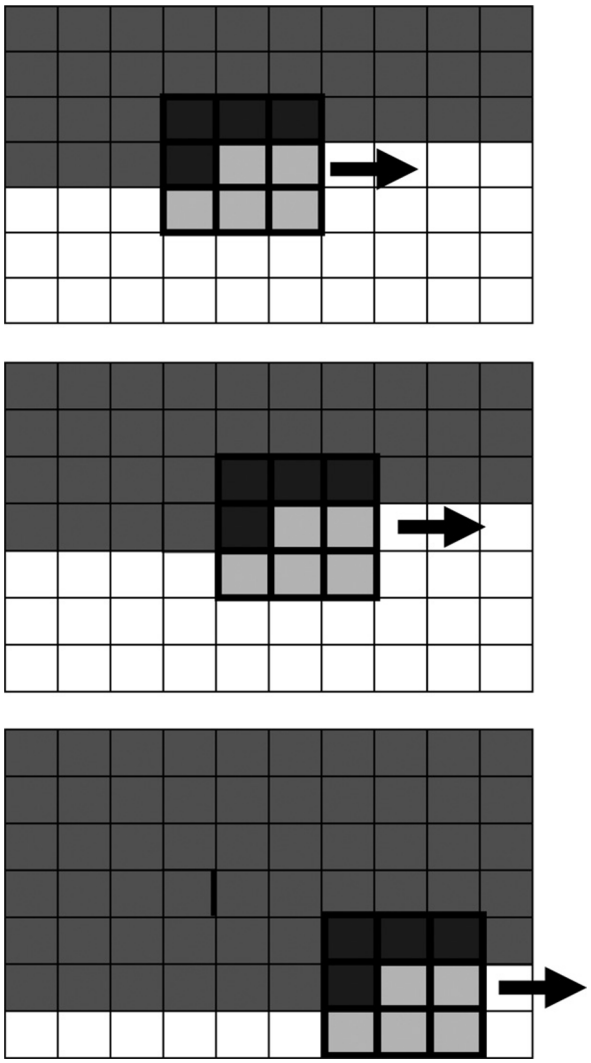

FIGURE 12.17

Performing convolutions using a digital mask. The convolution mask is applied to each pixel in the image. The value assigned to the central pixel results from multiplying each element in the mask by the gray value in the corresponding image, summing the result, and assigning the value to the corresponding pixel in a new image buffer. The operation is repeated for every pixel resulting in the processed image. Or different operations, a scalar multiplier and/or offset may be needed.

For example, consider a simple 3 × 3 convolution filter, which has the form:

1/9	1/9	1/9
1/9	1/9	1/9
1/9	1/9	1/9

Applied to a pixel with an intensity of 128 and surrounded by other intensity values as follows:

123	62	97
237	128	6
19	23	124

The gray value in the processed image at that pixel, therefore, would have a new value of $1/9(123+62+97+237+128+6+19+2+124) = 819/9 = 91$. Note that this convolution filter is simply an averaging filter identical to the operation described in Section 12.3 (in contrast, a median filter would have returned a value of 128). A 5 × 5 averaging filter would simply be a mask, which contains 1/25 in each pixel whereas a 7 × 7 averaging filter would contain 1/49 in each pixel. Since the speed of processing decreases with the size of the digital mask, the most frequently used filters are 3 × 3 masks.

In practice, the values found in the digital masks tend to be integer values with a divisor that can vary depending on the desired operation. In addition, because many operations can lead to resultant values, which are negative (since the values in the convolution filter can be negative), offset values are often used to prevent this from occurring. In the example of the averaging filter, the values in the kernel would be:

1	1	1
1	1	1
1	1	1

with a divisor value of 9 and an offset of zero. In general, for an 8-bit image, divisors and offsets are chosen so that all processed values following the convolution fall between 0 and 255.

Understanding the nature of convolution filters is absolutely necessary when using the microscope as a quantitative tool. User-defined convolution filters can be used to extract information specific for a particular application. When beginning to use these filters, it is important to have a set of standards, which the filters can be applied to in order to see if the desired effect has been achieved. In general, the best test objects for

convolution filters are simple geometric objects such as squares, grids, isosceles and equilateral triangles, circles, and so on. Many commercially available graphics packages provide such test objects in a variety of graphics formats. Examples of some widely used convolution masks are given in the following sections.

12.5.3.1 Point detection in a uniform field

Assume that an image consists of a series of grains on a constant background (e.g., a dark-field image of a cellular autoradiogram). The following 3×3 mask is designed to detect these points:

−1	−1	−1
−1	+8	−1
−1	−1	−1

When the mask encounters a uniform background, then the gray values in the processed center pixel will be zero. If, on the other hand, a value above the constant background is encountered, then its value will be amplified above that background and a high-contrast image will result.

12.5.3.2 Line detection in a uniform field

Similar to the point mask in the previous example, a number of line masks can be used to detect sharp, orthogonal edges in an image. These line masks can be used alone or in tandem to detect horizontal, vertical, or diagonal edges in an image. Horizontal and vertical line masks are represented as:

−1	−1	−1
+2	+2	+2
−1	−1	−1

−1	+2	−1
−1	+2	−1
−1	+2	−1

whereas, diagonal line masks are given as:

−1	−1	+2
−1	+2	−1
+2	−1	−1

+2	−1	−1
−1	+2	−1
−1	−1	+2

In any line mask, the direction of nonpositive values used reflects the direction of the line detected. When choosing the type of line mask to be utilized, the user must *a priori* know the directions of the edges to be enhanced.

12.5.3.3 Edge detection-computing gradients

Of course, lines and points are seldom encountered in natures and another method for detecting edges would be desirable. By far, the most useful edge detection procedure is one that picks up any inflection point in intensity. This is best achieved by using gradient operators, which take the first derivative of light intensity in both the x- and y-directions. One type of gradient convolution filters, which are often used, is the Sobel filter. An example of a Sobel filter, which calculates horizontal edges, is the Sobel North filter expressed as the following 3×3 kernel:

+1	+2	+1
0	0	0
−1	−2	−1

This filter is generally not used alone, but is instead used along with the Sobel East filter, which is used to detect vertical edges in an image. The 3×3 kernel for this filter is:

−1	0	+1
−2	0	+2
−1	0	+1

These two Sobel filters can be used to calculate both the angle of edges in an image and the relative steepness of intensity (i.e., the derivative of intensity with respect to position) of that image. The so-called Sobel Angle filter returns arctangent of the ratio of the resultant Sobel North filtered pixel value to the Sobel East filtered pixel value while the Sobel Magnitude filter calculates a resultant value from the square root of the sum of the squares of the Sobel North and Sobel East values.

In addition to Sobel filters, a number of different gradient filters can be used (specifically Prewitt or Roberts gradient filters) depending on the specific application. Figure 12.18 shows the design and outlines the basic properties of these filters, and Fig. 12.19 shows the effects of these filters on a fluorescence micrograph.

Name	Kernels	Uses
Gradient	$\begin{bmatrix} -1 & +1 & +1 \\ -1 & 2 & +1 \\ -1 & +1 & +1 \end{bmatrix}$	Detects the vertical edges of objects in an image.
Sobel	North: $\begin{bmatrix} +1 & +2 & +1 \\ 0 & 0 & 0 \\ -1 & -2 & -1 \end{bmatrix}$ East: $\begin{bmatrix} -1 & 0 & +1 \\ -2 & 0 & +2 \\ -1 & 0 & +1 \end{bmatrix}$	North detects horizontal edges; East detects vertical edges. North and East used to calculate Sobel Angle and Sobel Magnitude (see test). Filters should not be used independently; if horizontal or vertical detection is desired, use Prewitt.
Prewitt	North: $\begin{bmatrix} +1 & +1 & +1 \\ 0 & 0 & 0 \\ -1 & -1 & -1 \end{bmatrix}$ East: $\begin{bmatrix} -1 & 0 & +1 \\ -1 & 0 & +1 \\ -1 & 0 & +1 \end{bmatrix}$	North detects horizontal edges; East detects vertical edges.
Roberts	Northeast: $\begin{bmatrix} 0 & 1 \\ -1 & 0 \end{bmatrix}$ Northwest: $\begin{bmatrix} 1 & 0 \\ 0 & -1 \end{bmatrix}$	Northeast detects diagonal edges from top-left to bottom-right; Northwest detects diagonal edges from top-right to bottom-left.

FIGURE 12.18

Different 3 × 3 gradient filters used in imaging. Shown are four different gradient operators and their common uses in microscopy and imaging.

12.5.3.4 Laplacian filters

Laplacian operators calculate the second derivative of intensity with respect to position and are useful for determining whether a pixel is on the dark side or light side of an edge. Specifically, the Laplace-4 convolution filter, given as:

$$\begin{bmatrix} 0 & -1 & 0 \\ -1 & +4 & -1 \\ 0 & -1 & 0 \end{bmatrix}$$

detects the light and dark sides of an edge in an image. Because of its sensitivity to noise, this convolution mask is seldom used by itself as an edge detector. In order to keep all values of the processed image within 8 bits and positive, a divisor of 8 and an offset value of 128 are often employed.

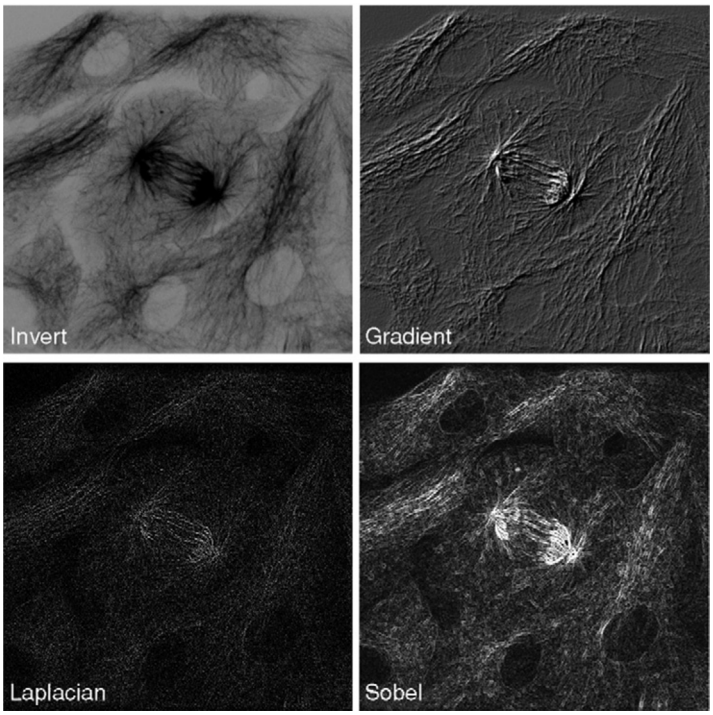

FIGURE 12.19

Different filters applied to a fluorescence image of a dividing mammalian cell. Inverse contrast LUT, gradient filter, Laplacian filter, Sobel filter.

The point detection filter shown earlier is also a kind of Laplace filter (known as the Laplace-8 filter). This filter uses a divisor value of 16 and an offset value of 128. Unlike the Laplace-4 filter, which only enhances edges, the Laplace-8 filter enhances edges and other features of the object.

12.6 THRESHOLDING

Image data may be globally segmented using a mask that differentiates objects based on their intensity values. This is referred to as thresholding, and seeks to differentiate an image into those pixels in the foreground (objects of interest) and those in the background (which will be ignored). In determining a threshold, the intensity value of a pixel, or the average intensity value for a defined region of pixels (say a 20×20 pixel box) is compared to a fixed value or threshold. Any pixel or region of pixels that is greater than the fixed value is kept; any pixel(s) below the threshold are discarded from the processed image (Figure 20). The processed image is then used for quantitative analysis, such as single particle tracking, where the threshold mask makes it easier to discriminate isolated objects (Jaqaman et al., 2008).

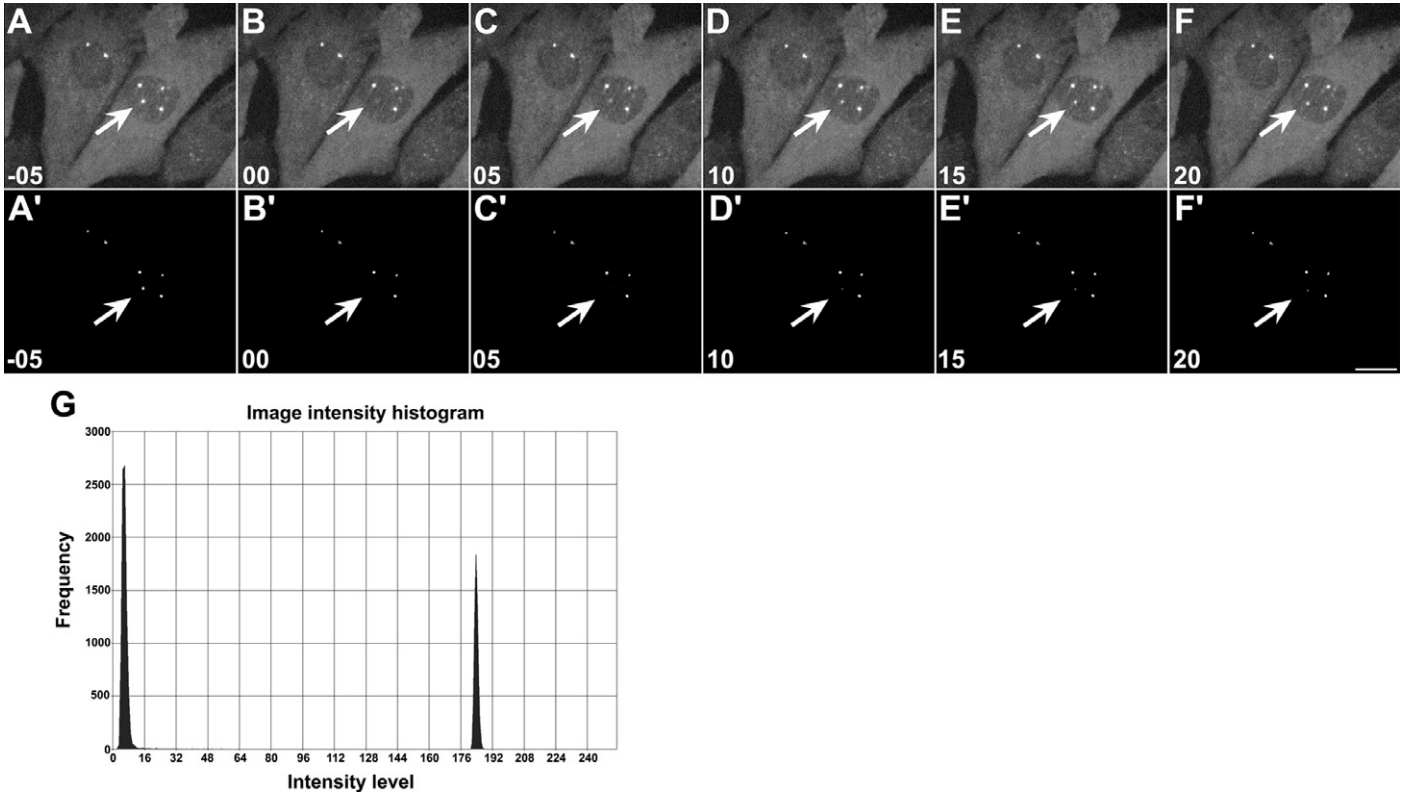

FIGURE 12.20

Image thresholding applied to fluorescence images. (A-F). Frames from a time-lapse series showing fluorescence recovery after photobleaching (FRAP) for a γ-tubulin-GFP expressing CHO cell. (A). The right cell has faint background fluorescence, a dark nuclear region that excludes GFP fluorescence, and four bright fluorescent spots, that represent re-duplicated centrosomes generated by cell cycle arrest in S-phase (Collins et al., 2010). (B). One centrosome (arrow) is photobleached using a laser (Photonics MicroPoint FRAP system). C-F. The fluorescence of the bleached spot returns, as the γ-tubulin bound to the centrosome exchanges with the soluble pool. (A'-F'). The same time-lapse sequence after undergoing global thresholding to segment the brightest regions of the images. The positions of the bright centrosomes are easily detected, and the background intensities have been driven to black. (G). Image intensity histogram showing a bimodal distribution, with a large number of near-black pixels between 0-16 gray levels, and a smaller intensity peak of bright pixels between 176-192 gray levels.

The determination of an optimum threshold can often be complicated. Too-high a threshold results in loss of information, whereas setting the threshold too low results in excessive noise. Determining the optimum threshold for an image can be simplified by examining the histogram for that image. Two prominent peaks, corresponding to two distinct intensity levels (a bright object, and a dark background) simplify the selection of a threshold values, which would lie between the peaks (Figure 20, G). However, in other cases, the image background may be uneven throughout the image, and there may be variance between the intensities of objects in the foreground. In such a case, finding a global threshold that differentiates between foreground and background may be difficult. Flat field correction and other processing steps may help, and the results can be analyzed by examining the resultant image intensity histogram, prior to thresholding. In other cases, using an iterative thresholding technique, such as described by Ridler & Calvard (1978) or Otsu (1979) can be used to determine the optimun global threshold value. In extreme cases, where uneven illumination and low contrast make global thresholding impossible, locally adaptive methods can be used, including sliding window or neighborhood processing methods (Niblack, 1986; Yan, Zhang, & Kube, 2005).

CONCLUSIONS

The judicious choice of image-processing routines can greatly enhance an image and can extract features, which are not otherwise possible. When applying digital manipulations to an image, it is imperative to understand the routines that are being employed and to make use of well-designed standards when testing them out. With the advent of high-speed digital detectors and computers, near real-time processing involving moderately complicated routines is now possible.

References

Andrews, H. C., & Hunt, B. R. (1977). *Digital image restoration*. Englewood Cliffs, NJ: Prentice-Hall.

Bates, R. H. T., & McDonnell, M. J. (1986). *Image restoration and construction*. New York, NY: Oxford University Press.

Cardullo, R. A. (1999). *Electronic and computer image enhancement in light microscopy*. *Encyclopedia of life sciences*. Hoboken, NJ: Wiley & Sons.

Castleman, K. R. (1979). *Digital image processing*. Englewood Cliffs, NJ: Prentice-Hall.

Chellappa, R., & Sawchuck, A. A. (1985). *Digital image processing and analysis*. New York, NY: IEEE Press.

Collins, E. S., Hornick, J. E., Durcan, T. M., Collins, N. S., Archer, W., Karanjeet, K. B., et al. (2010). Centrosome biogenesis continues in the absence of microtubules during prolonged S-phase arrest. *Journal of Cellular Physiology*, *225*, 454–465.

Erasmus, S. J. (1982). Reduction of noise in a TV rate electron microscope image by digital filtering. *Journal of Microscopy*, *127*, 29–37.

Gonzalez, R. C., & Wintz, P. (1987). *Digital image processing*. Reading, MA: Addison-Wesley.

Green, W. B. (1989). *Digital image processing: A systems approach*. New York, NY: Van Nostrand Reinhold.

Inoue, S. (1986). *Video microscopy*. New York, NY: Plenum.

Inoue, S., & Spring, K. R. (1997). *Video microscopy* (2nd ed.). New York, NY: Plenum.

Jahne, B. (1991). *Digital image processing*. New York, NY: Springer-Verlag.

Jaqaman, K., Loerke, D., Mettlen, M., Kuwata, H., Grinstein, S., Schmid, S. L., et al. (2008). Robust single-particle tracking in live-cell time-lapse sequences. *Nature Methods*, *5*, 695–702.

Niblack, W. (1986). *An introduction to image processing*. Englewood Cliffs, NJ: Prentice-Hall.

Otsu, N. (1979). A threshold selection method from gray-level histograms. *IEEE Transactions on Systems, Man, and Cybernetics*, *9*(1), 62–66.

Pratt, W. K. (1978). *Digital image processing*. New York, NY: Wiley.

Ridler, T. W., & Calvard, S. (1978). Picture thresholding using an iterative selection method. *IEEE Transactions on Systems, Man, and Cybernetics*, *8*(8), 630–632.

Russ, J. C. (1990). *Computer-assisted microscopy. The measurement and analysis of images*. New York, NY: Plenum.

Russ, J. C. (1994). *The image processing handbook*. Ann Arbor, MI: CRC Press.

Shotton, D. (1993). *Electronic light microscopy: Techniques in modern biomedical microscopy*. New York, NY: Wiley-Liss.

Yan, F., Zhang, H., & Kube, C. R. (2005). A multistage adaptive thresholding method. *Pattern Recognition Letters*, *26*, 1183–1191.

CHAPTER

65,000 Shades of Grey: Use of Digital Image Files in Light Microscopy

13

Sidney L. Shaw* **and Edward H. Hinchcliffe†**

*Biology Department, Indiana University, Bloomington, Indiana, and Department of Biology, University of North Carolina, Chapel Hill, North Carolina, USA

†Cellular Dynamics Section, Hormel Institute, University of Minnesota, Austin, Minnesota, USA

CHAPTER OUTLINE

Introduction **318**
13.1 What is An Image File? **320**
13.2 Bit Depth **320**
13.3 File Formats **322**
13.4 Sampling and Spatial Resolution **325**
13.5 Color **325**
13.6 Converting RGB to CMYK **327**
13.7 Compression **329**
13.8 Video Files **329**
13.9 Video Codecs **331**
13.10 Choosing a Codec **332**
13.10.1 Real Results 334
Conclusions **335**
Acknowledgments **335**
References **336**

Abstract

Computers dominate image capture and analysis in modern light microscopy. The output of an imaging experiment is a binary coded file, called an image file, which contains the spatial, temporal and intensity information present in the sample. Understanding what comprises an image file, and how these files are generated is necessary in order to optimize the use of the digital light microscope. In this chapter, we discuss image file formats, and the various components of these files, such as bit-depth, sampling rate, color theory, and compression, from the perspective of the non-computer scientist.

Methods in Cell Biology, Volume 114 **ISSN 0091-679X**
Copyright © 2013 Elsevier Inc. All rights reserved.
http://dx.doi.org/10.1016/B978-0-12-407761-4.00013-0

We also discuss the problem of proprietary file formats, and how these often are incompatible with certain types of imaging software. We present several solutions to this issue. Finally, we present the use of digital movie formats, compression routines, and provide some real world examples for optimizing the generation of digital movies.

INTRODUCTION

Digital microscopy is the recording of an image generated through the microscope into a binary coded file. Like photomicrography and cinemicrography, digital image files provide a permanent record of observations made in the microscope (Furness, 1997). Unlike these analog recording modes, digital micrographs can easily be assembled into sequences, to represent motion, or into projections to visualize spatial information in three dimensions, without having to first copy and convert these images into a digital format. The ultimate expression of the medium is the presentation of time-lapse motion picture sequences of 3D reconstructions (so-called 4D microscopy; see Salmon et al., 1998; Thomas, DeVries, Hardin & White, 1996).

In addition to representing purely visual information from a specimen, digital microscopy image files also contain quantitative temporal and spatial information, relating to the behavior, and/or specific events within cells. This is particularly powerful when using sophisticated fluorescent probes to detect and analyze individual molecules *in vivo*. The images contain quantitative data relating to protein concentration, enzyme kinetics, cellular dynamics, etc. To maximize the use of the digital microscope as a quantitative instrument, the temporal, spatial, and biochemical information obtained must be output into a form that can be analyzed, searched, shared, published in journals, displayed on websites, and presented at meetings. Mishandling the collection and storage of information contained within digital image files often leads to unfortunate outcomes. Thus, it becomes an important task to plan for the generation, manipulation, and storage of image-based data.

Most biologists have limited training in computer science or in areas of image processing. Often, the use of computers for biological imaging follows an "oral" tradition based on colleagues or collaborators. While such an approach can propagate useful information, it can also perpetuate misconceptions leading to bad digital habits. In many settings, standard protocols for a laboratory are developed without planning for storage, analysis, or eventual publication. The result is that digital imaging is not optimized, when it easily could be. The following chapter will deal with image files from the standpoint of a noncomputer scientist/graphics artist. The emphasis will be on understanding basic concepts and providing the individual biology researcher with the tools to make informed decisions about generating, manipulating, and storing graphics image files.

To begin, it is useful to consider the trajectory of your image data from initial collection to final publication. The majority of the images taken in the research laboratory are still used for the purpose of visually comparing a control to an experimental condition. The images can be from live cells or fixed material, 2D or 3D volumes, single frames, or time-lapse series. In each case, a collection of images will be taken

and stored as digital files for later review where the conditions of the experiment and details of the microscopy should be recorded, information that is referred to as "metadata," a topic that will be touched on later in this chapter. From these stored files, some level of analysis will be performed through human evaluations, often with considerable postprocessing of the original images for contrast and noise abatement or for creating 3D projections or movies. In limited cases, the image data will be subjected to more complicated analytical schemes using computational tools to extract numerical data (Cardullo & Hinchcliffe, 2007; Jaqaman et al., 2008; Walczak, Rizk, & Shaw, 2010; Waters, 2009). It is important that the processing and analytical steps be carefully recorded, as these need to be reported during publication. Finally, a select set of micrographs will be developed for presentations and for publication, with explicit instruction from a journal about format and resolution. All of the images should then be archived in a manner that permits search and retrieval in a manner consistent with laboratory notebooks and other data.

A key point to consider when generating and using digital image files is that the original, unprocessed images are data, a record of experimental results. These should be maintained as such, in an unmanipulated form. Any image-processing steps should be saved as a separate file, containing a processed image or a set of images. The same holds true for figures for presentation and/or publication, which are in essence "graphics." Though these graphics will contain images and measurements made from the data, they are separate and must be treated as such. In other words, files generated as graphics should never be used to generate data. Measurements should be made only from primary data files.

All of this data are collected using imaging software, and the software available has an enormous impact on how the data are captured, analyzed, and stored. In broad terms, there are two types of software commercially available for digital microscopy. The first is purpose written to drive an individual instrument and is usually provided as part of a "turn-key" imaging system. Often such software is tied to a particular instrument manufacturer and can only rarely interface with other instruments. This type of software can range from the basic, picture-taking packages designed for general digital photomicrography use, to highly sophisticated software, capable of analytical and quantitative measurements. The second type of software is designed primarily as an analytical tool and purpose built to work with most imaging platforms. This type of software is often capable of driving numerous devices from a wide range of manufacturers, such as microscopes, automated stages, cameras or other detectors, illumination and shuttering units, galvanometers, and laser-bleaching and -ablation devices. Because of their ability to interface with multiple instruments, such software packages offer great flexibility, and are used to drive many custom-built imaging systems. The choice of which type of system to choose is often based on capabilities and expertise in the lab or institute, as well as on budget considerations.

There is another type of software available called openware, freeware, or shareware. These packages are freely downloadable and are maintained and updated by a body of users. Packages such as the image-processing software *ImageJ* (http://rsbweb.nih.gov/ij/), formerly known as *NIH Image* for Macintosh and *Scion Imaging* for Windows, and the automated microscope control software MicroManager

(μManager: http://valelab.ucsf.edu/~MM/MMwiki/) are powerful tool that allow the user to drive image capture and analysis (Schneider, Rasband, & Eliceiri, 2012; Shaw, Salmon, & Quatrano, 1995). The only major difference between freeware and commercially available software packages is the availability of support versus cost to the researcher. On the shareware side, updates and added capabilities are determined by those users that can sit down and write the software. In the case of commercial packages, updates are dependent on users purchasing software licenses. Both routes can be used successfully, and the choice to use shareware is largely dependent on the level of computer science literacy in an individual laboratory; the cost of commercial software weighed against the time involved in obtaining support for the shareware (Wiley & Michaels, 2004).

13.1 WHAT IS AN IMAGE FILE?

The basic unit of digital imaging is an image file. Files can contain a simple image, or a complex, multiple-dimension experiment. An image is saved as a computer graphics file in one of two broad formats: (i) vector graphics and (ii) raster graphics (also called *bitmap files*). Vector graphics—commonly generated by drawing or plotting programs—consist of lines, curves, polygons, and other shapes that are specified mathematically to generate an image. Regions of these images are filled with gradations of gray or color. The advantage of a vector representation is that it exists without a defined spatial scale. To rescale the image, the computer recalculates the dimensions of each shape and redraws the image with sharp outlines and discrete tones. This format is ideal for representing diagrams and text where text does not lose resolution when output in different formats or resized. Vector-based graphics are not typically used for saving light microscopy data except in special cases, such as PALM and STORM, where the positions of individual molecules have been determined computationally and output as positions in space.

The major form of graphics file used for microscopy data is the raster graphic or bitmap image. The graphical information is saved and displayed as a grid of discrete picture elements (pixels). Because the intensity values at each point in the image are assigned to an independent pixel within the grid, bitmaps are the preferred way to store complex, continuous-tone images such as photographs (Fig. 13.1). Unlike vector graphics, a raster file has a fixed spatial scale. Rescaling the image requires either that the individual pixel elements change size or that the data are interpolated to create more or fewer pixels. Typical raster file formats include TIFF, DICOM, PICT, Joint Photographic Experts Group (JPEG), Graphics Interchange Format (GIF), and BMP. There are also raster graphics files associated with software packages, referred to a proprietary file formats (PFFs), which will be discussed later.

13.2 BIT DEPTH

The light intensity in the optical image is sampled or qualitized at each pixel position to create a digital intensity value or gray level. Just like spatial sampling, the sampling density determines with what fidelity the primary image data are captured.

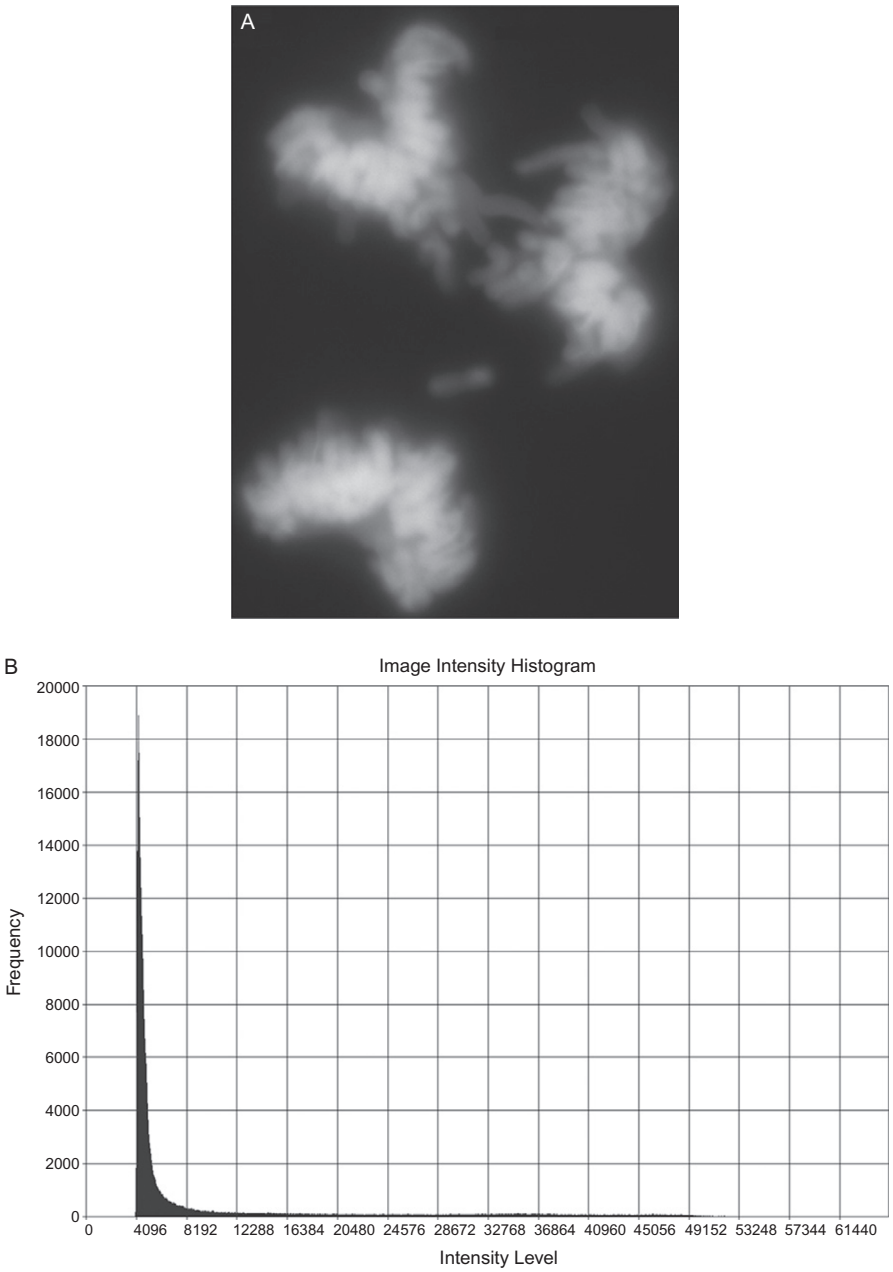

FIGURE 13.1

The raster image. (A) A grayscale image of chromosomes in a mitotic BSC-1 cell, labeled with DAPI. (B) The image intensity histogram for the image in (A). This 16-bit image has 65,535 gray levels, plus pure black (0). The majority of pixel intensities are close to black, representing the dark areas.

In this case, the fidelity of the data refers to how well the signal-to-noise ratio of the detector has been preserved in the recorded image. Digitizing an optical image means that the relative differences in light intensity are converted to relative intensity levels by some form of analog to digital converter (ADC). In simplest terms, an image detector, such as a CCD camera or a photomultiplier tube, converts photons comprising the image into electrons, and reads them out to an ADC as a voltage (Hinchcliffe & Sluder, 2003).

The ADC acts like a series of binary gates where at each gate, the ADC decides whether the voltage is greater than or less than a particular value. If the voltage is greater than that value, a "1" is sent to the computer and the gate value is subtracted from the voltage. If the voltage is less than that value, a "0" is assigned. The voltage then goes on to the next gate and the process is repeated. If a series of gates are set up in the ADC, where each gate value is half of the previous gate value, then the voltage gets divided into ever smaller amounts, corresponding ever smaller intensity differences. Collecting the output from an ADC with 4 gates would produce values from "0000" to "1111," corresponding to 2^4 possible intensity levels. Each binary value therefore constitutes a bit for the computer processor where the maximum intensity value of "1111" is reconstituted in this 4-bit sample as "$8+4+2+1$" or 15 out of a total range of 16 values (0–15). An ADC with 8 V dividing gates yields 2^8 possible values (0–255) where the first bit, often termed the "most significant bit" is 128 rather than 8 for the 4-bit image.

The bit depth of an image file determines how many intensity levels can be stored for each pixel, but it does not guarantee that the differences in gray levels are meaningful (Shaw, 2006). Contemporary computers store and process information in 8-bit increments termed bytes. Therefore, monochrome raster graphics are typically saved as 8-bit (256 gray levels) or 16-bit (65,536 gray levels) image files where each pixel is assigned one or two bytes of information, respectively. Digital cameras, photomultiplier tubes, the amplifiers that stream the voltage from the detector to the ADC, and the ADC itself all introduce errors in the form of extraneous electrons when recording the image to file. The variation in voltage "signal" caused by these stochastic errors constitutes an electronic "noise" that interferes with our ability to determine real differences between pixel intensity values after quantization. As the mean value of the electronic noise gets close to a particular ADC gate value, the decision to make that bit a "1" or a "0" becomes somewhat arbitrary.

13.3 FILE FORMATS

Selecting an image file format for storing your image data depends upon several considerations: the purpose of the graphics being represented, the file size, the imaging platform used, and the software available to manipulate the images. Commercial vendors commonly create machine or company-specific file types for the purpose of recording machine-specific parameters into the image data file. These so-called "metadata" are often used for specific postprocessing or visualization tasks where,

for example, the excitation and emission wavelengths are used to false color the image or the number of pixels per micron are used to generate scale bars. Converting your images from a PFF to a new file type that can be opened and manipulated across multiple software platforms will almost always eliminate the metadata and can ruin the primary image data if you are not careful to select an appropriate file type. There are several tools available to do this. Many proprietary files are now shared between imaging platforms, and some manufacturers offer a data viewing feature. There are also shareware software packages that will convert various PFFs to more common file formats (Linkert et al., 2010). These file types are significantly different from the JPEG and GIF files used more commonly in Websites and presentations.

TIFF

The Tagged Image File Format saves the image data without compression and with the option of encoding metadata into the first part of the file called the file header. TIFF is an excellent choice for saving and manipulating graphics files, particularly when these images will be utilized by several applications. TIFF images work equally well with grayscale or color images (Kay & Levine, 1992). TIFF files are often the basis for proprietary image file formats found in commercially available image capture and analysis programs, and most of these programs will output as 8-bit (grayscale), 16-bit (grayscale), or 24-bit (RGB) TIFF images. TIFFs can be saved uncompressed, or use a variety of compression regimes, including LZW compression, or JPEG compression (so-called JIFFs). TIFF is an excellent format to archive image data, because it is not software specific, and can be imported and opened by a variety of programs.

JPEG

Short for Joint Photographic Experts Group, JPEG is a ubiquitous file format for the distribution of digital images (see www.JPEG.org). Its major advantage is in the ability to provide outstanding visual images, particularly photographs, which can be highly compressed. JPEG is designed to exploit the limitations of the human vision: variations in brightness are perceived more than discrete changes in color (or grayscale). JPEG is intended for images that will be viewed by people and are an ideal format to use to present high-quality images with minimal file size (e.g., on a Website or in transferring images back and forth by e-mail or FTP). At its extreme, JPEG can represent an image using around one bit per pixel for storage, yet to the eye, this image looks indistinguishable from the original (see Kay & Levine, 1992). JPEG images are not designed for computer vision: the errors introduced by JPEG—even if they are invisible to the eye—make JPEGs unsuitable for quantitative analysis. This is compounded by the fact that JPEG files lack pixel intensity: the JPEG image looks fine to the eye but may lack some of the pixel-by-pixel information necessary for quantitative analysis (see Fig. 13.3). It is important to note that saving an image as a JPEG—even at the highest setting—introduces lossey file compression; information is discarded as the file is saved. For this reason, it is not recommended

that image files be archived as JPEGs, unless quantitative data are not required. Again, JPEGs are for graphics and presentation, not for analysis or archiving.

GIF

GIF is well suited for exchanging images between different programs, particularly across the web. Originally designed by CompuServe for this purpose, the GIF format has largely been replaced by the use of JPEG, particularly in the transfer of photographic images. However, JPEG will not completely replace GIF; for some types of images, GIF is superior in image quality, file size, or both. JPEG is superior to GIF for storing full-color or grayscale images of "realistic" scenes, such as photographs and continuous-tone images. Subtle variations in color are represented with less space by JPEG than by GIF, and yet, still provide a faithful representation. In JPEG, sharp edges tend to be blurred unless a high-quality setting is used. GIF is better for images with fewer colors, such as line drawings and simple cartoons that have sharp edges. GIF is only available in 256 color (not true color). Animated GIF images remain the standard for solid-color motion graphics output to the web, and the term GIF has been coopted to describe a short animation on the interweb, often depicting a politician or member of the entertainment community. Some of these animations can be quite humorous. For the scientist, these can be used to depict an animated graphic on a website.

BMP

Microsoft Windows Device-Independent Bitmap file is known as the BMP file. This is the standard Microsoft Windows raster file format. While it does not have many features, it can work for moving image around, especially between programs. When this is done, if it is best to convert the final image to another format, such as TIFF. Such conversions do not lead to image degradation, like that seen when converting a JPEG or GIF to a TIFF. BMP files are also used as the "desktop" image for Microsoft Windows (see Windows folder).

Proprietary file formats

Written to take advantage of a particular software package, PFF are usually based on TIFF architecture and include metadata (automatically generated by the imaging system) and notes input by the user. PFF files are ideal when working in the closed architecture of a commercial software package, where they allow ease of use and integration of software features (false coloring, scale bars, stored point spread functions for deconvolution, flat field corrections, background subtracts). Where PFFs have been problematic is in the use of cross-platforms, when system A cannot open a file from system B. There are several remedies for this. Many software packages now allow for opening and reading of cross-platform files, and many PFFs are open architecture, meaning that they can be utilized by multiple programs.

13.4 SAMPLING AND SPATIAL RESOLUTION

Converting what we see in the microscope into a digital bitmap or raster file requires that we sample the image intensity as discrete points in space. The density of samples taken per area determines how much of the available resolution we capture in the file up to the resolution limits of the optical system. Since the aperture of the microscope lens system typically limits the resolvable information from the specimen, oversampling the image by using many more pixels per area than necessary only increases the file size and does not produce a better quality image (Inoue & Spring, 1997). When referring to bitmap files, the resolution of the image file is typically specified as the final number of points that subdivide the raster image (e.g., 256×256 or 512×512) or simply as *pixels per line of printed material* (usually pixels per inch or *ppi*) or as *pixels per unit length of monitor* (usually as dots per inch or *dpi*) (see Inoue & Spring, 1997 for in-depth discussion of monitor resolution). Thus, an $8'' \times 10''$ image with a resolution of 150 ppi translates into a bitmap of 1200×1500 pixels. As the ppi or dpi increases, the size of each pixel to be displayed or printed gets smaller and vice versa.

Changing the size of a bitmap or raster image, where each pixel (of known dimensions) is mapped to a particular region of a fixed grid, must be handled carefully so that the original image data are not corrupted (Fig. 13.2). For electronic media, where the pixel size is not determined by a printed dot size, changing the size of the image ultimately requires changing the number of pixels. For example, a bitmap that is 500×500 pixels will yield a $5'' \times 5''$ image at 100 ppi. If this image is increased in size to $10'' \times 10''$, the bitmap must be converted to 1000×1000 pixels. The software used to rescale the image (such as Adobe Photoshop Adobe Systems Inc., Mountain View, CA) will typically redisplay the image at the new size without changing the actual dpi or ppi of the saved image data. However, if that image has been interpolated to 1000×1000 pixels, and saved as such, these data no longer constitute the raw scientific data that was captured at the microscope. Decreasing image size follows the same general rule.

Many different methods have been developed for interpolating to larger or smaller image sizes (see Kay & Levine, 1992), but all interpolation methods change your primary data. As journals continue to redefine their publication requirements for image data, it is critical that scientists creating figures in primarily vector-based (e.g. Adobe Illustrator) and raster-based (e.g. ImageJ, Adobe Photoshop) software clearly understand how their data are being altered through the process. All image manipulations should be reported with the figure to point out when evidentiary material used for a scientific claim is dependent upon image rescaling or processing.

13.5 COLOR

It is helpful to understand some basics of color theory in order to be able to properly manipulate color image files. Colors can be described in terms of their hue, saturation, and intensity (also referred to as *luminosity*). Hue denotes the color of an object (technically, hue represents the position on a standard color wheel, expressed in

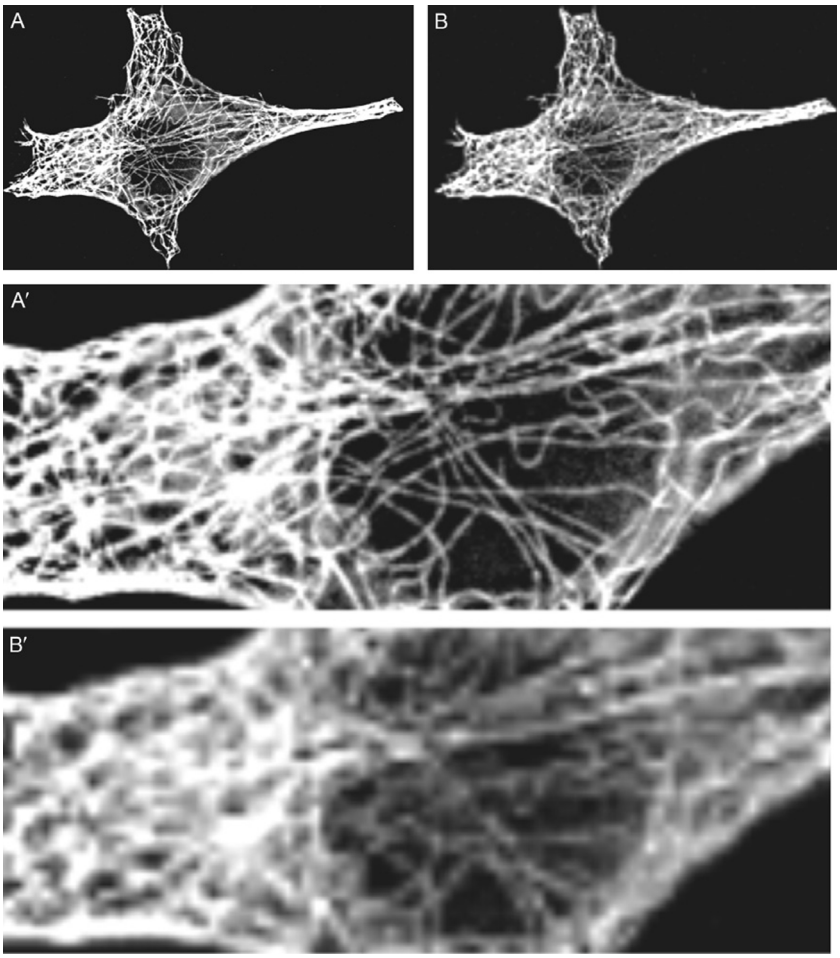

FIGURE 13.2

Re-sampling and interpolation. (A) Original image of a CHO cell stained with antibodies to α-tubulin. (B) The same image after it has been down-sampled and then re-sample to the original size. (A′/B′) Blowups of selected regions of (A and B). Note that the microtubules appear jagged, there is pixelation and the overall quality of the image in (B′) is poor. The interpolation routine for this demonstration was deliberately chosen to give poor results; most interpolation methods do much better.

degrees between 0 and 360). Compare the hue of a pair of dark cotton blue jeans with that in a pair of sky blue polyester Ban Lon pants. Saturation is the amount of pure white in the color. For example, the blue in a brand new pair of jeans is very saturated, whereas the blue in an old pair (or a pair that has been subjected to *acid wash*) is much less saturated. *Intensity* or *luminosity* denotes the brightness of an object: a

pair of blue jeans observed in bright sunlight will look different from the same pair of jeans in a dimly lit blues club, "round midnight."

There are two common (albeit not exclusive) methods that can be used to represent color in graphic image files. The first method is RGB, which mixes red, green, and blue light together in varying proportions. This is referred to as *additive color*, because adding all three colors in equal intensities creates white. It is easy to picture an RGB image as the overlaying of three-colored transparencies (one red, one green, and one blue); where the colors overlap, they create complementary colors such as cyan, magenta, and yellow. In an RGB image file, each pixel is assigned a specific intensity for each of the three different color channels. If the bit depth for each channel is set to 8, then this image is said to be 24-bit RGB, or 24-bit color (3×8-bits/channel). The result is 16.7 million color variations (often called 24-bit *true color*). True color has become the standard display mode of most computer monitors. *Note*: some color display systems support *32-bit true color display*. This is 24-bit RGB *plus* an 8-bit *alpha channel* that functions as a *mask* to specify how an individual pixel's colors should/will be merged when colors are overlaid. This alpha channel is crucial for transparent regions of an image and special effects. Also, many video cards support *32-bit giga color* (10 bits per channel RGB, *plus* a 2-bit alpha channel). This type of color representation is intended to give even more color information per channel, and the expense of transparency (often an Alpha channel is only needed for digital "fine" art, where transparent regions of the image are critical).

The second method commonly used to represent color in digital image files is called CMYK (*c*yan, *m*agenta, *y*ellow, and black; *K* represents black, so as not to be confused with blue). In CMYK images, the colors are *subtractive*. This is easiest to understand if thought of as ink printed onto a white piece of paper. Indeed, the use of CMYK inks is the standard mode for commercial color printing—including that for scientific journals—and is called *four-color process* printing (see below). If all four colors are overlaid in sufficient and equal amounts, then the resulting image is true black. If there is no ink (i.e. no color), then the page is white. In a CMYK image file, each pixel is assigned a percentage value for each of its four different color channels. If the bit depth for each channel is set to 8 (the standard), then this file is said to be *32-bit color* (not to be confused with *32-bit true color*—see above).

13.6 CONVERTING RGB TO CMYK

The range of colors generated by each method (*RGB* or *CMYK*) is referred to as the *color gamut* of that method (see Inoue & Spring, 1997). Because RGB and CMYK use different methods to reproduce color, the hues in RGB files may be *slightly* different from those represented in CMYK files. Also, CMYK has a smaller gamut of colors than RGB. The difference in color gamut between an RGB and a CMYK file is often blamed for the disappointing hues/saturation/intensity seen in multicolor digital microscopy images that have been converted from RGB to CMYK for publication in print journals. However, most, if not all color micrographs are

essentially grayscale images that subsequently have been pseudocolored to provide color information. As such, the gradations of red, green, and blue tones in these images are not subtle enough to cause the real problems observed during interconversion from RGB to CMYK. In fact, the interconversion of most digital images from RGB to CMYK does not present color management problems. This can be demonstrated by converting a digital photograph of family or loved ones (or both) from RGB to CMYK: the result is pleasing and true to the original image. The real problem for digital micrography (and cause for the less-than-optimal images generated) has its basis in the very nature of multiwavelength fluorescence micrographs themselves (see below).

Fluorescence images are composed of bright regions (where the fluorochrome is present) and a black background (where the fluorochrome is absent). In RGB mode, these types of images overlay very well, resulting in characteristic multichannel fluorescence micrographs. Where there is fluorescence overlap, there is a color shift to a complementary color; this color shift is often used to assay for colocalization of candidate molecules (i.e., red on green produces yellow). Remember that in an RGB image file, black represents the absence of pixel intensity. Therefore, where there is no overlap, the individual fluorochromes are contrasted with the pure black background. When output onto a RGB computer screen, these multicolor RGB fluorescence images are striking: they have deep, saturated colors and are combined with a rich, black background. However, when such an image is converted from RGB to CMYK for printing in a journal, the image becomes weak and sickly. This is the result of the switch from an additive color scheme (RGB) to a subtractive scheme (CMYK). The black background, which in RGB is the absence of intensity (no pixels), is converted to CMYK, which is represented by *maximum pixel intensities* for these regions (remember, the pure black regions in CMYK images are made up of equal percentages of C, M, Y, and K intensities for each pixel). After conversion, this black "ink" is overlaid onto the position of each fluorochrome present in the other layers. The effect is that the CMYK *black* regions act like a gray filter over the fluorescent image. The result is that the intensity of each "*bright*" pixel is diminished: also, the hue and the saturation of each pixel become altered.

To make matters worse, during the conversion from RGB to CMYK, the regions of the image that appear dark may be made up of varying intensities of C, M, Y, or K—they may not be true black. These pixels could be a dark maroon, a hunter green, a midnight blue, or a very deep golden brown. When each of these colors is highly saturated and has a faint intensity, the result is almost black. Thus, differing levels of color—masquerading as black—will be overlaid on the original pseudocolored image and change the hue, saturation, and intensity of individual pixel within the image, often in an unpredictable and uncontrollable fashion.

When preparing multicolor fluorescent images for publication, there are several ways to get around the unfortunate situation brought about by the conversion from RGB to CMYK. One way is to start by manipulating each color "layer" as an RGB image, until the desired intensities are found. Then the image is "flattened," and the layers are merged together. By flattening the image, the black pixels of the top layer

are discarded. Once the image has been flattened, it can be converted from RGB to CMYK. Thus, those pesky "black" pixels from the upper layer are gone, and the image will convert to CMYK with relatively high fidelity.

13.7 COMPRESSION

Because raster graphics require information to be saved for each pixel, bitmap files can be very large. This is particularly true for images that are 1000 pixels × 1000 pixels or larger (so-called mega pixel images). The size of these files also increases as the bit depth increases for each pixel. Large file sizes put stains on computer processing power, memory capacity, and storage (see Bertrand, 2001). One way to deal with the increase in file size is to introduce compression. To compress a file, the computer looks for patterns within the bitmap and tries to represent these patterns with as little information as possible. In addition, movie file formats also can use temporal compression, which looks for similarities between frames.

When a file is compressed, the computer can preserve all the original pixel information and represent this information in the resulting uncompressed image. This is said to be lossless compression, and the savings in file size come from how the information is processed and stored. Alternatively, the computer can discard information deemed irrelevant to be able to represent the final image. This is said to be lossey compression.

For digital microscopy, the use of compression—and the selection of a compression scheme—depends upon the requirements of the image and the imaging system. As a rule, it is best to acquire images with as little compression as possible (none at all would be best). Data analysis involving pixel intensities should be done on uncompressed files. These large files can be archived as is. The image can then be converted to a file type that supports compression, such as JPEG (Fig. 13.3). This is convenient for publishing on the Web or transferring via e-mail.

13.8 VIDEO FILES

In order to record dynamic changes in living cells, video records can be captured. Frames are captured at a specified interval, and a time-lapse sequence is generated. Such a technique is called time-lapse video microscopy. However, video actually refers to analog magnetic tape capture at 30 frames/s. Thus, it may be more accurate to describe digital motion picture capture from the microscope as digital cinemicrography rather than digital video. However, digital video microscopy persists as a standard term.

Video microscopy is used when the details of a series of events are required for analysis. Temporal analysis (relative to some fiduciary, such as a cell cycle transition event like nuclear envelope breakdown, or anaphase onset) or a terminal phenotype determination (cell division, cell death, cell movement) makes video

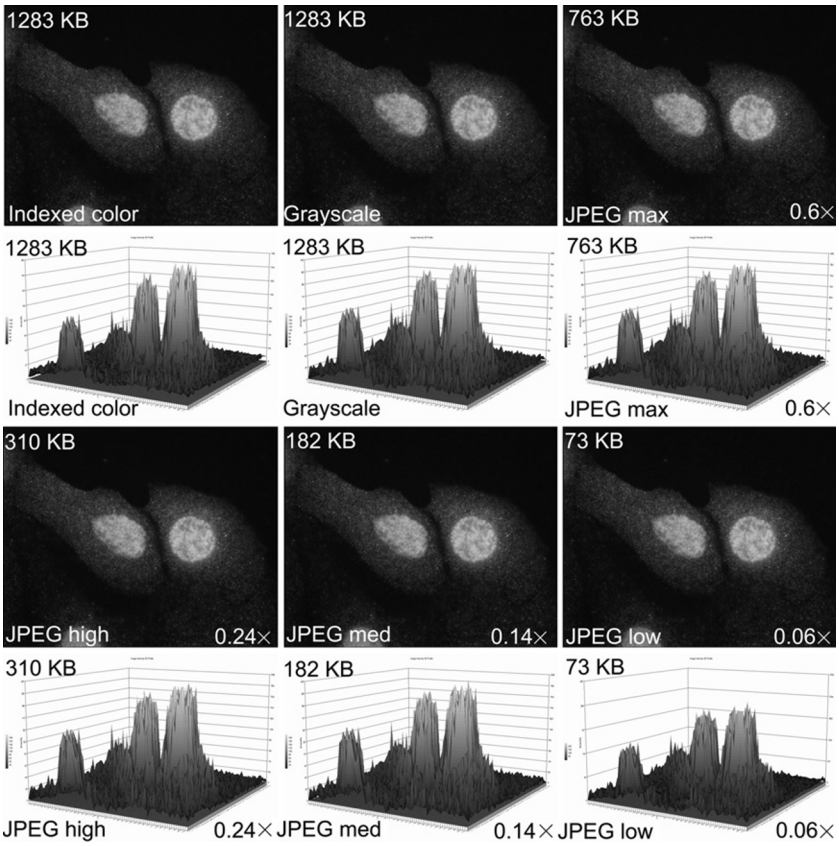

FIGURE 13.3

The effect of JPEG compression on image quality. Two cells labeled with a nuclear stain were imaged using a fluorescence microscope and saved as a TIFF file using indexed color. The file was then converted to a grayscale TIFF or JPEGs using a range of compression settings (maximum, high, medium, and low). Top panels show the original and converted micrographs, bottom panels show a 3D image intensity graphic of the bitmap. Notice that the image does not appear degraded, and that the image intensities for the original and converted images does not appear degraded until the lowest JPEG setting is used.

files particularly important. While there is a current emphasis on fluorescence microscopy, phase contrast and DIC imaging modes work great with video microscopy, and video microscope systems are easy and cost effective to assemble (see Durcan et al., 2008; Hinchcliffe, 2005; Salmon et al., 1998; Shaw et al., 1995).

The file format(s) used to store these digital motion picture sequences are in essence a series of raster graphics files, but with significant features. The most important are key frames and codecs (compression/decompression routines). Features that

are common to motion picture (movie) file formats include the ability to change image size, frame rate, bit depth, and codecs. Often, file formats are defined by the codec that they use (like Moving Picture Experts Group, MPEG or H.264).

AVI

Audio Video Interleave is considered the video standard for Windows. It is a special case of the Resource Interchange File Format. AVI is defined by Microsoft and is the most common format for audio/video data on the PC. AVI is an example of a *de facto* standard. For more information, see http://www.jmcgowan.com/avi.html.

QuickTime

Apple's video format, it also works well for PCs. This file type is well suited to editing and has similarities to the MP4 file format.

MPEG

MPEG is a version of JPEG for motion picture that allows significant compression of video files. MPEG makes extensive use of compression key frames, and therefore, requires more processing time. MPEG-1, layer 3 is an audio file format that provides significant compression of audio files. These files are known as *MP3*. MPEG-4 is the standardized format for DVDs. MPEG-4/part 14 or MP4 is the latest version of an ever-evolving group of file formats and specifications http://mpeg.chiariglione.org/.

TIFF sequence

This gives the ability of TIFF files to play as a motion picture sequence. The quality of TIFF sequences (or TIFF stacks) makes them particularly suited for quantitative analysis. However, this does introduce size limitations: the file size of TIFF stacks can be very large.

13.9 VIDEO CODECS

Because motion picture file formats have the potential to be very large (current video files in our lab are reaching 10s of gigabits), there is a great deal of emphasis on compression of the motion picture information. Video files present unique problems when being compressed. The image changes over time. Thus, there must be compression within an individual frame (*spatial compression*) just as in a conventional graphics file. In addition, the compression routine must have the ability to find similar regions within the images of the series as they change over time (called *temporal compression*). In digital video, there are three interactive features of compression routines that need to be dealt with: (i) compression of the information—for storage; (ii) decompression of the file—to allow viewing of the movie; and (iii) compression

key frames—signposts placed throughout the video file that allow the program to compare changes from frame to frame and minimize the amount of data that needs to be stored in the first place (see below).

Codecs can be symmetric or asymmetric. In a symmetric codec, compression and decompression occur at the same rate. Asymmetric codecs take more time to compress than decompress. This has an advantage in playback, but requires more time during video production. Central to any codec is the use of compression key frames. In a video sequence where very little changes (such as in many cinemicrography experiments), the computer will use unchanged regions of the image from frame to frame, and only have to describe the new (changing) regions. The compression routine references each frame on the previous one. When the scene changes entirely, a new reference frame must be generated. These reference frames are called key frames. Codecs insert key frames at varying intervals, and some codecs allow key frames to be inserted manually. For the video microscopist, key frames only come into play when the scene rapidly changes (a switch to a different imaging contrast mode during the experiment). Otherwise, the key frames specified by the codec can usually handle subtle changes.

A unique problem arises when video clips from different sources (and clips originally produced with different codecs) are pieced together into a final movie. If the final output is then saved with compression again, the clip is said to be *recompressed*. This does not provide any saving in file size and usually leads to degradation of the image, often in unpredictable ways. In order to ensure that video files are not recompressed, it is best to save an image sequence without compression, and only introduce a compression routine when the final movie is constructed.

It is important to note that video files require the proper codec to be decoded, that is, readout. As video codecs are constantly evolving, older files either need to be converted to a new format, or legacy codecs need to be maintained. Otherwise, video files can be rendered useless. Many older codecs can be found on the web, but it is a good idea to archive them, along with important video files, for future use.

There are too many codecs available to list here. However, one—H.264/MPEG-4 part 10 or Advanced Video Coding—is the current standard for BluRay disks and was developed by the ITU Telecommunication Standardization Sector (http://www.itu.int/en/ITU-T/Pages/default.aspx). This has become the default codec for generating QuickTime movies in many commercial imaging software packages.

13.10 CHOOSING A CODEC

There are a wide variety of video codecs available, and many of them are standard components of the Windows or Apple operating systems. Other codecs are provided as part of commercially available video editing programs, such as Adobe Premiere, Apple QuickTime, or Final Cut. Most commercial and freeware digital imaging software packages have the ability to output image sequences as AVIs or QuickTime movies. These are just as often designed to use one particular codec (usually

H.264). Finally, there are codecs that are designed to work with a specific software application or as part of hardware-based compression. Each of these compression routines is designed for a specific purpose, and there is no one *best* codec for video use. In order to optimize the output of digital cinemicrography, it is important to empirically determine which codec will work for a particular application.

What follows is a simple, step-by-step protocol for determining the suitability of a particular codec for an individual application.

1. Identify that program which will be used to play the final sequence (i.e., will this movie be for presentation in Microsoft PowerPoint, for playback from the web, or as a movie for temporal analysis in the lab). The final output program will determine which codec will work best.
2. Select a short sample movie to use as a test. This movie should be a clip taken from a candidate sequence of the type to be displayed (i.e. time-lapse of GFP or phase contrast). Match the bitmap dimensions to the output program (i.e. at least 640×480 for videos, 320×240 for web applications). These changes are made in the video editing software (see documentation provided with this software). The test clip should show examples of the type of detail needed in the final movie, but should be on the order of 5–40 MB (depending on the computer used). The small file size will facilitate rapid compression and playback. It is important that this test clip should be made from a sequence that was not previously compressed, otherwise recompression will occur.
3. Using a video editing program (such as Adobe Premiere or Apple QuickTime), convert the clip to a compressed form using a specific codec. For each codec, compress the clip with a range of compression settings (often referred to as "quality" setting) from best to worst. These setting are often represented as a number from 1 to 10 (10 being the highest quality and least compression). Alternatively, the quality setting may be a percentage (100% being the best quality and least compression). Start with four separate setting 100%, 50%, 25%, and 5%. Note the initial file size for the clip and the file size after compression, along with the time it takes to compress the file for each setting.
4. Open the resulting clips in the final output program (such as PowerPoint) and play each clip back, as it will be for the final presentation. Look for pixelation (indicative of too much spatial compression) or jerky play (too much temporal compression). Note the lowest setting which still provides an acceptable image.
5. For each setting, compare the four separate values for compression of this file: (i) degree of compression (change in file size from uncompressed to compressed), (ii) time of compression, (iii) quality of the image, and (iv) quality of the playback.
6. Repeat using another codec. By comparing the four criteria for a range of settings for each codec, the optimal codec and settings for a particular sequence file type can be found (Fig. 13.4). The trade-off is file size (storage) versus file quality (playback). The time it takes to compress the image is secondary, but does impact

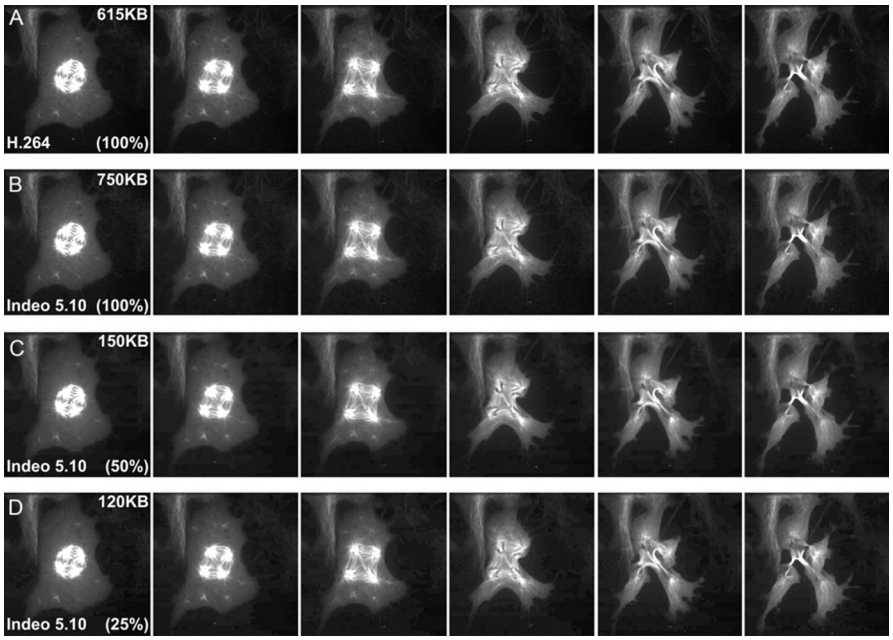

FIGURE 13.4

Selecting the appropriate compression/decompression routine (codec). A series of frames from a time series of a mitotic BSC-1 cell expressing α-tubulin-GFP and imaged with spinning disk confocal microscopy. This cell has assembled a tetrapolar spindle and proceeds through anaphase. This sequence was saved as a SlideBook file, with a final file size of 7.8 MB. The file was then saved using two different codecs. (A) Frames from the sequence saved as a QuickTime using H.264 (100% setting) and (B) as an AVI using the Intel Indeo 5.10 codec, and a range of compression settings. Compression settings are: (B) 100%, (C) 50%, and (D) 25%. Resulting file size for the entire compressed movie is shown in the right. There is little or no image degradation using H.264 compression. In the Indeo 5.10-compressed AVI files, there is noticeable degradation of the image, particularly, in the dark regions of the background.

the ability to manipulate the digital motion picture sequences. Remember, different codecs will be optimal for different file types. It is best to empirically determine the best codec for each sequence type (i.e., contrast mode or model system).

13.10.1 Real results

Using the protocol outlined above, a real cinemicrography digital file was generated and subjected to compression using two separate codecs, H.264 and Intel Indeo 5.10. For H.264, the highest quality was used, but this results in a fairly small file size. For Indeo 5.10, three different quality settings used employed (100%, 50%, and 25%).

The sample is a BSC-1 cell expressing α-tubulin-GFP (Hornick et al., 2008, 2011; Fig. 13.4). This cell was imaged using a Leica DM RXA2 microscope (Leica Microsystems, Deerfield, IL), equipped with a Yokagawa CSU-10 spinning disk, a Hammamatsu 9100 EM-CCD camera (Hammamatsu Photonics, Bridgewater, NJ), and SlideBook software (Intelligent Imaging Innovations, Denver, CO). The resulting AVI file was 31 frames, was saved without compression and ended up ~7.8 MB in size; each frame being 512 × 512 pixels, and 16 bit. The times it took to compress each movie file were measured: they were all about 1 min. The movie files were then analyzed for quality. An series of select frames from each compression routine is presented in Fig. 13.4.

For the H.264 codec, the 100% setting resulted in a file size of 615 KB, which is a compression of ~12.5 times over the original cropped movie!

Using Indeo Video 5.10, the 100% setting resulted in a file that is 750 KB, a compression of 10.4 times the original cropped file. In the case of Indeo Video 5.10, the 50% setting did not result in significant image degradation and yielded a file of 150 KB, a compression of five times that of the 100% setting. Further compression with this codec to 25% only trimmed 30 KB of the image size. Thus, for this movie file, 50% compression with Intel Indeo Video 5.10 gives the smallest file size a whopping 52 × compression! However, close inspection reveals significant image artifacts in the Indeo-compressed files. The H.264 codec does not generate these artifacts.

CONCLUSIONS

With the rebirth of light microscopy as an analytical and quantitative tool, the use and manipulation of digital graphics files has become essential for the cell/molecular biologist. Digital imaging has largely replaced 35-mm photography as a way to record micrographs. The basics of computer imaging can be mastered in little or no time. When used properly, digital image files allow for quantitative measurements of cellular activities. Proper use entails generating files with high bit depth (16 bit), and saving the files uncompressed. Images with lower bit depth (8 bit) can be used for presentation, and these files can be saved with compression to facilitate easy sharing and use in presentations.

Acknowledgments

We thank Katie Buchanan, Bill Burnip, Rich Cardullo, Paul Goodwin, Paul Jantzen, Karl Kilborn, Colin Monks, and Dee Sharma for providing helpful comments on the presentation of this material during the Analytical and Quantitative Light Microscopy (AQLM) course in Woods Hole. Both S. L. S. and E. H. H. are graduates of the 1995 AQLM course, and we would like to thank Dr. Ken Spring for his insight and humor during that course. Work in the authors' labs is supported by research grants from the National Science Foundation and National Institutes of General Medicine.

References

Bertrand, C. A. (2001). Color by numbers: Imaging large data. *Science*, *293*, 1335–1336.

Cardullo, R. A., & Hinchcliffe, E. H. (2007). Digital manipulation of fluorescence images: Noise reduction, contrast enhancement, and feature extraction. *Methods in Cell Biology*, *81*, 318–340.

Durcan, T., Halpin, E., Rao, T., Collins, N., Tribble, E., Hornick, J., et al. (2008). Tektin 2 is required for central spindle microtubule organization and the completion of cytokinesis. *The Journal of Cell Biology*, *181*, 595–603.

Furness, P. (1997). The use of digital images in pathology. *Journal of Pathology*, *183*, 253–263.

Hinchcliffe, E. H. (2005). Using long-term time-lapse imaging of mammalian cell cycle progression for laboratory instruction and analysis. *Cell Biology Education*, *4*, 284–290.

Hinchcliffe, E. H., & Sluder, G. (2003). Do not (mis-) adjust your set: Maintaining specimen detail in the video microscope. *Methods in Cell Biology*, *72*, 65–85.

Hornick, J. E., Bader, J. R., Tribble, E. K., Trimble, K., Breunig, J. S., Halpin, E. S., et al. (2008). Live-cell analysis of mitotic spindle formation in taxol-treated cells. *Cell Motility and the Cytoskeleton*, *65*, 595–613.

Hornick, J. E., Mader, C. C., Tribble, E. K., Bagne, C. C., Vaughan, K. T., Shaw, S. L., et al. (2011). Amphiastral mitotic spindle assembly in vertebrate cells lacking centrosomes. *Current Biology*, *21*, 598–605.

Inoue, S., & Spring, K. R. (1997). *Video microscopy: The fundamentals* (2nd ed.). New York: Plenum Press, 741.

Jaqaman, K., Loerke, D., Mettlen, M., Kuwata, H., Grinstein, S., Schmid, S. L., et al. (2008). Robust single-particle tracking in live-cell time-lapse sequences. *Nature Methods*, *5*, 695–702.

Kay, D. C., & Levine, J. R. (1992). *Graphics file formats*. Pennsylvania: Windcrest/McGraw-Hill Blue Ridge Summit, 278.

Linkert, M., Rueden, C. T., Allan, C., Burel, J.-M., Moore, W., Patterson, A., et al. (2010). Metadata matters: Access to image data in the real world. *The Journal of Cell Biology*, *189*, 777–782.

Salmon, E. D., Shaw, S. L., Waters, J., Waterman-Storer, C. M., Maddox, P. S., Yeh, E., et al. (1998). A high-resolution multimode digital microscope system. *Methods in Cell Biology*, *56*, 185–215.

Schneider, C. A., Rasband, W. S., & Eliceiri, K. W. (2012). NIH Image to ImageJ: 25 years of image analysis. *Nature Methods*, *9*, 671–675.

Shaw, S. L. (2006). Imaging the live plant cell. *The Plant Journal*, *45*, 573–598.

Shaw, S. L., Salmon, E. D., & Quatrano, R. (1995). Digital photography for the light microscope: Results with a gated, video-rate CCD camera and NIH-image software. *Biotechniques*, *19*, 946–955.

Thomas, C., DeVries, P., Hardin, J., & White, J. (1996). Four-dimensional imaging: Computer visualizations of 3D movements in living specimens. *Science*, *273*, 603–607.

Walczak, C. E., Rizk, R. S., & Shaw, S. L. (2010). The use of fluorescence redistribution after photobleaching for analysis of cellular microtubule dynamics. *Methods in Cell Biology*, *97*, 35–52.

Waters, J. C. (2009). Accuracy and precision in quantitative fluorescence microscopy. *The Journal of Cell Biology*, *185*, 1135–1148.

Wiley, H. S., & Michaels, G. S. (2004). Should software hold data hostage? *Nature Biotechnology*, *22*, 1037–1038.

CHAPTER

Quantitative Analysis of Digital Microscope Images 14

David E. Wolf*, Champika Samarasekera*, and Jason R. Swedlow†

*Sensor Technologies, LLC, Shrewsbury, Massachusetts, USA

†Division of Gene Regulation and Expression, College of Life Sciences, University of Dundee, Dundee, Scotland, United Kingdom

CHAPTER OUTLINE

14.1 So You Want to Do Digital Imaging ... 338
14.2 An Illustrative Example ... 339
14.3 What Is An Image? ... 340
14.4 What Kind of Quantitative Information Do You Want? ... 341
14.5 Quantitative Microscopy: A Tool Kit ... 341
14.6 Exercise 1: A Simple Calibration Curve, Relative Scale ... 342
14.7 Exercise 2: A Simple Calibration Curve, Absolute Scale ... 345
14.8 Exercise 3: Precision in a Calibration Curve ... 346
14.9 Standard Deviations, Standard Errors of the Mean, *t*-Tests, and Other Confusions ... 348
14.10 Dynamic Range, Do Not Waste It ... 350
14.11 Signal-to-Noise Ratio, *S/N*, and Signal-to-Background Ratio, *S/B* ... 350
14.12 Propagation of Error in Calculated Quantities ... 351
14.13 Exercise 4: Error Propagation in Imaging ... 352
14.14 Accuracy and Precision, Calibrating Against a Reference Standard ... 354
14.15 Flatfield Correction ... 354
14.16 Exercise 5: Flatfield Correction ... 355
14.17 Applications Requiring Spatial Corrections ... 355
14.18 Maximizing Resolution Before You Start ... 356
14.19 Exercise 6: Converting Pixels to Microns ... 357
14.20 Exercise 7: Imaging Warping ... 357
14.20.1 Ignoring the Problem ... 359
14.20.2 Dewarping Algorithms ... 360
14.21 Exercise 8: Two-Color Coincidence ... 361
14.22 Two-Camera and Two-Color Imaging ... 363
14.23 Putting It All Together ... 364

Methods in Cell Biology, Volume 114 ISSN 0091-679X
Copyright © 2007 Elsevier Inc. All rights reserved.
http://dx.doi.org/10.1016/B978-0-12-407761-4.00014-2

14.24 Appendix A. Error Propagation: A Generalized Equation 364
14.25 Appendix B. Image Translation and Rotation 366
Acknowledgments 367
References 367

Abstract

This chapter discusses quantitative analysis of digital microscope images and presents several exercises to provide examples to explain the concept. This chapter also presents the basic concepts in quantitative analysis for imaging, but these concepts rest on a well-established foundation of signal theory and quantitative data analysis. This chapter presents several examples for understanding the imaging process as a transformation from sample to image and the limits and considerations of quantitative analysis. This chapter introduces to the concept of digitally correcting the images and also focuses on some of the more critical types of data transformation and some of the frequently encountered issues in quantization. Image processing represents a form of data processing. There are many examples of data processing such as fitting the data to a theoretical curve. In all these cases, it is critical that care is taken during all steps of transformation, processing, and quantization.

Vor dem Gesetz steht ein Türhüter. Zu diesem Türhüter kommt ein Mann vom Lande und bittet um Eintritt in das Gesetz.[1]
Franz Kafka from "The Parable of the Law," Spiegal Online
http://gutenberg.spiegel.de/kafka/erzaehlg/gesetz.htm

14.1 SO YOU WANT TO DO DIGITAL IMAGING

Without doubt, the last decade has seen a virtual explosion of what might be termed quantitative microscopy techniques applied to biological problems. The average biologist must feel like Kafka's "man from the country." There is secret knowledge to be gotten if s/he is to gain entrance to the Law, in this case the laws of quantitation that govern a proper and meaningful measurement using a biological image. In the AQLM course, we have tried to expose both the theory and application of these laws. In a single 8-day course, we can only impart a basic sensitivity and understanding of the issues to our students and, perhaps most importantly, provide them resources and examples of where to go for the answers.

Our goal in this chapter is to present the basic concepts in quantitative analysis for imaging, but these concepts rest on a well-established foundation of signal theory

[1] Before the Law stood a gatekeeper. To this gatekeeper comes a man from the country, who begs entrance to the Law.

and quantitative data analysis. In this spirit, it would seem that the best way to begin here is with some critical references so that the reader will know where to go next. A thorough and lucid discussion of the foundations of signal processing in imaging is available in Goodman, 1996 "Introduction to Fourier Optics." A thorough discussion of the methods of image processing is in K. R. Castleman, 1979 "Digital Image Processing." For data analysis, there are a number of texts to consider, none clearer than Mandel, 1964 gem "The Statistical Analysis of Experimental Data." Other excellent books on the subject are Robinson, 2000 "Practical Strategies for Experimenting" and Beers, 1962 "Introduction to the Theory of Error." For discussions of critical issues in the curve fitting of data, the reader is referred to Bevington & Robinson, 2002 "Data Reduction and Error Analysis for the Physical Sciences," and Press, Teukolsky, Vetterling, & Flannery, 1992 "Numerical Recipes in C: The Art of Scientific Computing." Heed please the title of this last book; quantitative analysis is both science and art.

14.2 AN ILLUSTRATIVE EXAMPLE

Before we launch into our discussion, it is, perhaps, useful to begin with an illustrative example. In Fig. 14.1, we show two fluorescent objects in a microscope field. For the purposes of this example, what they are is not important. The objects look similar;

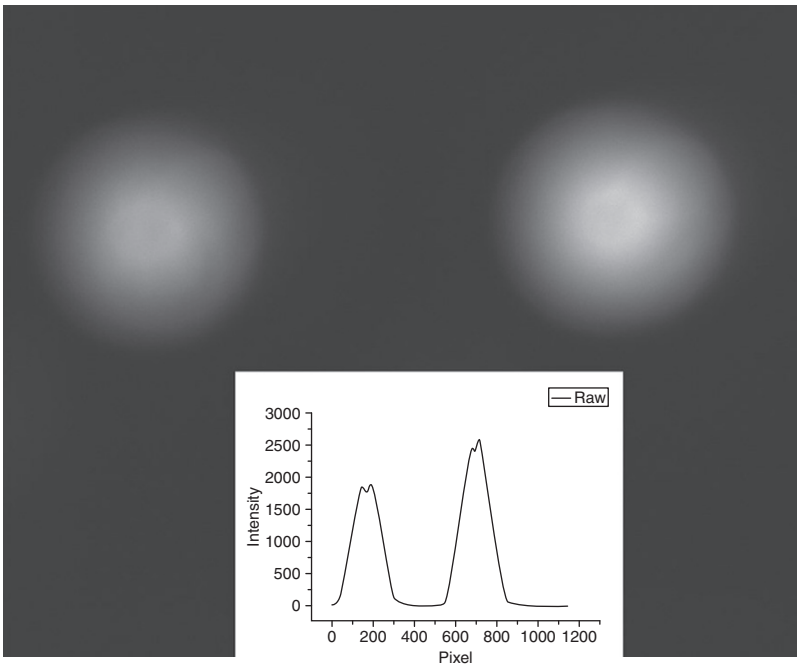

FIGURE 14.1

An image of two fluorescent objects, one at the center of the microscope field the other at the edge of the field, and their line profiles (inset).

one is near the center of the field, the other is near the edge and looks a bit fainter. In the Fig. 14.1 inset, we show intensity profiles across the center of the two objects and conclude that the object on the edge is indeed fainter. Before you rush off to publish this result, let us tell you a little secret. Figure 14.1 is a composite image where we have imaged the same object in two regions of the field. The apparent difference in brightness is not real. It results from the way that a microscope treats objects at the center of the field compared to the edges. This example provides the basis for the rest of what we will cover in this chapter, understanding the imaging process as a transformation from sample to image, and the limits and considerations of quantitative analysis.

14.3 WHAT IS AN IMAGE?

The microscope and all of our fancy digital imaging instrumentation form a black box (Fig. 14.2). Into the black box we put a signal—the sample. The black box transforms the sample and produces our image—a representation of the sample. In the parlance of mathematics and engineering, we say that the microscope transforms the sample and produces the image. If we call reality $R(x,y)$ with x and y the coordinates in object space, the transformation T, and the image $I(x',y')$ with x' and y' the coordinates in image space, then

$$I(x',y') = T * R(x,y). \tag{14.1}$$

This is directly analogous to the Fourier transform discussed in Appendix A of Chapter 2 by Wolf, this volume. Indeed, as is the case of the inverse Fourier transform, our job is to determine the inverse transform T^{-1} such that

$$R(x,y) = T^{-1} * I(x',y'). \tag{14.2}$$

Our goal is to reverse or correct any transformation that will perturb our quantitative result, so we must determine how the optics and electronics distort

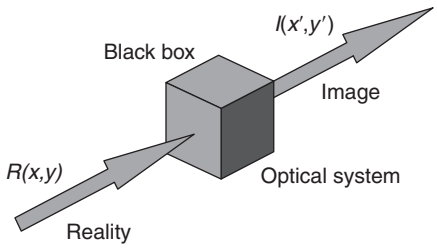

FIGURE 14.2

Optical systems as block boxes. Optical systems can be treated as black boxes. Reality in this case is a two-dimensional set of intensities: $R(x,y)$ enters the optical system and is transformed or distorted to produce the image $I(x',y')$. The goal of the video microscopist is to understand the mathematical rules of the transformation so that one can go backward from $I(x',y')$ to $R(x,y)$.

important aspects of the true object and produce the image. With this knowledge, we can digitally reverse the perturbation and correctly define the properties of the object. When one says that we need to know how the transformation takes place, we do not mean that we need to follow mathematically the tortuous route of light through the system. Rather we need to simply measure the transformation.

You will also note that we have used a cryptic $*$ in defining the process of transformation in Eq. (14.1). This is because different properties transform in different ways. They are not always linear and, as anyone who has meditated on transcendental functions for any length of time knows, not always analytically reversible. However, as one of our quantum mechanics professors once pointed out: "This is the age of computers!" That, after all, is what we are talking about here, taking an image and converting it digitally by computer processing to reality.

14.4 WHAT KIND OF QUANTITATIVE INFORMATION DO YOU WANT?

The particular kind of quantitative information that you want obviously depends on the experiment you are doing. Most analyses involve a measurement and comparison of either intensity or spatial relationships within an image.

14.5 QUANTITATIVE MICROSCOPY: A TOOL KIT

It is our purpose here to provide some simple exercises illustrative of critical issues in quantitative microscopy that you might perform in your own laboratory. It will also be apparent to the reader that these are not merely academic exercises. Rather these exercises can actually be used, in real-life situations to "calibrate" microscope imaging systems. Figure 14.3 shows a useful calibration tool kit containing four critical items: a vial of submicron fluorescent beads, a reticle or stage micrometer with 1 mm^2 ruled every 50 μm, a neutral density step filter, and a band-pass filter. The fluorescent beads are available from several commercial sources including: Invitrogen, CA; Bangs Laboratories, IN; and Polysciences, PA. Reticles are available from any major microscopy supplier such as Edmund Scientific, NJ (the one shown in Fig. 14.3 is from http://www.microscope-depot.com/reticles.asp?S=4). Step wedge neutral density filters can again be found from suppliers such as Edmund Scientific, NJ; Kodak, CT; Thor Laboratories, NJ; New port, MA; and Omega Optical, VT (the one shown in Fig. 14.3 is from Stouffer, Part No. T3110C http://www.stouffer.net/Productlist.htm). Band-pass filters may be obtained from Chroma Technology Corporation and Omega Optical, Inc. (the 600-nm band pass shown in Fig. 14.3 is from Omega Optical; it has a 10-nm bandwidth, https://www.omegafilters.com/index.php?page=prod_index).

FIGURE 14.3

Calibration toolkit consisting of a vial of submicron fluorescent beads, a reticle or stage micrometer, a neutral density step filter, and a band-pass filter.

14.6 EXERCISE 1: A SIMPLE CALIBRATION CURVE, RELATIVE SCALE[2]

The goal in this first exercise is to examine the relationship between input signal intensity and output signal intensity, in an attempt to determine whether we can be sure of the intensity relationships between objects in the image. Do the following:

1. Set up your microscope with a low power $\sim 10\times$ air objective.
2. Put a clean blank slide on the stage and focus on its top surface.
3. Align the Kohler illumination (Chapter 3 by Keller, volume 81, 2007).
4. Close down the brightfield diaphragm so that you can see the image of its iris in the eyepieces and then in the imaging camera.
5. Turn off all automatic settings on your camera and software. We want you to control the gain, dark current, and so on, not some circuit or software correction.

[2] All of the exercises in this chapter were performed on a Leica MZ 16 FA microscope with an RS Photometrics CoolSNAP camera and analyzed with Media Cybernetics Image Pro-Plus, version 5.1.1.38.

6. Set the camera exposure so that the intensity that you measure in the center of the field diaphragm is just short of the maximum signal possible. This means we want it to be just short of saturation. For a camera that outputs in bits, this is 256 for an 8-bit camera, 4096 for a 12-bit camera, and so on.
7. Take an image and record the intensity in the center of the field. One way to do this is to define a small area of interest like a square and measure the average intensity in that square.
8. Place one of the steps of the step wedge over the field diaphragm and repeat the measurement with the same exposure and gain settings.
9. Repeat this for as many steps as you can.

Step wedges and neutral density filters are, in general, defined in one of two ways: either as percentage of light transmitted or as optical density. A 50% transmittance filter, for instance, transmits 50% of the light. Percentage transmittance is related to optical density logarithmically through the relationship:

$$\%T = \frac{100}{10^{\mathrm{OD}}} \tag{14.3}$$

or

$$\log(\%T) = 2 - \mathrm{OD}. \tag{14.4}$$

10. Plot the output intensity as a function of the percentage transmittance. If you took a really complete data set, you might want to do this as a function of OD instead, essentially a logarithmic abscissa.

An example of such a data set is shown in Fig. 14.4A. Typically one sees a sigmoidal relationship, linear at the center but with asymptotic "tails" at the high and low ends. Modern CCD cameras when properly designed for quantitative measurements can be remarkably linear devices, but only over a defined dynamic range. Figure 14.4B tells you over what range the signal will indeed be linear. If you invert such a graph plotting input intensity as a function of output intensity, you will have a calibration curve for your system. If you take the trouble to use such a calibration curve, you can significantly improve the quantitative nature of your data. At the very least, you can finesse it and always stay in the linear range.

Notice how at zero input you are still getting a measurable output. This is the so-called dark current of the detector, and includes electrons that accumulate in the detector in the absence of any photons plus a digital offset that is added by the manufacturer. You will note a variation in the dark current. For modern CCDs, this tends to be dominated by readout noise. If you do not see a dark level, then you did not heed step 5. You have left on a dark current compensation circuit or algorithm. Fine you say; so what? Before you should use such an adjustment, you have to know that it is working correctly. Suppose this threshold is set too high. In that case, your data will be "clipped." The plot shown in Fig. 14.4A and B will then go through the origin, and you will be forced to make the erroneous conclusion that below a certain input level either the detector does not detect anything or somehow is subtracting photons.

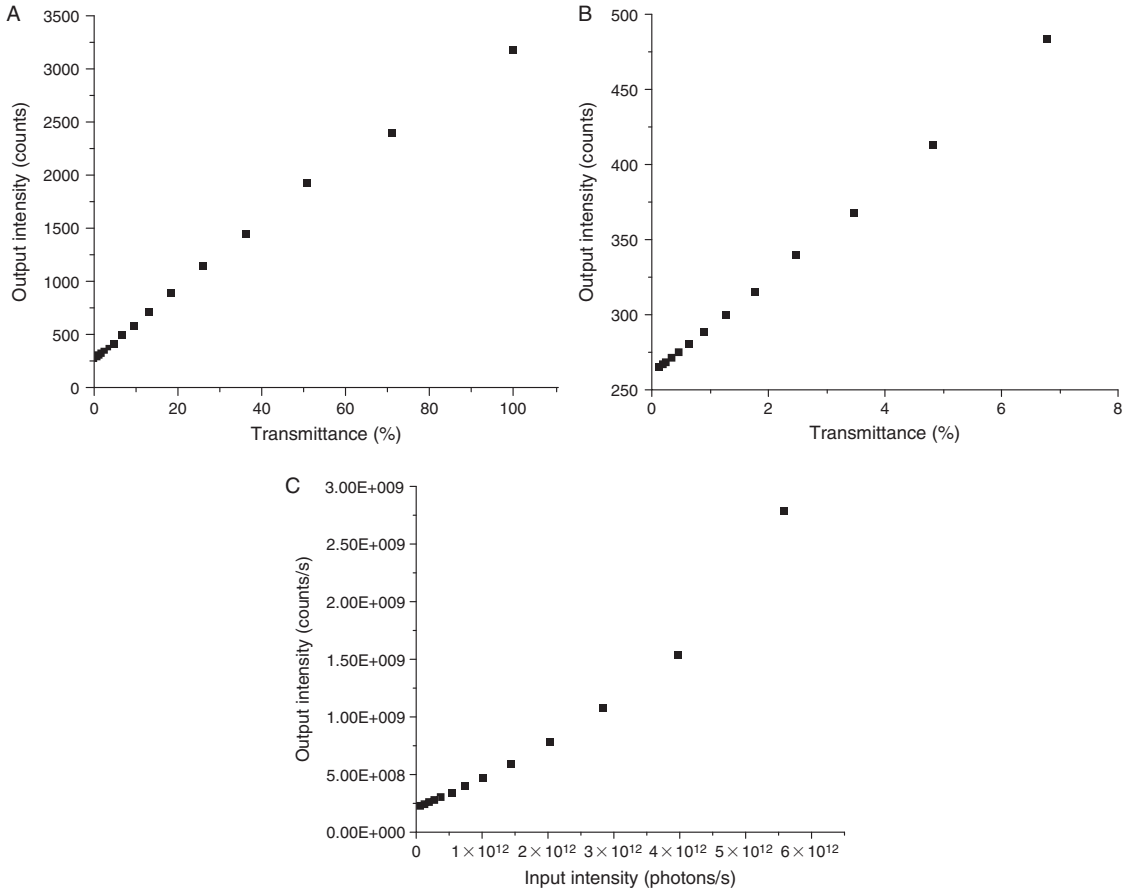

FIGURE 14.4

(A) A plot of the output intensity (counts) as a function of percentage transmittance. (B) A plot of the linear range of the output intensity (counts per second) as a function of percentage transmittance. (C) A plot of total output intensity (counts per second) as a function of input intensity (photons per second).

14.7 EXERCISE 2: A SIMPLE CALIBRATION CURVE, ABSOLUTE SCALE

So far Fig. 14.4A and B are relative measurements that are in terms of percentage transmittance. One can make it an absolute measurement with a little more work, provided you have access to two additional items: a high-quality photometer, otherwise known as a light meter, and an optical band-pass filter (Chapter 4 by Wolf, this volume) which passes light over a narrow (10–20 nm) band, somewhere in the visible range. Then one can proceed with a modified protocol from the first exercise:

1. Set up your microscope with a low power ~10× air objective.
2. Put a clean blank slide on the stage and focus on its top surface.
3. Align the Kohler illumination (Chapter 3 by Keller, volume 81, 2007).
4. Place the band-pass filter above the field diaphragm.
5. Close down the brightfield diaphragm so that you can see the image of its iris in the eyepieces and then in the imaging camera.
6. Turn off all automatic settings on your camera.
7. Set the camera exposure so that the intensity that you measure in the center of the field diaphragm is just short of the maximum signal possible.
8. Measure the intensity by placing the photometer above the filter. It is important that the photometer be such that all of the light is collected onto the photosensitive surface and that it be set to the wavelength at the center of the band pass.
9. Take an image and this time record the total intensity within the image of the iris. One way to do this is to define an area of interest like a square that includes the entirety of the iris and measure the total intensity in that area or by taking the average intensity per pixel and multiplying by the total number of pixels.
10. Place one of the steps of the step wedge over the field diaphragm and repeat the measurement with the same exposure and gain settings. You should not have to repeat the measurement with the photometer.
11. Repeat this for as many steps as you can.
12. Calculate the input light intensity at each level of attenuation.

At 100% transmittance, you obtain an intensity I_0 in watts per second. You can convert this to photons per second by dividing I_0 by the energy in Joules per photon, that is, by

$$E = \frac{hc}{\lambda * 10^{-9}}, \tag{14.5}$$

where h is Planck's constant $= 6.626068 \times 10^{-34}$ m^2 kg/s, c is the speed of light $=$ 299,792,458 m/s, and λ is the wavelength at the center of the band-pass filter expressed in nm. The intensity for the various steps will be the original intensity multiplied by the percentage transmittance, divided by 100.

13. Calculate the output light intensities as counts per second. You do this by dividing your measured count by the exposure time in seconds.

14. Plot the total output intensity in counts per second as a function of input intensity in photons per second.

The results of such a study are shown in Fig. 14.4C. There are a couple of interesting points to consider. First, the curve displays the dark count as an equivalent number of photons. Second, if we chose some point in the center of the linear region and subtract the dark count from the output value then we can define the collection efficiency of the microscope camera system as:

$$\varepsilon = \frac{\text{output} - \text{dark count}}{\text{input}}. \tag{14.6}$$

This efficiency is a total collection and conversion efficiency for your system. You can actually go the next step and convert your graph and efficiency to output photons per second, by going to the camera manufacturer's data sheets and/or the data sheets from the manufacturer of the specific chip in your CCD camera. These sheets will tell you how many counts you get per photon. If you think about it, this tells you approximately how many photons are striking the chip. You know how many you started out with, so the efficiency is then the collection efficiency of your optical system, with that particular objective. This can be a sobering number.

14.8 EXERCISE 3: PRECISION IN A CALIBRATION CURVE

The next issue to consider in your calibration curve is to consider your uncertainty otherwise known as error, or in more positive terms as precision. How precise are your measurements?

1. Repeat either Exercise 2 or Exercise 3 taking 10 independent measurements of each of the output intensities.
2. Calculate the mean and the standard deviation.
3. Plot the mean output intensities with the error bars set as the standard deviation as a function of the input intensity.

An example of such a plot is shown in Fig. 14.5. The errors plotted in Fig. 14.5 are very small because we have properly maximized our dynamic range. Nevertheless, every point has some error associated with it. To more clearly illustrate this, we have included an inset that plots the errors as a function of input intensity. Note that even the dark counts have an uncertainty. While absolute error is minimized at lower intensities, relative error is maximized. The obvious point is that you are not absolutely certain of the values. The precision of your measurements is usually expressed as a percentage of the mean.

What does this imprecision mean? If the source of this imprecision is random, and therefore normally distributed then, as illustrated in Fig. 14.6, 68.2% of the measured values will fall within ±one standard deviation, 95.4% within ±two standard deviations, and 99.7% between ±three standard deviations.

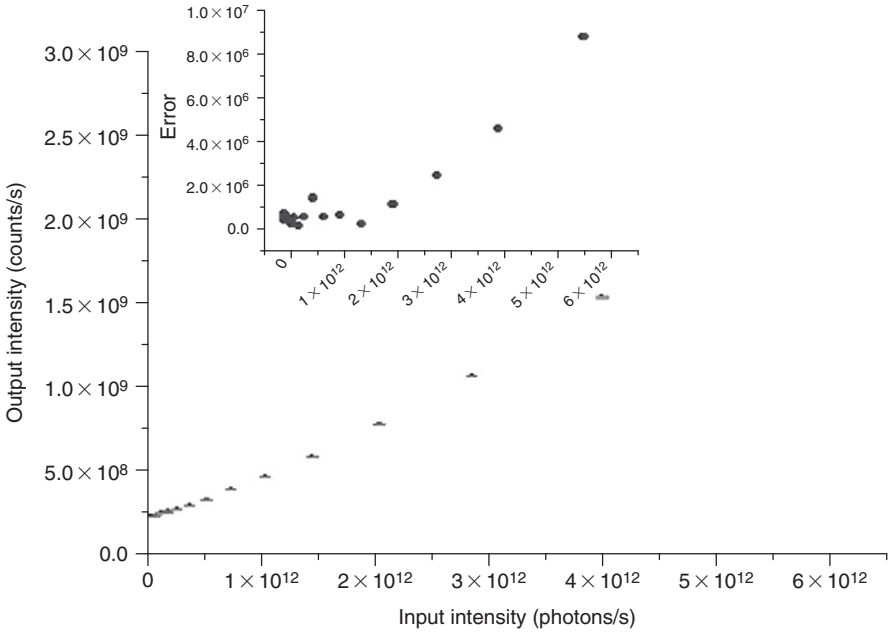

FIGURE 14.5

A plot of total output intensity (counts per second) as a function of input intensity (photons per second) with error bars and a plot of error as a function of input intensity (inset).

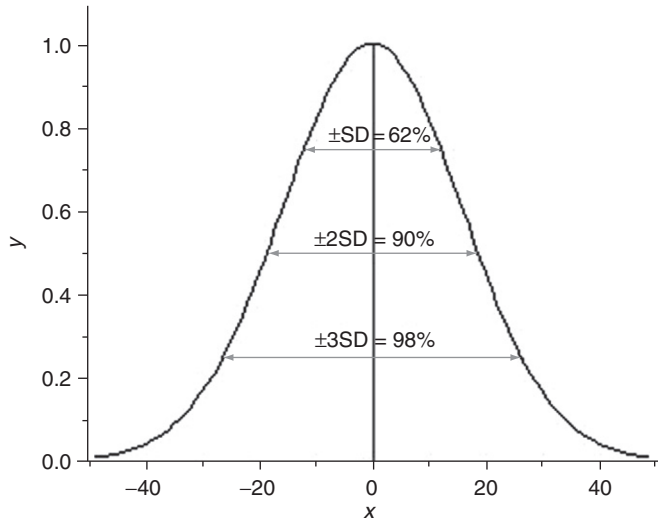

FIGURE 14.6

Gaussian distribution of imprecisions.

14.9 STANDARD DEVIATIONS, STANDARD ERRORS OF THE MEAN, *t*-TESTS, AND OTHER CONFUSIONS

Reviewers for quantitative journals tend to be sticklers for precision measurements. They want, at the very least, to see standard deviations or standard errors of the mean and the number of measurements associated with the determination of the mean. This is because they want to be able to determine the statistical significance of any statements that you make about your data.

One often hears one of two comments made regarding statistics:

1. They are just reporting standard errors instead of standard deviations in order to make bad data look good.
2. I do not need to report error and do a *t*-test because my system is not normally distributed.

Both of these statements are dead wrong!

The standard deviation reports the spread in measurements. The standard error reports the uncertainty that you have of the mean. Which one you report ultimately depends on the specific statement that you are making and supporting. Suppose that you are measuring the amount of some substance in a cell. If you want to say that cells express a variable amount of this substance, that the mean value is x and the variation is y, report the standard deviation as y. If on the other hand, you want to make a strong statement about the average value such as "the average production level in cells was found to be $x \pm y$," use standard error as y.

The "I don't need to use statistics because my data isn't normally distributed" argument requires a bit more explanation, but the bottom line is: yes you do! The theory of statistics is governed by what is referred to as *The Central Limit Theorem*. There is an excellent and extremely lucid discussion of this in Mandel's "The Statistical Analysis of Experimental Data." Mandel (p. 64) states *The Central Limit Theorem* as follows:

> *Given a population of values with a finite (non-infinite) variance, if we take independent samples from this population, all of size N, then the population formed by the averages of these samples will tend to have a Gaussian (normal) distribution, regardless of what the distribution of the original population; the larger N, the greater will be this tendency towards "normality." In simpler words: The frequency distribution of sample averages approaches normality, and the larger the samples, the closer is the approach.*

To which we add that in order for a *t*-test to be valid, the requirement of normality is on the frequency distribution of sample averages not on the frequency distribution of the individual measurements.

Let us illustrate this with an example from Mandel. Suppose that we have a school with 1000 classrooms. On this particular day, each of the classrooms has 100 seats and is overfilled. The teachers excuse everyone born in February or on the 31st of any month for day. We are left with only people born on a day from the 1st to 30th.

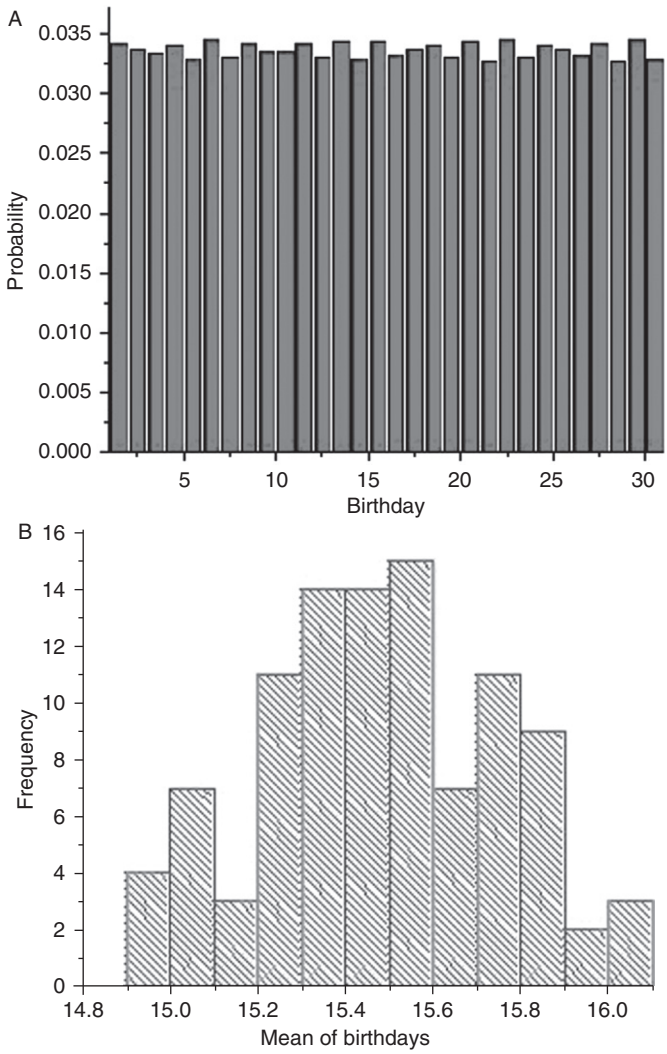

FIGURE 14.7

(A) A plot of the probabilities of the birthdays of 100 students (whose birthdays fell between the 1st and the 30th of a month) in 1000 classrooms. (B) A plot of the frequency distribution of the means of the birthdays of 100 students (whose birthdays fell between the 1st and the 30th of a month) in 1000 classrooms.

Barring some strange vagary of human reproduction, there is an equal probability of 1/30 of being born on any given date between 1 and 30. That is to say, the frequency distribution of birthdays is, as illustrated in Fig. 14.7A, a constant. We have simulated this situation with a random number generator and then calculated the mean

value obtained for each classroom. What is farther from a normal Gaussian distribution than this data set? In Fig. 14.7B, we plot the frequency distribution of the means. This distribution is clearly Gaussian in character. As predicted by *The Central Limit Theorem*, even this non-Gaussian data set yields a Gaussian distribution of means.

14.10 DYNAMIC RANGE, DO NOT WASTE IT

As explained in Chapter 8 by Spring, this volume, your detector stores an analog signal, typically a voltage, that must be converted to a digital signal. This is done with a device known as an analog-to-digital (or "A-to-D") converter. Suppose that one has a 12-bit camera. This means that the camera has a 12-bit A-to-D converter. If you set things up correctly so that the brightest objects of interest in your image are just short of saturation, then the camera will read intensities to a precision of $(1/2)^{12} = 1/4096 = 0.024\%$. By maximizing the use of dynamic range, you have maximized the precision attainable by your camera (this is why there were such small errors in Fig. 14.5). However, if instead you confine your measurement to only 40 gray levels, then you will only have a precision of $1/40 = 2.5\%$. You have increased the error associated with your measurements 100-fold. We can guarantee that you have enough sources of error in your system and experiment already. Do not introduce unnecessary error by improperly maximizing the dynamic range of your measurement! While it is not always possible to use the full dynamic range of a detector, this argument shows that always using as much as possible—for example, by binning pixels on a CCD—helps reduce systematic error in your measurements.

14.11 SIGNAL-TO-NOISE RATIO, *S/N*, AND SIGNAL-TO-BACKGROUND RATIO, *S/B*

Armed with what we hope is a heightened understanding of the importance of dynamic range and precision, let us revisit your data from Exercise 3. You will note that even the dark count or background has an uncertainty associated with it. Our data was generated with a CCD camera. Background in CCD cameras is dominated by the digital offset and readout noise and is close to a constant. If it were a constant then it might be possible to just subtract it from your measurements without affecting the precision of your measurements. However, it too has an imprecision associated with it and somehow this must be taken into account if we are to determine the overall precision (but note that a very high constant background limits dynamic range and degrades precision, as above). Before we explore this issue in greater depth, we can recognize that whatever the specifics of the mathematics are, our measurements will clearly be more precise, the greater the signal is relative to the error in the background. If we express the signal as S, its error as s; the background as B, and its error as N, for noise, then we want to maximize the signal-to-noise ratio, S/N. This is to be distinguished from the signal-to-background ratio which is S/B.

14.12 PROPAGATION OF ERROR IN CALCULATED QUANTITIES

Now let us ask more formally, if, as above, we have $S \pm s$ and $B \pm N$, what is the precision associated with the true signal $S - B$? What we are going to do here is provide you with the equations of error propagation and give you some examples of how to apply them. If you are interested in where these equations come from, they are derived in Appendix A.

Let us generalize this and say that we have two independent variables and their associated uncertainties $X \pm x$ and $Y \pm y$. We emphasize the requirement that the two variables do not depend on one another. For each possible mathematical operation with X and Y, how do we handle x and y?

For the addition of X and Y, we have that the sum is given by

$$(X + Y) + \sqrt{x^2 + y^2}. \tag{14.7}$$

For the subtraction of X and Y, we have that the difference is given by

$$(X - Y) + \sqrt{x^2 + y^2}. \tag{14.8}$$

Thus for addition or subtraction, the uncertainty is the square root of the sum of the squares of the uncertainties.

For multiplication of X and Y, we have that the product is given by

$$(XY)\left(1 + \sqrt{\left(\frac{x}{X}\right)^2 + \left(\frac{y}{Y}\right)^2}\right). \tag{14.9}$$

For division of X and Y, we have that the quotient is given by

$$\left(\frac{X}{Y}\right)\left(1 + \sqrt{\left(\frac{x}{X}\right)^2 + \left(\frac{y}{Y}\right)^2}\right). \tag{14.10}$$

Thus for multiplication or division, the fractional uncertainty is the square root of the sum of the squares of the fractional uncertainties.

For a general function of X and Y, call this $F(X,Y)$, the uncertainty, df, is given by

$$\mathrm{d}f = \sqrt{\left(\frac{\partial F}{\partial X}\right)^2 x^2 + \left(\frac{\partial F}{\partial Y}\right)^2 y^2}. \tag{14.11}$$

Probably the best way to understand this is to look at some examples. Consider again the data from Exercise 2. Here we find that the signal about midway up the curve is $S \pm s$ and the observed background or dark count was $D \pm d$. We can calculate the true signal, call it S_T, above background using Eq. (14.8) as:

$$S_T = (S - D) + \sqrt{d^2 + s^2}. \tag{14.12}$$

Similarly, we can calculate the signal to background S/B using Eq. (14.10) as:

$$\frac{S}{B} = \left(\frac{S}{D}\right)\left(1 \pm \sqrt{\left(\frac{d}{D}\right)^2 + \left(\frac{s}{S}\right)^2}\right). \tag{14.13}$$

Actually, if you think about it closely you will realize that the true S/B is S_T/D which is equivalent to $S/B - 1$. Subtracting a constant does not alter the uncertainty; as a result we have that

$$\frac{S_T}{B} = \frac{S}{B} - 1 = \left(\frac{S}{D} - 1\right) \pm \left(\frac{S}{D}\right)\sqrt{\left(\frac{d}{D}\right)^2 + \left(\frac{s}{S}\right)^2}. \tag{14.14}$$

This shows the basic process of error propagation. While it may appear cumbersome, it is done in steps, and can be automated using various software scripting tools. Suppose, for instance, that you are doing a two-color ratio calculation where you have two intensities, I_1 and I_2, with their two associated backgrounds, B_1 and B_2. Of course, each of these four quantities have their associated errors. Calculation of the error in the ratio, R, is given by

$$R = \frac{I_1 - B_1}{I_2 - B_2}. \tag{14.15}$$

One first calculates the errors in the numerator and the denominator using Eq. (14.8), and then in the R using Eq. (14.10).

This raises the question of when it is necessary to propagate error through calculations. In general, error must be propagated whenever a value is derived from the data that no longer captures the sources of variation in the image data. For example, when the signal contained within a defined region-of-interest is summed or averaged, the standard error should also be calculated, and this error should be propagated through any further calculations. However, any calculations performed with images (e.g., flatfield correction) maintain a representation of the error in the resulting image. In these cases, error propagation on a pixel-by-pixel level is not necessary.

14.13 EXERCISE 4: ERROR PROPAGATION IN IMAGING

As an exercise in error propagation in imaging applications and, in particular, in how to use Eq. (14.11), we would like you to try the following (Fig. 14.8):

1. As in Exercises 1 and 2, set up your microscope so that you are imaging your brightfield diaphragm.
2. Set your camera gain so that you are just short of saturation.
3. Set your area of interest so as to include the entire bright area of the diaphragm.
4. Measure the total intensity.
5. Turn off the lamp and wait 10 s.
6. Remeasure the area of interest and measure the dark intensity.
7. Turn the lamp back on and, with whatever tool your system provides, measure the diameter of the diaphragm.
8. Repeat steps 3–7 ten times and record your values.
9. Calculate the mean $\pm$ standard deviation for the intensity, $(I \pm i)$; the dark count, $(B \pm b)$; and the diameter, $(D \pm d)$.

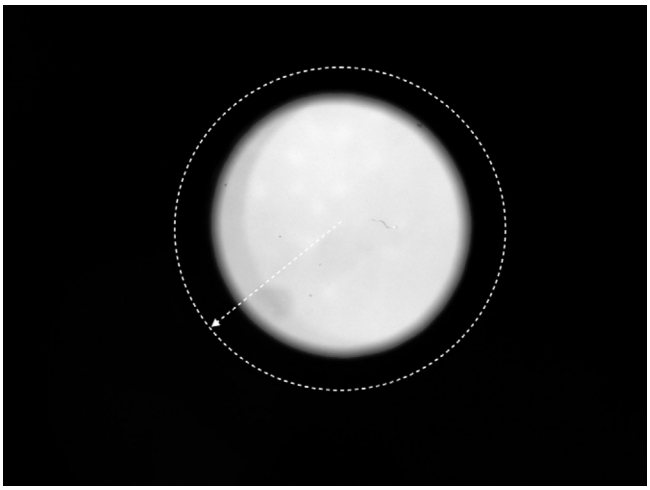

FIGURE 14.8

An image of the microscope diaphragm with a software defined area of interest (AOI) imposed.

We obtained an intensity of $(8.06 \times 10^8 \pm 1.3 \times 10^7)$ counts, a dark count of $(5.56 \times 10^7 \pm 2 \times 10^5)$ counts, and a diameter of (709 ± 3) pixels. Now the goal is to calculate the intensity per unit area. We recognize that there are probably easier ways to do this with your system, but the goal here is to learn how to propagate error. Also we recognize, that the diaphragm is not a perfect circle. So we have actually introduced error.

Calculating the intensity per unit area is pretty straightforward. It is

$$F = \frac{4I}{\pi D^2}. \tag{14.16}$$

To calculate the uncertainty, df, we must apply Eq. (14.11)

$$\begin{aligned} \mathrm{d}f &= \sqrt{\left(\frac{\partial F}{\partial I}\right)^2 i^2 + \left(\frac{\partial F}{\partial D}\right)^2 d^2}, \\ \mathrm{d}f &= \sqrt{\left(\frac{4}{\pi D^2}\right)^2 i^2 + \left(\frac{4I}{\pi}\right)^2 \left(\frac{-2}{D^3}\right)^2 d^2}, \\ \mathrm{d}f &= \sqrt{\left(\frac{4}{\pi D^2}\right)^2 i^2 + \left(\frac{8I}{\pi D^3}\right)^2 d^2}. \end{aligned} \tag{14.17}$$

If this is perplexing to you, remember that when taking a partial derivative you simply treat the other variable as if it were a constant. In our case we got (2042 ± 35) counts/pixel^2.

You may wonder why we told you to wait 10s after turning off the incandescent lamp in step 5. This is because incandescent lamps go off slowly. In particular, they continue to give off heat or infrared radiation which is potentially detectable by your camera, particularly if it is a CCD camera. This problem can be minimized by using an infrared absorption filter.

14.14 ACCURACY AND PRECISION, CALIBRATING AGAINST A REFERENCE STANDARD

So far we have discussed how you determine the errors obtained in a set of measured quantities and propagate them into a calculated quantity. In many situations, this is not the end of the process. Suppose, for instance, that you have measured, as described above, the ratio of two fluorescence intensities from a pH- or Ca^{2+}-sensitive fluorophore inside of a cell. You will have created a calibration curve of your ratio against pH or Ca^{2+} and you hope to use this calibration to determine the intracellular values of pH or Ca^{2+}. Typically, then you invert your calibration so that it reads out pH or Ca^{2+} as a function of ratio. You then make your measurements and if you are lucky, repeat measurements will give you a nice Gaussian distribution around the mean with the standard deviation describing your confidence level. By confidence, we mean here that you hope to say with confidence that the pH inside the cell is to a 95% confidence within two standard deviations of the value that you measured. Remember that standard deviation describes the precision.

However, suppose that you did your pH calibration with a pH electrode that had not been calibrated in the past month and the electrode had been left to dry out and form a disgusting crust. Under such circumstances, your measurements, while nicely clustered, could all be a pH unit off. How close you are to a true reference standard is known as accuracy and the amount of systematic error is referred to as bias.

We have seen, for instance in Exercise 3, that CCD cameras have a background dominated by readout noise. Readout is a DC level with a random noise about the DC level. The DC level represents a bias. Systematic sources of error, such as DC levels, add simply, while random sources of noise add as the sum of the squares as shown in Eq. (14.11). This sounds like an academic issue. However, keep these things in mind as you read about the various sources of noise in your detection systems in the camera chapters. You will encounter both classes of noise.

14.15 FLATFIELD CORRECTION

Now that your dynamic range is properly set and you have corrected for any nonlinearities in gain, we are ready to return to the problem in Fig. 14.1. You are ready to analyze an image. Why is it that the same object viewed at different points in the object plane can exhibit radically different intensities? This is because despite your best efforts at Kohler illumination of your fluorescence source, the illumination is not perfectly homogeneous across the field. Similarly, inhomogeneities may be introduced by other optics and by the camera's detector. In order to correct for these

inhomogeneities, the intensity profile of the image should be normalized to a reference image of a homogeneous fluorescence field. This is referred to as a flatfield correction, which corrects for inhomogeneities of illumination and detection.

To create a sample that is a homogeneous fluorescent surface, take a solution of a protein labeled with the same spectral characteristics as that being used in the experiment and let a drop of this sit on a coverslip for 20–30 min. (Do not allow this drop to dry! A film works better than a thick solution.) On gently washing away the drop, you will find that a film of fluorophore remains on the coverslip. You search out a region on the coverslip where the film is essentially homogeneous and then defocus very slightly to correct for any minor imperfections. At lower magnifications a piece of fluorescent tape works very well. At higher magnifications the imperfections start to become apparent and it is best to slightly defocus the detector while imaging the tape.

Before launching into the exercise an important consideration is bit depth. Images are normally stored as 16-bit integers. Digital division can be very tricky, and it is best to do these calculations as floating point. The results can then be scaled back to 16-bit integers by multiplying by a scalar.

14.16 EXERCISE 5: FLATFIELD CORRECTION

1. Chose a favorite fluorescent sample.
2. Create your homogeneous fluorescent reference film or tape.
3. Take an image of the homogeneous field. We will call this $H(x,y)$.
4. Take a background image in a region of no fluorescence: $B_H(x,y)$.
5. Background correct homogeneous field image: $H'(x,y) = H(x,y) - B_H(x,y)$
6. Take an image of your sample: $I(x,y)$.
7. Take a background image in a region of no fluorescence: $B_1(x,y)$.
8. Background correct your image: $I'(x,y) = I(x,y) - B_1(x,y)$.
9. Perform that flatfield correction: $F(x,y) = I'(x,y)/H'(x,y)$.

Figure 14.9 shows the results of such a flatfield correction applied to the images of Fig. 14.1. The images do indeed appear more similar in intensity than those of Fig. 14.1, and this is confirmed by the intensity scans seen in the Fig. 14.9 inset. Flatfield correction is a very effective method of normalizing intensity values across the field and removing some of the most common sources of systematic error from your images. It is an essential technique when measuring signal intensity differences between different regions of an image. It is also a means of producing excellent, publication quality images.

14.17 APPLICATIONS REQUIRING SPATIAL CORRECTIONS

While flatfield correction enables one to correct for inhomogeneities in illumination and detection across the field, it leaves open the question of whether the spatial relationship between points is accurate. In subsequent sections, we will examine the fundamental issue of spatial correction in imaging.

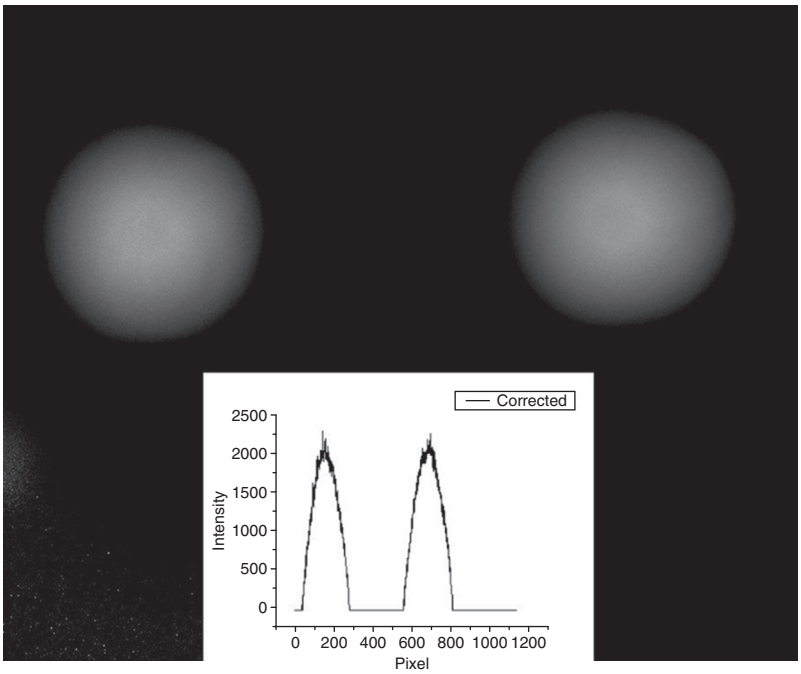

FIGURE 14.9

A flatfield corrected image, to get a true representation of intensities (inset) over an image of two fluorescent objects, one at the center of the microscope field the other at the edge of the field.

14.18 MAXIMIZING RESOLUTION BEFORE YOU START

Let us begin with the issue of obtaining accurate spatial information. A good place to begin is to discuss how resolution is classically defined. A complete discussion of this subject is outside of the scope of this chapter, and we refer the reader to Chapter 2 by Wolf, this volume. For our purposes, let us first follow our intuition, which tells us that resolution, defined as the smallest distance, r, between which two self-luminous points would still be distinguishable, should be related to wavelength. We then define the Rayleigh diffraction limit r as

$$r = 0.61\frac{\lambda}{\mathrm{NA}_{\mathrm{obj}}}, \tag{14.18}$$

where $\mathrm{NA}_{\mathrm{obj}}$ is the numerical aperture of your objective (you will find it written on the barrel of the objective). For a brightfield application, the NA of the condenser, $\mathrm{NA}_{\mathrm{cond}}$, also factors in, and Eq. (14.18) becomes

$$r = 1.22\frac{\lambda}{\mathrm{NA}_{\mathrm{obj}} + \mathrm{NA}_{\mathrm{cond}}}. \tag{14.19}$$

What this tells you is that for 500-nm light, and for an objective with an NA = 1.4, the resolution is going to be around 0.2 μm.

A striking point is that resolution does not involve any eyepiece or camera projection lens. These contribute what is called "empty magnification." They make images bigger but do not contribute any added detail.

Empty magnification can, in fact, be very important in digital imaging applications. Digital detectors can be thought of as arrays of individual pixel detectors. These are separated by some distance. Recognize that at the detector surface the resolution limit r in the object plane maps to a distance R, where

$$R = r(\text{objective magnification}) \times (\text{empty magnification}). \tag{14.20}$$

It is critical that this R be significantly greater than the interpixel distance. If it is not, your camera is going to reduce the resolution of your microscope.

14.19 EXERCISE 6: CONVERTING PIXELS TO MICRONS

An obvious point is that one will, in general, not want to express the size of objects or distances between points in an image in pixels. Rather distances and sizes will be expressed in microns. This raises the question of how one calibrates interpixel distances to microns, and yes, you guessed it this is going to require error propagation and an awareness of the issue of accuracy and bias. See Fig. 14.10.

1. Focus a ruling in your microscope. The one we use has boxes which are 50 μm apart. Try to get one of the crosses centered in the center of the field and try to get the vertical lines vertical and the horizontal lines horizontal.
2. Choose a relatively large separation, say, 200 μm and measure the distances, in pixels, between lines.
3. Repeat this 10 times.
4. Calculate the mean $\pm$ standard deviations. We got (285 $\pm$ 1) pixels.
5. Calculate the distance per pixel.

In our case 200 μm = (285 $\pm$ 1) pixels. So this is (200/285) μm/pixel. What about the error propagation? This is essentially an application of Eq. (14.10); however, since we must assume that the rulings on the reticle are accurate, the only source of error is in the pixel distance measurements. So percentage error is preserved and we get as our final answer [200/285(1 $\pm$ (1/285))] μm/pixel, or, (0.702 $\pm$ 0.004) μm/pixel. Note that the rulings are accurate is an assumption that there is no systematic error, that is, there is no bias.

14.20 EXERCISE 7: IMAGING WARPING

We next raise the question of whether the interpixel distance is the same regardless of where you are on the image. Look again at the image of the grid in Fig. 14.10. What we are going to do is to measure the intensity profile of this image, both in the x- and in

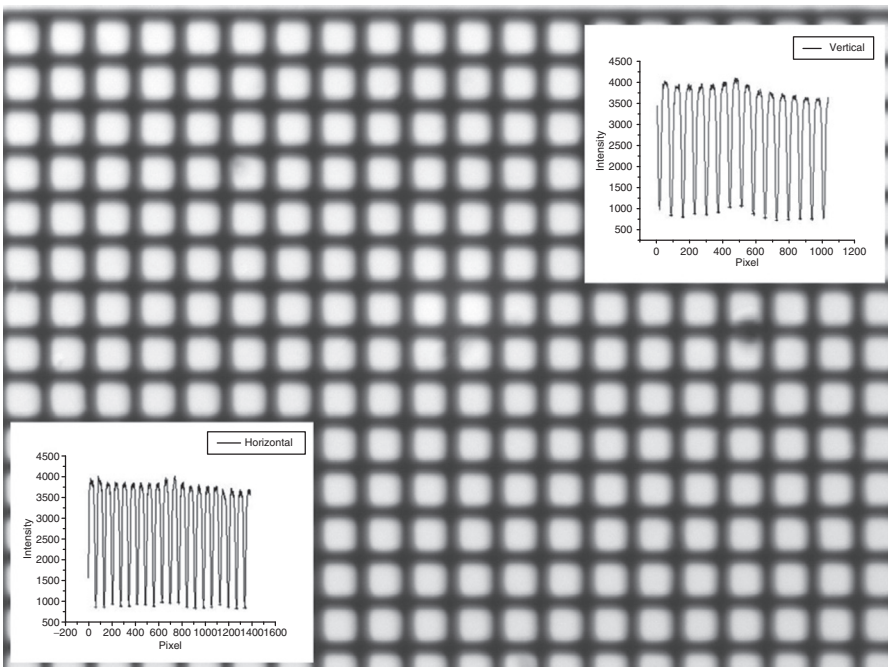

FIGURE 14.10

An image of a reticle with 1 mm^2 ruled every 50 μm.

the *y*-directions as one moves away from the center. We will then look at the position of the grid lines, so as to determine if there is any systematic variation in the image.

1. Take a focused image of the grid.
2. Measure the intensity profile, which goes approximately through the center in the horizontal and vertical directions.
3. Measure the distance in pixels between the various grid lines. If you want, you can convert these distances to microns.
4. Plot these distances on a graph.

In the case of our data (Fig. 14.11), we observed no distortion in the image. The data in both the *x*- and *y*-directions fell perfectly along straight lines. The straight lines are also shown in the plot and has an *R* value of 1.00. The statement that there is no distortion is not a random one. The criterion for no distortion is essentially that true points do not show statistically significant deviations from the line. This is why understanding the error associated with the measurements is so important. Another convenient way to look at the data is to plot the residuals from the line. In our case, there was no systematic deviation, but only random deviations (not shown). These problems will become more dramatic in objectives that are not corrected for one of the root causes of this phenomenon, namely spherical aberration.

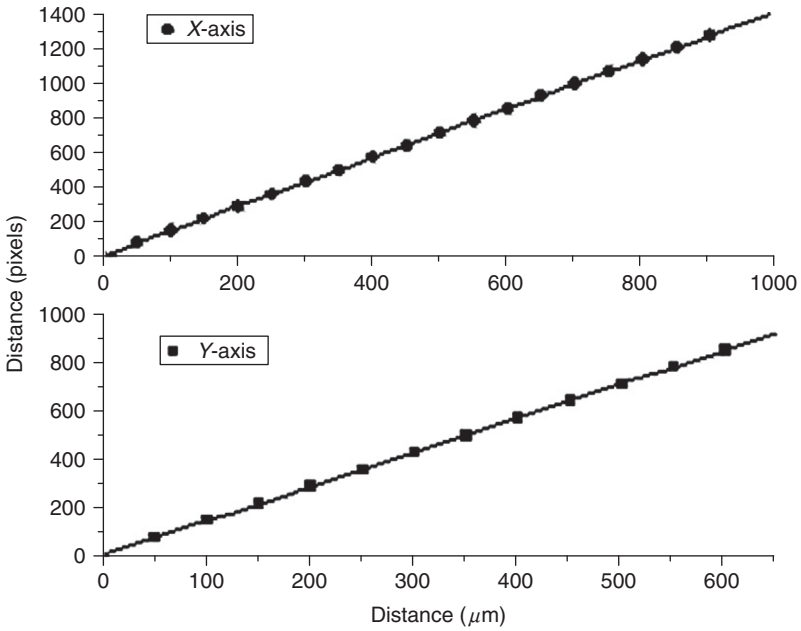

FIGURE 14.11

A plot of the distortion along the *x*- and *y*-axes.

The problem that we have been addressing here is how an imaging system distorts a rectilinear pattern. Unfortunately, rectilinear patterns are not transmitted true through the "black box" of your optical system. Figure 14.12 illustrates the two most common results: pincushion and barrel distortion. These distortions are not really surprising as, despite the best efforts of microscope designers, optical systems tend to focus to curved rather than planar surfaces, and the detector of your digital camera is more or less flat. You may also note that the edges of the image are slightly out of focus. You can not flatten a curved image surface to a flat detector surface without distortion.

The implications of warping can be very disturbing. Implicit in warping is the fact that magnification changes with position in your image. Also, if warping is different for different wavelengths, then the magnification becomes wavelength or color dependent. Warping is most common when using less-corrected lenses, especially in low-magnification experiments. How does one correct for this type of distortion?

14.20.1 Ignoring the problem

First some practical advice: Be aware that in some cases you can ignore this kind of distortion. Determine over what area of the center of the field this distortion remains less than a pixel. If you stay within that area, you can safely ignore it for most purposes.

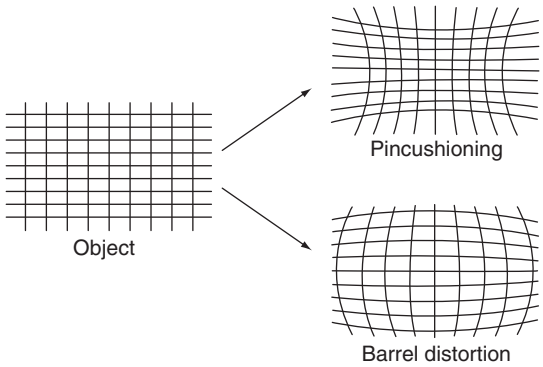

FIGURE 14.12

Pincushioning and barrel distortion. Because optical systems tend to focus to curved rather than to planar surfaces, rectilinear patterns in the object plane tend to produce "pincushioned" or "barrel-distorted" images. These can be corrected for as described in the text.

14.20.2 Dewarping algorithms

Many image-processing software packages come with "canned" software to dewarp an image. You should always make the effort to understand what the algorithm is doing. In the end, you are the judge of the validity of a particular algorithm for your applications.

An example of a dewarping algorithm is polynomial dewarping. This is a logical step up from a linear transformation. The idea is to assume that the shape of the distorted pattern in image space is a generalized polynomial of the rectilinear pattern of the object. For most purpose, a second-order polynomial will suffice. Again following our convention, the image coordinates (x',y') that correspond to a point in the object plane are given by

$$x' = a + bx + cy + dx^2 + exy + fy^2 \tag{14.21}$$

$$y' = A + Bx + Cy + Dx^2 + Exy + Fy^2 \tag{14.22}$$

where $a, b, c, d, e, f, A, B, C, D, E$, and F are constants. Because each point in object space has two coordinates, these 12 constants are determined by choosing six points in object space and measuring the values of (x',y') in the image. Typically, these points are chosen to be major intersections of your rectilinear grid; Eqs. (14.14) and (14.15) then enable you to calculate the constants. For example, suppose you use the point you define as the origin in the object plane, that is, $(x,y) = (0,0)$, which maps to a point (x',y') in the image plane, then Eqs. (14.21) and (14.22) tell us that $a = x'$ and $A = y'$, respectively.

Once the constants are determined, you are ready to dewarp your image. As in the cases of translation and rotation, this requires inversion of Eqs. (14.21) and (14.22). This looks like an algebraic nightmare (and it is!). However, there are several readily

available symbolic language software packages, such as Mathematica and Matlab, that can do this for you. Not only will they solve this equation for you, but many of them will generate software in your favorite computer language to do the calculation for you. This is not meant to be facetious. Modern personal computers have gotten so fast that imaging calculations like this, which a few years ago required array processors to accomplish in reasonable time, can now be accomplished in the blink of an eye.

14.21 EXERCISE 8: TWO-COLOR COINCIDENCE

A related problem to image warping is that of image translation. This becomes particularly important in multispectral applications where one wants images of the same object in two colors of fluorescence to be coincident spatially. Let us start off with a simple example. Suppose that you image a submicron fluorescent bead that you have positioned dead center in your microscope. Will it be at the center of your image? Probably not.

Exercise 8a for high numerical aperture systems

Let us try a simple experiment to attempt to measure this phenomenon.

1. Chose a submicron (0.1 or 0.2 μm) multispectral bead.
2. Put a dilute solution of these beads on a coverslip and allow time for them to settle onto the coverslip.
3. Invert the coverslip onto a microscope slide.
4. Remove excess buffer and seal with nail polish.
5. Use a high power, high numerical aperture objective (typical oil or water immersion) to view the sample.
6. Focus on a bead which is attached to the coverslip. Remember that microscopes are optimally designed to look at the interface between the coverslip and the aqueous medium. Then, make sure that the sample is also sharply focused in the image.
7. Take an image of the sample with one of the fluorescence filter cubes. Remember to be mindful of your dynamic range. As always, you do not want to be in a situation where you were using only a small fraction of the total dynamic range.
8. You may also find if you want to do this, it is useful to take a background image here for purposes of subtraction. It will be best to take both background images before you take the actual sample images, so that you do not have to change position when you change filter cubes.
9. Take a second image of the same bead only with a different fluorescence filter cube. Do not refocus, as part of this exercise is to determine whether the plane of focus is the same for the two colors.
10. Determine the location in terms of pixel coordinates of the bead in the two colors. Are they coincident? An interesting thing that you can do here is to portray the one image as green and the second image as red. You then create a composite image of these two color images. If the two signals are completely

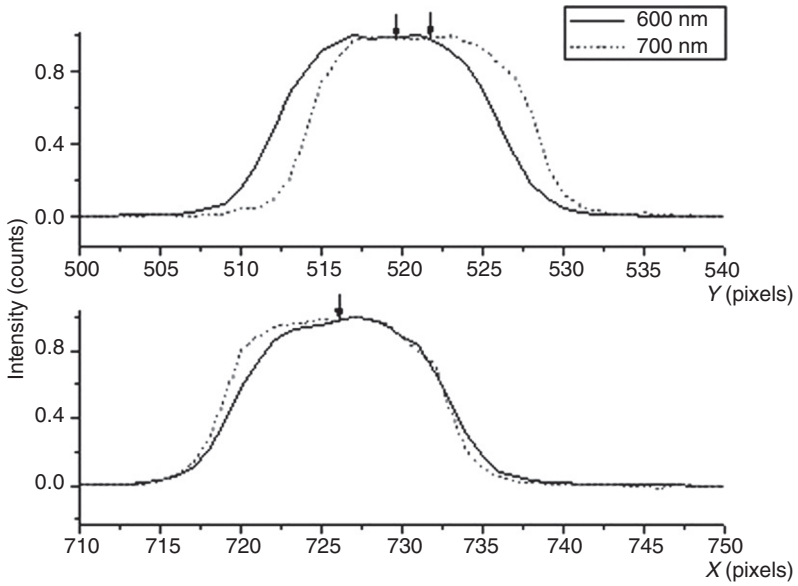

FIGURE 14.13

The shift of the center (denoted by arrows) of a pinhole at 600 and 700 nm in both the *x*- and the *y*-directions. The intensities at each wavelength have been normalized.

coincident, you will see nothing but yellow. However, if there is a shift, one side of the pseudo-color composite will be red, and the other side green.

Exercise 8b for low numerical aperture systems

For low numerical aperture systems such as stereoscopes, the following exercise may be more illuminating (Fig. 14.13). You will need in addition to the standard kit a pinhole aperture which is readily available from suppliers such as Thor, NJ and Edmund Optics, NJ. The one we used is a 150-μm aperture.

1. Place the aperture on the sample stage of the microscope and center it in the field of view.
2. Use an objective such that the aperture appears as small as possible.
3. Illuminate from below with an incandescent lamp source.
4. Take an image with the first fluorescence filter cube.
5. Measure the *x*- and *y*-coordinates in pixels of the center of the aperture.
6. Take an image with the second fluorescence filter cube.
7. Measure the *x*- and *y*-coordinates in pixels of the center of the aperture.
8. Repeat steps 4–7 for a total of 10 times.
9. Calculate for each filter cube the mean $\pm$ standard deviation of the *x*- and *y*-coordinates.

In doing this exercise we obtained the following values for the first cube (600 nm): $x_{600} = 726 \pm 1$, $y_{600} = 520 \pm 1$. For the second filter cube (700 nm),

we obtained $x_{700} = 726 \pm 1$, $y_{700} = 522 \pm 1$. The question then is whether either of these shifts is real, that is, statistically different from one another. Since the data was obtained in pairs it is best analyzed using a pairwise *t*-test, which requires going back to the original data rather than working with the means and standard deviations directly. When we do this we find that for the *x*-direction there is no significant difference, but in the *y*-direction there is a significant difference. Figure 14.13 shows the shift of the center of the pinhole (marked by arrows) in both the *x*- and *y*-directions (note that the intensities at each filter wavelength have been normalized).

The problem of a simple shift between two images taken at different wavelengths (often the result of using different fluorescence filters that act as optical wedges) is relatively straightforward to deal with. In general terms, if a bead is in position (x,y) in object space, its location will shift off in going to image space and will settle in at position (x',y'). Usually, these shifts are small and can be described by a simple pair of linear equations, such as

$$x' = x + a \tag{14.23}$$

and

$$y' = y + b \tag{14.24}$$

where a and b are constants. As already noted, this kind of correction becomes really important in applications such as color registration. Typically, the as and bs will be wavelength dependent, especially if you are changing wavelengths by shifting filter cubes. In addition, you cannot assume *a priori* that these shifts are independent of where in the object you are. The shifts may be greater at the edges of the image than at the center.

Equations (14.23) and (14.24) are easily inverted to obtain x and y. That, after all, is our goal: We want to know how a position in the image (x',y') translates to a position in the plane of the object. We have that

$$x = x' - a \tag{14.25}$$

and

$$y = y' - b \tag{14.26}$$

If the axes of the camera are not lined up with the horizontal and vertical axes of the microscope, then you will potentially observe rotations in addition to translations in the image. The problem of inverting rotational transformations is a little more complex. We defer this discussion to Appendix B.

14.22 TWO-CAMERA AND TWO-COLOR IMAGING

With the popularity of ratio imaging, one is often confronted by the problem of processing images from two cameras or two colors. In both of these cases, the images are not in perfect registration and there tend to be magnification differences. This is, in

fact, a very similar situation to the warping problem. The same generalized polynomial dewarping algorithm can be used to map an image obtained with one camera onto that obtained with the other. This is, in fact, one of the most common uses of dewarping algorithms.

14.23 PUTTING IT ALL TOGETHER . . .

Our goal so far has been to introduce the concept of digitally correcting your images. We have tried to focus on some of the more critical types of data transformation and some of the frequently encountered issues in quantitation. For a much more in-depth discussion of image processing, we refer you to Chapters 9, 10, 12, 14, 16, this volume; and Chapters 13, 15, 16, 18, volume 81, 2007 and several specialized texts (Baxes, 1984; Castleman, 1979; Pratt, 1991; Taylor & Wang, 1989; Wang & Taylor, 1989). Recognize that image processing represents a form of data processing. There are, of course, many other examples of data processing such as fitting your data to a theoretical curve. In all these cases, it is critical that care be taken during all steps of transformation, processing, and quantitation. However, since almost all of these occur in discrete steps it is usually straightforward, albeit essential, to track what you are doing.

14.24 APPENDIX A. ERROR PROPAGATION: A GENERALIZED EQUATION

Our goal in this chapter is to derive a generalized formula for error propagation. As pointed out in the chapter, error propagation is closely associated with curve fitting, and one often sees this fundamental relationship derived by chi-squared minimization. We will here take a more intuitive approach and recognize that the essential point or requirement is that the sources of error be independent. Independence is mathematically equivalent to orthogonality (Fig. 14.A.1). If we have a function,

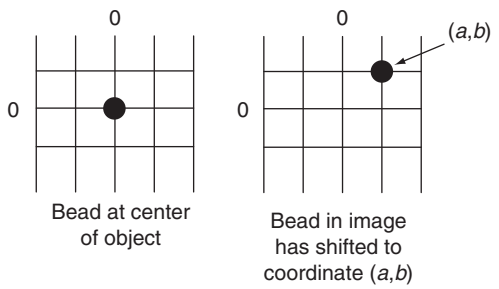

FIGURE 14.A.1

Linear transformation. One form of transformation in an optical system is linear translation. Here, we show a hypothetical bead at coordinate (0,0) in the reality or object plane. The optical system translates the bead to coordinate (*a,b*) in the image.

F, of two independent variables x and y [i.e., we have $F(x,y)$], then we can think of the two independent errors, dx and dy, as lying along two perpendicular axes, defined in terms of their unit vectors i and j. Then the directional derivative of $F(x,y)$ defines the uncertainty dF as

$$\mathrm{d}\vec{F} = \left(\frac{\partial F}{\partial x}\mathrm{d}x\right)\hat{i} + \left(\frac{\partial F}{\partial y}\mathrm{d}y\right)\hat{j} \tag{14.A1}$$

and equivalently that

$$\begin{aligned}(\mathrm{d}F)^2 &= \left(\frac{\partial F}{\partial x}\right)^2(\mathrm{d}x)^2 + \left(\frac{\partial F}{\partial y}\right)^2(\mathrm{d}y)^2 \\ \mathrm{d}F &= \sqrt{\left(\frac{\partial F}{\partial x}\right)^2(\mathrm{d}x)^2 + \left(\frac{\partial F}{\partial y}\right)^2(\mathrm{d}y)^2}\end{aligned} \tag{14.A2}$$

This is the general error propagation equation.

For addition or subtraction we have that

$$F(x,y) = x \pm y \tag{14.A3}$$

$$\frac{2F}{2x} = \frac{2F}{2y} = 1 \tag{14.A4}$$

and from Eq. (14.A2) that

$$\mathrm{d}F = \sqrt{(\mathrm{d}x)^2 + (\mathrm{d}y)^2} \tag{14.A5}$$

Thus for addition or subtraction the error is the square root of the sum of the squares.

For multiplication we have that

$$\begin{aligned}F(x,y) &= xy \\ \frac{2F}{2x} &= y \\ \frac{2F}{2y} &= x\end{aligned} \tag{14.A6}$$

Then using Eq. (14.A2) we obtain

$$\mathrm{d}F = \sqrt{y^2(\mathrm{d}x)^2 + x^2(\mathrm{d}y)^2} \tag{14.A7}$$

It is useful to divide Eq. (14.A6) by Eq. (14.A5). Thus

$$\frac{\mathrm{d}F}{F} = \sqrt{\frac{(\mathrm{d}x)^2}{x^2} + \frac{(\mathrm{d}y)^2}{y^2}} \tag{14.A8}$$

The same result can be readily obtained for division where

$$F(x,y) = \frac{x}{y} \tag{14.A9}$$

Thus for multiplication and division, the fractional error in F is the square root of the sum of the squares of the fractional errors in x and y. For multiplication and division, it is useful to extend and rewrite Eq. (14.A7) as

$$F \pm \mathrm{d}F = F\left(1 \pm \sqrt{\frac{(\mathrm{d}x)^2}{x^2} + \frac{(\mathrm{d}y)^2}{y^2}}\right) \tag{14.A10}$$

14.25 APPENDIX B. IMAGE TRANSLATION AND ROTATION

Above, we described the situation in which the camera's horizontal and vertical did not match the object's horizontal and vertical. A simple solution is to carefully rotate your camera until the axes match. This might not always be convenient. Alternatively, you might have a specific need to rotate an image about the center of the field. This can be done using a very similar process to that described for point translation. We will again use the convention that (x,y) describes the position in the object space and (x',y') describes the position in the image space (Fig. 14.A.2). If the image is rotated by an angle θ relative to the object, we have that

$$x' = x\cos\ \theta + y\sin\ \theta \tag{14.B1}$$

$$y' = y\cos\ \theta + x\sin\ \theta \tag{14.B2}$$

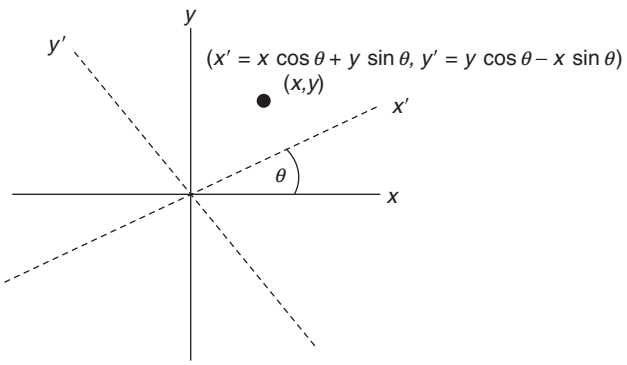

FIGURE 14.A.2

Rotational translation. Optical systems can also rotate. Here, the optical system rotates the object through an angle of θ so that a point with coordinates (x,y) in the object is located at (x',y') in the image.

On inversion, Eqs. (14.B1) and (14.B2) become

$$x = x' \cos\ \theta + y' \sin\ \theta \tag{14.B3}$$

$$y = x' \sin\ \theta + y' \cos\ \theta \tag{14.B4}$$

Of course, in a real world, you are liable to find a combination of translation and rotation, so the inversion becomes slightly more involved.

Acknowledgments

We are grateful for critical discussions with all of the faculty and students of the AQLM course. We are especially grateful to Drs. Jennifer Waters, John Murray, Mary-Ann Mycek, Kim Wicklund, Rainer Heintzmann, and Richard Cardullo, who helped in the design and execution of the quantitative microscopy exercises at AQLM. J.R.S. is a Wellcome Trust Senior Research Fellow.

References

Baxes, G. (1984). *Digital image processing*. Englewood Cliffs, NJ: Prentice Hall.

Beers, Y. (1962). *Introduction to the theory of error*. Boston, MA: Addison-Wesley.

Bevington, P. R., & Robinson, D. K. (2002). *Data reduction and error analysis for the physical sciences*. New York: McGraw-Hill.

Castleman, K. R. (1979). *Digital image processing*. Englewood, NJ: Prentice Hall.

Goodman, J. W. (1996). *Introduction to Fourier optics*. New York: McGraw-Hill.

Mandel, J. (1964). *The statistical analysis of experimental data*. New York: Dover Publications.

Pratt, W. (1991). *Digital image processing*. New York: Wiley.

Press, W. H., Teukolsky, S. A., Vetterling, W. T., & Flannery, B. P. (1992). *Numerical recipes in C*. New York: Cambridge University Press.

Robinson, G. K. (2000). *Practical strategies for experimenting*. New York: Wiley.

Taylor, D. L., & Wang, Y.-L. (1989). *Fluorescence microscopy of living cells in culture, Part A* (Vol. 29). San Diego, CA: Academic Press.

Wang, Y.-L., & Taylor, D. L. (1989). *Fluorescence microscopy of living cells in culture, Part B* (Vol. 30). San Diego, CA: Academic Press.

CHAPTER

15 Evaluating Optical Aberrations Using Fluorescent Microspheres: Methods, Analysis, and Corrective Actions

Paul C. Goodwin[*,†]

[*]*GE Healthcare, Issaquah, Washington, USA*

[†]*Department of Comparative Medicine, University of Washington, Seattle, Washington, USA*

CHAPTER OUTLINE

Introduction **370**
15.1 Rationale **371**
15.2 Methods **371**
15.3 Discussion **374**
15.3.1 Monochromatic Aberrations 374
15.3.1.1 Comatic Aberration 374
15.3.1.2 Astigmatic Aberration 374
15.3.1.3 Spherical Aberration 375
15.3.2 Polychromatic Aberrations 377
15.3.3 Determining the Source of Aberrations 382
15.3.4 A Word Regarding Mounting Media 383
Summary **384**
Acknowledgments **384**
References **385**

Abstract

Obtaining optimal performance from a microscopy system requires careful evaluation of the entire optics train of the imaging system. This evaluation starts with a fundamental evaluation of the optical components in the microscope. Concise and visual methods are provided for understanding the optical performance of the microscope as a system using subdiffraction fluorescent microspheres to evaluate both

Methods in Cell Biology, Volume 114 **ISSN 0091-679X**
Copyright © 2013 Elsevier Inc. All rights reserved.
http://dx.doi.org/10.1016/B978-0-12-407761-4.00015-4

monochromatic and polychromatic aberrations. Further practical guides are given to troubleshooting optical problems and final comments are made on optimizing sample preparation.

INTRODUCTION

The value of microscopy to a number of scientific disciplines is by now well established. In order to realize this value, a microscope must accomplish three goals: magnification, resolution, and contrast. Of these functions, magnification is the simplest to produce. Magnification is simply the ratio of the focal distance from a lens to the detector divided by the focal distance from the lens to the object. Since one could make an arbitrarily large focal distance from the lens to the detector, one could make phenomenal magnifications on the orders of millions of times magnification. So why are these large magnification systems not seen? This is because magnification without accompanying resolution and contrast is of little or no value. Rayleigh showed that resolution is dependent on the numerical aperture of the lens system. The numerical aperture is a description of the angle of light at which the object can be viewed. Resolution is limited by the diffraction of light and physical hard barriers. While Gustafsson et al. (Gustafsson, Agard, & Sedat, 1999) and others have shown synthetic methods of increasing the effective aperture of a lens through structured illumination, these diffraction barriers continue to limit resolution in most microscope systems. This leaves the microscopist with contrast or signal-to-background. Signal-to-background is the ability to differentiate between what is truly the signal that represents that object that is observed and the uncertainty that is independent of the object. Fundamentally, the difference between a relatively simple research microscope and a complex, high-end research microscope that costs up to one hundred times as much is the contrast that the latter system can generate. Magnification, as discussed above, is fundamentally generated by the ratio of the focal distances of the lenses in the microscope. Resolution and contrast, however, are dependent on the design and the implementation of the entire optical train. While it is tempting to assume that resolution and contrast are fixed, they are indeed variables due to this reliance on implementation. If a microscopist is to obtain the resolution and contrast for which they have invested considerable resources, they must be able to evaluate the optical performance of their system to assure that optical aberrations are not depriving them of the quality that they deserve. To make this determination, the microscopist needs methods to evaluate aberrations and their source. This chapter seeks to provide a practical guide to evaluating and troubleshooting complex optical system. It should be noted that these aberrations are relevant regardless of the overall microscopy method. In fact, it can probably be said that the more sophisticated the methods are for generating contrast (confocal, two-photon, structured illumination, etc.), the more affected the system will be by these aberrations. Likewise, these aberrations potentially affect the quality and quantification of all microscopy even in the most simple of optical systems.

15.1 RATIONALE

The overall optical performance of a microscope is the sum of the individual performances of each optical component. It is tempting to believe that the optical performance of every microscope is highly optimized such that the user is always working under ideal conditions. The optical performance of the microscope is achieved only under the most perfect conditions, and anything that introduces imperfections will decrease the performance of the optical system. The assumed perfect optical conditions are rarely achieved by the casual microscopist, and it is only with great diligence that ideal conditions can be created. How does the microscopist evaluate the performance of the microscope? How can the microscopist evaluate the optics of their microscope to achieve these ideal conditions? How can the microscopist determine the nature and source of aberrations and minimize these aberrations? The user must examine a well-defined optical sample and evaluate the performance relative to this known sample. One difficulty is that the samples that microscopist observe are generally too complex to serve as optical standards. For example, cells are three dimensional. Light is typically absorbed, refracted, and generated at different optical depths. The information from these different depths overlaps making it difficult to ascertain the actual optical performance. Moreover, a complex sample such as a cell is not known well enough to serve as a standard. Ideally, the optical standard would have a well-understood morphology, would be confined to a single, defined optical plane, and would be well isolated from other objects so as to not confuse the results. Furthermore, this specimen should be something that is easily created and replicated so that the microscopist can create it at will. A specimen that fulfills this requirement is the fluorescent microsphere.

A microsphere is typically a polystyrene bead that is infused with one or more fluorochrome. These beads are available in a variety of sizes and are infused with fluorochromes that are well suited to a number of optical filters. If the bead is smaller than the optical resolution of the microscope, its exact morphology does not affect the viewed image. A subresolution perfect sphere will generate the same optical pattern as a cube or, for that matter, one shaped like your favorite aunt. So the subresolution bead nicely fulfills the requirement for a known morphology, that is, it shape does not matter. Polystyrene microspheres are slightly charged so that they will tend to stick to glass. This makes them very easy to confine to a single optical plane. The separation of individual microspheres is relatively simple to affect by controlling the concentration of microspheres. Finally, microspheres are relatively easy to work with and slides containing fluorescent microspheres are simple and inexpensive to create. One such method is listed at the end of this chapter.

15.2 METHODS

Most microscopists work with samples that are three dimensional such as biological cells and materials. Even those whose work is primarily limited to a single plane (such as those observing artificial membranes and chromosome spreads) are affected

by the three-dimensional performance of the microscope, a point that will be demonstrated later in this chapter. So the evaluation of the microscope must be done in three dimensions, the lateral (x and y) and the axial (z). The microscopist must have a means to translate the bead laterally and to focus on different axial levels. Fortunately, most microscopes are well suited for this. Secondly, while it is possible that one could use a subresolution absorptive microsphere for this task, the contrast and ease of using fluorescence greatly facilitate this technique. If the user must evaluate a microscope not equipped with fluorescence optics, it is possible to perform some of these tests using what is colloquially referred to as a "star target," which is an opaque field with diffraction limited transparent "holes." For this chapter, we will limit our discussion to observations made with fluorescence microscopy; however, many of the principles are transferable to bright-field observations.

First of all, the microsphere should be used in a dark room and it is best if the user is well dark adapted, that is, the user's eyes should be accustomed to the dark. Many of the details of the optical performance are subtle and, since the beads are small, they are not terribly bright relative to room lights. Second, the microscope should be clean and free of dust and smudges that will impair optical performance. For evaluating objective lenses, it is important that both the front and rear lenses of the objective lens are properly cleaned. Third, it is important that the bead slide is also clean and free of dust and debris. Finally, it is important that the microscope is properly aligned and in good working order. The lamp used for the fluorescence illumination should be within the working lifetime of the bulb and should be on and allowed to stabilize for at least 30 min prior to use.

Once the sample is placed on the microscope stage, the appropriate excitation, emission, and dichromatic mirror filters are selected, and the appropriate focal plane is determined, it should be possible to observe the microsphere beads under fluorescence. The beads of a properly prepared bead slide are generally limited to just distal to the coverslip; however, it is possible for beads to be in solution or even to be attached to the slide surface of the slide. It is important that the user select beads that are just on the distal surface of the coverslip from the objective lens and not to focus on beads in the media or on the slide surface. High numerical aperture objective lenses are properly corrected for looking at objects placed just inside the coverslip. Any objects further into the slide (i.e., away from the objective lens) will be aberrated unless one either uses a lens with a correction collar or adjusts the refractive index of the immersion medium (see below). Once the proper focal plane is established, find an isolated bead that does not appear to have any beads adjacent to it. It is this object that we will now focus our attention upon.

The image of this bead is commonly referred to as the "Point Spread Function" or PSF. More correctly, the PSF is a point spread measurement in that it is a measurement of a physical phenomenon and not technically a function that describes that measurement; however, for simplicity and in keeping with tradition, we will refer to it as the PSF. For a good objective lens, the PSF should be highly symmetrical. Within the plane of focus, the PSF should appear as a point with some faint circles (airy disks) radiating from the central bright point (Fig. 15.1A). The rings should emanate from

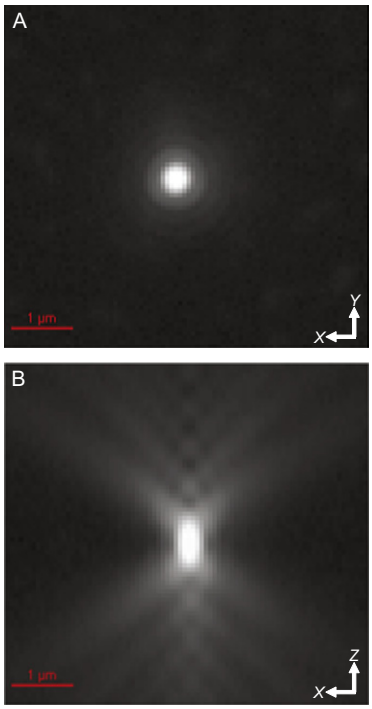

FIGURE 15.1

Ideal point spread function. Panel "A" is an *en face* view of a subdiffraction fluorescent bead through a 60×/1.42 PlanApo objective lens. Panel "B" is the same point spread function that has been digitally rotated 90° about the *X* axis in software. Notice that the axes are now *X* and *Z*. In both cases, the images are highly symmetrical laterally (A) and axially (B). These intensities in these images were squared to enhance the images for visualization.

the central bright point symmetrically; similar to the ripples from a pebble thrown into a still pond. As one focuses above or below the plane of best focus, these ripples (called rings) will change in intensity and phase, but the rings above and below the plane of best focus should diverge at the rate and be of the same magnitude. The rings should align with each other throughout focusing above and below the plane of best focus; that is, the center of the rings above, below, or in focus should all appear to arise from the same lateral position (Fig. 15.1B). A good PSF is the manifestation of all of the optical path lengths in the optical system being aligned. Under these ideal conditions, all of the rays of light that traverse through the optical system focus on the same points both laterally and axially (Fig. 15.2). Any divergence from this symmetry will most likely cause an aberration in the optical system. Each of these aberrations has a distinct source and descriptive term associated with it. These are described below.

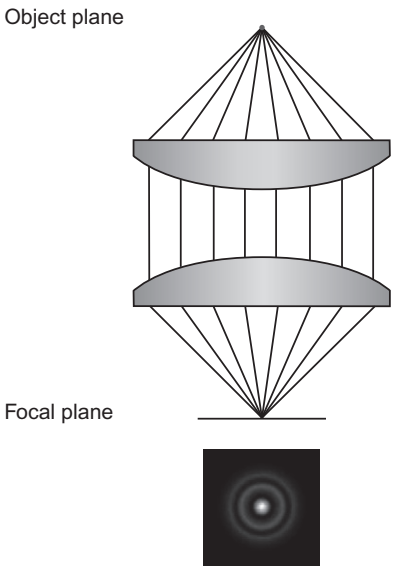

FIGURE 15.2

Ray path of a perfect lens. All rays in a perfect lens focus on the same point laterally and axially.

15.3 DISCUSSION

15.3.1 Monochromatic aberrations

15.3.1.1 Comatic aberration

Coma is an aberration that is typically seen at the edge of field-of-view (FOV). In a poor optical system, coma can even be seen in the middle of the FOV. In coma, there is a marked lack of radial symmetry, most easily seen when the object is slightly out of focus (Fig. 15.3). Coma is caused by rays that strike the lens elements in the optical path at oblique angles which is why it is most often a defect at the edge of the FOV. In lenses with comatic aberration, light from a point is projected through a lens such that rays that project through the lens at different angles focus onto different lateral positions in the focal plane (Fig. 15.4). Coma can be caused by tilted lenses or lens elements, by miscentration of lenses, or by smudges (such as finger prints) in the optical path. Coma can be caused by the sample if the cover glass is not orthogonal to the optical axis of the objective lens (see Arimoto and Murray, 2004).

15.3.1.2 Astigmatic aberration

Astigmatism is a common aberration of optical systems. Focusing an equal distance on the other side of the focal plane will exhibit elongation about the rotational axis orthogonal to the first elongation (Fig. 15.5). In astigmatism, the rays of light from objects that go through one axis of the lens do not focus on the same plane as objects

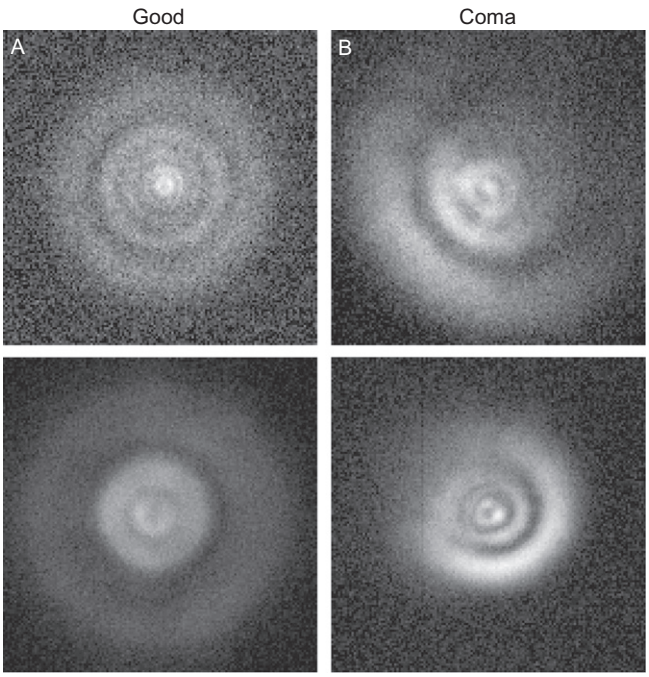

FIGURE 15.3

Coma. Column "A" shows examples of images from two different good lenses that do not exhibit coma. Column "B" shows examples of images from two different lenses that demonstrate moderate to significant coma. Notice the lack of radial symmetry in the diffraction rings in images from lenses that exhibit coma. In each case, the coma is easiest to see when the bead is defocused a few microns. These intensities in these images were squared to enhance the images for visualization.

with the orthogonal axis (Fig. 15.6). In the case of the PSF, in astigmatism, defocusing on one side of the plane of best focus will exhibit elongation in some rotational axis (e.g., horizontal). Astigmatism is most commonly caused by misalignment of the lens elements. Asigmatism will result when lens elements within the optical path are not centered on each other (i.e., their principle axes do not align) or when lenses are tilted relative to the principle optical axis.

15.3.1.3 Spherical aberration

Spherical aberration is the single most common optical defect in microscopy. Spherical aberration is marked by axial asymmetry. On one side of the plane of best focus, there will be sharp distinct diffraction rings. On the other side of the focus, the object will appear to extend for quite a distance and will not have distinct delineation (Fig. 15.7). Spherical aberration is caused when the rays of light that pass through the middle of the objective lens do not focus on the same plane as the rays that pass

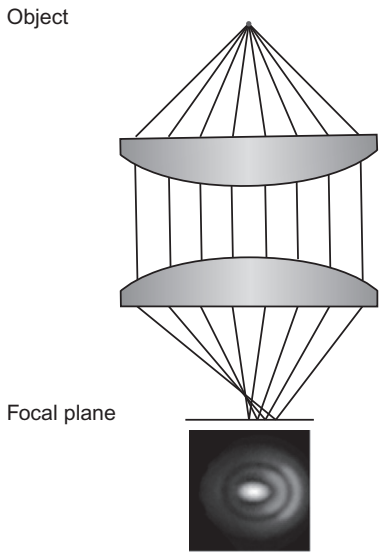

FIGURE 15.4

Coma ray trace. In a lens with coma, the rays from different parts of the lens focus on a different lateral position. This skews the airy disk and degrades resolution.

through the objective lens at the edge of the lens (Fig. 15.8). Spherical aberration is common because the sample contributes substantially to this aberration. Objective lens designs are optimized for observing samples through a cover glass and just on the surface of the cover glass that is distal from the objective lens. Without some form of correction, any other focal plane will be subject to spherical aberration. Since most biology takes place deeper into the sample than the surface of the cover glass, most images of biological samples have some degree of spherical aberration. For example, if one is looking into the middle of the nucleus of a mammalian cell, then they are looking 1–2 μm (or more) beyond the cover glass. Uncorrected, this distance is sufficient to significantly degrade the images and affect quantification. This effect can be easily seen in Fig. 15.9. In this figure, fluorescent microsphere beads are suspended in optical epoxy of constant refractive index. The beads are randomly distributed through a thickness of approximately 130 μm. As can be seen in the figure, spherical aberration is seen throughout the entire thickness except in a relatively narrow range of a few microns. For this illustration, high refractive index immersion oil was used to shift the ideal focus deeper on the sample (Hiraoka, Sedat, & Agard, 1990).

All of these aberrations, especially spherical aberration, substantially affect microscopy even when the microscopy is limited to a single focal plane because these aberrations severely degrade the contrast (signal-to-background) of the optical system.

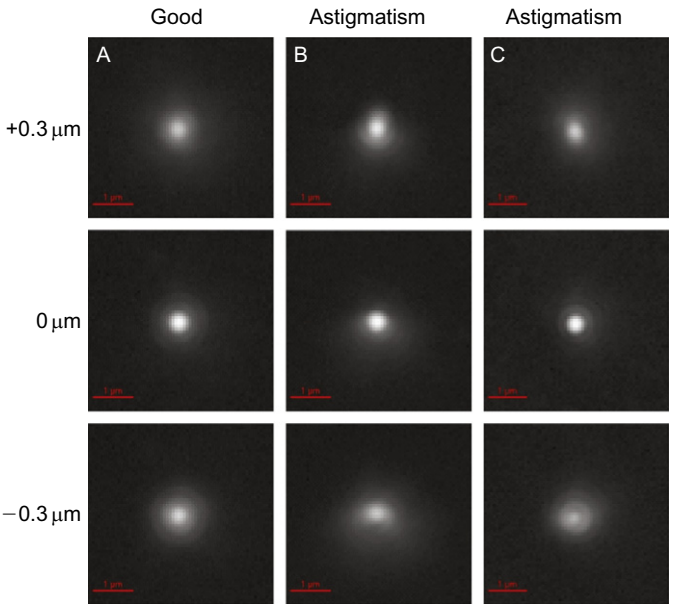

FIGURE 15.5

Astigmatism. Astigmatism is most easily seen above and below the plane of best focus. Column "A" shows a bead in focus as well as above and below that plane of best focus. Notice the symmetry of the bead above and below the plane of best focus. The images in columns "B" and "C" are from objective lenses with moderate astigmatism. Notice the apparent vertical elongation above and horizontal elongation below the plane of best focus. While the elongation due to astigmatism is not necessarily horizontal or vertical, the elongations are typically orthogonal above and below the plane of best focus. These intensities in these images were squared to enhance the images for visualization.

15.3.2 Polychromatic aberrations

Biology is multiparametric. Rarely does the scientist observe a single biomolecule without reference to other markers. Often, scientists prefer to combine multiple channels collected in parallel. This provides the opportunity to include in-sample controls and reference markers. Effectively, this is most often accomplished by observing multiple probes in the same sample (Brumbabugh, Schleifenbaum, Gasch, Sattler, & Schutlz, 2006; Scharer & Schutz, 2005; Schultz, Schleifenbaum, Goedhart, & Gadella, 2005). One of the simplest ways of accomplishing this is through judicious use of multiple wavelengths. For example, if one were to study the temporal localization of cyclins in mammalian cells, it is valuable to localize and visualize a given cyclin. It is much more informative to place that localization in context of important cell structures (such as the nucleus) and in relation to other cyclins. In a fixed

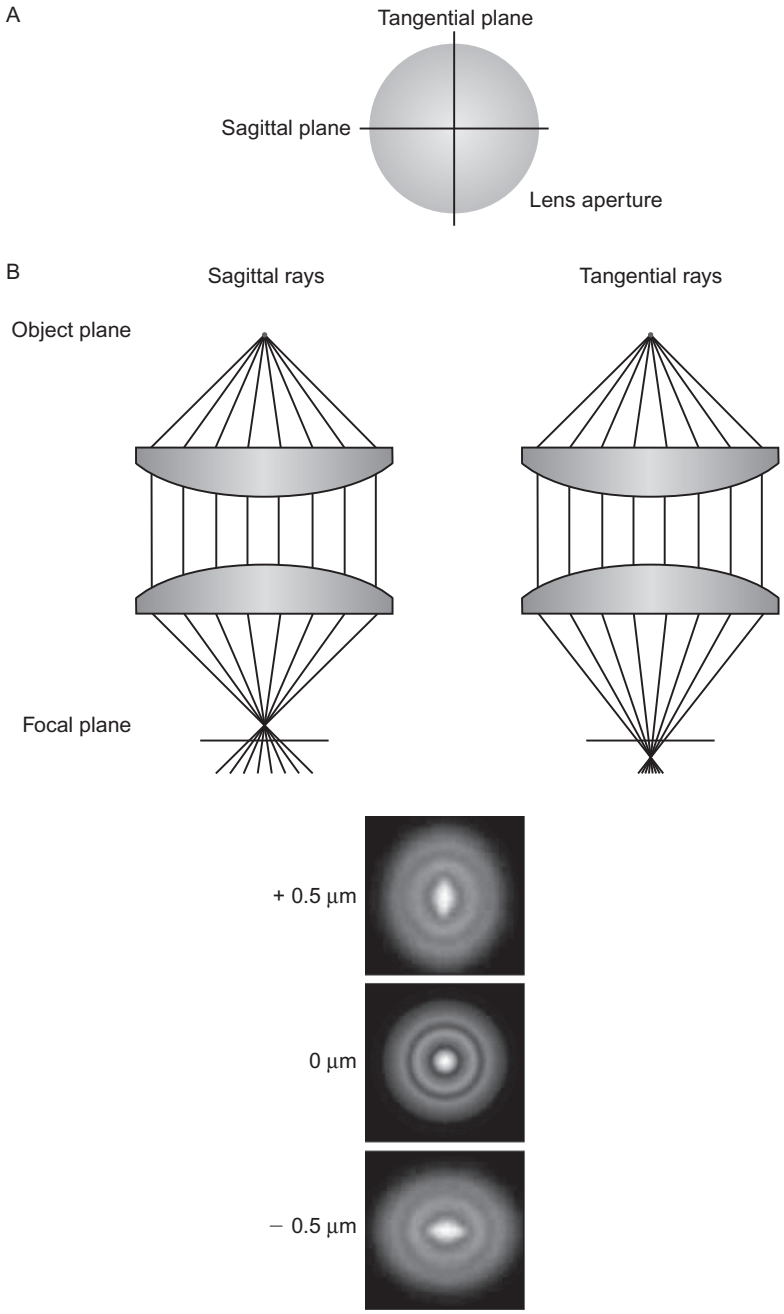

FIGURE 15.6

Ray path in astigmatism. In astigmatism, the rays that go through the lens along one plane (say the Sagittal plane) focus on a different focal plane than the rays that traverse the lens along a different, orthogonal plane (the Tangential plane). The interference of these rays causes elongation of the PSF that rotates 90° as one moves from the Sagittal to the Tangential focal plane.

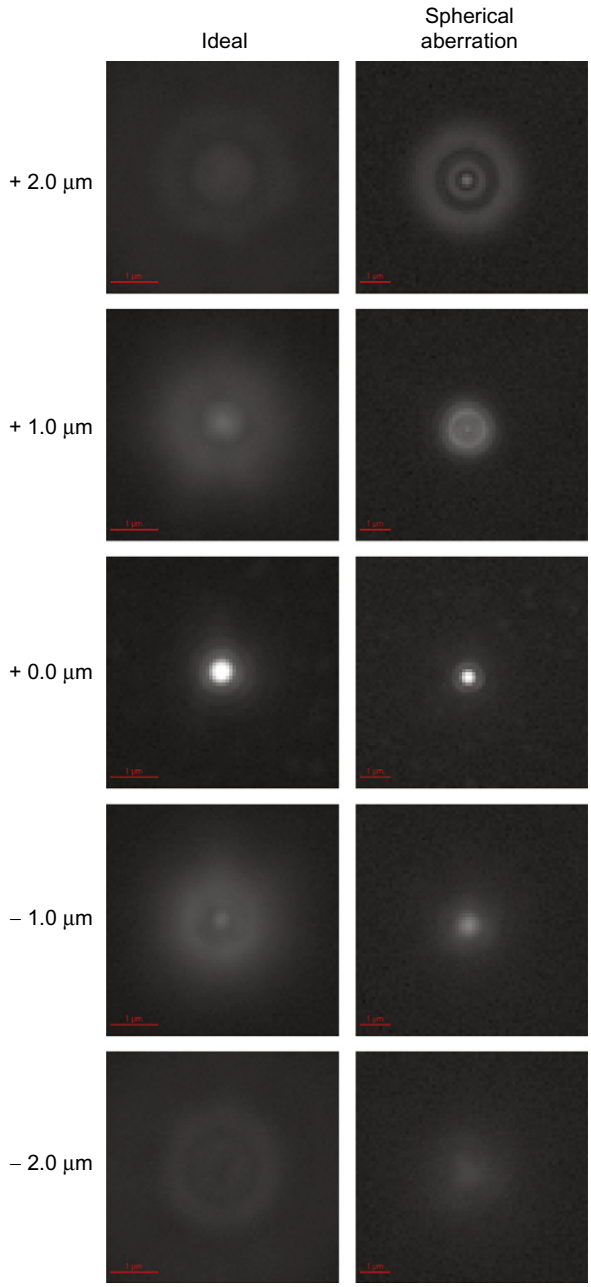

FIGURE 15.7

Spherical aberration. Spherical aberration is very common in all forms of microscopy. Spherical aberration is marked by asymmetrical defocus above and below the plane of best focus. In this example, notice in the "Ideal" lens how the object defocuses the same whether looking above or below the sample. With Spherical Aberration, there are sharp diffraction rings on one side of the focus and smearing in the opposite direction. These intensities in these images were squared to enhance the images for visualization.

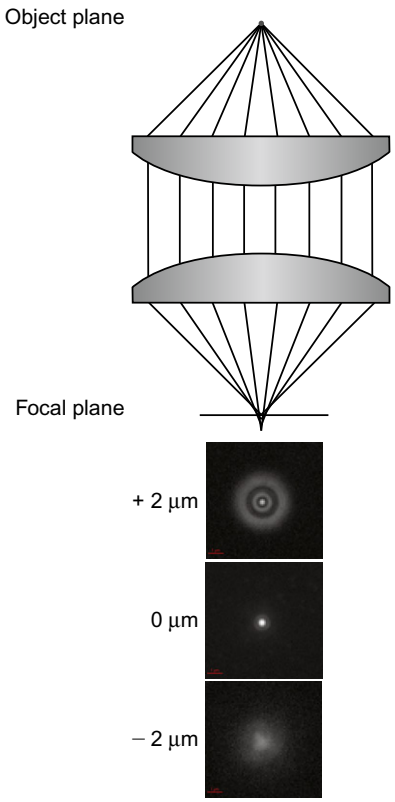

FIGURE 15.8

Ray path in spherical aberration. In spherical aberration, the rays from the lens focus on different depths. For example, rays from the center of the lens will focus on a different depth than the rays at the edges of the lens.

specimen, one may use DAPI to localize the nucleus, Alexa488-labeled antibodies to localize cyclin B, and Cyanine-3-labeled antibodies to localize cyclin E. If the optical system focuses the emission wavelengths of each of these probes to the same point in space, then localizing the relative positions of the probes is simple. If the wavelengths do not focus to the same point in space, there is chromatic aberration in the optical system, and accurately locating the relative positions of the probes is much more difficult. Chromatic aberrations may be either lateral or axial. Lateral chromatic aberrations are most often caused by alignment of the optical system, while axial chromatic aberrations are most often caused by either the design of the optical system or are the result of the monochromatic aberrations discussed in the previous section.

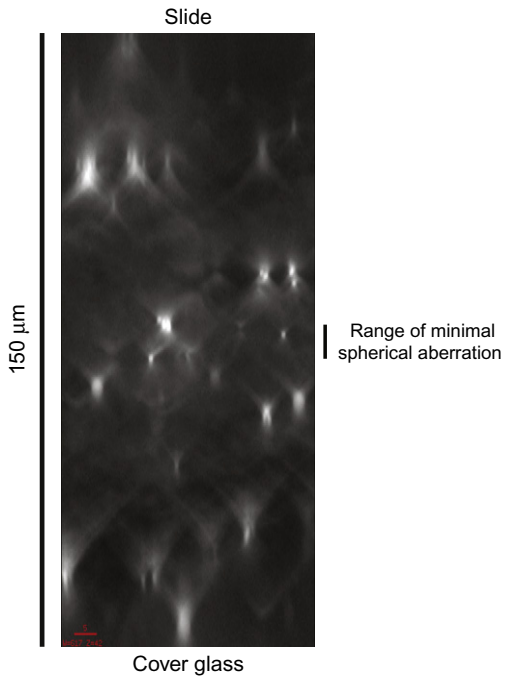

FIGURE 15.9

Spherical aberration as a function of focal depth. Microsphere beads embedded in optical epoxy with i.r. = 1.518. High refractive index immersion oil (1.530) was used to refocus the objective lens approximately 75 µm into the 150-µm specimen thickness. These intensities in these images were squared to enhance the images for visualization.

Lateral chromatic aberrations are rarely seen in properly designed optical system. In part, this is because these aberrations are fairly obvious even when observing histological sections with bright field. They can be seen in damaged or poorly made objective lenses but this is rare in modern research microscope. One common source of lateral aberrations is improper alignment of the optical system. Most of these can be corrected by properly aligning the microscope and detector. Lateral aberrations may be introduced by optical filters that can reside in the convergent light path between the tube lens and the detector. While locating filters into this portion of the light path is not always ideal, it is often the only alternative if one wishes to be able to automate the emission filters in the system. Placing these filters into the infinity space between the objective lens and the tube lens can constrain filter change speeds since any vibrations and misalignments in this space can degrade the image. Placing the emission filter in the convergent space greatly simplifies the mechanical design, but it can introduce chromatic aberrations if the filters are not the same thickness or if the filters are not orthogonal to the light path.

Axial chromatic aberration is a much more common aberration. Fundamentally, the shape of the lens elements within the microscope is such that the natural tendency is to refract light like a prism. Considerable care and effort go into the design of microscope optics to minimize these effects. Optical designers use exotic materials and optical coatings to minimize these effects, and lenses with optimal corrections (apochromatic lenses) are more expensive than lenses with fewer of these corrections (chromatic lenses). However, no matter how complex the optical design, it cannot fully account for the last elements in the optical path, that is, the sample. The immersion oil, the cover glass, and the medium bathing the sample all affect the axial chromatic aberrations. Dispersion is an optics term that describes the spectral separation of light through a medium. All of these last optical elements associated with the sample preparation can severely affect axial chromatic aberrations. In particular, the typical optical design is such that the sample is assumed to be sitting literally on the cover glass on the side opposite to the objective lens. As mentioned above, most of biology does not occur on the cover glass but is deeper into the sample. Thus, there is additional dispersion introduced into the optical system by the sample. Additionally, any of the monochromatic aberrations discussed in the above section will also introduce chromatic aberrations.

One final source of axial chromatic aberrations is rarely discussed, but the effect can be quite dramatic. When designing the microscope optics, assumptions are made as to refractive index of the air that surrounds the microscope. Anything that changes the refractive index of the air around the optics will worsen the axial chromatic aberration. The refractive index of the air is sensitive to its density so changes in temperature, humidity, and even air pressure can exacerbate these aberrations; thus, it is very important to carefully control the microscope environment to minimize these effects.

Even in a "fully" corrected optical system, there is some residual axial chromatic aberration. While it is possible for the designers to make these aberrations minimal, the microscopist is rarely willing to pay the costs associated with these highly corrected lenses. Furthermore, as discussed above, even if the microscope is fully corrected, the sample and environmental effects, if not controlled, will degrade even "perfect" microscope designs.

15.3.3 Determining the source of aberrations

As discussed in detail above, the aberrations discussed in this chapter can be in the optical design, the manufacture and alignment of the microscope, or in the sample preparation itself. Knowing the source of the aberrations is essential for eliminating them. For example, if the sample is responsible for the aberration, it is senseless to replace the microscope. How does one determine the source of the aberration? Fortunately, this is usually not terribly difficult. The aberrations will track the element which causes them. For example, if it is the sample, then the aberration will track with the sample, if it is the objective lens, it will track with the objective lens, etc.

When an aberration is detected, the first step is to examine the sample and the optics for any debris or hubris stuck to the surfaces. Common sources of such debris

include fingerprints, residual oil, dust, salts, and proteins. Such debris can be anywhere in the optical train including optical windows in the microscope and back apertures of objective lenses. If the debris or shadow of the debris can be seen through the eyepieces on the detector, then the debris must be close to a conjugate plane within the optical system; such as, on the cover glass, on the eyepieces, on the camera window, etc. Before placing a sample on the microscope, one should be sure to clean the sample of all debris, especially the cover glass. If the sample has previously been examined on a microscope, especially that of a different manufacture or from a different laboratory, all immersion oil should be removed from the cover glass. This can be done using a clean organic solvent and cotton-tipped swabs. One common choice for solvent is high-quality chloroform, but this should only be done in a very well-ventilated room or a fume hood as chloroform is hepatotoxic. Other choices include ether, absolute ethanol, and acetone. Some facilities will use commercial glass cleaners. Each of these choices has their own risks and benefits, but this is beyond the scope of this chapter.

The front and rear lens elements of objective lenses should be thoroughly cleaned. The objective lens should be examined for oil leaking into the lens. Dust should be removed from all windows and surfaces and the microscope should be covered when not in use. All of these steps will improve the performance of the microscope.

To isolate the source of aberrations, one can follow a simple triage plan. Examine the sample first. Carefully observe the nature of the aberration and especially any directionality to the asymmetries. Next, rotate the sample 180° in the sample holder. Did the aberration rotate with the sample or is it the same as before? Next, suspect the front surface of the objective lens. Clean the lens and reexamine the sample for aberrations. Next, loosen the lens in the objective turret and rotate the lens some noticeable amount (say 90°). Does the aberration rotate with the objective lens? If so, remove the lens and check that the rear lens is free of debris. Clean if necessary and repeat. If the aberration is not in the lens or the sample, then it must be in the stand or the detector. Follow the steps of move the element, check for aberration, fix if possible, retest, etc. until the aberration is isolated and corrected. If none of this works, then it may become necessary to call the manufacture of the microscope and ask for a service visit. Be sure to be prepared to discuss all steps that you have taken to isolate the source of the aberration.

15.3.4 A word regarding mounting media

There is one more source of aberration and poor imaging that is very common. While technically this is not an optical aberration, it has such a dramatic effect on microscopy that it is remiss to not broach it. This issue mostly affects fixed samples that are mounted under a cover glass. Individuals will spend hundreds of thousands of dollars on equipment. They will spend hundreds of man-hours and thousands of dollars on preparing antibodies and samples. Then in an effort to save a few minutes of time, they will reach for a premixed mounting medium. This is especially true in the case of mounting media that polymerize or gel. If the mounting medium is not

homogeneous in its optical properties, the media itself will act as thousands of microlenses and will scatter the light from sample. The net effect is to severely degrade the signal and to amplify the background of the image. These heterogeneities are most often caused by two sources. Many users make their own mounting media, often with antifade agents in them (such as DABCO, *n*-propyl-galate, etc.). These are most often made in buffered glycerol which is a good idea. Since buffered glycerol will not harden or gel, their direct use requires sealing the cover glass to slide interface to prevent the cover glass from moving. Often this is done with either fingernail polish or with a waxy seal such as VAYLAP. To avoid having to seal the slide, many scientists have taken to either adding a gel to the glycerol such as polyvinyl alcohol (PVA). The problem with PVA is that it does not homogeneously disperse throughout the buffered glycerol. This leaves clumps of PVA much like microscopic tapioca. Each of these clumps scatters light and degrades contrast as mentioned above.

An alternative often taken by scientists is to use a premixed mounting medium that hardens. Many of these are commercially available. These media are often nonmiscible with water. Since fully drying a specimen used for fluorescence often creates autofluorescence, scientists should avoid drying samples for fluorescence microscopy completely. When they add these nonmiscible mounting media to their prepared fluorescence samples, tiny bubbles of water form within the mounting media. Since water and the mounting media have different refractive indices, the loss of contrast is created. Many users further exacerbate the problem by purchasing mounting media that have nuclear stain (such as DAPI) premixed into the mounting medium. DAPI is fluorescent whether or not it is bound to DNA (though brighter when bound). With the concentration of DAPI in these premixed solutions, background fluorescence will almost always increase.

SUMMARY

The optical performance that we have come to expect exists only under ideal conditions. These conditions include the obvious optical components such as lenses and microscopy systems. Microscopists are remiss if they do not consider the less obvious optical components such as the sample and the environment. It is only in carefully testing and improving the entire optical train that the ideal imaging that the user seeks can be obtained.

Acknowledgments

The author would like to thank John Murray, University of Indiana, Bloomington for the embedded bead sample used in Fig. 15.9. The author is employed by GE Healthcare, Issaquah, Washington, USA and has financial interest in the company.

References

Arimoto, R., & Murray, J. M. (2004). A common aberration with water-immersion objective lenses. *Journal of Microscopy*, *216*(1), 49–51.

Brumbabugh, J., Schleifenbaum, A., Gasch, A., Sattler, M., & Schutlz, C. (2006). A dual parameter FRET probe for measuring PKC and PKA activity in living cells. *Journal of the American Chemical Society*, *128*(1), 24–25.

Gustafsson, M. G., Agard, D. A., & Sedat, J. W. (1999). I5M: 3D widefield light microscopy with better than 100 nm resolution. *Journal of Microscopy*, *195*(Pt 1), 10–16.

Hiraoka, Y., Sedat, J. W., & Agard, D. A. (1990). Determination of three-dimensional imaging properties of a light microscope system. Partioa confocal behavior in epifluorescence microscopy. *Biophysical Journal*, *57*(2), 325–333.

Scharer, O., & Schutz, C. (2005). Closing the gap between chemistry and biology. *ChemBioChem*, *6*(1), 3–5.

Schultz, C., Schleifenbaum, A., Goedhart, J., & Gadella, T. W., Jr. (2005). Multiparameter imaging for the analysis of intracellular signalling. *ChemBioChem*, *6*(8), 1323–1330.

CHAPTER

16 Ratio Imaging: Practical Considerations for Measuring Intracellular Ca^{2+} and pH in Living Cells

Nathan O'Connor and Randi B. Silver

Department of Physiology and Biophysics, Weill Medical College of Cornell University, New York, New York, USA

CHAPTER OUTLINE

Introduction **388**
16.1 Why Ratio Imaging? **388**
16.2 Properties of the Indicators BCECF and Fura-2 ..... **389**
16.2.1 Structure and Spectral Characteristics 389
16.2.2 Incorporation Into Intact Living Cells 392
16.2.3 Signal to Background 395
16.2.4 Possible Problems 395
16.3 Calibration of the Fluorescence Signal **396**
16.4 Components of An Imaging Workstation **401**
16.5 Experimental Chamber and Perfusion System: A Simple Approach **403**
Conclusion **405**
Acknowledgments **405**
References **405**

Abstract

This chapter discusses the use of ratiometric fluorescent probes for measuring intracellular pH (pH_i) and Ca_i^{2+} concentration at the single cell level. The development of sensitive and stable probes for monitoring pH_i and Ca_i^{2+} in living cells has provided the scientists with invaluable tools for studying a multitude of cellular processes. These probes afford a noninvasive and semiquantitative assessment of pH_i and Ca_i^{2+}, eliminating the need to impale cells with microelectrodes. The development and availability of membrane permeant Ca_i^{2+}- and pH-specific fluorescent probes coupled to major advances in the technology and design of low-light-level

Methods in Cell Biology, Volume 114 **ISSN 0091-679X**
Copyright © 2007 Elsevier Inc. All rights reserved.
http://dx.doi.org/10.1016/B978-0-12-407761-4.00016-6

charge-coupled devices geared toward biological applications, and improved microscope optics, have made it possible to visualize a two-dimensional fluorescence signal that is related to Ca_i^{2+} and pH_i. The chapter describes the basis for using dual excitation ratio imaging and tries to provide a framework for understanding and developing the technique for investigating the roles of Ca_i^{2+} and pH_i in cellular processes. The technique of quantitative ratio imaging for the measurement of pH_i and Ca_i^{2+} has revolutionized the field of cell physiology. Using the proper equipment and choosing the right dyes for the experimental needs should provide reliable and reproducible results. More importantly, the amount of data produced from each experiment, when analyzing pH_i and Ca_i^{2+} on an individual cell basis, yields valuable information on the heterogeneity of cellular responses.

INTRODUCTION

The development of sensitive and stable probes for monitoring intracellular pH (pH_i) and calcium (Ca_i^{2+}) in living cells has provided scientists with invaluable tools for studying a multitude of cellular processes. This chapter focuses on the use of ratiometric fluorescent probes for measuring pH_i and Ca_i^{2+} concentration at the single cell level. These probes afford a noninvasive and semi-quantitative assessment of pH_i and Ca_i^{2+}, eliminating the need to impale cells with microelectrodes. The development and availability of membrane permeant Ca^{2+}- and H^+-specific fluorescent probes coupled to major advances in the technology and design of low-light-level charge-coupled devices (CCDs) geared toward biological applications, and improved microscope optics, have made it possible to visualize a two-dimensional fluorescence signal that is related to Ca_i^{2+} and pH_i. This chapter describes the basis for using dual excitation ratio imaging and tries to provide a framework for understanding and developing the technique for investigating the roles of Ca_i^{2+} and pH_i in cellular processes.

16.1 WHY RATIO IMAGING?

The fluorescence emission of a probe may be influenced by a variety of factors. The uncertainties associated with quantitating single-wavelength fluorescence emission are apparent from the standard fluorescence equation:

$$F = f(\theta)g(\lambda)\Phi_F I_0 \varepsilon b c$$

where fluorescence emission of the probe (F) is related to a geometric factor [$f(\theta)$], the quantum efficiency of the detector [$g(\lambda)$], fluorescence quantum yield of the probe [Φ_F], excitation intensity [I_0], extinction coefficient of the probe [ε], optical pathlength [b], and fluorophore concentration [c] (Bright, Fisher, Rogowska, & Taylor, 1989). Fluorescence emission of a probe can also be influenced by cellular factors, like uneven loading of the dye or compartmentalization of the probe in intracellular organelles (Heiple & Taylor, 1981), as well as instrumentation noise, sample geometry, and intrinsic properties of the probe itself (Bright et al., 1989). These factors can all lead to difficulties in interpreting changes in a single-wavelength fluorescent probe.

These limitations have been overcome through the development of dual-wavelength fluorescent probes. Dual-wavelength indicators have a high affinity for binding their parameter of interest, like Ca^{2+} or H^+, and which contain fluorophores that fluoresce when the molecule is bound and unbound, but at two nonoverlapping wavelengths. The total fluorescence emitted from the probe represents two independent fluorescent forms of the dye originating from the same volume. The changes in fluorescence intensity of bound and unbound dye can be in the probe's excitation or emission spectrum. For the pH_i and Ca_i^{2+} probes discussed in this chapter, the fluorophore on the dye molecule shifts its excitation absorbance depending on whether the probe is bound or unbound to either H^+ or Ca^{2+}, so that the fluorescence emitted from these two excitation wavelengths represents the total fluorescence of the probe in the cytosol. The fluorescence measurements obtained with dual-wavelength probes are independent of both pathlength and intracellular dye concentration (Heiple & Taylor, 1981). It is this principle which underlies the efficacy of two widely used dual excitation ratiometric indicators form measuring pH_i and Ca_i^{2+}. Both 2′,7′-bis (carboxyethyl)-5(6)-carboxyfluorescein (BCECF) and Fura-2 shift their wavelength distribution of fluorescence excitation on binding H^+ and Ca^{2+}, respectively. Understanding the use of these two intracellular fluorescent dyes for understanding the roles of pH_i and Ca_i^{2+} in various cellular processes is the focus of this chapter.

16.2 PROPERTIES OF THE INDICATORS BCECF AND FURA-2

16.2.1 Structure and spectral characteristics

Figure 16.1 shows the chemical structures of BCECF and Fura-2. BCECF is a derivative of fluorescein with three additional carboxylate groups; two are attached by short alkyl chains, which raises the pK from 6.4 (for fluorescein) to a more physiological pK of 7.0 (Millard, Ryan, Webb, & Fewtrell, 1989). Fura-2, developed from the Ca chelator BAPTA, is the double aromatic analogue of EGTA with added fluorophores (Cobbold & Rink, 1987). Compared to its predecessor quin2, Fura-2 is a larger fluorophore with a much greater extinction coefficient and a higher quantum efficiency translating to 30-fold higher brightness per molecule (Cobbold & Rink, 1987). As shown in Fig. 16.1, both dyes are penta-anions and therefore hydrophilic and membrane impermeable in this form. The chemical structures of these dyes had to be modified to render them membrane permeable. Making these molecules neutral was accomplished by masking the negative charges on the structures with acetoxymethyl (AM) esters as shown at the right of Fig. 16.1 (BCECF/AM and Fura-2/AM). The loading of the neutral AM forms of the dyes into cells is discussed in more detail in Section 16.2.2.

As discussed above, a fundamental requirement of an indicator for quantitative ratio imaging is a differential sensitivity to its ligand at a specific wavelength relative to another wavelength. The measured fluorescence signal at these two wavelengths would then result in a ratio of fluorescence intensity reflecting the relative proportion of the bound and unbound forms of the indicator originating from the same volume. The excitation spectra in the following figures illustrate the wavelength specificity of BCECF for pH (Fig. 16.2) and Fura-2 for Ca^{2+} (Fig. 16.3).

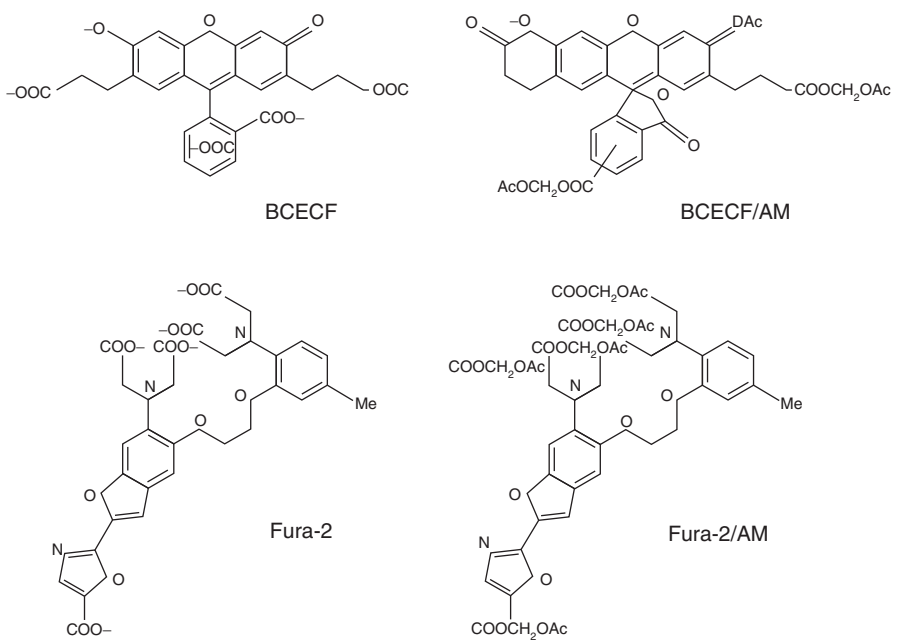

FIGURE 16.1

Chemical structures of BCECF and Fura-2. The free-acid and membrane-permeant forms of each dye are represented in the figure. Reprinted by kind permission from Molecular Probes, Inc. from the Handbook of Fluorescent Probes and Research Products, 9th Edition.

Excitation spectra of BCECF at various pH are shown in Fig. 16.2. To generate these curves, the free acid form of BCECF (2 μM) was added to aliquots of balanced HEPES-buffered salt solutions titrated to a known pH. The pH values of the samples ranged from 6.6–7.8. The BCECF in each sample of solution was excited by scanning the monochromater in the fluorimeter from 400–500 nm as shown on the abscissa. The corresponding emitted fluorescence intensity for each wavelength, collected at 520 nm, is shown on the ordinate. Figure 16.2 shows that between 490- and 500 nm, BCECF displays strong pH sensitivity. At these wavelengths the fluorescence intensity of BCECF increases as the pH of the solution becomes more alkaline. In contrast, at lower excitation wavelengths the fluorescence emitted from BCECF is pH independent. Therefore, in a given volume, alternately exciting the BCECF molecules at a pH sensitive wavelength with a pH insensitive wavelength yields the relationship of the changes in BCECF fluorescence signal at each wavelength with respect to the other. In Fig. 16.2, for example, the ratio of the emission intensity at 490 nm excitation, the pH-dependent wavelength, to the emission intensity at 440 nm excitation, the pH-independent wavelength, increases as pH becomes more alkaline and decreases as pH becomes more acidic.

The spectral characteristics of Fura-2 are shown in Fig. 16.3. Fura-2, developed by Grynkiewicz, Poenie, & Tsien, 1985, exhibits properties that make it ideal for ratio imaging. These properties are illustrated by the spectra in Fig. 16.3, showing

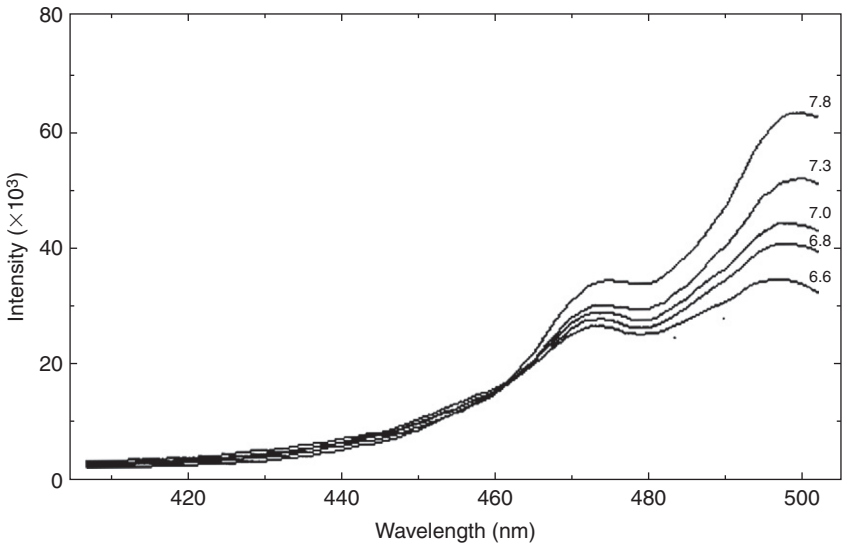

FIGURE 16.2

Excitation spectra of 2 μM BCECF at various pHs. The salt solution contained 130 mM KCl, 1 mM $MgCl_2$, 2 mM glucose, 2 mM $CaCl_2$, and 25 mM HEPES. The spectra (emission: 520 nm) were generated with a fluorimeter (Photon Technology Incorporated-Deltascan) scanning at 1-nm intervals and interfaced to an inverted microscope (Zeiss IM35) equipped with a Hamamatsu photomultiplier tube. Individual dishes placed on the stage of the microscope and aligned in the epifluorescent light path contained 250 μl of HEPES-buffered salt solution with 2 μM BCECF at the pHs indicated. The spectra have not been corrected for background noise. The peaks at 470 nm are due to xenon lamp output.

the shape of the excitation spectrum and the large dynamic range of the dye in a range of solutions containing varying concentrations of free Ca^{2+}. For Fura-2, the fluorescence intensity at 340-nm excitation is directly proportional and at 380-nm excitation inversely proportional to the free Ca^{2+} concentration. The ratio of the emitted intensities at 340- and 380-nm excitations can be used to determine the concentration of ionized Ca^{2+} in a given volume.

The BCECF and Fura-2 spectra demonstrate that these probes possess properties that make them prime candidates for dual excitation ratio imaging. From the BCECF and Fura-2 spectra, it should be apparent that by choosing the appropriate excitation wavelengths it is possible to have adequate emitted fluorescence intensity to generate a ratio of the fluorescent species of the dye bound and unbound in a given volume. Thus with both BCECF and Fura-2, a fundamental requirement for ratio imaging is met.

Going back to the standard fluorescence equation presented in Section 16.1, we are reminded of the many factors with the potential to influence the fluorescence signal without relation to actual changes in the parameter of interest. With dual-wavelength fluorescent probes, like Fura-2 and BCECF, interference from these factors is minimized. This principle is illustrated in Fig. 16.4 which shows the effect of

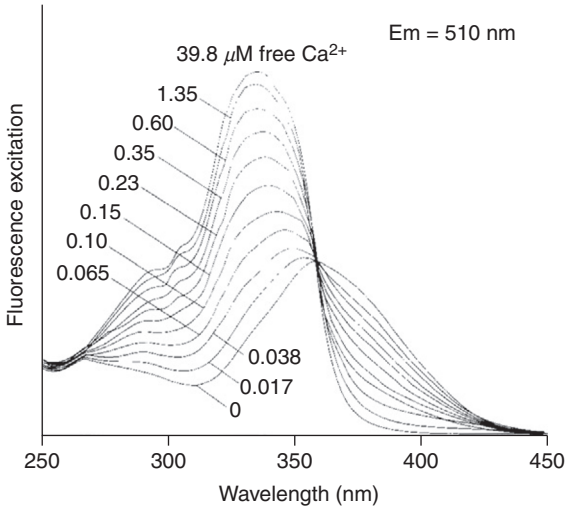

FIGURE 16.3

Excitation spectra of Fura-2 in a range of solutions containing 0–39.8 μM free Ca. Emission is at 510 nm. Reprinted by kind permission from Molecular Probes, Inc. from the Handbook of Fluorescent Probes and Research Products, 9th Edition.

changing the optical pathlength on the BCECF fluorescence signals. For this maneuver, BCECF free acid was dissolved in physiologically balanced salt solution buffered to a pH of 7.4. An aliquot of this solution was placed on a cover glass on the stage of an inverted epifluorescence microscope interfaced to an imaging system outfitted with the appropriate excitation and emission filters. The top panel of Fig. 16.4 shows the emitted BCECF fluorescence intensity from the 490- and 440-nm excitation wavelengths and the bottom panel is the ratio of the corresponding 490- and 440 nm signals. At the arrow, the focus or optical pathlength was changed. As shown in the top panel, both the 490- and 440 nm excitation fluorescence signals originating from the same volume decreased proportionately in response to the change in the focus. The corresponding 490/440 ratio remained constant as shown in the bottom panel. The changes in the fluorescence intensities were due to a mechanical factor, a change in the microscope focus. This simple example illustrates how factors other than the parameter of interest can affect fluorescence emission of a probe, but with dual-wavelength probes some of this interference can be minimized. It is also important to understand how a dye responds at its activated wavelength with respect to binding its parameter of interest. If the fluorescence intensity changes in a direction opposite from what is expected there may be interference from an unrelated factor.

16.2.2 Incorporation into intact living cells

As discussed in Section 16.2.1, the active forms of Fura-2 and BCECF are charged and not membrane permeable. The charged anionic forms of Fura-2 and BCECF can only be introduced into a cell with microinjection. To overcome the issue of

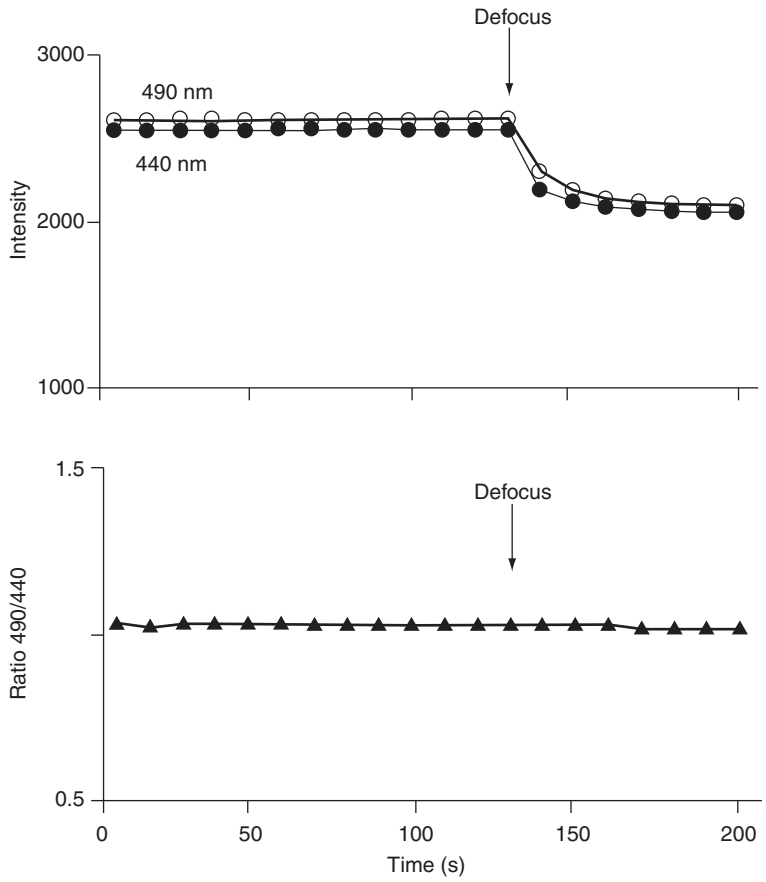

FIGURE 16.4

The effect of changing focus on the fluorescent signal from BCECF. A dish containing 2 μM BCECF free acid in 250 μl salt solution was placed on the stage of an inverted microscope. The top graph shows the individual traces for the emitted fluorescence excitation intensities at 490 nm (open circles) and 440 nm (closed circles) and the bottom graph is the ratio of 490/440. The focus was changed at the arrow. As shown in the top graph, both the 490- and 440 nm signals decreased with the change in focus; however, the 490/440 ratio remained the same.

membrane permeability, permeant, neutral forms of BCECF and Fura-2 were synthesized. This was a major accomplishment in dye chemistry for it permits diffusive entry of these dyes into cells (Cobbold & Rink, 1987). The membrane permeable analogues of BCECF and Fura-2 were created by replacing the negatively charged carboxylate groups of the molecule with neutral AM esters (Fig. 16.1) (Thomas, Buchsbaum, Zimniak, & Racker, 1979). In this formulation, the dye can diffuse across the cell without disruption of the cell membrane. Once the lipophilic form of the dye gets into the cytoplasm, esterases cleave off the hydrolyzable AM esters leaving the anionic form of the dye trapped inside the cell and free to bind its ligand

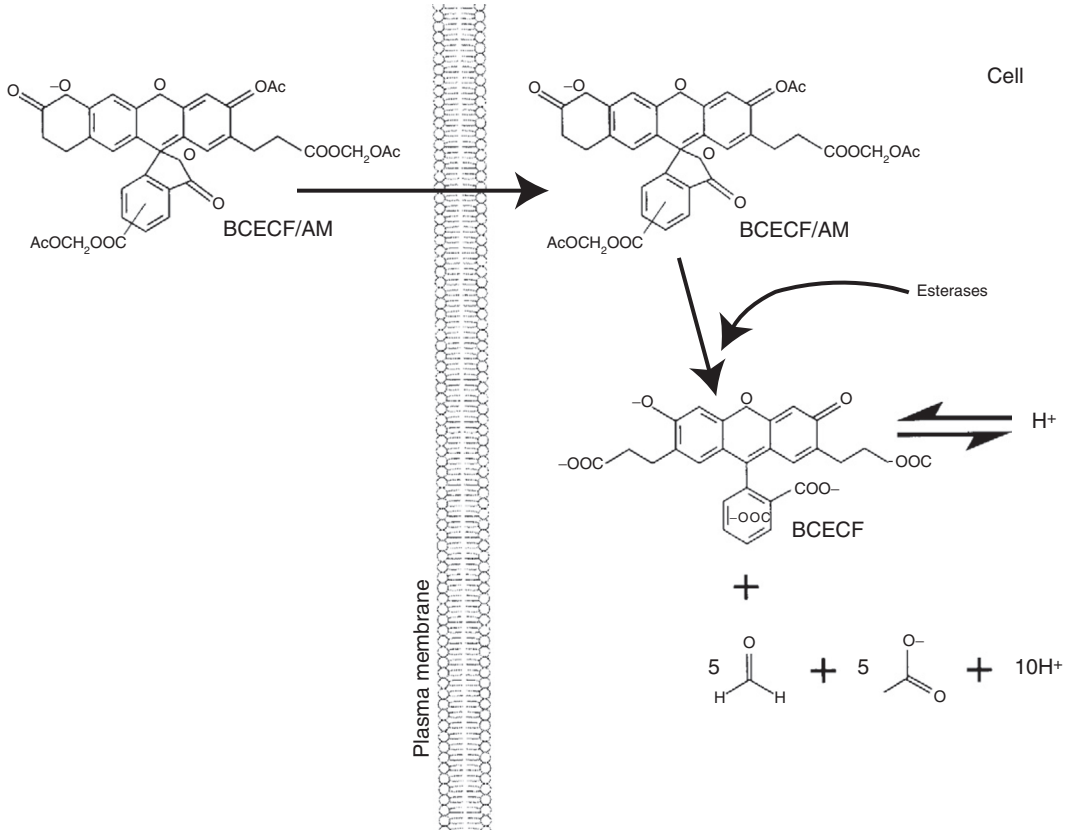

FIGURE 16.5

Schematic of BCECF/AM entering a cell and undergoing hydrolysis. The neutral molecule of BCECF is membrane permeable and readily diffuses into a cell. Once in the cytosol, endogenous esterases cleave the AM esters from the molecule leaving the polyanion trapped inside the cell where it will combine with the free H^+. A similar strategy applies for Fura-2. The chemical reaction depicted in the figure shows that for every BCECF/AM molecule hydrolyzed to its penta-anionic free acid, 5 molecules of formaldehyde, 5 molecules of acetate, and 10 protons are formed.

(i.e., H^+ or Ca^{2+}). This strategy is illustrated for BCECF in Fig. 16.5. Note that for every molecule of BCECF hydrolyzed in the cytosol, 5 molecules of formaldehyde, 5 molecules of acetate, and 10 protons are formed.

16.2.3 Signal to background

The loading concentration of the dye and the amount of time the cells need to be loaded will vary from cell type to cell type and need to be determined empirically. A good starting point is to expose cells to micromolar concentration of the AM form of the dye dissolved in medium or balanced salt solution, for about 60 min at room temperature. Once the extracellular dye is washed away, the loaded cells are ready to be used. The cells should be maintained in buffered salt solutions without phenol, amino acids, and vitamins because these components can fluoresce at wavelengths used to excite Fura-2, thereby interfering with the Fura-2 signal. As a rule the emitted fluorescence intensity of a probe should be at least two to three times greater than background signal. Tissue or cell autofluorescence should be measured prior to dye loading, with the imaging system configured exactly the way it will be used for the experiment. Optimal conditions for yielding a good fluorescence signal from cells will come from balancing loading of the dye into the cells with the appropriate combination of neutral density filters and excitation exposure time. It is important that the cells are not overloaded with the dyes for this can result in toxic accumulation of the end products of hydrolysis described above and buffering of steady-state Ca_i^{2+} and pH_i. At the beginning of an experiment, the pH_i and Ca_i^{2+} values measured with BCECF and Fura-2 should be representative of a resting, unperturbed state. When analyzing the experimental data, the background and autofluorescence should be subtracted from each excitation wavelength before determining the final ratio.

16.2.4 Possible problems

It has been reported in some tissues that hydrolysis of Fura-2/AM may be incomplete leaving partially cleaved forms of the dye which fluoresce at 380 nm (Thomas et al., 1979). Overloading cells with indicator may also lead to excessive compartmentalization of the dye in intracellular organelles, so that the emitted fluorescence may not adequately reflect a contribution of all of the intracellular compartments, which include the cytosol and the organelles (Thomas et al., 1979). Another potential problem to be aware of, if the cells are poorly loaded, is the possibility that hydrolyzed dye is transported out of the cell. It has been shown in certain cell types that once the AM form of the dye is cleaved into a penta-anion by intracellular esterases, it can be extruded from the cell by anion transporters in the plasma membrane. This movement of dye out of the cell can be inhibited by blocking the anion transporter with probenecid (Cardone et al., 1996; Di Virgilio, Steinberg, & Silverstein, 1990; Di Virgilio, Steinberg, Swanson, & Silverstein, 1988; Lakowicz, 1986).

16.3 CALIBRATION OF THE FLUORESCENCE SIGNAL

In order to assign a numerical value to the experimentally determined ratios it is necessary to calibrate the fluorescence signal. The easiest but most unreliable method for determining the pH_i and Ca_i^{2+} is by generating calibration curves on solutions that are titrated to known pH and $[Ca^{2+}]$ values to which the free acid form of the dye is added. Kits are commercially available for this purpose. The experimentally determined ratios generated on living cells are then extrapolated to fit these curves and the free H^+ and Ca^{2+} concentration can be generated. An underlying assumption of this technique is that the indicator acts in a similar fashion in salt solutions and cytoplasm, which may not be valid. This protocol often requires the use of viscosity correction factors to account for the difference in behavior of the dye inside the cell versus an external solution (Thomas et al., 1979).

A preferable method for calibrating the behavior of the dye inside the cell is to "clamp" the pH_i and Ca_i^{2+} to known values and measure the dye intensity at the corresponding wavelengths. Ideally, this clamp is performed at the end of each experiment on the field of cells. Specific ionophores or carriers are incorporated into the plasma membrane of the cells allowing one to set the Ca_i^{2+} or pH_i to known values. Equilibrium between the external solution and internal environment of the cell is assumed. The corresponding fluorescence signals from the two excitation wavelengths at these known values are then used to calibrate the experimentally determined ratios.

One commonly used technique for calibrating BCECF in cells is the high potassium/nigericin clamp protocol of Silver et al., 2002. With this protocol, pH_i is set to known values at the end of an experiment by exposing the cells to the K^+/H^+ antiporter, nigericin, in the presence of potassium solutions titrated to known pH. With the nigericin present, K^+ and H^+ gradients across the cell membrane are collapsed so that $[K]_i/[K]_o$ is equal to $[H]_i/[H]_o$. BCECF, with a pK $\sim$ 7.0, changes its fluorescence intensity at 490 nm proportionally between pH 6.4 and pH 7.8. Clamping pH_i/pH_o in the experimental cells with nigericin to values between 6.4 and 7.8 yields a linear relationship. The slope and *y* intercept of this relationship are then used to convert the experimentally determined ratios to pH_i values. Figure 16.6 shows how this calibration technique is done. Figure 16.6A–C show intensity-modulated display (IMD) colored ratiometric images of a field of BCECF-loaded cells excited at 490 nm and 440 nm at three different time points during an experiment. The IMD colors range from red (alkaline) to blue (acid). Figure 16.6A shows the 490/440 fluorescence in a field of cells at the beginning of the experiment and represents basal pH_i values. Figure 16.6B and C were generated at the end of the experiment during the nigericin clamp at pH 7.8 (Fig. 16.6B) and 6.5 (Fig. 16.6C). With the appropriate software, each cell in the field can generate its own slope and intercept from the linear relationship generated by the nigericin clamp. The linear relationship derived from the nigericin clamp for one of the cells in this field is shown in Fig. 16.6D. By calculating the slope and *y* intercept of the relationship, the experimentally determined ratios can be converted to pH_i. An example of the conversion of the 490/440 ratio to pH_i is shown for the

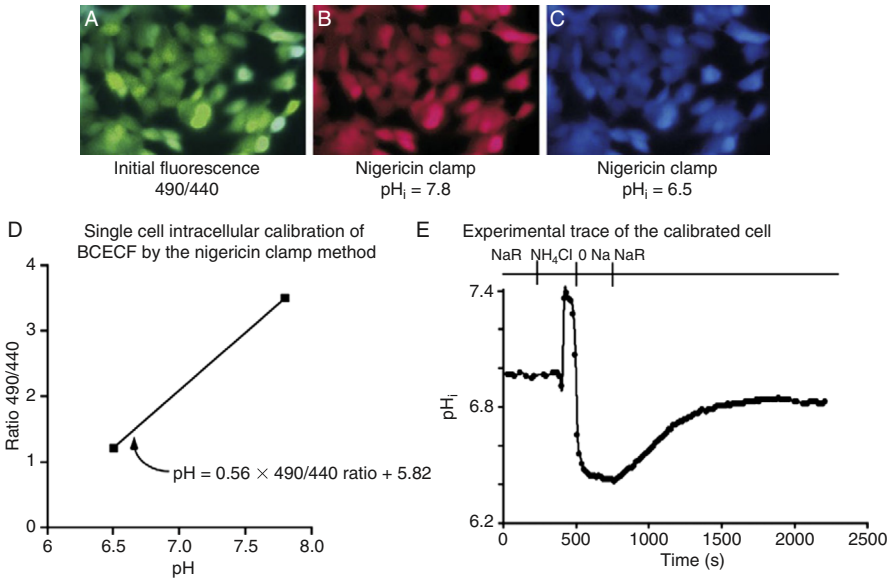

FIGURE 16.6

Top: Three representative ratiometric pseudocolor images of cells loaded with BCECF and excited at 490 nm and 440 nm, emission at 520 nm. The range of pseudocolor goes from red (alkaline) to dark blue (acid). (A) is an image of the initial fluorescence in these cells at the beginning of an experiment, with the cells bathed in Hepes buffered Ringer's solution. (B) and (C) are pseudocolor images of the same field of cells clamped to pH_i 7.8 (B) and pH_i 6.5 (C), with nigericin. Bottom: (D) represents the calibration of BCECF using the nigericin clamp protocol, in one cell from the field above. Intracellular and extracellular pH were equilibrated with the H^+/K^+ exchanger, nigericin (10 μM), and potassium solutions titrated to the indicated pH. The slope and intercept defined by the line was used to convert the experimentally determined 490/440 ratio to pH_i. (E) The experimental trace from this cell expressed as pH_i as a function of time.

cell whose values were used to calculate the slope and y intercept in Fig. 16.6D. Figure 16.6E is the trace of pH_i versus time and shows the Na^+-dependent pH_i recovery response of a cell acutely exposed to an NH_4Cl prepulse.

Intracellular calibration of Fura-2 can also be carried out in the cells with the Ca^{2+} ionophore ionomycin. This procedure is done at the end of an experiment similar to the nigericin technique described for BCECF. Calibration of the Fura-2 signal is achieved by determining both the maximum 340/380 ratio and the minimum 340/380 ratio of Fura-2 in the field of cells being studied. The maximum Fura-2 ratio is achieved with saturating levels of Ca^{2+} (2 mM) and the minimum Fura-2 ratio is attained in the presence of the Ca^{2+} chelator EGTA with no added Ca^{2+}, both in the presence of ionomycin. Ca_i^{2+} concentrations measured at intermediate ratios are calculated according to the relationship described for Fura-2 by Grynkiewicz et al., 1985

$$[Ca^{2+}] = K_d \frac{R - R_{min}}{R_{max} - R} \frac{S_{f2}}{S_{b2}}$$

where K_d is the effective dissociation constant (224 nM) at 37 °C, S_{f2} is the free or unbound signal at 380 nm, and S_{b2} is the Ca^{2+}-bound dye signal at 380 nm.

Figure 16.7A and B is an example of how Fura-2 is calibrated in cells. Figure 16.7A shows four IMD colored ratiometric images of Fura-2-loaded cells, excited at 340 nm and 380 nm, at four different time points during an experiment. The IMD colors range from red (>1 μM Ca^{2+}) to blue (<10 nM Ca^{2+}). Panel A shows the 340/380 IMD ratio of the cells at the beginning of the experiment and corresponds to a time point during interval A on the representative trace from a cell in this field (Fig. 16.7B). Panel B is a time point in which the cells were exposed to a depolarizing high potassium solution thereby opening voltage sensitive Ca^{2+} channels in the cell membrane. The IMD image has changed from dark green to bright green/yellow under this condition, which translates to an increase in Ca_i^{2+}. This time point corresponds to point B on the trace in Fig. 16.7B. Panels C and D represent images during the calibration of Fura-2 in the cells, with C being the R_{max}, also indicated by C in the trace of Fig. 16.7B and D being the R_{min} indicated in Fig. 16.7B.

Figure 16.7B shows the 340 nm and 380 nm signals as well as the ratio and the calibrated Ca_i^{2+} value for a single cell in the field of cells shown in Fig. 16.7A. The cells are initially bathed with a Hepes buffered solution. At the first arrow, the superfusate is changed to a high potassium solution. As mentioned above, depolarization by high extracellular K^+ leads to an influx of Ca^{2+} evidenced by a decrease in the 380 nm signal and an increase in the 340 nm signal, resulting in a transient increase in the 340/380 ratio. In order to convert the changes in the 340/380 ratio to Ca_i^{2+} values, the intracellular Fura-2 was calibrated. As indicated on the trace ionomycin was added to the superfusate in the presence and absence of extracellular Ca^{2+}. Addition of ionomycin in the presence of extracellular Ca^{2+} leads to a massive influx of Ca^{2+} through the ionomycin pore and yields the R_{max}. This results in an increase in the 340 nm and a decrease in the 380 nm signals resulting in a maximum 340/380 ratio of 3.2 from an initial ratio of 0.9. For generating a R_{min}, ionomycin remained present in the extracellular fluid and extracellular Ca was replaced with EGTA. Under this condition, the 340 signal goes down and the 380 signal increases resulting in the minimum 340/380 ratio (R_{min}) as shown in the trace. The values obtained from this intracellular calibration of Fura-2, are then plugged into the equation described above in order to convert the experimental 340/380 ratios, to Ca_i^{2+}. For this cell the initial Ca_i^{2+} started at 100 nM. With the K^+-induced depolarization, the Ca_i^{2+} went up to 250 nM which was immediately regulated back down to basal levels.

The calibration of intracellular BCECF and Fura-2 shown in Figs. 16.6 and 16.7 demonstrates the utility of dual-wavelength ratiometric imaging for measuring pH_i and Ca_i^{2+}. It is important to monitor the behavior of the dye at the level of the individual wavelengths as well as with the ratio. In order to maximize the amount of usable data acquired from a field of cells and to monitor variability of responses on a

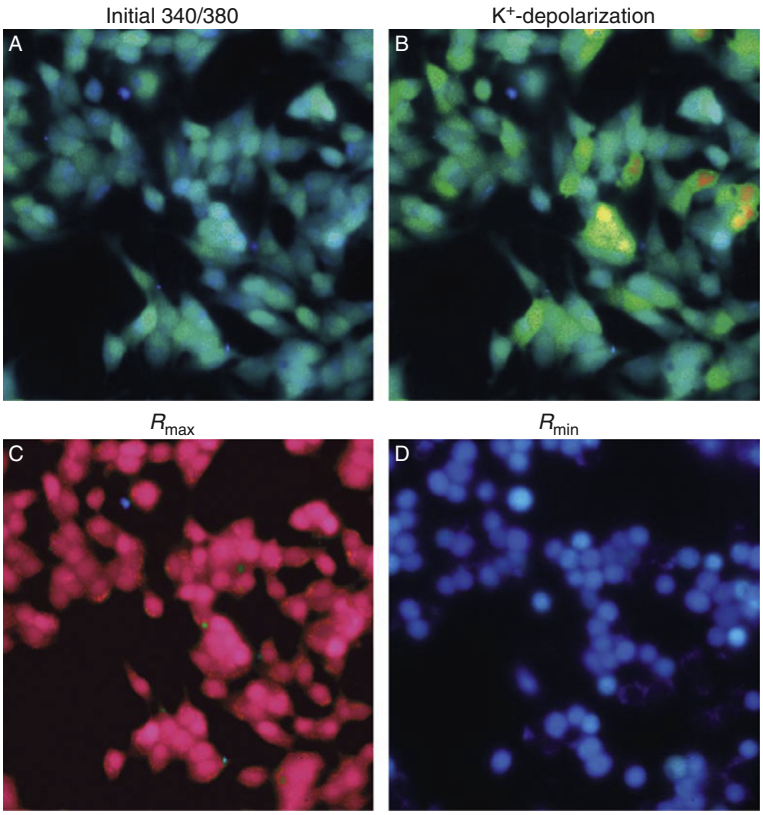

FIGURE 16.7A

Four representative ratiometric pseudocolor images of cells loaded with Fura-2 and excited at 340 nm and 380 nm, emission at 510 nm. The range of pseudocolor goes from blue (<10 nM Ca^{2+}) to red (>1000 nM Ca^{2+}). (A) is an image of the initial fluorescence in these cells at the beginning of an experiment, with the cells bathed in Hepes buffered Ringer's solution and corresponds to a time point from A in the traces in Fig. 16.7B. (B) is an image from the experiment after the bathing solution was changed to a high potassium solution, which depolarized the cells. This image corresponds to a time point from B in the traces in Fig. 16.7B. These cells express a voltage sensitive Ca^{2+} channel in the membrane. The switch to a K^+-depolarizing solution resulted in an opening of these channels and an influx of Ca^{2+} from the extracellular fluid. The pseudocolor image is bright green/yellow indicating that the 340/380 ratio increased. (C) is an image from the experiment during the maneuver to calibrate the Fura-2 in the cell, specifically the R_{max} value, and corresponds to a time point during C in the trace in Fig. 16.7B. Ionomycin (10 μM) was added to the extracellular Ringer's solution which resulted in a massive influx of Ca^{2+} from the extracellular fluid. This caused a large increase in the 340/380 ratio. (D) is an image from the experiment during the maneuver to calibrate the Fura-2 in the cell, specifically the R_{min}value, and corresponds to a time point during D in the trace in Fig. 16.7B. Ionomycin (10 μM) was added to the Ca^{2+} free extracellular solution, which also contained EGTA. This maneuver resulted in a massive efflux of Ca^{2+} from the cell resulting in a decrease in the 340/380 ratio.

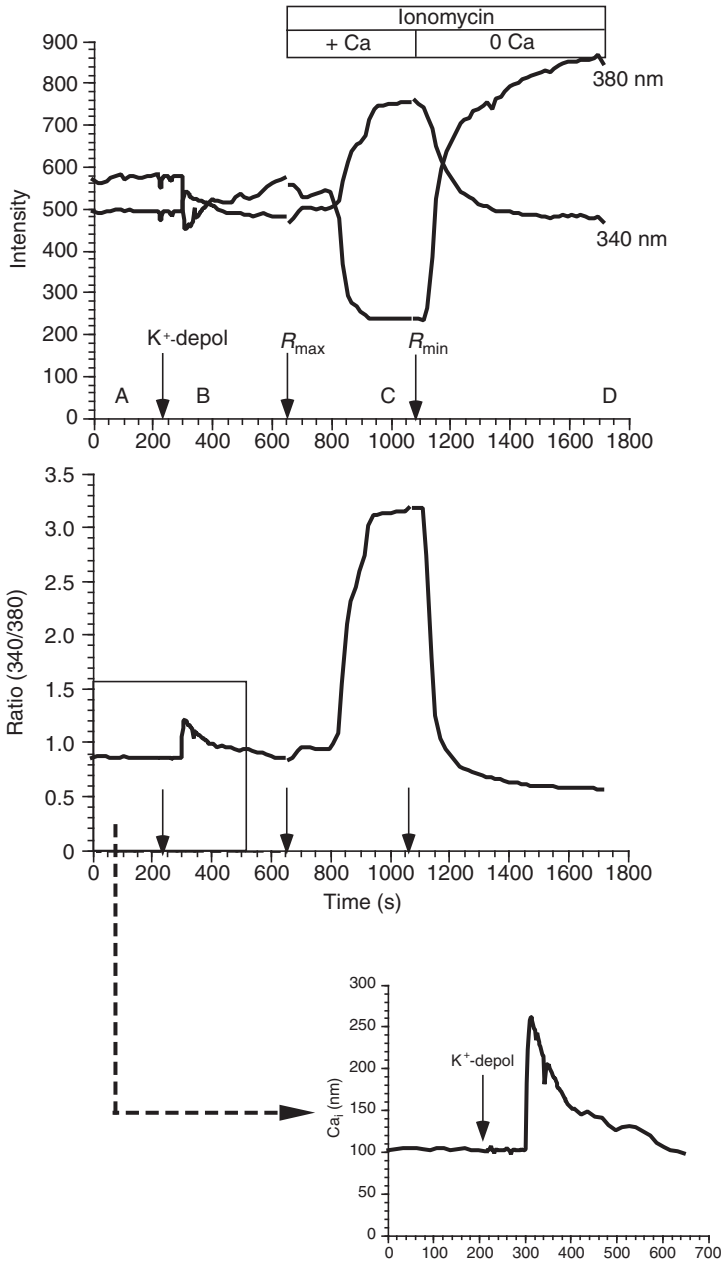

FIGURE 16.7B

The responses of a single cell in the field of cells shown in the pseudocolor images in Fig. 16.7A showing the changes in the 340 nm and 380 nm intensities (top), the 340/380 ratio (middle), and the corresponding Ca_i^{2+}, values based on the Fura-2 calibration in this cell (bottom). Arrows indicate where the solution was changed during the experiment as described above.

cell-to-cell basis, it is imperative that each cell monitored during the experiment generates its own calibration curve based on the behavior of the dye in the cell. Imaging software is available for this purpose.

Be mindful that meaningful interpretations of $[Ca^{2+}]$ and pH measurements require not only careful calibration, but also the maintenance of physiological conditions throughout the experimental protocol. The tissue/cell preparation should be superfused with balanced salt solutions at the appropriate pH.

16.4 COMPONENTS OF AN IMAGING WORKSTATION

Figure 16.8 is a schematic of an imaging workstation. The fluorescence light path begins with a high-energy xenon or mercury lamp housed at the rear of the microscope (Fig. 16.8A) or away from the imaging workstation in an external excitation wavelength controller (Fig. 16.8C), delivering its light via a fiber optic cable or liquid light guide. Xenon lamps provide a continuous light output from 270–700 nm (Tsien, 1989), except around 450–485 nm where one sees some sharp lines similar to those seen in the BCECF spectra in Fig. 16.1. Mercury lamps produce a higher intensity than xenon lamps but this output is not continuous; rather it is concentrated in lines so these lamps are only suitable if the lines coincide with the peak excitation of the fluorophore. A high energy light source providing the optimal output of intensity in the excitation range needed should be chosen. A 75–175 W xenon lamp works well for both Fura-2 and BCECF measurements. It is also important that the lamp is focused and provides a flat and evenly illuminated field.

Output from the lamp passes through the appropriate excitation filters housed in a shuttered, motorized filter wheel (Fig. 16.8B) or in adjacent slots in the external wavelength controller (Fig. 16.8C). These devices change excitation wavelengths and control the duration of the illuminating light. In the configuration of Fig. 16.8C, a galvanometer is used to swing the excitation light beam into incidence with one of the excitation filters. The galvanometer is able to rapidly change its position, resulting in a wavelength-switching time of $\sim$2 ms.

To minimize photobleaching and photodynamic damage to cells, fluorescence excitation can be shuttered off except during the brief periods required to record an image. Additionally, the intensity of the excitation light can be attenuated toward the minimum level required to obtain a useful emission intensity level. In many filter wheels, a neutral density filter fits in the same slot as the excitation filter. In the galvanometer-based system, the excitation light beam can be oriented such that the entrance pupil of the liquid light guide is not filled. This results in a lower intensity, but still relatively homogeneous, excitation light beam exiting the light guide. Attenuation of excitation intensity can also be used to equalize two disparate excitation wavelength intensities.

Light of two alternating wavelengths enters the optical axis of the microscope and encounters a filter cube housing an appropriate dichroic mirror and emission filter (Fig. 16.8D). The mirror and emission filter should pass the appropriate wavelengths

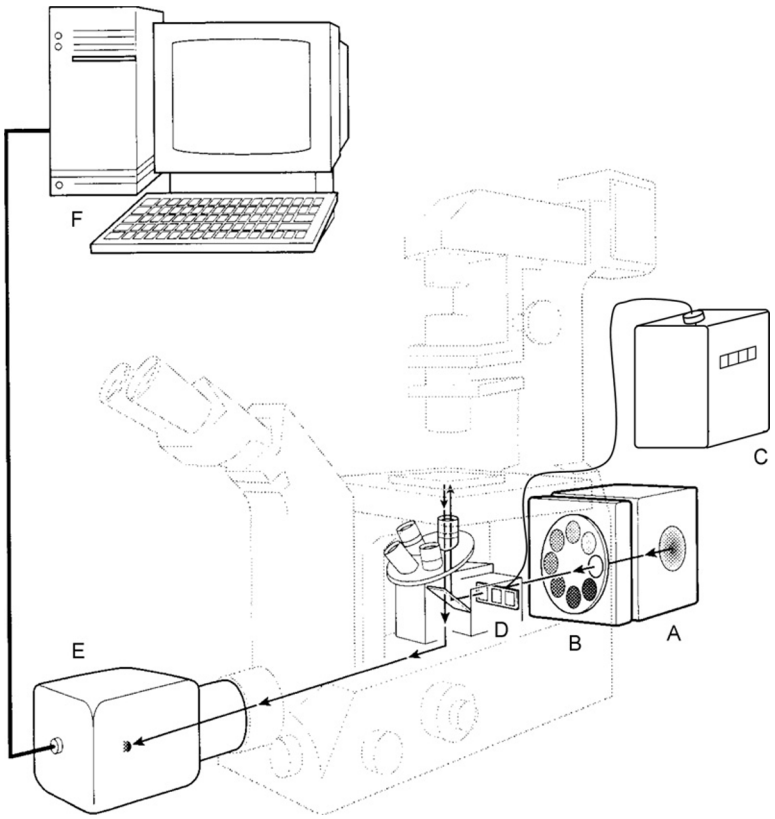

FIGURE 16.8

Schematic of an imaging workstation. The components include either a high energy lamp (A) connected to a shutter-controlled filter wheel (B) attached directly to the back of the microscope or an external excitation wavelength controller delivering light via a light guide (C). The dichroic mirror and emission filter are housed in the base of the nosepiece (D). The low-light-level imaging device (E) is interfaced to a port on the microscope. The image processor and operating system are housed in the computer (F) that controls the entire workstation.

as efficiently as possible. Emission filters with high transmission characteristics are widely commercially available (Erdogan, 2006). The dual-purpose dichroic mirror reflects the exciting light up through the objective to the sample sitting in the chamber on the stage of the microscope. The emitted fluorescence travels back down through the objective and is transmitted through the dichroic mirror and emission filter to the detector (Fig. 16.8E). An inverted epifluorescence microscope outfitted with high numerical aperture (NA) oil or glycerin immersion objectives (>1.25) is best for low-light-level imaging. The light-collecting efficiency of an objective varies approximately with the square of the NA.

The basic requirements for a detector or camera used in low-light-level imaging are wide dynamic range and linear response within the range of detection. Intensified video cameras and frame transfer CCDs can both be used for ratio imaging. An advantage of the frame transfer CCD is its potential to image over a wide dynamic range of intensities. This is sometimes the only option for performing quantitative ratio imaging on all cells viewed in a field of view. For example, at a given camera gain with a fixed gray-level scale of 0-255, a cell population may not have homogenous loading. This can be due to a variety of reasons like differences in intrinsic esterase activities or differences in subcellular compartment volumes. In experimental situations of this nature, a frame transfer camera with an expanded grayscale would be very helpful. A camera containing a frame transfer chip (E2V) with 16-bit readout has a gray scale 256 times greater than a standard digital camera and goes from 0 to 65,535 gray levels.

Another advantage of using the frame transfer type device for ratio imaging is the speed at which it records an image pair. This is possible because, in the camera, the chip has half of its surface covered by an opaque mask. The first excitation wavelength signal is recorded on the unmasked side and electronically transferred to the masked side (Bright et al., 1989). The second excitation wavelength signal is then recorded while the first is being read off the masked side of the chip. This allows the recording of two images in rapid succession with on-chip transfer of an image taking less than 2 ms (Bright et al., 1989).

The best way to decide which detector is most suitable is to test various detection devices with your biological specimen. If possible try to perform an intracellular calibration of the dye to see how the detection device performs at the maximum and minimum range of signals. A discussion of the properties of different types of low-light-level cameras may be found elsewhere in this volume.

A host computer (Fig. 16.8F), which includes the operating system and an image processor, controls the entire workstation. The operating system controls the shutter and filter wheel and coordinates the acquisition and analysis of the ratio images. The image processor is required for data acquisition and decreases processing time over that of the computer, permitting readout of the experimentally acquired images close to real time (Bright et al., 1989).

16.5 EXPERIMENTAL CHAMBER AND PERFUSION SYSTEM: A SIMPLE APPROACH

As important as choosing the right components of the imaging workstation is finding an experimental chamber and perfusion system that is easy to use and assemble. This section describes a simple chamber and a perfusion system routinely used in the laboratory, which may be useful to others.

Figure 16.9 is a diagram of a perfusion apparatus consisting of a Lucite rack from which glass syringes are suspended (Fig. 16.9A). Solutions are gravity fed into a six-port Hamilton valve with six individual inputs and one output (Fig. 16.9B). The

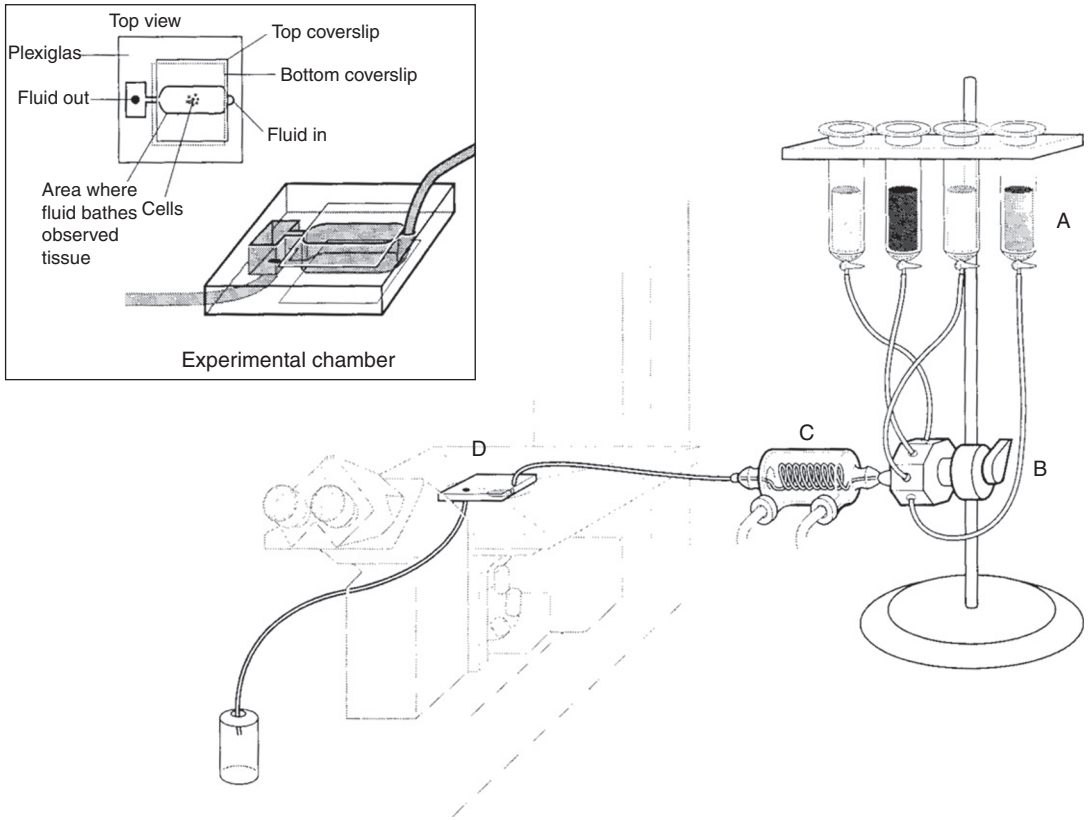

FIGURE 16.9

Diagram of experimental perfusion setup and chamber. The perfusion apparatus consists of a ring stand with a rack holding glass syringes (A). Each syringe is attached to an input on a Hamilton valve (B) via tubing. The output from the Hamilton valve goes into a miniature water-jacketed glass coil (C) (Radnotti Glass Technology, Monrovia, CA) where it is warmed to 37 °C. Output from the coil enters the experimental chamber (D) mounted on the stage of an inverted microscope.

solution exiting from the output port then goes directly into a miniature water-jacketed glass coil (Fig. 16.9C) (Radnotti Glass Technology, Monrovia, CA) for regulating solution temperature. The warmed solution (37 °C) then enters the experimental chamber (Fig. 16.9D) which fits on the stage of the inverted epifluorescence microscope. The experimental chamber, which was designed to fit on the stage of an inverted microscope, is diagrammed in more detail in the inset of Fig. 16.9. It consists of a piece of Lucite fitted on the bottom and top with interchangeable coverslips (No. 1.5 thickness and 22 mm^2) which are temporally attached to the chamber with Dow Corning high vacuum grease. The specimen area of the chamber contains an entry port for accommodating the entering perfusate and an exit port to convey the perfusate to a reservoir sitting at a lower level. The chamber volume is roughly 600 μl exchanged at a rate of about 2 ml/min. For an inverted microscope, the experimental cells must rest on the surface of the coverslip, which constitutes the bottom of the chamber. This is essential due to the small working distance of many of the high-NA objectives required for performing low-light-level imaging experiments. For example, the Nikon Fluor 40× oil immersion objective with NA 1.3 has a working distance of 0.22 mm when used with a No. 1.5 coverslip of 0.17-mm thickness. With this combination of objective and coverslip there is enough working distance to view cells adherent to the coverslip surface facing the chamber. A coverslip is also placed on the top of the chamber to maintain temperature, laminar flow, and optimal optical conditions for viewing the cells.

CONCLUSION

In conclusion, the technique of quantitative ratio imaging for the measurement of pH_i and Ca_i^{2+} has revolutionized the field of cell physiology. Using the proper equipment and choosing the right dyes for your experimental needs should provide reliable and reproducible results. More importantly the amount of data produced from each experiment, when analyzing pH_i and Ca_i^{2+} on an individual cell basis, yields valuable information on the heterogeneity of cellular responses (Rink, Tsien, & Pozzan, 1982; Silver et al., 2001) and will open up new areas for understanding the roles of pH_i and Ca_i^{2+} in signal transduction.

Acknowledgments

This work was generously supported by NIH Grants DK-060726 and HL-73400. The authors would like to acknowledge the contributions of Drs. A. C. Reid and L. Ma.

References

Bright, G. R., Fisher, G. W., Rogowska, J., & Taylor, D. L. (1989). Fluorescence ratio imaging microscopy. In D. L. Taylor & Y. Wang (Eds.), *Methods in cell biology*, Vol. 30, (pp. 157–192). San Diego: Academic Press.

Cardone, M. H., Smith, B. L., Mennitt, P. A., Mochly-Rosen, D., Silver, R. B., & Mostov, K. E. (1996). Signal transduction by the polymeric immunoglobulin receptor suggests a role in regulation of receptor transcytosis. *The Journal of Cell Biology*, *133*, 997–1005.

Cobbold, P. H., & Rink, T. J. (1987). Fluorescence and bioluminescence measurement of cytoplasmic free calcium. *The Biochemical Journal*, *248*, 313–328.

Di Virgilio, F., Steinberg, T. H., & Silverstein, S. C. (1990). Inhibition of Fura-2 sequestration and secretion with organic anion transporter blockers. *Cell Calcium*, *11*, 57–62.

Di Virgilio, F., Steinberg, T. H., Swanson, J. A., & Silverstein, S. C. (1988). Fura-2 secretion and sequestration in macrophages. A blocker of organic anion transport reveals that these processes occur via a membrane transport system for organic anions. *Journal of Immunology*, *140*, 915–920.

Erdogan, T. (2006). New optical filters improve high-speed multicolor fluorescence imaging. *Biophotonics International*, *13*, 34–39.

Grynkiewicz, G. M., Poenie, M., & Tsien, R. Y. (1985). A new generation of Ca^{2+} indicators with greatly improved fluorescence properties. *The Journal of Biological Chemistry*, *260*, 3440–3450.

Heiple, J. M., & Taylor, D. L. (1981). An optical technique for measurement of intracellular pH in single living cells. *Kroc Foundation Series*, *15*, 21–54.

Lakowicz, J. R. (1986). *Principles of fluorescence spectroscopy* (Vol. 24). New York: Plenum Press.

Millard, P. J., Ryan, T. A., Webb, W. W., & Fewtrell, C. (1989). Immunoglobulin *E. coli* receptor cross-linking induces oscillations in intracellular free ionized calcium in individual tumor mast cells. *The Journal of Biological Chemistry*, *264*, 19730–19739.

Rink, T. J., Tsien, R. Y., & Pozzan, T. (1982). Cytoplasmic pH and free Mg^{2+} in lymphocytes. *The Journal of Cell Biology*, *95*, 189–196.

Silver, R. B., Mackins, C. J., Smith, N. C. E., Koritchneva, I. L., Lefkowitz, K., Lovenberg, T., et al. (2001). Coupling of histamine H_3 receptors to neuronal Na^+/H^+ exchange: A protective mechanism in myocardial ischemia. *Proceedings of the National Academy of Sciences of the United States of America*, *98*, 2855–2859.

Silver, R. B., Poonwasi, K. S., Seyedi, N., Wilson, S., Lovenberg, T. W., & Levi, R. (2002). Decreased intracellular calcium mediates the histamine H_3-receptor induced attenuation of norepinephrine exocytosis from cardiac sympathetic nerve endings. *Proceedings of the National Academy of Sciences of the United States of America*, *99*, 501–506.

Thomas, J. A., Buchsbaum, R. N., Zimniak, A., & Racker, E. (1979). Intracellular pH measurements in Ehrlich ascites tumor cells utilizing spectroscopic probes generated *in situ*. *Biochemistry*, *18*, 2210–2218.

Tsien, R. Y. (1989). Fluorescent probes of cell signalling. *Annual Review of Neuroscience*, *12*, 227–253.

CHAPTER

Quantitative Fluorescence Microscopy and Image Deconvolution

17

Jason R. Swedlow

Division of Gene Regulation and Expression, College of Life Sciences, University of Dundee, Dundee, Scotland, United Kingdom

CHAPTER OUTLINE

Introduction **408**
17.1 Quantitative Imaging of Biological Samples Using Fluorescence Microscopy **409**
17.1.1 Quantitative Fluorescence—Detectors 409
17.1.2 Quantitative Fluorescence—Limits on Linearity 409
17.1.2.1 Illumination Variations 410
17.1.2.2 Detector Noise 410
17.1.2.3 Photon Shot Noise 411
17.1.3 Quantitative Fluorescence—Characterizing the Performance of an Imaging System 411
17.1.4 Preprocessing of Images for Quantitative Analysis 413
17.1.5 Processing Data for Quantitative Analysis 413
17.1.6 Methodologies for Quantitative Imaging 416
17.2 Image Blurring in Biological Samples **417**
17.2.1 Approaches for Image Deblurring by Deconvolution 419
17.2.1.1 Deblurring or Neighbor-Based Methods 419
17.2.1.2 Restoration Methods 420
17.2.2 Image Deconvolution: Effects and Results 421
17.2.3 Image Deconvolution: Practical Issues 421
17.3 Applications for Image Deconvolution **423**
Concluding Remarks **423**
Acknowledgments **424**
References **424**

Methods in Cell Biology, Volume 114
ISSN 0091-679X
http://dx.doi.org/10.1016/B978-0-12-407761-4.00017-8
Copyright © 1998 Elsevier Inc. All rights reserved.

Abstract

Quantitative imaging and image deconvolution have become standard techniques for the modern cell biologist because they can form the basis of an increasing number of assays for molecular function in a cellular context. There are two major types of deconvolution approaches—deblurring and restoration algorithms. Deblurring algorithms remove blur but treat a series of optical sections as individual two-dimensional entities and therefore sometimes mishandle blurred light. Restoration algorithms determine an object that, when convolved with the point-spread function of the microscope, could produce the image data. The advantages and disadvantages of these methods are discussed in this chapter. Image deconvolution in fluorescence microscopy has usually been applied to high-resolution imaging to improve contrast and thus detect small, dim objects that might otherwise be obscured. Their proper use demands some consideration of the imaging hardware, the acquisition process, fundamental aspects of photon detection, and image processing. This can prove daunting for some cell biologists, but the power of these techniques has been proven many times in the works cited in the chapter and elsewhere. Their usage is now well defined, so they can be incorporated into the capabilities of most laboratories.

A major application of fluorescence microscopy is the quantitative measurement of the localization, dynamics, and interactions of cellular factors. The introduction of green fluorescent protein and its spectral variants has led to a significant increase in the use of fluorescence microscopy as a quantitative assay system. For quantitative imaging assays, it is critical to consider the nature of the image-acquisition system and to validate its response to known standards. Any image-processing algorithms used before quantitative analysis should preserve the relative signal levels in different parts of the image. A very common image-processing algorithm, image deconvolution, is used to remove blurred signal from an image. There are two major types of deconvolution approaches, deblurring and restoration algorithms. Deblurring algorithms remove blur, but treat a series of optical sections as individual two-dimensional entities, and therefore sometimes mishandle blurred light. Restoration algorithms determine an object that, when convolved with the point-spread function of the microscope, could produce the image data. The advantages and disadvantages of these methods are discussed.

INTRODUCTION

Fluorescence microscopy has experienced a revolution in the last 10 years. This mode of imaging has been transformed by the labeling of proteins with GFP from a specialized technique into a standard assay for molecular function (Chalfie, Tu, Euskirchen, Ward, & Prasher, 1994; Patterson, Day, & Piston, 2001; Stearns, 1995). In addition, the cost of imaging hardware has dropped and new imaging techniques have appeared for measuring molecular interactions and dynamics, often in living cells. The applications of these technologies has made quantitative analysis of

digital microscope images a required part of the cell biologist's toolbox. In this chapter, I review some of the principles of quantitative imaging and then discuss one of the most common image-processing applications that depends on rigorous application of quantitative imaging: image deconvolution.

17.1 QUANTITATIVE IMAGING OF BIOLOGICAL SAMPLES USING FLUORESCENCE MICROSCOPY

Quantitative imaging has long been a cornerstone of fluorescence microscopy. The use of small molecule fluorophores that preferentially localize to a cellular compartment or report the concentration of a specific cellular ion (Tsien & Waggoner, 1995), especially those appropriate for ratio imaging (Silver, 1998), have traditionally been the most quantitatively accurate probes for fluorescence microscopy. Antibody-based localization in indirect immunofluorescence faithfully reported the localization of the antibody but often suffered from variable antigen accessibility and differences in extraction or fixation. More recently, the use of genetically encoded fluorescence based on GFP and its spectral variants (Tsien, 1998) ensures that, assuming there is no proteolytic cleavage of the GFP fusion protein, each fluorophore molecule is spatially and quantitatively linked to a single molecule of the protein under study. This capability is now commonly used as the basis for the quantitative study of protein localization, dynamics, and interactions (Lippincott-Schwartz, Snapp, & Kenworthy, 2001).

17.1.1 Quantitative fluorescence—detectors

Detectors for fluorescence microscopy are now routinely provided on commercially available turnkey systems. Laser scanning confocal microscopes (LSCMs) and multiphoton microscopes (MPMs) use photomultiplier tubes (PMTs) to detect the small number of photons emanating from the in-focus image plane. Wide-field microscopes (WFMs) and spinning disk confocal microscopes (SDCMs) image a large field simultaneously and thus require the use of an array of detectors to record an image. Charge-coupled device (CCD) cameras have become the standard detector used in these microscope systems. Both PMTs and CCDs provide high sensitivity and linear response over their dynamic range and thus, when used appropriately, can form the basis of a linear fluorescence microscope-based detection system (Art, 1995; Inoué & Spring, 1997).

17.1.2 Quantitative fluorescence—limits on linearity

It is one thing to design a microscope system for quantitative imaging; it is quite another thing to use it so that all measurements are, in fact, in the linear range of the detection system. First and foremost, the intrinsic sources of noise in the imaging system should be identified and minimized. In the author's experience, noise can

derive from anywhere in the optical train, but is most commonly caused by illumination instabilities, the detector electronics, or mechanical or thermal fluctuations in the sample or microscope body. Any combination of these effects will add noise to any image measurement, thus decreasing its dynamic range and accuracy. It is critical that these sources not be ignored or taken for granted just because, for instance, a commercial supplier claims them to be "minimized."

17.1.2.1 Illumination variations

In fluorescence microscopy, a major source of noise is the variation of light flux coming from either the lamp or the laser used as an illumination source. In WFMs, the lamps used as sources can suffer significant power deviations of up to 10% on timescales of milliseconds to seconds. These fluctuations become more dramatic as the lamp ages. For applications requiring repeated imaging (i.e., optical sectioning or time-lapse), these variations cause stochastic changes during the acquisition of each image. The result is that the total fluorescence excitation light varies between images, resulting in deviations in fluorescence signal derived from the imaging system, not the sample. Stabilized power supplies for these lamps are available, and these can partially suppress this problem. Preferably these deviations can be measured, either during data collection or subsequently from the image data, and then corrected by a software correction algorithm (Chen, Swedlow, Grote, Sedat, & Agard, 1995).

For laser scanning confocal microscopes, recent studies have identified power deviations of the order of 1%–10% in the standard gas lasers used in commercial turnkey systems, apparently caused by changes in the plasma discharge (Swedlow, Hu, Andrews, Roos, & Murray, 2002; Zucker & Price, 2001). They are significant because they occur on the microsecond timescale, which is on the order of the dwell time of the laser at each pixel in a scanning microscope. These variations cause pixel-to-pixel variations in illumination intensities. In principle, these can be corrected by measuring illumination variations with a rapid detector, although use of this approach failed to correct the observed deviations (Swedlow et al., 2002). Regardless of their source, illumination power deviations can contribute a significant source of noise in fluorescence imaging and should therefore be assessed and corrected as much as possible.

17.1.2.2 Detector noise

A second major source of noise in imaging systems derives from the detectors used to record the fluorescence signals. In PMTs this largely results from spurious electrons generated by the high voltages within the PMT (Art, 1995; Pawley, 1994). This problem grows as the PMT gain is increased. In addition, our recent work revealed a second source of detector noise that we were unable to unambiguously characterize, but that appeared to be associated with the amplifier circuitry associated with the PMT detector (Swedlow et al., 2002). For CCDs, each time a pixel is "read," there is an uncertainty, usually expressed as the rootmean-square (RMS)

number of electrons (e^-) that is added to the value measured at each pixel. This source of noise is stochastic and varies pixel by pixel and is therefore very hard to remove. In the authors' labs, we try to use CCDs with less than 6 e^- RMS, especially for low-light-level imaging. Regardless of the detector used, measurements made near the lower end of the dynamic range of the detector will have a significant noise content. Consequently, any attempts to make critical measurements at these signal levels will have significant noise deviations and thus not be "linear." The best solution is to either record higher signal levels, so that detector noise comprises less of the total signal, or to use a more sensitive, lower-noise detector (see Inoué & Spring, 1997, for a full description of detector types, performance, and limitation).

17.1.2.3 Photon shot noise

The detection of photons is inherently a statistical process, with the uncertainty in the detection being given by $(N)^{1/2}$, where N is the number of photons counted (Pawley, 1995a). As the number of photons counted increases, the relative uncertainty in the measurement decreases. This uncertainty is referred to as photon shot noise. To minimize this source of noise, it seems reasonable to try to collect as many photons as possible. In fluorescence imaging, especially when imaging photosensitive live cells, it is only possible to collect small numbers of photons, because only limited amounts of fluorescence excitation can be tolerated by the cell or tissue (Swedlow & Platani, 2002). For this reason, it is often the case that photon shot noise is a significant source of noise in fluorescent microscope images.

17.1.3 Quantitative fluorescence—characterizing the performance of an imaging system

Before proceeding with a quantitative measurement, it is critical that the imaging system be characterized and any sources of systematic noise be minimized. A number of helpful articles are available to aid in the characterization of different systems (Murray, 1998; Sheppard, Gan, Gu, & Roy, 1995; Zucker & Price, 2001). In the author's lab, to characterize the overall performance of the detection system and characterize the linearity of an imaging system's response, we have also used a distribution of large beads (InSpeak 2.5-μm beads, Molecular Probes, Inc.) made up of beads with six different concentrations of a fluorophore spanning over two orders of magnitude. The beads are spread on a coverslip, and many hundreds of beads are imaged. The selection of fluorescence excitation and duration and detector settings must be chosen so that the whole range of beads can be visualized without saturating the detector. After imaging, the fluorescence in each bead is summed and the distribution of the measured bead fluorescence is plotted on a histogram (Fig. 17.1; Swedlow et al., 2002). This analysis reveals two aspects of the quantitative limits of the imaging system. First, the relative fluorophore concentrations of each bead population can be compared to those measured independently by FACS to test whether the microscope is working as a reasonably linear detector. Second, the coefficients of

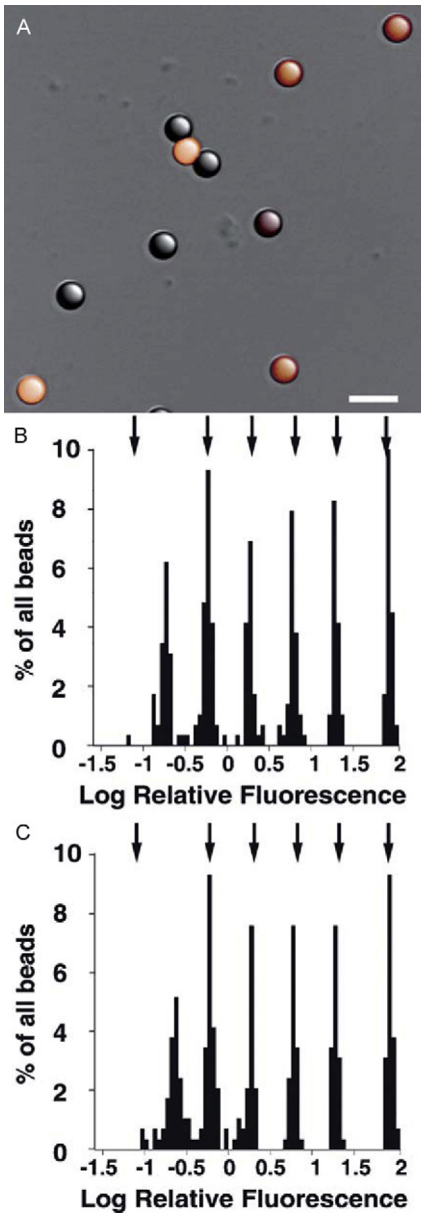

FIGURE 17.1

WFM imaging of calibrated fluorescent standards. (A) Merged fluorescence and DIC image of a mixture of 2.5-μm polystyrene beads with seven different fluorophore densities. Fluorescence from the beads with the three highest fluorophore densities is bright enough to make them appear colored in this image, whereas beads with the lower fluorophore densities appear gray. Scale bar, 5 μm. (B) Quantitative analysis of fluorescent bead image.

variation within each bead population reveal how the contributions of systematic and photon shot noise discussed above are contributing to each of the measurements. For the wide-field microscope shown analyzed in Fig. 17.1, we found that the coefficients of variation were essentially unchanged over the five brightest bead populations, covering over two orders of magnitude of the system's dynamic range (Table 17.1). We observed a clear increase in the coefficient of variation for the weakest bead population. Although the median of this population appeared in an appropriate position (Fig. 17.1), the measurement clearly contained a higher uncertainty (Table 17.1). Measurements made within this dynamic range of the detector would therefore contain significant noise.

17.1.4 Preprocessing of images for quantitative analysis

Before performing quantitative analyses, digital image data often must be preprocessed, or filtered to minimize various types of systematic noise. One example of this is the flat-field correction of the CCD field used in wide-field imaging. This step corrects for illumination variation across the area of the CCD as well as any systematic differences in pixel response within the CCD array. This step is usually critical to prevent quantitative results from being affected by systematic errors in illumination or signal detection (Agard, Hiraoka, Shaw, & Sedat, 1989).

A second example of quantitative image preprocessing corrects the time-dependent illumination variation discussed above. In the WFM, illumination changes that occur between frames in a series of optical sections or a time-lapse movie must be corrected before further quantitative processing is performed. Direct measurement of the excitation flux in each frame is possible, but it can only be made if the illumination system of the microscope includes suitable photon detectors. Alternatively, illumination changes can be measured and corrected by simply summing the fluorescence signal in each frame and then fitting the summed signals to a polynomial (Chen et al., 1995).

17.1.5 Processing data for quantitative analysis

Before performing any processing algorithms on image data, it is important to consider whether the operation will preserve the quantitative relationships in the data. In many cases, quantitative relationships will not be preserved. This is often desirable, as the resulting changes in contrast can help identify objects, edges, and so forth by visual inspection (Russ, 1992). However, if the interpretation of an image requires

Total fluorescence in three-dimensional images of 290 beads was determined by summing an identical volume in each bead and normalized to put all measurements on the same scale. Relative bead fluorescence was also determined by FACS and similarly normalized. Arrows show the positions of the median fluorescence of each bead population measured by FACS. (C) Same dataset as (B) but after image restoration by iterative deconvolution. Figure adapted from Swedlow et al. (2002). Copyright 2002 National Academy of Sciences, USA.

Table 17.1 Statistical Analysis of Noise in Measurements of Fluorescent Beads

Beads[a]	WFM/Raw	WFM/Decon	FACS[b]
.3	.35	.24	.20
1	.09	.10	.10
3	.08	.08	.08
10	.09	.08	.07
30	.07	.08	.06
100	.06	.07	.06

[a]*Nominal relative bead fluorophore density as specified by manufacturer.*
[b]*Coefficients of variation for beads used for WFM measured by FACS.*
Note*: Values are coefficients of variation (standard deviation/arithmetic mean) for each of the bead populations measured in Fig. 17.1. The central 80% of each population was used to calculate the mean. Background was subtracted as described in Eq. (17.1). Between 30 and 45 beads were used for each bead population assayed by microscopy. From each population 1200–1500 beads were used for FACS assay. Table adapted from Swedlow* et al. *(2002). Copyright 2002 National Academy of Sciences, USA.*

quantitative analysis, care must be taken to ensure that the algorithm used preserves quantitative relationships.

As an example of the effects of processing algorithms, consider the image in Fig. 17.2, recorded with a CCD camera with a wide-field microscope. This is a large bead that contains fluorescent dye on its surface, but not in its interior. The images shown in Fig. 17.2A show the same bead imaged under five different relative illumination levels. The LUT(look-up table) on each image is adjusted to show the minimum and maximum signal detected by the detector, a CCD camera. Each image is labeled with the relative level of illumination, expressed as a percentage. The line plots through the center of the bead reveal the relative differences between the background, the shell of fluorescence, and the unlabeled center of the bead. These same images are shown after processing with low-pass (Fig. 17.2B) and high-pass (Fig. 17.2C) convolution filters (Russ, 1992). Note that the low-pass filter improves the visibility of the bead, but also significantly changes the relative fluorescence measurements shown in the line plots. The relative intensities are apparently identical for the three brightest images (100, 50, 10); nearly the same for the next brightest image (1), but incorrect for the dimmest image (0.1). Use of the high-pass filter makes the bead invisible in the lowest signal image and also dramatically changes the relative intensities measured within the bead.

The convolution operations in Fig. 17.2 dramatically affected the relative intensities within the bead test image. At first glance, this may suggest that these and even more sophisticated processing and filtering schemes should not be used for quantitative image analysis. In fact, a common approach is to use the results of these methods as the basis for a mask that defines which pixels are to be included in an analysis and which are to be excluded. For example, although the 0.1% image in Fig. 17.2A is quite noisy, the result from the low-pass convolution in Fig. 17.2B

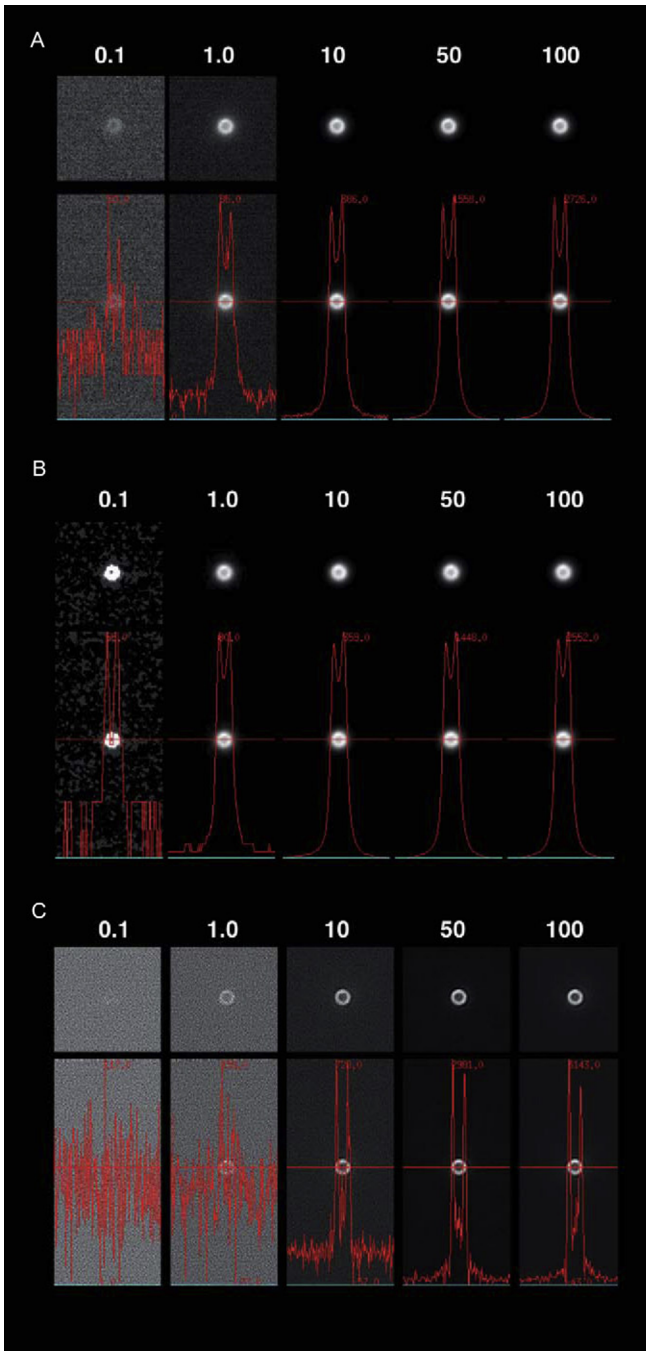

FIGURE 17.2

Effects of standard image processing methods on relative fluorescence measurements. A 5-μm bead with fluorophore concentrated on its surface was imaged in a fluorescence

Continued

might be used to define the area within Fig. 17.2A that was to be subjected to quantitative analyses. Such strategies are quite common and thus define a critical role for nonlinear image-processing methods within quantitative imaging.

17.1.6 Methodologies for quantitative imaging

The applications for quantitative analysis in fluorescence microscopy have exploded over the last few years (Lippincott-Schwartz et al., 2001). A large number of them depend on the determination of the fluorescence signal within a subregion of an image. As discussed above, as most digital microscopes are linear detectors and GFP fluorescence shows us the concentration of protein at specific sites (unlike antibody-based immunofluorescence), such measurements are now routine. Notable applications using summed fluorescence include fluorescence recovery after photobleaching (FRAP), fluorescence loss in photo-bleaching (FLIP), fluorescence resonance energy transfer (FRET), and fluorescence lifetime imaging (FLIM) as well as simple measurements of fluorescence change in different cellular compartments. The basic principles in measuring the fluorescence in an image involve five steps:

1. Identifying the object in two or three dimensions to be measured
2. Summing the fluorescence signal in the object
3. Measuring the area or volume in the object (number of pixels or voxels)
4. Identifying a second area considered to be representative of background
5. Measuring the summed fluorescence and area/volume in the background.

With these values, the background corrected fluorescence in the object can be calculated as follows:

$$F'_{\text{obj}} = \sum_{i=1}^{i=N_{\text{obj}}} F_{\text{obj}_i} - N_{\text{obj}} \frac{\sum_{j=1}^{j=N_{\text{bkg}}} F_{\text{bkg}_j}}{N_{\text{bkg}}}, \tag{17.1}$$

where F is the fluorescence signal measured at each pixel i or j, obj is the object area or volume, bkg is the selected background area or volume, and N is the number of pixels in the selected object or background. This equation sums the fluorescence in an object,

---

microscope repeatedly while varying the neutral density filter placed between the excitation light beam and the sample (Transmittance = 100%, 50%, 10%, 1%, and 0.1%) while keeping all other imaging parameters the same. (A) Raw images from the microscope. (B) The images in (A) were processed with a low-pass convolution filter. (C) The images in (A) were processed with a high-pass convolution filter. Each image is shown alone and superimposed with a line plot through the center of the bead to indicate the relative intensities in the image and is presented using a LUT set to the individual images minimum and maximum signal. Each line plot is also scaled to the minimum and maximum signal in the individual image. J. R. S. thanks Paul Goodwin, Applied Precision, LLC, for recording this data at the 2002 Analytical and Quantitative Light Microscopy Course, Marine Biological Laboratory.

calculates the background contribution per pixel, and then corrects the summed object fluorescence by the number of pixels in the object multiplied by background per pixel. This background correction is critical to help reveal subtle changes in fluorescence.

17.2 IMAGE BLURRING IN BIOLOGICAL SAMPLES

One of the major challenges facing the cell biologist using digital imaging is the intrinsic thickness of cells and tissues. In most fluorescence imaging (and especially when imaging live cells), it is critical to gather and measure as many photons as possible to reduce photon shot noise. Objective lenses with high numerical aperture or light-gathering power are therefore usually used (for the definition and description of basic microscope optics, see Inoué & Spring, 1997). They also tend to be the lenses with the greatest resolving power, so that small objects can be detected and resolved. Unfortunately these lenses have a relatively narrow depth of field, so they produce an image that combines in-focus information from the focal plane and blurred, out-of-focus information from elsewhere in the sample. The degradation of the in-focus signal by blurring decreases contrast and thus prevents individual objects from being resolved. The density of the blurred light increases linearly with the thickness of the sample. In practice, blurring becomes a significant problem in cells more than 10–20 μm thick (depending on the density of the fluorescence signal).

The blurring of a sample by an objective lens is represented by the point-spread function (PSF). The PSF can be either calculated by a variety of formulae (e.g., Gibson & Lanni, 1991) or directly measured by imaging a subresolution fluorescent bead using the same optical setup as will be used for samples (Wallace, Schaefer, & Swedlow, 2001). The blurring of the bead by the objective lens can be described by a convolution operation where the PSF operates on every point in the image:

$$\text{image}(x,y,z) = \int_{-\infty}^{\infty}\int_{-\infty}^{\infty}\int_{-\infty}^{\infty} \text{psf}(x-x', y-y', z-z') * \text{object}(x',y',z')\,dx'\,dy'\,dz',$$

where the image is the recorded data, the object is the sample on the microscope, and (x,y,z) is the coordinate system of the microscope. Note that the PSF and this convolution are three-dimensional. The equation can be written more succinctly as

$$\text{image} = \text{object} \otimes \text{psf}, \tag{17.2}$$

where the symbol $\otimes$ connotes a convolution. The equation means that every source of fluorescence in a sample is spread into the three-dimensional distribution that is the PSF (Fig. 17.3). To obtain these images, a small, 0.1-μm bead was imaged in a WFM and optical sections were collected from 4 μm below to 4 μm above the bead. Because the beads are significantly smaller than the resolution limit of the microscope (Inoué & Spring, 1997; Wallace et al., 2001), they contain no structural information visible by the WFM [see Goodman, 1996 for a thorough treatment of resolution in optics]. In the fluorescence microscope, these beads are essentially point sources and therefore reveal the PSF of the microscope. Figure 17.3 shows the PSF viewed from the side, so that the optical axis is running vertically through the center of the bead. The

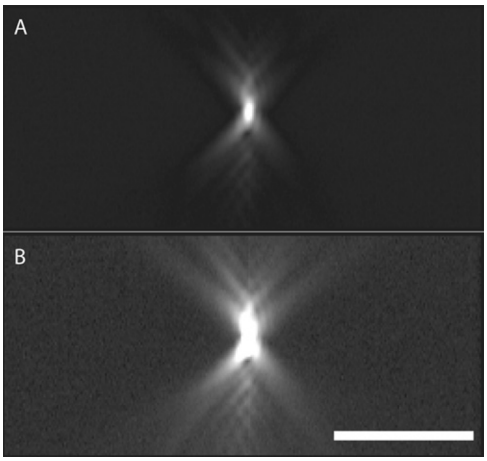

FIGURE 17.3

PSF of a high–numerical aperture lens. Optical sections of a 0.1-μm fluorescent bead were recorded with a 100 $\times$ 1.4 oil immersion lens. These were then rotated 90° to create an orthogonal (or so called "*x*–*z*" view) of the PSF. The images show a slice through the PSF where the vertical axis of the image is parallel to the optical axis of the microscope. (A) Image of PSF scaled so to show the minimum and maximum of the signal in the image. (B) The same image as (A), but scaled with a logarithmic gamut to highlight the lower-level out-of-focus information. Scale = 5 μm.

inverted cones above and below the in-focus bead are the blurred light emanating from the bead. It is clear that there is significant out-of-focus light even from a single bead. In a cell or tissue, with point sources spread throughout the sample volume, the density of blurred light can easily dominate the in-focus signal.

It is important to note that Fig. 17.3 shows a single bead in an optically clear medium. This highly idealized specimen is a far cry from the optical properties of a real specimen, especially an embryo or tissue. These samples contain significant amounts of material that can scatter light. Scattering is a random phenomenon and thus cannot be modeled using expressions similar to Eq. (17.2). For this reason, scattering can only be minimized or eliminated by changing aspects of the optical path, although there may be applications in the future where the refractive index heterogeneities that cause scattering can be measured *in situ* and corrected (Kam, Hanser, Gustafsson, Agard, & Sedat, 2001).

It is possible to use either optical or computational methods to reduce the amount of blurred light in an image. The most common optical methods involve LSCMs and MPMs. LSCMs excite the sample point by point by scanning the sample with a diffracted-limited beam and remove blurred light by passing fluorescence emission through a pinhole confocal with the specimen plane of the microscope (Inoué, 1995). MPMs also scan the sample with a diffraction-limited beam, but they limit the fluorophore excitation to a small volume by ensuring that fluorophore excitation can only

occur where the excitation light flux is highest, just at the point of focus of the scanned beam (Denk & Svoboda, 1997). A large number of methods and configurations are available, and the interested reader should consult any number of texts for a full discussion of these methods (e.g., Pawley, 1995b).

An alternative strategy involves the use of the imaging equation [Eq. (17.2)] in sophisticated image processing methods to discern in-focus and out-of-focus signal. These methods attempt to reverse the effects of convolution of the PSF in the light microscope and are thus referred to as deconvolution methods. A large number of reviews on these methods have been produced (Agard, 1984; Agard et al., 1989; McNally, Karpova, Cooper, & Conchello, 1999; Shaw, 1993; Swedlow, Sedat, & Agard, 1997; Wallace et al., 2001). The interested reader should visit these texts as well for detailed descriptions of this methodology. In this section, I discuss the general design and use of these deconvolution algorithms and their use in wide-field and spinning disk confocal fluorescence microscopy.

17.2.1 Approaches for image deblurring by deconvolution

17.2.1.1 Deblurring or neighbor-based methods

There are two general families of deconvolution algorithms. The first are known as deblurring or neighbor-based algorithms. These methods are fundamentally two-dimensional in nature: they seek to identify the contribution of out-of-focus fluorescence in each optical section and remove it. These algorithms deblur one section at a time by considering the image as a sum of the in-focus signal and the out-of-focus signal from neighboring sections. In their simplest form, they consider a given optical section and its immediate neighbors:

$$\text{image}_n = \text{object}_n \otimes \text{psf}_n + \text{object}_{n+1} \otimes \text{psf}_{n+1} + \text{object}_{n-1} \otimes \text{psf}_{n-1}, \qquad (17.3)$$

where n is the optical section number. In this treatment, each of these terms is a two-dimensional function at a specific focal plane. Given the PSF shown in Fig. 17.3, this is clearly an approximation, but it works surprisingly well, especially when a low numerical aperture lens or relatively large section spacings are used. In these cases the approximation that most of the out-of-focus signal in section n derives from section $n-1$ and $n+1$ is roughly correct.

To calculate object_n, Eq. (17.3) can be rearranged; however, it still depends on object_{n-1}, and object_{n+1}. Obviously these are not known, so to speed the calculation these values are substituted with the appropriate optical sections in the image data:

$$\text{image}_n = \text{object}_n \otimes \text{psf}_n + \text{image}_{n+1} \otimes \text{psf}_{n+1} + \text{image}_{n-1} \otimes \text{psf}_{n-1}.$$

This approximation and the limitation of the solution to only one optical section and its neighbors add error to the calculated solution for object_n. Nonetheless, neighbor-based solutions can be calculated rapidly, usually within a few seconds, and are used frequently to quickly assess an image. Because of the errors in the method, they should not be relied on to provide quantitatively accurate data. This is most easily

seen if one considers the image model in Eq. (17.3) in a sample containing a bright object four sections away from n. Using Eq. (17.3), any blurred light in section n will be considered to be "signal," with blurred signal coming from $n+1$ and $n-1$. Clearly this would produce erroneous results. For these reasons, deblurring or neighbor-based methods should not be used for quantitative analysis.

A special case for these methods arises when one is deblurring single optical sections; that is a two-dimensional image. There are many implementations of this so-called "no neighbors" deconvolution. This processing is fundamentally two-dimensional, and all structure in the image, whether deriving from a real object or from blurred fluorescence will be enhanced by this method. Again, the results from this approach can produce images with improved contrast, but these data should not be subjected to quantitative analysis.

17.2.1.2 Restoration methods

An alternative set of methods for deconvolving digital microscope images are known as restoration methods. These methods use the imaging equation [Eq. (17.2)] to obtain an estimate of the object: If the object were known or could be estimated, convolution with the PSF would generate the image data:

$$\text{image} = \hat{o} \otimes \text{psf},$$

where $\hat{o}$ represents an estimate or guess at the object. In general, these methods are iterative and progress through the following steps:

1. $\hat{i}^{(k)} = \hat{o}^{(k)} \otimes \text{psf}$
2. $\hat{o}^{(k+1)} = \hat{o}^{(k)} \frac{\text{image}}{\hat{i}^{(k)}}$
3. if $\hat{o}^{(k+1)} < 0$, then $\hat{o}^{(k+1)} = 0$
4. $k = k + 1$,

where $\hat{i}$ represents the guess after blurring with the psf and k is the iteration number. All of these functions are three-dimensional; the coordinate system (x, y, z) has been left out for simplicity.

In step 1, restoration methods start with a guess $\hat{o}^{(k)}$ at the object (usually the original data) and convolve this guess with the psf to give a blurred guess $\hat{i}^{(k)}$. In step 2, the blurred guess $\hat{i}^{(k)}$ is compared with the image data; this comparison is used to update the guess $\hat{o}^{(k)}$ to generate a new guess $\hat{o}^{(k+1)}$. The exact form of this update of $\hat{o}^{(k)}$ to $\hat{o}^{(k+1)}$ represents the major difference between different methods. Originally, a number of methods were developed, tested, and published (Agard, 1984; Agard et al., 1989; Carrington, 1990; Conchello, 1998; Schaefer, Schuster, & Herz, 2001). The form shown here in step 2 is based on the ratio of the image and $\hat{i}^{(k)}$. In step 2, the blurred guess $\hat{i}^{(k)}$ as suggested by Gold, 1964 and implemented for digital microscope images by Agard (Agard et al., 1989). In step 3, the new guess is subjected to a nonnegativity constraint: Any values in $\hat{o}^{(k+1)}$ that are less than 0 are set equal to 0. This ad hoc constraint was added to help stabilize restoration methods during their early applications (Agard, 1984). More recent analysis

indicates that this step is used infrequently in at least some methods and that eliminating it does not affect the quantitative nature of the final restored result (Swedlow et al., 2002). This is important because without the non-negativity constraint, this restoration method becomes linear. Finally, in step 4, the iteration number is increased and the process is then repeated, starting at step 1, until a stable $\hat{o}^{(k+1)}$ is achieved.

One notable extension of this approach is known as blind deconvolution, where both the object and the PSF are not known and derived from the image data (Holmes, 1992; Holmes et al., 1995). The strategy in this approach is similar to that outlined above with three main differences. First, the convolution in step 1 is performed with a guess at the PSF, which initiates with a calculated PSF based on the known imaging parameters (numerical aperture, wavelength, etc.). The update, as in many nonblind methods, is then performed using a maximum liklihood method (Holmes et al., 1995). In step 3, the guess at the object is constrained by nonnegativity, as above, but the guess at the PSF is constrained to lie within a volume described by a calculated PSF. With these constraints, blind deconvolution can be used for image restoration and is available as a commercial product from a number of vendors.

17.2.2 Image deconvolution: effects and results

The major effect of deconvolution algorithms is an improvement in the contrast in an image by a reduction in blur. Deblurring algorithms accomplish this by estimating and removing blur. Restoration algorithms generate an estimate of the object and, in so doing, partially restore blurred signal to its in focus position. This allows blurred signal to be used, to some extent at least, as in focus signal. This results in an improvement in the signal-to-noise ratio, as shown by the decrease in the coefficients of variations measured after restoration in each of the bead populations in Table 17.1. Note also that the relative intensities in an image are largely preserved after restoration (Fig. 17.1B, C), and thus, this approach preserves quantitative relationships and therefore may be used to improve image contrast in preparation for quantitative image analysis. An example of the improvement in image contrast after image restoration is shown in Fig. 17.4. There is a clear visual improvement in the contrast in the image (Fig. 17.4A, B) but also an improvement in the signal-to-noise, as shown by the line plots (Fig. 17.4C, D).

17.2.3 Image deconvolution: practical issues

Restoration is only sensibly applied to three-dimensional datasets, as they treat both the image and the PSF as a three-dimensional entity. In practice, the steps listed above are calculated by a series of Fourier transforms, as these represent a convenient and efficient way to calculate convolutions (Bracewell, 1986). The hardware requirements for these calculations, including fast CPUs and significant memory requirements (see Wallace et al., 2001) are now routinely available in desktop computers, so restoration can be used by most microscopists.

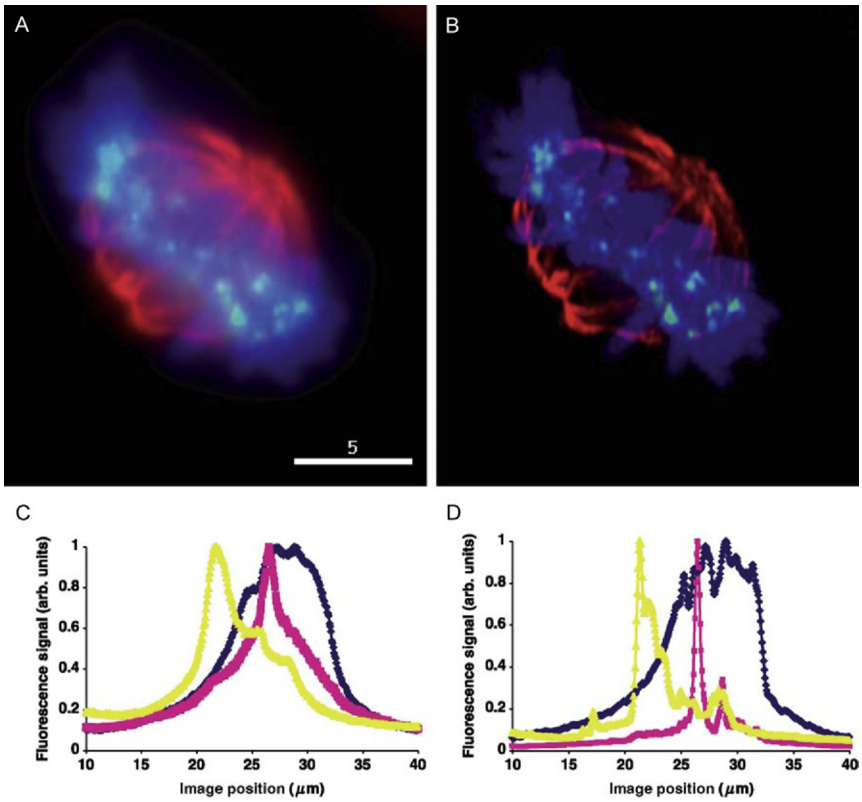

FIGURE 17.4

Restoration of images of a mitotic HeLa cell. A metaphase HeLa cell stably expressing a fusion of the aurora-B kinase and GFP was fixed with 3.7% CH_2O and stained with a mouse monoclonal antitubulin antibody and DAPI. The antitubulin was detected with an anti-mouse IgG antibody conjugated to Texas Red. Optical sections covering the whole cell were recorded with a DeltaVision Restoration Microscope (Applied Precision, LLC, Issaquah, WA) and deconvolved using a constrained iterative restoration algorithm (Swedlow et al., 1997). Images are projections through 2 μm of the data stack. (A) Image before restoration with constrained iterative deconvolution. (B) Image after restoration with constrained iterative deconvolution. (C) Line plot showing fluorescence signal values in image before deconvolution along line shown in (A). DAPI (blue), aurora-B-GFP kinase (yellow), and antitubulin (magenta) are plotted on a scale so that each graph is normalized to its maximum value. (D) Same as (C), but along identical line in deconvolved image. Note the dramatic increase in contrast.

In the last few years, restoration algorithms have been extended and developed by a number of commercial software vendors (although see http://3dmicroscopy.wustl.edu/~xcosm/ and http://www.msg.ucsf.edu/IVE/ for notable exceptions). Most of these methods remain proprietary, so it has become difficult to definitively

understand the differences between various algorithms. Besides the exact form of the update (step 2), there are many differences in the ways images are preprocessed and handled during the restoration calculation. There are a great number of implementation issues that, although not part of the actual algorithm discussed above, greatly affect the performance and speed of the algorithms (Agard et al., 1989; Swedlow et al., 1997; Wallace et al., 2001). As a user, the best strategy is to test different methods on images familiar to you and to assess the performance for yourself.

17.3 APPLICATIONS FOR IMAGE DECONVOLUTION

Image deconvolution in fluorescence microscopy has usually been applied to high-resolution imaging to improve contrast and thus detect small, dim objects that might otherwise be obscured (Dernburg et al., 1996; Femino, Fay, Fogarty, & Singer, 1998; Monks, Freiberg, Kupfer, Sciaky, & Kupfer, 1998). Because of their ability to at least partially use blurred light, restoration algorithms have been especially useful for low-light-level imaging in living cells (Carrington et al., 1995; Platani, Goldberg, Lamond, & Swedlow, 2002; Swedlow et al., 2002; Swedlow, Sedat, & Agard, 1993; Swedlow et al., 2002; Wilkie & Davis, 2001). Traditionally, these algorithms have been applied to images from WFMs, although there have been some efforts to use deconvolution algorithms on image data from LSCMs (Highett, Beven, & Shaw, 1993; Holmes et al., 1995; Shaw & Rawlins, 1991). Recently, spinning disk confocal microscopes (SDCMs) have been developed that scan the specimen with an array of beams generated by holes in a Nipkow disk (Inoue & Inoué, 2002). These microscopes generate a confocal image that can be directly viewed or projected onto a CCD camera and have recently found many applications in cell biology. Application of commercial restoration algorithms to SDCM data has proven quite effective in images from many different cell types (Boes et al., 2002; Maddox, Moree, Canman, & Salmon, 2002).

CONCLUDING REMARKS

Quantitative imaging and image deconvolution have become standard techniques for the modern cell biologist because they can form the basis of an increasing number of assays for molecular function in a cellular context. Their proper use demands some consideration of the imaging hardware, the acquisition process, fundamental aspects of photon detection, and image processing. This can prove daunting for some cell biologists, but the power of these techniques has been proven many times in the works cited in this article and elsewhere. Their usage is now well-defined, so they can be incorporated into the capabilities of most laboratories.

Acknowledgments

The work from my laboratory is supported by grants from the Wellcome Trust and Cancer Research UK. J. R. S. is a Wellcome Trust Senior Research Fellow.

References

Agard, D. A. (1984). Optical sectioning microscopy: Cellular architecture in three dimensions. *Annual Review of Biophysics and Bioengineering*, *13*, 191–219.

Agard, D. A., Hiraoka, Y., Shaw, P., & Sedat, J. W. (1989). Fluorescence microscopy in three dimensions. *Methods in Cell Biology*, *30*, 353–377.

Art, J. (1995). Photon detectors for confocal microscopy. In J. B. Pawley (Ed.), *Handbook of biological confocal microscopy* (pp. 183–196). New York: Plenum.

Boes, M., Cerny, J., Massol, R., Op den Brouw, M., Kirchhausen, T., Chen, J., et al. (2002). T-cell engagement of dendritic cells rapidly rearranges MHC class II transport. *Nature*, *418*, 983–988.

Bracewell, R. N. (1986). *The Fourier transform and its applications*. New York: McGraw-Hill.

Carrington, W. (1990). Image restoration in 3D microscopy with limited data. *Proceedings of SPIE (International Society of Optical Engineering)*, *1205*, 72–83.

Carrington, W. A., Lynch, R. M., Moore, E. D., Isenberg, G., Fogarty, K. E., & Fay, F. S. (1995). Super resolution three-dimensional images of fluorescence in cells with minimal light exposure. *Science*, *268*, 1483–1487.

Chalfie, M., Tu, Y., Euskirchen, G., Ward, W. W., & Prasher, D. C. (1994). Green fluorescent protein as a marker for gene expression. *Science*, *263*, 802–805.

Chen, H., Swedlow, J. R., Grote, M., Sedat, J. W., & Agard, D. A. (1995). The collection, processing, and display of digital three-dimensional images of biological specimens. In J. Pawley (Ed.), *Handbook of biological confocal microscopy* (pp. 197–210). New York: Plenum Press.

Conchello, J. A. (1998). Super resolution and convergence properties of the expectation-maximization algorithm for maximum-likelihood deconvolution of incoherent images. *Journal of the Optical Society of America. A*, *15*, 2609–2619.

Denk, W., & Svoboda, K. (1997). Photon upmanship: Why multiphoton imaging is more than a gimmick. *Neuron*, *18*, 351–357.

Dernburg, A. F., Broman, K. W., Fung, J. C., Marshall, W. F., Philips, J., Agard, D. A., et al. (1996). Perturbation of nuclear architecture by long-distance chromosome interactions. *Cell*, *85*, 745–759.

Femino, A. M., Fay, F. S., Fogarty, K., & Singer, R. H. (1998). Visualization of single RNA transcripts *in situ*. *Science*, *280*, 585–590.

Gibson, S. F., & Lanni, F. (1991). Experimental test of an analytical model of aberration in an oil-immersion objective lens used in three-dimensional light microscopy. *Journal of Optical Society of America*, *8*, 1601–1613.

Gold, R. (1964). An iterative unfolding method for response matrices. *Argonne National Laboratory* ANL-6984.

Goodman, J. W. (1996). *Introduction to Fourier optics*. New York: McGraw-Hill.

Highett, M. I., Beven, A. F., & Shaw, P. J. (1993). Localization of 5 S genes and transcripts in *Pisum sativum* nuclei. *Journal of Cell Science*, *105*, 1151–1158.

Holmes, T. J. (1992). Blind deconvolution of quantum-limited imagery: Maximum likelihood approach. *Journal of the Optical Society of America. A*, *9*, 1052–1061.
Holmes, T. J., Bhattacharya, S., Cooper, J. A., Hanzel, D., Krishnamurthi, V., Lin, W.-C., et al. (1995). Light microscopic images reconstructed by maximum likelihood deconvolution. In J. Pawley (Ed.), *Handbook of biological confocal microscopy* (pp. 389–402). New York: Plenum Press.
Inoué, S. (1995). Foundations of confocal scanned imaging in light microscopy. In J. Pawley (Ed.), *Handbook of biological confocal microscopy* (pp. 1–17). New York: Plenum Press.
Inoue, S., & Inoué, T. (2002). Direct-view high-speed confocal scanner: The CSU-10. *Methods in Cell Biology*, *70*, 87–127.
Inoué, S., & Spring, K. R. (1997). *Video microscopy*. New York: Plenum Press.
Kam, Z., Hanser, B., Gustafsson, M. G. L., Agard, D. A., & Sedat, J. W. (2001). Computational adaptive optics for live three-dimensional biological imaging. *Proceedings of the National Academy of Sciences of the United States of America*, *98*, 3790–3795.
Lippincott-Schwartz, J., Snapp, E., & Kenworthy, A. (2001). Studying protein dynamics in living cells. *Nature Reviews. Molecular Cell Biology*, *2*, 444–456.
Maddox, P. S., Moree, B., Canman, J. C., & Salmon, E. D. (2002). A spinning disk confocal microscope system for rapid high resolution, multimode, fluorescence speckle microscopy and GFP imaging in living cells. *Methods in Enzymology*, *360*, 597–617.
McNally, J. G., Karpova, T., Cooper, J., & Conchello, J. A. (1999). Three-dimensional imaging by deconvolution microscopy. *Methods*, *19*, 373–385.
Monks, C. R., Freiberg, B. A., Kupfer, H., Sciaky, N., & Kupfer, A. (1998). Three-dimensional segregation of supramolecular activation clusters in T cells. *Nature*, *395*, 82–86.
Murray, J. M. (1998). Evaluating the performance of fluorescence microscopes. *Journal of Microscopy*, *191*, 128–134.
Patterson, G., Day, R. N., & Piston, D. (2001). Fluorescent protein spectra. *Journal of Cell Science*, *114*, 837–838.
Pawley, J. B. (1994). The sources of noise in three-dimensional data sets. In J. Stevens (Ed.), *Three-dimensional confocal microscopy* (pp. 47–94). New York: Academic Press.
Pawley, J. (1995a). Fundamental limits in confocal microscopy. In J. Pawley (Ed.), *Handbook of biological confocal microscopy* (pp. 19–37). New York: Plenum Press.
Pawley, J. (1995b). *Handbook of confocal microscopy* (2nd ed.). New York: Plenum Press.
Platani, M., Goldberg, I., Lamond, A. I., & Swedlow, J. R. (2002). Cajal body dynamics and association with chromatin are ATP-dependent. *Nature Cell Biology*, *4*, 502–508.
Russ, J. C. (1992). *The image processing handbook*. Boca Raton, FL: CRC Press.
Schaefer, L. H., Schuster, D., & Herz, H. (2001). Generalized approach for accelerated maximum likelihood based image restoration applied to three-dimensional fluorescence microscopy. *Journal of Microscopy*, *204*, 99–107.
Shaw, P. J. (1993). Computer reconstruction in three-dimensional fluorescence microscopy. In D. Shotton (Ed.), *Electronic light microscopy* (pp. 211–230). New York: Wiley-Liss.
Shaw, P. J., & Rawlins, D. J. (1991). The point-spread of a confocal microscope: Its measurement and use in deconvolution of 3-D data. *Journal of Microscopy*, *163*, 151–165.
Sheppard, C. J. R., Gan, X., Gu, M., & Roy, M. (1995). Signal-to-noise in confocal microscopes. In J. B. Pawley (Ed.), *Handbook of biological confocal microscopy* (pp. 363–402). New York: Plenum.
Silver, R. B. (1998). Ratio imaging: Practical considerations for measuring intracellular calcium and pH in living tissue. *Methods in Cell Biology*, *56*, 237–251.

Stearns, T. (1995). Green fluorescent protein. The green revolution. *Current Biology*, *5*, 262–264.

Swedlow, J. R., Hu, K., Andrews, P. D., Roos, D. S., & Murray, J. M. (2002). Measuring tubulin content in *Toxoplasma gondii*: A comparison of laser-scanning confocal and wide-field fluorescence microscopy. *Proceedings of the National Academy of the United States of America*, *99*, 2014–2019.

Swedlow, J. R., & Platani, M. (2002). Live cell imaging using wide-field microscopy and deconvolution. *Cell Structure and Function*, *27*, 335–341.

Swedlow, J. R., Sedat, J. W., & Agard, D. A. (1993). Multiple chromosomal populations of topoisomerase II detected *in vivo* by time-lapse, three-dimensional wide field microscopy. *Cell*, *73*, 97–108.

Swedlow, J. R., Sedat, J. W., & Agard, D. A. (1997). Deconvolution in optical microscopy. In P. A. Jansson (Ed.), *Deconvolution of images and spectra* (pp. 284–309). New York: Academic Press.

Tsien, R. Y. (1998). The green fluorescent protein. *Annual Review of Biochemistry*, *67*, 509–544.

Tsien, R. Y., & Waggoner, A. (1995). Fluorophores for confocal microscopy: Photophysics and photochemistry. In J. B. Pawley (Ed.), *Handbook of biological confocal microscopy* (pp. 267–280). New York: Plenum.

Wallace, W., Schaefer, L. H., & Swedlow, J. R. (2001). A working person's guide to deconvolution in light microscopy. *BioTechniques*, *31*, 1076–1097.

Wilkie, G. S., & Davis, I. (2001). *Drosophila* wingless and pair-rule transcripts localize apically by dynein-mediated transport of RNA particles. *Cell*, *105*, 209–219.

Zucker, R. M., & Price, O. (2001). Evaluation of confocal microscopy system performance. *Cytometry*, *44*, 273–294.

CHAPTER

Practical Aspects of Quantitative Confocal Microscopy

18

John M. Murray

Department of Biology, Indiana University, Bloomington, Indiana, USA

CHAPTER OUTLINE

Introduction **428**
18.1 Setting Up for Quantitative Imaging **428**
18.1.1 Spot-Scanning Confocals 428
18.1.2 Disk-Scanning or Swept-Array Confocals 430
18.2 Correcting Nonuniformities (Flat Fielding) **430**
18.2.1 Additive Correction 430
18.2.2 Multiplicative Correction 431
18.3 Limitations to Exact Quantitation **432**
18.3.1 Limitations on Accuracy 432
18.3.2 Limitations on Precision 433
18.4 Evaluating and Comparing Performance **438**
References **440**

Abstract

Confocal microscopes are in principle well suited for quantitative imaging. The 3D fluorophore distribution in a specimen is transformed by the microscope optics and detector into the 2D intensity distribution of a digital image by a linear operation, a convolution. If multiple 2D images of the specimen at different focal planes are obtained, then the original 3D distribution in the specimen can be reconstructed. This reconstruction is a low-pass spatially filtered representation of the original, but quantitatively preserves relative fluorophore concentrations, with of course some limitations on accuracy and precision due to aberrations and noise. Given appropriate calibration, absolute fluorophore concentrations are accessible. A few simple guidelines are given for setting up confocal microscopes and checking their performance. With a little care, the images collected should be suitable for most types of quantitative analysis.

Methods in Cell Biology, Volume 114
ISSN 0091-679X
http://dx.doi.org/10.1016/B978-0-12-407761-4.00018-X
Copyright © 2013 Elsevier Inc. All rights reserved.

INTRODUCTION

In principle, confocal microscopes should be capable of generating excellent quantitative data. The 3D fluorophore distribution in a specimen is transformed by the microscope optics and detector into the 2D intensity distribution of a digital image by a linear operation, a convolution. If multiple 2D images of the specimen at different focal planes are obtained, then a low-pass spatially filtered representation of the original 3D distribution in the specimen can be reconstructed in a way that quantitatively preserves relative fluorophore concentrations, with of course some limitations on accuracy and precision due to aberrations and noise. Given appropriate calibration, absolute fluorophore concentrations are accessible.

To retain in the images all of the quantitative information passed by the microscope, it is necessary to set up the system properly, but fortunately this is easy to do.

18.1 SETTING UP FOR QUANTITATIVE IMAGING

18.1.1 Spot-scanning confocals

Spot-scanning confocals typically utilize PMT detectors, for which the gain is continuously adjustable over an enormous range by changing the voltage applied to the dynode chain. The gain (PMT voltage) must be set carefully on these instruments to avoid detector saturation. In addition, there is an "offset" or "dark adjust" that needs to be set to avoid detector underflow. Finally, the laser power must be set low enough to avoid depopulating the ground state of the fluorophore. If significant ground-state depletion occurs, then fluorescence emission does not increase linearly with illumination intensity (Fig. 18.1). Note that ground-state depletion will be much more severe for molecules in the focal plane than for those slightly displaced in Z, due to the rapid falloff of illumination intensity with Z when using a high numerical aperture objective lens. In this situation, fluorophores in the focal plane will give rise to less fluorescence than expected and be underrepresented in the image relative to fluorophores out of the focal plane. In other words, ground-state depletion destroys the quantitative relationship between image intensities and the fluorophore distribution in the specimen.

Here is a recipe for setting up the PMT detector and laser for quantitative imaging and for ensuring that the damage to the sample due to photobleaching or phototoxicity is within acceptable limits.

For this preliminary setup, choose an area of the intended specimen that is equivalent to the area to be imaged, but is not the best area. (It may be destroyed during this setup phase). Steps 4–7 will probably have to be iterated several times to optimize all the parameters.

1. Choose the appropriate filters/laser line combination.
2. Decide what pixel spacing is required to obtain the information needed from this particular sample and set the magnification/electronic zoom factor accordingly. Do not oversample (i.e., pixel spacing should be close to the Nyquist limit).

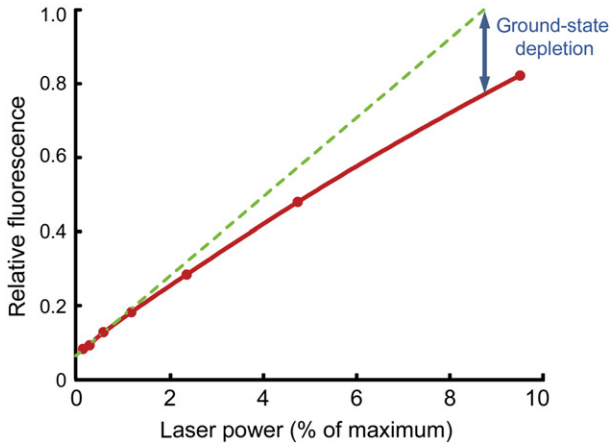

FIGURE 18.1

Nonlinear response of emitted fluorescence to illumination intensity. At low illumination intensity, fluorescence emission increases in strict proportion to laser power. At higher intensity, emitted fluorescence (solid red line) is less than predicted (green dashed line), because the population of molecules in the ground state has been depleted.

3. Get a ballpark estimate for the imaging parameters: set the pinhole diameter initially to be ~1 Airy disk. Set the PMT voltage to maximum. Set the laser to the minimum intensity that gives a decent signal at this PMT voltage.
4. Find the linear range of the *detector*. To display the images, use an LUT that highlights underflow and overflow in color, but is grayscale in between.
   a. Define the baseline: scan with the laser off at the scan speed to be used for data collection and set the offset/dark adjust so that the screen intensity is minimized, but there are no pixels at zero intensity.
   b. Define the maximum intensity: find a region of the specimen that is likely to be the brightest, and with the laser on, decrease the PMT voltage until the average intensity is ~75% of the maximum, or lower if necessary to keep the fraction of saturated pixels insignificant.
5. Find the linear range for the *specimen*: check that the recorded fluorescence emission increases linearly with increase in laser power up to at least twice the intensity to be used for imaging. If the fluorescence does not increase exactly in proportion to laser power (i.e., ground-state depletion is occurring), one must sacrifice temporal resolution (work with lower laser power and longer scan times) or spatial resolution (decrease laser power and increase pinhole size, increase pixel size), or both.
6. Determine the exposure required to achieve an acceptable image quality (i.e., adjust the scan speed (pixel dwell time) and number of scans averaged per frame

to achieve an SNR that is adequate for the intended observations or measurements).

7. Check that the level of illumination is below the "unacceptable damage" threshold: with the laser set to the intensity to be used for data collection, monitor the intensity in a selected small area of the specimen over the course of numerous repeated scans. One would like to be able to scan long enough to collect all the needed information before the cumulative photobleaching reaches 50% (probably <20% for live cells). If the fluorescence is bleaching too much, you will have to sacrifice spatial resolution (increase pixel size, decrease laser power) or photometric resolution (decrease laser power, dwell time, or number of scans averaged per frame), or both. For time-lapse imaging, one may also have to sacrifice time resolution (work with lower laser power and longer intervals between time points).

18.1.2 Disk-scanning or swept-array confocals

Confocals in which multiple spots of illumination are used in parallel, such as disk-scanning or "swept-field" instruments, typically use CCD cameras as detectors. The gain on these detectors is adjustable over a much smaller range, and the number of photons needed to saturate the detector at typical gain levels is much higher than for PMT detectors, making detector saturation much less of a problem for most specimens. Additionally, because the illumination is split among thousands of spots instead of being focused into a single spot, it is difficult to achieve laser powers sufficient to cause significant ground-state depletion. Setup of these instruments is thus much simpler than for spot-scanning confocals. It is necessary merely to choose a combination of image integration time and laser power that limits the intensities recorded from the brightest regions of the specimen to something less than the detector full-well value (i.e., less than 4095 for a 12-bit CCD camera).

18.2 CORRECTING NONUNIFORMITIES (FLAT FIELDING)

Ideally, the proportionality factor relating fluorophore concentration in the specimen to digital intensity in the image would be a constant, but in practice small variations in this factor over the field of view are common. Corrections for these nonuniformities can and should be applied before the image data are used for quantitative purposes. In general, two types of corrections need to be applied, one additive and the other multiplicative.

18.2.1 Additive correction

Additive corrections are applied to compensate for nonuniformities that are independent of local image intensity. Figure 18.2 shows examples for PMT and CCD detectors. To measure this nonuniformity, an image is collected with the illumination off

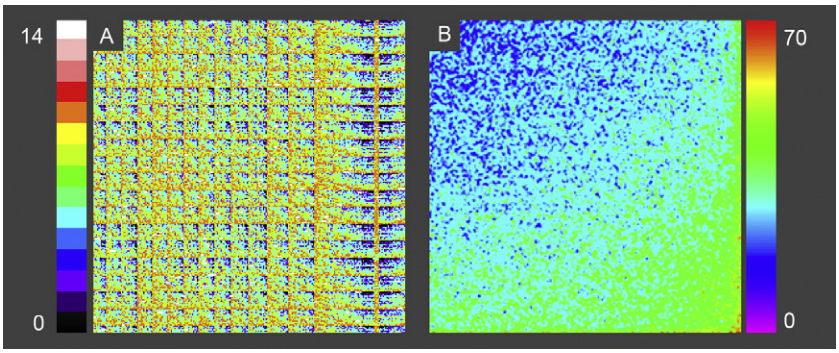

FIGURE 18.2

Dark-current images from spot-scanning and disk-scanning confocal. (A) 250 × 250 pixel region from an image collected on the Zeiss LSM510 spot-scanning confocal, showing patterned noise artifacts in the dark current. Displayed intensities range from 0 to 14 counts (255 maximum). (B) 512 × 512 pixel image from a CCD detector showing a "hot-spot" with higher dark current in the lower right corner. Displayed intensities range from 0 to 70 counts (4095 maximum).

(a "dark current" image). This image is first scaled to match the exposure time used for collecting the real data, then subtracted from each image in the dataset. This correction procedure is straightforward for CCD detectors, but often problematic for PMT detectors because the nonuniformities arise from periodic noise in the detector electronics and give rise to patterned fluctuations (Fig. 18.2A) that shift position with every frame. Hence, the particular pattern of nonuniformities observed in the "dark current" image is unlikely to match the pattern in the data images. Fortunately, with proper adjustment of the offset, the size of the nonuniformities in PMT dark current is usually small compared to the noise in the data.

18.2.2 Multiplicative correction

Multiplicative corrections are applied to compensate for nonuniformities that are proportional to local image intensity. This type of nonuniformity is measured by collecting an image of a *thin* (e.g., <1 μm thick) sample known to have a spatially uniform distribution of fluorophore. It is important to maximize the SNR in the image of this specimen, for example, by using the longest possible exposure length while avoiding detector saturation. It is also critical to use exactly the same magnification, position within the field of view, and pinhole size as used for the real data. Figure 18.3 shows examples for CCD- and PMT-based instruments. Nonuniformities of this type are common due to defects in the optics of the system that lead to variation in illumination intensity across the field of view. Nonuniform transmittance of emitted fluorescence to the detector is also frequent, due to deviations from precise

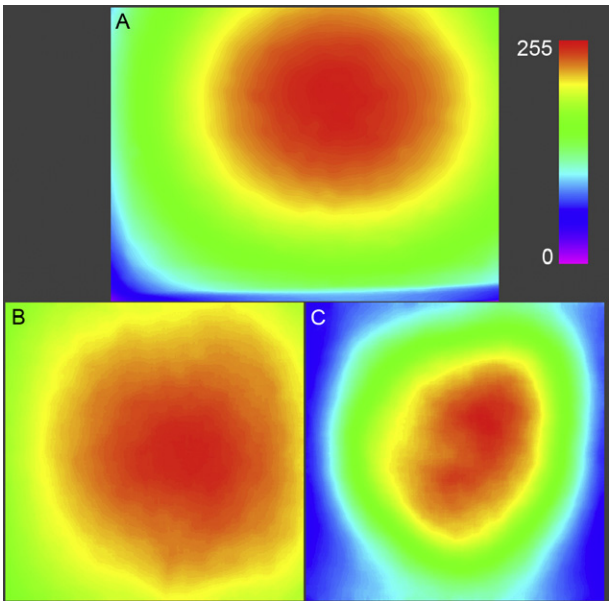

FIGURE 18.3

Images of a uniformly fluorescent thin specimen from a scanning disk (A) and spot-scanning confocal with completely open pinhole (B) or pinhole set to 1 Airy disk radius (C).

superposition of the illuminated and detected focal spots. Nonuniformity arising from the latter characteristically worsens with increasing lens N.A. and decreasing pinhole diameter. Single-pixel defects in CCD chips are also common. The image of the uniformly fluorescent specimen is adjusted by applying any necessary additive corrections and then normalized so that the local average in the brightest region of the image has a value of 1.0. To avoid nonsensical values in the division to follow, it is prudent to trim extremely low or extremely high pixels in the normalized result (e.g., enforce a minimum value of 0.1 and a maximum of 10). Each image of the specimen dataset is adjusted by the additive correction discussed above, and then divided by this trimmed, normalized image of the uniform specimen.

18.3 LIMITATIONS TO EXACT QUANTITATION

18.3.1 Limitations on accuracy

If nonlinearities due to ground-state depletion are avoided, then the remaining significant photometric inaccuracy results from residual aberrations in the objective lens, particularly axial and lateral chromatic aberration, and errors in the scanning hardware that lead to variation in pixel dwell time across the field of view. Confocal

microscopes are particularly susceptible to chromatic aberrations (Keller, 1995; Sandison, Williams, Wells, Strickler, & Webb, 1995). The effect is to dramatically attenuate image intensities in a non-uniform way across the field of view, generally worsening with distance from the optical axis. The pattern of attenuation often differs for different emission wavelengths.

Most errors due to the scanning hardware will be compensated by the flat-fielding corrections described above. If the specimen is very thin (so thin that using a confocal microscope would not be sensible), the multiplicative correction described above will also suffice to compensate for the effects of chromatic aberration. However, for a specimen thicker than a micron or so, curvature of field interacts with axial and lateral chromatic aberration so as to make it impossible to compensate completely for their effects unless the precise 3D distribution of fluorophore in the specimen is already known, a situation that would seem to render microscopy superfluous. A more detailed description of this problem is given in Chapters 5 and 7 of Pawley (1995).

18.3.2 Limitations on precision

In considering the images obtained from a confocal microscope, the question of whether their quality can be improved will always be faced if the goal is to use the images for quantitative analysis. The defect that is most likely to interfere with quantitative applications is the limited SNR in confocal images, particularly from spot-scanning confocals. In principle, the SNR achieved in an image of a fluorescent specimen ought ultimately to be limited only by the inevitable Poisson noise associated with stochastic absorption, excitation, and reemission of a finite number of photons. The highest achievable SNR in a single image will therefore never be greater than the square root of the number of photons/pixel in the image. An upper limit to the achievable SNR is set by $\sqrt{W}$, where W is the "well capacity," the number of photons/pixel at detector saturation.

In practice, other sources of noise are usually present, degrading the SNR to something less than $\sqrt{W}$. The total noise in an image can be thought of as the sum of a component that increases in proportion to the exposure time or signal (e.g., Poisson or "shot" noise from signal, background, and dark current) plus an exposure-independent component (e.g., camera read noise). These noise components can also be characterized as "inescapable" (Poisson noise arising from the signal itself) and "possibly avoidable" (all other sources). Therefore, in order to determine what the limits on precision in the data ought to be, that is, how much of the noise in a dataset is "inescapable," it is clearly necessary to know how many photons went into making the image.

For a Poisson distribution, variance is numerically equal to mean. If the digital intensity values were numerically equal to the number of photons arriving at each image pixel, then the image variances ("noise" squared) would equal the average intensity, and the expected SNR would be simply the square root of the image intensities $\left(\text{SNR} = S/N = S/\sqrt{S} = \sqrt{S}\right)$ However, the digital intensity values are related to the number of arriving photons by an unknown proportionality factor. One needs to know this proportionality factor in order to decide how many photons contributed

to the image, information that is necessary to decide whether the observed noise in the image is the inescapable Poisson minimum, or whether one could do better. The purpose of this section is to describe how that proportionality factor can be measured.

Not every photon that arrives at the detector actually contributes to the image. Some photons are simply not detected. The quantum efficiency (QE) relates the number of photons arriving at the detector to the number of *countable events* (defined below). The QE is always less than 1; some photons are simply not detected at all and do not give rise to a *countable event*. A graph of QE versus wavelength is usually on the specification sheet provided by the detector's manufacturer.

A *countable event* for a CCD detector is the generation of a photo-electron in the CCD chip; for a PMT, a *countable event* is a pulse of electrons exiting the end of the dynode chain in response to a photon absorbed at the photocathode. For either type of detector, the number of *countable events* in a given time interval is simply a constant fraction (the QE) of the number of photons arriving in that interval, and thus fluctuates stochastically as does the number of arriving photons. In both the CCD- and PMT-based instruments, additional electronics downstream of the detector convert *countable events* to the digital number that is output for each pixel. The proportionality factor relating number of *countable events* to output digital value is the effective *scaling* imposed by this additional electronics, that is, the number of *countable events* that corresponds to an increment of 1 in the digital output value.

One can determine the product of *scaling* (call it $\boldsymbol{c}$) and QE (which we will denote as $\boldsymbol{e}$) by measuring the relationship between the mean and variance of pixel intensities. For a true Poisson variate, such as the number of arriving photons, the variance is equal to the mean. However, only a fraction $\boldsymbol{e}$ of the arriving photons gives rise to *countable events*, and this number is then scaled by $\boldsymbol{c}$ to give the digital intensity value in the output image. Thus, the variance computed from image digital intensity values is related to the Poissonian variance of arriving photon numbers by $\boldsymbol{e^2c^2}$ The *slope* of a graph of variance versus average digital intensity has the value ($\boldsymbol{ec}$); the reciprocal of the *slope* is the number of arriving photons needed for a digital intensity increment of 1. The *y-intercept* of the graph can be used to find the sum of all noise components not correlated with the signal.

The protocol for collecting the needed data is described separately below for CCD- and PMT-based confocals.

1. for a CCD detector:
   - **a.** With no light going to the camera (room lights and any nearby computer monitors off, laser off), but microscope otherwise configured as for image collection, acquire an image with very short (e.g., 10 ms) exposure. Find the mean intensity of this image. This is the "offset," a constant value (i.e., variance = 0), independent of exposure time and image intensity.
   - **b.** Turn the laser on. Adjust the laser power to give an image intensity just above background noise with a 10-ms exposure.
   - **c.** Acquire two images in rapid succession with a 10-ms exposure, changing nothing in between. These two images should be identical so that any

difference between them can be attributed to noise. First find the *average pixel intensity* in the images (call it $\boldsymbol{D}$). Then subtract one image from the other. Add a constant to avoid negative values (e.g., image1 − image2 + 1000). Find the standard deviation of this difference image, square it, and divide by 2. This number is the *variance* of a single pixel in the image.

d. Repeat this acquisition and calculation for pairs of images taken at 20, 40, 80, 160 ms. . ., up to ~70% of detector saturation.

e. Plot *variance* versus ($\boldsymbol{D} - \mathit{offset}$) and from the least squares fit of a straight line, obtain the *slope* ($\boldsymbol{ec}$) and *intercept*.

f. The arithmetic:

$\mathbf{P}$ = average number of arriving photons/pixel (variance = $\mathbf{P}$)

$\boldsymbol{r}$ = exposure-independent noise (countable events/pixel)
(average = 0, variance = $\boldsymbol{r}^2$)

$\boldsymbol{D}$ = average pixel intensity, as a digital number (gray-levels)

$1/\boldsymbol{c}$ = number of countable events needed to give an increment of 1 in the digital intensity value

$\boldsymbol{e}$ = detector quantum efficiency

$$\boldsymbol{D} = \boldsymbol{ec}\mathbf{P} + \langle \boldsymbol{cr} \rangle + \mathit{offset} = \boldsymbol{ec}\mathbf{P} + \mathit{offset}$$

$$\text{variance of } \boldsymbol{D} = \boldsymbol{e}^2\boldsymbol{c}^2\mathbf{P} + \boldsymbol{c}^2\boldsymbol{r}^2 \qquad = \boldsymbol{ec}(\boldsymbol{D} - \mathit{offset}) + \boldsymbol{c}^2\boldsymbol{r}^2$$

To calculate the exposure-independent noise, one must know the value of $\boldsymbol{e}$ (QE, usually available from the manufacturer's spec sheet):

$\boldsymbol{r}$ = (QE × sqrt[*intercept*])/*slope*

If this value is much larger than the camera read noise, then avoidable extra noise is being added to the images, and some detective work is needed to find the source (Fig. 18.4).

2. for a PMT detector:

The protocol is messier than for the CCD detector. Due to the large fluctuations in illumination intensity in most spot-scanning confocals (Swedlow, Hu, Andrews, Roos, & Murray, 2002), one cannot use the system lasers as illumination for this test (i.e., a significant amount of the noise correlated with the signal would be due to the laser fluctuations, rather than Poisson noise). The quartz-halogen lamp used for visual transmitted light observation and the mercury arc lamp used for visual epifluorescence observation are also unsuitable due to residual line frequency (60 or 120 Hz) modulation of their output. A stable illumination source can be obtained by simply positioning a battery powered incandescent light source (e.g., a flashlight with a heated filament bulb, NOT an LED) over the objective. Unfortunately, the output of this type of light source is not easily controlled, so the number of photons reaching the PMT must be varied by some other method. With a little trial and error

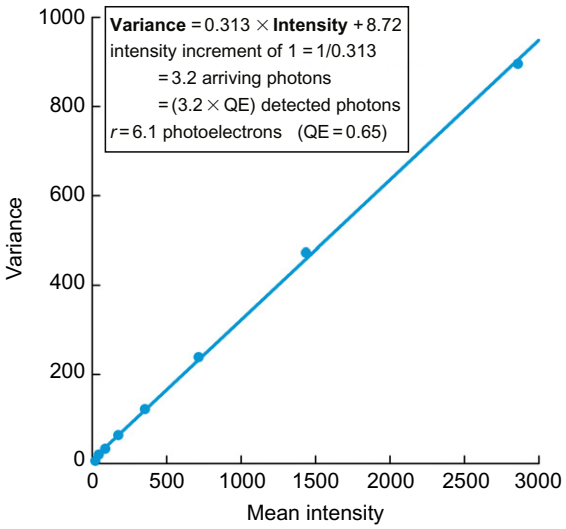

FIGURE 18.4

Calibration of a CCD detector by measuring variance as a function of intensity.

experimentation, the required wide range of signal intensities can usually be achieved by combining different pinhole diameters with different dichromatic mirrors and emission filters. The final complication is that the measurement needs to be done for different PMT voltages spanning the range normally used for real specimens (Figs. 18.5 and 18.6).

Here is a recipe for collecting the needed data:

For display of the images, use a "pseudocolor" LUT that highlights underflow and overflow in color, but is grayscale in between. It is also extremely useful to display a continuously updated histogram of image pixel intensities.

a. With no light input, but with the microscope otherwise configured as for image collection, acquire an image. Find the mean intensity of this image. This is the "*offset*," a constant value (i.e., variance = 0), independent of exposure time and image intensity. Use the "offset adjust" or "dark current" controls to make this value small (<10), but with no zero pixels. Repeat this measurement for different PMT voltages over the range commonly used for data collection with real specimens. The *offset* will probably be nearly the same over this range.

b. Turn the light source on. Set the PMT voltage to the lowest value used for any specimen. Adjust the position of the flashlight, the filters, the pinhole diameter, and other parameters to give an average intensity of ~80% saturation.

c. Scan two images in rapid succession and store them. Adjust the filter, light source, or pinhole to decrease the average intensity ~2-fold, and collect another pair of images. Repeat with average intensities of ~20%, 10%, and 5% of saturation.

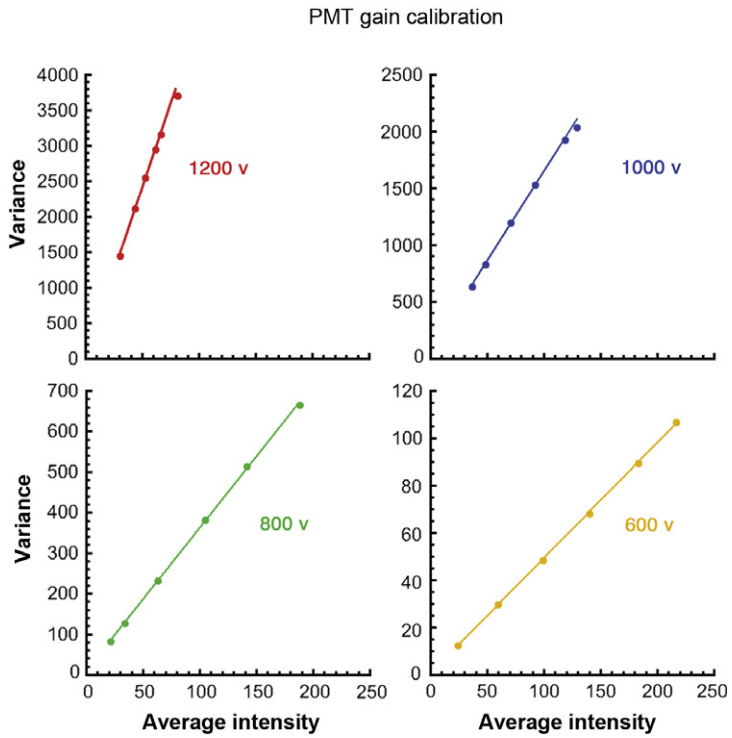

FIGURE 18.5

Plots of data used to calibrate the gain of a PMT. Image variance was measured as a function of image intensity for four different PMT voltage settings.

d. These pairs of images should be identical, so any difference between them can be attributed to noise. First find the average intensity in each pair (=***D***). Subtract one member of each pair from the other, adding a constant to avoid negative values (e.g., image1 − image2 + 128). Find the standard deviation of this difference image, square it, and then divide by 2. This number is the *variance* of ***D***.

e. Plot the *variance* versus (***D*** − *offset*), and obtain the slope (***e*** × ***c***) and *intercept* of the best straight line through the data.

f. Repeat steps (b)–(e) for 5 or 6 PMT voltages spanning the range normally used for real specimens. As the PMT voltage is increased, the range of intensities will need to be drastically reduced (e.g., average intensity restricted to 5–20% of maximum) in order to avoid detector saturation. The proportion of saturated pixels (intensity = 255 or 4095 for 8-bit or 12-bit digitization) should be kept below 2%.

g. Plot log(1/(***e*** × ***c***)) versus PMT voltage. The data fall on a gently curved line, with curvature low enough that linear interpolation is sufficient to generate values for PMT voltages between the data points.

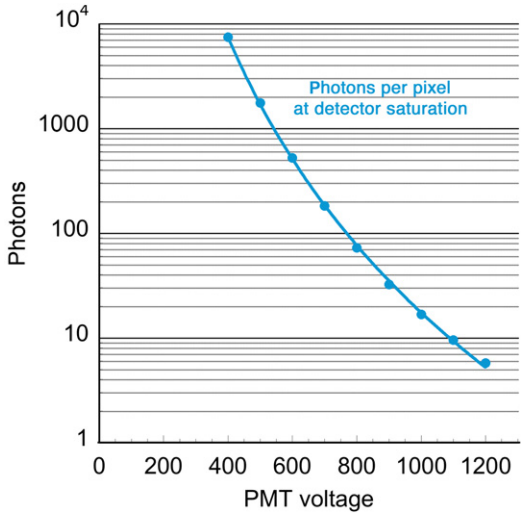

FIGURE 18.6

Calibration of a PMT detector. The number of photons required to give the maximum pixel intensity value is plotted as a function of voltage applied to the PMT. Note that at the highest voltage, only ~6 photons are needed to saturate the detector.

18.4 EVALUATING AND COMPARING PERFORMANCE

It is valuable to have an assay for evaluating the performance of a confocal microscope and for comparing the performance of different systems. Better performance may be defined as achieving a higher "image quality" at equivalent 3D resolution under the constraints imposed by working with typical living biological specimens. Some useful measures of image quality include image contrast, SNR, and the precision of quantitative measurements based on image pixel intensities. The constraints imposed by biological specimens include the PSF-degrading effects of specimen thickness, the need to efficiently remove out-of-focus background, and, most importantly, the limitations imposed on illumination time–intensity by photobleaching and phototoxicity. Clearly, if there were no restrictions on the illumination dose that could be used, then, other things being equal, longer exposure, and brighter illumination would give higher image SNR, up to the limit allowed by maximum detector capacity. Thus, performance criteria must include the overall efficiency of photon acquisition, and comparisons between systems must be carried out with equal dosage of illumination.

An assay that satisfies these requirements has been described in detail elsewhere (Murray, Appleton, Swedlow, & Waters, 2007). Briefly, the approach is to acquire images at high magnification of fluorescent beads that are small relative to the resolving power of the microscope and are labeled with both a red and a green fluorophore. The beads are mounted over a solution of the green fluorophore whose concentration is adjusted to give a level of out-of-focus background comparable

to that seen with biological specimens. The illumination system on each microscope is calibrated by measuring the photobleaching of a standardized specimen, whose photobleaching is a measure of the illumination time-irradiance integral. When this time-irradiance integral is held constant, the quality of the images of the small fluorescent beads becomes a system-independent measure of the performance that is sensitive to light throughput, 3D resolution, background removal, and intrinsic noise.

Figure 18.7 shows a montage of typical images of the fluorescent beads obtained from different types of microscopes at various concentrations of background fluorophore. Those measurements revealed that the precision of all types of digital microscope imaging systems used for 3D microscopy could be substantially improved. Improvements in precision would immediately increase the value of these systems for live-cell imaging, where the loss of precision typically cannot be compensated by collecting more photons.

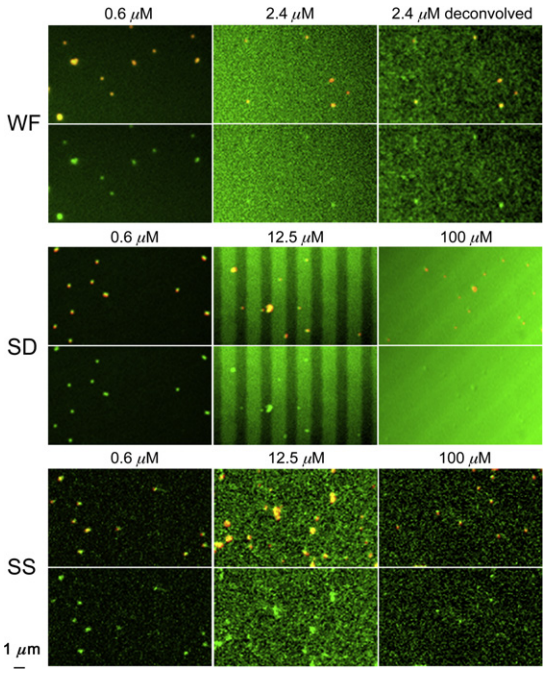

FIGURE 18.7

Montage of images of beads with different amounts of out-of-focus fluorescence from widefield (WF), spinning disk (SD), and spot-scanning (SS) confocal microscopes. The concentration of green fluorophore in the background solution is given above each image. For this figure, nonlinear contrast stretching has been employed to optimize single bead visibility in the green channel in the images with high background. The smallest objects visible in the red channel are single beads. Larger objects are clusters of multiple beads.

Adapted from Murray et al. (2007).

References

Keller, H. E. (1995). Objective lenses for confocal microscopy. In J. B. Pawley (Ed.), *Handbook of biological confocal microscopy* (pp. 111–126). New York: Plenum.

Murray, J. M., Appleton, P. L., Swedlow, J. R., & Waters, J. C. (2007). Evaluating performance in three-dimensional fluorescence microscopy. *Journal of Microscopy*, *228*, 390–405.

Pawley, J. B. (1995). *Handbook of biological confocal microscopy*. New York: Plenum Press.

Sandison, D. R., Williams, R. M., Wells, K. S., Strickler, J., & Webb, W. W. (1995). Quantitative fluorescence confocal laser scanning microscopy (CLSM). In J. B. Pawley (Ed.), *Handbook of biological confocal microscopy* (pp. 39–53). New York: Plenum.

Swedlow, J. R., Hu, K., Andrews, P. D., Roos, D. S., & Murray, J. M. (2002). Measuring tubulin content in Toxoplasma gondii: A comparison of laser-scanning confocal and wide-field fluorescence microscopy. *Proceedings of the National Academy of Sciences of the United States of America*, *99*, 2014–2019.

CHAPTER

19 Theoretical Principles and Practical Considerations for Fluorescence Resonance Energy Transfer Microscopy

Richard A. Cardullo

Department of Biology, The University of California, Riverside, California, USA

CHAPTER OUTLINE

Introduction **442**
19.1 Principles and Basic Methods of FRET **442**
19.1.1 Basic Principles of Nonradiative FRET 442
19.1.2 Methodologies for Measuring Transfer Efficiencies in Solutions 444
19.1.3 Practical Considerations for all FRET Measurements 447
19.2 FRET Microscopy **448**
19.2.1 The Microscope 449
19.2.2 Fluorescence Illumination 450
19.2.2.1 Light Sources 450
19.2.2.2 Wavelength Selectors 451
19.2.2.3 Detectors 452
19.2.3 Typical FRET Systems: CFP–YFP as an Example 453
19.2.3.1 A Steady-State FRET System 454
19.2.3.2 Fluorescence Lifetime FRET Systems: Time Versus Frequency Domains 454
Conclusions **455**
Acknowledgments **455**
References **455**

Abstract

Typically, light microscopic methodologies using conventional optics are limited by the diffraction limit yielding resolutions that cannot be reached lower than approximately 200 nm. However, using appropriate donor–acceptor pairs, nonradiative fluorescence resonance energy transfer (FRET) allows the microscopist to detect,

Methods in Cell Biology, Volume 114 **ISSN 0091-679X**
Copyright © 2007 Elsevier Inc. All rights reserved.
http://dx.doi.org/10.1016/B978-0-12-407761-4.00019-1

and in some cases quantify, molecular interactions on the order of Angstroms. In this chapter, the basic principles of FRET are introduced using both steady state and lifetime modes to detect the close association of fluorescent donor and acceptor molecules. The basic design of experiments and optical and imaging components is discussed to create a microscope that is capable of monitoring dynamic molecular associations in living cells.

INTRODUCTION

As discussed elsewhere in this volume, the resolution of the light microscope is limited by diffraction and is, at best, about 0.2 μm. On a molecular scale this translates to a distance of 2000 Å (200 nm), which means that resolving molecular interactions is an impossible feat using a light microscope. On the other hand, using fluorescence intensity information, one is able to quantitatively detect molecular interactions and motions. Perhaps the most powerful tool for this purpose is nonradiative fluorescence resonance energy transfer (FRET) which can quantitatively detect associations between molecules with Angstrom resolution. Until recently, this methodology has been restricted to populations of molecules using steady-state fluorimeters or lifetime instruments. However, with recent technological advances in microscopes, light source, and detectors, FRET is now possible within single cells.

In the first part of this chapter, the basic principles of FRET will be described focusing on both steady-state and time-resolved methodologies. The second part of the chapter will discuss different kinds of FRET microscopes, emphasizing the specific pieces of equipment that are required for making quantitative or qualitative determinations of molecular associations.

19.1 PRINCIPLES AND BASIC METHODS OF FRET

Nonradiative FRET is a quantum mechanical phenomenon that occurs between two fluorescent molecules. The precise way in which these molecules interact allows distance measurements to be made on a molecular scale. In this section, we introduce the basic concepts of FRET at a simple level. A more detailed treatment can be found elsewhere (Cardullo, 1992, Cardullo, 2002).

19.1.1 Basic principles of nonradiative FRET

The method of nonradiative FRET allows separation between fluorescent molecules to be made with Angstrom resolution over distances between 10 and 100 Å. The technique was first conceived of by Förster, 1959, for historical review) and has been used to measure intra- and intermolecular distances between, for instance, different reactive sites on a protein, proteins and lipids in a model system, or proteins on the cell surface. Because of its sensitivity over molecular distances, the technique has been dubbed "the spectroscopic ruler" (Stryer & Haugland, 1967). Although

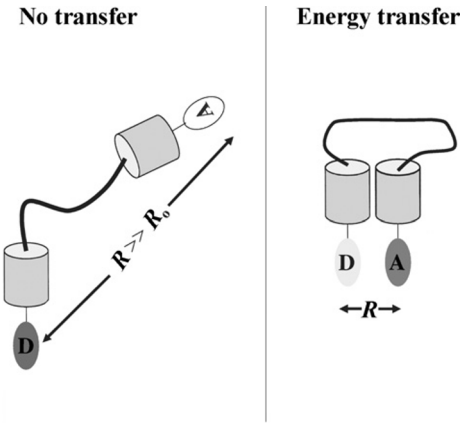

FIGURE 19.1

Principle of FRET between a donor molecule, D, and an acceptor molecule, A. In this case, a single macromolecule (such as a protein) is labeled with both D and A. Initially, D and A are separated by a sufficiently large distance so that transfer does not occur and the fluorescence intensity of the donor, measured at the donor emission peak, is maximal. When the protein undergoes a conformational change leading to a separation of D and A that is typically on the order of tens of Angstroms, then there is a nonradiative transfer of energy from the donor to the acceptor resulting in a quenching of donor and a sensitized emission of the acceptor. See text for details.

extremely useful for probing macromolecular interactions, FRET is a sophisticated technique that requires exact determination of critical spectroscopic parameters. To emphasize these parameters, it is critical to understand the mechanism of electronic energy transfer in fluorescence assays.

The principle of FRET is simple and is shown in Fig. 19.1. A donor molecule absorbs light at some frequency that temporarily places that molecule into a higher energetic electronic state. Before the electron can decay back down to its ground state, the proximity of another molecule results in the nonradiative transfer of energy from the donor molecule to an acceptor molecule by a dipole-induced dipole interaction. The donor molecule has therefore given up its energy to an acceptor molecule where it can now decay radiatively at its characteristic fluorescence emission wavelength. In using FRET, only one of the two molecules needs to be fluorescent. However, most users of this technique employ both fluorescent donor and acceptor molecules whose spectrofluorometric properties become modulated when energy transfer occurs.

When designing molecules in which energy transfer will occur, three conditions must be met:

1. The donor emission spectrum must overlap the acceptor absorbance spectrum.
2. The donor and acceptor fluorophores must be sufficiently aligned so that an acceptor dipole can be induced by the donor.

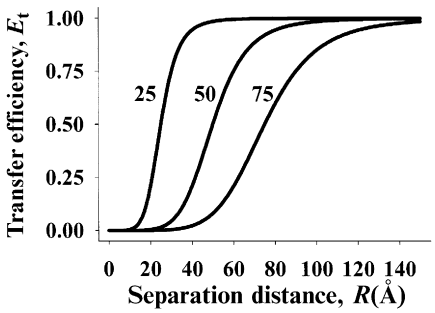

FIGURE 19.2

Theoretical transfer efficiency curves as a function of the separation distance, R, between donor, D, and acceptor, A. Numbers represent theoretical R_0 values of 25, 50, and 75 Å.

3. The donor and acceptor must be separated by some minimum distance so that the probability of energy transfer is high.

When these conditions are met, the probability of transfer, also known as the transfer efficiency, E_t, is related by the Förster equation:

$$E_t = \frac{R_0^6}{R^6 + R_0^6} \tag{19.1}$$

where R is the separation distance between the donor and acceptor fluorophores and R_0 is the separation distance for a particular donor–acceptor pair where the transfer efficiency equals 0.5 (Fig. 19.2). It is because the transfer efficiency falls off inversely as the sixth power of the separation distance, the FRET is a useful tool for measuring molecular distances both quantitatively and qualitatively. The transfer efficiency, and therefore the molecular separation distance, can be determined by either measuring donor lifetimes or measuring steady-state methods.

19.1.2 Methodologies for measuring transfer efficiencies in solutions

There are four major ways to measure the transfer efficiency due to FRET when the donor is excited, they include:

1. A decrease in the donor lifetime.
2. A decrease in the steady-state fluorescence emission intensity of the donor (donor quenching).
3. An increase in the steady-state fluorescence emission intensity of the acceptor (sensitized emission).
4. A change in the fluorescence polarization.

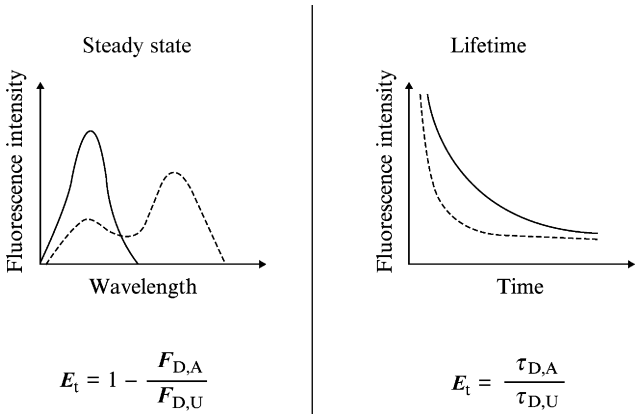

FIGURE 19.3

FRET can be quantified using either steady-state or lifetime measurements. (A) In steady-state FRET, there is a decrease in the fluorescence intensity of the donor along with the sensitized emission of the donor. Microscopes are designed to either measure fluorescence intensities at discrete wavelengths corresponding to the donor and acceptor emission peaks or by gathering emission spectra when the donor is excited. (B) In lifetime FRET, there is a decrease in the lifetime of the donor fluorophore in the presence of acceptor. Solid lines represent the presence of the donor in the absence of acceptor and dashed lines in the presence of acceptor.

Of these four methods, 1 and 2 are the most widely used and the most amenable for measuring transfer efficiencies in microscopes and we will focus on these two methods (Fig. 19.3).

A molecule can lose energy by a number of both radiative and nonradiative mechanisms:

$$k_t = k_r + k_{nr},$$

where k_t is the overall rate constant for radiative (k_r) and nonradiative (k_{nr}) processes. In the absence of nonradiative processes, the donor fluorophore will decay at some characteristic rate. However, when a competing nonradiative process occurs (e.g., FRET), there is a *decrease* in the lifetime of the donor. In general, the transfer efficiency, E_t, is given by:

$$E_t = \frac{\tau_{D,A}}{\tau_{D,U}}, \tag{19.2}$$

where $\tau_{D,A}$ is the excited state lifetime of the donor in the presence of acceptor and $\tau_{D,U}$ is the excited state lifetime in the absence of acceptor. Using a fluorescence lifetime machine, measurements of donor lifetimes in the presence and absence of acceptor can be made, and the transfer efficiency can be calculated directly from Eq. (19.2). The advantage of lifetime measurements is that they are extremely sensitive so that

accurate determinations of E_t can be made (Herman, 1989). However, few investigators have ready access to this equipment as it is expensive and difficult to maintain.

As opposed to fluorescence lifetime equipment, most investigators have access to a steady-state fluorimeter and it is possible to make fairly accurate determinations of transfer efficiency using such instrumentation (Gordon, 1988). The degree of energy transfer can be quantified as a decrease in the donor's fluorescence emission intensity (donor quenching) or by an increase in the fluorescence emission intensity of the acceptor (sensitized emission). The most common method is to quantify the transfer efficiency by measuring the amount of donor quenching in the presence and absence of acceptor. In this mode, the transfer efficiency is:

$$E_t = 1 - \frac{F_{D,A}}{F_{D,U}}, \tag{19.3}$$

where $F_{D,A}$ is the fluorescence intensity of the donor in the presence of acceptor (i.e., the transfer condition) and $F_{D,U}$ is the fluorescence intensity in the absence of acceptor. In the case of ligand–receptor interactions or nucleic acid hybridization, the measurement of $F_{D,U}$ (Fig. 19.2) must be made with an unlabeled complementary molecule. By measuring $F_{D,U}$ (or $\tau_{D,U}$) in this way, other donor quenching mechanisms besides FRET are accounted for. Often it is more convenient to express the transfer efficiency using the degree of donor emission quenching rather than measuring the fluorescence intensities directly. In this case:

$$E_t = \frac{q_{D,A} - q_{D,U}}{1 - q_{D,U}}. \tag{19.4}$$

Whether one is making lifetime of steady-state measurements, an accurate determination of R_0 must be made. Measurements of R_0 are easily achieved if certain spectral parameters can be measured. In general, R_0 is given by:

$$R_0 = 9.765 \times 10^3 (\kappa^2 J(\lambda) Q_D n^{-4})^{1/6}, \tag{19.5}$$

where $J(\lambda)$ is the overlap integral (in cm^3/M) between the donor emission spectrum and the acceptor absorbance spectrum, κ^2 is the orientation factor between donor and acceptor, Q_D is the quantum yield of the donor in the absence of acceptor, and n is the refractive index of the medium between donor and acceptor (Fig. 19.4). Quantitatively, the overlap integral can be calculated as:

$$J(\lambda) = \int_0^\infty \varepsilon(\lambda) f(\lambda) \lambda^4 d\lambda, \tag{19.6}$$

where $\varepsilon(\lambda)$ is the molar extinction coefficient of the acceptor and $f(\lambda)$ is the normalized fluorescence spectrum of the donor which is defined as:

$$f(\lambda)d\lambda = \frac{F(\lambda)d\lambda}{\int_0^\infty F(\lambda)d\lambda} \tag{19.7}$$

and $F(\lambda)$ is the fluorescence emission intensity of the donor. The orientation factor, κ^2 is perhaps the most troublesome factor since its numerical value can vary

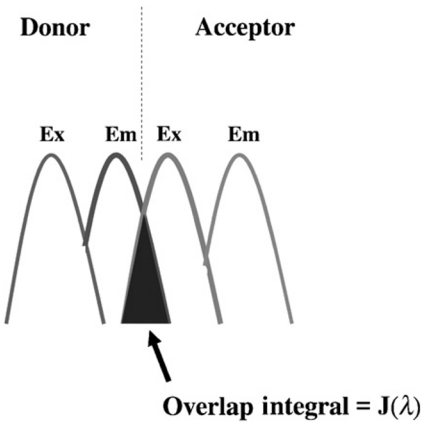

FIGURE 19.4

FRET occurs only when there is a significant overlap between the donor emission and the acceptor excitation spectra. In general, the overall value of the transfer efficiency is dependent on R_0, a value that includes the overlap integral and the relative orientation of the donor and acceptor molecules.

anywhere between 0 and 4. In reality, the orientation between a population of donor and acceptor molecules are randomly oriented both spatially and temporally. It can also be shown that under randomizing conditions, the average value of κ^2 ($\langle\kappa^2\rangle$) is equal to 2/3 (Dale, 1979). For most macromolecular interactions in solutions, using a value of κ^2 of 2/3 is entirely appropriate and even minor polarizations of donor and acceptor molecules will not lead to major variations in the determination of R_0. However, in certain geometries, the investigator using energy transfer as a quantitative tool must be conscious of the possibility that certain molecular interactions may lead to extreme values in κ^2. In particular, energy transfer in highly polarizing situations, such as biological membranes or nucleic acids, may lead to situations where dipoles are either orthogonally aligned (leading to no possibility for a dipole-induced dipole interaction) with a resulting κ^2 value of 0, or aligned in parallel so that κ^2 is equal to 4.

19.1.3 Practical considerations for all FRET measurements

Whether using FRET for quantitatively detecting interactions between complementary molecules in solution or for designing experiments using a FRET microscope described in Section 19.2, a number of measurements and controls must always be performed in order to minimize artifacts and maximize signal-to-noise ratios to obtain the highest quality images. These include:

1. *Determining the background fluorescence of the sample*. Measure the background fluorescence intensities of all samples in the absence of labeled molecules using the appropriate wavelengths for FRET measurements.

2. *Determine the fluorescence intensity of the donor*. Ideally, this should be in a range where the fluorescence emission intensity varies linearly with fluorophore concentration. This reading will be the baseline value for determining the amount of quenching that occurs in the presence of a complementary molecule that contains the acceptor fluorophore.
3. *Determine the fluorescence intensity of the donor in the presence of the unlabeled complementary molecule*. In an ideal experiment, the unlabeled complementary molecule would not modulate the fluorescence intensity of the donor after binding. However, this is often not the case and the fluorescence emission intensity of the donor generally changes on binding. In the case of polynucleic acids, hybridization of an unlabeled strand quenches the donor molecule on the labeled complementary strand (Cardullo, Agrawal, Flores, Zamecnik, & Wolf, 1988). This degree of quenching [$q_{D,U}$ in Eq. (19.4)] can depend on a number of different parameters, including the number of nucleotide pairs in the hybrid, the length of the hydrocarbon spacer between the terminal nucleotide and the fluorophore, the temperature, and the ionic strength of the solution. In some cases, especially those involving imaging, the best way to measure the donor fluorescence intensity in the absence of acceptor is to photobleach the acceptor fluorophore after the two labeled molecules associate with one another (Kenworthy, 2001).
4. *Determine the fluorescence intensity of the donor in the presence of the acceptor-labeled complement*. The amount of quenching in the presence of acceptor ($q_{D,A}$) is used along with the amount of quenching in the absence of acceptor-labeled complement ($q_{D,U}$) to determine the transfer efficiency using Eq. (19.4).

It is important to note that in the absence of these kinds of controls, modulation of fluorescence intensities or lifetimes using a microscope system may be due to other factors besides FRET.

19.2 FRET MICROSCOPY

In theory, FRET should be readily achievable in an imaging microscope system if accurate detection of the donor and the acceptor fluorescence intensities, or lifetimes, can be made. In most cases, because of difficulties in accurately quantifying parameters such as R_0 and κ^2, a FRET microscope is not generally used for quantifying interactions between molecules but rather is best used for localizing those interactions within a cell. In this mode, all that is needed is sufficient signal-to-noise resolution to determine whether any increase in transfer efficiency can be mapped onto pixels. This requires either that fluorescence intensities can be accurately determined at both donor and acceptor wavelengths for steady-state measurements or that accurate lifetime measurements can be made using a fluorescence lifetime imaging microscopy (FLIM). In either case, care must be taken to ensure that high-quality fluorescence images are obtained in the absence of artifacts resulting from differential response of optical or electronic elements at different wavelengths. Consequently, all aspects of microscope design from the choice of objectives, light sources, and cameras must be

taken into account. In this section, we will discuss the required instrumentation for FRET microscopy studies using either a steady-state or FLIM instrument.

19.2.1 The microscope

FRET microscopes can be either upright or inverted depending on the particular application and need for manipulating samples. In an upright microscope, cells either can be prepared and imaged through a coverslip or, alternatively, can be attached to glass coverslips and imaged from above using high numerical aperture (NA) long-working distance objectives that may be immersed in a physiologically buffered solution that surrounds the sample. In contrast, inverted microscopes image cells from below using high NA short-working distance objectives and coverslips. In either case, one can have easy access to the cells of interest when microscopy is combined with patch-clamp recordings, pressure injections, amperometry, or similar experimental manipulations.

As discussed elsewhere in this volume, although a microscope has many components that are responsible for the delivery of excitation light to the sample and emission light to the detector, the singularly most important part is the choice of objective(s). Magnification, NA, aberration, and spectral properties are some of the factors that need to be taken into account when choosing objectives for FRET. In cellular microscopy, the majority of work is performed using magnifying powers greater than 40× to allow for intracellular localization of donor-acceptor pairs. NA of the objective is an important for two reasons: First, a high NA maximizes the resolution of the system which is an especially important feature when donor-acceptor pairs may be localized within intracellular domains or organelles. Second, the NA dictates the efficiency of the objective to collect light, a feature especially important with fluorescence measurements since selected multiple wavelengths of light are passing through the objective. As the magnification of the objective increases, more light needs to be gathered by the lens, which is readily available when using objectives with NAs greater than 1.3. Use of appropriate immersion fluids between the objectives and the sample in either upright (by immersing the lens in physiological saline) or inverted configurations (by immersing the lens in oil below the coverslip and the sample) increases the NA when compared to the air interface.

Although objectives should be devoid of spherical and spatial aberrations, this is usually a trade-off feature. In general, as the number of components that make up the objective lens decreases, the loss of light is decreased, but often at the expense of some spherical aberration. The transmittance of objectives is also important and, for FRET, differences in transmission can be a critical factor in both the magnitude of the absolute signal in signal-to-noise and the donor and acceptor channels. This is especially true in the UV when the investigator may be using intercalating dyes for detecting interactions with nucleic acids or when using other some of the newer high-efficiency probes in the lower wavelengths. This has recently become an issue in FRET microscopy when blue fluorescent protein (BFP) is used as a donor since the objective must have excellent transmittance in near UV range. Indeed, the best (albeit the most expensive) would be to use an objective that contains quartz

optical components. However, some companies offer more economical alternatives that have adequate transmittance down to 340 such as Fluor and SuperFluor objectives.

The FRET microscope must also provide the appropriate transmission optics to locate and position the cell of interest and to correlate fluorescent signals within known cellular regions or organelles. In general, some form of contrast enhancement is desirable. A simple insertion of green interference filters in the path can be acceptable to observe some cell types (e.g., neurons), while for flatter cells (e.g., astrocytes or spermatozoa) additional contrast is often necessary. As discussed elsewhere in this volume, the most commonly used methods for enhancing contrast are phase and differential interference contrasts (DICs). Phase contrast reduces the amount of light due to the presence of the phase ring in the objective but otherwise does not compromise fluorescence imaging. In DIC microscopy, polarizers are introduced into the light path, which not only reduce the intensity of fluorescence emission but also change the polarization of light. Consequently, polarizers should be removed (usually mounted on a slider) to yield optimal fluorescence imaging.

The feasibility of using FRET at subdiffractional levels of visible light has been demonstrated. In these experiments, Kirsch, Subramaniam, Jenei, & Jovin, 1999 used scanning near-field optical microscopy with uncoated glass fiber tips for light delivery to detect FRET between donor and acceptor molecules. Although not widely used, the use of near-field microscopy may ultimately offer distinct advantages over diffraction-limited methods that require the use of objectives.

19.2.2 Fluorescence illumination

In a standard epifluorescence microscope, the light emitted from a source is directed by associated optics into the back aperture of the microscope and then through an objective. As in all elements of the microscope, the optical components in this path must be capable of transmission of the relevant light wavelengths (i.e., excitation and emission wavelengths for both the donor and acceptor fluorophores). Since the total transmittance depends on the number of individual components comprising the system, a reduction in the number of optical elements is advisable. Excitation wavelength selectors, dichroic mirrors, and emission selectors are all additional components in the delivery of the excitation wavelengths and recovery of emission wavelengths in the FRET microscope.

19.2.2.1 Light sources

The most commonly used sources of light for fluorescence microscopy are mercury (Hg) and xenon (Xe) arc lamps. Although Hg lamps have some usable intensity maxima (e.g., as with fluorescein, rhodamine, and BFP excitation wavelengths), Xe arc lamps provide relatively even spectral radiance and, as with ratio imaging, are the light source of choice for FRET applications. When these lamps are combined with monochromators or appropriate filters, one can select the required excitation wavelengths to generate a complete spectrum for FRET. Since these lamps produce large

amounts of emission in the infrared (IR), it is necessary to use a heat filter prior to the entry of light into the microscope. Such filters are most commonly mounted at the back aperture of the microscope. Alternatively, optical fibers or liquid light guides can be used to deliver the light to the back of the microscope or directly to the sample.

Lasers offer more coherent light whose intensities are at acceptable levels only at discrete wavelengths. Argon and nitrogen lasers can be used in conjunction with commercially available dye modules to generate light at a variety of different wavelengths. For example, a pulsed nitrogen laser with a principal line at 337 nm can be used to cover the range from 360 to 950 nm when combined with appropriate dye modules. Although applicable for steady-state FRET, this pulsed laser is not a choice for FLIM applications due to a pulse time ($\sim$3 ns) on the order of the lifetime of most fluorophores. Instead, lasers that offer temporal resolution of $\sim$100 ps are required for FRET using FLIM. One option is to use a laser-pumped Ti:sapphire-pulsed IR laser that is tunable between 700 and 1000 nm, with or without a frequency doubler, yielding 350- to 1000-nm excitation wavelengths. Additionally, pulsed lasers can be used to "freeze" images, similar to a flash with a camera.

Finally, light-emitting diodes (LEDs) have shown promise in FLIM applications in cuvettes. However, at the present time their light emission is not sufficient to combine them with complex optical systems that are used in imaging single cells.

19.2.2.2 Wavelength selectors

When a broad-spectrum (multiwavelength) source of light is used, the wavelength of light is selected at three points: at the excitation selector, at the dichroic mirror, and at the emission selector. This is most commonly achieved using glass (fused silica) filters. Increasingly, however, various kinds of monochromators are used for selecting excitation and emission wavelengths for microscopic applications such as FRET. Further, acousto-optical tunable filters (AOTFs) can be used for specific applications such as blending wavelengths from different laser sources in confocal microscopy and in frequency-domain FLIM. Liquid crystal tunable filters (LCTFs) can also be used for selecting emission, but not excitation, wavelengths although these filters will also polarize the light as well.

Two major filter types used in fluorescence microscopy are colored filter glass and thin-film-coated filters. Color glass filters are relatively inexpensive and their spectral characteristics are insensitive to their angle of incidence, but there is a limited selection with their band-pass types having poor slopes and often low peak transmittance. Therefore, the most commonly used filters for FRET contain thin-film coatings, either metallic or interference coating. Metallic coatings are used for mirrors or neutral density filters. Interference coatings can be used to design almost any filter type, including band-pass exciters and emitters, long-pass and short-pass filters, and dichroic mirrors. This flexibility is inherent in the composition of stacked thin layers of material. Filters and filter sets ("cubes") commonly used for FRET applications are listed in Tables 19.1 and 19.2.

Monochromators are frequently used in FRET applications. In essence, a monochromator produces a single spectral line from a broad-spectrum source. The most

Table 19.1 Standard Fluorescence Microscope Filter Sets Used for GFP Variant Probes

GFP Variant Filter Sets	Exciter	Dichroic	Emitter
BFP	387RDF28	410DRLP	450RDF58
CFP	440DF21	455DRLP	480DF30
YFP	500RDF25	525DRLP	545RDF35
GFP	475RDF40	505DRLP	535RDF45

B, blue; C, cyan; Y, yellow; and G, green

Table 19.2 Fluorescence Microscope Filter Sets Used for Different Donor/Acceptor GFP Variant Probe Combinations

FRET Filter Sets	Exciter	Dichroic	Emitter 1	Emitter 2
CFP–YFP	440DF21	455DRLP	480DF30	535DF26
BFP–GFP	365HT25	400DCLP	450DF65	535DF45

common type is a Czerny-Turner monochromator, utilizing a grating to disperse light, whose wavelength is chosen using an exit slit. Monochromators can be tunable and changing between two wavelengths requires speeds down to the millisecond range. In FRET applications where typically a ratiometric approach is used, one can use a beam splitter with two static monochromators, or use a single tunable monochromator at the emission end.

AOTFs are most commonly used to filter laser light. They have found commercial applications in confocal microscopes (and FRET) and are used there to mix light emitted from different lasers. In these filters, the light passes through a crystal (tellurium oxide), which acoustically vibrates when driven by radio frequencies. This basically creates a diffraction grating, and by varying the frequency of vibrations, one can quickly tune the filter to diffract out any wavelength of light at ~2-nm full-width at half maximum (FWHM). These filters are used to modulate light frequencies in frequency-domain FLIM.

LCTF is another electronically tunable optical filter, consisting of several horizontally stacked units. Each unit is composed of a liquid crystal sandwiched by sheet polarizers. With these filters, one can electronically tune the wavelength within a few milliseconds. These filters can be used for FRET only at the emission end since they are thermally unstable and cannot receive direct light from either an Hg or an Xe light source.

19.2.2.3 Detectors

Traditional FRET experiments use a single camera together with wavelength selectors at the emission end to capture a pair of emission images: one at the donor's emission wavelength and the other at the acceptor's emission wavelength due to

excitation of the donor fluorophore. There are number of ways to rapidly switch wavelengths, including rotating filter wheels, motorized sliders, LCTFs, and tunable monochromators. These methods are relatively inexpensive with excellent spatial resolution, but all suffer in providing adequate temporal resolution (e.g., switching emission filters results in at least a 100-ms delay).

Ideally, one should be able to simultaneously collect information for both the donor and acceptor fluorophores. This can be achieved by splitting the emission light into two spectral channels, one corresponding to the donor's emission and the other to the acceptor's emission, that are then routed to individual detectors. This method greatly improves temporal resolution, although problems with registration between the two detectors are often difficult to achieve. Consequently, this type of system is relatively complex and expensive. An alternative is to use a single camera with an image splitter. In this system, each light channel is routed to its own half of the imaging array. This gives excellent temporal resolution and reduces the cost at expense of reduction in spatial resolution.

In order to record planar information for fluorescent preparations, a camera is required (except for confocal configurations described subsequently). Most commonly used cameras currently used for FRET applications are either ICCDs (intensified charged coupled device) or CCCDs (cooled CCD), having analog and digital outputs, respectively. ICCDs have no lag time and show high sensitivity throughout a range required for imaging FRET emissions. Gen III intensifiers are mostly used today to amplify the light prior to delivering light to the CCD chip. The readout from the chip is synchronized to a standard analog video signal. The limiting factor in quality of images generated by an ICCD is the quality of the intensifier. A CCD is an imaging device whose sensor consists of semiconductor layers divided into electronic traps. Incident photons create electron-hole pairs accumulating charge that is proportional to the arriving photon flux. The readout of a resulting potential from each pixel is then digitized for display and stored in a computer. Signals can be integrated for variable amounts of time until read out. Since the noise is mainly result from thermal generation of electrons, cooling of the detector increases signal-to-noise ratio.

Confocal microscopy as well as near-field microscopy have been employed in FRET imaging. Since in both cases spatial information is built up on a point by point basis, photomultiplier tubes can be used as fluorescent detectors to generate a two (or three)-dimensional image. PMTs can also be used for fast temporal detection in combination with wide-field fluorescence microscopes. In these kinds of photometry applications, an aperture can be inserted into a secondary imaging plane at the emission end of the microscope to define a region of interest such as a group of cells, a single cell, or a portion of a cell.

19.2.3 Typical FRET systems: CFP–YFP as an example

As shown previously, the most common ways to monitor FRET is to use either a steady-state approach in which donor quenching the presence of acceptor is used to calculate transfer efficiencies or a lifetime instrument is used to monitor decrease

in donor lifetime in the presence of acceptor. Since applications of FRET microscopy are increasingly using GFP variant constructs as donor and acceptor pairs for detecting specific protein-protein interactions (Anderson, Sanderson, Gerwig, & Peychl, 2006; Xu, Brzostowski, & Jin, 2006; Zeng et al., 2006), this section will focus on that particular application. A general description of GFP, its variants, and their uses in fluorescence microscopy can be found in Chapter 6 by Straight, volume 81, 2007. Using the considerations described in these sections, three systems are described for measuring FRET between a CFP-labeled donor and a YFP-labeled acceptor.

19.2.3.1 A steady-state FRET system

The following is a description of a typical FRET system for CFP–YFP acceptor-donor pairs. A microscope equipped with a 40× SuperFluor objective for maximum transmission of light is connected to a 100-W Xe arc lamp used for sample excitation. The duration of the sample's exposure to light is controlled by an electronic shutter to minimize photobleaching. The light exiting the lamp housing, containing a focusing lens, is routed to the back aperture of the microscope. In the light path, there is a holder containing three filter sets: CFP, YFP, and FRET filter sets (Tables 19.1 and 19.2). The fluorescence emission is collected using one filter set at a time and then the sample is imaged with an ICCD camera. When ratiometric imaging is used, a pair of images corresponding to emission wavelengths at 480 and 535 nm due to excitation at 440 nm reports donor and acceptor emission intensity values. In order to access the transfer efficiency, YFP (the acceptor) has to be bleached since this will maintain the association between the two labeled molecules but will result in obtaining an unquenched value for the donor. This is accomplished by excitation of the YFP with a 525/40-nm band-pass filter to minimize bleaching of the donor CFP. Monitoring of bleaching success can be accomplished using a YFP filter set. The increase in fluorescence of CFP as recorded by looking at the CFP donor emission channel is a direct measure of the transfer efficiency (E_t) which can be calculated using the following equation:

$$E_t = 1 - \left(\frac{\text{CFP intensity before YFP photobleach}}{\text{CFP intensity after YFP photobleach}}\right).$$

19.2.3.2 Fluorescence lifetime FRET systems: time versus frequency domains

In this configuration, a 440-nm laser line is used as the excitation wavelength. A laser (535 nm; Coherent Verdi) pumped pulsed (76 MHz;150 fs) Ti:sapphire IR laser, which is tunable between 700- and 1000-nm wavelengths, is used here to achieve the necessary wavelength and time resolution. The laser is tuned at 880 nm and light exiting from the laser is passed through a frequency doubler resulting in 440-nm light. This pulsed light is delivered to the back aperture of the microscope and used to illuminate living cells. The emitted light is filtered through a 480/30-nm filter and amplified at image intensifier, and then integrated on a CCD chip coupled to an

intensifier. This gated intensifier is synchronized to the laser. After laser pulse excitation, the image intensifier with the coupled camera acquires images at different time delays. Provided that integration times during acquisition of the individual images are the same, it is possible to make a comparison of the fluorescence lifetimes by acquiring two images at two different delay times with respect to the excitation pulse. For example, in this system, CFP lifetimes decrease from 2.2 to 1.6 ns in the presence of acceptor (Elangovan, Day, & Periasamy, 2002).

For frequency-domain FLIM, the continuous excitation light originating from a laser is modulated at radio frequencies (typically at 10–100 MHz) using an AOTF. Two radio frequency synthesizers whose phase settings are computer controlled are used to produce a repetitive signal (e.g., a sinusoidal wave). One frequency synthesizer drives the modulation of the AOTF, while the other drives the modulation of an image intensifier. The emission light is focused onto an image intensifier. Thus, fluorescence emission is demodulated, phase-shifted, and captured onto a CCD. Image acquisition and shutter control at the excitation are also computer interfaced and controlled. A more detailed description on FLIM can be found in Chapter 24 by Chang et al, volume 81, 2007.

CONCLUSIONS

The first FRET microscope was constructed over a quarter of a century ago (Fernandez & Berlin, 1976), although recent advances in imaging technology and the development of wavelength selection devices have made this powerful technique popular among investigators interested in studying the interactions between molecules in cells. Using steady-state methods, it is now possible to construct a relatively low-cost system that can detect molecules within cells. In contrast, lifetime measurements allow for the determination of more quantitative data to be obtained. Coupled with the advent of the development of new fluorescent probes such as the green fluorescent protein and other genetically engineered reporters (Zhang, Campbell, Ting, & Tsien, 2002), the future of this technology is sure to reveal molecular associations both within cells and on cell surfaces that were previously detected only using nonmicroscopic methods (Nagy et al., 2002; Zimmermann, Rietdorf, Girod, Georget, & Pepperkok, 2002).

Acknowledgments

The author wishes to thank Dr. David Wolf (Sensor Technologies, Shrewsburg, MA) and Dr. Vladimir Parpura (University of California, Riverside) for valuable discussions on FRET.

References

Anderson, K. I., Sanderson, J., Gerwig, S., & Peychl, J. (2006). A new configuration of the Zeiss LSM 510 for simultaneous optical separation of green and red fluorescent protein pairs. *Cytometry. Part A*, *69*, 920–929.

Cardullo, R. A. (1992). Nonradiative fluorescence resonance energy transfer. In C. Kessler (Ed.), *Nonradioactive labeling and detection of biomolecules* (pp. 414–423). Heidelberg, Germany: Springer-Verlag.

Cardullo, R. A. (2002). Principles of non-radiative FRET: The spectroscopic ruler. *Microscopy and Analysis*, *15*, 19–21.

Cardullo, R. A., Agrawal, S., Flores, C., Zamecnik, P., & Wolf, D. E. (1988). Detection of nucleic acid hybridization by nonradiative fluorescence resonance energy transfer. *Proceedings of the National Academy of Sciences of the United States of America*, *85*, 8790–8794.

Dale, R. E. (1979). The orientation factor in intramolecular energy transfer. *Biophysical Journal*, *26*, 161–194.

Elangovan, M., Day, R. N., & Periasamy, A. (2002). Nanosecond fluorescence resonance energy transfer-fluorescence lifetime imaging microscopy to localize the protein interactions in a single living cell. *Journal of Microscopy*, *205*, 3–14.

Fernandez, R. M., & Berlin, R. D. (1976). Cell surface distribution of lectin receptors determined by resonance energy transfer. *Nature*, *264*, 411–415.

Förster, T. (1959). Transfer mechanisms of electronic excitation. *Discussions of the Faraday Society*, *264*, 7–17.

Gordon, G. W. (1988). Quantitative fluorescence resonance energy transfer measurements using fluorescence microscopy. *Biophysical Journal*, *74*, 2702–2713.

Herman, B. (1989). Resonance energy transfer microscopy. *Methods in Cell Biology*, *30*, 219–243.

Kenworthy, A. K. (2001). Imaging protein-protein interactions using fluorescence resonance energy transfer microscopy. *Methods*, *24*, 289–296.

Kirsch, A. K., Subramaniam, V., Jenei, A., & Jovin, T. M. (1999). Fluorescence resonance energy transfer detected by scanning near-field optical microscopy. *Journal of Microscopy*, *194*, 448–454.

Nagy, P., Vereb, G., Sebestyen, Z., Horvath, G., Lockett, S. J., Damjanovich, S., et al. (2002). Lipid rafts and the local density of ErbB proteins influence the biological role of homo- and heteroassociations of ErbB2. *Journal of Cell Science*, *115*, 4251–4262.

Stryer, L., & Haugland, R. P. (1967). Energy transfer: A spectroscopic ruler. *Proceedings of the National Academy of Sciences of the United States of America*, *58*, 719–726.

Xu, X., Brzostowski, J. A., & Jin, T. (2006). Using quantitative fluorescence microscopy and FRET imaging to measure spatiotemporal signaling events in single living cells. *Methods in Molecular Biology*, *346*, 281–296.

Zeng, W., Sward, H. E., Malnasi-Csizmadia, A., Wakelin, S., Wooley, R. J., Sheema, G. S., et al. (2006). Resonance energy transfer between green fluorescent protein variants: Complexities revealed with myosin fusion proteins. *Biochemistry*, *45*(35), 10482–10491.

Zhang, J., Campbell, R. E., Ting, A. Y., & Tsien, R. Y. (2002). Creating new fluorescent probes for cell biology. Nature Reviews. *Molecular Cell Biology*, *3*, 906–918.

Zimmermann, T., Rietdorf, J., Girod, A., Georget, V., & Pepperkok, R. (2002). Spectral imaging and linear un-mixing enables improved FRET efficiency with a novel GFP2-YFP FRET pair. *FEBS Letters*, *531*, 245–249.

CHAPTER

20 Fluorescence Lifetime Imaging Microscopy for Quantitative Biological Imaging

Leng-Chun Chen, William R. Lloyd, III, Ching-Wei Chang, Dhruv Sud, and Mary-Ann Mycek

Department of Biomedical Engineering, University of Michigan, Ann Arbor, Michigan, USA

CHAPTER OUTLINE

Introduction to Fluorescence Lifetime Imaging Microscopy 458
20.1 Fluorophore Excited-State Lifetime: τ 460
20.1.1 Basic Theory 460
20.1.2 Key Features of Fluorescence Lifetime Sensing 462
20.2 Methods for Creating Fluorescence Lifetime Maps 465
20.2.1 Time Domain 465
20.2.1.1 Time-Gated FLIM 465
20.2.1.2 TCSPC FLIM 467
20.2.2 Frequency Domain 469
20.2.3 Data Analysis Methods 471
20.2.3.1 RLD and Analytical Least-Squares Algorithms 471
20.2.3.2 Iterative Least-Squares Analysis with Multiexponential Fitting 472
20.2.3.3 Least-Squares Analysis with Laguerre Polynomial Fitting 472
20.2.3.4 Phasor Plot Analysis 473
20.2.3.5 Improving Precision of Fluorescence Lifetime Maps 474
20.3 FLIM Techniques for Quantitative Biological Imaging 477
20.3.1 FLIM Detection of FRET Events 477
20.3.2 Intracellular Molecular Diffusion Rates Measured Via FCS-FLIM 479
20.3.3 Multispectral-FLIM 480
20.3.4 MP-FLIM of Endogenous Tissue Fluorophores 482
Summary 483
Acknowledgment 483
References 484

Methods in Cell Biology, Volume 114 **ISSN 0091-679X**
Copyright © 2013 Elsevier Inc. All rights reserved.
http://dx.doi.org/10.1016/B978-0-12-407761-4.00020-8

Abstract

Fluorescence lifetime imaging microscopy (FLIM) is a method for measuring fluorophore lifetimes with microscopic spatial resolution, providing a useful tool for cell biologists to detect, visualize, and investigate structure and function of biological systems. In this chapter, we begin by introducing the basic theory of fluorescence lifetime, including the characteristics of fluorophore decay, followed by a discussion of factors affecting fluorescence lifetimes and the potential advantages of fluorescence lifetime as a source of image contrast. Experimental methods for creating lifetime maps, including both time- and frequency-domain experimental approaches, are then introduced. Then, FLIM data analysis methods are discussed, including rapid lifetime determination, multiexponential fitting, Laguerre polynomial fitting, and phasor plot analysis. After, data analysis methods are introduced that improve lifetime precision of FLIM maps based upon optimal virtual gating and total variation denoising. The chapter concludes by highlighting several recent FLIM applications for quantitative biological imaging, including Förster resonance energy transfer-FLIM, fluorescence correlation spectroscopy-FLIM, multispectral-FLIM, and multiphoton-FLIM.

INTRODUCTION TO FLUORESCENCE LIFETIME IMAGING MICROSCOPY

There has been significant growth in the use of fluorescence in the biological sciences during the past few decades (Lloyd, Chen, & Mycek, 2013; Lloyd, Chen, Wilson, & Mycek, 2013). Besides environmental monitoring, clinical chemistry, DNA sequencing, and genetic analysis by fluorescence *in situ* hybridization, fluorescence is used for cell identification and sorting in flow cytometry, and to reveal the localization and movement of intracellular substances in cellular imaging by means of fluorescence microscopy (Lakowicz, 2006).

Microscopic imaging of steady-state fluorescence intensity is routinely employed for studies in cell biology to reveal information regarding cellular morphology, intracellular ion concentrations, protein binding, lipid content, and membrane status (Rudolph & Kempe, 1997). However, intensity-based measurements are vulnerable to artifacts such as variation in excitation source intensity, detector gain setting, optical loss in the optical path and/or sample, variation in sample fluorophore concentration, photobleaching, and microscope focusing. Further, fluorophores with similar excitation and emission spectra may be impossible to differentiate with steady-state fluorescence intensity imaging.

Fluorophore lifetime is the property describing on average how rapidly an excited-state fluorophore decays. Accordingly, fluorescence lifetime imaging microscopy (FLIM) is a technique for producing spatially resolved images of fluorophore lifetime, providing another dimension of information for visualizing fluorophores and an additional source of contrast (Chang & Mycek, 2012b). As an example, and as can be inferred from Table 20.1, flavin adenine dinucleotide (FAD) is

Table 20.1 Endogenous and exogenous fluorophores used in cell biology (ISS; Urayama & Mycek, 2003)

Fluorophore	Solvent	Excitation max [nm]	Emission max [nm]	Life time [ns]
Endogenous				
Tryptophan	Water	295	353	3.1
Tyrosine	Water	275	304	3.6
Phenylalanine	Water	260	282	6.8
NAD(P)H	Water	350	460	0.4
FAD	Water	450	525	4.7
FMN	Water	450	525	2.3
Exogenous				
ATTO 565	Water	561	585	3.4
Rhodamine B	Water	562	583	1.68
Cy3	PBS	548	562	0.3
Cy5	PBS	646	664	1
DAPI	TRIS/ EDTA	341	496	0.16
FITC	PB pH 7.8	494	518	4.1
Fluorescein	PB pH 7.5	495	517	4
GFP	Buffer pH 8	498	516	3.2
Hoechst 33342	TRIS/ EDTA	336	471	0.35
Lucifer Yellow	Water	428	535	5.7

The standard fluorophores have single-exponential decay fluorescence lifetimes. PBS, phosphate-buffered saline, pH 7.4; TRIS/EDTA (1 mM, pH 7.4), tris*(hydroxymethyl)aminomethane/ ethylenediamine-tetraacetic acid; PB, phosphate buffer.*

distinguished from flavin mononucleotide with fluorescence lifetime approaches such as FLIM, as can ATTO 565 from Rhodamine B, despite the fact that their fluorescence spectra overlap. Further, fluorescence lifetime is known to be sensitive to the fluorophore's local environment and can reveal information on pH, oxygenation, temperature, and molecular associations (Lakowicz, 2006; Tadrous, 2000). For example, Fig. 20.1 illustrates the capability of FLIM to study Förster resonance energy transfer (FRET or FLIM-FRET), which reports on molecular associations. Here, FLIM-FRET was employed to monitor the localization of pre-mRNA splicing in a cell nucleus (Ellis et al., 2008). These results showed that spatial mapping with FLIM-FRET revealed differences in splicing factors interactions within complexes located in separate subnuclear domains.

Section 1 begins with the basics of fluorescence lifetime sensing, including the characteristics of fluorophore excited-state decay, a discussion of factors affecting fluorescence lifetimes, and the usefulness of fluorophore lifetimes as a source of contrast. Then, in Section 2, both time-domain (TD) and frequency-domain (FD) approaches to measure fluorescence lifetimes and their associated data analysis methods will be

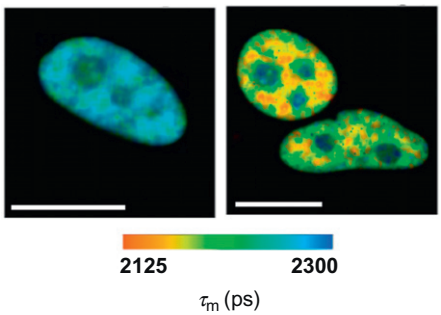

FIGURE 20.1

Intensity-based FRET measurements are limited by the typical assumption that FRET occurs in all observable donor molecules and the resulting complexity of data analysis. Alternatively, FLIM-FRET measurements are not limited by such an assumption. FLIM-FRET measurements can provide robust measurements that depend on the physical fluorescence lifetime and are thus internally calibrated with relatively straightforward data analysis methods. Such quantification is achieved by measuring fluorescence lifetime, which directly relates to the environment and binding state of a fluorescent molecule. Here, FLIM-FRET was employed to monitor nuclear pre-mRNA splicing, a process necessary for the functional coding sequence ligation. Living HeLa cells were monitored with FLIM to map the localization of the interaction between the splicing protein (U1 70K) and a serine/arginine-rich protein (SF2/ASF), which plays a key role in constitutive and alternating splicing. HeLa cells were transfected with EGFP-U1 70K (donor) and cotransfected with either mCherry-C1 or mCherry-SF2/AFS (acceptor). The donor fluorescence lifetime in HeLa cells was measured in the presence of either mCherry-C1 (negative control, left) or mCherry-SF2/AFS (right). Cotransfection of EGFP-U1 70K and mCherry-SF2/AFS resulted in a reduction of the mean donor lifetime, which is indicative of FRET. Scale bar: 10 μm (Ellis, Lleres, Denegri, Lamond, & Caceres, 2008).

described. Various applications of FLIM, ranging from FLIM-FRET, fluorescence correlation spectroscopy-FLIM (FCS-FLIM), multispectral-FLIM (MS-FLIM), and multiphoton-FLIM (MP-FLIM), will be highlighted in Section 3, followed by a Section "Summary".

20.1 FLUOROPHORE EXCITED-STATE LIFETIME: τ

20.1.1 Basic theory

Figure 20.2 is a simplified version of a Jablonski diagram to illustrate the molecular fluorescence process, where S_0 and S_1 are the ground and first excited electronic states, respectively, and the horizontal lines represent different vibrational states of the fluorophore. In condensed phases, after absorption of a photon, almost all excited molecules rapidly relax to the lowest vibrational level of the first excited state, from which they return to the ground state via: nonradiative or radiative decay process. The radiative decay rate Γ depends on the electronic properties of an isolated fluorophore. Molecular

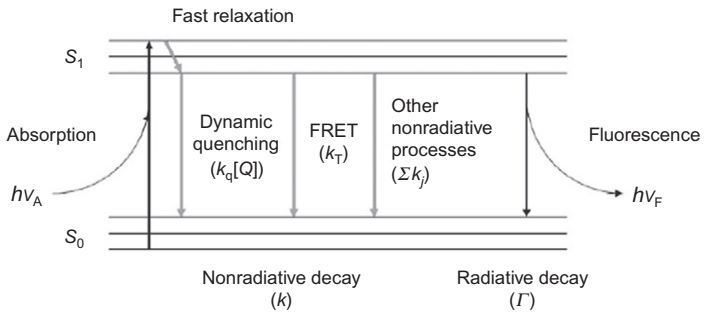

FIGURE 20.2

Simplified Jablonski diagram. k_q, Bimolecular quenching constant; $[Q]$, Quencher concentration (see Section 1.2); k_T, energy transfer rate constant (see Section 3.1); k_j, rate constant for nonradiative processes other than dynamic quenching and FRET (Chang, Sud, & Mycek, 2007).

interactions, such as dynamic (or collisional) quenching (see Section 1.2) and FRET (see Section 3.1), are accounted for in the nonradiative decay rate k.

Radiative decay is responsible for fluorescence emission, which provides detectable photons. However, since both decay processes depopulate fluorescent molecules in the first excited state, with fluorophore population $N(t)$, the overall decay of fluorescence emission intensity, proportional to $N(t)$, is attributed to both decay rates. In the simplest case, fluorescence decay follows the stochastic exponential decay as shown in Eqs. (20.1) and (20.2).

$$\frac{dN(t)}{dt} = -(\Gamma + k)N(t) \tag{20.1}$$

$$N(t) = N_0 e^{-(\Gamma+k)t} = N_0 e^{-t/\tau} \tag{20.2}$$

where N_0 is the initial number of fluorescent molecules in the first excited state, and

$$\tau = \frac{1}{\Gamma + k} \tag{20.3}$$

is the fluorescence lifetime, indicative of the average time a molecule spends in the excited state prior to returning to the ground state. Both nonradiative and radiative decay rates affect the value of τ, as shown in Eq. (20.3). Another important property of fluorophores is the quantum yield Q, defined as the ratio of the number of emitted photons to the number of absorbed photons, which is given by

$$Q = \frac{\Gamma}{\Gamma + k} \tag{20.4}$$

Note that $0 \leq Q \leq 1$ and Q can be close to unity if $k \ll \Gamma$. Generally, higher Q means higher fluorescence efficiency, which is usually favored in fluorescence applications. Commonly employed fluorophores such as tryptophan has a Q of 0.13, Rhodamine B has a Q of 0.31, Cy3 has a Q of 0.04, and fluorescein has a Q of

0.95 (ISS; Urayama & Mycek, 2003). Although Q can be used as a source of contrast, experimental protocols for estimating Q are strict and controlled, making such protocols difficult to apply in biological samples.

20.1.2 Key features of fluorescence lifetime sensing

Fluorescence lifetime is an intrinsic property of a fluorophore and is insensitive to a variety of intensity-based artifacts. Factors such as variations in excitation source intensity, detection gain setting, optical loss in the optical path and/or sample, variation in sample fluorophore concentration, photobleaching, and microscope focusing will all affect measured fluorescence intensities, but will leave the intrinsic excited-state fluorophore lifetime unchanged (Lloyd, Wilson, Chang, Gillispie, & Mycek, 2010). In addition, due to the nature of nonradiative decay processes, fluorescence lifetimes are sensitive to the fluorophore's microenvironment, including factors such as temperature, pH, oxygen concentration, polarity, molecular associations (binding), ion concentration, and relaxation through collisional (dynamic) quenching and FRET. Figure 20.3 is an example of the intensity-independent nature of FLIM measurements; here, the measured fluorescence lifetime, an intrinsic property of the fluorescent molecule, remains unaffected by variations in fluorophore concentration (within limits). As expected, these same variations in fluorophore concentration were shown to directly impact the measured fluorescence intensity.

Fluorescence quenching is generally classified into two primary types: static and dynamic. The concepts of static and dynamic quenching are shown in Fig. 20.4. Static quenching occurs due to the formation of nonfluorescent complexes via the interaction between fluorophores and other molecules in solution known as

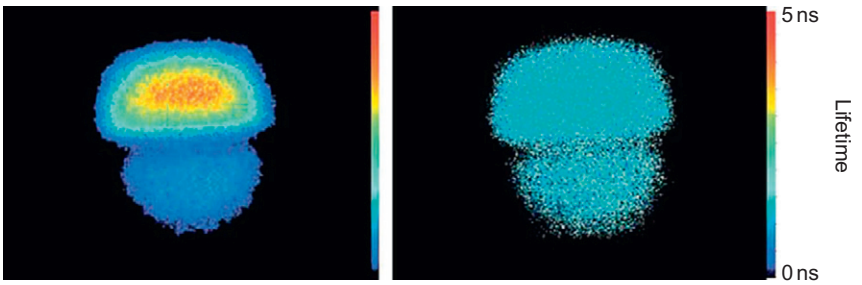

FIGURE 20.3

Intensity-independent fluorophore lifetimes recovered by FLIM. Despite a factor of four difference in POPOP concentration and hence signal intensity (left), the three-gate protocol lifetime map (right) showed identical mean lifetimes for the two POPOP samples. The images were of POPOP in ethanol solutions in two quartz capillaries. The capillary interface was on the diameter, with the circular region as the illumination area. The intensity images were background subtracted before calculation of lifetime map (Urayama et al., 2003).

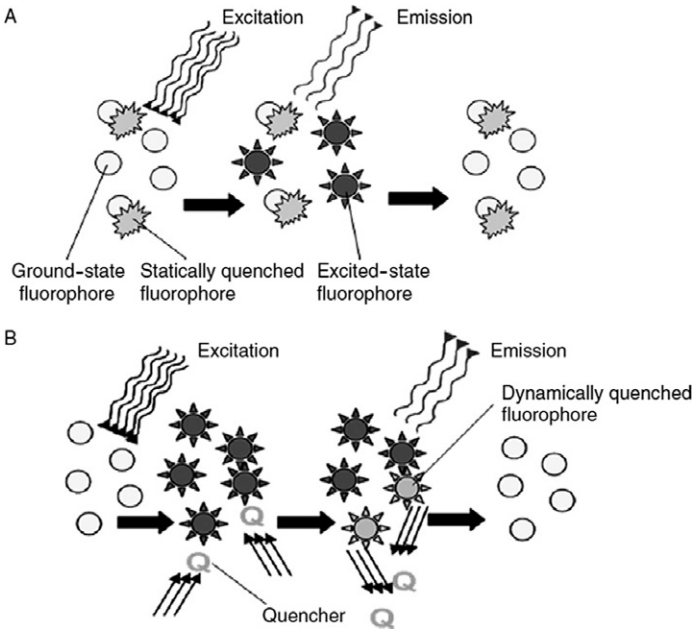

FIGURE 20.4

Static quenching (A) occurs due to the formation of nonfluorescent complexes from the interaction between fluorophores and other molecules in solution known as quenchers. Lifetime imaging is insensitive to static quenching. On the other hand, dynamic quenching (B) happens during the decay process, when excited-state fluorophores are de-excited upon contact with the quenchers. As a result, detected lifetime will be shortened (Chang et al., 2007).

quenchers. Fluorescence lifetime imaging is insensitive to static quenching, as other unbound (hence still fluorescent) fluorophores retain their fluorescent properties. On the other hand, dynamic (or collisional) quenching happens during the fluorescence decay process, when some excited-state fluorophores are de-excited upon contact with the quenchers and follow a nonradiative decay process (see Fig. 20.2), which leads to a faster decay of excited-state fluorophore population and hence a shorter fluorescence lifetime.

Therefore, measuring fluorescence lifetime provides a means of probing the local fluorophore environment. FLIM was reported (Sanders, Draaijer, Gerritsen, Houpt, & Levine, 1995) for quantitative pH determination in living cells with the fluorescent probe c.SNAFL-1. It was found that a lifetime-based approach was easier to employ than the traditional intensity-based ratiometric, while still providing accurate information regarding intracellular pH. Another FLIM-based pH measurement was presented in Lin, Herman, and Lakowicz (2003), which suggested that FLIM can be employed to measure the intracellular pH of resting cells, and to follow the pH fluctuations inside cells after environmental perturbations.

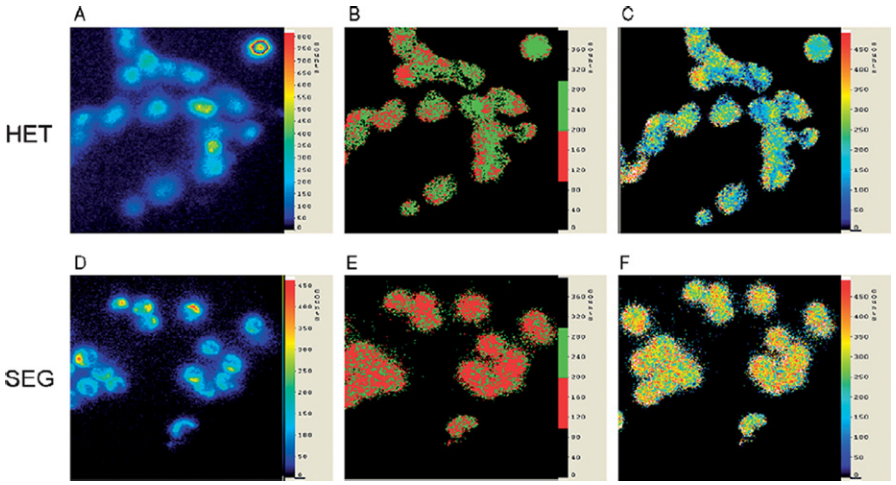

FIGURE 20.5

RTDP fluorescence intensity (A and D), lifetime in nanoseconds (B and E), and oxygen in micromolar (C and F) maps of normal human squamous esophageal epithelial cells (HET) (A–C) and Barrett's adenocarcinoma esophageal cells (SEG) (D–F). The intensity images (A and D) could not be reliably used to discriminate between the two different cell lines. The binary lifetime maps (B and E), on the other hand, plainly indicate different lifetimes for these two cellular species, with the SEG recording lower lifetimes than the HET. For the given case, $\tau_{HET} = 225$ ns and $\tau_{SEG} = 170$ ns. The mean lifetime difference was found to be $\Delta\tau = 44 \pm 7.48$ ns. Logically, this translated into higher oxygen levels in the SEG versus the HET using the calibration derived, as can be seen in the oxygen distribution maps (C and F) (Sud, Mehta, et al., 2006; Sud, Zhong, Beer, & Mycek, 2006).

Measurements of dissolved oxygen concentration in single living cells were previously demonstrated (Gerritsen, Sanders, Draaijer, & Levine, 1997; Mehta et al., 2007; Sud, Mehta, et al., 2006; Sud & Mycek, 2009; Sud, Zhong, Beer, & Mycek, 2006; Zhong, Urayama & Mycek, 2003), including one example shown in Fig. 20.5. Because the probe's fluorescence emission was found to be dynamically quenched by oxygen, the probe's lifetime was directly dependent upon local oxygen concentration and could be used for quantitative estimation of oxygen in living cells via FLIM. Molecular associations such as binding of the endogenous fluorophore nicotinamide adenine dinucleotide (NADH) to malate dehydrogenase have been imaged with FLIM (Lakowicz, Szmacinski, Nowaczyk, & Johnson, 1992) by using the increase in NADH lifetime upon binding as a source of contrast. NADH lifetime increased by ~150% and was much easier to detect than the blue shift of the emission spectrum that was only ~20% of the full-width at half-maximum in fluorescence intensity measurement.

Finally, FRET between the phospholipids NBD-PE (energy donor) and LRB-PE (energy acceptor) was employed to monitor endosomal fusion in single living cells

(Oida, Sako, & Kusumi, 1993). Excellent reviews providing further historical FLIM background can be found in French, So, Dong, Berland, and Gratton (1998), Gadella (1999), Tadrous (2000), van Munster and Gadella (2005), and Wallrabe and Periasamy (2005).

20.2 METHODS FOR CREATING FLUORESCENCE LIFETIME MAPS

The objective of both TD and FD measurements is to recover the lifetime parameter that describes fluorescence decay, thereby providing additional information that is not measured during steady-state intensity measurements. Both TD and FD methods (equivalent and related by the Fourier Transform) have comparable temporal resolution and discrimination, and benefit from the continual evolution of imaging technologies. The choice of FLIM instrumentation therefore depends on the particular application: FD FLIM uses any continuous wave light source and is better suited for evaluating short-lifetime measurements, while TD FLIM is optimal for flexible, large temporal range systems, and especially apt for long-lifetime measurements.

A more thorough and mathematically rigorous discussion of TD and FD approaches can be found in the previous edition of this book (Chang et al., 2007). In this edition, we emphasize emerging data analysis methods for FLIM (Section 2.3) that have been employed since the publication of the previous edition.

20.2.1 Time domain

Measuring fluorescence lifetime (τ) via TD methods involves reconstructing the exponential decay of fluorescence intensity over time, which can be accomplished in a variety of ways including the most commonly used techniques of gated integration and time-correlated single photon counting (TCSPC), each of which is further described below.

20.2.1.1 Time-gated FLIM

Figure 20.6 illustrates the instrumentation and concepts of the gated integration TD approach for measuring lifetime τ. A mode-locked or cavity-dumped laser, or a discharge source, is typically used to provide pulsed excitation. The excitation light pulse is split by a beam-splitter into two paths, one of which excites the sample on the microscope stage, while the other triggers the timing of an electronically gated charge-coupled device (CCD) camera, with programmable timing delays. After sample excitation, the fluorescence emission is collected by the CCD during gated detection. During the time period the CCD gate is open, the received fluorescence intensity signal is integrated (a convolution with the gated detector gain). Gates with different temporal delays provide different regions of the recorded signal waveform, making it possible to reconstruct the exponential decay curve.

Following the instrumentation setup in Fig. 20.6, the resulting fluorescence is a convolution of the sample's intrinsic fluorescence decay with the excitation

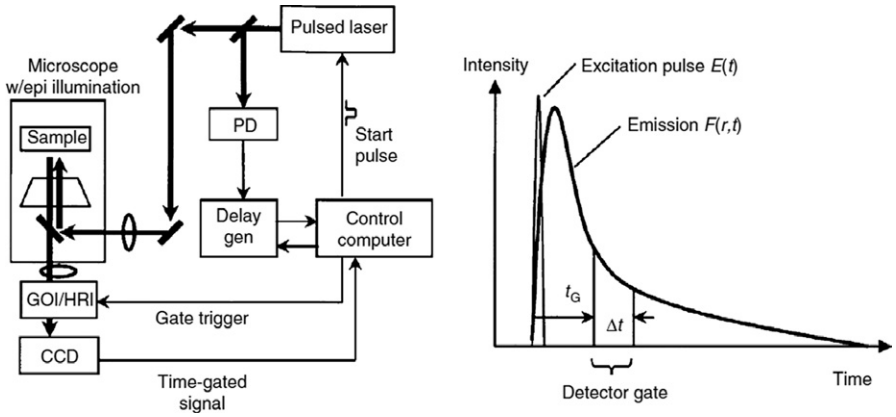

FIGURE 20.6

Time-domain lifetime imaging instrumentation and concepts (Sud, Mehta, et al., 2006; Sud, Zhong, Beer, & Mycek, 2006; Urayama & Mycek, 2003). The variable *r* indicates parameters that are spatially varying. Abbreviations for instrument schematics: PD, photodiode; delay gen, delay generator; GOI, gated optical intensifier; HRI, high-rate imager; CCD, charge-coupled device (camera); thick solid lines, light path; thin solid line, electronic path.

profile (the instrument response function) $E(t)$. For a sample with a spatially dependent j-component multiexponential lifetime, the fluorescence signal $F(r, t)$ is therefore

$$F(r,t) = E(t) \otimes \sum_j \alpha_j(r) \mathrm{e}^{-\left(\frac{t}{\tau_j(r)}\right)} = \int_{-\infty}^{t} E(t') \sum_j \alpha_j(r) \mathrm{e}^{-\left(\frac{t-t'}{\tau_j(r)}\right)} \mathrm{d}t' \tag{20.5}$$

where $\tau_j(r)$ and $\alpha_j(r)$ are the lifetime and amplitude of the jth component, respectively. The variable r emphasizes the spatial dependence of the fluorescence lifetime such as a pixel location on an area detector (e.g., a CCD camera). $E(t)$ is determined by replacing the sample with a reference with very short lifetime (unresolvable by system), so that the decay is effectively a delta-function. With $E(t)$ known, the lifetime $\tau_j(r)$ is fit to measured decays by using deconvolution algorithms, such as least-squares iterative reconvolution.

Because $F(r, t)$ detection must preserve both spatial and temporal information, a gated intensified CCD (ICCD) camera is often used. The ICCD can be switched on and off within a few nanoseconds, allowing it to control the exact timing of the signal incident onto the CCD. The fluorescence is imaged during a short interval $G(t)$

representing the gated detector gain, characterized by a rise time, fall time, and gate width. For a gate opening at time t_G, the detected image $D(r,t_G)$ is given by

$$D(r,t_G) = \int_{-\infty}^{\infty} G(t' - t_G)F(r,t')\mathrm{d}t' \tag{20.6}$$

The temporally and spatially resolved decay of the sample fluorescence is then reconstructed by imaging at various t_G, which is synchronized to the excitation pulse by using a photodiode coupled with electronics capable of variable delays.

However, deconvolution using iterative algorithms requires a well-sampled signal profile and can be computationally intensive and is usually not practical. Instead, pico- and femto-second sources, which can be regarded as delta-function excitation sources (time response is faster than system), are employed to eliminate the need for $E(t)$ deconvolution because fluorophore lifetimes are in the 0.1- to 10-ns regime. Also, the effects of $G(t)$ convolution can be minimized by using ratios of detected intensities (described in Section 2.3.1) or ICCD's with gate widths as fast as tens of picoseconds (Dowling, Hyde, Dainty, French, & Hares, 1997), so that $G(t)$ deconvolution may not be necessary.

20.2.1.2 TCSPC FLIM

In addition to gated detection, TCSPC has also been implemented for TD FLIM (Becker, Bergmann, & Weiss, 2002; Böhmer et al., 2001; Bugiel, König, & Wabnitz, 1989; Ghiggino, Harris, & Spizzirri, 1992). Figure 20.7 illustrates the concepts of TCSPC. The sample is excited with a high repetition rate excitation

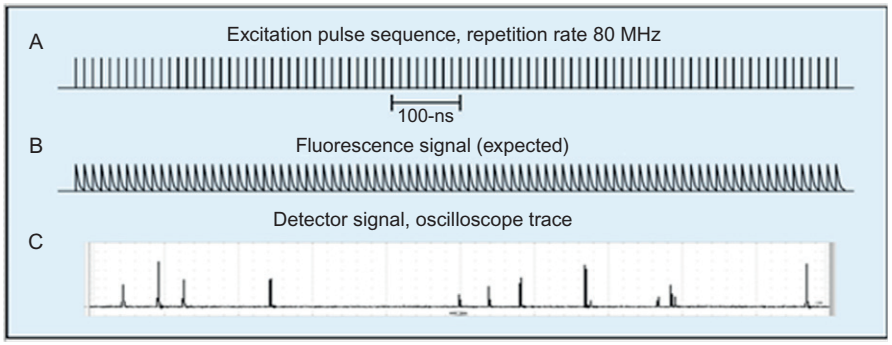

FIGURE 20.7

Illustration of time-correlated single photon counting (TCSPC). (A) A pulsed excitation source, here shown with a repetition rate of 80 MHz, is employed to repetitively excite a sample. (B) The expected fluorescence signal, if measured from each excitation pulse, would approximate an exponential pulse train. (C) However, the detected signal, here measured by an oscilloscope, is visibly different to that in part (B). The measured pulses are the detection of a single photon event, typically measured at a rate near $10^7\ \mathrm{s}^{-1}$. Once binned across time, these single observed fluorescence events accumulate into a fluorescence decay similar to Fig. 20.6 (right) (Becker, 2012).

source. With a sample with high quantum yield, each excitation pulse could generate a detectable fluorescence decay. In practice, this is not the case. Two primary reasons are users employing low excitation energy to limit potential photodamage to biological samples and weakly fluorescent samples. Therefore, TCSPC instead records fluorescence events with single-photon sensitivity and with time-correlated memory. Such memory records the first detected fluorescence photon as well as the time associated with the photon, and does not measure any later fluorescence. Therefore, the user can create a time-correlated histogram by binning individual recordings at the same time frames. TCSPC can be very accurate as the accuracy of the time measurement is not limited by the width of the detector gate. In addition, TCSPC has high efficiency, which records nearly every fluorescence photon detected, as compared with the time-gating scheme.

For TCSPC measurements (Lakowicz, 2006), a photomultiplier tube (PMT) is used to monitor each excitation pulse in order to produce a start signal to trigger the voltage ramp of a time-to-amplitude converter (TAC), which will be stopped upon detection of first emitted photon, providing an output pulse with a voltage proportional to the time between the start and stop signals. A multichannel analyzer converts the voltage to a time channel using an analog-to-digital converter (ADC). According to different time bins, where the photons are recorded, a probability histogram of counts is constructed versus time channels, from which the waveform of exponential decay is revealed.

An alternative is the reversed start–stop scheme, in which for each time period, the TAC is activated and starts ramping up voltage when the first photon is received. The voltage increase is stopped when a pulse is received, which can be either the pulse from the next period, or, if considering possible jitter of the pulses, a delayed pulse from the same period (the pulse that actually excited the photon). The reversal of time axis in the final data can be compensated for electronically. The advantage of the reversed start–stop scheme is that the TAC does not have to be constantly activated and reset in every period, considering the fact that in most periods actually no photon is recorded. However, reversed start–stop may cause some type of counting loss distortion.

With excitation pulses, dead-time-related distortion (one type of counting loss effect) may occur when using reversed start–stop scheme, since TAC/ADC dead time (when the TAC/ADC is processing signals) may extend into a subsequent pulse period. This will favor photon recording in the later part of pulse period. Dead-time-related distortion cannot be easily corrected, because the dead time may vary with the TAC voltage, and the transition from the dead time to the next active time may cause ripple in the TAC characteristic (Becker, 2005).

The photon counting rate is usually set to be only $\sim$1% to avoid a pile-up effect (another type of counting loss effect). The pile-up effect distorts the TCSPC data and makes the decay appear faster than is the case, since any photons detected after receiving the first photon will not be recorded. Simulations have been done to characterize the pile-up effect (Demas, 1983; Salthammer, 1992). The counting loss effect and its correction are described in Becker, 2005.

20.2.2 Frequency domain

The basic principle of FD FLIM is illustrated in Fig. 20.8 for a wide-field imaging system, though this approach is readily applicable to confocal systems (Fig. 20.9; Booth & Wilson, 2004). A sinusoidally modulated light source is used for excitation.

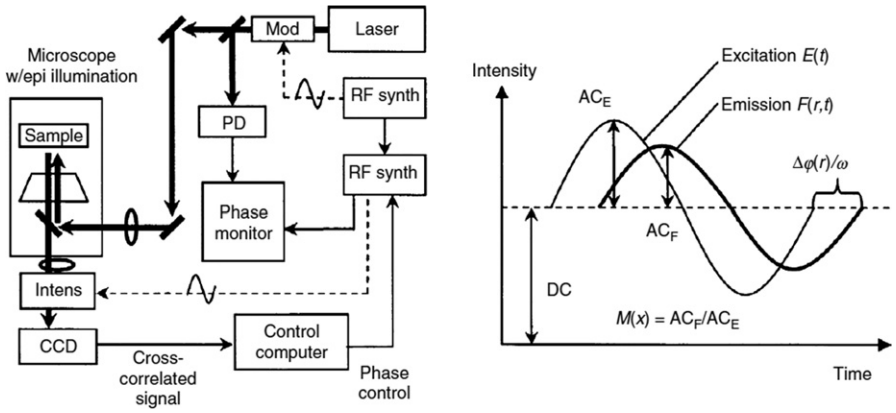

FIGURE 20.8

Frequency-domain lifetime imaging instrumentation and concepts (Urayama & Mycek, 2003). The variable *r* indicates parameters that are spatially varying. Abbreviations for instrument schematics: PD, photodiode; CCD, charge-coupled device (camera); RF synth, RF synthesizer; mod, intensity modulator; thick solid lines, light path; thin solid line, electronic path; dashed line, RF signal path.

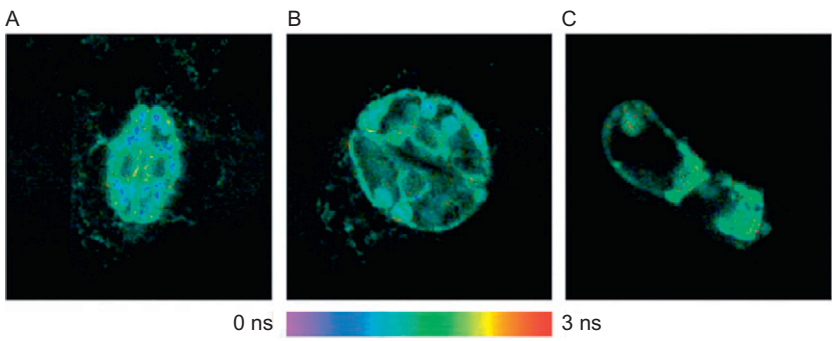

FIGURE 20.9

Combined fluorescence intensity and phase lifetime images of *Nicotiana tabacum* specimens with a confocal system. The fluorescence is a combination of autofluorescence and GFP fluorescence. (A and B) Stomata of leaves in which the endoplasmic reticulum was labeled with GFP5. (C) A trichrome of a leaf with GFP5-labeled Golgi. The hue of the images represents the fluorescence lifetime corresponding to the scale shown from 0 to 3 ns. The image widths are: (A) 100 μm, (B) 70 μm, and (C) 65 μm (Booth & Wilson, 2004).

The resulting sample emission is also sinusoidally modulated at the same frequency as the excitation, but is shifted in phase and is demodulated to some extent, that is, has a reduced modulation depth. Fluorescence lifetime can be directly calculated by changes in phase delay and demodulation. For measuring different lifetimes, different modulating source frequencies need to be used. Note that the measured phase delay φ between excitation and emission is in the range 0–90°, although arbitrarily long delays (>90°) can be introduced by optical delay lines. Demodulation of the emission is measured as a factor M (Fig. 20.8), which has a value of 0–1. It follows that at low frequencies, emission from samples with low lifetimes (fast decays) will follow the excitation faithfully; hence, the phase delay will be nearly 0° and the demodulation nearly 1. As the modulation frequency is increased, the finite lifetime of the fluorophore prevents this and is reflected in a phase delay as well as demodulation of the emission. At extremely high excitation frequencies, phase delay will be 90° while demodulation will be 0.

The phase delay and demodulation, plotted over a range of frequencies, provide the frequency response of the sample. Typically, the plot is limited to a "useful frequency" range in which changes in phase and demodulation are frequency dependent. As a general rule, the center frequency of this plot is approximately the reciprocal of the fluorescence lifetime (i.e., $1/\tau$). Hence, typical biological fluorophores such as NAD(P)H and collagen with lifetimes of few nanoseconds need excitation sources modulated at 1–200 MHz. Long-lived fluorophores such as platinum and ruthenium–ligand complexes have lifetimes of microseconds and hence the modulation is tens of kHz to 1 MHz. Lifetimes in the low picoseconds (e.g., Rose Bengal, 90 ps) require modulated sources at frequencies of approximately 2 GHz.

A detailed treatment of standard FD FLIM instrumentation and its variants can be found elsewhere (Lakowicz, 2006). Briefly, radio frequency modulation (MHz range) of a light source is done via acousto- or electro-optic modulators. The light source can be CW (argon-ion laser, arc lamps) or even a high repetition rate pulsed laser. On the detection side, cross-correlation is used to extract low-frequency phase and demodulation information by modulating the detector at a frequency offset from the modulation frequency, a scheme known as heterodyne detection. For sync operation, the same RF synthesizer is hence used for modulating the light source as well as providing the reference signal for the intensifier on the CCD.

One difficulty of FD measurements is accurate estimation of phase angle and modulation at high frequencies. In heterodyne detection, the signal waveform at the modulation frequency F is convolved with a reference waveform at frequency $F + \Delta F$ ($\Delta F = 10$–100 Hz). The slow response of the CCD acts as a low-pass filter that removes the high frequency component in the resulting waveform and provides an easily detectable, slowly varying signal with the phase and modulation information. Another approach known as homodyne detection involves setting $\Delta F = 0$. The resulting signal (after low-pass filtering) is a static-phase-dependent signal. A detailed treatment of FD data analysis can be found in Urayama and Mycek (2003).

20.2.3 Data analysis methods

FLIM measures a three-dimensional data cube, containing both spatial and temporal information. Analyzing FLIM measurements is, therefore, more involved than analyzing intensity-based measurements. Five methods are introduced in this section: (i) rapid lifetime determination (RLD) and analytical least-squares algorithms, (ii) iterative least-squares analysis with multiexponential fitting, (iii) least-squares analysis with Laguerre polynomial fitting, (iv) phasor plot analysis, and (v) methods for improving precision of fluorescence lifetime maps. Methods detailed focus on rapid, accurate, and high-throughput FLIM analysis.

20.2.3.1 RLD and analytical least-squares algorithms

An analytic RLD algorithm can be used to analyze time-gated FLIM data (Bugiel et al., 1989; Sharman, Periasamy, Ashworth, Demas, & Snow, 1999; Wang, Uchida, Coleman, & Minami, 1991). As an example of how using intensity ratios eliminate gate parameters and of analytic lifetime determination, consider a sample with a single-exponential lifetime excited by a negligibly short excitation pulse. For an effective gate width Δt, the gated detector signal at time t is as follows

$$D(r,t) = \int_{t}^{t+\Delta t} \alpha e^{-\left(\frac{t'}{\tau(r)}\right)} dt' = \alpha\tau\left[e^{-\left(\frac{t}{\tau(r)}\right)} - e^{-\left(\frac{t+\Delta t}{\tau(r)}\right)}\right] \tag{20.7}$$

A spatially resolved lifetime τ (r) can be determined by using two images gated at times t_1 and t_2 (Wang, Periasamy, Herman, & Coleman, 1992), so that

$$\tau(r) = \frac{t_2 - t_1}{\ln\frac{D(r,t_1)}{D(r,t_2)}} \tag{20.8}$$

Note that the gate width cancels from the ratio. Because the lifetime determination is analytic and requires only two gates, a two-dimensional image of lifetimes can be constructed rapidly. The acquisition of only two gates allows one to measure the lifetime map in real time, since image acquisition and processing take a fraction of a second (Cubeddu, Comelli, D'Andrea, Taroni, & Valentini, 2002). In practice, a two-gate scheme can be sensitive to noise, therefore methods using N gates (N typically equal to 5–10; Cubeddu et al., 2002) can be used with least-squares method to increase data redundancy and give more stable results. In this case, lifetime images were calculated on a pixel-by-pixel basis by

$$\tau_p = -\frac{N\left(\sum t_i^2\right) - \left(\sum t_i\right)^2}{N\sum t_i \ln I_{i,p} - \left(\sum t_i\right)\left(\sum \ln I_{i,p}\right)} \tag{20.9}$$

where N is the number of images, $I_{i,p}$ is the intensity of pixel p in image i, and t_i is the gate delay of image i. All sums are over i.

For more complicated fluorescence decays, double exponential (Cubeddu et al., 2002; Sharman et al., 1999) and nonexponential decays (Lee et al., 2001) have been considered.

20.2.3.2 Iterative least-squares analysis with multiexponential fitting

Iterative least-squares analysis can be performed to analyze TCSPC-FLIM data. The goal of iterative least-squares method is to minimize goodness of fit (χ^2) by varying the values of model parameters. χ^2 is expressed as follows

$$\chi^2 = \sum_{k=1}^{n} \frac{1}{\sigma_k^2} [N(t_k) - N_c(t_k)]^2 = \sum_{k=1}^{n} \frac{[N(t_k) - N_c(t_k)]^2}{N(t_k)} \tag{20.10}$$

where n is the total number of channels, $N(t_k)$ is the observed count number in channel k, $N_c(t_k)$ is the calculated count number in channel k from model prediction, and σ_k^2 is the variance of $N(t_k)$, which is equal to $N(t_k)$ from Poisson statistics. χ^2 is actually a variance-weighted least-squares statistic that will have a value close to the number of measurements channels for good fits, which follows statistical χ^2 distribution.

Suppose the FLIM data are being analyzed in terms of the multiexponential model in Eq. (20.5), then the values of τ_j and α_j are varied until χ^2 is a minimum, which occurs when $N(t_k)$ and $N_c(t_k)$ are most closely matched. In practice, a table of χ_R^2, reduced χ^2 (defined as the division of χ^2 by the degrees of freedom) distribution, showing the p-values for various χ_R^2 values with different degrees of freedom, will help decide how well the model fits the data. Since systematic errors in the data can easily result in a 10–20% elevation of χ_R^2, a model would be acceptable if p-value is not statistically significant at 5% significant level (Lakowicz, 2006).

20.2.3.3 Least-squares analysis with Laguerre polynomial fitting

The Laguerre deconvolution method was proposed for time-resolved fluorescence analysis in 1993 (Marmarelis, 1993), first being demonstrated for rapid analysis of single fluorescence decays and only recently demonstrated for fast FLIM analysis (Jo, Fang, & Marcu, 2005; Pande & Jo, 2011). Since then, Laguerre analysis has been employed for a variety of fluorescence lifetime and FLIM applications, ranging from brain tumor (Sun et al., 2010) to oral carcinoma detection (Sun et al., 2009). Advantages of Laguerre deconvolution compared with multiexponential fitting include no *a priori* assumptions about the modeled decay behavior of the data, rapid fitting via least-squares estimation, and a unique "best" fit.

Laguerre analysis is based on the Laguerre expansion of the kernel technique. Each measured decay is fit to one set of unique and discrete Laguerre functions on an orthonormal basis given as follows

$$h(r,n) = \sum_{j=0}^{L-1} c_j(r) b_j^{\alpha}(n) \tag{20.11}$$

with

$$b_j^{\alpha}(n) = \alpha^{(n-j)/2}(1-\alpha)^{1/2}\sum_{k=0}^{j}(-1)^k\binom{n}{k}\binom{j}{k} \tag{20.12}$$

where $c_j(r)$ are the Laguerre expansion coefficients to be solved for at each pixel p, L is the number of Laguerre functions to be used to model the fluorescent data, and $b_j^{\alpha}(n)$ represents the jth Laguerre function. The α value used must be between 0 and 1. For fluorescence decays with longer average lifetimes, higher α values will yield better fits.

Laguerre analysis has been employed for FLIM analysis because the model can fit each image pixel simultaneously. Such an approach has been shown to reduce analysis time by at least two orders of magnitude (Jo et al., 2005). For example, in 480×736 FLIM images, Laguerre analysis was shown to take <60 s (Sun et al., 2010).

20.2.3.4 Phasor plot analysis

Phasor plot analysis is based on well-established procedures originally developed to analyze dielectric relaxation experiments, that is, a sample's transient responses to repeated perturbations (Hill, 1969). In fluorescence, this method was applied to analyze FD FLIM data, as the modulated excitation light is the perturbation and the fluorescence emission is the relaxation. In recent years, phasor analysis was further developed to offer a simple, graphical, and rapid algorithm for interpreting FD FLIM data that were obtained after single excitation frequency from samples exhibiting more than one fluorescence lifetime (Clayton, Hanley, & Verveer, 2004; Redford & Clegg, 2005).

In FD experiments, phasor analysis transformed the modulation, M, and the phase, φ, (see Fig. 20.8) of the emission with respect to the excitation into

$$x = M\cos\varphi \tag{20.13}$$

and

$$y = M\sin\varphi. \tag{20.14}$$

A pair of x and y values represents a phasor vector on the phasor plot.

TD FLIM can also be analyzed with phasor analysis because the excitation pulse frequency can be transformed into phasor space similarly to the sinusoidal excitation frequency of FD FLIM. To provide an instantaneous (excluding complex fitting procedures) view of the fluorescence decay in TD experiments, the FD FLIM phasor plot analysis was modified (Digman, Caiolfa, Zamai, & Gratton, 2008). Fluorescence decays, $F(t)$, at each pixel of an image were transformed into a phasor plot by

$$x = \frac{\int_0^{\infty} F(t)\cos(\omega t)\mathrm{d}t}{\int_0^{\infty} F(t)\mathrm{d}t} \tag{20.15}$$

and

$$y = \frac{\int_0^\infty F(t)\sin(\omega t)\mathrm{d}t}{\int_0^\infty F(t)\mathrm{d}t}, \tag{20.16}$$

where ω is the laser repetition angular frequency. Each pixel of the image gives a point on the phasor plot. If the fluorescence decay is single exponential, the coordinates x and y become

$$x = \frac{1}{1+(\omega\tau)^2} \tag{20.17}$$

and

$$y = \frac{\omega\tau}{1+(\omega\tau)^2}. \tag{20.18}$$

The two coordinates lie on the semicircle of a phasor plot, as shown in blue in Fig. 20.10A.

The analysis is performed by observing clustering of pixels in specific regions of the phasor plot, providing a global view of FLIM images. The method can also be used in a reciprocal mode in which each point of the phasor plot is mapped, and pseudocolored, to a pixel of the image (Fig. 20.10). Since every molecular species has a specific phasor vector, located in specific regions, users can identify molecules by their position on the phasor plot. Therefore, the phasor/polar plots analysis makes the interpretation of FLIM data accessible to the nonexpert.

20.2.3.5 Improving precision of fluorescence lifetime maps

Precise fluorophore lifetime mapping is vitally important to quantifying the biological microenvironment. One challenge to precise lifetime mapping is that all measurements must be obtained without perturbing living cells—a difficult task. The experimenter may be tempted to use high power and long measurement times to acquire high-quality images, but such conditions could damage the cells and fluorophores. The opposite can also be true. Low-light and fast measurements will maintain cell viability, but may not produce images with high signal-to-noise ratio. Temporal optimization and spatial denoising methods were developed to address this problem and enhance the precision of acquired FLIM data.

For time-gated FLIM, optimal temporal gating techniques using either Monte Carlo simulations or analytical error propagation analysis were developed to reduce the illumination light dose, while additionally improving the precision of lifetime analysis (Chang & Mycek, 2010b; Sharman et al., 1999). Relative standard deviation (RSD), defined as the standard deviation divided by the mean value, was calculated over a determined FLIM image assuming only Poisson noise. The optimal gating parameters, the gate width and the time interval between the starting points of

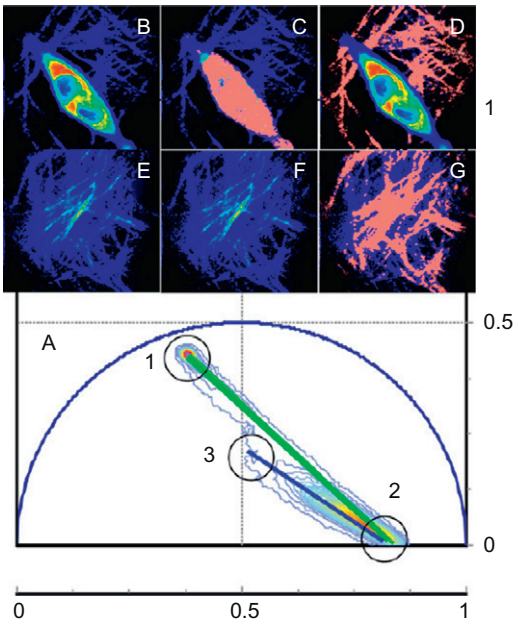

FIGURE 20.10

Phasor plot analysis for analyzing time-domain FLIM data offers several key advantages compared with conventional time-domain FLIM data analysis techniques. The analysis is instantaneous without complex fitting procedures and the phasor plot provides a visual representation of the fluorescence decay, making the FLIM technique accessible to an untrained user. Here, fluorescence intensity images were acquired from (B) CHO-K1 cells transfected with paxillin EGFP in a three-dimensional collagen matrix and (E) only the collagen matrix. Each fluorescence image pixel was transformed into (A) phasor space. All pixels contained within cursor Position 1 on the phasor plot were pseudocolored pink in images (C) and (F), corresponding to the EGFP expression. The pixels contained within Position 2 were pseudocolored pink in images (D) and (G), corresponding to the collagen fluorescence. Position 3 represents weak fluorescence background. The color-coded images show homogeneous EGFP or collagen signals, demonstrating a precise characterization of the cellular microenvironment (Digman et al., 2008).

two consecutive gates, were determined by minimizing the RSD. In addition to optimal temporal gating, image denoising methods were employed to enhance time-gated and TCSPC-FLIM data for precise lifetime mapping.

Figure 20.11 shows that both optimal virtual gating and the total variation (TV) denoising method, commonly used in medical imaging systems for selective smoothing and hence edge preserving, reduced RSD of TCSPC-FLIM data in live cells (Chang & Mycek, 2010a). In particular, when combining the two methods sequentially, the resulting RSD was lower than when either method was employed alone. One advantage of this newly developed, TV-based spatial denoising method

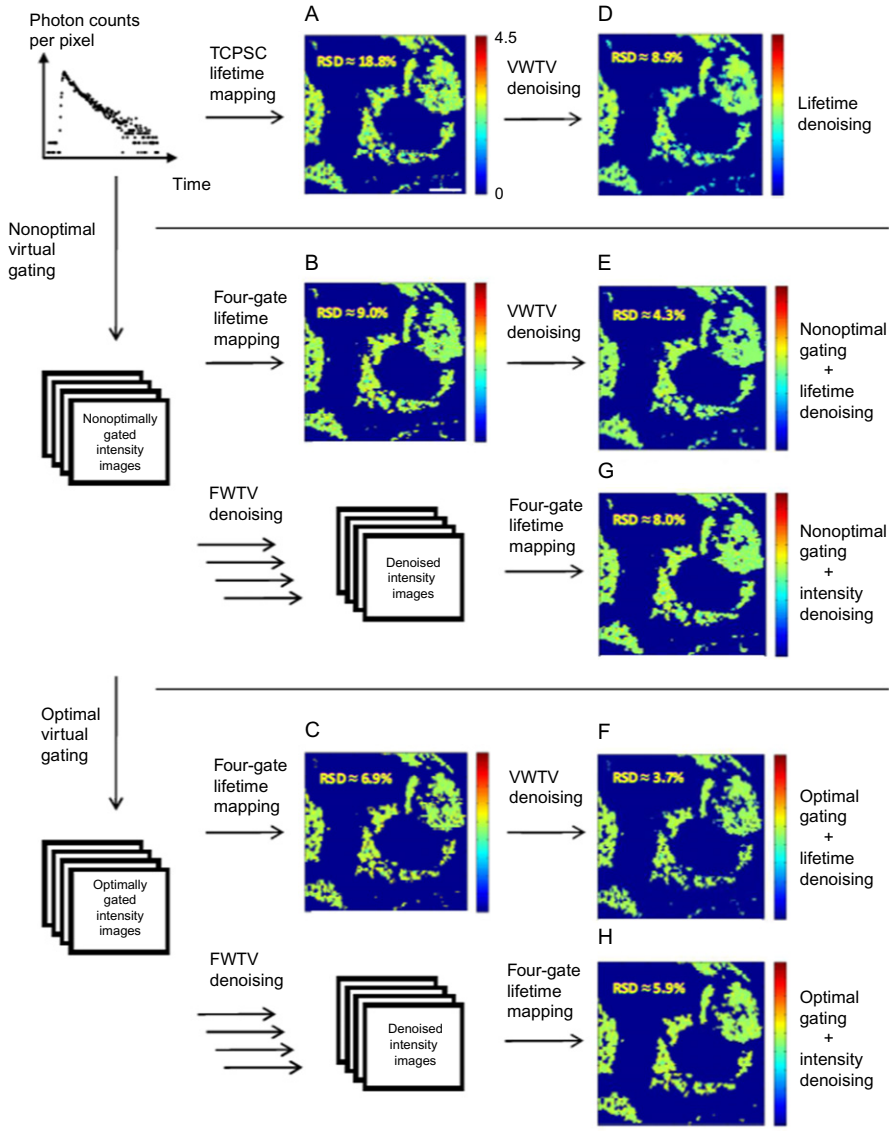

FIGURE 20.11

Temporal optimization and spatial denoising methods can be applied to previously acquired FLIM measurements to improve lifetime precision of live-cell images. Here, multiphoton microscopy was employed to image live LLC-PK1 cells expressing mEmerald-EB3. Temporal optimization improved lifetime precision shown from (A) the TCSPC lifetime map to (C) the optimal virtual-gated lifetime map, indicated by the decreased RSDs. Total variation denoising techniques further improved lifetime precision, yielding reduced RSDs in (D)–(H). In addition, employing the denoising method combined with optimal virtual gating notably improved the precision of (C). RSD represents relative standard deviation, an indicator for the lifetime uncertainty. FWTV, *f*-weighted total variation; VWTV, variance-weighted total variation (Chang et al., 2010a).

is its versatility: the technique can be employed to denoise intensity images at each gate or it can directly denoise a lifetime map with either Poisson or non-Poisson distributed noise (Chang & Mycek, 2010a, 2010b, 2012a).

20.3 FLIM TECHNIQUES FOR QUANTITATIVE BIOLOGICAL IMAGING

The applications that follow are examples of FLIM that were chosen to highlight the broad range of FLIM applications, spanning both endogenous and exogenous fluorescence measurements. These measurements include subcellular resolution to detect protein–protein interactions (e.g., FRET) and molecular diffusion (e.g., FCS). Additionally, the examples demonstrate applications of FLIM for quantitative biological imaging via exogenous and/or sample endogenous fluorophores for several biological systems, including cells, tissues, and organs.

20.3.1 FLIM detection of FRET events

Förster (or fluorescence) resonance energy transfer theory was developed by Professor Theodor Förster (Förster, 1948), and it describes the mechanism for experimental techniques developed to measure spatial distance between two (or multiple) fluorophores. Cell biologists exploit FRET to measure the distance between two sites on a macromolecule, the distance between two proteins attached with fluorophores, and hence whether and how these two proteins interact. FRET is regarded as an *in vivo* "nanoscale ruler," since it can be monitored in living cells, and the distance for FRET to occur is usually within several nanometers, and on the same scale as the dimensions of biological macromolecules. The diameter of many proteins, the distance within which proteins interact in living cells, the thickness of biological membranes, and the distance between sites on multisubunit proteins are typically within this scale.

FRET mandates the presence of at least one donor–acceptor (D–A) pair having a D–A distance associated therewith, although more than one such pairs and hence distances can be involved. Readers interested in more details are referred to Chapter 15 in Lakowicz, 2006. FRET occurs when the donor emission spectrum overlaps with the acceptor excitation spectrum. After donor excitation, energy will be transferred nonradiatively if the D–A pair is in close proximity (i.e., via the nonradiative pathway illustrated in Fig. 20.2 without photo emission), as a result of long-range dipole–dipole interaction between the D–A pair. In other words, the acceptor does not reabsorb the photons emitted from the donor as a means of energy transfer, which also implies that the intervening solvent or molecule has little effect on the efficiency of FRET. A common use of FRET is to monitor any phenomena with changes in the D–A distance, such as conformational changes of a macromolecule, or the cleavage of a macromolecule by enzymes. FRET can be measured with endogenous (using tryptophan as a donor, Table 20.1) or exogenous fluorophores (e.g., CFP-YFP) as D–A pairs in cell biology (Becker et al., 2005).

How close exactly for the D–A pair will FRET occur? Quantitatively, Förster distance is defined as the distance at which the energy transfer efficiency is 50% and the energy transfer efficiency (E) is defined as

$$E = \frac{k_T}{\tau_D^{-1} + k_T} \tag{20.19}$$

where τ_D is the donor lifetime in the absence of an acceptor and k_T is the energy transfer rate from a donor to an acceptor. k_T is given by

$$k_T = \frac{1}{\tau_D}\left(\frac{R_0}{r}\right)^6 \tag{20.20}$$

where R_0 is the Förster distance and r is the D–A distance. In Eq. (20.20), when $r = R_0$, $E = 50\%$, as described in the definition of Förster distance. Also, the dependence of k_T on r is highly nonlinear and strong when the D–A distance is near R_0; when $r = 2R_0$, the energy transfer efficiency drops to only 1.56%, according to Eqs. (20.19) and (20.20).

In order to detect FRET efficiently, D–A pairs with longer R_0 are preferred. The typical value of R_0 is in the range of 20–60 Å, depending on the extent of D–A spectra overlap, the D–A orientation, the refractive index of the medium, and the quantum yield (see Eq. 20.4) of the donor in the absence of an acceptor. Since D–A orientation is usually assumed to be dynamic and random, while refractive index of the medium typically treated as a constant for biomolecules in aqueous solution, in usual cases R_0 is considered dependent only on the optical properties of the fluorophore pairs and is approximately fixed for a given D–A pair.

FRET can be measured with either steady-state or time-resolved data (Jares-Erijman & Jovin, 2003); the donor lifetime is shortened and the donor intensity is lowered if FRET occurs. FRET-FLIM combines FRET and lifetime imaging, often with considerable advantages over intensity-based FRET. The main advantage is that FRET-FLIM eliminates possibilities that results are biased from intensity-based measurement artifacts that could modify results by more than the FRET efficiency (Chang, Wu, Merajver, & Mycek, 2009; Zhong et al., 2007).

Figure 20.12 presents results from a time-lapsed FRET-FLIM study that measured chromatin compaction at the scale of nucleosomal arrays in live cells from metaphase to telophase (Lleres et al., 2009). A human cell line coexpressing histone H2B tagged to express either enhanced green fluorescent proteins (EGFP) or mCherry fluorescent proteins was monitored. FRET occurred between EGFP- and mCherry-tagged histones on separate nucleosomes. The number of FRET events increases when chromatin compacts. The FRET map spatially illustrated the degree of compaction for the entire set of chromosomes (Fig. 20.12). A heterogeneous population of different FRET efficiencies was seen in metaphase (blue and green regions), which subsequently became more homogeneous and reached maximum as the cell progressed into late anaphase. These data are consistent with extensive higher order folding of chromatin fibers occurring during the anaphase.

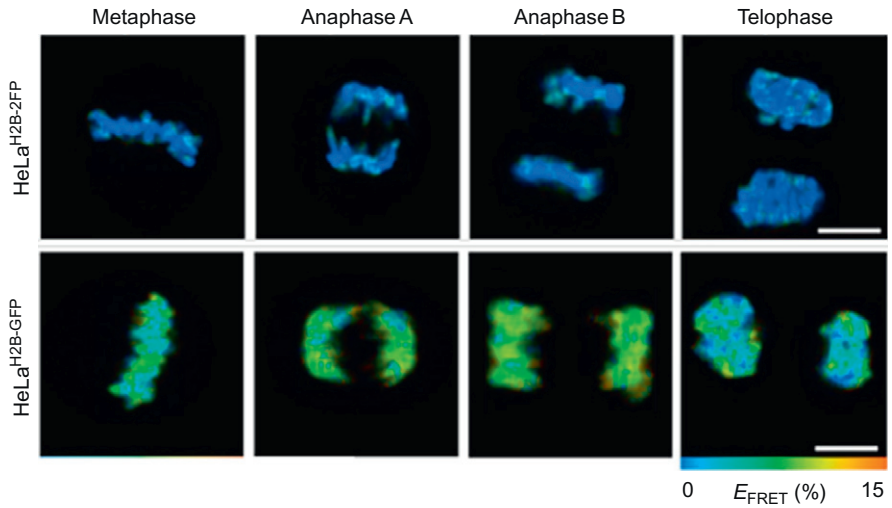

FIGURE 20.12

FLIM-FRET was used to assess chromatin compaction within chromosomes of live cells at different stages of mitosis. FRET map derivation is detailed in Section 3.1. HeLa cells (top, control) expressing only histone H2B tagged to enhanced green fluorescent protein (EGFP) ($HeLa^{H2B\text{-}GFP}$) or (bottom, experimental) coexpressing H2B tagged to either EGFP or mCherry FPs ($HeLa^{H2B\text{-}2FP}$) were compared. FRET occurs between FP-tagged histones and was increased during chromatin compaction. $HeLa^{H2B\text{-}2FP}$ cells at different stages during mitosis show variations in compaction level, observed as different FRET efficiency populations. The variation was throughout the length of all chromosomes, reaching maximum FRET efficiency in late anaphase. Alternatively, $HeLa^{H2B\text{-}GFP}$ did not show the FRET variation. Scale bar: 10 μm (Lleres, James, Swift, Norman, & Lamond, 2009).

In addition, a two-photon FRET-FLIM system for protein localization was characterized (Chen & Periasamy, 2004), and plasma membrane organization in cowpea protoplasts was studied using FRET-FLIM with different GFP-fused proteins (Vermeer, van Munster, Vischer, & Gadella, 2004). A FRET-FLIM-based detection, performed in FD, was employed to monitor protein kinase Cα (PKCα) molecules immunostained with both Cy3 (donor) and Cy5 (acceptor). FRET occurred only on phosphorylated PKCα molecules (Ng et al., 1999). A review on FRET-FLIM has provided a table of commonly used FRET fluorophore pairs for FLIM studies (Wallrabe & Periasamy, 2005).

20.3.2 Intracellular molecular diffusion rates measured via FCS-FLIM

The advent of photon counting techniques such as TCSPC has resulted in the development of statistical methods for sample analysis, broadly classified as FCS. As mentioned earlier, benefits of FLIM lie in obtaining information other than,

and complementary to, fluorophore concentration and localization; this includes the molecular environment and protein grouping and/or interactions. By measuring variations in fluorescence intensity at a single image pixel over time, FCS provides single-point measurements of kinetic and diffusion properties of fluorescent molecules, as well as their concentration and aggregation state. The detection volume in confocal systems is in the subfemtometer range, and the number of fluorescent molecules in this small space will typically be one.

FCS can also be used to cover dynamic phenomena on a submicrosecond timescale. FCS-FLIM provides a very useful fluorescence modality which can be implemented on confocal systems, and commercial integrated products are available for this purpose. FCS has been reported early on for studying the mobility of small solutes in the cytoplasm of living cells (Berland, So, & Gratton, 1995). Kask, Palo, Ullmann, and Gall (1999) used FCS for monitoring restriction-enzyme-mediated cleavage of DNA hybrids by using fluorescently labeled complementary oligonucleotides. A two channel confocal fluorescence lifetime microscope was used for FCS and FLIM, since the timing information down to a picosecond scale offered the possibility not only to reconstruct fluorescence decay of each pixel for FLIM but also to analyze the fluorescence fluctuation correlation function of any single spot of interest (Wahl, Koberling, Patting, Rahn, & Erdmann, 2004). Healthy and sorbitol-stressed cells expressing a GFP-MK2 fusion protein were studied with TCSPC and analyzed with lifetime imaging and FCS (Becker et al., 2006). In stressed cells, while FLIM results demonstrated a lifetime reduction and translocation of the proteins to the cytoplasm, FCS of one single spot showed slower diffusion with higher correlation amplitude, possibly indicating the aggregation of the proteins. Reviews on FCS and FLIM can also be found in Breusegem, Levi, and Barry (2006) and Hink, Bisselin, and Visser (2002).

20.3.3 Multispectral-FLIM

Multispectral-FLIM (ms-FLIM) leverages the primary advantages of fluorescence spectroscopy and FLIM imaging into one measurement (Becker, Bergmann, & Biskup, 2007; Lloyd et al., 2010). That is, ms-FLIM enables the user to perform spectral unmixing to isolate individual fluorophore contributions from a multi-fluorophore samples, akin to fluorescence spectroscopy, while additionally allowing the user to measure the effect of the microenvironment on an individual fluorophore in a given spectral band, akin to fluorescence lifetime imaging. Collecting FLIM images in multiple wavelength bands increases the overall measurement time, but the advantageous gains in data breadth described below can overcome such a limitation.

The advantages from fluorescence spectroscopy and FLIM imaging provide the most benefit when measured samples contain multiple fluorophores with broad emission spectra, whether exogenous, endogenous, or both. Such samples often contain a fluorophore that will be prominent in the collected signal, making the contributions from less prominent fluorophores very small and more difficult to analyze.

One advantage to FLIM imaging, as mentioned earlier, is the measurement of functional and spatial fluorophore information. ms-FLIM takes this one step further: through FLIM image acquisition at multiple wavelengths, functional information can be analyzed from multiple fluorophores. One such example involving endogenous fluorescence is the simultaneous detection of NAD(P)H and FAD, two biologically relevant molecules related to cellular metabolism. In this case, these fluorophores can be preferentially detected with emission detection less than ~500 nm for NAD(P)H and greater than ~500 nm for FAD (Skala et al., 2007).

Figure 20.13 shows typical data collected with an ms-FLIM instrument (Becker et al., 2007). Here, a fresh mouse kidney section was excited with 750-nm two-photon excitation, and images were collected in 16 evenly spaced wavelength

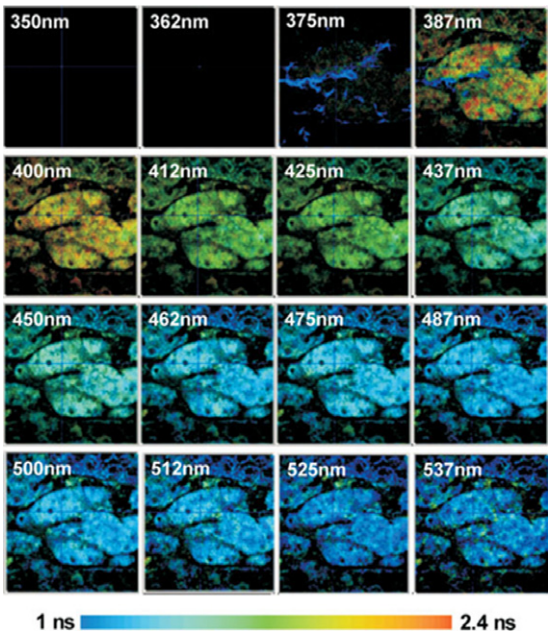

FIGURE 20.13

Multispectral fluorescence lifetime imaging microscopy (ms-FLIM) increases data depth of standard FLIM measurements. Here, ms-FLIM measurements were acquired by measuring FLIM images with a fixed excitation wavelength and varying emission wavelength bandpasses. Such data enable the user to spatially and spectrally resolve fluorescence. Here, ms-FLIM images were measured from unstained mouse kidney after 2-photon excitation at 750 nm (Zeiss LSM510 NLO microscope with Becker–Hickl FLIM detection). While characteristic fluorescence was similar among all wavelengths spatially, there are marked differences in average fluorescence lifetime, ranging from ~2–2.4 ns at 387 nm to ~1 ns or less at 537 nm, underscoring the ability for quantitative analysis of multiple tissue fluorophores (Becker et al., 2007).

regions from 350 to 537 nm. FLIM maps of average lifetime are shown for each wavelength region. There is an observable decrease in average lifetime from low-emission wavelengths (<400 nm) to middle-emission wavelengths (412–450 nm) to high wavelengths (>462 nm), which can be attributed to the detection of different relative contributions of endogenous fluorophores in each wavelength region. Collection time for the image was 10 min, resulting from a low power level to reduce sample photobleaching and photodamage. With a higher sample fluorescence, common in some applications involving exogenous fluorescence, multispectral images were collected in 20 s with a fixed excitation wavelength (Becker et al., 2007).

One future application of ms-FLIM can be for enhanced FLIM-FRET detection. With measurements in multiple wavelength ranges, the user will have an easier task to separate the donor and acceptor lifetimes. Additionally, it will be easier to separate out background fluorescence (Becker et al., 2007).

For greater fluorophore separation, state-of-the-art excitation sources can be combined with ms-FLIM setups to achieve multiwavelength detection after multiwavelength excitation (Owen et al., 2007). This application involves more selective fluorophore targeting than common ms-FLIM setups. Moreover, multiwavelength excitation allows for greater precision in resolving individual fluorophores and the effect of the microenvironment (Skala et al., 2007).

20.3.4 MP-FLIM of endogenous tissue fluorophores

Multiphoton excitation microscopy provides high axial (optical sectioning) and lateral resolution, reduced out of focus photobleaching/photodamage, and is optimal for deep tissue imaging (Helmchen & Denk, 2005). The high sensitivity of multiphoton microscopy imaging makes it ideal for measuring endogenous tissue fluorophores.

Endogenous tissue fluorophores such as NAD(P)H, FAD, collagen, elastin, and keratin report on tissue microenvironment without chemical staining (Zipfel et al., 2003). In particular, intracellular NAD(P)H and FAD molecules are involved in mitochondrial metabolic pathways (Heikal, 2010). Therefore, measurements of such endogenous fluorophores are label-free indicators of tissue metabolism.

Figure 20.14 illustrates NAD(P)H- and FAD-binding states measured with a multiphoton-FLIM system. *In vivo* label-free measurements to monitor precancerous epithelia were performed on 22 hamster cheek pouches (Skala et al., 2007). A significant decrease in the contribution and lifetime of protein-bound NADH was observed in both low- and high-grade epithelial precancers compared with normal epithelial tissues. In addition, a significant increase in the protein-bound FAD lifetime and a decrease in the contribution of protein-bound FAD were observed in high-grade precancers only. Increased intracellular variability in the NADH and FAD fluorescence lifetimes were observed in precancerous cells compared with normal cells.

Label-free multiphoton-FLIM was also employed to characterize normal human epidermis at different skin sites and in patients of different ages (Benati et al., 2011), monitor metastasis and the tumor microenvironment in tissues (Provenzano, Eliceiri, & Keely, 2009), and monitor cell viability for tissue engineering applications

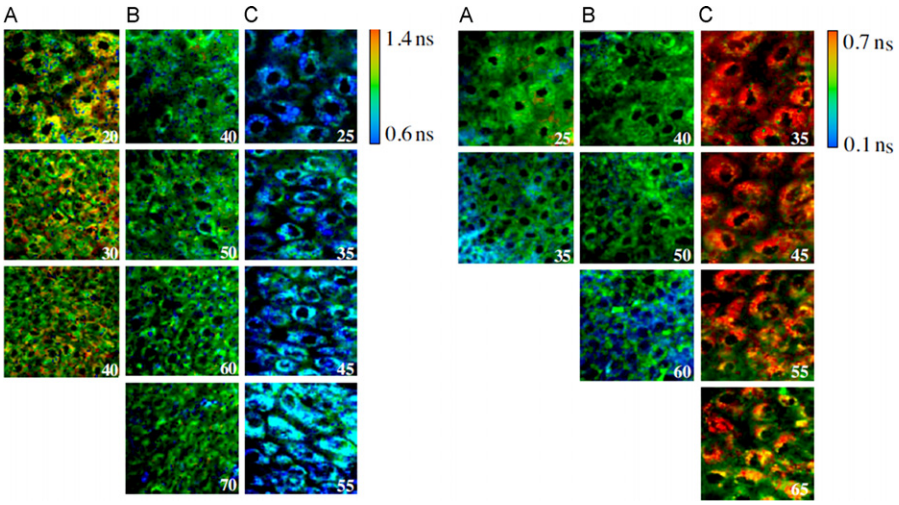

FIGURE 20.14

Multiphoton TCSPC-FLIM was employed to distinguish (A) normal, (B) low-grade precancer, and (C) high-grade precancer promoted in a hamster cheek pouch model. *In vivo* multiphoton TCSPC-FLIM images of (left) mean NADH and (right) mean FAD suggested that the averaged NADH lifetime decreases and the average FAD lifetime increases with precancer development. The lifetime and contribution of free and protein-bound NADH and FAD were shown to characterize the precancer development in Skala et al. (2007). Images were acquired with excitation at 800 nm and emission centering at 490 nm (with a 490 short-pass filter) for NADH, excitation at 890 nm and emission between 400 and 600 nm for FAD.

(Lloyd et al., 2012) via measurements of endogenous tissue fluorophores, demonstrating its potential for future clinical use.

SUMMARY

In this chapter, the basic concepts, key advantages, data analysis methods, and several applications of FLIM are discussed. Continuing advances in technology for microscopy and the developing appreciation that fluorescence lifetime is a sensitive means for quantitatively evaluating microenvironment will likely help make FLIM a critical research tool for cell biology by providing new ways for life scientists to detect, visualize, and investigate structure and function in biological systems.

Acknowledgment

This work was supported in part by the National Institutes of Health grant NIH R01-DE-01943 (to M.-A. M.).

References

Becker, W. (2005). *Advanced time-correlated single photon counting techniques* Vol. 81. Berlin, Heidelberg: Springer Verlag.

Becker, W. (2012). *The bh TCSPC handbook* (5th ed.). Berlin, Germany: Becker & Hickl GmbH. *http://www.becker-hickl.com/handbook.htm*.

Becker, W., Bergmann, A., & Biskup, C. (2007). Multispectral fluorescence lifetime imaging by TCSPC. *Microscopy Research and Technique*, *70*(5), 403–409.

Becker, W., Bergmann, A., Haustein, E., Petrasek, Z., Schwille, P., Biskup, C., et al. (2005). Fluorescence lifetime images and correlation spectra obtained by multi-dimensional TCSPC. *Multiphoton Microscopy in the Biomedical Sciences V*, *5700*, 144–151.

Becker, W., Bergmann, A., Haustein, E., Petrasek, Z., Schwille, P., Biskup, C., et al. (2006). Fluorescence lifetime images and correlation spectra obtained by multidimensional time-correlated single photon counting. *Microscopy Research and Technique*, *69*(3), 186–195.

Becker, W., Bergmann, A., & Weiss, G. (2002). Lifetime imaging with the Zeiss LSM-510. *Proceedings of SPIE*, *4620*, 30–35.

Benati, E., Bellini, V., Borsari, S., Dunsby, C., Ferrari, C., French, P., et al. (2011). Quantitative evaluation of healthy epidermis by means of multiphoton microscopy and fluorescence lifetime imaging microscopy. *Skin Research and Technology*.

Berland, K. M., So, P. T. C., & Gratton, E. (1995). Two-photon fluorescence correlation spectroscopy—Method and application to the intracellular environment. *Biophysical Journal*, *68*(2), 694–701.

Böhmer, M., Pampaloni, F., Wahl, M., Rahn, H.-J., Erdmann, R., & Enderlein, J. (2001). Time-resolved confocal scanning device for ultrasensitive fluorescence detection. *The Review of Scientific Instruments*, *72*(11), 4145–4152.

Booth, M. J., & Wilson, T. (2004). Low-cost, frequency-domain, fluorescence lifetime confocal microscopy. *Journal of Microscopy*, *214*(Pt 1), 36–42.

Breusegem, S. Y., Levi, M., & Barry, N. P. (2006). Fluorescence correlation spectroscopy and fluorescence lifetime imaging microscopy. *Nephron Experimental Nephrology*, *103*(2), e41–e49.

Bugiel, I., König, K., & Wabnitz, H. (1989). Investigation of cell by fluorescence laser scanning microscopy with subnanosecond time resolution. *Lasers in the Life Sciences*, *3*(1), 47–53.

Chang, C.-W., & Mycek, M.-A. (2010a). Precise fluorophore lifetime mapping in live-cell, multi-photon excitation microscopy. *Optics Express*, *18*(8), 8688–8696.

Chang, C.-W., & Mycek, M.-A. (2010b). Enhancing precision in time-domain fluorescence lifetime imaging. *Journal of Biomedical Optics*, *15*(5), 056013.

Chang, C.-W., & Mycek, M.-A. (2012a). Quantitative molecular imaging in living cells via FLIM. In C. D. Geddes (Ed.), *Reviews in fluorescence 2010* (pp. 173–198). New York: Springer.

Chang, C.-W., & Mycek, M.-A. (2012b). Total variation versus wavelet-based methods for image denoising in fluorescence lifetime imaging microscopy. *Journal of Biophotonics*, *5*(5–6), 449–457.

Chang, C.-W., Sud, D., & Mycek, M.-A. (2007). Fluorescence lifetime imaging microscopy. In G. Sluder & D. Wolf (Eds.), *Methods in cell biology*, Vol. 81. London, UK: Elsevier Inc (Chapter 24).

Chang, C.-W., Wu, M., Merajver, S. D., & Mycek, M.-A. (2009). Physiological fluorescence lifetime imaging microscopy improves Förster resonance energy transfer detection in living cells. *Journal of Biomedical Optics*, *14*(6), 060502.

Chen, Y., & Periasamy, A. (2004). Characterization of two-photon excitation fluorescence lifetime imaging microscopy for protein localization. *Microscopy Research and Technique*, *63*(1), 72–80.

Clayton, A. H. A., Hanley, Q. S., & Verveer, P. J. (2004). Graphical representation and multicomponent analysis of single-frequency fluorescence lifetime imaging microscopy data. *Journal of Microscopy*, *213*, 1–5.

Cubeddu, R., Comelli, D., D'Andrea, C., Taroni, P., & Valentini, G. (2002). Time-resolved fluorescence imaging in biology and medicine. *Journal of Physics D: Applied Physics*, *35*, R61–R76.

Demas, J. N. (1983). *Excited state lifetime measurements*. New York: Academic Press.

Digman, M. A., Caiolfa, V. R., Zamai, M., & Gratton, E. (2008). The phasor approach to fluorescence lifetime imaging analysis. *Biophysical Journal*, *94*(2), L14–L16.

Dowling, K., Hyde, S. C. W., Dainty, J. C., French, P. M. W., & Hares, J. D. (1997). 2-D fluorescence lifetime imaging using a time-gated image intensifier. *Optics Communications*, *135*, 27–31.

Ellis, J. D., Lleres, D., Denegri, M., Lamond, A. I., & Caceres, J. F. (2008). Spatial mapping of splicing factor complexes involved in exon and intron definition. *The Journal of Cell Biology*, *181*(6), 921–934, (Research Support, Non-U.S. Gov't).

Förster, T. (1948). Intermolecular energy migration and fluorescence. *Annals of Physics*, *2*, 55–75.

French, T., So, P. T. C., Dong, C. Y., Berland, K. M., & Gratton, E. (1998). Fluorescence lifetime imaging techniques for microscopy. *Methods in Cell Biology*, *56*, 277–304.

Gadella, T. W. J., Jr. (1999). Fluorescence lifetime imaging microscopy (FLIM): Instrumentation and application. In W. T. Masons (Ed.), *Fluorescent and luminescent probes for biological activity* (pp. 467–479). San Diego, CA: Academic Press.

Gerritsen, H. C., Sanders, R., Draaijer, A., & Levine, Y. K. (1997). Fluorescence lifetime imaging of oxygen in living cells. *Journal of Fluorescence*, *7*(1), 11–16.

Ghiggino, K. P., Harris, M. R., & Spizzirri, P. G. (1992). Fluorescence lifetime measurements using a novel fiber-optic laser scanning confocal microscope. *The Review of Scientific Instruments*, *63*(5), 2999–3002.

Heikal, A. A. (2010). Intracellular coenzymes as natural biomarkers for metabolic activities and mitochondrial anomalies. *Biomarkers in Medicine*, *4*(2), 241–263.

Helmchen, F., & Denk, W. (2005). Deep tissue two-photon microscopy. *Nature Methods*, *2*(12), 932–940 (Review).

Hill, N. E. (1969). *Dielectric properties and molecular behaviour*. London/New York: Van Nostrand Reinhold.

Hink, M. A., Bisselin, T., & Visser, A. J. (2002). Imaging protein-protein interactions in living cells. *Plant Molecular Biology*, *50*(6), 871–883.

ISS. Lifetime data of selected fluorophores. http://www.iss.com/resources/fluorophores.html.

Jares-Erijman, E. A., & Jovin, T. M. (2003). FRET imaging. *Nature Biotechnology*, *21*(11), 1387–1395.

Jo, J. A., Fang, Q., & Marcu, L. (2005). Ultrafast method for the analysis of fluorescence lifetime imaging microscopy data based on the laguerre expansion technique. *IEEE Journal of Quantum Electronics*, *11*(4), 835–845.

Kask, P., Palo, K., Ullmann, D., & Gall, K. (1999). Fluorescence-intensity distribution analysis and its application in biomolecular detection technology. *Proceedings of the National Academy of Sciences of the United States of America*, *96*(24), 13756–13761.

Lakowicz, J. R. (2006). *Principles of fluorescence spectroscopy* (3rd ed.). New York: Springer.

Lakowicz, J. R., Szmacinski, H., Nowaczyk, K., & Johnson, M. L. (1992). Fluorescence lifetime imaging of free and protein-bound NADH. *Proceedings of the National Academy of Sciences of the United States of America*, *89*(4), 1271–1275.

Lee, K. C. B., Siegel, J., Webb, S. E. D., Leveque-Fort, S., Cole, M. J., Jones, R., et al. (2001). Application of the stretched exponential function to fluorescence lifetime imaging. *Biophysical Journal*, *81*, 1265–1274.

Lin, H. J., Herman, P., & Lakowicz, J. R. (2003). Fluorescence lifetime-resolved pH imaging of living cells. *Cytometry. Part A*, *52*(2), 77–89.

Lleres, D., James, J., Swift, S., Norman, D. G., & Lamond, A. I. (2009). Quantitative analysis of chromatin compaction in living cells using FLIM-FRET. *The Journal of Cell Biology*, *187*(4), 481–496.

Lloyd, W. R., Chen, L.-C., Kuo, S., Marcelo, C. L., Feinberg, S. E., & Mycek, M.-A. (2012). Fluorescence lifetime imaging microscopy (FLIM) studies of living primary human cells for applications in tissue regeneration. *Proceedings of SPIE*, *8226*, 82260E–82266E.

Lloyd, W. R., Chen, L.-C., & Mycek, M. A. (2013). Fluorescence spectroscopy. In S. P. Morgan, S. J. Matcher, & F. Rose (Eds.), *Optical techniques in regenerative medicine*. Boca Raton, FL: CRC Press.

Lloyd, W. R., Chen, L.-C., Wilson, R. H., & Mycek, M.-A. (2013). Biophotonics: Clinical fluorescence detection. In D. J. Maitland, & J. E. Moore, Jr., (Eds.), *Biomedical technology and devices handbook*. (2nd ed.). Boca Raton, FL: CRC Press.

Lloyd, W., Wilson, R. H., Chang, C.-W., Gillispie, G. D., & Mycek, M.-A. (2010). Instrumentation to rapidly acquire fluorescence wavelength-time matrices of biological tissues. *Biomedical Optics Express*, *1*(2), 574–586.

Marmarelis, V. Z. (1993). Identification of nonlinear biological systems using Laguerre expansions of kernels. *Annals of Biomedical Engineering*, *21*, 573–589.

Mehta, G., Mehta, K., Sud, D., Song, J. W., Bersano-Begey, T., Futai, N., et al. (2007). Quantitative measurement and control of oxygen levels in microfluidic poly(dimethylsiloxane) bioreactors during cell culture. *Biomedical Microdevices*, *9*(2), 123–134.

Ng, T., Squire, A., Hansra, G., Bornancin, F., Prevostel, C., Hanby, A., et al. (1999). Imaging protein kinase C alpha activation in cells. *Science*, *283*(5410), 2085–2089.

Oida, T., Sako, Y., & Kusumi, A. (1993). Fluorescence lifetime imaging microscopy (flimscopy)—Methodology development and application to studies of endosome fusion in single cells. *Biophysical Journal*, *64*(3), 676–685.

Owen, D. M., Auksorius, E., Manning, H. B., Talbot, C. B., de Beule, P. A., Dunsby, C., et al. (2007). Excitation-resolved hyperspectral fluorescence lifetime imaging using a UV-extended supercontinuum source. *Optics Letters*, *32*(23), 3408–3410.

Pande, P., & Jo, J. A. (2011). Automated analysis of fluorescence lifetime imaging microscopy (FLIM) data based on the Laguerre deconvolution method. *IEEE Transactions on Bio-Medical Engineering*, *58*(1), 172–181.

Provenzano, P. P., Eliceiri, K. W., & Keely, P. J. (2009). Multiphoton microscopy and fluorescence lifetime imaging microscopy (FLIM) to monitor metastasis and the tumor microenvironment. *Clinical & Experimental Metastasis*, *26*(4), 357–370.

Redford, G. I., & Clegg, R. M. (2005). Polar plot representation for frequency-domain analysis of fluorescence lifetimes. *Journal of Fluorescence*, *15*(5), 805–815.

Rudolph, W., & Kempe, M. (1997). Trends in optical biomedical imaging. *Journal of Modern Optics*, *44*(9), 1617–1642.

Salthammer, T. (1992). Numerical simulation of pile-up distorted time-correlated single photon counting (TCSPC) data. *Journal of Fluorescence*, *2*(1), 23–27.

Sanders, R., Draaijer, A., Gerritsen, H. C., Houpt, P. M., & Levine, Y. K. (1995). Quantitative pH imaging in cells using confocal fluorescence lifetime imaging microscopy. *Analytical Biochemistry*, *227*(2), 302–308.

Sharman, K. K., Periasamy, A., Ashworth, H., Demas, J. N., & Snow, N. H. (1999). Error analysis of the rapid lifetime determination method for double-exponential decays and new windowing schemes. *Analytical Chemistry*, *71*(5), 947–952.

Skala, M. C., Riching, K. M., Gendron-Fitzpatrick, A., Eickhoff, J., Eliceiri, K. W., White, J. G., et al. (2007). In vivo multiphoton microscopy of NADH and FAD redox states, fluorescence lifetimes, and cellular morphology in precancerous epithelia. *Proceedings of the National Academy of Sciences of the United States of America*, *104*(49), 19494–19499.

Sud, D., Mehta, G., Mehta, K., Linderman, J. J., Takayama, S., & Mycek, M.-A. (2006). Optical imaging in microfluidic bioreactors enables oxygen monitoring for continuous cell culture. *Journal of Biomedical Optics*, *11*, 050504.

Sud, D., & Mycek, M.-A. (2009). Calibration and validation of an optical sensor for intracellular oxygen measurements. *Journal of Biomedical Optics*, *14*(2), 020506.

Sud, D., Zhong, W., Beer, D. G., & Mycek, M.-A. (2006). Time-resolved optical imaging provides a molecular snapshot of altered metabolic function in living human cancer cell models. *Optics Express*, *14*(10), 4412–4426.

Sun, Y., Hatami, N., Yee, M., Phipps, J., Elson, D. S., Gorin, F., et al. (2010). Fluorescence lifetime imaging microscopy for brain tumor image-guided surgery. *Journal of Biomedical Optics*, *15*(5), 056022.

Sun, Y., Phipps, J., Elson, D. S., Stoy, H., Tinling, S., Meier, J., et al. (2009). Fluorescence lifetime imaging microscopy: in vivo application to diagnosis of oral carcinoma. *Optics Letters*, *34*(13), 2081–2083.

Tadrous, P. J. (2000). Methods for imaging the structure and function of living tissues and cells: 2 Fluorescence lifetime imaging. *Journal of Pathology*, *191*(3), 229–234.

Urayama, P. K., & Mycek, M.-A. (2003). Fluorescence lifetime imaging microscopy of endogenous biological fluorescence. In M.-A. Mycek & B. W. Pogue (Eds.), *Handbook of biomedical fluorescence* (pp. 211–236). New York: Marcel Dekker, Inc.

Urayama, P. K., Zhong, W., Beamish, J. A., Minn, F. K., Sloboda, R. D., Dragnev, K. H., et al. (2003). A UV-visible fluorescence lifetime imaging microscope for laser-based biological sensing with picosecond resolution. *Applied Physics B-Lasers Optics*, *76*(5), 483–496.

van Munster, E. B., & Gadella, T. W. J. (2005). Fluorescence lifetime imaging microscopy (FLIM). *Advances in Biochemical Engineering/Biotechnology*, *95*, 143–175.

Vermeer, J. E., van Munster, E. B., Vischer, N. O., & Gadella, T. W., Jr. (2004). Probing plasma membrane microdomains in cowpea protoplasts using lipidated GFP-fusion proteins and multimode FRET microscopy. *Journal of Microscopy*, *214*(Pt 2), 190–200.

Wahl, M., Koberling, F., Patting, M., Rahn, H., & Erdmann, R. (2004). Time-resolved confocal fluorescence imaging and spectrocopy system with single molecule sensitivity and sub-micrometer resolution. *Current Pharmaceutical Biotechnology*, *5*(3), 299–308.

Wallrabe, H., & Periasamy, A. (2005). Imaging protein molecules using FRET and FLIM microscopy. *Current Opinion in Biotechnology*, *16*(1), 19–27.

Wang, X. F., Periasamy, A., Herman, B., & Coleman, D. (1992). Fluorescence lifetime imaging microscopy (FLIM): Instrumentation and applications. *Critical Reviews in Analytical Chemistry*, *23*(5), 369–395.

Wang, X. F., Uchida, T., Coleman, D. M., & Minami, S. (1991). A two-dimensional fluorescence lifetime imaging system using a gated image intensifier. *Applied Spectroscopy*, *45*(3), 360–366.

Zhong, W., Urayama, P., & Mycek, M.-A. (2003). Imaging fluorescence lifetime modulation of a ruthenium-based dye in living cells: The potential for oxygen sensing. *Journal of Physics D: Applied Physics*, *36*(14), 1689–1695.

Zhong, W., Wu, M., Chang, C. W., Merrick, K. A., Merajver, S. D., & Mycek, M. A. (2007). Picosecond-resolution fluorescence lifetime imaging microscopy: A useful tool for sensing molecular interactions in vivo via FRET. *Optics Express*, *15*(26), 18220–18235.

Zipfel, W. R., Williams, R. M., Christie, R., Nikitin, A. Y., Hyman, B. T., & Webb, W. W. (2003). Live tissue intrinsic emission microscopy using multiphoton-excited native fluorescence and second harmonic generation. *Proceedings of the National Academy of Sciences of the United States of America*, *100*(12), 7075–7080.

CHAPTER

21 Fluorescence Correlation Spectroscopy: Molecular Complexing in Solution and in Living Cells

Dylan A. Bulseco and David E. Wolf
Sensor Technologies, LLC, Shrewsbury, Massachusetts, USA

CHAPTER OUTLINE

Introduction **490**
21.1 Studying Biological Systems With FCS **491**
21.1.1 First Principles 491
21.1.2 Defining a Small Sample Volume: The Confocal Principle 493
21.1.3 What Exactly is FCS? 494
21.1.4 What Can We Study with FCS? 497
21.1.5 Molecular Complexing in Solution 501
21.1.6 FCS Measurements in Living Cells 504
21.1.7 Molecular Complexing in Living Cells 505
21.2 Designing and Building An FCS Instrument **509**
21.2.1 Overview: The Experimental Setup 509
21.2.2 Primary Components of an FCS Instrument 511
21.2.3 Laser Illumination 511
21.2.3.1 Laser Power 512
21.2.3.2 Wavelengths Available 512
21.2.3.3 Laser Stability 512
21.2.3.4 Fiber-Optic Coupling of Laser 512
21.2.3.5 Beam Steering 513
21.2.3.6 System Alignment 513
21.2.4 Optics 514
21.2.4.1 Telescoping Beam Expander 515
21.2.4.2 Selecting Dichromatic Mirrors and Filters 515
21.2.4.3 High-NA Objective 515
21.2.5 Photon Counting 515
21.2.5.1 PMT 516
21.2.5.2 APD 516

Methods in Cell Biology, Volume 114 **ISSN 0091-679X**
Copyright © 2007 Elsevier Inc. All rights reserved.
http://dx.doi.org/10.1016/B978-0-12-407761-4.00021-X

21.2.6 Digital Correlator 516
21.2.6.1 Correlator.com 516
21.2.6.2 ALV 517
21.2.7 Data Acquisition and Analysis 517
21.2.7.1 Random Noise and Optimized Signals 517
21.2.7.2 Autocorrelation Analysis 518
21.2.7.3 Fitting Correlation Curves 518
21.2.7.4 Measuring Stoichiometry 519
21.2.7.5 Calculation of Beam Diameter and Confocal Volume 519
21.3 What are the Current Commercial Sources of FCS? 520
21.4 Summary 520
Acknowledgments 520
References 521

Abstract

This chapter describes how the microscope can be used to measure a fluorescence signal from a small, confined volume of the sample—the confocal volume—and how these measurements are used to quantitate the dynamics and complexing of molecules, the technique of fluorescence correlation spectroscopy (FCS). FCS represents a significant example of how the microscope can be used to extract information beyond the resolution limit of classical optics. FCS enables studying events at the level of single molecules. With FCS, one can measure the diffusion times and the interaction of macromolecules, the absolute concentration of fluorescently labeled particles, and the kinetics of chemical reactions. Practical applications of FCS include studies on ligand–receptor binding, protein–protein and protein–DNA interactions, and the aggregation of fluorescently labeled particles. The chapter focuses on the principles of FCS, demonstrates how FCS is used to study macromolecular interactions in solution and in living cells, and examines critical experimental parameters that must be considered. The chapter also discusses the minimum requirements for building a microscope-based FCS instrument and illustrates the key criteria for both instrument sensitivity and analysis of FCS data. It can be used to study single molecules both in solution and in living cells and can be used to monitor a variety of macromolecular interactions. When used as an *in vitro* technique, FCS measurements are easy to conduct and can be made on simplified instrumentation. When used *in vivo* on living cells, many additional factors must be considered when evaluating experimental data. Despite these concerns, FCS represents a new approach that has broad applicability for the determination of molecular stoichiometry both *in vivo* and *in vitro* for a variety of membrane and soluble receptor systems.

INTRODUCTION

In this chapter, we will discuss how the microscope can be used to measure a fluorescence signal from a small, confined volume of the sample, the confocal volume, and

how these measurements are used to quantitate the dynamics and complexing of molecules, the technique of fluorescence correlation spectroscopy (FCS). Beyond being an important technique in the arsenal of modern biophysics, biochemistry, and cell biology, FCS represents a significant example of how the microscope can be used to extract information beyond the resolution limit of classical optics. FCS enables us to study events at the level of single molecules. With FCS, one can measure the diffusion times and the interaction of macromolecules, the absolute concentration of fluorescently labeled particles, and the kinetics of chemical reactions. Practical applications of FCS include studies on ligand–receptor binding, protein–protein and protein–DNA interactions, and the aggregation of fluorescently labeled particles. For comprehensive reviews on the theory and applications of FCS, see Rigler, 1995; Widengren & Rigler, 1998; Schwille, 2001; Hess & Webb, 2002; Berland, 2004; Elson, 2004; Foldes-Papp, 2006; Frieden, Chattopadhyay, & Elson, 2002; Hink, Bisselin, & Visser, 2002; Lippincott-Schwartz, Snapp, & Kenworthy, 2001; Medina & Schwille, 2002; Pramanik, 2004; Thompson, Lieto, & Allen, 2002; Vukojevic et al., 2005.

This chapter is divided into two sections. In the first section, we discuss the principles of FCS, demonstrate how FCS is used to study macromolecular interactions in solution and in living cells, and examine critical experimental parameters that must be considered. In the second section, we discuss the minimum requirements for building a microscope-based FCS instrument and illustrate key criteria for both instrument sensitivity and analysis of FCS data.

21.1 STUDYING BIOLOGICAL SYSTEMS WITH FCS

21.1.1 First principles

Suppose that you have a solution of some solute in a beaker. Suppose that we have precisely V liters of this solution and that it is at a molar concentration, C. How many molecules (N) of solute are in the beaker? The answer is, of course, $N = CVA$, where A is Avogadro's number. A key point to realize is that this is a closed system. If you take care not to let the system evaporate, that is, if you keep it closed, you will always find N molecules in the beaker. However, suppose you had a way of looking at a subvolume within the beaker, call this v, where $v < V$ (Fig. 21.1). How many molecules will you find in this subvolume? Your first answer is likely to be $n = CvA$. However, you need to be careful. Suppose, for instance, that v is a small subvolume ($v < V$) whose diameter is less than the average distance between solute molecules? In this case, there is a reasonably high probability that the volume will contain zero molecules, a similar probability that it will contain one molecule, and progressively lower probabilities that there are two, three, and so on molecules in the volume (Fig. 21.1). It is only on average that you get the number n. The longer the time over which the sample is averaged, the more likely the average will be n. If we call the probabilities respectively P_i, then

$$n = 0P_0 + 1P_1 + 2P_2 + 3P_3 + \ldots + NP_N, \tag{21.1}$$

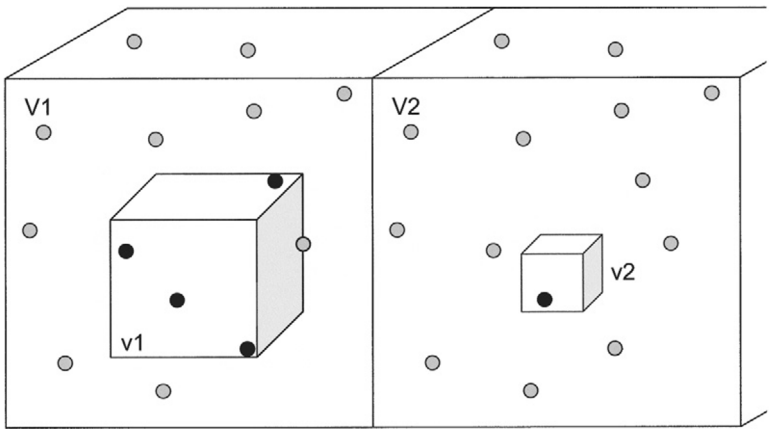

FIGURE 21.1

Illustration of volume (V1 and V2) and subvolume (v1 and v2) when detection volume is larger (v1) and smaller (v2) than the average distance between diffusing particles.

where N is again the total number of molecules in the beaker and where

$$1 = P_0 + P_1 + P_2 + P_3 + \ldots + P_N. \tag{21.2}$$

Now suppose that you did this measurement M times. You would have M values of n_K. You could then calculate the standard deviation (SD) of your measurements about the mean value n in the usual way:

$$\mathrm{SD} = \sum_{K=1}^{M} \frac{(n_K - n)^2}{(M-1)}. \tag{21.3}$$

It is actually rather straightforward to calculate the SD, provided you know the probabilities P_i. The reader is referred to Howard Berg's wonderful book, *Random Walks in Biology* (Berg, 1993) for this derivation. It turns out that

$$\mathrm{SD} = \sqrt{n}. \tag{21.4}$$

Therefore, just as in radioactive decay, another random process, we get

$$n \pm \sqrt{n}. \tag{21.5}$$

It is important to note that these equations are fully generalizable and therefore apply to any volume v. We see that the percentage variation of the measurement SD over mean is given by $(1/\sqrt{n})100$. For an average value of $n = 100$, the percentage variation therefore is 10%, and for $n = 10{,}000$, it is 1%.

It is also important to recognize that in a solution in which molecules are free to diffuse, you can actually focus on a single subvolume and let the random diffusion of molecules into and out of this volume replace scanning from subvolume to subvolume. In this case, the stochastic fluctuation occurs over time but the same equations apply. The timescale of the fluctuations is defined by the characteristic diffusion

time. If the volume is a sphere with radius ω, then this time is given as $\omega^2/2D$, $\omega^2/4D$, $\omega^2/6D$ for one-, two-, and three-dimensional diffusion, respectively. If we anticipate our later discussion and assume that we are studying a cylindrical rather than a spherical volume, then we have two time constants for diffusion, $\omega_1^2/4D$ and $h^2/2D$, where ω is the radius of the cylinder and h is the length. Again we refer the reader to Howard Berg's book for a discussion of the random walk of molecules in solution (Berg, 1993). The reader is further referred to Charles L. Dodgson's description of the dance of the molecules, referred to as the Dodo's Caucus-Race, in his *Alice's Adventures in Wonderland* (Carroll, 2000).

> *(And as you might like to try the thing yourself, some winter day. I will tell you how the Dodo managed it.)*
>
> *First it marked out a racecourse, in a sort of circle ('the exact shape doesn't matter' it said), and there all the party were placed along the course, here and there. There was no 'One, two, three and away' but they began running when they liked, and left off when they liked, so it was not easy to know when the race was over. However, when they had been running half an hour or so, and were quite dry again, the Dodo suddenly called out, 'The race is over!' and they all crowded round it, panting, and asking, 'But who has won?'*

21.1.2 Defining a small sample volume: the confocal principle

FCS takes advantage of confocal optics and improved electronics to increase signal and to reduce noise. Figure 21.2 illustrates the formation of a confocal volume with a focused light source, such as a monochromatic laser. In Chapter 1 by Sluder and Nordberg, this volume, the concept of conjugate focal planes in the microscope is described. In a confocal microscope, apertures at the conjugate image planes are used to confine the interrogated region of the sample to a small diffraction-limited volume. Optics are designed to reduce out-of-focus light and to limit image detection to the desired focal plane of in-focus light (the sample plane), which increases contrast and effective resolution. This is achieved by first minimizing the detection volume by illumination with a laser beam focused to the limit of resolution with a high numerical aperture (NA) objective. Second, out-of-focus light is eliminated by introducing a field pinhole or aperture in the conjugate image plane and before the detector. This serves to limit detection to the plane in which the object is focused, which is depicted in Fig. 21.2 by the box at beam waist of the illumination volume. Signals from planes either above or below the object plane are focused either above or below the conjugate image plane and are therefore collected inefficiently. That is, fluorescence signals from these out-of-focus planes are excluded by the field aperture and are therefore not recorded by the detector. It is therefore clear that only those fluorescently labeled particles that diffuse into the laser-excitation volume emit fluorescence and that only those precisely at the object plane will be "visible" to the photon detector. In this way, FCS takes advantage of the confocal principle to improve the signal-to-noise ratio, which enables one to realize single-molecule detection limits.

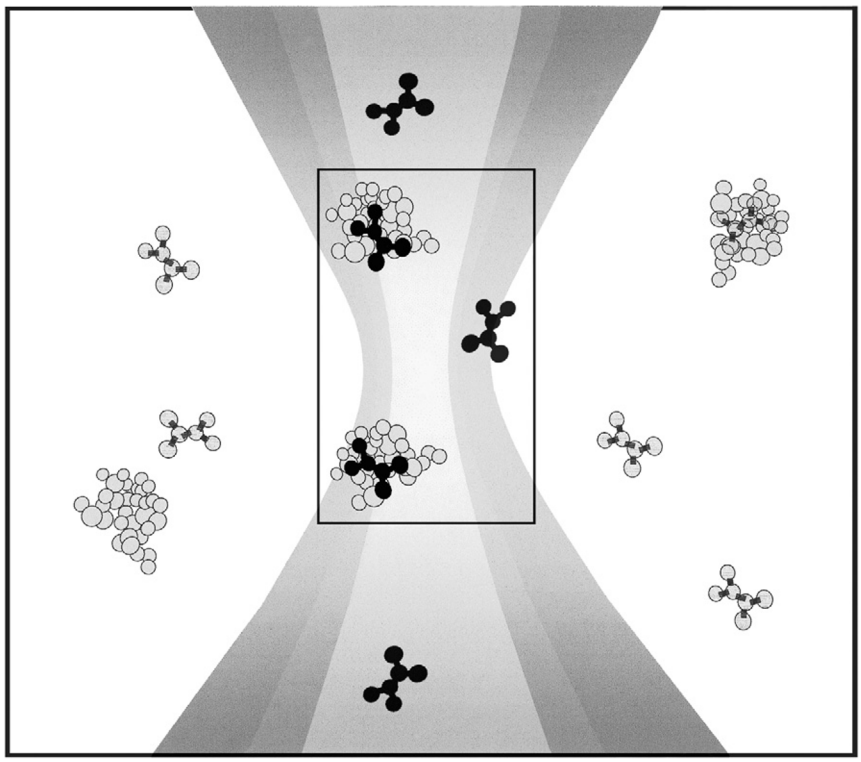

FIGURE 21.2

Confocal illumination and detection volumes. Only those particles that diffuse into the confocal volume will be detected by the photon counter.

21.1.3 What exactly is FCS?

When optimal confocal optics and electronics are used, FCS is a single-molecule detection method that can be carried out in small (femtoliter) volumes. As described above, a tightly focused laser beam defines this confocal volume, and the diffusion of fluorescently labeled particles into and out of this illuminated volume determines the pattern of fluorescence intensity fluctuation. From these data, one can extract both qualitative (presence or absence of interaction) and quantitative (diffusion times, stoichiometry of interactions, concentration of interacting particles, and kinetics of this interaction) information about the macromolecules being studied.

The concept of FCS evolved from work on dynamic light scattering [for a comprehensive review of dynamic light scattering, see Berne & Pecora, 2000]. FCS was first proposed in the early 1970s (Elson & Magde, 1974; Magde, Elson, & Webb, 1974) but was not a practical technique for biological samples because of high noise and low sensitivity. Despite these technical limitations, pioneering work of this

period used FCS to study diffusion in lipid bilayers (Fahey et al., 1977), lateral transport on cell membranes (Elson, Schlessinger, Koppel, Axelrod, & Webb, 1976), chemical kinetics (Magde, 1976; Magde, 1977), and the molecular weight of DNA (Weissman, Schindler, & Feher, 1976). In the 1980s, FCS was coupled with the technique of total internal reflection and became a powerful tool for studying surface–solution interactions (Axelrod, Thompson, & Burghardt, 1983) and antibody–hapten interaction at surfaces (Thompson & Axelrod, 1983). Advances in autocorrelation electronics, detectors, and confocal microscopy have improved detection limits, shortened measurement times, and increased our ability to resolve multiple correlation times (Rigler, 1995; Widengren & Rigler, 1998). This has led to a renaissance in the application of FCS to biological systems (Berland, 2004; Elson, 2004; Foldes-Papp, 2006; Frieden et al., 2002; Hess & Webb, 2002; Hink et al., 2002; Lippincott-Schwartz et al., 2001; Medina & Schwille, 2002; Pramanik, 2004; Rigler, 1995; Schwille, 2001; Thompson et al., 2002; Vukojevic et al., 2005; Widengren & Rigler, 1998).

FCS can be implemented in two ways—autocorrelation and cross correlation. Autocorrelation measures the persistence of a single fluorescent particle in the confocal volume. It temporally correlates fluorescence intensity fluctuations (Fig. 21.3A) as labeled particles diffuse into and out of the detection volume. Statistical analysis of fluorescence-intensity fluctuations results in an autocorrelation curve (Fig. 21.3B) that shows the decay of temporal correlation in fluorescence intensity over time. The autocorrelation function is given by

$$G(\tau) = 1 + \frac{\langle \delta I(t)\delta I(t+\tau)\rangle}{\langle I\rangle^2}, \tag{21.6}$$

where the δI's refer to the deviations of the intensity about the mean. Cross correlation extends standard autocorrelation FCS by introducing two different fluorescent labels with distinct excitation and emission properties that can be detected in the same confocal volume. It temporally correlates the intensity fluctuations of two distinguishable labels. Coincidence of these fluorescent labels on the same macromolecule is detected as a change in amplitude, R, at short time points, τ, and the amplitude of the cross-correlation function is directly proportional to the concentration of dual-labeled fluorescent particles. The cross-correlation function is given by

$$r(\tau) = \frac{\langle \delta I_i(t)\delta I_j(t+\tau)\rangle}{SD_i SD_j}. \tag{21.7}$$

The correlation function of Eq. (21.7) is the form commonly used in statistics, which goes to 1 for perfect cross correlation and to 0 for no cross correlation. Instrumentally, it is simpler to define the cross-correlation function in a manner analogous to Eq. (21.6) for the autocorrelation function

$$R(\tau) = 1 + \frac{\langle \delta I_i(t)\delta I_j(t+\tau)\rangle}{I_i I_i}. \tag{21.8}$$

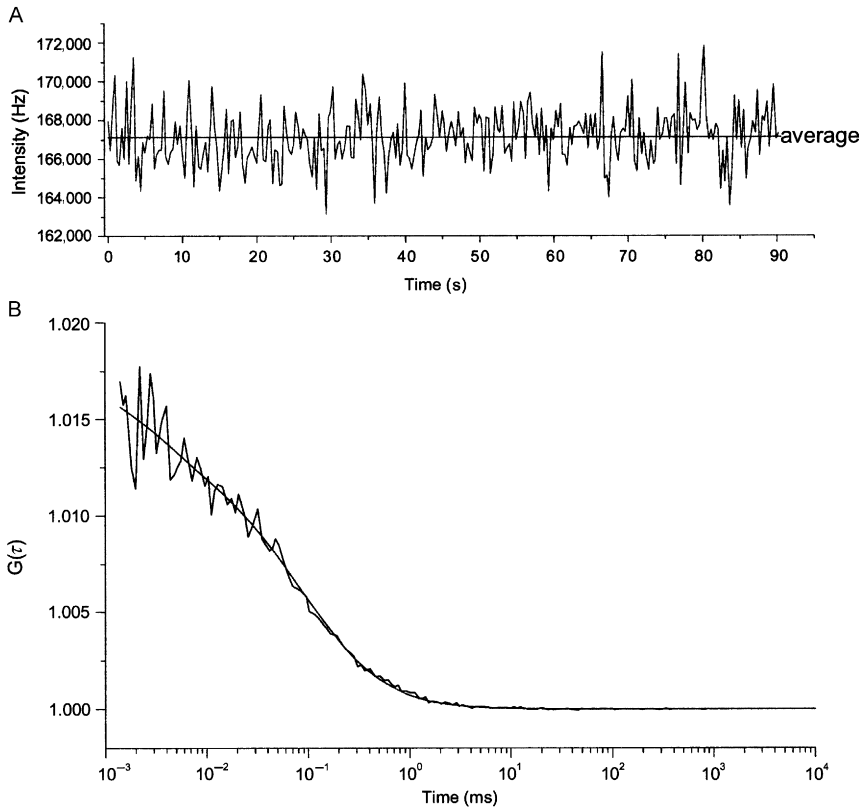

FIGURE 21.3

FCS is a statistical technique that temporally correlates fluorescence intensity fluctuations. (A) Fluorescence intensity fluctuates over time around an average intensity. (B) Autocorrelation curve shows the decay of temporal correlation over time.

This form is simpler to calculate in real time from an ongoing data stream and has the further advantage that when $I_i = I_j$, then $R(\tau) = G(\tau)$.

The relaxation time for correlation relates to stochastic processes of randomization such as diffusion, whereas the size of these fluctuations relates to the number of molecules or particles involved in the stochastic process. Autocorrelation functions are used to analyze these fluctuations and yield information on diffusion coefficients, aggregation state chemical concentration, chemical reaction kinetics, and stoichiometry of macromolecules (Elson & Magde, 1974; Magde et al., 1974) in solution as well as in the plasma membrane of living cells (Brock, Hink, & Jovin, 1998; Elson et al., 1976; Lippincott-Schwartz et al., 2001; Maertens, Vercammen, Debyser, & Engelborghs, 2005; Pramanik, 2004; Schwille, Oehlenschlager, & Walter, 1996; Vukojevic et al., 2005; Widengren & Rigler, 1998). FCS, in either autocorrelation or cross-correlation mode, is an ideal method to study the interactions of macromolecules.

Figure 21.4A illustrates the diffusion of a labeled particle, such as a rhodamine-conjugated Fab fragment, through a confocal volume. Only these particles in the illumination volume fluoresce, and detection is further limited to particles precisely within the defined confocal object plane. It is important to note here that FCS is sensitive to both the number and size of the particles that diffuse through the confocal volume. When fluorescently labeled particles bind to large macromolecular targets such as whole IgG (Fig. 21.4B) or self-aggregate to form complexes (Fig. 21.4C), the autocorrelation curves reflect the appearance of these large, slow-diffusing complexes.

Nonlinear regression is used to fit data to the three-dimensional autocorrelation function [Eq. (21.9)] for samples in solution. Parameter estimates are calculated for particle number (N), triplet state fraction (T), triplet state correlation time (τ_T), particle fraction (F_i), and diffusion time (τ_{Di}) for diffusing particle species i. The structure parameter, K^2 where $K = \omega_2/\omega_1$ [ω_2 and ω_1 being the exp(–2) beam radii in the z and x directions, respectively], is determined separately and held constant for each fit

$$G(\tau) = 1 + \left(\frac{1}{N}\right)(1 - T + T\exp(-\tau/\tau_T))\left(\sum_i \frac{F_i}{(1+\tau/\tau_{D_i})(1+\tau/K^2\tau_{D_i})^{1/2}}\right). \tag{21.9}$$

21.1.4 What can we study with FCS?

FCS can be used to study any fluorescently labeled molecule with single-molecule detection limits either in solution or in living cells. In other words, FCS can be used to monitor the interaction of labeled molecules with unlabeled or labeled targets, using autocorrelation or cross correlation, respectively. FCS experiments conducted in solution are simpler, which results in unambiguous experiments and simplified instrument design. Sample volumes may be as small as 1 μl (although confocal detection volumes are actually a few femtoliters), limited only by potential evaporation during the measurement. If the sample volume is large enough, precise positioning of the confocal detection volume is not critical, although laser power, buffer autofluorescence, and experimental or data analysis artifacts must still be addressed. Finally, when working with low concentrations in small volumes, one must mitigate adsorption of macromolecules to the cover glass by inclusion of NP-40 or Pluronic acid. Using FCS to study living cells requires special consideration. Cells are highly compartmentalized, with intracellular structures interspersed within an aqueous, cytosolic volume that is on the order of a few picoliters. Diffusion of soluble proteins may be affected by modulating binding proteins, increased cytosolic viscosity, and interfering structural proteins. In addition to precise positioning within the cell, researchers must be careful to use low laser power, consider the effects of background autofluorescence and photobleaching, and critically evaluate the results obtained.

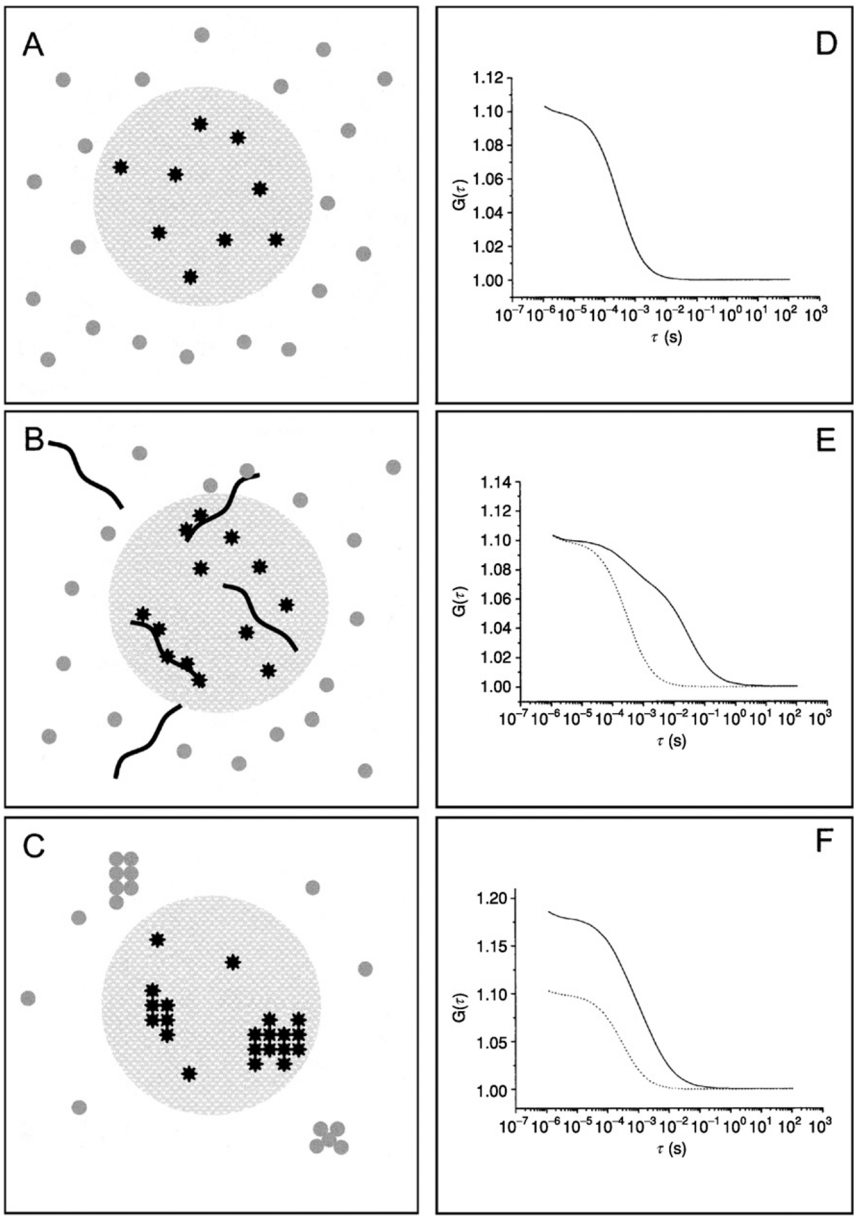

FIGURE 21.4

Illustration of FCS detection. Only those labeled particles that diffuse into and out of the laser-illuminated volume (stars) and are precisely in the object plane defined by the confocal optics will be detected by the photon counter. (A) Single-labeled particles, rhodamine-labeled Fab fragments, for example, emitting fluorescence when in the illumination volume.

Continued

Two features of FCS make it a useful tool for studying macromolecular interactions: FCS can resolve multiple diffusing components, and FCS is sensitive to changes in aggregation state of the fluorophore. Figure 21.5A shows how an autocorrelation curve can be used to discriminate fast- and slow-diffusing particles. Nonlinear curve fitting results in parameter estimates for two diffusing fractions with distinctly different diffusion times. Binding of small, fast-diffusing particles, to a large macromolecule (as illustrated in Fig. 21.4B), results in formation of a new, slower-diffusing component that can be used to monitor binding events. This is depicted in Fig. 21.4E, which shows the curve from Fig. 21.4D superimposed (dotted line) on results obtained for samples shown in Fig. 21.4B (solid line). This is further illustrated by the rightward shift in the autocorrelation curve as diffusion time is increased (Fig. 21.5B). The intercept of the correlation function at time $\tau = 0$ is the reciprocal of the average number of fluorescent particles in the sample and can be used as a measure of receptor complexing or aggregation (as illustrated in Fig. 21.4C). If the number of fluorescent particles in the detection volume is decreased, or if these fluorescent particles aggregate to form fewer, large complexes, the intercept at time $\tau = 0$ is increased. This is depicted in Fig. 21.4F, which shows the curve from Fig. 21.4D superimposed (dotted line) on results obtained for samples shown in Fig. 21.4C (solid line). This is further illustrated by the increased intercept of the correlation curve as time τ approaches 0, as the number of particles in the confocal detection volume is decreased (Fig. 21.5C). These two principles can therefore be used to monitor macromolecular interactions in small volumes and form the basis of many screening applications for protein–protein, protein–DNA, and DNA–DNA interactions.

A brief list of selected published applications of FCS follows. These include studies on translational diffusion and transport (Fahey et al., 1977), chemical kinetics (Magde, 1976), molecular aggregation (Berland, 1997; Brown & Royer, 1997; Meyer & Schindler, 1988; Palmer & Thompson, 1987; Palmer & Thompson, 1989), ligand binding (Matayoshi & Swift, 2001; Pramanik & Ekberg, 2001; Pramanik & Rigler, 2001; Rudiger, Haupts, Moore, & Pope, 2001; Zhong et al., 2001), enzymatic activity (Clair, 1997; Meyer-Almes & Auer, 2000; Moore et al., 1999), nucleic acid interactions *in vivo* and *in vitro* (Kinjo & Rigler, 1995; Politz, Browne, Wolf, & Pederson, 1998; Schwille, Haupts, Maiti, & Webb, 1999), monitoring PCR reactions (Walter, Schwille, & Eigen, 1996), screening phage display results (Lagerkvist, Foldes-Papp, Persson, & Rigler, 2001), active transport velocity in plants (Kohler, Schwille, Webb, & Hanson, 2000), and single-molecule detection (Foldes-Papp, Demel, & Tilz, 2001; Foldes-Papp, Demel, & Tilz, 2002). FCS,

(B) Binding of labeled particles to a large binding protein such as whole IgG. (C) Aggregation of labeled particles to form large complexes. (D) Sample autocorrelation curve for the particles detected in (A). (E) Sample autocorrelation curve for particles detected in (B) (solid). Autocorrelation curve from (D) included for comparison (dotted). (F) Sample autocorrelation curve for the particles detected in (C) (solid). Autocorrelation curve from (D) included for comparison (dotted).

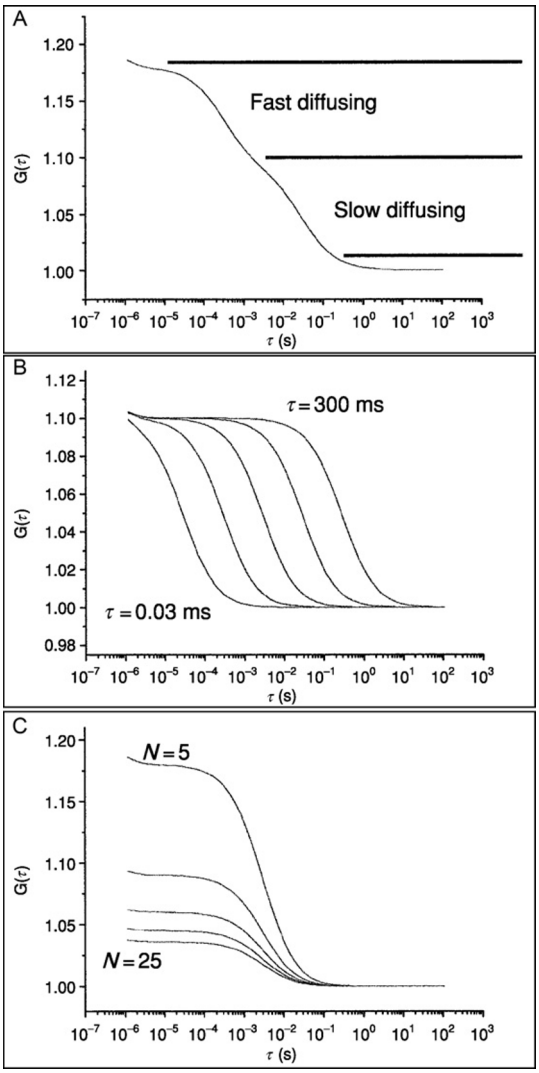

FIGURE 21.5

Features of FCS that are used to detect the interaction of macromolecules. (A) FCS can be used to detect multiple diffusing components. This curve illustrates detection of fast- and slow-diffusing particles. (B) The FCS autocorrelation curve shifts to the right as diffusion time (and hence particle size) increases. (C) The intercept, as τ approaches 0, is increased as the number of particles in the confocal detection volume is decreased.

therefore, enables one to study single macromolecules as well as large, labeled particles such as proteins binding to beads or bacteria expressing human receptors (Van Craenenbroeck et al., 2001).

21.1.5 Molecular complexing in solution

FCS is ideally suited for the study of protein–protein interactions in solution. In addition to single-molecule detection limits, it can be run in homogeneous assay format, which eliminates the need to separate bound from free label, and it requires small sample volumes (microliters), which reduce reagent requirements. To illustrate this, we have quantified molecular complexing and stoichiometry of interacting macromolecules using the binding of Rh-Fab to rabbit IgG. Figure 21.6A shows representative curves of Rh-Fab in solution either alone (solid line) or in the presence of 4-μM IgG (dotted line). This figure clearly illustrates how the key principles previously discussed can be used to monitor binding: the binding of Rh-Fab to IgG results in a predominately slower-diffusing fraction, as indicated by the rightward shift in the autocorrelation curve; and as Rh-Fab/IgG aggregates are formed, the particle number (N) is decreased as is indicated by the increased intercept as τ approaches 0.

The formation of a large Rh-Fab/IgG complex results in the appearance of a slow-diffusing component. Figure 21.6B shows that the slow-diffusing fraction is increased at higher IgG concentrations and saturates when IgG is greater than 1 μM. To quantify this interaction, we must first revisit the three-dimensional autocorrelation function [Eq. (21.9)] presented above.

FCS is based on statistical analysis of fluorescence intensity fluctuations. It is important to recognize that there are two major sources of stochastic fluctuations in the fluorescence signal in FCS experiments. The first occurs on the microsecond time scale and results from intersystem crossing of the fluorophores between the singlet and triplet states. The second occurs on the millisecond time scale and results from diffusion of the macromolecules into and out of the confocal volume. This observation has two ramifications: first, the fluctuations observed between singlet and triplet states are governed by the number of fluorophores in the confocal volume, whereas diffusional fluctuations are governed by the number of particles, and second, fluctuations resulting from intersystem crossing and particle diffusion are completely independent. For these reasons, we restate the three-dimensional autocorrelation function as

$$G(\tau) = 1 + \frac{T}{N_M}\exp(-\tau/\tau_T) + \frac{1-T}{N_P}\left(\sum_i \frac{F_i}{(1+\tau/\tau_{D_i})(1+\tau/K^2\tau_{D_i})^{1/2}}\right), \tag{21.10}$$

where N_M and N_P are the average number of fluorophore molecules and average number of particles in the sample volume, respectively. It should be noted that in the case where $N_M = N_P = N$, Eq. (21.10) reduces to Eq. (21.9), which has been derived elsewhere (Elson & Qian, 1989).

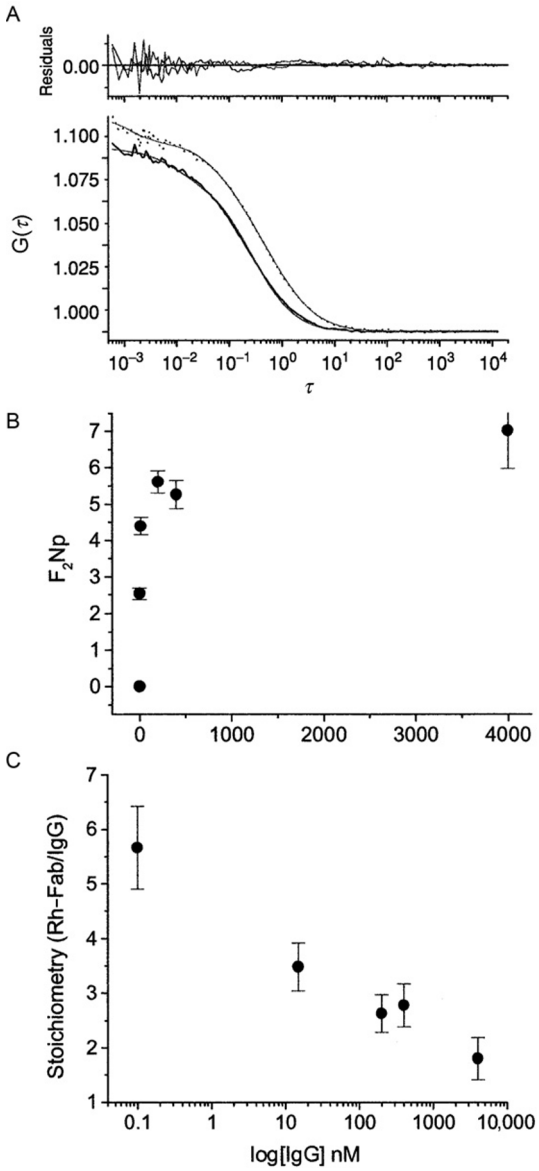

FIGURE 21.6

Molecular complexing in solution. (A) Rh-Fab alone (solid line) and with 4-μM IgG (dotted line). Residuals (top panel) were obtained after fitting the data to Eq. (21.11). (B) Fraction of slow-diffusing particles saturates as IgG concentration is increased. (C) Stoichiometry of Rh-Fab binding to IgG in solution.

To further simplify this relationship, we assume that T is constant in our measurements. Our findings indicate that this is a valid assumption as long as laser power is held constant and samples are subjected to low laser illumination (25–40 μW). This results in Eq. (21.11):

$$G(\tau) = 1 + \frac{1}{N'_M}\exp(-\tau/\tau_T) + \frac{1}{N_P}\left(\sum_i \frac{F_i}{(1+\tau/\tau_{D_i})(1+\tau/K^2\tau_{D_i})^{1/2}}\right), \quad (21.11)$$

which is identical to Eq. (21.10) when $N_M = N'_M T$ and $N_P = N'_P(1-T)$.

Fitted parameters for particle number (N'_P) and diffusion time (τ_{D_i}) were obtained for Rh-Fab/IgG data presented in Fig. 21.6A by fitting to Eq. (21.11). Data for Rh-Fab alone were best fit to a single fast-diffusing component ($i = 1$), whereas Rh-Fab + IgG was best fit to two diffusing components ($i = 2$; fast and slow). Analysis of Rh-Fab alone resulted in $N'_P = 11.3$ and $\tau_{D1} = 189$ μs, whereas in the presence of 4-μM IgG, $N'_P = 9.0$ with diffusion times of $\tau_{D1} = 130$ μs and $\tau_{D2} = 884$ μs.

Molecular stoichiometry was determined by titrating Rh-Fab (10 nM) with increasing concentrations of IgG. The autocorrelation curves were analyzed with Eq. (21.11) and parameters used to calculate stoichiometry as described below. First, a calibration factor, r, which is the number of fluorophores per Fab, is calculated using parameters obtained for Rh-Fab measurements alone and Eq. (21.12):

$$r = \frac{N'_M}{N'_P} \quad (21.12)$$

We can then define stoichiometry (S) conceptually as

$$S = \frac{\text{Number of Fabs in slow complex}}{\text{Number of complexes}}$$

where S is given by

$$S = \frac{\text{Total Fabs} - \text{fast-diffusing Fabs}}{\text{Number of complexes}}$$

Using the parameters defined in Eqs. (21.11) and (21.12), a general relationship for stoichiometry can be written as

$$S = \frac{N'_M/r - F_1 N'_P}{F_2 N'_P}, \quad (21.13)$$

where N'_M is the number of fluorophore molecules, N'_P is the number of diffusing particles distributed between slow (F_1) and fast (F_2) diffusing classes, and $F_2 N'_P$ defines the total number of slow-diffusing complexes formed.

Figure 21.6C shows the stoichiometry (S) of Rh-Fab bound per IgG as IgG concentration is increased. This indicates that there are about six Fab binding sites per IgG, when multiple Fabs are bound at the lowest IgG concentration. As more IgG is added, the number of bound Rh-Fab per IgG is decreased, as binding is distributed

over all available binding sites. These findings show that FCS can be used to measure molecular stoichiometry in solution by analysis of multiple autocorrelation curves. We next implemented this analysis in living cells expressing gp75, the low-affinity nerve growth factor receptor (NGFR).

21.1.6 FCS measurements in living cells

The first successful FCS measurements made on cell membranes were reported in the mid-1970s (Elson et al., 1976). This pioneering work demonstrated the feasibility of using FCS to study dynamic cellular events, in this case, lateral diffusion in the plasma membrane, in living cells. With the genomes of many organisms now well characterized, an increasing emphasis is being placed on understanding protein function. Furthermore, it is critical to understand how this function is modulated by interactions with other proteins in the context of a cell. For these reasons, FCS is an important technique to consider when investigating dynamic interactions in living cells.

As a result, the application of FCS to the study of intracellular proteins *in vivo* has grown in recent years, and the critical factors that govern successful measurements have been more clearly defined. The fundamental issues to consider are the precise location of the confocal volume in a cell, the effect of autofluorescence on FCS measurements, and the effect of laser power on apparent diffusion times (Brock et al., 1998; Brock & Jovin, 1998; Widengren & Rigler, 1998). Positioning of the confocal detection volume will affect the nature and quality of *in vivo* FCS data. Cell compartmentalization, cytoskeletal elements, internal membranes, and organelles result in microdomains that will be sampled differently as the position of the confocal detection volume is changed (Brock et al., 1998). Figure 21.7 illustrates how the relative fractions of fast- and slow-diffusing particles will change as the position of the detection volume is moved relative to the plasma membrane. For detection volume A (Fig. 21.7), only slow-diffusing membrane receptors will be detected. If the detection volume is slightly displaced, it is clear how one might detect both fast- and slow-diffusing particles (Fig. 21.7B) or only fast-diffusing particles (Fig. 21.7C). A related and perhaps more difficult problem to solve is the process of membrane ruffling over time in response to perturbation of the signaling systems being studied (Ridley, 1994).

Measurement artifacts present potential problems when using FCS to study living cells. Both photobleaching and autofluorescence result in reduced signal quality but can be overcome with diligent selection of experimental conditions. First, specific fluorescent signal should be at least tenfold higher than background autofluorescence. Second, fluorophores such as Alexa (Molecular Probes, Eugene, OR) can be used that show reduced photobleaching. Finally, when studying living cells, low laser power is essential to avoid cell damage and to minimize photobleaching and fluorophore depletion in cellular compartments.

The choice of fluorophore is critical when using FCS to study protein interactions in living cells. As mentioned previously, Alexa dyes (Molecular Probes) are

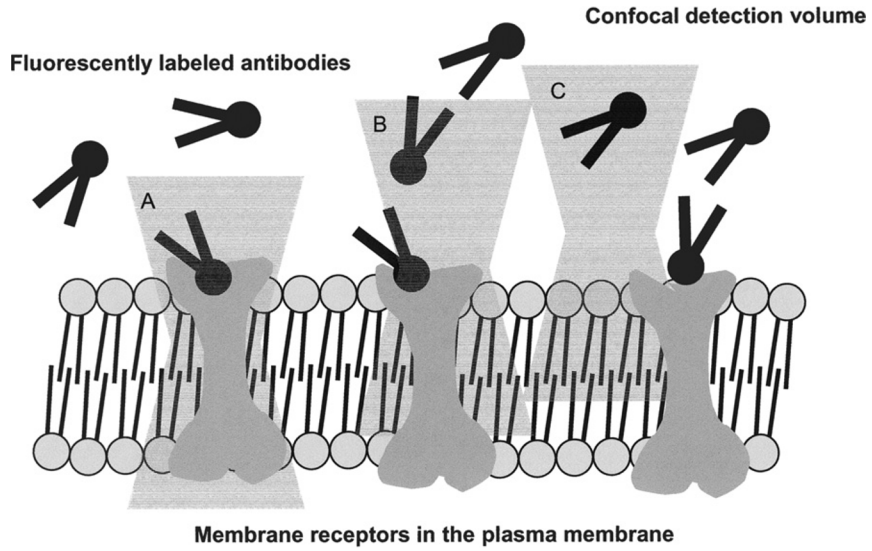

FIGURE 21.7

Precise positioning of the confocal volume affects reproducible FCS measurements of receptors in the plasma membrane.

especially useful because of reduced photobleaching. Green fluorescent protein (GFP) and spectral-shifted GFP mutants are effective tags for any *in vivo* study using fluorescence microscopy, as these are expressed as fusion proteins, which creates targeted cellular markers. When used with FCS, though, additional care must be taken when evaluating results because of potential artifacts related to GFP "blinking" (Dittrich, Malvezzi-Campeggi, Jahnz, & Schwille, 2001; Haupts, Maiti, Schwille, & Webb, 1998; Malvezzi-Campeggi, Jahnz, Heinze, Dittrich, & Schwille, 2001) or proteolytic cleavage of GFP from the fusion protein. Although beyond the scope of this chapter, it is important to point out that the application of two-photon excitation for cross-correlation FCS provides an excellent approach to studying live cells [for review, see Schwille et al., 1996; Schwille, 2001; Kim & Schwille, 2003; Lippincott-Schwartz et al., 2001; Vukojevic et al., 2005].

21.1.7 Molecular complexing in living cells

Application of FCS to living cells requires diligent experimental approaches as well as sensible evaluation of data. First, we made FCS measurements of lipophilic dye, $DiIC_{16}$, both in solution and in the plasma membranes of living A875 human melanoma cells. $DiIC_{16}$ is ideal for FCS measurements in plasma membranes of living cells for two reasons: first, the quantum yield of $DiIC_{16}$, which forms micelles in solution, is very low compared to $DiIC_{16}$ in cell membranes, and second, $DiIC_{16}$ remains in the plasma membrane after extensive washing of free dye from the sample

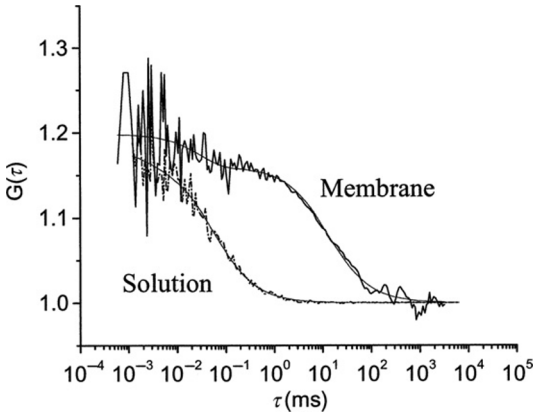

FIGURE 21.8

FCS measurements of $DiIC_{16}$ in solution and in the plasma membrane of a living cell.

chamber. FCS measurements made on $DiIC_{16}$ in the cell membrane are easily distinguished from $DiIC_{16}$ in solution (Fig. 21.8). In general, membrane measurements are characterized by longer correlation times but may exhibit both fast- and slow-diffusing components, which in part, depend on the precise placement of the confocal detection volume. We next combined FCS measurements of a membrane receptor in living cells with stoichiometry calculations, as described above.

The same rationale presented above for the three-dimensional autocorrelation function also applies to the two-dimensional autocorrelation function. Separation of N attributed to intersystem crossing and particle diffusion for the two-dimensional autocorrelation function is presented in Eq. (21.14)

$$G(\tau) = 1 + \frac{1}{N'_M}\exp\left(\frac{-\tau}{\tau_T}\right) + \frac{1}{N'_P}\left(\sum_i \frac{F_i}{1+\tau/\tau_{D_i}}\right) \tag{21.14}$$

The low-affinity NGFR gp75 is endogenously expressed by the human melanoma cell line, A875. FCS measurements were made with an Alexa-488 conjugated Fab fragment specific for gp75 on A875 cells before (Fig. 21.9, dotted line) and after (Fig. 21.9, solid line) exposure to 180-nM nerve growth factor (NGF) for 5 min. The data were fit to Eq. (21.14), using nonlinear regression, and the resulting parameters used to calculate stoichiometry. First, the calibration factor, r, was determined using measurements ($n = 20$) of Alexa-Fab alone ($r = 1.74 \pm 0.14$). Next, we made FCS measurements on different locations on 16 unique A875 cells both before and after treatment with NGF. Average fitted values were used to calculate S using Eq. (21.13). The stoichiometry of Alexa-Fab bound per gp75 particle was determined to be (1.12 ± 0.12) for untreated and (0.94 ± 0.10) for NGF-treated cells. These calculated molecular stoichiometries do not significantly differ from 1.0 for untreated

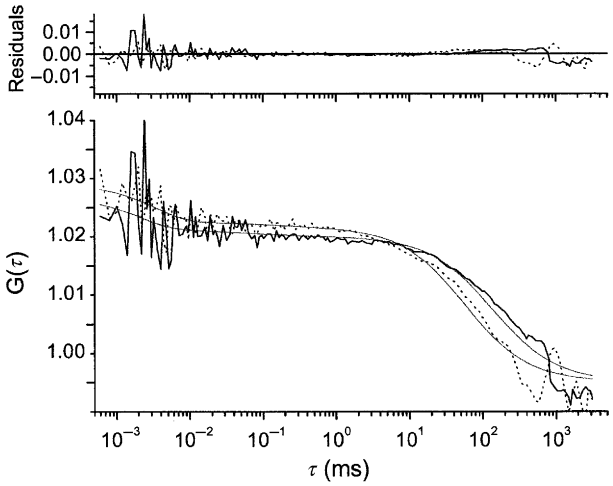

FIGURE 21.9

FCS measurements of the low-affinity nerve growth factor receptor, gp75, in the presence (solid) and absence of NGF. Residuals (top panel) were obtained after fitting to Eq. (21.14).

(student's two-tailed t-test, $p \leq 0.41$) and NGF-treated (student's two-tailed t-test, $p \leq 0.55$) cells, indicating that gp75 is a monomer in A875 cells.

It is critical to point out that estimation of stoichiometry is dependent on several experimental factors. First, according to this approach, theoretical values for monomers, dimers, trimers, and tetramers must be 1, 2, 3, and 4, respectively, if and only if 100% of all available binding sites are filled (e.g., 100% fractional occupancy) with the labeled probe used in the study, and if all receptor complexes are composed of receptors that have one bound labeled probe per receptor. Unlabeled receptors are therefore "invisible" to FCS but may still participate in the formation of receptor oligomers. We know that gp75 has a single antigenic epitope for the Alexa-Fab used in this study. Because the number of observed Fabs per particle is dependent on the fractional occupancy of these binding sites, we must take this into consideration when calculating receptor stoichiometry. Fractional occupancy (p) is dependent both on the affinity (K_D) of the Fab for its binding site and the concentration of Fab ($[L]$) used in each experiment and can be calculated by $p = [L]/([L] + K_D)$. Our experiments were conducted with Alexa-Fab at a concentration of 320 nM. Because the affinity of Alexa-Fab for gp75 was independently determined to be 313 $\pm$ 98 nM (data not shown), we assume a fractional occupancy (p) of 0.51.

Figure 21.10A shows the probability relationships that predict the number of measured Fabs per receptor particle for fractional occupancy p. In deriving these relationships, it is again important to recognize that FCS only measures receptors with at least one Fab bound to them. Unoccupied receptors are not detected. Theoretical curves for monomers, dimers, trimers, and tetramers as a function of p are shown in

A

Monomer	p/p
Dimer	$2p/(2p - p^2)$
Trimer	$3p/(3p - 3p^2 + p^3)$
Tetramer	$4p/(4p - 6p^2 + 4p^3 - p^4)$

B

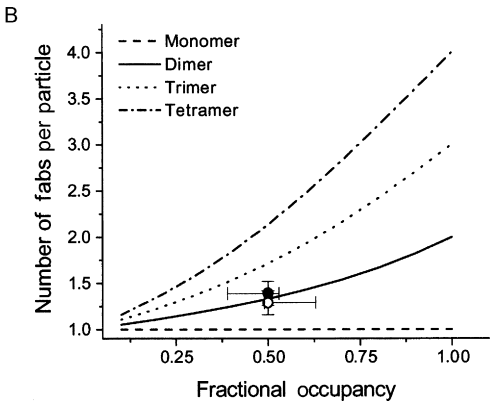

FIGURE 21.10

Calculated stoichiometry values are dependent on fractional occupancy. (A) Probability relationships used to predict the number of measured Fabs per receptor particle, which is dependent on fractional occupancy *p*. (B) Theoretical curves for monomers, dimers, trimers, and tetramers as a function of fractional occupancy *p*.

Fig. 21.10B. Note that for monomers, the number of measured Fabs per particle is independent of fractional occupancy and equals 1.0. As discussed above, we found that the number of Fabs per particle for gp75 did not significantly deviate from 1.0 for untreated and NGF-treated cells. Furthermore, Fabs per particle for untreated (1.12 ± 0.12) and NGF-treated (0.94 ± 0.10) cells were significantly lower (student's one-tailed *t*-test, $p \leq 0.02$ and $p \leq 0.0001$ for untreated and NGF-treated cells, respectively) than the value predicted for a dimer (1.34) when receptor fractional occupancy is 0.51. Therefore, our findings demonstrate that gp75 receptors are monomers before NGF treatment and that NGF does not result in receptor complexing.

This study demonstrates that FCS can be used to quantify the interactions of membrane receptors *in vivo*. Furthermore, it shows the additional complexity that is introduced when studying macromolecules in living cells. Our studies were routinely conducted at low laser power ($<25\ \mu$W) but were only successful when the Fab was conjugated to Alexa-488. The same study was attempted with the fluorescein-conjugated form of the Fab without success, mostly because of problems associated with rapid photobleaching.

21.2 DESIGNING AND BUILDING AN FCS INSTRUMENT

21.2.1 Overview: the experimental setup

The remainder of this chapter is focused on describing the factors to consider when building a microscope-based FCS instrument. A schematic of the FCS experimental setup is shown in Fig. 21.11, and a photograph (Fig. 21.12A) of the final instrument built in our laboratory on a Zeiss Axiovert 35 is also shown. The illumination source was a CW Ar laser (Lexel Laser, Model 95-2Ar), which was focused through the epiil-lumination port of a Zeiss Axiovert 35. The laser was coupled to the microscope in two different ways: using a wavelength-optimized single-mode fiber aligned through a

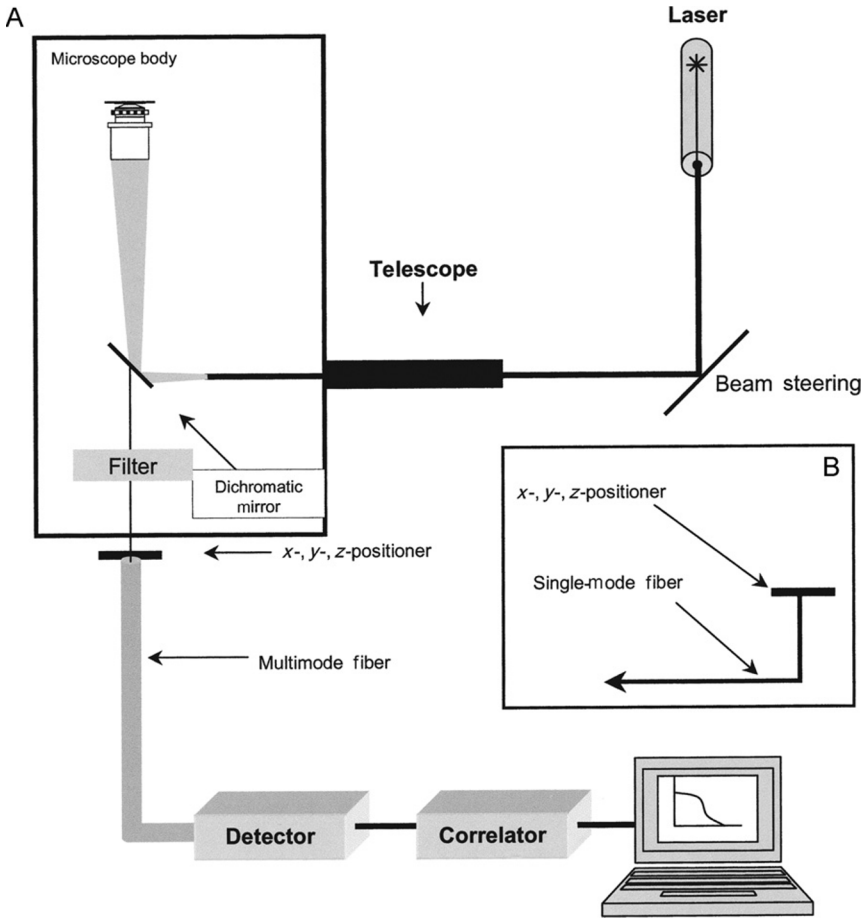

FIGURE 21.11

Schematic of FCS instrument built on a Zeiss Axiovert 35 microscope in our laboratory with beam steering (A) and fiber coupling (B).

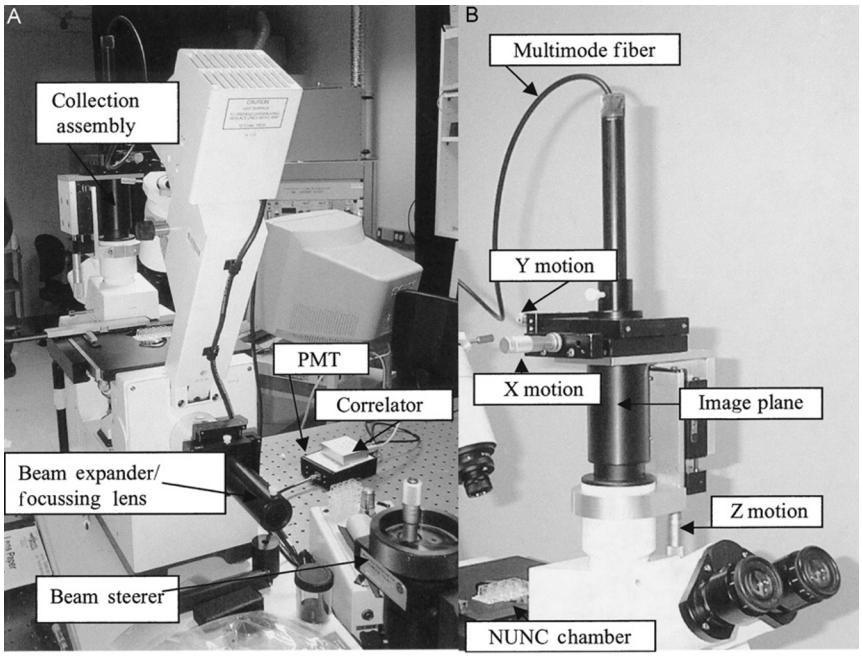

FIGURE 21.12

FCS instrument built in our laboratory.

FiberPort micropositioning device (Optics for Research), which provides both focusing as well as alignment for optimal laser to fiber launch, or using mirrors to steer the beam. When fiber coupling was used, a snap-on lens was used to collimate the laser light. For both fiber coupled and beam steering, the laser light was focused through a lens in a telescope device attached to the epiillumination port of the microscope. Incoming light was aligned with x–y positioners, and focus on the back aperture of the objective adjusted with the telescope. A Zeiss 63×, 1.2-NA water-immersion objective was used to refocus the laser onto the sample to be studied. The emitted fluorescent light was collected through the same objective and passed through a 50- or 100-μm multimode fiber, placed at the conjugate image plane, which served both as the pinhole and the collection fiber. The pinhole served to reject out-of-focus light, and the multimode fiber carried the emitted fluorescence light to a photomultiplier tube (PMT; Correlator.com, using a Hamamatsu HC120-08 PMT module) for photon counting. Positive TTL pulses from the PMT were sent to the digital correlator (Correlator.com, Flex2K-12Dx2 multiple tau) via coaxial cables with BNC connectors. The digital correlator was connected to a desktop or laptop computer via a USB port.

Laser power output was regulated in light control mode and attenuated using neutral density filters. Samples were characteristically exposed to 20–50 μW of laser power after optical attenuation, as measured at the object plane. Regulation of laser

power was a critical consideration for the FCS experimental setup to ensure optimal laser stability and to minimize photobleaching of cell membrane samples. Laser instability may be observed as systematic oscillations in photon counts and is therefore correlated.

21.2.2 Primary components of an FCS instrument

Five primary components are necessary to build an FCS instrument. Although each component is essential, one can choose from a variety of commercially available hardware solutions. We, therefore, discuss the key factors to consider when selecting these components:

- Laser illumination
- Optics
- Photon detection
- Correlator
- Data acquisition and analysis

The laser selected must meet stability, power, and excitation wavelength requirements. Optics between the laser (input) and photon detector (output) determine the beam diameter, confocal volume, and, ultimately, photon detection efficiency. A multimode fiber (100-μm diameter) was positioned in the conjugate image plane and simultaneously served both as pinhole before the detector and to carry the light signal to the photon detector. The photon detector selected must have low dark count rates and output positive TTL pulses, which are counted and processed by the digital correlator. The digital correlator, which was connected to a computer via USB port, was used to acquire photon counts, dual autocorrelation, or cross-correlation data. Relevant data processing and analysis was conducted using Origin. Visit our Web site (www.biosensorgroup.com/fcs) for more details on the software developed in our laboratory as well as the hardware used to build our FCS instrument.

21.2.3 Laser illumination

The laser selected for an FCS machine must meet stability, power, and excitation wavelength criteria. We must first assume that the laser beam intensity profile is Gaussian or TEM_{00} mode. It is important to attain the correct mode structure, otherwise, data analysis routines developed for FCS are not applicable. For our FCS instrument, we used a water-cooled, 2-W, argon ion laser (Lexel Laser Model 95-2Ar). The laser was tuned to ensure TEM_{00} mode structure. Laser light input was coupled to a Zeiss Axiovert 35 microscope by direct beam steering or via single-mode, wavelength-optimized fiber optics. Although fiber-optic coupling resulted in greater than 50% light loss, both techniques required further attenuation and worked adequately for the illumination of biological samples.

21.2.3.1 Laser power

FCS instruments do not require high-power lasers. The output of a 5-mW laser is adequate to illuminate biological samples whether coupled by beam steering or fiber optics and often requires additional attenuation. To minimize interconversion between singlet and triplet states, laser power should be kept as low as possible for the sample being studied. We typically exposed our samples to 20–50 μW of laser power after total attenuation. Note that the power per unit area is the critical parameter to control.

21.2.3.2 Wavelengths available

One of the most important factors when selecting a laser is excitation wavelength. Available wavelengths will depend on the type of laser selected. Ion lasers (argon or argon/krypton) produce multiple laser lines in wavelengths from around 457 to 568 nm. Ion lasers can be single line, tunable multiline, or simultaneous multiline, with power levels from 20–30 mW to 10 W. If single wavelengths are to be used, helium-neon (HeNe) lasers provide lines at either 543 or 635 nm. In addition, solid-state diode lasers are available from ultraviolet through infrared wavelengths, including visible laser lines at 430, 473, 488, 490, 491, 532, 633, or 658 nm at a variety of power levels from a few milliwatts to tens of milliwatts. The Cobolt Dual Calypso (www.cobolt.se) is a dual-line diode-pumped solid-state laser with both 491 and 532 nm laser lines combined into a single beam. The final criterion to determine is the stability of the laser selected.

21.2.3.3 Laser stability

In addition to desired wavelength, laser stability is the most important property to consider. Because FCS requires temporal correlation of fluorescent intensity fluctuations, any systematic noise in laser output in the measurement time domain will be correlated and reflected in the autocorrelation curve. We have evaluated a number of HeNe and diode lasers with inherent instability, which made their use in FCS problematic. Although the level of background noise that can be tolerated in an FCS instrument is dependent on collection efficiency and the assay application to be implemented, minimizing systematic laser output fluctuations should be a high priority and will provide the greatest degree of flexibility and sensitivity.

21.2.3.4 Fiber-optic coupling of laser

The laser light source may be coupled to the epiillumination port of the microscope through single-mode fiber optics. Although polarization-maintaining (PM) fibers are often used for this coupling, we have found that wavelength-optimized (e.g., 488/514 nm) single-mode fibers that are not PM fibers work adequately. The critical parameter is the efficient launching of the input laser light into the fiber, which requires both focusing the laser and alignment with micropositioners.

Alignment of the laser launch into the fiber is a critical step in building a fiber-coupled FCS instrument. Selection of the fiber launch coupling port, therefore, is critical. We chose to use the Optics for Research FiberPort miniature micropositioner, outfitted with optics designed to focus the input laser beam into the single-mode

fiber. Alignment is accomplished using two *xy* adjustment and three *z*/tilt/yaw screws, which enables both translational and tilt adjustment. We have been able to attain less than 50% coupling efficiency with this fiber port, which is sufficient for illumination of biological samples. In fact, further attenuation of the laser input before the fiber port is necessary to keep laser power within the single-mode fiber specifications. Improper laser-to-fiber launch alignment will result in damage to the fiber and alteration of the laser beam intensity profile.

Other fiber coupling hardware is available from a variety of other manufacturers. The Point Source kineFLEX kinematic single-mode fiber delivery system uses PM fibers and includes alignment hardware to optimize fiber launch. OZ Optics sells a variety of component-level laser-to-fiber delivery systems that can be customized for specific needs. Contact one of these product manufacturers for more details.

The primary advantage of fiber-coupling laser input is the benefit of modularity. This enables one to easily switch laser sources without difficult realignment tasks and without increasing the complexity of the input light path by the addition of dichroics and mirrors. We have also successfully used beam steering to direct laser input to the epiillumination port of the microscope.

21.2.3.5 Beam steering

Laser beam steering was accomplished using the beam steerer setup shown in Fig. 21.12A. It consists of two mirrors with positional controls that enable one to direct the laser beam to enter the microscope along the optical axis. Pinholes were placed in the light path between the laser and beam steerer and the beam steerer and microscope. This facilitated alignment of the input laser light in the correct plane and along the optical axis. Correct input alignment was verified by focusing on an image of the spot on fluorescent tape. When the input beam was on the optical axis, the image appeared symmetrical above and below the plane of focus. If not aligned on the optical axis, the image appeared as an ellipse and was skewed on either side of the spot's center as we focused above and below the focal plane.

21.2.3.6 System alignment

Overall alignment of the FCS system is critical to optimize signal collection efficiency and to ensure Gaussian laser beam intensity profiles. Alignment is required between the laser output and input into the microscope and between the pinhole/collection fiber optic and the conjugate image plane. If the laser is fiber coupled to the microscope, then launching of the laser beam into the fiber is critical (as described above). If the laser is directed into the microscope with a beam steerer, then alignment using pinholes and mirror adjustment is required (as described above).

Positioning the multimode fiber pinhole and collection fiber is critical to optimize efficient collection of photons. Collection efficiency is greatly reduced when the detector is not aligned correctly in the conjugate image plane. We have used differential drive micrometers in the *x*–*y* dimensions with a 0.5- to 25-μm per revolution precision (Thorlabs). We found that this level of precision in the *z*-axis was not necessary

and have used a micrometer with 500-μm per revolution precision. To test collection efficiency, we have characterized autocorrelation curves obtained with HPLC purified water, 1-nM R6G, and 10-nM R6G. The goals were to minimize counts obtained with water (no fluorophore) and maximize counts obtained in the presence of low fluorophore concentrations (Fig. 21.13). The final counts per particle (CPP) obtained for R6G was used as a general measure of instrument efficiency.

21.2.4 Optics

The optical requirements for laser illumination depend on your microscope. The minimum lenses required are a high-NA objective and those required to build the telescoping beam expander. Ideally, minimizing optical components between the object plane and photon detector will improve collection efficiency and reduce potential reflection and autofluorescence artifacts.

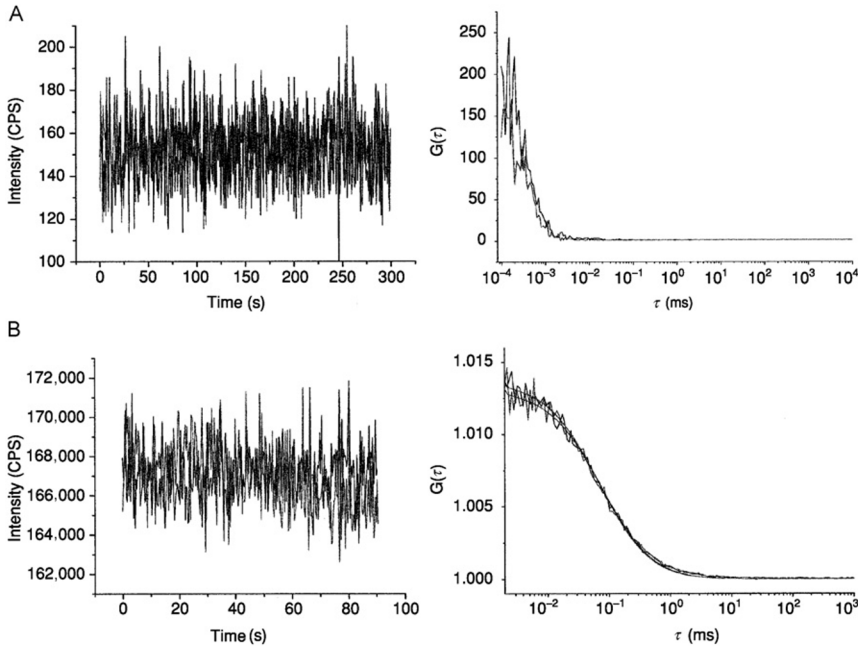

FIGURE 21.13

FCS measurements made on HPLC water and R6G in water to characterize our instrument. (A) Fluorescence intensity fluctuations (left panel) and autocorrelation curve (right panel) of measurements made on HPLC water. (B) Fluorescence intensity fluctuations (left panel) and autocorrelation curve (right panel) of measurements made on R6G in water.

21.2.4.1 Telescoping beam expander

To minimize the confocal volume, it was necessary not only to focus the beam at the object plane but also to fill the back focal plane of the objective. To accomplish this, we used a telescoping lens and beam expander to focus the laser beam on the back focal plane of the objective. Because it is difficult to obtain a comprehensive schematic of the Zeiss Axiovert 35, we empirically determined the optimal position of the telescoping beam expander to minimize focused laser beam diameter. The assumption of Gaussian beam intensity profile appears to be valid, as determined by analysis of R6G diffusion times in water (Fig. 21.13B). For a comprehensive evaluation of Gaussian beam profiles and the effect on FCS, see Hess, Huang, Heikal, & Webb, 2002.

21.2.4.2 Selecting dichromatic mirrors and filters

The emission filters and dichromatic mirrors used for FCS will depend on the fluorophore being used. Specific excitation and the emission properties of the fluorophore probe will determine what filter sets are required for the microscope. More than likely, the appropriate filter sets already exist for your microscope, and one must only consider whether or not the properties are optimal for the FCS experiments being considered.

21.2.4.3 High-NA objective

A number of excellent water-immersion objectives with high NAs are available. We have chosen to use a Zeiss 63× water-immersion 1.2-NA objective in our FCS system, which includes a selection collar for coverslip thickness. Water immersion offers the advantage that the path through aqueous media is constant regardless of how deeply into the sample one is focused. The only factors that affect the precise position of the image and of the confocal volume are the thickness and the angle relative to the optical axis of the coverslip. Subtle variations caused by these factors are compensated for by the micropositioners at the image planes, enabling precise alignment of the confocal aperture in the image plane.

21.2.5 Photon counting

Low-noise photon counting is essential for optimal FCS instrumentation. Signal-to-noise ratios are affected by the nature of the photon-counting device used. There are two primary options available—a photon-counting APD from Perkin-Elmer or idQuantique, or a PMT such as the one used on our FCS instrument. Although APD and PMT modules with low dark counts (25–100 cps) can be obtained, the spectral response of APDs and PMTs differs somewhat. Optimal detection at longer (red) wavelengths requires use of an APD, as the efficiency of PMTs drops off dramatically as one approaches 600 nm.

21.2.5.1 PMT

The photon counter used in our system was purchased from Correlator.com. It is based on the Hamamatsu HC120-08 PMT, with an amplifier/discriminator module and additional circuitry to prevent damage caused by high-intensity input. It uses an FC fiber optic connector for optical input and BNC cable to take positive TTL pulse output to the digital correlator. The PMT has low noise ($\leq$50 cps) with 20-ns pulse-pair resolution and a pulse width of 10 ns. Although this PMT is no longer available from Hamamatsu, several models with similar features are available.

21.2.5.2 APD

Both Perkin-Elmer and idQuantique offer single photon-counting APD modules. Perkin-Elmer Models SPCM-AQR-14, SPCM-AQR-15, and SPCM-AQR-16 are photon-counting APD modules with dark counts of 100, 50, and 25 cps, respectively. Models typically used in FCS instruments exhibited dark current counts of 100 or fewer counts per second. Perkin-Elmer also offers a single photon-counting array module with four independent channels (SPCM-AQ4C). Each of these models is available with fiber coupling to FC connectors. IdQuantique's id100 series of APDs are available in either free-space or fiber-coupled formats. The active area diameters of models id100-20 and id100-50 are 20 and 50 μm, respectively, with dark current counts of $<$50 cps.

21.2.6 Digital correlator

We have selected a digital hardware correlator from Correlator.com for our FCS system. Although hardware performance is excellent, the data acquisition and analysis software is not designed for FCS, but rather quasi-elastic light-scattering experiments, and there is no built-in data analysis features for FCS experiments. Because of this, we have developed, with the assistance of Correlator.com and OriginLab, data acquisition and analysis software that uses the graphical capabilities and data analysis tools of Origin (www.originlab.com).

21.2.6.1 Correlator.com

The Flex2K-12$\times$2 multiple tau external digital correlator (www.correlator.com) was used to acquire photon count data and for autocorrelation curves. It is a real-time, highly stable correlator that is easy to use and set up. It has a theoretical sampling time of 12.5 ns and accepts two TTL inputs from PMT modules via BNC connectors for dual autocorrelation or cross-correlation data acquisition. Correlation data is transferred to computer via USB port. In addition, the digital correlator can be run in photon-counting mode (in two channels) to enable photon-counting histograms (PCH) or fluorescence intensity distribution analysis (FIDA) analysis but requires processing of the incoming data before analysis. Correlator.com offers a number of other multiple tau digital correlators in the Flex02 series.

21.2.6.2 ALV

ALV (www.alvgmbh.de) digital correlators are available as an external model that is interfaced with a PCI bus card in a desktop computer (ALV-5000/EPP and the ALV-60×0/EPP series). Although their ISA bus card (ALV-5000/E) is no longer part of their product line, ALV continues to support this hardware. The original Zeiss Confocor was built with the ALV-5000/E, as were many laboratory-built instruments. The primary advantage offered by the ALV correlator is that it currently provides superior software.

21.2.7 Data acquisition and analysis

Correlator.com provides basic data acquisition software with the external digital correlator to collect photon counts, dual autocorrelation, or cross-correlation data. Although acquisition is sufficient, it is not ideal for FCS data visualization and analysis. We have therefore written integrated data acquisition and analysis modules using Origin. Visit our Web site (*www.biosensorgroup.com/fcs*) for more details on the data processing and analysis software developed in our laboratory.

21.2.7.1 Random noise and optimized signals

Reliable FCS measurements require an instrument that achieves high signal-to-noise ratios. There are two primary sources of random errors in any fluorescence measurement. The first is background noise that originates from intrinsic fluorescence of optics or sample preparations, back-reflections in fiber optics, and stray light from out-of-focus fluorescence. The second source is electronic noise, which is an intrinsic property of the detector used and includes the limitations imposed by photon-counting statistics. Although the first source of background noise can be minimized by careful selection of components and instrument alignment, the second is integral to the measured signal and is reflected in the signal-to-noise ratio that can be achieved in any measurement.

Shot noise is generated by random variation in emission from the PMT photocathode. Contributions from shot noise are present in all FCS autocorrelation measurements, which further complicate fluctuation analysis. Figure 21.13A, right panel, is the autocorrelation curve of HPLC water that shows the contribution of shot noise at short correlation times. The relative signal error caused by shot noise can be reduced with long sample measurement times or with high photon count rates. Shot noise is dependent on the detected fluorescence intensity—it increases as the square root of signal intensity. Therefore, signal-to-noise ratio is effectively increased at sufficiently high photon count rates. See the following references for detailed discussions on signal-to-noise-ratio, the sources of random errors, and shot noise (Hess et al., 2002; Magde et al., 1974; Qian & Elson, 1990; Saffarian & Elson, 2003).

Our goal was to optimize FCS measurements in solution using two criteria. First, FCS measurements of HPLC-purified water were made to characterize the overall background noise of our instrument. We typically observed between 100 and 200 cps for these measurements (Fig. 21.13A, left panel), whereas R6G were typically

on the order of 160,000–180,000 cps (Fig. 21.13B, left panel). Second, we characterized CPP for R6G measurements. The values that we typically observed varied from around 30 to around 100 CPP. Before conducting experiments, we optimized the FCS system for detection of around 100 CPP for R6G in water and for low background counts.

21.2.7.2 Autocorrelation analysis

Analysis of FCS data is a difficult yet critical step in obtaining biologically relevant information from experiments conducted in solution or in living cells. Parameters obtained by nonlinear curve fitting to the three-dimensional autocorrelation function [Eq. (21.9)] provides information on the average number of particles in the confocal volume (N), the time (τ_T) and fraction (T) of triplet state, and the diffusion time (τ_{Di}) and fraction (F_i) of i diffusing particles under examination.

These results may then be used to calculate the diffusion coefficient (D), stoichiometry as described above (S), confocal volume, and concentration of fluorescently labeled particle. In addition, validation of the FCS system using the reference standard, R6G, enables one to calculate laser beam diameter and confocal volume for the system.

The diffusion coefficient is converted from diffusion time (τ) using the relationship:

$$D_i = \frac{\omega_1^2}{4\tau_{D_i}},$$

where ω_1 is the illumination volume waist radius and is a constant property of the FCS instrument. Several steps involving the analysis of R6G in water are required to determine K^2 and ω_1. First, autocorrelation curves of R6G in water are obtained and analyzed to determine the structure parameter, K^2, where $K = \omega_2/\omega_1$, using a fixed diffusion coefficient value for R6G ($D = 2.8 \times 10^{-10}$ m^2/s). This value of K^2 is then fixed for all subsequent analysis of three-dimensional autocorrelation data using Eq. (21.9). ω_1 is determined using the following equation:

$$\omega_i = \sqrt{4D_{\tau_D}},$$

assuming the diffusion coefficient for R6G as above and the best fit value for diffusion time, τ, obtained by curve fitting. The value for $\omega_2 = K\omega_1$, which is then used to calculate confocal volume with the relationship, is volume $= 2\pi\omega_1^2\omega_2$ (in units m^3).

21.2.7.3 Fitting correlation curves

Nonlinear curve fitting is used to extract parameter information from FCS data using biologically relevant models. One selects the model to apply for the analysis and chooses the degree of complexity or number of distinct components for the fit. Often, selection of more complicated models results in "better fits," as additional parameters are introduced that can be "squeezed" independently to produce further minimization of the sum-of-squares of the residuals. Although one can visually inspect the

residuals to determine whether the selected model results in a better fit, an F-test should be applied to compare results. It is important to note that the F-test is limited to the analysis of more complex forms of the same model, for example, one and two or two and three diffusing components of the three-dimensional model presented in Eq. (21.9) but it is not intended to compare different models [e.g., Eqs. (21.9) and (21.11)].

21.2.7.4 Measuring stoichiometry

Stoichiometry of interacting macromolecules is an important parameter to characterize for dynamic systems. FCS is readily used to qualitatively detect macromolecular interactions using either autocorrelation or cross correlation. Quantitative measure of these interactions requires more stringent experimental conditions as well as additional computational steps, as described above.

Distribution analysis of photon counts has been recently introduced as a new method of fluorescence fluctuation analysis. PCH, also known as FIDA, is the most widely accepted method to quantitatively characterize macromolecular interactions. PCH and FIDA were introduced at about the same time by two independent laboratories (Chen, Muller, Ruan, & Gratton, 2002; Hillesheim & Muller, 2003; Palo et al., 2002; Palo, Mets, Jäger, Kask, & Gall, 2000; Perroud, Huang, & Zare, 2005) but are based on similar principles. Although autocorrelation measures the temporal decay of correlation, PCH and FIDA measure the probability distribution of fluctuations. It has the advantage of analyzing photon intensity streams and is not dependent on the autocorrelation function and the ability to distinguish between fast- and slow-diffusing components. These techniques provide information on number and relationship between interacting classes or species of particles and can be used to measure ligand–receptor binding and the formation of oligomeric species (Chen, Muller, So, & Gratton, 1999; Kask et al., 2000; Palo et al., 2000; Rudiger et al., 2001). The technique used in our laboratory determines molecular stoichiometry by autocorrelation function analysis when two distinct diffusing components can be distinguished, as described above.

21.2.7.5 Calculation of beam diameter and confocal volume

R6G was used as the standard to characterize our FCS system. R6G (5 nM) was used to determine structure parameter (K^2) as described above. For the data shown in Fig. 21.13B, the structure parameter was determined to be 11.73. This value was fixed for all subsequent data collected on that particular day. We have found this value to vary between experiments, usually in the range of 3–20. Analysis of R6G data resulted in an average diffusion time of 73.6 μs for R6G in our FCS system. Using these data and the relationships described above, we determined the illumination beam diameter to be 0.6 μm and the confocal volume to be $\sim$0.5 fl. This value should be borne in mind when considering power levels described in this chapter.

21.3 WHAT ARE THE CURRENT COMMERCIAL SOURCES OF FCS?

FCS instruments are available from a number of commercial sources. ISS (www.iss.com) and Carl Zeiss (www.zeiss.com) were the first commercial systems available. Both systems share similar features—can function in autocorrelation and cross-correlation modes, can be configured for either single-photon or multiphoton excitation, can collect photon counts for PCH analysis or FIDA, and can work well for both solution and cellular systems. The ISS Alba Fluorescence Correlation Spectroscopy System can additionally be upgraded for steady-state and lifetime measurements, and the user can choose to use an Olympus or Nikon epifluorescence microscope. The Zeiss Confocor II is limited to Zeiss microscopes and optics but can be equipped with a laser scanning module that creates a full-featured confocal microscope. In addition, the Zeiss Confocor II offers software that enables researchers to visualize cells and select the specific location at which to collect correlation data.

Other sources of FCS instrumentation include Hamamatsu, Leica, Becker & Hickl, and Sensor Technologies, Inc. The FCS instrument produced by Sensor is optimized for measurements made in solution using both autocorrelation and cross-correlation modes. The unique feature of this instrument is its portability. It is based on a simplified design and is a small-footprint, benchtop instrument that is self-contained and easily transported. In addition to data acquisition and analysis software, Sensor Technologies also offers FCS-optimized reagent kits for rapid development of FCS-based assays. Visit the Sensor Technologies Web site at www.biosensorgroup.com/fcs for more details.

21.4 SUMMARY

FCS is an important technique for biophysicists, biochemists, and cell biologists. FCS represents an example of how one can make use of the microscope and electronics to extract information beyond the resolution limit of classical optics. It can be used to study single molecules both in solution and in living cells and can be used to monitor a variety of macromolecular interactions. When used as an *in vitro* technique, FCS measurements are easy to conduct and can be made on simplified instrumentation. When used *in vivo* on living cells, many additional factors must be considered when evaluating experimental data. Despite these concerns, FCS represents a new approach that has broad applicability for the determination of molecular stoichiometry both *in vivo* and *in vitro* for a variety of membrane and soluble receptor systems.

Acknowledgments

We thank Christine Thompson and Alonzo Ross for providing experimental assistance and gp75 clones, and Leya Bergquist and Roxanne Wellman for their assistance in preparing

figures for this chapter. D.A.B. completed portions of this work while supported by NIH Training Grant NS-07366. D.E.W. was supported by a grant from the National Institutes of Health (NS28760). The content of this publication is solely the responsibility of the authors and does not represent the views of these funding agencies.

References

Axelrod, D., Thompson, N. L., & Burghardt, T. P. (1983). Total internal inflection fluorescent microscopy. *Journal of Microscopy*, *129*, 19–28.

Berg, H. C. (1993). *Random walks in biology*. Princeton, NJ: Princeton University Press.

Berland, K. M. (1997). Fluorescence correlation spectroscopy: New methods for detecting molecular associations. *Biophysical Journal*, *72*, 1487–1488.

Berland, K. M. (2004). Fluorescence correlation spectroscopy: A new tool for quantification of molecular interactions. *Methods in Molecular Biology*, *261*, 383–398.

Berne, B. J., & Pecora, R. (2000). *Dynamic light scattering: With applications to chemistry, biology and physics*. Mineola, NY: Dover Publications.

Brock, R., Hink, M. A., & Jovin, T. M. (1998). Fluorescence correlation microscopy of cells in the presence of autofluorescence. *Biophysical Journal*, *75*, 2547–2557.

Brock, R., & Jovin, T. M. (1998). Fluorescence correlation microscopy (FCM)—Fluorescence correlation spectroscopy (FCS) taken into the cell. *Cellular and Molecular Biology (Noisy-le-Grand, France)*, *44*, 847–856.

Brown, M. P., & Royer, C. (1997). Fluorescence spectroscopy as a tool to investigate protein interactions. *Current Opinion in Biotechnology*, *8*, 45–49.

Carroll, L. (2000). *Alice's adventures in wonderland*. (Vol. 35). New York, NY: Penguin Publishing, 239.

Chen, Y., Muller, J. D., Ruan, Q., & Gratton, E. (2002). Molecular brightness characterization of EGFP *in vivo* by fluorescence fluctuation spectroscopy. *Biophysical Journal*, *82*, 133–144.

Chen, Y., Muller, J. D., So, P. T., & Gratton, E. (1999). The photon counting histogram in fluorescence fluctuation spectroscopy. *Biophysical Journal*, *77*, 553–567.

Clair, J. J. (1997). Analysis of highly disfavored processes through pathway-specific correlated fluorescence. *Proceedings of the National Academy of Sciences of the United States of America*, *94*, 1623–1628.

Dittrich, P., Malvezzi-Campeggi, F., Jahnz, M., & Schwille, P. (2001). Accessing molecular dynamics in cells by fluorescence correlation spectroscopy. *Biological Chemistry*, *382*, 491–494.

Elson, E. L. (2004). Quick tour of fluorescence correlation spectroscopy from its inception. *Journal of Biomedical Optics*, *9*, 857–864.

Elson, E. L., & Magde, D. (1974). Fluorescence correlation spectroscopy. I. Conceptual basis and theory. *Biopolymers*, *13*, 1–27.

Elson, E. L., & Qian, H. (1989). Interpretation of fluorescence correlation spectroscopy and photobleaching recovery in terms of molecular interactions. *Methods in Cell Biology*, *30*, 307–332.

Elson, E. L., Schlessinger, J., Koppel, D. E., Axelrod, D., & Webb, W. W. (1976). Measurement of lateral transport on cell surfaces. *Progress in Clinical and Biological Research*, *9*, 137–147.

Fahey, P. F., Koppel, D. E., Barak, L. S., Wolf, D. E., Elson, E. L., & Webb, W. W. (1977). Lateral diffusion in planar lipid bilayers. *Science*, *195*, 305–306.

Foldes-Papp, Z. (2006). What it means to measure a single molecule in a solution by fluorescence fluctuation spectroscopy. *Experimental and Molecular Pathology*, *80*, 209–218.

Foldes-Papp, Z., Demel, U., & Tilz, G. P. (2001). Ultrasensitive detection and identification of fluorescent molecules by FCS: Impact for immunobiology. *Proceedings of the National Academy of Sciences of the United States of America*, *98*, 11509–11514.

Foldes-Papp, Z., Demel, U., & Tilz, G. P. (2002). Detection of single molecules: Solution-phase single-molecule fluorescence correlation spectroscopy as an ultrasensitive, rapid and reliable system for immunological investigation. *Journal of Immunological Methods*, *260*, 117–124.

Frieden, C., Chattopadhyay, K., & Elson, E. L. (2002). What fluorescence correlation spectroscopy can tell us about unfolded proteins. *Advances in Protein Chemistry*, *62*, 91–109.

Haupts, U., Maiti, S., Schwille, P., & Webb, W. W. (1998). Dynamics of fluorescence fluctuations in green fluorescent protein observed by fluorescence correlation spectroscopy. *Proceedings of the National Academy of Sciences of the United States of America*, *95*, 13573–13578.

Hess, S. T., Huang, S., Heikal, A. A., & Webb, W. W. (2002). Biological and chemical applications of fluorescence correlation spectroscopy: A review. *Biochemistry*, *41*, 697–705.

Hess, S. T., & Webb, W. W. (2002). Focal volume optics and experimental artifacts in confocal fluorescence correlation spectroscopy. *Biophysical Journal*, *83*, 2300–2317.

Hillesheim, L. N., & Muller, J. D. (2003). The photon counting histogram in fluorescence fluctuation spectroscopy with non-ideal photodetectors. *Biophysical Journal*, *85*, 1948–1958.

Hink, M. A., Bisselin, T., & Visser, A. J. (2002). Imaging protein-protein interactions in living cells. *Plant Molecular Biology*, *50*, 871–883.

Kask, P., Palo, K., Fay, N., Brand, L., Mets, U., Ullmann, D., et al. (2000). Two-dimensional fluorescence intensity distribution analysis: Theory and applications. *Biophysical Journal*, *78*, 1703–1713.

Kim, S. A., & Schwille, P. (2003). Intracellular applications of fluorescence correlation spectroscopy: Prospects for neuroscience. *Current Opinion in Neurobiology*, *13*, 583–590.

Kinjo, M., & Rigler, R. (1995). Ultrasensitive hybridization analysis using fluorescence correlation spectroscopy. *Nucleic Acids Research*, *23*, 1795–1799.

Kohler, R. H., Schwille, P., Webb, W. W., & Hanson, M. R. (2000). Active protein transport through plastid tubules: Velocity quantified by fluorescence correlation spectroscopy. *Journal of Cell Science*, *113*, 3921–3930.

Lagerkvist, A. C., Foldes-Papp, Z., Persson, M. A., & Rigler, R. (2001). Fluorescence correlation spectroscopy as a method for assessment of interactions between phage displaying antibodies and soluble antigen. *Protein Science*, *10*, 1522–1528.

Lippincott-Schwartz, J., Snapp, E., & Kenworthy, A. (2001). Studying protein dynamics in living cells. *Nature Reviews. Molecular Cell Biology*, *2*, 444–456.

Maertens, G., Vercammen, J., Debyser, Z., & Engelborghs, Y. (2005). Measuring protein-protein interactions inside living cells using single color fluorescence correlation spectroscopy. Application to human immunodeficiency virus type 1 integrase and LEDGF/p75. *The FASEB Journal*, *19*, 1039–1041.

Magde, D. (1976). Chemical kinetics and fluorescence correlation spectroscopy. *Quarterly Reviews of Biophysics*, *9*, 35–47.

Magde, D. (1977). Concentration correlation analysis and chemical kinetics. *Molecular Biology, Biochemistry, and Biophysics*, *24*, 43–83.

Magde, D., Elson, E. L., & Webb, W. W. (1974). Fluorescence correlation spectroscopy. II. An experimental realization. *Biopolymers*, *13*, 29–61.

Malvezzi-Campeggi, F., Jahnz, M., Heinze, K. G., Dittrich, P., & Schwille, P. (2001). Light-induced flickering of DsRed provides evidence for distinct and interconvertible fluorescent states. *Biophysical Journal*, *81*, 1776–1785.

Matayoshi, E., & Swift, K. (2001). *Applications of FCS to protein-ligand interactions: Comparison with fluorescence polarization.* Berlin: Springer-Verlag.

Medina, M. A., & Schwille, P. (2002). Fluorescence correlation spectroscopy for the detection and study of single molecules in biology. *BioEssays*, *24*, 758–764.

Meyer, T., & Schindler, H. (1988). Particle counting by fluorescence correlation spectroscopy. Simultaneous measurement of aggregation and diffusion of molecules in solutions and in membranes. *Biophysical Journal*, *54*, 983–993.

Meyer-Almes, F. J., & Auer, M. (2000). Enzyme inhibition assays using fluorescence correlation spectroscopy: A new algorithm for the derivation of kcat/KM and Ki values at substrate concentrations much lower than the Michaelis constant. *Biochemistry*, *39*, 13261–13268.

Moore, K. J., Turconi, S., Ashman, S., Ruediger, M., Haupts, U., Emerick, V., et al. (1999). Single molecule detection technologies in miniaturized high throughput screening: Fluorescence correlation spectroscopy. *Journal of Biomolecular Screening*, *4*, 335–354.

Palmer, A. G., III., & Thompson, N. L. (1987). Molecular aggregation characterized by high order autocorrelation in fluorescence correlation spectroscopy. *Biophysical Journal*, *52*, 257–270.

Palmer, A. G., III., & Thompson, N. L. (1989). Fluorescence correlation spectroscopy for detecting submicroscopic clusters of fluorescent molecules in membranes. *Chemistry and Physics of Lipids*, *50*, 253–270.

Palo, K., Brand, L., Eggeling, C., Jager, S., Kask, P., & Gall, K. (2002). Fluorescence intensity and lifetime distribution analysis: Toward higher accuracy in fluorescence fluctuation spectroscopy. *Biophysical Journal*, *83*, 605–618.

Palo, K., Mets, U., Jäger, S., Kask, P., & Gall, K. (2000). Fluorescence intensity multiple distributions analysis: Concurrent determination of diffusion times and molecular brightness. *Biophysical Journal*, *79*, 2858–2866.

Perroud, T. D., Huang, B., & Zare, R. N. (2005). Effect of bin time on the photon counting histogram for one-photon excitation. *Chemphyschem*, *6*, 905–912.

Politz, J. C., Browne, E. S., Wolf, D. E., & Pederson, T. (1998). Intranuclear diffusion and hybridization state of oligonucleotides measured by fluorescence correlation spectroscopy in living cells. *Proceedings of the National Academy of Sciences of the United States of America*, *95*, 6043–6048.

Pramanik, A. (2004). Ligand-receptor interactions in live cells by fluorescence correlation spectroscopy. *Current Pharmaceutical Biotechnology*, *5*, 205–212.

Pramanik, A., & Ekberg, K. (2001). C-peptide binding to human cell membranes: Importance of Glu27. *Biochemical and Biophysical Research Communications*, *284*, 94–98.

Pramanik, A., & Rigler, R. (2001). Ligand-receptor interactions in the membrane of cultured cells monitored by fluorescence correlation spectroscopy. *Biological Chemistry*, *382*, 371–378.

Qian, H., & Elson, E. L. (1990). On the analysis of high order moments of fluorescence fluctuations. *Biophysical Journal*, *57*, 375–380.

Ridley, A. J. (1994). Membrane ruffling and signal transduction. *BioEssays*, *16*, 321–327.

Rigler, R. (1995). Fluorescence correlations, single molecule detection and large number screening. Applications in biotechnology. *Journal of Biotechnology*, *41*, 177–186.

Rudiger, M., Haupts, U., Moore, K. J., & Pope, A. J. (2001). Single-molecule detection technologies in miniaturized high throughput screening: Binding assays for G protein-coupled receptors using fluorescence intensity distribution analysis and fluorescence anisotropy. *Journal of Biomolecular Screening*, *6*, 29–37.

Saffarian, S., & Elson, E. L. (2003). Statistical analysis of fluorescence correlation spectroscopy: The standard deviation and bias. *Biophysical Journal*, *84*, 2030–2042.

Schwille, P. (2001). Fluorescence correlation spectroscopy and its potential for intracellular applications. *Cell Biochemistry and Biophysics*, *34*, 383–408.

Schwille, P., Haupts, U., Maiti, S., & Webb, W. W. (1999). Molecular dynamics in living cells observed by fluorescence correlation spectroscopy with one- and two-photon excitation. *Biophysical Journal*, *77*, 2251–2265.

Schwille, P., Oehlenschlager, F., & Walter, N. G. (1996). Quantitative hybridization kinetics of DNA probes to RNA in solution followed by diffusional fluorescence correlation analysis. *Biochemistry*, *35*, 10182–10193.

Thompson, N. L., & Axelrod, D. (1983). Immunoglobulin surface-binding kinetics studied by total internal reflection with fluorescence correlation spectroscopy. *Biophysical Journal*, *43*, 103–114.

Thompson, N. L., Lieto, A. M., & Allen, N. W. (2002). Recent advances in fluorescence correlation spectroscopy. *Current Opinion in Structural Biology*, *12*, 634–641.

Van Craenenbroeck, E., Vercammen, J., Matthys, G., Beirlant, J., Marot, C., Hoebeke, J., et al. (2001). Heuristic statistical analysis of fluorescence fluctuation data with bright spikes: Application to ligand binding to the human serotonin receptor expressed in *Escherichia coli* cells. *Biological Chemistry*, *382*, 355–361.

Vukojevic, V., Pramanik, A., Yakovleva, T., Rigler, R., Terenius, L., & Bakalkin, G. (2005). Study of molecular events in cells by fluorescence correlation spectroscopy. *Cellular and Molecular Life Sciences*, *62*, 535–550.

Walter, N. G., Schwille, P., & Eigen, M. (1996). Fluorescence correlation analysis of probe diffusion simplifies quantitative pathogen detection by PCR. *Proceedings of the National Academy of Sciences of the United States of America*, *93*, 12805–12810.

Weissman, M., Schindler, H., & Feher, G. (1976). Determination of molecular weights by fluctuation spectroscopy: Application to DNA. *Proceedings of the National Academy of Sciences of the United States of America*, *73*, 2776–2780.

Widengren, J., & Rigler, R. (1998). Fluorescence correlation spectroscopy as a tool to investigate chemical reactions in solutions and on cell surfaces. *Cellular and Molecular Biology (Noisy-le-Grand, France)*, *44*, 857–879.

Zhong, Z. H., Pramanik, A., Ekberg, K., Jansson, O. T., Jornvall, H., Wahren, J., et al. (2001). Insulin binding monitored by fluorescence correlation spectroscopy. *Diabetologia*, *44*, 1184–1188.

CHAPTER

Breaking the Resolution Limit in Light Microscopy

22

Rainer Heintzmann[*,1] **and Gabriella Ficz**[†,2]

[*]*Randall Division of Cell and Molecular Biophysics, King's College London, London, United Kingdom*

[†]*Laboratory of Developmental Genetics and Imprinting, The Babraham Institute, Cambridge, United Kingdom*

CHAPTER OUTLINE

Introduction 526
22.1 What is Resolution? 529
22.2 Methods Within the Combined Illumination and Detection Abbe Limit 534
22.3 Methods Circumventing the Abbe Limit 537
22.4 A Comment on Near Field Methods and Pendry's Lens 540
22.5 Key Points 541
Acknowledgment 542
References 542
Further Reading 544

Abstract

The advancement in fluorescence microscopy has dramatically enhanced the obtainable optical resolution enabling the users to inspect the structures of interest at finer and finer level of detail. This chapter describes some of these methods and how they break the classical resolution limit. The labeling of targets, such as individual genetic

[1]Rainer Heintzmann (*1970) studied Physics in Osnabrück, Germany. After his Ph.D. in Heidelberg (Supervisor Professor Dr. C. Cremer), he continued his work on fluorescence microscopy development for 5 years in the laboratory of Dr. Thomas Jovin, MPI for Biophysical Chemistry, Göttingen, Germany. He now heads the Nanoimaging research group at King's College London, United Kingdom.
[2]Gabriella Ficz (*1978) studied Biology in Iasi, Romania. After her Ph.D. in Göttingen, Germany (Supervisor Dr. D. Arnd-Jovin), she now works on mammalian epigenetics and reprogramming within the group of Dr. W. Reik, The Babraham Institute, Cambridge, United Kingdom.

Methods in Cell Biology, Volume 114 **ISSN 0091-679X**
Copyright © 2006 by Oxford University Press. Reprinted with permission.
http://dx.doi.org/10.1016/B978-0-12-407761-4.00022-1

loci, specific proteins, or organelles, is possible inside living cells, which led to the extensive use of fluorescence microscopy in life sciences. Other microscopic modes usually lack this high specificity but sometimes provide other useful information such as the orientation of molecular species in polarization microscopy. Modes, such as differential interference contrast, phase contrast, or dark field, are useful to discriminate and follow cells or structures within them without the need for specific labeling. However, classically the resolution of all of these light microscopic modes was far below that of the electron microscope, and only some recent approaches have made significant progress in resolution increase. Recently, many microscopy methods have dramatically enhanced the resolution. Gradually, these methods are now applied to solve biological problems. The most promising approaches are all based on fluorescence and use either nonlinear interaction of light with the sample (STED, nonlinear structured illumination, dynamic saturation optical microscopy, or saturation in the time domain) or precise localization of individual particles or molecules with subsequent image generation.

INTRODUCTION

Fluorescence microscopy has been an essential tool for biologists over many years especially after the discovery of the green fluorescent protein and the possibility of tagging virtually every protein with it. Advances in fluorescence microscopy have dramatically enhanced the obtainable optical resolution (Garini, Vermolen, & Young, 2005) enabling the users to inspect structures of interest at finer and finer level of detail. The aim of our chapter is to describe some of these methods (Table 22.1) and how they break the classical resolution limit.

Usually, if the aim is to see the structure of a cell down to molecular detail one has to resort to electron microscopy or electron tomography (Baumeister, 2005). However, this requires sample fixation which by itself can alter the microstructure, even when preparative methods such as shock freezing or high-pressure freeze substitution are used. In addition, it is not easily possible to label and distinguish multiple targets inside the cell. The common approaches such as tagging with metal particles of different sizes (van den Pol, 1989) help to some extent but usually serve as mere indicators that in the vicinity of these metal particles the structure of interest can be expected. Finally, but most importantly, electron microscopy at this level of resolution is not possible for living samples.

Light optical microscopy and especially fluorescence microscopy does not suffer from the above problems. The labeling of targets such as individual genetic loci, specific proteins, or organelles is possible inside living cells which led to the extensive use of fluorescence microscopy in life sciences (Mahy, Perry, Gilchrist, Baldock, & Bickmore, 2002). Other microscopic modes usually lack this high specificity, but do sometimes provide other useful information such as the orientation of molecular species in polarization microscopy (Kawata, Inouye, & Ichimura, 2004). Modes such as differential interference contrast (DIC), phase contrast, or dark field are useful to discriminate and follow cells or structures within them without the need for specific labeling.

Table 22.1 Fluorescence Microscopy Methods

Method	Common Abbreviations	Abbe Applies	Remarks	Best Resolution (nm)	References
Wide-field	WF	Yes	The resolution depends on the numerical aperture (NA) (not the magnification). High NA is achieved by immersion objectives. The sample has to be immersed in the same refractive index as immersion medium.	~230 (*xy*), ~1000 (*z*)	Pawley, 2006
Confocal	CLSM, LSM	Yes	In theory: twice the resolution of wide-field microscopy. Local dose of light is very high for a short time. Potentially more photodamage. Photons are blocked by the pinhole, wasting useful information. Fine with living cells.	~180 (*xy*), ~500 (*z*)	Pawley, 2006
4Pi	4Pi (type A, B, C)	Yes	A second lens is used and adjusted to coherently participate in the imaging. Demonstrated with living cells, multiple foci preferred.	~200 (*xy*), ~90 (*z*)	Bewersdorf et al., 2006; Pawley, 2006
I^5M	I^5M	Yes	Similar to the above except no scanning needed and an incoherent full wide-field illumination is used from both sides. Potentially faster.	~230 (*xy*), ~90 (*z*)	Gustafsson et al., 1999
Localization	PALM, STORM, PAINT	Yes	Optics within the Abbe limit, but the task (localizing single particles) is not restricted to it. PALM, STORM, and PAINT managed (for the first time) to reconstitute full images from many thousand localized molecules. Particle discrimination by color, fluorescence lifetime, blinking, bleaching, photo-activation followed by bleaching and transient binding. Not demonstrated in 3D, no living cells yet.	~20 (*xy*)	Betzig et al., 2006; Bystricky et al., 2004; Danuser & Waterman-Storer, 2006; Gordon et al., 2004; Heilemann et al., 2002; Hildenbrand et al., 2005; Kellermayer, 2005; Kubitscheck et al., 2005; Lacoste et al., 2000; Lidke et al., 2005; Mahy et al., 2002; Ober et al., 2004; Qu et al., 2004; Rust et al., 2006; Sharonov & Hochstrasser, 2007; Syed et al., 2006; Yildiz et al., 2003

Continued

Table 22.1 Fluorescence Microscopy Methods—cont'd

Method	Common Abbreviations	Abbe Applies	Remarks	Best Resolution (nm)	References
Structured illumination	SIM, PEM, LMEM, HELM, Lattice Microscopy	Yes	Currently ~10 CCD images required for a slice. So far, no 3D data published. Requires extensive image processing. Potentially fast. No living cells demonstrated yet.	~100 (XY)	Chung et al., 2006; Gustafsson, 2000; Heintzmann & Cremer, 1999; Pawley, 2006
Nonlinear structured illumination	SPEM, SSIM	No	Currently ~100 CCD images required for one single reconstructed plane. Sample must not move within this time. No living cells demonstrated yet.	~50 (*xy*)	Gustafsson, 2005; Heintzmann et al., 2002
Two photon	2P	No	Nonlinear gain in resolution is cancelled by longer wavelength. Inherent sectioning without a pinhole. Only in-plane bleaching. Deep tissue possible due to long illumination wavelength. Fine with living cells.	~200 (*xy*), ~400 (*z*)	Pawley, 2006
Stimulated emission depletion	STED	No	The saturation of the stimulated emission circumvents the Abbe limit. Combination with 4Pi possible. Not yet demonstrated in 3D. No living cells demonstrated yet.	~16 (*x*), ~20 (*xy*), ~50 (*z*)	Donnert et al., 2006; Hell & Wichmann, 1994; Kittel et al., 2006; Willig et al., 2006a,b,c; Pawley, 2006
Evanescent wave	TIRFM	No	Resolution improvement only along *z*. Can be combined with structured illumination. Contact to surface of different refractive index required. Fine with living cells. 3D stacks not demonstrated.	~230 (*xy*), ~100 (*z*)	Axelrod, 2003; Pawley, 2006
Near field	SNOM, NSOM	No	Only applicable if scanning tip is in close proximity (<10 nm) to the sample. Living cells possible. 3D stacks not yet demonstrated.	~30 (*xy*), ~10 (*z*)	Kawata et al., 2004; Wabuyele et al., 2005

Abbreviations: WF, wide-field; CLSM, confocal laser scanning microscopy; LSM, laser scanning microscopy; 4Pi, stands for the full solid angle of a sphere; Type A, coherent illumination; B, coherent detection; C, coherent illumination and detection; I^5M, incoherent interference illumination image interference; PALM, photoactivated localization microscopy; STORM, stochastic optical reconstruction microscopy; PAINT, points accumulation for imaging in nanoscale topography; SIM, structured illumination microscopy; PEM, patterned excitation microscopy; LMEM, laterally modulated excitation microscopy; HELM, harmonic excitation microscopy; SPEM, saturated patterned excitation microscopy; SSIM, saturated structured illumination microscopy; 2P, two photon; STED, stimulated emission depletion.

However, classically the resolution of all of these light microscopic modes was far below that of the electron microscope and only some recent approaches have made significant progress in resolution increase.

22.1 WHAT IS RESOLUTION?

The term "resolution" has to be distinguished from "sensitivity," "sampling," and "precision." Below we will try to clarify the meaning of these terms.

One can have a very sensitive light microscopic system which makes it possible to see single virus particles or even single fluorescent molecules (Betzig et al., 2006; Kittel et al., 2006; Lacoste et al., 2000; Sharonov & Hochstrasser, 2007). This only means we would have single molecule *sensitivity*, but the size of such a molecule in the image could, for example, still correspond to 0.5 μm in the sample coordinate system, which would be a relatively poor optical resolution.

Another common confusion is the difference between resolution and *sampling*, which relates to magnification. It is easy to magnify an image of the sample by optical means to any desired degree; however, the process of magnification does not increase the optical resolution, at best it preserves it. When an image of the sample is detected by our eyes, or for example a CCD camera, it gets "sampled" into a discrete set of measured intensity values, one for each detector element (such as a photosensitive cell in the eye). These sampling points correspond to nominal positions in the coordinate system of the object under investigation, without a limit to their density. The magnification has to be adjusted such that the finest level of detail present in the image is still measured (sampled) by at least two such detector elements, but any denser sampling will not yield new information about the sample. For a detailed discussion on sampling in optical microscopy, see Heintzmann, 2006; Heintzmann & Ficz, 2006. Magnification significantly beyond this limit is sometimes called "empty magnification." When there is a noise attributable to the readout process of the detector (read noise), such empty magnification should be avoided as it deteriorates the image quality.

In many cases, there can be very specific questions in biology which are to be answered by microscopic imaging. Such questions could be: "What is the spatial distance between two specific genetic loci in the nucleus or between two molecules on the cell surface?" To answer these questions, there is no need for a resolution in the order of this distance, but the error of localization (the reciprocal of the localization *precision*) needs to be below this expected distance. This means that the distance between the estimated and the true center position of the object has to be below the distance between the two objects. Localization precision can be far higher than the optical resolution (Pawley, 2006; Rust, Bates, & Zhuang, 2006), e.g., the localization error of single molecules can be smaller than 10 nm on a system of 200-nm optical resolution and we can use this even for relative position determination between multiple loci, as long as we are able to discriminate between the target genes (or other small structures) in our image. Such discrimination can be achieved by using multiple colors (Bystricky, Heun, Gehlen, Langowski, & Gasser, 2004; Lidke, Rieger, Jovin, & Heintzmann, 2005; Ober, Ram, & Ward, 2004), differences in fluorescence lifetime

(Heilemann et al., 2002), photobleaching (Gordon, Ha, & Selvin, 2004; Rust et al., 2006), the individuality of statistical blinking events (Lippincott-Schwartz & Patterson, 2003), photoactivation (Betzig et al., 2006; Sharonov & Hochstrasser, 2007), and transient binding (Heintzmann & Sheppard, 2007). The higher the resolution the better the localization precision, but how much better than the optical resolution depends strongly (with a square root dependence) on the number of photons collected from each target. An impressive application of the localization idea was to observe the molecular steps of Myosin V (Syed, Snyder, Franzini-Armstrong, Selvin, & Goldman, 2006; Yildiz et al., 2003). Another interesting application was to follow the kinetics of the receptor-mediated entry of NTF2 and transport of NTF2 and transportin 1, with and without transport substrate, into the nucleus (Lacoste et al., 2000). The method of speckle microscopy (Danuser & Waterman-Storer, 2006) uses precise localization for the tracking of molecular clusters to reveal their temporal behavior. Nanosizing (Inoue & Oldenbourg, 1998) can be used to address the question of the size of biological particles of known shape.

Even when objects are not point-like structures, the position of features like straight edges (e.g., tubulin fibers) or planes (e.g., plasma membrane) can often be determined very precisely by microscopy methods. All of these methods are based on localization precision, which should not be confused with the term resolution as discussed below.

When we talk about high *resolution* of an optical instrument in this chapter, we mean the ability to see a structure at a high level of detail. There are various ways to define the term resolution more precisely which are discussed in the two separate boxed sections (Boxes 22.1 and 22.2). The reader who is uninterested in the technical details of resolution definition may skip the boxed sections.

For classical treatments of the resolution proven see Chapter 1 by Sluder and Nordberg, this volume; and Chapter 2 by Wolf, this volume.

Although the definitions of resolution [FWHM (*F*ull *W*idth of the PSF measured at *H*alf its *M*aximum) see Fig. 22.1, Rayleigh and Sparrow limit] mentioned in the boxed section "The point spread function" (Box 22.1) may be useful in some cases, we would like to use a different limit called the Abbe limit (see boxed section "The Abbe limit," Box 22.2) within this chapter, as this limit has a very direct relationship to which light rays are captured by the objective lens of the microscope.

It is interesting to note that the ability to precisely localize can be turned into a genuine "resolution" when many closely spaced particles can be discriminated. From the precise localization of these particles, a picture can be constructed by painting dots at each localized position. A method termed "Pointillism" (Lippincott-Schwartz & Patterson, 2003). A very successful way of discriminating closely spaced molecules is using a repetitive cycle of faint photoactivation followed by bleaching of the activated molecules (Betzig et al., 2006; Sharonov & Hochstrasser, 2007). In every cycle only very few molecules get activated, so the chance of PSF overlap is small and the localization thus very precise. In fixed samples, it was possible to reconstruct impressive images of a cryo-prepared thin section from a COS-7 cell-expressing CD63 (lysosomal transmembrane protein) tagged with Kaede and dEosFP-tagged cytochrome *c* oxidase import sequence in mitochondria of COS-7 cells down to a

Box 22.1 THE POINT SPREAD FUNCTION: THE SAMPLE AS A SUM OF POINTS

The point spread function (PSF) describes how a very small (in theory infinitesimally small) emitter gets imaged by an imaging system.

As a sample can be thought of consisting of many points (in the limit infinite) each with its own strength, the image can be described as an equivalent sum of corresponding PSFs. Most optical systems (called "linear shift invariant") can be idealized as having a position independent PSF, where emitters at every position in the field image to the same PSF shape.[3] This feature simplifies optical theory significantly as the imaging operation can then be described by a mathematical operation called "convolution."

In Fig. 22.1, two examples of typical PSFs of a wide-field fluorescence microscope are shown. As can be seen, the PSF sizes are quite different for the numerical apertures[4] of 1.3 and 0.3. Imaging with a microscope is as if painting the object points with a brush of the size of the PSF. A useful resolution measure is thus this size taken at the full width of the PSF measured at half its maximum (FWHM) (Fig. 22.1). Thinking about the situation of three-dimensional (3D) samples to "paint," one will have to envision the whole "painting" operation as a 3D process with the appropriate 3D PSF which would then yield an entire 3D focus series.

In the in-focus PSF at low NA, the intensity reaches zero value at a well-defined closest distance (see arrow in Fig. 22.1). The circle of the PSF inside the first zero position is called the Airy disc and its radius is called the Rayleigh distance.

The *Rayleigh resolution limit* uses the example of two point-like objects and defines the resolution as the distance, where the maximum in the image of each of these objects occurs at the position (Fig. 22.1) where the image of the other object has its first intensity minimum.[5]

The *Sparrow limit* is the distance between such point objects of equal intensity at which a dip half way between them ceases to be visible in the superposition of their images (the first two derivatives of the intensity curve along the connecting line become zero).

All these limits can be to some degree changed by optical engineering approaches that vary the amount to which some light rays contribute to the image (sometimes referred to as apodization). Such modification usually introduces higher side-lobes (a side-lobe can be seen just right of where the arrow labeled "zero intensity" points to in Fig. 22.1), which are unwanted. Due to their nonabsolute nature, these limits could be called "soft," whereas the Abbe limit as discussed in the other boxed section (Box 22.1) is a "hard" limit in the sense that apodization approaches do not alter it. The Abbe limit makes an exact statement about which information about the sample is transmitted by the microscope.

resolution of about 20 nm (Betzig et al., 2006). Currently, a problem is the rather long imaging time well above an hour for a single 2D image, but further development should obviate this. An alternative is to exploit the transient binding of fluorophores, yielding rare bursts of signal which can be localized (Heintzmann & Sheppard, 2007).

[3] A very common optical aberration which violates the linear shift invariance is field-dependent astigmatism.

[4] $\mathrm{NA} = n \sin(\alpha)$, with the refractive index of the embedding medium n and the half-opening angle of the objective being α.

[5] For high NA (Fig. 22.1), the intensity does not reach zero at this minimum and the minimum position is not accurately predicted by the commonly used paraxial approximation: $d = 0.61\lambda/\mathrm{NA}$.

Box 22.2 THE ABBE LIMIT: THEORY OF THE SAMPLE AS A SUM OF WAVES

The Abbe limit corresponds to the distance of the finest periodical structure, which can be imaged by an optical microscope.

To understand the importance of the Abbe limit, it is useful to first think of a sample being a periodical structure. The simplest case could be a series of lines (in 2D) or even planes of alternating brightness (in 3D) describing the distribution of fluorophores. Such a restriction to a specific sample structure may seem to be far fetched at first, but it can be shown (when we also allow negative adundances), that an arbitrary sample structure (e.g., an image with cells) can always be described in this picture as a simple additive superposition of such periodical structures (waves). This would normally imply an infinite amount of waves, each with an individual orientation, wavelength, and phase shift. Mathematics shows that in a somewhat magical way these waves can cancel each other in the dark sample areas and in total sum up such that the exact brightness structure of the sample can be represented in this way. In two dimensions, each of these waves would be like a sinusoidal line grating, a series of positive and negative line-like features. If we can understand how images are formed of these wave structures, we can still represent the final image as the sum on these individual images of wave structures.

Why is such a periodic wave structure sample especially useful for discussing the resolution of optical systems? All classical far field optical systems have a well-defined fixed lower limit to the distance between these periodical structures in the sample to be at all present in its image. In the case of methods based on imaging scattered, diffracted, or refracted light from the sample, such as transmission, phase contrast, DIC, dark field, and others, this fixed limit can be easily understood: the light leaving the sample needs to be captured by the objective lens of the microscopy system to contribute to the image by interference[6] (Fig. 22.2A). Due to the laws of diffraction, a finer periodic (grating-like) structure will lead to the light leaving the object at a higher angle hitting the objective closer to its finite aperture limit and diffraction from a very fine periodic structure will miss the objective lens (Fig. 22.2B, see discussion in Chapter 14 by Wolf et al., this volume). Thus, the aperture of the objective defines this resolution limit. When altering the incident direction of the light away from normal incidence to the plane of focus, the diffracted light will also emerge at a different angle. In this way, under oblique illumination, light which would miss the objective lens at normal incidence can then be directed into the acceptance angle of the objective. However, also in this case a limit is placed by the available angular range (thus the $NA_{illumination}$) of the condenser optics. Finally, even if one could illuminate an object under all possible angles and detect the light leaving the sample under all possible angles, there would still be a very finite resolution to the image. As the diffracted angles relate to the period of the grating in relation to the wavelength of light in the medium, the finest possible grating that could be observed in this way is spaced at half this wavelength. As the wavelength in a medium is smaller (by the refractive index of this medium) than in vacuum or air, the best resolution is achieved by embedding the sample and the front side of the objective lens in a medium of high refractive index. This is usually done with oil immersion (with $n = 1.518$). The combination of the refractive index of the medium and the angle of detection (aperture half angle α) is conveniently summarized in the definition of the numerical aperture [$NA = n \sin(\alpha)$]. This NA, together with the illumination angles and the wavelength thus define the Abbe resolution limit:

[6]The surprising bit about interference is that depending on the mutual phase of the light, bright light (e.g., from the left part of the lens) plus bright light (e.g., from the right part of the lens) can yield darkness at a specific position in the image.

$$d_{\text{min}} = \frac{\lambda}{\text{NA}_{\text{illumination}} + \text{NA}_{\text{detection}}}. \tag{22.1}$$

In *fluorescence*, the situation is slightly different, as the light from different fluorescent molecules has to be incoherently[7] added as intensity instead of being added as coherent amplitude (intensity and phase), since their emitted light has a random mutual phase relationship. The image of each such molecule will nevertheless be formed by the rays leaving this molecule and by their coherent interference for each wavelength in the image plane (Fig. 22.2C). There is a spatial frequency limit to such an image of a point as defined by the limiting angles and thereby also here similar restrictions to the resolution do apply. For the detection of a wide-field fluorescence microscopy, the corresponding Abbe limit becomes:

$$d_{\text{min}} = \frac{\lambda}{2\text{NA}_{\text{detection}}}. \tag{22.2}$$

This factor of 2 in Eq. (22.2), when compared with $\text{NA}_{\text{detection}}$ in Eq. (22.1), stems from the fact that in a incoherent fluorescence PSF the finest detail stems from mutual interference of the highest angled rays (e.g., left with right side), whereas in transmission the finest scattering structure would be defined by the difference of the incident illuminating ray (in the middle of the aperture) and the highest angled rays that are captured (e.g., at the side of the aperture).

The rays striking the objective lens at the highest angle (being closest to the edge of the aperture in the back focal plane) define the finest possible fluorescent periodic structure which can be resolved. Even finer structures would only be imaged as a homogeneous level of brightness with no modulation whatsoever.

One may now wonder, whether changing the fluorescence illumination method could help to further enhance the resolution. This turns out to be a good approach. However, just illuminating at an oblique angle in fluorescence microscopy will not change anything since the emitted light of a molecule cannot interfere with the illumination or the light emitted from any other molecule. It is necessary to generate local intensity differences in the sample in order to gain resolution. In the main text, a few of these systems with a nonuniform illumination will be discussed.

In analogy to the above discussion on the Abbe limit, a similar limit exists to describe the finest possible intensity feature in the illumination light field that can be generated, when illuminating through the objective lens. Usually the fluorescent sample reacts linearly to the incident light intensity, which means its emitted light is proportional to the incident light at this specific sample position. This multiplication leads to the fact that the two Abbe limits (for illumination and detection) can simply be added yielding a new *combined Abbe limit*. Although some authors using these effects have called the new resolution limit "beyond" the Abbe limit, we like to call this combined illumination and detection limit still within the Abbe limit, in the sense that the microscopy system adheres to a limit obtained by the addition of the illumination and the detection Abbe limit.

[7]Incoherent light means light which cannot generate interference, whereas coherent light can interfere.

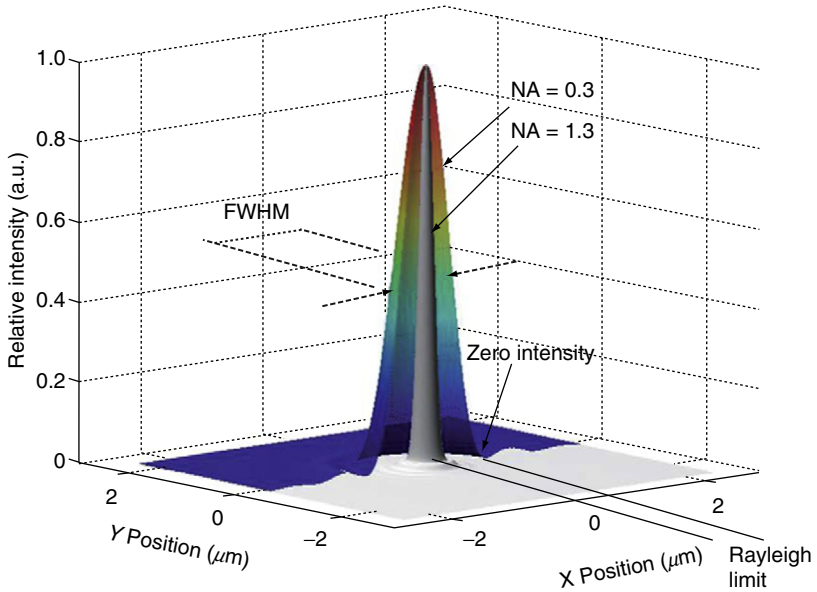

FIGURE 22.1

The point spread function (PSF). Two PSFs are shown, one for high numerical aperture (NA = 1.3 in gray) and one for NA = 0.3 (slightly transparent shades). As can be seen, the low-NA PSF is wide and has well-defined positions of zero intensity, leading to the definition of the Rayleigh limit. For this, PSF also the definition of full width measured at half the maximum (FWHM) is shown. The high-NA PSF (uniformly gray peak in the middle) is much finer but does not have the rings of zero intensity.

22.2 METHODS WITHIN THE COMBINED ILLUMINATION AND DETECTION ABBE LIMIT

A number of modern microscopy techniques such as confocal, 4Pi, and structured illumination microscopy achieve their high resolution (see Box 22.2 "The Abbe limit") by a spatially nonuniform illumination (Table 22.1). Nonuniform illumination implies that adjacent positions in the sample can receive different illumination intensities. Below we will detail on how the resolution enhancement is achieved for these methods.

In confocal microscopy, the sample is illuminated with a focused beam, which is then raster scanned over it. The emitted fluorescent light is imaged onto a pinhole, whose diameter can be adjusted. Due to the combined effects of illumination and detection, this procedure does indeed enhance the resolution beyond that of a standard wide-field fluorescence microscope. If the pinhole is very small, the light distribution used for illumination is very similar to the spatial sensitivity map of light detection from the sample. For light particles (photons) to reach the detector, a

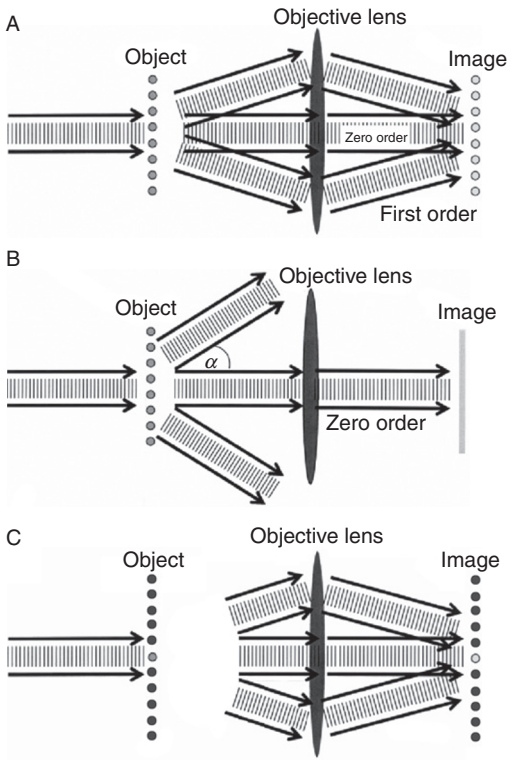

FIGURE 22.2

The Abbe limit. (A) Diffraction of a parallel light beam from a periodic grating structure (only the zero and first diffraction orders are shown). (B) Diffracted light from a fine periodical structure already fails to fall within the angular acceptance range of the objective lens. The image can thus only be formed from the undiffracted zero order yielding a flat image of equal intensity. (C) For fluorescence the emitters have to be considered independently and intensity will be added. Nevertheless, the finest resolution (constituent of the PSF) is still defined by the biggest angle of emitted light rays that were captured and refocused.

particular sample point needs to be illuminated (e.g., 1/10 probability) and light emitted from this point needs to be detected (e.g., 1/10 detection probability). This chance of illumination and detection (in the above example $1/10 \times 1/10 = 1/100$) in combination with a linear response of the sample leads to the resulting PSF of the overall system to be the product of the illumination and detection PSFs. Discussed in terms of periodic distributions inside the sample, this confocal system is now, in principle, able to pick up a twofold finer periodicity.

However, in practice this is almost never achieved as the fine details (high spatial frequency[8]) are suppressed so much that they get lost in the noise. To make matters worse, a closed pinhole would not detect any light, which leads to pinhole diameters

[8]The spatial frequency is the number of cycles per meter of a periodic pattern.

in the range of the diameter of an Airy disc (where the first theoretical minimum occurs in the image of a point) to be used in biological experiments. In this case, even features slightly finer than the standard uniform widefield-illumination Abbe limit cannot be resolved as they get lost in the noise. This reduces the in-plane performance of a confocal microscope back to that of a uniform illumination system; however, the increased sectioning ability of confocal microscopes is important and led to their success.

By altering the intensity and phase of the light which gets sent into or detected from the sample under different angles, a technique often referred to as "apodization" or pupil plane filtering, the high spatial frequencies can be emphasized, getting the practical performance a bit closer to the theoretical limit of twice the widefield resolution with uniform illumination (Akduman et al., 1998; Cichocki, Martinez-Corral, Kowalczyk, & Andres, 1998). Nevertheless, to our knowledge, no such system has ever been successful enough to make it into the market.

The I^5M and the 4Pi type C microscope take both the illumination aperture and the detection aperture to their extreme (Bewersdorf, Schmidt, & Hell, 2006; Gustafsson, Agard, & Sedat, 1999). As the name 4Pi suggests (a full sphere has a solid angle of 4π), the idea is to get as close as possible to illumination (and detection) from all sides of the sample. For practical reasons, the best approximation is achieved by combining two objective lenses opposed to another along the z (optical axis)-direction to act as a single lens. To do so, the two optical paths from laser and detector to the sample (through the top and through the bottom objectives) need to be identical in length both for the illumination and detection wavelengths (4Pi type C microscope). From the discussion above, it can be seen that the maximal possible numerical aperture (becoming identical to the refractive index) is obtained along the optical axis (z) connecting the two opposing objectives, whereas little changes along the x- and y-directions. Thus, for illumination the resolution limit is $\lambda_{ex}/(2n)$ and for detection it is $\lambda_{em}/(2n)$, with λ being the respective wavelengths of excitation and emission. This means the finest periodical fluorescent structure which can be detected in a 4Pi (type C with visible excitation) microscope is about $\lambda/(4n)$, which amount to $\sim$100 nm along the optical axis for glycerol embedding and a wavelength around 500 nm. However, considering the in-plane directions (x and y), this realization of the 4Pi concept has not increased the numerical aperture (and thus the resolution) as compared to a standard confocal microscope. Noticeably the lateral resolution, albeit in theory improved by a factor of $\sim$2, suffers also from the same problem as standard confocal microscopes, with practically no xy-resolution improvement in comparison to a uniform illumination microscope detectable for reasonable pinhole sizes. Nevertheless, the enormous improvement along the axial direction is worthwhile (Fig. 22.3B). Features in only slightly different planes would normally blur together in one image plane, but are now separated nicely in a 4Pi microscope. This leads also to a much cleaner appearance of individual slices of a 4Pi dataset. Similar arguments apply to the I^5M method, where incoherent illumination is used (Gustafsson et al., 1999).

The methods of structured illumination (Chung, Kim, & So, 2006; Gustafsson, 2000; Heintzmann & Cremer, 1999) exploit the fact that the excitation and emission Abbe limit can be added. The highest possible spatial frequency is intentionally

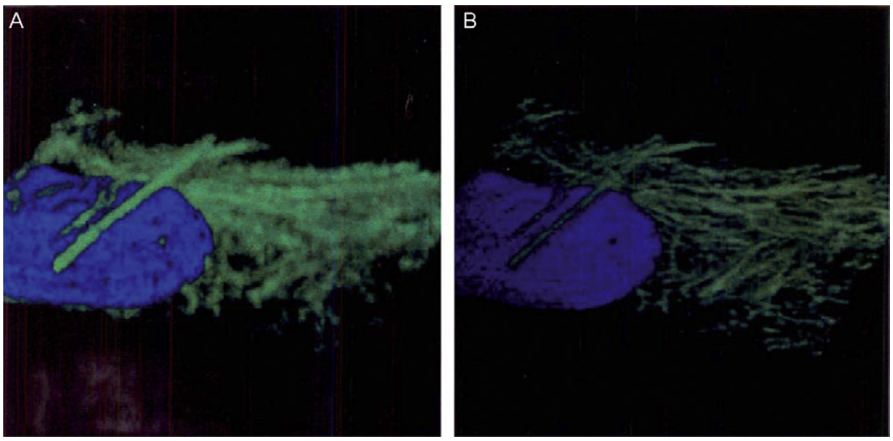

FIGURE 22.3

Confocal and 4Pi images. Comparison of volume-rendered images of the actin cytoskeleton and the nucleus of muscle support tissue endothelial cells. The nucleus was stained with DAPI and the actin cytoskeleton with Alexa488-phalloidin. (A) Two-photon confocal view of the sample and (B) two-photon 4Pi (type A) view (after three-point deconvolution) of the sample. The improved resolution and better discrimination of biological structures is visible. This dataset corresponds to a width of 23.4 μm, a height of 2.9 μm, and a depth of 30.0 μm.

introduced during excitation via a fine sinusoidal illumination pattern in the sample volume. This is achieved by projecting a fine grating[9] into the sample under coherent illumination conditions, which allows the contrast of the excitation structure to be maximal. A high-resolution image can be reconstructed (Fig. 22.4) from a series of images under different positions (and orientations) of the excitation pattern. In comparison to confocal microscopy, structured illumination captures high spatial frequencies of the sample much more efficiently and thus allows for a true factor of two resolution improvement (Gustafsson, 2000), albeit at the expense of requiring extensive computational reconstruction.

22.3 METHODS CIRCUMVENTING THE ABBE LIMIT

The most advanced high-resolution microscopy methods use some form of nonlinearity to avoid the restrictions of the Abbe limit. Below, the importance of the nonlinearity is motivated and exemplified with two-photon microscopy, nonlinear structured illumination, and stimulated emission depletion (STED) microscopy.

As mentioned in the boxed section "The Abbe Limit," the linear[10] response of the sample led us to define the combined illumination and detection Abbe limit as a

[9] Or by directly interfering laser beams.

[10] "Linear" means that the fluorescence is simply proportional to the amount of illumination intensity. A double input light intensity means double fluorescence emission intensity generated. The straight multiplication of input intensity with fluorophore concentration (brightness of the sample) leads to the addition of the illumination and the detection Abbe limit.

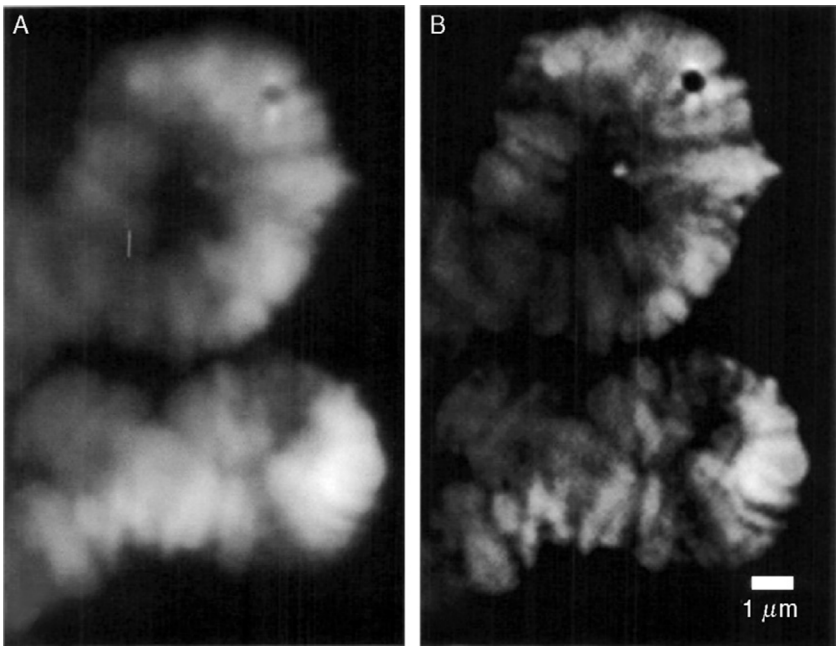

FIGURE 22.4

Linear structured illumination of *Drosophila* polytene chromosomes stained with Sytox Green. (A) Wide-field image obtained by summing all the individual images under structured illumination. (B) Reconstruction of the sample from the structured illumination data (five phases, two angles).

fundamental limit in far field microscopy. This limit, however, does not apply if this linear relationship can be violated. Abbe's theory has to be modified if the emitted light can only be described by a *nonlinear*[11] dependence of emission on the local excitation intensity. As it turns out, the highest exponent present in a polynomial expansion of the nonlinear dependence between excitation and emission defines the resolution limit (Hell, 2004). Every exponent in such an expansion of the nonlinear dependence of emission on local excitation can be thought of a number of additional multiplications, each adding another excitation Abbe limit to the dependence.

The simplest nonlinear dependence is encountered in two-photon microscopy. Due to the probabilistic nature of the two-photon absorption process (both photons need to interact with the fluorophore at the same time), the chance for a fluorescent molecule to be in the excited state is proportional to the square of the incident intensity at a specific position in the sample. Thus, also the emitted light intensity is proportional to this square of the excitation intensity. As a result, two-photon

[11]"Nonlinear" means that the generated fluorescence is not any longer proportional to the illumination intensity.

microscopy indeed circumvents the Abbe limit by a factor of two in the excitation pathway. However, this improvement is bought at the expense of a roughly twofold longer excitation wavelength leading to essentially no additional gain, when compared with a standard single-photon excitation in a confocal microscope. However, the significant advantage of two-photon microscopy is the reduced absorption and scattering, allowing to image deeper into tissue and the inherent confocality due to the squaring of the excitation intensity obviating the need for a pinhole on the emission path. Another advantage of the square dependence is the reduction of sidelobe height, which is particularly useful in 4Pi microscopy.

However, other processes can achieve this nonlinear dependency with the help of visible light and are also not limited to a maximal exponent of two in the polynomial expansion. The simplest case is saturation of the excited state of fluorophores by intense illumination (Hell, 2004). Practically, this can be realized as a microscopy method by combining the nonlinearity with the concept of structured illumination (Gustafsson, 2005; Hell, 2004) or by detecting high harmonics in the time domain under temporally sinusoidally modulated illumination intensity in a confocal system (Fujita, Kobayashi, Nakamura, & Kawata, 2006). Also, the spatial nonuniformity of a depletion, bleaching, or light-induced inactivation process (dynamic saturation optical microscopy, Enderlein, 2005) can be used, which is again a nonlinear saturation effect. All of these methods are still in a developmental stage and some of them (nonlinear structured illumination, dynamic saturation optical microscopy) require a substantial amount of image processing, since the high-resolution information contained in the measured data has to be computationally extracted.

The most successful method so far is STED microscopy (Hell & Wichmann, 1994; Kubitscheck et al., 2005; Willig, Keller, Bossi, & Hell, 2006; Willig et al., 2006; Willig, Rizzoli, Westphal, Jahn, & Hell, 2006; Fig. 22.5). The method itself is slightly more complex, but has the advantage of obtaining a directly scanned image without the need of image processing. The idea is to deactivate fluorophores surrounding the center of the scanning spot by stimulated emission[12] caused by a second beam (the doughnut-shaped STED-beam) with a wavelength being within the emission spectrum of the fluorophore. If this was only done with a relatively dim STED-beam, this method would add another linear term, leading only to a moderate resolution improvement. However, driving this STED-beam into saturation establishes the required nonlinearity of high order. The center of this STED-beam is expected to have zero intensity, leaving the fluorophores unchanged in their excitation state. If a little bit of STED-beam is present at a location only slightly away from its center (zero intensity) position, its interaction with the fluorophore is long enough to push the latter into the ground state. This will force emission of light at the wavelength of the STED-beam, which can be specifically blocked by appropriate filters allowing most of the spontaneous fluorescence emission to pass. Also a temporal discrimination is possible. It has been demonstrated that STED can be applied to imaging of

[12]Stimulated emission is the physical effect that a fluorophore is more likely to emit a photon higher than the rate of photons with identical properties passing by.

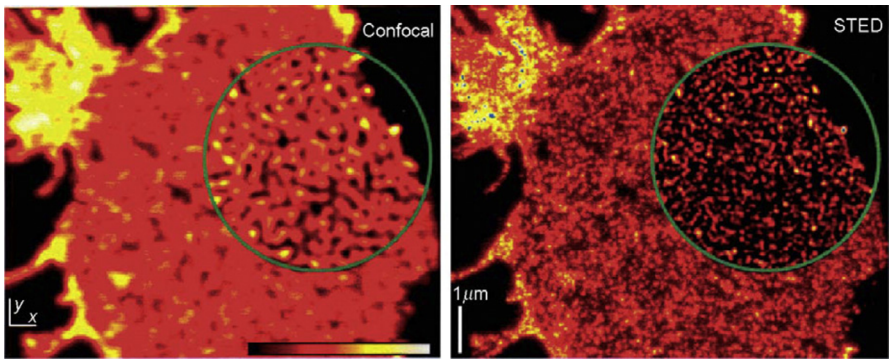

FIGURE 22.5

Stimulated emission depletion image. Revealing the nanopattern of the SNARE protein SNAP-25 on the plasma membrane of a mammalian cell. Confocal (A) versus STED image (B) of the antibody-tagged proteins. The encircled areas show linearly deconvolved data. STED microscopy provides a substantial leap forward in the imaging of protein self-assembly; here it reveals for the first time that SNAP-25 is ordered in clusters of <60-nm average size. Reproduced with permission of the Institute of Physics from reference Willig et al. (2006a).

endogenous markers such as GFP (Willig et al., 2006). By allowing the triplet states to relax between successive excitations, the fluorescence yield in STED microscopy could be dramatically improved (Donnert et al., 2006).

A practical rule of thumb can be established as alteration to Abbe's equation (Hildenbrand et al., 2005), with the aim to estimate a resolution criterion considering the limited signal-to-noise ratio available. However, such a rule of thumb should not be taken to be a new Abbe limit, as the Abbe limit sets a fixed limit to linear resolution methods, whereas the suggestion in Hildenbrand et al., 2005 is an approximation to the width of the directly obtained PSF, which may or may not be a good indicator of the smallest periodical structure that can be discriminated for a given noise level in the system. In principle, all of the saturation-based nonlinear methods have infinite resolution, but the high-resolution information becomes obscured by the noise.

22.4 A COMMENT ON NEAR FIELD METHODS AND PENDRY'S LENS

Obviously, the distribution of emitting fluorophores in the sample can have any structure and is not constrained by the Abbe limit. The sample is just as it is with no limit to its periodical constituents but the light intensity is known to fall off by an inverse square law with distance to each emitting molecule. Such a light distribution within the sample would also not be limited by the Abbe limit. The discrepancy to the light detection discussed so far arises from the fact that in the theory above we only considered light waves that are able to propagate (so-called far field waves). However,

Maxwell's equations in a homogeneous medium allow also for a different kind of oscillating electromagnetic fields called evanescent (or near field) waves. These solutions of the Maxwell's equations in a homogeneous medium decay exponentially in a direction of space. Even worse, the finer the (diffracting) sample structure causing these evanescent waves is, the quicker their decay over distance. In the optical regime, these evanescent waves become usually undetectable after about 1 μm.

Scanning near field optical microscopy (SNOM) methods place a probe (a tip, a scatterer of particles that can fluoresce or resonantly be excited) close enough to the sample structure to measure these evanescent fields (Wabuyele, Culha, Griffin, Viallet, & Vo-Dinh, 2005). From the above, it becomes clear that near field methods are constrained to imaging surfaces. An additional problem is that at these small distances to the sample the interaction of the tip with the electromagnetic field can change the local field and the interpretation of the images may become difficult. As with the nonlinear methods described, the Abbe limit does not apply to the near field. Practically, SNOM achieves a resolution down to about 30 nm in a watery environment. An interesting perspective is the measurement of tip-enhanced Raman scattering (Kellermayer, 2005).

Another particular example of a near field effect is evanescent wave microscopy (Axelrod, 2003). Here an exponentially decaying intensity distribution can be generated close to a surface by illumination above the critical angle of total internal reflection (TIRF) of a planar interface between an optically dense medium (e.g., glass, $n = 1.518$) and a less dense medium (e.g., water, $n = 1.33$). In contrast to SNOM, this evanescent wave just extends along z and the resolution improvement gained is also just oriented along z. However, the main advantage of TIRF is a relatively sharp discrimination between (usually membrane and vesicular) sample structures close to the optical interface (depending on the illumination angle closer than about 200 nm) and structures further away from this interface. For cells which are adherently grown to this interface, this method is interesting as vesicles in the interior of the living cell can be suppressed and only structures tethered to or fused with the plasma membrane are present in the image.

The idea of the "perfect lens" has arisen (Qu, Wu, Mets, & Scherer, 2004), which is also based on using nonpropagating waves. Pendry realized that a medium of negative refractive index (e.g., a thin slab of silver) would lead to exponentially growing waves within this medium. This effect can in theory make up for the exponentially decreasing evanescent waves outside the medium such that they theoretically have similar levels at the focus as in the sample space. This effect has been demonstrated experimentally for light at small distances (Fang, Lee, Sun, & Zhang, 2005) but it still remains to be shown how much the nonideal media used for such lenses can reamplify the "lost" evanescent waves and to which maximal distance such an ideal lens could work.

22.5 KEY POINTS

Recently, many microscopy methods have dramatically enhanced the resolution. Gradually, these methods are now applied to solve biological problems. The most promising approaches are all based on fluorescence and use either nonlinear

interaction of light with the sample (STED, nonlinear structured illumination, dynamic saturation optical microscopy, or saturation in the time domain) or precise localization of individual particles or molecules with subsequent image generation.

Acknowledgment

This chapter is reprinted with modification from Heintzmann & Ficz, 2006.

We would like to thank Klaus Suhling, Matthias Krause, Peter Fraser, and Vassilios Sarafis for useful comments on the chapter. Furthermore, we thank Ondrej Mandula, Liisa Hirvonen, and Yannick Colpin for their contribution to the structured illumination setup and the image reconstruction (Fig. 22.4). Darren Williams and Guy Tear are thanked for preparing the polytene squash sample.

References

Akduman, I., Brand, U., Grochmalicki, J., Hester, G., Pike, R., & Bertero, M. (1998). Superresolving masks for incoherent high-numerical-aperture scanning microscopy in three dimensions. *Journal of the Optical Society of America. A*, *15*, 2275–2287.

Axelrod, D. (2003). Total internal reflection fluorescence microscopy in cell biology. *Methods in Enzymology*, *361*, 1–33.

Baumeister, W. (2005). From proteomic inventory to architecture. *FEBS Letters*, *579*, 933–937.

Betzig, E., Patternson, G. H., Sougrat, R., Lindwasser, O. W., Olenych, S., Bonifacino, J. S., et al. (2006). Imaging intracellular fluorescent proteins at near-molecular resolution. *Science*, *313*, 1642–1645.

Bewersdorf, J., Schmidt, R., & Hell, S. W. (2006). Comparison of I^5M and 4Pi-microscopy. *Journal of Microscopy*, *222*, 105–117.

Bystricky, K., Heun, P., Gehlen, L., Langowski, J., & Gasser, S. M. (2004). Long-range compaction and flexibility of interphase chromatin in budding yeast analyzed by high-resolution imaging techniques. *Proceedings of the National Academy of Sciences of the United States of America*, *101*, 16495–16500.

Chung, E., Kim, D., & So, P. T. C. (2006). Extended resolution wide-field optical imaging: Objective-launched standing-wave total internal reflection fluorescence microscopy. *Optics Letters*, *31*, 945–947.

Cichocki, T., Martinez-Corral, M., Kowalczyk, M., & Andres, P. (1998). Annular binary filters for controlling the axial behaviour of optical systems. *Journal of Modern Optics*, *45*, 227–237.

Danuser, G., & Waterman-Storer, C. M. (2006). Quantitative fluorescent speckle microscopy of cytoskeleton dynamics. *Annual Review of Biophysics and Biomolecular Structure*, *35*, 361–387.

Donnert, G., Keller, J., Medda, R., Andrei, M. A., Rizzoli, S. O., Luhrmann, R., et al. (2006). Macromolecular-scale resolution in biological fluorescence microscopy. *Proceedings of the National Academy of Sciences of the United States of America*, *103*, 11440–11445.

Enderlein, J. (2005). Breaking the diffraction limit with dynamic saturation optical microscopy. *Applied Physics Letters*, *87*, Art. No. 097105.

Fang, N., Lee, H., Sun, C., & Zhang, X. (2005). Sub-diffraction-limited optical imaging with a silver superlens. *Science*, *308*, 534–537.

Fujita, K., Kobayashi, M., Nakamura, O., & Kawata S. (2006). *Fluorescence microscope and observation method Patent* WO/2006/061947.

Garini, Y., Vermolen, B. J., & Young, I. T. (2005). From micro to nano: Recent advances in high-resolution microscopy. *Current Opinion in Biotechnology*, *16*, 3–12.

Gordon, M. P., Ha, T., & Selvin, P. R. (2004). Single-molecule high-resolution imaging with photobleaching. *Proceedings of the National Academy of Sciences of the United States of America*, *101*, 6462–6465.

Gustafsson, M. G. L. (2000). Surpassing the lateral resolution limit by a factor of two using structured illumination microscopy. *Journal of Microscopy*, *198*, 82–87.

Gustafsson, M. G. L. (2005). Nonlinear structured-illumination microscopy: Wide-field fluorescence imaging with theoretically unlimited resolution. *Proceedings of the National Academy of Sciences of the United States of America*, *102*, 13081–13086.

Gustafsson, M. G. L., Agard, D. A., & Sedat, J. W. (1999). I^5M:3D widefield light microscopy with better than 100 nm axial resolution. *Journal of Microscopy*, *195*, 10–16.

Heilemann, M., Herten, D. P., Heintzmann, R., Cremer, C., Müller, C., Tinnefeld, P., et al. (2002). High-resolution colocalization of single dye molecules by fluorescence lifetime imaging microscopy. *Analytical Chemistry*, *74*, 3511–3517.

Heintzmann, R. (2006). Band-limit and appropriate sampling in microscopy. In J. E. Celis (Ed.), *Cell biology: A laboratory handbook*, Vol. 3, (pp. 29–36). London: Elsevier Academic Press Chapter 3.

Heintzmann, R., & Cremer, C. (1999). Lateral modulated excitation microscopy: Improvement of resolution by using a diffraction grating. *Proceedings of SPIE*, *3568*, 185–196.

Heintzmann, R., & Ficz, G. (2006). Breaking the resolution limit in light microscopy. *Briefings in Functional Genomics & Proteomics*, *5*(4), 289–301.

Heintzmann, R., & Sheppard, C. J. R. (2007). The sampling limit in fluorescence microscopy. *Micron*, *38*, 145–149.

Hell, S. W. (2004). Strategy for far-field optical imaging and writing without diffraction limit. *Physics Letters A*, *326*, 140–145.

Hell, S. W., & Wichmann, J. (1994). Breaking the diffraction resolution limit by stimulated emission: Stimulated-emission-depletion fluorescence microscopy. *Optics Letters*, *19*, 780–782.

Hildenbrand, G., Rapp, A., Spori, U., Wagner, C., Cremer, C., & Hausmann, M. (2005). Nanosizing of specific gene domains in intact human cell nuclei by spatially modulated illumination light microscopy. *Biophysical Journal*, *88*, 4312–4318.

Inoue, S., & Oldenbourg, R. (1998). Microtubule dynamics in mitotic spindle displayed by polarized light microscopy. *Molecular Biology of the Cell*, *9*, 1603–1607.

Kawata, S., Inouye, Y., & Ichimura, T. (2004). Near-field optics and spectroscopy for molecular nano-imaging. *Science Progress*, *87*, 25–49.

Kellermayer, M. S. (2005). Visualizing and manipulating individual protein molecules. *Physiological Measurement*, *26*, R119–R153.

Kittel, R. J., Wichmann, C., Rasse, T. M., Fouquet, W., Schmidt, M., Schmid, A., et al. (2006). Bruchpilot promotes active zone assembly, Ca^{2+} channel clustering, and vesicle release. *Science*, *312*, 1051–1054.

Kubitscheck, U., Grunwald, D., Hoekstra, A., Rohleder, D., Kues, T., Siebrasse, J. P., et al. (2005). Nuclear transport of single molecules: Dwell times at the nuclear pore complex. *The Journal of Cell Biology*, *168*, 233–243.

Lacoste, T. D., Michalet, X., Pinaud, F., Chemla, D. S., Alivisatos, A. P., & Weiss, S. (2000). Ultrahigh-resolution multicolor colocalization of single fluorescent probes. *Proceedings of the National Academy of Sciences of the United States of America*, *97*, 9461–9466.

Lidke, K. A., Rieger, B., Jovin, T. M., & Heintzmann, R. (2005). Superresolution by localization of quantum dots using blinking statistics. *Optics Express*, *13*, 7052–7062.

Lippincott-Schwartz, J., & Patterson, G. H. (2003). Development and use of fluorescent protein markers in living cells. *Science*, *300*, 87–91.

Mahy, N. L., Perry, P. E., Gilchrist, S., Baldock, R. A., & Bickmore, W. A. (2002). Spatial organization of active and inactive genes and noncoding DNA within chromosome territories. *The Journal of Cell Biology*, *157*, 579–589.

Ober, R. J., Ram, S., & Ward, S. E. (2004). Localization accuracy in single-molecule microscopy. *Biophysical Journal*, *86*, 1185–1200.

Pawley, J. B. (2006). *Handbook of biological confocal microscopy* (3rd ed., pp. 265–279). USA: Springer.

Qu, X., Wu, D., Mets, L., & Scherer, N. F. (2004). Nanometer-localized multiple single-molecule fluorescence microscopy. *Proceedings of the National Academy of Sciences of the United States of America*, *101*, 11298–11303.

Rust, J. M., Bates, M., & Zhuang, X. (2006). Sub-diffraction-limit imaging by stochastic optical reconstruction microscopy (STORM). *Nature Methods*, *3*, 793–796. doi:http://dx.doi.org/10.1038/nmeth 929.

Sharonov, A., & Hochstrasser, R. M. (2007). Wide-field subdiffraction by accumulated binding of diffusing probes. *Proceedings of the National Academy of Sciences of the United States of America*, *103*, 18911–18916.

Syed, S., Snyder, G. E., Franzini-Armstrong, C., Selvin, P. R., & Goldman, Y. E. (2006). Adaptability of myosin V studied by simultaneous detection of position and orientation. *The EMBO Journal*, *25*, 1795–1803.

van den Pol, A. N. (1989). Neuronal imaging with colloidal gold. *Journal of Microscopy*, *155*, 27–59.

Wabuyele, M. B., Culha, M., Griffin, G. D., Viallet, P. M., & Vo-Dinh, T. (2005). Near-field scanning optical microscopy for bioanalysis at nanometer resolution. *Methods in Molecular Biology*, *300*, 437–452.

Willig, K. I., Keller, J., Bossi, M., & Hell, S. W. (2006). STED microscopy resolves nanoparticle assemblies. *New Journal of Physics*, *8*, Art. No. 106.

Willig, K. I., Kellner, R., Medda, R., Hein, B., Jakobs, S., & Hell, S. W. (2006). Nanoscale resolution in GFP-based microscopy. *Nature Methods*, doi:http://dx.doi.org/10.1038/nmeth922.

Willig, K. I., Rizzoli, S. O., Westphal, V., Jahn, R., & Hell, S. W. (2006). STED microscopy reveals that synaptotagmin remains clustered after synaptic vesicle exocytosis. *Nature*, *440*, 935–939.

Yildiz, A., Forkey, J. N., McKinney, S. A., Ha, T., Goldman, Y. E., & Selvin, P. R. (2003). Myosin V walks hand-over-hand: Single fluorophore imaging with 1.5 nm localization. *Science*, *300*, 2061–2066.

Further Reading

Heintzmann, R., Jovin, T. M., & Cremer, C. (2002). Saturated patterned excitation microscopy (SPEM)—A novel concept for optical resolution improvement. *Journal of the Optical Society of America. A*, *19*, 1599–1609.

Pendry, J. B. (2000). Negative refraction makes a perfect lens. *Physical Review Letters*, *85*, 3966–3969.

CHAPTER

Circumventing Photodamage in Live-Cell Microscopy

23

Valentin Magidson* **and Alexey Khodjakov*,†**

*Wadsworth Center, NYS Department of Health, Albany, New York, USA

†Rensselaer Polytechnic Institute, Troy, New York, USA

CHAPTER OUTLINE

Introduction 545
23.1 Light Intensity and Exposure Time 548
23.2 Optimization of Excitation Spectrum 551
23.3 Hardware Synchronization 554
23.4 Avoiding Unnecessary Irradiation via Intelligent Illumination 556
Conclusions 558
References 559

Abstract

Fluorescence microscopy has become an essential tool in cell biology. This technique allows researchers to visualize the dynamics of tissue, cells, individual organelles, and macromolecular assemblies inside the cell. Unfortunately, fluorescence microscopy is not completely "noninvasive" as the high-intensity excitation light required for excitation of fluorophores is inherently toxic for live cells. Physiological changes induced by excessive illumination can lead to artifacts and abnormal responses. In this chapter, we review major factors that contribute to phototoxicity and discuss practical solutions for circumventing photodamage. These solutions include the proper choice of image acquisition parameters, optimization of filter sets, hardware synchronization, and the use of intelligent illumination to avoid unnecessary light exposure.

INTRODUCTION

Live-cell microscopy always involves a compromise between the desire to achieve the best possible image quality and the necessity to maintain cells live and happy on the microscope stage. One must always remember that fluorescence is an inherently

Methods in Cell Biology, Volume 114 **ISSN 0091-679X**
Copyright © 2013 Elsevier Inc. All rights reserved.
http://dx.doi.org/10.1016/B978-0-12-407761-4.00023-3

inefficient process—emission is orders of magnitude weaker than the intensity of excitation light. Photon flux required to generate a sufficiently strong signal from typical fluorophores (fluorescent proteins or chemical dyes) is damaging to the cells. Deleterious effects of light primarily arise due to generation of chemically reactive spices such as free radicals and specifically singlet and triplet forms of oxygen. As oxygen is required for respiratory-chain reactions, scavenging this molecule from the environment inevitably changes the cell's physiology. Thus, although oxygen scavengers, for example, oxyrase, have been successfully used in short-term live-cell recordings (Rodionov & Borisy, 1997; Zhai, Kronebusch, & Borisy, 1995), this approach is not applicable when the goal is to obtain data from physiologically normal and healthy cell populations. In this case, the only practical solution for minimizing deleterious effects of light is to avoid any unnecessary irradiation. In turn, this is achieved via optimization of the hardware and proper experimental strategies.

Gradual decrease in fluorescence intensity due to light-induced degradation of fluorophores (termed "photobleaching") is usually considered to be the main impediment in live-cell imaging (Fig. 23.1A). However, the fact is that light intensity sufficient to induce prominent photobleaching also inevitably changes homeostasis of the cell. Bleached cells are damaged! In fact, physiology of a typical mammalian cell is severely affected even under illumination conditions that cause only minimal changes in fluorescence intensity of the green fluorescent protein (GFP) or similar fluorophores (Fig. 23.1B). However, manifestation of physiological changes can be delayed (Fig. 23.1C), and photodamage often remains unnoticed in shorter term experiments.

Assessing the extent of photodamage inflicted by excessive illumination is difficult. Cells from various organisms exhibit dramatically different sensitivity to light. Embryos of *Drosophila melanogaster* and *Caenorhabditis elegans* are significantly more resilient to high-intensity illumination than mammalian cells. Wide variability in light tolerance is also common among different cell types originating from the same organism. For example, many types of transformed cells progress through the cell cycle under conditions that induce a permanent G2 block in untransformed cell lines of the same origin (Mikhailov, Patel, McCance, & Rieder, 2007). Further, even within the same population, individual-cell response to excessive illumination is often heterogeneous. We find that the great majority of untransformed human cells (RPE1) complete cell division in less than 30 min under low-light illumination. Higher doses of light tend to increase the duration of mitosis and sometimes arrest mitotic progression altogether. However, a significant number of cells (~25%) still manages to progress through mitosis *with normal timing* under illumination conditions that completely arrest mitosis in ~30% of cells within the same population (Schilling et al., 2012). Thus, in their response to intense light cells follow the "Anna Karenina" principle (Diamond, 1997) which originated from the opening sentence of the famous Leo Tolstoy's novel: "Happy families are all alike; every unhappy family is unhappy in its own way." In biological terms, the meaning of Anna Karenina's principle is that the suboptimal environmental conditions common when cells are maintained on the microscope stage (excessive illumination, errant temperature control, unusual tonicity, and/or pH of the culture media) often result in extreme variability in behavior of individual cells within a uniform population. This artificially

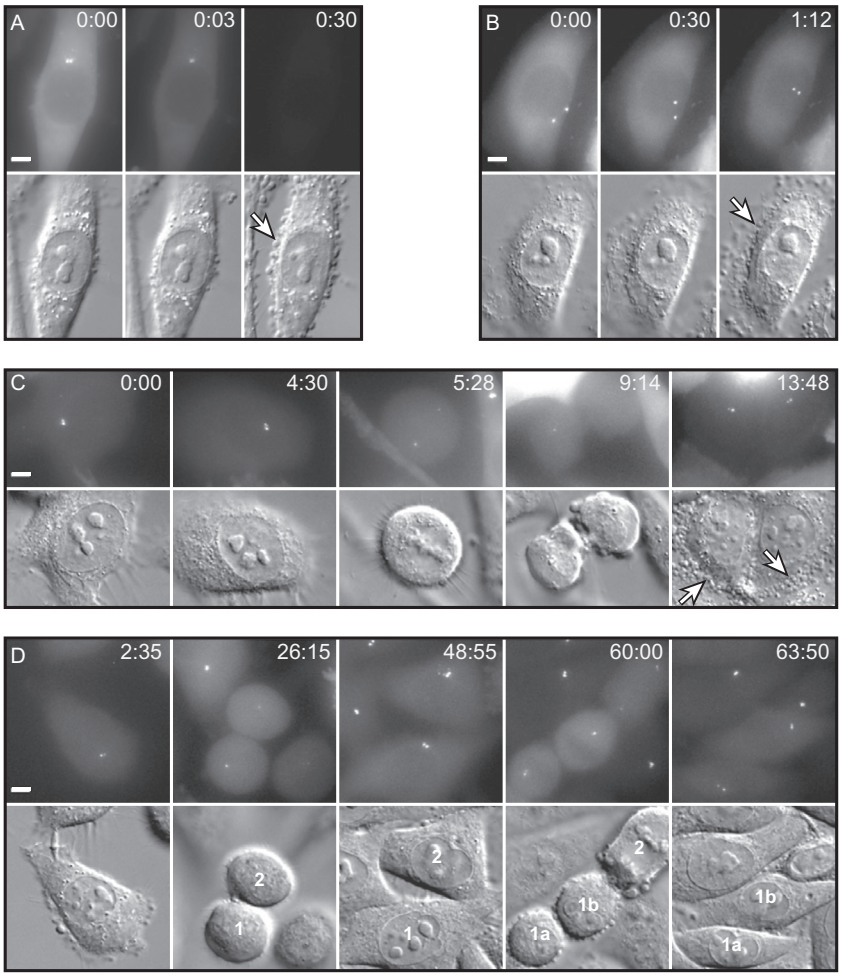

FIGURE 23.1

Photobleaching and photodamage effects in GFP microscopy. (A) 3D fluorescence time-lapse (30-s intervals) recorded on a standard research-grade imaging workstation. Fluorescence intensity gradually decreases (photobleaching) under these conditions. Concurrent with photobleaching, physiology of the cell changes as evident from the formation of membrane blebs (0:30, arrow). (B) Lower intensity of the excitation light circumvents photobleaching. However, photodamage remains severe as evident from the appearance of membrane blebs at later time points (1:12, arrow). (C) Increasing intervals between time points from 30 s to 2 min further delays manifestation of photodamage. In this sequence, the cell enters mitosis 5 h after initiation of the time-lapse. However, cell division is abnormally long (~3 h) and both daughter cells ultimately develop membrane blebs (13:48, arrow). (D) Further increase in time intervals (to 5 min) allows cells to remain healthy and undergo multiple cell cycles during 64-h recording (progeny of cell #2 is not shown due to space restrictions). HeLa cells constitutively expressing Centrin1-GFP to label centrioles. Fluorescence recorded in wide-field mode. Excitation light generated by a Xenon lamp (XBO-75) filtered with infra-red (KG-5) and ultraviolet (GG-420) absorption filters in addition to the GFP filters. Top rows in each panel present maximal intensity projections of the entire *Z*-stack. Bottom rows present individual DIC images selected from *Z*-stacks. Time shown as hours:minutes. Scale bars = 5 μm.

induced heterogeneity in the behavior of "unhappy" cells can distort the outcome of the experiment.

It is not uncommon for stressed cells to appear unaffected by light until they reach a certain transition point within the cell cycle. For example, most mammalian cells will initiate chromosome condensation and display other hallmarks of mitotic entry such as centrosome activation under intense illumination. However, many of these cells reverse progression through the cell cycle during mid-prophase and return to a G2-like state with completely decondensed chromatin and inactivated centrosomes. The percentage of cells that undergo cell cycle reversion is greater if the population is stressed by antimicrotubule drugs (Khodjakov & Rieder, 1999). Unfortunately, such a stage-specific effect on the cell cycle implies that photodamage would not be detected unless the experiment is sufficiently long to include the point at which the damaging effects are manifested.

Additional complications arise from the cumulative nature of stress. Exposure to one stressful factor often increases sensitivity of the cell to other insults, and unfortunately, this synergism often occurs in live-microscopy experiments. For example, physical removal of the centrosome from mammalian cells has been reported to result in a cell cycle arrest during G1 phase of the cell cycle (Hinchcliffe, Miller, Cham, Khodjakov, & Sluder, 2001; Khodjakov & Rieder, 2001). The conclusion was based on time-lapse recordings that demonstrated lack of cell cycle progression in acentrosomal cells while cells with centrosomes within the same field of view divided repeatedly. Therefore, the result was interpreted as a solid indication that centrosomes were required to support cell cycle progression (Hinchcliffe et al., 2001; Khodjakov & Rieder, 2001). However, subsequent investigations revealed that lowering the intensity of excitation light allows acentrosomal cells to progress through the entire cell cycle (Uetake et al., 2007). The reason for the G1 arrest observed in the original centrosome-removal studies was that cells already stressed by the removal of centrosome become more sensitive to intense light. Similarly, cells tend to become sensitized by treatments with various drugs, siRNA, or other environmental insults. This sensitization can be suppressed to an extent by inhibition of p38 kinase (Mikhailov, Shinohara, & Rieder, 2005; Uetake et al., 2007), a major component of the stress-response pathway. Germane here is that microscopy conditions that do not induce detectable deleterious effects in healthy cell populations can become damaging when applied to cells whose health is already compromised by other types of stress. A great care must be taken in every live-cell experiment to limit light exposure to the level absolutely necessary for obtaining images of the sufficient quality. Exceeding this level is dangerous as it clouds interpretation of the experimental outcome.

23.1 LIGHT INTENSITY AND EXPOSURE TIME

Achieving the full resolution of an optical system is only possible when the ratio of useful signal to noise in the image is sufficiently high. All other factors being equal, the same number of photons can be captured by the detector during a shorter exposure

time at higher intensity of excitation light versus less intense excitation and longer exposure. In fact, these alternative sets of acquisition parameters yield comparable image quality and similar level of photobleaching in conventional imaging of fixed cells. However, in live-cell imaging phototoxicity depends not only on the irradiation dose but also on how exactly this dose was delivered. The differences are due to both photochemistry and physiological responses of the cell.

In the elementary fluorescence cycle, absorption of a photon converts the low-energy "ground-state" fluorophore into an "excited" molecule. The lifetime of the excited state is short (nanoseconds) and return to the ground state is accompanied by the emission of a new, longer wavelength photon. This basic cycle is complicated by the existence of additional transitions such as decay of the excited molecule into a still energized but nonfluorescent "triplet" state. The lifetime of triplets is relatively long (microseconds) and these molecules can absorb additional photons before their energy dissipates (Fig. 23.2A). Additional absorption results in a further energy increase and facilitate chemical transformations that ultimately cause destruction of the fluorophore (Donnert, Eggeling, & Hell, 2007).

The existence of multiple excited states with various lifetimes and various predispositions to chemical breakdown implies that the rate of photobleaching depends on numerous factors and in particular on whether the excitation light is delivered continuously or in pulses. Extremely short pulses (shorter than the lifetime of excited fluorophores) separated by intervals that exceed the lifetime of the nonfluorescent but photobleaching-prone triplets have been shown to substantially reduce photobleaching in single-spot-scanning confocal microscopy (Donnert et al., 2007). However, implementation of this approach is difficult as relatively long pauses between the pulses are required for the dangerous triplet states to decay. These pauses would reduce the speed of a single-spot confocal imaging system by as much as 100-fold. Potential solutions to this problem include simultaneous scanning of the sample with multiple beams (Bingen, Reuss, Engelhardt, & Hell, 2011) as well as utilizing extremely fast scanners to direct each pulse to a nonirradiated spot. With the latter approach, extremely short dwell times ($\sim$50 ns) have been shown to noticeably decrease photobleaching and improve viability of brain cells imaged via multiphoton confocal microscopy (Chen et al., 2012). Thus, the use of relatively sparse but short high-intensity pulses is beneficial in certain types of microscopy.

However, the situation is reversed in wide-field and spinning-disk confocal microscopy that are most commonly used for long-term recordings of live cells. In these applications, decreasing the intensity of excitation light along with the appropriate increase in the exposure time reduces phototoxicity.

While specific studies on the physiology of cellular responses to dim versus bright light are scarce, the notion that illumination becomes a damaging factor only above a certain threshold level is intuitive. Most organisms are adapted to life under continuous illumination, and cells possess mechanisms that can repair a certain amount of damage inflicted by environmental factors such as radiation. As long as this protective capacity is not overwhelmed, illumination would not trigger an emergency stress response. In fact, cultured human cells continue to undergo normal

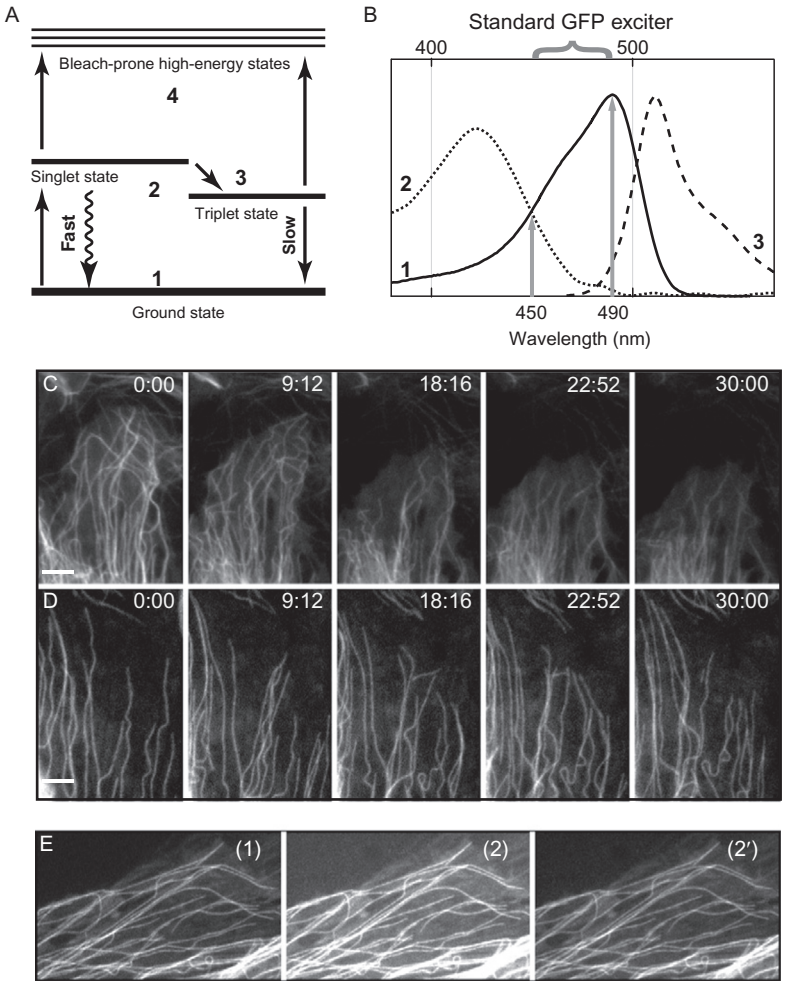

FIGURE 23.2

Dependence of photodamage on the spectrum of excitation. (A) Various states of fluorophore excitation. (1) Ground-state fluorophore, (2) singlet-state excited molecule, (3) nonfluorescent triplet state, and (4) higher energy chemically reactive states. (B) Spectral properties of GFP. (1) Absorption spectrum of ground-state GFP molecules. (2) Absorption spectrum of already excited GFP molecules. (3) Fluorescence emission spectrum. Curly bracket denotes spectral range of excitation filters used in standard GFP filter cubes. Notice that 490-nm wavelength is efficiently absorbed by ground state but not excited molecules. In contrast, 450-nm light is absorbed by both states. (C and D) Comparison of photobleaching and photodamage induced by wide versus narrow excitation filters. Photobleaching is prominent in (C), recorded with a standard GFP exciter (450–490-nm band-pass). Also notice that the cell retracts its leading edge in response to excessive illumination. In contrast, photobleaching as well as morphological changes are minimal in

cell cycles under continuous illumination at the intensities sufficient for phase-contrast and/or DIC recordings (our unpublished observation). Unfortunately, light flux used in a typical GFP time-lapse even with a sensitive CCD camera is greater than the intensity of direct sunshine (~0.2 vs. 0.13 W/cm^2, Schilling et al., 2012). "Sunburn" becomes unavoidable! Lower excitation intensities are not practical as they would require exceedingly long exposure times not compatible with the dynamic nature of live cells. Thus, real-life live-cell fluorescence recordings are conducted at the excitation intensity known to induce phototoxicity. This dictates special considerations in the layout of imaging systems specifically designed for life-cell experiments. Below, we outline main aspects of a microscopy workstation that need to be specifically optimized to minimize photodamage.

23.2 OPTIMIZATION OF EXCITATION SPECTRUM

One of the parameters that determine the extent of photodamage in live-cell microscopy is the quality of the excitation light. Standard filter sets, well suited for fixed-cell microscopy, often are not ideal in live-cell experiments. In the latter case, circumventing deleterious effects of irradiation should take priority over maximization of total fluorescence intensity.

Standard commercial filter sets are usually designed to maximize excitation by utilizing a relatively large portion of the fluorophore's absorption spectrum. Excitation filters with spectral width ~40 nm are commonly offered for GFP imaging (Fig. 23.2B). Though these filters do offer excellent signal strength, excitation with seemingly less efficient narrow-band filters is advantageous when a large number of images need to be acquired in live cells. An example of a marked decrease in photobleaching and photodamage due to a narrower excitation filter is illustrated in Fig. 23.2. Notice that although the quality of images recorded with a wider exciter is initially higher, the intensity of GFP signal gradually degrades throughout the course of recording (Fig. 23.2C). In contrast, with a very narrow exciter matched to the absorption maximum photobleaching is unnoticeable after 30 min of recording (Fig. 23.2D). In addition to prominent photobleaching, the cell followed with a wider

(D), recorded with a narrow 488 ± 1-nm laser-line filter. Both recordings were conducted at 2-s intervals but neutral-density filters and shorter exposure times were used in (C) to decrease the difference in the amount of light delivered to the sample (notice that intensities are similar at 0:00 in both sequences). Time shown as minutes:seconds. (E) Effects of emission filter on image quality. (1) Standard combination of filters used in spinning-disc confocal microscopy. (2) Same object recorded with no emission filter. Although the amount of noise increases slightly, improved brightness is beneficial in single-color live-cell recording. (2′) Adjusting the look-up table of (2) creates an image virtually indistinguishable from that recorded with the proper emission filter (cf. 1 and 2′). PtK$_2$ cells constitutively expressing α-tubulin-GFP to label microtubules. Scale bars = 5 μm.

Spectra are adapted from Rankin et al. (2011).

excitation filter becomes photodamaged as manifested by the retractions of the initially extended lamella (Fig. 23.2C). In contrast, no change in the cell morphology occurs when GFP is excited with almost monochromatic light. Therefore, imaging conditions are not stressful in this case.

Several mechanisms can contribute to the increase in photodamage observed upon wide-spectrum excitation. One is that photons with shorter wavelength are more likely to cause chemical breakdown of the fluorophore because of their higher energy. Not intuitive to a biologist is that the difference in energy between a 490-nm photon (absorption maximum for the GFP, Fig. 23.2B) versus a 450-nm photon (50% of absorption maximum for the GFP; Fig. 23.2B) is 0.225 eV. This difference corresponds to an increase in the temperature of a single molecule by 2300 °C (in gas). Obviously, such a prominent and localized energy increase beyond the level necessary for exciting the fluorophore is dangerous for the molecule. Another mechanism involves the difference in absorption spectra of the ground-state versus long-lifetime triplet-state fluorophores (Rankin et al., 2011). The latter tend to absorb shorter wavelengths with higher efficiency (Fig. 23.2B). As absorption by the triplets leads to the formation of bleach-prone high energy states, excitation with wavelengths shorter than the absorption maximum can potentially increase photobleaching. Yet, additional phototoxicity observed upon wider-spectrum excitation can arise due to collateral excitation of endogenous chromophores such as cytochromes that are always present in the cell. Photodamage of these molecules ultimately triggers stress-response pathways. Irrespective of the exact mechanism(s), empirical observations demonstrate that narrower exciters spectrally matched to the absorption maximum of the fluorophore diminish deleterious effects of fluorescence imaging in live cells.

An added benefit of extremely narrow excitation is that it can render emission filters unnecessary. We find that rejection of the excitation light by modern dichroic mirrors is often sufficient to capture "clean" spinning-disc confocal fluorescence images without a dedicated emission filter (Fig. 23.2E). Elimination of the emission filter increases the intensity of fluorescence because the entire spectrum of emission light is captured. A corollary is that the intensity of excitation can be lowered by several percent. Although the gain may seem insignificant, in live-cell recordings even a minute decrease in illumination intensity is advantageous particularly when a large number of images need to be acquired. Obviously, emission filters cannot be omitted when cells are labeled with more than one fluorophore.

Dependence of photobleaching/photodamage on the excitation spectrum often becomes a limiting factor in multicolor live-cell imaging. Absorption spectra of fluorescent proteins are usually wide (Chudakov, Matz, Lukyanov, & Lukyanov, 2010). This feature implies that red-shifted proteins absorb wavelengths used for excitation of green-shifted fluorescent proteins. This absorption is unavoidable even when monochromatic laser light is used (Fig. 23.3A), and it is manifested as "cross talk" between the green- and red-channels (Fig. 23.3B). The importance of cross talk for the interpretation of protein colocalization and quantification of signals is actively discussed in the literature. However, less attention is given to the fact that cross talk also

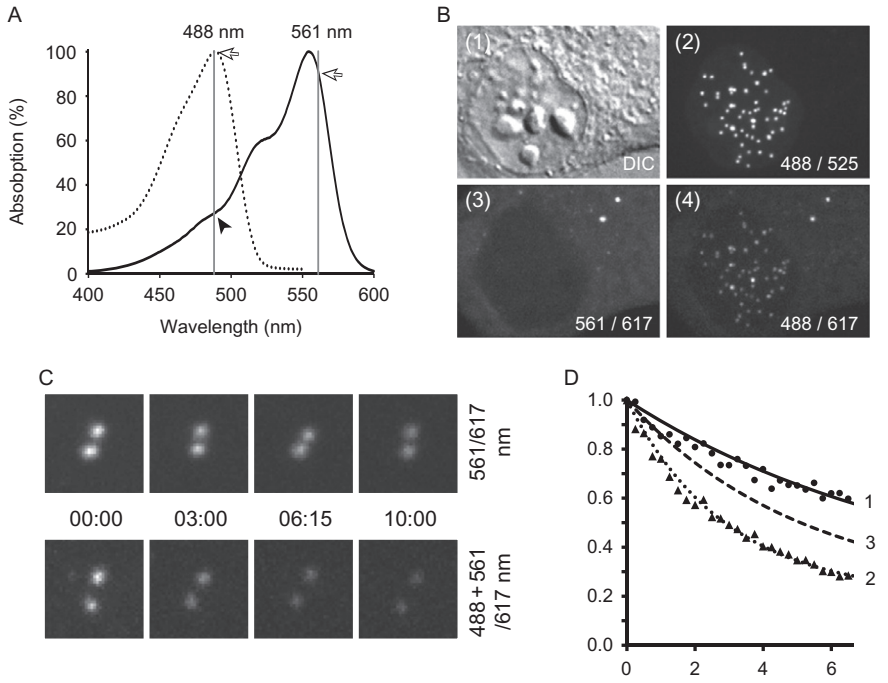

FIGURE 23.3

Disproportionate increase in photobleaching observed in multicolor recordings. (A) Absorption spectra of GFP (dashed line) and tdTomato (solid line). Arrows and arrowhead mark the efficiency of absorption for the wavelengths commonly used to excite these fluorophores. Notice that tdTomato absorbs ~27% of the 488-nm light. (B) Human RPE1 cell expressing CenpA-GFP and Centrin1-tdTomato. DIC image is shown in (1). Panels (2) and (3) present the green (488-nm excitation/525-nm emission) and red (561-nm excitation/617-nm emission) fluorescence channels. Notice that CenpA-GFP localizes inside the nucleus while Centrin-tdTomato targets centrioles in the cytoplasm. Thus, FRET between these proteins is not possible. Image in (4) shows red fluorescence induced by 488-nm excitation. The presence of GFP signal in the red channel is due to the wide emission spectrum of this fluorophore (bleeds through). tdTomato signal is due to excitation of this protein by the 488-nm light. (C) Selected frames from time-lapse recordings of cells similar to one shown in (B). Top row illustrates stability of Centrin-tdTomato fluorescence in a single-color recording. Bottom row illustrates a prominent increase in photobleaching of Centrin-tdTomato when both the green- and red-channels are recorded. (D) Quantification of photobleaching. Curves 1 and 2 correspond to the top and bottom rows in panel (C). Curve 3 is theoretical prediction of tdTomato photobleaching in a two-color recording that accounts for the partial excitation by the 488-nm laser light. As evident from these curves, the extent of photobleaching observed in the experiment is much greater that the theoretical expectation.

accelerates the rate of photobleaching for the red-shifted fluorophores. Furthermore, an important property of multicolor recordings is that the severity of photobleaching for red-shifted proteins can far exceed the rate formally expected due to the absorption-spectra overlap. Comparing to single-color recordings, photobleaching of the fluorescent protein tdTomato roughly doubles in experiments that involve recording both green- and red-fluorescence channels (excitation with similar intensities of 488- and 561-nm lasers; Fig. 23.3D). This is significantly higher than expected as tdTomato absorbs less than 30% at 488 nm. The additional increase in photobleaching can be attributed to the same effects as increase in phototoxicity upon off-peak excitation discussed earlier in this chapter. The 488-nm wavelength, optimal for GFP excitation, corresponds to the dangerous shorter-than-optimal part of the absorption spectrum for red-shifted proteins. Therefore, damaging effects of 488-nm excitation on tdTomato are more pronounced than those caused by the 561-nm "on-peak" light.

Overlap between the excitation spectra of different fluorophores in a multicolor recording can be minimized by a careful selection of fluorescent-proteins pairs. For example, TagRFP-T has same spectral peaks as tdTomato (555 nm) but its absorption at 488 nm is only ~10% (Shaner et al., 2008). However, complete elimination of unintentional excitation is not currently possible and the additional stress inflicted by the second fluorophore needs to be considered in experimental designs. Somewhat paradoxically, in many cases, a practical solution for avoiding excessive photodamage in experiments that require visualization of more than one object is to tag all objects with the same fluorophore. This approach has been proven quite beneficial when the objects are morphologically distinct (Chang, Svitkina, Borisy, & Popov, 1999; Tran, Marsh, Doye, Inoue, & Chang, 2001) or when morphologically similar objects exhibit distinctly different behavior (Magidson et al., 2011).

23.3 HARDWARE SYNCHRONIZATION

As even fully optimized monochromatic excitation is nevertheless toxic, great care must always be taken to minimize the irradiation dose. Ideally, cells should be illuminated only during the period necessary to acquire the image. However, in real life, actual exposure time often includes a useless "overhead" due to imprecise synchronization between the various hardware components. Relatively simple adjustments in the configuration of the imaging system help to minimize the overhead and sometime virtually eliminate it.

Acquisition of a fluorescence image is a complex routine that involves several steps: the shutter must open and then close, the detector needs to be switched from dormant state to image acquisition and then "readout" state, and finally the image needs to be transferred to the computer memory. In a typical workstation, each of these individual steps is triggered by a command generated by the computer. The commands are issued sequentially and a mechanism needs to be in place to ensure that the next command is not executed prematurely, prior to the completion of the previous step. Most commonly, software designers rely on a return code from

the hardware—receiving this code by the computer confirms that the previous step has been completed and the process can advance further. This is a lengthy process particularly when acquisition routine is complex (e.g., collecting a *Z*-series in multiple colors). It is noteworthy that communication speed is not directly related to the computer processor clock. Somewhat paradoxically, replacing an old computer with a faster model may actually increase the overhead particularly when the workstation comprises newer and older hardware components (due to space limitations this technical issue is not discussed here).

The overhead can be quite long; particularly, in those microscopy workstations that are assembled in-house from individual parts acquired with little consideration for how well these components can communicate with one another when integrated into a common imaging system. Our surveying of various instruments in our own laboratory and elsewhere reveals that a typical overhead on a mid-range research-grade imaging workstation is on the order of 100–200 ms (Fig. 23.4). Thus, a single fluorescent snapshot with the nominal exposure (CCD photon-accumulation time) of

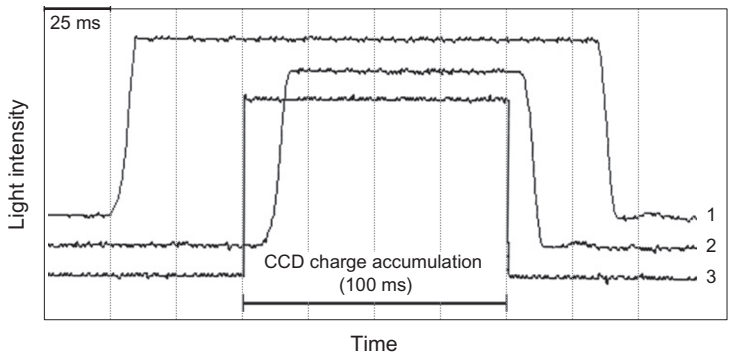

FIGURE 23.4

Actual exposure times for different types of synchronization and different light sources. In all cases, nominal exposure time is set to 100 ms in the commercial software package that controls the imaging workstation. Actual exposure time is measured by a photodetector placed near the focal plane of the objective lens. The output of the detector is recorded by an oscilloscope. Curve 1 represents a standard configuration where excitation light generated by a mercury burner is shuttered with a mechanical shutter and the hardware (CCD camera and shutters) is synchronized via computer control. As evident from this example, the actual exposure exceeds the nominal by almost twofold (190 vs. 100 ms). Curve 2 is recorded with the same hardware but the shutter and camera are directly synchronized (details in the text). In this configuration, unnecessary exposure is limited to the time required to close the shutter. Notice that the shutter begins to open when the camera is already in the charge accumulation mode and it closes after charge accumulation is completed. For curve 3, the mercury burner and mechanical shutters were replaced with a light-emitting diode (LED). In this case, due to fast on/off time of the LED, the actual exposure is virtually the same as the nominal exposure time.

50 ms can actually subject the cell to ~250-ms irradiation. In extreme cases, we saw imaging systems driven by popular commercial software with overheads in excess of 1 s. Such an extreme variability in the overhead is likely to be one of the main reasons for why the extent of photobleaching/photodamage seems to be so variable in different laboratories. It is also noteworthy that overhead time remains fairly constant for a particular imaging workstation. Therefore, the contribution of overhead to phototoxicity is greater when short exposure times are desired. For example, a 100-ms overhead doubles the irradiation dose for 100-ms nominal exposures but it only adds 20% to 500-ms nominal exposures. Thus, the real-life relationship between the exposure time and light intensity is often nonreciprocal. Recordings tend to be less toxic when conducted at the longest allowable exposure time and congruently the lowest possible level of excitation light.

Overheads caused by computer/hardware communications can be eliminated by employing direct synchronization between the camera and shutters. Many research grade CCD cameras offer an "exposure out" connectors that generate an electric signal only when the camera acquires photons. This signal can be used as a trigger to initiate shutter opening or closing at a precise time. In fact, this type of hardware synchronization is used in several high-end commercial imaging systems. Further, major manufacturers of scientific CCD cameras offer proprietary synchronization cables that allow researchers to enable direct synchronization as an after-market solution for both commercially acquired and in-house assembled workstations. We routinely employ this solution in our laboratory (Fig. 23.4) and can attest that it results in a marked decrease in photobleaching/phototoxicity.

The second source of overhead is due to relatively long time required for opening and closing of mechanical shutters (Fig. 23.4). This problem is not commonly found in confocal systems where the light is blocked by almost instantaneous acousto-optic tunable filters. However, in wide-field microscopy mechanical shutters are common and their limited speed is an important limitation particularly for multidimensional time-lapses. Fortunately, modern light sources such as light-emitting diodes (LED) now make the use of mechanical shutters in imaging workstations unnecessary. In sharp contrast to tungsten filaments and arc burners, LEDs transition between the dark and light-emitting states in less than a microsecond which is insignificant in a typical live-cell recording. Thus, fast light sources combined with proper hardware control enable complete elimination of the exposure overhead (Fig. 23.4).

23.4 AVOIDING UNNECESSARY IRRADIATION VIA INTELLIGENT ILLUMINATION

A fundamental limitation in conventional microscopy (both wide field and confocal) is that acquiring a single image exposes every focal plane of the sample to the same amount of light. This means that phototoxicity inflicted by recording a *Z*-series is similar to phototoxicity inflicted by the same number of in-focus images. Unfortunately, in a typical *Z*-series only some planes contain in-focus images while others

capture nothing but defocused "blur." Yet, these useless images contribute to phototoxicity by increasing cumulative exposure. Recently, several clever techniques have been introduced that help to avoid capturing images of "empty parts" of the sample. Some of these techniques require significant modifications of the microscope's optical path. Their implementation requires a significant investment in new equipment. Others rely on computer algorithms and thus can be retroactively enabled on older instruments.

Most notable hardware-based approaches to decreasing phototoxicity include selective plane illumination microscopy (SPIM) (Huisken, Swoger, Del Bene, Wittbrodt, & Stelzer, 2004), its more recent variant termed Bessel-beam Plane Illumination (Planchon et al., 2011), and controlled light exposure microscopy (CLEM) (Hoebe et al., 2007).

In Bessel-beam microscopy and SPIM, the object is illuminated at an angle to the optical axis of the microscope by a thin light sheet. This radical departure from the classic microscope design ensures that only a single plane within the object is illuminated at any given time. The rest of the object remains in the dark. Images obtained by Bessel-beam microscopy are spectacular in both resolution and clarity, particularly when this technique is combined with structured illumination (Gao et al., 2012). Bessel beams are expected to significantly decrease phototoxicity; however, this approach has not been extensively tested in routine investigations as specialized instruments are just becoming commercially available.

CLEM offers a way to decrease phototoxicity in classic point-scanning confocal microscopes by introducing a feedback sensor that measures the rate of photon accumulation at each diffraction-limited spot. As fluorescently labeled objects are by definition bright, slow accumulation of the signal during exposure indicates that the spot contains no object. Therefore, a full exposure for this spot is not required. In contrast, pixels with rapid increase in signal need to be fully exposed and recorded. This clever way of attenuating irradiation dose for individual spots within the same image results in a significant decrease in cumulative exposure. However, implementation of CLEM is expensive, and it is not compatible with wide-field and spinning-disc confocal modalities.

Dose-decreasing illumination is also being developed for wide-field and spinning-disc confocal microscopy. Recently, a simple software-based approach, termed Predictive-Focus Illumination (PFI), was introduced (Schilling et al., 2012). In PFI, a full-range *Z*-series is recorded only once at the first time point of the series. At subsequent time points, *Z*-range is restricted to a small number of focal planes centered on the object-of-interest (OOI) whose position is estimated by a tracking algorithm (Fig. 23.5). OOI is defined by the user or can be automatically detected by the computer. All necessary computations (OOI detection and tracking) are done during the lapse between consecutive time points. While the exact benefits of PFI depend on the number of OOIs and their distribution in space, this approach has been shown to decrease cumulative light exposure up to fivefold in certain types of 3D time-lapses (Schilling et al., 2012). Noteworthy is that PFI requires no hardware modification and thus can be implemented by end users in the environment of a cell biology laboratory (software to enable PFI is freely available; see Schilling et al., 2012).

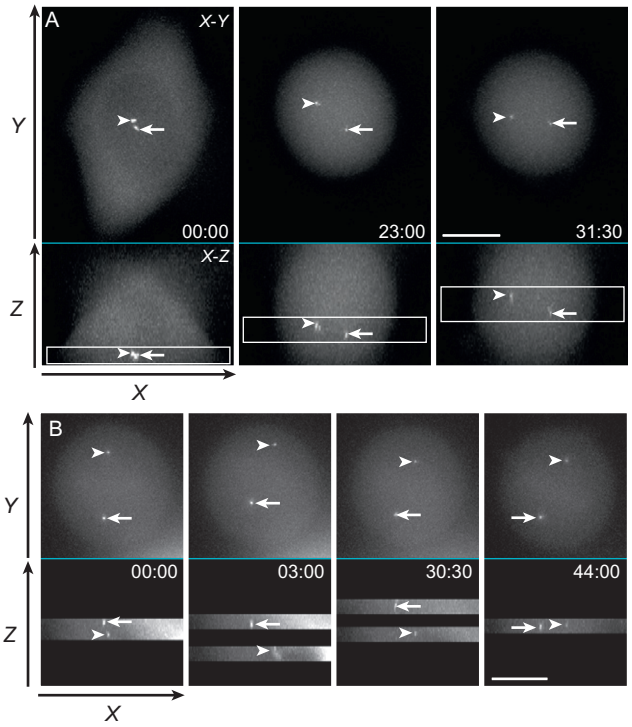

FIGURE 23.5

Example of an adaptive illumination technique. (A) Selected frames from a 3D time-lapse of centrosome movements during cell division in human (HeLa) cells. These cells become rounded during mitosis and the centrosomes move extensively in all three dimensions. Approximately, 50 *Z*-planes need to be captured at every time point to ensure that both centrosomes remain in focus throughout the recording. Only few of these planes contain information pertinent to the centrosome behavior (white boxes). (B) Predictive-focus illumination dramatically decreases the number of necessary exposures. In this technique, short *Z*-series centered on the predicted positions of the objects-of-interest are recorded at every time point. Notice that when the objects separate in *Z*, their positions are tracked individually. Top and bottom halves of each panel presents *X*–*Y* and *X*–*Z* maximal projections of 3D volumes. Time is in minutes:seconds. Bar = 10 μm.

CONCLUSIONS

Live-cell fluorescence microscopy is not a truly noninvasive observation technique. The number of images that can be captured before the cell becomes damaged is fundamentally limited. Sooner or later, the cell is likely to change its physiological state in response to stress induced by high-intensity excitation light. This limitation needs to be considered in the design of every live-cell fluorescence experiment. For

example, inexperienced investigators would browse through the sample in fluorescence mode in search of the cell to record. However, even a brief look at the cell with one's eyes takes 5–10 s which means that it subjects the sample to the same amount of irradiation as recording 50–100 images at 100-ms exposures. This "curiosity damage" can be easily avoided by using completely safe phase-contrast or DIC microscopy to choose the cell and position it. Understanding limitations inherent in live-cell fluorescence microscopy helps to recognize problems and avoid artifacts.

References

Bingen, P., Reuss, M., Engelhardt, J., & Hell, S. W. (2011). Parallelized STED fluorescence nanoscopy. *Optics Express*, *19*, 23716–23726.

Chang, S., Svitkina, T. M., Borisy, G. G., & Popov, S. V. (1999). Speckle microscopic evaluation of microtubule transport in growing nerve processes. *Nature Cell Biology*, *1*, 399–403.

Chen, X., Leischner, U., Varga, Z., Jia, H., Deca, D., Rochefort, N. L., et al. (2012). LOTOS-based two-photon calcium imaging of dendritic spines in vivo. *Nature Protocols*, *7*, 1818–1829.

Chudakov, D. M., Matz, M. V., Lukyanov, S., & Lukyanov, K. A. (2010). Fluorescent proteins and their applications in imaging living cells and tissues. *Physiological Reviews*, *90*, 1103–1163.

Diamond, J. M. (1997). Guns, germs, and steel: The fates of human societies. New York: W.W. Norton.

Donnert, G., Eggeling, C., & Hell, S. W. (2007). Major signal increase in fluorescence microscopy through dark-state relaxation. *Nature Methods*, *4*, 81–86.

Gao, L., Shao, L., Higgins, C. D., Poulton, J. S., Peifer, M., Davidson, M. W., et al. (2012). Noninvasive imaging beyond the diffraction limit of 3D dynamics in thickly fluorescent specimens. *Cell*, *151*, 1370–1385.

Hinchcliffe, E. H., Miller, F. J., Cham, M., Khodjakov, A., & Sluder, G. (2001). Requirement of a centrosomal activity for cell cycle progression through G 1 into S phase. *Science*, *291*, 1547–1550.

Hoebe, R. A., Van Oven, C. H., Gadella, T. W. J., Dhonukshe, P. B., Van Noorden, C. J. F., & Manders, E. M. M. (2007). Controlled light-exposure microscopy reduces photobleaching and phototoxicity in fluorescence live-cell imaging. *Nature Biotechnology*, *25*, 249–253.

Huisken, J., Swoger, J., Del Bene, F., Wittbrodt, J., & Stelzer, E. H. (2004). Optical sectioning deep inside live embryos by selective plane illumination microscopy. *Science*, *305*, 1007–1009.

Khodjakov, A., & Rieder, C. L. (1999). The sudden recruitment of g-tubulin to the centrosome at the onset of mitosis and its dynamic exchange throughout the cell cycle, do not require microtubules. *The Journal of Cell Biology*, *146*, 585–596.

Khodjakov, A., & Rieder, C. L. (2001). Centrosomes enhance the fidelity of cytokinesis in vertebrates and are required for cell cycle progression. *The Journal of Cell Biology*, *153*, 237–242.

Magidson, V., O'Connell, C. B., Loncarek, J., Paul, R., Mogilner, A., & Khodjakov, A. (2011). The spatial arrangement of chromosomes during prometaphase facilitates spindle assembly. *Cell*, *146*, 555–567.

Mikhailov, A., Patel, D., McCance, D. J., & Rieder, C. L. (2007). The G2 p38-mediated stress-activated checkpoint pathway becomes attenuated in transformed cells. *Current Biology*, *17*, 2162–2168.

Mikhailov, A., Shinohara, M., & Rieder, C. L. (2005). The p38-mediated stress-activated checkpoint. A rapid response system for delaying progression through antephase and entry into mitosis. *Cell Cycle*, *4*, 57–62.

Planchon, T. A., Gao, L., Milkie, D. E., Davidson, M. W., Galbraith, J. A., Galbraith, C. G., et al. (2011). Rapid three-dimensional isotropic imaging of living cells using Bessel beam plane illumination. *Nature Methods*, *8*, 417–423.

Rankin, B. R., Moneron, G., Wurm, C. A., Nelson, J. C., Walter, A., Schwarzer, D., et al. (2011). Nanoscopy in a living multicellular organism expressing GFP. *Biophysical Journal*, *100*, L63–L65.

Rodionov, V. I., & Borisy, G. G. (1997). Microtubule treadmilling in vivo. *Science*, *275*, 215–218.

Schilling, Z., Frank, E., Magidson, V., Wason, J., Loncarek, J., Boyer, K., et al. (2012). Predictive-focus illumination for reducing photodamage in live-cell microscopy. *Journal of Microscopy*, *246*(2), 160–167.

Shaner, N. C., Lin, M. Z., McKeown, M. R., Steinbach, P. A., Hazelwood, K. L., Davidson, M. W., et al. (2008). Improving the photostability of bright monomeric orange and red fluorescent proteins. *Nature Methods*, *5*, 545–551.

Tran, P. T., Marsh, L., Doye, V., Inoue, S., & Chang, F. (2001). A mechanism for nuclear positioning in fission yeast based on microtubule pushing. *The Journal of Cell Biology*, *153*, 397–411.

Uetake, Y., Loncarek, J., Nordberg, J. J., English, C. N., La Terra, S., Khodjakov, A., et al. (2007). Cell cycle progression and de novo centriole assembly after centrosomal removal in untransformed human cells. *The Journal of Cell Biology*, *176*, 173–182.

Zhai, Y., Kronebusch, P. J., & Borisy, G. G. (1995). Kinetochore microtubule dynamics and the metaphase-anaphase transition. *The Journal of Cell Biology*, *131*, 721–734.

CHAPTER

24

A User's Guide to Localization-Based Super-Resolution Fluorescence Imaging

Graham T. Dempsey

Department of Chemistry and Chemical Biology, Harvard University, Cambridge, Massachusetts, USA

CHAPTER OUTLINE

Introduction **562**
24.1 Fluorescent Probe Selection **565**
24.1.1 Spatial Resolution and Important Probe Properties 565
24.1.2 Choosing Probes 567
24.1.2.1 Single-Color Fixed-Cell Imaging 567
24.1.2.2 Multicolor Fixed-Cell Imaging 570
24.1.2.3 Live-Cell Imaging 571
24.2 Sample Preparation **571**
24.2.1 Immunohistochemistry 571
24.2.2 Fluorescent Proteins 574
24.2.3 Alternative Labeling Approaches 575
24.3 Instrumentation **575**
24.3.1 Excitation Pathway 576
24.3.1.1 Laser Sources 576
24.3.1.2 Intensity and Temporal Modulation 578
24.3.1.3 Illumination Schemes 578
24.3.2 Microscope 578
24.3.2.1 Microscope Body 578
24.3.2.2 Dichroic Mirrors and Emission Filters 578
24.3.2.3 Objective Lens 579
24.3.3 Detection Pathway 579
24.3.3.1 Camera 579
24.3.3.2 3D Imaging 580
24.3.3.3 Multichannel Detection 580
24.3.4 Focus Lock 580
24.3.5 Computer 581

Methods in Cell Biology, Volume 114 **ISSN 0091-679X**
Copyright © 2013 Elsevier Inc. All rights reserved.
http://dx.doi.org/10.1016/B978-0-12-407761-4.00024-5

24.4 Data Collection and Analysis 581
24.4.1 Data Collection 581
24.4.1.1 Fiducial Markers for Drift Correction 581
24.4.1.2 Single-Color 2D and 3D Imaging 582
24.4.1.3 Multicolor Imaging 582
24.4.1.4 Live-Cell Imaging 583
24.4.2 Data Analysis 584
24.4.2.1 Peak Finding 584
24.4.2.2 Gaussian Fitting 584
24.4.2.3 Displaying the STORM Image 585
24.4.2.4 Drift Correction 585
24.4.2.5 Filtering the STORM Image 586
24.4.2.6 Multicolor STORM Considerations 587
24.4.2.7 Live-Cell STORM Considerations 587
Summary and Outlook 587
Acknowledgments 588
References 588

Abstract

Advances in far-field fluorescence microscopy over the past decade have led to the development of super-resolution imaging techniques that provide more than an order of magnitude improvement in spatial resolution compared to conventional light microscopy. One such approach, called Stochastic Optical Reconstruction Microscopy (STORM) uses the sequential, nanometer-scale localization of individual fluorophores to reconstruct a high-resolution image of a structure of interest. This is an attractive method for biological investigation at the nanoscale due to its relative simplicity, both conceptually and practically in the laboratory. Like most research tools, however, the devil is in the details. The aim of this chapter is to serve as a guide for applying STORM to the study of biological samples. This chapter will discuss considerations for choosing a photoswitchable fluorescent probe, preparing a sample, selecting hardware for data acquisition, and collecting and analyzing data for image reconstruction.

INTRODUCTION

An important advance in light microscopy over the past decade has been the realization of super-resolution fluorescence imaging, which overcomes the diffraction-limited spatial resolution of conventional optical systems (Hell, 2007; Huang, Babcock, & Zhuang, 2010). One implementation, referred to as Stochastic Optical Reconstruction Microscopy (STORM), emerged from the convergence of two key insights: (1) the position of a fluorophore can be determined with high precision using its fluorescence image and (2) individual fluorophores in a labeled sample

can be imaged sequentially rather than simultaneously. The shape of each individual emitter image is an Airy pattern, commonly referred to as the point spread function (PSF), which can be approximated by a Gaussian distribution (Fig. 24.1A) and fit to an accuracy of ~1 nm in the lateral dimensions (Gelles, Schnapp, & Sheetz, 1988; Thompson, Larson, & Webb, 2002; Yildiz et al., 2003). While PSF-fitting works well for isolated molecules, a typical imaging specimen may have thousands of fluorophores whose images overlap when they emit fluorescence simultaneously. Overcoming this limitation requires the use of probes whose fluorescence can be modulated between an emissive "on" state and a dark "off" state. By intermittently turning on a sparse, stochastic subset of fluorophores, the individual positions of each molecule can be determined. The process of sparse activation and localization is repeated for different subsets of fluorophores until a sufficient number of position measurements accumulate to map out the structure of interest.

The basic concept of STORM is shown in Fig. 24.1B. This approach is commonly referred to as either STORM (Rust, Bates, & Zhuang, 2006) or (fluorescence) photoactivated localization microscopy ((F)PALM) (Betzig et al., 2006; Hess, Girirajan, & Mason, 2006). Although other names, such as direct STORM (Heilemann, van de

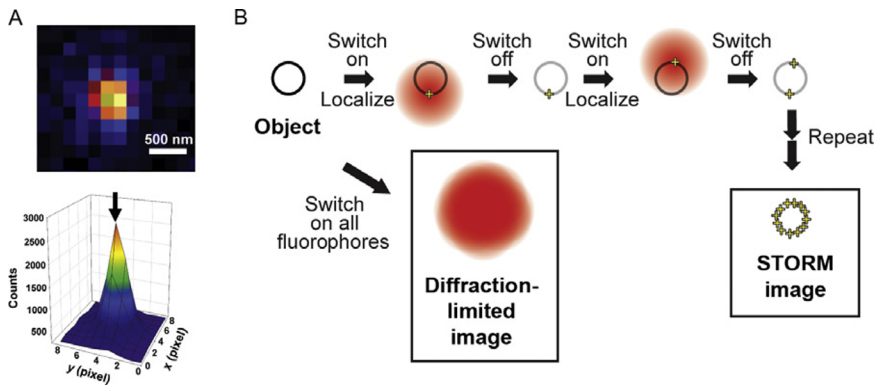

FIGURE 24.1

Principles of single-molecule localization and STORM. (A) (Upper panel) Electron multiplying charge-coupled device (EMCCD) image of a single fluorescent molecule, where the color gradient represents the number of counts (dark is low counts, light is high counts). Due to diffraction, the image is blurred to several hundred nanometers. (Lower panel) Intensity distribution of the molecule shown in the upper panel. The distribution resembles a Gaussian function, which can be used to determine the molecule centroid (black arrow) to subdiffraction-limit precision. (B) A circular, subdiffraction-limit-sized object is densely labeled with fluorophores. Exciting these fluorophores (shown as a solid circles) simultaneously results in the diffraction-limited case, where the circular feature is obscured. However, by turning on a single fluorophore, the position of that fluorophore (shown as a "+") can be determined by Gaussian fitting. The molecule is turned off and a different molecule turned on. The process is repeated until sufficient localizations map the object structure.

Cartoon adapted from Dempsey, Vaughan, Chen, Bates, and Zhuang (2011).

Linde, Mukherjee, & Sauer, 2009; Heilemann et al., 2008) and ground-state depletion with individual molecule return (Fölling et al., 2008), have been created to describe this approach when used with different probes and fluorescence modulation strategies, each technique utilizes the same principles of sparse activation and precise single-molecule localization. For simplicity, the technique will be referred to as STORM.

STORM can be used to attain more than a 10-fold improvement in spatial resolution in the lateral and axial dimensions. For two-dimensional (2D) STORM, 20–30 nm lateral resolution can be routinely achieved. For extension to three-dimensional (3D) imaging, a variety of methods have been developed. These include optical astigmatism (Huang, Wang, Bates, & Zhuang, 2008), multifocal plane imaging (Juette et al., 2008), interferometry (Shtengel et al., 2009), and a double-helix PSF (Pavani et al., 2009). For astigmatism-based 3D STORM, a cylindrical lens is inserted into the detection pathway to change the PSF shape in the x and y directions depending on the position of the fluorophore relative to the focal plane (Fig. 24.2A). The fluorescence image can then be fit to an elliptical Gaussian function, where the centroid is used to determine the x–y position and the shape used to determine the z-position. Here, the achievable axial resolution for a single objective

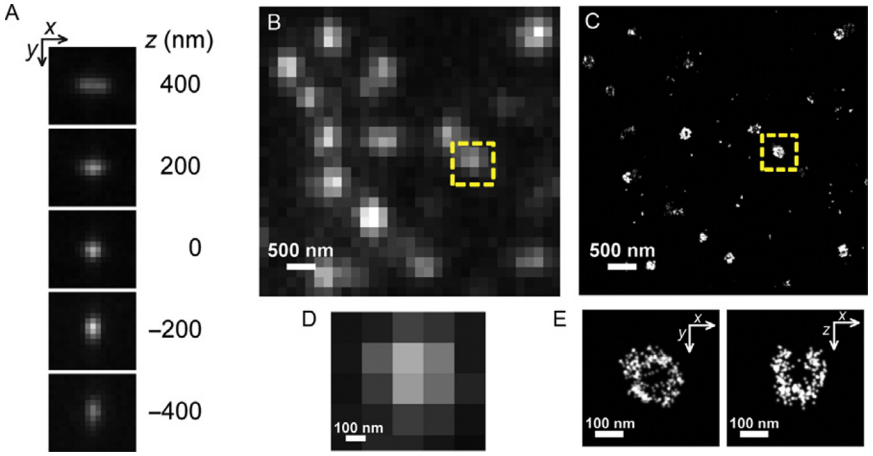

FIGURE 24.2

3D STORM. (A) Single-bead image taken at different z-positions. At $z=0$, the image is symmetric. At positions above and below the focal plane, the image becomes elliptical in the x and y directions, respectively. The image shape can be used to assign a z-position to each molecule. (B) Conventional and (C) 3D STORM image of CCPs in a BS-C-1 cell. CCPs are spherically shaped endocytic vesicles. A comparison of the (D) conventional and (E) STORM image is shown for the boxed, dotted region. The left and right panels in (E) are x–y and x–z cross sections, respectively, which reveal the hollow spherical structure.

(C) and (E) from Dempsey et al. (2011).

is 50–60 nm (Huang, Wang, et al., 2008). A comparison of a 3D STORM image with a conventional fluorescence image of clathrin-coated pits (CCPs), in a fixed cell is shown in Fig. 24.2B–E.

Although simple in principle, successful implementation of STORM requires carefully choosing a high-performing fluorescent probe, preparing a sample with ultrastructural preservation, selecting an instrument with appropriate hardware, and analyzing data for high-resolution image reconstruction. Presented in this chapter are the important general considerations for each aspect, with a focus on the practical implementation of STORM in the laboratory.

24.1 FLUORESCENT PROBE SELECTION

A critical choice for STORM is the type of fluorescent probe. Most STORM probes are either fluorescent proteins (FPs) or organic dyes. The advantages and disadvantages of each will be discussed. The choice of probe ultimately depends on the intended application, and discussing all possibilities is beyond the scope of this chapter. In the following sections, I focus on common imaging modes, namely single-color, multicolor, and live-cell imaging, with recommended starting points. The recommended probes and buffer components for each imaging mode are summarized in Table 24.1. For a more detailed evaluation of photoswitching performance for many organic dyes used for STORM, see Dempsey et al., 2011. For a review of some FP photoswitching properties, see Lippincott-Schwartz & Patterson, 2009. Before discussing specific probes, let us first examine important probe properties that impact spatial resolution and image quality.

24.1.1 Spatial resolution and important probe properties

One of the key determining factors of spatial resolution in a STORM image is the number of detected photons per fluorescent event. The uncertainty, $\sigma_{x,y}$, of Gaussian fitting to a molecule image scales approximately as:

$$\sigma_{x,y} \sim \frac{\sigma_{\mathrm{PSF}}}{\sqrt{N}} \tag{24.1}$$

where σ_{PSF} is the standard deviation (SD) of the microscope PSF and N is the number of detected photons (Thompson et al., 2002). The inverse-square-root dependence in this expression arises from the statistical uncertainty of multiple measurements, where each photon is a measurement of the molecule position. Collecting more photons reduces the localization uncertainty.

A second determinant of spatial resolution is the localization density, or the number of identified probes per given region, and is best understood using the Nyquist sampling theorem (Shroff, Galbraith, Galbraith, & Betzig, 2008): to resolve a spatial feature of frequency f requires a minimum sampling frequency of $2f$. This implies

Table 24.1 Probes and imaging buffers for different applications

Application	Probe(s)	Imaging solution						
		Buffer	GLOX (v/v) (%)	Glucose (w/v) (%)	MVAA (mM)	BME (mM)	MEA (mM)	TCEP (mM)
Fixed-cell, single-color imaging	Alexa 647, DyLight 750, or Atto 488	pH 7–9	1	1–10	–	100	–	–
		pH 7–9	1	1–10	–	–	10	–
		pH 7–9	1	1–10	1	–	–	25
	mEos2 or PA-mCherry	PBS	–	–	–	–	–	–
Highest resolution, fixed-cell, single-color imaging	Reduced Cy3B	pH 7–9	1	1–10	1	–	–	–
Fixed-cell, multireporter imaging	Alexa 647 and DyLight 750 and/or Atto 488	pH 7–9	1	1–10	–	100	–	–
		pH 7–9	1	1–10	–	–	10	–
		pH 7–9	1	1–10	1	–	–	25
	Alexa 647 and mEos2 and/or DyLight 750	pH 7–9	1	1–10	–	100	–	–
		pH 7–9	1	1–10	–	–	10	–
Fixed-cell multiactivator imaging	Alexa 405–Alexa 647 and/or Cy2–Alexa 647 and/or Cy3–Alexa 647	pH 7–9	1	1–10	–	–	10	–
Live-cell, single-color imaging	Alexa 647	DMEM; low serum; no phenol red	1	2.5	–	70	–	–
	mEos2 or PA-mCherry	DMEM; low serum; no phenol red	–	–	–	–	–	–

This list is intended to be a starting point, as other probes are available. Note that 1% GLOX is 0.5 mg/mL glucose oxidase (Sigma–Aldrich) and 40 μg/mL catalase (Sigma–Aldrich).

that the maximum achievable spatial resolution, r, can be approximated as twice the average distance between neighboring probes or:

$$r \sim \frac{2}{M^{1/d}} \tag{24.2}$$

where M is the localization density and d is a dimensionality of one, two, or three (1D, 2D, or 3D, respectively). For example, a diffraction-limited, 2D object such as a 100×100 nm solid square requires $\sim$100 localizations to resolve the object at 20 nm resolution. Extension to 3D requires even more localizations.

Several probe properties are required given the demands for achieving high-spatial resolution. The first is a high number of detected photons per photoswitching event. Brighter probes enable higher optical resolution. The second property is a high contrast due to a low-duty cycle (DC) and high-contrast ratio. The DC is the fraction of time a molecule spends in the fluorescent state (Bates, Huang, & Zhuang, 2008; Dempsey et al., 2011). The maximum number of probes that can be localized in a diffraction-limited region scales approximately with the inverse of the DC. To localize 100 molecules in a diffraction-limited region, for example, requires that each probe have a DC of $\leq$1/100 or spend $\geq$99% of the time in a dark state. A low-DC ensures that a single molecule is on at any time. The contrast ratio is the ratio of the fluorescence in the bright state following activation to the fluorescence in the dark state. For some probes, residual fluorescence from the dark form can reduce the signal to noise of the activated state, especially at high labeling densities. For this reason, a high-contrast ratio is beneficial. A third property is the photostability or propensity of the probe to photobleach. High photostability ensures that a sufficient number of probes can be localized to satisfy the Nyquist requirement. The effects of these probe properties on image reconstruction are explored in Fig. 24.3. Other properties such as number of switching cycles, the times between dark/bright states, and switching homogeneity are also important to consider, but are beyond the scope of this chapter (Dempsey et al., 2011).

24.1.2 Choosing probes

24.1.2.1 Single-color fixed-cell imaging

A recommended starting probe for single-color imaging of fixed samples is the carbocyanine dye Alexa 647 (Life Technologies) or its structural analogue Cy5 (GE Healthcare), the highest performing reversible photoswitches to date. These dyes give high photons ($\sim$5000), a low-DC ($<$0.001), high photostability, and a high number of switching cycles (Dempsey et al., 2011). Photoswitching to a dark state occurs upon illumination with red laser light, in the presence of specific chemical components: an oxygen scavenging system to reduce photobleaching, a primary thiol to induce photoswitching (Bates, Blosser, & Zhuang, 2005; Dempsey, Bates, et al., 2009; Heilemann, Margeat, Kasper, Sauer, & Tinnefeld, 2005), and a buffer to maintain a stable pH (see Table 24.1). Different thiols and thiol concentrations can change the photoswitching properties of dyes (Dempsey et al., 2011).

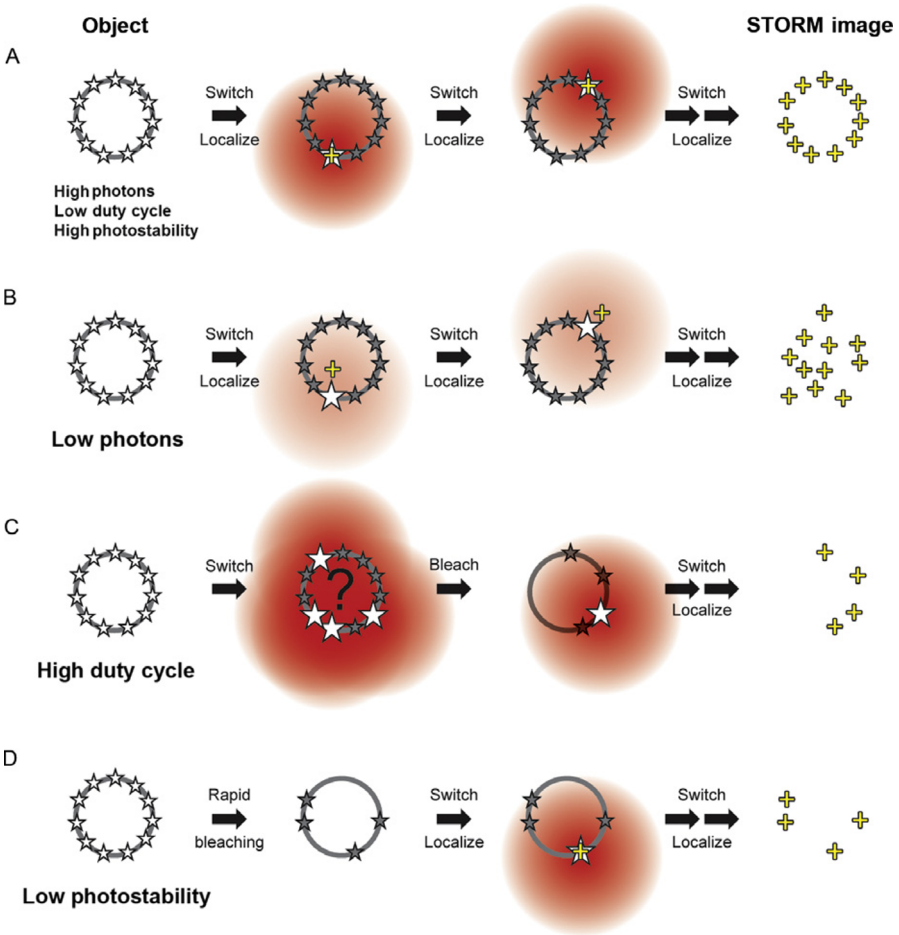

FIGURE 24.3

Photoswitchable probe properties and their impact on STORM images. (A–D) A subdiffraction-sized circle is labeled with probes, whose positions are shown as stars. The fluorescence image is shown as a solid circle and the determined centroid as "+." (A) A probe with high photon number, low DC, and high photostability can resolve the circular feature of the object. (B) If the photon number is too low, the increased error in localizing each molecule will give the appearance of a filled rather than open circle. (C) If the DC is too high, the overlapping fluorescence images from having multiple molecules emit per diffraction-limited spot will preclude the identification of any one probe. Achieving single-molecule density requires either reducing the labeling density or bleaching the sample, and a sufficient number of localizations can no longer be identified to resolve the circle. (D) Similarly, if the photostability is too low, a significant number of molecules will photobleach before being localized, leading to a sparse localization density.

Using 2-mercaptoethylamine (MEA), for example, not only results in a lower photon number than 2-mercaptoethanol (BME) for Alexa 647/Cy5 but also gives a lower DC. Activation from the dark state is either spontaneous or can be promoted by illumination with violet light. Alternatively, Cy5 and Alexa 647 can be paired with activating fluorophores to promote recovery from the dark state at low activation light intensities (Bates, Huang, Dempsey, & Zhuang, 2007). If Alexa 647 is not an option, other dyes, such as Cy7 (Life Technologies), Alexa 750 (Invitrogen), DyLight 750 (Pierce), Atto 488 (Sigma–Aldrich), or Alexa 488 (Invitrogen) can be used, although often at worse performance (∼1000 photons). For a discussion of the best performing dyes under different buffer and imaging conditions, see Dempsey et al., 2011. It has recently been discovered that the nucleophile *tris*(2-carboxyethyl)phosphine (TCEP; Sigma–Aldrich) can be used in place of the thiol for photoswitching of Alexa 647 and Alexa 750/DyLight 750 (Vaughan, Dempsey, Sun, & Zhuang, 2013). The use of TCEP enables significantly more photons per switching event for Alexa 750/DyLight 750 (∼3000 for TCEP vs. ∼800 for thiol).

The photoactivatable FP mEos2 (McKinney, Murphy, Hazelwood, Davidson, & Looger, 2009) is also a good option for single-color imaging as it displays a higher brightness (∼1200 photons) and contrast ratio compared to most other FPs. mEos2 begins in a blue-shifted fluorescent state, and upon illumination with violet light, a fraction of molecules are activated to a red-shifted fluorescent state that can be imaged with yellow light. The irreversible photoactivation of mEos2 does not require special buffer additives, and imaging can be performed in a standard physiological pH buffer, such as phosphate-buffered saline (PBS). A new, optimized variant of mEos2 called mEos3 shows a lower tendency toward oligomerization and slightly improved brightness (Zhang et al., 2012). A number of FP alternatives to mEos2 exist. These include, but are not limited to, PA-GFP (Patterson & Lippincott-Schwartz, 2002), tdEos (Wiedenmann et al., 2004), Dendra2 (Gurskaya et al., 2006), mkikGR (Habuchi, Tsutsui, Kochaniak, Miyawaki, & van Oijen, 2008), PA-mCherry (Subach et al., 2009), YFP (Biteen et al., 2008), Dronpa (Habuchi et al., 2005), Dreiklang (Brakemann et al., 2011), and rsEGFP (Grotjohann et al., 2011). Often, PA-mCherry is a good second choice if mEos2 is not an option. In general, however, different FPs have to be tested for each specific application, as the photoswitching performance and oligomerization tendencies can vary significantly.

For applications that demand ultrahigh resolution of ∼5 nm or better, reductively caged cyanines and rhodamines are a good option (Vaughan, Jia, & Zhuang, 2012). Fluorophores such as Cy3B, Atto 488, Cy3, Alexa 647, and Cy5.5 can be reduced to a dark form using sodium borohydride. Illumination with UV light activates the probe from the dark form to the ground state, upon which the activated dye can be imaged under conditions that allow tens to hundreds of thousands of photons to be collected in a single event. The imaging buffer includes an oxygen scavenger system and a mixture of methyl viologen and ascorbic acid (MVAA; Sigma–Aldrich) to prevent unwanted blinking of the dye (Vogelsang et al., 2008). The best performing dye for this method, in terms of both photon number (∼200,000) and fraction of fluorescence

recovery after UV activation (40%), is Cy3B. It should be noted, however, that imaging with reductive caging is generally limited to slower imaging speeds compared to Alexa 647 with thiol or mEos2.

24.1.2.2 Multicolor fixed-cell imaging

Multicolor imaging can be performed in two general formats, multireporter or multiactivator. Multireporter STORM distinguishes probes based on the emission color of the photoswitchable probe, or reporter. The primary advantage is the low channel-to-channel crosstalk when using probes with well-separated emission spectra. For this reason, the multireporter approach is best for imaging two or more structures that have a high degree of colocalization at subdiffraction resolution. The disadvantages are that the dyes used for different color channels are of varying performance in terms of photoswitching properties, and channel alignment is nontrivial. For organic dyes, it is recommended that one of the probes used is Alexa 647 and the other is either Alexa 750/Cy7/DyLight 750 or Atto 488/Alexa 488. Combinations of FPs can be used, but are often limited by the fluorescence of the preactivated form of many photoactivatable FPs that occupies one of the possible spectral bandwidths. Sequential imaging strategies have been devised to circumvent this with some success (Shroff et al., 2007). Alternatively, PA-GFP in combination with PA-mCherry can be used with limited spectral overlap (Subach et al., 2009). Hybrid approaches that combine FPs with organic dyes, such as mEos2 with Alexa 647, are also possible.

Multiactivator imaging is performed using photoswitchable dye pairs, where the reporter fluorophore used for single-molecule localization is paired with a shorter wavelength activator fluorophore that reactivates the reporter from a dark state to the bright state. The activator dye provides a sensitive, independent control over the fraction of reporters that is on at a given time. Different activator dyes have spectrally distinct absorption spectra, which allow probe pairs to be distinguished by the wavelength of activation light. This principle has been successfully demonstrated using either Alexa 647 (or Cy5) or Alexa 750 (or Cy7) as reporter dyes paired with Alexa 405, Cy2, and Cy3 (Bates, Dempsey, Chen, & Zhuang, 2012; Bates et al., 2007). The advantages of this approach are the use of the highest performing dye (Alexa 647), the absence of chromatic aberrations, and perfect color channel alignment. The principle disadvantage, however, is the relatively high crosstalk between channels from two primary sources: activation with the incorrect activation wavelength and nonspecific activation. The latter, and often more significant source, refers to spontaneous activation from the dark state that leads to incorrect channel assignment. The contribution of nonspecific activation to crosstalk becomes most detrimental in samples where the target structures are of largely different abundances. The nonspecific activation rate of the higher copy number targets can overwhelm the lower copy number targets. Crosstalk can be minimized for the multiactivator approach by using MEA in place of BME (Table 24.1) and further subtraction performed during analysis (Section 4). In general, when imaging two or more interacting structures that are spatially distinct and of similar abundance, the multiactivator approach can be used.

24.1.2.3 Live-cell imaging

Live-cell STORM introduces additional considerations when choosing probes. The first consideration is the trade-off between temporal and spatial resolution. Achieving a particular spatial resolution requires the collection of a sufficient number of localizations to satisfy the Nyquist criterion, as discussed previously. This collection process, however, requires a certain amount of time that is ultimately limited by a probe's photoswitching kinetics and restricts the time scales that can be investigated. FPs, such as tdEos and mEos2, are currently limited to relatively slow switching speeds, where time resolutions of ~30 s can be attained for spatial resolutions of ~40 and ~80 nm in the lateral and axial dimensions, respectively (Jones, Shim, He, & Zhuang, 2011; Shroff et al., 2008). Alternatively, Alexa 647 can be used to achieve ~0.5 s time resolution at a spatial resolution of ~25 and ~50 nm in the lateral and axial dimensions, respectively. Other organic dyes, such as Atto 655, TMR, and Oregon Green, have also been used, but with varying degrees of success due to lower photon numbers and faster photobleaching rates compared to Alexa 647 (Jones et al., 2011; Wombacher et al., 2010).

The second set of challenges arises from targeting probes to specific cellular structures. Highly-charged organic dyes are especially difficult to use when labeling live cells due to their inability to permeate the cell membrane. Many organic dyes are decorated with charged chemical groups that are important for dye solubility in aqueous buffers, as well as for maintaining photoswitching properties (unpublished data). Alexa 647, for example, is highly negatively charged with sulfonates that render the dye cell impermeable. Charged dyes can be loaded into cells by bead loading or electroporation, at the expense of possible cell perturbation, and such approaches have enabled Alexa 647 to be used in live-cell STORM (Jones et al., 2011). In addition to being cell impermeable in many cases, organic dyes are not naturally genetically targeted like FPs and require special targeting methods discussed below.

24.2 SAMPLE PREPARATION

The most important goals of sample preparation for STORM are ultrastructure preservation and high labeling density and specificity. A general rule-of-thumb is that a low quality conventional fluorescence image will give a low quality super-resolution image. STORM will not transform a poorly prepared sample to a well-prepared one! Given the large sample space of potential STORM applications, it is recommended that the reader refer to protocols in the literature for labeling particular protein targets. This section focuses on common sample preparations and labeling approaches and discusses important factors that require optimization.

24.2.1 Immunohistochemistry

A common sample preparation strategy for STORM is to use immunohistochemistry (IHC). STORM is generally compatible with standard IHC protocols involving fixation, blocking, permeabilization, and direct or indirect antibody labeling. A good

starting point for optimization is to canvas the literature, especially when electron microscopy has been previously performed on the target structures. A complete description of these topics is beyond the scope of this chapter. Detailed discussion of the perils and potential artifacts of immunofluorescence can be found elsewhere (Schnell, Dijk, Sjollema, & Giepmans, 2012). This section highlights the importance of fixative, permeabilization reagent, and antibodies for preserving ultrastructure while maintaining antigenicity and labeling specificity.

The most common fixatives include cross-linking reagents (Electron Microscopy Sciences) such as paraformaldehyde (PFA), glutaraldehyde (GA), or combinations of the two. Standard organic solvents, such as methanol and acetone, can also be used. The choice of fixative is critical, as it can lead to ultrastructure damage (Fig. 24.4A–C). In some cases, strong fixatives such as GA can block access of an antibody to an epitope and should be used with caution. The optimization of fixation conditions should include different fixative types, concentrations, buffers, incubation times, and temperatures. For MeOH, a common usage is 100% at −20 °C. PFA concentrations often range from 2% to 4% and GA from 0.1% to 2%, both at room temperature.

When studying intracellular components, a permeabilization reagent will need to be chosen. Methanol, in addition to serving as a fixative, also permeabilizes the cellular membrane by dissolving lipids. Nonionic detergents, such as Triton X-100 or NP-40 (Sigma–Aldrich), can also be used to extract the cellular membrane. Transient permeabilization reagents, such as saponin (Sigma–Aldrich), may also be used. Localization artifacts can result if an improper permeabilization reagent is used (Fig. 24.4D–F). As in the case of fixatives, optimization of the permeabilization step should include different reagent types, concentrations, and incubation times as well as tests for permeabilization during or after fixation. A good starting point for detergent concentrations is between 0.05% and 0.5% (v/v). Lower concentrations are especially important if the target of interest is a membrane protein that could be extracted during this step.

In addition to fixation and permeabilization, antibodies will need to be selected and labeled with photoswitchable dyes. Primary antibodies for tens of thousands of different proteins are commercially available from vendors such as Abcam, Sigma–Aldrich, and Milipore, to name just a few. For secondary detection, antibodies can be found against many species and from a variety of vendors, such as Jackson Immunoresearch. Indirect IHC using labeled secondary antibodies is a good place to start for several reasons. For one, direct primary labeling can be nontrivial for some antibodies. The reasonably high concentrations needed for labeling may not be available and primaries often come with additional components, such as BSA, that can also be labeled with the antibody. Second, dye labeling can sometimes compromise the epitope-binding region of the antibody, reducing the labeling density. Last, the use of secondary detection can provide higher labeling densities when multiple secondaries bind a single primary. Alternatively, primary labeling may be needed. For one, a single tier of antibodies enables higher spatial resolution compared to two tiers provided by secondary detection (a standard IgG antibody is ∼10–15 nm in size). Second, if two or more targets have primary antibodies made from the same species secondary detection can be

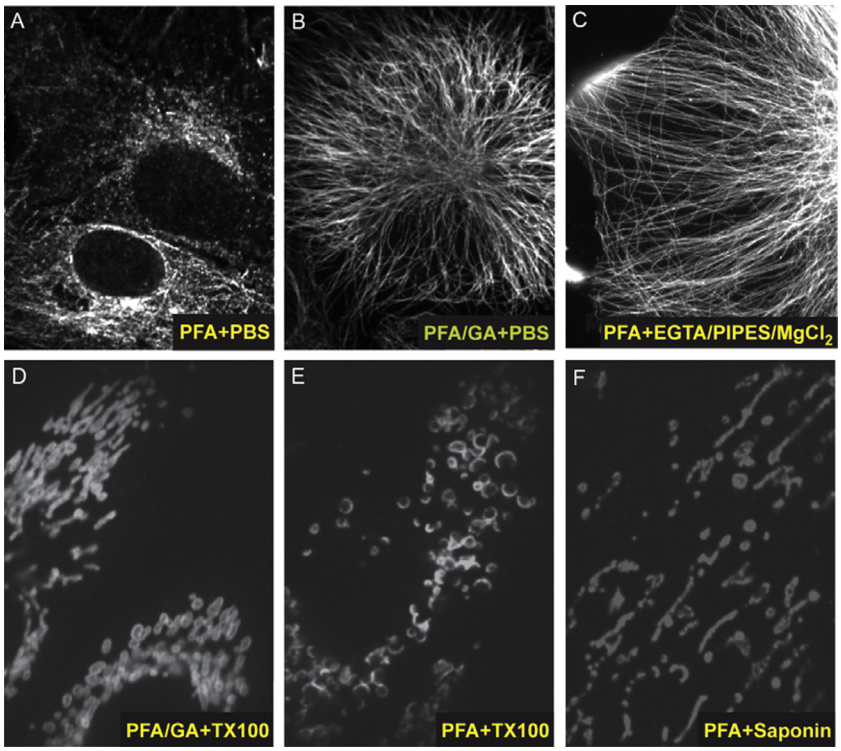

FIGURE 24.4

Importance of ultrastructure preservation during sample preparation. (A–C) Conventional fluorescence micrographs demonstrating the effect of fixative on microtubule ultrastructure. (A) Fixation of BS-C-1 cells with 3% PFA in PBS leads to degradation of the microtubule filaments. (B) However, fixation with 3% PFA and 0.1% GA in PBS or (C) fixation using a buffer containing EGTA, PIPES, and $MgCl_2$ preserves the microtubule ultrastructure. (D–F) Conventional fluorescence micrographs of the mitochondrial protein, TOM20, demonstrating the effect of permeabilization on mitochondria ultrastructure. (D) Cells fixed with 3% PFA and 0.1% GA and permeabilized with 0.05% Triton X-100 (TX100) show densely stained mitochondria, with the expected, elongated morphology. (E) Omitting GA from the immunostaining procedure, however, results in swollen, round mitochondrial structures with an unexpected asymmetric staining pattern. In some cases, the mitochondria rupture. (F) Using a gentler, transient detergent, in this case 0.05% saponin, restores the elongated mitochondria shapes and the uniform labeling density.

Images provided by Dr. Joshua Vaughan.

limited. Whether labeling primaries or secondaries, the labeling procedure is similar. Protocols for labeling antibodies with STORM probes have been described in detail elsewhere (Dempsey et al., 2011; Dempsey, Wang, & Zhuang, 2009).

Once antibodies are chosen and labeled, the conditions for epitope binding can be optimized. Typical optimization of primary and secondary antibody binding for immunofluorescence includes different antibody types, concentrations, and incubation times and temperatures. A good starting point for antibody concentrations when using cultured cells is ~1–10 μg/mL for primaries and ~2–5 μg/mL for secondaries. Samples should be washed thoroughly between antibody additions to reduce nonspecific antibody labeling. Finally, one can perform a second fixation step at the end of IHC to covalently link the antibodies, preserving the sample for longer periods (~1 month or longer in some cases).

24.2.2 Fluorescent proteins

A second approach to sample preparation is the use of FPs. In the simplest configuration, a DNA plasmid is created with a FP encoded at the N- or C-terminus of the gene of interest and the plasmid is either stably or transiently transfected into a specific cell line for expression. For details about making fusion constructs and the various methods of transfecting cell lines, please refer to *Molecular Cloning manuals*. Some important aspects are mentioned here.

When preparing FP fusions, a careful choice of FP must be made. As discussed, FPs vary widely in their performance and the degree to which oligomerization impacts protein localization. This will need to be tested for each protein target. In addition to oligomerization tendencies, the maturation time and temperature should be considered, especially for live-cell imaging. The length of time required for proper fluorophore maturation may not be compatible with the time scale of the process under investigation, as maturation ranges from minutes to hours for different FPs. For example, mEos2 requires >2 h for proper maturation (McKinney et al., 2009). Refer to the previous references for maturation times of different FPs.

In addition to FP choice, there are other considerations. For design of a plasmid, several different promoters may need to be tested to find the optimal expression levels. In addition to the promoter, the linker length between the FP and the protein target may need to be optimized in the event that labeling density is low. The linker length can sometimes adversely affect protein targeting. The method of transfection should also be chosen carefully. Transient transfection for expression of fusion constructs is a common method for investigating proteins in cultured cells using STORM. One can use different transfection reagents or electroporation for introducing DNA into cells. Electroporation often has higher transfection efficiency than transfection reagents such as Lipofectamine (Life Technologies). In both cases, the conditions for transfection should be optimized. Once transfected, plated cells will typically express for 18–24 h before imaging. For fixed samples, the fixation considerations mentioned above also hold true when using FPs, but it should also be confirmed that the FP photoswitching properties are not compromised following treatment with fixatives and detergents.

24.2.3 Alternative labeling approaches

An expression system consisting of a peptide tag and a fluorophore substrate can be used for labeling. These systems combine the genetic encoding capability of FPs with the superior probe properties of organic dyes. The tag–substrate interaction can be either covalent or noncovalent and either self-mediated or enzymatically coupled. A variety of tag expression systems are available, and a detailed discussion of these labeling systems can be found elsewhere (Crivat & Taraska, 2012; Fernández-Suárez & Ting, 2008). As an example, consider the SNAP-tag system used for live-cell STORM with Alexa 647 (Jones et al., 2011). The SNAP-tag is a mutant of the enzyme O6-alkyguanine-DNA alkyltransferase, which reacts to form a covalent bond with benzylguanine (BG) derivatives (Keppler et al., 2004). In this case, cells can be transfected with a plasmid encoding the protein of interest with a SNAP-tag fused to the N- or C-terminus. Cells express the protein for 18–24 h, upon which a fluorescently labeled BG-Alexa 647 substrate (New England Biolabs) is loaded into cells by nucleofection or bead loading to bind to the SNAP-tag. After 18–24 h, labeled cells are then ready for imaging in fixed or live cells. SNAP-tags enable the higher performing organic dyes to be used rather than FPs. The downside, however, is that the overexpression of a SNAP-tagged protein can lead to localizations artifacts seen with FPs. Furthermore, the delivery of fluorescently labeled BG derivatives across the cellular membrane can be a challenge.

Hybrid approaches combining protein overexpression and IHC are also available for targeted labeling. In some applications, an antibody may not be available or bind effectively to the desired target. In addition, the same target may also be incompatible with FPs. In this case, one can try epitope tags, such as myc or HA, where a target protein is expressed with an epitope tag and antibodies against those tags can be used to label with photoswitchable probes. Another recent development uses nanobodies or small, $\sim$2 nm, antigen-binding fragments from camelid antibodies (Ries, Kaplan, Platonova, Eghlidi, & Ewers, 2012). Nanobodies are currently only demonstrated for targeting GFP and RFP for STORM.

Cellular structures other than proteins can also be labeled for STORM. One can use membrane-specific, lipophilic dyes, such as DiI and DiD from Invitrogen or organelle markers such as Mito-, ER-, or Lyso-tracker from Invitrogen. By simply incubating cultured cells with micromolar concentrations of these dyes for $<$5 min, cellular membranes and specific organelles can be labeled for live-cell STORM (Shim et al., 2012). For STORM of DNA or RNA structure, fluorescence *in situ* hybridization has been used (Lubeck & Cai, 2012). Last, other small-molecule labels can be utilized, such as Alexa 647-phalloidin for targeting the actin cytoskeleton with high specificity and labeling density (Xu, Babcock, & Zhuang, 2012; Xu, Zhong, & Zhuang, 2013).

24.3 INSTRUMENTATION

This section covers the key hardware requirements for a STORM setup. It should be noted that commercial versions of these setups are currently available from vendors such as Nikon, Leica, Zeiss, and others, albeit at higher price tags than a home-built

system. A schematic of a 3D, multicolor STORM instrument is shown in Fig. 24.5. A STORM setup begins with an optical surface, such as an 8–18″ thick steel optical table, that is used for dampening vibrations and mounting optical components. The table should be placed in a separate room in the basement or other location relatively free of unwanted vibrational and optical noise sources.

24.3.1 Excitation pathway

24.3.1.1 Laser sources

Lasers come in a wide variety, from mixed-gas to solid-state. When available, solid-state lasers are usually the best option. They are quiet, compact, easy to use, and come in numerous wavelengths and output powers. Mixed-gas lasers, such as an

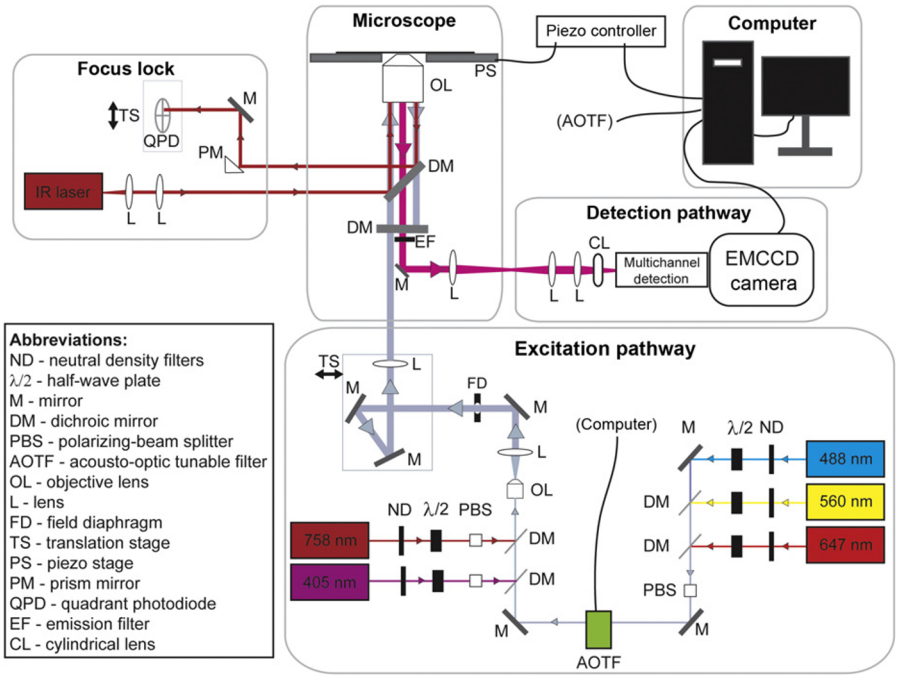

FIGURE 24.5

Example STORM instrument. Example laser sources are listed. The AOTF has a limited bandwidth so that the 405 and 758 nm lasers are directed to the microscope using a separate optical path. The various beams are combined using DMs and the excitation light is expanded to fill the illumination area. A TS is equipped with two steering mirrors and a lens for focusing the light to the back focal plane of the OL. The TS allows one to switch between TIRF and epi-illumination. The excitation light reflects off of the DM toward the sample. The detected fluorescence from the sample passes through the DM and the EF. The light is relayed toward the EMCCD, passing through the CL for 3D imaging and a multichannel detection device for multireporter imaging. A focus lock is shown as a separate pathway.

Ar–Kr gas laser, for example, provide several visible and NIR wavelengths at high output power (>100 mW) from a single source, but have large operating power requirements, high maintenance demands, and can be noisy.

There are two general considerations when choosing lasers: the wavelength and output power. The wavelength should be chosen to match the absorption peak of the fluorescent probe for efficient photon absorption. The laser power, and ultimately the laser intensity at the sample, will determine the switching kinetics of the probes that are used. For imaging and switching probes to a dark state, stronger powers are typically required for faster switching speeds. As an example, for 60 Hz imaging of Alexa 647 photoswitching on a 256×256 pixel EMCCD camera ($45\ \mu m \times 45\ \mu m$ field of view), $\sim 2\ kW/cm^2$ of laser intensity can be used. Assuming a system efficiency of 33%, this corresponds to ~ 50 mW of power at the sample from a ~ 150 mW laser. It is generally recommended, if possible, to use imaging intensities of ~ 1–$3\ kW/cm^2$ for the highest signal to noise for most probes. Activation lasers, on the other hand, can be used at much lower intensities, ~10–1000-fold less than that of the imaging lasers. Activation lasers with ~10 mW or more power are preferred to allow for the full dynamic range of activation. Recommendations for laser sources are given in Table 24.2.

Table 24.2 Laser sources used for different STORM probes

Probe(s)	Laser	Vendor	Gas or solid-state?	λ (nm)	Power (mW)
Alexa 647/Cy5 (imaging)	Innova 70C	Coherent	Gas	647	150
	Visible fiber	MPB communications	Solid-state	647	200–1500
	Diode-pumped	Crystalaser	Solid-state	656	50–300
Alexa 750/DyLight 750/Cy7 (imaging)	Innova 302C	Evergreen	Gas	752	150
	Tapered amplifier	Toptica	Solid-state	758	1000
Atto 488/Alexa 488 (imaging), Cy2 (activation), mEos2/PA-mCherry (preactivated)	Sapphire	Coherent	Solid-state	488	10–500
	Innova 70C	Coherent	Gas	488	200
mEos2/PA-mCherry (imaging), Cy3 (activation)	Visible fiber	MPB communications	Solid-state	560	200–2000
	Sapphire	Coherent	Solid-state	561	50–200
	Innova 70C	Coherent	Gas	568	50
Direct activation, Alexa 405 (activation)	CUBE	Coherent	Solid-state	405	100

24.3.1.2 Intensity and temporal modulation

Often during an experiment, one will need to adjust the laser power and exposure independently. This can be performed in two ways. The first way uses mechanical shutters with neutral density (ND) filters and polarization optics for each laser line. Shutters, from vendors such as Uniblitz, are simple to implement, but relatively slow with a maximum switching speed of just a few hundred Hertz. ND filters provide coarse manual power control and polarization optics (half-wave plate combined with a polarizing beam splitter) provide finer manual tuning. The second option, and recommended one, is to use an acousto-optic tunable filter (AOTF). The AOTF, from vendors such as Crystal Technology, provides both fast (MHz) temporal modulation and a high dynamic range for computer-controlled intensity adjustment. AOTFs are generally more complicated to implement and have a limited bandwidth. Some lasers, such as the 405 nm CUBE laser, use internal modulation.

24.3.1.3 Illumination schemes

The most common illumination scheme uses total internal reflection fluorescence (TIRF)/epifluorescence. A versatile setup allows for simple switching between TIRF and epi-illumination. For samples that are imaged close to the optical surface, TIRF can be used to enable high signal to noise and maximum laser intensity. Alternatively, oblique incidence between TIRF and epi-illumination can be used for samples that are <5 μm in thickness to allow for moderate rejection of out-of-focus fluorescence. Imaging at higher depths requires epi-illumination. Alternatively, two-photon (York, Ghitani, Vaziri, Davidson, & Shroff, 2011) or light-sheet illumination (Cella Zanacchi et al., 2011) schemes can be used.

24.3.2 Microscope

24.3.2.1 Microscope body

An inverted fluorescence microscope is the easiest frame to use for a STORM setup. Commercial inverted frames such as the Olympus IX-71 and Nikon TiU are good options.

24.3.2.2 Dichroic mirrors and emission filters

The dichroic mirrors and emission filters should be chosen carefully based on the selected probes as well as the available laser sources. Typically, dichroics used for STORM reflect and transmit several wavelengths with high efficiency. For most single-color or multiactivator imaging, extended reflectivity dichroics with high transmission efficiency ($>95\%$) of the probe emission and a highly reflective ($>95\%$) bandwidth for efficient reflection of the imaging and activation lasers can be used. For multireporter STORM, custom polychroic mirrors are used that have the reflectivity optimized for the appropriate excitation wavelengths and the passband optimized for the given reporter probes. As laser sources are typically used, excitation filters are generally not required. However, emission filters should be chosen to maximize the passband and to ensure that residual imaging laser light is not

Table 24.3 Dichroics and emitters used for different STORM probes at the corresponding laser wavelengths

Probes	λ (nm)	Dichroic	Emitter	Vendor
Atto 488/Alexa 488	488	T495LP	ET535/50	Chroma
mEos2/PA-mCherry	560	Di01-R561	FF01-617/73	Semrock
Cy5/Alexa 647	647	Z660DCXRU	ET700/75m	Chroma
Alexa 750/DyLight 750/Cy7	758	Q770DCXR	HQ800/60m	Chroma

Each dichroic is also compatible with 405 nm excitation. The dichroic/emitter listed for Cy5/Alexa 647 can be used for multiactivator STORM. For multireporter STORM, custom polychroic mirrors from Chroma can be purchased.

transmitted toward the detector. See Table 24.3 for dichroics and emitters used for different probes at selected excitation wavelengths.

24.3.2.3 Objective lens

When choosing an objective lens, two important considerations are the numerical aperture and the choice of water versus oil immersion. Two objectives with high performance in terms of photon collection and low background for STORM are the Olympus 100× 1.4NA UPlanSApo and Nikon Apo TIRF 1.49NA. For imaging deeper samples, a water immersion objective more closely matches the index of refraction of the aqueous sample, reducing chromatic aberrations. More sophisticated dual-objective geometries with opposing objective lenses have been created either for interferometric 3D imaging (Shtengel et al., 2009) or for increased resolution through higher photon collection and reduced localization errors (Xu et al., 2012).

24.3.3 Detection pathway

24.3.3.1 Camera

The ideal camera for STORM has high-quantum efficiency (QE) and low read noise for efficient single-molecule detection. The current standard is the back-illuminated EMCCD camera, which can achieve ~70–90% QE for wavelengths between ~400 and 800 nm with <1–2 photoelectrons read noise. Vendors include Andor and Hamamatsu. Additional considerations are the imaging speed and the pixel and chip size. For fixed-cell imaging and live-FP imaging, acquisition speeds of >30 Hz for a 45 μm × 45 μm pixel area can be used. For most live-cell imaging of dyes, faster speeds of >200 Hz for a reduced 20 μm × 20 μm pixel area can be used. The final pixel size is chosen to match the SD of the PSF for optimal localization precision (Thompson et al., 2002), which is typically ~150–160 nm. This can be easily achieved when using a 100× magnification objective and an EMCCD with a physical pixel size of 16 μm with no additional magnification. The Andor DU897 (512 × 512 pixels), Andor DU897 ULTRA (512 × 512 pixels), Andor DU887 (512 × 512 pixels), and, for faster imaging speeds, the Andor DU860 (128 × 128

pixels) are reliable options. Note that the DU860 has a larger physical pixel size and may require additional magnification for the optimal final pixel size. CMOS cameras from companies such as Hamamatsu and Andor are emerging as possible replacements to the EMCCD technology. CMOS arrays offer larger fields of view for larger imaging areas, with faster acquisition speeds, and comparable QE to EMCCDs.

24.3.3.2 3D imaging

For astigmatism-based 3D STORM, a cylindrical lens is placed into the detection pathway before the camera. The choice of cylindrical lens focal length is important. A 1-m focal length is a good starting point. Ideally, the lens provides a round, uniform image shape when the molecule is in focus as well as high sensitivity such that the molecule's shape change can be easily detected over a z-range of ± 400 nm (Fig. 24.2A). Cylindrical lenses with focal lengths that are too short often result in nonuniform image shapes, while focal lengths that are too long may have limited sensitivity. The focal length and position of the cylindrical lens in the detection path should be determined empirically.

24.3.3.3 Multichannel detection

For multireporter imaging, a special detection system is often required. In the simplest configuration, one can image each channel with a different dichroic mirror and emission filter, where filters are changed mechanically between imaging of each probe. This approach suffers from difficulties in nanoscale alignment of channels due to mechanical switching of the optical components. A more robust approach is to use a dual-view or quad-view detection system, which can be home-built or purchased from companies such as Photometrics. Channel alignment can then be performed during data analysis (Section 4). Multichannel detection systems with a single laser source and dyes with partially overlapping spectra can be used for ratiometric-type STORM (Shim et al., 2012; Testa et al., 2010).

24.3.4 Focus lock

Maintaining a precise focal position during an experiment can be a challenge due to axial drift between the cover glass of the sample and the objective lens. For 2D imaging, drift reduces the sharpness of the fluorophore images leading to less precise single-molecule localization. For 3D imaging, the z-position will be incorrectly determined. To counter axial drift, a feedback system that maintains the focus, or focus lock, is used. The basic construction is a laser, preferably an IR source such as a 975-nm laser diode from Thorlabs, directed toward the sample in TIRF illumination along a distinct optical path. The laser reflects off of the sample and returns as spatially distinct from the incoming beam. The reflected light is detected using a position-sensitive detector, such as a quadrant photodiode. In the event of axial sample drift, the position of the beam on the detector shifts. To correct for this shift, a feedback control loop instructs either a piezo stage or an objective positioner (Mad City Labs and Physik Instrumente) to change the z-position until the original

focal position is restored. This maintains the focus to within ~40 nm and additional drift correction is performed during data analysis (Section 4). Focus lock features can also be found on many commercial microscopes, such as the Nikon Perfect Focus.

24.3.5 Computer

Finally, to coordinate the various devices requires a computer with appropriate control software. The general computer requirements are a medium to high-end workstation, such as a Dell with >5 k RPM SATA hard drives that are adequately fast for writing data acquired from the camera. To process many of the incoming and outgoing digital and analogue signals, data acquisition (DAQ) cards from National Instruments can be used. For controlling the instruments, custom software is written in either Python or LabVIEW programming languages. The major software controls are the camera acquisition, the focus lock, and the AOTF or other laser modulation.

24.4 DATA COLLECTION AND ANALYSIS

This section discusses basic data collection procedures for different applications as well as the standard STORM analysis routine. For detailed procedures of specific experimental designs mentioned throughout the chapter, please refer to the relevant references. Additional details on the STORM analysis routine can be found elsewhere (Dempsey, Wang, et al., 2009). A number of more sophisticated analysis routines are also available for improved fitting precision (Laurence & Chromy, 2010; Mortensen, Churchman, Spudich, & Flyvbjerg, 2010), faster processing speeds (Quan et al., 2010; Zhu, Zhang, Elnatan, & Huang, 2012), and higher molecular densities (Holden, Uphoff, & Kapanidis, 2011; Mukamel, Babcock, & Zhuang, 2012). The interested reader can refer to these references for more details.

24.4.1 Data collection

For simplicity, this discussion focuses on cultured cells. A simple cell line to use when possible is either BS-C-1 or Cos7 cells, which are relatively thin (~5–10 μm) when adhered to a glass substrate. Typically, cells are plated at around 50–75% confluency either on coverslips or in LabTek 8-well chambers (Nunc) using #1.5 glass. Prior to imaging, it is assumed that the appropriate imaging solution is added (Table 24.1) and the required laser lines are aligned to the sample using the appropriate dichroics and emission filters (Tables 24.2 and 24.3).

24.4.1.1 Fiducial markers for drift correction

Sample drift from thermal changes and mechanical perturbations that occur during data acquisition will need to be corrected in the final STORM image. Fiducial markers, whose positions can be tracked in x, y, and z, provide a record of the sample

drift during an experiment and are ideal for thinner samples with low localization densities or for live-cell samples. These markers can be 50–200 nm fluorescent beads that will appear in the frames of the STORM movie when immobilized to the surface on which the samples are being imaged. An overly dense field of beads should be avoided as single molecules may not be detectable in the region surrounding the bead.

24.4.1.2 Single-color 2D and 3D imaging

For 3D imaging, a calibration curve should be generated prior to each imaging session, as the individual calibration may change over time. Small (50–200 nm) fluorescent beads visible in the imaging channel are immobilized on a #1.5 glass coverslip at low density such that individual beads are well separated when viewed on the EMCCD camera. With the cylindrical lens in place, the sample is focused such that the images of the individual beads are round and symmetric ($\sim z = 0$). Using the piezo stage or the objective positioner, the sample or objective is scanned over a z-range from -500 to $+500$ nm relative to the $z = 0$ position. During this time, a fluorescence movie of the bead images is collected. The ellipticity of the bead images should change from the x to the y direction over this scanning range. The actual z-position for each frame should also be recorded so that the z-position can be matched to the molecule shape. This step can be repeated two to three times for different fields of view. Creating the calibration curve is discussed in the next section.

Consider a sample labeled with Alexa 647. To search for cells labeled with Alexa 647, the red laser power is turned sufficiently low to prevent photoswitching. Once a cell is chosen, the sample is focused on the desired imaging plane and the focus lock is engaged. Before data acquisition, the camera frame rate and gain should be set. The frame rate should be optimized for the photoswitching speed of the probe such that a single fluorescent switching event occupies $\sim$1–2 frames. The gain should be set to maximize the signal to noise. If a conventional fluorescence image is desired, it can be recorded at this stage. To begin acquisition of the STORM movie, the imaging laser is turned on at high power (see Section 3) to switch molecules to a dark state. For samples with markedly high labeling density, the initial stage of switching the fluorophores to a dark state may require seconds to minutes to reach single-molecule density. As the number of single molecules in the field decreases due to photobleaching, the violet activation laser can be switched on at low power and ramped up slowly over the course of the movie to maintain emitter density. The number of movie frames collected will depend on the imaging target, but is typically in the range of thousands to tens of thousands. For thicker specimens, the sample can be scanned in z to obtain z-sections that are later pieced together during analysis (Huang, Jones, Brandenburg, & Zhuang, 2008).

24.4.1.3 Multicolor imaging

If performing 3D multicolor STORM, a z-calibration movie should be recorded in the same manner described above. For multireporter imaging, however, a set of 3D calibration movies should be acquired for each spectral channel. The focal shift

between color channels due to chromatic aberrations should be noted at this stage and the calibration and imaging be performed by compensating for this shift.

In addition to *z*-calibration, a separate set of position mapping movies need to be recorded when performing multireporter STORM. For proper alignment of two or more channels into a common reference frame, the *x*-, *y*-, and *z*-positions of each channel need to be correctly matched. For example, in the case of two detection channels, fluorescent beads are chosen such that the fluorescence of each bead can be detected in both channels. The beads are immobilized to a glass coverslip at low density as described for *z*-calibration. Tens of movies are recorded for different fields of view. For 3D imaging, tens of movies should be recorded for at least five different *z*-positions, 0, $\pm$250, and $\pm$500 nm. These movies are used to generate a mapping function, described below, that is applied to the data for channel alignment.

For multireporter STORM data acquisition, channels are typically imaged sequentially, from the NIR to blue wavelengths to avoid bleaching by the high power imaging lasers. Each channel is imaged as described for single-color imaging. The time between imaging each channel should be minimized to prevent significant sample drift between channels.

For multiactivator STORM acquisition, consider a two-color experiment using Alexa 405–Alexa 647 and Cy3–Alexa 647 dye pairs. Before beginning data acquisition, a laser sequence is created that has two basic parts, activation and imaging. The laser sequence synchronizes the laser exposures to each camera frame so that color identification can be performed during data analysis. An example sequence would be: one frame of violet activation light, four frames of red imaging light, one frame of green activation light, and four frames of red imaging light. This 10 frame sequence is repeated throughout the course of the experiment. The number of chosen imaging frames depends on the number of frames required to switch Alexa 647 back to the dark state. Due to the intrinsic DC of each probe, however, there will be a fraction of molecules that turn on spontaneously in any given frame. Once the laser sequence is set, STORM acquisition begins. Again, the activation laser power is adjusted to maximize the number of single molecules per frame for each of the two channels.

24.4.1.4 Live-cell imaging

For live-cell imaging, cells are kept at 37 °C in a standard cell incubator up until imaging is performed. It is preferable, when possible, to first find the cells of interest using low laser intensity illumination and record the stage positions using an automated *x*–*y* stage before adding the final imaging buffer. In this way, buffer can be added and the cells imaged immediately, maximizing the window of cell viability. A temperature stabilized microscope stage and objective can be used to maintain temperatures preferred for cell health. Imaging is performed similarly to that described for single-color fixed samples, but with faster frame rates required for higher temporal resolution. Activation needs to be carefully monitored to ensure a uniform distribution of localizations between time slices in the final STORM movie.

24.4.2 Data analysis

This discussion is based on custom analysis software written in programming languages that include IDL, C++, and MATLAB. For commercial instruments, a data analysis software package should be included. There are also open source analysis routines for processing STORM data (Henriques et al., 2010).

24.4.2.1 Peak finding

STORM data consists of a stack of hundreds to thousands of image frames, with each frame being a 2D array of pixel intensities. The first stage in the data analysis is locating the pixel positions of the fluorescent molecules above the background noise. A background value is first computed using a frame with low fluorophore density, where the background equals the median of the pixels in the selected frame. Once the background is determined, a threshold is set as a minimum peak height or number of SDs above the background. The user then tests the chosen threshold on a subset of movie frames to identify peak pixel values above the threshold. The central pixel of each identified position is compared to its surrounding pixels, and the positions in which the central pixel $\geq$ surrounding pixels are selected for further analysis.

24.4.2.2 Gaussian fitting

Peaks identified in each frame are fit with an elliptical Gaussian function, f, to determine the molecule centroid position in the lateral plane as well as the image widths along x and y, which can be used for determining the axial centroid position for 3D imaging (Huang, Wang, et al., 2008). This function is given by:

$$f(x,y) = h \quad \exp\left(-\frac{1}{2}\left(\frac{(x-x_0)^2}{{w_x}^2} + \frac{(y-y_0)^2}{{w_y}^2}\right)\right) + b \tag{24.3}$$

here, h is the peak height, (x_0, y_0) is the lateral centroid position, w_x and w_y are the image widths in x and y, respectively, and b is the background. For 2D imaging, the width parameters, w_x and w_y, can be used to reject molecules that are too wide. For 3D imaging, these parameters are compared to a calibration curve. The calibration curve is generated from the fluorescent bead data described above. The bead images in each frame are fit to an elliptical Gaussian function to determine $w_{x\text{cal}}$ and $w_{y\text{cal}}$. The median value of the widths are determined for each frame and, using the known relative z-position for each frame, a plot of $w_{x\text{cal}}$, $w_{y\text{cal}}$ versus z can be made. The plots are then fit to a defocusing curve:

$$w_{x\,\text{cal},y\,\text{cal}}(z) = w_0\sqrt{1 + \left(\frac{z-c}{d}\right)^2 + A\left(\frac{z-c}{d}\right)^3 + B\left(\frac{z-c}{d}\right)^4} \tag{24.4}$$

where w_0 is the width of the molecule in the focal plane at $z=0$ (where the molecule image is round and symmetric), c is the offset of the molecule from the focal plane at $z=0$, d is the microscope depth, and A and B are the coefficients that account for the non-ideality of the detection optics. A z-position can be assigned to

each fluorescent molecule in the STORM data by minimizing the relative distance of $w_x^{1/2}$ and $w_y^{1/2}$ from the calibration curve. The expression that is minimized is given as:

$$\sqrt{\left(w_x^{1/2} - w_{x\,\mathrm{cal}}^{1/2}\right)^2 + \left(w_y^{1/2} - w_{y\,\mathrm{cal}}^{1/2}\right)^2} \tag{24.5}$$

Last, the effects of focal shift and spherical aberration should be corrected using a linear scaling factor. For a discussion of the effects of spherical aberration on z-position determinations using astigmatism-based imaging, see Huang, Jones, et al., 2008 and Huang, Wang, et al., 2008.

Additional parameters can be determined from the fitted peaks. First, the total counts for each molecule image can be computed as $2\pi w_x w_y h$ and then converted to photons using a camera calibration of analogue-to-digital counts per photoelectron for a given gain setting. Molecules that are localized for multiple consecutive frames and are within one pixel from each other can be linked together into a single on event or trail. The cumulative photons from all frames in the trail can be used to increase the localization precision. Last, other parameters such as the molecule sharpness and roundness can be determined.

24.4.2.3 Displaying the STORM image

The centroid positions can now be rendered as a STORM image. The simplest display is to plot each position as a single marker. Alternatively, each position can be plotted as a Gaussian distribution, whose width is weighted by the number of photons that are collected for the corresponding fluorescent event (see Eq. 24.1). In this case, high photon events are plotted as bright, sharp peaks, and lower photon events are plotted as dim, broad peaks. In the case of 3D STORM, each of the localizations can be assigned a color based on the z-position.

24.4.2.4 Drift correction

Correction of sample drift can be performed at this stage. If fiducial markers were used for data collection, the marker positions for each frame or subset of frames in the movie can be tracked in x, y, and z by Gaussian fitting. The net average displacement of the beads from the start of the movie is then subtracted from each of the STORM localizations. Alternatively, the localizations themselves can be used. In this case, the localizations of the STORM image are subdivided into segments corresponding to different parts of the movie (e.g., the STORM image reconstructed from frames 0–1000, 1001–2000, 2001–3000, etc.) and a cross-correlation function (2D for the x–y dimensions/1D for the z dimension) computed for each window relative to the initial window. The centroid position of the function is determined by Gaussian fitting. The resultant drift versus time trace is interpolated for all movie frames and is then subtracted for each of the STORM localizations.

24.4.2.5 Filtering the STORM image

The STORM image can be filtered to remove false localizations that arise from different sources of noise. The sharpness parameter can be used to remove single pixel camera noise and the roundness parameter can be used in 2D STORM images to reject peaks that are heavily skewed, often arising from overlapping fluorescent molecules in the raw data. Localizations that show exceptionally long trail lengths and higher than expected photon numbers can be rejected, as these sometimes arise from sample dirt. Localizations that show particularly low photon values can also be rejected, as these can often be attributed to cellular autofluorescence that is incorrectly localized. And last, a density filter can be used such that sparse, spurious localizations can be rejected. The basic analysis workflow, from peak finding to filtering the final STORM image, is summarized in Fig. 24.6. Additional analysis steps are needed for multicolor and live-cell imaging applications.

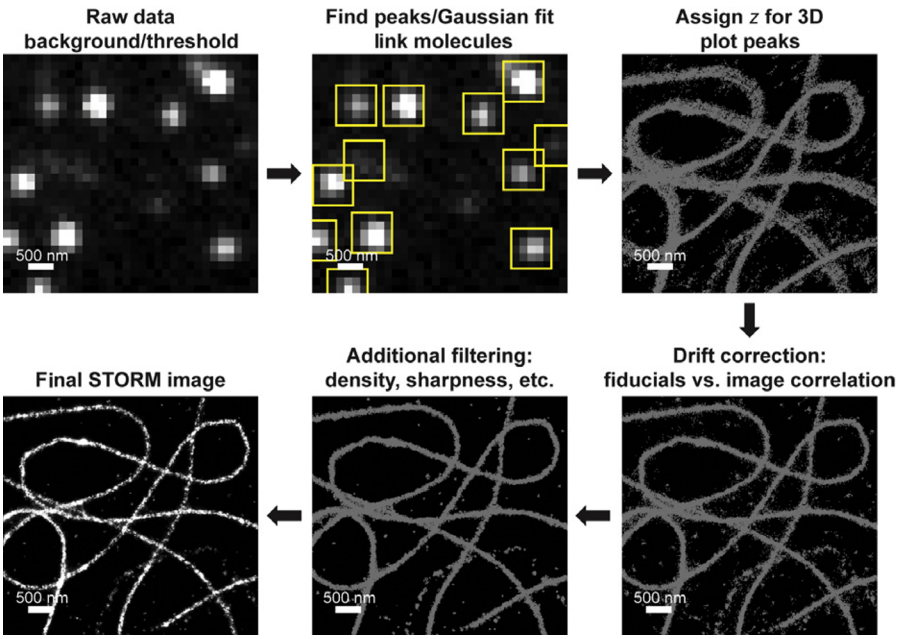

FIGURE 24.6

Analysis workflow for reconstructing a STORM image of microtubules. From the raw data, peaks are found within each frame (indicated by the boxed regions) after determining the background and threshold. The identified peaks are fit with an elliptical Gaussian function and linked across frames. In the case of 3D STORM, the *z*-position is determined using the calibration curve. The peaks can be rendered as a STORM image, in this case using markers for each localization. The drift is corrected using image correlation. Additional filtering of the image can be performed before rendering the final STORM image with a width-weighted Gaussian for each localization.

Image adapted from Vaughan et al. (2013).

24.4.2.6 Multicolor STORM considerations

For multiactivator STORM applications, color assignment must be performed. As mentioned previously, a laser sequence of alternating activation and imaging frames is used such that the laser exposures are synchronized with each frame of the movie. Molecules that are identified in the first frame following an activation frame are assigned to the corresponding color as a specific localization. Molecules that are identified in red frames not following an activation event and whose trail does not originate in the first red frame are considered nonspecific localizations. As mentioned above, crosstalk between channels can lead to incorrect color identification. This crosstalk can be dealt with in part using a statistical cross talk subtraction method (Bates et al., 2012, 2007; Dani, Huang, Bergan, Dulac, & Zhuang, 2010) equivalent to linear unmixing used in conventional fluorescence microscopy (Carlsson & Mossberg, 1992).

For multireporter STORM, channel alignment is needed. Using the bead mapping movies described above, a warping polynomial can be calculated. The polynomial accounts for both linear translations and higher order distortions between channels. Once warping is applied, the spherical aberration correction and drift correction can be performed.

24.4.2.7 Live-cell STORM considerations

When performing live-cell STORM, the final STORM data can be subdivided to create a time series in order to show high-resolution dynamics. In this case, the recorded STORM movie can be parsed into nonoverlapping time segments of a chosen length, and a STORM image reconstructed for each time slice. The choice of segment length will be a major determinant of the achieved spatial resolution. Longer time segments will allow for more localizations per slice, and a higher Nyquist spatial resolution (see Eq. 24.2). However, this comes at the expense of a reduced temporal resolution. Conversely, shorter time segments, and better temporal resolution, can be chosen, but at reduced Nyquist spatial resolution. The choice of time segment will depend on the application and the required spatial resolution.

SUMMARY AND OUTLOOK

This chapter describes the basic guidelines for performing STORM. To summarize, here are some helpful rules to follow. First, use the best performing probe possible, rather than simply the most convenient. Second, preserving ultrastructure is essential to successful sample preparation. Any preparation method that either greatly diminishes labeling density or leads to localization artifacts ultimately compromises the final STORM image. Third, a good STORM setup requires reasonably strong laser sources and high, as possible, photon collection efficiencies. Last, use the simplest experimental design possible that can still answer your question. Often, it is best to begin with single-color, fixed-cell imaging tests before attempting more complex multicolor and live-cell imaging designs.

With this technique, what new biological insights can we hope to gain? Within the past few years, we have seen applications emerging in fields ranging from bacteriology to neuroscience. Super-resolution techniques have revealed previously unseen nanoscale spatial organization and ultrastructure of cellular features, such as synapses (Dani et al., 2010), the actin cytoskeleton (Kanchanawong et al., 2010; Xu et al., 2012; Xu et al., 2013), and the bacterial nucleoid (Wang, Li, Chen, Xie, & Zhuang, 2011). The ability to perform high-resolution, multicolor, 3D imaging also enables the study of protein colocalization with an unprecedented level of detail. And last, the ability to resolve individual components at the nanoscale, such as single proteins (Greenfield et al., 2009) or genes of interest (Lubeck & Cai, 2012), now allows for systems biology-type investigation of networks within single cells. These are just a few of the recent exciting insights of STORM and surely more are on the horizon.

Acknowledgments

A special thank you to Joshua Vaughan, Sara Jones, and Colenso Speer for their critical reading of the manuscript and to Xiaowei Zhuang for financial support.

References

Bates, M., Blosser, T. R., & Zhuang, X. (2005). Short-range spectroscopic ruler based on a single-molecule optical switch. *Physical Review Letters*, *94*(10), 108101.

Bates, M., Dempsey, G. T., Chen, K. H., & Zhuang, X. (2012). Multicolor super-resolution fluorescence imaging via multi-parameter fluorophore detection. *ChemPhysChem*, *13*(1), 99–107.

Bates, M., Huang, B., Dempsey, G. T., & Zhuang, X. (2007). Multicolor super-resolution imaging with photo-switchable fluorescent probes. *Science*, *317*(5845), 1749–1753.

Bates, M., Huang, B., & Zhuang, X. (2008). Super-resolution microscopy by nanoscale localization of photo-switchable fluorescent probes. *Current Opinion in Chemical Biology*, *12*(5), 505–514.

Betzig, E., Patterson, G. H., Sougrat, R., Lindwasser, O. W., Olenych, S., Bonifacino, J. S., et al. (2006). Imaging intracellular fluorescent proteins at nanometer resolution. *Science*, *313*(5793), 1642–1645.

Biteen, J. S., Thompson, M. A., Tselentis, N. K., Bowman, G. R., Shapiro, L., & Moerner, W. E. (2008). Super-resolution imaging in live Caulobacter crescentus cells using photoswitchable EYFP. *Nature Methods*, *5*(11), 947–949.

Brakemann, T., Stiel, A. C., Weber, G., Andresen, M., Testa, I., Grotjohann, T., et al. (2011). A reversibly photoswitchable GFP-like protein with fluorescence excitation decoupled from switching. *Nature Biotechnology*, *29*(10), 942–947.

Carlsson, K., & Mossberg, K. (1992). Reduction of cross-talk between fluorescent labels in scanning laser microscopy. *Journal of Microscopy*, *167*(1), 23–37.

Cella Zanacchi, F., Lavagnino, Z., Perrone Donnorso, M., Del Bue, A., Furia, L., Faretta, M., et al. (2011). Live-cell 3D super-resolution imaging in thick biological samples. *Nature Methods*, *8*(12), 1047–1049.

Crivat, G., & Taraska, J. W. (2012). Imaging proteins inside cells with fluorescent tags. *Trends in Biotechnology*, *30*(1), 8–16.

Dani, A., Huang, B., Bergan, J., Dulac, C., & Zhuang, X. (2010). Superresolution imaging of chemical synapses in the brain. *Neuron*, *68*(5), 843–856.

Dempsey, G. T., Bates, M., Kowtoniuk, W. E., Liu, D. R., Tsien, R. Y., & Zhuang, X. (2009). Photoswitching mechanism of cyanine dyes. *Journal of the American Chemical Society*, *131*(51), 18192–18193.

Dempsey, G. T., Vaughan, J. C., Chen, K. H., Bates, M., & Zhuang, X. (2011). Evaluation of fluorophores for optimal performance in localization-based super-resolution imaging. *Nature Methods*, *8*(12), 1027–1036.

Dempsey, G. T., Wang, W., & Zhuang, X. (2009). Fluorescence imaging at sub-diffraction-limit resolution with stochastic optical reconstruction microscopy. In P. Hinterdorfer & A. M. van Oijen (Eds.), *Handbook of single-molecule biophysics* (pp. 95–127). New York: Springer Science and Business Media.

Fernández-Suárez, M., & Ting, A. Y. (2008). Fluorescent probes for super-resolution imaging in living cells. *Nature Reviews. Molecular Cell Biology*, *9*(12), 929–943.

Fölling, J., Bossi, M., Bock, H., Medda, R., Wurm, C. A., Hein, B., et al. (2008). Fluorescence nanoscopy by ground-state depletion and single-molecule return. *Nature Methods*, *5*(11), 943–945.

Gelles, J., Schnapp, B. J., & Sheetz, M. P. (1988). Tracking kinesin-driven movements with nanometre-scale precision. *Nature*, *331*(6155), 450–453.

Greenfield, D., McEvoy, A. L., Shroff, H., Crooks, G. E., Wingreen, N. S., Betzig, E., et al. (2009). Self-organization of the Escherichia coli chemotaxis network imaged with super-resolution light microscopy. *PLoS Biology*, *7*(6), e1000137.

Grotjohann, T., Testa, I., Leutenegger, M., Bock, H., Urban, N. T., Lavoie-Cardinal, F., et al. (2011). Diffraction-unlimited all-optical imaging and writing with a photochromic GFP. *Nature*, *478*(7368), 204–208.

Gurskaya, N. G., Verkhusha, V. V., Shcheglov, A. S., Staroverov, D. B., Chepurnykh, T. V., Fradkov, A. F., et al. (2006). Engineering of a monomeric green-to-red photoactivatable fluorescent protein induced by blue light. *Nature Biotechnology*, *24*(4), 461–465.

Habuchi, S., Ando, R., Dedecker, P., Verheijen, W., Mizuno, H., Miyawaki, A., et al. (2005). Reversible single-molecule photoswitching in the GFP-like fluorescent protein Dronpa. *Proceedings of the National Academy of Sciences of the United States of America*, *102*(27), 9511–9516.

Habuchi, S., Tsutsui, H., Kochaniak, A. B., Miyawaki, A., & van Oijen, A. M. (2008). mKikGR, a monomeric photoswitchable fluorescent protein. *PLoS One*, *3*(12), e3944.

Heilemann, M., Margeat, E., Kasper, R., Sauer, M., & Tinnefeld, P. (2005). Carbocyanine dyes as efficient reversible single-molecule optical switch. *Journal of the American Chemical Society*, *127*(11), 3801–3806.

Heilemann, M., van de Linde, S., Mukherjee, A., & Sauer, M. (2009). Super-resolution imaging with small organic fluorophores. *Angewandte Chemie International Edition in English*, *48*(37), 6903–6908.

Heilemann, M., van de Linde, S., Schuttpelz, M., Kasper, R., Seefeldt, B., Mukherjee, A., et al. (2008). Subdiffraction-resolution fluorescence imaging with conventional fluorescent probes. *Angewandte Chemie International Edition in English*, *47*(33), 6172–6176.

Hell, S. W. (2007). Far-field optical nanoscopy. *Science*, *316*(5828), 1153–1158.

Henriques, R., Lelek, M., Fornasiero, E. F., Valtorta, F., Zimmer, C., & Mhlanga, M. M. (2010). QuickPALM: 3D real-time photoactivation nanoscopy image processing in ImageJ. *Nature Methods*, *7*(5), 339–340.

Hess, S. T., Girirajan, T. P. K., & Mason, M. D. (2006). Ultra-high resolution imaging by fluorescence photoactivation localization microscopy. *Biophysical Journal*, *91*(11), 4258–4272.

Holden, S. J., Uphoff, S., & Kapanidis, A. N. (2011). DAOSTORM: An algorithm for high-density super-resolution microscopy. *Nature Methods*, *8*(4), 279–280.

Huang, B., Babcock, H., & Zhuang, X. (2010). Breaking the diffraction barrier: Super-resolution imaging of cells. *Cell*, *143*(7), 1047–1058.

Huang, B., Jones, S. A., Brandenburg, B., & Zhuang, X. (2008). Whole-cell 3D STORM reveals interactions between cellular structures with nanometer-scale resolution. *Nature Methods*, *5*(12), 1047–1052.

Huang, B., Wang, W., Bates, M., & Zhuang, X. (2008). Three-dimensional super-resolution imaging by stochastic optical reconstruction microscopy. *Science*, *319*(5864), 810–813.

Jones, S. A., Shim, S. H., He, J., & Zhuang, X. (2011). Fast, three-dimensional super-resolution imaging of live cells. *Nature Methods*, *8*(6), 499–508.

Juette, M. F., Gould, T. J., Lessard, M. D., Mlodzianoski, M. J., Nagpure, B. S., Bennett, B. T., et al. (2008). Three-dimensional sub-100 nm resolution fluorescence microscopy of thick samples. *Nature Methods*, *5*(6), 527–529.

Kanchanawong, P., Shtengel, G., Pasapera, A. M., Ramko, E. B., Davidson, M. W., Hess, H. F., et al. (2010). Nanoscale architecture of integrin-based cell adhesions. *Nature*, *468*(7323), 580–584.

Keppler, A., Kindermann, M., Gendreizig, S., Pick, H., Vogel, H., & Johnsson, K. (2004). Labeling of fusion proteins of O6-alkylguanine-DNA alkyltransferase with small molecules in vivo and in vitro. *Methods*, *32*(4), 437–444.

Laurence, T. A., & Chromy, B. A. (2010). Efficient maximum likelihood estimator fitting of histograms. *Nature Methods*, *7*(5), 338–339.

Lippincott-Schwartz, J., & Patterson, G. H. (2009). Photoactivatable fluorescent proteins for diffraction-limited and super-resolution imaging. *Trends in Cell Biology*, *19*(11), 555–565.

Lubeck, E., & Cai, L. (2012). Single-cell systems biology by super-resolution imaging and combinatorial labeling. *Nature Methods*, *9*(7), 743–748.

McKinney, S. A., Murphy, C. S., Hazelwood, K. L., Davidson, M. W., & Looger, L. L. (2009). A bright and photostable photoconvertible fluorescent protein. *Nature Methods*, *6*(2), 131–133.

Mortensen, K. I., Churchman, L. S., Spudich, J. A., & Flyvbjerg, H. (2010). Optimized localization analysis for single-molecule tracking and super-resolution microscopy. *Nature Methods*, *7*(5), 377–381.

Mukamel, E. A., Babcock, H., & Zhuang, X. (2012). Statistical deconvolution for superresolution fluorescence microscopy. *Biophysical Journal*, *102*(10), 2391–2400.

Patterson, G. H., & Lippincott-Schwartz, J. (2002). A photoactivatable GFP for selective photolabeling of proteins and cells. *Science*, *297*(5588), 1873–1877.

Pavani, S. R., Thompson, M. A., Biteen, J. S., Lord, S. J., Liu, N., Twieg, R. J., et al. (2009). Three-dimensional, single-molecule fluorescence imaging beyond the diffraction limit by using a double-helix point spread function. *Proceedings of the National Academy of Sciences of the United States of America*, *106*(9), 2995–2999.

Quan, T. W., Li, P. C., Long, F., Zeng, S. Q., Luo, Q. M., Hedde, P. N., et al. (2010). Ultra-fast, high-precision image analysis for localization-based super resolution microscopy. *Optics Express*, *18*(11), 11867–11876.

Ries, J., Kaplan, C., Platonova, E., Eghlidi, H., & Ewers, H. (2012). A simple, versatile method for GFP-based super-resolution microscopy via nanobodies. *Nature Methods*, *9*(6), 582–584.

Rust, M. J., Bates, M., & Zhuang, X. (2006). Sub-diffraction-limit imaging by stochastic optical reconstruction microscopy (STORM). *Nature Methods*, *3*(10), 793–795.

Schnell, U., Dijk, F., Sjollema, K. A., & Giepmans, B. N. (2012). Immunolabeling artifacts and the need for live-cell imaging. *Nature Methods*, *9*(2), 152–158.

Shim, S. H., Xia, C., Zhong, G., Babcock, H. P., Vaughan, J. C., Huang, B., et al. (2012). Super-resolution fluorescence imaging of organelles in live cells with photoswitchable membrane probes. *Proceedings of the National Academy of Sciences of the United States of America*, *109*(35), 13978–13983.

Shroff, H., Galbraith, C. G., Galbraith, J. A., & Betzig, E. (2008). Live-cell photoactivated localization microscopy of nanoscale adhesion dynamics. *Nature Methods*, *5*(5), 417–423.

Shroff, H., Galbraith, C. G., Galbraith, J. A., White, H., Gillette, J., Olenych, S., et al. (2007). Dual-color superresolution imaging of genetically expressed probes within individual adhesion complexes. *Proceedings of the National Academy of Sciences of the United States of America*, *104*(51), 20308–20313.

Shtengel, G., Galbraith, J. A., Galbraith, C. G., Lippincott-Schwartz, J., Gillette, J. M., Manley, S., et al. (2009). Interferometric fluorescent super-resolution microscopy resolves 3D cellular ultrastructure. *Proceedings of the National Academy of Sciences of the United States of America*, *106*(9), 3125–3130.

Subach, F. V., Patterson, G. H., Manley, S., Gillette, J. M., Lippincott-Schwartz, J., & Verkhusha, V. V. (2009). Photoactivatable mCherry for high-resolution two-color fluorescence microscopy. *Nature Methods*, *6*(2), 153–159.

Testa, I., Wurm, C. A., Medda, R., Rothermel, E., von Middendorf, C., Fölling, J., et al. (2010). Multicolor fluorescence nanoscopy in fixed and living cells by exciting conventional fluorophores with a single wavelength. *Biophysical Journal*, *99*(8), 2686–2694.

Thompson, R. E., Larson, D. R., & Webb, W. W. (2002). Precise nanometer localization analysis for individual fluorescent probes. *Biophysical Journal*, *82*(5), 2775–2783.

Vaughan, J. C., Dempsey, G. T., Sun, E., & Zhuang, X. (2013). Phosphine-quenching of cyanine dyes as a versatile tool for fluorescence microscopy. *Journal of the American Chemical Society*, *135*(4), 1197–1200.

Vaughan, J. C., Jia, S., & Zhuang, X. (2012). Ultrabright photoactivatable fluorophores created by reductive caging. *Nature Methods*, *9*(12), 1181–1184.

Vogelsang, J., Kasper, R., Steinhauer, C., Person, B., Heilemann, M., Sauer, M., et al. (2008). A reducing and oxidizing system minimizes photobleaching and blinking of fluorescent dyes. *Angewandte Chemie International Edition in English*, *47*(29), 5465–5469.

Wang, W., Li, G. W., Chen, C., Xie, X. S., & Zhuang, X. (2011). Chromosome organization by a nucleoid-associated protein in live bacteria. *Science*, *333*(6048), 1445–1449.

Wiedenmann, J., Ivanchenko, S., Oswald, F., Schmitt, F., Röcker, C., Salih, A., et al. (2004). EosFP, a fluorescent marker protein with UV-inducible green-to-red fluorescence conversion. *Proceedings of the National Academy of Sciences of the United States of America*, *101*(45), 15905–15910.

Wombacher, R., Heidbreder, M., van de Linde, S., Sheetz, M. P., Heilemann, M., Cornish, V. W., et al. (2010). Live-cell super-resolution imaging with trimethoprim conjugates. *Nature Methods*, *7*(9), 717–719.

Xu, K., Babcock, H. P., & Zhuang, X. (2012). Dual-objective STORM reveals three-dimensional filament organization in the actin cytoskeleton. *Nature Methods*, *9*(2), 185–188.

Xu, K., Zhong, G., & Zhuang, X. (2013). Actin, spectrin, and associated proteins form a periodic cytoskeletal structure in axons. *Science*, *339*(6118), 452–456.

Yildiz, A., Forkey, J. N., McKinney, S. A., Ha, T., Goldman, Y. E., & Selvin, P. R. (2003). Myosin V walks hand-over-hand: Single fluorophore imaging with 1.5-nm localization. *Science*, *300*(5628), 2061–2065.

York, A. G., Ghitani, A., Vaziri, A., Davidson, M. W., & Shroff, H. (2011). Confined activation and subdiffractive localization enables whole-cell PALM with genetically expressed probes. *Nature Methods*, *8*(4), 327–333.

Zhang, M., Chang, H., Zhang, Y., Yu, J., Wu, L., Ji, W., et al. (2012). Rational design of true monomeric and bright photoactivatable fluorescent proteins. *Nature Methods*, *9*(7), 727–729.

Zhu, L., Zhang, W., Elnatan, D., & Huang, B. (2012). Faster STORM using compressed sensing. *Nature Methods*, *9*(7), 721–723.

CHAPTER

Quantitative Ratiometric Imaging of FRET-Biosensors in Living Cells

25

Désirée Spiering[*,†], Jose Javier Bravo-Cordero[*,†], Yasmin Moshfegh[*,†], Veronika Miskolci[*,†], and Louis Hodgson[*,†]

[*]*Department of Anatomy and Structural Biology, Albert Einstein College of Medicine of Yeshiva University, Bronx, New York, USA*

[†]*Gruss Lipper Biophotonics Center, Albert Einstein College of Medicine of Yeshiva University, Bronx, New York, USA*

CHAPTER OUTLINE

Introduction **594**
25.1 Image Processing Methods **596**
25.1.1 "Single-Chain" Systems 596
25.1.1.1 Flatfield Correction (Shading Correction) 597
25.1.1.2 Background Subtraction 599
25.1.1.3 Morphing 600
25.1.1.4 Image Masking 600
25.1.1.5 X–Y *Translational Registration* 601
25.1.1.6 Ratio Calculation 601
25.1.1.7 Photobleach Correction 602
25.1.2 "Dual-Chain" Systems 602
25.1.2.1 Quantitative Bleedthrough Calibration 603
25.1.2.2 Ratio Versus $[FRET]_{Corr}$ 603
25.1.2.3 Photobleach Correction 603
25.2 Imaging Considerations and Caveats, Pitfalls **604**
25.2.1 How to Keep Cells Happy 604
25.2.2 Minimizing Photobleaching 604
25.2.3 Motion Artifacts 605
25.2.4 Thickness Artifacts 605
Summary **607**
Acknowledgments **607**
References **607**

Methods in Cell Biology, Volume 114
Copyright © 2013 Elsevier Inc. All rights reserved.
ISSN 0091-679X
http://dx.doi.org/10.1016/B978-0-12-407761-4.00025-7

Abstract

Biosensors based on FRET have been useful in deciphering the dynamics of protein activation events in living cells at subcellular resolutions and in time scales of seconds. These new systems allow observations of dynamic processes which were not possible previously using more traditional biochemical and cell biological approaches. The image data sets obtained from these sensors require careful processing in order to represent the actual protein activation events. Here, we will cover the basic approaches useful for processing the raw image data sets into relativistic ratiometric measurements, capable of depicting relative differences in the protein activation states within a single cell. We will discuss in detail the approaches for genetically encoded, single-chain biosensor systems based on FRET, as well as those that are based on intermolecular, dual-chain design. Additionally, the same analysis can be utilized for biosensor systems using solvatochromic dyes (Nalbant, Hodgson, Kraynov, Toutchkine, & Hahn, 2004), useful for detection of endogenous protein activation states.

INTRODUCTION

Fluorescent biosensors based on the Forster resonance energy transfer (FRET) have now been established as powerful tools, allowing direct observations of protein activation states (posttranslational modification, comformational change, or protein–protein interactions) in living cells in their native environment (Hahn & Toutchkine, 2002; Honda et al., 2001; Itoh et al., 2002; Machacek et al., 2009; Miyawaki & Tsien, 2000; Nakamura, Kurokawa, Kiyokawa, & Matsuda, 2006; Nalbant, Hodgson, Kraynov, Toutchkine, & Hahn, 2004; Pertz, Hodgson, Klemke, & Hahn, 2006; Ting, Kain, Klemke, & Tsien, 2001; Zaccolo et al., 2000; Zhang, Ma, Taylor, & Tsien, 2001). The term "biosensor" implies that it is capable of reporting information other than the bulk localization changes of the protein, usually through molecular engineering, which are typically not possible to observe using traditional biochemical and cell biological methods. A few examples of these sensors are shown in Fig. 25.1. The primary detection modality is via the FRET, where the changes in the distance between the FRET donor and acceptor molecules as well as the angle of dipole coupling can significantly impact the amount of FRET transfer that occurs in a given state of the biosensor (Hodgson, Pertz, & Hahn, 2008; Hodgson, Shen, & Hahn, 2010; Lakowicz, 1983; Lankawoicz, 1986; Piston & Kremers, 2007; Stryer, 1978; Stryer & Haugland, 1967). Therefore, the "optimization" of the total FRET change as a function of all-on versus the all-off conditions of the biosensor in a cell constitutes the major developmental effort of these molecular constructs (Hodgson et al., 2008). Once properly optimized, however, the biosensors can reveal in real time and at subcellular spatial resolutions, the posttranslational modification states (or, activation states, binding events, etc.) of the protein of interest, which is not possible to do using traditional approaches. In order to harness their power, appropriate microscopy techniques and image processing approaches become critical components to obtaining meaningful readouts. Here, we outline the

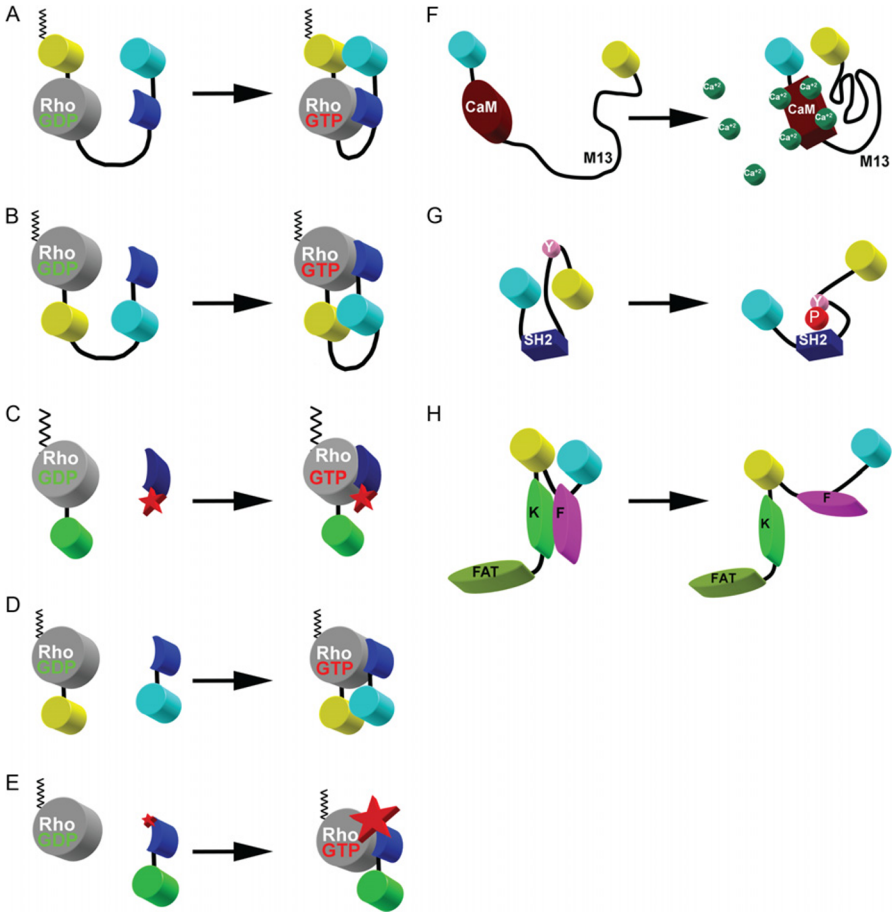

FIGURE 25.1

Schematic drawings of some of the available types of biosensors which the image processing techniques presented here can be used. (A) Rho family GTPase biosensors in which the FRET donor and acceptor are placed on the N-/C-terminals of the molecule (Itoh et al., 2002; Kurokawa & Matsuda, 2005). This design does not allow for the correct interaction with the upstream guanine nucleotide dissociation inhibitor (GDI). (B) Rho family GTPase biosensor in which the full-length Rho GTPase is placed on the C-terminus, maintaining the correct C-terminal posttranslational modification of the GTPase thereby allowing for the correct GTPase–GDI interaction (Pertz et al., 2006). (C) The original Rac1 FLAIR biosensor, in which the binding of the small binding domain labeled with Alexa-546 to the activated, EGFP-labeled GTPase (bound to GTP), resulted in FRET between the EGFP (donor) and Alexa-546 (acceptor) (Kraynov et al., 2000). (D) Similar to (C) but fully genetically encoded version utilizing the FRET between ECFP and EYFP (Machacek et al., 2009). (E) MeroCBD biosensor for detecting the activity of endogenous, unlabeled GTPase (Nalbant et al., 2004). Solvent-polarity sensing dye is attached to a small binding domain (also labeled with EGFP).

(Continued)

basic image processing methods, useful for single-chain as well as dual-chain versions of the ratiometric FRET-biosensors. The approaches we outline here will give relativistic readouts of FRET ratios in cells expressing the biosensor. The ratiometric measurements of a system in which the FRET donor and acceptor halves are placed within single-chain system (Fig. 25.1A, B, and F–H) allows for the use of FRET/CFP ratio as a simple estimate of the relative FRET, as the concentrations of the FRET donors and acceptors are stoichiometrically equimolar everywhere within a cell (Miyawaki et al., 1997). However, it is important to note that the resulting ratiometric data is nonlinear in relation to the FRET efficiency changes; therefore, such data will be useful for observing the relativistic differences in FRET ratio within a single cell, or in an experiment performed under the same conditions using the same optical microscopy system. There are more rigorous methods available (Bastiaens & Squire, 1999; Hinde, Digman, Welch, Hahn, & Gratton, 2012; Zal & Gascoigne, 2004) in which the microscopy modality as well as the processing are performed in terms of the efficiency of FRET, that is, involving fluorescence lifetime imaging, etc. However, for routine purposes and for relativistic comparison purposes, the traditional ratiometric approach is still highly efficient and useful, especially if correct assumptions are made and users are aware of its limitations as well as its capabilities.

25.1 IMAGE PROCESSING METHODS

25.1.1 "Single-chain" systems

Ratiometric biosensor systems of the "single-chain" design broadly includes: (1) single-chain fluorescent protein–FRET-based systems, (2) sensors that require ratiometric calculations in which the intensity modulating fluorophore signal is ratioed against a constant intensity fluorophore signal, wherein both fluorophores are attached on the same molecule, or (3) single fluorophore that modulates the fluorescence emission intensities at two different emission wavelengths which are then

Figure 25.1—Cont'd Upon binding to active GTPase, the local solvent polarity changes due to the binding event, thus the fluorescence emission intensity from the dye changes. By monitoring the ratio between the dye intensity modulation and the EGFP emission, the activation states of the endogenous GTPase can be observed. (F) Cameleon biosensor for calcium ion concentration measurements (Miyawaki et al., 1997). (G) Substrate-based biosensor for focal adhesion kinase (FAK) (Seong et al., 2011). This biosensor uses a substrate which the activated FAK will phosphorylate, and this changes the conformation within the molecule to affect FRET. The substrate-based biosensor detects the local "balance" of the upstream kinase and phosphatase activities; thus, they are not strictly measuring the activities of kinases. (H) FAK biosensor that detects the activation of the molecule through sensing the conformational change (Cai et al., 2008). In the strict sense, this biosensor detects the "activation" of FAK through sensing the exposure of the kinase domain ("K").

ratioed. For the purpose of this section, the procedure for the CFP–YFP FRET biosensor based on single-chain design will be described. The extension of the approach to these other systems should be straightforward.

25.1.1.1 Flatfield correction (shading correction)

We routinely use an arc-lamp-based illumination system for the widefield imaging of FRET-biosensors (Hodgson, Nalbant, Shen, & Hahn, 2006; Spiering & Hodgson, 2012). In this case, the arc-lamp condenser and fluorescence illumination train introduce shading effects in the field of view (FOV) where the center of the FOV is brighter than the periphery of the FOV (Fig. 25.2). This effect can be minimized by a careful adjustment of the condenser focus setting, or the use of other illumination modes including solid-state and laser illumination systems coupled to correctly configured beam expanders. Therefore, it is advisable to assess the extent of the field illumination unevenness prior to initiating any FRET biosensor imaging by simply mounting a chamber containing some imaging media and take a set of images of the blank FOV. In order to assess the extent of the field unevenness, make a linescan measurement diagonally across the FOV and observe the resulting intensity values across the FOV (Fig. 25.2). Any deviations from uniformity require the correction outlined here. The basic equation for the flatfield corrections is:

$$[\mathrm{IMAGE}]_{\mathrm{Corrected}} = \frac{\left\{[\mathrm{IMAGE}]_{\mathrm{Raw}} - [\mathrm{DC}] + \overline{[\mathrm{DC}]}\right\} \times [\mathrm{SF}]}{\left\{[\mathrm{SHADE}] - [\mathrm{DC}] + \overline{[\mathrm{DC}]}\right\}}. \tag{25.1}$$

The three components necessary for this correction are: (1) Data image stack for the CFP and FRET ([IMAGE]), (2) corresponding shading images in CFP and FRET ([SHADE]), (3) dark-current image set for the exposure times used in CFP

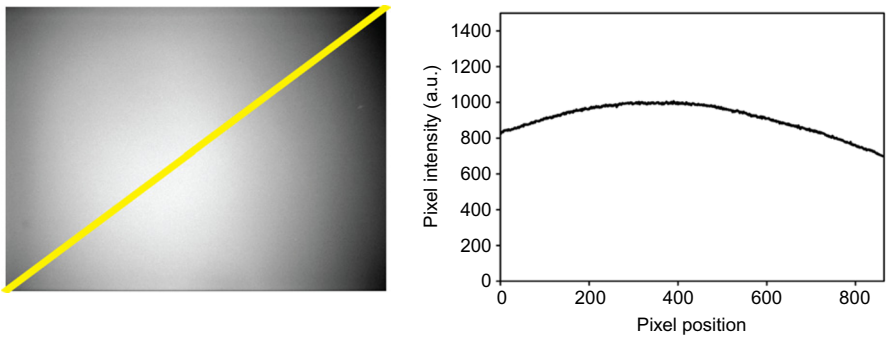

FIGURE 25.2

Shading present in the field of view. (Left) An empty field of view is imaged, and the linescan measurement (yellow diagonal line) line is shown. (Right) The corresponding linescan measurement of the empty field of view.

and FRET image acquisitions ([DC]; $\overline{[DC]}$ denotes average pixel intensity value of the [DC] image used), and (4) a scaling factor ([SF]) to account for the floating point considerations. Following the calculation of the flatfield correction, a 3×3 median filter is applied in order to eliminate any hot pixels.

25.1.1.1.1 Shading images

Shading images are images of the blank FOV taken at *identical* conditions and settings (neutral density filters used, camera exposure times, and the CCD sensor mode used) as the actual data sets. Things that can directly affect the shading within an FOV are the focus location, relative amount of the lens immersion oil used and the volume and the type of media that exists above the specimen plane. All of these factors contribute to creating and affecting the specific shading of the data images in widefield microscopy and all must be accounted for. Here, a good practice is to keep a log notebook of the excitation neutral density filters and exposure times used for each time-lapse data set taken for CFP and FRET as one proceeds with the imaging experiments throughout the day. Another key point is the use of frame averaging when obtaining the shading images. We routinely take 20 FOVs and average in order to produce one shading correction image. This greatly reduces the stochastic noise (Hodgson et al., 2006).

25.1.1.1.2 Dark-current correction images

Dark-current correction images are taken at the exact exposure times used for each of CFP and FRET, but without any illumination. When obtaining these images, it is best to completely shut out the illumination paths; we routinely manually close off the fluorescence illumination train by using a sliding manual shutter and flipping the bottom camera port mirror to prevent any stray light entry into the CCD. These images correct for the thermal noise and readout noise associated with the CCD camera operation. The frame averaging is useful, and we routinely take 20 FOVs and average to produce the dark-current correction images for CFP and FRET. When Eq. (25.1) is used, the average pixel value of the dark-current correction image is added back as a single constant to both the raw data image and the shading image after the dark-current subtraction. This is done in order to maintain the pedestal intensity value within the FOV the same as prior to the operation.

25.1.1.1.3 Scaling factor

Scaling factor is used to account for the floating point calculation operation. Two things that determine the choice of the scaling factor are: (1) the typical intensity differences between the average intensity value within the shading image compared to the brightest intensity pixels in the data image and (2) the 16-bit depth in which the computations and the resulting tiff images must reside. The first point depends on the bit depth of the digitizer used in the CCD, whether this is 12, 14, or 16 bits, on the amount of autofluorescence in the medium, and the expression levels of the biosensor. Typically, the maximum possible value within the appropriate bit range is divided by the average intensity value of the shading image. This value in our system is usually in the order of 10–20. Therefore, in order to stay within the 16-bit space,

the scaling factor of 1000 is chosen. Once this value is set, one should be consistent for both the CFP and FRET data sets.

25.1.1.2 Background subtraction

Flatfield corrected, median-filtered images are then processed for background subtraction. Because of the flatfield correction, the cell-free areas within the FOV should have more or less uniform intensity level (Fig. 25.3). Select a small area away from the cell where there is no background debris and measure the average intensity value within such an area. Here, it is important to scroll through the time-lapse stack of images to make sure that no debris or cell protrusions come into the selected region as a function of time. The measured background intensity values will be different from frame to frame in a time-lapse series (due possibly to photobleaching of the autofluorescence in the imaging media, addition of stimulation media, etc.); therefore, it is important to measure the average value at each time point and subtract the

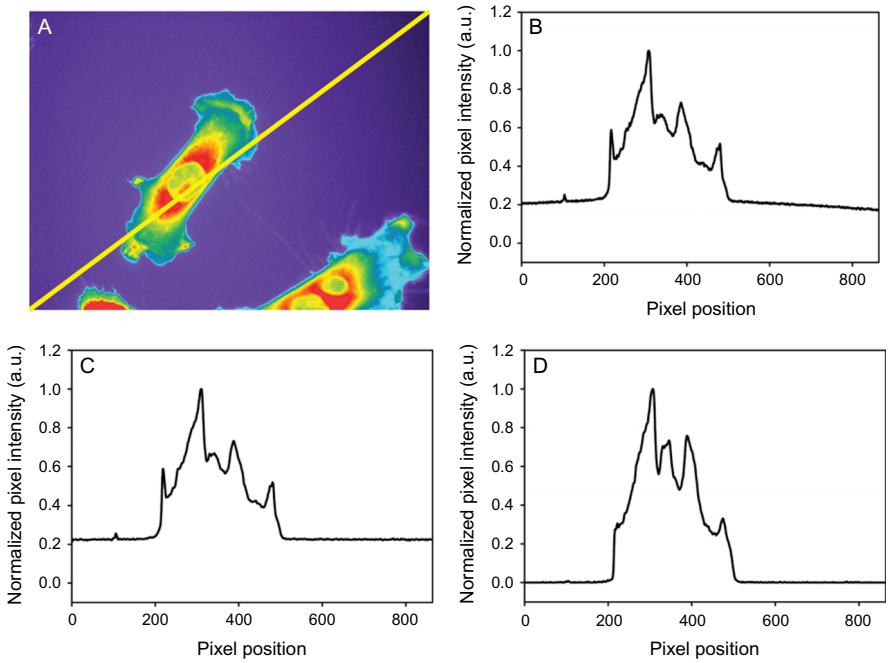

FIGURE 25.3

Effect of the shading correction on the background of images. (A) Raw image of a cell expressing a biosensor is shown. The yellow line corresponds to the linescan measurement location. (B) Linescan measurement of (A). (C) Linescan measurement of (A) after shading correction. (D) Linescan measurement of (A) after shading correction and background subtraction.

appropriate intensity value from each image plane in a time series. This means that one cannot simply measure the background value from the first image plane and subtract such a value from all image planes in a time-lapse series.

25.1.1.3 Morphing

In order to achieve a pixel-by-pixel matching of the CFP and FRET channels of the data set, a careful alignment of the data set is essential. When using multiple cameras to capture simultaneously the CFP, FRET, and any other fluorescence channels (Spiering & Hodgson, 2012), mounting of the cameras assigned to each channel will never be perfect; even the relative magnifications at each camera port could be different and these effects are compounded since different wavelengths of emission channels will impart differential lateral chromatic effects as a function of the location within a FOV. Even if a single camera is used to acquire sequentially CFP and FRET channels, the lateral chromatic dispersion will be dependent on the emission wavelengths so the pixel-by-pixel matching using computational methods is desired. In order to address this, a field of multispectral beads (Tetraspeck beads, Invitrogen) is used to produce a set of calibration images in CFP and FRET channels. Such calibration images are used to construct a set of morphing filters using programs such as Matlab, to result in pixel-by-pixel matching accuracy of sub-1/10th of a pixel (Hodgson et al., 2010). Particle tracking (Crocker & Grier, 1996) based morphing algorithm for Matlab which is useful for achieving this can be provided through contacting the authors of this chapter.

25.1.1.4 Image masking

In preparation for ratio calculations, the CFP and FRET image sets should be intensity thresholded and masked. The basic idea of masking is to set the regions that are outside of the cell uniformly zero, as the background subtraction of a single averaged value from every pixel in the FOV does not necessarily produce uniformly zero values outside the cell due to stochastic nature of the intensity distribution within the background regions. If the background regions are not masked to set equal to zero, noisy appearance in the ratio will be a problem (Fig. 25.4). Because of the changing total fluorescent intensity levels inside the cell as a function of time due primarily to photobleaching, images at the beginning of the time-lapse series are usually much brighter than those at the end of a time series. If a single intensity threshold value is used to produce the mask, it is likely to result in either overselection or underselection of cell area depending on how the thresholding is performed. To overcome this, we typically equalize the average intensity levels in a whole time series using image processing software, and use the equalized time series to threshold in order to produce the binary mask with the least amount of impact from the changing intensity levels due to photobleaching. Once such threshold value is determined, then a binary mask (pixel values inside the cell area is one and outside is zero) is produced for every time point in the time-lapse series. This series of binary masks is then multiplied into the CFP and FRET image sets to produce the masked CFP and FRET image sets. Here, it is important to produce the binary masks independently for CFP and FRET. Alternatively, an automated thresholding and masking (segmentation) approach is also available (Shen et al., 2006).

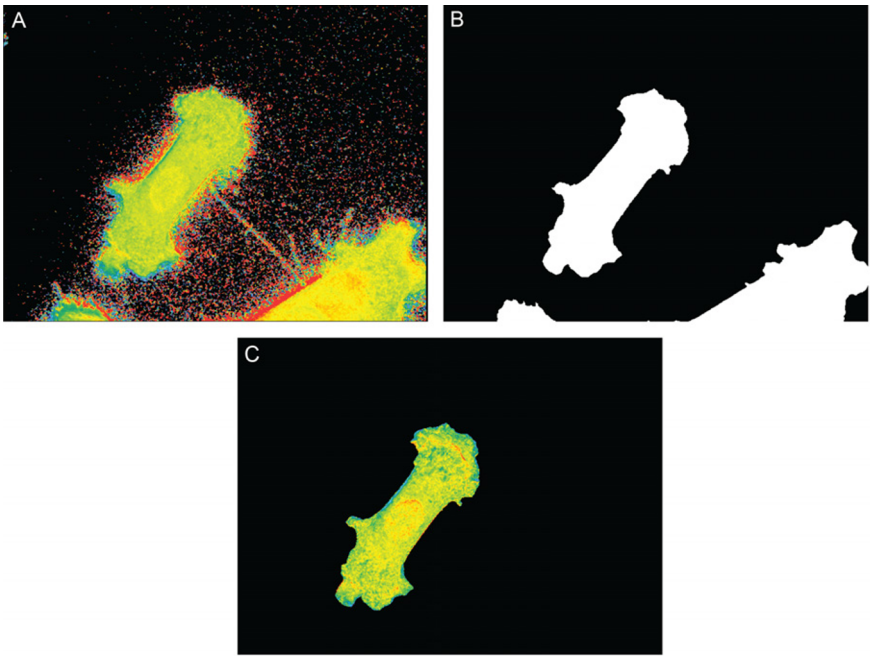

FIGURE 25.4

Effect of masking on the final ratio image. (A) Ratio image without masking. (B) Binary mask created using the intensity-based thresholding. (C) Ratio image after applying the binary mask to the data.

25.1.1.5 X–Y translational registration

We apply the *X–Y* subpixel translational registration to morphed and masked CFP and FRET image sets to correct for any image centering differences. This stems from the mounting of the two cameras used for simultaneous acquisition being not perfectly centered in the FOV with respect to each other. In situations, where the morphing-based registration may not be critical (single camera used, dual-excitation single-emission dye used, emission filters placed within the infinity space of the microscope), *X–Y* subpixel registration may also be sufficient in some cases. We use a previously published approach to achieve subpixel registration using an automated algorithm, available through contacting the authors of this chapter (Shen et al., 2006). Since this method is based on the optimization of the global cross-correlation coefficient between the two masked images, it works the best if there is only one cell within the FOV to attain the matching between two image sets.

25.1.1.6 Ratio calculation

Once the registration is complete, FRET image is divided by the CFP image. Here again, the floating point operation consideration is necessary. We previously showed the effect of the scaling factor on the resulting ratio histogram distribution (Hodgson

et al., 2006). Here, the dynamic range of the biosensor response between all-on versus all-off is important to consider when choosing a scaling factor. Our FRET-biosensors typically result in the dynamic range of 1:2–1:25, depending on the design and the construction. Therefore, we routinely use 1000 as the scaling factor to stay within the 16-bit depth.

25.1.1.7 Photobleach correction

The photobleaching effect of the resulting ratio image set depends on the rates of FRET donor and acceptor photobleaching during a time-lapse imaging session. Thus, this effect can be optimized by choosing photostable variants of fluorescent proteins. We have previously reported a method to correct for photobleaching of the Rho family GTPase biosensors during live cell time-lapse imaging (Hodgson et al., 2006). Here, the key point is to recall and to consider carefully the assumptions associated with this approach involving the biexponential fit method that we applied to our Rho GTPase sensors previously (Hodgson et al., 2006). The Rho family GTPases is such that the great majority of the GTPases are kept in an inactive state in complex with GDI, and only less than 5% of the total GTPase is activated at spatially distinct locations at any given time (Del Pozo et al., 2002). It is only possible to assume the biexponential intensity decay model because of this biological feature of the Rho family GTPases; where a great majority of the biosensor will remain in an inactive state and thus bleaching at a constant rate. This allows for a direct measurement of the average intensity change per time in the ratio data to approximate the rate of photobleaching by a biexponential function. When using a fluorescent biosensor other than for the Rho family GTPases, the biological regulation of such molecule must be carefully considered in ordered to determine whether or not this assumption holds.

25.1.2 "Dual-chain" systems

Ratiometric biosensor systems of the "dual-chain" design (i.e., Rac1 and RhoA sensors; Machacek et al., 2009) require additional calibration steps in order to account for the nonequimolar distribution of the FRET donor and acceptor halves of the biosensor components. This involves constructing calibration plots using cells expressing only the CFP or the YFP, and measuring the relative bleedthroughs of each signal into the FRET emission channel upon respective CFP or YFP excitation. The calibration curve is used to determine the amounts of bleedthrough and these values are then subtracted from the raw FRET intensity data to produce the corrected FRET images. Because of the need for such calibrations due to the nonequimolar distribution of the sensor halves, we image in sequence a set of CFP, FRET, and YFP images at every time point of a time-lapse series. The same calibrations outlined here can be applied to single-chain biosensor data sets to reduce the equimolar-associated assumptions or in cases if other analysis techniques including the efficiency-FRET (Zal & Gascoigne, 2004) are required so as to translate the measured relative ratios into absolute FRET transfer efficiencies.

25.1.2.1 Quantitative bleedthrough calibration

Because of the nonequimolar distribution of the FRET donor and acceptor halves of the biosensor in a given location within a cell, one must account for the amounts of bleedthroughs.

a. CFP bleedthrough into the FRET channel: After the completion of imaging, calibration is performed using cell expressing only CFP. Here, images are taken at identical conditions as the actual imaging experiments, and the CFP and the FRET channel emissions are measured.

b. YFP excitation by CFP excitation light: Here, calibration is performed using cells expressing only YFP. Images are taken at identical conditions as the actual imaging experiments, and the CFP-excited FRET channel emission is measured followed by YFP channel direct excitation and emission. The YFP emission into the CFP emission channel is usually negligible so we do not carry this quantity over in our calculations.

c. Once the above set of images are obtained, they are processed (dark-current correction, flatfield correction, and background subtraction), and the pixel-by-pixel measurements are made to correlate between: (1) CFP calibration: FRET channel intensity per CFP channel intensity and (2) YFP calibration: FRET channel intensity per YFP channel intensity. These correlations are then linearly regressed through the origin (0,0) and the slope of the corresponding regression function becomes the correction factor with which to determine the bleedthroughs for each channel, according to the following equation:

$$[\mathrm{FRET}]_{\mathrm{Corr}} = [\mathrm{FRET}]_{\mathrm{Raw}} - \alpha[\mathrm{CFP}] - \beta[\mathrm{YFP}] \tag{25.2}$$

where α is the slope of the CFP calibration correlation and β is the slope of the YFP calibration correlation. Methods to automate this process are available.

25.1.2.2 Ratio versus $[\mathrm{FRET}]_{\mathrm{Corr}}$

When bleedthrough corrections are made as above in Section 1.2.1, the resulting $[\mathrm{FRET}]_{\mathrm{Corr}}$ can be used to study the total FRET occurring in a cell. When this is ratioed against CFP and the CFP is attached to the GTPase, then the ratio is indicative of the relative FRET per localization of the GTPase. Both of these measures are useful in interpreting biological readouts such as whether the accumulation of $[\mathrm{FRET}]_{\mathrm{Corr}}$ is due to per GTPase activity levels being elevated (higher Ratio) or the spatial accumulation of modestly activated GTPase (lower Ratio) may be contributing to the increased $[\mathrm{FRET}]_{\mathrm{Corr}}$ (in the absence of elevated Ratio). These parameters should both be used to interpret the observed activation patterns.

25.1.2.3 Photobleach correction

A similar assumption as the single-chain sensor case applies here for the GTPase biosensor. Other types of sensors must be carefully considered in terms of the biological function so as to determine whether or not the observed photobleach rate can be attributed to majority of inactive material passively bleaching. The biexponential

correction should be directly applicable to $[FRET]_{Corr}$; however, correction of the Ratio ($[FRET]_{Corr}/[CFP]$) requires additional considerations. The Ratio is based on the following (Vanderklish et al., 2000):

$$R = \frac{[FRET]_{Corr}}{[CFP]} = \frac{[FRET]_{Raw} - \alpha[CFP] - \beta[YFP]}{[CFP]} \tag{25.3}$$

Rearranging Eq. (25.3) yields:

$$R = \frac{[FRET]_{Raw}}{[CFP]} - \beta\frac{[YFP]}{[CFP]} - \alpha \tag{25.4}$$

In Eq. (25.4), α is a constant therefore simply measuring the biexponential decay pattern of the $[FRET]_{Raw}/[CFP]$ and $[YFP]/[CFP]$ parameters, correcting them based on the fits, and linearly combining the corrected fractions with the appropriate α and β parameters, one can obtain the photobleach corrected Ratio. Algorithm to automate this is available.

25.2 IMAGING CONSIDERATIONS AND CAVEATS, PITFALLS

25.2.1 How to keep cells happy

The key to keeping cells alive and happy during imaging is rigorous light management. In order to avoid photodamaging cells, it is best to select the minimal intensity of excitation light to achieve the desired signal saturation in the CCD dynamic range (80% saturation of the dynamic range of the CCD) within reasonable exposure times. We routinely place neutral density filters in the excitation light path to significantly attenuate the light intensity. The usual target for the exposure times for our biosensor is approximately 600–1000 ms to achieve 80% saturation of the CCD dynamic range. We find that to achieve the same level of signal saturation levels, longer exposures at lower light intensity tend to minimize photodamage compared to rapid exposures using high intensity excitation light. This is due to the difference in the rate of reactive oxygen species production between the two conditions and in the slower situation, cells appear to process these oxygen radicals more effectively (Hodgson et al., 2010).

25.2.2 Minimizing photobleaching

Photobleaching of fluorescent material stems from the production of reactive oxygen species and how such oxygen radicals attack the fluorophore rendering it in nonfluorescent state. Therefore, it is critical to minimize spurious irradiation. We find it useful to set up a trigger device controlling the shutter system to rapidly open/close the fluorescence shutter and then place this device near the microscope controls. When trying to locate cells using the eyepiece, immediately close the shutter upon finding a potential cell target and switch to DIC for fine tuning the stage placement, focus, etc. In the DIC transillumination pathway, we use LED-based system with defined light

wavelength spectra that do not overlap with any of the excitation spectra of the fluorophores used to prevent spurious fluorescence excitation. Additional methods to control photobleaching includes bubbling the media with Argon gas to displace the dissolved oxygen and then to use Oxyfluor reagent (www.oxyrase.com) to remove oxygen from the media to minimize the formation of the reactive oxygen species. Such aggressive oxygen management may not be ideal or applicable in situations where long imaging duration is required. However, for imaging conditions where rapid kinetics is measured in the time scales of seconds to minutes, these approaches are useful.

25.2.3 Motion artifacts

When taking ratiometric image sets with a single camera where filter wheels are used to switch between different excitation/emission conditions, the time it takes to complete a single cycle of data acquisition can result in artifactual ratio signals simply from the motion of the cells. The use of simultaneous acquisition using multiple cameras, or the use of CCD image splitting device (dual/quad-view: photometrics) will eliminate these issues. However, if only a single camera system is available, one can estimate the extent of such motion effects by simply obtaining: (1) CFP, (2) FRET, and (3) CFP; in one data acquisition cycle. Comparing the ratio patterns of FRET (2) to the first CFP (1) acquired versus the last CFP (3) acquired, should be indicative of how much motion artifacts may be present in the ratiometric data. Once the extent of the motion artifact is determined, it is important to also keep the order of image acquisitions the same between each experiment so as to maintain this effect consistent between data sets.

25.2.4 Thickness artifacts

Depending on the distribution patterns of the biosensor within a cell and how the active versus the inactive compartments partition in different parts of a cell (i.e., plasma membrane vs. cytoplasmic, etc.), there will be a dilution effect in measured ratio values as a function of the cell thickness. In a traditional two-dimensional microscopic imaging, a three-dimensional cell is projected onto a 2D image plane; therefore, information in the z-dimension is lost and integrated into a single point in the plane. When examining cellular protein activities using biosensors, it is desirable to correct for the effects of cell thickness, especially for membrane bound proteins that specifically partition between membrane and bulk compartments as a function of protein activation. For the GTPase biosensor, because it is a membrane-active protein, this correction is not a simple division by the cell thickness to normalize for the thickness and is therefore more complex. The model we generated is:

$$\mathrm{FRET} = \mathrm{FRET_m} + \mathrm{FRET_c} \tag{25.5}$$

$$\mathrm{CFP} = \mathrm{CFP_m} + \mathrm{CFP_c}, \tag{25.6}$$

where FRET and CFP are the actual fluorescence of FRET and CFP measured by each CCD pixel in a camera, $FRET_m$ is the plasma membrane FRET fluorescence, and $FRET_c$ is cytoplasmic FRET fluorescence, CFP_m is the plasma membrane CFP fluorescence, and CFP_c is cytoplasmic CFP fluorescence. From Eqs. (25.5) and (25.6), for the volume above the pixel area:

$$\mathrm{FRET} = \mathrm{FRET_m} + \rho_{\mathrm{FRET}} Ah \tag{25.7}$$

$$\mathrm{CFP} = \mathrm{CFP_m} + \rho_{\mathrm{CFP}} Ah, \tag{25.8}$$

where ρ_{FRET} and ρ_{CFP} are the fluorescence densities of FRET and CFP (cytoplasmic, inactive state of the biosensor), respectively, A is the pixel area, and h is the thickness of the cell at the pixel coordinate. From empirical image data, FRET/CFP has a maximum value of α in a cell. The maximum value occurs at the thinnest part of the cell, and assuming this part of the cell has negligible cytoplasm:

$$\mathrm{FRET_m} = \alpha \mathrm{CFP_m} \tag{25.9}$$

Therefore, from Eqs. (25.7) and (25.8):

$$\frac{\mathrm{FRET}}{\mathrm{CFP}} = \frac{\alpha \mathrm{CFP} + \rho_{\mathrm{FRET}} Ah}{\mathrm{CFP} + \rho_{\mathrm{CFP}} Ah} \tag{25.10}$$

The cell thickness effect can be elucidated by plotting FRET/CFP versus h as shown in Eq. (25.10). Figure 25.5 shows the result of fitting the experimental data to

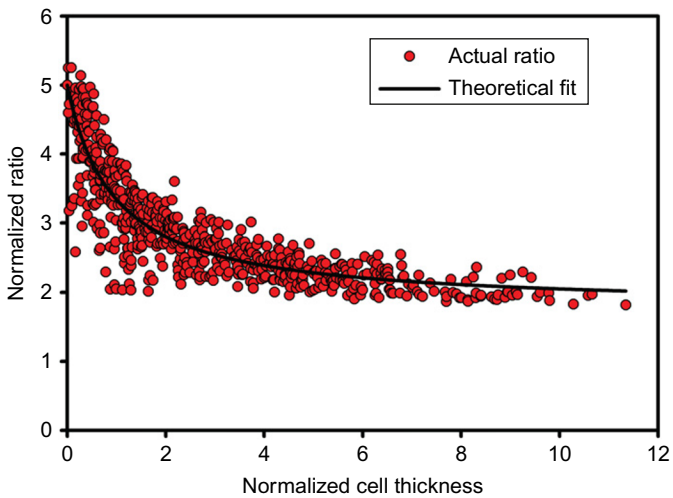

FIGURE 25.5

Effect of cell thickness of biosensor ratio measurements. The normalized ratio values at different regions of interests within a single-cell data were plotted against the normalized cell thickness indicator fluorescence intensity (red dots). The theoretical model derived in Eq. (25.10) was used to fit the data (solid line).

Eq. (25.10). As can be seen from the figure, the cell thickness has a dilution effect on sensing GTPase activity. With this relation known, a thickness indicator, such as a fluorescent dextran, can be introduced into the cell to measure h, and protein activity can be corrected accordingly.

SUMMARY

Here, we presented an overview of the procedures to follow when analyzing the image data from single-chain and bimolecular FRET-biosensors for the Rho family GTPases. The automation journals for the Metamorph software, as well as the computer codes written for Matlab program are available to automate almost all parts of the quantitative processing. These codes can be obtained by contacting the authors.

Acknowledgments

This work was funded by GM093121 (D. S., J. J. B.-C., and L. H.), "Sinsheimer Foundation Young Investigator Award" (L. H.), and T32GM007491 (Y. M. and V. M.).

References

Bastiaens, P. I., & Squire, A. (1999). Fluorescence lifetime imaging microscopy: Spatial resolution of biochemical processes in the cell. *Trends in Cell Biology*, *9*(2), 48–52.

Cai, X., Lietha, D., Ceccarelli, D. F., Karginov, A. V., Rajfur, Z., Jacobson, K., et al. (2008). Spatial and temporal regulation of focal adhesion kinase activity in living cells. *Molecular and Cellular Biology*, *28*(1), 201–214. doi:http://dx.doi.org/10.1128/MCB.01324-07, MCB.01324-07 [pii].

Crocker, J. C., & Grier, D. G. (1996). Methods of digital video microscopy for colloidal studies. *Journal of Colloid and Interface Science*, *179*, 298–310.

Del Pozo, M. A., Kiosses, W. B., Alderson, N. B., Meller, N., Hahn, K. M., & Schwartz, M. A. (2002). Integrins regulate GTP-Rac localized effector interactions through dissociation of Rho-GDI. *Nature Cell Biology*, *4*(3), 232–239.

Hahn, K. M., & Toutchkine, A. (2002). Live cell fluorescent biosensors for activated signaling proteins. *Current Opinion in Cell Biology*, *14*, 167–172.

Hinde, E., Digman, M. A., Welch, C., Hahn, K. M., & Gratton, E. (2012). Biosensor Forster resonance energy transfer detection by the phasor approach to fluorescence lifetime imaging microscopy. *Microscopy Research and Technique*, *75*(3), 271–281. doi:http://dx.doi.org/10.1002/jemt.21054 [Research Support, N.I.H., Extramural].

Hodgson, L., Nalbant, P., Shen, F., & Hahn, K. (2006). Imaging and photobleach correction of Mero-CBD, sensor of endogenous Cdc42 activation. *Methods in Enzymology*, *406*, 140–156.

Hodgson, L., Pertz, O., & Hahn, K. M. (2008). Design and optimization of genetically encoded fluorescent biosensors: GTPase biosensors. *Methods in Cell Biology*, *85*, 63–81.

Hodgson, L., Shen, F., & Hahn, K. (2010). Biosensors for characterizing the dynamics of rho family GTPases in living cells. *Current Protocols in Cell Biology*, Chapter 14, Unit 14.11.11–26.

Honda, A., Adams, S. R., Sawyer, C. L., Lev-Ram, V., Tsien, R. Y., & Dostmann, W. R. (2001). Spatiotemporal dynamics of guanosine 3',5'-cyclic monophosphate revealed by a genetically encoded, fluorescent indicator. *Proceedings of the National Academy of Sciences of the United States of America*, *98*(5), 2437–2442.

Itoh, R. E., Kurokawa, K., Ohba, Y., Yoshizaki, H., Mochizuki, N., & Matsuda, M. (2002). Activation of rac and cdc42 video imaged by fluorescent resonance energy transfer-based single-molecule probes in the membrane of living cells. *Molecular and Cellular Biology*, *22*(18), 6582–6591.

Kraynov, V. S., Chamberlain, C., Bokoch, G. M., Schwartz, M. A., Slabaugh, S., & Hahn, K. M. (2000). Localized Rac activation dynamics visualized in living cells. *Science*, *290*(5490), 333–337.

Kurokawa, K., & Matsuda, M. (2005). Localized RhoA activation as a requirement for the induction of membrane ruffling. *Molecular Biology of the Cell*, *16*(9), 4294–4303. doi: http://dx.doi.org/10.1091/mbc.E04-12-1076, E04-12-1076 [pii].

Lakowicz, J. R. (1983). *Energy transfer principles of fluorescence spectroscopy*. New York: Plenum Press, 305–341.

Lankawoicz, J. R. (1986). *Distance measurements by energy transfer Principles of fluorescence spectroscopy*. NY: Springer, NY, 312–316.

Machacek, M., Hodgson, L., Welch, C., Elliott, H., Pertz, O., Nalbant, P., et al. (2009). Coordination of Rho GTPase activities during cell protrusion. *Nature*, *461*(7260), 99–103.

Miyawaki, A., Llopis, J., Heim, R., McCaffery, J. M., Adams, J. A., Ikura, M., et al. (1997). Fluorescent indicators for Ca^{2+} based on green fluorescent proteins and calmodulin [see comments]. *Nature*, *388*(6645), 882–887.

Miyawaki, A., & Tsien, R. Y. (2000). Monitoring protein conformations and interactions by fluorescence resonance energy transfer between mutants of green fluorescent protein. *Methods in Enzymology*, *327*, 472–500.

Nakamura, T., Kurokawa, K., Kiyokawa, E., & Matsuda, M. (2006). Analysis of the spatiotemporal activation of rho GTPases using Raichu probes. *Methods in Enzymology*, *406*, 315–332. doi:http://dx.doi.org/10.1016/S0076-6879(06)06023-X [Research Support, Non-U.S. Gov't].

Nalbant, P., Hodgson, L., Kraynov, V., Toutchkine, A., & Hahn, K. M. (2004). Activation of endogenous Cdc42 visualized in living cells. *Science*, *305*(5690), 1615–1619.

Pertz, O., Hodgson, L., Klemke, R. L., & Hahn, K. M. (2006). Spatiotemporal dynamics of RhoA activity in migrating cells. *Nature*, *440*(7087), 1069–1072.

Piston, D. W., & Kremers, G. J. (2007). Fluorescent protein FRET: The good, the bad and the ugly. *Trends in Biochemical Sciences*, *32*(9), 407–414. doi:http://dx.doi.org/10.1016/j.tibs.2007.08.003, S0968-0004(07)00191-0 [pii].

Seong, J., Ouyang, M., Kim, T., Sun, J., Wen, P. C., Lu, S., et al. (2011). Detection of focal adhesion kinase activation at membrane microdomains by fluorescence resonance energy transfer. *Nature Communications*, *2*, 406. doi:http://dx.doi.org/10.1038/ncomms1414 [Evaluation Studies Research Support, N.I.H., Extramural Research Support, Non-U.S. Gov't Research Support, U.S. Gov't, Non-P.H.S.].

Shen, F., Hodgson, L., Rabinovich, A., Pertz, O., Hahn, K., & Price, J. H. (2006). Functional proteometrics for cell migration. *Cytometry. Part A*, *69*(7), 563–572.

Spiering, D., & Hodgson, L. (2012). Multiplex imaging of Rho family GTPase activities in living cells. *Methods in Molecular Biology*, *827*, 215–234. doi:http://dx.doi.org/10.1007/978-1-61779-442-1_15.

Stryer, L. (1978). Fluorescence energy transfer as a spectroscopic ruler. *Annual Review of Biochemistry*, *47*, 819–846.

Stryer, L., & Haugland, R. P. (1967). Energy transfer: A spectroscopic ruler. *Proceedings of the National Academy of Sciences of the United States of America*, *58*(2), 719–726.

Ting, A. Y., Kain, K. H., Klemke, R. L., & Tsien, R. Y. (2001). Genetically encoded fluorescent reporters of protein tyrosine kinase activities in living cells. *Proceedings of the National Academy of Sciences of the United States of America*, *98*(26), 15003–15008.

Vanderklish, P. W., Krushel, L. A., Holst, B. H., Gally, J. A., Crossin, K. L., & Edelman, G. M. (2000). Marking synaptic activity in dendritic spines with a calpain substrate exhibiting fluorescence resonance energy transfer. *Proceedings of the National Academy of Sciences of the United States of America*, *97*(5), 2253–2258.

Zaccolo, M., De Giorgi, F., Cho, C. Y., Feng, L., Knapp, T., Negulescu, P. A., et al. (2000). A genetically encoded, fluorescent indicator for cyclic AMP in living cells. *Nature Cell Biology*, *2*(1), 25–29.

Zal, T., & Gascoigne, N. R. (2004). Photobleaching-corrected FRET efficiency imaging of live cells. *Biophysical Journal*, *86*(6), 3923–3939.

Zhang, J., Ma, Y., Taylor, S. S., & Tsien, R. Y. (2001). Genetically encoded reporters of protein kinase A activity reveal impact of substrate tethering. *Proceedings of the National Academy of Sciences of the United States of America*, *98*(26), 14997–15002.

CHAPTER

Tip-Enhanced Raman Spectroscopy for the Base Interrogation of DNA

26

Noah Kolodziejski

Radiation Monitoring Devices, Watertown, Massachusetts, USA

CHAPTER OUTLINE

Introduction and Motivations **612**
Tip-Enhanced Raman Spectroscopy 612
26.1 Materials **614**
26.1.1 AFM/TERS System Construction 614
26.1.2 Tip Preparation 614
26.2 Methods **615**
26.2.1 AFM/TERS System Construction 615
26.2.2 TERS Silver Tip Production 617
26.2.3 Alignment 618
26.2.4 Sample Preparation: Wet Stamping of DNA Solution to Form Highly Ordered Arrays 621
26.3 Discussion **624**
26.3.1 Evaluating Sequencing Resolution 624
Summary **627**
References **627**

Abstract

A combination of scanning probe and Raman microscopies allows for the label-free chemical mapping of surfaces with spatial resolutions one to two orders of magnitude below the diffraction limit. Because Raman spectroscopy provides a highly specific molecular "fingerprint," the resulting spectra allow speciation of even highly similar chemical compounds. The surface enhancement phenomenon allows Raman signals from a species to be enhanced by many orders of magnitude within the vicinity (~10 nm) of a source of free electrons such as a noble metal. Presenting the metal surface as a single highly localized point, and moving this point with angstrom accuracy across a distributed, heterogenous surface while collecting Raman spectra, is what is known as tip-enhanced Raman spectroscopy, or TERS.

Methods in Cell Biology, Volume 114 **ISSN 0091-679X**
Copyright © 2013 Elsevier Inc. All rights reserved.
http://dx.doi.org/10.1016/B978-0-12-407761-4.00026-9

INTRODUCTION AND MOTIVATIONS

When photons of energy *hv* encounter matter, most of those scattered are observed to be at the same energy as the incident photons. A very small number of the photons will lose energy, exciting the molecule into very short-lived "virtual states" of electron cloud polarization, scattering away with a lower energy and longer wavelength. These photons are shifted in wavelength, with an energy loss corresponding to a specific vibrational mode of the scattering molecule's electron cloud. Collecting a spectrum of many such "Raman" photons reveals sharp spectral peaks, each corresponding to a particular vibrational mode. Because the permitted vibrational modes of a molecule are discrete and precise, and depend on every atom and their relative orientations, a Raman spectrum is a very specific identifier of molecular species.

Unfortunately, the weak scattering cross section of the Raman effect ($\approx 10^{-29}$ cm^2/molecule) provides only one isotropically scattered Raman-shifted photon for every 10^7 incident upon the sample (Smith & Dent, 2005). For this reason, single-molecule analysis was beyond the reach of Raman spectroscopists until the discovery of surface-enhanced Raman spectroscopy, or SERS. SERS generally refers to the massive increase of molecular scattering intensity (by 10^6–10^{10}) (Le Ru, Blackie, Meyer, & Etchegoin, 2007; Smith & Dent, 2005) in the immediate vicinity (≈ 5 nm) of a metal surface whose dimensions and orientation allow the metal to act as a "nanoantenna," and whose electrons resonate with the frequency of incoming light. SERS has been widely researched and exploited as a trace analysis method (Etchegoin et al., 2003; Lacerna, 1993; Vo-Dinh, Hiromoto, Begun, & Moody, 1984), advancing to the point that SERS spectra from single molecules are published with regularity (Etchegoin & Le Ru, 2008; Kneipp et al., 1997; Le Ru, Meyer, & Etchegoin, 2006; Nie & Emery, 1997).

Though SERS has high sensitivity and molecular specificity, it is rarely a highly repeatable technique in traditional practice and is ill suited for the detection of DNA bases in a quantitative manner. The reasons for this are twofold: first, SERS relies upon proximity between the analyte and the plasmonic surface. In the majority of SERS implementations, issues of surface chemistry and electrostatic interaction complicate the meeting of the surface with many analytes. Second, SERS is a technique used in aggregate, on randomly created SERS-active surfaces (on the order of 5 nm, even ordered patterning techniques are quite disordered), meaning that many molecules and many plasmonic "hot spots" are normally imaged within one diffraction-limited spot. The spatial resolution is therefore limited at best, and even nonexistent for traditional SERS analysis of long heterogeneous molecules such as DNA.

Tip-enhanced Raman spectroscopy

A combination of scanning probe microscopy and SERS, tip-enhanced Raman spectroscopy (TERS) allows for Raman imaging with resolution well below the diffraction limit (Novotny & Stranick, 2006). This technique takes advantage of the highly refined techniques of either atomic force microscopy (AFM), scanning tunneling microscopy (STM), or even the less mature shear force microscopy (SFM) to provide positional resolution. In the simplest depiction, one floods a discrete nanoscale metalized scanning

probe with photons; the enhancement volume is confined to the region directly below the tip (Fig. 26.1). Taking the difference spectrum between tip engaged and tip retracted yields the SERS spectrum for the volume whose diameter is roughly equal to the radius of curvature of the tip (Steidtner & Pettinger, 2008).

With established protocols, AFM and STM tips with 10^9–10^{11} enhancement ratios and sub-10-nm radii are produced with some regularity. We have found evidence in our laboratory that for AFM/TERS studies on DNA, resolution is increased even further due to one-dimensional confinement of stretched, immobilized DNA. We will concentrate only on our efforts in AFM/TERS in this chapter.

The motivations for work in TERS are many and varied, though in this chapter we will concentrate on the most basic techniques required to detect spectra indicating the base content of immobilized DNA by TERS. The clinical relevance of DNA that is modified beyond what can be detected by modern sequencing technologies is only now becoming clear. For instance, there is growing evidence that implicates oxidation of DNA bases in Alzheimer's, traumatic brain injury, Down syndrome, and Parkinson's disease. Our laboratory's ultimate goal of single-base sequencing of DNA simultaneously sensitive to multiple molecular damage and modification sites is an important for gaining understanding of the control that nonsequence information contained within genotype has over phenotypic expression in multiple disorders.

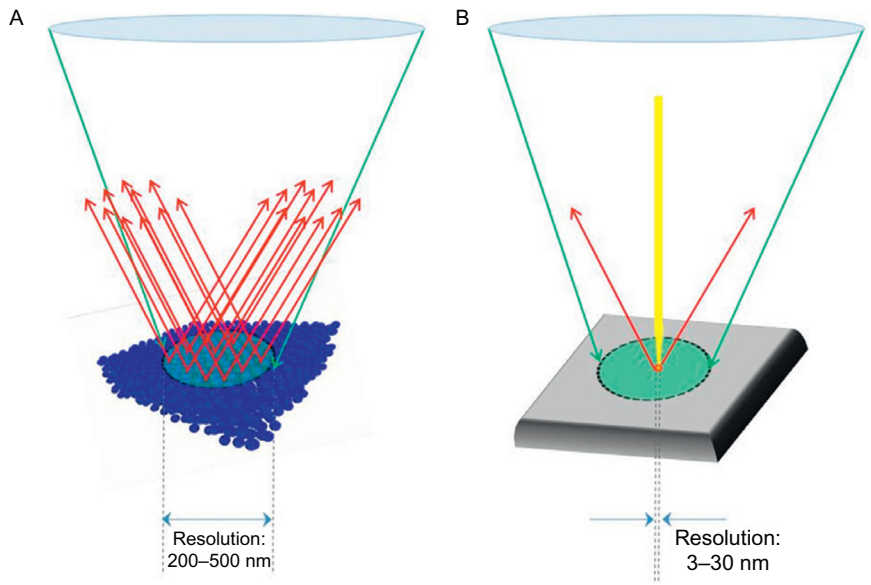

FIGURE 26.1

Comparison of two methods for enhancing Raman signals: (A) Traditional SERS techniques, such as illuminating a metal colloid incubated with analyte, are limited by the Abbe diffraction resolution limit of $\approx\lambda/2$. (B) In TERS, a large region is flooded with photons as a nanoscale metal tip of known position is introduced. Analyte under the tip is exclusively subjected to enhancements that range from 10^6 to 10^{12}. Enhancement volume is, at first order, limited by the radius of curvature of the metal tip.

The vast majority of the information presented here was learned by constructing and using a "home-built" AFM/TERS system over the bulk of 2011 under an NIH grant (HHSN261201000115C). We will cover the salient points of instrument construction, tip coating, DNA immobilization on glass, and finally integration of the parts to make a working TERS system. Within each subsection in Section **2**, we will present hard-learned recommendations based upon what has worked and not worked for us. The user must take these recommendations not as hard truths (there are so few in a technique so dependent on empirical results rather than first principles), but as guidelines around which to structure their first efforts.

The breadth of this chapter precludes the depth and thoroughness needed to guide a user step-by-step through the entire process. Further, while the reputation of TERS as notoriously difficult need not be your experience, even with careful planning and significant resources the user should expect significant time to be consumed in learning the details, workings, and expert operation of the AFM/TERS system as well as by customizing their equipment and process.

26.1 MATERIALS

26.1.1 AFM/TERS system construction

1. Atomic Force microscope, with sample scanning, preferably a system which can be mounted atop an inverted microscope (Asylum Research MFP-3d ca. 2006, the user can choose between most top-mounted, biological AFMs)
2. Inverted light microscope (Olympus IX-71 or equivalent)
3. Raman long-pass 45° dichroic and filters for coupling laser light into microscope and filtering laser input, TERS signal (Semrock, Inc.)
4. 532-nm CW or quasi-CW Laser in the milliwatt range (CrystaLaser)
5. Spectrometer with (water or passively) cooled and back-thinned spectroscopic CCD (.5m Acton SP2150, Princeton Instruments PIXIS)
6. High stability kinematic mirror mounts (5), two with differential or piezo adjusters (Thorlabs, Newton, NJ)
7. High-extinction nonsheet polarizer, zero-order 1/2 waveplate, and Radial polarizer (Thorlabs, Radial polarizer from Arcoptix, Z-Pol, or homemade)
8. Various high-modulus optomechanical mounts. If it is a removable or adjustable element, it should be exceedingly precise and repeatable (various suppliers)

26.1.2 Tip preparation

1. Sputtering system with either RF plasma etch or multiple targets (Denton Desk II)
2. $1 \times 99.999\%$ purity silver target and $1 \times 99.995\%$ purity aluminum target (Alfa-Aesar)
3. Si tapping mode AFM tips (NT-MDT NSG-10)

All other materials are detailed in later sections

26.2 METHODS

26.2.1 AFM/TERS system construction

The work of assembling an AFM/TERS system is often lamented to be extremely difficult. While this had to be the case for TERS systems based upon earlier AFMs, there is no reason why a user with reasonable optical skills cannot prepare their own TERS system today, or improve upon the resolution and performance of the newer crop of commercial TERS systems.

The recent ubiquitization of standard AFM/Raman techniques has precipitated the creation of several commercial AFM's which can be converted for TERS with relative ease. There are even some off-the-shelf TERS systems at the time of this paper's publication which boast of being able to achieve reliable TERS with no system modifications. It should be noted that while the construction of the basic TERS system outlined here is not terribly difficult, achieving reliable, high performance which allows for mapping with resolutions in the tens of nanometers requires moderate to extensive informed modification of a home-built system, or careful operation and some modification of a commercial TERS system. Noise, thermal drift and hysteresis in the AFM/optical train, as well as creation of data collection software (for home-built systems) are the primary challenges outside of the area of tip fabrication, and while we will outline some rules-of-thumb at reducing sources of error, each system is unique and requires different remedies. It is in shortening the time until achieving reliable mapping that commercial off-the-shelf TERS systems truly excel at saving time and producing results, due to their software/hardware integration. For the custom-made system outlined here, the time to TERS mapping from initial system bolt-together was approximately 4 months for a highly experienced optical physicist.

An AFM/TERS system can be constructed in many different ways, though in general most systems can be described in their essence to be a quasi-confocal microscope whose confocal volume is at the apex of an AFM tip. The three most common optical layouts for TERS: side illumination, epi-illumination, and top-illumination, each present different advantages. In practice, the limited NA of side illumination makes top- or epi-illumination favorable in most circumstances. The TERS system described here is an epi-illuminated system, though conversion between modes would not be fundamentally difficult for the reader as long as their AFM allows optical access to the cantilever from above.

As the layout of a TERS system is similar to that of a confocal or fluorescence microscope, many groups construct their instrument atop a commercial inverted light microscope (ILM). The engineered maturity of commercial ILMs yields convenience, user familiarity, and reasonably low thermal drift and high resistance to acoustical noise. While we have found that the ILM adds very little vibrational noise ($\sim$1–3 pm), we have found that ILMs suffer from thermal drift of the objective lens in the z (focusing) axis. For some commercial TERS systems, this translates directly to x-axis drift of the optical beam, as the mirror is mounted upon the turret itself. This should be corrected by

independently mounting the turning mirror. At best, drift in the z-axis will affect TERS signals due to defocusing. For our instrument, the x–y thermal drift within the AFM head and sample stage was similar on-or-off the microscope and was highly dependent upon stable room temperature and minimal user handling. For an open system like ours which was in a $\pm 2\,^{\circ}\mathrm{C}$ controlled room, the thermal drift was excessively high (as much as 10 nm/min) making long mapping experiments with high resolutions nearly impossible without careful thermal shielding. The model AFM used in our home-built system was particularly unsuited to be fit with an incubator or shield to reduce thermal drift, as electronics in the head become appreciably hot during use.

In terms of practical usability, we found that the benefit of using an ILM lay in the ability to scan samples for fluorescent markers which can be used to locate regions of TERS interest. This work is best done first at low followed by high magnification, which is particularly simple with a turret. A low-magnification option also allows rough alignment with the tip/AFM head after tip changes. The ILM also presents the opportunity to switch between eyepiece, spectrometer coupling, and camera imaging with minimal vibration. If the thermal drift in the optical turret assembly is problematic, and if fluorescent or bright field imaging of the sample at low magnification is not required, one can avoid the thermal drift of an optical turret assembly altogether. This can be done by either immobilizing the z-axis of the turret, using a commercial TERS system which does not rely upon the turret at all or can be modified as such, or removing the AFM head and constructing what is essentially an ILM of one's own. Our very general recommendation is that for a home-built TERS system, an ILM may be quite valuable, though the value is less apparent in a high-end commercial TERS system, whose lenses are not hot-swappable for various (worthwhile) reasons.

Shown in Fig. 26.2, our home-built TERS system was constructed with the invaluable aid and generosity of Dr Jeeseong Hwang at NIST, who lent to us several months of laboratory space, the AFM, and his advice on the construction.

Once a user has chosen an AFM, integration with an ILM is straightforward. Once the AFM is affixed atop the ILM, bolt entire apparatus to a passive floating optical table (18″ thickness is recommended to increase mass and decrease vibration). Achieving TERS with an active isolation table requires either that the laser and optics be on said table or single-mode fiber coupled the system. Install the laser and coupling optics; the laser should encounter at least three mirrors before hitting the beam steering mirror, to allow for complete alignment correction when the system is moved or elements swapped. Five hundred and thirty-two nanometer is recommended in this work, though a tunable laser or a supercontinuum laser with an adjustable Raman filter can introduce the possibility of enhanced resonance Raman. The laser should be coupled into the system with an ND filter wheel to adjust power, placed before any user-adjusted mirror. This filter wheel should exhibit high resistance to pitch and yaw variation from filter-to-filter (it is exceedingly important for ease-of-use that the beam not "walk" on the tip while changing laser powers). The same positional accuracy requirements holds for all optical elements that intersect the. The coupling mirror in the inverted microscope is either an AFM-controlled steering mirror (ideal, but only available on the newest commercial TERS systems),

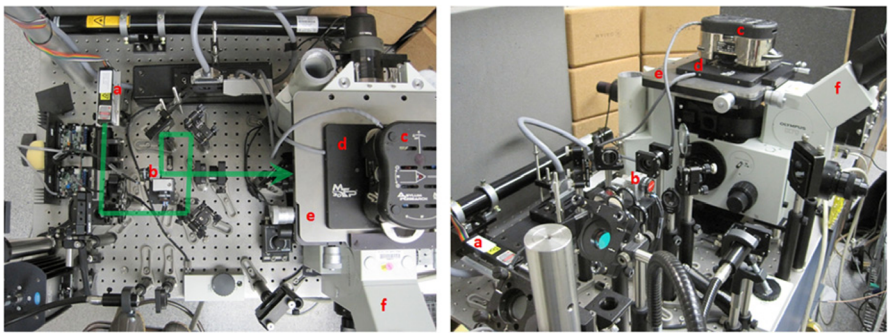

FIGURE 26.2

Left: Top view of author's experimental setup. Beamline is traced in green. Right: Side view of TERS setup, showing microscope more clearly. (a) Laser, (b) scanning galvanometer, (c) AFM head, (d) AFM sample scanning stage, (e) microscope coarse sample stage, and (f) ILM.

or as in our case, a 50/50 beamsplitter swappable with a 45° long-pass Raman dichroic. Note that many such dichroics will "scramble" polarization. On the bottom or side port of the ILM, a mirror can deliver light through an ultrasteep long-pass Raman filter or notch filter to an objective lens focused upon the spectrometer's input slit or pinhole. A pinhole maximizes the confocal filtering of the collected light, decreasing background from scattering and out-of-plane photons.

For selection of an objective lens, in general for epi- or top-illuminated TERS, extremely high numerical apertures are favored, as marginal rays with incident polarizations in the axis of the tip-sample gap are most likely to contribute to TERS signal. For this reason and others, radial polarization is touted as superior for TERS (Dorn, Quabis, & Leuchs, 2003; Hayazawa, Saito, & Kawata, 2004). With any lens, one can experiment with polarizations and blocking of the central portion of the beam to reduce scattered background, as well as heat transfer from photons of suboptimal polarization/incidence angle. We found out best results with a total internal reflection (Olympus TIRF, 1.4 NA) objective lens.

The user should familiarize themselves with the operation of the AFM, and how to minimize noise and thermal drift in the lab. In this work, tapping mode was used, though various modes of noncontact are also possible on DNA. Contact mode was found to destroy the DNA sample.

26.2.2 TERS silver tip production

With the simplest version of the production procedure we outline here, we have observed TERS signals from DNA with ~50% of the tips produced. The Ag coating was performed in a small SEM-type sputtering chamber (Desk II, Denton Vacuum,

Inc.). Production of the tips began with the receipt of NSG10 tips from NTMDT, Inc. The tips were then transferred, still in their gel packs (shipping and storage method commonly used in the industry), to the sputtering chamber, and after a 5–60 s RF plasma etch, 99.999% silver was sputtered onto the assembly at a pressure of 75–100 mTorr (Argon) and sputtering current of 45 mA. Sputtering rate (thickness/time) was calibrated by AFM, and layers of 15, 40, 60, and 400 nm were deposited. While coating outside of the gel packs is likely preferable, we have found success with predeposition RF etching with gel packs. When we do not use gel packs, we still coat most of the interior of our long-term tip storage vessel with Ag to create a sacrificial sulfuric fouling surface.

Once TERS is achieved, attention should be turned to the issue of preserving the usable service life of the tips, which with bare Ag was only several minutes under illumination, with TERS signal dropping noticeably and nonlinearly (estimated to be logarithmic) over seconds to tens of seconds. Based upon our experience, we believe that imaging wear is not the primary cause, as each tip was utilized for at least 10 min, occasionally hours, of imaging before locating, recording an image of, and measuring TERS on DNA. This fact coupled with the quasi-logarithmic nature of the signal degradation suggests the localized optical field, via, for instance, heat and contact-mediated annealing, is to blame.

Significantly, we found that coating the silver with a thin (1–5 nm) passivation layer of Al extended the service life of the tips to several hours of imaging, with a shelf life on the order of weeks and even months. The aluminum would ideally be sputtered in a dual target system with a turbo pump and a planetary stage. In actuality, the aluminum was swapped into the sputterer after breaking vacuum; and the unit was only rotary vane pumped, with no sample rotation. When repumped down with aluminum as the target, the system was normally RF plasma etched for 5–20 s at ~5 mA, though this step was not found to be critical. The aluminum is then sputtered while a shutter shields the tips, to expose fresh Al on the target and encapsulate contaminants in the chamber. This "cleansing" sputter is carried out for as long as several minutes. With an Al overcoat, catastrophic TERS signal degradation due to tip crashing/excessive speed and sample swapping accounted for most cases of Al-coated tip "death."

More significantly, TERS signal was found to be difficult to achieve with several other models and brands of tip, even the NSG30 tips from the same supplier, supposedly identical in all ways but resonance frequency.

26.2.3 Alignment

Once the system is set up to perform TERS and tips are produced, the process of alignment begins. Alignment of the optical field with the tip and maintenance of that alignment is, aside from tip manufacturing, commonly said to be the most difficult and tedious part of performing TERS. Several of the AFM manufacturers which produce off-the-shelf TERS systems have attempted to ease this process by using a confocal microscope system to handle the input and output optics. Inside

this box, not only is there housed every optical component we have already outlined as required for TERS, save the scanning mirror and objective lens, but also there is a confocal photomultiplier tube aligned to detect backscattered light. In commercial TERS software systems, the system automatically scans the beam across the tip, mapping the confocal scattering back to the photomultiplier. The user can then select a "hot spot" of plasmonic activity on which to align the beam. This is very useful, though in the author's experience not required, as the hot spots can be seen with the naked eye through the eyepieces of the ILM as one uses a high-precision galvanometer or piexo-controlled mirror to walk the beam across the focal plane. When aligned with a hot spot, a pattern of concentric diffraction rings appear at the beam waist. The location of this phenomenon is highly symmetrical and repeatable, and repeated scanning across the tip in both axes by the user with even a differential micrometer-controlled stage (use an external adjuster with any optical element you manually align before or during an experiment to prevent thermal drift from body heat) was found to be sufficient to produce reliable TERS signals.

All or some of the following steps should be followed when swapping tips, samples, or simply aligning the system from gross misalignment:

1. Place standard Si cantilever into cantilever holder, and assemble system for AFM, with glass cover slip/sample.
2. Couple broadband light from a tungsten lamp or LED, either far-field fiber coupled into the space between the AFM tip and the sample stage, or more elegantly, free space coupled through a movable pellicle beamsplitter into the optical train.
3. Focus on top cover glass surface. Approach Si cantilever with coarse adjusters nearly to the surface while observing through the ILM eyepieces, with low mag objective if possible, moving the AFM head so that the tip is centered in the optical field.
4. Set the AFM to work in tapping mode with an amplitude of $\sim$5 nm. Engage the tip via software, confirming that the tip remains centered.
5. Turn on laser, and move to center of optical field. Try to make the focal spot coincident with the tip by moving both as close to the center of the field as possible.
6. Retract tip via software and move sample stage so that approximate area to be TERS imaged is centered in the optical field. Turn off broadband source and reengage tip.
7. Scan via AFM and confirm location of TERS-relevant sample area. It is now at the center of the optical field and coarsely aligned. Retract tip.
8. Replace tip with metalized TERS tip and engage. Turn on broadband source, and without moving the sample, use the AFM software to recenter the tip in the optical field. If the TERS tip is properly metalized, the user will see a glowing bright spot surrounded by dark in the broadband bright field image. This is the tip apex. Note that metalized, though damaged or otherwise

TERS inactive tips also glow. One can often detect worn or crushed tips via the shape of the bright spot using this method. Turn on or unblock the laser.

9. Utilizing TERS software or eyepiece and kinematic mirror mount/galvanometer, walk the laser focus past the tip, and center on hot spot.
10. Block laser and scan sample.
11. "Zoom in" on the portion of the sample which is TERS relevant using AFM software, and unblock laser, using ≤ 1 μW power at sample. Look for TERS spectrum on spectrometer, move tip around, and increase laser power if no TERS is sufficient or signal is insufficient for imaging (the user will get a feel for how much laser power the tip can handle before softening or ruining the sample).
12. Image or acquire individual TERS spectra.
13. If no spectrum is found, note several things: If the tip is TERS active, the authors have find that it emits a "fluorescence-like glow" of background light, which can help indicate if your spectrometer is still aligned with your confocal-illuminated volume. Be sure also that you are integrating for at least 100 ms during alignment.
14. When TERS was first observed for a new tip, the authors spend <10 s confirming that the signal is maximized via walking the beam to compensate for thermal drift away from the hot spot. Between scans, the author would also look through the eyepieces to observe that the diffraction rings indicating hot spot alignment were still symmetrical (note the laser power and never stare into a laser with more than 200 μW delivered to the sample).
15. Always remember to block/reduce laser power during all processes which are not acquiring spectra. Use the minimum power for all efforts until spectra are to be recorded. Excess heat from input light anneals, softens, and deforms AFM TERS tips and can oxidize/denature a sample (STM and shear force TERS tips are more forgiving in this respect, as their solid metal construction can delocalize and dissipate more thermal energy).

The instructions are specified for a TERS system with a differentially or piezo-controlled mirror/galvanometer to scan the laser beam, as well as x–y scanning on both the sample and the tip. If a system has only sample scanning (as did our MFP-3d), it is still possible to align via moving the entire stage assembly with micrometers that will be included in the system. In order to not lose light into the spectrometer, it is wise to not use a pinhole, but a multimode fiber optic to deliver light to the spectrometer.

We often utilized polarization modification and blocked the central portion of the beam to reduce heat load while maintaining TERS signal. None of the data presented in this report, however, used a blocked beam. We discovered that without being very precise in creating radial polarization, or illuminating annularly, there was little to no benefit from such efforts. I recommend exploring these options oneself, albeit with care and precision. All data were taken with fairly well-scrambled linearly polarized light, filling the back aperture of the objective.

26.2.4 Sample preparation: Wet stamping of DNA solution to form highly ordered arrays

Our linearization technique is a modified form of a procedure published on generating DNA nanostrand arrays (Guan, Lee, 2005) by "stamping" a substrate with PDMS wetted with molecularly combed DNA. We used fluorescence imaging to monitor the results. The technique works for dsDNA or ssDNA, though most of our experience is in dsDNA, as it can be dyed with more efficient dyes for troubleshooting the process. The technique here is presented for λ-phage DNA to get the user started in imaging DNA, but was not altered for shorter, engineered DNA segments which can be used to determine axial resolution, which are described later.

A 1-cm-thick PDMS slab is prepared on a clean (alcoholic KOH or piranha etched if not kept in clean room conditions), flat silicon wafer. PDMS is then cut out into $\sim$2 cm $\times$ 2 cm squares and peeled from the silicon wafer. PDMS is cleaned before each use by soaking in DI with 30% Micro-90 solution and sonicating for 15 min. At the same time, a microscope cover slip (Electron Microscopy Sciences, 1 oz, 25 mm diameter, cat. #72,195) and one standard thickness glass slide (Gold Seal, Inc.) are prepared after washing in distilled water and soaking in 50/50 alcoholic KOH solution for 2 h. Glass and PDMS are then rinsed in DI for approx. 30 min. All substrates are then dried with dry nitrogen or left to drip-dry in a biological safety HEPA hood.

Next about 1 μl of 250 μg/ml phage DNA (Sigma–Aldrich, naturally methylated) is mixed with 1 μl of 1–10 μM solution of YOYO-1 (dsDNA) or SYBR-2 (ssDNA). The mix is incubated for $\sim$2 h in the dark. For linearizing ssDNA, DNA is simultaneously incubated and denatured at 90 °C for $\sim$1 h, and coverslips are heated to 80 °C.

After incubation, a 1 μl drop is placed on the clean microscope slide and the PDMS, silicon wafer side down, is placed on top of the droplet. As shown in Fig. 26.3, a pressure of $\sim$10–25 pounds per square inch is applied. The fluid escaping from the sides is dried with N_2 gas or the corner of a Kimwipe. The PDMS is then quickly peeled off in one direction, placed on the second cover glass, gently pressed to adhere the DNA, and then peeled off in the same direction as before. The mechanism of linearization is postulated to be molecular combing along the receding meniscus. The cover slip is then used for imaging the DNA with high-magnification fluorescence microscopy or AFM, while the thicker microscope slide can be discarded or cleaned in KOH for reuse. For unlabeled DNA, the procedure is identical, substituting TRIS for the dye. Upon finding evidence of the DNA supercoiling (>2 nm height), it is diluted down 10 $\times$, and/or a fresh sample is ordered. We found that it is necessary to order a fresh sample nearly every 2 weeks, as when the DNA was "old," it would form yarn-like balls which would not comb straight.

As seen in Fig. 26.4, the DNA is highly linearized on the glass cover slip. Further observation indicates that the vast majority of linearized DNA molecules are individual dsDNA strands, as the observed lengths of stained DNA are largely homogenous, at between 20 and 25 μm (the intercalation of YOYO-1 dye is known to lengthen the stacking distance of dsDNA. Supercoiling or another mechanism of

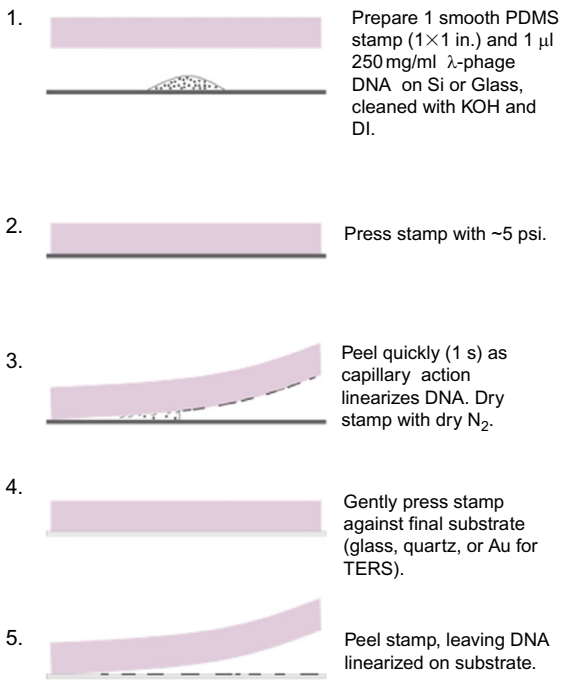

FIGURE 26.3

Wet stamping procedure. Process is highly sensitive to surface preparation. DNA is denatured at 90 °C before stamping to achieve ssDNA linearization.

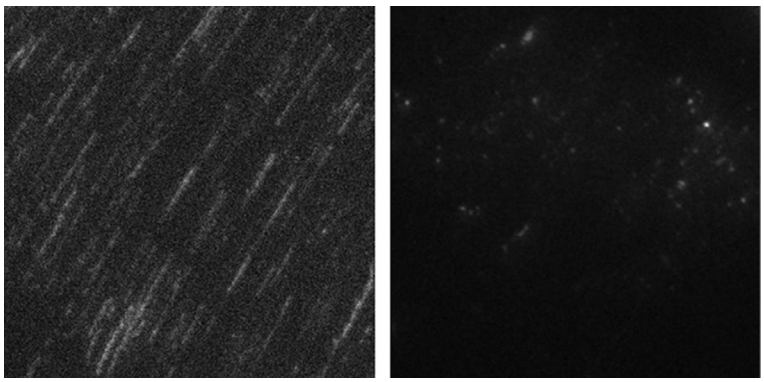

FIGURE 26.4

Fluorescence micrographs of linearized dsDNA prepared by PDMS stamping/molecular combing and stained with 1 μM YOYO-1 dye. Left: Control dye solution without DNA. Right: Linearized dsDNA. Excitation is 488 nm and emission filter is centered around 532 nm with FWHM 30 nm.

DNA agglomeration is expected to result in a broad spectrum of lengths, which are not apparent from observation under the fluorescence microscope).

We coated and tested over 200 cantilevers during the length of our work with Ag coatings. TERS tip yields (measured by observable signal over 1 s integrations at 0.1 mW, 532 nm on DNA) increased to over 80% by the end of programmatic work, due to process refinements already mentioned (Cleanliness of the target swap in sputtering and predeposition sputtered cleaning of targets).

Ultrathick coatings can also be used with success. Other researchers have found that such thicknesses of Ag form a large sphere (200 nm diameter) at the apex of the tip, presumed to be due to nucleation and electrostatic charge concentration. Tips produced in such a manner yielded surprisingly high-resolution (<40 nm) AFM and TERS images, and more consistent TERS yield. We cannot yet explain this, but assume that the 400 nm coated tips may exhibit exceptional surface roughness on the nanoscale (Fig. 26.5) accounting for the high-resolution TERS activity. Preliminary results showed that 200–400 nm coated tips would occasionally exhibit ultrahigh TERS resolutions of ~10 nm. Future studies will utilize TEM or high-resolution SEM to image the probes and determine if nanoscale roughness accounts for this tremendously high resolution.

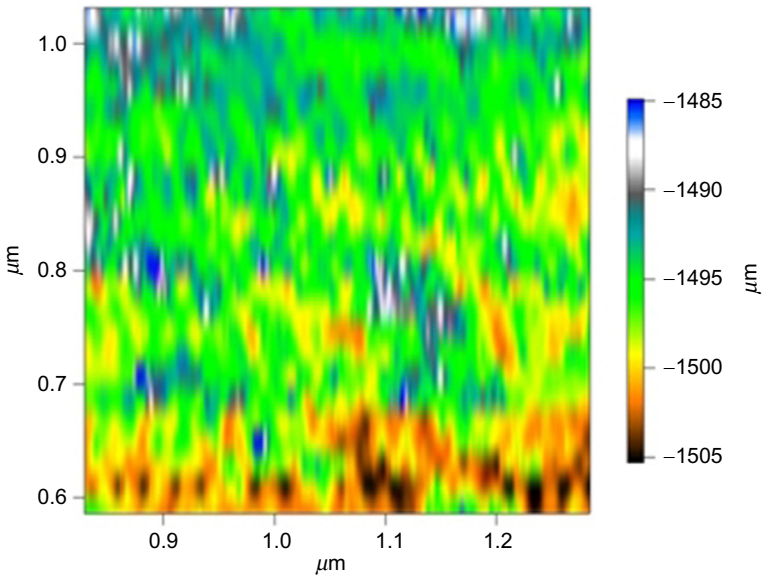

FIGURE 26.5

AFM micrograph (450 nm × 450 nm) of Ag sputtered on flat portion of an Si cantilever. Ag is 400-nm thick and displays roughness features on the order of ~10 × 10 × 10 nm in dimension. Each feature is of appropriate size to act as a plasmonic nanoantenna.

26.3 DISCUSSION

26.3.1 Evaluating sequencing resolution

As an exercise, we will present the reader with the ultimate results of the efforts that inspired our discussion and observations thus far. Between the basic presentation of TERS on DNA that we have presented instructions for, and our ultimate goal of single-base resolution, we have made progress on tip manufacture which is beyond the scope of this chapter. With our most high enhancement and resolution tips from these efforts, we set about to design and test a preliminary experimental design, which when we upgrade our system to a lower-drift state-of-the-art AFM/TERS system (AIST-NT), we can ultimately use to evaluate resolutions approaching single-base levels.

In order to evaluate the axial resolution of the system on DNA, we created and scanned DNA strands with alternating "homopolymeric" lengths of repeating Watson/Crick pairs (Fig. 26.6). These engineered DNA strands were made at RMD's Molecular Biology Laboratory, by Dr Daniel Hall, with a mixture of $(A/T)_{10}$ and $(G/C)_{10}$ "sticky ended" oligos ligated together. As a result, the one-for-one alternating sequence seen in Fig. 26.6 is idealized, and in actuality, the 50/50 mixture of oligos will arrange themselves randomly. We were able to produce these oligos at variable lengths up to 10 kb. We also have a more laborious procedure to ensure a nonrandom one-for-one sequence. Unfortunately, any procedures for creating oligos are outside the scope of this chapter.

As a result of thermal drift convolved by 1 s integration times, following along the DNA was difficult, as the tip would end up "falling off" of the DNA strand in less than 10 s of placement. The pattern followed by the tip is represented in atop the AFM micrograph in Fig. 26.7. Each step across the DNA is 6 nm, while each step in the axial direction is 3 nm. Example spectra are pictured at various points along the raster scan in Fig. 26.7. Future work with our new instrument will be able to use smaller step sizes, as lower thermal drift will allow for longer experiments.

With the ~1 kb long, alternating 10-base pair engineered DNA strands represented in Fig. 26.6, and the particularly high enhancement tips available after 6 months of process refinement, we arrived at three typical spectra from engineered DNA (Fig. 26.8), which we attempted to correlate to either $(A/T)_{10}$ or $(G/C)_{10}$. While the spectra varied between two basic spectra as the tip stepped along the DNA, which suggests resolutions of ~3 nm, these are not base assignments but correlations, presented in a preliminary manner, which will require further work to determine the validity thereof. It should be noted that this data was taken after the system was moved to Radiation Monitoring Devices (Watertown, MA) from NIST (Gaithersburg, MD), and thus the system used a ~1/8-m spectrograph, and as a result spectral resolution suffered, further complicating our evaluation.

Of the three spectra, spectrum 2 is the most unique shown in Fig. 26.8. The most striking differences come from the presence of the adenine peak at 1051 cm^{-1} and the presence of two thymine peaks at 1398 and 1538–1546 cm^{-1}. The presence of these

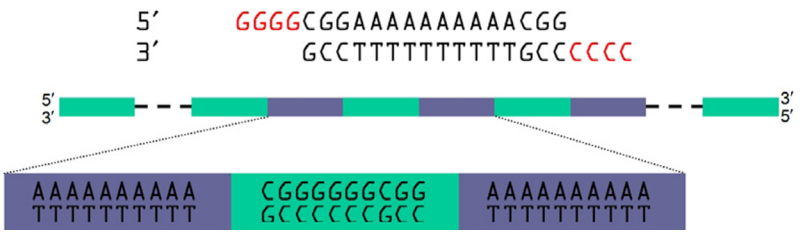

FIGURE 26.6

Engineered DNA design produced by RMD. Total lengths varied with production technique and ranged from 300 to 10 kb. The length of each homopolymeric region could be varied from 10 to 30 bp. Regions longer than 30 bp (up to 1 kb) required another ligation step to join blunt-ended homopolymers.

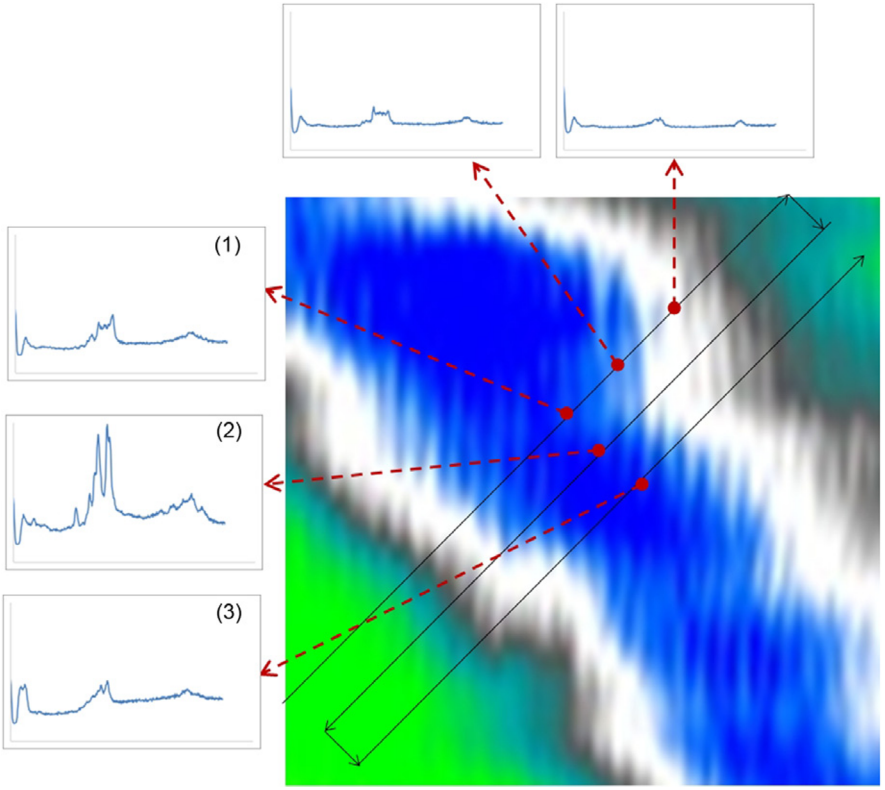

FIGURE 26.7

TERS scanning region (20 nm × 20 nm) of engineered DNA segment. Data for sequencing resolution were taken along the raster scan pattern pictured. Spectra from various points are shown, including spectra 1, 2, and 3 which were used for sequencing analysis. TERS resolution across the strand is 8–15 nm HWHM, while TERS resolution along the strand (sequencing axis) is ~3 nm. The cause of this asymmetry is unknown.

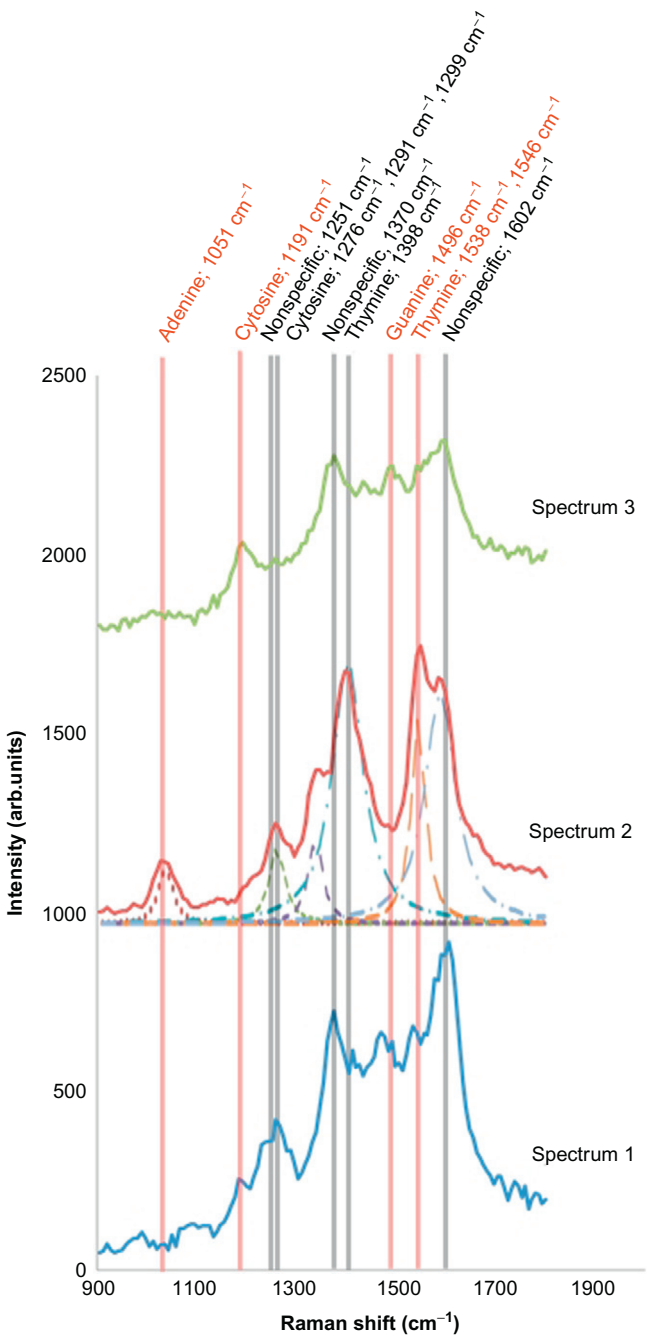

FIGURE 26.8

Three spectra from 3 nm steps along engineered DNA. By identifying strong and specific band assignments (shown in red), we are able to perform a preliminary assignment of nucleobase contribution. Data are normalized for clarity.

unique peaks (Treffer, Lin, Bailo, Deckert-Gaudig, & Deckert, 2011), along with the absence of the guanine peak at 1496 cm^{-1} and cytosine peak at 1191 cm^{-1}, agrees more favorably with an assignment of A/T base pairs than it does with G/C pairs.

Analysis of spectra 1 and 3 shows clear spectral differences from spectrum 2. The guanine peak at 1496 cm^{-1}, in particular, is strongly represented in spectra 1 and 3, while being largely absent from spectrum 2. Cytosine is also evident in spectra 1 and 3, and absent from spectrum 2. Variation in the nonspecific and specific peaks between spectrum 1 and 3 would be expected due to the helicity of the DNA molecule exposing a varying mixture of common bonds to the polarization of the E-field. A solution to this is to use fixed ssDNA in future work. We observe that spectrum 1 and 3 correlate most robustly to G/C base pairs, though a higher resolution spectrometer is needed to accurately quantitate the unique peaks without the interference of other, common peaks.

SUMMARY

TERS is a powerful technology which is quickly approaching a state of maturity that will allow what was once extremely difficult and largely academic to become a more common practical analysis technique. Whereas the vast majority of TERS papers from just 5 years ago addressed the technology of TERS, it is recent that applications in biology and materials science have precipitated the use of TERS to solve real world problems. We have demonstrated and instructed the user on how to scan DNA for base content with resolutions below 50 nm with tips that they can produce with high yield in an inexpensive SEM-type sputtering machine. We also provided advice on increasing resolution to approach the final results presented in this chapter, the tips for which were all produced in the same SEM-type desktop sputterer. We are hopeful that in the near future, techniques under development in our laboratory, as well as yours and others, will allow for single-base resolutions from TERS. This will open the world of the epigenome and allow for real-time, long read-length simultaneous sequencing of methylated, oxidized, and otherwise modified nucleobases in clinically relevant DNA.

References

Dorn, R., Quabis, S., & Leuchs, G. (2003). Sharper focus for a radially polarized light beam. *Physical Review Letters*, *91*, 233901.

Etchegoin, P. G., & Le Ru, E. C. (2008). A perspective on single molecule SERS: Current status and future challenges. *Physical Chemistry Chemical Physics*, *10*, 6079.

Etchegoin, P., Maher, R. C., Cohen, L. F., Hartigan, H., Brown, R. J. C., Milton, M. J. T., et al. (2003). New limits in ultrasensitive trace detection by surface enhanced Raman scattering (SERS). *Chemical Physics Letters*, *375*(1–2), 84–90.

Guan, J., & Lee, L. J. (2005). Generating highly ordered DNA nanostrand arrays. *Proceedings of the National Academy of Sciences of the United States of America*, *102*(51), 18321–18325.

Hayazawa, N., Saito, Y., & Kawata, S. (2004). Detection and characterization of longitudinal field for tip-enhanced Raman spectroscopy. *Applied Physics Letters*, *85*, 6239.

Kneipp, K., Wang, Y., Kneipp, H., Perelman, L. T., Itzkan, I., Dasari, R. R., et al. (1997). Single molecule detection using surface-enhanced Raman scattering (SERS). *Physical Review Letters*, *78*, 1667–1670.

Lacerna, J. J. (1993). Combining fingerprinting capability with trace analytical detection: Surface-enhanced raman spectrometry. *Analytica Chimica Acta*, *283*(1), 607–622.

Le Ru, E. C., Blackie, E., Meyer, M., & Etchegoin, P. G. (2007). SERS enhancement factors: A comprehensive study. *The Journal of Physical Chemistry*, *111*, 13794–13803.

Le Ru, E. C., Meyer, M., & Etchegoin, P. G. (2006). Proof of single-molecule sensitivity in surface enhanced Raman scattering (SERS) by means of a two-analyte technique. *The Journal of Physical Chemistry. B*, *110*(4), 1944–1948.

Nie, S. M., & Emery, S. R. (1997). Probing single molecules and single nanoparticles by surface-enhanced Raman scattering. *Science*, *275*(5303), 1102–1106.

Novotny, L., & Stranick, S. (2006). Near-field optical microscopy and spectroscopy with pointed probes. *Annual Review of Physical Chemistry*, *57*, 303–331.

Smith, E., & Dent, W. (2005). *Modern Raman spectroscopy*. Chichester: John Wiley & Sons.

Steidtner, J., & Pettinger, B. (2008). Tip-enhanced Raman spectroscopy and microscopy on single dye molecules with 15 nm resolution. *Physical Review Letters*, *100*, 236101.

Treffer, R., Lin, X., Bailo, E., Deckert-Gaudig, T., & Deckert, V. (2011). Distinction of nucleobases—A tip-enhanced Raman approach. *Beilstein Journal of Nanotechnology*, *2*, 628–637.

Vo-Dinh, T., Hiromoto, M. Y. K., Begun, G. M., & Moody, R. L. (1984). Surface-enhanced Raman spectroscopy for trace organic analysis. *Analytical Chemistry*, *56*(9), 1667–1670.

Index

Note: Page numbers followed by, followed by *f* indicate figures, *t* indicate tables, and *b* indicate boxes.

A

Abbe limit
  far field microscopy, 537–538
  nonlinear dependency, 537–539
  nonlinearity, 537
  signal-to-noise ratio, 540
  STED-beam, 539–540, 540*f*
  two-photon microscopy, 538–539
  wave structure sample, 532*b*
Acousto-optical tunable filter (AOTF), 451, 452, 576*f*, 578
Additive correction, 430–431, 431*f*
Aequorea aequorea, 100–101
Aequorin protein. *See Aequorea aequorea*
AFM. *See* Atomic force microscopy (AFM)
Airy disk and microscope resolution
  circular aperture diffraction, 39–41
  Fourier series and transforms, 19–20
  numerical aperture, 20–23
  point source of light, 19–20
  Rayleigh's criterion, 20–23
  resolution definitions, 20, 22*f*
  spherical wavelets emission, 23
Analog-to-digital converter (ADC), 196, 350
Analog to digital unit, 252
AOTF. *See* Acousto-optical tunable filter (AOTF)
Aperture diaphragm, 53–55, 135
Astigmatism, 374–375, 377*f*, 378*f*
Atomic fluorescence
  angular momentum, 74
  atomic adsorbance and emission spectra, 73
  electronic orbitals, 74
  Jablonski diagram, 73, 73*f*
  Planck's radiation law, 73
  singlet state, 74
  spectrum, helium-neon laser, 73–74, 74*f*
Atomic force microscopy (AFM)
  materials, 614
  methods
    confocal volume, 615
    epi-illumination, 615
    home-built system, 615–616
    ILM, 615–616
    noise, thermal drift and hysteresis, 615
    Raman filter, 616–617
    Raman techniques, 615
    side illumination, 615
    software/hardware integration, 615
    top-illumination, 615
Audio video interleave (AVI), 331
Auto-expose functions, 143
Axial polychromatic aberrations, 377–380, 382

B

Back focal plane (BFP), 57, 62–63, 64–65
Band-pass emission filter, 137–138
Barrier filter. *See* Emission filter
Bayer mosaic filter, 171–172, 171*f*
BCECF. *See* 2′7′-Bis (carboxyethyl)-5(6)-carboxyfluorescein (BCECF)
Beer's law, 72
BFP. *See* Back focal plane (BFP)
Binocular phototubes. *See* Trinocular tubes
Biological samples
  image blurring
    deconvolution algorithms (*see* Deconvolution algorithms)
    LSCMs and MPMs, 418–419
    optical/computational methods, 418–419
    PSF, 417–418, 418*f*
    WFM, 417–418
  quantitative fluorescence microscopy
    CCD cameras, 409
    detector noise, 410–411
    FLIM, 421
    FLIP, 421
    FRAP, 421
    FRET, 421
    GFP, 408–409
    illumination variations, 410
    imaging system, 411–413, 412*f*, 414*t*
    photon shot noise, 411
    PMTs, 409
    processing algorithms, 413–416, 415*f*
    quantitative image preprocessing, 413
    WFMs and SDCMs, 409
2′7′-Bis (carboxyethyl)-5(6)-carboxyfluorescein (BCECF)
  IMD colored ratiometric images, 396–397, 397*f*
  intact living cells, 392–395, 394*f*
  nigericin clamp protocol, 396–397, 397*f*
  nigericin technique, 397–398
  structure and spectral characteristics

2′7′-Bis (carboxyethyl)-5(6)-carboxyfluorescein (BCECF) *(Continued)*
carboxylate groups, 389
chemical structures, 389, 390*f*
dual excitation ratio imaging, 391
dual-wave-length fluorescent probes, 391–392
fluorescence signals, 391–392, 393*f*
pH, 389, 390, 391*f*
Black level. *See* Offset control
Blind deconvolution, 421
Blooming, 154, 165
Blue fluorescent protein (BFP), 449–450
Brightness, camera settings. *See* Offset control

C

Camera noise (N_{camera}), 255–256
CCD camera. *See* Charge-coupled device (CCD) camera
Cell culture media, 131–132
Central limit theorem, 348, 348
CFP. *See* Cyan fluorescent protein (CFP)
Charge-coupled device (CCD) camera
architecture
frame-transfer device, 169
full-frame device, 168–169
interline-transfer device, 169
sensors, 169–170, 170*f*
binning, 143–144, 143*f*, 170–171, 227–228
camera noise, 142
CCCD (*see* Cooled charge-coupled device (CCCD) camera)
charge storage capacity, 165
charge transfer efficiency, 166
color
Bayer mosaic filter, 171–172, 171*f*
depth of penetration, photon, 173
frame-sequential color cameras, 172–173, 173*f*
liquid crystal filter, 172–173
spatial resolution, 171–172
strategies, 171
three-CCD color camera, 172, 172*f*
video cameras, 236
components, 164
dark noise, 165, 221
depletion layer, 164–165
digital still cameras, 236
dynamic range, 167–168, 225–226
EBCCD, 175
electron-bombarded CCD, 175
electronic imaging, 164–165
electronic noise, 165
EMCCD (*see* Electron multiplier charge-coupled device (EMCCD) camera)
exposure time, 142–143
fast-scan CCD cameras, 231
in fluorescence microscopy, 176–178
frame rate and speed, 227
gain, 141–142, 226–227
HAD technology, 164–165
ICCD (*see* Intensified charge-coupled device (ICCD) camera)
image integration, 168
image-intensified CCD, 173–174, 175
imaging detector development, 178
intensified cameras (*see* Intensified cameras)
internal image amplification cameras
electron bombardment camera, 235
on-chip multiplication gain, 234–235
linearity and uniformity, 224–225
on-chip multiplication, 175–176
photon statistical noise, 165
quantum efficiency, 141–142, 166–167
readout, 245, 246*f*
readout noise, 220–221, 247
scan formats, 170
sensitivity and quantum efficiency
conversion factors, 218, 219*f*
fill factor, 218
noise equivalent floor, 216
quoting sensitivity, 218
radiant sensitivity, 217–218
spectral response, 217, 217*f*
shading, 166
shot/photon noise, 220
signal noise, 143
signal-to-noise ratio, 218–220, 221–222, 222*f*, 227–228
SIT cameras, 237
slow-scan CCD cameras, 229–231
spatial resolution, 222–224, 223*f*, 227–228
time response, 225
video CCD cameras, 228–229
working process, 164, 245–246
Charge transfer efficiency (CTE), 166
Circumventing photodamage, live-cell microscopy
Anna Karenina's principle, 546–548
Bessel-beam microscopy, 557
Caenorhabditis elegans, 546–548
CLEM, 557
confocal fluorescence images, 552
dose-decreasing illumination, 557
Drosophila melanogaster, 546–548
GFP, 546, 547*f*, 553*f*

hardware synchronization, 554–556, 555*f*
light intensity and exposure time, 548–551, 550*f*
photobleaching, 552–554, 553*f*
phototoxicity, 556–557
SPIM, 557
standard commercial filter sets, 551–552
stress-response pathway, 548
tdTomato, 554
wide-spectrum excitation, 552
Clipping, 154
Color-corrected negative lens. *See* "Telan" lens
Color video cameras, 236
Comatic aberration, 374, 375*f*, 376*f*
Complementary metal-oxide semiconductor (CMOS) camera, 216, 237–238, 245
Condenser
carrier, 55
numerical aperture
dry condenser, 53, 54*f*
objective, 52, 53*f*
research-type condensers, 53
perfect, 52, 52*f*
Confocal microscopy
3D fluorophore distribution, 428
disk-scanning/swept-array confocals, 430
limitations
accuracy, 432–433
CCD detector, 434, 436*f*
countable events, 434
noise components, 433
PMT detector, 435, 437*f*, 438*f*
Poisson distribution, 433–434
quantitative analysis, 433
SNR, 433
live-cell fluorescence imaging, 133, 134
nonuniformities correction
additive correction, 430–431, 431*f*
multiplicative correction, 431–432, 432*f*
performance evaluation
fluorescent beads, 439, 439*f*
image quality, 438
photobleaching, 438
phototoxicity, 438
spot-scanning confocals, 428–430, 429*f*
Contrast stretching
exposure time, 157
offset and gain adjustment
DIC images, cultured cells, 157, 158*f*
fluorescence image, 159, 161*f*
histogram, 159, 160*f*, 161*f*
increasing gain, 158–159
specimen detail of interest identification, 157
primary considerations, 157
Controlled light exposure microscopy (CLEM), 557, 615
Conversion efficiency (CE), 252
Convolution, 531
digital mask
averaging filter, 308
edge detection-computing gradients, 310, 311*f*, 312*f*
filter size, 306
intensities reassinging, 306, 307*f*
Laplacian filters, 311–312
line detection, 309–310
point detection, 309
thresholding, 312–314, 313*f*
graphical representation, 304, 305*f*
impulse function, 305
processing steps, 304
properties, 304–305
Cooled charge-coupled device (CCCD) camera, 248, 248*f*
CCD chip, 248
full-well capacity (FWC), 248
Hamamatsu C4880 dual mode (*see* Hamamatsu C4880 dual mode cooled CCD camera)
intrascene dynamic range, 248
noise effects, 258–259, 259*f*
noise reduction, 248
readout amplifier noise, 165–166
sensitivity, 276
shading, 279
SNR, 248
spatial resolution, 277
temporal resolution, 278
usability, 280
Cooled sCMOS (CsCMOS) camera, 248–249
Cyan fluorescent protein (CFP), 109–110, 115
Cylindrical Bessel function, 41

D

Deblurring/neighbor-based algorithms, 419–420, 421
Deconvolution algorithms
deblurring/neighbor-based algorithms, 419–420, 421
restoration methods, 420–421, 422–423
Detectable signal change (DS)
definition, 261–263
increasing signal
detector area, 265
higher QE, 263–264

Detectable signal change (DS) *(Continued)*
microscope objectives and magnification factors, 266
on-chip signal integration, 264–265, 266*t*
noise reduction
averaging images, 266–267
camera noise, 270
signal amplification, 270
signal intensification (*see* Signal intensification)
Detector calibration
CCD, 434, 436*f*
PMT, 435, 437*f*, 438*f*
Dichromatic mirror, 95, 136–137, 190*f*, 191, 515
Differential interference contrasts (DICs), 450
Digital camera
contrast stretching (*see* Contrast stretching)
exposure time, 154
gain, 155–156, 156*f*
gray-level information
histogram, 152
line scan plot, 152–153
over-and underexposed pixel detection software, 154
pixel colorization, 154
pixel value measurement, 152
vs. image display controls, 159–161
offset control, 154, 155*f*
Digital images
bit depth, 320–322
color, 325–327
compression, 329, 330*f*
file formats
BMP, 324
GIF, 324
JPEG, 323
PFF, 324
TIFF, 323
image-processing steps, 319
imaging software, 319–320
live-cells
CCD camera, 141–144
focus maintenance, 144–145
shutters, 144
quantitative temporal and spatial information, 318
raster graphics, 320, 321*f*
RGB to CMYK conversion, 327–329
sampling and spatial resolution, 325, 326*f*
vector graphics, 320
video codecs
asymmetric codecs, 332
key frames, 332
legacy codecs, 332
spatial compression, 331–332
suitability determination, 332–335, 334*f*
symmetric codecs, 332
temporal compression, 331–332
video files
AVI, 331
features, 330–331
MPEG, 331
QuickTime, 331
TIFF sequence, 331
Digital imaging system
microscope automation and camera control, 183*f*, 185*f*, 201–202
software packages, 202–203
Digital mask
averaging filter, 308
edge detection-computing gradients, 310, 311*f*, 312*f*
filter size, 306
intensities reassinging, 306, 307*f*
Laplacian filters, 311–312
line detection, 309–310
noise reduction, 292–293, 294*f*
point detection, 309
thresholding, 312–314, 313*f*
Digital microscope images
analog-to-digital converter, 350
black box, 340, 340*f*
calibration curve
absolute scale, 344*f*, 345–346
precisions, 346–347, 347*f*
relative scale, 342–344, 344*f*
cryptic *, 341
empty magnification, 357
error propagation, 351–354, 353*f*, 364–366, 364*f*
flatfield correction, 354–355, 356*f*
imaging warping
barrel distortion, 359, 360*f*
distortion plot, 358, 359*f*
grid lines, 357–358
pincushion, 359, 360*f*
polynomial dewarping, 360
spherical aberration, 358
intensity profiles, 339–340, 339*f*
pixels conversion, 357, 358*f*
quantitative information, 341
quantitative microscopy, 341, 342*f*
Rayleigh diffraction limit, 356–357
reference standard, 354
rotational translation, 366–367, 366*f*

signal-to-background ratio, 350
signal-to-noise ratio, 350
spatial corrections, 355
standard deviations, 348–350, 349*f*
standard errors, 348–350, 349*f*
two-camera and two-color imaging, 363–364
two-color coincidence, 361–363, 362*f*
Digital microscopy, cameras. *See* Charge-coupled device (CCD) camera
Digital still cameras, 236
Digitizer count (DC), 252
Dirac Delta Function, 35
Discosoma, 104
Disk-scanning/swept-array confocals, 430
DNA oxidation, 613
drFP583 protein, 104
dsRed protein, 104, 105*f*
Dual-chain systems
CFP/YFP excitation, 602
photobleach correction, 603–604
quantitative bleedthrough calibration, 603
ratio *vs.* $[FRET]_{Corr}$, 603
Dynamic range (DR)
CCCD camera, 248
CsCMOS camera, 249
definition, 261–262
EMCCD camera, 251
ICCD/ IsCMOS camera, 250
increasing signal
detector area, 265
higher QE, 263–264
microscope objectives and magnification factors, 266
on-chip signal integration, 264–265, 266*t*
noise reduction
averaging images, 266–267
camera noise, 270
signal amplification, 270
signal intensification (*see* Signal intensification)

E

Electron-bombarded charge-coupled device (EBCCD), 175
Electron bombardment camera, 235
Electronic imaging, 164–165, 218–220, 221, 244–245
Electronic shuttering, 169
Electron multiplier charge-coupled device (EMCCD) camera, 141–142, 251*f*, 563*f*, 577, 579–580, 582
fast frame rates, 250–251
Gain Aging, 252
high and low light imaging, 250–251
impact ionization, 251, 252
multiplication register, 251–252
noise effects, 260–261, 261*f*
relative readout noise, 251
sensitivity, 276
shading, 279
spatial resolution, 278
temporal resolution, 278
usability, 281
EMCCD. *See* Electron multiplier charge-coupled device (EMCCD) camera
Emission filter, 95, 109, 110*f*, 136–137, 140–141, 191, 381, 401–402, 515, 552, 553*f*, 578–579
Empty magnification, 9–10, 529
Endogenous tissue fluorophores, 482
Enhanced green fluorescent proteins (EGFP), 478
Epiillumination optics
condenser diaphragm, 189
dual filter wheel and epishutter, 189, 190*f*
emission filter, 191
field stops, 190–191
filter cube turret, 191
heat reflection filter, 189
Köhler illumination, 189
longitudinal chromatic aberration, 191
mercury lamp housing, 189
multiple band-pass dichromatic mirror, 190*f*, 191
Eyepiece/ocular
benefits of, 60
10 × eyepieces, 59
fixed-focus eyepiece, 59
high-eyepoint, 59
Nyquist criterion, 60
useful magnification range, 59–60

F

Fast-scan CCD cameras, 231
FCS. *See* Fluorescence correlation spectroscopy (FCS)
Field diaphragm, 50–51, 64–65, 135
Field iris diaphragm. *See* Field diaphragm
Field stop. *See* Field diaphragm
Filters
Bayer mosaic filter, 171–172, 171*f*
and chromatic mirrors, 109, 110*f*
dichromatic mirror, 136–137
emission filter, 136–137
excitation filter, 136–137
IR blocking filter, 50
liquid crystal filter, 172–173
ND filters, 135

Filters *(Continued)*
selection automation, 137–138
wavelength selection
absorbing glass filters, 93–94
fluorescence emission spectrum, 92–93, 93*f*
interference filters, 93–94
percentage transmission, 92–93, 93*f*
Finite tube length microscope
cross section, 2–3, 4*f*
geometric optics, 3*f*
vs. infinity-corrected microscope optics, 4, 5*f*
intermediate image plane, 2–3
objective lens and ocular lens, 2, 3*f*
photo-detecting surface, 2–3
specimen image magnification, 6
"telan" lens, 4, 5*f*
Flat-fielding corrections
additive correction, 430–431, 431*f*
multiplicative correction, 431–432, 432*f*
Flavin adenine dinucleotide (FAD), 458–459
FLIM. *See* Fluorescence lifetime imaging microscopy (FLIM)
Fluorescence
atomic, 73–74
cell structures, 70
depolarization, 80–81
excited state
lifetime, 76–77
saturation, 77
filters, wavelength selection, 92–94, 93*f*
light absorption
absorbance measurement, 71–72, 71*f*, 72–73
Beer's law, 72
fluorophore density, 72–73
light intensity, 71–72
optical density, 72
measurement
in steady state, 82–83
in time-domain (*see* Lifetime measurement)
microscope, 94–95
monochromator construction, 83
nonradiative decay mechanisms, 77–78
organic molecular, 74–76
photomultiplier tube construction, 84
quantum efficiency (QE), 76–77
resonance energy (*see* Fluorescence resonance energy transfer (FRET))
Fluorescence correlation spectroscopy (FCS)
biological systems
Alexa-Fab affinity, 507
antibody–hapten interaction, 494–495
autocorrelation, 495–496, 496*f*
confocal principle, 493, 494*f*
cross correlation, 495–496, 496*f*
$DiIC_{16}$, solution and plasma membrane, 505–506, 506*f*
discriminate fast-and slow-diffusing particles, 499
dynamic light scattering, 494–495
fluorescently labeled molecule, 497
lipid bilayers, 494–495
living cells, 504–505, 505*f*
low-affinity NGFR gp75, 506–507, 507*f*
macromolecules interaction, 499, 500*f*
modulating binding protein, 497
molecular complexing in solution, 501–504, 502*f*
molecules, 491–492, 492*f*
monomers, dimers, trimers, and tetramers, 507–508, 508*f*
multiple diffusing components, 499
probability relationships, 507–508, 508*f*
radioactive decay, 492
rhodamine-conjugated Fab fragment, 497, 498*f*
single-molecule detection method, 494
structure parameter, 497
surface-solution interactions, 494–495
two-dimensional autocorrelation function, 506
commercial sources, 520
data acquisition and analysis
autocorrelation analysis, 518
beam diameter and confocal volume, 519
fitting correlation curves, 518–519
random noise and optimized signal, 517–518
stoichiometry, 519
digital correlator
ALV, 517
correlator.com, 516
FLIM, 479–480
laser illumination, 511–514
beam steering, 513
fiber-optic coupling, 512–513
laser power, 512
laser stability, 512
system alignment, 513–514, 514*f*
wavelength, 512
laser power output, 510–511
ligand-receptor binding, 490–491
optics
dichromatic mirrors and filters, 515
high-NA objective, 515
photon counting, 515–516
telescoping beam expander, 515

photon counting
APD, 516
PMT, 516
primary components, 511
protein-DNA interaction, 490–491
protein-protein interaction, 490–491
single molecules, 490–491
TEM 00 mode structure, 511
Zeiss Axiovert 35 microscope, 509–510, 509*f*
Fluorescence intensity, 77
Fluorescence lifetime imaging microscopy (FLIM), 416
endogenous and exogenous fluorophores, 459*t*
FAD, 458–459
fluorescence lifetime sensing, 459–460
fluorophore excited-state lifetime
intensity-based artifacts, 462
intensity-independent nature, 462, 462*f*
Jablonski diagram, 460–461, 461*f*
LRB-PE, 464–465
NADH, 464
nonradiative decay, 461
phospholipids NBD-PE, 464–465
quantitative pH determination, 463
radiative decay, 461
RTDP fluorescence intensity, 464*f*
static and dynamic quenching, 462–463, 463*f*
tryptophan, 461–462
maps (*see* Fluorescence lifetime maps)
pre-mRNA splicing, 458–459
quantitative biological imaging
FCS, 479–480
FRET events, 448–449, 458–459, 460*f*, 477–479, 479*f*
MP-FLIM, endogenous tissue fluorophores, 482–483, 483*f*
multispectral-FLIM, 480–482, 481*f*
Rhodamine B, 458–459
Fluorescence lifetime maps
data analysis methods
analytical least-squares algorithms, 471–472
iterative least-squares analysis, multiexponential fitting, 472
least-squares analysis, Laguerre polynomial fitting, 472–473
Monte Carlo simulations, 474–475
phasor plot analysis, 473–474
Poisson noise, 474–475
RSD, 474–475
temporal optimization and spatial denoising methods, 475–477, 476*f*
frequency domain (FD), 469–470, 469*f*
time domain (TD) methods
TCSPC film, 467–468, 467*f*
time-gated FLIM, 465–467, 466*f*
Fluorescence loss in photobleaching (FLIP), 116–117, 416
Fluorescence microscopy
FLIM (*see* Fluorescence lifetime imaging microscopy (FLIM))
fluorescence fundamentals (*see* Fluorescence)
FPALM, 563–564
FRET microscopy (*see* Fluorescence resonance energy transfer (FRET) microscopy)
mode, 133–134
power of, 95–96
Fluorescence photoactivated localization microscopy (FPALM), 563–564
Fluorescence recovery after photobleaching (FRAP), 116–117, 416
Fluorescence resonance energy transfer (FRET)
dipole-induced dipole interaction, 79
donor emission and acceptor excitation spectra, 78–79, 78*f*
excited state lifetime, 78–79
hyperchromicity, 80
mechanism, 78–79, 79*f*
oligonucleotide hybridization, 80, 80*f*
spectroscopic ruler, 78–79
transfer efficiency, 79, 80
donor quenching mechanism, 446
donor's fluorescence emission intensity, 446
fluorescence intensity, 444*f*, 446
fluorescence lifetime equipment, 446
molar extinction coefficient, 446–447
overlap integral, 446–447
radiative and nonradiative mechanisms, 445–446
steady-state/lifetime measurements, 444–445, 445*f*
Fluorescence resonance energy transfer (FRET) microscopy, 416
Angstrom resolution, 442
BFP, 449–450
cellular microscopy, 449
cellular regions/organelles, 450
CFP-YFP
protein-protein interactions, 453–454
steady-state approach, 454
time *vs.* frequency domains, 454–455
DIC microscopy, 450
donor and acceptor fluorescence intensities, 448–449
fluorescence illumination
detectors, 452–453

Fluorescence resonance energy transfer (FRET) microscopy *(Continued)*
epifluorescence microscope, 450
light sources, 450–451
wavelength selectors, 451–452, 452*t*
fluorescence intensity information, 442
light microscope, 442
microscope, 449–450
nonradiative, 442–444, 443*f*, 444*f*
numerical aperture (NA), 449
practical considerations
acceptor-labeled complement, 448
background fluorescence, 447
fluorescence emission intensity, 448
unlabeled complementary molecule, 448
spherical and spatial aberrations, 449–450
transfer efficiency
donor quenching mechanism, 446
donor's fluorescence emission intensity, 446
fluorescence intensity, 444*f*, 446
fluorescence lifetime equipment, 446
molar extinction coefficient, 446–447
overlap integral, 446–447
radiative and nonradiative mechanisms, 445–446
steady-state/lifetime measurements, 444–445, 445*f*
Fluorescent microspheres
contrast, 370
magnification, 370
optical aberrations (*see* Optical aberrations)
optical performance, 371
polystyrene microspheres, 371
PSF, 372–373, 373*f*, 374*f*
resolution, 370
three-dimensional performance, 371–372
Fluorescent probe
live-cell imaging, 571
multicolor fixed-cell imaging, 570
probes and imaging buffers, 565, 566*t*
single-color fixed-cell imaging, 567–570
spatial resolution and probe properties, 565–567, 568*f*
Fluorescent protein (FP)
GFP (*see* Green fluorescent protein (GFP))
imaging
filters and chromatic mirrors, 109, 110*f*
fixation, 112
FP selection, 109–111
fusion construction, 111–112
intracellular environments, 114–115, 116*f*
multiwavelength, 114
optical system components, 108
protein dynamic measurements, 116–117
protein-protein interactions in vivo, 115
super-resolution, 117
time-lapse, 112–114, 113*f*
unwanted fluorescence reduction, 108–109
Fluorophore
density, 72–73
live-cell fluorescence imaging, 127–128
Förster resonance energy transfer (FRET)
biosensors, Rho family GTPases
dual-chain systems (*see* Dual-chain systems)
motion artifacts, 605
photobleaching, 604–605
single-chain systems (*see* Single-chain systems)
thickness artifacts, 605–607, 606*f*
FLIM detection, 458–459, 460*f*
chromatin compaction, 478, 479*f*
donor-acceptor (D-A) pair, 477, 478
donor emission spectrum, 477
EGFP/mCherry fluorescent proteins, 478
energy transfer efficiency, 478
Förster distance, 477
intensity-based measurement artifacts, 478
macromolecule, 477
metaphase, 478
nanoscale ruler, 477
phosphorylated PKCα molecules, 479
steady-state/time-resolved data, 478
GFP, 115
Fourier series
Airy disk, 19–20
Dirac Delta Function, 35
electric field wave equation, 34
Fourier/reciprocal space, 27, 27*f*
Fourier transform, 33, 34–35
inverse Fourier transform, 35
$2n+1$ coefficients, 32, 33
sine/cosine representation, 33–34
$S_n(x)$ function, 31–32
step function, 33
FP. *See* Fluorescent protein (FP)
Frame-sequential color cameras, 172–173, 173*f*
Frame-transfer CCD, 169
Fraunhoffer diffraction, 40
FRET. *See* Fluorescence resonance energy transfer (FRET)Förster resonance energy transfer (FRET)
Full-frame CCD, 168–169
Fura-2 shift
autofluorescence, 395
fluorescence intensity, 395

hydrolysis, 395
intact living cells, 392–395, 394*f*
intracellular organelles, 395
structure and spectral characteristics
Ca^{2+}, 389, 390–391, 392*f*
Ca chelator BAPTA, 389
chemical structures, 389
dual excitation ratio imaging, 391
dual-wave-length fluorescent probes, 391–392
fluorophore, 389
spectral characteristics, 390–391, 392*f*

G

Gating, ICCD, 175
GFP. *See* Green fluorescent protein (GFP)
Green fluorescent protein (GFP), 408–409, 546, 547*f*
chromophore formation, 101–103
identification, 100–101
mutagenesis
Discosoma, 104
dsRed chromophores, 104–105, 105*f*
excitation and emission spectrum, 104
fluorescent protein characteristics, 104–105, 106*t*
PA-GFP, 105–107, 107*f*
red fluorescent protein, 104–105
RSFPs, 105–107, 107*f*
structure, 103–104
Green's theorem, 37

H

Halogen regenerative cycle, 45–47
Hamamatsu C4880 dual mode cooled CCD camera
dark and background reference image subtraction, 195*f*, 199
features, 193–194
intensity measurements, 198
light intensity, 195*f*, 198
position measurements, 198
quantum efficiency, 190*f*, 194–195, 195*f*
readout
analog-to-digital converter, 196
binning, 197–198, 197*f*
fast-scan mode, 196
image size, 196
noise, 199
slow-scan mode, 196
transfer time, 196
shading, 199–200
signal-to-noise, 200–201, 200*f*
thermal noise, 198–199, 198*f*
Heterodyne detection, 91
Hole-accumulator-diode (HAD), 164–165
Homodyne detection, 91, 92*f*
Huygens' principle, 14–15, 39

I

ICCD. *See* Intensified charge-coupled device (ICCD) camera
Image deconvolution, 423. *See also* Deconvolution algorithms
Image intensification, 173–174
Image-intensified CCD camera, 173–174, 175. *See also* Intensified charge-coupled device (ICCD) camera
Image processing
contrast enhancement
contrast enhancement factor, 297–299
contrast routines, 294–295
gray values, 295–297, 297*f*
image transfer function (ITF), 296–297, 298*f*
LUT, 299, 301*f*, 302*f*
nonlinear ITF, 299, 300*f*
convolution (*see* Convolution)
image digitization, 286–288, 287*f*
noise reduction
averaging *vs.* median filters, 293–294, 295*f*, 296*f*
digital mask, 292–293, 294*f*
image subtraction, 292, 293*f*
temporal averaging, 290–291, 290*f*, 291*f*
transforms
forward transformation, 301–303
Fourier transform, 301–303
frequency domain cutoff filters, 303–304, 304*f*
image smoothing and noise removal, 303
inverse transformation kernel, 301–303
Imaging warping
barrel distortion, 359, 360*f*
distortion plot, 358, 359*f*
grid lines, 357–358
pincushion, 359, 360*f*
polynomial dewarping, 360
spherical aberration, 358
Immunohistochemistry (IHC), 571, 573*f*
Infinity-correction, 58
Infinity optics microscopes
vs. finite tube-length microscopes, 5*f*, 6
infinity space, 6
intermediate image plane, 6
"telan" lens, 5*f*, 6
tube lenses, 6
Infinity space, 58

Intensified cameras
  disadvantages, 233
  fast-scan scientific CCD, 234
  fiber optic coupling, 233
  high time resolution, 233
  ICCD (*see* Intensified charge-coupled device (ICCD) camera)
  IsCMOS (*see* Intensified sCMOS (IsCMOS) camera)
  lens coupling, 233
  setup, 231–233, 232*f*
  types, 233
  video CCD, 234
  with video readout, 280
Intensified charge-coupled device (ICCD) camera, 173–174, 175, 249–250, 250*f*
  gating, 175
  geometric distortion, 279
  shading, 279
  spatial resolution, 277–278
  temporal resolution, 278–279
  usability, 280–281
Intensified photon counting cameras, 269, 270
Intensified sCMOS (IsCMOS) camera, 249–250, 250*f*
  geometric distortion, 279
  usability, 280–281
Intensity-modulated display (IMD), 396–397, 397*f*
Interline-transfer CCD, 169
Intermediate image plane, 2–3, 6
Internal image amplification cameras
  electron bombardment camera, 235
  on-chip multiplication gain, 234–235
Intersystem crossing, 74–76
Intracellular Ca^{2+} and pH measurements
  BCECF (*see* 2′7′-Bis (carboxyethyl)-5(6)-carboxyfluorescein (BCECF))
  dual-wavelength indicators, 389
  experimental chamber and perfusion system, 403–405, 404*f*
  fluorescence emission, 388
  fluorescence signal calibration
    Ca^{2+} ionophore ionomycin, 397–398
    calibration technique, 396–397, 397*f*
    clamp, 396
    Fura-2-loaded cells, 398, 399*f*
    H^{+} and Ca^{2+} concentration, 396
    Hepes buffered solution, 398
    IMD, 396–397, 397*f*, 398, 399*f*
    nigericin, 396–397, 397*f*
  Fura-2 shift (*see* Fura-2 shift)
  imaging workstation, 401–403, 402*f*
Inverse Fourier transform, 35
IR blocking filter, 50
IsCMOS. *See* Intensified sCMOS (IsCMOS) camera

J

Jablonski diagram
  atomic fluorescence, 73, 73*f*
  organic molecular fluorescence, 74–76, 75*f*
Joint photographic experts group (JPEG), 323

K

Kirchoff's scalar theory of diffraction, 35–36
Koehler illumination, 135
  benefits, 61
  components, 61–62
  conjugated light paths
    illumination pathway, 62–63, 64*f*
    imaging pathway, 64–65, 64*f*, 65*f*
  Koehler, August, 60–61, 61*f*
  working process, 62
Köhler illumination, 189

L

Label-free multiphoton-FLIM, 482–483
Laguerre analysis, 472–473
Laguerre polynomial fitting, 472–473
Lamp collector, 49–50, 51*f*
Laser scanning confocal microscopes (LSCMs), 409
Lateral chromatic aberration (LCA), 56
Lateral polychromatic aberrations, 377–380, 381
Lifetime measurement
  boxcar-gated detection, 85–87, 86*f*, 87*f*, 88*f*
  deconvolution process, 90
  excited state lifetime, 84–85
  exponential decay times, 85
  phase modulation method
    heterodyne detection, 91
    homodyne detection, 91, 92*f*
    phase modulation imaging microscopy, 92
    point spread function, 90
    spatial frequencies, 90
    spectrofluorimeter, 90–91, 91*f*
  photomultiplier response, 85, 86*f*
  photon correlation method, 89, 89*f*
  streak camera method, 87–89, 88*f*
Light amplification by stimulated emission of radiation (LASER), 49
Light-emitting diodes (LEDs), 48, 49, 49*f*
Light microscopy
  digital images (*see* Digital images)
  frame-sequential color cameras, 172–173
  image processing (*see* Image processing)

resolution limit (*see* Resolution limit)
single-chip CCD, 171–172
Light source
artificial sources, 44, 45*f*
gas discharge/arc lamps, 47–48, 49*f*
incandescent light bulb, tungsten filament, 44–45, 46*f*
laser light sources, 49
LEDs, 48, 49, 49*f*
pre-aligned bulbs, 47
tungsten-halogen bulbs, 45–47, 47*f*
Xenon bulbs, 47–48
Linear shift invariant, 531
Liquid crystal filter, 171, 172–173
Liquid crystal tunable filters (LCTFs), 451, 452
Live-cell fluorescence imaging
cell health and troubleshooting, 146–147
challenges, 126, 127
checklist, 127, 127*t*
digital images (*see* Digital images, live-cells)
fluorescence microscopy mode
confocal microscopy, 133, 134
TIRF microscopy, 134
wide-field microscopy, 133
microscope stand, 132–133
nD imaging, 145–146
objective lens (*see* Objective lens)
signal-to-noise ratio, 126
spatial resolution, 126
specimen preparation
cell culture media, 131–132
chambers, 129–131
fluorophore selection, 127–128
photobleaching prevention, 132
spherical aberration and light scattering, 128–129
temperature maintenance, 131
wide-field illumination (*see* Wide-field illumination)
Lookup table (LUT), 299, 301*f*, 302*f*
Low light cameras
advanced technology
convenience, 283
high sensitivity, 282
high spatial resolution, 282
high temporal resolution, 282
CCD camera (*see* Charge-coupled device (CCD) camera)
CMOS camera, 216, 237–238, 245
detection efficiency, 214–215, 214*t*
DR (*see* Dynamic range (DR))
DS (*see* Detectable signal change (DS))
filters and dichroic mirrors, 214
fluorescence imaging, 212–213
geometric distortion, 279
image acquisition, 238
image intensity, 213–214
numerical aperture, 214
optical components, 213–214
sCMOS (*see* sCMOS camera)
sensitivity
comparison, 275–276, 276*f*
gray level scale, 252, 254*t*
high sensitivity, 252
image brightness, 252
SNR (*see* Signal-to-noise ratio (SNR))
Luminous field diaphragm. *See* Field diaphragm

M

Maxwell's wave equation, 31
Metadata, 322–325
Microchannel plate (MCP), 174
Microscope
finite tube length microscope (*see* Finite tube length microscope)
infinity optics microscopes (*see* Infinity optics microscopes)
mounting video camera
basic considerations, 8–9
camera pixel number and resolution, 10
empty magnification, 9–10
objectives
coverslip selection, 8
mixing and matching, 7–8
types of, 6–7
Microscope alignment
illumination section
aperture diaphragm, 53–55
condenser (*see* Condenser)
field diaphragm, 50–51
illumination path components, 50
Koehler illumination (*see* Koehler illumination)
lamp collector, 49–50, 51*f*
light source (*see* Light source)
stage and specimen holder, 55–56
imaging section
camera mount, 59
eyepiece/ocular, 59–60
inclined binocular tube, 59
infinity space, 58
intermediate image plane, 59
nosepiece turret, 58
objective (*see* Objectives)

Microscope alignment *(Continued)*
trinocular tubes, 59
tube lens, 58
Microscope image formation, optics
Abbe's theory, 31
diffraction problems, 36, 36*f*
Fourier/reciprocal space
characteristic spatial frequency, 23–24, 24*f*
Fourier series, 27, 27*f*
Fourier transforms, 27
frequency amplitudes, 26–27, 26*f*
optical ringing, 26
step function, 25–26, 25*f*, 26–27
Green's theorem, 37
Huygens' principle, 14–15, 39
Kirchoff's scalar theory of diffraction, 35–36
microscope resolution
Airy disk (*see* Airy disk and microscope resolution)
back focal plane, 29–30
and contrast, 30–31, 30*f*
diffraction grating, 28–29, 28*f*
resolution limit, 28–29
scalar spherical waves, 36
single-slit diffraction, 18–19, 19*f*, 20*f*
solution for plane, 37–39
superposition of waves
constructive and destructive interference, 13*f*, 14
electric field vector, 13–14
superposition of sine waves, 13, 13*f*
superposition theorem, 14
Young's experiment (*see* Young's experiment)
Monochromatic aberrations
astigmatism, 374–375, 377*f*, 378*f*
coma, 374, 375*f*, 376*f*
spherical aberration
asymmetrical defocus, 375–376, 379*f*
focal depth, 375–376, 381*f*
ray path, 375–376, 380*f*
sharp diffraction rings, 375–376, 379*f*
Monochromator, 83
Multidimensional imaging. *See* nD imaging
Multiexponential fitting, 472
Multimode digital microscope system, 182*f*
anaphase *in vitro* imaging, 203–205, 205*f*
components, 181–182, 183*f*
DE-DIC system, 185*f*, 203, 204*f*
DIC imaging, 185, 185*f*
digital imaging system
microscope automation and camera control, 183*f*, 185*f*, 201–202
software packages, 202–203
epiillumination optics
condenser diaphragm, 189
dual filter wheel and epishutter, 189, 190*f*
emission filter, 191
field stops, 190–191
filter cube turret, 191
heat reflection filter, 189
Köhler illumination, 189
longitudinal chromatic aberration, 191
mercury lamp housing, 189
multiple band-pass dichromatic mirror, 190*f*, 191
fluorescence optical components, 182–184, 185*f*
fluorescence photoactivation, 182–184, 205–206, 206*f*
GFP-dynein-labeled microtubules, yeast, 207–208, 208*f*
Hamamatsu C4880 dual mode cooled CCD camera (*see* Hamamatsu C4880 dual mode cooled CCD camera)
immunofluorescent specimens, 208, 209*f*
mitotic mutant analysis, 181
multiple optical modes, 181
Nikon FXA upright microscope (*see* Nikon FXA upright microscope)
optical sections, 186
phase contrast, 185, 185*f*
photobleaching and photodamage, 184
tissue cells migration, 206–207, 207*f*
transillumination optics
band-pass filter, 192
focus control, 193
ground-glass diffuser, 192
heat-reflecting filter, 192
Köhler illumination, 192
quartz-halogen lamp, 191
thermal isolation, 192
transshutter, 192
vibration isolation, 182*f*, 193
Multiphoton excitation microscopy, 482
Multiphoton-FLIM (MP-FLIM), 482, 483*f*
Multiphoton microscopes (MPMs), 409
Multiplicative correction, 431–432, 432*f*
Multispectral fluorescence lifetime imaging microscopy (msFLIM), 480–482, 481*f*
Multiwavelength imaging, 114

N

NA. *See* Numerical aperture (NA)
nD imaging, 145–146
Neutral density (ND) filters, 135, 147, 183*f*, 189, 401
Nicotinamide adenine dinucleotide (NADH), 464
Nikon FXA upright microscope, 182*f*, 183*f*

filter wheel, 183*f*, 188–189
focus determination, 188
imaging optics, 186–189
magnification changer, 187, 187*f*
matching condenser, 186
Normarski prism, 188–189
objective numerical aperture, 186
phase contrast, 188
set up, 186
Nonradiative fluorescence resonance energy transfer (FRET), 442–444, 443*f*, 444*f*
Numerical aperture (NA), 214, 370, 401–402
Airy disk and microscope resolution, 20–23
dry condenser, 53, 54*f*
and magnification, 186, 266
objective, 52, 53*f*, 129, 186, 356–357, 449, 493
objective lens, 108, 176, 372, 417, 418*f*, 428, 579, 617
point spread function (PSF), 534*f*
research-type condensers, 53
resolution and brightness, 138–139
spherical aberration, 129

O

Objective lens, 2, 3*f*, 579
aberration correction, 139–140
infinity-corrected, 8
magnification, 139
numerical aperture, 108, 138–139, 176, 372, 417, 418*f*, 428, 617
phase and DIC, 140–141
spherical aberration, 139, 140
Objectives
BFP, 57
infinity optics, 56
LCA correction, 56
mixing and matching, 7–8
mounting media and cover slips, 57
Offset control, 154
Older Zeiss and Leica objectives, 8–9
Olympus and Nikon objectives, 7, 8–9
Optical aberrations
monochromatic aberrations
astigmatism, 374–375, 377*f*, 378*f*
coma, 374, 375*f*, 376*f*
spherical aberration, 375–376, 379*f*, 380*f*, 381*f*
mounting media, 383–384
polychromatic aberrations
axial, 377–380, 382
lateral, 377–380, 381
source determination, 382–383
Optimal gating, 474–475

P

Parfocal, 59
Pectiniidae, 105–107
Phase objective lens, 140–141
Phasor analysis, 473–474
Photoactivatable fluorescent protein (PA-FP), 117
Photoactivatable green fluorescent protein (PA-GFP), 105–107, 107*f*
Photoactivated localization microscopy (PALM), 117, 563–564
Photobleaching, 78
fluorescent protein, 116–117
Oxyrase/OxyFluor, 132
Photomultiplier tubes (PMTs), 82, 84, 409
Photon counting camera, 268–269, 269*f*, 270
Photosensitive surface, 164–165
Physical optics. *See* Superposition of waves
Picture elements, 164
Piezoelectric devices, 146
Pixel colorization, 154
Plan achromats, 6–7
Plan apochromats, 6–7
Planck's radiation law, 73
Plan fluorite lenses, 6–7
Point spread function (PSF), 372–373, 373*f*, 374*f*, 417–418, 531*b*, 534*f*
Polarization, fluorescence, 80–81, 81*f*
Polychromatic aberrations
axial, 377–380, 382
lateral, 377–380, 381
Polynomial dewarping, 360
Proprietary file formats (PFF), 324
Protein dynamics, 101, 105–107
PSF. *See* Point spread function (PSF)

Q

Quantitative microscopy, 341, 342*f*
Quantum efficiency (QE)
CCD camera, 166–167
live-cell imaging, 141–142

R

Raman filter, 616–617
Raster graphics, 320, 321*f*
Ratio imaging. *See* Intracellular Ca^{2+} and pH measurements
Ratiometric biosensor systems
dual-chain systems (*see* Dual-chain systems)
single-chain systems (*see* Single-chain systems)
Rayleigh diffraction limit, 356–357
Rayleigh resolution limit, 531, 534*f*
Rayleigh's criterion, 20–23

Readout amplifier noise, 165–166
Readout noise, 246, 247
Red fluorescent protein (RFP), 104–105
Relative standard deviation (RSD), 474–475
Resolution limit
  Abbe limit (*see* Abbe limit)
  apodization, 536
  confocal and 4Pi images, 536, 537*f*
  empty magnification, 529–530
  fluorescence microscopy methods, 526, 527*t*
  I^5M and the 4Pi type C microscope, 536
  light optical microscopy, 526
  linear structured illumination, 536–537, 538*f*
  near field methods and pendry's lens, 540–541
  pinhole diameters, 535–536
  Pointillism, 530–534
  precision, 529–530
  PSF, 531*b*, 534*f*
  sampling, 529
  sensitive light microscopic system, 529
  spatially nonuniform illumination, 527*t*, 534
Restoration methods, 420–421, 422–423
Reversible protein highlighting process, 105–107
Reversibly switchable fluorescent proteins (RSFPs), 105–107, 107*f*

S

Scanning near field optical microscopy (SNOM) methods, 541
Scanning tunneling microscopy (STM), 613
Scientific applications, 165, 172
sCMOS camera
  advantages, 247
  cooled sCMOS, 248–249
  Global Shutter mode, 246
  IsCMOS, 249–250, 250*f*
  noise effects, 259–260, 260*f*
  readout, 246–247, 247*f*
  Rolling Shutter mode, 246
  sensitivity, 276
  shading, 279
  spatial resolution, 277
  temporal resolution, 278
  usability, 280
  working process, 246
Selective plane illumination microscopy (SPIM), 557
Sensitive cameras, 212–213
SERS. *See* Surface-enhanced Raman spectroscopy (SERS)
Signal amplification cameras. *See* Electron multiplier charge-coupled device (EMCCD) camera
Signal intensification
  multiphoton and single photon, 268–269, 269*f*
  multiplication noise, 267
  photon counting camera, 269, 269*f*, 270
  relative noise reduction, 267
  relative read noise, ICCD camera, 267–268, 268*f*
Signal shot noise (N_{shot}), 255
Signal-to-noise ratio (SNR)
  camera noise (N_{camera}), 255–256
  formula, 255
  vs. light level, 257–258, 257*f*, 258*t*
  required levels
    high light image, 271, 274*f*
    integration time, 274
    low-noise camera, 275
    multiplication noise, 274–275
    signal multiplication cameras, 274
    1 s photon counting, 271, 272*f*
    1/30 s photon counting, 271, 271*f*
    10 s photon counting, 271, 272*f*
    100 s photon counting, 271, 273*f*
    1000 s photon counting, 271, 273*f*
  sensitivity, 253
  signal calculation, 255
  signal shot noise (N_{shot}), 255
  total noise (N), 256–257
Silicon intensified target (SIT) cameras, 237
Single-chain systems
  background subtraction, 599–600, 599*f*
  flatfield correction (shading correction)
    arc-lamp-based illumination system, 597–598
    CFP, 597–598
    dark-current correction images, 598
    field of view (FOV), 597–598, 597*f*
    scaling factor, 598–599
    shading images, 598
  image masking, 600, 601*f*
  morphing, 600
  photobleach correction, 602
  ratio calculation, 601–602
  X-Y translational registration, 601
Single-pass emission filters, 137–138
Single-slit Fraunhoffer diffraction, 18–19
Slow-scan CCD cameras, 229–231
SNR. *See* Signal-to-noise ratio (SNR)
Sparrow limit, 531
Spectrofluorimeter, 82, 82*f*
Spherical aberration
  asymmetrical defocus, 375–376, 379*f*
  focal depth, 375–376, 381*f*
  ray path, 375–376, 380*f*
  sharp diffraction rings, 375–376, 379*f*

Spinning disk confocal microscopes (SDCMs), 409
Split-FP systems, 117
Spot-scanning confocals, 428–430, 429*f*
Step function, 25–26, 25*f*, 26–27, 33
Stochastic optical reconstruction microscopy (STORM)
  computer, 581
  data analysis
    drift correction, 585
    filtering, 586, 586*f*
    Gaussian fitting, 584–585
    molecules, 587
    Nyquist spatial resolution, 587
    peak finding, 584
    photon events, 585
    software package, 584
  data collection
    fiducial markers, drift correction, 581–582
    live-cell imaging, 583
    multicolor imaging, 582–583
    single-color 2D and 3D imaging, 582
  detection pathway
    camera, 579–580
    3D imaging, 564–565, 564*f*, 580
    multichannel detection, 580
  excitation pathway
    intensity and temporal modulation, 578
    laser sources, 576–577, 576*f*, 577*t*
    TIRF, 578
  fluorescent probe selection (*see* Fluorescent probe)
  focus lock, 580–581
  Gaussian distribution, 563*f*
  microscope
    dichroic mirrors and emission filters, 578–579
    inverted fluorescence microscope, 578
    objective lens, 579
  PALM, 563*f*
  sample preparation
    fluorescent proteins, 574
    immunohistochemistry (IHC), 571, 573*f*
    peptide tag and fluorophore substrate, 575
    ultrastructure preservation, 571
Stoke's shift, 74–76
Superposition of waves
  constructive and destructive interference, 13*f*, 14
  electric field vector, 13–14
  sine waves, 13, 13*f*
  superposition theorem, 14
Superposition theorem, 14
Super-resolution fluorescence imaging. *See* Stochastic optical reconstruction microscopy (STORM)
Super-resolution imaging, 117
Surface-enhanced Raman spectroscopy (SERS), 165–166, 612

T

Tagged image file format (TIFF), 323, 331
"Telan" lens, 4, 5*f*, 6
TERS. *See* Tip-enhanced Raman spectroscopy (TERS)
Three-CCD color camera, 172, 172*f*
Time-correlated single photon counting (TCSPC), 467–468, 467*f*, 472
Time-lapse imaging, 112–114, 113*f*
Tip-enhanced Raman spectroscopy (TERS)
  AFM system construction (*see* Atomic force microscopy (AFM))
  alignment, 618–620
  discrete nanoscale metalized scanning probe, 612–613, 613*f*
  evaluating sequencing resolution
    AFM micrograph, 624, 625*f*
    homopolymers, 625*f*
    spectrum 2, 624–627, 626*f*
    Watson/Crick pairs, 624, 625*f*
  Raman effect, 612
  Raman photons, 612
  sample preparation, 621–623, 622*f*, 623*f*
  SERS, 612
  silver tip production, 617–618
  STM, 613
  tip preparation, 617–618
TIRF microscopy, 134
Total internal reflection fluorescence (TIRF), 578
Total noise (*N*), 256–257
Total variation (TV) denoising method, 475–477, 476*f*
Transillumination optics
  band-pass filter, 192
  focus control, 193
  ground-glass diffuser, 192
  heat-reflecting filter, 192
  Köhler illumination, 192
  quartz-halogen lamp, 191
  thermal isolation, 192
  transshutter, 192
  vibration isolation, 182*f*, 193
Trinocular tubes, 59
Tube lens, 43–67, 56
Two-slit interference. *See* Young's experiment

V

Video CCD cameras, 228–229, 234
Video codecs
  asymmetric codecs, 332
  key frames, 332
  legacy codecs, 332
  spatial compression, 331–332
  suitability determination, 332–335, 334*f*
  symmetric codecs, 332
  temporal compression, 331–332

W

Wide-field fluorescence microscope, 531, 533, 534–535
Wide-field illumination
  diaphragms, 135, 136*f*
  filter sets
    absorption and emission spectra, 137
    dichromatic mirror, 136–137
    emission filter, 136–137
    excitation filter, 136–137
    selection automation, 137–138
    transmission spectra, 137
  light source, 134–135
Wide-field microscopes (WFMs), 409

Y

Yellow fluorescent protein (YFP), 109, 115
Young's experiment
  double-slit interference pattern, 15–17, 17*f*
  Huygens' construct, 15–17, 16*f*
  phase shift source, 15–17, 16*f*
  time-averaged intensity, 18
  time-dependent wave, 17

Volumes in Series

Founding Series Editor
DAVID M. PRESCOTT

Volume 1 (1964)
Methods in Cell Physiology
Edited by David M. Prescott

Volume 2 (1966)
Methods in Cell Physiology
Edited by David M. Prescott

Volume 3 (1968)
Methods in Cell Physiology
Edited by David M. Prescott

Volume 4 (1970)
Methods in Cell Physiology
Edited by David M. Prescott

Volume 5 (1972)
Methods in Cell Physiology
Edited by David M. Prescott

Volume 6 (1973)
Methods in Cell Physiology
Edited by David M. Prescott

Volume 7 (1973)
Methods in Cell Biology
Edited by David M. Prescott

Volume 8 (1974)
Methods in Cell Biology
Edited by David M. Prescott

Volume 9 (1975)
Methods in Cell Biology
Edited by David M. Prescott

Volume 10 (1975)
Methods in Cell Biology
Edited by David M. Prescott

Volume 11 (1975)
Yeast Cells
Edited by David M. Prescott

Volume 12 (1975)
Yeast Cells
Edited by David M. Prescott

Volume 13 (1976)
Methods in Cell Biology
Edited by David M. Prescott

Volume 14 (1976)
Methods in Cell Biology
Edited by David M. Prescott

Volume 15 (1977)
Methods in Cell Biology
Edited by David M. Prescott

Volume 16 (1977)
Chromatin and Chromosomal Protein Research I
Edited by Gary Stein, Janet Stein, and Lewis J. Kleinsmith

Volume 17 (1978)
Chromatin and Chromosomal Protein Research II
Edited by Gary Stein, Janet Stein, and Lewis J. Kleinsmith

Volume 18 (1978)
Chromatin and Chromosomal Protein Research III
Edited by Gary Stein, Janet Stein, and Lewis J. Kleinsmith

Volume 19 (1978)
Chromatin and Chromosomal Protein Research IV
Edited by Gary Stein, Janet Stein, and Lewis J. Kleinsmith

Volume 20 (1978)
Methods in Cell Biology
Edited by David M. Prescott

Advisory Board Chairman
KEITH R. PORTER

Volume 21A (1980)
Normal Human Tissue and Cell Culture, Part A: Respiratory, Cardiovascular, and Integumentary Systems
Edited by Curtis C. Harris, Benjamin F. Trump, and Gary D. Stoner

Volume 21B (1980)
Normal Human Tissue and Cell Culture, Part B: Endocrine, Urogenital, and Gastrointestinal Systems
Edited by Curtis C. Harris, Benjamin F. Trump, and Gray D. Stoner

Volume 22 (1981)
Three-Dimensional Ultrastructure in Biology
Edited by James N. Turner

Volume 23 (1981)
Basic Mechanisms of Cellular Secretion
Edited by Arthur R. Hand and Constance Oliver

Volume 24 (1982)
The Cytoskeleton, Part A: Cytoskeletal Proteins, Isolation and Characterization
Edited by Leslie Wilson

Volume 25 (1982)
The Cytoskeleton, Part B: Biological Systems and *In Vitro* Models
Edited by Leslie Wilson

Volume 26 (1982)
Prenatal Diagnosis: Cell Biological Approaches
Edited by Samuel A. Latt and Gretchen J. Darlington

Series Editor
LESLIE WILSON

Volume 27 (1986)
Echinoderm Gametes and Embryos
Edited by Thomas E. Schroeder

Volume 28 (1987)
***Dictyostelium discoideum:* Molecular Approaches to Cell Biology**
Edited by James A. Spudich

Volume 29 (1989)
Fluorescence Microscopy of Living Cells in Culture, Part A: Fluorescent Analogs, Labeling Cells, and Basic Microscopy
Edited by Yu-Li Wang and D. Lansing Taylor

Volume 30 (1989)
Fluorescence Microscopy of Living Cells in Culture, Part B: Quantitative Fluorescence Microscopy—Imaging and Spectroscopy
Edited by D. Lansing Taylor and Yu-Li Wang

Volume 31 (1989)
Vesicular Transport, Part A
Edited by Alan M. Tartakoff

Volume 32 (1989)
Vesicular Transport, Part B
Edited by Alan M. Tartakoff

Volume 33 (1990)
Flow Cytometry
Edited by Zbigniew Darzynkiewicz and Harry A. Crissman

Volume 34 (1991)
Vectorial Transport of Proteins into and across Membranes
Edited by Alan M. Tartakoff

Selected from Volumes 31, 32, and 34 (1991)
Laboratory Methods for Vesicular and Vectorial Transport
Edited by Alan M. Tartakoff

Volume 35 (1991)
Functional Organization of the Nucleus: A Laboratory Guide
Edited by Barbara A. Hamkalo and Sarah C. R. Elgin

Volume 36 (1991)
***Xenopus laevis:* Practical Uses in Cell and Molecular Biology**
Edited by Brian K. Kay and H. Benjamin Peng

Series Editors
LESLIE WILSON AND PAUL MATSUDAIRA

Volume 37 (1993)
Antibodies in Cell Biology
Edited by David J. Asai

Volume 38 (1993)
Cell Biological Applications of Confocal Microscopy
Edited by Brian Matsumoto

Volume 39 (1993)
Motility Assays for Motor Proteins
Edited by Jonathan M. Scholey

Volume 40 (1994)
A Practical Guide to the Study of Calcium in Living Cells
Edited by Richard Nuccitelli

Volume 41 (1994)
Flow Cytometry, Second Edition, Part A
Edited by Zbigniew Darzynkiewicz, J. Paul Robinson, and Harry A. Crissman

Volume 42 (1994)
Flow Cytometry, Second Edition, Part B
Edited by Zbigniew Darzynkiewicz, J. Paul Robinson, and Harry A. Crissman

Volume 43 (1994)
Protein Expression in Animal Cells
Edited by Michael G. Roth

Volume 44 (1994)
***Drosophila melanogaster:* Practical Uses in Cell and Molecular Biology**
Edited by Lawrence S. B. Goldstein and Eric A. Fyrberg

Volume 45 (1994)
Microbes as Tools for Cell Biology
Edited by David G. Russell

Volume 46 (1995)
Cell Death
Edited by Lawrence M. Schwartz and Barbara A. Osborne

Volume 47 (1995)
Cilia and Flagella
Edited by William Dentler and George Witman

Volume 48 (1995)
***Caenorhabditis elegans:* Modern Biological Analysis of an Organism**
Edited by Henry F. Epstein and Diane C. Shakes

Volume 49 (1995)
Methods in Plant Cell Biology, Part A
Edited by David W. Galbraith, Hans J. Bohnert, and Don P. Bourque

Volume 50 (1995)
Methods in Plant Cell Biology, Part B
Edited by David W. Galbraith, Don P. Bourque, and Hans J. Bohnert

Volume 51 (1996)
Methods in Avian Embryology
Edited by Marianne Bronner-Fraser

Volume 52 (1997)
Methods in Muscle Biology
Edited by Charles P. Emerson, Jr. and H. Lee Sweeney

Volume 53 (1997)
Nuclear Structure and Function
Edited by Miguel Berrios

Volume 54 (1997)
Cumulative Index

Volume 55 (1997)
Laser Tweezers in Cell Biology
Edited by Michael P. Sheetz

Volume 56 (1998)
Video Microscopy
Edited by Greenfield Sluder and David E. Wolf

Volume 57 (1998)
Animal Cell Culture Methods
Edited by Jennie P. Mather and David Barnes

Volume 58 (1998)
Green Fluorescent Protein
Edited by Kevin F. Sullivan and Steve A. Kay

Volume 59 (1998)
The Zebrafish: Biology
Edited by H. William Detrich III, Monte Westerfield, and Leonard I. Zon

Volume 60 (1998)
The Zebrafish: Genetics and Genomics
Edited by H. William Detrich III, Monte Westerfield, and Leonard I. Zon

Volume 61 (1998)
Mitosis and Meiosis
Edited by Conly L. Rieder

Volume 62 (1999)
Tetrahymena thermophila
Edited by David J. Asai and James D. Forney

Volume 63 (2000)
Cytometry, Third Edition, Part A
Edited by Zbigniew Darzynkiewicz, J. Paul Robinson, and Harry Crissman

Volume 64 (2000)
Cytometry, Third Edition, Part B
Edited by Zbigniew Darzynkiewicz, J. Paul Robinson, and Harry Crissman

Volume 65 (2001)
Mitochondria
Edited by Liza A. Pon and Eric A. Schon

Volume 66 (2001)
Apoptosis
Edited by Lawrence M. Schwartz and Jonathan D. Ashwell

Volume 67 (2001)
Centrosomes and Spindle Pole Bodies
Edited by Robert E. Palazzo and Trisha N. Davis

Volume 68 (2002)
Atomic Force Microscopy in Cell Biology
Edited by Bhanu P. Jena and J. K. Heinrich Hörber

Volume 69 (2002)
Methods in Cell–Matrix Adhesion
Edited by Josephine C. Adams

Volume 70 (2002)
Cell Biological Applications of Confocal Microscopy
Edited by Brian Matsumoto

Volume 71 (2003)
Neurons: Methods and Applications for Cell Biologist
Edited by Peter J. Hollenbeck and James R. Bamburg

Volume 72 (2003)
Digital Microscopy: A Second Edition of Video Microscopy
Edited by Greenfield Sluder and David E. Wolf

Volume 73 (2003)
Cumulative Index

Volume 74 (2004)
Development of Sea Urchins, Ascidians, and Other Invertebrate Deuterostomes: Experimental Approaches
Edited by Charles A. Ettensohn, Gary M. Wessel, and Gregory A. Wray

Volume 75 (2004)
Cytometry, 4th Edition: New Developments
Edited by Zbigniew Darzynkiewicz, Mario Roederer, and Hans Tanke

Volume 76 (2004)
The Zebrafish: Cellular and Developmental Biology
Edited by H. William Detrich, III, Monte Westerfield, and Leonard I. Zon

Volume 77 (2004)
The Zebrafish: Genetics, Genomics, and Informatics
Edited by William H. Detrich, III, Monte Westerfield, and Leonard I. Zon

Volume 78 (2004)
Intermediate Filament Cytoskeleton
Edited by M. Bishr Omary and Pierre A. Coulombe

Volume 79 (2007)
Cellular Electron Microscopy
Edited by J. Richard McIntosh

Volume 80 (2007)
Mitochondria, 2nd Edition
Edited by Liza A. Pon and Eric A. Schon

Volume 81 (2007)
Digital Microscopy, 3rd Edition
Edited by Greenfield Sluder and David E. Wolf

Volume 82 (2007)
Laser Manipulation of Cells and Tissues
Edited by Michael W. Berns and Karl Otto Greulich

Volume 83 (2007)
Cell Mechanics
Edited by Yu-Li Wang and Dennis E. Discher

Volume 84 (2007)
Biophysical Tools for Biologists, Volume One: *In Vitro* Techniques
Edited by John J. Correia and H. William Detrich, III

Volume 85 (2008)
Fluorescent Proteins
Edited by Kevin F. Sullivan

Volume 86 (2008)
Stem Cell Culture
Edited by Dr. Jennie P. Mather

Volume 87 (2008)
Avian Embryology, 2nd Edition
Edited by Dr. Marianne Bronner-Fraser

Volume 88 (2008)
Introduction to Electron Microscopy for Biologists
Edited by Prof. Terence D. Allen

Volume 89 (2008)
Biophysical Tools for Biologists, Volume Two: *In Vivo* Techniques
Edited by Dr. John J. Correia and Dr. H. William Detrich, III

Volume 90 (2008)
Methods in Nano Cell Biology
Edited by Bhanu P. Jena

Volume 91 (2009)
Cilia: Structure and Motility
Edited by Stephen M. King and Gregory J. Pazour

Volume 92 (2009)
Cilia: Motors and Regulation
Edited by Stephen M. King and Gregory J. Pazour

Volume 93 (2009)
Cilia: Model Organisms and Intraflagellar Transport
Edited by Stephen M. King and Gregory J. Pazour

Volume 94 (2009)
Primary Cilia
Edited by Roger D. Sloboda

Volume 95 (2010)
Microtubules, in vitro
Edited by Leslie Wilson and John J. Correia

Volume 96 (2010)
Electron Microscopy of Model Systems
Edited by Thomas Müeller-Reichert

Volume 97 (2010)
Microtubules: In Vivo
Edited by Lynne Cassimeris and Phong Tran

Volume 98 (2010)
Nuclear Mechanics & Genome Regulation
Edited by G.V. Shivashankar

Volume 99 (2010)
Calcium in Living Cells
Edited by Michael Whitaker

Volume 100 (2010)
The Zebrafish: Cellular and Developmental Biology, Part A
Edited by: H. William Detrich III, Monte Westerfield and Leonard I. Zon

Volume 101 (2011)
The Zebrafish: Cellular and Developmental Biology, Part B
Edited by: H. William Detrich III, Monte Westerfield and Leonard I. Zon

Volume 102 (2011)
Recent Advances in Cytometry, Part A: Instrumentation, Methods
Edited by Zbigniew Darzynkiewicz, Elena Holden, Alberto Orfao, William Telford and Donald Wlodkowic

Volume 103 (2011)
Recent Advances in Cytometry, Part B: Advances in Applications
Edited by Zbigniew Darzynkiewicz, Elena Holden, Alberto Orfao, Alberto Orfao and Donald Wlodkowic

Volume 104 (2011)
The Zebrafish: Genetics, Genomics and Informatics 3rd Edition
Edited by H. William Detrich III, Monte Westerfield, and Leonard I. Zon

Volume 105 (2011)
The Zebrafish: Disease Models and Chemical Screens 3rd Edition
Edited by H. William Detrich III, Monte Westerfield, and Leonard I. Zon

Volume 106 (2011)
Caenorhabditis elegans: Molecular Genetics and Development 2nd Edition
Edited by Joel H. Rothman and Andrew Singson

Volume 107 (2011)
Caenorhabditis elegans: Cell Biology and Physiology
2nd Edition
Edited by Joel H. Rothman and Andrew Singson

Volume 108 (2012)
Lipids
Edited by Gilbert Di Paolo and Markus R Wenk

Volume 109 (2012)
Tetrahymena thermophila
Edited by Kathleen Collins

Volume 110 (2012)
Methods in Cell Biology
Edited by Anand R. Asthagiri and Adam P. Arkin

Volume 111 (2012)
Methods in Cell Biology
Edited by Thomas Müler Reichart and Paul Verkade

Volume 112 (2012)
Laboratory Methods in Cell Biology
Edited by P. Michael Conn

Volume 113 (2013)
Laboratory Methods in Cell Biology
Edited by P. Michael Conn